nanomaterials

Special Issue Reprint

Nanotechnologies and Nanomaterials

Selected Papers from CCMR

Volume II

Edited by
Jihoon Lee and Ming-Yu Li

mdpi.com/journal/nanomaterials

MDPI

Nanotechnologies and Nanomaterials: Selected Papers from CCMR—Volume II

Nanotechnologies and Nanomaterials: Selected Papers from CCMR—Volume II

Editors

Jihoon Lee
Ming-Yu Li

MDPI

Basel • Beijing • Wuhan • Barcelona • Belgrade • Novi Sad • Cluj • Manchester

Editors
Jihoon Lee
Department of Electronic
Engineering, College of
Electronics and Information,
Kwangwoon University
Seoul
Korea

Ming-Yu Li
School of Science, Wuhan
University of Technology
Wuhan
China

Editorial Office
MDPI
St. Alban-Anlage 66
4052 Basel, Switzerland

This is a reprint of articles from the Special Issue published online in the open access journal *Nanomaterials* (ISSN 2079-4991) (available at: https://www.mdpi.com/journal/nanomaterials/special_issues/nano_CCMR_Series).

For citation purposes, cite each article independently as indicated on the article page online and as indicated below:

Lastname, A.A.; Lastname, B.B. Article Title. *Journal Name* **Year**, *Volume Number*, Page Range.

Volume II
ISBN 978-3-7258-0881-6 (Hbk)
ISBN 978-3-7258-0882-3 (PDF)
doi.org/10.3390/books978-3-7258-0882-3

Volume I-II
ISBN 978-3-7258-0807-6 (Hbk)
ISBN 978-3-7258-0808-3 (PDF)

Contents

About the Editors

Jihoon Lee

Jihoon Lee received his Ph.D. degree in Microelectronics and Photonics from the University of Arkansas, Fayetteville, AR, USA, in 2008, and a Management of Business Administration degree from Sam M. Walton College of Business, University of Arkansas, Fayetteville, AR, USA, in 2006. In 2009, he joined the faculty of Kwangwoon University, Seoul, South Korea, where he is currently a professor in the Department of Electronics Engineering, College of Electronics and Information. His current research interests include the fabrication and characterization of various hybrid metals and semiconductors, quantum- and nanostructures, and their applications in biosensors, detectors, and energy.

Ming-Yu Li

Ming-Yu Li is a faculty member at Wuhan University of Technology (WUT). He received his Ph.D. in Electronic Engineering from Kwangwoon University, South Korea, in 2016. He served as a postdoctoral fellow for 3 years at Huazhong University of Science and Technology (HUST). His research interests focus on nanomaterial synthesis, nanostructure fabrication and characterization, functional materials, and optoelectronic devices. He has published more than 92 research papers in international journals and has authorized more than 16 patents.

nanomaterials

Article

Fabrication and Photocatalytic Properties of Zinc Tin Oxide Nanowires Decorated with Silver Nanoparticles

Jia-Chi Su [1], Tsung-Lin Hsieh [1], Shu-Meng Yang [1], Shao-Chun Chao [1] and Kuo-Chang Lu [1,2,*]

[1] Department of Materials Science and Engineering, National Cheng Kung University, Tainan 701, Taiwan; n56081412@ncku.edu.tw (J.-C.S.); n56091255@gs.ncku.edu.tw (T.-L.H.); n56074287@gs.ncku.edu.tw (S.-M.Y.); n56104375@gs.ncku.edu.tw (S.-C.C.)
[2] Core Facility Center, National Cheng Kung University, Tainan 701, Taiwan
* Correspondence: gkclu@mail.ncku.edu.tw; Tel.: +886-6-275-7575 (ext. 62920)

Abstract: With the continuous advancement of high-tech industries, how to properly handle pollutants has become urgent. Photocatalysis is a solution that may effectively degrade pollutants into harmless molecules. In this study, we synthesized single crystalline Zn_2SnO_4 (ZTO) nanowires through chemical vapor deposition and selective etching. The chemical bath redox method was used to modify the ZTO nanowires with Ag nanoparticles to explore the photocatalytic properties of the nanoheterostructures. The combination of the materials here is rare. Optical measurements by photoluminescence (PL) and UV–Vis show that the PL spectrum of ZTO nanowires was mainly in the visible light region and attributed to oxygen vacancies. The luminescence intensity of the nanowires was significantly reduced after modification, demonstrating that the heterojunction could effectively reduce the electron-hole pair recombination. The reduction increased with the increase in Ag decoration. The conversion from the UV–Vis absorption spectrum to the Tauc Plot shows that the band gap of the nanowire was 4.05 eV. With 10 ppm methylene blue (MB) as the degradation solution, ZTO nanowires exhibit excellent photodegradation efficiency. Reusability and stability in photodegradation of the nanowires were demonstrated. Photocatalytic efficiency increases with the number of Ag nanoparticles. The main reaction mechanism was confirmed by photocatalytic inhibitors. This study enriches our understanding of ZTO-based nanostructures and facilitates their applications in water splitting, sewage treatment and air purification.

Keywords: zinc tin oxide; nanowires; chemical vapor deposition; surface modification; photocatalysis; reactive radical species

Citation: Su, J.-C.; Hsieh, T.-L.; Yang, S.-M.; Chao, S.-C.; Lu, K.-C. Fabrication and Photocatalytic Properties of Zinc Tin Oxide Nanowires Decorated with Silver Nanoparticles. *Nanomaterials* **2022**, *12*, 1201. https://doi.org/10.3390/nano12071201

Academic Editors: Jihoon Lee and Ming-Yu Li

Received: 2 March 2022
Accepted: 31 March 2022
Published: 3 April 2022

1. Introduction

Previous studies indicate that industrial dyes and textile dyes are the largest organic pollutants, causing increasing environmental pollution [1,2]. About 10–20% of the world's dye production is lost during the dying process and discharged into textile wastewater. Due to water pollution, advanced oxidation processes (AOPs) have been rapidly developed as an innovative water treatment technology [3,4]. The principle of AOPs is to generate highly reactive transition substances based on the catalytic properties of materials, such as H_2O_2, $\cdot OH^-$ and $\cdot O_2{}^-$ for organic compounds which are difficult to decompose. Semiconductors are often used as catalysts in AOPs, such as TiO_2, ZnO and Fe_2O_3, which have been demonstrated to degrade organic compounds effectively, finally mineralizing them into harmless carbon dioxide and water [5].

Zinc tin oxide, also known as ZTO, is a non-toxic ternary oxide semiconductor (A_2BO_4, inverse spinel structure) with high conductivity, low visible light adsorption, high electron mobility and excellent thermal stability. Ternary metals have higher chemical stability as compared to binary metal oxides. ZTO nanostructures have been fabricated for various important applications, including optical sensors [6,7], gas sensors [8,9], dye-sensitized solar cells [10,11] and photocatalysts [12–14]. In the past few years, different techniques have been applied in synthesizing one-dimensional ZTO nanostructures, including the hydrothermal method [15,16], CVD [7,17] and the template method [18], among which CVD is the best choice since it is more economical and environmentally friendly [19,20].

In terms of photocatalytic applications, surface modification of precious metals is frequently used to increase photocatalytic efficiency, such as Ag [21–23], Pd [24] and Pt [25], which can form Schottky contact through the junction between the metal and semiconductor and lower the recombination efficiency of electron-hole pairs to enhance photocatalytic properties.

In this work, we studied ZTO NWs and Ag-ZTO NWs as efficient photocatalysts in water treatment for environmental pollution. We synthesized ZTO NWs by the chemical vapor deposition (CVD) method via the vapor–liquid–solid (VLS) route and modified the nanowires using the chemical bath redox method. The 1 at% Ag-ZTO NWs and 3 at% Ag-ZTO NWs were fabricated with different amounts of $AgNO_3$. All three kinds of nanowires were characterized by SEM, TEM, XRD, EDS, XPS and PL to identify their structures and phases.

2. Materials and Methods

2.1. Synthesis of ZTO and Ag-ZTO Nanowires

ZTO NWs were synthesized with a three-zone tube furnace via catalyst-assisted chemical vapor deposition (CVD) through a vapor–liquid–solid (VLS) growth mechanism. The mixture of zinc oxide powder (0.12 g) (Alfa Aesar, Ward Hill, MA, USA purity 99.9%) and active charcoal (0.12 g) (Sigma-Aldrich, St. Louis, MO, USA) was loaded into an alumina boat and placed in the second heating zone. Tin oxide powder (0.03 g) (Alfa Aesar, Ward Hill, MA, USA purity 99.9%) and active charcoal (0.03 g) were mixed with the same ratio and placed in the third heating zone. A 10 nm-thick Au layer on the silicon substrate was deposited by the E-beam evaporation system. Nanowire growth was based on the vapor−liquid−solid (VLS) mechanism with Au as catalyst. The alumina boat of sonically cleaned Si (100) substrates with a 10 nm thin Au layer was placed downstream outside the third heating zone. The temperatures of the second and third heating zones were raised to 955 and 905 °C for 1.5 h, respectively. Argon gas was introduced with the flow rate of 100 sccm. After the reaction, the furnace was cooled down to room temperature naturally. The single phase ZTO NW substrate was immersed in 12 mM sodium borohydride ($NaBH_4$) (98+%, Acros Organics, Morris Plains, NJ, USA) solution, which was then titrated with silver nitrate solution (0.01 and 0.03 g) of deionized water (pH = 7, ionic strength = 0.001 M) and $AgNO_3$ to form Ag-ZTO NWs as shown in Figure S1.

2.2. Electrical Measurements

To fabricate the nanodevice for single nanowire electrical resistivity measurements, ZTO NWs and Ag-ZTO NW substrates were immersed into deionized water (pH = 7, I = 0.001 M) and sonicated to separate the nanowires from the substrate. The solution with nanowires was dripped on an as-prepared Si/SiO_2 substrate with four independent Ag electrodes with 400 nm-thick platinum to which the nanowire was connected by a focus ion beam (FIB, FEI Nova-200 NanoLab Compatible, Hillsboro, OR, USA). The electrical m easurements of a single nanowire here were based on the method previously reported by Gu et al. [26], which can eliminate the voltage drop and contact resistance during measurement to obtain more accurate results. The schematic illustration and setup of the electrical measurements are shown in Figure S5.

2.3. Photodegradation

The photodegradation performance of ZTO and Ag-ZTO NWs was evaluated with 10 ppm methylene blue (0.5 g/100 mL) (Sigma-Aldrich, St. Louis, MO, USA) in deionized water (pH = 7, I = 0.001 M) as shown in the experimental setup of Figure 5g. The sample was placed at the bottom of a beaker perpendicular to the simulated solar light lamp. We stirred 5 mL MB in the beaker using a magnetic stirrer in the darkroom for 30 min to reach an adsorption–desorption balance for UV–Vis absorption measurement as the MB initial concentration C_0. During the illumination of the Xe lamp (105 W/m^2, Oriel® LCS-100™ Small Area Sol1A), we took 0.5 mL MB per 30 min for the UV–Vis absorption measurement as C_t. The photodegradation efficiency was then calculated according to Equation (1) [27]:

$$\text{Degradation}(\%) = \left(1 - \frac{C_t}{C_0}\right) \cdot 100\% \tag{1}$$

2.4. Radical Trapping Experiment

To understand the major reactive species in the MB photodegradation experiment, radical scavengers were added to inhibit different radical work during the photodegradation process. In this study, 1 mM ethylenediaminetetraacetic acid (EDTA) was used to inhibit h+, 1 mM tert-butanol (TBA) was used to inhibit $\cdot OH$ and 1 mM 1,4-benzoquinone (BQ) was used to inhibit $\cdot O_2{}^-$. Other procedures were the same as the photodegradation experiment. Lower photodegradation efficiency after adding a specific scavenger corresponds to higher importance of the reactive species.

2.5. Characterization

Morphologies and structures of ZTO and Ag-ZTO NWs were characterized by field-emission scanning electron microscopy (FESEM, Hitachi SU8000, Tokyo, Japan), X-ray diffractometry (XRD, Bruker D8 Discover with GADDS, Fitchburg, WI, USA), transmission electron microscopy (TEM, JEOL-2100F, CS STEM, Tokyo, Japan), Energy-dispersive X-ray spectroscopy (EDS) and X-ray photoelectron spectroscopy (XPS, PHI 5000 VersaProbe, ULVAC-PHI, Kanagawa, Japan). Photoluminescence (PL, HORIBA LabRAM HR, Longjumeau, France) and UV–Vis spectrophotometry (PerkinElmer LAMBDA 950, Waltham, MA, USA) were utilized for optical and photocatalysis properties.

3. Results and Discussion

3.1. Morphology and Structure Analysis of ZTO NWs and Ag-ZTO NWs

3.1.1. SEM and XRD Analysis

It has been difficult to fabricate pure ternary nanowires with a furnace; for example, synthesis of Zn_2SnO_4 (ZTO) nanowires frequently comes with simultaneous synthesis of ZnO and SnO_2 [28]. Therefore, ZnO/ZTO NWs were chosen for synthesis, and we used 12.5 mM aqueous hydrochloric acid (HCl) to remove the ZnO phase. Figure S2a,b show the SEM images of before and after the selective etching process; Figure S1c shows the XRD pattern after the selective etching process, indicating that we successfully obtained single phase ZTO NWs. Figure 1a,b show the high-density ZTO NWs had a length of over 10 μm and diameter of about 40–80 nm. Figure 1c is the SEM image after modification of Ag nanoparticles. Figure 1d shows the XRD patterns for ZTO NWs, 1 at% Ag-ZTO NWs and 3 at% Ag-ZTO NWs; the peaks located at 17.7° (111), 29.2° (220) and 34.4° (311) correspond to ZTO (JCPDS no.74-2184), while the peaks at 38.3° (111) and 44.5° (200) correspond to Au (JCPDS no.99-0056) because of the VLS growing mechanism. Since the diffraction peaks of Ag (JCPDS no. 87-0719) and Au are almost the same, the diffraction peaks of Au appear wider after modification of Ag.

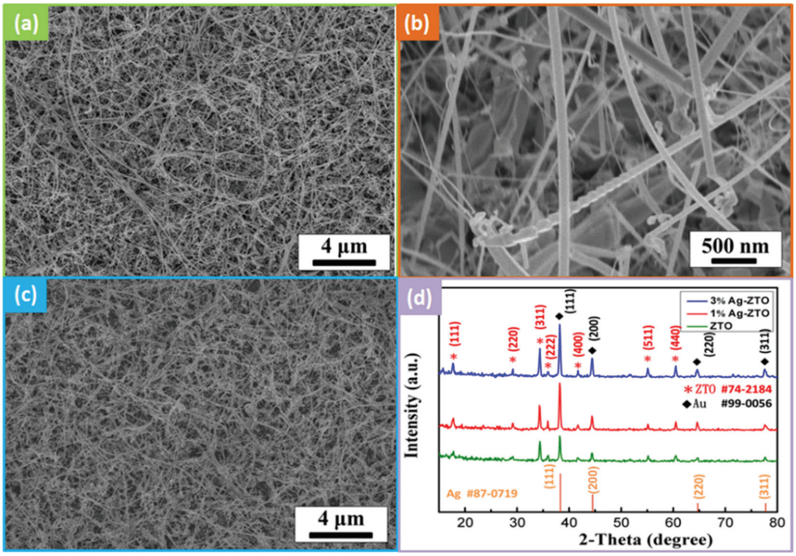

Figure 1. Morphologies of ZTO NWs and Ag-ZTO NWs. (**a**) Low magnification SEM image of ZTO NWs. (**b**) High magnification SEM image of ZTO NWs. (**c**) Low magnification SEM image of Ag-ZTO NWs. (**d**) XRD pattern of ZTO NWs and Ag-ZTO NWs.

3.1.2. HRTEM and EDS Analysis

Figure 2a is a HRTEM image of the ZTO nanowire, where the interplanar spacings, 0.5 and 0.31 nm, correspond to (111) and (220) planes of Zn_2SnO_4, and the inset is the selected area electron diffraction (SAED) pattern corresponding to the diffraction peaks in the XRD analysis. Figure 2b,c are SEM images of 1 at% Ag-ZTO NWs and 3 at% Ag-ZTO NWs, respectively; more Ag nanoparticles with a diameter of 5–20 nm were on the surface of the latter. Figure 2d is a HRTEM image of Ag-ZTO NW, where the interplanar spacings of the nanowire are the same as those of the ZTO NW in Figure 2a; additionally, attached on the surface is a particle with an interplanar spacing of 0.24 nm, corresponding to the (111) plane of Ag. Based on the XRD and TEM analysis, the nanoparticles were confirmed to be Ag. Figure S4a,b show the EDS studies of 1 at% Ag-ZTO and 3 at% Ag-ZTO NW; Figure S4c,d show the mapping of 1 at% Ag-ZTO and the 3 at% Ag-ZTO NW. EDS analysis indicates that ZTO NWs are nonstoichiometric compounds, but XRD and XPS studies confirm that the structure and valence of elements are correct.

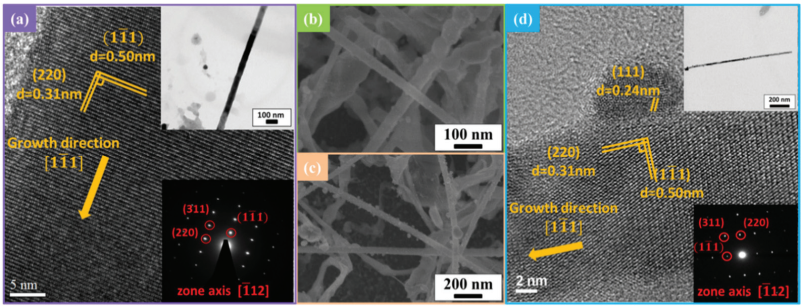

Figure 2. Morphology and structure analysis of ZTO NWs and Ag-ZTO NWs. (**a**) HRTEM image of ZTO NWs. (**b**) SEM image of 1 at% Ag-ZTO NWs. (**c**) SEM image of 3 at% Ag-ZTO NWs. (**d**) HRTEM image of Ag-ZTO NWs.

3.1.3. XPS Analysis

XPS analysis was conducted to further investigate the composition of Ag-ZTO NWs. The valence states of the elements in the nanowires can be confirmed by XPS curve fitting as shown in Figure 3a–d. Figure 3a shows the $2p_{1/2}$ and $2p_{3/2}$ orbitals of zinc, the binding energies of which were 1021.7 and 1044.7 eV, coherent with the previously reported energy difference of 23 eV [29]; the two characteristic peaks correspond to two valence states, Zn^0 and Zn^{2+}. Figure 3b reveals two characteristic peaks of $3d_{5/2}$ and $3d_{3/2}$ orbitals of tin, which were from Sn^{2+} and Sn^{4+}, the binding energies of which are about 486.7 and 495.1 eV, respectively. The binding energy of the 3d orbitals between Sn^{2+} and Sn^{4+} states is very close. It is known from the previous report [30] that the binding energy for Sn^{4+} is bigger than that for Sn^{2+}, demonstrating that the blue line denotes Sn^{4+}, while the red line denotes Sn^{2+}. Figure 3c indicates that the oxygen binding energy of ZTO NWs mainly resulted from oxygen in the lattice and oxygen vacancies, the binding energies of which were 530.8 and 532 eV, respectively [31]. After surface modification, Figure 3d shows the binding energies of $3d_{5/2}$ and $3d_{3/2}$ orbitals of silver were 367.6 and 373.6 eV, respectively [32].

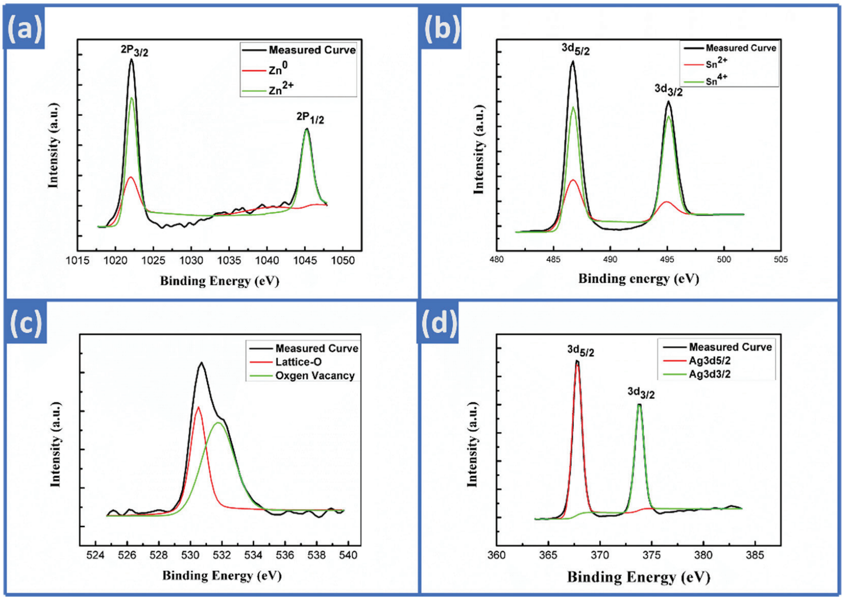

Figure 3. XPS analysis for Ag-ZTO NWs. (**a**) Zn 2p, (**b**) Sn 3d, (**c**) O 1s, (**d**) Ag 3d.

3.1.4. UV–Vis and PL Analysis

To explore the optical properties of ZTO NWs and Ag-ZTO NWs, it is important to determine the band gap. Figure 4a is the room temperature UV–Vis absorption spectra of ZTO NWs and 3 at% Ag-ZTO NWs; both had a significant increase in absorption at a wavelength less than 325 nm. The absorption spectrum feature at 350–450 nm corresponds to impurities or oxygen vacancy levels. The band gap of the nanowires was calculated with Tauc's equation [12]:

$$(\alpha h\nu)^{1/n} = A(h\nu - E_g) \tag{2}$$

where α is the adsorption coefficient of the material, A is a proportionality constant and n is a constant exponentially different based on the types of semiconductors, being 1/2 for direct bandgap semiconductors. The inset of the UV–Vis spectra is the Tauc Plot. According to the tangent of the diagram, the band gaps of ZTO NWs and 3 at% Ag-ZTO NWs were 4.05 and 4.04 eV, which are close to the previously reported value (3.92 eV). The wider band gap for the ZTO NWs may be attributed to their smaller sizes [14]. The similar absorption edges before and after Ag modification indicate that their bandgap energy difference is negligible [22,23].

Figure 4b shows the PL spectra for a 325 nm laser for ZTO NWs and Ag-ZTO NWs at room temperature, exhibiting a wide emission band from 425 to 750 nm with a central wavelength of 580 nm. Various emission peaks might contribute to the wide PL spectrum. The green fluorescent signal around the 560 nm peak was emitted from the conduction band (CB) to oxygen vacancies ($V^{+}{}_{0}$) [33]. The orange fluorescent signal around the 590 nm peak was attributed to oxygen vacancies and interstitial tin vacancies. The red fluorescent signal around the 650 nm peak resulted from interstitial zinc and tin vacancies [34]. In the PL analysis, oxygen vacancies mostly resulted from the large surface area of nanowire and lack of oxygen due to nanowire growth by three zone furnaces; thus, many oxygen vacancies existed in the nanowires. During nanowire growth, oxygen vacancies tended to diffuse from the interior to the surface; thus, the oxygen vacancy concentration on the surface was greater than that in the interior of the nanowires [35]. The excited electrons were captured by the metastable energy band caused by the oxygen vacancies and then released to recombine with holes [29]. Therefore, oxygen vacancies improved photocatalytic performance by reducing the recombination rate of electron-hole pairs. After Ag modification, the photoluminescence intensity decreased dramatically, the reason behind which is discussed in the photodegradation section.

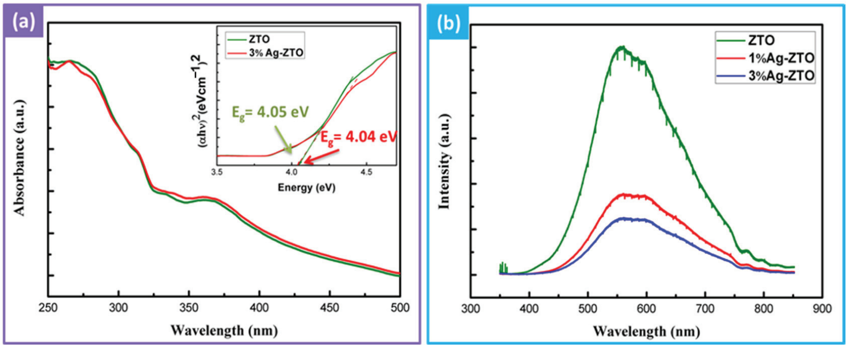

Figure 4. Optical properties of ZTO NWs and Ag-ZTO NWs. (**a**) UV–Vis spectra (**b**) PL spectra.

3.2. Growth Mechanism

Figure S3 is the schematic illustration of the ZTO NW growth mechanism. Zinc oxide powder and tin oxide powder were reduced to $Zn_{(v)}$ and $Sn_{(v)}$ through the carbothermic reduction method based on Equations (3) and (4). At 900 °C, the Au catalyst on the surface of the silicon substrate was transformed to liquid and reacted with $Zn_{(v)}$ and $Sn_{(v)}$ to form an Au–Zn–Sn liquid alloy. As the carrier gas delivered more precursors to the substrate, the Au–Zn–Sn liquid alloy was supersaturated, precipitated and oxidized into ZTO NWs. The ZTO nanowires grew longer with the continuous precipitation of the droplets according to Equation (5):

$$\mathrm{ZnO}_{(s)} + \mathrm{C}_{(s)} \overset{\Delta}{\rightarrow} \mathrm{Zn}_{(v)} + \mathrm{CO}_{(v)} \tag{3}$$

$$\mathrm{SnO}_{2(s)} + \mathrm{C}_{(s)} \overset{\Delta}{\rightarrow} \mathrm{Sn}_{(v)} + \mathrm{CO}_{2(v)} \tag{4}$$

$$\mathrm{Au}_{(l)} + 2\mathrm{Zn}_{(v)} + \mathrm{Sn}_{(v)} + 2\mathrm{O}_{2(v)} \overset{\Delta}{\rightarrow} \mathrm{Zn}_2\mathrm{SnO}_{4(s)} + \mathrm{Au}_{(s)} \tag{5}$$

3.3. Electrical Measurements of Single ZTO NW and Ag-ZTO NW

Figure S5a shows the schematic illustration of the electrical measurements and Figure S5b–d are SEM images of ZTO NW, 1 at% Ag-ZTO NW and 3 at% Ag-ZTO NW connected to Ag electrodes, respectively. Each single nanowire was measured 8 times, including

R13, R14, R23 and R24, by applying positive and negative voltages. The I-V measurements for ZTO NW, 1 at% Ag-ZTO NW and 3 at% Ag-ZTO NW are shown in Figures S6–S8, respectively. Based on Table 1, the resistivity of ZTO NW here was 6.01×10^{-5} Ω·m, which is better than previous studies [36]; the resistivity of 1 at% Ag-ZTO NW and 3 at% Ag-ZTO NW was 2.1×10^{-4} and 4.3×10^{-4} Ω·m, indicating the resistivity increase after surface modification.

Table 1. Electrical resistivity measurements of ZTO NW, 1 at% Ag-ZTO NW and 3 at% Ag-ZTO NW.

	ZTO NW	**1 at% Ag-ZTO NW**	**3 at% Ag-ZTO NW**
Resistivity	6.01×10^{-5} Ω·m	2.1×10^{-4} Ω·m	4.3×10^{-4} Ω·m

3.4. Photocatalytic Properties of ZTO NWs and Ag-ZTO NWs

3.4.1. Photodegradation Activities

Methylene blue (MB) is a heterocyclic dye with wide industrial applications, being frequently used for coloring paper, as a temporary hair colorant and for dyeing cottons, wools and so on. Additionally, it has been extensively used in human and veterinary medicine for several therapeutic and diagnostic procedures. It cannot be degraded through the conventional water treatment process due to its complex aromatic structures, hydrophilic nature and high stability against light, temperature, water, chemicals, etc.; thus, it may cause substantial environmental pollution. Although MB is not considered to be a very toxic dye, it can result in very harmful effects on living things, such as breathing difficulties, vomiting, diarrhea and nausea. Therefore, many efforts have been made to remove MB from water [37,38], and we chose it to investigate the photodegradation activities of ZTO NWs and Ag-ZTO NWs. MB has a very strong characteristic peak at 663 nm [39]; the efficiency of photodegradation can be calculated based on the change of the absorption peak of MB. Figure 5a shows the UV–Vis absorption spectra of MB degraded by ZTO NWs, while Figure 5b,c show the UV–Vis absorption spectra of MB degraded by 1 at% Ag-ZTO NWs and 3 at% Ag-ZTO NWs. It can be seen that the absorption spectra of 3 at% Ag-ZTO NWs have the most obvious change; therefore, 3 at% Ag-ZTO NWs have the best degradation efficiency. Figure 5d reveals the change of MB concentration versus time. The red line denotes ZTO NWs, which degraded 85% of MB in 120 min; the blue line denotes 1 at% Ag-ZTO NWs, which degraded 94% of MB in 120 min and the green line denotes 3 at% Ag-ZTO NWs, degrading 80% of MB in the first 60 min and degrading 96% in 120 min. To obtain a better understanding of the kinetics of photodegradation, pseudo-first-order equation was used as shown in Equation (6) [40]:

$$\ln\left(\frac{C_0}{C_t}\right) = \kappa t \tag{6}$$

where κ is the rate constant and t means time. Figure 5e shows the comparison of the rate constants for ZTO NWs, 1 at% Ag-ZTO NWs and 3 at% Ag-ZTO NWs, which were 0.0157, 0.023 and 0.025 min^{-1}, respectively. These results demonstrate the enhanced photodegradation performance with the silver modification.

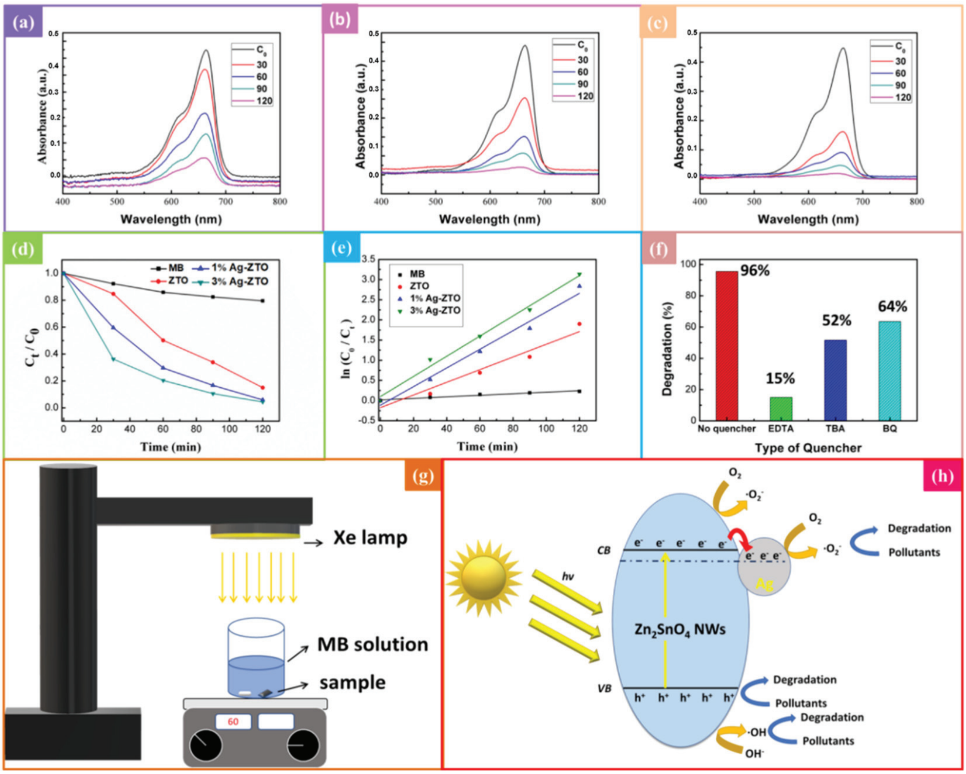

Figure 5. Photocatalytic properties of ZTO NWs and Ag-ZTO NWs were evaluated with 10 ppm methylene blue in deionized water (pH = 7, I = 0.001 M). The UV–Vis absorbance spectra of (**a**) ZTO NWs, (**b**) 1 at% Ag-ZTO NWs, (**c**) 3 at% Ag-ZTO NWs towards MB dye. (**d**,**e**) Comparison of photocatalytic activities between ZTO NWs and Ag-ZTO NWs. (**f**) Comparison of photocatalytic activities among different scavengers for 3 at% Ag-ZTO NWs. (**g**) Schematic illustration of photodegradation experimental setup. (**h**) Schematic illustration for photodegradation mechanism of Ag-ZTO NWs.

3.4.2. Effect of Reactive Free Radicals

To understand the influence of different reactive free radicals in the photodegradation process, the reaction of each free radical was inhibited by adding scavengers [41,42]. The 3 at% Ag-ZTO NWs were added to ethylenediaminetetraacetic acid (EDTA), tert-butanol (TBA) and benzoquinone (1,4-benzoquinone, BQ) as the scavengers of h^+, $\cdot OH$ and $\cdot O_2^-$, respectively. EDTA was used as a scavenger of h^+. The reaction between h^+ and EDTA is as follows: $EDTA + h^+ \rightarrow CO_2 + H_2O$. TBA was used as a scavenger of $\cdot OH$. BQ was used as a scavenger of $\cdot O_2^-$, which can trap superoxide anions via an electron transfer mechanism: $BQ + \cdot O_2^- \rightarrow \cdot BQ^- + O_2$. Figure 5f shows the change in the photodegradation efficiency after adding different scavengers. The original efficiency of 3 at% Ag-ZTO NWs was 96% in 120 min; after adding EDTA, TBA and BQ, the efficiency was reduced to 15%, 52% and 63%, respectively. The results indicate that adding EDTA led to the highest inhibition, followed by TBA and BQ. The degree of effects for reactive species in photodegradation is $h^+ > \cdot OH > \cdot O_2^-$ with the major mechanisms shown in Equations (7)–(9):

$$Zn_2SnO_4 + hv\ (\geq E_g) \rightarrow Zn_2SnO_4\ (h_{cb}{}^+) + Zn_2SnO_4\ (e^-) \tag{7}$$

$$Zn_2SnO_4\ (h_{cb}{}^+) + OH^- \rightarrow \cdot OH \tag{8}$$

$$(h_{cb}{}^+, \cdot OH) + Dye\ (MB) \rightarrow CO_2 + H_2O + \text{degraded products} \tag{9}$$

3.4.3. Reliability and Stability

To study the stability of ZTO NWs and Ag-ZTO NWs, three consecutive cycles of MB degradation were conducted. Figure S9c shows that the photodegradation efficiencies were 96%, 84% and 82%, respectively. The decrease in degradation rate may be attributed to the photo-corrosion of the nanowire surface or the accumulation of contaminants on the nanowire surface; however, the degradation efficiency of the second and third times tends to be stable. As previously reported [12–14], the degradation efficiency of MB decreases by 10–20% before the photocatalyst is reused, while our degradation efficiency dropped about 14% and became stable following the typical curve, indicating that 3 at% Ag-ZTO NWs are expected to be a reusable photocatalyst. Additionally, the XRD pattern in Figure S9d reveals that the ZTO NWs still had great crystallinity after multiple cycles.

3.4.4. Photodegradation Mechanism

Figure 5h is the schematic illustration for the photodegradation mechanism of Ag-ZTO NWs. As the ZTO NWs were illuminated, the electrons in the valence band were excited to the conduction band to form electron-hole pairs at the NW surface. Electrons in the conduction band reacted with oxygen to form superoxide radicals ($\cdot O_2^-$), while the holes in the valence band could react with pollutants and the hydroxide ions (OH^-) to generate hydroxyl radicals ($\cdot OH$), thereby degrading the pollutants. With the ZTO NWs modified with silver, the excited electrons diffused to the silver particles [43], reducing the recombination rate of electron-hole pairs. The PL intensity is proportional to the electron-hole recombination rate; thus, the PL intensity decreased after Ag modification. When the recombination efficiency of electron-hole pairs was reduced, the electrons and holes had more opportunities to react with pollutants, increasing the degradation rate.

4. Conclusions

Single crystalline Zn_2SnO_4 (ZTO) nanowires were successfully synthesized by chemical vapor deposition and selective etching. Silver nanoparticles were modified on the surface of ZTO nanowires using the chemical bath redox method to fabricate 1 at% Ag-ZTO NWs and 3 at% Ag-ZTO NWs. The structures of ZTO NWs and Ag-ZTO NWs were confirmed by EDS, XRD, XPS and HRTEM. The PL intensity decrease after surface modification reflects the decrease in the electron-hole pair recombination efficiency, which is beneficial for photocatalysis. The single ZTO NW shows low electrical resistivity of $6.01 \times 10^{-5}\ \Omega\cdot$m. A total of 96% of MB was degraded by 3 at% Ag-ZTO NWs in 120 min. h^+ and $\cdot OH$ were the main reactants of photodegradation. After multiple cycles, the nanowires maintained degradation efficiency well without apparent change in terms of structure and morphology, showing reliability in photocatalysis.

Supplementary Materials: The following supporting information can be downloaded at: https://www.mdpi.com/article/10.3390/nano12071201/s1, Figure S1: Schematic illustration for fabrication of Ag-ZTO NWs. Figure S2: SEM images and XRD pattern of ZTO NWs before and after selective etching. (a) SEM image before selective etching (b) SEM image after selective etching (c) comparison of XRD patterns before and after selective etching. Figure S3: Schematic illustration of growth mechanism for ZTO NWs. Figure S4: EDS and mapping images of 1 at% Ag-ZTO NW and 3 at% Ag-ZTO NW. (a) EDS analysis of 1 at% Ag-ZTO NW (b) EDS analysis of 3 at% Ag-ZTO NW (c) mapping images of 1 at% Ag-ZTO NW (d) mapping images of 3 at% Ag-ZTO NW. Figure S5: Electrical measurement setup for ZTO NWs and Ag-ZTO NWs. (a) Schematic illustration of the electrical measurements. SEM images of (b) ZTO NW (c) 1 at% Ag-ZTO NW (d) 3 at% Ag-ZTO NW connected to 4 electrodes. Figure S6: I–V measurements of single ZTO nanowire (a) R_{13+} (b) R_{13-} (c) R_{14+} (d) R_{14-} (e) R_{23+} (f) R_{23-} (g) R_{24+} (h) R_{24-}. Figure S7: I–V measurements of single 1 at% Ag-ZTO nanowire (a) R_{13+} (b) R_{13-} (c) R_{14+} (d) R_{14-} (e) R_{23+} (f) R_{23-} (g) R_{24+} (h) R_{24-}. Figure S8: I–V measurements of single 3 at% Ag-ZTO nanowire (a) R_{13+} (b) R_{13-} (c) R_{14+} (d) R_{14-} (e) R_{23+} (f) R_{23-} (g) R_{24+} (h) R_{24-}. Figure S9: Photocatalytic reliability of ZTO NWs and Ag-ZTO NWs. (a) Degradation behaviors of ZTO NWs for three repeated cycles (b) degradation behaviors of 1 at%

Ag-ZTO NWs for three repeated cycles (c) degradation behaviors of 3 at% Ag-ZTO NWs for three repeated cycles (d) XRD pattern after the third cycle of degradation.

Author Contributions: Conceptualization, J.-C.S. and K.-C.L.; Data curation, J.-C.S.; Formal analysis, J.-C.S.; Supervision, K.-C.L.; Writing—original draft, J.-C.S.; Writing—review and editing, T.-L.H., S.-M.Y., S.-C.C. and K.-C.L. All authors have read and agreed to the published version of the manuscript.

Funding: This research was supported by the Ministry of Science and Technology of Taiwan through Grant MOST 108-2221-E-006-139-MY3. The research was also supported in part by Higher Education Sprout Project, Ministry of Education to the Headquarters of University Advancement at National Cheng Kung University (NCKU).

Data Availability Statement: Not applicable.

Acknowledgments: The authors gratefully acknowledge the use of EM000800 of MOST 110-2731-M-006-001 belonging to the Core Facility Center of National Cheng Kung University.

Conflicts of Interest: The authors declare that they have no competing interests.

References

1. Konstantinou, I.K.; Albanis, T.A. TiO_2-assisted photocatalytic degradation of azo dyes in aqueous solution: Kinetic and mechanistic investigations: A review. *Appl. Catal. B* **2004**, *49*, 1–14. [CrossRef]
2. Neppolian, B.; Choi, H.C.; Sakthivel, S.; Arabindoo, B.; Murugesan, V. Solar light induced and TiO_2 assisted degradation of textile dye reactive blue 4. *Chemosphere* **2002**, *46*, 1173–1181. [CrossRef]
3. Chong, M.N.; Jin, B.; Chow, C.W.; Saint, C. Recent developments in photocatalytic water treatment technology: A review. *Water Res.* **2010**, *44*, 2997–3027. [CrossRef] [PubMed]
4. Cheng, M.; Zeng, G.; Huang, D.; Lai, C.; Xu, P.; Zhang, C.; Liu, Y. Hydroxyl radicals based advanced oxidation processes (AOPs) for remediation of soils contaminated with organic compounds: A review. *Chem. Eng. J.* **2016**, *284*, 582–598. [CrossRef]
5. Chan, S.H.S.; Wu, T.Y.; Juan, J.C.; Teh, C.Y. Recent developments of metal oxide semiconductors as photocatalysts in advanced oxidation processes (AOPs) for treatment of dye waste-water. *J. Chem. Technol. Biotechnol.* **2011**, *86*, 1130–1158. [CrossRef]
6. Li, L.; Lou, Z.; Shen, G. Flexible broadband image sensors with SnS quantum dots/Zn_2SnO_4 nanowires hybrid nanostructures. *Adv. Funct. Mater.* **2018**, *28*, 1705389. [CrossRef]
7. Li, L.; Gu, L.; Lou, Z.; Fan, Z.; Shen, G. ZnO quantum dot decorated Zn_2SnO_4 nanowire heterojunction photodetectors with drastic performance enhancement and flexible ultraviolet image sensors. *ACS Nano* **2017**, *11*, 4067–4076. [CrossRef]
8. Tharsika, T.; Haseeb, A.S.M.A.; Akbar, S.A.; Sabri, M.F.M.; Wong, Y.H. Gas sensing properties of zinc stannate (Zn_2SnO_4) nanowires prepared by carbon assisted thermal evaporation process. *J. Alloys Compd.* **2015**, *618*, 455–462. [CrossRef]
9. Thanh, H.X.; Trung, D.D.; Trung, K.Q.; Van Dam, K.; Van Duy, N.; Hung, C.M.; Hoa, N.D.; Van Hieu, N. On-chip growth of single phase Zn_2SnO_4 nanowires by thermal evaporation method for gas sensor application. *J. Alloys Compd.* **2017**, *708*, 470–475. [CrossRef]
10. Lana-Villarreal, T.; Boschloo, G.; Hagfeldt, A. Nanostructured zinc stannate as semiconductor working electrodes for dye-sensitized solar cells. *J. Phys. Chem. C* **2007**, *111*, 5549–5556. [CrossRef]
11. Tan, B.; Toman, E.; Li, Y.; Wu, Y. Zinc stannate (Zn_2SnO_4) dye-sensitized solar cells. *J. Am. Chem. Soc.* **2007**, *129*, 4162–4163. [CrossRef] [PubMed]
12. Jain, S.; Shah, A.P.; Shimpi, N.G. An efficient photocatalytic degradation of organic dyes under visible light using zinc stannate (Zn_2SnO_4) nanorods prepared by microwave irradiation. *Nano Struct. Nano Objects* **2020**, *21*, 100410. [CrossRef]
13. Shi, L.; Dai, Y. Synthesis and photocatalytic activity of Zn_2SnO_4 nanotube arrays. *J. Mater. Chem. A* **2013**, *1*, 12981–12986. [CrossRef]
14. Rovisco, A.; Branquinho, R.; Deuermeier, J.; Freire, T.; Fortunato, E.; Martins, R.; Barquinha, P. Shape Effect of Zinc-Tin Oxide Nanostructures on Photodegradation of Methylene Blue and Rhodamine B under UV and Visible Light. *ACS Appl. Nano Mater.* **2021**, *4*, 1149–1161. [CrossRef]
15. Zhu, H.; Yang, D.; Yu, G.; Zhang, H.; Jin, D.; Yao, K. Hydrothermal synthesis of Zn_2SnO_4 nanorods in the diameter regime of sub-5 nm and their properties. *J. Phys. Chem. B* **2006**, *110*, 7631–7634. [CrossRef] [PubMed]
16. Zhao, Q.; Deng, X.; Ding, M.; Huang, J.; Ju, D.; Xu, X. Synthesis of hollow cubic Zn_2SnO_4 sub-microstructures with enhanced photocatalytic performance. *J. Alloys Compd.* **2016**, *671*, 328–333. [CrossRef]
17. Zeng, J.; Xin, M.D.; Li, K.; Wang, H.; Yan, H.; Zhang, W.J. Transformation process and photocatalytic activities of hydrothermally synthesized Zn_2SnO_4 nanocrystals. *J. Phys. Chem. C* **2008**, *112*, 4159–4167. [CrossRef]
18. Shi, J.B.; Wu, P.F.; Lin, H.S.; Lin, Y.T.; Lee, H.W.; Kao, C.T.; Liao, W.H.; Young, S.L. Synthesis and characterization of single-crystalline zinc tin oxide nanowires. *Nanoscale Res. Lett.* **2014**, *9*, 1–6. [CrossRef]
19. Shen, C.L.; Yang, S.M.; Lu, K.C. Single Crystalline Higher Manganese Silicide Nanowire Arrays with Outstanding Physical Properties through Double Tube Chemical Vapor Deposition. *Nanomaterials* **2020**, *10*, 1880. [CrossRef]

20. Huang, W.J.; Yang, S.M.; Liao, T.T.; Lu, K.C. Synthesis of morphology-improved single-crystalline iron silicide nanowires with enhanced physical characteristics. *CrystEngComm* **2021**, *23*, 3270–3275. [CrossRef]
21. Yao, Y.C.; Dai, X.R.; Hu, X.Y.; Huang, S.Z.; Jin, Z. Synthesis of Ag-decorated porous TiO_2 nanowires through a sunlight induced reduction method and its enhanced photocatalytic activity. *Appl. Surf. Sci.* **2016**, *387*, 469–476. [CrossRef]
22. Wang, F.; Yang, H.; Zhang, Y. Enhanced photocatalytic performance of $CuBi_2O_4$ particles decorated with Ag nanowires. *Mater. Sci. Semicond. Process.* **2018**, *73*, 58–66. [CrossRef]
23. Ye, Y.; Yang, H.; Li, R.; Wang, X. Enhanced photocatalytic performance and mechanism of Ag-decorated $LaFeO_3$ nanoparticles. *J. Solgel Sci. Technol.* **2017**, *82*, 509–518. [CrossRef]
24. Zhang, L.; Du, L.; Yu, X.; Tan, S.; Cai, X.; Yang, P.; Gu, Y.; Mai, W. Significantly enhanced photocatalytic activities and charge separation mechanism of Pd-decorated ZnO–graphene oxide nanocomposites. *ACS Appl. Mater. Interfaces* **2014**, *6*, 3623–3629. [CrossRef] [PubMed]
25. Simon, T.; Carlson, M.T.; Stolarczyk, J.K.; Feldmann, J. Electron transfer rate vs recombination losses in photocatalytic H_2 generation on Pt-decorated CdS nanorods. *ACS Energy Lett.* **2016**, *1*, 1137–1142. [CrossRef]
26. Gu, W.; Choi, H.; Kim, K. Universal approach to accurate resistivity measurement for a single nanowire: Theory and application. *Appl. Phys. Lett.* **2006**, *89*, 253102. [CrossRef]
27. Körbahti, B.K.; Rauf, M.A. Application of response surface analysis to the photolytic degradation of Basic Red 2 dye. *Chem. Eng. J.* **2008**, *138*, 166–171. [CrossRef]
28. Arafat, M.M.; Ong, J.Y.; Haseeb, A.S.M.A. Selectivity shifting behavior of Pd nanoparticles loaded zinc stannate/zinc oxide (Zn_2SnO_4/ZnO) nanowires sensors. *Appl. Surf. Sci.* **2018**, *435*, 928–936. [CrossRef]
29. Lin, J.H.; Huang, Y.J.; Su, Y.P.; Liu, C.A.; Devan, R.S.; Ho, C.H.; Wang, Y.P.; Lee, H.W.; Chang, C.M.; Liou, Y.; et al. Room-temperature wide-range photoluminescence and semiconducting characteristics of two-dimensional pure metallic Zn nanoplates. *RSC Adv.* **2012**, *2*, 2123–2127. [CrossRef]
30. Jie, L.; Chao, X. XPS examination of tin oxide on float glass surface. *J. Non Cryst. Solids* **1990**, *119*, 37–40. [CrossRef]
31. Bai, S.; Chen, C.; Tian, Y.; Chen, S.; Luo, R.; Li, D.; Chen, A.; Liu, C.C. Facile synthesis of α-MoO_3 nanorods with high sensitivity to CO and intrinsic sensing performance. *Mater. Res. Bull.* **2015**, *64*, 252–256. [CrossRef]
32. Han, S.W.; Kim, Y.; Kim, K. Dodecanethiol-derivatized Au/Ag bimetallic nanoparticles: TEM, UV/VIS, XPS, and FTIR analysis. *J. Colloid Interface Sci.* **1998**, *208*, 272–278. [CrossRef] [PubMed]
33. Arooj, S.; Xu, T.; Hou, X.; Wang, Y.; Tong, J.; Chu, R.; Liu, B. Green emission of indium oxide via hydrogen treatment. *RSC Adv.* **2018**, *8*, 11828–11833. [CrossRef]
34. Ali, M.B.; Barka-Bouaifel, F.; Elhouichet, H.; Sieber, B.; Addad, A.; Boussekey, L.; Férid, M.; Boukherroub, R. Hydrothermal synthesis, phase structure, optical and photocatalytic properties of Zn_2SnO_4 nanoparticles. *J. Colloid Interface Sci.* **2015**, *457*, 360–369.
35. Deng, B.; Da Rosa, A.L.; Frauenheim, T.; Xiao, J.P.; Shi, X.Q.; Zhang, R.Q.; Van Hove, M.A. Oxygen vacancy diffusion in bare ZnO nanowires. *Nanoscale* **2014**, *6*, 11882–11886. [CrossRef]
36. Karthik, K.R.G.; Andreasson, B.P.; Sun, C.; Pramana, S.S.; Varghese, B.; Sow, C.H.; Mathews, N.; Wong, L.H.; Mhaisalkar, S.G. Physical and electrical properties of single Zn_2SnO_4 nanowires. *Electrochem. Solid State Lett.* **2010**, *14*, K5. [CrossRef]
37. Bayomie, O.S.; Kandeel, H.; Shoeib, T.; Yang, H.; Youssef, N.; El-Sayed, M.M. Novel approach for effective removal of methylene blue dye from water using fava bean peel waste. *Sci. Rep.* **2020**, *10*, 7824. [CrossRef]
38. Hou, C.; Hu, B.; Zhu, J. Photocatalytic degradation of methylene blue over TiO_2 pretreated with varying concentrations of NaOH. *Catalysts* **2018**, *8*, 575. [CrossRef]
39. Yao, J.; Wang, C. Decolorization of methylene blue with sol via UV irradiation photocatalytic degradation. *Int. J. Photoenergy* **2010**, *2010*, 1–6. [CrossRef]
40. Rauf, M.A.; Ashraf, S.S. Fundamental principles and application of heterogeneous photocatalytic degradation of dyes in solution. *Chem. Eng. J.* **2009**, *151*, 10–18. [CrossRef]
41. Cavalcante, R.P.; Dantas, R.F.; Bayarri, B.; González, O.; Giménez, J.; Esplugas, S.; Junior, A.M. Photocatalytic mechanism of metoprolol oxidation by photocatalysts TiO_2 and TiO_2 doped with 5% B: Primary active species and intermediates. *Appl. Catal. B* **2016**, *194*, 111–122. [CrossRef]
42. Chen, D.; Ray, A.K. Removal of toxic metal ions from wastewater by semiconductor photocatalysis. *Chem. Eng. Sci.* **2001**, *56*, 1561–1570. [CrossRef]
43. Deng, Q.; Duan, X.; Ng, D.H.L.; Tang, H.; Yang, Y.; Kong, M.; Wu, Z.; Cai, W.; Wang, G. Ag nanoparticle decorated nanoporous ZnO microrods and their enhanced photocatalytic activities. *ACS Appl. Mater. Interfaces* **2012**, *4*, 6030–6037. [CrossRef] [PubMed]

nanomaterials

Article

3D-Printable Oxygen- and Drug-Carrying Nanocomposite Hydrogels for Enhanced Cell Viability

Ravi Kumar [1,2] and Nermin Seda Kehr [1,2,*]

[1] Physikalisches Institute, Westfälische Wilhelms-Universität Münster, Wilhelm-Klemm-Straße 10, 48149 Münster, Germany; ravikapoorsaini@gmail.com
[2] Center for Soft Nanoscience (SON), Westfälische Wilhelms-Universität Münster, Busso-Peus-Straße 10, 48149 Münster, Germany
* Correspondence: seda@uni.muenster.de

Abstract: Nanocomposite (NC) hydrogels have been widely studied due to their tunable biochemical/physical properties for tissue engineering and biomedical applications. Nanoparticles (NPs) that can carry bioactive hydrophilic/hydrophobic molecules and provide sustained release within hydrogels are an ideal all-in-one-platform for local drug delivery applications. Dual delivery of different bioactive molecules is desired to achieve synergetic therapeutic effect in biomedical applications. For example, the co-administration of drug molecules and oxygen (O_2) is an ideal choice to improve cell viability, while reducing the harmful effects of hypoxia. Therefore, we prepared drug-loaded O_2-carrying periodic mesoporous organosilica (PMO-PFC) NPs and their 3D-printable hydrogel precursors based on gelatin methacryloyl (GelMa) to fabricate 3D-scaffolds to improve cell-viability under both normoxia (21% O_2) and hypoxia (1% O_2) conditions. We used rutin as the hydrophobic drug molecule to demonstrate that our O_2-carrying PMO-PFC NPs can improve hydrophobic drug loading and their sustained delivery over 7 days, while supporting sustained O_2-delivery for 14 days under hypoxia conditions. Furthermore, the fibroblast cells were interacted with NC hydrogel scaffolds to test their impact on cell-viability under both normoxia and hypoxia conditions. The improved rheological properties suggest the prepared NC hydrogels can be further tested or used as an injectable hydrogel. The improved mechanical properties and 3D printability of NC hydrogels indicate their potential use as artificial tissue constructs.

Keywords: NC hydrogel; drug-delivery; oxygen-carrying hydrogels; 3D-printing

Citation: Kumar, R.; Kehr, N.S. 3D-Printable Oxygen- and Drug-Carrying Nanocomposite Hydrogels for Enhanced Cell Viability. *Nanomaterials* **2022**, *12*, 1304. https://doi.org/10.3390/nano12081304

Academic Editors: Jihoon Lee and Ming-Yu Li

Received: 17 March 2022
Accepted: 9 April 2022
Published: 11 April 2022

1. Introduction

Nanocomposite (NC) hydrogels are crosslinked three-dimensional (3D) polymer networks embedded with nanoparticles (NPs) and have been used in tissue engineering and biomedical applications [1,2]. NC hydrogels mimic the extracellular matrix (ECM) environment, and tunable biochemical/physical properties can control cell functions such as cell adhesion, migration, proliferation, and differentiation. NC hydrogels are stimuli-responsive, hydrophilic, biocompatible, biodegradable and have excellent physical properties, such as mechanical toughness, elasticity, resistance against compression, and a high degree of swelling-deswelling. Several types of NPs (for example, carbon-based NPs, inorganic NPs, metal/metal oxide NPs, etc.) have been combined by physical or chemical interactions with polymeric chains of hydrogels, which results in novel properties in electronics, biosensors and biomedical applications [1–6]. By tailoring functionality of embedded NPs, NC hydrogels have opened new opportunities to develop advance biomaterials for tissue engineering and controlled drug delivery. The embedded NPs can serve as effective drug-carriers for both hydrophilic and hydrophobic drug molecules. The loading efficiency and controlled release of drugs can also be enhanced by the porous structure of hydrogels and large surface area and pores of NPs.

Numerous state-of-the-art approaches were demonstrated to fabricate NC hydrogels for controlled and site-specific drug delivery [7–9]. For example, Hou et al. [10] prepared a NC hydrogel using pH-responsive graphene oxide (GO) encapsulated with an anti-cancer drug (curcumin), thereby showing site-specific release to the proximal colon. In another example, Pacelli et al. [11] prepared a GelMa-based hydrogel embedded with nanodiamonds as a drug-carrier (dexamethasone, Dex), to promote the osteogenic differentiation of human adipose stem cells (hASCs). Zhao et al. [12] described Fe_3O_4 NPs incorporated into magnetic field-responsive NC hydrogels, thereby demonstrating the controlled release of bovine serum albumin (BSA) as the model drug. Alvarez et al. [13] described NC hydrogels consisting of silica NPs and collagen loaded with gentamicin/rifamycin drugs for wound-healing dressings and also investigated antibacterial activity. Motealleh et al. described alginate-based hydrogels made of periodic mesoporous organosilica with an antibacterial tetracycline (Tet) drug. The 3D-printed hydrogels showed a release of Tet for seven days and enhanced fibroblast cell proliferation [14]. Several studies also demonstrated the advanced application of NC hydrogels as local drug delivery systems due to their injectability and in situ forming abilities [8,15–17]. Furthermore, NC hydrogels can be used to fabricate 3D-scaffolds with tunable porosity and structure that are similar to tissue-like constructs due to their shear thinning and viscoelastic properties [18–20]. NPs that can carry bioactive molecules and provide sustained biomolecule release within hydrogels are ideal all-in-one-platforms for local drug delivery applications. Therefore, NC hydrogels are promising 3D functional artificial tissue constructs for drug delivery, and able to improve cellular attachment, proliferation, differentiation, and migration.

Rutin (quercetin-3-O-rutinoside) is a naturally occurring bioflavonoid found in vegetables and fruit. It has low solubility in water, thus showing poor stability and bioavailability [21]. Rutin, however, has various pharmacological activities (for example, antibacterial, antiprotozoal, antitumor, anti-inflammatory, antiallergic, antiviral etc.) [22]. Rutin-coated nanosystems have been demonstrated in various therapeutic objectives and have shown enhanced aqueous solubility, bioavailability and stability [23–26]; however, there are few studies conducted into loading rutin into hydrogels [27–29].

O_2 is the most vital nutrient for cell survival and signal cascading to regulate cellular activities. The hypoxia condition occurs when there is insufficient (lower than normal oxygen level) and heterogeneous oxygen distribution within the body tissues, which leads to cell apoptosis, tissue necrosis, transplantation failures, and failures in tissue formation. Over the years, researchers demonstrated different approaches to O_2-releasing hydrogels (either by introducing O_2-releasing molecules within hydrogels or by embedding O_2-releasing nanoparticles within NC hydrogels) to provide sufficient O_2 to the tissues [30–32]. Commonly used O_2-releasing materials are solid inorganic peroxides (for example, calcium peroxide and sodium percarbonate), hydrogen peroxide, and perfluorocarbons (PFCs). Alemdar et al. [32] prepared a GelMa-based hydrogel incorporated within calcium peroxide for O_2 delivery in cardiac cells and demonstrated reduced hypoxia-induced cell death by limiting the necrosis. Kang et al. [33] investigated oxygen-generating alginate (OGA) hydrogel as a bioactive acellular matrix for enhanced wound healing. Patil et al. [34] demonstrated the use of methacrylamide chitosan modified with perfluorocarbon chains (MACF) to construct hydrogel dressings for treating dermal wounds. In another example, Li et al. [35] constructed hydrogels consisting of perfluorocarbons conjugated to methacrylamide chitosan to promote stem cell proliferation. Park et al. [36] reported a hyperbaric oxygen-generating (HOG) hydrogel consisting of thiolated gelatin and calcium peroxide, which promoted wound healing and neovascularization. However, these engineered functional tissues have low oxygen diffusion for in vitro and in vivo applications. In a scaffold, O_2 can diffuse a limited distance of 100–200 μm so providing sufficient O_2 to bigger non-vascularized scaffolds is an issue for in vivo application. The non-homogenous distribution of O_2 through the non-vascularized scaffolds can also limit the repair to damaged tissue. Therefore, the incorporation of O_2-releasing materials within scaffolds is suggested to provide sufficient O_2 to the cells to maintain metabolic activity during the period of blood vessel ingrowth and repair of tissue. Co-delivery of different bioactive molecules is desired to achieve synergetic therapeutic effects in biomedical applications [37–39]. For example, the co-administration of drug molecules and oxygen (O_2) is an ideal choice to improve cell viability, while reducing the harmful effects of hypoxia. The co-administration of O_2 and drug molecules via NPs into NC hydrogels and the subsequent impact on cell viability have been studied only by a few researchers. For example, Newland et al. [40] described the simultaneous release of oxygen and doxorubicin from a gellan gum hydrogel loaded with calcium peroxide and the chemotherapeutic drug doxorubicin under normoxia and hypoxia. Motealleh et al. [41] prepared an alginate-based periodic mesoporous organosilica-consisting NC hydrogel to improve O_2 release under the hypoxia condition, enhance healthy cell viability and decrease the viability of malignant and immortal cells in the presence of an anti-cancer drug.

We, therefore, aim to generate drug molecules loaded with O_2-carrying NPs and their 3D-printable hydrogel precursors to fabricate 3D-scaffolds to improve cell viability under both normoxia and hypoxia conditions. To achieve this, we will use rutin as the hydrophobic drug molecule to demonstrate that our O_2-carrying organic-inorganic NPs can improve hydrophobic drug loading and its sustained delivery over seven days, while supporting sustained O_2-delivery for 14 days under hypoxia conditions. Recently, we demonstrated the preparation of rutin-loaded O_2-carrying NPs, and their impact on fibroblast and Colo 818 cell viability under normoxia and hypoxia conditions on a 2D-cell culture plate [42]. A 3D biomaterial network can mimic the 3D tissue environment better than a 2D-cell culture plate [43]. Therefore, in the current study, we use similar NPs to generate injectable NC hydrogels to fabricate 3D-scaffolds to improve cell viability in 3D biomaterial network. We synthesized the oxygen-carrying nanoparticles (PMO-PFCs) and the surface of the PMO-PFCs was functionalized with a hydrophobic drug (rutin). Rutin-coated PMO-PFCs were further coated with a biodegradable and cell-adhesive bipolymer poly-d-lysine (PDL) for stability. Later, rutin-coated PMO-PFCs were incorporated into a gelatin methacryloyl (GelMa) -based hydrogel network. The NC-hydrogel scaffolds were prepared by lyophilization and measured for their capability to release oxygen under normoxia and hypoxia conditions. The drug release (rutin) profile was also observed at different pH for seven days. To demonstrate the enhanced cell viability under normoxia and hypoxia conditions, the NC-hydrogel scaffolds were interacted with the fibroblast cells. The morphology of the cells was examined by nuclei- and actin-staining after the cell experiment. The NC hydrogels were also characterized for rheological and mechanical properties. To summarize, drug-coated NC hydrogel shows sustained O_2 over a period of 14 days and drug release at different pH values for seven days. The antioxidant effect of rutin, O_2 release, and cell-adhesive coating (PDL) on PMO-PFCs slightly supported the cell viability under the hypoxia condition.

2. Materials and Methods

2.1. Materials

Hexadecyltrimethylammonium bromide (CTAB, 98%), [1H,1H,2H,2H perfluorooctyltriethoxysilane (PFC)], [1,2-bis(triethoxysilyl)ethane (BTEE, 96%)], Hoechst 33342 nuclei dye, [2′,7′-dichlorodihydrofluorescein diacetate (DCFHDA)], trypsin, poly-d-lysine (PDL), alginic acid sodium salt, powder gelatin (from porcine skin), methacrylic anhydride (MA), N-vinylcoprolactane (VC), eosin Y, triethanolamine (TEA), and the WST-1 assay were ordered from Sigma-Aldrich, Darmstadt, Germany. Rutin-trihydrate was purchased from Roth GmbH, Karlsruhe, Germany. Ammonia (32%), ethanol (absolute, for analysis) and hydrochloric acid (32%, for analysis) were bought from Merck, Darmstadt, Germany. Phalloidin Alexa Fluor 488 was purchased from Invitrogen, Life technology Europe, Bleiswijk, Netherlands. Primary dermal fibroblasts: normal, human, and adult cells were purchased from ATCC, Manassas, VA, USA. Human Colo 818 (malignant melanoma) cells were bought from DSMZ, Braunschweig Germany. The Dulbecco's Modified Eagle Medium (DMEM) [supplemented with 1% (*v/v*) penicillin/streptomycin, 2% (*v/v*) L-glutamate, and 10% (*v/v*) fetal bovine serum (FBS)], penicillin/ streptomycin, phosphate-buffered saline (PBS), and L-glutamate were obtained from Sigma-Aldrich, Darmstadt, Germany.

2.2. Synthesis of Periodic Mesoporous Organosilica (PMO-PFC)

Briefly, 30 mL ethanol (99.8%) and 90 mL deionized (DI) water were mixed by magnetic stirrer in a 250 mL round-bottom flask. While stirring, 485 mg CTAB and 270 µL NH_3 (32%) were added and stirred for 1 h at room temperature (RT). Then, 1.74 mL (1.67 g, 4.7 m mol) BTEE and PFC (0.59 g, 1.16 m mol, 0.44 mL in 3 mL ethanol) were added and stirred for additional 48 h at RT. After 48 h and while still being stirred, 50 mL ethanol (99%) was added, followed by 1.4 mL HCl (32 wt%) which was slowly added to the mixture and stirred for 6 h at 50 °C to remove the CTAB. The reaction mixture was transferred to 15 mL falcon tubes and centrifuged (6500 rpm, Hettich EBA 200 small centrifuge from Andreas Hettich GmbH & Co.KG, Tuttlingen, Germany) for 15 min at RT. The supernatant was discarded and the PMO-PFC particles were washed a further 3 times with ethanol by centrifugation. The tubes with particles were left with open lids to dry for 2 days at RT.

2.3. Loading of Rutin to PMO-PFC Particles

An amount of 100 mg of PMO-PFC particles and rutin trihydrate (80 mg) were mixed together with 0.4 mL ethanol, sonicated for 20 min and stirred for 10 min at RT. Then, 1.1 mL DI water was added and sonicated again for 5 min. The mixture was stirred overnight at RT and then centrifuged for 15 min to collect the rutin-coated PMO-PFC particles. The coated particles were further washed with DI water and dried overnight. The supernatant was collected for the purpose of measuring rutin concentration. The amount of rutin loaded into the PMO-PFC particles was determined by means of spectrophotometric analyses. 300 µL of supernatant was added to a 96-well plate and the absorbance measured at 352 nm by a UV-vis spectrometer. The concentration of free rutin was calculated by using a calibration curve (Figure S1). The amount of loaded rutin was the amount of rutin added initially minus the amount of free rutin in the supernatant. The loaded efficiency (E%) was calculated according to the equation below:

$$E\% = (\text{amount of rutin added-amount of free rutin})/(\text{amount of rutin added}) \times 100$$

2.4. Coating of Poly-d-lysine (PDL) to Ru(PMO-PFC) Particles

An amount of 50 mg of Ru(PMO-PFC) was added to 1.5 mL PDL solution (0.5 mg/mL in DI water) in a 2 mL Eppendorf tube, sonicated for 20 min, and then stirred for 1 day at RT. The mixture was then centrifuged for 15 min and the supernatant was used to calculate the released rutin by means of spectrophotometric analyses. The absorbance and E% were measured as explained in the above section and supporting information. The product was dried, lids open, at RT.

2.5. Preparation of GelMa

Gelatin methacryloyl (GelMa) was synthesized according to the previous study [44]. First, gelatin (20 g) was dissolved in PBS (600 mL) at 60 °C for 1 h by stirring. Then, methacrylic anhydride (16 mL) was added dropwise to the mixture and continuously stirred for 2 h at 50 °C. The entire mixture was then transferred into dialysis membrane tubes (with 12–14 kDa) and kept in autoclaved DI water for 7 days at 50 °C to remove unreacted methacrylic anhydride. The water was replaced every day with fresh prewarmed and autoclaved DI water. After 7 days, the solution was filtered with a vacuum filter (110 mm pore size) and then lyophilized to achieve a dried GelMa foam.

2.6. Preparation of NC Hydrogel and Scaffold

A GelMa stock solution was first prepared with GelMa (1 g, 10 *w/v*%) in PBS (10 mL) mixed with eosin Y in PBS (0.1 mM) as a photoinitiator, TEA as a co-initiator (133 µL, 1.3 *w/v*%), and VC as a co-monomer (0.1 g, 1.0 *w/v*%) and kept at 80 °C for 10 min in order to dissolve GelMa. For the scaffold, the stock GelMa solution was mixed with particle (1 mg/mL) and alginate (70 mg/mL). The hydrogel solution was homogeneously mixed by spatula and the mixed solution was transferred into a syringe. The hydrogel solution was then filled into a hexagon template (side—0.25 cm, height—0.4 cm, volume = ca. 65 μL) by syringe and photo-crosslinked with visible light (450–550 nm) for 120–180 s, using FocalSeal (Genzyme Biosurgical, Cambridge, MA, USA). For ionic crosslinking of Alg, the templates were covered with 2.5 mM $CaCl_2$ solution in DI water for 20 min. For rheology, cross-linked hydrogel was removed from the templates and used for the measurement. For scaffolds, the templates were frozen at −20 °C for 1 day and then lyophilized with a freeze dryer. The hexagon template was removed and the scaffolds were ready to use for experimentation. For mechanical properties, the cylindrical scaffolds (10 mm diameter, 10–13 mm height) were freeze dried and prepared similarly to the above-mentioned method.

2.7. Rutin Release from Rutin-Coated GelMa-Based Scaffold

First, the rutin-coated GelMa-based scaffold (freeze-dried) was placed in DMEM (1 mL, pH-6 and 7.4) in a 2 mL Eppendorf tube at RT. After each incubation time, the media was collected and centrifuged for 10 min. The supernatant was transferred into a new Eppendorf tube and fresh media was added to the scaffold and left at RT until the next incubation time (adding up the previous incubation time). The collected supernatants were used to measure the absorbance of rutin for each incubation time by spectrophotometric analyses. The concentration of released-rutin was calculated by using a calibration curve similar to the method discussed in the supporting information (Figure S1).

2.8. Measurement of O_2 Content from Scaffold

The O_2 content of the cell culture media and scaffold containing cell culture media was determined using an oxygen sensor (OXY-1 SMA trace, Pre Sens Precision Sensing GmbH, Regensburg, Germany). All samples were incubated either in normoxia (21% O_2) or hypoxia conditions (1% O_2) for 14 days. To generate the hypoxia condition, we used a hypoxia box saturated with a gas mixture of 1% O_2 + 5% CO_2 + 94% N_2. First, the scaffold-containing media was placed in a hypoxia box closed with a rubber cap and saturated with 1% O_2, and the oxygen level measured after the given incubation time. Similar was done for the normoxia condition without saturating with 1% O_2.

2.9. 3D Printing of Hydrogels

To show the printability of prepared NC hydrogels, NC hydrogels were prepared with particles (1 mg/mL) and alginate (70 mg/mL). The hydrogel mixture was homogenously mixed by spatula and transferred into a special syringe for 3D printing. The hexagon structure (ca. 2.3 × 2.3 cm) was designed with the inbuilt software of a Cellink 3D printer (CELLINK, Boston, MA, USA) for layer-by-layer deposition (3 layers). Particles containing hydrogels were printed (using Cellink HeartWare version 2.4.1) in a hexagon structure, and crosslinked with visible light (450–550 nm) for 120–180 s using FocalSeal (Genzyme Biosurgical, Cambridge, MA, USA), for covalent photo-crosslinking of GelMA, and then with a 2.5 mM $CaCl_2$ solution for ionic crosslinking of Alg. The syringe temperature and printing plate temperature were set at 37 °C. A needle with an inner diameter of 0.41 mm was used for printing, and the speed of the syringe was 20 mm s^{-1}. To prepare the scaffolds, the samples were frozen at −20 °C and then lyophilized with a freeze dryer, yielding the 3D-printed scaffolds.

2.10. Cell Viability in the Scaffolds

First, PMO-PFC, Ru(PMO-PFC), and Ru(PMO-PFC)PDL particles(1 mg/mL) -prepared scaffolds were placed on a culture plate. The cells were thawed from −80 °C and carefully seeded on the culture plate with pre-warmed media. After overnight incubation at 37 °C and 5% CO_2, cells were washed with PBS and harvested by trypsinization. Then, cells were collected by adding pre-warmed media and centrifuged for 3 min. The supernatant was discarded and the cell pallet was collected by adding 1 mL pre-warmed media. Cells were counted in hemocytometer and the particle-coated scaffolds were incubated with 10^4 cells for 1 day and 7 days under hypoxia and normoxia conditions at 37 °C and 5% CO_2. For control, the cells were seeded on scaffold without particles (only the GelMa-based scaffold). After incubation period, the scaffolds with cells were washed with PBS (2×) and incubated with cell proliferation reagent WST-1 assay (10 vol% in media) for 3 h. Cell viability was measured at 460 nm by scanning the plate with a UV-vis spectrophotometer.

2.11. Co-Staining of Cells

Cells were seeded separately on the scaffolds and incubated for 1 day and 7 days at 37 °C and 5% CO_2 under hypoxia and normoxia conditions. Then, the cells were fixed with paraformaldehyde (4%). After 20 min, scaffolds were washed with PBS (2×) and the nuclei-staining was performed with Hoechst 33342 dye [stock solution (16.2 mM), diluted 1:2000 in PBS] at RT for 20 min. Then, scaffolds were washed with PBS (2×) and incubated with 0.1% Triton X-100 in PBS for 30 min at RT. Scaffolds were then washed with PBS (3×), and co-stained with phalloidin Alexa Fluor 488 [5 μL of the methanolic stock solution (6.6 μM) of phalloidin Alexa Fluor 488, diluted in 200 μL of PBS containing 3% bovine serum albumin] for f-actin staining. Scaffolds were kept overnight at room temperature and stored in the dark. Afterward, the scaffolds were washed with PBS (2×) and ready for imaging.

2.12. Characterization

Scanning electron microscopy (SEM) was performed on a Zeiss cross beam 340 scanning electron microscope, to determine the morphology of the particles. The average size of the particles from SEM images was measured by ImageJ from 35 NPs. An Inlens-Duo detector (secondary electron (SE) detector) for particles and a SESI detector (SE, and secondary ion detector) for the hydrogels were used. Zeta potential measurements and dynamic light scattering (DLS) were conducted using a Malvern Zetasizer Nano Series. A Nikon ECLIPSE Ts2R fluorescence microscope was used to determine the cell morphology and fluorescence imaging. Cell viability was measured using a Tecan Infinite 200 PRO spectrophotometer. A Christ Alpha 1-2-LD plus freeze-dryer was used to produce porous hydrogel scaffolds. An INKREDIBLE 3D bioprinter (CELLINK, Boston, MA, USA) was used to print all nanocomposite hydrogels into computer-designed 3D structures. Rheological measurements were carried out using an MCR 302 rheometer (Anton Paar, Ashland, VA, USA) with a 25 mm diameter parallel-plate geometry measuring system. A material testing machine (type 066590, ZwickRoell GmbH & Co. KG, Ulm, Germany) was used to determine the compression modulus of the samples.

2.13. Statistical Methods

Experiments were performed three times. The results are shown as average values with standard deviations. Significance tests were conducted using a single factor ANOVA test. Significance levels were depicted as * for $p \leq 0.05$, ** for $p \leq 0.01$, and *** for $p \leq 0.001$, where p is the probability value and a statistical measurement used to validate a hypothesis against observed data.

3. Results

3.1. Preparation and Characterization of Rutin-Coated PMO-PFC Particles

The synthesis of PMO-PFC particle was performed according to a previous study [41]. The PFCs are excellent candidates for O_2-releasing materials, but the hydrophobic and non-aqueous nature of PFCs can exert a sudden release of O_2 [45]. Therefore, the internal and external surfaces of NPs were functionalized with PFCs. Next, rutin was encapsulated into the PMO-PFC system (denoted as Ru(PMO-PFC)) as drug molecules via hydrophobic forces generated by PFC. It is important to note that non-PFC coated periodic mesoporous organosilica is insufficient for hydrophobic rutin encapsulation. Rutin is a naturally occurring bioflavonoid and has a wide range of pharmacological properties. The poor water solubility of rutin limits its bioavailability; researchers have, therefore, incorporated rutin into the nanosystems to enhance their stability and bioavailability. We calculated around 90% loading efficiency of rutin into PMO-PFCs. The hydrophobic nature of rutin allows entrapment into PMO-PFC particles by hydrophobic forces [46]. The calibration curve of rutin in water and calculations are given in the Supplementary Information (Figure S1). Further, to enhance the stability of the whole system in biological and physiochemical conditions, a biodegradable polymer, PDL, was coated over the rutin-functionalized PMO-PFCs, denoted as Ru(PMO-PFC)PDL. During the PDL-coating process, an amount of rutin is expected to release into the supernatant. Therefore, we calculated around 83% loading efficiency after the PDL coating into the rutin-encapsulated PMO-PFC particles. The characterization of the functionalized nanoparticles was performed by scanning electron microscopy (SEM), dynamic light scattering (DLS), and zeta potential measurement. The measured zeta potential and size distribution values are shown in Table 1. The changes in the zeta potential from -6.98 ± 0.28 to -14.94 ± 0.47 mV indicate a combined deposition/adsorption process of rutin on the surface of the PMO-PFCs, because rutin displays different solubility in water at different temperatures that is attributed to the different interaction forces such as van der Waals forces and hydrogen bonding (Peng et al.) [47]. The deposition/adsorption of rutin on the surface of PMO-PFCs, increases the value of the zeta potential; the negative value may be due to its hydroxyl groups, which indicates the whole particles now have more negative zeta potential. This result also indicates the deposition/adsorption of rutin on the external surface of PMO-PFC. Further, the size of the particles increases from 238.30 ± 32.18 to 457.60 ± 60.89 nm. After the PDL (positively charged polymer)-coating of Ru(PMO-PFC), a positive increase in the zeta potential indicates the successful coating of the polymer matrix on the Ru(PMO-PFC) via electrostatic interaction. The morphology of the nanoparticles is shown in SEM image (Figure 1A). The average size of the particles in DLS and SEM is different, which is most likely due to the aggregation of the hydrophobic particles in the aqueous solution during the DLS measurement. Furthermore, the increase in the size of the Ru(PMO-PFC)PDL can be due to the swelling of the PDL on the surface of the particles.

Table 1. Zeta potential (mean value ± standard deviation) and size measurement (mean value ± standard deviation) of particles. ANOVA: $p < 0.01$ (**), $p < 0.001$ (***) and ^{a} = significant difference between PMO-PFC and Ru(PMO-PFC), ^{b} = significant difference between Ru(PMO-PFC) and Ru(PMO-PFC)PDL. Number of repeated experiments (N) = 3.

Sample	Zeta Potential (mV)	Size (nm)
PMO-PFC	-6.98 ± 0.28	238.30 ± 32.18
Ru(PMO-PFC) ^{a}	-14.94 ± 0.47 ***	457.60 ± 60.89 **
Ru(PMO-PFC)PDL ^{b}	44.50 ± 1.52 ***	520.76 ± 20.11 ***

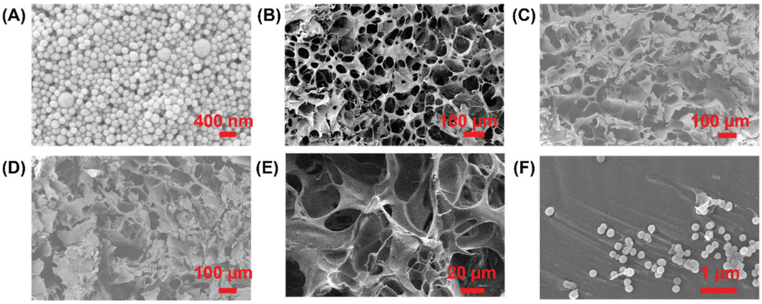

Figure 1. SEM images of PMO-PFCs (**A**), G+PMO-PFC (**B**), G+Ru(PMO-PFC) (**C**), G+Ru(PMO-PFC)PDL (**D**), zoom-in image of hydrogel (**E**) and PMO-PFCs inside the hydrogel network (**F**).

3.2. Characterization of NC Hydrogels

After successful functionalization of rutin to PMO-PFCs and PDL coating on Ru(PMO-PFC), the hydrogel precursor and scaffolds were prepared as described in the Method section. The scaffolds with PMO-PFC, Ru(PMO-PFC) and Ru(PMO-PFC)PDL are denoted as G+PMO-PFC, G+Ru(PMO-PFC), G+Ru(PMO-PFC)PDL, respectively. The hydrogels were also characterized for morphological properties by SEM (Figure 1B–E). The SEM images show the porous structure of the prepared scaffolds. The average size of the PMO-PFCs is 143 ± 12 nm (Figure 1A). The zoom-in image (Figure 1F) shows the distribution of PMO-PFCs within hydrogel network. The aggregation of PMO-PFCs is expected, due to the hydrophobic nature of the particles.

Rheologic properties such as viscosity (η), storage (G′) and loss modulus (G″), are important factors to determine the injectability of the hydrogel. The ability of hydrogels to change viscosity in response to the changes in shear stress is crucial for injectable hydrogels. Hydrogels with a lower viscosity and lower storage and loss moduli are typically easier to inject than hydrogels with a high viscosity and high storage and loss moduli. The viscosity of the G+PMO-PFC, G+Ru(PMO-PFC) and G+Ru(PMO-PFC)PDL hydrogels decreases with increasing shear rate and demonstrates the shear thinning property (Figure 2A). Storage and loss moduli are the elastic and viscous responses of a hydrogel to oscillatory shear. A higher storage modulus than loss modulus for the G+PMO-PFC, G+Ru(PMO-PFC) and G+Ru(PMO-PFC)PDL hydrogels over the entire range of angular velocities demonstrates their viscoelastic properties (Figure 2B). The shear thinning and viscoelastic properties of prepared NC hydrogels show their ability for use as injectable hydrogels and as hydrogel precursors for printing 3D scaffolds. For the compression test, the cylindrical scaffolds were prepared according to the earlier-mentioned method. The NC-hydrogel scaffolds show a higher compression modulus than the GelMa-based scaffold at 100 N (Figure 2C), indicating stronger mechanical compressive properties of NC hydrogel, due to incorporation of NPs. This is due to the non-covalent interactions between the polymer networks of hydrogel- and O_2-carrying NPs. The G+Ru(PMO-PFC) shows a higher compression modulus than the GelMa-based scaffold and G+PMO-PFC, perhaps because of the interaction of GelMa with the hydroxyl-groups of the rutin. G+Ru(PMO-PFC)PDL shows more stiffness (highest compression modulus among others) due to the distribution of hydrophilic PDL-coated particles within the hydrogel network. The swelling and degradation of the scaffold were also measured (Figures S2 and S3). The G+PMO-PFC, G+Ru(PMO-PFC), and G+Ru(PMO-PFC)PDL scaffolds exhibited a low swelling ratio and less degradation compared with the GelMa-based scaffold (see Supplementary Information). To summarize, the prepared NC-hydrogel scaffolds show better rheological properties which enables them to be used as injectable and printable hydrogels. The enhanced mechanical properties also make these NC hydrogels potential candidates for constructing an artificial tissue construct.

3.3. 3D Printing of NC Hydrogels

A 3D-printable hydrogel is an emerging area for tissue engineering because of the bioavailability and biodegradability of hydrogels, and their capabilities for cell adhesion, proliferation and differentiation. The improved mechanical and elastic properties of NC hydrogels make them suitable candidates for the strong and durable artificial organ implantations [48]. To demonstrate the printability of the prepared NC hydrogels, NC hydrogels were printed into a hexagonal structure using the Cellink 3D printer. Figure 3 shows the 3D hexagons printed in this way (Figure 3, top images). The crosslinked and freeze-dried scaffolds retained their shape fidelity (Figure 3, lower images).

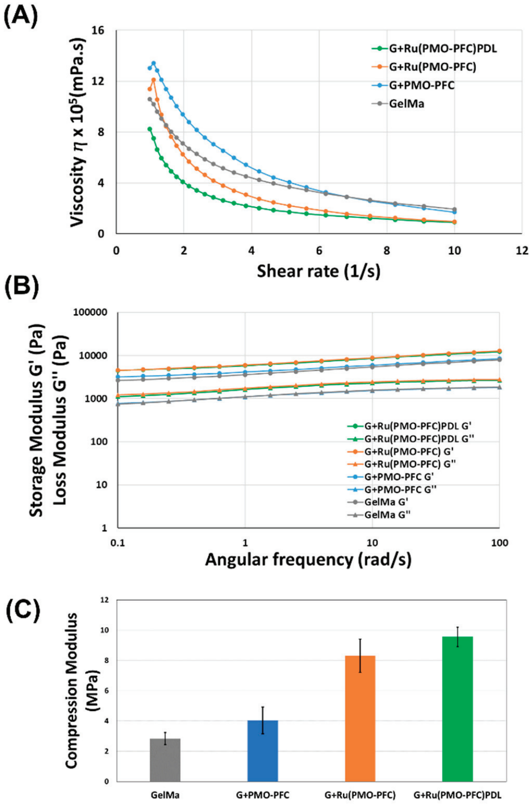

Figure 2. Rheological and mechanical properties of NC hydrogels. Viscosity vs shear rate (**A**), the storage modulus is shown by circle and loss modulus by triangle marker vs angular frequency (**B**), and compression modulus for each hydrogel scaffold (**C**).

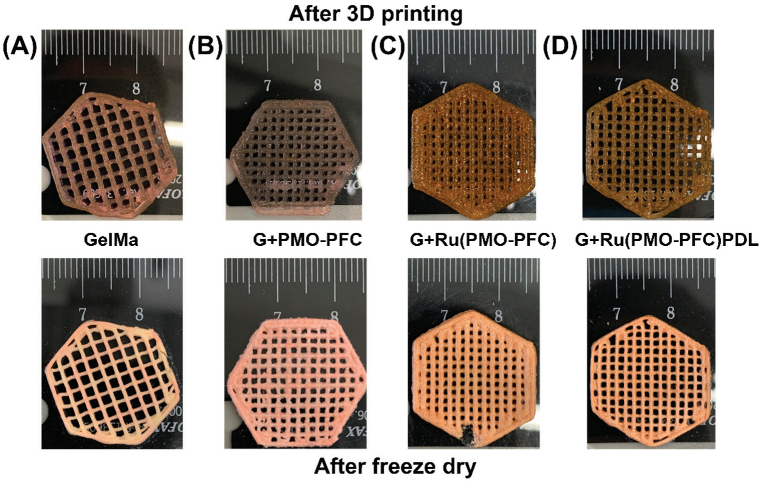

Figure 3. Photograph of 3D printed scaffolds of GelMa (**A**), G+PMO-PFC (**B**), G+Ru(PMO-PFC) (**C**) and G+Ru(PMO-PFC)PDL (**D**) (The top images are after printing; bottom images are after crosslinking and freeze-drying process).

3.4. Oxygen Release from NC Hydrogel Scaffold

To test the oxygen-carrying capacity of PMO-PFC-containing scaffolds, the scaffolds were placed in Dulbecco's Modified Eagle Medium (DMEM) and their O_2 content was measured by an oxygen sensor under normoxia and hypoxia conditions. The scaffold-containing media was kept in a hypoxia box at normoxia (Figure 4A) and hypoxia (Figure 4B) conditions for given incubation times. Under the hypoxia condition, O_2 content increases for the media with G+PMO-PFC and remains constant or higher than others for the longer period (Figure 4B), while that of the particle-free scaffold (GelMa, control) decreases after 3 h and shows almost zero O_2 content over the longer period. A similar trend is observed with media without any scaffold. However, the media with G+PMO-PFC in normoxia conditions shows constant O_2 content over the period of 4 days and then starts decreasing after 4 days. However, the decrease in O_2 content is slower in G+PMO-PFC than that in the GelMa-based scaffold (particle-free scaffold). For G+PMO-PFC, the oxygen-carrying nanoparticles release O_2 under hypoxia and normoxia conditions. It is important to note that under normoxia conditions, the scaffolds in the media interact with air, while under hypoxia they are in a closed hypoxia box at about 1% O_2. Therefore, the release of O_2 from PMO-PFC-containing scaffolds was different under normoxia and hypoxia conditions. To summarize, scaffolds containing PMO-PFC particles continuously release oxygen in the hypoxia condition and maintain oxygen levels in normoxia conditions (at least for 4 days) as compared with particle-free scaffolds.

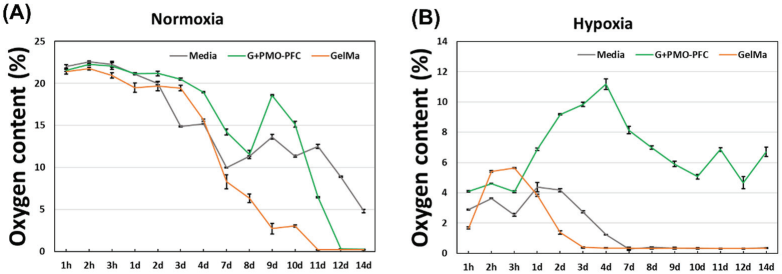

Figure 4. O_2 content of NC hydrogel scaffold under normoxia (**A**) and hypoxia condition (**B**).

3.5. Rutin Release from Rutin-Functionalized NC Hydrogel Scaffold

Rutin release from the NC scaffolds was studied to show the ability of bio-functional PMO-PFC particles for sustained drug release into the hydrogel. The initial amount of rutin per G+Ru(PMO-PFC) scaffold was ca. 46.7 µg and 42.3 µg for the G+Ru(PMO-PFC)PDL scaffold (see the supporting information for the calculation). The rutin release was performed at pH 7.4 (physiological environment) and pH 6 (tumor cell environment). Briefly, the G+Ru(PMO-PFC) and G+Ru(PMO-PFC)PDL scaffolds were placed in media for the given incubation time (30 min to 7 days) at room temperature. After reach incubation time, the media was replaced by fresh media and the absorbance of collected media was measured by UV spectroscopy. The concentration of rutin into media was then calculated from the calibration curve. The cumulative release profile (Figure 5) shows sustained release for pH 7.4 and pH 6. It is observed that at pH 6 the release of rutin is slightly higher than the release at pH 7.4 for both scaffolds. The percentage graph is shown in Figure S4. The slower and constant drug released from the hydrogels could be beneficial at a specific site until the natural tissue regenerates or is replaced by implanted artificial tissue. The slightly higher release at pH 6 could be beneficial, for example, for anticancer drug release at the tumor site. The results show that the release of rutin from NC hydrogels is sustained but not significantly pH dependent.

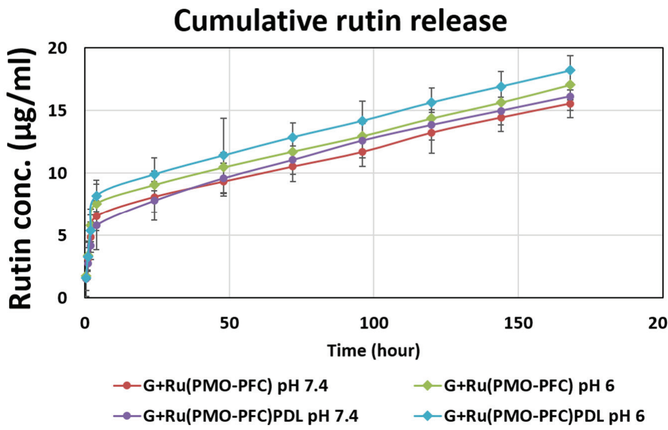

Figure 5. Rutin release (µg/mL) from NC-hydrogel scaffolds at pH 7.4 and pH 6.

3.6. Cell-Viability Experiment on NC-Hydrogel Scaffolds

To test the bio-functionality and cell-adhesiveness of the prepared NC-hydrogel scaffolds, fibroblasts cells (FBs) were used. FBs are the most common cell type present in connective tissue and play an important role in tissue repair and wound healing. For the cell experiment, the scaffolds were placed into the well plate and cells (10^4) were incubated for 1 day and 7 days, at 37 °C and 5% CO_2. The cell proliferation reagent WST-1 was used for the spectrophotometric quantification of cell viability. Figure 6 shows the cell experiment data for cell viability versus each sample for the number of incubation days. The data were normalized to the control sample (GelMa, 1day under normoxia) for each condition and incubation time. Hypoxia conditions occur when there is insufficient (lower than normal oxygen level) and heterogeneous oxygen distribution within the body tissues, which can reduce cell growth and proliferation. Hypoxia can reduce cell apoptosis, tissue necrosis, transplantation failure, and failure in tissue formation. However, oxygen-carrying particles within NC-hydrogel scaffolds can release oxygen and increase proliferation.

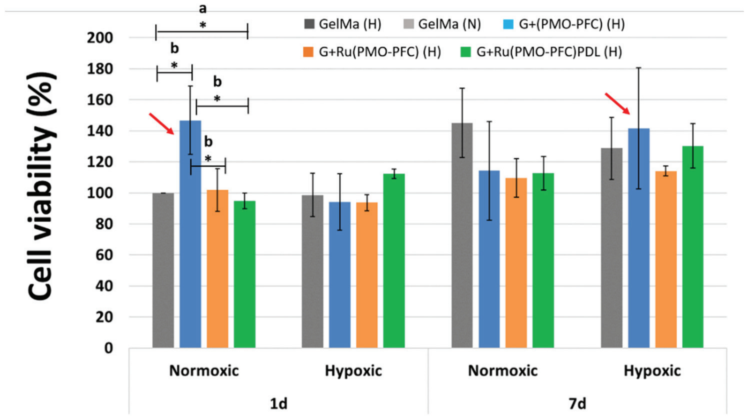

Figure 6. Cell viability of FB cells under normoxia and hypoxia conditions for 1 day and 7 days incubation times. The red arrow shows the sample with the highest effect on cell viability. ANOVA: $p < 0.05$ (*), a = significant difference between four groups, b = significant difference between two groups. Number of repeated experiments (N) = 3.

Our results show (Figure 6) that, at one day normoxia, no significant difference in the number of viable cells was observed for G+Ru(PMO-PFC) and G+Ru(PMO-PFC)PDL compared to GelMa-based scaffolds, while G+(PMO-PFC) exhibited approximately 47% more cell viability than GelMa, demonstrating the positive impact of O_2-carrying PMO-PFC on enhanced cell viability under normoxic conditions. However, under hypoxia conditions, after one day of incubation, we observed only an enhanced effect of G+Ru(PMO-PFC)PDL on cell viability (approximately 14% increase in cell viability). On the other hand, cell viability increased under normoxia from one day to seven days by approximately 45, 7, and 19% for GelMa, G+Ru(PMO-PFC) and G+Ru(PMO-PFC)PDL, respectively. However, these results were not significant for GelMa, so the effects of releasing O_2 and/or rutin on cell viability after seven days of incubation under normoxia are not apparent. Under hypoxia conditions, after seven days of incubation, cell viability was slightly lower than under normoxia only for GelMa. However, we observed a slight increase in cell viability in G+(PMO-PFC), G+Ru(PMO-PFC) and G+Ru(PMO-PFC)PDL, respectively. Furthermore, cell viability from one day to seven days also showed an increase in cell viability under hypoxia conditions due to sustained O_2 release, the antioxidant effect of rutin suppressing oxidative stress induced by hypoxia [23], and the cell-adhesive GelMa and PDL coating.

In general, our results for one day hypoxia, and seven days' normoxia and hypoxia showed no significant differences (Figure 6); we, therefore, compared the effects of G+(PMO-PFC), G+Ru(PMO-PFC), and G+Ru(PMO-PFC)PDL on cell viability under hypoxia conditions with the effects of the particle-free GelMa-based scaffold under normoxia conditions (Figure 7). We aimed, in fact, to maintain cell viability under hypoxia using O_2 delivery particles similar to cell viability under normoxia conditions. We observed that incorporation of only G+Ru(PMO-PFC)PDL (H) into GelMa was able to increase cell viability under hypoxia (H) conditions more than cell viability in GelMa under normoxia (N) conditions for a one-day incubation period. While GelMa (H), G+(PMO-PFC) (H), and G+Ru(PMO-PFC) (H) showed approximately 2%, 6%, and 7% less cell viability than GelMa (N), G+Ru(PMO-PFC)PDL (H) showed a 12% higher cell viability than GelMa (N). This result indicates the synergistic positive effect of O_2, rutin and PDL on cell viability under hypoxia conditions. After seven days of incubation, all samples displayed less cell viability under hypoxia than normoxia conditions. However, G+(PMO-PFC) (H) showed the best result compared with the other samples. Cell viability for GelMa (H), G+Ru(PMO-PFC) (H), and G+Ru(PMO-PFC)PDL (H) was 11, 21, and 10% less than GelMa (N), respectively, while cell viability for G+(PMO-PFC) (H) was only 2% less than GelMa (N). These results indicate that G+Ru(PMO-PFC)PDL and G+(PMO-PFC) can be used for one- and seven-day incubation periods, respectively, to improve or support cell viability under hypoxia conditions. Furthermore, their impact on cell viability increased over time, showing that they can support viability of cells for longer incubation times.

To summarize, the scaffold containing G+(PMO-PFC) was the best sample that increased cell viability under normoxia only after one day of incubation (Figure 6, red arrow), while it supported cell viability under hypoxia similar to normoxia but only after seven days of incubation (Figure 7, red arrow). On the other hand, G+Ru(PMO-PFC)PDL was the best sample that allowed us to increase cell viability under hypoxia slightly more than under normoxia conditions, although this effect was significant only after one day of incubation (Figure 7, dark red arrow).

Fluorescence microscopy was used to examine the morphology of the cells on the samples (Figure 8). For this, cells were incubated on NC-hydrogel scaffolds under normoxia and hypoxia for 1 day to 7 days. After incubation period, cells were nuclei- stained with Hoechst 33342 dye and actin-stained with phalloidin Alexa Fluor 488 dye. Degraded scaffolds with FB cells on the culture plate were then imaged by microscope. We observed that the FB cells on the scaffolds had a circular shape instead of their usual elongated and stretched shape. The ECM nature of hydrogels helps the cells to grow in different shapes and the shapes of the cells can be manipulated by biochemical clues and the mechanical properties of the scaffolds [49,50].

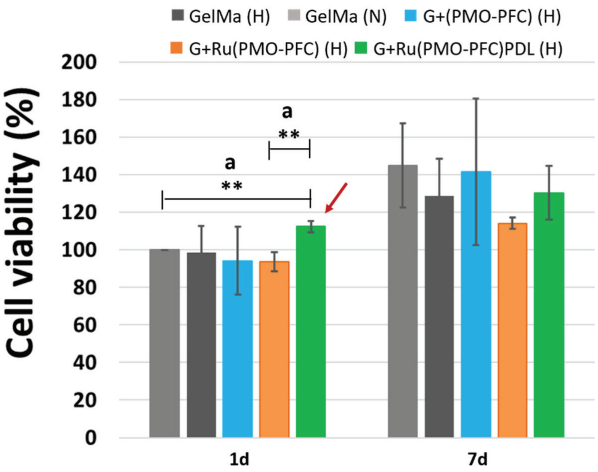

Figure 7. Comparison of the effects of G+(PMO-PFC), G+Ru(PMO-PFC), and G+Ru(PMO-PFC)PDL on cell viability under hypoxia conditions with the effects of the particle-free GelMa-based scaffold under normoxia conditions (H = hypoxia; N = normoxia). The dark red arrow shows the sample with the highest effect on cell viability. ANOVA: $p < 0.01$ (**), a = significant difference between two groups. Number of repeated experiments (N) = 3.

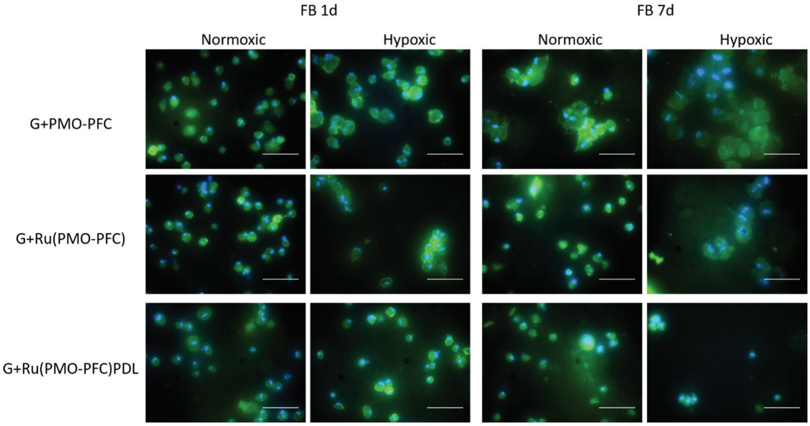

Figure 8. Fluorescence images of FB cells on NC-hydrogel scaffolds under normoxia and hypoxia conditions for 1d and 7d incubation times. Scale bar equals 50 µm.

4. Conclusions

We successfully described a method for the fabrication of NC hydrogels for co-administration of hydrophobic drug molecules and O_2 delivery. NC hydrogels provide sustained O_2 content over a 14-day period under hypoxia and normoxia conditions. The release experiment also suggests the sustained drug release for seven days. The beneficial effects of nontoxic and antioxidant rutin, cell-adhesive coating of PMO-PFCs in the 3D hydrogel networks, and O_2 release from the scaffolds on cell viability were observed only for G+(PMO-PFC and G+Ru(PMO-PFC)PDL under specific conditions and incubation times. G+(PMO-PFC) promoted cell viability under normoxia only after one day of incubation and under hypoxia after seven days of incubation. G+Ru(PMO-PFC)PDL increased cell viability more under hypoxia than under normoxia conditions in one day of incubation, demonstrating the synergistic effect of O_2 release, rutin, and PDL on cell viability. However, our results show that our systems still need to be improved to achieve better cell viability under hypoxia conditions. The improved rheological properties suggest the prepared NC hydrogels can be further tested or used as an injectable hydrogel. The enhanced mechanical properties and 3D-printability of NC hydrogels may be used for artificial tissue constructs. Therefore, overall performance of prepared NC hydrogels makes an alternate attractive route for injectable hydrogel in local area delivery and tissue regeneration for implantation. This can be further investigated for wound dressing to test the pharmacological properties of rutin for in vivo application.

Supplementary Materials: The following supporting information can be downloaded at: https://www.mdpi.com/article/10.3390/nano12081304/s1, Figure S1: Calibration curve of rutin in water at wavelength of 352 nm (A). The absorbance spectra of supernatant after rutin coating of PMO-PFCs (B); Figure S2: Swelling ratio of GelMa and NC hydrogels at 1day and 7 days; Figure S3: Degradation of GelMa and NC hydrogels at 1 day and 7 days; Figure S4: Rutin release in percentage for scaffolds at different pH value.

Author Contributions: R.K. and N.S.K. designed the experiments. R.K. performed all the experiments and the characterization of the materials. R.K. wrote the first draft; R.K. and N.S.K. edited the manuscript. All authors have read and agreed to the published version of the manuscript.

Funding: We thank the Deutsche Forschungsgemeinschaft (KE 1577/7-2) for funding.

Institutional Review Board Statement: Not applicable.

Informed Consent Statement: Not applicable.

Data Availability Statement: Not applicable.

Conflicts of Interest: The authors declare no conflict of interest.

References

1. Gaharwar, A.K.; Peppas, N.A.; Khademhosseini, A. Nanocomposite Hydrogels for Biomedical Applications. *Biotechnol. Bioeng.* **2014**, *111*, 441–453. [CrossRef] [PubMed]
2. Rafieian, S.; Mirzadeh, H.; Mahdavi, H.; Masoumi, M.E. A review on nanocomposite hydrogels and their biomedical applications. *Sci. Eng. Compos. Mater.* **2019**, *26*, 154–174. [CrossRef]
3. Lavrador, P.; Esteves, M.R.; Gaspar, V.M.; Mano, J.F. Stimuli-Responsive Nanocomposite Hydrogels for Biomedical Applications. *Adv. Funct. Mater.* **2020**, *31*, 2005941. [CrossRef]
4. Huang, J.; Liu, F.; Su, H.; Xiong, J.; Yang, L.; Xia, J.; Liang, Y. Advanced Nanocomposite Hydrogels for Cartilage Tissue Engineering. *Gels* **2022**, *8*, 138. [CrossRef]
5. Lee, J.H. Injectable hydrogels delivering therapeutic agents for disease treatment and tissue engineering. *Biomater. Res.* **2018**, *22*, 27. [CrossRef] [PubMed]
6. Nichol, J.W.; Koshy, S.T.; Bae, H.; Hwang, C.M.; Yamanlar, S.; Khademhosseini, A. Cell-laden microengineered gelatin methacrylate hydrogels. *Biomaterials* **2010**, *31*, 5536–5544. [CrossRef]
7. Song, F.; Li, X.; Wang, Q.; Liao, L.; Zhang, C. Nanocomposite Hydrogels and Their Applications in Drug Delivery and Tissue Engineering. *J. Biomed. Nanotechnol.* **2015**, *11*, 40–52. [CrossRef] [PubMed]
8. Rizzo, F.; Kehr, N.S. Recent Advances in Injectable Hydrogels for Controlled and Local Drug Delivery. *Adv. Healthc. Mater.* **2020**, *10*, 2001341. [CrossRef]
9. Tutar, R.; Motealleh, A.; Khademhosseini, A.; Kehr, N.S. Functional Nanomaterials on 2D Surfaces and in 3D Nanocomposite Hydrogels for Biomedical Applications. *Adv. Funct. Mater.* **2019**, *29*, 1904344. [CrossRef]
10. Hou, L.; Shi, Y.; Jiang, G.; Liu, W.; Han, H.; Feng, Q.; Ren, J.; Yuan, Y.; Wang, Y.; Shi, J.; et al. Smart nanocomposite hydrogels based on azo crosslinked graphene oxide for oral colon-specific drug delivery. *Nanotechnology* **2016**, *27*, 315105. [CrossRef]
11. Pacelli, S.; Maloney, R.; Chakravarti, A.R.; Whitlow, J.; Basu, S.; Modaresi, S.; Gehrke, S.; Paul, A. Controlling Adult Stem Cell Behavior Using Nanodiamond-Reinforced Hydrogel: Implication in Bone Regeneration Therapy. *Sci. Rep.* **2017**, *7*, 6577. [CrossRef] [PubMed]
12. Zhao, W.; Odelius, K.; Edlund, U.; Zhao, C.; Albertsson, A.-C. In Situ Synthesis of Magnetic Field-Responsive Hemicellulose Hydrogels for Drug Delivery. *Biomacromolecules* **2015**, *16*, 2522–2528. [CrossRef]
13. Alvarez, G.S.; Hélary, C.; Mebert, A.M.; Wang, X.; Coradin, T.; Desimone, M.F. Antibiotic-loaded silica nanoparticle–collagen composite hydrogels with prolonged antimicrobial activity for wound infection prevention. *J. Mater. Chem. B* **2014**, *2*, 4660. [CrossRef] [PubMed]

14. Motealleh, A.; Kart, D.; Czieborowski, M.; Kehr, N.S. Functional Nanomaterials and 3D-Printable Nanocomposite Hydrogels for Enhanced Cell Proliferation and for the Reduction of Bacterial Biofilm Formation. *ACS Appl. Mater. Interfaces* **2021**, *13*, 43755–43768. [CrossRef] [PubMed]
15. Motealleh, A.; Dorri, P.; Kehr, N.S. Injectable polymer/nanomaterial composites for the fabrication of three-dimensional biomaterial scaffolds. *Biomed. Mater.* **2020**, *15*, 045021. [CrossRef] [PubMed]
16. Zhou, L.; Chen, F.; Hou, Z.; Chen, Y.; Luo, X. Injectable self-healing CuS nanoparticle complex hydrogels with antibacterial, anti-cancer, and wound healing properties. *Chem. Eng. J.* **2021**, *409*, 128224. [CrossRef]
17. Dimatteo, R.; Darling, N.J.; Segura, T. In situ forming injectable hydrogels for drug delivery and wound repair. *Adv. Drug Deliv. Rev.* **2018**, *127*, 167–184. [CrossRef]
18. Spicer, C.D. Hydrogel scaffolds for tissue engineering: The importance of polymer choice. *Polym. Chem.* **2020**, *11*, 184–219. [CrossRef]
19. Nezhad-Mokhtari, P.; Ghorbani, M.; Roshangar, L.; Soleimani Rad, J. A review on the construction of hydrogel scaffolds by various chemically techniques for tissue engineering. *Eur. Polym. J.* **2019**, *117*, 64–76. [CrossRef]
20. El-Sherbiny, I.M.; Yacoub, M.H. Hydrogel scaffolds for tissue engineering: Progress and challenges. *Glob. Cardiol. Sci. Pract.* **2013**, *2013*, 38. [CrossRef]
21. Gullón, B.; Lú-Chau, T.A.; Moreira, M.T.; Lema, J.M.; Eibes, G. Rutin: A review on extraction, identification and purification methods, biological activities and approaches to enhance its bioavailability. *Trends Food Sci. Technol.* **2017**, *67*, 220–235. [CrossRef]
22. Ganeshpurkar, A.; Saluja, A.K. The Pharmacological Potential of Rutin. *Saudi Pharm. J.* **2017**, *25*, 149–164. [CrossRef] [PubMed]
23. Negahdari, R.; Bohlouli, S.; Sharifi, S.; Maleki Dizaj, S.; Rahbar Saadat, Y.; Khezri, K.; Jafari, S.; Ahmadian, E.; Gorbani Jahandizi, N.; Raeesi, S. Therapeutic benefits of rutin and its nanoformulations. *Phytother. Res.* **2020**, *35*, 1719–1738. [CrossRef] [PubMed]
24. Júlio, A.; Caparica, R.; Costa Lima, S.A.; Fernandes, A.S.; Rosado, C.; Prazeres, D.M.F.; Reis, S.; Santos de Almeida, T.; Fonte, P. Ionic Liquid-Polymer Nanoparticle Hybrid Systems as New Tools to Deliver Poorly Soluble Drugs. *Nanomaterials* **2019**, *9*, 1148. [CrossRef]
25. Wu, H.; Su, M.; Jin, H.; Li, X.; Wang, P.; Chen, J.; Chen, J. Rutin-Loaded Silver Nanoparticles With Antithrombotic Function. *Front. Bioeng. Biotechnol.* **2020**, *8*, 1356. [CrossRef]
26. Hu, B.; Dai, F.; Fan, Z.; Ma, G.; Tang, Q.; Zhang, X. Nanotheranostics: Congo Red/Rutin-MNPs with Enhanced Magnetic Resonance Imaging and H2O2-Responsive Therapy of Alzheimer's Disease in APPswe/PS1dE9 Transgenic Mice. *Adv. Mater.* **2015**, *27*, 5499–5505. [CrossRef]
27. Mishra, S.; Mishra, S.R.; Soni, H. Efficacy of Hydrogel Containing Rutin in Wound Healing. *EAS J. Pharm. Pharmacol.* **2021**, *3*, 161–167. [CrossRef]
28. Zhao, L.; Qi, X.; Cai, T.; Fan, Z.; Wang, H.; Du, X. Gelatin hydrogel/contact lens composites as rutin delivery systems for promoting corneal wound healing. *Drug Deliv.* **2021**, *28*, 1951–1961. [CrossRef]
29. Tran, N.Q.; Joung, Y.K.; Lih, E.; Park, K.D. In Situ Forming and Rutin-Releasing Chitosan Hydrogels As Injectable Dressings for Dermal Wound Healing. *Biomacromolecules* **2011**, *12*, 2872–2880. [CrossRef]
30. Farris, A.L.; Rindone, A.N.; Grayson, W.L. Oxygen delivering biomaterials for tissue engineering. *J. Mater. Chem. B* **2016**, *4*, 3422–3432. [CrossRef]
31. Camci-Unal, G.; Alemdar, N.; Annabi, N.; Khademhosseini, A. Oxygen-releasing biomaterials for tissue engineering. *Polym. Int.* **2013**, *62*, 843–848. [CrossRef] [PubMed]
32. Alemdar, N.; Leijten, J.; Camci-Unal, G.; Hjortnaes, J.; Ribas, J.; Paul, A.; Mostafalu, P.; Gaharwar, A.K.; Qiu, Y.; Sonkusale, S.; et al. Oxygen-Generating Photo-Cross-Linkable Hydrogels Support Cardiac Progenitor Cell Survival by Reducing Hypoxia-Induced Necrosis. *ACS Biomater. Sci. Eng.* **2016**, *3*, 1964–1971. [CrossRef] [PubMed]
33. Kang, J.I.; Park, K.M.; Park, K.D. Oxygen-generating alginate hydrogels as a bioactive acellular matrix for facilitating wound healing. *J. Ind. Eng. Chem.* **2019**, *69*, 397–404. [CrossRef]
34. Patil, P.S.; Fountas-Davis, N.; Huang, H.; Michelle Evancho-Chapman, M.; Fulton, J.A.; Shriver, L.P.; Leipzig, N.D. Fluorinated methacrylamide chitosan hydrogels enhance collagen synthesis in wound healing through increased oxygen availability. *Acta Biomater.* **2016**, *36*, 164–174. [CrossRef]
35. Li, H.; Wijekoon, A.; Leipzig, N.D. Encapsulated Neural Stem Cell Neuronal Differentiation in Fluorinated Methacrylamide Chitosan Hydrogels. *Ann. Biomed. Eng.* **2013**, *42*, 1456–1469. [CrossRef]
36. Park, S.; Park, K.M. Hyperbaric oxygen-generating hydrogels. *Biomaterials* **2018**, *182*, 234–244. [CrossRef]
37. Hyun, H.; Yoo, Y.; Kim, S.; Ko, H.; Chun, H.; Yang, D. Hydrogel-Mediated DOX·HCl/PTX Delivery System for Breast Cancer Therapy. *Int. J. Mol. Sci.* **2019**, *20*, 4671. [CrossRef]
38. Darge, H.F.; Andrgie, A.T.; Hanurry, E.Y.; Birhan, Y.S.; Mekonnen, T.W.; Chou, H.-Y.; Hsu, W.-H.; Lai, J.-Y.; Lin, S.-Y.; Tsai, H.-C. Localized controlled release of bevacizumab and doxorubicin by thermo-sensitive hydrogel for normalization of tumor vasculature and to enhance the efficacy of chemotherapy. *Int. J. Pharm.* **2019**, *572*, 118799. [CrossRef]
39. Song, H.; Yang, P.; Huang, P.; Zhang, C.; Kong, D.; Wang, W. Injectable polypeptide hydrogel-based co-delivery of vaccine and immune checkpoint inhibitors improves tumor immunotherapy. *Theranostics* **2019**, *9*, 2299–2314. [CrossRef]
40. Newland, B.; Baeger, M.; Eigel, D.; Newland, H.; Werner, C. Oxygen-Producing Gellan Gum Hydrogels for Dual Delivery of Either Oxygen or Peroxide with Doxorubicin. *ACS Biomater. Sci. Eng.* **2017**, *3*, 787–792. [CrossRef]

41. Motealleh, A.; Schäfer, A.H.; Fromm, O.; Kehr, N.S. 3D-Printed Oxygen-Carrying Nanocomposite Hydrogels for Enhanced Cell Viability under Hypoxic and Normoxic Conditions. *Biomacromolecules* **2021**, *22*, 4758–4769. [CrossRef] [PubMed]
42. Kumar, R.; Kehr, N.S. Oxygen and Drug-carrying Periodic Mesoporous Organosilicas for Enhanced Cell Viability under Normoxic and Hypoxic Conditions. *Int. J. Mol. Sci.* 2022; *manuscript in preparation*.
43. Jensen, C.; Teng, Y. Is It Time to Start Transitioning From 2D to 3D Cell Culture? *Front. Mol. Biosci.* **2020**, *7*, 33. [CrossRef] [PubMed]
44. Zhu, M.; Wang, Y.; Ferracci, G.; Zheng, J.; Cho, N.-J.; Lee, B.H. Gelatin methacryloyl and its hydrogels with an exceptional degree of controllability and batch-to-batch consistency. *Sci. Rep.* **2019**, *9*, 6863. [CrossRef]
45. Riess, J.G. Understanding the Fundamentals of Perfluorocarbons and Perfluorocarbon Emulsions Relevant toIn VivoOxygen Delivery. *Artif. Cells Blood Substit. Biotechnol.* **2009**, *33*, 47–63. [CrossRef] [PubMed]
46. Fang, R.; Jing, H.; Chai, Z.; Zhao, G.; Stoll, S.; Ren, F.; Liu, F.; Leng, X. Study of the physicochemical properties of the BSA: Flavonoid nanoparticle. *Eur. Food Res. Technol.* **2011**, *233*, 275–283. [CrossRef]
47. Peng, B.; Li, R.; Yan, W. Solubility of Rutin in Ethanol + Water at (273.15 to 323.15) K. *J. Chem. Eng. Data* **2009**, *54*, 1378–1381. [CrossRef]
48. Advincula, R.C.; Dizon, J.R.C.; Caldona, E.B.; Viers, R.A.; Siacor, F.D.C.; Maalihan, R.D.; Espera, A.H. On the progress of 3D-printed hydrogels for tissue engineering. *MRS Commun.* **2021**, *11*, 539–553. [CrossRef] [PubMed]
49. Sarker, B.; Singh, R.; Silva, R.; Roether, J.A.; Kaschta, J.; Detsch, R.; Schubert, D.W.; Cicha, I.; Boccaccini, A.R. Evaluation of Fibroblasts Adhesion and Proliferation on Alginate-Gelatin Crosslinked Hydrogel. *PLoS ONE* **2014**, *9*, e107952. [CrossRef]
50. Liu, H.; Wu, M.; Jia, Y.; Niu, L.; Huang, G.; Xu, F. Control of fibroblast shape in sequentially formed 3D hybrid hydrogels regulates cellular responses to microenvironmental cues. *NPG Asia Mater.* **2020**, *12*, 45. [CrossRef]

nanomaterials

Article

Damage Accumulation Phenomena in Multilayer (TiAlCrSiY)N/(TiAlCr)N, Monolayer (TiAlCrSiY)N Coatings and Silicon upon Deformation by Cyclic Nanoindentation

Anatoly I. Kovalev [1,2,*], Vladimir O. Vakhrushev [1,2], Ben D. Beake [3], Egor P. Konovalov [1,2], Dmitry L. Wainstein [1,2], Stanislav A. Dmitrievskii [1], German S. Fox-Rabinovich [4] and Stephen Veldhuis [4]

[1] State Scientific Centre, I.P. Bardin Central Research Institute for Ferrous Metallurgy, 23/9 bdg, 2, Radio Str., 105005 Moscow, Russia; gareq1211@gmail.com (V.O.V.); filin.capmer@gmail.com (E.P.K.); d_wainstein@sprg.ru (D.L.W.); info@sprg.ru (S.A.D.)
[2] Surface Phenomena Researches Group, LLC, Staropimenovsky Lane, 6, bdg. 1, off. 4, 127006 Moscow, Russia
[3] Micro Materials Ltd., Willow House, Yale Business Village, Ellice Way, Wrexham LL13 7YL, UK; ben@micromaterials.co.uk
[4] Department of Mechanical Engineering (JHE-316), McMaster University, 1280 Main Street West, Hamilton, Ontario, ON L8S 4L7, Canada; gfox@mcmaster.ca (G.S.F.-R.); veldhu@mcmaster.ca (S.V.)
* Correspondence: a_kovalev@sprg.ru; Tel.: +7-495-777-94-10

Citation: Kovalev, A.I.; Vakhrushev, V.O.; Beake, B.D.; Konovalov, E.P.; Wainstein, D.L.; Dmitrievskii, S.A.; Fox-Rabinovich, G.S.; Veldhuis, S. Damage Accumulation Phenomena in Multilayer (TiAlCrSiY)N/(TiAlCr)N, Monolayer (TiAlCrSiY)N Coatings and Silicon upon Deformation by Cyclic Nanoindentation. *Nanomaterials* **2022**, *12*, 1312. https://doi.org/10.3390/nano12081312

Academic Editors: Jihoon Lee and Ming-Yu Li

Received: 1 March 2022
Accepted: 6 April 2022
Published: 11 April 2022

Abstract: The micromechanism of the low-cycle fatigue of mono- and multilayer PVD coatings on cutting tools was investigated. Multilayer nanolaminate (TiAlCrSiY)N/(TiAlCr)N and monolayer (TiAlCrSiY)N PVD coatings were deposited on the cemented carbide ball nose end mills. Low-cycle fatigue resistance was studied using the cyclic nanoindentation technique. The obtained results were compared with the behaviour of the polycrystalline silicon reference sample. The fractal analysis of time-resolved curves for indenter penetration depth demonstrated regularities of damage accumulation in the coatings at the early stage of wear. The difference in low-cycle fatigue of the brittle silicon and nitride wear-resistant coatings is shown. It is demonstrated that when distinguished from the single layer (TiAlCrSiY)N coating, the nucleation and growth of microcracks in the multilayer (TiAlCrSiY)N/(TiAlCr)N coating is accompanied by acts of microplastic deformation providing a higher fracture toughness of the multilayer nanolaminate (TiAlCrSiY)N/(TiAlCr)N.

Keywords: micro-impact fatigue; wear hard coatings; study state cutting; fractal analysis

1. Introduction

Simple and complex ion-plasma PVD coatings based on titanium and aluminium nitrides are widely used in the metalworking industry to improve the wear resistance of cutting tools. There are several concepts for designing such coatings. The first one is based on the permanent increasing of the hardness of the nitrides. Such coatings are aimed on the passive wear resistance during cutting and they are destroyed due to damage accumulation [1]. Chemical and phase composition of the second group of hard coatings is selected in a way that provides favourable conditions for their tribo-oxidation when protective oxide films are dynamically formed on the surface of the cutting tool [2]. These amorphous oxide films have a thickness of several nanometres. They radically reduce the friction and thermal conductivity coefficients in the wear region [3]. In this way, such coatings are adapting themselves to severe tribological conditions manifesting to the greatest extent in conditions of high-speed dry cutting.

Nanolaminate multilayer coatings for cutting tools have been proposed in the last decade as a more promising alternative to traditional monolayer coatings. Multilayer coatings show high hardness, crack resistance, and toughness when compared with monolayer coatings. The general idea of the surface engineered, multilayer PVD coatings is to design their composition and architecture that provides adaptive spatio-temporal behaviour of the coating [3,4]. This generation of coatings provides the following: the highest possible adhesion to the substrate; the ability of the coating layer to accumulate and dissipate energy simultaneously that is typical for nanostructures; and high surface protection/lubrication with an additional objective of better wear behaviour in a highly loaded contact with a workpiece and a chip.

The main advantage of multilayer coatings is associated with obstruction of the transboundary propagation of microcracks. Ultimately, the cutting tool coatings break down, but we can extend their operational resource by controlling their architecture and physico-chemical transformations in the cutting zone. In recent years, the mechanisms of degradation of cutting tool coatings have been studied by microstructural methods. However, these very detailed studies have discussed superhard coatings on late wear stages. The coatings had a weak interlayer adhesive strength [5] or were multilayer ceramic–metallic or nitride–metallic coatings TiN/Ti characterized by a sharp difference in the elastic-plastic properties of individual layers [6]. The wear of hard coatings has a multi-stage mechanism. Obviously, the phase composition of the wear products of PVD coatings is also changed during various stages of cutting.

The running-in stage is the most aggressive in terms of its external impact on the cutting tool. It largely determines the further behaviour of the tool during cutting. Protection against damage accumulation is the first and the most significant function of the coating at this stage. Indeed, features of a defective structure formation in wear-resistant coatings at the initial stage of wear are not studied sufficiently regardless of the fact that this stage determines the further service of the cutting tool. Nanolaminate multilayer composites deformed in the wear zone are complicated objects for structural studies because the accumulation of crystal lattice defects including their influence on tool wear during operation is an unusual task. The aim of this work was the investigation of damage accumulation in multilayer adaptive coatings at the running-in stage and their influence on subsequent stages of wear.

Nanoindentation impact testing is one of the representative methods of mechanical testing providing rich information about the elastic–plastic properties of materials. This method allows studying physical and mechanical properties at the nanoscale down to interatomic distances inaccessible to common mechanical testing techniques such as standard Vickers, Berkovich, Knoop, and Rockwell hardness tests [7–9]. Until now, theoretical and experimental studies in this area have looked for ways to improve the accuracy in determining the strength, toughness, and ductility values for various materials basing on indentation data [10–12]. Nanoindentation is one of the most significant methods to measure mechanical properties of surface layers and thin films in submicron regions [13].

This method allows measuring the alteration in micromechanical properties of the nanolaminate coating in course of cyclic deformation. Statistical processing of time series allows us to analyse the influence of previous events on subsequent ones. The successful experience of such application of cyclic nanoindentation was demonstrated in a study on the wear of PVD multilayer coatings [14]. In this work, damage accumulation in solid, single layer (TiAlCrSiY)N and multilayer (TiAlCrSiY)N/(TiAlCr)N PVD coatings at the initial wear stage was investigated. These results were compared with the destruction of hard and brittle silicon.

2. Materials and Methods

The multilayer $Ti_{0.2}Al_{0.55}Cr_{0.2}Si_{0.03}Y_{0.02}N/Ti_{0.25}Al_{0.65}Cr_{0.1}N$ and monolayer $Ti_{0.2}Al_{0.55}Cr_{0.2}Si_{0.03}Y_{0.02}N$ coatings were deposited using $Ti_{0.2}Al_{0.55}Cr_{0.2}Si_{0.03}Y_{0.02}$ and $Ti_{0.25}Al_{0.65}Cr_{0.1}$ targets that were correspondingly fabricated by a powder metallurgical process on cemented carbide ball nose end mills WC-Co substrate in an R&D-type hybrid PVD coater (Kobe Steel Ltd., Koube, Japan) using a plasma-enhanced arc source. The multilayer coating had 30 bilayers. WC-Co samples were heated up to about 500 °C and cleaned by Ar ion etching. During the PVD process, an Ar-N_2 gas mixture was fed to the chamber at a pressure of 2.7 Pa with nitrogen partial pressure of 1.3 Pa. The arc source was operated at 100 A for a 100 mm diameter × 16 mm thick target. The other deposition parameters were bias voltage 100 V and substrate rotation 5 rpm. The thickness of the coating studied was around 3 μm for the film characterization and micro-scale impact testing. The coating has a nanocrystalline multi-layered microstructure with alternating nanolayers periods of 20–30 nm [15,16] and a hardness of 30 GPa measured using the nanoindentation method at room temperature and 28 GPa at 500 °C [17]. Under micromechanical testing these coatings were compared with polycrystalline Si. Micromechanical characteristics were determined using a Micro Materials NanoTest System setup. A trigonal diamond pyramid with the angle of 65.3° penetrated the sample with coating at the loads of 25 mN, 30 mN, 40 mN, and 50 mN. The cyclic load and unloading with the period of 4 s were repeated many times for 5 min. The penetration depth vs. the cyclic loading time was registered automatically. Prior to indentation tests, the calibration of the indenter tip was carried out employing a fused silica sample. Cyclic nanoindentation loading were carried out on three different samples of Si, monolayer, and multilayer coated systems and the penetration depth versus time was recorded continuously at a constant indentation rate of 0.05 s^{-1}.

These studies allowed for modelling the behaviour of the material at low-cycle fatigue. In the micro-impact test there is a quasi-static indentation before the first actual impact. The on-load indentation depth (h_0) associated with this is recorded and used to confirm that the depth zero is measured correctly and that the test did not impact an anomalous region of the surface. Subsequently, the probe depth is recorded "on-load" for every impact. A detailed description of cyclic nanoindentation technique is given in [2]. In our case, all micro-impact tests were carried out by one diamond indenter to exclude the influence of probe geometry [18].

3. Results and Discussion

Cutting tools are operating under low-cycle fatigue conditions. At the initial stage of cutting tool wear, elastic–plastic deformation is observed, accompanied by strain hardening and active nucleation, and accumulation of crystal lattice imperfections. The micro-cracking completes these processes of plastic deformation. In this regard, the resistance of the coating to low-cycle fatigue can affect the operational resource of the cutting tool.

Indicative displacement/penetration vs. time curves for four different indentation maximum loads ranging from 25 mN to 50 mN are shown in Figure 1. During the first few impacts, the depth increases rapidly, gradually slowing to approach a plateau where the depth is almost unchanged with each successive impact. The monolayer coating compared to the multilayer one is characterised by lower resistance to cyclic loading already at the earliest stage of the testing. Moreover, already in the first 30 s, the indenter penetration in the single layer coating was about 1000 nm, and penetration depth increases rapidly. A sharp jump on the curve means the formation of forked microcracks propagating to a big depth. In the multilayer coating, plastic deformation was developed gradually with some incubation time, and after 50 s the maximal penetration depth did not exceed 280 nm at the bug jump. This is comparable to the propagation of microdefects through six bilayers. During the incubation time, at almost 20 s from the start of the experiment, up to 50 s, the swings were about 30–50 nm of the penetration depth corresponding to the nucleation and propagation of cracks in one layer. After 50 s, the depth of penetration of the indenter into the monolayer coating was bigger than for the multilayer one. This means a higher level of damage accumulation at this stage of the test in the monolayer coating.

Comparable results of Si nanoimpact with spherical indenter were presented in [19].

For silicon reference samples, the results of cyclic nanoindentation differ significantly from the nitride coatings behaviour. Silicon is an extremely brittle material. It is known that depending on the load during nanoindentation, a series of phase transitions occurs in silicon. In the literature, such effects are associated with the formation of new phases, in particular, Si–II phase with an increase in the load and Si–III/Si–XII phases at the reset [19].

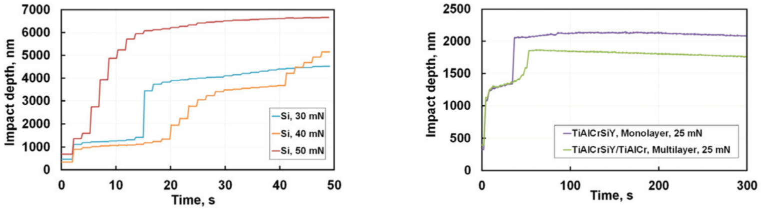

(**a**) (**b**)

Figure 1. Short-term indenter penetration depth at 30–50 mN, 50 s for Si reference sample (**a**) and for monolayer and multilayer coatings at 25 mN, 300 s (**b**).

The increase of maximal load to 40 and 50 mN radically changes nanoindentation curves probably associated with phase transitions already initiated at the initial stage of cyclic testing because it correlates with dependences of such phase transformations on the load and loading rate described in [20]. After a short incubation period, the elastoplastic deformation in this brittle material develops, accompanied by the formation of a sufficient amount of dislocation sources forming initial microcracks, which are then merged into main ones. Nanoindentation curves demonstrate discontinuities of a spontaneous rise in the indenter penetration depth. In this case, the characteristic time of such a jump is much shorter than the experiment sampling time equal to 0.05 s. This means that Si–II → Si–III/Si–XII phase transition is accompanied by a rapid expansion of the crystalline lattice volume in a new phase of structural transformations, which leads to peak stress growth exceeding the critical ones for the formation of brittle cracks.

These discontinuities known in the literature as pop-ins and pop-outs [21] manifest themselves as sudden steps crack propagation in both loading and unloading stages. It is comprehensible that the occurrence of a pop-in is strongly connected with free length of crack propagation. The length of free propagation for such microfractures depends on the crystalline structure of different silicon polymorphic phases. A significant differentiation in jumps of the indenter penetration on these curves occurs due to variations in free propagation length of brittle microcracks. As we see in silicon, microcracks can unite and propagate over considerable distances comparable with pop-in jumps.

Conversion of test results to the dependence of contact stress from test time allows for a better understanding of the development of microstructural defects. These contact stresses could be calculated using well-known equations for hardness but one should take into account the presence of both elastic and plastic components of deformation while the microhardness values refer only to the plastic deformation of the sample. When assessing the microhardness of a heterophase layered nanocomposite, the microhardness of a bilayer is calculated taking into account the volume fraction of phases [12]. Assuming that elastoplastic properties of layers in a TiAlCrSiYN/TiAlCrN multilayer coating do not differ significantly, the contact stress σ can be determined from the generally accepted expression:

$$\sigma = \mathrm{P}_{\mathrm{max}}/\mathrm{A}, \tag{1}$$

where A is the actual projected contact area indenter with material at maximal load $\mathrm{P}_{\mathrm{max}}$.

In modern nanoindentation systems, the hardness is defined without the optical control of final residual imprint. A as defined by area function is directly determined from the "load-displacement curve" [22]. A dependence of hardness and contact stress in our case on the indenter penetration depth h can be represented as:

$$\sigma = 0.00387\ \mathrm{P}_{\mathrm{max}}/\mathrm{h}^2, \tag{2}$$

where h is the penetration depth. It is clear that σ includes components of elastic and plastic deformation, and we neglect (similarly to Vickers hardness measurement procedure) the formation of cracks near the impression.

Figure 2 presents the re-calculated results of cyclic nanoindentation for polycrystalline silicon (a) and coatings (b). The stresses of cracks initiation and propagation for coatings are significantly lower than those for silicon. The results for silicon are presented in Stress (MPa). It is most probable that steps of constant stresses for Si at loads of 30 mN and 50 mN correspond to the activation of dislocation sources or due to the joining of lateral cracks. The sharp drop in stress occurrences is due to their relaxation during coalescence and rapid propagation of brittle cracks. The noticeable difference in curves for 30, 40, and 50 mN can be explained by phase transformations that already developed at the initial moments of nanoindentation.

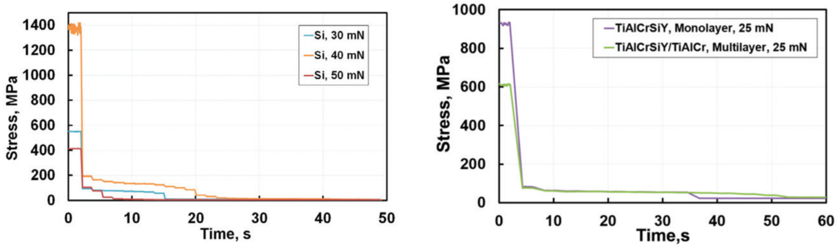

(**a**) (**b**)

Figure 2. Dependence of stress on the cyclic nanoindentation time at 30–50 mN, 70 s for Si reference (**a**) and at 25 mN, 70 s for monolayer and multilayer coatings (**b**).

Silicon exhibits a phase transformation at pressures 9 to 16 GPa. Cubic diamond (Si-I) phase is transformed into the metallic one β-tin (Si-II) and accompanied by a densification (volume contraction) of about 20%. Experiments also indicate that the first phase formed from Si-II in 10–12 GPa, under slow decompression, was Si-XII (or R8-rhombohedral structure with eight atoms per unit cell), leading to a 9% expansion of material [23]. At further decompressing of Si, the degree of rhombohedral distortion gradually decreases and a mixture of Si-XII and Si-III phases (bcc 8 body-centred cubic structure with 16 atoms per unit cell) is produced, whereas the Si-XII remains at ambient pressure. Various investigations [20–25] have shown the probability of phase transformations in silicon during nanoindentation. One can assume that slip bands are arising during nanoindentation under load localisation, and their hindering provides peak stresses initiating phase transformations in local shear bands at a lower level in the range of 30–50 mN than was described in the literature [23].

One can see in Figures 1 and 2 that opposed to brittle silicon, the single- and multilayer coatings behave as constant values of stresses and penetration depth achieved at indentation time from 5 to 35 s. This stage of cyclic nanoindentation is developing at a depth of about 100 nm. We can assume that dislocation sources are initiated at this time. Microplastic deformation in these coatings is developing without flashy growth of microcracks. For later impact testing times microcracks in the monolayer coating are nucleating and growing to the critical length. Stresses in the multilayer coating remain stable during a long enough time when microcracks grow, reaching their critical length. Then, microcracks grow without increasing the applied stresses propagating into the volume, which leads to stress relaxation. Microplastic deformation of a multilayer coating takes a much longer time and stops with gradual stress-decreasing as a result of the initiation and propagation of microcracks into the coating layers depth of about 280 nm corresponding to six TiAlCrSiYN/TiAlCrN bilayers. Formation of hills around indentations in the case of microplastic deformation and its absence at brittle cracking was previously shown on SEM images of imprints in [2,14] (Figure 3).

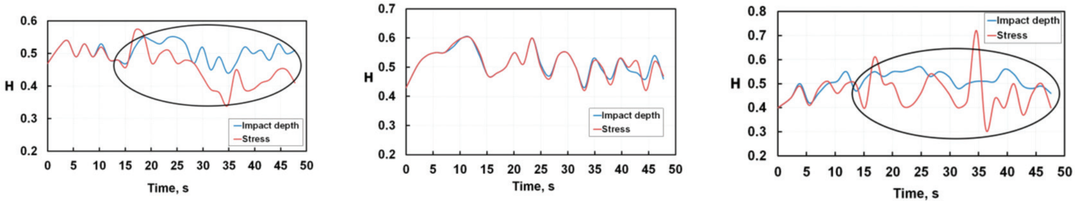

(**a**) (**b**) (**c**)

Figure 3. Cyclic variations of Hurst exponents for fatigue tests of silicon at 30 mN (**a**), 40 mN (**b**), and 50 mN (**c**) loads.

In accordance with the Mises principle [24], microplastic deformation can develop in neighbouring regions in the presence of compatible deformation. It can be assumed that a high number of interfaces in a multilayer coating should sharply reduce the plasticity due to the disarrangement in compatibility in the transfer of the dislocation slip between layers, but such a coating has a big margin of toughness compared with the monolayer coating. This is clearly seen when we compare indentation depth stabilisation from 7 s to 52 s of the impact. There are two reasons for this phenomenon. The first is that a good crystallographic conformity exists between the TiAlCrSiYN and TiAlCrN layers during their epitaxial growth. The second reason is that the initiation and growth of microcracks in each of the layers in the multilayer coating prevails over their transboundary propagation. At the same time, the mature substructure and the small thickness of several nanometre layers can significantly reduce peak Peierls stresses [26] and slow the growth of microcracks to their critical size. The stabilisation of the indentation depth and the constancy of stresses at long test times up to 300 s (Figures 1 and 2) may be due to the strain hardening and the stabilization of coating plastic deformation at the selected indentation load.

The monolayer coating has lower impact toughness and it is fractured with cascade formation of brittle cracks throughout the entire volume of the material. In the multilayer coating, microcracking is developing in several layers by sequential propagating of microcracks between layers. This process is energy-consuming with one comparing to simple crack branching in a monolayer. Obviously, during wear of coatings as in course of cyclic nanoindentation tests, mechanical load is accompanied by microplastic deformation, microcrack formation, and strain hardening.

It was of considerable interest to study the influence of initial stages of coating degradation on further ones. For this purpose, the indentation curves shown in Figures 1 and 2 were subjected to fractal analysis.

We used the Hurst exponent as a tool measuring the long-term influence of previous events on subsequent ones developed during nanoimpact tests. To determine the Hurst exponent, nanoindentation curves presented in Figures 1 and 2 for 300 s of testing were rescaled in short time intervals corresponding to individual jumps. For each series, the following was determined: the end of the time series, the average value of the penetration depth in each series, the difference between the maximum and minimum values (R), standard deviation (S), and number of measurements (pulses) (N). The Hurst parameter (H) was calculated using the following formula:

$$H = \log(R/S)/\log(N/2), \tag{3}$$

In this analysis three ranges of the Hurst exponent are considered. The H value of 0.5 corresponds to a stochastic uncorrelated process. In this case, the prior and posterior events are divorced from each other. The current process does not determine the following one. If $0 \leq H < 0.5$, the process is unstable similar to the "white noise" when a mean reversion is observed. A Hurst exponent in the range of $0.5 < H < 1$ represents a sequence of events coupled in time. Here, events inherit from previous ones, and each previous event affects the next one. In terms of chaotic dynamics, the process sensitivity to initial conditions is observed in this case. Moreover, such long-term memory is preserved over the whole analysed time series. That is, short-term processes will affect further short-term processes, and long-term processes will affect further long-term processes. At H exceeding 0.5, the time series is a fractal and the series of self-similar processes are observed in it.

Figure 3 shows the cyclic variation of the Hurst exponent for nanoimpact tests of silicon. The blue colour corresponds to calculations based on Figure 1 depth-time plots; the red colour corresponds to the calculation based on Figure 2 stress-time. As one can see, weakly interdependent processes are observed only in the very initial period up to 15 s of nanoindentation at a load of 40 mN. This means that in the initial period of testing there is a close relationship between the microcracks initiation and their propagation. In all other cases during nanoindentation, the Hurst exponent value is less than 0.5, and degradation of silicon develops as a stochastic process. At the 40 mN load, the curves of the Hurst exponent calculated from the drop-in stresses or the increase in the depth of the crater, are in alignment, but at other loads the divergence of the curves becomes noticeable after 15 s. These regions are marked by ovals on the plots. Most likely this difference in Hurst exponents is observed because at this fatigue stage, the cascade of the lateral branching of cracks develops in silicon, and the real contact area between indenter and material distinguishes from what one expects for a given penetration depth. As the Hurst exponent value for silicon is on average about 0.5, its fatigue brittle fracture occurs as a stochastic process, when in the simplest case the branching of cracks does not relate to the number of their nucleation centres.

Comparing Figures 3 and 4, one can see that the wear of both monolayer and multilayer coatings differs significantly from the degradation of silicon: Hurst exponents are staying above 0.5 up to 300 s of the fatigue tests.

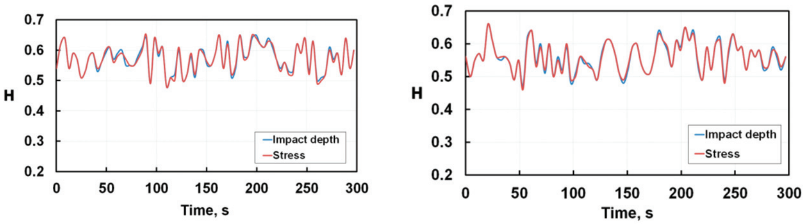

(**a**) (**b**)

Figure 4. Cyclic variations of Hurst exponents for nanoindentation tests of monolayer (**a**) and multilayer (**b**) coatings.

Analysing the features of the plots in Figure 4, we can see that the Hurst exponent H fluctuates within $0.5 < H < 0.66$. For each coating the Hurst exponents coincide completely regardless of calculation method. This means that during fatigue tests the ductility of the coatings is high and brittle degradation of the material near the indenter print is not observed as distinguished from silicon. Each fluctuation peak $H = F(t)$ signifies the accumulation of coherent structural transformations and their subsequent relaxation. Microplastic deformation and relaxation of accumulated micro-stresses occur at initial moments of the tests. The average level of the Hurst criterion is slightly higher for the multilayer coating than for the single layer one. This means that the processes of structural self-organization in both coatings are sufficiently high and that if the Hurst exponent is higher than 0.5 for a long series of observations, the long-term memory of events becomes significant.

Since the Hurst exponent is reliably higher than 0.5 during testing of up to 300 s, both coatings are damaged gradually due to the slow growth of previously initiated microcracks. Analysing Figures 2 and 4, we can conclude that the multilayer coating has an increased low-cycle fatigue resistance compared to the monolayer coating. In the entire range of fatigue tests, microplastic deformations in the monolayer coating are developing for a short time at the very initial moment of loading. Subsequently, cracks are nucleating and propagating by the brittle fracture mechanism through nitride, spontaneously and at high speed without any interrelation. The multilayer coating is characterised by a big toughness margin. So, the fatigue in this coating develops with the presence of an incubation period when the initiation and propagation of microcracks is accompanied by microplastic deformation and relaxation of accumulated stresses without brittle degradation of coatings.

4. Conclusions

At the early stage of wear, microcracks under the influence of localised stresses are nucleating and propagating in the coatings. During the incubation period, the nucleation of cracks is accompanied by microplastic deformation, which significantly increases the stage of damage accumulation and influences on cracks branching in the volume and on the interfaces. In the monolayer coating the nucleation and growth of brittle microcracks occurs throughout the whole deformed volume. During low-cycle fatigue tests the structural self-organization is quite high in both multilayer TiAlCrSiYN/TiAlCrN and monolayer TiAlCrSiYN coatings. In this case, the multilayer coating is characterised by larger toughness. In these coatings, fatigue structural changes are interrelated in contrast to silicon where the low-cycle fatigue develops as a stochastic accumulation of imperfections.

Author Contributions: Conceptualization, A.I.K.; methodology, A.I.K., D.L.W. and B.D.B.; validation, V.O.V., D.L.W., E.P.K. and S.A.D.; formal analysis, V.O.V. and E.P.K.; investigation, B.D.B., E.P.K. and G.S.F.-R.; writing—original draft preparation, A.I.K. and D.L.W.; writing—review and editing, B.D.B. and S.V.; visualization, E.P.K. and S.A.D. All authors have read and agreed to the published version of the manuscript.

Funding: This research was funded by the Russian Science Foundation, RSF project No. 21-79-10044 and by Natural Sciences and Engineering Research Council of Canada NSERC Grant NETGP 479639-15.

Institutional Review Board Statement: Not applicable.

Informed Consent Statement: Not applicable.

Data Availability Statement: Not applicable.

Conflicts of Interest: The authors declare no conflict of interest.

References

1. Vereschaka, A.A.; Sitnikov, N.; Volosova, M.; Seleznev, A.; Sotova, C.; Bublikov, J. Investigation of Properties of the Zr,Hf-(Zr,Hf)N-(Zr,Hf,Me,Al)N Coatings, Where Me Means Cr, Ti, or Mo. *Coatings* **2021**, *11*, 1471. [CrossRef]
2. Chowdhury, S.; Beake, B.; Yamamoto, K.; Bose, B.; Aguirre, M.; Fox-Rabinovich, G.; Veldhuis, S.C. Improvement of Wear Performance of Nano-Multilayer PVD Coatings under Dry Hard End Milling Conditions Based on Their Architectural Development. *Coatings* **2018**, *8*, 59. [CrossRef]
3. Fox-Rabinovich, G.; Kovalev, A.; Aguirre, M.H.; Yamamoto, K.; Veldhuis, S.; Gershman, I.; Rashkovskiy, A.; Endrino, J.L.; Beake, B.; Dosbaeva, G.; et al. Evolution of self-organization in nano-structured PVD coatings under extreme tribological conditions. *Appl. Surf. Sci.* **2014**, *297*, 22–32. [CrossRef]
4. Fox-Rabinovich, G.; Kovalev, A.; Veldhuis, S.; Yamamoto, K.; Endrino, J.L.; Gershman, I.S.; Rashkovskiy, A.; Aguirre, M.H.; Wainstein, D.L. Spatio-temporal behaviour of atomic-scale tribo-ceramic films in adaptive surface engineered nano-materials. *Sci. Rep.* **2015**, *5*, 8780. [CrossRef] [PubMed]
5. Vereschaka, A.; Grigoriev, S.; Chigarev, A.; Milovich, F.; Sitnikov, N.; Andreev, N.; Sotova, C.; Bublikov, J. Development of a Model of Crack Propagation in Multilayer Hard Coatings under Conditions of Stochastic Force Impact. *Materials* **2021**, *14*, 260. [CrossRef] [PubMed]
6. Krella, A. Resistance of PVD Coatings to Erosive and Wear Processes: A Review. *Coatings* **2020**, *10*, 921. [CrossRef]
7. Mott, B.W. *Micro-Indentation Hardness Testing*; Butterworths Scientific Publications: London, UK, 1956.
8. Bauccio, M. *ASM Metals Reference Book*, 3rd ed.; ASM International: Materials Park, OH, USA, 1993.
9. Tabor, D. *Hardness of Metals*; Clarendon Press: Oxford, UK, 1951.
10. Chenga, Y.T.; Cheng, C.M. Scaling, dimensional analysis, and indentation measurements. *Mater. Sci. Eng. R Rep.* **2004**, *44*, 91–149. [CrossRef]
11. Zhang, S. *Handbook of Nanostructured Thin Films and Coatings Mechanical Properties*, 1st ed.; CRC Press: Boca Raton, FL, USA, 2010.

12. Puchi-Cabrera, E.S.; Staia, M.H.; Iost, A. Modeling the composite hardness of multilayer coated systems. *Thin Solid Film.* **2015**, *578*, 53–62. [CrossRef]
13. Golovin, Y.I. Nanoindentation and mechanical properties of solids in submicrovolumes, thin near-surface layers, and films: A Review. *Phys. Solid State* **2008**, *50*, 2205–2236. [CrossRef]
14. Kovalev, A.I.; Rashkovskiy, A.Y.; Fox-Rabinovich, G.S.; Veldhuis, S.; Beake, B.D. Regularities of Tribooxidation and Damageability at the Early Stage of Wear of Single-Layer (TiAlCrSiY)N and Multilayer (TiAlCrSiY)N/(TiAlCr)N Coatings in the Case of High-Speed Cutting. *Prot. Met. Phys. Chem. Surf.* **2016**, *52*, 517–525. [CrossRef]
15. Fox-Rabinovich, G.; Beake, B.; Yamamoto, K.; Aguirre, M.; Veldhuis, S.C.; Dosbaeva, G.K.; Elfizy, A.; Biksa, A.; Shuster, L.S. Structure, properties and wear performance of nano-multilayered TiAlCrSiYN/TiAlCrN coatings during machining of Ni-based aerospace superalloys. *Surf. Coat. Technol.* **2010**, *204*, 3698–3706. [CrossRef]
16. Fox-Rabinovich, G.S.; Yamamoto, K.; Beake, B.D.; Kovalev, A.I.; Aguirre, M.H.; Veldhuis, S.C.; Dosbaeva, G.K.; Wainstein, D.L.; Biksa, A.; Rashkovskiy, A. Emergent behavior of nano-multilayered coatings during dry high-speed machining of hardened tool steels. *Surf. Coat. Technol.* **2010**, *204*, 3425–3435. [CrossRef]
17. Fox-Rabinovich, G.S.; Gershman, I.S.; Yamamoto, K.; Aguirre, M.H.; Covelli, D.; Arif, T.; Aramesh, M.; Shalaby, M.A.; Veldhuis, S. Surface/interface phenomena in nano-multilayer coating under severing tribological conditions. *Surf. Interface Anal.* **2017**, *49*, 584–593. [CrossRef]
18. Beake, B.D.; Bergdoll, L.; Isern, L.; Endrino, J.L.; Fox-Rabinovich, G.S.; Veldhuis, S.C. Influence of probe geometry in micro-scale impact testing of nano-multilayered TiAlCrN/NbN coatings deposited on WC-Co. *Int. J. Refract. Met. Hard Mater.* **2021**, *95*, 105441. [CrossRef]
19. Wang, S.; Liu, H.; Xu, L.; Du, X.; Zhao, D.; Zhu, B.; Yu, M.; Zhao, H. Investigations of Phase Transformation in Monocrystalline Silicon at Low Temperatures via Nanoindentation. *Sci. Rep.* **2017**, *7*, 8682. [CrossRef]
20. Ctvrtlik, R.; Tomastik, J.; Ranc, V. Nanoindentation-Induced Phase Transformation in Silicon Thin Films. *Key Eng. Mater.* **2014**, *586*, 112–115. [CrossRef]
21. Alexandros, D.; Sidiropoulos, E.H.; Avraam, A.K.; Elias, C.A. “Pop-in” and “pop-out” effect in monocrystalline silicon. *Stat. Investig. J. Mech. Behav. Mater.* **2017**, *26*, 65–71.
22. Malzbender, J.; den Toonder, J.M.J.; Balkenende, A.R.; de With, G. Measuring mechanical properties of coatings: A methodology applied to nano-particle-filled sol-gel coatings on glass. *Mater. Sci. Eng. R Rep.* **2002**, *36*, 47–103. [CrossRef]
23. Crain, J.; Ackland, G.J.; Maclean, J.R.; Piltz, R.O.; Hatton, P.D.; Pawley, G.S. Reversible pressure-induced structural transitions between metastable phases of silicon. *Phys. Rev. B* **1994**, *50*, 13043. [CrossRef]
24. Lee, W.S.; Chang, S.L. Load Dependence of Nanoindentation Behaviour and Phase Transformation of Annealed Single-Crystal Silicon. *Mater. Trans.* **2015**, *56*, 726–732. [CrossRef]
25. Nagy, P.; Horvát, P.; Pető, G.; Kálmán, E. Nanoindentation of silicon. *Mater. Sci. Forum* **2009**, *604–605*, 29–36. [CrossRef]
26. Kamimura, Y.; Edagawa, K.; Takeuchi, S. Experimental evaluation of the Peierls stresses in a variety of crystals and their relation to the crystal structure. *Acta Mater.* **2013**, *61*, 294–309. [CrossRef]

nanomaterials

Article

One-Dimensional Nanoscale Si/Co Based on Layered Double Hydroxides towards Electrochemical Supercapacitor Electrodes

Osama Saber [1,2,*], Sajid Ali Ansari [1,*], Aya Osama [1] and Mostafa Osama [1]

[1] Department of Physics, College of Science, King Faisal University, P.O. Box 400, Al-Ahsa 31982, Saudi Arabia; 217044956@student.kfu.edu.sa (A.O.); 214110595@student.kfu.edu.sa (M.O.)
[2] Egyptian Petroleum Research Institute, Nasr City, P.O. Box 11727, Cairo 11765, Egypt
* Correspondence: osmohamed@kfu.edu.sa (O.S.); sansari@kfu.edu.sa (S.A.A.); Tel.: +966-13-589-9440 (O.S.)

Abstract: It is well known that layered double hydroxides (LDHs) are two-dimensional (2D) layered compounds. However, we modified these 2D layered compounds to become one-dimensional (1D) nanostructures destined for high-performance supercapacitors applications. In this direction, silicon was inserted inside the nanolayers of Co-LDHs producing nanofibers of Si/Co LDHs through the intercalation of cyanate anions as pillars for building nanolayered structures. Additionally, nanoparticles were observed by controlling the preparation conditions and the silicon percentage. Scanning electron microscopy, X-ray diffraction, Fourier transform infrared spectroscopy and thermal analyses have been used to characterize the nanolayered structures of Si/Co LDHs. The electrochemical characterization was performed by cyclic voltammetry and galvanic charge–discharge technique in 2M KOH electrolyte solution using three-electrode cell system. The calculated specific capacitance results indicated that the change of morphology from nanoparticles or plates to nanofibers had a positive effect for improving the performance of specific capacitance of Si/Co LDHs. The specific capacitance enhanced to be 621.5 F g^{-1} in the case of the nanofiber of Si/Co LDHs. Similarly, the excellent cyclic stability (84.5%) was observed for the nanofiber. These results were explained through the attribute of the nanofibrous morphology and synergistic effects between the electric double layer capacitive character of the silicon and the pseudo capacitance nature of the cobalt. The high capacitance of ternary Si/Co/cyanate LDHs nanocomposites was suggested to be used as active electrode materials for high-performance supercapacitors applications.

Keywords: Si/Co LDHs; 1D nanostructures; nanofibers; cyclic voltammetry; charge–discharge method; supercapacitors

Citation: Saber, O.; Ansari, S.A.; Osama, A.; Osama, M. One-Dimensional Nanoscale Si/Co Based on Layered Double Hydroxides towards Electrochemical Supercapacitor Electrodes. *Nanomaterials* **2022**, *12*, 1404. https://doi.org/10.3390/nano12091404

Academic Editors: Ming-Yu Li and Jihoon Lee

Received: 16 March 2022
Accepted: 15 April 2022
Published: 20 April 2022

1. Introduction

The current global energy situation has become more critical because of environmental problems and climate change. Therefore, the urgent and continued need for clean energy has pushed the development of novel alternative sources of energy that are capable of transforming energy as well as storing energy for longer durations [1–5]. Therefore, there is an urgent need for an abundance of energy storage devices such as fuel cells, batteries, and super capacitors (electrochemical capacitors), which are low cost, environmentally friendly, more effective, and easier to manufacture. The interests in supercapacitors are being stimulated due to the potential connection between traditional capacitors and batteries [6–8]. Supercapacitors (SCs), also called ultra-capacitors, are considered to be a new type of energy storage/conversion device due to their high-power density, fast charging/discharging rate, long lifecycle, wide operating temperature range, as well as its maintenance-free and ecofriendly features. Due to its excellent properties, it is used in different application systems such as hybrid electric vehicles, electronic devices, mortar starter, memory backup system, industrial power and energy management [9–11].

Generally, supercapacitors or electrochemical supercapacitors can be divided into two major categories based on its charging mechanism [12]. The first one is electric double layer capacitors (EDLCs), which store capacity or electrical energy through the adsorption/desorption between the electrode–electrolyte interface and carbon-based materials. These are used as active materials for fabricating electrodes. The second is pseudo capacitors, wherein energy is based on the faradic process at the surface of the electrode in the electrolyte solution and the charge accumulates through the redox reaction. Conducting polymers and transition metal oxide and hydroxide have been used in pseudo capacitors. Pseudo capacitive electrode materials, especially binary metal oxides or hydroxides, have been proven to be an outstanding specific capacitance material. Recently, transition metal silicate oxide or hydroxides have focused on positive electrode materials due to their higher theoretical capacity, easy synthesis, and low cost [13–15]. For example, Zhang et al. synthesized three-dimensional $Zn_4Si_2O_7(OH)_2{\cdot}H_2O$ which were used in supercapacitive device applications [16].

Among the binary metal hydroxides materials, layered double hydroxides (LDHs) are promising capacitive materials for many electrochemical processes because they have layered structures that contain positive and negative charges which can act as active sites for electrochemical processes [17]. The positive charges of the nanolayers of LDHs are produced from the presence of di- and trivalent metals in order arrangements inside nanolayers. To neutralize the positive charges of the nanolayers, selective anionic species are intercalated to act as pillars for building the nanolayered structures of LDHs [18]. These structures showed a high performance in different fields such as catalysis [19], magnetic and optical applications [20], lithium-ion batteries [21] and particularly, supercapacitors [22,23]. For supercapacitors [24,25], the stable-layered structures of LDHs can attain the demands of efficient supercapacitors such as long-life cycling at a high current density. For example, a high energy density with 95% retention after 10,000 cycles was reported for CoS/NiCo LDHs [26]. Additionally, a maximum energy density 35 Wh kg^{-1} was observed for NiAl LDHs/Ni-MOF [27].

In recent years, [28], Si-based materials have attracted attention in electrochemical processes because of their high theoretical capacity 4200 mA h g^{-1}. Si–C–Cu composites [29] and Si–C microspheres [30,31] which showed an enhanced electrochemical performance. Therefore, many researchers have tried to combine silicon with LDHs for increasing the electrochemical performance, but it was difficult because the structure of LDHs depends on di- and trivalent elements. Recently, Li et al. [32] reported that Si supported on NiAl LDHs increased the performance of anode material in lithium batteries. Additionally, the pseudo-capacitive performance of Ni_3Si_2 nanowires was observed by Goh's group, indicating 54.8 C g^{-1} at 0.5 A g^{-1} in the case it was grown on a Ni-coated Si substrate and 313 C g^{-1} at 0.5 A g^{-1} for Ni foil [33]. In addition, higher specific capacitance (760 F g^{-1} at 0.5 A g^{-1}) was observed for Ni_3Si_2 nanowires grown on Ni foam by Jiang et al. [34]. A good supercapacitor performance was observed through preparing the single-crystalline Co_2Si nanowires producing ~983 μF cm^{-2} at 2 μA cm^{-2} [35].

To the best of our knowledge, there is no one working on the applications of Si/Co LDHs for supercapacitors. Therefore, in the current study, series of Si/Co LDHs were prepared and transformed to become nanofibers through the confinement of cyanate anions inside nanolayered structures. The optimized Si/Co LDHs electrode material exhibited excellent electrochemical performance in 2M KOH electrolytic solution; the specific capacitance of Si/Co LDHs electrodes was up to 621.5 F g^{-1} at 2 A g^{-1} and the capacitance retention was approximately 86.5% after 3000 continuous charge/discharge cycles. This study can provide a reference for future studies of morphological control and provide the strategies to enhance the performance of supercapacitor electrode materials. Additionally, nanofibers may be useful for designing and fabricating nano-devices.

2. Materials and Methods

2.1. Preparation of Nanostructures

The hydrolysis of urea depends on temperature [36]. By controlling the temperature of the aqueous solution of urea, it decomposes at a slow rate whilst producing ammonium carbonate or cyanate through two stages. During the slow decomposition of urea, the reaction medium is converted from acidic into alkaline, which leads to precipitating the nanostructures of Si/Co LDHs. Therefore, the urea was used in this reaction as a pH controller and precipitant. Series of Si/Co LDHs were prepared after mixing aqueous solutions of cobalt nitrate (0.03 M), urea (0.5 M) and silicon chloride (0.0096 M) under vigorous stirring. The reaction is sensitive for the temperature. Therefore, it was precisely adjusted at 80 °C. Depending on the time of the reaction, series of Si/Co samples were prepared. After 16 h, the sample was separated and washed by the distilled water. This sample was coded by SiCo-1-16. By continuing the heating process, the second sample was separated after 20 h and coded by SiCo-1-20. By further heating for 26 h and 36 h, the third and fourth samples were separated and coded by SiCo-1-26 and SiCo-1-36.

By increasing the molar ratio of Si/Co from 0.25 to 0.33, the fifth sample was precipitated after heating for 36 h of the same procedure. After washing and filtration, the product was dehydrated under vacuum at room temperature. The sample was labeled here after as Si/Co-2-36.

2.2. Physical Characterization

The morphology of the prepared samples was determined by scanning electron microscopy (SEM). The JEOL JSM-6330F (Tokyo, Japan) was used for imaging solid prepared materials. By using powder X-ray diffraction a Rigaku RINT 2200 (Tokyo, Japan), the structure of the prepared materials was determined through a source of radiation Cu Kα (filtered) at $\lambda = 0.154$ nm with angles between 1.8° and 50°. A Seiko SSC 5200 apparatus (Tokyo, Japan) was used for measuring the thermal analyses of the prepared materials using three techniques (differential thermal gravimetric—DTG; thermal gravimetric—TGA; and differential thermal analysis—DTA). The thermal analyses were measured under a flow of nitrogen and were carried out up to 800 °C with a heating rate of 10 °C/min. In order to determine the functional groups of the prepared materials, Horiba FT-720 (Tokyo, Japan) has used for performing Fourier transform infrared (FT-IR) spectroscopy using potassium bromide discs in the range of 400–4000 cm^{-1}.

2.3. Electrochemical Measurements

Electrochemical performance of all the electrodes was examined in a three-electrode system with a Pt sheet, a Ag/AgCl electrode used as a reference and counter electrode, respectively. To fabricate the working electrode firstly, slurry active material was prepared by adding 80 wt% of the Si/Co LDH, 10 wt% of activated carbon (AC), 10 wt% of polyvinylidene fluoride (PVDF) in anhydrous 1-Methyl-2-pyrrolidinone (NMP) and mixed properly using a magnetic stirrer at ambient temperature and the slurry of active material coated on chemically cleaned nickel foam of 1 × 1 area with mass loading at approximately 1 mg before drying in an oven at 90 °C for 12 h. All electrochemical measurements were carried out in 2M KOH aqueous solution using CV and CD analysis.

3. Results and Discussion

3.1. Scanning Electron Microscopy

Scanning electron microscopy is an important technique for determining the morphology of Si/Co LDHs. In order to obtain clear images, the samples were coated by a thin film of platinum before measurements. However, whilst the SEM images of the natural samples of layered double hydroxides showed platy morphology, the current samples of Si/Co LDH exhibited an alternative morphology. Figure 1a shows the SEM images of sample Si/Co-1-16. It indicates that the sample Si/Co-1-16 has fibers in the nano scale. In addition, there are a few nanoparticles being observed in Figure 1a. These results were confirmed through measuring the SEM images of sample Si/Co-1-26 as shown in Figure 1b and Figure S1. Clear fibrous morphology was observed in a wide area of the sample Si/Co-1-26, as seen in Figure S1a. By magnifying, it showed clear nanofibers in the shape of aggregates and bundles, as seen in Figure S1b,c. In the other locations, the individual nanofibers were observed, indicating that the fibers of Si-Co-1-26 are in the nanoscale with a diameter of 50 nm, as shown in Figure S1c,d.

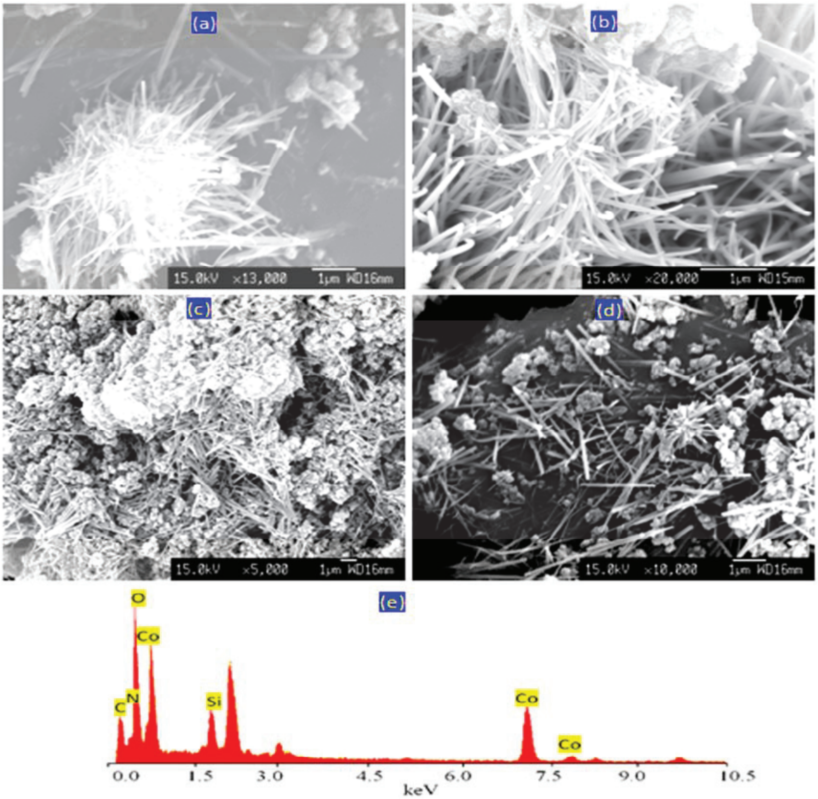

Figure 1. SEM images of samples (**a**) SiCo-1-16; (**b**) SiCo-1-26; (**c**,**d**) SiCo-2-36; and (**e**) EDX analysis of SiCo-1-26.

By increasing the molar ratio of Si/Co from 0.25 to 0.33, SEM images of Si/Co-2-36 showed nanoparticles in addition to a fibrous structure, as shown in Figure 1c,d. Additionally, Figure 1c revealed the aggregates of both nanofibers and the nanoparticles, together indicating the presence of two phases. The appearance of nanoparticles after increasing the content of silicon indicated that the extra silicon separated from the LDH structure to build new phase.

By comparing with the familiar plate-like morphology of LDHs, the nano-fibrous morphology of Si/Co LDH is unusual because the structure of LDHs consists of nanolayers with interlayered anions acting as pillars. In the usual LDHs, it is logical because the nanolayers of the majority of LDHs are composed of di- and tri-valent cations. Therefore, one positive charge (+1) was produced and neutralized with one negative charge (one pillar or one anion). However, in our study, the tetravalent silicon was used inside the nanolayers with cobalt. Therefore, a positive charge (+2) was produced and neutralized by two anions. Therefore, the nanofibers were formed through a mechanism which will be explained later in the subsequent sections.

Energy-dispersive X-ray spectrometry (EDX) analysis has provided clear information of the different elements in the outermost layers of the nanofibers of LDHs. Cobalt and silicon in addition to oxygen were detected in the wide area of the SEM image of SiCo-1-26 as shown in Figure 1e. Additionally, the signals of both nitrogen and carbon are clearly observed in Figure 1e, indicating the presence of cyanate and nitrate anions.

X-ray photoelectron spectroscopy (XPS), which is also known as electron spectroscopy for chemical analysis (ESCA), was used for measuring the oxidation state of cobalt in sample SiCo-1-26. According to the electron binding energy of Co ($2p_{3/2}$) for sample SiCo-1-26, it was 785 eV, as shown in Figure S2. By comparing with the binding energy of cobalt in CoO (783–781 eV) [37,38] and in Co_2O_3 (781–779 eV) [37,38], the presence of cobalt as divalent cations was confirmed because the value 785 eV was near to the divalent cation (783 eV) and far from the trivalent cation (781 eV).

3.2. Fourier Transform Infrared Spectroscopy

Fourier transform infrared spectroscopy was utilized to detect the interlayered anions of Si/Co LDH and determine its functional groups. Figure 2 showed the FT-IR spectrum of the nanofibers of Si/Co LDHs.

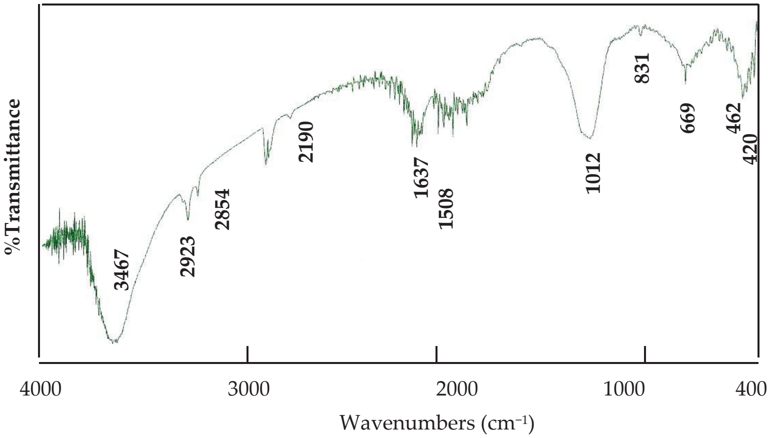

Figure 2. Infrared spectrum of the sample SiCo-1-26.

Fourier transform infrared spectroscopy was utilized to detect the interlayered anions of Si/Co LDH and determine its functional groups. Figure 2 showed the FT-IR spectra of the nanofibers of Si/Co LDHs. The clear absorption bands, which were observed at 3467 cm^{-1} and 1637 cm^{-1}, confirmed the presence of both the hydroxyl groups and the interlayered water. Additionally, Figure 2 showed small bands at 2923 cm^{-1} and 2854 cm^{-1}, indicating the formation of hydrogen bonds between the interlayered water and anions. These characteristic bands confirmed the formation of the LDH structure. The absorption band of the interlayered cyanate anions was observed at 2190 cm^{-1}. Additionally, the peak at 1012 cm^{-1} which was due to stretching mode of C–N was confirmed the presence of cyanate anions. In addition, the presence of nitrate anions was confirmed by two bands at 1508 cm^{-1} and 1384 cm^{-1}. Additionally, the vibrational mode of nitrate (υ_4) was observed at 669 cm^{-1}. Characteristic peaks for O–Si–O appeared as a broad peak at 1012 cm^{-1} while the band observed at 462 cm^{-1} is due to Si–O–Co [39], as shown in Figure 2.

3.3. Powder X-ray Diffraction

Figure 3 displays the X-ray diffraction patterns of the prepared products after the different reaction times 16–36 h. Figure 3(a) showed that the sample SiCo-1-16, which precipitated after reaction time 16 h, has a non-crystalline structure.

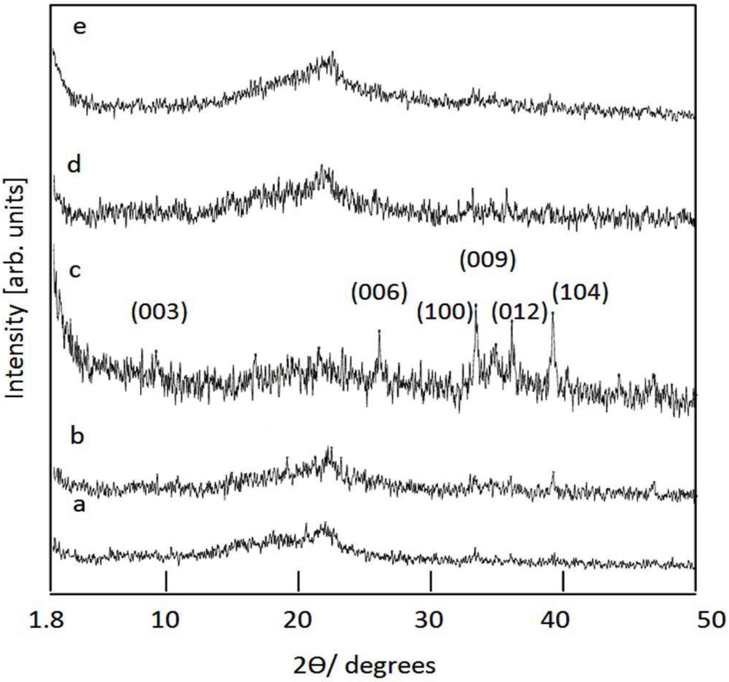

Figure 3. X-ray diffraction of Si/Co LDH: (a) SiCo-1-16; (b) SiCo-1-20; (c) SiCo-1-26; (d) SiCo-1-36; and (e) SiCo-2-36.

In case the reaction time increased to 20 h, weak peaks started to grow as shown in Figure 3(b). During a reaction time lasting between 26 h and 36 h, the weak peaks became more observable in the diagram of sample SiCo-1-26, as shown in Figure 3(c). The main peaks of the layered double structure were observed at 0.79 nm, 0.36 nm and 0.26 nm, indicating the reflections of planes [003], [006], and [009], respectively. According to the spacing for plane [003], the parameter (c) was calculated to be 2.37 nm. By comparing with the (c) value of the synthetic and natural LDHs, a little shift was observed for the prepared Si/Co LDHs. Additionally, other peaks were observed at a spacing of 0.27 nm, 0.26 nm, 0.25 nm and 0.23 nm. According to Gastuche et al. and Saber et al. [40,41], these peaks agree with the diffuse non-basal reflections of the planes (100), (101), (012) and (104) of an LDH structure and confirm that the Si/Co LDHs has disordered structure. These data agree with the results which are previously published for Zn-Si LDH [41] and concluded that the presence of silicon inside the nanolayers of LDHs caused the distortion of the nanolayered structures of LDHs.

By increasing the molar ratio of Si/Co, an amorphous structure was observed for the sample Si/Co-2-36, as shown in Figure 3(e). This means that the presence of a high silicon content caused strong distortion for the layered structure because of creating a new phase, which is consistent with the SEM results.

According to the SEM images and XRD results, in addition to the XPS and EDX spectra, the effect of reaction and aging time plays an important role for building the nanofibers of Si/Co LDHs. Figure 4 shows the schematic representation of the synthesis of 1D nanofibers.

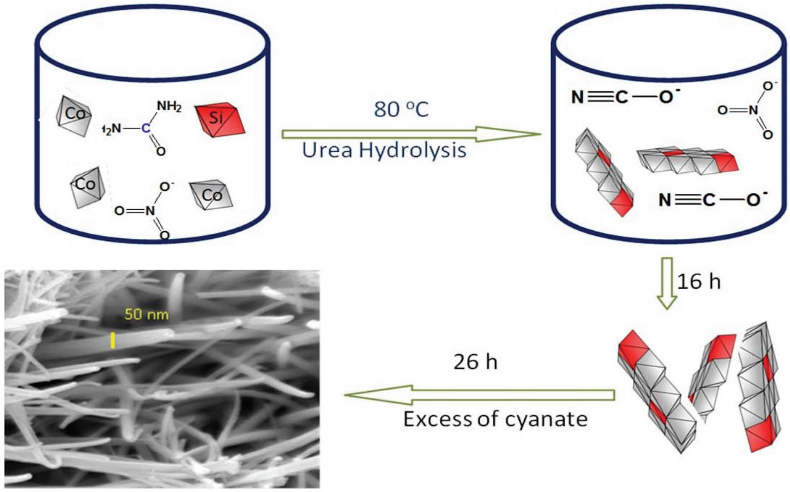

Figure 4. Schematic representation of the synthesis of 1D nanofibers.

3.4. Thermal Analyses

The thermal behavior of samples SiCo-1-16 and SiCo-1-36 was determined by measuring the thermal gravimetric (TGA), differential thermal gravimetric (DTG) and differential thermal analyses (DTA). Figure 5a showed that the total weight loss of SiCo-1-16 was 21% and accomplished after heating at 500 °C, while the total weight loss of SiCo-1-36 was 27% and observed at 601 °C, as shown in Figure 5b. This means that the Si/Co LDHs needed more reaction time than 16 h to be completely formed. By studying the details of thermal analyses, the TG diagrams revealed that the intercalated water and surface water were lost through two stages in a similar way for both samples SiCo-1-16 and SiCo-1-36. At 100 °C, the surface water of both samples was easily lost and was 7–8 wt%, which is consistent with the clear peak in the DTG curve.

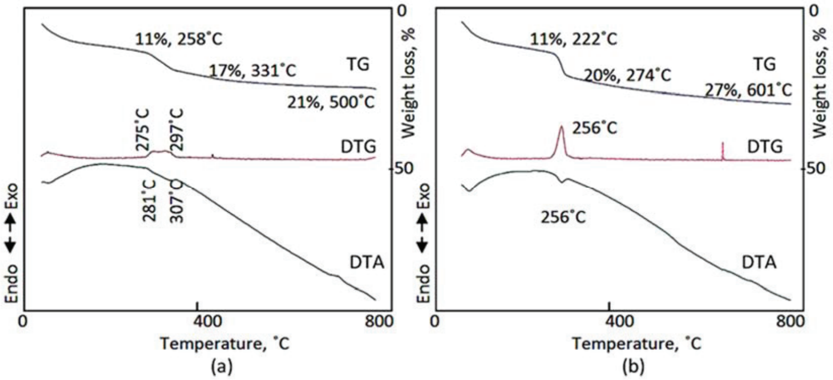

Figure 5. Thermal analyses of: (**a**) SiCo-1-16; and (**b**) SiCo-1-36.

The DTA curve confirmed that by observing the endothermic peak at 80 °C, the water molecules which strongly bonded with the interlayered anions were lost at higher temperatures of 222–258 °C for both samples and were 3–4 wt%. The decomposition of the interlayered anions of sample SiCo-1-16 happened in two steps. The first step was 6 wt% and occurred at 331 °C. The second step was 4 wt% and took place at 500 °C. The DTG curve revealed two peaks at 275 °C and 297 °C, confirming the presence of two interlayered anions. Additionally, the dual interlayered anions were confirmed by DTA curve. However, in the case of sample SiCo-1-36, the first anion 9 wt% was sharply lost at 274 °C, exhibiting an endothermic peak in the DTA curve and a sharp peak in the DTG curve at 256 °C. Meanwhile, the second anion 7 wt% was gradually lost at up to 601 °C with the dihydroxylation process of the nanolayers. These results concluded that the nanofibers of Si/Co LDH formed after 26 h of reaction time. During this time, the dual anions of cyanate and nitrate intercalated with a large amount of water inside the interlayered space.

3.5. Formation Mechanism of One-Dimensional Nanofibers

The usual geometry and morphology of Co-Al LDHs are two-dimensional layered structures with a hexagonal shape [42]. In the current structure, a one-dimensional structure was observed for Si/Co LDHs. According to the difference between the usual LDHs and the current LDHs, the mechanism of conversion from a 2D material to a 1D structure can be applied for explaining this behavior. The current Si/Co LDH creates cationic nanolayers with positive charges (+2) on silicon because of the combination between the divalent cobalt and the tetravalent silicon. In addition, the FI-IR results and thermal analyses confirmed the presence of cyanate anions (CNO^-) and nitrate anions which can be used as pillars for building the LDH structure and neutralizing the positive charges (+2) of the nanolayers of Si/Co. These cyanate anions were produced through urea hydrolysis while the nitrate anions were released from the precursor of cobalt. Urea is a very weak Bronsted base ($pK_b = 13.8$). By controlling the temperature, urea is slowly hydrolyzed and decomposed to form ammonium cyanate, converting the medium of the reaction from an acidic nature (pH = 3) to alkaline nature (pH = 8).

This process needs a long time to produce enough amounts of cyanate anions in addition to achieving an alkaline medium for precipitating LDHs. Therefore, SEM images showed that the better quality of nanofibers was obtained after 26 h of the reaction. The positive charges (+2), which produced from the combination between cobalt and silicon, attracted the cyanate anions and/or nitrate anions which were identified by FTIR and thermal analyses. The comparison between the structure and the size of both nitrate and cyanate anions indicated that the intercalation of cyanate anions to build LDHs is more favorable because of its straight structure. By competition with the nitrate anions, the pull of two cyanate anions (−1) toward the silicon cation (+2) is occurred through only one side as shown in Figure 6. The steric hindrance between these two anions created strong repulsion forces inside the interlayered region of LDH. These forces pushed and pressed on the nanolayers, especially on their edges leading to curling and curving for the nanolayers producing nanofibers as shown in Figure 6.

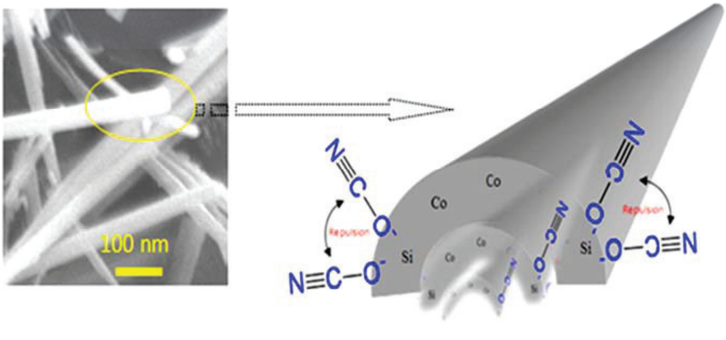

Figure 6. Schematic representation of 1D nanofiber.

3.6. Electrochemical Studies

Electrochemical supercapacitor properties of the nano size one-dimensional Si/Co LDH samples explored in three-electrode system. The system based on one-dimensional Si/Co LDHs as a working electrode, platinum sheet as a counter electrode, Ag/AgCl as a compared electrode, and 2 moles of KOH electrolyte. A collection of the effective electrochemical method such as cyclic voltammetry (CV) and Galvano static charge–discharge (GCD) applied to investigate the electrochemical properties of the SiCo-1-16, SiCo-1-26, SiCo-1-36 and Si/Co-2-36 LDH electrode materials. The voltage range of the optimal capacitance of the Si/Co LDHs was measured by the CV curves under the scan rate of 5 mV/s and the optimal range was from 0.0 V to 0.45 V (Figure 7a).

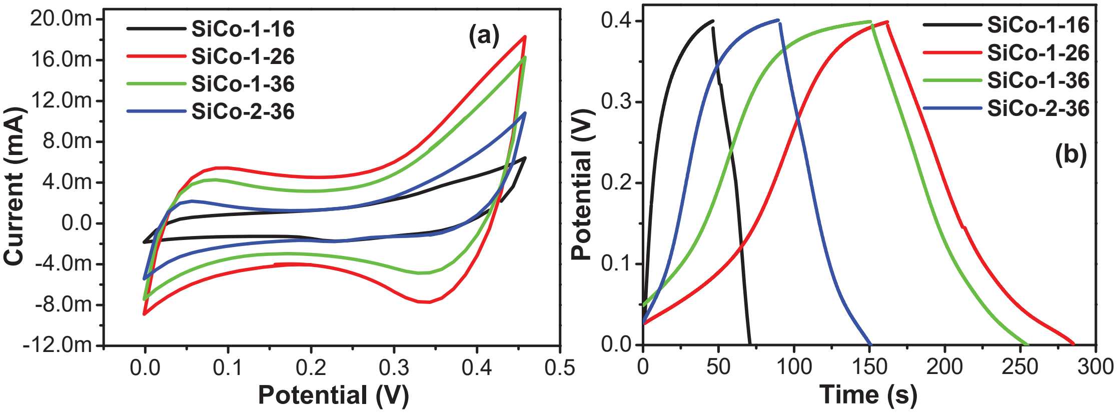

Figure 7. Comparative (**a**) CV curves of the SiCo-1-16, SiCo-1-26, SiCo-1-36, and SiCo-2-36 LDH electrodes at fix scan rate of 5 mV/s; and (**b**) CD curves of SiCo-1-16, SiCo-1-26, SiCo-1-36, and SiCo-2-36 LDH electrodes at fixed current density of 2 A g^{-1}.

Figure 7a represents the comparative CV graphs of the SiCo-1-16, SiCo-1-26, SiCo-1-36 and Si/Co-2-36 LDH electrodes at a fixed scan rate, which reveals the impact of the synthesis time duration and mole ratio of Si/Co on their electrochemical properties. All four samples of Si/Co LDH with a different synthesis time duration and different mole ratio of Si/Co show regular CV curves and all four samples have a couple of redox peaks between approximately 0.05 and 0.35 V at a fixed scan rate of 5 mV/s, which indicates the faradic nature [43,44]. It is well known that the charges are stored with respect to the area under the CV curves. The redox peak assigned the reaction of Co^{2+}/Co^{3+} in the Si/Co LDH in alkaline electrolytic solution [44–46]. From CV curves, it can be seen that the SiCo-1-26 sample's large integrated area in the CV curve as compared to other samples of Si/Co LDH indicates a higher specific capacitance provided by the SiCo-1-26 sample electrode. This enhanced performance of the SiCo-1-26 LDH electrode is due to the nano fibrous morphology of the material, which secondly might be due to the synergetic effect between silicon as EDLC and the pseudocapacitive nature of cobalt. Changing the synthesis time duration also affects the morphology of the electrode material, which affects the specific capacitance of the electrode material. In the case of the SiCo-1-36 electrode, which was due to a long synthesis time, the nano fibers became thick, which is responsible for the decrease in the capacitance of the electrode material (SiCo-1-36). In the case of SiCo-2-36 from the SEM images, it can be clearly seen that the nanoparticles adhere to the nanofibers and both nanofibers and nanoparticles aggregate together, hindering the capacitive performance of the SiCo-2-36 electrode.

The comparative GCD data are also proposed in Figure 7b at the current density of 2 A/g^{-1} and in the potential range of the 0.0 to 0.4 V. All the electrodes demonstrate rapid response and excellent electrochemical reversibility, confirming the faradic behavior of electrodes. Moreover, the specific capacitance of these samples calculated from the length of charge/discharge curve and from Equation (S1) mention inside the electronic supplementary information of the Si/Co LDH electrodes confirm this result precisely. The SiCo-1-16, SiCo-1-26, SiCo-1-36 and Si/Co-2-36 LDH electrodes depicted the highest calculated specific capacitance of 140 F g^{-1}, 621.5 F g^{-1}, 515 F g^{-1} and 326.5 F g^{-1} at the current density of 2 A g^{-1} [47,48], respectively. The SiCo-1-26 LDH electrode has the largest specific capacitance (621.5 F g^{-1}) as compared to the SiCo-1-16 (140 F g^{-1}), SiCo-1-36 (515 F g^{-1}) and Si/Co-2-36 (326.5 F g^{-1}) LDH electrodes; moreover, the calculated CD result coordinates well with the CV result.

Figure 8 depicted the CV curves of all the electrode samples SiCo-1-16, SiCo-1-26, SiCo-1-36 and Si/Co-2-36 LDH, respectively, at different scan rates between 5 mV s^{-1} and 70 mV s^{-1}, and within the potential range of 0.0–0.45 V verses Ag/AgCl standard electrode. CV curves of all the samples show the redox peak or redox activity on the electrode surface, which clearly indicates the pseudocapacitor behavior of the electrode material. Moreover, from the CV curves, the oxidation–reduction peaks can be observed, which move towards to the higher and lower potential due to the reinforced electric polarization and feasible kinetic irreversibility of the electrolytic ion on the electrode surface. The electrode material which displayed the redox peak in the CV analysis should not be presumed to be a pseudocapacitor, as the electrode keep altering over the whole potential window. Consequently, the electrochemical supercapacitive performance of all the Si/Co LDH electrodes were measured in terms of the specific capacity instead of specific capacitance [27].

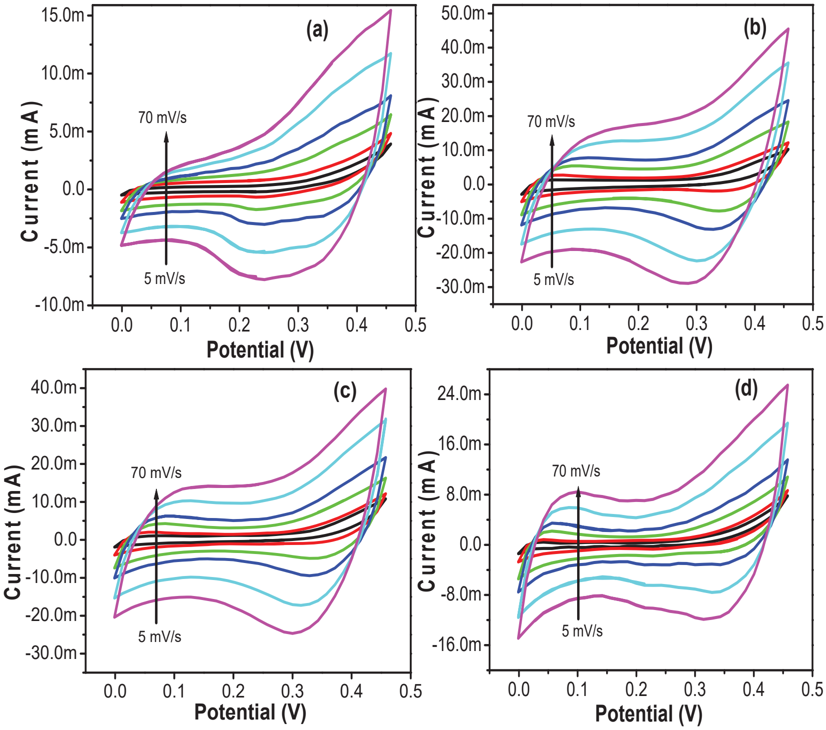

Figure 8. CV curves of the (**a**) SiCo-1-16; (**b**) SiCo-1-26; (**c**) SiCo-1-36; and (**d**) SiCo-2-36 LDH electrodes at different scan rates.

For better applicability, the electrochemical behavior of the prepared electrodes was directly evaluated by the galvanostatic charge–discharge (GCD) method at different current densities. Figure 9 shows the CD curves of the SiCo-1-16, SiCo-1-26, SiCo-1-36 and SiCo-2-36 LDHs electrodes at the current densities ranging from 2 A g^{-1} to 10 A g^{-1}. The calculated specific capacitance of the electrode material with respect to the altering synthesis time duration are as follows: in the case of SiCo-1-16, the LDH electrodes at 2, 3, 5, 7 and

10 A g^{-1} are 140, 120, 125, 119, 112.5 F g^{-1}, the SiCo-1-36 LDH electrode at 515, 427.5, 400, 350, 325 F g^{-1} and in the case of the SiCo-1-26 LDH electrode, the estimated specific capacitances are approximately 621.5, 510, 475, 437.5, 375 F g^{-1}, respectively. As compared to the SiCo-1-16 and SiCo-1-36 LDH electrodes, the SiCo-1-26 LDH electrode delivered a long time charge/discharge performance due to its unique (nano size particle mixed fibrous) morphology, which provided the larger surface area and more active sites for the electrolyte intercalation/deintercalation during the CD process and maximized the utilization of the SiCo-1-26 LDH electrode.

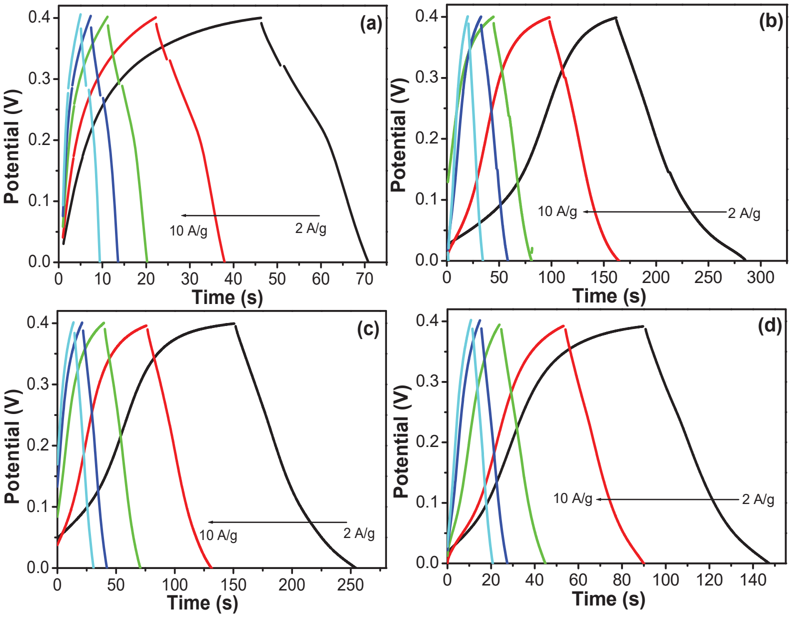

Figure 9. GCD curves of the (**a**) SiCo-1-16; (**b**) SiCo-1-26; (**c**) SiCo-1-36; and (**d**) SiCo-2-36 LDH electrodes at different current densities.

To understand the effect of the ratio of the Si and Co material on the morphology and electrochemical performance of Si/Co LDH electrodes, the CV and GCD data profile of the SiCo-2-36 LDH electrode are proposed in Figure 6. From the CV curve (Figure 7a), it is clearly shown that the sample shows a small integrated area which displays that the capacitance of SiCo-2-36 LDH electrode decreased. The CD curve (Figure 7b) also depicted the lower performance of the SiCo-2-36 LDH electrode due to the aggregation of the nanoparticles and nanofibers. The specific capacitance of the SiCo-1-16, LDH electrode at 2, 3 5, 7 and 10 A g^{-1} are 326.5, 303, 265, 211.75, 200 F g^{-1}, respectively. Figure 10a represents the calculated specific capacitance of the prepared electrodes (SiCo-1-16, SiCo-1-26, SiCo-1-36 and Si-Co-2-36 LDHs electrodes) at different current densities. From Figure 10a, it clearly shows that with the increasing current density, the specific capacitance of the synthesized electrodes decreased due to the decreased penetration of the electrolyte at higher current.

The long-term stability performance of the electrode material is one of the most important concerns in energy storage applications. Generally, metal oxides suffer from the poor cyclic stability because of degradation [49,50]. The cyclic stability test and the coulombic efficiency (Figure S3) of the optimized SiCo-1-26 LDH electrode were analyzed by the GCD analysis at 5 A g^{-1} for continuous 3000 charge/discharge cycles. From Figure 10b, it is clearly shown that in the 400 initial cycles, the capacitance of the electrode material rapidly decreases due to the active site saturation of the surface of electrodes during the charge–discharge mechanism stability of the electrode. As shown in Figure 10b, the nano size particle mixed fibrous retained 84.5% of the specific capacitance after 3000 cycles. The better performance of the SiCo-1-26 LDH electrode material was due to the nano size particle mixed fibrous morphology, which provided more active sites during the electrochemical test and helped stabilize the overall structure of the nanocomposite during the continuous charging–discharge process up to 3000 cycles.

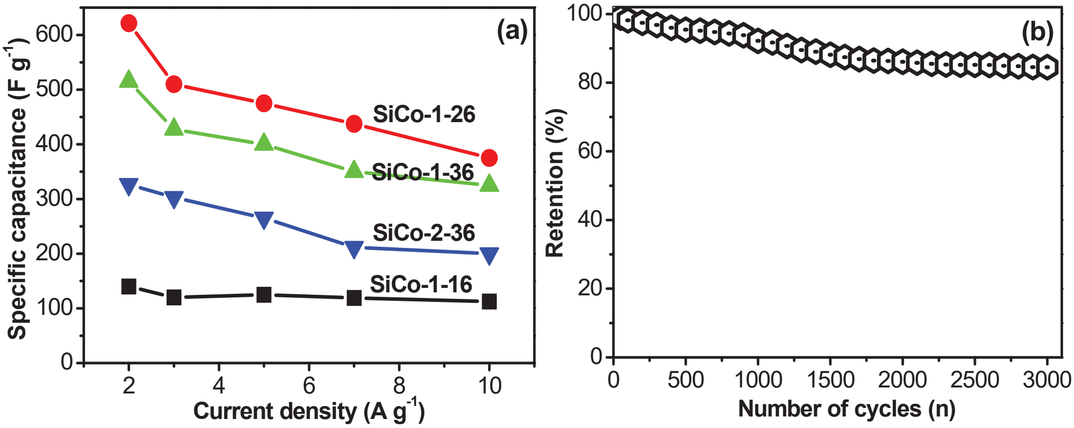

Figure 10. (**a**) Calculated specific capacitance of the SiCo-1-16, SiCo-1-26, SiCo-1-36 and Si/Co-2-36 LDH electrodes at different current densities; and (**b**) cyclic stability of SiCo-1-26 LDH electrodes over 3000 cycles.

4. Conclusions

In the current study, a dual objective was attained by preparing the Si/Co nanofibers and obtaining a new candidate for supercapacitor electrodes. The SEM images showed that the prepared Si/Co LDHs, which were prepared after a reaction time of 26 h, had nanofibers which were 50 nm in diameter. Additionally, the X-ray diffraction, FTIR and thermal analyses showed that these LDHs have two interlayered anions; cyanate and nitrate. The steric hindrance between the two bulky anions inside the interlayered region of LDHs led to strong repulsion forces between them, causing curling for the nanolayers of LDH-producing nanofibers.

The electrochemical characterization indicated that the change of the plate-like morphology, which is the familiar morphology of LDHs, to that of nanofibers, had the positive effect of improving the performance of the specific capacitance of Si/Co LDHs. The specific capacitance increased to 621.5 F g^{-1} in the case of the nanofiber of Si/Co LDHs. In addition, the excellent cyclic stability arrived to 84.5%. Furthermore, the nanofibers helped stabilize the overall structure of the nanocomposite during the continuous charging–discharge process up to 3000 cycles. Finally, the high capacitance of the ternary system of the Si/Co/cyanate nanofibers was suggested to be used as active electrode materials for high-performance supercapacitors applications.

Supplementary Materials: The following supporting information can be downloaded at: https://www.mdpi.com/article/10.3390/nano12091404/s1, Figure S1: SEM images of the sample SiCo-1-26 at different magnification (a) 10 µm, (b) 100 nm, and (c,d) 50 nm; Figure S2: XPS analysis for SiCo-1-26; Figure S3: Coulombic efficiency profile of the optimized electrode examined at current density of 7 A g^{-1}.

Author Contributions: Conceptualization, O.S.; methodology, O.S. and S.A.A.; software, M.O. and A.O.; validation, O.S. and M.O.; formal analysis, O.S. and S.A.A.; investigation, O.S., S.A.A., A.O. and M.O.; resources, O.S.; data curation, O.S., M.O. and A.O.; writing—original draft preparation, O.S. and S.A.A.; writing—review and editing, O.S. and S.A.A.; visualization, M.O.; supervision, O.S.

and S.A.A.; project administration, O.S.; funding acquisition, O.S. All authors have read and agreed to the published version of the manuscript.

Funding: This research was funded by the Deanship of Scientific Research in King Faisal University (Saudi Arabia), grant number GRANT74 and the APC was funded by the same grant number GRANT74.

Data Availability Statement: Data are available in a publicly accessible repository.

Acknowledgments: The authors acknowledged the Deanship of Scientific Research at King Faisal University for financial support under the Research Annual Track (Grant No. GRANT74).

Conflicts of Interest: The authors declare no conflict of interest.

References

1. Zheng, Y.; Zheng, S.; Xu, Y.; Xue, H.; Liu, C.; Pang, H. Ultrathin two-dimensional cobalt-organic frameworks nanosheets for electrochemical energy storage. *Chem. Eng. J.* **2019**, *373*, 1319–1328. [CrossRef]
2. Yuan, M.; Guo, X.; Liu, Y.; Pang, H. Si-based materials derived from biomass: Synthesis and applications in electrochemical energy storage. *J. Mater. Chem. A* **2019**, *7*, 22123. [CrossRef]
3. Chhetri, K.; Dahal, B.; Tiwari, A.P.; Mukhiya, T.; Muthurasu, A.; Ojha, G.P.; Lee, M.; Kim, T.; Chae, S.H.; Kim, H.Y. Controlled Selenium Infiltration of Cobalt Phosphide Nanostructure Arrays from a Two-Dimensional Cobalt Metal–Organic Framework: A Self-Supported Electrode for Flexible Quasi-Solid-State Asymmetric Supercapacitors. *ACS Appl. Energy Mater.* **2021**, *4*, 404–415. [CrossRef]
4. Pan, Z.; Yang, J.; Zhang, Y.; Gao, X.; Wang, J. Quasi-solid-state fiber-shaped aqueous energy storage devices: Recent advances and prospects. *J. Mater. Chem. A* **2020**, *8*, 6406–6433. [CrossRef]
5. Wang, X.; Zhang, Y.; Zheng, J.; Jiang, H.; Dong, X.; Liu, X.; Meng, C. Fabrication of vanadium sulfide (VS4) wrapped with carbonaceous materials as an enhanced electrode for symmetric supercapacitors. *J. Colloid Interface Sci.* **2020**, *574*, 312–323. [CrossRef] [PubMed]
6. Deka, B.K.; Hazarika, A.; Kim, J.; Kim, N.; Jeong, H.E.; Park, Y.-B.; Park, H.W. Bimetallic copper cobalt selenide nanowire-anchored woven carbon fiber-based structural supercapacitors. *Chem. Eng. J.* **2019**, *355*, 551–559. [CrossRef]
7. Chhetri, K.; Tiwari, A.P.; Dahal, B.; PrasadOjha, G.; Mukhiya, T.; Lee, M.; Kim, T.; Chae, S.H.; Muthurasu, A.; Kim, H.Y. A ZIF-8-derived nanoporous carbon nanocomposite wrapped with Co_3O_4-polyaniline as an efficient electrode material for an asymmetric supercapacitor. *J. Electroanaly. Chem.* **2020**, *856*, 113670. [CrossRef]
8. Sun, H.; Zhu, J.; Baumann, D.; Peng, L.; Xu, Y.; Shakir, I.; Huang, Y.; Duan, X. Hierarchical 3D electrodes for electrochemical energy storage. *Nat. Rev. Mater.* **2019**, *4*, 45–60. [CrossRef]
9. Jiang, H.; Yang, L.; Li, C.; Yan, C.; Lee, P.S.; Ma, J. High–rate electrochemical capacitors from highly graphitic carbon–tipped manganese Oxide/Mesoporous Carbon/Manganese Oxide Hybrid Nanowires. *Energy Environ. Sci.* **2011**, *4*, 1813. [CrossRef]
10. Miller, J.R.; Simon, P. Electrochemical capacitors for energy management. *Science* **2008**, *321*, 651. [CrossRef]
11. Ansari, S.A.; Parveen, N.; Han, T.H.; Ansari, M.O.; Cho, M.H. Fibrous polyaniline@manganese oxide nanocomposites as supercapacitor electrode materials and cathode catalysts for improved power production in microbial fuel cells. *Phys. Chem. Chem. Phys.* **2016**, *18*, 9053. [CrossRef] [PubMed]
12. Wang, Y.; Song, Y.; Xia, Y. Electrochemical capacitors: Mechanism, materials, systems, characterization, and applications. *Chem. Soc. Rev.* **2016**, *45*, 5925–5950. [CrossRef] [PubMed]
13. Wang, X.; Zhang, Y.; Zheng, J.; Liu, X.; Meng, C. Hydrothermal synthesis of VS4/CNTs composite with petal-shape structures performing a high specific capacity in a large potential range for high-performance symmetric supercapacitors. *J. Colloid Interface Sci.* **2019**, *554*, 191–201. [CrossRef] [PubMed]
14. Owusu, K.A.; Qu, L.; Li, J.; Wang, Z.; Zhao, K.; Yang, C.; Hercule, K.M.; Lin, C.; Shi, C.; Wei, Q.; et al. Low-crystalline iron oxide hydroxide nanoparticle anode for high-performance supercapacitors. *Nat. Commun.* **2017**, *8*, 14264. [CrossRef] [PubMed]
15. Zheng, J.; Zhang, Y.; Meng, C.; Wang, X.; Liu, C.; Bo, M.; Pei, X.; Wei, Y.; Liv, T.; Cao, G. V_2O_3/C nanocomposites with interface defects for enhanced intercalation pseudo capacitance. *Electrochim. Acta* **2019**, *318*, 635–643. [CrossRef]
16. Zhang, Y.; Jiang, H.; Wang, Q.; Meng, C. In-situ hydrothermal growth of $Zn_4Si_2O_7(OH)_2{\cdot}H_2O$ anchored on 3D N, S-enriched carbon derived from plant biomass for flexible solid-state asymmetrical supercapacitors. *Chem. Eng. J.* **2018**, *352*, 519–529. [CrossRef]
17. Wu, X.; Jiang, L.; Long, C.; Wei, T.; Fan, Z. Dual support system ensuring porous Co-Al hydroxide nanosheets with ultrahigh rate performance and high energy density for supercapacitors. *Adv. Funct. Mater.* **2015**, *25*, 1648–1655. [CrossRef]
18. Wang, Q.; O'Hare, D. Recent advances in the synthesis and application of layered double hydroxide (LDH) nanosheets. *Chem. Rev.* **2012**, *112*, 4124–4155. [CrossRef]
19. Feng, J.-T.; Lin, Y.-J.; Evans, D.G.; Duan, X.; Li, D.-Q. Enhanced metal dispersion and hydrodechlorination properties of a Ni/Al_2O_3 catalyst derived from layered double hydroxides. *J. Catal.* **2009**, *266*, 351–358. [CrossRef]

20. Liu, Z.; Ma, R.; Osada, M.; Iyi, N.; Ebina, Y.; Takada, K.; Sasaki, T. Synthesis, anion exchange, and delamination of Co-Al layered double hydroxide: Assembly of the exfoliated nanosheet/polyanion composite films and magneto-optical studies. *J. Am. Chem. Soc.* **2006**, *128*, 4872–4880. [CrossRef]
21. Li, Q.; Yi, Z.; Cheng, Y.; Wang, X.; Yin, D.; Wang, L. Microwave-assisted synthesis of the sandwich-like porous Al_2O_3/RGO nanosheets anchoring NiO nanocomposite as anode materials for lithium-ion batteries. *Appl. Surf. Sci.* **2018**, *427*, 354–362. [CrossRef]
22. Zhao, J.; Xu, S.; Tschulik, K.; Compton, R.G.; Wei, M.; O'Hare, D.; Evans, D.G.; Duan, X. Molecular-scale hybridization of clay monolayers and conducting polymer for thin-film supercapacitors. *Adv. Funct. Mater.* **2015**, *25*, 2745–2753. [CrossRef]
23. Zhao, J.; Chen, J.; Xu, S.; Shao, M.; Zhang, Q.; Wei, F.; Ma, J.; Wei, M.; Evans, D.G.; Duan, X. Hierarchical NiMn layered double hydroxide/carbon nanotubes architecture with superb energy density for flexible supercapacitors. *Adv. Funct. Mater.* **2014**, *24*, 2938–2946. [CrossRef]
24. Zhang, L.; Wang, J.; Zhu, J.; Zhang, X.; San Hui, K.; Hui, K.N. 3D porous layered double hydroxides grown on graphene as advanced electrochemical pseudocapacitor materials. *J. Mater. Chem. A* **2013**, *1*, 9046. [CrossRef]
25. Li, Z.; Shao, M.; Zhou, L.; Zhang, R.; Zhang, C.; Han, J.; Wei, M.; Evans, D.G.; Duan, X. A flexible all-solid-state micro-supercapacitor based on hierarchical CuO@ layered double hydroxide core shell nanoarrays. *Nano Energy* **2016**, *20*, 294–304. [CrossRef]
26. Guan, X.; Huang, M.; Yang, L.; Wang, G.; Guan, X. Facial design and synthesis of CoS_x/Ni-Co LDH nanocages with rhombic dodecahedral structure for high performance asymmetric supercapacitors. *Chem. Eng. J.* **2019**, *372*, 151–162. [CrossRef]
27. Zheng, W.; Sun, S.; Xu, Y.; Yu, R.; Li, H. Sulfidation of hierarchical NiAl LDH/Ni-MOF composite for high-performance supercapacitor. *Chem. Electro. Chem.* **2019**, *6*, 3375–3382. [CrossRef]
28. Gao, P.; Huang, X.; Zhao, Y.; Hu, X.; Cen, D.; Gao, G.; Bao, Z.; Mei, Y.; Di, Z.; Wu, G. formation of Si hollow structures as promising anode materials through reduction of silica in $AlCl_3$-NaCl molten salt. *ACS Nano* **2018**, *12*, 11481–11490. [CrossRef]
29. Zhang, H.; Zong, P.; Chen, M.; Jin, H.; Bai, Y.; Li, S.; Ma, F.; Xu, H.; Lian, K. Situ synthesis of multilayer carbon matrix decorated with copper particles: Enhancing the performance of Si as anode for Li-ion batteries. *ACS Nano* **2009**, *13*, 3054–3062. [CrossRef]
30. Yi, Z.; Qian, Y.; Cao, C.; Lin, N.; Qian, Y. Porous Si/C microspheres decorated with stable outer carbon interphase and inner interpenetrated Si@C channels for enhanced lithium storage. *Carbon* **2019**, *149*, 664–671. [CrossRef]
31. Prakash, S.; Zhang, C.; Park, J.D.; Razmjooei, F.; Yu, J.S. Silicon core-mesoporous shell carbon spheres as high stability lithium-ion battery anode. *J. Colloid Interface Sci.* **2019**, *534*, 47–54. [CrossRef] [PubMed]
32. Li, Q.; Wang, Y.; Lu, B.; Yu, J.; Yuan, M.; Tan, Q.; Zhong, Z. Fabing Su. Hollow core-shell structured Si@NiAl-LDH composite as highperformance anode material in lithium-ion batteries. *Electrochim. Acta* **2020**, *331*, 135331. [CrossRef]
33. Ramly, M.M.; Omar, F.S.; Rohaizad, A.; Aspanut, Z.; Rahman, S.A.; Goh, B.T. Solid-phase diffusion controlled growth of nickel silicide nanowires for supercapacitor electrode. *Appl. Surf. Sci.* **2018**, *456*, 515–525. [CrossRef]
34. Jiang, Y.; Li, Z.; Li, B.; Zhang, J.; Niu, C. Ni_3Si_2 nanowires grown in situ on Ni foam for high-performance supercapacitors. *J. Power Sources* **2016**, *320*, 13–19. [CrossRef]
35. Lee, J.; Yoo, C.Y.; Lee, Y.A.; Park, S.H.; Cho, Y.; Jun, J.H.; Kim, W.Y.; Kim, B.; Yoon, H. Single-crystalline Co_2Si nanowires directly synthesized on silicon substrate for high-performance micro-supercapacitor. *Chem. Engin. J.* **2019**, *370*, 973–979. [CrossRef]
36. Saber, O.; Kotb, H.M.; Osama, M.; Khater, H.A. An Effective Photocatalytic Degradation of Industrial Pollutants through Converting Titanium Oxide to Magnetic Nanotubes and Hollow Nanorods by Kirkendall Effect. *Nanomaterials* **2022**, *12*, 440. [CrossRef]
37. Barrioni, B.R.; Norris, E.; Jones, J.R.; Pereira, M.M. The influence of cobalt incorporation and cobalt precursor selection on the structure and bioactivity of sol–gel-derived bioactive glass. *J. Sol-Gel Sci. Technol.* **2018**, *88*, 309–321. [CrossRef]
38. Saber, O. Preparation and characterization of a new nano layered material, Co–Zr LDH. *J. Mater. Sci.* **2007**, *42*, 9905–9912. [CrossRef]
39. Wakahara, A.; Fujiwara, T.; Okada, H.; Yoshida, A.; Ohshima1, T.; Itho, H. Energy-Back-Transfer Process in Rare-Earth Doped AlGaN. *Mater. Res. Soc. Symp. Proc.* **2005**, *866*, 391–396. [CrossRef]
40. Gastuche, M.C.; Brown, G.; Mortland, M. Mixed magnesium-aluminum hydroxides. *Clay Miner.* **1967**, *7*, 177–201. [CrossRef]
41. Saber, O.; Tagaya, H. Preparation of a new nano-layered materials and organic–inorganic nano-hybrid materials Zn–Si LDH. *J. Porous Mater.* **2009**, *16*, 81–89. [CrossRef]
42. Salak, A.N.; Vieira, D.E.L.; Lukienko, I.M.; Shapovalov, Y.O.; Fedorchenko, A.V.; Fertman, E.L.; Pashkevich, Y.G.; Babkin, R.Y.; Shilin, A.D.; Rubanik, V.V.; et al. High-Power Ultrasonic Synthesis and Magnetic-Field-Assisted Arrangement of Nanosized Crystallites of Cobalt-Containing Layered Double Hydroxides. *Chem. Eng.* **2019**, *3*, 62. [CrossRef]
43. Parveen, N.; Ansari, S.A.; Ansari, M.O.; Cho, M.H. Manganese dioxide nanorods intercalated reduced graphene oxide nanocomposite toward high performance electrochemical supercapacitive electrode materials. *J. Colloid Interface Sci.* **2017**, *506*, 613–619. [CrossRef] [PubMed]
44. Donga, X.; Yub, Y.; Zhang, Y.; Xu, Z.; Jiang, H.; Meng, C.; Huang, C. Synthesis of cobalt silicate nanosheets with mesoporous structure and high surface area as the promising electrode for high-performing hybrid supercapacitor. *Electrochim. Acta* **2021**, *380*, 138225. [CrossRef]

45. Wang, Q.; Zhang, Y.; Jiang, H.; Li, X.; Cheng, Y.; Meng, C. Designed mesoporous hollow sphere architecture metal (Mn, Co, Ni) silicate: A potential electrode material for flexible all solid-state asymmetric supercapacitor. *Chem. Eng. J.* **2019**, *362*, 818–829. [CrossRef]
46. Rong, Q.; Long, L.-L.; Zhang, X.; Huang, Y.X.; Yu, H.-Q. Layered cobalt nickel silicate hollow spheres as a highly stable supercapacitor material. *Appl. Energy* **2015**, *153*, 63–69. [CrossRef]
47. Parveen, N.; Hilal, M.; Han, J.I. Newly Design Porous/Sponge Red Phosphorus@ Graphene and Highly Conductive Ni2P Electrode for Asymmetric Solid State Supercapacitive Device with Excellent Performance. *Nano-Micro Lett.* **2020**, *12*, 25. [CrossRef]
48. Parveen, N.; Ansari, S.A.; Al-Arjan, W.S.; Ansari, M.O. Manganese dioxide coupled with hollow carbon nanofiber toward high-performance electrochemical supercapacitive electrode materials. *J. Sci. Adv. Mater. Devices* **2021**, *6*, 472–482. [CrossRef]
49. Dong, X.; Yu, Y.; Jing, X.; Jiang, H.; Hu, T.; Meng, C.; Huang, C.; Zhang, Y. Sandwich-like honeycomb Co_2SiO_4/rGO/honeycomb Co_2SiO_4 structures with enhanced electrochemical properties for high-performance hybrid supercapacitor. *J. Power Source* **2021**, *492*, 229643. [CrossRef]
50. Zhang, Y.; Wang, C.; Dong, X.; Jiang, H.; Hu, T.; Meng, C.; Huang, C. Alkali etching metal silicates derived from bamboo leaves with enhanced electrochemical properties for solid-state hybrid supercapacitors. *Chem. Eng. J.* **2021**, *417*, 127964. [CrossRef]

nanomaterials

Article

A Detailed Insight into Acoustic Attenuation in a Static Bed of Hydrophilic Nanosilica

Syed Sadiq Ali [1], Agus Arsad [2], SK Safdar Hossain [1] and Mohammad Asif [3,*]

[1] Department of Chemical Engineering, King Faisal University, P.O. Box 380, Al-Ahsa 31982, Saudi Arabia; ssali@kfu.edu.sa (S.S.A.); snooruddin@kfu.edu.sa (S.S.H.)
[2] UTM-MPRC Institute for Oil and Gas, School of Chemical and Energy Engg, Faculty of Engineering, Universiti Teknologi Malaysia, Johor Bahru 81310, Malaysia; agus@utm.my
[3] Department of Chemical Engineering, King Saud University, P.O. Box 800, Riyadh 11421, Saudi Arabia
* Correspondence: masif@ksu.edu.sa; Tel.: +966–11–4676849

Abstract: The commercial utilization of bulk nanosilica is widespread in concrete, rubber and plastics, cosmetics and agriculture-related applications, and the market of this product is projected to exceed USD 5 billion by 2025. In this investigation, the local dynamics of a nanosilica bed, excited with sinusoidal acoustic waves of different frequencies, were carefully monitored using sensitive pressure transducers to obtain detailed insights into the effectiveness of sound waves as a means of energy transport inside the bed. The evolution of wave patterns and their frequency and power distributions were examined both in the freeboard and in the static bed. These results were compared with those obtained by using an empty column. The acoustic frequency strongly affected the signal power. The average power of the acoustic signal in the freeboard region was twice higher than that for the empty column, whereas the same (power) ratio decreased to approximately 0.03 inside the bed for 300 Hz. However, at 360 Hz, the power ratio was substantially lower at 0.24 and 0.002 for the freeboard and the granular bed, respectively, thereby indicating tremendous attenuation of acoustic waves in the granular media at all frequencies.

Keywords: acoustic vibrations; nanosilica; frequency analysis; attenuation; freeboard region; granular bed

Citation: Ali, S.S.; Arsad, A.; Hossain, S.S.; Asif, M. A Detailed Insight into Acoustic Attenuation in a Static Bed of Hydrophilic Nanosilica. *Nanomaterials* **2022**, *12*, 1509. https://doi.org/10.3390/nano12091509

Academic Editors: Jihoon Lee and Ming-Yu Li

Received: 21 March 2022
Accepted: 27 April 2022
Published: 28 April 2022

1. Introduction

Ultrafine particles are widely used in process industries and laboratories owing to their tremendously large surface area, which enhances the surface-based rate processes. However, processing these particles is often challenging due to strong interparticle forces (IPFs), which lead to the formation of large agglomerates and compromise the effectiveness of these particles in actual applications. During the two-phase gas-solid processing, agglomeration may lead to poor interphase mixing, low heat, and mass transfer rates, thereby compromising the efficiency of the overall process [1–5].

Fluidization technology can be used to promote efficient interphase mixing between the gas phase and the resident solid phase of the bed. This technique improves the heat and mass transfer rates and lowers the energy consumption by limiting the pressure drop to the effective weight of the bed [6–10]. However, the physical properties of the solid phase have an important bearing on the nature of the fluidization. The fluidization of fine and ultrafine particles is particularly challenging due to the presence of strong IPFs, which leads to an uneven and non-homogeneous fluidization. To counteract the effect of IPFs, fluidization assistance is often employed by inputting additional energy. This approach helps improve the fluidization hydrodynamics by lowering the minimum fluidization velocity (U_{mf}), increasing the bed expansion and suppressing the hysteresis phenomenon caused by the bed's non-homogeneities [11–16].

One of the most widely reported assisted fluidization techniques in the literature is acoustic vibration, where sound waves act as a source of additional energy needed to overcome the IPFs [17,18]. In fact, the application of acoustics, especially nanoacoutics, in different areas of science, engineering, and medicine is a growing area of research [19]. Many studies have investigated the effect of the acoustic frequency and amplitude on fluidization hydrodynamics by monitoring the minimum fluidization velocity in the presence of sound waves. For example, Zhu et al. [20] varied the sound pressure level (SPL) and frequency in a short fluidized bed of hydrophobic nanoparticles and found that the acoustic field helped lower the U_{mf} and improve the bed homogeneity when the amplitude exceeded 95 dB. They detected a stronger effect of the sound at a lower frequency and higher amplitude. However, at frequencies greater than 2000 Hz, the effect of acoustics was reportedly negligible. Apart from lowering the minimum fluidization velocity, sound assistance can also improve the stability of the fluidized bed by suppressing the density fluctuations, thereby promoting segregation based on the density difference [21]. The improved hydrodynamics of sound–assisted fluidized beds can enhance the carbon capture efficacy of activated carbon, and impart greater homogeneity to a bed of binary nano-powders during their fluidization [22,23]. Similarly, the use of acoustics was reported to enhance the fluidization quality and drying rate of lignite, thereby resulting in a better product quality [24].

Xu et al. [25] studied the effect of acoustic waves on the fluidization of Geldart groups C and A particles in a shallow fluidized bed (height: 4–5 cm) by placing the sound source below the distributor. For both groups of particles, sound waves of 120 Hz frequency were most effective in lowering the U_{mf}, whereas the theoretical resonant frequency was predicted to be 81 Hz. The authors also measured the SPL above the bed. However, at a fixed amplitude and frequency, the SPL values mostly decreased with the velocity increase for the group C particles. Meanwhile, SPL values recorded above the bed were relatively unaffected for group A particles above 1.5 cm/s. The authors argued that this behavior can be used to distinguish groups A and C particles.

Herrera et al. [26] examined the formation of standing waves in fluidized beds of fine particles as a function of frequency by placing a sound source at the top of a 0.9 m long column and by measuring the SPLs at different positions along the bed height. The SPL profiles along the height showed good agreement with the classical one-dimensional wave model that accounted for the attenuation phenomenon due to the damping of acoustic vibrations in the fluidized bed. By using shallow beds (height: 4.5–8.3 cm), they obtained velocity of sound as low as 24 m/s for a 40-m fly ash fluidized above the minimum bubbling velocity. Kumar et al. [27] investigated the acoustic attenuation characteristics of a 1.9 m long fixed bed with different packings. By conducting the nonlinear regression of experimental data and using the predictions of the classical wave model, they calculated the attenuation coefficient and acoustic velocity in the bed and found that the attenuation increased along with frequency and decreased along with the increasing bed void fraction. Increasing in the void fraction also increased the acoustic velocity and natural frequencies.

Cherntongchai et al. [28] determined the U_{mf} of a sound-assisted shallow fluidized bed (height $\approx$ 8.0 cm) of group A particles in the frequency range 50 Hz–500 Hz using a sound source located at the top of a long fluidization column with SPL fixed at 80 dB. By assuming that the SPL at the top of the bed is same as that of the sound source located at the top of the fluidization column, they predicted the formation of standing waves at different frequencies used in their experiments following the approach of Herrera et al. [26]. However, they did not consider the sound attenuation in the fluidized bed. They attributed the U_{mf} decrease at 50 Hz to the formation of a standing wave with $kL = \pi/2$, where k was the wave number, and L is the height of the fluidized bed.

Al-Ghurabi et al. [29] monitored the pressure transients at different locations along the height of a 370-mm long sound-assisted fluidized bed of hydrophilic particles with strong agglomeration behavior. They found that the pressure fluctuations at the resonant frequency were significantly higher than those obtained at non-resonant frequencies, whereas the mean values of the pressure drop were mostly unaffected by the frequency. Surprisingly, the sound waves at frequencies significantly different from the resonant frequency hardly affected the bed hydrodynamics. Moreover, the gas velocity mitigated the effect of acoustic vibrations as the vigorous solid motion at high velocities absorbed the momentum of the sound waves. During their downward propagation, the sound waves undergo significant attenuation since the acoustic intensity, characterized by pressure fluctuations, in the lower bed region was significantly smaller than that in the upper region.

Among assisted fluidization techniques, sound-assisted fluidization has been widely investigated owing to its potential application as a low-cost alternative to the energy-intensive assisted fluidization technique of mechanical vibration. While most studies have mainly focused on improving fluidization hydrodynamics as discussed above, a deeper insight into the evolution of the wave structures and the strength of the acoustic field in the free board region and the granular bed has been clearly lacking in the literature. This study sets out to fill this gap by investigating the effect of sound waves along the height of a granular bed of highly porous nanosilica at different frequencies. The sound velocity, while being approximately 343 m/s in the air (and therefore in the free-board region with a negligible particle concentration) can be as low as 20 m/s in the granular bed [26]. The presence of these two acoustically interacting yet physically separate regions would lead to the evolution of different wave patterns given that the natural frequencies of standing waves are critically dependent upon the sound velocity. Unlike in previous studies where the sound effects were mainly characterized by fluidization behavior (e.g., minimum fluidization velocity), this work directly monitors the acoustic waves (with frequencies ranging from 200 Hz to 400 Hz emitted from the source) in the bed and the freeboard region by using sensitive pressure transducers. The highest acoustic frequency (i.e., 400 Hz) used was below the Nyquist frequency of 500 Hz. The experimental results were also compared with that of an empty column to clearly delineate the effect of the granular bed on the evolution and attenuation of wave structures. Such a study that clearly sheds light on the limitation of the sound waves as means of the fluidization assistance has in fact been long overdue. Results of this investigated clearly reveal that the effect of acoustic vibrations is mainly limited to the upper part of the granular bed. Even at a depth of 0.5 m from the upper bed interface with a sound source of 125 dB, the signal attenuation becomes too significant that any perceived effect of sound waves on the fluidized bed hydrodynamics hardly appears justifiable.

2. Experimental

2.1. Experimental Setup

The detailed schematic of the experimental setup is reported in Figure 1. A 1.5 m tall transparent perspex column with 0.07 m internal diameter (ID) was used as the test section. A 0.3 m long plenum was used as the calming section. A distributor, with 2 mm holes and 2.7% opening, was used to separate the test section from the calming section. The distributor was covered with a nylon mesh of pore size 20 μm to prevent the solid particles from passing through the holes of the distributor. A 0.3 m long and 0.15 m ID disengagement section was placed at the top of the test-section to minimize the entrainment losses. Acoustic vibrations were generated using a downward-facing loudspeaker placed above the disengagement section at a distance of approximately 1.75 m from the distributor. The loudspeaker was connected to the audio port of a laptop through an amplifier. A MATLAB program (MathWorks, Natick, MA, US) was used to generate sinusoidal waveform of the required frequency.

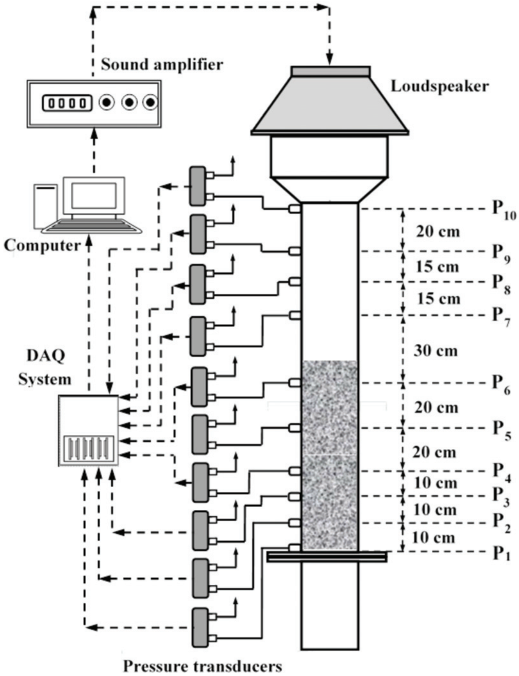

Figure 1. Schematic of the experimental set-up.

The acoustic waves were monitored using 10 different pressure transducers as shown in Figure 1. The positions of the pressure ports from the distributor are presented in Table 1, where the distances from the distributor (x) are normalized with respect to the distance of the sound source (i.e., L = 1.75 m) to yield dimensionless distance, $\overline{x}$, from the distributor. Highly sensitive bidirectional differential pressure transducers (PX163-005BD5V, Omega, Norwalk, CT, US) with a response time of 1 ms and a bandwidth of 1 kHz were used. The range of these transduces were ± 5 in H_2O (i.e., ±1244 Pa) to ensure an accurate measurement of low-pressure events taking place in our acoustically perturbed system. The pressure transducers were connected to a data acquisition (DAQ) system (USB-6289, National Instruments, Austin, TX, US), operated using the LabVIEW software (National Instruments, Austin, TX, US). The pressure transient data were acquired at a rate of 1000 Hz.

Table 1. Location of pressure ports with distances measured from the distributor.

Pressure Port	**P1**	**P2**	**P3**	**P4**	**P5**	**P6**	**P7**	**P8**	**P9**	**P10**
Location, x (m)	0.01	0.1	0.2	0.3	0.5	0.7	1.0	1.15	1.3	1.5
Location $\overline{x}$ (m/m)	0.01	0.06	0.11	0.17	0.29	0.40	0.57	0.66	0.74	0.86

2.2. Nanosilica Powder

Hydrophilic nanosilica (Aerosil 200, Evonik Industries AG, Essen, Germany) with a reported primary size of 12 nm and specific surface of 200 m^2/g were used in our experiments. In a powdered bed, these materials have a porosity of approximately 0.977 and a tapped density of approximately 50 kg/m^3. In dry dispersion, the nanosilica mainly takes the form as multi-level agglomerates with a wide size distribution varying from 2 µm to 100 µm [30,31].

2.3. Measurements and Calibration

The pressure fluctuations can be characterized as the root mean square of sound pressure, p_{rms}, which is the standard deviation of the recorded pressure transients or root mean square when the average pressure is zero

$$p_{rms} = \sqrt{\frac{1}{(N-1)}\sum_{i=1}^{N}\left(P_i - \overline{P}\right)^2} \tag{1}$$

where N is the number of data points, p_i is the instantaneous pressure in Pa, and $\overline{P}$ is its average value.

p_{rms} can be converted into SPL (dB) as

$$\mathrm{SPL} = 20\log_{10}\left[\frac{p_{rms}}{P_{ref}}\right] \tag{2}$$

where $p_{ref} = 2 \times 10^{-5}$ Pa is the reference pressure. However, to obtain precise SPL values in the experiments, a calibration was performed to interpolate SPL with p_{rms} using a Bruel and Kjaer, Type 4231 (Nærum, Denmark) sound pressure level meter. To this end, the pressure and SPL were recorded simultaneously by plugging both the SPL meter and pressure traducers in the same pressure tap. As shown in Figure 2, the pressure transducer output in terms of Pa can be related to SPL (dB) as

$$\mathrm{SPL} = 9.646ln(p_{rms}) + 83.05 \tag{3}$$

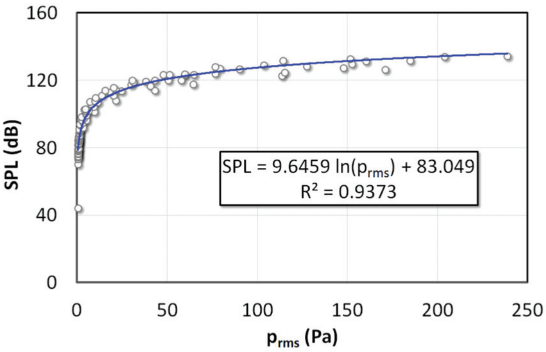

Figure 2. Calibration of the SPL meter with respect to root mean square pressure amplitude.

2.4. Methodology

The sound pressure level of the acoustic source (i.e., loud-speaker) was fixed at 125 dB. Two sets of experiments were carried out by varying the sound frequency and recording the pressure dynamics at 1000 Hz. An empty column was used in the first set of experiments, whereas a nanosilica bed was employed in the second set of experiments. The height of the bed was set to 0.78 m in the experiments. The experiments were carried out by varying frequencies in the range of 200 Hz to 400 Hz (i.e., 200, 220, 240, 270, 300, 320, 340, 360, 380, and 400 Hz).

3. Mathematical Model

3.1. Empty Bed

When an acoustic wave travels from one medium to another, a part of incident wave is reflected by the interface, whereas the other portion transmits though the interface to another medium. When the reflected wave overlaps the incident wave, a new waveform called standing waves is generated due to the superimposition of incident and reflected waves, which is termed as standing wave. The pressures of the reflected and transmitted acoustic waves at the interface are related with that of the incident wave in terms of the impedances of these two media as follows [32]:

$$\frac{p_r}{p_i} = \frac{z_2 - z_1}{z_2 + z_1} \tag{4}$$

$$\frac{p_t}{p_i} = 2\frac{z_2}{z_2 + z_1} \tag{5}$$

where p_i is the pressure of the incident wave, p_r and p_t are the pressures of the reflected and transmitted waves, respectively. The z_1 and z_2 are the specific acoustic impedances of the first medium and second media.

The one dimensional propagation of plane acoustic pressure waves in air can be described as [26,32]:

$$\frac{\partial^2 p}{\partial t^2} - c^2\frac{\partial^2 p}{\partial x^2} = 0 \tag{6}$$

where c is the speed of the acoustic wave in the medium, and t and x are the temporal and spatial coordinates, respectively. The longitudinal sound waves travel from the source towards the distributor, which acts as a closed boundary. The reflected wave from the distributor forms a standing wave when superimposing the incident wave. The general solution of Equation (6) is given as [32]

$$p(x,t) = \sqrt{(A+B)^2 cos^2(kx) + (A-B)^2 sin^2(kx)}\ cos(\omega t - \phi) \tag{7}$$

where

$$\phi = tan^{-1}\left(\frac{(A-B)}{(A+B)}tan(kx)\right) \tag{8}$$

Here, $k = \frac{\omega}{c} = \frac{2\pi f}{c} = \frac{2\pi}{\lambda}$, is the wave number, f is the frequency, ω is the angular frequency, and λ is the wavelength.

For the case of an empty column, the boundary is the distributor, which is a rigid thick perspex plate with a specific acoustic impedance of 3.2×10^6 Pa·m^{-1}s [33]. Given that the specific acoustic impedance of air is 415 Pa·m^{-1}s, we have $z_2 \gg z_1$, and hence $p_r \approx p_i$ in Equation (4). The amplitudes of the incident and reflected waves are equal. Therefore,

$$p(x,t) = P_0\sqrt{\frac{cos^2(kx)}{cos^2(kL)}}\ cos(\omega t) \tag{9}$$

where P_0 is the amplitude of the waves originating from the source of acoustic vibrations (i.e., loudspeaker).

The standing wave formation results in the development of nodes and antinodes in the closed column that can be predicted as follows using amplitude term in Equation (9)

$$kL = (2n-1)\frac{\pi}{2}; \qquad n = 1,\ 2,\ 3, \ldots\ldots \tag{10}$$

which corresponds to the pressure antinodes or displacement nodes. Therefore, $kL = \pi/2$ gives rise to the first harmonic with one node and one antinode. For the case with L= 1.75 m and 27 °C, the fundamental frequency is approximately 50 Hz. Note that closed pipe will allow only odd harmonics. Therefore, the frequency of the third, fifth, and seventh harmonics will be 149, 249, and 348 Hz, respectively, given that the velocity of sound at 27 °C is approximately 348 m/s.

3.2. Static Granular Bed of Ultrafine Particles

During the propagation of acoustic waves through the freeboard region, part of the pressure intensity transverses through the interface and contributes to the augmentation of energy in the granular bed, whereas the remaining energy is reflected as shown in Figure 3. The upper layer of the bed acts as the first interface for the reflection and refraction of the acoustic waves. The transmitted wave p_{t1} travels through the bed and reaches the distributor at the bottom, which acts as the second interface. The reflected wave p_{r1} from the first interface superimposes with the incident wave p_{i1} to form a standing wave in the freeboard. However, the resultant standing wave in the freeboard is different from the standing waves formed in the completely empty column due to the difference between the two media. The fraction of sound intensity that is transmitted to the other medium and the one that is reflected back can be calculated by using the acoustic power transmission coefficient, α_t and acoustic power reflection coefficient, α_r [32].

$$\alpha_t = \frac{I_t}{I_i} = \frac{{p_t}^2 z_1}{{p_i}^2 z_2} \tag{11}$$

$$\alpha_r = \frac{I_r}{I_i} = \frac{{p_r}^2}{{p_i}^2} \tag{12}$$

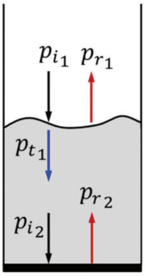

Figure 3. Incidence, reflection and transmission of acoustic waves from the bed interface and the distributor.

Substituting Equations (3) and (4) into Equations (11) and (12) yields

$$\alpha_t = \frac{4z_1 z_2}{(z_1 + z_2)^2} \tag{13}$$

$$\alpha_r = \frac{(z_2 - z_1)^2}{(z_1 + z_2)^2} \tag{14}$$

The specific acoustic impedance can be calculated as [34]

$$z = \rho_b c \tag{15}$$

The velocity of sound in a medium is calculated as [35,36]

$$c = \frac{1}{\sqrt{\rho_b\left(\frac{\varepsilon}{K_g} + \frac{(1-\varepsilon)}{K_p}\right)}} \tag{16}$$

where K_g and K_p are the bulk moduli of the gas and solid particles in the bed, respectively. For air, $K_g = 1.01 \times 10^5$ Pa, and $K_P = 3.67 \times 10^7$ Pa for SiO_2. The speed of sound in the granular bed is therefore 45.4 m/s, whereas specific values of impedance are 2152.43 Pa m^{-1}s and 415 Pa m^{-1}s for the bed and air, respectively. Equations (13) and (14) are then used to calculate the acoustic power transmission coefficient, $\alpha_t = 0.54$ and acoustic power reflection coefficient, $\alpha_r = 0.46$. However, when the acoustic wave reaches the distributor, complete reflection takes place at the rigid distributor interface $\left(z_2 = 3.2 \times 10^6 \text{ Pa m}^{-1}\text{s}\right)$, leading to $\alpha_r \approx 1$ in Equation (14), given that $z_2 \gg z_1$. Moreover, in the particles bed, we have $p_{t1} > p_{r2}$ due to the attenuation of acoustic resulting from the energy absorption by the nanosilica bed.

4. Results and Discussion

This section initially presents the experimental data for the empty column for different sound frequencies recorded at several locations along the height of the closed column shown in Figure 1. The case of the highly porous static bed of ultrafine nanosilica is considered afterwards. Unlike previous studies that were mostly carried out using shallow beds, using sensitive pressure transducers in this work allowed utilization of a relatively long bed with a height of 0.78 m. The sound amplitude and recoding locations were kept the same as the ones for the empty column to examine the evolution and attenuation of the wave patterns during their downward propagation through the nanosilica particle bed toward the distributor.

4.1. Empty Column Dynamics under Acoustic Vibrations

Although the experiments were carried out for 10 different frequencies ranging from 200 Hz to 400 Hz, Figure 4 shows the experimental data only for three selected acoustic frequencies (i.e., 220, 240 and 360 Hz) to examine how the difference in frequencies, whether small or large, affects the evolution of wave patterns in the empty column. The normalized distance of the measurement point from the distributor is shown as the boxed legend. Although the difference between 220 Hz and 240 Hz was not substantial, yet their wave dynamics significantly differed. For instance, the 240 Hz acoustics, demonstrated localized high-density pattern, resulting from the presence of different waves with close frequencies. Interestingly, the location closest to the sound source (i.e., $\overline{x}$ = 0.86) in Figure 4a,b (at 220 Hz and 240 Hz) had much smaller fluctuations compared with farther away location at $\overline{x}$ = 0.74. The amplitude of acoustic waves subsequently decreased while moving away from the source until reaching $\overline{x}$ = 0.40 (Figure 4a,b), which was slightly below the midpoint of the empty column. However, the wave amplitude demonstrated a modest increase farther away from the acoustic source (i.e., $\overline{x}$ = 0.29) before decreasing at $\overline{x}$ = 0.17 and progressively increasing in the lower portion of the closed empty column. The highest degree of disturbance was observed slightly above the distributor at $\overline{x}$ = 0.06, whereas a substantial attenuation in magnitude was observed immediately above the distributor. The difference in sound frequency, albeit insignificant, critically influenced the acoustic amplitude. For instance, at the same locations (e.g., at $\overline{x}$ = 0.06) the amplitude of acoustic disturbance for 240 Hz was almost twice as large as that for 220 Hz.

When the frequency increased to 360 Hz (Figure 4c), the fluctuations mostly showed a significant increase compared to those observed at the corresponding locations for 220 Hz and 240 Hz. For instance, at $\overline{x}$ = 0.06, the amplitudes of pressure fluctuations were as high as ±1000 Pa. By contrast, the fluctuations were substantially mitigated at other locations (e.g., $\overline{x}$ = 0.40, 0.17, and 0.01). The dependence of the wave amplitude on the location was mainly due to the superposition of the incidence wave with the one reflected from the distributor, which resulted in the formation of standing waves. Theoretically, there should have been a displacement node (or pressure antinode) at the distributor that acts as a closed boundary. On the contrary, the amplitude at this location was smaller than that at $\overline{x}$ = 0.06, which could be an artefact of the perforations present on the distributor. According to the wave model, when a closed empty column is subjected to acoustics of 360 Hz (i.e., $kL \cong 7.2\pi/2$), which is close to the seventh harmonic (i.e., the third overtone) a standing wave with four nodes and an equal number of antinodes is formed.

The pressure transients in Figure 4 comprise of waves of different frequencies even though an acoustic wave of a single frequency was introduced in the column. This aspect of the acoustics dynamics is explored to obtain deep insights into this phenomenon by carefully analyzing the signals in the frequency domain. For the case of the 220 Hz acoustics shown in Figure 5a, two small-amplitude yet prominent peaks of comparable magnitude corresponding to 220 Hz and 320 Hz were observed at $\overline{x}$ = 0.86. Interestingly, peak of

320 Hz was more prominent than that of 220 Hz. Therefore, the total standard deviation of the acoustic fluctuations at $\overline{x}$ = 0.74 was 175 Pa, followed by 160 Pa at $\overline{x}$ = 0.06, where several acoustic frequencies were present, apart from the prominent peak at 220 Hz. The high amplitude waves at widely varying locations inside the column indicates the presence of pressure antinodes. Meanwhile, the lowest standard deviation of 25 Pa was recorded at $\overline{x}$ = 0.40, which indicates the presence of a pressure node. Low standard deviations of 44, 49, 54, and 51 Pa were also observed at $\overline{x}$ = 0.86, 0.66. 0.57, and 0.17, respectively.

Figure 5b illustrates the case of 240 Hz acoustics. Unlike in 220 Hz, a prominent peak appeared only for 240 Hz at $\overline{x}$ = 0.74, whereas smaller peaks around the one at 240 Hz appeared at $\overline{x}$ = 0.66. The spread of other frequencies around the 240 Hz peak was not as wide as that around 220 Hz peak. This phenomenon can be observed across different locations where the pressure transients were recorded, and resulted in the evolution of localized high-density wave patterns as shown in Figure 4b. The highest standard deviation of 301 Pa, which indicates a pressure antinode, was recorded at $\overline{x}$ = 0.06 (near the distributor), and was almost twice that obtained for 220 Hz sound waves. The second highest standard deviation of 210 Pa was recorded much closer to the sound source at $\overline{x}$ = 0.74.

The amplitude spectra of the pressure signals recorded at different locations when the column was excited with the 360 Hz frequency sound waves are shown in Figure 5c. The high magnitude fluctuations at $\overline{x}$ = 0.74, 0.57, 0.29, and 0.06 seen in Figure 4c can be ascribed to the formation of antinodes. However, unlike the 220 Hz and 240 Hz acoustic waves considered before, the prominent amplitude peak was almost exclusively contributed by 360 Hz acoustic disturbances. The standard deviation of the pressure fluctuations near the distributor (i.e., at $\overline{x}$ = 0.06) was 650 Pa (SPL = 146 dB), which was even higher than the 125 dB amplitude used for the sound source. At $\overline{x}$ = 0.40, the lowest degree of fluctuation was observed with a standard deviation of 16 Pa, which corresponded to an SPL of 110 dB.

The predictions of the wave equation for the closed column at selected frequencies are shown in Figure 6, which plots the variation of the sound pressure level (SPL) with the distance above the distributor. The formation of pressure nodes and antinodes at various locations along the height of the fluidization column indicates a clear trend with a changing frequency. As the frequency increased, the nodes and antinodes also increased in number and shifted their positions. For example, the mathematical model predicted pressure nodes at $\overline{x}$ = 0.17 and at $\overline{x}$ = 0.23 above the distributor at 360 Hz (i.e., $kL \cong 7.2\pi/2$), which is clearly supported by the experimental data shown in Figure 4c. Another node was observed at $\overline{x}$ = 0.69, which closely corresponds to the behavior observed at $\overline{x}$ = 0.74 (Figure 4c). A notable difference was also observed in the amplitudes of the standing waves by changing the source frequency. The amplitudes of standing waves generated with a 360 Hz source frequency is significantly higher than those of standing waves generated at lower frequency even though the experimental configuration remained the same. This behavior was also clearly reflected in the experimental data shown in Figures 3 and 4.

Figure 7 compares the experimental data for 240 Hz and 360 Hz. In both cases, a clear discrepancy was observed at the lower boundary. The wave amplitude at the distributor, which was a pressure antinode, was smaller than that of the point immediately above it (i.e., $\overline{x}$ = 0.06). Such difference can be mainly attributed to the perforations on the distributor, which mitigate the development of a displacement node at the distributor. However, the model predictions and the experimental data showed an overall good agreement for the case of 360 Hz. Meanwhile, some discrepancies were noted for the case of 240 Hz due to the presence of waves of other frequencies.

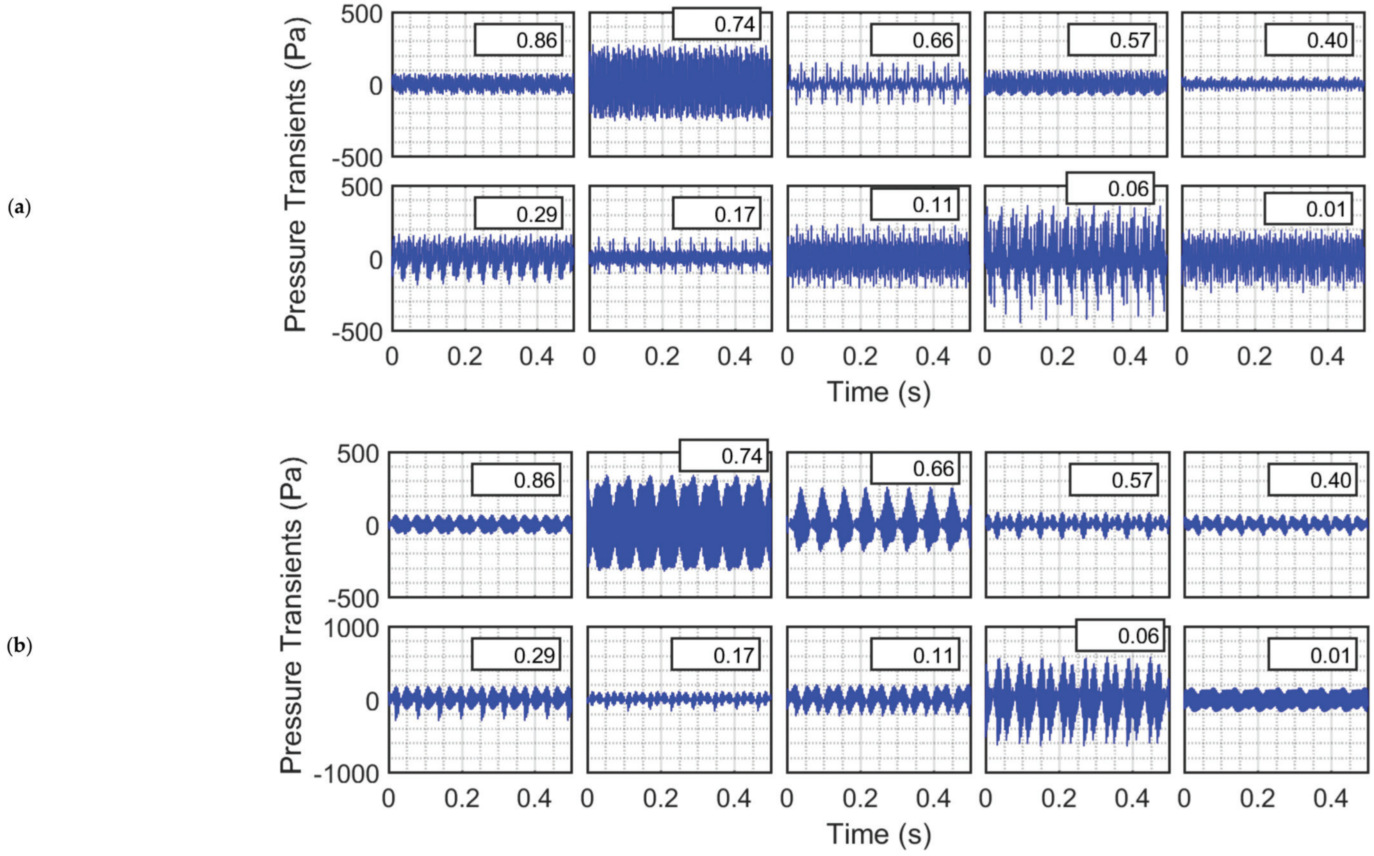

Figure 4. *Cont.*

(c)

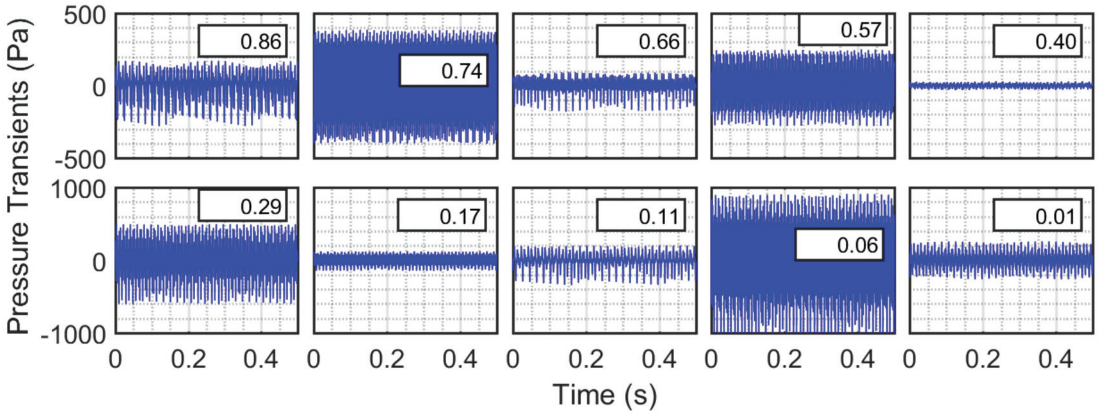

Figure 4. Local pressure transients in a closed empty column excited with sound waves of frequencies (**a**) 220, (**b**) 240, and (**c**) 360 Hz.

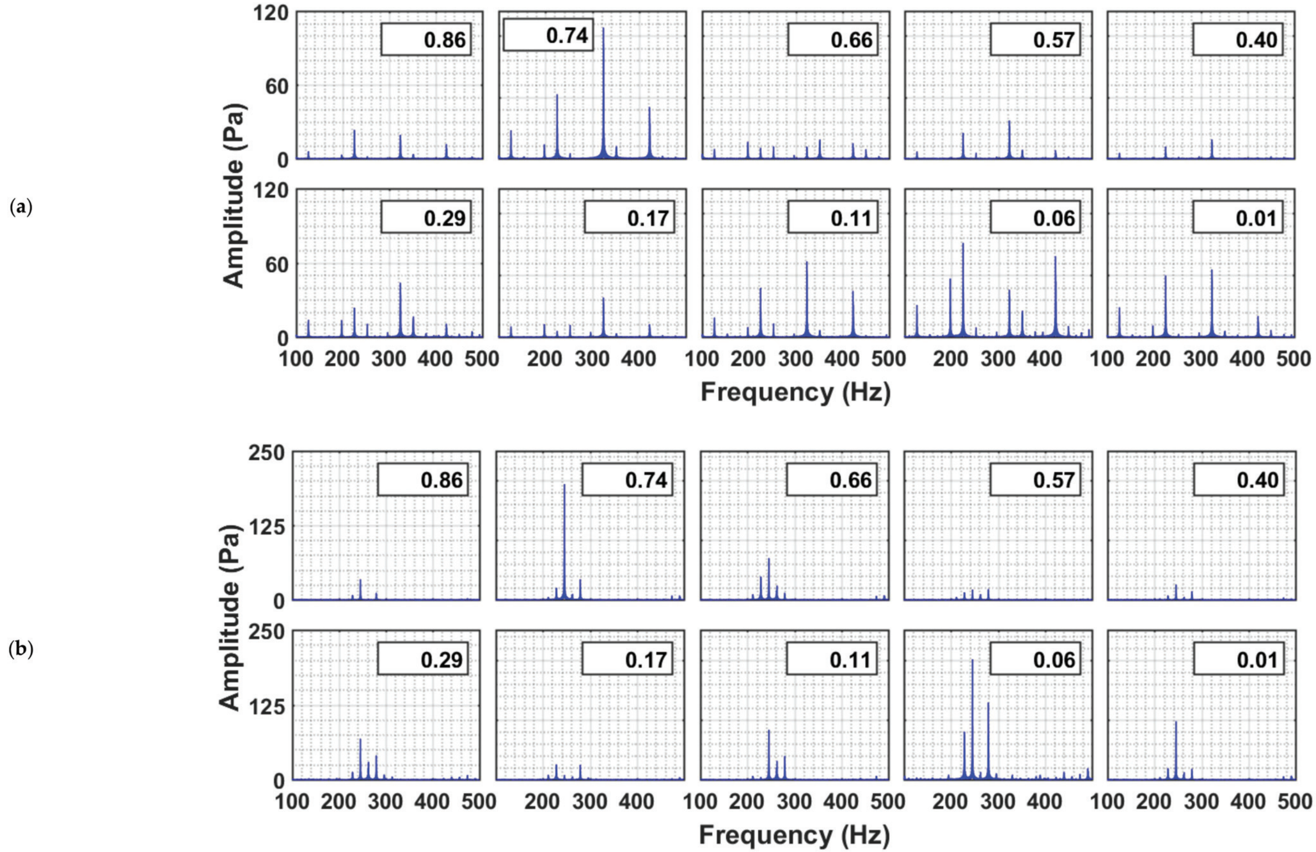

Figure 5. *Cont.*

(**c**)

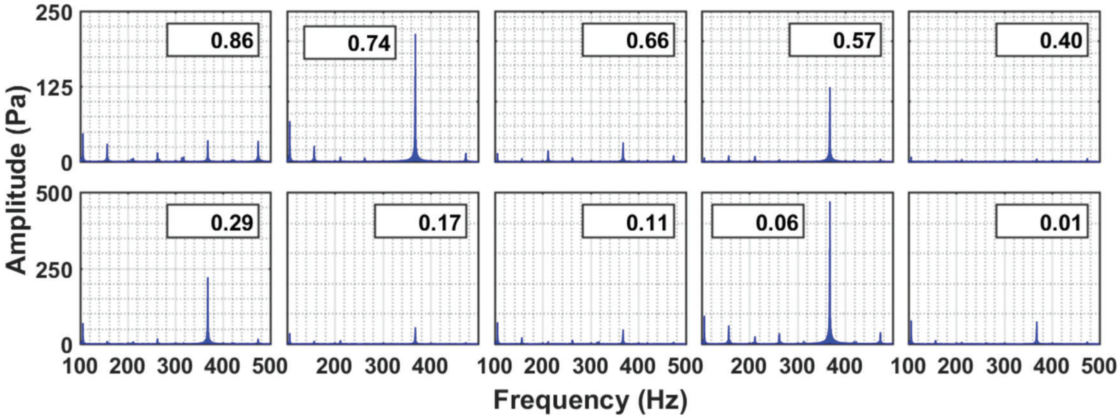

Figure 5. Frequency spectra of the local pressure transients in a closed empty column subjected to sound waves of frequencies (**a**) 220, (**b**) 240, and (**c**) 360 Hz.

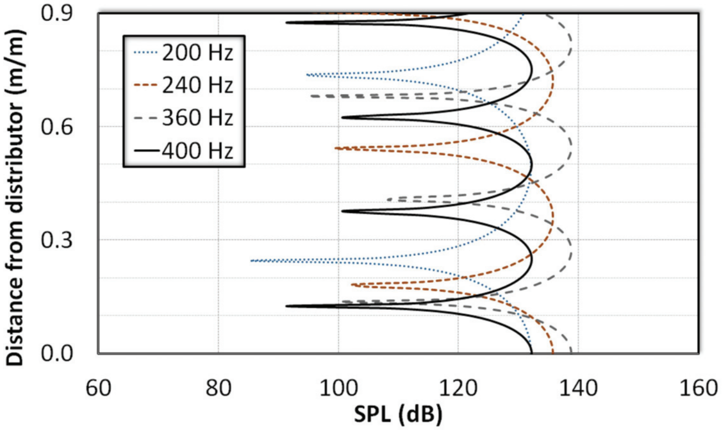

Figure 6. Model predictions of sound pressure level in an empty column subjected to sound waves of different frequencies.

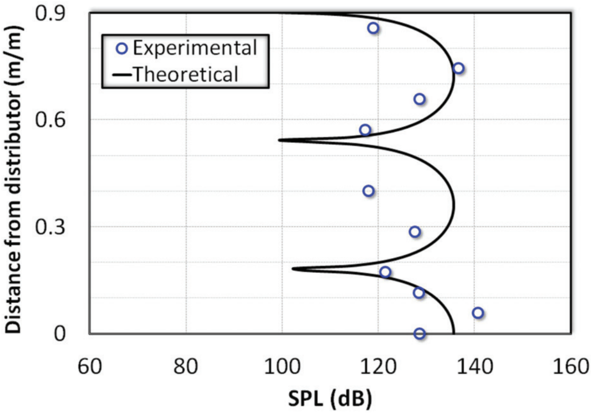

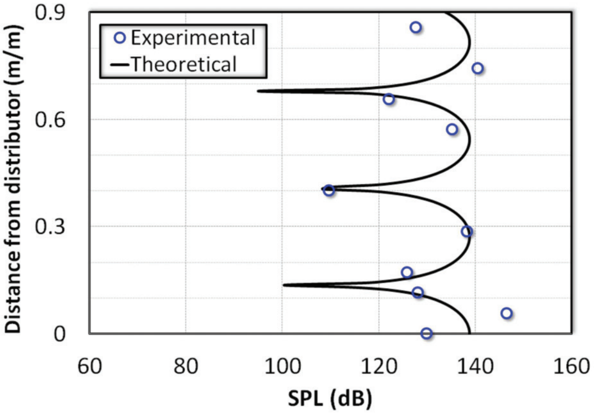

Figure 7. Comparison of model predictions with experimental data in an empty column subjected to sound waves of frequencies (**a**) 240 Hz and (**b**) 360 Hz.

4.2. Static Granular Nanosilica Bed Dynamics under Acoustic Vibrations

Figure 8 shows the behavior when the column is filled with nanosilica up to the height of 78 cm. Two different frequencies (i.e., 240 and 360 Hz) are considered here. Figure 8a presents the case of 240 Hz. The behavior in the freeboard region was similar to that observed for the case of an empty column as far as amplitudes are concerned. For instance, at $\overline{x}$ = 0.74, the standard deviations for the empty column and the nanosilica bed are 210.4 Pa and 210.8 Pa, respectively. Moreover, the pressure transients appeared to be superimposition of waves of different frequencies. Even the uppermost region of the bed at $\overline{x}$ = 0.40 did not show any significant difference. However, the sound intensity was significantly attenuated in the bed owing to the presence of nanosilica powder. At $\overline{x}$ = 0.06, the standard deviation was only 13.3 Pa, whereas that of empty column was 301.2 Pa. The Y-scale varies from −50 Ps to 50 Pa in the second row of the figure, whereas that in the first row varies within the ±500 Pa range.

For the same bed height, the effect of the 360 Hz acoustic waves was different than that of 240 Hz waves (Figure 8b). The amplitude of waves recorded in the freeboard region was mostly lower than those observed in the empty column even for locations close to the sound source and far from the boundary of the granular nanosilica bed (e.g., at $\overline{x}$ = 0.86). A significant difference was also observed in the freeboard region at $\overline{x}$ = 0.57, where an antinode turned into a node due to the presence of the bed. This phenomenon indicates the formation of a new standing wave pattern that evolved as a result of the interference of the reflected waves from the bed interface and the distributor. However, the magnitude of the wave had a lower resultant amplitude due to the absorption of sound energy by the granular medium as indicated by Equations (13) and (14). As seen in Figure 8b, the main difference was observed for the transients occurring inside the granular nanosilica bed. While the fluctuations for the empty bed varied by ± 600 Pa, less than ±40 Pa variations were observed in the locations inside the bed. For instance, at $\overline{x}$ = 0.06, the difference in the standard deviation was almost 100 times; 6.5 Pa (101 dB) for the nanosilica bed and 650 Pa (146 dB) for the empty column. Interestingly, the difference in the standard deviations between $\overline{x}$ = 0.40 (20.3 Pa, immediately below the top interface), and $\overline{x}$ = 0.29 (19.4 Pa, well within the bed) was negligible, although one would expect the sound waves to attenuate along with increasing penetration depth inside the bed. This phenomenon can be attributed to the evolution of a new standing wave pattern inside the porous granular nanosilica bed.

In the frequency domain (Figure 9), several peaks simultaneously appeared in the neighborhood of the dominant frequency (i.e., 240 Hz), when the system was excited with 240 Hz frequency. This phenomenon can be clearly observed in the freeboard region and the upper part of the granular bed. However, as the acoustic waves traveled down the granular bed, the other frequency components were filtered out, thereby retaining only the dominant frequency component. The bed excited with 360 Hz sound waves demonstrated similar behavior. In most cases, the dominant peak at 360 Hz was clearly visible. Although attenuated, the dominant frequency wave was retained by the granular nanosilica bed while filtering out the other frequencies.

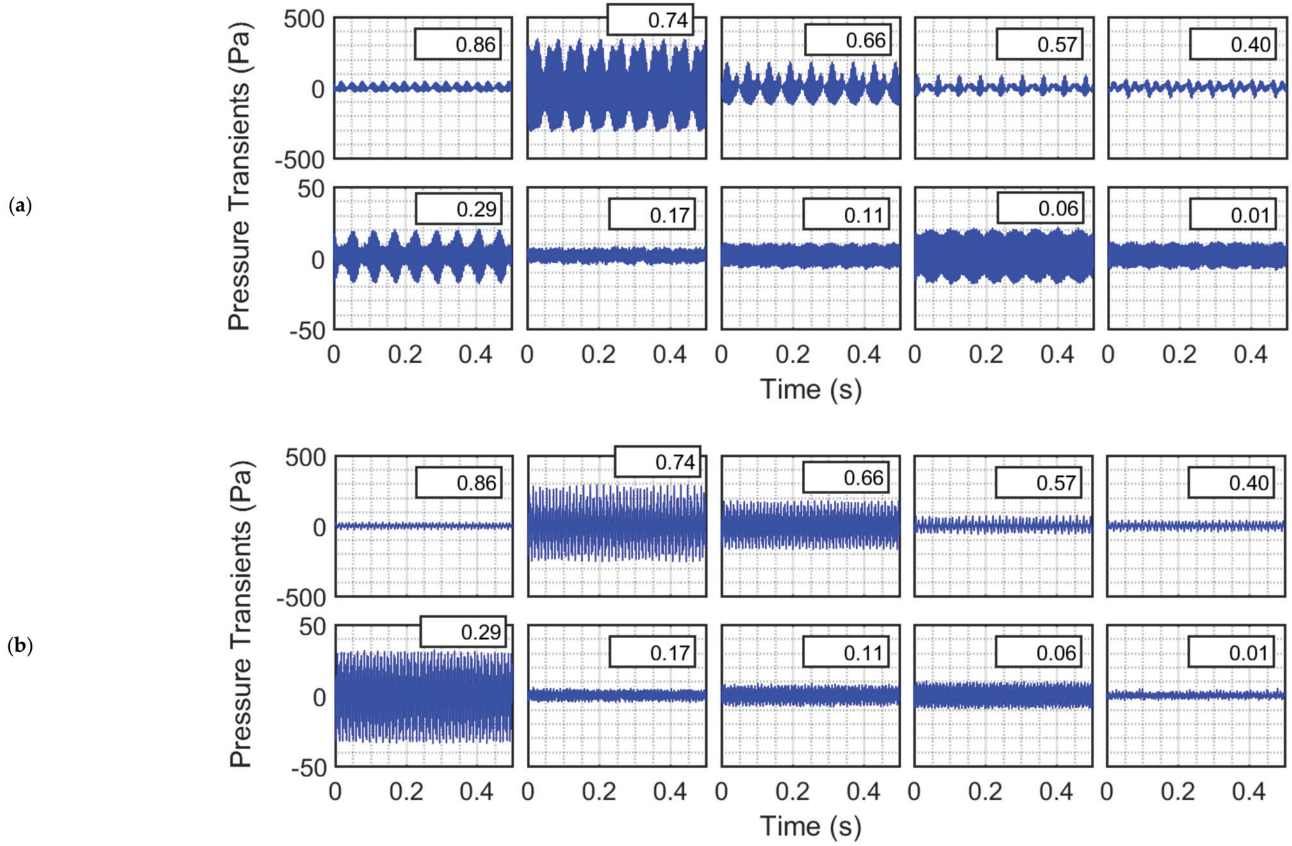

Figure 8. Pressure transients in a nanosilica bed and freeboard region excited with sound waves of frequencies (**a**) 240 Hz and (**b**) 360 Hz.

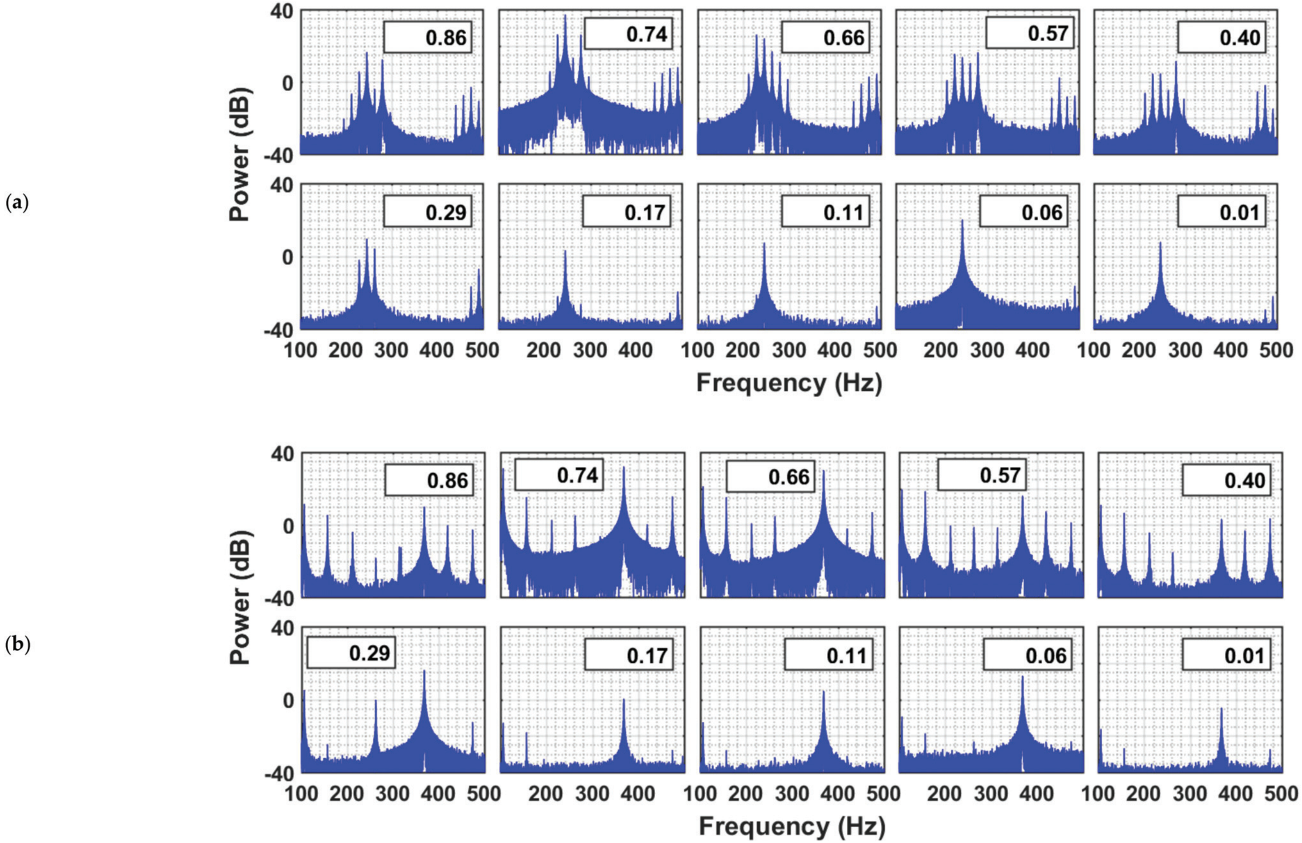

Figure 9. Power spectra of pressure transients in a nanosilica bed and freeboard region excited with sound waves of frequencies (**a**) 240 Hz and (**b**) 360 Hz.

4.3. Signal Power

The average power of the signal for the empty column and nanosilica bed was evaluated by integrating or summing the power spectra over the frequency. Figure 10 presents signal power only for selected frequencies (i.e., 220, 240, 360, and 380 Hz) in addition to the mean signal power of all frequencies considered in this study. Figure 10a considers the case of the empty column and clearly shows the peaks and troughs due to the existence of pressure nodes and antinodes. The sound waves of 360 Hz exhibited prominent peaks and troughs. These results were supported by the theoretical predictions in Figure 6. The dominant frequency was the main contributor to the signal power. When the column was partially filled with nanosilica, a significant change can be observed in the power profiles along the bed height as shown in Figure 10b. The nearly thousand-fold decrease in the magnitude of power inside the bed could be ascribed to the absorption of sound energy. In fact, the penetration of sound energy was limited only to the upper part of the bed. In this study, the bed height was set to 0.78 m (i.e., $\overline{x}$ = 0.45), and the first pressure port from the top of the bed was located at $\overline{x}$ = 0.40 (i.e., 0.70 m from the distributor). Despite a significant dissipation of the sound energy, the clear presence of peaks and troughs indicate the evolution of the standing wave pattern inside the bed. A pressure node was observed at $\overline{x}$ = 0.17 and an antinode was reported at $\overline{x}$ = 0.06 near the distributor. Meanwhile, the freeboard region, despite the absorption of energy in the bed, was not similarly affected as far as the power is concerned. Another noteworthy difference was observed between Figure 10a,b. The prominent peaks and troughs of 360 Hz sound waves in the empty column were suppressed due to the presence of the bed. In sum, changing the frequency of the sound waves does not significantly impact the power transmission inside the bed.

The power transmission and dissipation due to the presence of the granular nanosilica bed were further explored by comparing the power deep inside the bed at a distance of $\overline{x}$ = 0.06 from the distributor with the corresponding value for the empty column. The case of the freeboard region at $\overline{x}$ = 0.74 was also considered. The ratios for both cases are presented in Figure 11a. The ratio for the freeboard region mostly varied from 0.5 to 5. Interestingly, the average signal power (i.e., pressure fluctuations) at 300 Hz and 320 Hz in the freeboard region was almost five time larger than that in the empty column due to the shifting of the pressure antinode in response to the presence of the granular static bed. Meanwhile, the higher value of frequencies above 340 Hz resulted in significantly lower ratios. A similar trend was also observed for deep inside the bed at $\overline{x}$ = 0.06. However, the average signal power in the absence of the bed was 200 to 10,000 times higher than that in the presence of a bed, which clearly demonstrates that the presence of a granular nanosilica bed results in a significant power attenuation.

(**a**)

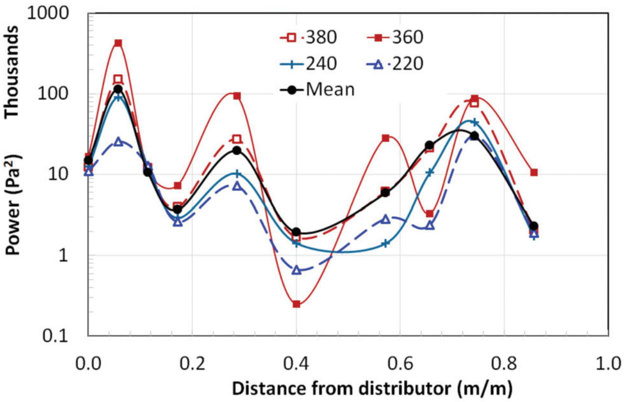

Figure 10. *Cont.*

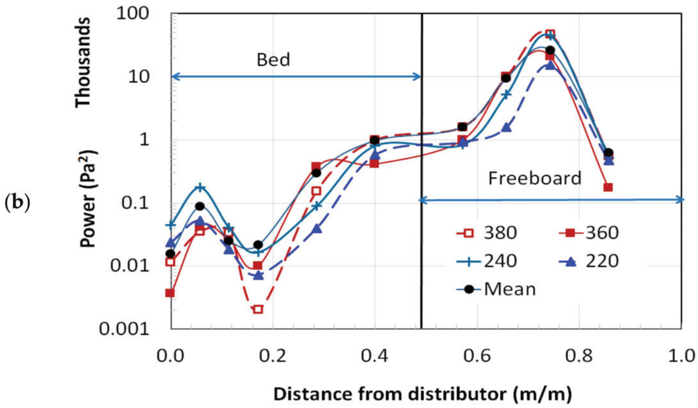

Figure 10. Power distribution of sound waves along the column length for (**a**) empty column and (**b**) nanosilica bed.

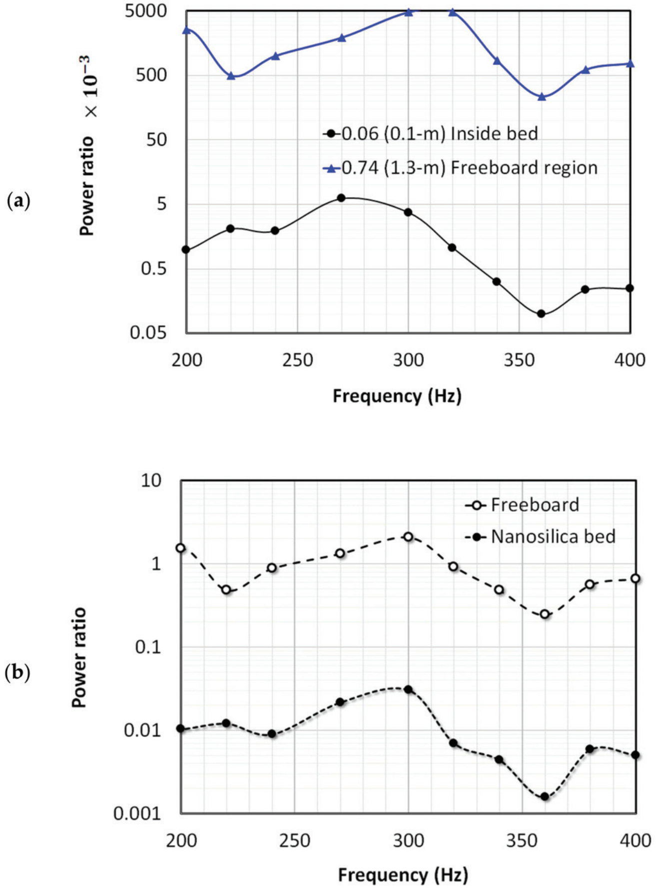

Figure 11. Effect of frequency on the acoustic attenuation (**a**) at a specific point inside the bed and in the freeboard region, and (**b**) the average effect for the entire bed and the freeboard region (the empty column values are used as reference).

Only a single location, each for the freeboard and the bed, where the peak fluctuations occurred has been considered so far in the above. The overall average signal powers for the freeboard region extending from $\overline{x}$ = 0.57 to 0.86 and for the granular bed region extending from $\overline{x}$ = 0.0 to 0.40 were also computed. Figure 11b compares the average powers thus obtained with the corresponding values for the empty bed to gain further insights into the region-wise signal attenuations. The observed trend was similar to that shown in Figure 11a where local ratios are presented. A smaller ratio was observed at 360 Hz since the signal power at this frequency was most pronounced in the empty column. However, the presence of the granular nanosilica bed mitigated its effect, resulting in lower values of power ratios.

5. Conclusions

Unlike previous studies that mostly used SPL meters, sensitive pressure transduces were utilized in this work to monitor the wave patterns generated in the closed empty column and static granular bed subjected to acoustic disturbance by placing a sound source at the top of the column. The amplitudes of the signal (i.e., pressure fluctuations) differed across various locations along the height of the column, indicating the evolution of standing wave patterns. Although the sound source was excited with a single frequency, the frequency domain analysis of the signal revealed the presence of disturbances of other frequencies. However, the granular nanosilica bed filtered the disturbances and retained only the dominant frequency component of the signal. A careful comparison of the disturbances between the empty column and the static granular bed revealed a significant dissipation of the signal power as the waves propagated downward the bed toward the distributor. The effect of the sound waves could only be observed in the upper region of the bed. Compared with the empty column, the signal power decreased by several orders of magnitude along with increasing distance from the upper interface of the bed. The sound frequency clearly affected the signal strength. However, contrary to the case of the empty column, the locations of pressure nodes and antinodes were not affected by the change of the frequency in the nanosilica bed.

Author Contributions: Conceptualization, S.S.A. and M.A.; methodology, S.S.A. and M.A.; software, S.S.A.; validation, S.S.A.; formal analysis, S.S.A.; resources, M.A.; data curation, S.S.A.; writing—original draft preparation, S.S.A.; writing—review and editing, A.A. and S.S.H.; visualization, S.S.A. and M.A.; supervision, M.A.; funding acquisition, S.S.H. All authors have read and agreed to the published version of the manuscript.

Funding: This research was funded by the Deanship of Scientific Research at King Faisal University through Grant No. 1811012 under the Research Group Support Track.

Institutional Review Board Statement: Not applicable.

Informed Consent Statement: Not applicable.

Acknowledgments: The authors acknowledge the Deanship of Scientific Research at King Faisal University for its financial support under the Research Group Support Track (Grant No. 1811012).

Conflicts of Interest: The authors declare no conflict of interest.

Nomenclature

c	speed of acoustic wave in the medium (m/s)
I	acoustic intensity
K	bulk modulus
p_{rms}	root mean square of sound pressure
N	number of data points
p_i	instantaneous pressure/incident pressure (Pa)
p_r	reflected pressure (Pa)
p_t	transmitted pressure (Pa)
$\overline{P}$	average value of p_i
P_0	amplitude of the waves originating from the source (Pa)
SPL	sound pressure level (dB)
x	distance from the distributor along the bed height (m)
$\overline{x}$	dimensionless distance from the distributor, i.e., $\overline{x} = x/L$ (m/m)
z	specific acoustic impedance
L	height of the acoustics source from distributor (m)
Greek symbols	
μ	air viscosity at room temperature (N·s m^{-2})
k	wave number
f	acoustic frequency
ω	angular frequency
λ	wavelength
α	acoustic power transmission coefficient
ρ_b	bulk density of the medium (kg/m^3)
ε	bed porosity

References

1. Karimi, F.; Haghshenasfard, M.; Sotudeh-Gharebagh, R.; Zarghami, R.; Mostoufi, N. Multiscale characterization of nanoparticles in a magnetically assisted fluidized bed. *Particuology* **2020**, *51*, 64–71. [CrossRef]
2. Ali, S.S.; Arsad, A.; Asif, M. Effect of modified inlet flow strategy on the segregation phenomenon in pulsed fluidized bed of ultrafine particles: A collapse bed study. *Chem. Eng. Processing - Process Intensif.* **2021**, *159*, 108243. [CrossRef]
3. Raganati, F.; Chirone, R.; Ammendola, P. Gas–solid fluidization of cohesive powders. *Chem. Eng. Res. Des.* **2018**, *133*, 347–387. [CrossRef]
4. Shabanian, J.; Chaouki, J. Influence of interparticle forces on solids motion in a bubbling gas-solid fluidized bed. *Powder Technol.* **2016**, *299*, 98–106. [CrossRef]
5. Ali, S.S.; Al-Ghurabi, E.H.; Ajbar, A.; Mohammed, Y.A.; Boumaza, M.; Asif, M. Effect of Frequency on Pulsed Fluidized Beds of Ultrafine Powders. *J. Nanomater.* **2016**, *2016*, 12. [CrossRef]
6. Fedorov, A.V.; Yazykov, N.A.; Bulavchenko, O.A.; Saraev, A.A.; Kaichev, V.V.; Yakovlev, V.A. CuFeAl Nanocomposite Catalysts for Coal Combustion in Fluidized Bed. *Nanomaterials* **2020**, *10*, 1002. [CrossRef] [PubMed]
7. Ali, S.S.; Asif, M. Fluidization of nano-powders: Effect of flow pulsation. *Powder Technol.* **2012**, *225*, 86–92. [CrossRef]
8. Asif, M.; Al-Ghurabi, E.H.; Ajbar, A.; Kumar, N.S. Hydrodynamics of Pulsed Fluidized Bed of Ultrafine Powder: Fully Collapsing Fluidized Bed. *Processes* **2020**, *8*, 807. [CrossRef]
9. Lee, J.-R.; Lee, K.-S.; Park, Y.-O.; Lee, K.-W. Fluidization characteristics of fine cohesive particles assisted by vertical vibration in a fluidized bed reactor. *Chem. Eng. J.* **2020**, *380*, 122454. [CrossRef]
10. Ali, S.S.; Basu, A.; Alfadul, S.M.; Asif, M. Nanopowder Fluidization Using the Combined Assisted Fluidization Techniques of Particle Mixing and Flow Pulsation. *Appl. Sci.* **2019**, *9*, 572. [CrossRef]
11. Hoorijani, H.; Reza, Z.; Kamal, N.; Navid, M. Investigating the hydrodynamics of vibro-fluidized bed of hydrophilic titanium nanoparticles. *Chem. Eng. Res. Des.* **2021**, *174*, 486–497. [CrossRef]
12. An, K.; Andino, J.M. Enhanced fluidization of nanosized TiO_2 by a microjet and vibration assisted (MVA) method. *Powder Technol.* **2019**, *356*, 200–207. [CrossRef]
13. Al-Ghurabi, E.H.; Shahabuddin, M.; Kumar, N.S.; Asif, M. Deagglomeration of Ultrafine Hydrophilic Nanopowder Using Low-Frequency Pulsed Fluidization. *Nanomaterials* **2020**, *10*, 388. [CrossRef] [PubMed]
14. Ali, S.S.; Asif, M. Effect of particle mixing on the hydrodynamics of fluidized bed of nanoparticles. *Powder Technol.* **2017**, *310*, 234–240. [CrossRef]
15. Zhao, Z.; Liu, D.; Ma, J.; Chen, X. Fluidization of nanoparticle agglomerates assisted by combining vibration and stirring methods. *Chem. Eng. J.* **2020**, *388*, 124213. [CrossRef]

16. Al-Ghurabi, H.E.; Ajbar, A.; Asif, M. Improving Fluidization Hydrodynamics of Group C Particles by Mixing with Group B Particles. *Appl. Sci.* **2018**, *8*, 1469. [CrossRef]
17. Ajbar, A.; Bakhbakhi, Y.; Ali, S.; Asif, M. Fluidization of nano-powders: Effect of sound vibration and pre-mixing with group A particles. *Powder Technol.* **2011**, *206*, 327–337. [CrossRef]
18. Xu, X.; Fu, Y.; Song, S.; Dong, L.; Lv, B.; Chen, Z.; Tian, Y.; Chen, J. Fluidization and separation characteristics of a gas–solid separation fluidized bed in the presence of an acoustic field. *Chem. Eng. Res. Des.* **2021**, *169*, 46–53. [CrossRef]
19. Peng, C.; Chena, M.; Spicerb, J.B.; Jiang, X. Acoustics at the nanoscale (nanoacoustics): A comprehensive literature review. Part I: Materials, devices and selected applications. *Sens. Actuators A Phys.* **2021**, *332*, 112719. [CrossRef]
20. Zhu, C.; Liu, G.; Yu, Q.; Pfeffer, R.; Dave, R.N.; Nam, C.H. Sound assisted fluidization of nanoparticle agglomerates. *Powder Technol.* **2004**, *141*, 119–123. [CrossRef]
21. Lv, B.; Deng, X.; Chen, J.; Fang, C.; Zhuc, X. Effects of sound fields on hydrodynamic and dry beneficiation of fine coal in a fluidized bed. *Sep. Purif. Technol.* **2021**, *254*, 117575. [CrossRef]
22. Ammendola, P.; Chirone, R.; Raganati, F. Fluidization of binary mixtures of nanoparticles under the effect of acoustic fields. *Adv. Powder Technol.* **2011**, *22*, 174–183. [CrossRef]
23. Ammendola, P.; Chirone, R. Aeration and mixing behaviours of nano-sized powders under sound vibration. *Powder Technol.* **2010**, *201*, 49–56. [CrossRef]
24. Si, C.; Wu, J.; Wang, Y.; Zhang, Y.; Liu, G. Effect of acoustic field on minimum fluidization velocity and drying characteristics of lignite in a fluidized bed. *Fuel Processing Technol.* **2015**, *135*, 112–118. [CrossRef]
25. Xu, C.; Cheng, Y.; Zhu, J. Fluidization of fine particles in a sound field and identification of group C/A particles using acoustic waves. *Powder Technol.* **2006**, *161*, 227–234. [CrossRef]
26. Herrera, C.A.; Levy, E.K.; Ochs, J. Characteristics of acoustic standing waves in fluidized beds. *AIChE J.* **2002**, *48*, 503–513. [CrossRef]
27. Kumar, T.S.; Patle, M.K.; Sujith, R.I. Characteristics of acoustic standing waves in packed-bed columns. *AIChE J.* **2007**, *53*, 297–304. [CrossRef]
28. Cherntongchai, P.; Chaiwattana, S.; Leruk, R.; Panyaruean, J.; Sriboonnak, S. Influence of standing wave characteristics on hydrodynamic behaviours in sound-assisted fluidization of Geldart group A powder. *Powder Technol.* **2019**, *350*, 123–133. [CrossRef]
29. Al-Ghurabi, E.H.; Ali, S.S.; Alfadul, S.M.; Shahabuddin, M.; Asif, M. Experimental investigation of fluidized bed dynamics under resonant frequency of sound waves. *Adv. Powder Technol.* **2019**, *30*, 2812–2822. [CrossRef]
30. Ali, S.S.; Hossain, S.K.S.; Asif, M. Dynamics of partially collapsing pulsed fluidized bed. *Can. J. Chem. Eng.* **2021**, *99*, 2333–2344. [CrossRef]
31. Ali, S.S.; Al-Ghurabi, E.H.; Ibrahim, A.A.; Asif, M. Effect of adding Geldart group A particles on the collapse of fluidized bed of hydrophilic nanoparticles. *Powder Technol.* **2018**, *330*, 50–57. [CrossRef]
32. Reynolds, D.D. *Engineering principles of acoustics: Noise and Vibration Control/Douglas D. Reynolds*; Allyn and Bacon: Boston, MA, USA, 1981.
33. Regtien, P.; Dertien, E. 9-Acoustic sensors. In *Sensors for Mechatronics*, 2nd ed.; Regtien, P., Dertien, E., Eds.; Elsevier Publishing: Amsterdam, The Netherlands, 2018; pp. 267–303.
34. Hansen, C.H. Fundamentals of acoustics. In *Occupational Exposure to Noise: Evaluation, Prevention and Control*; Goelzer, B.H., Hansen, C.H., Sehrndt, G.A., Eds.; World Health Organization: Geneva, Switzerland, 2001.
35. Kaliyaperumal, S.; Barghi, S.; Zhu, J.; Briens, L.; Rohani, S. Effects of acoustic vibration on nano and sub-micron powders fluidization. *Powder Technol.* **2011**, *210*, 143–149. [CrossRef]
36. Atkinson, C.M.; Kytömaa, H.K. Acoustic wave speed and attenuation in suspensions. *Int. J. Multiph. Flow* **1992**, *18*, 577–592. [CrossRef]

nanomaterials

Article

Variations in the Physical Properties of RF-Sputtered CdS Thin Films Observed at Substrate Temperatures Ranging from 25 °C to 500 °C

Sangwoon Lee [1], Juna Kim [1], Seokhee Lee [1], Hyun-Jin Cha [1], Chang-Sik Son [2], Young-Guk Son [1,*] and Donghyun Hwang [2,*]

[1] School of Materials Science and Engineering, Pusan National University, Busan 46241, Korea; 201983325@pusan.ac.kr (S.L.); kja6037@pusan.ac.kr (J.K.); leesh91@pusan.ac.kr (S.L.); jk260df@pusan.ac.kr (H.-J.C.)
[2] Division of Materials Science and Engineering, Silla University, Busan 46958, Korea; csson@silla.ac.kr
* Correspondence: ykson@pusan.ac.kr (Y.-G.S.); dhhwang@silla.ac.kr (D.H.); Tel.: +82-10-4553-0034 (Y.-G.S.); +82-10-3156-4055 (D.H.)

Abstract: CdS films with a wide range of substrate temperatures as deposition parameters were fabricated on Corning Eagle 2000 glass substrates using RF magnetron sputtering. The crystallographic structure, microscopic surface texture, and stoichiometric and optical properties of each CdS film deposited at various substrate temperatures were observed to be highly temperature-dependent. The grown CdS thin films revealed a polycrystalline structure in which a cubic phase was mixed based on a hexagonal wurtzite phase. The relative intensity of the H(002)/C(111) peak, which represents the direction of the preferential growth plane, enhanced as the temperatures climbed from 25 °C to 350 °C. On the contrary, the intensity of the main growth peak at the higher temperatures of 450 °C and 500 °C was significantly reduced and exhibited amorphous-like behavior. The sharp absorption edge revealed in the transmission spectrum shifted from the long wavelength to the short wavelength region with the rise in the substrate temperature. The bandgap showed a tendency to widen from 2.38 eV to 2.97 eV when the temperatures increased from 25 °C to 350 °C. The CdS films grown at the temperatures of 450 °C and 500 °C exhibited glass-like transmittance with almost no interference fringes of light, which resulted in wide bandgap values of 3.09 eV and 4.19 eV, respectively.

Keywords: cadmium sulfide; thin film; substrate temperature; RF magnetron sputtering; physical property

Citation: Lee, S.; Kim, J.; Lee, S.; Cha, H.-J.; Son, C.-S.; Son, Y.-G.; Hwang, D. Variations in the Physical Properties of RF-Sputtered CdS Thin Films Observed at Substrate Temperatures Ranging from 25 °C to 500 °C. *Nanomaterials* **2022**, *12*, 1618. https://doi.org/10.3390/nano12101618

Academic Editor: Marianna Kemell

Received: 15 March 2022
Accepted: 29 April 2022
Published: 10 May 2022

1. Introduction

Cadmium sulfide (CdS) is a "Group II-VI compound semiconductor formed by cadmium (Cd) belonging to Group IIB metallic elements and sulfur (S) included in Group VI non-metallic elements" [1]. CdS is one of the *n*-type semiconductor materials exhibiting a bandgap of 2.42 eV [2]. Due to these characteristics, it is mainly applied to optoelectronic devices such as photovoltaics [3,4]. Moreover, several researchers are focusing on CdS because it can be applied to devices, such as piezoelectric, photonic, and thin-film transistors [5–7]. CdS thin films are deposited using various techniques, such as "sputtering" [8], "molecular beam epitaxy (MBE)" [9], "chemical vapor deposition (CVD)" [10], "chemical bath deposition (CBD)" [11], and "spray pyrolysis" [12]. Each of these deposition techniques has its own set of advantages and disadvantages. One of the widely utilized deposition process techniques for fabricating CdS films more efficiently is radio-frequency (RF) magnetron sputtering. RF magnetron sputtering enables better adhesion, wider coverage, higher uniformity, the convenience of thickness control, and higher film density at relatively low substrate temperatures in the film manufacturing process compared to other deposition techniques [8]. The physical characteristics of RF magnetron sputtered CdS thin films are directly dependent on deposition parameters, such as "the substrate temperature, working pressure, gas flow rate, growth time, and RF power" [8,13,14]. Among these deposition parameters, "the substrate temperature is the main experimental factor that determines the crystallographic, optical and electrical properties of thin films" [13,14]. The surface texture and thickness of the grown thin film also change significantly corresponding to the marginal variation in the substrate temperature during the sputtering process. Moreover, the desired phase can be obtained if the substrate temperature is sufficiently high despite insufficient sputtering power or deposition pressure. N. Akcay et al. "fabricated CdS thin films with the thickness of 50 nm or less at the substrate temperature of 200 °C using RF magnetron sputtering and applied it as the buffer layer for CZTS thin-film solar cells" [13]. Das et al. "demonstrated the effect of the temperatures on various properties of RF-sputtered CdS thin films grown at substrate temperatures ranging from 25 °C to 300 °C" [14]. In a previous study, we also discussed "the structural and optical properties of CdS thin films prepared at the temperatures between 25 °C and 250 °C" [15]. Most studies on the application of CdS films as buffer layers explain the physical properties at substrate temperatures below 300 °C. However, the characteristics of the devices may be determined based on the characteristics of CdS films exhibited at substrate temperatures above 300 °C when the CdS film is applied as a junction layer for electronic devices other than the buffer layer of solar cells [16–18]. Therefore, further research on the physical properties of CdS thin films over a wide range of substrate temperatures is required.

In this paper, CdS thin films were fabricated on glass substrates by RF magnetron sputtering by applying a wider range of substrate temperatures (25–500 °C) as experimental parameters than in previous studies. In particular, the singularity of structural and optical property fluctuations seen at 450 °C and 500 °C is a unique result that has not been previously reported in other papers. Additionally, we discussed in depth how deposition temperatures affect the structural, morphological, compositional, and optical aspects of CdS thin films.

2. Materials and Methods

2.1. Deposition of CdS Thin Films

CdS thin films with various substrate temperatures were prepared on Corning Eagle 2000 glass substrates by RF magnetron sputtering. Corning Eagle 2000 glass substrate features a strain point of 666 °C and a softening point of 985 °C and has better thermal stability than soda-lime glass, which has a strain point of 520 °C and a softening point of 820 °C. The CdS target used in the sputtering process was 4 mm thick, 50 mm in diameter, and 99.99% pure (4N). A 25×25 mm^2 glass was used as the substrate for CdS thin-film deposition, and the fine glass particles generated during glass cutting were blown away using a nitrogen gun. Glass substrates were placed in a beaker containing deionized (DI) water and ultrasonically cleaned for 10 min to remove residual organic substances on the surface of the substrate. The substrates were immersed in a beaker containing a 99% or higher purity of acetone, ethyl alcohol, and isopropyl alcohol, followed by ultrasonic cleaning for 5 min after each post-primary cleaning. The surfaces of the substrates after ultrasonic cleaning were dried using a nitrogen gun and immediately loaded into a vacuum chamber to minimize external contamination. The initial vacuum degree of the chamber for the sputtering process was 5.0×10^{-6} Torr (0.667 mPa) or less using a turbopump. Moreover, 55 sccm of argon gas was introduced into the chamber through a mass flow controller. The surface impurities of the CdS target were removed by performing pre-sputtering for 30 min at an RF power of 60 W and a deposition pressure of 3.0×10^{-2} Torr (4 Pa) before the deposition of a CdS thin film. The substrate was isolated from the target by a movable shutter during the pre-sputtering and cleaning of the target surface. Thereafter, CdS thin films were deposited on the substrates for 15 min by increasing the RF power to 120 W and adjusting the temperature from 25 °C to 500 °C at the same deposition pressure.

2.2. Characterization of CdS Thin Films

The crystallographic characteristics of the CdS thin films were analyzed using X-ray diffraction (XRD, D8 Advance, Bruker, Billerica, MA, USA) with a Cu Kα radiation wavelength (λ) of 0.15406 nm. The surface morphology, grain size, film thickness, and elemental composition of the CdS thin films were evaluated by a field emission scanning electron microscope (FESEM, S-4800, HITACHI, Tokyo, Japan) and an energy dispersive X-ray spectrometer (EDS, 7953-H, Horiba, Kyoto, Japan) attached as an additional accessory. The optical transmittance was observed under a wavelength variable of 190 to 1100 nm through an ultraviolet-visible (UV–Vis) spectrometer (UV-1800, SHIMADZU, Kyoto, Japan). The energy bandgap was calculated based on the data collected from the transmittance measurements.

3. Results and Discussion

3.1. Structural Properties of CdS Thin Films

Figure 1 illustrates the XRD patterns of CdS thin films deposited at various substrate temperatures (T_s) measured at 2 theta (θ) diffraction angles ranging from 20° to 80°. The deposited CdS films were mixed in hexagonal (H) and cubic (C) structures (JCPDS No. 01-077-2306 and 01-080-0019) [19]. According to the JCPDS card showing information about the CdS crystal system, it is difficult to ascertain a distinct Miller index for the XRD pattern represented at 2θ diffraction angles of 26.5° and 54.6°. This is due to the 2θ angles representing the hexagonal and cubic structures as being 26.53° and 26.55°, respectively, with the difference between the two angles being only 0.02. The angular difference between the hexagonal and cubic structures expressed at 54.64° and 54.67°, respectively, is also very insignificant at 0.03. Therefore, the diffraction peaks appearing at these two angles can be expressed by the Miller indices of H(002)/C(111), which represent the mixture of hexagonal and cubic phases [19,20].

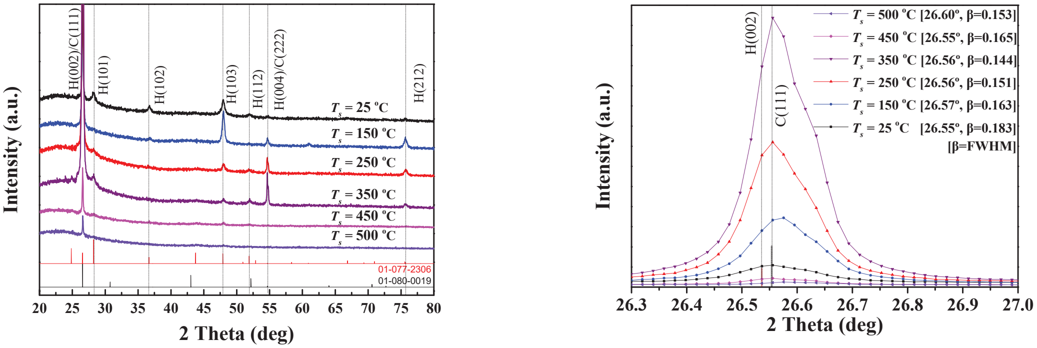

(**a**) (**b**)

Figure 1. (**a**) XRD results of CdS thin films fabricated at various substrate temperatures, and (**b**) the details of the H(002)/C(111) peaks corresponding to the main diffraction plane in the XRD patterns.

The peaks for the H(002)/C(111) plane representing the preferential growth orientation were observed at a diffraction angle of 26.5° [21,22]. Relatively weak peaks corresponding to the H(101), H(102), H(103), H(112), and H(212) planes representing the hexagonal structure were observed at diffraction angles of 28.2°, 36.6°, 47.8°, 51.9°, and 75.6°, respectively. As the temperature ascended to 350 °C, the intensity of the principal diffraction peaks increased proportionately. However, the intensity of the dominant peaks dropped dramatically for the films grown at higher temperatures (450 °C and 500 °C). The intensity of the peak on the H(004)/C(222) plane at a diffraction angle of 54.6° depended on the substrate temperature at the main peaks. The full width at half maximum (FWHM) of the H(002)/C(111) peaks for CdS thin films deposited at a variety of substrate temperatures is summarized in Table 1.

The FWHM values were analyzed using DIFFRAC.SUITE software, which was provided by Bruker. The Scherrer formula ($D = 0.9\lambda/\beta cos\theta$) was used to determine the crystallite size [23]. The crystallite size of the CdS thin film at 25 °C was 46.6 nm. The crystallite size gradually increased to 52.3 nm at 150 °C, 56.4 nm at 250 °C, and 59.2 nm at 350 °C, corresponding to the increase in substrate temperature. However, for the films formed at 450 °C and 500 °C, the crystallite size was reduced to 51.7 nm and 55.7 nm, respectively.

Table 1. Detailed values representing the structural properties of CdS thin films fabricated at various substrate temperatures.

Substrate Temperature (°C)	2 Theta (deg)	FWHM Value (deg)	Crystallite Size by XRD (nm)	Grain Size by FESEM (nm)	Thickness by FESEM (nm)
25	26.55	0.183	46.6	43.3	333
150	26.57	0.163	52.3	49.4	378
250	26.56	0.151	56.4	65.4	437
350	26.56	0.144	59.2	77.2	396
450	26.55	0.165	51.7	47.8	254
500	26.60	0.153	55.7	55.3	569

3.2. Morphological and Compositional Properties of CdS Thin Films

Figure 2 represents the FESEM images of the surface morphology and cross-section of the prepared CdS thin films at various substrate temperatures. The crystal grains with an average diameter of 43.3 nm are closely bonded to each other to form a thin-film surface in the CdS film prepared at the temperature of 25 °C. A temperature of 25 °C corresponds to a relatively low temperature in terms of promoting “initial nucleation and providing a high density of nuclei to obtain a surface texture” [24]. When growing a thin film by sputtering, if the substrate temperature is raised while fixing the deposition time, sufficient activation energy for nucleation and growth is supplied according to the temperature increase during the deposition process. Therefore, the substrate temperature becomes an effective process condition to improve the density and thickness of the thin film and the grain size [25]. The average grain size value for CdS films improved to 77.2 nm when the temperature was elevated to 350 °C. Moreover, the spacing of adjacent grain boundaries also widened. The average thickness of the CdS film deposited at 25 °C was measured to be 333 nm. The thickness of the film grew with increasing temperatures to 378 nm at 150 °C and 437 nm at 250 °C. Through these observations, it could be seen that the thickness of the CdS thin film deposited by the sputtering process gradually improved with the substrate temperature up to 250 °C. The thickness of the films deposited at 350 °C and 450 °C, on the other hand, plummeted to 396 nm and 254 nm, respectively. The decrement in the thickness of the films observed at the temperatures between 350 °C and 450 °C is due to the re-evaporation phenomenon occurring at higher substrate temperatures above 300 °C [24,26]. The surface and cross-sectional images of the CdS thin film deposited at 450 °C show that the crystals grew in extremely irregular directions under these conditions. The crystal growth irregularities were more pronounced in the images of CdS films deposited at the temperature of 500 °C, exhibiting a shape that resembled nanorods. The surface morphology and thickness variations occurring at high temperatures over 450 °C are consistent with the amorphization tendency observed in the XRD results. The structural and optical singularities at 450 °C and 500 °C were observed for the first time during our research.

The results of the EDS analysis of the chemical composition are listed in Table 2. The average values of the four different points are indicated. The atomic percentage of Cd was higher than that of S for CdS films deposited at temperatures between 25 °C and 350 °C. The atomic percentage of Cd represents a continuously decreasing trend with increasing substrate temperature. The reduction of Cd content is presumed to be due to the surface mobility and vapor pressure of the Cd element being higher than that of the

S element, so that the Cd atoms preferentially escape from the CdS film along with the rise in the substrate temperature [14]. The atomic ratio of elemental S to Cd in the films grown at the temperatures between 250 °C and 350 °C was approximately equal to the stoichiometric composition of CdS. Conversely, the atomic percentage of S was higher than that of Cd at 450 °C and 500 °C. The S/Cd ratio was also calculated to be 1.14 and 1.09, which are values that deviate from the stoichiometric composition. The results of the EDS investigation show that the deterioration of the crystallinity and the non-uniformity of the surface microstructure of the CdS thin films grown at substrate temperatures of ≥450 °C can be attributed to the collapse of the stoichiometry induced by the volatilization of the Cd element [27–29].

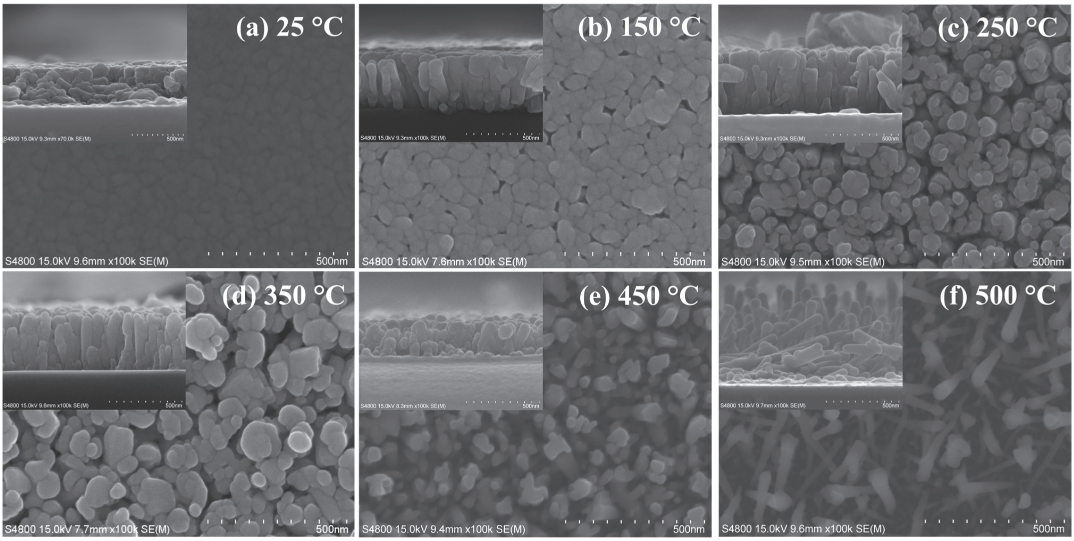

Figure 2. Surface morphology and cross-sectional FESEM images of CdS thin films at (**a**) T_s = 25 °C, (**b**) T_s = 150 °C, (**c**) T_s = 250 °C, (**d**) T_s = 350 °C, (**e**) T_s = 450 °C and (**f**) T_s = 500 °C.

Table 2. Values of the variation in the chemical composition of CdS thin films grown at various substrate temperatures.

Substrate Temperature (°C)	Cd (Atomic %)	S (Atomic %)	S/Cd Ratio
25	53.15	46.85	0.88
150	51.59	48.41	0.94
250	50.89	49.11	0.97
350	50.87	49.13	0.97
450	46.57	53.43	1.14
500	47.76	52.24	1.09

3.3. Optical Properties of CdS Thin Films

Figure 3 shows the optical transmittance results for CdS thin films fabricated over a wide substrate temperature range. The sharp absorption edge of the CdS thin film deposited at 350 °C was observed near the wavelength of 500 nm. However, at higher temperatures between 450 °C and 500 °C, the absorption edge wavelengths were confirmed at 300 nm and 270 nm, respectively. The average transmittance of the room-temperature-sputtered CdS thin film measured for wavelengths between 500 to 1100 nm was 66%. The transmittance values for the CdS thin film improved to 76.3% at 150 °C, 82.8% at 250 °C, 81.5% at 350 °C, and 91.2% at 450 °C with the increase in the substrate temperature. At a substrate temperature of 500 °C, the transmittance decreased to 88.8% compared to the immediately preceding condition. The absorption edge of the transmittance spectra at substrate temperatures of 450 °C and 500 °C shifted to the shorter wavelength region. The blue shift of the absorption edge is thought to be related to the shape of the crystal's growth. We previously mentioned the singularity of the shape variation of the surface and cross-section of CdS films grown at 450 °C and 500 °C through the SEM results in Figure 2. In the deposited films under these conditions, the spacing between adjacent crystal grains is unusually wide. It also indicates that the crystal growth was randomly grown in an irregular direction rather than perpendicular to the substrate. Due to these results, it is thought that the transmittance pattern of the deposited CdS film in this temperature range exhibits an amorphous-like behavior. Moreover, the interference fringes of light observed in the 500 to 1100 nm wavelength range were absent. This may be due to the volatilization of the Cd element, which occurs when exposed to temperatures above 450 °C, as indicated in Table 2.

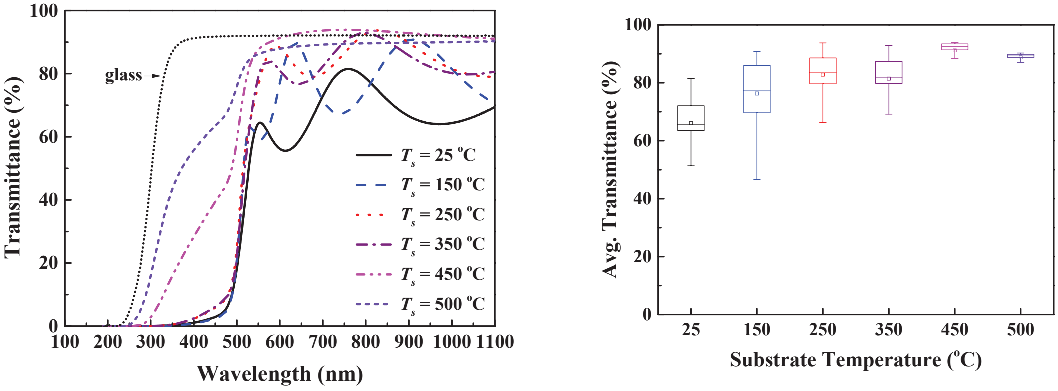

(**a**) (**b**)

Figure 3. Optical transmittance spectral results for CdS thin films fabricated at various substrate temperatures: (**a**) transmittance spectrum and (**b**) average transmittance distribution.

The energy bandgap of the CdS thin film was "calculated by substituting the absorption coefficient (α) derived from the transmission spectrum into the following Tauc equation" and is shown in Figure 4 [30].

$$(\alpha h v)^{1/n} = A(h v - E_g) \tag{1}$$

In this equation, "A is the constant for the effective mass (M) associated with the bands, and h is Planck's constant. The frequency of the incident radiation is v, the bandgap of that material is E_g, and the exponent n is the transition probability" [14,30]. The transition probability, n, was calculated by substituting the value of the direct allowed transition (1/2) in Equation (1). The E_g was determined by approximating the $(\alpha h v)^2$ graph on the y-axis corresponding to the photon energy (hv) extrapolated to $\alpha = 0$ with a straight line [2,31]. The bandgap of the CdS thin film deposited at a substrate temperature of 25 °C was 2.38 eV. "This bandgap value is higher than the bulk of CdS at 300 K (2.42 eV)" [32]. The bandgap value widened from 2.39 eV to 2.97 eV as the substrate temperature was raised from 150 °C to 350 °C. The analysis of XRD patterns (Figure 1), FESEM images (Figure 2), and EDS data (Table 2) established that substrate temperatures of up to 350 °C were effective deposition parameters for the formation of CdS thin films. Therefore, it can be considered that this temperature range has a positive effect on the grain size, crystal structure, and stoichiometric composition in the growth stage of the CdS thin films. The band gaps at higher substrate temperatures (450 °C and 500 °C) were 3.09 eV and 4.19 eV, respectively. This steep increase in the bandgap is due to the blue shifting of the transmission spectrum following the amorphous nature of the CdS thin films. It should be noted here that the measured bandgap values under these substrate temperature conditions may be somewhat inaccurate. The thickness of the film is one of the important parameters when plotting the bandgap with the Tauc equation. The cross-sectional SEM image of the 450 °C samples shown in Figure 2 represents a higher density than the 500 °C samples. The thickness of the sample at 450 °C was calculated based on the average of the points where the particles grown perpendicular to the substrate were densely distributed. At a substrate temperature of 500 °C, grain growth occurs randomly in a direction perpendicular or oblique to the substrate. Since the length of each grown crystal is different, it is only possible to estimate the film thickness rather than accurately measuring the film thickness. The film thickness of the sample was calculated based on the average length of crystals grown at perpendicular or very close angles. Therefore, depending on which viewpoint is applied, the thickness of the film deposited at 500 °C may differ from the value of 569 nm shown in Table 2; the actual thickness is estimated to be much thinner than that value. For these reasons, the inhomogeneous substrate coverage observed at 450 °C was further aggravated at 500 °C, leading to accelerated amorphous behavior and an increased bandgap [33].

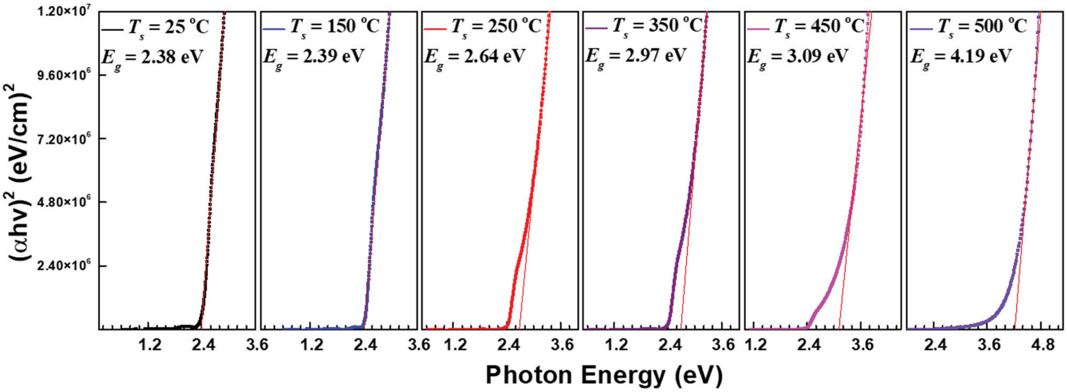

Figure 4. Energy band gap of CdS thin films as determined by transmittance spectroscopy.

4. Conclusions

In this study, we comprehensively analyzed the effect of substrate temperature on the structural, compositional, and optical properties of RF-sputtered CdS thin films. All CdS thin films grown at various substrate temperatures (25–500 °C) showed a polycrystalline structure with mixed hexagonal (H) and cubic (C) phases. The diffraction peak for the H(002)/C(111) plane was observed at 26.5°, indicating a preferential growth orientation. The diffraction intensity for the main peak showed a tendency to significantly improve more than twofold as the substrate temperature increased from 25 °C to 350 °C. In contrast, the intensity for the peak at the temperature conditions of 450 °C and 500 °C decreased and showed a value significantly lower than that of the CdS film deposited at 25 °C. FESEM image analysis confirmed that substrate temperature has a respectable effect on morphological changes such as the surface and thickness of CdS thin films. In particular, in the image of the CdS thin film grown at 500 °C, it was confirmed that crystal growth was performed in an arbitrary direction rather than perpendicular to the substrate. The distance between the grains was also observed to widen compared to the lower substrate temperature, revealing non-uniform crystal growth. The stoichiometric ratio (S/Cd) of the CdS films grown at 250 °C and 350 °C showed the same value of 0.97. This value is slightly less than the stoichiometric ratio of bulk CdS. The volatilization of Cd was observed in CdS films prepared at higher temperatures (450 °C and 500 °C). Therefore, the chemical composition of the films represents an S-rich stoichiometry. The sharp absorption edge of the CdS thin film fabricated at a substrate temperature of 25 °C was observed near a wavelength of 500 nm, and the average transmittance was 66%. Subsequently, the transmittance of the film was enhanced to about 81.5% and 91.2% at temperatures of 350 °C and 450 °C, respectively. At the substrate temperature of 500 °C, the transmittance decreased slightly compared to the previous condition and showed a value of approximately 88.8%. The band gaps of the CdS thin films grown at substrate temperatures of 25 °C and 150 °C were 2.38 eV and 2.39 eV, respectively, which were close to those of bulk CdS. The bandgap of the CdS thin film deposited at the higher substrate temperature presented a tendency to widen in proportion to the increase in temperature.

Author Contributions: Conceptualization, S.L. (Sangwoon Lee) and D.H.; methodology, C.-S.S. and Y.-G.S.; formal analysis, S.L. (Sangwoon Lee); investigation, S.L. (Sangwoon Lee), J.K., S.L. (Seokhee Lee) and H.-J.C.; resources, C.-S.S. and Y.-G.S.; writing—original draft preparation, S.L. (Sangwoon Lee) and D.H.; writing—review and editing, S.L. (Sangwoon Lee), C.-S.S., Y.-G.S. and D.H.; visualization, S.L. (Sangwoon Lee), J.K., S.L. (Seokhee Lee) and H.-J.C.; supervision, Y.-G.S. and C.-S.S.; project administration, D.H.; funding acquisition, C.-S.S. All authors have read and agreed to the published version of the manuscript.

Funding: This work was supported by the National Research Foundation of Korea (NRF) grant funded by the Korea government (MSIT) (No. NRF-2018R1A5A1025594), and was supported by the Korea Institute of Energy Technology Evaluation and Planning (KETEP) and the Ministry of Trade, Industry & Energy (MOTIE) of the Republic of Korea (No. 20183010014260 and 20193010014850).

Data Availability Statement: Not applicable.

Conflicts of Interest: The authors declare no conflict of interest.

References

1. Dawood, Y.Z. The influence of substrate temperature on CdS thin films properties prepared by pulse laser deposition on glass substrates. *Energy Procedia* **2017**, *119*, 536–544. [CrossRef]
2. Das, N.S.; Ghosh, P.K.; Mitra, M.K.; Chattopadhyay, K.K. Effect of film thickness on the energy band gap of nanocrystalline CdS thin films analyzed by spectroscopic ellipsometry. *Physica E* **2010**, *42*, 2097–2102. [CrossRef]
3. Hur, S.G.; Kim, E.T.; Lee, J.H.; Kim, G.H.; Yoon, S.G. Characterization of photoconductive CdS thin films prepared on glass substrates for photoconductive-sensor applications. *J. Vac. Sci. Technol. B* **2008**, *26*, 1334–1337. [CrossRef]
4. Yasmeen, Z.; Salah, Q.; Saba, J.; Najiba, A. Effect of Substrate Temperature on the Morphological and Optical Properties of Nanocrystalline ZnO Films Formed By DC Magnetron Sputtering. *J. Appl. Phys.* **2015**, *7*, 59–63.
5. Ashok, C.; Rao, K.V.; Chakra, C.S.; Rajendar, V.; Narayanan, R.L. Fabrication and Characterization of CdS Thin Films for the Solar Cell Applications. *Int. J. ChemTech Res.* **2014**, *66*, 3367–3370.
6. Demir, R.; Gode, F. Structural, optical and electrical properties of nanocrystalline cds thin films grown by chemical bath deposition method. *Chalcogenide Lett.* **2015**, *12*, 43–50.
7. Stefko, R. Investigation of the features of acousto-electric oscillation in cadmium sulfide. *Sov. J. Commun. Technol. Electron.* **1991**, *36*, 127–132.
8. Rondiya, S.; Rokade, A.; Funde, A.; Kartha, M.; Pathan, H.; Jadkar, S. Synthesis of CdS thin films at room temperature by RF-magnetron sputtering and study of its structural, electrical, optical and morphology properties. *Thin Solid Films* **2017**, *631*, 41–49. [CrossRef]
9. Oliva, A.; Solıs-Canto, O.; Castro-Rodrıguez, R.; Quintana, P. Formation of the band gap energy on CdS thin films growth by two different techniques. *Thin Solid Films* **2001**, *391*, 28–35. [CrossRef]
10. Kamran, M.A.; Majid, A.; Alharbi, T.; Iqbal, M.W.; Ismail, K.; Nabi, G.; Li, Z.A.; Zou, B.S. Novel Cd-CdS micro/nano heterostructures: Synthesis and luminescence properties. *Opt. Mater.* **2017**, *73*, 527–534. [CrossRef]
11. Khan, Z.R.; Shkir, M.; Ganesh, V.; Alfaify, S.; Yahia, I.S.; Zahran, H.Y. Linear and Nonlinear Optics of CBD Grown Nanocrystalline F Doped CdS Thin Films for Optoelectronic Applications: An Effect of Thickness. *J. Electron. Mater.* **2018**, *47*, 5386–5395. [CrossRef]
12. Shkir, M.; Ashraf, I.M.; Chandekar, K.V.; Yahia, I.S.; Khan, A.; Algarni, H.; AlFaify, S. A significant enhancement in visible-light photodetection properties of chemical spray pyrolysis fabricated CdS thin films by novel Eu doping concentrations. *Sens. Actuators A-Phys.* **2020**, *301*, 111749. [CrossRef]
13. Akcay, N.; Zaretskaya, E.P.; Ozcelik, S. Development of a CZTS solar cell with CdS buffer layer deposited by RF magnetron sputtering. *J. Alloys Compd.* **2019**, *772*, 782–792. [CrossRef]

14. Das, N.K.; Chakrabartty, J.; Farhad, S.F.U.; Sen Gupta, A.K.; Ahamed, E.M.K.I.; Rahman, K.S.; Wafi, A.; Alkahtani, A.A.; Matin, M.A.; Amin, N. Effect of substrate temperature on the properties of RF sputtered CdS thin films for solar cell applications. *Results Phys.* **2020**, *17*, 103132. [CrossRef]
15. Hwang, D.H.; Hui, K.N.; Choi, J.K.; Son, Y.G. Substrate Temperature Effects on Structural and Optical Properties of Radio Frequency Sputtered CdS Thin Films. *Sci. Adv. Mater.* **2014**, *6*, 2233–2237. [CrossRef]
16. Dondapati, H.; Santiago, K.; Pradhan, A.K. Influence of growth temperature on electrical, optical, and plasmonic properties of aluminum:zinc oxide films grown by radio frequency magnetron sputtering. *J. Appl. Phys.* **2013**, *114*, 143506. [CrossRef]
17. Nakajima, Y.; Murata, H.; Saitoh, N.; Yoshizawa, N.; Suemasu, T.; Toko, K. Low-Temperature (400 degrees C) Synthesis of Multilayer Graphene by Metal-Assisted Sputtering Deposition. *ACS Omega* **2019**, *4*, 6677–6680. [CrossRef]
18. Zhang, W.; Zhu, G.S.; Zhi, L.; Yang, H.J.; Yang, Z.P.; Yu, A.B.; Xu, H.R. Structural, electrical and optical properties of indium tin oxide thin films prepared by RF sputtering using different density ceramic targets. *Vacuum* **2012**, *86*, 1045–1047. [CrossRef]
19. Nieto-Zepeda, K.E.; Guillen-Cervantes, A.; Rodriguez-Rosales, K.; Santos-Cruz, J.; Santos-Cruz, D.; Olvera, M.D.L.; Zelaya-Angel, O.; Santoyo-Salazar, J.; Hernandez-Hernandez, L.A.; Contreras-Puente, G.; et al. Effect of the sulfur and fluorine concentration on physical properties of CdS films grown by chemical bath deposition. *Results Phys.* **2017**, *7*, 1971–1975. [CrossRef]
20. Echendu, O.K.; Dejene, F.B.; Dharmadasa, I.M.; Eze, F.C. Characteristics of Nanocrystallite-CdS Produced by Low-Cost Electrochemical Technique for Thin Film Photovoltaic Application: The Influence of Deposition Voltage. *Int. J. Photoenergy* **2017**, *2017*, 3989432. [CrossRef]
21. Hashim, U.; Rahman, K.A.; Hakim; Othman, M.A. CdS Film Thickness Characterization By RF Magnetron Sputtering. *AIP Conf. Proc.* **2009**, *1136*, 253–258.
22. Moon, B.S.; Lee, J.H.; Jung, H. Comparative studies of the properties of CdS films deposited on different substrates by RF sputtering. *Thin Solid Films* **2006**, *511*, 299–303. [CrossRef]
23. Warren, B.E. *X-ray Diffraction*; Courier Corporation: Chelmsford, MA, USA, 1990.
24. Kim, D.; Park, Y.; Kim, M.; Choi, Y.; Park, Y.S.; Lee, J. Optical and structural properties of sputtered CdS films for thin film solar cell applications. *Mater. Res. Bull.* **2015**, *69*, 78–83. [CrossRef]
25. Martil, I.; Gonzalezdiaz, G.; Sanchezquesada, F. Temperature and Bias Effects on the Electrical-Properties of Cds Thin-Films Prepared by Rf Sputtering. *Thin Solid Films* **1984**, *114*, 327–334. [CrossRef]
26. Feldmeier, E.M.; Fuchs, A.; Schaffner, J.; Schimper, H.J.; Klein, A.; Jaegermann, W. Comparison between the structural, morphological and optical properties of CdS layers prepared by Close Space Sublimation and RF magnetron sputtering for CdTe solar cells. *Thin Solid Films* **2011**, *519*, 7596–7599. [CrossRef]
27. Ojeda-Barrero, G.; Oliva-Aviles, A.I.; Oliva, A.I.; Maldonado, R.D.; Acosta, M.; Alonzo-Medina, G.M. Effect of the substrate temperature on the physical properties of sprayed-CdS films by using an automatized perfume atomizer. *Mater. Sci. Semicond. Proc.* **2018**, *79*, 7–13. [CrossRef]
28. Barman, B.; Bangera, K.V.; Shivakumar, G.K. Effect of substrate temperature on the suitability of thermally deposited cadmium sulfide thin films as window layer in photovoltaic cells. *Superlattices Microstruct.* **2018**, *123*, 374–381. [CrossRef]
29. Ouachtari, F.; Rmili, A.; Elidrissi, B.; Bouaoud, A.; Erguig, H.; Elies, P. Influence of bath temperature, deposition time and S/Cd ratio on the structure, surface morphology, chemical composition and optical properties of CdS thin films elaborated by chemical bath deposition. *J. Mod. Phys.* **2011**, *2*, 1073–1082. [CrossRef]
30. Pankove, J.I. *Optical Processes in Semiconductors*; Prentice-Hall: Hoboken, NJ, USA, 1971; Volume 92.
31. Banerjee, R.; Jayakrishnan, R.; Ayyub, P. Effect of the size-induced structural transformation on the band gap in CdS nanoparticles. *J. Phys.-Condens. Matter* **2000**, *12*, 10647–10654. [CrossRef]
32. Dongre, J.K.; Nogriya, V.; Ramrakhiani, M. Structural, optical and photoelectrochemical characterization of CdS nanowire synthesized by chemical bath deposition and wet chemical etching. *Appl. Surf. Sci.* **2009**, *255*, 6115–6120. [CrossRef]
33. Memarian, N.; Rozati, S.M.; Concina, I.; Vomiero, A. Deposition of Nanostructured CdS Thin Films by Thermal Evaporation Method: Effect of Substrate Temperature. *Materials* **2017**, *10*, 773. [CrossRef] [PubMed]

nanomaterials

MDPI

Review

A Review on Current Designation of Metallic Nanocomposite Hydrogel in Biomedical Applications

Nur Syafiqah Farhanah Dzulkharnien [1] and Rosiah Rohani [1,2,*]

[1] Department of Chemical & Process Engineering, Faculty of Engineering and Built Environment, Universiti Kebangsaan Malaysia, UKM, Bangi 43600, Selangor, Malaysia; p115201@siswa.ukm.edu.my
[2] Research Centre for Sustainable Process Technology, Faculty of Engineering & Built Environment, Universiti Kebangsaan Malaysia, UKM, Bangi 43600, Selangor, Malaysia
* Correspondence: rosiah@ukm.edu.my

Abstract: In the past few decades, nanotechnology has been receiving significant attention globally and is being continuously developed in various innovations for diverse applications, such as tissue engineering, biotechnology, biomedicine, textile, and food technology. Nanotechnological materials reportedly lack cell-interactive properties and are easily degraded into unfavourable products due to the presence of synthetic polymers in their structures. This is a major drawback of nanomaterials and is a cause of concern in the biomedicine field. Meanwhile, particulate systems, such as metallic nanoparticles (NPs), have captured the interest of the medical field due to their potential to inhibit the growth of microorganisms (bacteria, fungi, and viruses). Lately, researchers have shown a great interest in hydrogels in the biomedicine field due to their ability to retain and release drugs as well as to offer a moist environment. Hence, the development and innovation of hydrogel-incorporated metallic NPs from natural sources has become one of the alternative pathways for elevating the efficiency of therapeutic systems to make them highly effective and with fewer undesirable side effects. The objective of this review article is to provide insights into the latest fabricated metallic nanocomposite hydrogels and their current applications in the biomedicine field using nanotechnology and to discuss the limitations of this technology for future exploration. This article gives an overview of recent metallic nanocomposite hydrogels fabricated from bioresources, and it reviews their antimicrobial activities in facilitating the demands for their application in biomedicine. The work underlines the fabrication of various metallic nanocomposite hydrogels through the utilization of natural sources in the production of biomedical innovations, including wound healing treatment, drug delivery, scaffolds, etc. The potential of these nanocomposites in relation to their mechanical strength, antimicrobial activities, cytotoxicity, and optical properties has brought this technology into a new dimension in the biomedicine field. Finally, the limitations of metallic nanocomposite hydrogels in terms of their methods of synthesis, properties, and outlook for biomedical applications are further discussed.

Keywords: metallic; nanocomposite; hydrogel; nanotechnology; drug delivery; tissue engineering; wound care

Citation: Dzulkharnien, N.S.F.; Rohani, R. A Review on Current Designation of Metallic Nanocomposite Hydrogel in Biomedical Applications. *Nanomaterials* **2022**, *12*, 1629. https://doi.org/10.3390/nano12101629

Academic Editors: Ming-Yu Li and Jihoon Lee

Received: 20 April 2022
Accepted: 7 May 2022
Published: 10 May 2022

1. Introduction

Nanotechnology is one of the latest fields in science and engineering; it deals with the design of nanoscale devices and systems, where the dimensions of the particles are less than 100 nm [1]. Since the 20th century, the advancement of nanotechnology through exploration and evolution has driven it to become one of the crucial domains for closing the gaps, both in the research and the industrial fields. The significant properties, such as the antimicrobial and electrocatalytic properties, thermal stability, luminescence, etc., can be transformed by nanotechnology and will eventually be applied to manifold applications, such as tissue engineering, biotechnology, biomedicine [2], cosmetics [3], food [4], textiles [5,6], and others. Some of the applications of nanotechnology in various fields are illustrated in Figure 1.

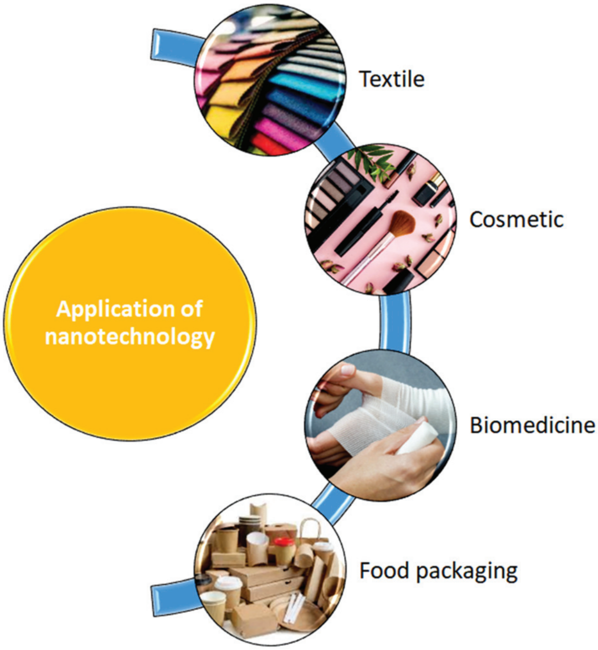

Figure 1. Involvement of nanotechnology in various industrial fields.

An extensive investigation of the drug delivery systems aided by nanotechnology has revealed excellent site-specific delivery and drug release properties to control targeted diseases. Over the past 2 years, the severe acute respiratory syndrome-associated coronavirus (SARS-CoV-2) pandemic has overwhelmed global healthcare systems. Thus, it is crucial that a rapid, early, accurate, cost-effective, and on-site diagnosis be invented to accommodate the spread of such viral diseases, including via nanotechnology. Ibrahim et al. [7] reviewed the effectiveness of gold (Au) and silver nanoparticles (Ag NPs) as biosensors in the detection of pathogenic RNA viruses. According to them, these NPs possess excellent characteristics, such as good biocompatibility, broad structural variety, and notable bio-imitative behaviours, for the efficient detection of pathogens.

Meanwhile, at present, the utilization of NPs can lead to unfavourable and longer-term side effects [8,9]. There is insufficient understanding of the particle size, morphology, absorption by immune system cells, safety risks, and toxicity, which are major concerns during the uptake of drugs [10]. Meanwhile, in the field of tissue engineering, despite the ability of nanocomposite materials to minimize the effects of tissue injury and artificial organ tissue, the fundamental knowledge about bio-mimic materials incorporated with nanotechnology is still lacking in this area, and thorough investigative studies supported by clinical approval are required [11]. Although biomedicine nanotechnology has brought the healthcare sector to a new level, challenges in the design of these nanomaterials, such as poor reproducibility, specificity, efficacy, affordability, and adverse side effects, still need to be diligently overcome. In view of this, the present review article selectively focuses on the evolution of metallic nanocomposite hydrogels in recent years and their applications in the field of biomedicine, specifically in drug delivery, wound care, and tissue engineering.

A lot of research work has been carried out to extensively explore the fabrication of nanomaterials for use in the field of biomedicine [10,11]. These nanomaterials, which comprise selected materials integrated with NPs, are produced by various techniques, including both physical and chemical methods, as well as by considering the correlation between their particle size and morphology through either in vivo or in vitro studies. The fabrication process involves the selection of suitable techniques and materials for the synthesis of the nanomaterials. Therefore, the next section will further discuss the types and methods of the synthesis of NPs to gain a comprehensive understanding of the reported techniques being used to fabricate NPs.

2. Types and Methods of Synthesis of Nanoparticles

Various nanostructures, such as micelles, liposomes, dendrimers, metallic NPs, and nano-coatings, have been utilized in the development of nanotechnology, especially in the biomedicine field [12–16]. Among the various known NPs, metal or metal oxide NPs are the most promising ones due to their antibacterial properties in association with a high surface-to-volume ratio [17]. The potential of NPs as antibacterial agents is dependent on their size, structure, and morphological behaviour, which could lead to different applications in the biomedical field, such as drug delivery, wound healing, and tissue engineering. Arokiyaraj et al. (2017) [18] elucidated the finding that Ag NPs extracted from the *Rheum palmatum* root exhibited an average particle size of 121.5 nm, with a zone of inhibition of 13–15 mm against the *S. aureus* and *P. aeruginosa*, produced through the well diffusion method. Recently, Feroze et al. (2020) [19] reported that the average size of Ag NPs synthesized from fungal metabolites of *Penicillium oxalicum* ranged from 60 to 80 nm. Their results demonstrated a better antibacterial performance, with a maximum zone of inhibition of 17.5 ± 0.5 mm (against the *S. aureus* and *S. dysenteriae*) and 18.3 ± 0.60 mm (against the *S. typhi),* using a similar method. Both of the referred works signified that the antibacterial activities of NPs are directly correlated to the size of the NPs, where the smaller the size of the particles, the higher their surface-to-volume ratio, thereby leading to their better performance as antibacterial agents.

NPs are known as particulate dispersions or solid particles or groups of atoms with dimensions in the range of 1–100 nm. Alterations to the surface area and/or volume of the NPs will lead to modifications of their properties, such as their mechanical, thermal, optical, and catalytic behaviour, which can be exploited in diverse applications, such as in the biological fields [20,21]. In the last decade, the fabrication of NPs based on polysaccharides [22], polymers [23,24], and plant-derived bioactive compounds [25] incorporated with active drugs has proven to be efficient in treating various pathological conditions.

The synthesis of NPs can be classified into two major methodologies, namely the bottom-up and top-down methods. Generally, in the bottom-up approach, atoms, molecules, or small particles are joined together to form a nanostructured building block of NPs. A few examples of the use of the bottom-up approach in the preparation of NPs are physical and chemical vapour deposition, liquid state synthesis, chemical reduction, gas phase, and the solvothermal methods [26]. In contrast, the synthesis of NPs using the top-down technique involves reducing the size of the bulk material via different physical and chemical treatments. Some of the physical techniques that are commonly used in the top-down method are lithography, laser ablation, sputtering deposition, pulsed electrochemical etching, and vapour deposition [27]. The techniques that have been discussed herein are illustrated in Figure 2.

The utilization of different techniques and materials in the fabrication of NPs yields NPs with distinct properties, such as variations in the particle size and structure, morphology, and intrinsic behaviour. The bar chart in Figure 3 illustrates the average particle size of ZnO NPs synthesized using a variety of techniques. The chart indicates the different techniques and solvents used to obtain a distinct particulate size, eventually leading to a variety of significant properties in the ZnO NPs. Among all the techniques mentioned, the ZnO NPs produced by the solvothermal method exhibited a small particle size distribution, which was actually less than 10 nm. The use of ethanol as a solvent led to the formation of small, highly-dispersed ZnO NPs with a uniform shape and size [28]. This finding showed that the solvent plays an important role in the synthesis of ZnO NPs. A similar work by Thareja et al. (2007) [29] supported the use of water and alcohol as solvents to produce smaller-sized ZnO NPs (17 nm), which were significantly smaller than the size of the ZnO NPs (70 nm) produced through the use of acetone as the liquid media in the laser ablation method. In contrast, Hasanpoor et al. [30] described the fabrication of ZnO NPs using the microwave irradiation technique, where the nanoparticles displayed a particle size ranging from 50–150 nm and had a variety of morphologies at the different radiation powers of 540 W and 680 W. In fact, the morphological properties of the ZnO NPs also varied with the use of different techniques and solvents during the synthesis of the ZnO NPs, as presented in Figure 3. Therefore, the particle size and morphology of the NPs are dependent on the preparation technique and the solvent used for the construction of the NPs.

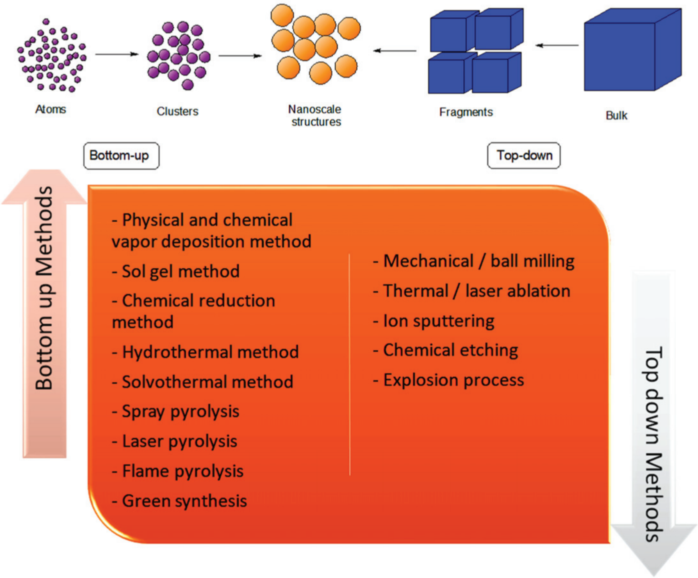

Figure 2. List of different bottom-up and top-down methods commonly used for NP synthesis.

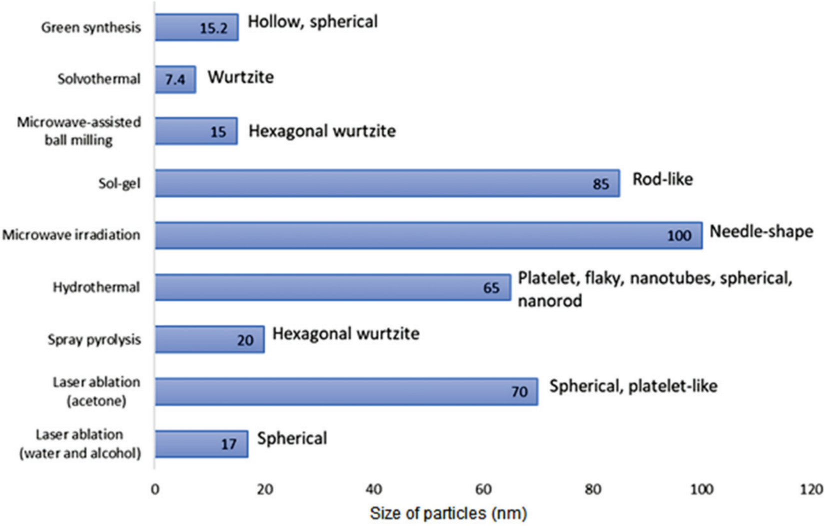

Figure 3. Comparison of the average size of particles (in nm) and morphological structures of ZnO NPs synthesized using different techniques: solvothermal [28], laser ablation [29], microwave irradiation [30], green synthesis [31], microwave-assisted ball milling [32], sol-gel [33], hydrothermal [34], and spray pyrolysis [35].

Nowadays, scientists have come to realize that most of the conventional methods (physical and chemical techniques) used for the synthesis of NPs can have major adverse effects on humans and nature. The physical methods used for the preparation of NPs include mechanical/ball milling, chemical etching and precipitation, microwave decomposition, thermal/laser ablation, and so on [36,37]. These methods come at a high cost in terms of resources, energy, time, and space and are considered as inconvenient for application in the research and industrial fields [38]. Meanwhile, common conventional methods that utilize chemicals, such as solvent extraction–evaporation, solvent diffusion, organic phase separation, sol gel, laser pyrolysis, and others, are usually associated with the utilization of hazardous organic solvents that are harmful to the environment and can affect the physiological structure [39]. In fact, these chemical methods can lead to the formation of toxic by-products and involve expensive, complicated, and laborious processes, which are unfavourable to the ecosystem, and lab work [40]. For that reason, it is necessary to use alternative synthesis pathways to eliminate most of the adverse effects, especially in an effort to minimize the disposal of waste and to avoid the possible use of hazardous and toxic materials. Despite the unique features of NPs that are beneficial for diverse applications, numerous nanomaterials have also exhibited toxicity at the nanoscale level. In order to eliminate this issue of toxicity, researchers and scientists have explored the fabrication of bio-nanoparticles by incorporating green chemistry into nanotechnology with the use of plants, microbes, etc. [41]. The green synthesis method has become a promising route to be explored by scientists as it uses biological sources, such as plant, bacteria, or fungi, to develop eco-friendly, non-hazardous, and biocompatible NPs. The plant-mediated green synthesis of NPs is a well-known method that utilizes plant extracts. This green synthesis method has gained significant attention among researchers exploring the different behaviours/properties of NPs in relation to the various type of plants used [42]. Sur et al. (2018) [43] utilized biosynthesized Ag NPs obtained from Reetha (*Sapindus mukorossi*) and Shikakai (*Acacia concinna*) plant extracts as an effective surface-enhanced Raman scattering (SERS) active substrate for the rapid identification of harmful bacteria, such as *Mycobacterium tuberculosis*. In another work, reported by da Silva et al. (2019) [44], a rare transition metal oxide of zirconia NPs (ZrO_2 NPs) was successfully fabricated using *Euclea natalensis* plant extract as a bio-reducing agent. Recently, Abel et al. (2021) [45] reported on the green synthesis of ZnO NPs via an aqueous coffee leaf extract *(Coffee arabica)*, which served as a reducing agent to stabilize the particle length. This had a valuable antibacterial potency on pathogens in wounds. Meanwhile, Phang et al. (2021) [46] elucidated the potential of using CuO NPs from the water extracts of papaya (*Carica papaya* L.) peel biowaste as a photocatalyst for the degradation of palm oil mill effluent (POME) in wastewater treatment under ultraviolet (UV) irradiation. It was noticed that about 66% of the COD was reduced in the POME solution with the use of the biosynthesized CuO NPs under UV light irradiation for 3 h, indicating the degradation of soluble proteins and carbohydrates in the POME. The result showed that there was an improvement in the photocatalytic degradation of POME in the presence of the CuO NPs when compared to the absence of the NPs in dark conditions. Thus, the research work proved that NPs are considered as a promising photocatalyst in accelerating the treatment of POME wastewater.

Overall, physical and chemical methods have been developed to produce NPs. Nevertheless, these approaches may have a negative impact on the environment, human health, and the ecosystem. A few of the major concerns that have arisen in the production of NPs are to do with their high cost, hazardous nature, and the formation of toxic by-products. In order to overcome these issues, the development of an alternative route that is eco-friendly, affordable, and facilitates the creation a sustainable ecosystem is highly necessary. Green synthesis has become an alternative option and a promising pathway to replace the physical and chemical methods for the preparation of NPs as it is biocompatible and environmentally friendly. The rising popularity of the green synthesis method has triggered scientists to produce NPs from diverse sources, such as plant, bacteria, fungi, and algae. However, microorganisms, such as bacteria, fungi, and yeast, are exposed to the risk of culture contamination, tedious operations, and less control over the size of the NPs. Meanwhile, plant-mediated bio-synthesis has received wide attention for the fabrication of NPs due to the abundance of sources and the various choices of flora that can be explored. A review on the fabrication of metal or metal oxide NPs derived from plants will be presented in the following section.

3. Recent Advances on Plant-Mediated Nanoparticles

Recently, NPs synthesized from metals (i.e., Ag, gold (Au)) and metal oxides (i.e., ZnO, titanium oxide (TiO_2), copper oxide (CuO), iron oxide (Fe_2O_3), and alumina (Al_2O_3)) have attracted tremendous attention in the research world due to their potential as strong antibacterial agents as a consequence of their large surface-area-to-volume ratio [47]. The introduction of transition materials into their structures makes them the best candidates for the synthesis of metal-based NPs as they possess partially filled d-orbitals in their elements, which makes them more redox-active (easier to reduce to zerovalent atoms), a feature that facilitates the aggregation of their NPs [48].

Usman et al. (2019) [49] prepared a series of gold NPs (Au NPs) at various concentrations of palm oil leaf extract via the ultrasound radiation technique. They confirmed that increasing the concentration of the palm oil leaf extract (POLE) during synthesis resulted in an increase in the average particle size and a decrease in the polydispersity index (PDI) of the synthesized Au NPs. In another work, by Ramimoghadam et al. (2013) [50], ZnO NPs were successfully synthesized using palm olein (PO) as a bio template via the hydrothermal method. Their findings showed that the particle size distribution tended to exhibit a dual mesoporous distribution, namely micro- and nano-structures with various volumes of PO. Ismail et al. (2019) [51] also worked on the effect of using honey on copper nanoparticles (Cu-NPs) via a green method aided by ultrasonic irradiation. An evaluation of the antibacterial assay and its cytotoxicity against selected bacteria and mammalian cell lines, respectively, revealed that the Cu NPs without honey had a higher cytotoxicity and higher killing activity compared to Cu NPs with honey. A study by Sharma and co-workers (2020) [38] reported on the potential photocatalytic and antimicrobial activities of synthesized ZnO NPs via the green synthesis technique. This study further revealed that the largest zone of inhibition was predominantly attained by *B. subtilis*, followed by *E. coli* and *S. aureus*. Furthermore, the minimum inhibitory concentration (MIC) and minimum bactericidal concentration (MBC) values were between 195 and 3125 $\mu g\ mL^{-1}$ and 6250 and 12,500 $\mu g\ mol^{-1}$, respectively, with these outcomes being lower than the values reported in previous findings [52,53], where the chemical-based approach had been chosen as the method of synthesis. Eventually, the ZnO NPs synthesized via the green method clearly showed that the plant-mediated ZnO NPs were more efficient as antibacterial agents. Table 1 shows a list of the NPs fabricated via green synthesis over the past five years (2018–2022). According to the table, a variety of metal or metal oxide NPs from various plant sources are considered as potential antimicrobial agents that can kill or inhibit the growth of various microorganisms. It is believed that these plant-mediated NPs can be utilized in diverse applications and industries where there is a high risk of contamination by bacteria and fungi.

Table 1. List of nanoparticles with their applications.

Nanoparticles	Technique	Pathogens	Application	Reference
CuO	Green synthesis (Aloe vera leaf extract)	*A. hydrophila, P. fluorescens, F. branchiophilum*	Fisheries	[54]
ZnO	Green synthesis (*Curcuma longa* L.)	*B. subtilis, K. pneumonia, B. licheniformis, E. coli, A. niger, C. albicans.*	Wound care	[55]
CuO	Green synthesis (*Carica papaya* leaves)	*B. subtilis, B. megaterium, B. cereus, S. epidermidis, E. coli, K. pneumonia, K. oxytoca, S. typhimurium.*	Textiles	[56]
Ag	Green synthesis (Mahua oil cake (MOC) of *Madhuca latifolia* L.)	*S. aureus, S. faecalis, L. monocytogenesi, E. coli, S. typhimurium*	Food packaging	[57]
Ag	Green synthesis (*Crocus sativus* L. wastages)	*E. coli, P. aeruginosa, K. pneumonia, S. flexneri, B. subtilis*	Biomedicine	[58]
Ag	Green synthesis (*Capsicum Annuum var Annuum*)	-	Tissue engineering	[59]
Au (gold)	Green synthesis (*Hubertia ambavilla*)	-	Cosmetics	[60]
Fe_3O_4	Green synthesis (*Lagenaria siceraria*)	*E. coli, S. aureus*	Drug delivery	[61]
Palladium (Pd)	Green synthesis (gum harri (*Anogeissus latifollia*)	*P. aeruginosa, S. aureus*	Catalyst	[62]
$AgNO_3$, $Cu(NO_3)_2$, $Ce(NO_3)_3$, $La(NO_3)_3$, $Zn(NO_3)_2$	Green synthesis (*Senna occidentalis*)	*E. coli, S. aureus, C. globosum, A. alternata*	Paint coating	[63]
CdO	Green synthesis (green tea)	-	Electronic devices	[64]

Nevertheless, most of the metal and metal oxide NPs, such as ZnO NPs, Ag NPs, TiO_2 NPs, and others, are highly toxic to human health and have become a major concern with regard to clinical and pharmaceutical handling. Cytotoxicity, oxidative stress, and mitochondrial dysfunction can occur in various cell lines due to the reduction in Zn-dependent enzymes and transcription factors by an increase in [Zn^{2+}] ions, as a result of the dissolution of ZnO NPs in the extracellular region [65,66]. This was supported by Chen et al. (2019) [67], who stated that the cytotoxicity of ZnO NPs in HepG2 cells is dependent on the size or concentration of the ZnO NPs. According to Aadli et al. (2019) [68], lignin-functionalised Ag NPs have a toxic effect on MCF-7 cancer cells in a dose-dependent manner, and they suggested that the cell toxicity of Ag NPs might possibly be due to the generation of reactive oxygen species (ROS), such as hydrogen peroxide or their conversion into highly reactive hydroxyls or superoxide radicals. Niska et al. (2018) [69] mentioned in a review that TiO_2 NPs also have a toxic effect, whereby the NPs accumulate on the surface of human keratinocytes (HaCaT cells), are absorbed by endocytosis, and generate ROS to cause mitochondrial damage to DNA and genotoxicity in human keratinocytes.

Thus, it is necessary to select a suitable method and the raw materials for a proper design of nanomaterials to reduce the toxicity of the substances. One such potential method involves reducing the dissolution of the toxic particulates to eventually hinder or lessen the toxicity of the materials. This can be done by modifying the composition or by doping in an extra component to improve the stability of the NPs. In addition, the addition of exogenous chelating agents in the synthesis may help to reduce the toxicity of the dissolved ions [70]. Díez-Pascual et al. (2015) [71] investigated the wound healing potential of polymeric films reinforced with chitosan-modified ZnO NPs and suggested that the modification of the ZnO NPs with chitosan reduced their cytotoxicity towards human cells. This was attributed to the increase in size of the NPs due to the physical attachment of biopolymers to the ZnO surface. Norouzi et al. (2021) [72] reported an insignificant loss of cell viability in HFF cells at a concentration of less than 500 µg/mL of polyvinyl alcohol/ZnO NPs (PVA/ZnO) through a cytotoxicity assay. The result showed that at concentrations below 500 µg/mL, the cell viability of HFF cells was higher than 82.8%, thereby indicating that PVA/ZnO NPs are non-toxic to human cells at that concentration level. The findings on the cytotoxicity of ZnO NPs from the above works were compared with the reported works [73], and it was revealed that there was an improvement in the toxicity of NPs on human cells when PVA was integrated into the NPs.

Recently, hybrid hydrogels together with nanotechnology have shown a significant potential to be used as antimicrobial agents. Some of the latest research work related to nanocomposites that has been reported in the open literature will be discussed in the subsequent subtopic.

4. Innovation of Metallic Nanocomposite Hydrogels

Recently, hydrogels have been attracting much attention among scientists due to their fascinating ability to absorb and retain a sufficient amount of water. A hydrogel comprises a network of monomers or polymers linked together by hydrogen bonds, electrostatic interactions, hydrophobic interactions, or covalent bonds to form a hydrophilic 3-D polymer network [74]. The medical application of nanotechnology, which is recognized in an emerging field known as nano-medicine, is still under development.

Farjadian et al. (2019) [75] evaluated the thermo- and pH-responsive characteristics of nano-carrier drug delivery platforms based on lysine-modified poly (vinylcaprolactam) (PVCL) crosslinked by poly (ethylene glycol) diacrylate (PEGDA) to form a nano-hydrogel conjugated with doxorubicin (DOX). The release profile of PVCL-DOX revealed that the highest release of 80% was obtained at 40 °C and pH 5 within 72 h, which indicates that the substance can suitably adhere to cancer sites. Additionally, PVCL-DOX showed an efficient response in killing cancer cells in in vitro studies on MCF-7 cell lines compared to that of the free DOX. This indicates that the prepared substance has a potential to be utilized as an effective anti-cancer agent. Meanwhile, Abbaszadeh et al. (2020) [76] fabricated a novel chitosan-based quercetin nanohydrogel (ChiNH/Q) and highlighted that the nanocomposite had distinct antitumour and anti-inflammatory properties that could regulate the proliferation of breast cancer cells. This was a novel finding as it demonstrated, for the first time, the application of ChiNH/Q on the global genomic DNA methylation profile of HEPG2 cells. A study into the antitumour properties of the prepared ChiNH/Q revealed that the level of methylated cytosine was significantly higher (1.01%) than the free-Q and ChiNH-treated cells (0.993% and 0.992%, respectively). This demonstrated the efficiency of this nanohydrogel in inhibiting tumour cells by decreasing the DNA methyltransferases (DNMTs) gene expression and also by increasing the global DNA methylation in HepG2 cancer cells. In another work, Kamiński et al. (2020) [77] investigated the potential behaviour of the synthesized polymer hydrogel, HydroGel Bacterial Cellulose (HGBC), which originated from a kombucha-derivative, as a replacement for synthetic materials, such as polyamide (nylon), polyester, acrylic, Kevlar, etc., in the textile industry, especially for use by astronauts in space. This HGBC material is one of the future innovations that is being explored widely due to its excellent mechanical durability, good swelling properties, fire-resistance, and comfort. Figure 4 shows photographs of the finished materials using HGBC for clothing.

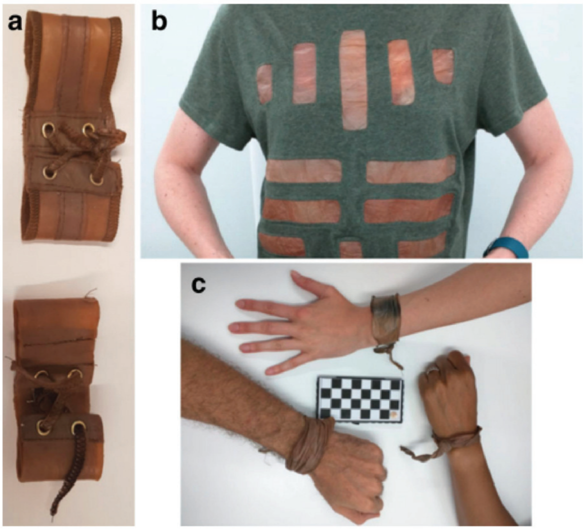

Figure 4. Photographs of (**a**) wristband, (**b**) T-shirt sewn with fabric coated HGBC, (**c**) condition of wristband after 2 weeks. Adapted from Ref. [77].

Nevertheless, one drawback of using hydrogels on their own is their low mechanical strength, especially when used as scaffolds, which require high mechanical strength with good tolerance of compression and elasticity. This low mechanical property hinders their utilization for handling and loading in different parts of the body. Thus, the insertion of metallic NPs into hydrogels to form metallic nanocomposite hydrogels can increase the entanglements in its polymeric matrix to yield a high mechanical strength [78]. Dil et al. (2018) [79] reported on the antibacterial potential of novel porous gelatine silver/AcA (NPGESNC-AcA) nanocomposite hydrogels through free radical polymerization. According to their study, the gelation hydrogel with Ag NPs gave a better performance against *E. coli* (Gram-negative bacteria) compared to *S. aureus* (Gram-positive bacteria). This result may be due to the fact that the cell walls of Gram-negative bacteria have a thinner lipid layer that could have facilitated the penetration of the released Ag NPs into the bacterial cell membrane to eventually destroy them. Gholamali et al. (2019) [80] developed a new drug delivery system comprising oxidized starch/CuO nanocomposite hydrogels through the in situ method. They performed in vitro drug release profiles at different concentrations of CuO NPs on the hydrogels to determine the cumulative release of the drug from the metallic nanocomposite hydrogels. The reduced cumulative release of the drug, ibuprofen, with respect to increases in the concentration of NPs in an acidic environment was attributed to the role played by the CuO NPs as the primary precursor of the prolonged drug release behaviour. The outcome showed that a lower concentration of CuO NPs in the hydrogel matrix provided a better drug release profile, making it suitable for controlled drug delivery. In another work, Ahmadian et al. (2019) [81] also obtained a similar outcome with regard to the drug delivery potential of polyvinyl alcohol/CuO (PVA/CuO) nanocomposite hydrogels at pH 7.4. It was observed that as the number of CuO NPs increased, the drug release rate was lowered because the entrapped drug molecules could not easily diffuse into the contacted hydrogel network. Katas et al. (2021) [82] successfully synthesized Ag NPs using a spent mushroom substrate (SMS) as a reducing agent. The NPs were then incorporated with genipin-crosslinked gelatine hydrogels as a wound dressing. The biosynthesized AgNP hydrogel proved to be an effective antibacterial material against *S. aureus*, *P. aeruginosa*, *Bacillus subtilis* (*B. subtilis*), and *Escherichia coli* (*E. coli*).

Concurrently, any change in the size of the NPs is expected to alter their physical and chemical properties due to an increase or decrease in their surface area. Meanwhile, the hydrophilic properties and high-water content of hydrogels could cause outstanding mechanical and swelling properties. Thus, combining NPs and hydrogels under the same mechanism is a technological development that will result in nanocomposites with outstanding properties for applications in drug delivery, wound dressing, agriculture, textiles, and others. The fabrication of nanocomposite hydrogels incorporated with metallic NPs is still new, and thus, comprehensive and extensive studies are essential to obtain a full picture of the functionality of these types of nanocomposites in various applications. In this review, the focus on the utilization of metallic nanocomposite hydrogels in the field of biomedicine will be discussed in the next subtopic.

5. Functionalization of Biobased Metallic Nanocomposite Hydrogels in Biomedicine Applications

5.1. Drug Delivery Systems

It has been ascertained worldwide that the use of NPs for drug delivery involves complex research, with promising outcomes being generated from in vitro studies and small animal models. Nevertheless, research into the use of these nanomaterials on humans is still limited due to the translational gap that exists between animal and human studies. It has been observed that the behaviour and functionality of nanomedicines in the body are associated with the physiological and pathological differences between animal model species and humans [83].

Nanotechnology is a novel solution for overcoming the bottleneck in the issue of complexity owing to the fast development of nanoscience and the magnificent performance of nanomaterials. A nano-drug delivery system comprises nanomaterials with the full potential to enhance the stability and water solubility of drugs, extend the cycle time, elevate the uptake rate of target cells or tissues, and reduce enzyme degradation, thereby improving the safety and effectiveness of the drugs [84]. Two main aspects in the fabrication of metallic nanocomposite hydrogels are their pore size and their water intake, which must be taken into account during the drug-loading process to achieve the optimum release rate of the drugs into the targeted cells. The pore size of the nanocomposite hydrogel must fit the size of the immobilized drugs, while a high-water content is necessary to create a convenient environment for the immobilization of the drugs [85].

The schematic diagram in Figure 5 illustrates the drug delivery mechanism. In brief, Figure 5a shows that the drugs, made up of polymers, are loaded into the metallic nanocomposite hydrogel through physical or chemical attachments [86]. Next, this nanomaterial is administered into the patient's body via an injection and is then transported into the blood vessels, as depicted in Figure 5b. At a certain point, due to the different environments at the site of the tumour, such as the presence of enzymes or a difference in pH, temperature, electric field, and redox potential, this condition could trigger the smart nanomaterial to release the drug loaded in the nanocomposite to interact with the tumour cells. The drug/therapeutic agent can be released from the nanocomposite hydrogel through three mechanisms, namely (i) diffusion-controlled or (ii) chemically controlled degradation or (iii) swelling-controlled mechanisms. As shown in Figure 5c, the immobilization of these drugs in the targeted tissues can cause the partial or complete destruction of tumour cells [87,88].

Amiri et al. (2017) [89] successfully prepared novel alginate/$CoFe_2O_3$ metallic nanocomposite beads (Alg/CFO MNPs) hydrogels in the presence of caffeine via the co-precipitation method. This work is claimed to be the first to deal with a combination of alginate hydrogel beads with magnetite cobalt ferrite nanoparticles (CFO MNPs) as a drug carrier. The in vitro study proved that the release profile of this nanocomposite hydrogel was elevated at neutral pH compared to an acidic environment, which influenced the diffusion of drugs into the nanomaterials. In an acidic environment, the hydrogels are mainly surrounded by carboxylic acid and easily undergo protonation, which eventually results in a decline in drug diffusion. Basu and co-workers (2018) [90] developed semi-interpenetrating-hydrogel-silver nanocomposites (SNA) via a facile and simple green methodology through the free radical copolymerization of sodium alginate/polyacrylamide (NaAlg/PAAm) onto *Dolichos biflorus* Linn, which acted as a reducing agent. According to their study, the loading efficiency of the drug was greatly induced by the concentration of the drug and the impregnation time. Both factors contributed to the high increase in the drug loading in the initial phase, which eventually dropped off at a certain concentration and time. These effects may be attributed to the high drug diffusion level during the early loading stage. Meanwhile, Chen et al. (2018) [91] successfully fabricated Au NPS from carrageenan oligosaccharide (CAO) hydrogels, which were used as the reducing and capping agent. They investigated the antitumour activities of their synthesized NPs on colorectal cancer and breast cancer in vitro. Based on the synthetic route and mechanism shown in Figure 6, there was a reduction of Au^{3+} to Au^0 ions in the reaction system, indicating the formation of Au NPs. Meanwhile, the CAO, which acted as a capping agent, was added to obtain CAO-Au-NPs nanocomposite hydrogels. The CAO was surrounded by gold atoms to form nano-sized particles.

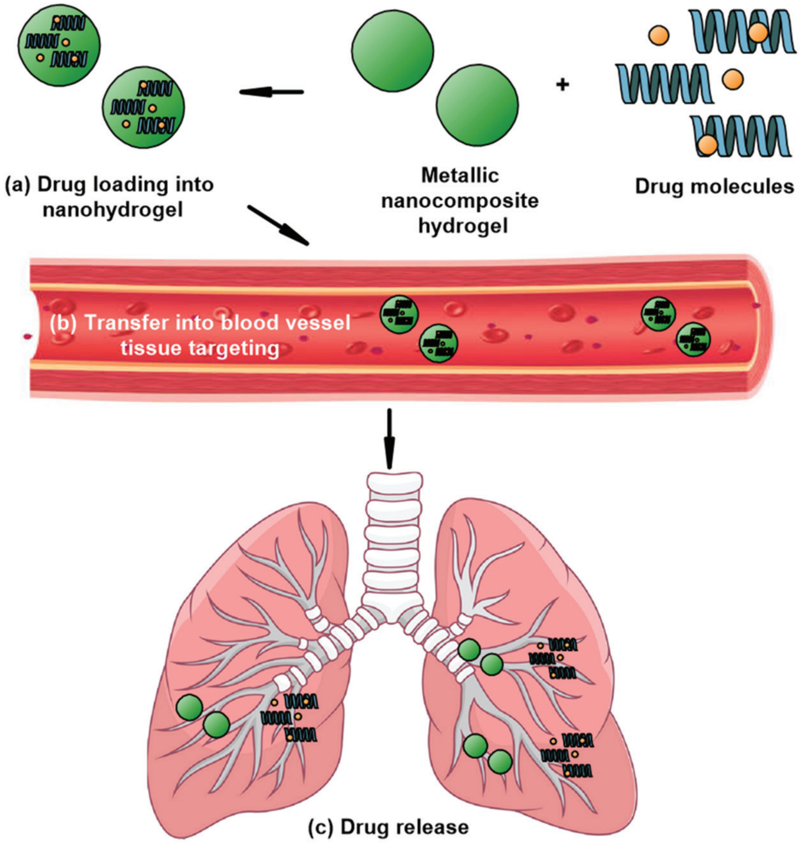

Figure 5. The proposed schematic diagram showing stages of drug delivery mediated by metallic nanocomposite hydrogel: (**a**) drug loading into metallic nanocomposite hydrogel, (**b**) immobilization of metallic nanocomposite hydrogel in blood vessel to targeted tissues, and (**c**) drug release process.

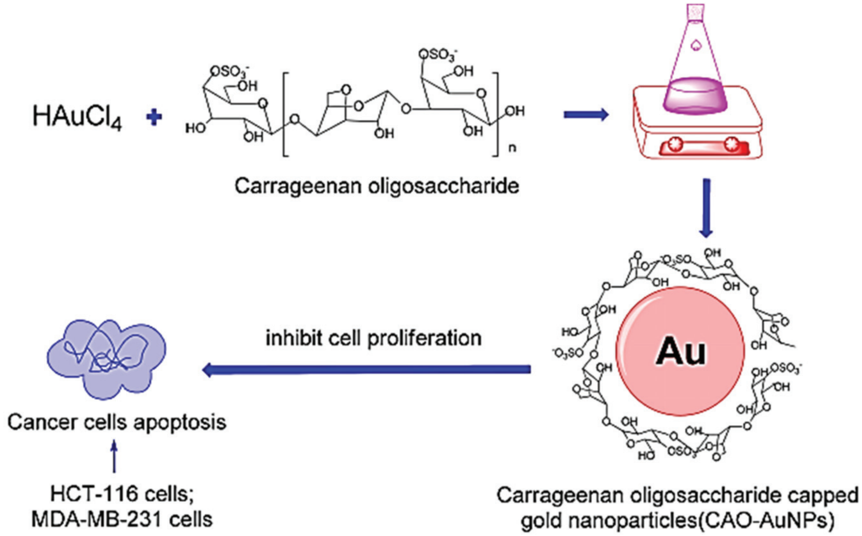

Figure 6. Schematic diagram showing the mechanism of carrageenan oligosaccharide (CAO) hydrogel capped the gold nanoparticles (Au-NPs). Subsequently, the cytotoxicity test of CAO-AuNPs nanocomposite hydrogel on cancer cells (HCT-116 cells and MDA-MB-231 cells) was also conducted. Adapted from Ref. [91].

Organic–inorganic hybrid hydrogels based on an interpenetrating polymer network (IPN) synthesized from polyaspartic-acid-based polymers embedded with Ag, CuO, and ZnO NPs were successfully designed by Sattari et al. (2018) [92]. In general, the fusion of NPs and IPN hydrogels increased the stability of the drug, curcumin, in the network and eventually caused a slower release of the drug. In addition, Sattari and co-workers also concluded that the pH environment affected the release of curcumin from the synthesized hydrogel, where it was observed that there was an increased release of the drug from the hydrogel at its natural pH due to an increase in the electrostatic repulsion and a reduction of the hydrogen bonds between the ionic groups. Recently, Nagaraja et al. [93] elaborated on the potential use of natural polymer-based stimuli-responsive silver nanocomposite hydrogels (TGIAVE-Ag) obtained through a simple redox polymerization and a green method using an aqueous extract of *Terminalia belliricia* seeds. The prepared TGIAVE-Ag exhibited excellent antimicrobial activity with a large inhibition zone ranging between 12–18 mm against *K. pneumonia, P. aeruginosa, E. coli*, and *S. aureus* as Gram-positive and Gram-negative bacteria, through the disc diffusion method. They suggested that the Ag NPs generated free radicals and Ag^+ ions, which led to the formation of pits and the eventual death of the cells.

In general, natural sources are used to synthesize green NPs, which act as a reducing and stabilizing agent, before the metal atoms are reduced to metal ions. These nano-scale particles will eventually combine with the hydrophilic hydrogels, which commonly contain –OH, –COOH, $–CONH_2$, –CONH, and $–SO_3H$, to elevate the rate of drug diffusion into the targeted cells. Tumour cells or tissues usually behave differently in the environment compared to normal cells, and therefore, the materials must be able to withstand the changes in the behaviour of tumour cells while transporting the drugs. Metallic nanocomposite hydrogels have shown their ability to adapt to external stimuli, such as pH, temperature, and enzymes, at the tumour site, thus enhancing the diffusion rate of the therapeutic agent in the drug delivery system. In addition to drug delivery, these nanomaterials have also exhibited a potential in wound care applications, which will be discussed in the following subsection.

5.2. Wound Care Applications

Skin is the largest organ of the body and comprises multiple components and functions. The outer layer of the skin is composed of dead cells and the epidermis, which acts as a protection against the environment. The dermis or so-called middle layer, which consists of living cells with a network of blood vessels and nerves, is responsible for the detection of any external stimulus and the thermal regulation of the enclosed body. The inner layer of the skin is mainly formed of fat, and its function is to insulate the body against shock. A wound is caused by a physical trauma, where the skin is torn, cut, or punctured (an open wound) or where a blunt force trauma causes a contusion (a closed wound) [94].

There are two types of wounds, namely acute wounds and chronic wounds. In general, acute wounds are injuries with minimal microbial load or zero infection, scab generation, and immune cell infiltration in the beginning stage. Consequently, acute wounds can be repaired within a short period of time [95]. On the other hand, chronic wounds take a longer time to repair due to the challenging process of being reimposed into the normal anatomical structure and functions [96].

Wound healing is typically divided into four different phases, namely: (i) haemostasis, (ii) inflammation, (iii) proliferation, and (iv) remodelling [20]. Figure 7 shows a schematic diagram of the flow of the wound healing process. These phases are clarified in the following points:

(i) Stage 1: Haemostasis—once the skin experiences an injury, the haemostasis process will generate platelet clotting, accompanied by the formation of a fibrin matrix that acts as a scaffold for cell infiltration [97].

(ii) Stage 2: Inflammation—the second stage, which is the inflammation process, will start immediately after blood clotting, and it takes around 24 h to 4–6 days to complete the process. In this stage, proteolytic enzymes and pro-inflammatory cytokines will be secreted over the immune cells around the wound area. These inflammatory cells produce reactive oxygen species (ROS), which are responsible for protecting the organism from bacteria and infections. Gram-positive bacteria, such as *S. aureus* and *S. pyogenes*, can be found predominantly in the first stage of infection, while Gram-negative bacteria (i.e., *E. coli* and *P. aeruginosa*) dwell in wounds that have already developed. In this context, an extensive understanding of cell-material interactions is vital to trigger an exploration of new biomaterials. The discovery of new biomaterials, including nanocomposite hydrogels, which can mimic the microenvironment of the skin, is essential to enhance the rate of wound healing, especially in chronic diabetic patients. The metallic nanocomposite hydrogel should be able to target the macrophages to become regenerative and, eventually, be able to regulate the excretion of signalling molecules. Consequently, a polymeric matrix offers structural support and carries information to be passed to the cells for their in-growth.

(iii) Stage 3: Proliferation—all foreign particles and tissue debris are eliminated from the wound by neutrophils and macrophages, thus preventing infections [98]. The activation of the support system following the arrival of the neutrophils at the lesion is associated with the loss of granules in the platelet, the liberation of chemotactic signals by the necrotic tissue, and bacterial deterioration.

(iv) Stage 4: Remodelling—finally, the system will eventually evolve by causing the macrophages to react to injuries. These cells are in charge of the phagocytosis of fibrin and cellular debris, and they release the macrophage-derived growth factor (MDGF) for fibroblasts and endothelial cells [97].

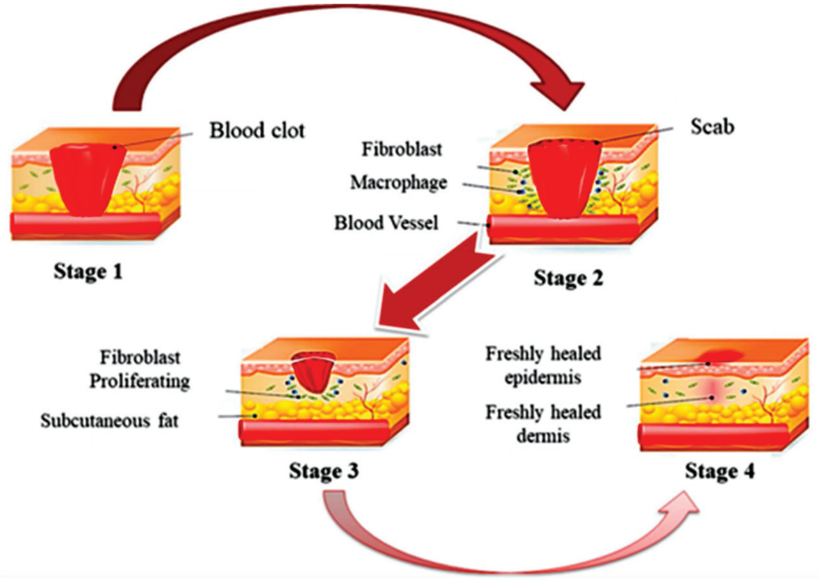

Figure 7. Illustration on the wound healing process. The four stages of wound healing, which are (i) Stage 1: Hemostasis phase; (ii) Stage 2: Inflammatory phase; (iii) Stage 3: Proliferation phase; and (iv) Stage 4: Remodeling phase. Reprinted with permission from Ref. [98]. Copyright 2020 Elsevier.

The materials used to cover or treat wounds have also evolved from simple wound covers into commercial wound dressings, with the latest one involving smart technology. Originally, common materials, such as honey, animal oils or fats, cobwebs, mud, leaves, moss, or animal dung in a crude form were used as wound dressings, and later, two or more of these components were combined for convenience of use and to improve their clinical effectiveness. Up to the end of the 19th century, absorbent sheets were produced by scraping sheets of old linen with sharp knives. These were eventually replaced by cotton in the middle of the 20th century [94]. Wound dressings, such as gauze, sterilized absorbent cotton, and bandages, are commonly found in clinical practices due to their low cost. However, these dressings can only provide physical protection and are limited in their wound healing mechanisms when it comes to maintaining a moist environment and preventing infections [96]. Nowadays, smart wound dressing has emerged as a promising strategy for enhancing wound care management by modifying the materials to another level of innovation in advanced wound dressing technologies. The developed smart wound dressing is not only able to provide physical protection but can also act as a diagnostic sensor that is able to monitor the condition of a wound and apply a proper treatment to promote the healing process [99,100].

Recently, the emergence of metallic nanocomposite hydrogels in wound healing applications has driven these nanotechnologies into new inventions in the science and engineering fields. The role of these nanocomposite hydrogels in wound care is dominantly favourable due to their fascinating biocompatibility, controllable physical characteristics, natural drug-loading system, and abundance of functional groups [101]. A study by Haseeb and co-workers (2017) [102] revealed that their fabricated wound dressing containing silver nanoparticles (Ag NPs), produced from linseed hydrogels (LSH), showed excellent antimicrobial and wound dressing properties. Based on their antimicrobial activity, it was found that the LSH-Ag NPs actively inhibited the growth of several bacteria and fungi, such as the *S. mutans*, *S. epidermidis*, *P. aeruginosa*, *E. coli*, *S. aureus*, *B. Subtilis*, *A. odontolyticus*, and *A. niger* strains. Additionally, the LSH films impregnated with Ag NPs showed a wound closure of 100% for rabbits on the 15th day. A similar outcome was obtained from a commercialized Band-Aid dressing on the excised wound of a group of healthy male rabbits. Nevertheless, the excised wounds on a rabbit patched with the LSH-Ag NPs film displayed a faster recovery compared to the standard Band-Aid dressing.

Next, Ezealisiji et al. (2019) [103] reported on the successful synthesis of ZnO NPs nanocomposite hydrogels, using a *Solanum torvum* extract as the bio template, which were tested for their effects on the hepatic and renal functions of Wistar rats. They found that the moisturizing and humectant properties of the hydrogels enhanced the diffusion of the nanomaterials into the skin by reversibly agitating the stratum corneum, which eventually contributed to an added driving force for the transference of the nanomaterials into the skin. Later, the metallic nanocomposite hydrogels resulted in the initiation of oxidative stress, mitochondrial impairment, and DNA denaturation, while accelerating apoptosis of the skin structure. Another work by Batool et al. (2021) [55] revealed the effectiveness of ZnO-NPs/silica gel hydrogels (ZnO-NP/SG) fabricated from *Aloe barbadensis* leaf extract for wound healing in male albino mice. The prepared wound dressing showed a promising potential for the control of bacterial growth as it is biocompatible and can accelerate wound healing behaviours in mice, which proves its therapeutic ability. According to Batool et al., the high concentration of ZnO-NP/SG loaded at 30 ppm resulted in a higher wound recovery rate than in the control sample. Meanwhile, it was found that at a concentration of 15 ppm, it was capable of healing 95% of the wound within 11 days. These results showed that the ZnO-NP/SG dressing had a better control of bacterial growth, was biocompatible, and accelerated wound healing properties in mice, thereby indicating its therapeutic ability.

In summary, metallic nanocomposite hydrogels are considered as ideal materials for offering a protective barrier against bacterial infections, as well as in promoting the rate of wound healing, as they are biodegradable, biocompatible, non-toxic, antimicrobial, biologically adhesive, biologically active, and haemostatic. The moist condition of this nanomaterial is able to prevent wound dehydration, which could slow down the wound healing process. At the same time, the NPs embedded in the hydrogels are responsible for acting as an antimicrobial agent by inhibiting the formation and growth of bacterial or fungal strains. In fact, it has been proven in extensive research studies that nanocomposite hydrogels can replace the conventional Band-Aid dressings available in the market due to their potential to enhance the wound healing process at a faster rate than the standard Band-Aid dressings. With a deeper understanding and with further studies into nanocomposite hydrogels, these smart nanomaterials can be commercialized in the market in the future and can be safely used, either in daily life or in the clinical field. Next, the functionality of metallic nanocomposite hydrogels in tissue engineering applications will be explored and discussed in the subsequent sub-topic.

5.3. Tissue Engineering and Regenerative Medicine (TERM)

Many factors can contribute to the burden of orthopaedic trauma, and these mostly involve bone and cartilage fractures due to road accidents, work and sports injuries, degenerative diseases, such as osteoporosis, osteoarthritis, cancer, cystic fibrosis, and hereditary bone diseases, such as marrow abortion. The abrasion implications defined by bone defects, bone fractures, severe pain, fever, redness, and others demand a proper reformation and rehabilitation [104]. Moreover, various physiological signals, such as biochemical, mechanical, and electrical signals, are essential in the process of tissue regeneration. Tissue impairment normally produces local physiological electricity, followed by the interchanging transmission of electrical signals between cells. The emergence of external electrical signals in the tissue regeneration system can cause changes in the electrical charges between the cells and can stimulate the adherence, migration, proliferation, and differentiation of stem cells. Thus, it is essential to select suitable electrically active materials that are capable of transferring electrical signals through, for instance, a scaffold to build a biomimetic electro-micro-environment for the purpose of stem cell differentiation [105].

In order to cater for injuries and diseases, the development of tissue engineering has shown a great potential for innovation in clinical applications. Tissue engineering and regenerative medicine (TERM) comprise a restoration process and the substitution or regeneration of damaged tissues, which are difficult to repair. Figure 8 presents the tissue engineering approaches that are commonly practised. Prior to the development of the tissue or organ, it is essential to isolate some cells from a small tissue biopsy performed on the patient to gain an understanding of the characteristics of the specific tissue cells, as depicted in Figure 8a. The isolated cells are then expanded and seeded into three-dimensional (3D) scaffolds that mimic the natural extracellular matrices (ECM) of the targeted tissue, where they undergo proliferation as well as differentiation, as shown in Figure 8b–d. The scaffolds are responsible for transporting the cells to the targeted site in the patient's body, enhancing cell-biomaterial interactions, aiding cell adhesion, and enabling sufficient gases, nutrients, and growth factors to be transported to the seed cells to maintain the survival, proliferation, and differentiation of the cells. Subsequently, these cell-loaded scaffolds are transplanted into the patient by injecting or implanting the fabricated tissue at the desired site via surgery, as depicted in Figure 8e [106]. Thus, it is essential that the materials be fabricated according to the needs in the TERM applications by taking into account certain factors, such as the cell proliferation, the type of cells at the targeted site, and the signal connection.

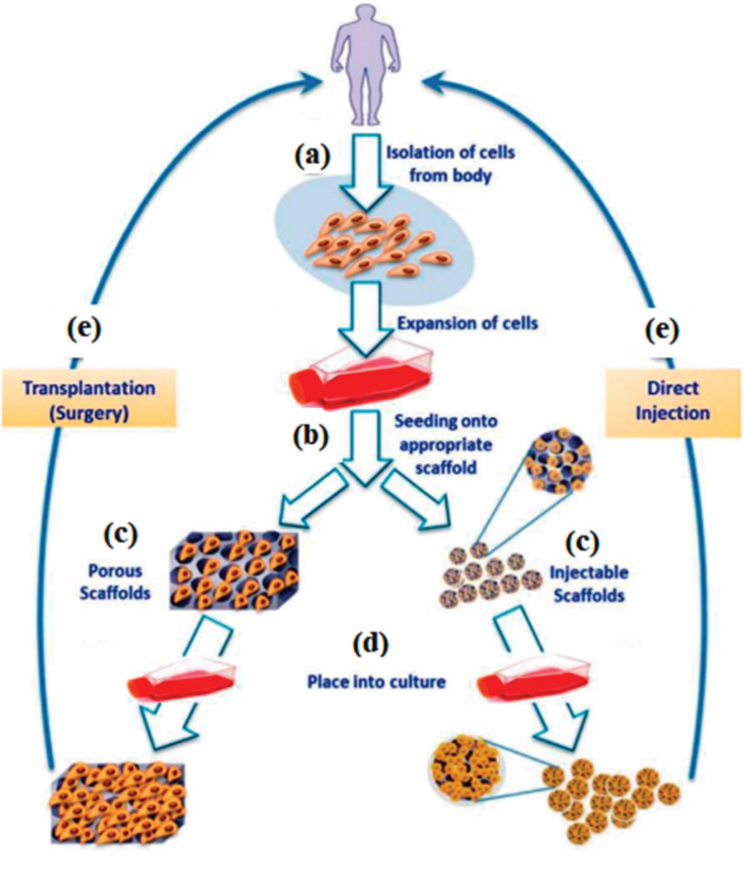

Figure 8. Schematic illustration demonstrated the most common tissue engineering mechanism, starting with (**a**) isolation of cells from body, (**b**) implantation cells onto scaffold, (**c**,**d**) cell proliferation, and (**e**) transplantation or injection. Adapted from Ref. [106].

Nowadays, the transplantation of tissues acquired from a healthy donor (an allograft) or from a patient's own body (an autograft) is one of the many options available to patients.

However, a few drawbacks that could occur during tissue transplantation are the lack of donor tissue, the possibility of infection, the high chance of tissue rejection, and faulty graft guts [107]. Over the past 5 years, numerous techniques, such as supercritical fluid technology and 3D printing, have been widely used to fashion the scaffolds for tissue engineering [108]. Hakimi et al. (2018) [109] invented a remarkable portable 3D bioprinter (weight < 0.8 g) with a microfluidic cartridge that can be utilized for the bioprinting of skin sheets. The study demonstrated a successful in situ bioprinting on porcine and murine wound models, where the wounds were fully covered with a homogeneous layer according to the thickness of the wound. The wounds treated with the in situ deposited sheet stopped bleeding approximately 5 min later and were able to achieve haemostasis after 10 min. Such portable 3D printers can be revolutionized in the current healthcare market, especially for emergency cases such as burn trauma that require immediate treatment [110].

Meanwhile, a metallic nanocomposite hydrogel possesses a network that acts as an artificial scaffold, which can be fitted into a 3D microenvironment. This approach has become an innovative technique in the modern TERM field, where the main goal of the TERM is to assemble functional constructs of tissues or organs by restoring and maintaining the damaged tissues or whole organs. In addition, this nanocomposite hydrogel has unique properties, such as high-water content, biocompatibility, stimuli-responsive features, and bio-responsive functions, which could offer various materials of choice for manifold TERM applications [111,112]. Although they possess water-bearing properties, the common hydrogel matrices are unable to conduct electrical signals and can obstruct the signal connection between cells. Nowadays, the development of conductive hydrogels offers a more promising potential in the tissue engineering field compared to the common hydrogels due to their capacity to stimulate electrical signals between cells and promote a physiological microenvironment for electroactive tissues [105].

Various research works have been established to create biomaterials that can mimic the microenvironment of the skin. Previously, Zulkifli et al. (2017) [113] reported on the fabrication of low-toxicity hydroxyethyl cellulose/silver NPs (HEC/Ag NPs) nanocomposite hydrogel scaffolds, which are ideal for skin tissue engineering applications. Rakhshaei et al. (2019) [114] prepared chitosan-gelatine/ZnO nanocomposite hydrogel scaffolds (CS-GEL/nZnO) through in situ synthesis and studied the cytocompatibility of the nanomaterial on normal human dermal fibroblast cells (HFF2). In comparison to the previous report [115], where the NPs were simply added to the matrix of the scaffold, the production of this nanomaterial through in situ synthesis was clearly able to elucidate a higher antibacterial and lower cytotoxicity effect because the ZnO NPs were well distributed in the polymeric matrix. Thus, the in situ synthesis of CS-GEL/nZnO hydrogels is strongly recommended for biomedical applications, especially for skin tissue engineering. Recently, Zhou et al. (2020) [111] reviewed the proliferation and expansion of cardiomyocytes using Au NPs fused with a silk-based hydrogel (SF/ECM). They reported that the uniform distribution of Au NPs in the matrix provided a favourable conductivity and had a biological effect on cardiac repair, where this metallic nanocomposite hydrogel was able to effectively decrease the size of infarct tissue from 89% to 65%.

In brief, TERM is one of the vital fields of biomedicine, and a detailed understanding of its mechanism and conceptualization is still required if it is to be applied in real-life applications. Although a hydrogel contains a certain amount of water and is biocompatible, the hydrogel itself possesses a low viscosity and is unable to conduct electrical signals, which makes it unfavourable for utilization in TERM. Thus, to satisfy the requirements for its use as a scaffold, the hydrogel matrix must be modified to obtain the required structure and properties. A few factors, such as cell proliferation, adhesion, migration, and signalling, must be considered in the engineered tissues prior to the fabrication of the metallic nanocomposite hydrogels to enable them to be used for the treatment of organ failures resulting from diseases and injuries. Combinations of the selected NPs and hydrogels can be tailored to create crosslinked networks with enhanced mechanical strength and electrical, optical, magnetic, and biomedical properties. In addition, nanocomposite hydrogels can be used as a temporary alternative to replace burnt or injured tissue as they have the ability to mimic the microenvironment of human tissue. However, inventions using this nanotechnology are still limited and must be further established in the future. Thus, the next section gives an overview of the limitations and future perspective of metallic nanocomposite hydrogel technology in order to identify important ideas that can be used to overcome the current limitations of this technology.

6. Limitations and Future Perspective of Metallic Nanocomposite Hydrogel Technology

In brief, the fabrication of metallic nanocomposite hydrogels containing NPs from various natural sources through green synthesis has shown a tremendous potential for diverse applications, especially in the biomedicine field. In previous studies in the literature [116,117], conventional hydrogels suffered from poor mechanical strength and fast/abrupt biodegradation limits, thus making them unfavourable for most applications [118]. Meanwhile, the instability of NPs in aqueous solutions has become a major constraint to the advancement of novel nanomaterials [119]. Therefore, various emerging technologies to reinforce hydrogels composed of nanomaterials are being identified to close the gap by enhancing the strength and elastic modulus of these nanocomposites. Although publications on NPs and hydrogels abound, publications on the fabrication of hydrogels incorporated with metallic NPs are still limited and need to be explored further. In the fabrication or modification of metallic nanocomposite hydrogels, a few factors, such as structural modification, material stability, processability, and solubility, which might affect the production, must be taken into consideration as these conditions will vary greatly and have an impact on the hydrogel cross-linking materials [120]. From another perspective, there are also concerns with regard to the adverse effects of the cytotoxicity of the nanomaterials used due to the controversial interaction between the uncertain mechanisms of the NPs and cells [121]. Therefore, the selection of the best materials and techniques for the preparation of these novel antimicrobial metallic nanocomposite hydrogels is crucial, and a few factors need to be taken into consideration in observing their biocompatibility with cell growth and their precise functions.

7. Conclusions

The introduction of biosynthesized metallic nanocomposite hydrogels has become a new alternative route for the replacement of non-biodegradable synthetic materials. The excellent properties of metallic nanocomposite hydrogels, such as their small size, moist condition, biodegradability, high thermal stability, conductivity, and good mechanical strength, have greatly affected the development of nanotechnology for various application fields, such as in biomedicine, coatings, food industry, packing, and others. In this review, a few of the current fabricated metallic nanocomposite hydrogels and their use in the field of biomedicine, such as in drug delivery, wound healing, and TERM, were discussed extensively. In addition to that, the limitations on the use of these metallic nanocomposite hydrogels were briefly explained at the end of this review. The most crucial challenge with regard to biosynthesized metallic nanocomposite hydrogels is that their complex mechanism and interaction with biomolecules have not been clearly distinguished. In addition, parameters such as the size, shape, agglomeration, purity, surface area, surface charge, functionalization, storage stability, and adverse cytotoxicity of the metallic nanocomposite hydrogels must also be considered during the synthesis of these nanocomposite. Overall, in-depth and comprehensive studies on the mechanism and compatibility of metallic nanocomposite hydrogels on human cells need to be carried out to create advanced smart wound dressings in the near future.

Author Contributions: Conceptualization, N.S.F.D.; investigation, N.S.F.D.; writing—original draft preparation, N.S.F.D.; supervision, R.R.; writing—review and editing, R.R.; funding acquisition, R.R. All authors have read and agreed to the published version of the manuscript.

Funding: The APC was funded by Universiti Kebangsaan Malaysia under Geran Universiti Penyelidikan [GUP/2021/027].

Institutional Review Board Statement: Not applicable.

Informed Consent Statement: Not applicable.

Data Availability Statement: No new data were created or analyzed in this study. Data sharing is not applicable to this article.

Acknowledgments: The authors would like to express their gratitude to Universiti Kebangsaan Malaysia for their assistance and encouragement.

Conflicts of Interest: The authors declare no conflict of interest.

References

1. Nasrollahzadeh, M.; Sajadi, S.M.; Sajjadi, M.; Issaabadi, Z. An introduction to nanotechnology. In *Interface Science and Technology*; Elsevier: Amsterdam, The Netherlands, 2019; Volume 28, pp. 1–27.
2. Wu, D.; Zhou, J.; Creyer, M.N.; Yim, W.; Chen, Z.; Messersmith, P.B.; Jokerst, J.V. Phenolic-enabled nanotechnology: Versatile particle engineering for biomedicine. *Chem. Soc. Rev.* **2021**, *50*, 4432–4483. [CrossRef] [PubMed]
3. Ahmad, U.; Ahmad, Z.; Khan, A.A.; Akhtar, J.; Singh, S.P.; Ahmad, F.J. Strategies in development and delivery of nanotechnology based cosmetic products. *Drug Res.* **2018**, *68*, 545–552. [CrossRef] [PubMed]
4. Enescu, D.; Cerqueira, M.A.; Fucinos, P.; Pastrana, L.M. Recent advances and challenges on applications of nanotechnology in food packaging. A literature review. *Food Chem. Toxicol.* **2019**, *134*, 110814. [CrossRef]
5. Vasantharaj, S.; Sathiyavimal, S.; Saravanan, M.; Senthilkumar, P.; Gnanasekaran, K.; Shanmugavel, M.; Manikandan, E.; Pugazhendhi, A. Synthesis of ecofriendly copper oxide nanoparticles for fabrication over textile fabrics: Characterization of antibacterial activity and dye degradation potential. *J. Photochem. Photobiol. B Biol.* **2019**, *191*, 143–149. [CrossRef] [PubMed]
6. Asif, A.; Hasan, M.Z. Application of nanotechnology in modern textiles: A review. *Int. J. Curr. Eng. Technol.* **2018**, *8*, 227–231.
7. Ibrahim, N.; Jamaluddin, N.D.; Tan, L.L.; Mohd Yusof, N.Y. A Review on the Development of Gold and Silver Nanoparticles-Based Biosensor as a Detection Strategy of Emerging and Pathogenic RNA Virus. *Sensors* **2021**, *21*, 5114. [CrossRef]
8. Mohammadpour, R.; Dobrovolskaia, M.A.; Cheney, D.L.; Greish, K.F.; Ghandehari, H. Subchronic and chronic toxicity evaluation of inorganic nanoparticles for delivery applications. *Adv. Drug Deliv. Rev.* **2019**, *144*, 112–132. [CrossRef]
9. Nikolova, M.P.; Chavali, M.S. Metal oxide nanoparticles as biomedical materials. *Biomimetics* **2020**, *5*, 27. [CrossRef]
10. Nobile, S.; Nobile, L. Nanotechnology for biomedical applications: Recent advances in neurosciences and bone tissue engineering. *Polym. Eng. Sci.* **2017**, *57*, 644–650. [CrossRef]
11. Kaushik, A. Biomedical nanotechnology related grand challenges and perspectives. *Front. Nanotechnol.* **2019**, *1*, 1. [CrossRef]
12. Chandarana, M.; Curtis, A.; Hoskins, C. The use of nanotechnology in cardiovascular disease. *Appl. Nanosci.* **2018**, *8*, 1607–1619. [CrossRef]
13. Kalhapure, R.S.; Renukuntla, J. Thermo-and pH dual responsive polymeric micelles and nanoparticles. *Chem.-Biol. Interact.* **2018**, *295*, 20–37. [CrossRef] [PubMed]
14. Gao, A.; Hu, X.-L.; Saeed, M.; Chen, B.-F.; Li, Y.-P.; Yu, H.-J. Overview of recent advances in liposomal nanoparticle-based cancer immunotherapy. *Acta Pharmacol. Sin.* **2019**, *40*, 1129–1137. [CrossRef] [PubMed]
15. Ambekar, R.S.; Choudhary, M.; Kandasubramanian, B. Recent advances in dendrimer-based nanoplatform for cancer treatment: A review. *Eur. Polym. J.* **2020**, *126*, 109546. [CrossRef]
16. Spirescu, V.A.; Șuhan, R.; Niculescu, A.-G.; Grumezescu, V.; Negut, I.; Holban, A.M.; Oprea, O.-C.; Bîrcă, A.C.; Vasile, B.Ș.; Grumezescu, A.M. Biofilm-Resistant Nanocoatings Based on ZnO Nanoparticles and Linalool. *Nanomaterials* **2021**, *11*, 2564. [CrossRef] [PubMed]
17. Khodashenas, B.; Ghorbani, H.R. Synthesis of silver nanoparticles with different shapes. *Arab. J. Chem.* **2019**, *12*, 1823–1838. [CrossRef]
18. Arokiyaraj, S.; Vincent, S.; Saravanan, M.; Lee, Y.; Oh, Y.K.; Kim, K.H. Green synthesis of silver nanoparticles using Rheum palmatum root extract and their antibacterial activity against Staphylococcus aureus and Pseudomonas aeruginosa. *Artif. Cells Nanomed. Biotechnol.* **2017**, *45*, 372–379. [CrossRef]
19. Feroze, N.; Arshad, B.; Younas, M.; Afridi, M.I.; Saqib, S.; Ayaz, A. Fungal mediated synthesis of silver nanoparticles and evaluation of antibacterial activity. *Microsc. Res. Tech.* **2020**, *83*, 72–80. [CrossRef]
20. Rajendran, N.K.; Kumar SS, D.; Houreld, N.N.; Abrahamse, H. A review on nanoparticle based treatment for wound healing. *J. Drug Deliv. Sci. Technol.* **2018**, *44*, 421–430. [CrossRef]
21. Najm, A.; Chowdhury, M.; Munna, F.; Chelvanathan, P.; Selvanathan, V.; Aminuzzaman, M.; Techato, K.; Amin, N.; Akhtaruzzaman, M. Impact of Cadmium Salt Concentration on Cds Nanoparticles Synthesized By Chemical Precipitation Method. *Chalcogenide Lett.* **2020**, *17*, 537–547.
22. Zhang, J.; Zhan, P.; Tian, H. Recent updates in the polysaccharides-based Nano-biocarriers for drugs delivery and its application in diseases treatment: A review. *Int. J. Biol. Macromol.* **2021**, *182*, 115–128. [CrossRef]

23. Miao, Q.; Xie, C.; Zhen, X.; Lyu, Y.; Duan, H.; Liu, X.; Jokerst, J.V.; Pu, K. Molecular afterglow imaging with bright, biodegradable polymer nanoparticles. *Nat. Biotechnol.* **2017**, *35*, 1102–1110. [CrossRef] [PubMed]
24. Deirram, N.; Zhang, C.; Kermaniyan, S.S.; Johnston, A.P.; Such, G.K. pH-responsive polymer nanoparticles for drug delivery. *Macromol. Rapid Commun.* **2019**, *40*, 1800917. [CrossRef] [PubMed]
25. Xu, C.; Cao, L.; Zhao, P.; Zhou, Z.; Cao, C.; Li, F.; Huang, Q. Emulsion-based synchronous pesticide encapsulation and surface modification of mesoporous silica nanoparticles with carboxymethyl chitosan for controlled azoxystrobin release. *Chem. Eng. J.* **2018**, *348*, 244–254. [CrossRef]
26. Jamkhande, P.G.; Ghule, N.W.; Bamer, A.H.; Kalaskar, M.G. Metal nanoparticles synthesis: An overview on methods of preparation, advantages and disadvantages, and applications. *J. Drug Deliv. Sci. Technol.* **2019**, *53*, 101174. [CrossRef]
27. Balasooriya, E.R.; Jayasinghe, C.D.; Jayawardena, U.A.; Ruwanthika RW, D.; de Silva, M.R.; Udagama, P.V. Honey mediated green synthesis of nanoparticles: New era of safe nanotechnology. *J. Nanomater.* **2017**, *2017*, 5919836. [CrossRef]
28. Shamhari, N.M.; Wee, B.S.; Chin, S.F.; Kok, K.Y. Synthesis and characterization of zinc oxide nanoparticles with small particle size distribution. *Acta Chim. Slov.* **2018**, *65*, 578–585. [CrossRef]
29. Thareja, R.; Shukla, S. Synthesis and characterization of zinc oxide nanoparticles by laser ablation of zinc in liquid. *Appl. Surf. Sci.* **2007**, *253*, 8889–8895. [CrossRef]
30. Hasanpoor, M.; Aliofkhazraei, M.; Delavari, H. Microwave-assisted synthesis of zinc oxide nanoparticles. *Procedia Mater. Sci.* **2015**, *11*, 320–325. [CrossRef]
31. Selim, Y.A.; Azb, M.A.; Ragab, I.; HMAbd El-Azim, M. Green synthesis of zinc oxide nanoparticles using aqueous extract of Deverra tortuosa and their cytotoxic activities. *Sci. Rep.* **2020**, *10*, 3445. [CrossRef]
32. Chen, D.; Ai, S.; Liang, Z.; Wei, F. Preparation and photocatalytic properties of zinc oxide nanoparticles by microwave-assisted ball milling. *Ceram. Int.* **2016**, *42*, 3692–3696. [CrossRef]
33. Hasnidawani, J.; Azlina, H.; Norita, H.; Bonnia, N.; Ratim, S.; Ali, E. Synthesis of ZnO nanostructures using sol-gel method. *Procedia Chem.* **2016**, *19*, 211–216. [CrossRef]
34. Osman DA, M.; Mustafa, M.A. Synthesis and characterization of zinc oxide nanoparticles using zinc acetate dihydrate and sodium hydroxide. *J. Nanosci. Nanoeng.* **2015**, *1*, 248–251.
35. Ghaffarian, H.R.; Saiedi, M.; Sayyadnejad, M.A.; Rashidi, A.M. Synthesis of ZnO nanoparticles by spray pyrolysis method. *Iran. J. Chem. Chem. Eng.* **2011**, *30*, 1–6.
36. Tajau, R.; Rohani, R.; Hamid SS, A.; Adam, Z.; Janib SN, M.; Salleh, M.Z. Surface functionalisation of poly-APO-b-polyol ester cross-linked copolymers as core–shell nanoparticles for targeted breast cancer therapy. *Sci. Rep.* **2020**, *10*, 21704. [CrossRef] [PubMed]
37. Sagadevan, S.; Lett, A.; Fatimah, I.; Lokanathan, Y.; Léonard, E.; Oh, W.-C.; Hossain, M.M.; Johan, M.R. Current trends in the green syntheses of tin oxide nanoparticles and their biomedical applications. *Mater. Res. Express* **2021**, *8*, 82001. [CrossRef]
38. Sharma, S.; Kumar, K.; Thakur, N.; Chauhan, S.; Chauhan, M. The effect of shape and size of ZnO nanoparticles on their antimicrobial and photocatalytic activities: A green approach. *Bull. Mater. Sci.* **2020**, *43*, 20. [CrossRef]
39. Mohanraj, V.; Chen, Y. Nanoparticles-a review. *Trop. J. Pharm. Res.* **2006**, *5*, 561–573. [CrossRef]
40. Herman, A.; Herman, A.P. Nanoparticles as antimicrobial agents: Their toxicity and mechanisms of action. *J. Nanosci. Nanotechnol.* **2014**, *14*, 946–957. [CrossRef]
41. Jadoun, S.; Arif, R.; Jangid, N.K.; Meena, R.K. Green synthesis of nanoparticles using plant extracts: A review. *Environ. Chem. Lett.* **2021**, *19*, 355–374. [CrossRef]
42. Paiva-Santos, A.C.; Herdade, A.M.; Guerra, C.; Peixoto, D.; Pereira-Silva, M.; Zeinali, M.; Mascarenhas-Melo, F.; Paranhos, A.; Veiga, F. Plant-mediated green synthesis of metal-based nanoparticles for dermopharmaceutical and cosmetic applications. *Int. J. Pharm.* **2021**, *597*, 120311. [CrossRef] [PubMed]
43. Sur, U.K.; Ankamwar, B.; Karmakar, S.; Halder, A.; Das, P. Green synthesis of Silver nanoparticles using the plant extract of Shikakai and Reetha. *Mater. Today Proc.* **2018**, *5*, 2321–2329.
44. Da Silva, A.F.V.; Fagundes, A.P.; Macuvele, D.L.P.; de Carvalho, E.F.U.; Durazzo, M.; Padoin, N.; Soares, C.; Riella, H.G. Green synthesis of zirconia nanoparticles based on Euclea natalensis plant extract: Optimization of reaction conditions and evaluation of adsorptive properties. *Colloids Surf. A: Physicochem. Eng. Asp.* **2019**, *583*, 123915. [CrossRef]
45. Abel, S.; Tesfaye, J.L.; Shanmugam, R.; Dwarampudi, L.P.; Lamessa, G.; Nagaprasad, N.; Benti, M.; Krishnaraj, R. Green synthesis and characterizations of zinc oxide (ZnO) nanoparticles using aqueous leaf extracts of coffee (*Coffea arabica*) and its application in environmental toxicity reduction. *J. Nanomater.* **2021**, *2021*, 3413350. [CrossRef]
46. Phang, Y.-K.; Aminuzzaman, M.; Akhtaruzzaman, M.; Muhammad, G.; Ogawa, S.; Watanabe, A.; Tey, L.-H. Green Synthesis and Characterization of CuO Nanoparticles Derived from Papaya Peel Extract for the Photocatalytic Degradation of Palm Oil Mill Effluent (POME). *Sustainability* **2021**, *13*, 796. [CrossRef]
47. García-Barrasa, J.; López-de-Luzuriaga, J.M.; Monge, M. Silver nanoparticles: Synthesis through chemical methods in solution and biomedical applications. *Cent. Eur. J. Chem.* **2011**, *9*, 7–19. [CrossRef]
48. Supraja, N.; Prasad, T.; Gandhi, A.D.; Anbumani, D.; Kavitha, P.; Babujanarthanam, R. Synthesis, characterization and evaluation of antimicrobial efficacy and brine shrimp lethality assay of Alstonia scholaris stem bark extract mediated ZnONPs. *Biochem. Biophys. Rep.* **2018**, *14*, 69–77. [CrossRef] [PubMed]

49. Usman, A.I.; Aziz, A.A.; Noqta, O.A. Green sonochemical synthesis of gold nanoparticles using palm oil leaves extracts. *Mater. Today Proc.* **2019**, *7*, 803–807. [CrossRef]
50. Ramimoghadam, D.; Hussein MZ, B.; Taufiq-Yap, Y.H. Synthesis and characterization of ZnO nanostructures using palm olein as biotemplate. *Chem. Cent. J.* **2013**, *7*, 71. [CrossRef]
51. Ismail, N.A.; Shameli, K.; Wong, M.M.-T.; Teow, S.-Y.; Chew, J.; Sukri, S.N.A.M. Antibacterial and cytotoxic effect of honey mediated copper nanoparticles synthesized using ultrasonic assistance. *Mater. Sci. Eng. C* **2013**, *104*, 109899. [CrossRef]
52. Sirelkhatim, A.; Mahmud, S.; Seeni, A.; Kaus NH, M.; Ann, L.C.; Bakhori, S.K.M.; Hasan, H.; Mohamad, D. Review on zinc oxide nanoparticles: Antibacterial activity and toxicity mechanism. *Nano-Micro Lett.* **2015**, *7*, 219–242. [CrossRef] [PubMed]
53. Shahid, S.; Khan, S.; Ahmad, W.; Fatima, U.; Knawal, S. Size-dependent bacterial growth inhibition and antibacterial activity of Ag-doped ZnO nanoparticles under different atmospheric conditions. *Indian J. Pharm. Sci.* **2018**, *80*, 173–180. [CrossRef]
54. Kumar, P.V.; Shameem, U.; Kollu, P.; Kalyani, R.; Pammi, S. Green synthesis of copper oxide nanoparticles using Aloe vera leaf extract and its antibacterial activity against fish bacterial pathogens. *BioNanoScience* **2015**, *5*, 135–139. [CrossRef]
55. Batool, M.; Khurshid, S.; Qureshi, Z.; Daoush, W.M. Adsorption, antimicrobial and wound healing activities of biosynthesised zinc oxide nanoparticles. *Chem. Pap.* **2021**, *75*, 893–907. [CrossRef]
56. Turakhia, B.; Divakara, M.B.; Santosh, M.S.; Shah, S. Green synthesis of copper oxide nanoparticles: A promising approach in the development of antibacterial textiles. *J. Coat. Technol. Res.* **2020**, *17*, 531–540. [CrossRef]
57. Biswal, A.K.; Misra, P.K. Biosynthesis and characterization of silver nanoparticles for prospective application in food packaging and biomedical fields. *Mater. Chem. Phys.* **2020**, *250*, 123014. [CrossRef]
58. Bagherzade, G.; Tavakoli, M.M.; Namaei, M.H. Green synthesis of silver nanoparticles using aqueous extract of saffron (*Crocus sativus* L.) wastages and its antibacterial activity against six bacteria. *Asian Pac. J. Trop. Biomed.* **2017**, *7*, 227–233. [CrossRef]
59. Luna-Sánchez, J.; Jiménez-Pérez, J.; Carbajal-Valdez, R.; Lopez-Gamboa, G.; Pérez-González, M.; Correa-Pacheco, Z. Green synthesis of silver nanoparticles using Jalapeño Chili extract and thermal lens study of acrylic resin nanocomposites. *Thermochim. Acta* **2019**, *678*, 178314. [CrossRef]
60. Haddada, M.B.; Gerometta, E.; Chawech, R.; Sorres, J.; Bialecki, A.; Pesnel, S.; Spadavecchia, J.; Morel, A.-L. Assessment of antioxidant and dermoprotective activities of gold nanoparticles as safe cosmetic ingredient. *Colloids Surf. B Biointerfaces* **2020**, *189*, 110855. [CrossRef]
61. Kanagasubbulakshmi, S.; Kadirvelu, K. Green synthesis of iron oxide nanoparticles using Lagenaria siceraria and evaluation of its antimicrobial activity. *Def. Life Sci. J.* **2017**, *2*, 422–427. [CrossRef]
62. Kora, A.J.; Rastogi, L. Green synthesis of palladium nanoparticles using gum ghatti (*Anogeissus latifolia*) and its application as an antioxidant and catalyst. *Arab. J. Chem.* **2018**, *11*, 1097–1106. [CrossRef]
63. Barberia-Roque, L.; Obidi, O.F.; Gámez-Espinosa, E.; Viera, M.; Bellotti, N. Hygienic coatings with bioactive nano-additives from Senna occidentalis-mediated green synthesis. *NanoImpact* **2019**, *16*, 100184. [CrossRef]
64. Mohanraj, K.; Balasubramanian, D.; Jhansi, N.; Bakkiyaraj, R.; Chandrasekaran, J. Structural, Optical and electrical properties of green synthesis CdO nanoparticles and its Ag/CdO/P-Si junction diode fabricated via JNS pyrolysis technique. *Int. J. Thin Films Sci. Technol.* **2017**, *6*, 87–91. [CrossRef]
65. Pandurangan, M.; Kim, D.H. In vitro toxicity of zinc oxide nanoparticles: A review. *J. Nanoparticle Res.* **2015**, *17*, 158. [CrossRef]
66. Yu, Z.; Li, Q.; Wang, J.; Yu, Y.; Wang, Y.; Zhou, Q.; Li, P. Reactive oxygen species-related nanoparticle toxicity in the biomedical field. *Nanoscale Res. Lett.* **2020**, *15*, 115. [CrossRef]
67. Chen, P.; Wang, H.; He, M.; Chen, B.; Yang, B.; Hu, B. Size-dependent cytotoxicity study of ZnO nanoparticles in HepG2 cells. *Ecotoxicol. Environ. Saf.* **2019**, *171*, 337–346. [CrossRef]
68. Aadil, K.R.; Pandey, N.; Mussatto, S.I.; Jha, H. Green synthesis of silver nanoparticles using acacia lignin, their cytotoxicity, catalytic, metal ion sensing capability and antibacterial activity. *J. Environ. Chem. Eng.* **2019**, *7*, 103296. [CrossRef]
69. Niska, K.; Zielinska, E.; Radomski, M.W.; Inkielewicz-Stepniak, I. Metal nanoparticles in dermatology and cosmetology: Interactions with human skin cells. *Chem.-Biol. Interact.* **2018**, *295*, 38–51. [CrossRef]
70. Buchman, J.T.; Hudson-Smith, N.V.; Landy, K.M.; Haynes, C.L. Understanding nanoparticle toxicity mechanisms to inform redesign strategies to reduce environmental impact. *Acc. Chem. Res.* **2019**, *52*, 1632–1642. [CrossRef]
71. Díez-Pascual, A.M.; Díez-Vicente, A.L. Wound healing bionanocomposites based on castor oil polymeric films reinforced with chitosan-modified ZnO nanoparticles. *Biomacromolecules* **2015**, *16*, 2631–2644. [CrossRef]
72. Norouzi, M.A.; Montazer, M.; Harifi, T.; Karimi, P. Flower buds like PVA/ZnO composite nanofibers assembly: Antibacterial, in vivo wound healing, cytotoxicity and histological studies. *Polym. Test.* **2021**, *93*, 106914. [CrossRef]
73. Vasile, O.R.; Serdaru, I.; Andronescu, E.; Truşcă, R.; Surdu, V.A.; Oprea, O.; Ilie, A.; Vasile, B.Ş. Influence of the size and the morphology of ZnO nanoparticles on cell viability. *Comptes Rendus Chim.* **2015**, *18*, 1335–1343. [CrossRef]
74. Chirani, N.; Yahia, L.; Gritsch, L.; Motta, F.L.; Chirani, S.; Farè, S. History and applications of hydrogels. *J. Biomedical Sci.* **2015**, *4*, 1–23.
75. Farjadian, F.; Rezaeifard, S.; Naeimi, M.; Ghasemi, S.; Mohammadi-Samani, S.; Welland, M.E.; Tayebi, L. Temperature and pH-responsive nano-hydrogel drug delivery system based on lysine-modified poly (vinylcaprolactam). *Int. J. Nanomed.* **2019**, *14*, 6901. [CrossRef] [PubMed]

76. Abbaszadeh, S.; Rashidipour, M.; Khosravi, P.; Shahryarhesami, S.; Ashrafi, B.; Kaviani, M.; Sarabi, M.M. Biocompatibility, cytotoxicity, antimicrobial and epigenetic effects of novel chitosan-based quercetin nanohydrogel in human cancer cells. *Int. J. Nanomed.* **2020**, *15*, 5963. [CrossRef] [PubMed]
77. Kamiński, K.; Jarosz, M.; Grudzień, J.; Pawlik, J.; Zastawnik, F.; Pandyra, P.; Kołodziejczyk, A.M. Hydrogel bacterial cellulose: A path to improved materials for new eco-friendly textiles. *Cellulose* **2020**, *27*, 5353–5365. [CrossRef]
78. Rafieian, S.; Mirzadeh, H.; Mahdavi, H.; Masoumi, M.E. A review on nanocomposite hydrogels and their biomedical applications. *Sci. Eng. Compos. Mater.* **2019**, *26*, 154–174. [CrossRef]
79. Dil, N.N.; Sadeghi, M. Free radical synthesis of nanosilver/gelatin-poly (acrylic acid) nanocomposite hydrogels employed for antibacterial activity and removal of Cu (II) metal ions. *J. Hazard. Mater.* **2018**, *351*, 38–53. [CrossRef]
80. Gholamali, I.; Hosseini, S.N.; Alipour, E.; Yadollahi, M. Preparation and characterization of oxidized starch/CuO nanocomposite hydrogels applicable in a drug delivery system. *Starch-Stärke* **2019**, *71*, 1800118. [CrossRef]
81. Ahmadian, Y.; Bakravi, A.; Hashemi, H.; Namazi, H. Synthesis of polyvinyl alcohol/CuO nanocomposite hydrogel and its application as drug delivery agent. *Polym. Bull.* **2019**, *76*, 1967–1983. [CrossRef]
82. Katas, H.; Mohd Akhmar, M.A.; Suleman Ismail Abdalla, S. Biosynthesized silver nanoparticles loaded in gelatine hydrogel for a natural antibacterial and anti-biofilm wound dressing. *J. Bioact. Compat. Polym.* **2021**, *36*, 111–123. [CrossRef]
83. Mitchell, M.J.; Billingsley, M.M.; Haley, R.M.; Wechsler, M.E.; Peppas, N.A.; Langer, R. Engineering precision nanoparticles for drug delivery. *Nat. Rev. Drug Discov.* **2021**, *20*, 101–124. [CrossRef] [PubMed]
84. Deng, Y.; Zhang, X.; Shen, H.; He, Q.; Wu, Z.; Liao, W.; Yuan, M. Application of the nano-drug delivery system in treatment of cardiovascular diseases. *Front. Bioeng. Biotechnol.* **2020**, *7*, 489. [CrossRef]
85. Chyzy, A.; Tomczykowa, M.; Plonska-Brzezinska, M.E. Hydrogels as potential nano-, micro-and macro-scale systems for controlled drug delivery. *Materials* **2020**, *13*, 188. [CrossRef] [PubMed]
86. Raza, A.; Hayat, U.; Rasheed, T.; Bilal, M.; Iqbal, H.M. Redox-responsive nano-carriers as tumor-targeted drug delivery systems. *Eur. J. Med. Chem.* **2018**, *157*, 705–715. [CrossRef]
87. Dalwadi, C.; Patel, G. Application of nanohydrogels in drug delivery systems: Recent patents review. *Recent Pat. Nanotechnol.* **2015**, *9*, 17–25. [CrossRef] [PubMed]
88. Roointan, A.; Farzanfar, J.; Mohammadi-Samani, S.; Behzad-Behbahani, A.; Farjadian, F. Smart pH responsive drug delivery system based on poly (HEMA-co-DMAEMA) nanohydrogel. *Int. J. Pharm.* **2018**, *552*, 301–311. [CrossRef]
89. Amiri, M.; Salavati-Niasari, M.; Pardakhty, A.; Ahmadi, M.; Akbari, A. Caffeine: A novel green precursor for synthesis of magnetic $CoFe_2O_4$ nanoparticles and pH-sensitive magnetic alginate beads for drug delivery. *Mater. Sci. Eng. C* **2017**, *76*, 1085–1093. [CrossRef]
90. Basu, S.; Samanta, H.S.; Ganguly, J. Green synthesis and swelling behavior of Ag-nanocomposite semi-IPN hydrogels and their drug delivery using Dolichos biflorus Linn. *Soft Mater.* **2018**, *16*, 7–19. [CrossRef]
91. Chen, X.; Zhao, X.; Gao, Y.; Yin, J.; Bai, M.; Wang, F. Green synthesis of gold nanoparticles using carrageenan oligosaccharide and their in vitro antitumor activity. *Mar. Drugs* **2018**, *16*, 277. [CrossRef]
92. Sattari, S.; Dadkhah Tehrani, A.; Adeli, M. pH-responsive hybrid hydrogels as antibacterial and drug delivery systems. *Polymers* **2018**, *10*, 660. [CrossRef] [PubMed]
93. Nagaraja, K.; Rao, K.M.; Reddy, G.V.; Rao, K.K. Tragacanth gum-based multifunctional hydrogels and green synthesis of their silver nanocomposites for drug delivery and inactivation of multidrug resistant bacteria. *Int. J. Biol. Macromol.* **2021**, *174*, 502–511. [CrossRef] [PubMed]
94. Rajendran, S. *Advanced Textiles for Wound Care*; Woodhead Publishing: Sawston, UK, 2018.
95. Mihai, M.M.; Dima, M.B.; Dima, B.; Holban, A.M. Nanomaterials for wound healing and infection control. *Materials* **2019**, *12*, 2176. [CrossRef] [PubMed]
96. Shi, C.; Wang, C.; Liu, H.; Li, Q.; Li, R.; Zhang, Y.; Liu, Y.; Shao, Y.; Wang, J. Selection of appropriate wound dressing for various wounds. *Front. Bioeng. Biotechnol.* **2020**, *8*, 182. [CrossRef]
97. Tottoli, E.M.; Dorati, R.; Genta, I.; Chiesa, E.; Pisani, S.; Conti, B. Skin wound healing process and new emerging technologies for skin wound care and regeneration. *Pharmaceutics* **2020**, *12*, 735. [CrossRef]
98. Moeini, A.; Pedram, P.; Makvandi, P.; Malinconico, M.; d'Ayala, G.G. Wound healing and antimicrobial effect of active secondary metabolites in chitosan-based wound dressings: A review. *Carbohydr. Polym.* **2020**, *233*, 115839. [CrossRef]
99. Almeida, I.B.; Teixeira LG, B.; de Carvalho, F.O.; Silva, É.R.; Nunes, P.S.; Dos Santos, M.R.V.; de Souza Araújo, A.A. Smart Dressings for Wound Healing: A Review. *Adv. Ski. Wound Care* **2021**, *34*, 1–8. [CrossRef]
100. Farahani, M.; Shafiee, A. Wound healing: From passive to smart dressings. *Adv. Healthc. Mater.* **2021**, *10*, 2100477. [CrossRef]
101. Yang, Z.; Huang, R.; Zheng, B.; Guo, W.; Li, C.; He, W.; Wei, Y.; Du, Y.; Wang, H.; Wu, D. Highly Stretchable, Adhesive, Biocompatible, and Antibacterial Hydrogel Dressings for Wound Healing. *Adv. Sci.* **2021**, *8*, 2003627. [CrossRef]
102. Haseeb, M.T.; Hussain, M.A.; Abbas, K.; Youssif, B.G.; Bashir, S.; Yuk, S.H.; Bukhari, S.N.A. Linseed hydrogel-mediated green synthesis of silver nanoparticles for antimicrobial and wound-dressing applications. *Int. J. Nanomed.* **2017**, *12*, 2845. [CrossRef]
103. Ezealisiji, K.M.; Siwe-Noundou, X.; Maduelosi, B.; Nwachukwu, N.; Krause, R.W.M. Green synthesis of zinc oxide nanoparticles using Solanum torvum (L) leaf extract and evaluation of the toxicological profile of the ZnO nanoparticles–hydrogel composite in Wistar albino rats. *Int. Nano Lett.* **2019**, *9*, 99–107. [CrossRef]

104. Qasim, M.; Chae, D.S.; Lee, N.Y. Advancements and frontiers in nano-based 3D and 4D scaffolds for bone and cartilage tissue engineering. *Int. J. Nanomed.* **2019**, *14*, 4333. [CrossRef] [PubMed]
105. Jiang, L.; Wang, Y.; Liu, Z.; Ma, C.; Yan, H.; Xu, N.; Gang, F.; Wang, X.; Zhao, L.; Sun, X. Three-dimensional printing and injectable conductive hydrogels for tissue engineering application. *Tissue Eng. Part B Rev.* **2019**, *25*, 398–411. [CrossRef] [PubMed]
106. El-Sherbiny, I.M.; Yacoub, M.H. Hydrogel scaffolds for tissue engineering: Progress and challenges. *Glob. Cardiol. Sci. Pract.* **2013**, *2013*, 38. [CrossRef] [PubMed]
107. Ng, J.Y.; Obuobi, S.; Chua, M.L.; Zhang, C.; Hong, S.; Kumar, Y.; Gokhale, R.; Ee, P.L.R. Biomimicry of microbial polysaccharide hydrogels for tissue engineering and regenerative medicine–A review. *Carbohydr. Polym.* **2020**, *241*, 116345. [CrossRef] [PubMed]
108. Nabavinia, M.; Khoshfetrat, A.B.; Naderi-Meshkin, H. Nano-hydroxyapatite-alginate-gelatin microcapsule as a potential osteogenic building block for modular bone tissue engineering. *Mater. Sci. Eng. C* **2019**, *97*, 67–77. [CrossRef]
109. Hakimi, N.; Cheng, R.; Leng, L.; Sotoudehfar, M.; Ba, P.Q.; Bakhtyar, N.; Amini-Nik, S.; Jeschke, M.G.; Günther, A. Handheld skin printer: In situ formation of planar biomaterials and tissues. *Lab A Chip* **2018**, *18*, 1440–1451. [CrossRef]
110. Chouhan, D.; Dey, N.; Bhardwaj, N.; Mandal, B.B. Emerging and innovative approaches for wound healing and skin regeneration: Current status and advances. *Biomaterials* **2019**, *216*, 119267. [CrossRef]
111. Zhao, H.; Liu, M.; Zhang, Y.; Yin, J.; Pei, R. Nanocomposite hydrogels for tissue engineering applications. *Nanoscale* **2020**, *12*, 14976–14995. [CrossRef]
112. Zulkifli, M.Z.A.; Kamarudin, N.H.N.; Nordin, D. Polycaprolactone/Chlorophyllin Sodium Copper Salt Nanofibrous Mats Prepared by Electrospinning for Soft Tissue Engineering. *J. Kejuruter.* **2019**, *2*, 68–76.
113. Zulkifli, F.H.; Hussain FS, J.; Zeyohannes, S.S.; Rasad, M.S.B.A.; Yusuff, M.M. A facile synthesis method of hydroxyethyl cellulose-silver nanoparticle scaffolds for skin tissue engineering applications. *Mater. Sci. Eng. C* **2017**, *79*, 151–160. [CrossRef] [PubMed]
114. Rakhshaei, R.; Namazi, H.; Hamishehkar, H.; Kafil, H.S.; Salehi, R. In situ synthesized chitosan–gelatin/ZnO nanocomposite scaffold with drug delivery properties: Higher antibacterial and lower cytotoxicity effects. *J. Appl. Polym. Sci.* **2019**, *136*, 47590. [CrossRef]
115. Sudheesh Kumar, P.; Lakshmanan, V.-K.; Anilkumar, T.; Ramya, C.; Reshmi, P.; Unnikrishnan, A.; Nair, S.V.; Jayakumar, R. Flexible and microporous chitosan hydrogel/nano ZnO composite bandages for wound dressing: In vitro and in vivo evaluation. *ACS Appl. Mater. Interfaces* **2012**, *4*, 2618–2629. [CrossRef] [PubMed]
116. Kumar, B.; Isloor, A.M.; Kumar, G.; Asiri, A.M. Nanohydroxyapatite reinforced chitosan composite hydrogel with tunable mechanical and biological properties for cartilage regeneration. *Sci. Rep.* **2019**, *9*, 15957. [CrossRef] [PubMed]
117. Xu, X.; Liu, Y.; Fu, W.; Yao, M.; Ding, Z.; Xuan, J.; Li, D.; Wang, S.; Xia, Y.; Cao, M. Poly (N-isopropylacrylamide)-based thermoresponsive composite hydrogels for biomedical applications. *Polymers* **2020**, *12*, 580. [CrossRef]
118. Mohamed, A.L.; Elmotasem, H.; Salama, A.A. Colchicine mesoporous silica nanoparticles/hydrogel composite loaded cotton patches as a new encapsulator system for transdermal osteoarthritis management. *Int. J. Biol. Macromol.* **2020**, *164*, 1149–1163. [CrossRef]
119. Wen, S.; Shuang-Ting, Y.; Yue-Liang, W.; Long-Hua, G. Preparation of Noble Metal Nanoparticles and Hydrogel Composite Materials and Their Application in Analytical Chemistry. *Chin. J. Anal. Chem.* **2021**, *49*, 676–685.
120. Xiang, J.; Shen, L.; Hong, Y. Status and future scope of hydrogels in wound healing: Synthesis, materials and evaluation. *Eur. Polym. J.* **2020**, *130*, 109609. [CrossRef]
121. Tan, H.-L.; Teow, S.-Y.; Pushpamalar, J. Application of metal nanoparticle–hydrogel composites in tissue regeneration. *Bioengineering* **2019**, *6*, 17. [CrossRef]

nanomaterials

MDPI

Review

Recycling and Reutilizing Polymer Waste via Electrospun Micro/Nanofibers: A Review

Xiuhong Li [1], Yujie Peng [1], Yichen Deng [1], Fangping Ye [1], Chupeng Zhang [1,*], Xinyu Hu [1,*], Yong Liu [2,*] and Daode Zhang [1]

[1] School of Mechanical Engineering, Hubei University of Technology, Wuhan 430068, China; 20200005@hbut.edu.cn (X.L.); pengyj1024@163.com (Y.P.); denyichen@163.com (Y.D.); yefangping@hbut.edu.cn (F.Y.); hgzdd@126.com (D.Z.)

[2] Beijing Key Laboratory of Advanced Functional Polymer Composites, College of Materials Science and Engineering, Beijing University of Chemical Technology, Beijing 100029, China

* Correspondence: zcp1988123@126.com (C.Z.); 19991012@hbut.edu.cn (X.H.); yongliu@mail.buct.edu.cn (Y.L.)

Abstract: The accumulation of plastic waste resulting from the increasing demand for non-degradable plastics has led to a global environmental crisis. The severe environmental and economic drawbacks of inefficient, expensive, and impractical traditional waste disposal methods, such as landfills, incineration, plastic recycling, and energy production, limit the expansion of their applications to solving the plastic waste problem. Finding novel ways to manage the large amount of disposed plastic waste is urgent. Until now, one of the most valuable strategies for the handling of plastic waste has been to reutilize the waste as raw material for the preparation of functional and high-value products. Electrospun micro/nanofibers have drawn much attention in recent years due to their advantages of small diameter, large specific area, and excellent physicochemical features. Thus, electrospinning recycled plastic waste into micro/nanofibers creates diverse opportunities to deal with the environmental issue caused by the growing accumulation of plastic waste. This paper presents a review of recycling and reutilizing polymer waste via electrospinning. Firstly, the advantages of the electrospinning approach to recycling plastic waste are summarized. Then, the studies of electrospun recycled plastic waste are concluded. Finally, the challenges and future perspectives of electrospun recycled plastic waste are provided. In conclusion, this paper aims to provide a comprehensive overview of electrospun recycled plastic waste for researchers to develop further studies.

Keywords: electrospinning; recycling; reutilizing; plastic waste

Citation: Li, X.; Peng, Y.; Deng, Y.; Ye, F.; Zhang, C.; Hu, X.; Liu, Y.; Zhang, D. Recycling and Reutilizing Polymer Waste via Electrospun Micro/Nanofibers: A Review. *Nanomaterials* **2022**, *12*, 1663. https://doi.org/10.3390/nano12101663

Academic Editor: Takuya Kitaoka

Received: 10 April 2022
Accepted: 7 May 2022
Published: 13 May 2022

1. Introduction

Synthetic polymers such as polyethylene terephthalate (PET), polystyrene or expanded polystyrene (PS) and polyamide (PA) have been widely applied in various commercial and household applications since the 1940s owing to their fascinating properties of low-cost, light weight, corrosion-resistance, and processability [1]. The conveniences and benefits of plastic products have significantly increased their production, leading to a large amount of disposed plastic in landfills. Due to the low biodegradation of plastic waste, the resulting accumulation of white pollution seen everywhere causes adverse environmental issues not only to human beings but also to wildlife such as birds [2,3]. Therefore, figuring out effective methods to deal with plastic waste is urgent.

Landfills, incineration, plastic recycling, and energy production are the current post-consumer treatments for the disposal of plastic waste, as shown in Table 1 [4–10]. In addition to recycling, the other three approaches have drawbacks, such as waste of space (landfills), high cost (energy production), and toxic byproducts (incineration), which restricts their further development as treatments for plastic waste. Additionally, the traditional recycling method aims to eliminate plastic waste rather than encourage its beneficial, value-added reuse. Modern recycling is a superior choice for utilizing plastic waste in valuable products in response to the circular economy. This minimizes the accumulation of plastic waste to alleviate environmental concern and realizes reutilization to create economic value.

Table 1. Various management methods of plastic waste and their influence.

Management	Advantages	Disadvantages	Ref.
Landfill	Convenience	Occupies large space/ Difficult to decompose	[4]
Incineration	Recovery of thermal energy/ Reduction in the weight and volume of waste	Harmful to the environment	[5]
Mechanical pulverization (Physical recycling)	Reused as materials compounded with additives	Remanufactured products with worse properties	[6]
Microbial decomposition	Reduces secondary pollution	Needs special conditions Releases methane gas	[7,8]
Thermal decomposition (Chemical recycling)	Low pollution/ High utilization rate/ High value of products	Relatively complicated	[6,9]
Physical and chemical modification reuse	Recycled products with good properties and values/ Less secondary pollution	Needs high-level techniques and high costs	[6]
Mechanical recycling	Economical/ Environmental	Difficult to recycle complex and contaminated polymer waste/Intense energy consumption	[9,10]

Therefore, cost-effective recycling technologies and higher-value applications should be developed. Due to their specific chemical and physical properties, such as high surface ratio, high porosity, light weights and small diameters nanomaterials have attracted lots of attention in various fields, including bioengineering, electronic devices, energy storage, etc. [11–15]. Commonly, nanomaterials can be prepared by drawing [16], template synthesis [17], phase separation [18], self-assembly [19], centrifugal spinning [20], and electrospinning [14,21]. Electrospinning is the primary choice for fabricating nanomaterials, especially micro/nanofibers, due to its simplicity, low costs, and efficiency. Furthermore, the materials for electrospinning are various, and polymers are the most used. Therefore, electrospinning is a promising way to reuse polymeric waste, turning plastic waste into higher-value products [22]. Many studies have changed recycled plastic waste into fibers [23,24]. Zander et al. prepared nanofibers from pure and mixed waste, including polyethylene (PET), polystyrene (PS), and polycarbonate (PC) by electrospinning and established that their mechanical performance is better than that of commercial polymers with the same molecular weight [25].

Similarly, Esmaeili and colleagues synthesized PET, PS, and PC nano/microfibers by solution electrospinning and investigated the effect of various operational parameters, especially needle diameter and spinning voltage, on the properties of the obtained fibers [26]. Thus, to offer a platform for reviewing the potential of electrospinning in reutilizing plastic waste, this review mainly discusses the advantages of electrospinning for recycling and reutilizing plastic waste and focuses on the electrospinning studies to date of the main plastic waste types containing PET, PS, and PA. In the final section, the challenges and future perspectives of electrospun recycled plastic waste are addressed.

2. Advantages of Electrospinning for Reutilizing Polymeric Waste

Electrospinning is a versatile and straightforward technique for fabricating micro/nanofibers employing electrostatic force, which uses polymer solutions or melts as raw materials. A conventional electrospinning system consists of three major components: a spinneret (supplying polymer sources), a high voltage power supply (providing electric forces), and a collector (collecting micro/nanofibers), as shown in Figure 1 [27]. During the process, the polymer solution or melt forms a "Taylor cone" at the end of the spinneret by continuously increasing the spinning voltage between the spinneret and the collector [28]. As the applied voltage exceeds a certain critical value, a polymer jet is ejected from the "Taylor cone" tip, which then solidifies into micro/nanofibers in the collector. The electrospinning technique possesses several attractive merits: simplicity, low cost, mass production, and wide application. There are three primary advantages of the electrospinning technique when recycling and reutilizing plastic waste, as shown in Figure 2 [29–39].

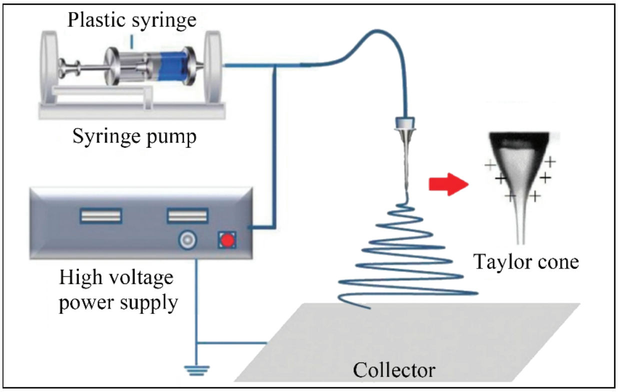

Figure 1. The mechanism of electrospinning. Reprinted from ref. [27].

2.1. Diversity of Electrospinning Materials

Electrospinning can recycle and utilize plastic waste owing to the technique's diversity of polymer sources. Traditional electrospinning can be classified into solution electrospinning [40] and melt electrospinning [41], based on the state of the polymer used. In solution electrospinning, if the polymers can be matched with appropriate solvents, they can be electrospun into micro/nanofibers. Additionally, melt electrospinning is proposed to give a chance for the polymers lacking suitable solvents used in solution electrospinning, which expands the polymer choices used in electrospinning. Thus, the two types of electrospinning methods are complementary, making the method adaptable for a variety of materials. It is obvious that the common raw materials for electrospinning are polymers, including natural polymers, synthetic polymers, and hybrid blends [42–44]. Fortunately, most polymeric waste belongs to synthetic polymers such as PET, PS, PA, and so on, which can be easily electrospun into micro/nanofibers with appropriate electrospinning processing conditions [25,45,46]. Furthermore, the use of additives (such as nanoparticles) in the raw materials is feasible, leading to a wider range of material choices for recycling and utilizing plastic waste. The diversity of electrospinning materials is the first advantage of electrospinning for recycling and using polymeric waste.

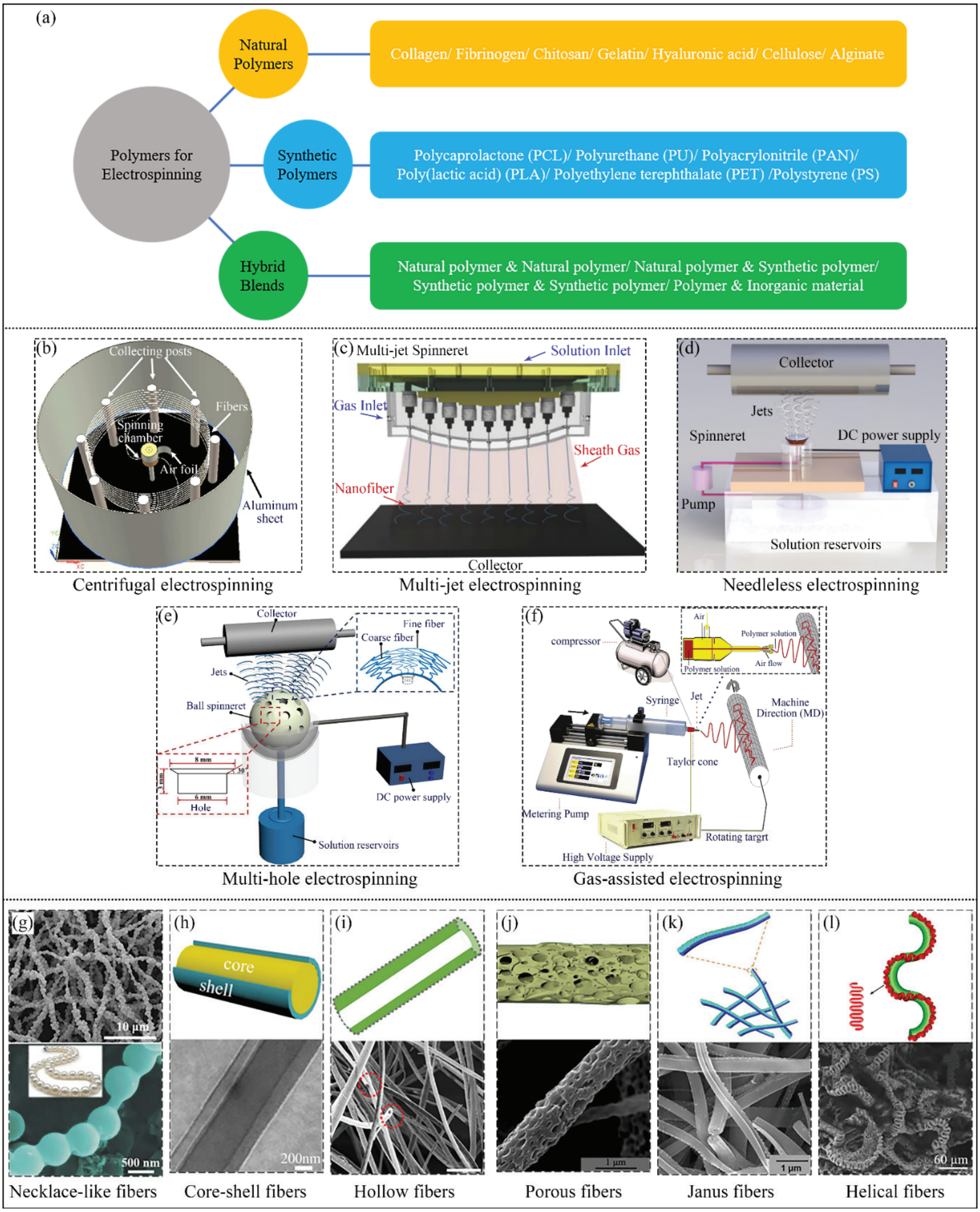

Figure 2. (**a**) Materials for electrospinning (**b**–**f**). Various technologies for electrospinning: (**b**) centrifugal electrospinning [29], (**c**) multi-jet electrospinning [30], (**d**) needleless electrospinning [31], (**e**) multi-hole electrospinning [32], and (**f**) gas-assisted electrospinning [33] (**g**–**l**) Special structures of electrospun fibers: (**g**) necklace-like fibers [34], (**h**) core-shell fibers [35], (**i**) hollow fibers [36], (**j**) porous fibers [37], (**k**) Janus fibers [38]. and (**l**) helical fibers [39]. (**b**,**j**) Reprinted with permission from ref. [29,37]. Copyright American Chemical Society. (**c**–**i**) Reprinted with permission from ref. [30–36]. Copyright Elsevier. (**k**) Reprinted with permission from ref. [38]. Copyright 2019 Springer. (**l**) Reprinted with permission from ref. [39]. Copyright 2020 Royal Society of Chemistry.

2.2. Variety of Modified Electrospinning Techniques

Electrospinning has attracted lots of attention in a wide range of applications due to its simplicity, flexibility, and applicability. However, some challenges exist in traditional electrospinning, such as the residues of organic/toxic solvents (solution electrospinning), complex systems, large fiber diameters (melt electrospinning), and low production rates. To satisfy the requirements of upscaling electrospinning production, multiple modified electrospinning techniques have been developed to solidify their foundation for expanded nanotechnological applications. To realize mass production of electrospinning, needleless electrospinning [47,48], multi-jet electrospinning [49], multi-hole electrospinning [50], gas-assisted electrospinning [51], and centrifugal electrospinning [52] have been demonstrated. Among these modified electrospinning fabrication methods, the needleless electrospinning systems have evolved into many different configurations based on the moving state of the spinnerets, classified into two types: rotating spinnerets and stationary spinnerets. As for the rotating spinnerets in needleless electrospinning, multiple jets are automatically introduced by the movement and vibration of the spinnerets. In comparison, stationary spinnerets in needleless electrospinning utilize external forces, such as magnetic forces, gravity, and gas bubbles to produce multiple jets [48]. Multi-jet and multi-hole electrospinning apply the exact mechanism to alter one jet to several jets by increasing the number of nozzles. In addition, gas-assisted electrospinning and centrifugal electrospinning add other forces to help the electrospinning process upscale fiber production.

Unlike conventional single nozzle electrospinning, all the above-mentioned modified electrospinning techniques can produce multiple jets simultaneously, leading to mass production of micro/nanofibers. That is to say, various electrospinning techniques create a large number of opportunities to transform plastic waste into valuable products for commercial applications. This is the second advantage of electrospinning techniques for recycling and reutilizing plastic waste.

2.3. The Complexity of Electrospinning Structures

It is known that the electrospun fibers are usually nonwoven, which limits their applications in a variety of areas such as bioengineering, electronic components and flexible devices. Therefore, many strategies, including management of the electrospinning process and configurations, have been proposed to manufacture ordered fibers [53]. For example, Xia et al. reported that uniaxially aligned nanofibers were prepared by electrospinning with a collector consisting of two separate pieces of electrically conductive substrate [54]. Similarly, Li et al. also obtained uniaxially aligned electrospun fibers by a different way of using a rotating cylinder collector and two oppositely placed metallic needles with opposite voltages in 2006 [55]. Moreover, magnetic-assisted electrospinning was established to fabricate aligned fibrous arrays by Jiang et al. [56]. Those studies import external forces or apply special collectors to prepare ordered fibers by electrospinning. However, it is still hard to control a single jet during electrospinning, even with those modified methods. Fortunately, direct-writing electrospinning (DWE), combining electrospinning with 3Dprinting, was created and can tune a single electrospun jet to the designed path during the fabrication process. This was first proposed by Kameoka and colleagues [57] to prepare patterned fibers using a low spinning voltage and a small spinning distance. Subsequently, numerous studies have been published to take advantage of this technique to obtain specially designed structures [58–61]. The appearance of the DWE method offers a novel way of fabricating complicated structures with fabulous functions. Furthermore, an electrospinning approach called coaxial electrospinning is suitable for preparing core-shell structures [62–65]. According to the above discussion, it can be concluded that electrospinning can produce fibers with lots of structures, such as hollow structures, multilayer structures, porous structures, core/shell structures, and so on, which offers diverse opportunities for plastic waste to be electrospun into different patterns adaptable to a growing number of applications [66–71].

3. Typical Polymer Waste and Reutilization via Electrospinning

In the second section, the advantages of electrospinning for recycling and reutilizing plastic waste are summarized. It is easy to see that electrospinning is an amazing recycling technique for turning plastic waste into high-value products. Thus, lots of studies focus on preparing plastic waste via electrospinning and are shown in Table 2 [25,72–89]. In the following parts, the types of polymer waste reutilized through electrospinning are illustrated in detail.

Table 2. Summary of polymeric products (membranes or fibers) prepared from plastic waste sources of PET, PS, PA, etc., via electrospinning.

Products	Origin Waste Source	Performance Discussion (Indicator)	Application	Ref.
PET, PS, PC nanofibers	Water bottles, styrofoam, Compact discs (CDs)	Elastic moduli: 15 to 60 MPa/ High water filtration efficiency (over 99%) of 1 μm particles	Ultra/micro filtration	[25]
Tough mesomorphic fiber membranes	Coca Cola bottles (500 mL)	Fiber diameters: 0.4 to 4.3 μm/ High strength (62.5 MPa), modulus (1.39 GPa), toughness (65.5 MJ m^{-3})/ High absorption capacity of smoke residuals (43 × its own weight)	Smoke filtration	[72]
PET nanofibrous membranes	Beverage bottles	Fiber diameters: 95 ± 37 nm/ High filtering efficiency (more than 98% for particles over 120 nm)	Filtration media in face mask	[73]
PET membranes	PET bottles	Fiber diameters: 1.29 μm/ High mechanical resistance (4 MPa)/ High collection efficiency (98.4%) and low-pressure drop (212 Pa)	Air filters	[74]
PET fibers	Clear soda packaging	Mean fiber diameter: 3.25 to 0.65 μm/ Mechanical strength: 3.2 to 4.5 MPa/ High filtration efficiency (up to 99%)	Air/gas filtration	[75]
PET membranes	Plastic water bottles	Fiber diameters: 100 nm/ High filtration efficiency (more than 99% of particles as small as 500 nm/6 log reductions for Gram-negative and Gram-positive bacteria)	Water filtration	[76]
Electrochemical active microporous carbon structure	Used PET bottles	The medium combines double-layer and redox reaction pseudocapacitance characteristics.	Energy storage	[77]
PET films on paper and textile materials	Used mineral water bottles	The impregnated with PET do not absorb water droplets.	Waterproof materials	[78]
PET nanofibers	Used grade PET bottles, PET granule	Minimum fiber diameters: 61 to 93 nm (Produced by melt-electrospinning)	-	[79]
PET nanofibers	Clear PET bottles	Fiber diameters: 45 to 65 μm	-	[80]
Colored PET nanofibers	Recycled PET bottles	Good colorfastness/ Good mechanical strength	Advanced colorful applications	[81]
PET nanofiber mats	Recycled PET bottles	Good colorfastness/ Good mechanical strength/ Low processing temperature/ Minimum dyeing time	Advanced apparel applications	[82]

Table 2. *Cont.*

Products	Origin Waste Source	Performance Discussion (Indicator)	Application	Ref.
PET/lignin nanofibers	Waste water bottles	Average fiber diameter: 191 ± 60 nm	Separators/ filters	[83]
Sooth uniform PET nanofibers	Waste PET materials	Minimum average fiber diameter: 105.03 ± 36.79 nm	-	[84]
Lignin/recycled PET fibrous mats	Waste water bottles	Average fiber diameter: 80 to 781 nm	-	[85]
Carbon nanofibers	Used PET water bottles	Average fiber diameter: 191 ± 60 nm/ The C content of the nanofibers: 94.3%	Advanced separation	[86]
Adsorptive membranes	PET bottle waste	Cr(VI) removal capacity (5.54 mg/50 mg)/ Reusability (93.7% adsorption effectiveness after five cycles)	Removal of hexavalent chromium from water	[87]
PDMS functionalized PET fibrous membranes	Recycled PET pellets	Superoleophilic properties (oil contact angle of 0°)/ Anti-water-fouling properties/ High flux (~20,000 L m^{-2} h^{-1})/ High separation efficiency (>98%)	Oil/water separation	[88]
Conductive PET nanofibers	Water bottles	Average fiber diameter of copper-coated r-PET nanofibers (700 nm)/ Low electrical resistance (0.1 Ω)/ Flexible/ Good mechanical strength	Wearable electronics/ Flexible sensors/Energy storage	[89]

3.1. PET

PET is a common synthetic thermoplastic polyester prepared by polycondensation, which can be reused by heating. This plastic has a low crystallization rate, high melting point, and facile processing. Based on the fabricating process and thermal history, it can exist in the form of amorphous (transparent) and semicrystalline (opaque or white). Owing to its superior physicochemical properties, such as chemical resistance and thermal stability and non-toxicity, PET can be employed in numerous fields, especially as one of the most suitable packaging plastics for storing various liquids, including water, soft drinks and milk, and oil. However, the scarcity of space, accumulation threats to the environment, and proliferation of pathogenic microorganisms make recycling PET inevitable. As mentioned before, the traditional recycling approaches of plastic waste have merits and demerits [90]. One of the best chances for recycling and reutilizing plastic waste such as PET is to recreate them as new functional products with special functions via electrospinning. Electrospinning is a technology that can fabricate fibers with diameters in the micro/nano scale, which are an order of magnitude lower than that of fibers produced by conventional melt-blown spinning [91]. Based on the publications related to recycling and reutilizing PET waste by electrospinning, there are several ways to make the best use of recycled PET.

3.1.1. Directly Electrospun Recycled PET into Micro/Nanofibers for Different Applications

Most of the electrospun recycled PET micro/nanofibers are applied for filtration. For instance, Andersson et al. developed a tough mesomorphic fiber membrane with recycled PET by electrospinning, which shows a good performance for smoke filtration, as shown in Figure 3 [72]. The IR-absorbance of the fiber mat increases in the 3000–2850 cm^{-1} and 3500–3200 cm^{-1} ranges after smoke filtration, indicating that the CH and OH are absorbed by fiber mats, respectively. Additionally, the absorption of hydrocarbons/alcohols increases with decreasing the fiber diameter. Similarly, Nosko et al. found that the electrospun recycled PET fibers with an average diameter of around 95 nm show an enhanced filtration efficiency of particles with a size of about 120 nm, and the fibers exhibit good vapor permeability and breathability, which can be promising filtration media for personal protection [73]. Except for using electrospun recycled PET for filtration, researchers have also studied the effects of electrospinning processing parameters on the filtration efficiency of the electrospun recycled fibers. For example, Aguiar and colleagues used recycled PET to develop microfiber membranes and evaluated their properties as air filter media for nanoparticles by changing the solution concentrations [74]. In the same year, they electrospun the same membrane by adjusting solution concentrations and tuning the needle diameter, electrospinning processing time, and collector rotation speed [75]. All the above publications are about the air filtration of electrospun recycled PET fibers [92]. There are also studies focused on water filtration. Zander et al. prepared recycled PET nanofibers via solution electrospinning which can be employed for water filtration [76]. They tested the performance of the filter by passing through an aqueous solution of latex fluorescent beads ranging from 30 to 2000 nm. The result shows that the filters are effective in removing the beads with diameters of 1 and 2 μm in the solution, but they are ineffective for removing the particles under 500 nm. Similarly, Attila et al. electrospun recycled PET to polymer fibers with diameters ranging from 200 to 600 nm, with potential use in filtration [93]. In addition, electrospun recycled PET can be applied in energy storage [77], antibiotics [94], electromagnetic shielding, [95] and so on. Karashanova et al. demonstrated that electrospun recycled PET on paper and textile materials results in a waterproof coating, possibly used for protective clothing and waterproof paper [78]. The above researches utilized solution electrospinning to treat recycled PET. Moreover, Yazdanshenas et al. used melt electrospinning to prepare nanofibers from PET bottles [79]. Additionally, Militky and colleagues applied melt electrospinning to fabricate PET nanofibers from recycled PET bottles and studied the effects of the processing parameters on the morphology of the fibers [80].

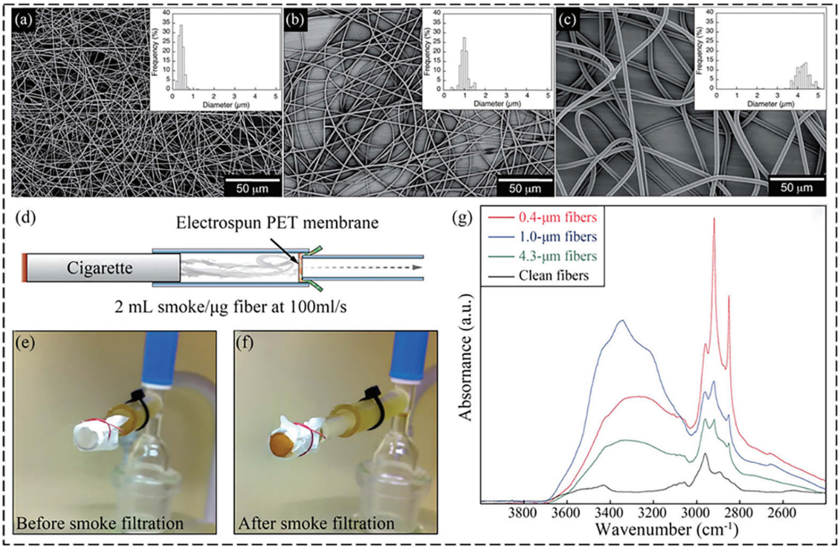

Figure 3. (**a**–**c**) Micrographs of electrospun fibers with different concentrations of PET: (**a**) 10 wt%, (**b**) 15 wt%, (**c**) 20 wt%. (**d**) Schematic illustration of smoke filtration testing (**e**–**f**). Photographs of fiber mats: (**e**) before and (**f**) after smoke filtration testing. (**g**) IR-spectroscopy of clean fiber mats and smoke-exposed fiber mats with average fiber diameters of 0.4, 1.0 and 4.3 mm. Reprinted with permission from ref. [72]. Copyright 2015 Royal Society of Chemistry.

3.1.2. Recycled PET as a Raw Source of Electrospinning for Mechanism Research

Electrospun PET fibers can become functional materials and be used as raw sources to perform mechanism studies. For instance, Khatri and colleagues conducted a kinetics and thermodynamic study on the dyeability of electrospun waste PET fibers and found that the obtained fibers display excellent properties, such as superior colorfastness, strong mechanical strength, low processing temperature, etc. [82]. In another study, they utilized recycled PET to fabricate colored nanofibers through electrospinning and they conducted physicochemical studies of the obtained fibers [81]. Zuburtikudis et al. attempted to adjust the electrospinning variables to tailor the average fiber diameter of electrospun lignin/recycled PET fibers [83]. Ahmed et al. conducted a similar study by using the Taguchi design experiment to obtain the optimum electrospinning experimental conditions for recycled PET [84]. However, Marzouqi and colleagues employed the same materials, lignin/recycled-PET, as electrospun raw materials to study the effect of the obtained fibers' nanoscale dimensions on the carbonization process, which is significant in optimizing the carbonization process [85].

3.1.3. Combine Electrospinning with Other Techniques to Fabricate Functionalized Fibers

In addition to using electrospinning as a method of recycling, researchers also combined electrospinning with other techniques to obtain functionalized fibers. Zuburtikudis et al. fabricated carbon nanofibers by electrospinning a mix of lignin and recycled PET with a carbonization process [86]. Similarly, Attia et al. fabricated lignin-based fibers from a blend of recycled lignin and PET by electrospinning, which can be used to remove methylene blue dye in water [96]. In another study, Khorram and colleagues prepared adsorptive membranes for chromium removal from wastewater with electrospun recycled PET fibers treated with cold plasma and functionalized with chitosan. The results show that the functionalized chitosan electrospun membranes with the plasma treatment possess the highest adsorption capacity compared with membranes without plasma treatment and neat nanofibrous PET [87]. In the study by Sakai et al., a functional fibrous membrane with recycled PET for oil/water separation was fabricated by a two-step method. Firstly, the recycled PET was electrospun into a fibrous membrane and then the membrane was dip-coated with polydimethylsiloxane (PDMS) [88]. In another study by Li et al., hierarchical porous recycled PET was manufactured into fibers, also via two steps: electrospinning and solvent post-treatment, which showed the high efficiency of aerosols and virus capture [97]. Figure 4 illustrates the whole preparation process of the mentioned fibers in [97].

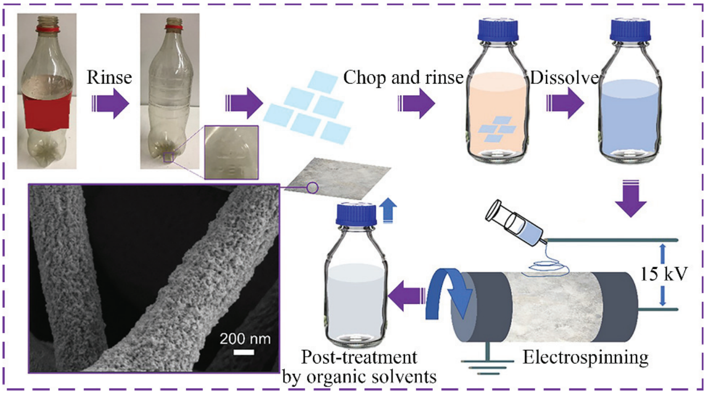

Figure 4. Process of recycled PET electrospinning and post-treatment. Reprinted with permission from ref. [97]. Copyright 2021 American Chemical Society.

Furthermore, Siyal and colleagues synthesized electrospun recycled PET nanofibers with excellent conductivity and good mechanical strength by electrospinning and electroless deposition methods [89]. In another study, Sinha-Ray et al. used a novel supersonic solution blowing method consisting of an electrospinning scheme coupled with a supersonic converging-diverging de Laval nozzle connected with an air compressor to prepare recycled PET mats for filtration of PM0.1–2 [98]. Apart from preparing functional fibers, one study by Naguib et al. manufactured core-shell fibrous mats in two steps: fabricating recycled PET to fibers by electrospinning and then coating the polyaniline by chemically polymerization, which can be utilized as a potential supercapacitor device (Figure 5) [99].

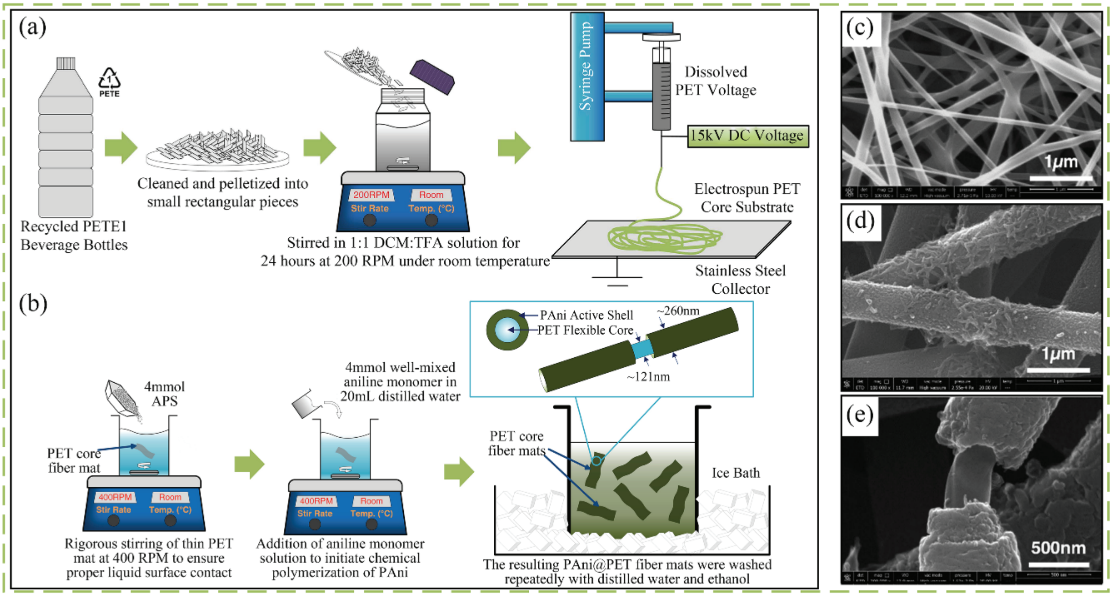

Figure 5. (**a**) Process of fabricating the PET core fibers from the recycled PETE1 recyclable beverage bottles. (**b**) The production process of PAni@PET core-shell fibers. (**c**) Morphology of the pure PET fibrous core. (**d**) PAni@PET core-shell structure. (**e**) SEM photograph of the exposed core. Reprinted with permission from ref. [99]. Copyright 2016 IOP Publishing.

3.1.4. Electrospun Recycled PET Incorporated with Additives to Obtain Fibers with Unique Properties

To endow better mechanical properties and unique properties (e.g., filtration efficiency) to the electrospun recycled PET fibers, some groups put additives into the recycled PET during electrospinning [100–104]. One type of additive is polymers. For example, Manuel et al. fabricated composite fibers consisting of recycled PET, purchased polyacrylonitrile (PAN) and styrene via electrospinning and investigated their mechanical properties [101]. The composite presents high values of hardness and elastic modulus, which are 4.5 and 7.5 times those of PAN fiber values, respectively. Petrik et al. reported that electrospun recycled PET fibers modified with 2-(aminomethyl) pyridine could be an adsorber for Cu^{2+} from an aqueous solution [102]. Hu et al. prepared two kinds of nanofibrous membranes for membrane distillation with the recycled PET waste via electrospinning. One was pristine and the other was modified with 1H,1H,2H,2H-perfluorodecyltriethoxysilane (FAS), showing a better endurance performance [103]. In another study by Goh et al., a soft, flexible, fluffy and 3D aerogel was made with waste PET for the water treatment of heavy metals and energy harvesting [104]. The aerogel was chemically modified by coating polydopamine (PDA) and soaking with PEI to improve its efficiency and versatility. As shown in Figure 6, the preparation process and the SEM images of the 3D aerogel are presented.

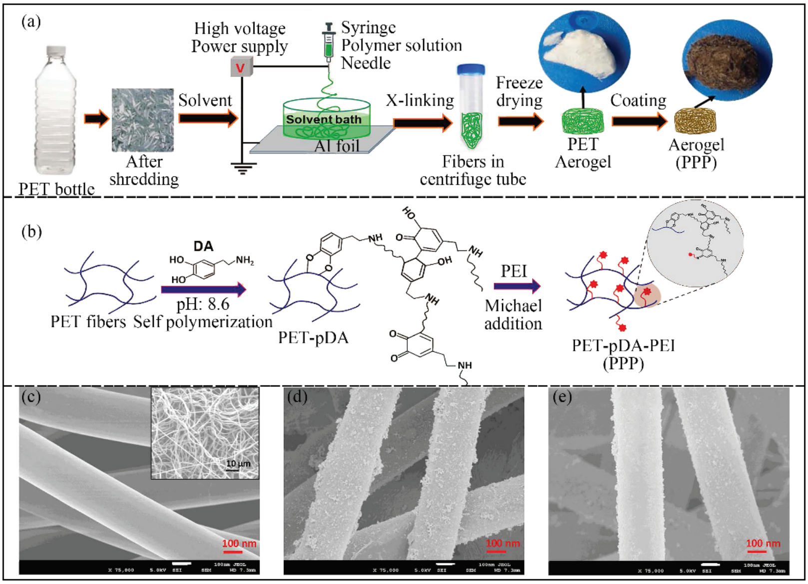

Figure 6. (**a**) Process of fabricating the 3D PPP aerogel from PET bottles. (**b**) Mechanisms for Michael addition reaction occurred during the surface modification process. (**c**–**e**) FESEM images of fibers: (**c**) pristine PET fibers, (**d**) pDA coated fibers (PET-pDA), and (**e**) PET-pDA-PEI (PPP) fibers. Reprinted with permission from ref. [104]. Copyright 2021 Elsevier.

Apart from using synthetic polymers as additives in the above studies, some researchers also employed natural polymers. Sangermano et al. fabricated a nanofibrous membrane with recycled PET and chitosan for oil/water separation and discussed the effect of chitosan concentrations on separation performance [105]. The PET nanofiber membranes may possess amphiphilic properties after being modified by hydrophilic chitosan. Furthermore, the morphology, the chemical composition and wettability of the membranes are related to the chitosan concentrations in the solutions, which affects the selective separation behavior of the membranes. Alena et al. demonstrated that electrospun PET/silk fibroin–composite fibers can be used as aerosol filtration membranes for dirt, bacteria, and viruses [106]. The other type of additive is nanoparticles. Latifi et al. obtained a nanofiber web with recycled PET and nano iron oxide via electrospinning, which possesses microwave absorption characterization and wettability [107]. Alirezazadeh and colleagues electrospun a micro/nanofibrous core-sheath yarn with recycled PET wrapped by PAN containing dimethyl 5-sodium sulfoisophthalate nanoparticles and examined its wicking behavior for filtration [108]. Vanegas et al. revealed that electrospinning the recycled PET and zinc oxide nanoparticles together could obtain fibers with antibacterial and antifungal properties [94]. In a study by Hou et al., icephobic nanocomposite electrospun membranes from recycled PET modified with SiO_2 exhibited high electromagnetic shielding efficiency with superhydrophobic and icephobic performance [95].

3.2. PS

Expanded (EPS) and extruded (XPS) polystyrene, also named styrofoam, is a thermoplastic polymer used in many areas, including the electronics and packaging industries, because of its versatility, light weight, thermal stability, cleanliness, and low cost [109]. The extensive applications of EPS make it one of the abundant plastic wastes because it degrades at a prolonged rate in the natural environment and can exist for years. In addition, EPS is toxic to organisms and tends to accumulate surrounding mercury compounds, leading to a harsh influence on the environment [110,111]. Therefore, it is also significant to transform recycled EPS into valuable products by electrospinning.

Many publications have demonstrated that recycled PS can be fabricated into functional fibers by the electrospinning technique [112]. Shin et al. conducted a series of studies on recycled EPS via electrospinning [45]. In 2005, they obtained electrospun fibers with recycled EPS and natural solvent, which benefits the environment [113]. Then, Shin et al. mixed micro-glass fibers with the electrospun EPS fibers and found the fibers' separation efficiency improved for filtration of water-in-oil emulsions [114–116]. The applications of electrospun recycled EPS are commonly for filtration. For example, Khairurrijal et al. researched electrospun recycled EPS for air filtration [117–119]. In 2018, they synthesized nanofiber membranes from waste high-impact PS using the electrospinning method, which showed a suitable application in air filtration based on the contact angle measurement and air-filtration test [117]. One year later, Khairurrijal et al. electrospun recycled EPS to nanofiber mats with different morphology, including smooth fiber, wrinkled fibers, and beaded fibers with various diameters, suitable for air filtration, with high mechanical strength, ultra-hydrophobic surface, and high-quality factors [118].

In addition, to expand the origins of the recycled EPS, Khairurrijal and colleagues fabricated nanofibrous membranes for air filtration with recycled EPS waste from various sources, including food packaging, EPS craft, instant noodle cups, and electronics packaging by the electrospinning technique [119]. Another study by Demir et al. prepared fibrous mats using recycled PS by electrospinning method, which can be applied to treat protein-based solid contents of body fluid medical waste [120] and is a promising adsorbent for remediation of oily wastewater [121]. In another study, the mass production of stacked styrofoam nanofibers was realized through a multi-nozzle electrospinning system with a drum collector [122].

Furthermore, researchers also electrospun recycled EPS with additives to improve the properties of the obtained fibers. The mentioned authors, Khairurrijal et al., electrospun a composite membrane with recycled styrofoam and TiO_2, which can be applied to degrade wastewater [123]. In a study by Asmatulu et al., nanocomposite fibers with super-hydrophobicity characters were synthesized by electrospinning recycled EPS foam added with titanium nanoparticles and aluminum microparticles of different proportions, promising candidates for water collection, water filtration, tissue engineering, and composites [124]. The results showed that the contact angle of the as-prepared nanocomposites was 157° and their fog water collection capacity was more than 1.35 L/m^2. In addition, the cost of the nanocomposite materials was only USD 2.67, which can provide the minimum daily water consumption for a two-member household (6 L). Rahman et al. reported that superhydrophobic–hydrophilic nanocomposite fibers with the same materials were electrospun for atmospheric clean water production, which was inspired by the fog-harvesting capability of Stenocara beetles [124,125]. Dandin et al. prepared nanocomposite fibers by electrospinning recycled PS with multiwall carbon nanotubes (MWCNTs) and NiZn ferrite, providing a way for turning plastic waste into high-value new products for several industrial applications, such as transportation, construction, and energy [126]. In addition, to combine other nanomaterials to fabricate electrospun recycled PS with various functions, the researcher also applied electrospinning and post-treatment techniques to obtain functional recycled PS products. For instance, Jalal et al. prepared PS cation exchange membranes from recycled PS waste packing by electrospinning and post sulfonation reactions, which plays an essential role in hydrogen fuel cells [127].

3.3. PA

Polyamide (PA) is a semicrystalline polymer with good physicochemical properties which is often used in the form of fibers for a broad set of fields, including fashion, automotive, electronics, etc. Currently, PA production is continuously growing to satisfy the requirements of applications, resulting in an important proportion of polymer waste [128]. Compared with recycled PET and EPS, there is less research about recycled PA.

Janalikova et al. prepared a fibrous antibacterial membrane with recycled PA and monoacylglycerol (MAG) blend by electrospinning, which also showed a filtration potential similar to electrospun PET and PS [46]. Another study by Arenas et al. reported a sustainable nanofibrous sound absorption membrane with recycled PA6 and polyvinyl alcohol (PVA) by needleless electrospinning. The resulting membrane showed a high porosity and airflow resistivity [129].

3.4. Other Plastic Waste

In addition to the recycled PET, PS, and PA via electrospinning, there are other plastic wastes such as lactic acid (LA), acrylonitrile butadiene styrene (ABS), polyvinyl chloride (PVC), etc. that can be recycled and reutilized by this technique. Kim et al. utilized a novel lactic-assisted 3D electrospinning to produce a low-density 3D polycaprolactone/lactic acid fibrous mesh (3D-PCLS) with recycled LA waste, which can be applied in bone tissue engineering [130]. Khairurrijal et al. used ABS waste to prepare a nanofiber membrane by electrospinning, which can potentially be employed as air filtration media [131]. They also investigated the critical concentration of PVC waste morphology from particles to fibers by electrospinning [132]. Park et al. collected waste polyvinyl(butyral) (W-PVB) from windshields [133]. They fabricated carbon nanofibers from the composites of W-PVB and natural cellulose by electrospinning, carbonization, and the KOH activation approach, which are beneficial for removing the rhodamine B from water.

4. Summary and Outlook

Accumulation of plastic waste in landfills has become one of the most significant environmental issues today. Recycling and reutilizing plastic waste into high-value products like micro/nanomaterial is an efficient and viable strategy. Electrospinning is undoubtedly a superior method to transform plastic waste into functional fibers, foams, and other materials. In this review, the advantages of electrospinning in reusing plastic waste and the present advances in recycling and reutilizing plastic waste via electrospinning were briefly summarized. As a versatile method for reusing plastic waste, electrospinning mainly possesses three merits: (1) diverse choices of materials offer plenty of opportunities to reutilize various types of plastic waste as raw materials for electrospinning; (2) novel electrospinning techniques provide limitless possibilities for turning plastic waste into profitable products; and (3) various electrospun structures make plastic waste adaptable for applying in numerous areas. Regarding the superior benefits of electrospinning for recycling and reutilizing plastic waste, the developments in changing plastic waste into a high-value product via electrospinning were discussed based on the common types of plastic waste, PET, PS, and PA.

In the future, electrospinning will certainly be a promising way to recycle and reutilize plastic waste owing to the advantages mentioned. Although electrospun plastic waste has already been profoundly and extensively studied, there are still possibilities and perspectives that need to be further explored. Future advances are potentially concluded from the following aspects: (1) employment of additives, such as nanofillers, with plastic waste or mixed plastic waste to endow the electrospun composites with special functions; (2) deep research on the optimization of electrospun processing parameters for different types of plastic waste to fabricate high-value products with designed properties; (3) further developments for solution electrospinning with natural, non-toxic solvent, or usage of a solvent-free manner such as melt electrospinning in order to realize green manufacturing; (4) combination of electrospinning with other techniques to prepare micro/nano functional fibers(or membranes) with unique structures for expanded explorations of potential industrial applications; and (5) intensive studies on the mass production of electrospun plastic waste to fulfill commercialization.

Author Contributions: Conceptualization, X.L. and Y.L.; writing—original draft preparation, X.L., Y.P. and Y.D.; review and editing, F.Y., C.Z. and D.Z.; supervision, X.H. and Y.L.; funding acquisition, X.L. All authors have read and agreed to the published version of the manuscript.

Funding: This work was supported by the National Natural Science Foundation of China (Grant No. 52003078), the Department of Science and Technology of Hubei Province (Grant No. 2020BIB012), the Doctoral Scientific Research Foundation of Hubei University of Technology (Grant No. BSQD2020002), and the Hubei Key Laboratory of Modern Manufacturing Quality Engineering Foundation (Grant No. KFJJ-2020005).

Institutional Review Board Statement: Not applicable.

Informed Consent Statement: Not applicable.

Data Availability Statement: Not applicable.

Conflicts of Interest: The authors declare no conflict of interest.

References

1. Saleem, J.; Riaz, M.A.; McKay, G. Oil Sorbents from Plastic Wastes and Polymers: A Review. *Hazard. Mater.* **2018**, *341*, 424–437. [CrossRef] [PubMed]
2. Basto, M.N.; Nicastro, K.R.; Tavares, A.I.; McQuaid, C.D.; Casero, M.; Azevedo, F.; Zardi, G.I. Plastic Ingestion in Aquatic Birds in Portugal. *Mar. Pollut. Bull.* **2019**, *138*, 19–24. [CrossRef] [PubMed]
3. Thakur, S.; Verma, A.; Sharma, B.; Chaudhary, J.; Tamulevicius, S.; Thakur, V.K. Recent Developments in Recycling of Polystyrene Based Plastics. *Curr. Opin. Green Sustain. Chem.* **2018**, *13*, 32–38. [CrossRef]
4. Hopewell, J.; Dvorak, R.; Kosior, E. Plastics Recycling: Challenges and Opportunities. *Philos. Trans. R. Soc. B Biol. Sci.* **2009**, *364*, 2115–2126. [CrossRef]
5. Bujak, J.W. Thermal utilization (treatment) of plastic waste. *Energy* **2015**, *90*, 1468–1477. [CrossRef]
6. Pan, D.; Su, F.M.; Liu, C.T.; Guo, Z.H. Research progress for plastic waste management and manufacture of value-added products. *Adv. Compos. Hybrid Mater.* **2020**, *3*, 443–461. [CrossRef]
7. Lambert, S.; Wagner, M. Environmental Performance of Bio-based and Biodegradable Plastics: The Road Ahead. *Chem. Soc. Rev.* **2017**, *46*, 6855–6871. [CrossRef]
8. Haider, T.P.; Völker, C.; Kramm, J.; Landfester, K.; Wurm, F.R. Plastics of the Future? The Impact of Biodegradable Polymers on the Environment and on Society. *Angew. Chem. Int. Ed.* **2019**, *58*, 50–62. [CrossRef]
9. Al-Salem, S.M.; Lettieri, P.; Baeyens, J. Recycling and Recovery Routes of Plastic Solid Waste (PSW): A Review. *Waste Manag.* **2009**, *29*, 2625–2643. [CrossRef]
10. Briassoulis, D.; Hiskakis, M.; Babou, E. Technical specifications for mechanical recycling of agricultural plastic waste. *Waste Manag.* **2013**, *33*, 1516–1530. [CrossRef]
11. Zare, Y. Recent Progress on Preparation and Properties of Nanocomposites from Recycled Polymers: A Review. *Waste Manag.* **2013**, *33*, 598–604. [CrossRef]
12. Qasim, S.B.; Zafar, M.S.; Najeeb, S.; Khurshid, Z.; Shah, A.H.; Husain, S.; Rehman, I.U. Electrospinning of Chitosan-Based Solutions for Tissue Engineering and Regenerative Medicine. *Int. J. Mol. Sci.* **2018**, *19*, 407. [CrossRef]
13. Guo, H.T.; Chen, Y.M.; Li, Y.; Zhou, W.; Xu, W.H.; Pang, L.; Fan, X.M.; Jiang, S.H. Electrospun Fibrous Materials and Their Applications for Electromagnetic Interference Shielding: A Review. *Compos. Part A Appl. Sci. Manuf.* **2021**, *143*, 106309. [CrossRef]
14. Xue, J.J.; Wu, T.; Dai, Y.Q.; Xia, Y.N. Electrospinning and Electrospun Nanofibers: Methods, Materials, and Applications. *Chem. Rev.* **2019**, *119*, 5298–5415. [CrossRef]
15. Peng, S.J.; Li, L.L.; Hu, Y.X.; Srinivasan, M.; Cheng, F.Y.; Chen, J.; Ramakrishna, S. Fabrication of Spinel One-Dimensional Architectures by Single-Spinneret Electrospinning for Energy Storage Applications. *ACS Nano* **2015**, *9*, 1945–1954. [CrossRef]
16. Dong, Z.X.; Kennedy, S.J.; Wu, Y.Q. Electrospinning Materials for Energy-Related Applications and Devices. *J. Power Sources* **2011**, *196*, 4886–4904. [CrossRef]
17. Ondarçuhu, T.; Joachim, C. Drawing a Single Nanofibre over Hundreds of Microns. *Europhys. Lett.* **1998**, *42*, 215. [CrossRef]
18. Rafii-Tabar, H. Modelling the Nano–scale Phenomena in Condensed Matter Physics via Computer-Based Numerical Simulations. *Phys. Rep.* **2000**, *325*, 239–310. [CrossRef]
19. Liu, G.J.; Ding, J.F.; Qiao, L.J.; Guo, A.; Dymov, B.P.; Gleeson, J.T.; Hashimoto, T.; Saijo, K. Polystyrene-Block-Poly(2-cinnamoylethyl methacrylate) Nanofibers-Preparation, Characterization, and Liquid Crystalline Properties. *Chem. Eur. J.* **1999**, *5*, 2740–2749. [CrossRef]
20. Whitesides, G.M.; Grzybowski, B. Self-Assembly at All Scales. *Science* **2002**, *295*, 2418–2421. [CrossRef]
21. Lim, C.T. Nanofiber Technology: Current Status and Emerging Developments. *Prog. Polym. Sci.* **2017**, *70*, 1–17. [CrossRef]
22. Asmatulu, R.; Davluri, S.; Khan, W. Fabrications of CNT Based Nanocomposite Fibers from the Recycled Plastics. In Proceedings of the ASME 2009 International Mechanical Engineering Congress and Exposition, Lake Buena Vista, FL, USA, 13–19 November 2009. [CrossRef]
23. Isık, T.; Horzum, N.; Demir, M.M.; Muñoz-espí, R.; Crespy, D. A Recycling Route of Plastics Via Electrospinning: From Daily Wastes to Functional Fibers. In *Green Electrospinning*; Horzum, N., Demir, M.M., Muñoz-Espí, R., Crespy, D., Eds.; De Gruyter: Berlin, Germany, 2019; pp. 239–264. [CrossRef]

24. Yasin, S.; Bakr, Z.H.; Ali, G.A.M.; Saeed, I. Recycling Nanofibers from Polyethylene Terephthalate Waste Using Electrospinning Technique. In *Waste Recycling Technologies for Nanomaterials Manufacturing*; Makhlouf, A.S.H., Ali, G.A.M., Eds.; Springer: Cham, Switzerland, 2021; pp. 805–821. ISBN 978-3-030-68031-2. [CrossRef]
25. Zander, N.E.; Sweetser, D.; Cole, D.P.; Gillan, M. Formation of Nanofibers from Pure and Mixed Waste Streams Using Electrospinning. *Ind. Eng. Chem. Res.* **2015**, *54*, 9057–9063. [CrossRef]
26. Esmaeili, E.; Deymeh, F.; Rounaghi, S.A. Synthesis and Characterization of the Electrospun Fibers Prepared from Waste Polymeric Materials. *Int. J. Nano Dimens* **2017**, *8*, 171–181. [CrossRef]
27. Chen, K.; Chou, W.; Liu, L.; Cui, Y.; Xue, P.; Jia, M. Electrochemical Sensors Fabricated by Electrospinning Technology: An Overview. *Sensors* **2019**, *19*, 3676. [CrossRef]
28. Taylor, G.I. Electrically Driven Jets. *Proc. R. Soc. Lond. Ser. A Math. Phys. Sci.* **1969**, *313*, 453–475. [CrossRef]
29. Ren, L.Y.; Ozisik, R.; Kotha, S.P.; Underhill, P.T. Highly Efficient Fabrication of Polymer Nanofiber Assembly by Centrifugal Jet Spinning: Process and Characterization. *Macromolecules* **2015**, *48*, 2593–2602. [CrossRef]
30. Zheng, G.F.; Jiang, J.X.; Wang, X.; Li, W.W.; Liu, J.; Fu, G.; Lin, L.W. Nanofiber Membranes by Multi-Jet Electrospinning Arranged as Arc-Array with Sheath Gas for Electrodialysis Applications. *Mater. Des.* **2020**, *189*, 108504. [CrossRef]
31. Xiong, J.; Liu, Y.; Li, A.L.; Wei, L.; Wang, L.M.; Qin, X.H.; Yu, J.Y. Mass Production of High-Quality Nanofibers via Constructing Pre-Taylor Cones with High Curvature on Needleless Electrospinning. *Mater. Des.* **2020**, *197*, 109247. [CrossRef]
32. Quan, Z.Z.; Wang, Y.H.; Zu, Y.; Qin, X.H.; Yu, J.Y. A Rotary Spinneret for High Output of Electrospun Fibers with Bimodal Distribution. *Eur. Polym. J.* **2021**, *159*, 110707. [CrossRef]
33. Aminyan, R.; Bazgir, S. Fabrication and Characterization of Nanofibrous Polyacrylic Acid Superabsorbent Using Gas-Assisted Electrospinning Technique. *React. Funct. Polym.* **2019**, *141*, 133–144. [CrossRef]
34. Kong, X.Z.; Zheng, Y.C.; Wang, Y.P.; Liang, S.Q.; Cao, G.Z.; Pan, A.Q. Necklace-Like Si@ C Nanofibers as Robust Anode Materials for High Performance Lithium Ion Batteries. *Sci. Bull.* **2019**, *64*, 261–269. [CrossRef]
35. Ma, L.; Shi, X.J.; Zhang, X.X.; Li, L.L. Electrospinning of Polycaprolacton/Chitosan Core-Shell Nanofibers by a Stable Emulsion System. *Colloid Surf. A-Physicochem. Eng. Asp.* **2019**, *583*, 123956. [CrossRef]
36. Gao, J.F.; Song, X.; Huang, X.W.; Wang, L.; Li, B.; Xue, H.G. Facile Preparation of Polymer Microspheres and Fibers with a Hollow Core and Porous Shell for Oil Adsorption and Oil/Water Separation. *Appl. Surf. Sci.* **2018**, *439*, 394–404. [CrossRef]
37. Zhang, D.; Jin, X.Z.; Huang, T.; Zhang, N.; Qi, X.D.; Yang, J.H.; Zhou, Z.W.; Wang, Y. Electrospun Fibrous Membranes with Dual-Scaled Porous Structure: Super Hydrophobicity, Super Lipophilicity, Excellent Water Adhesion, and Anti-Icing for Highly Efficient Oil Adsorption/Separation. *ACS Appl. Mater. Interfaces* **2019**, *11*, 5073–5083. [CrossRef]
38. Cao, X.Y.; Deng, J.P.; Pan, K. Electrospinning Janus Type CoOx/C Nanofibers as Electrocatalysts for Oxygen Reduction Reaction. *Adv. Fiber Mater.* **2020**, *2*, 85–92. [CrossRef]
39. Su, Y.C.; Taskin, M.B.; Dong, M.D.; Han, X.J.; Besenbacher, F.; Chen, M.L. A Biocompatible Artificial Tendril with a Spontaneous 3D Janus Multi-Helix-Perversion Configuration. *Mat. Chem. Front.* **2020**, *4*, 2149–2156. [CrossRef]
40. Salas, C. 4-Solution electrospinning of nanofibers. In *Electrospun Nanofibers*; Afshari, M., Ed.; Woodhead Publishing: Cambridge, UK, 2017; pp. 73–108. ISBN 978-0-08-100907-9. [CrossRef]
41. Larrondo, L.; Manley, R.S.J. Electrostatic Fiber Spinning from Polymer Melts. I. Experimental Observations on Fiber Formation and Properties. *J. Polym. Sci Polym. Phys. Ed.* **1981**, *19*, 909–920. [CrossRef]
42. Bhardwaj, N.; Kundu, S.C. Electrospinning: A fascinating fiber fabrication technique. *Biotechnol. Adv.* **2010**, *28*, 325–347. [CrossRef]
43. King, W.E.; Bowlin, G.L. Near-Field Electrospinning and Melt Electrowriting of Biomedical Polymers-Progress and Limitations. *Polymers* **2021**, *13*, 1097. [CrossRef]
44. Liu, Y.; Li, K.; Mohideen, M.M.; Ramakrishna, S. *Melt Electrospinning: A Green Method to Produce Superfine Fibers*; Elsevier Inc.: Amsterdam, The Netherlands, 2019; ISBN 978-0-12-816220-0.
45. Shin, C. A New Recycling Method for Expanded Polystyrene. *Packag. Technol. Sci.* **2005**, *18*, 331–335. [CrossRef]
46. Opálková Šišková, A.; Pleva, P.; Hrůza, J.; Frajová, J.; Sedlaříková, J.; Peer, P.; Kleinová, A.; Janalíková, M. Reuse of Textile Waste to Production of the Fibrous Antibacterial Membrane with Filtration Potential. *Nanomaterials* **2022**, *12*, 50. [CrossRef]
47. Wang, X.; Niu, H.T.; Lin, T.; Wang, X.G. Needleless Electrospinning of Nanofibers with a Conical Wire Coil. *Polym. Eng. Sci.* **2009**, *49*, 1582–1586. [CrossRef]
48. Lin, T. Needleless Electrospinning: A Practical Way to Mass Production of Nanofibers. *J. Text. Sci. Eng.* **2012**, *2*, 1–3. [CrossRef]
49. Yamashita, Y.; Ko, F.; Tanaka, A.; Miyake, H. Characteristics of Elastomeric Nanofiber Membranes Produced by Electrospinning. *J. Text. Eng.* **2007**, *53*, 137–142. [CrossRef]
50. Varabhas, J.S.; Chase, G.G.; Reneker, D.H. Electrospun Nanofibers from a Porous Hollow Tube. *Polymer* **2008**, *49*, 4226–4229. [CrossRef]
51. Wang, X.F.; Um, I.C.; Fang, D.F.; Okamoto, A.; Hsiao, B.S.; Chu, B. Formation of Water-Resistant Hyaluronic Acid Nanofibers by Blowing-Assisted Electro-Spinning and Non-Toxic Post Treatments. *Polymer* **2005**, *46*, 4852–4867. [CrossRef]
52. Liao, C.C.; Hou, S.S.; Wang, C.C.; Chen, C.Y. Electrospinning Fabrication of Partially Crystalline Bisphenol a Polycarbonate Nanofibers: The Effects of Molecular Motion and Conformation in Solutions. *Polymer* **2010**, *51*, 2887–2896. [CrossRef]
53. Silva, P.M.; Torres-Giner, S.; Vicente, A.A.; Cerqueira, M.A. Management of Operational Parameters and Novel Spinneret Configurations for the Electrohydrodynamic Processing of Functional Polymers. *Macromol. Mater. Eng.* **2022**, 2100858. [CrossRef]

54. Li, D.; Wang, Y.L.; Xia, Y.N. Electrospinning of Polymeric and Ceramic Nanofibers as Uniaxially Aligned Arrays. *Nano Lett.* **2003**, *3*, 1167–1171. [CrossRef]
55. Pan, H.; Li, L.M.; Hu, L.; Cui, X.J. Continuous Aligned Polymer Fibers Produced by a Modified Electrospinning Method. *Polymer* **2006**, *47*, 4901–4904. [CrossRef]
56. Yang, D.; Lu, B.; Zhao, Y.; Jiang, X. Fabrication of Aligned Fibrous Arrays by Magnetic Electrospinning. *Adv. Mater.* **2007**, *19*, 3702–3706. [CrossRef]
57. Kameoka, J.; Orth, R.; Yang, Y.; Czaplewski, D.; Mathers, R.; Coates, G.W.; Craighead, H.G. A Scanning Tip Electrospinning Source for Deposition of Oriented Nanofibres. *Nanotechnology* **2003**, *14*, 1124. [CrossRef]
58. Sun, D.H.; Chang, C.; Li, S.; Lin, L.W. Near-Field Electrospinning. *Nano Lett.* **2006**, *6*, 839–842. [CrossRef]
59. Brown, T.D.; Brown, T.D.; Hutmacher, D.W. Direct Writing by Way of Melt Electrospinning. *Adv. Mater.* **2011**, *23*, 5651. [CrossRef]
60. Brown, T.D.; Slotosch, A.; Thibaudeau, L.; Taubenberger, A.; Loessner, D.; Vaquette, C.; Dalton, P.D.; Hutmacher, D.W. Design and Fabrication of Tubular Scaffolds via Direct Writing in a Melt Electrospinning Mode. *Biointerphases* **2012**, *7*, 13. [CrossRef]
61. He, X.X.; Zheng, J.; Yu, G.F.; You, M.H.; Yu, M.; Ning, X.; Long, Y.Z. Near-Field Electrospinning: Progress and Applications. *J. Phys. Chem. C* **2017**, *121*, 8663–8678. [CrossRef]
62. Loscertales, I.G.; Barrero, A.; Guerrero, I.; Cortijo, R.; Marquez, M.; Gañán-Calvo, A.M. Micro/Nano Encapsulation Via Electrified Coaxial Liquid Jets. *Science* **2002**, *295*, 1695–1698. [CrossRef]
63. Yarin, A.L. Coaxial Electrospinning and Emulsion Electrospinning of Core-Shell Fibers. *Polym. Adv. Technol.* **2010**, *33*, 310–317. [CrossRef]
64. Lu, Y.; Xiao, X.D.; Fu, J.; Huan, C.M.; Qi, S.; Zhan, Y.J.; Zhu, Y.Q.; Xu, G. Novel Smart Textile with Phase Change Materials Encapsulated Core-Sheath Structure Fabricated by Coaxial Electrospinning. *Chem. Eng. J.* **2018**, *355*, 532–539. [CrossRef]
65. Huang, B.Y.; Zhang, Z.X.; Zhao, C.H.; Cairang, L.M.; Bai, J.L.; Zhang, Y.X.; Mu, X.M.; Du, J.W.; Wang, H.; Pan, X.J.; et al. Enhanced Gas-Sensing Performance of Zno@In2o3 Core@Shell Nanofibers Prepared by Coaxial Electrospinning. *Sens. Actuator B-Chem.* **2018**, *255*, 2248–2257. [CrossRef]
66. Wang, C.; Wang, J.; Zeng, L.; Qiao, Z.; Liu, X.; Liu, H.; Zhang, J.; Ding, J. Fabrication of Electrospun Polymer Nanofibers with Diverse Morphologies. *Molecules* **2019**, *24*, 834. [CrossRef]
67. Chen, L.F.; Lu, Y.; Yu, L.; Lou, X.W. Designed Formation of Hollow Particle-Based Nitrogen-Doped Carbon Nanofibers for High-Performance Supercapacitors. *Energy Environ. Sci.* **2017**, *10*, 1777–1783. [CrossRef]
68. Wu, J.; Wang, N.; Wang, L.; Dong, H.; Zhao, Y.; Jiang, L. Electrospun Porous Structure Fibrous Film with High Oil Adsorption Capacity. *ACS Appl. Mater. Interfaces* **2012**, *4*, 3207–3212. [CrossRef]
69. Lin, M.F.; Xiong, J.Q.; Wang, J.X.; Parida, K.; Lee, P.S. Core-Shell Nanofiber Mats for Tactile Pressure Sensor and Nanogenerator Applications. *Nano Energy* **2018**, *44*, 248–255. [CrossRef]
70. Pais, V.; Mota, C.; Bessa, J.; Dias, J.G.; Cunha, F.; Fangueiro, R. Study of the Filtration Performance of Multilayer and Multiscale Fibrous Structures. *Materials* **2021**, *14*, 7147. [CrossRef]
71. Li, R.; Cheng, Z.Q.; Yu, X.B.; Wang, S.; Han, Z.L.; Kang, L.J. Preparation of Antibacterial PCL/PVP-AgNP Janus Nanofibers by Uniaxial Electrospinning. *Mater. Lett.* **2019**, *254*, 206–209. [CrossRef]
72. Strain, I.N.; Wu, Q.; Pourrahimi, A.M.; Hedenqvist, M.S.; Olsson, R.T.; Andersson, R.L. Electrospinning of recycled PET to generate tough mesomorphic fibre membranes for smoke filtration. *J. Mater. Chem. A* **2015**, *3*, 1632–1640. [CrossRef]
73. Šišková, A.O.; Frajová, J.; Nosko, M. Recycling of poly(ethylene terephthalate) by electrospinning to enhanced the filtration efficiency. *Mater. Lett.* **2020**, *278*, 128426. [CrossRef]
74. Bonfim, D.P.F.; Cruz, F.G.S.; Bretas, R.E.S.; Guerra, V.G.; Aguiar, M.L. A Sustainable Recycling Alternative: Electrospun PET-Membranes for Air Nanofiltration. *Polymers* **2021**, *13*, 1166. [CrossRef]
75. Bonfim, D.P.F.; Cruz, F.G.S.; Guerra, V.G.; Aguiar, M.L. Development of Filter Media by Electrospinning for Air Filtration of Nanoparticles from PET Bottles. *Membranes* **2021**, *11*, 293. [CrossRef]
76. Zander, N.E.; Gillan, M.; Sweetser, D. Recycled PET Nanofibers for Water Filtration Applications. *Materials* **2016**, *9*, 247. [CrossRef] [PubMed]
77. Mirjalili, A.; Dong, B.; Pena, P.; Ozkan, C.S.; Ozkan, M. Upcycling of Polyethylene Terephthalate Plastic Waste to Microporous Carbon Structure for Energy Storage. *Energy Storage* **2020**, *2*, e201. [CrossRef]
78. Angelov, R.R.; Georgieva, B.C.; Karashanova, D.B. Films of Recycled Polyethylene Terephthalate, Obtained by Electrospraying, for Paper and Textile Impregnation. In Proceedings of the Scientific Session on Advanced Materials and Technologies, Sofia, Bulgaria, 10–11 October 2016; pp. 156–160. [CrossRef]
79. Rajabinezhad, H.; Khajavi, R.; Rashidi, A.; Mansouri, N.; Yazdanshenas, M.E. Recycling of Used Bottle Grade Polyethylene Terephthalate to Nanofibers by Melt-Electrospinning Method. *Int. J. Environ. Res.* **2009**, *3*, 663–670.
80. Naksuwan, P.; Komárek, M.; Salačová, J.; Militký, J. The Study of Recycled Poly (Ethylene Terephthalate) Nanofibres from PET Bottle. *Appl. Mech. Mater.* **2016**, *848*, 3–6. [CrossRef]
81. Mehdi, M.; Mahar, F.K.; Qureshi, U.A.; Khatri, M.; Khatri, Z.; Ahmed, F.; Kim, I.S. Preparation of Colored Recycled Polyethylene Terephthalate Nanofibers from Waste Bottles: Physicochemical Studies. *Adv. Polym. Technol.* **2018**, *37*, 2820–2827. [CrossRef]
82. Mahar, F.K.; Mehdi, M.; Qureshi, U.A.; Brohi, K.M.; Zahid, B.; Ahmed, F.; Khatri, Z. Dyeability of Recycled Electrospun Polyethylene Terephthalate (PET) Nanofibers: Kinetics and Thermodynamic Study. *J. Mol. Liq.* **2018**, *248*, 911–919. [CrossRef]

83. Svinterikos, E.; Zuburtikudis, I. Tailor-Made Electrospun Nanofibers of Biowaste Lignin/Recycled Poly(Ethylene Terephthalate). *J. Polym. Environ.* **2017**, *25*, 465–478. [CrossRef]
84. Abbas, J.A.; Said, I.A.; Mohamed, M.A.; Yasin, S.A.; Ali, Z.A.; Ahmed, I.H. Electrospinning of Polyethylene Terephthalate (PET) Nanofibers: Optimization Study Using Taguchi Design of Experiment. *IOP Conf. Ser. Mater. Sci. Eng.* **2018**, *454*, 12130. [CrossRef]
85. Svinterikos, E.; Zuburtikudis, I.; Al-Marzouqi, M. The Nanoscale Dimension Determines the Carbonization Outcome of Electrospun Lignin/Recycled-PET Fibers. *Chem. Eng. Sci.* **2019**, *202*, 26–35. [CrossRef]
86. Svinterikos, E.; Zuburtikudis, I. Carbon Nanofibers from Renewable Bioresources (Lignin) and a Recycled Commodity Polymer [Poly(Ethylene Terephthalate)]. *Appl. Polym. Sci.* **2016**, *133*. [CrossRef]
87. Khorram, M.; Mousavi, A.; Mehranbod, N. Chromium Removal Using Adsorptive Membranes Composed of Electrospun Plasma-Treated Functionalized Polyethylene Terephthalate (PET) with Chitosan. *J. Environ. Chem. Eng.* **2017**, *5*, 2366–2377. [CrossRef]
88. Doan, H.N.; Vo, P.P.; Hayashi, K.; Kinashi, K.; Sakai, W.; Tsutsumi, N. Recycled PET as a PDMS-Functionalized Electrospun Fibrous Membrane for Oil-Water Separation. *J. Environ. Chem. Eng.* **2020**, *8*, 103921. [CrossRef]
89. Hussain, N.; Mehdi, M.; Yousif, M.; Ali, A.; Ullah, S.; Hussain Siyal, S.; Hussain, T.; Kim, I.S. Synthesis of Highly Conductive Electrospun Recycled Polyethylene Terephthalate Nanofibers Using the Electroless Deposition Method. *Nanomaterials* **2021**, *11*, 531. [CrossRef] [PubMed]
90. Shojaei, B.; Abtahi, M.; Najafi, M. Chemical Recycling of Pet: A Stepping-Stone toward Sustainability. *Polym. Adv. Technol.* **2020**, *31*, 2912–2938. [CrossRef]
91. Li, H.Y.; Bubakir, M.M.; Xia, T.; Zhong, X.F.; Ding, Y.M.; Yang, W.M. Mass production of ultra-fine fibre by melt electrospinning method using umbellate spinneret. *Mater. Res. Innov.* **2014**, *18*, 921–925. [CrossRef]
92. Lyu, C.; Zhao, P.; Xie, J.; Dong, S.; Liu, J.; Rao, C.; Fu, J. Electrospinning of Nanofibrous Membrane and Its Applications in Air Filtration: A Review. *Nanomaterials* **2021**, *11*, 1501. [CrossRef]
93. Gergely, A.; Kántor, J.; Bitay, E.; Biró, D. Electrospinning of Polymer Fibres Using Recycled PET. *Acta Mater. Transylvanica* **2019**, *2*, 19–26. [CrossRef]
94. Vázquez, K.; Vanegas, P.; Cruzat, C.; Novoa, N.; Arrué, R.; Vanegas, E. Antibacterial and Antifungal Properties of Electrospun Recycled PET Polymeric Fibers Functionalized with Zinc Oxide Nanoparticles. *Polymers* **2021**, *13*, 3763. [CrossRef]
95. Tas, M.; Musa, U.G.; Ahmed, I.; Xu, F.; Smartt, C.; Hou, X.H. Functionalised SiO2 Modified Icephobic Nanocomposite Electrospun Membranes for Outdoor Electromagnetic Shielding Applications. *Polymer* **2022**, *240*, 124499. [CrossRef]
96. Attia, A.A.M.; Abas, K.M.; Ahmed Nada, A.A.; Shouman, M.A.H.; Šišková, A.O.; Mosnáček, J. Fabrication, Modification, and Characterization of Lignin-Based Electrospun Fibers Derived from Distinctive Biomass Sources. *Polymers* **2021**, *13*, 2277. [CrossRef]
97. Song, J.; Zhao, Q.; Meng, C.; Meng, J.M.; Chen, Z.D.; Li, J.S. Hierarchical Porous Recycled PET Nanofibers for High-Efficiency Aerosols and Virus Capturing. *ACS Appl. Mater. Interfaces* **2021**, *13*, 49380–49389. [CrossRef] [PubMed]
98. Kakoria, A.; Chandel, S.S.; Sinha-Ray, S. Novel Supersonically Solution Blown Nanofibers from Waste PET Bottle for Pm0.1-2 Filtration: From Waste to Pollution Mitigation. *Polymer* **2021**, *234*, 124260. [CrossRef]
99. Shi, H.T.H.; Naguib, H.E. Highly Flexible Binder-Free Core-Shell Nanofibrous Electrode for Lightweight Electrochemical Energy Storage Using Recycled Water Bottles. *Nanotechnology* **2016**, *27*, 325402. [CrossRef] [PubMed]
100. Santos, R.P.O.; Rodrigues, B.V.M.; Ramires, E.C.; Ruvolo, A.C.; Frollini, E. Bio-Based Materials from the Electrospinning of Lignocellulosic Sisal Fibers and Recycled PET. *Ind. Crops Prod.* **2015**, *72*, 69–76. [CrossRef]
101. Chinchillas-Chinchillas, M.J.; Orozco-Carmona, V.M.; Alvarado-Beltran, C.G.; Almaral-Sanchez, J.L.; Sepulveda-Guzman, S.; Jasso-Ramos, L.E.; Castro-Beltran, A. Synthesis of Recycled Poly(ethylene terephthalate)/Polyacrylonitrile/Styrene Composite Nanofibers by Electrospinning and Their Mechanical Properties Evaluation. *J. Polym. Environ.* **2019**, *27*, 659–669. [CrossRef]
102. Totito, T.C.; Laatikainen, K.; Pereao, O.; Bode-Aluko, C.; Petrik, L. Adsorptive Recovery of Cu^{2+} from Aqueous Solution by Polyethylene Terephthalate Nanofibres Modified with 2-(Aminomethyl)Pyridine. *Appl. Sci.* **2021**, *11*, 11912. [CrossRef]
103. Xu, G.R.; An, X.C.; Das, R.; Xu, K.; Xing, Y.L.; Hu, Y.X. Application of Electrospun Nanofibrous Amphiphobic Membrane Using Low-Cost Poly (Ethylene Terephthalate) for Robust Membrane Distillation. *J. Water Process. Eng.* **2020**, *36*, 101351. [CrossRef]
104. Roy, S.; Maji, P.K.; Goh, K.L. Sustainable Design of Flexible 3D Aerogel from Waste PET Bottle for Wastewater Treatment to Energy Harvesting Device. *Chem. Eng. J.* **2021**, *413*, 127409. [CrossRef]
105. Baggio, A.; Doan, H.N.; Vo, P.P.; Kinashi, K.; Sakai, W.; Tsutsumi, N.; Fuse, Y.; Sangermano, M. Chitosan-Functionalized Recycled Polyethylene Terephthalate Nanofibrous Membrane for Sustainable On-Demand Oil-Water Separation. *Glob. Chall.* **2021**, *5*, 2000107. [CrossRef]
106. Opálková Šišková, A.; Mosnáčková, K.; Hrůza, J.; Frajová, J.; Opálek, A.; Bučková, M.; Kozics, K.; Peer, P.; Eckstein Andicsová, A. Electrospun Poly(ethylene Terephthalate)/Silk Fibroin Composite for Filtration Application. *Polymers* **2021**, *13*, 2499. [CrossRef]
107. Mohammadkhani, F.; Montazer, M.; Latifi, M. Microwave Absorption Characterization and Wettability of Magnetic Nano Iron Oxide/Recycled PET Nanofibers Web. *J. Text. Inst.* **2019**, *110*, 989–999. [CrossRef]
108. Abbaszadeh, A.; Ravandi, S.A.H.; Valipouri, A.; Alirezazadeh, A. Investigating the Wicking Behavior of Micro/Nanofibrous Core-Sheath PET-PAN Yarn Modified by Dimethyl 5-Sodium Sulfoisophthalate. *J. Appl. Polym. Sci.* **2019**, *136*, 48185. [CrossRef]
109. Ho, B.T.; Roberts, T.K.; Lucas, S. An Overview on Biodegradation of Polystyrene and Modified Polystyrene: The Microbial Approach. *Crit. Rev. Biotechnol.* **2018**, *38*, 308–320. [CrossRef] [PubMed]

110. Raza, Z.A.; Abid, S.; Banat, I.M. Polyhydroxyalkanoates: Characteristics, Production, Recent Developments and Applications. *Int. Biodeterior. Biodegrad.* **2018**, *126*, 45–56. [CrossRef]
111. Graca, B.; Bełdowska, M.; Wrzesień, P.; Zgrundo, A. Styrofoam Debris as a Potential Carrier of Mercury within Ecosystems. *Environ. Sci. Pollut. Res.* **2014**, *21*, 2263–2271. [CrossRef]
112. Alayande, S.O.; Dare, E.O.; Akinlabi, A.K.; Ajao, J.A.; Pelemo, D.A.; Fasasi, A.Y.; Osinkolu, G.A. Recycling of Expanded Polystyrene via Electrospinning Technique. *Niger. J. Mater. Sci.* **2012**, *3*, 71–75.
113. Shin, C.; Chase, G.G. Nanofibers from Recycle Waste Expanded Polystyrene Using Natural Solvent. *Polym. Bull.* **2005**, *55*, 209–215. [CrossRef]
114. Shin, C.; Chase, G.G.; Reneker, D.H. Recycled Expanded Polystyrene Nanofibers Applied in Filter Media. *Colloid Surf. A Physicochem. Eng. Asp.* **2005**, *262*, 211–215. [CrossRef]
115. Shin, C. Filtration Application from Recycled Expanded Polystyrene. *J. Colloid Interfaces Sci.* **2006**, *302*, 267–271. [CrossRef]
116. Shin, C.; Chase, G.G. Separation of Liquid Drops from Air by Glass Fiber Filters Augmented with Polystyrene Nanofibers. *J. Dispers. Sci. Technol.* **2006**, *27*, 5–9. [CrossRef]
117. Zulfi, A.; Munir, M.M.; Hapidin, D.A.; Rajak, A.; Edikresnha, D.; Iskandar, F.; Khairurrijal, K. Air Filtration Media from Electrospun Waste High-Impact Polystyrene Fiber Membrane. *Mater. Res. Express* **2018**, *5*, 35049. [CrossRef]
118. Rajak, A.; Hapidin, D.A.; Iskandar, F.; Munir, M.M.; Khairurrijal, K. Controlled Morphology of Electrospun Nanofibers from Waste Expanded Polystyrene for Aerosol Filtration. *Nanotechnology* **2019**, *30*, 425602. [CrossRef] [PubMed]
119. Rajak, A.; Hapidin, D.A.; Iskandar, F.; Munir, M.M.; Khairurrijal, K. Electrospun Nanofiber from Various Source of Expanded Polystyrene (EPS) Waste and Their Characterization as Potential Air Filter Media. *Waste Manag.* **2020**, *103*, 76–86. [CrossRef] [PubMed]
120. Isik, T.; Demir, M.M. Medical Waste Treatment via Waste Electrospinning of PS. *Fiber. Polym.* **2018**, *19*, 767–774. [CrossRef]
121. Isik, T.; Demir, M.M. Tailored Electrospun Fibers from Waste Polystyrene for High Oil Adsorption. *Sustain. Mater. Technol.* **2019**, *18*, e00084. [CrossRef]
122. Munir, M.M.; Nuryantini, A.Y.; Iskandar; Suciati, T.; Khairurrijal, K. Mass Production of Stacked Styrofoam Nanofibers Using a Multinozzle and Drum Collector Electrospinning System. *Adv. Mater. Res.* **2014**, *896*, 20–23. [CrossRef]
123. Rajak, A.; Munir, M.M.; Abdullah, M.; Khairurrijal, K. Photocatalytic Activities of Electrospun TiO2/Styrofoam Composite Nanofiber Membrane in Degradation of Waste Water. *Mater. Sci. Forum* **2015**, *827*, 7–12. [CrossRef]
124. Uddin, M.N.; Desai, F.J.; Subeshan, B.; Rahman, M.M.; Asmatulu, E. Sustainable Atmospheric Fog Water Generator through Superhydrophobic Electrospun Nanocomposite Fibers of Recycled Expanded Polystyrene Foams. *Surf. Interfaces* **2021**, *25*, 425602. [CrossRef]
125. Uddin, M.N. Electrospun Nanocomposite Fibers of Recycled Polystyrene Foams: An Efficient Atmospheric Fog Water Generator. In Proceedings of the 16th Annual Symposium on Graduate Research and Scholarly Projects, Wichita, KS, USA, 1 May 2020; p. 64.
126. Khan, W.S.; Asmatulu, R.; Davuluri, S.; Dandin, V.K. Improving the Economic Values of the Recycled Plastics Using Nanotechnology Associated Studies. *J. Mater. Sci. Technol.* **2014**, *30*, 854–859. [CrossRef]
127. Jalal, N.M.; Jabur, A.R.; Hamza, M.S.; Allami, S. Sulfonated Electrospun Polystyrene as Cation Exchange Membranes for Fuel Cells. *Energy Rep.* **2020**, *6*, 287–298. [CrossRef]
128. Žagar, E.; Češarek, U.; Drinčić, A.; Sitar, S.; Shlyapnikov, I.M.; Pahovnik, D. Quantitative Determination of PA6 and/or PA66 Content in Polyamide-Containing Wastes. *ACS Sustain. Chem. Eng.* **2020**, *8*, 11818–11826. [CrossRef]
129. Ulrich, T.; Arenas, J.P. Sound Absorption of Sustainable Polymer Nanofibrous Thin Membranes Bonded to a Bulk Porous Material. *Sustainability* **2020**, *12*, 2361. [CrossRef]
130. Hwang, T.I.; Kim, J.I.; Lee, J.; Moon, J.Y.; Lee, J.C.; Joshi, M.K.; Park, C.H.; Kim, C.S. In Situ Biological Transmutation of Catalytic Lactic Acid Waste into Calcium Lactate in a Readily Processable Three-Dimensional Fibrillar Structure for Bone Tissue Engineering. *ACS Appl. Mater. Interfaces* **2020**, *12*, 18197–18210. [CrossRef] [PubMed]
131. Zulfi, A.; Hapidin, D.A.; Munir, M.M.; Iskandar, F.; Khairurrijal, K. The Synthesis of Nanofiber Membranes from Acrylonitrile Butadiene Styrene (ABS) Waste Using Electrospinning for Use as Air Filtration Media. *RSC Adv.* **2019**, *9*, 30741–30751. [CrossRef] [PubMed]
132. Zulfi, A.; Rezeki, Y.A.; Edikresnha, D.; Munir, M.M.; Khairurrijal, K. Synthesis of Fibers and Particles from Polyvinyl Chloride (PVC) Waste Using Electrospinning. *IOP Conf. Ser. Mater. Sci. Eng.* **2018**, *367*, 12014. [CrossRef]
133. Park, J.C.; Kim, J.C.; Park, S.; Kim, D.W. Efficient Waste Polyvinyl(butyral) and Cellulose Composite Enabled Carbon Nanofibers for Oxygen Reduction Reaction and Water Remediation. *Appl. Surf. Sci.* **2020**, *510*, 145505. [CrossRef]

nanomaterials

Article

Theoretical Study on Electronic, Magnetic and Optical Properties of Non-Metal Atoms Adsorbed onto Germanium Carbide

Lin Zhang [1] and Zhen Cui [2,*]

[1] School of Science, Xi'an University of Technology, Xi'an 710048, China; zhangliner@xaut.edu.cn
[2] School of Automation and Information Engineering, Xi'an University of Technology, Xi'an 710048, China
* Correspondence: zcui@xaut.edu.cn

Abstract: Nine kinds of non-metal atoms adsorbed into germanium carbide (NM-GeC) systems wereare investigated by first-principles calculations. The results show that the most stable adsorption positions vary with the NM atoms, and C-GeC exhibits the strongest adsorption. The adsorption of NM atoms causes changes in the electronic, optical and magnetic properties of the GeC system. F- and Cl-GeC turn into magnetic metals, P-GeC becomes a half-metal and H- and B-GeC appear as non-magnetic metals. Although C- and O-GeC remain non-magnetic semiconductors, N-GeC presents the behaviors of a magnetic semiconductor. Work function decreases in H-, B- and N-SiC, reaching a minimum of 3.37 eV in H-GeC, which is 78.9% of the pristine GeC. In the visible light region, redshifts occur in the absorption spectrum of C-GeC , with strong absorption in the wavelength range from 400 to 600 nm. Our analysis shows that the magnetism in semiconducting NM-GeC is attributed to the spinning state of the unbonded electrons of the NM atoms. Our study demonstrates the applications of NM-GeC in spintronics, optoelectronics and photovoltaic cells, and it provides a reference for analyzing magnetism in semiconducting NM materials.

Keywords: non-metal; germanium carbide; absorption energy; work function; absorption spectrum

Citation: Zhang, L.; Cui, Z. Theoretical Study on Electronic, Magnetic and Optical Properties of Non-Metal Atoms Adsorbed onto Germanium Carbide. *Nanomaterials* **2022**, *12*, 1712. https://doi.org/10.3390/nano12101712

Academic Editors: Jihoon Lee and Ming-Yu Li

Received: 17 April 2022
Accepted: 12 May 2022
Published: 17 May 2022

1. Introduction

Graphene with a planar structure has attracted significant attention in academia and industries for its unique mechanical, electrical and thermal properties [1,2]. However, the zero-band gap and difficulties in integration with silicon-based systems hinder the application of graphene in electronics [3], which facilitates the exploration of other alternative two-dimensional (2D) atomic crystals [4–6]. An increasing number of new 2D materials have been investigated by first-principles calculations, including not only single-atom crystals [7,8], but also II–VI group compounds [9], III–V group compounds [10,11] and IV-IV group compounds [12–14]. These 2D materials have shown their advantages in the fields of spintronics [15,16], optoelectronics [17–20], energy conversion [21,22], catalysis [23–26] and gas sensing [27–29].

As the compounds of group IV elements, 2D silicon carbide (SiC) and germanium carbide (GeC) have stable planar honeycomb structures and exhibit similar properties to graphene [30,31]. Both of them are semiconductors whose band gaps are comparable to the energy of water oxidation and reduction [32,33]. Although 2D GeC exhibits excellent compatibility with silicon-based microelectronic devices [34], there are fewer studies on GeC than there are on SiC. To expand the applications of 2D GeC, impurity atoms are injected to modulate physical and chemical properties by doping or adsorption [35,36]. Previous studies on other 2D materials provide many effective analyses for property variations induced by dopants. For example, impurity atoms lead to the redistribution of charge and induce magnetism near the host atoms. The ferromagnetic states in transition metals (TM) atoms of adsorbed 2D materials are caused by the occupation mode of the *d* orbital hybridization of the TM atoms [37,38]. Magnetism in non-metal (NM) doped 2D blue phosphorene is related to the sp^3 orbital hybridization of the NM atoms [39]. In addition, the interaction force between impurity atoms and neighboring atoms adjusts the bandgap of 2D materials and leads to the modulation of the absorption spectrum and emission electron capability [37].

Until now, some progress has been made in studying GeC systems. NM atoms adsorbed onto GeC (NM-GeC), such as 1H-GeC, have been predicted to be promising materials for digital circuits and light-emitting diodes [40]. Surface-functionalized GeC monolayers with F and Cl have demonstrated their advantage in opto-electronic devices for their strong absorption in the near ultraviolet light region [41]. The effective growth of GeC films has been achieved [42]. However, regularity conclusions on GeC systems are still lacking. In this work, nine kinds of NM-GeC structures are constructed based on optimum thermodynamics. The electrical, magnetic and optical properties of NM-GeC are discussed systematically. F-, Cl-, P- and N-GeC exhibit magnetism. H-GeC presents a stronger electron-emitting capacity than other NM-GeC systems. In the absorption spectrum of C-GeC, redshift occurs in the visible light region. These performances expand the applications of NM-GeC in spintronics, optoelectronics and photovoltaic cells. Discussions on the magnetism of NM-GeC provide a reference for other materials of adsorbed 2D NM atoms.

2. Computational Methods and Theoretics

All first-principles calculations were performed with the Vienna Ab initio Simulation Package (VASP) based on density functional theory [43]. The parameterized exchange-correlation interactions were analyzed by the Generalized Gradient Approximation of the Perdew–Burke–Ernzerhof function [44–46]. A basis with a 550 eV cut-off energy of plane-waves was set to achieve high computational accuracy. Pristine 2D GeC was constructed with a $4 \times 4 \times 1$ supercell configuration. To minimize the effect of the interaction between the adatoms, only one non-metal atom was injected, and the corresponding coverage concentration was 3.125%. All the possible adsorption positions were marked in the GeC supercell, as shown in Figure 1a. T_C was above the C atom, T_{Ge} was above the Ge atom, T_H was above the middle of the Ge-C bond and T_B was above the center of the hexagonal structure. A vacuum layer with a height of 20 Å was constructed along the vertical direction of the GeC plane to eliminate the interlayer interaction of periodic structures. The Brillouin zone was sampled by a set of $3 \times 3 \times 1$ Monkhorst–Pack k-point grids [47]. All structures were fully relaxed until the Hellmann–Feynman force on each atom was less than 0.01 eV/Å, and the total energy change converged to 10^{-5} eV/atom or less. Local field effects were considered with random-phase approximation (RPA) [48].

The possibility of each NM-GeC structure was examined by calculating the corresponding adsorption energy,

$$E_{\mathrm{ad}} = E_{\mathrm{NM+GeC}} - (E_{\mathrm{GeC}} + E_{\mathrm{NM}}) \tag{1}$$

where E_{ad} is the adsorption energy of the NM-SiC system. $E_{\mathrm{NM+GeC}}$, E_{GeC} and E_{NM} represent the energies of the final NM-GeC, the original isolated GeC and the isolated NM atom, respectively. A negative E_{ad} indicates that the adsorption process is thermodynamically favorable and that the NM-GeC system is more stable than the original system. However, the most likely structure corresponds to the system with the lowest adsorption energy. Therefore, the adsorption energies were compared at all the possible adsorption positions. The following discussions are all based on the most stable structures.

The adsorption of NM atoms caused the redistribution of charges, leading to changes in optical, electrical and magnetic properties. Charge density differences were introduced to display the charge transfer before and after the adsorption,

$$\Delta\rho = (\rho_{\mathrm{GeC}} + \rho_{\mathrm{NM}}) - \rho_{\mathrm{Total}} \tag{2}$$

where $\Delta\rho$ is the charge density difference (CDD) of the system. ρ_{Total}, ρ_{GeC} and ρ_{NM} represent the charge densities of the non-metal atoms adsorbed onto GeC, of the pristine GeC, and of the isolated non-metal atom, respectively.

The redistribution of charge implies that new covalence bonds were formed between the adatom and the substrate atoms, which led to the change in the ability of the system to bind electrons. The work function was calculated to evaluate the electron-emitting capacity of NM-GeC,

$$W = e\phi - E_{\mathrm{F}} \tag{3}$$

where W is the work function, e is the charge of an electron, ϕ is the electrostatic potential in the vacuum near the surface and E_{F} is the Fermi level. The smaller that the work function is, the stronger that the electron-emitting capacity is.

As important optical parameter coefficients, the absorption coefficients of the pristine and NM-GeC were investigated by frequency-dependent dielectric response theory [49,50],

$$\alpha(\omega) = \sqrt{2}\omega\left[\frac{\sqrt{\varepsilon_1^2(\omega)+\varepsilon_2^2(\omega)}-\varepsilon_1(\omega)}{2}\right]^{1/2} \tag{4}$$

where ω represents the photon frequency, and $\varepsilon_1(\omega)$ and $\varepsilon_2(\omega)$ are the real and imaginary parts of the complex dielectric function, respectively.

Spin-polarized charges were introduced to the analysis of the magnetic properties of the pristine GeC and NM-GeC,

$$\rho = \rho_{\mathrm{up}} - \rho_{\mathrm{down}} \tag{5}$$

where ρ is the spin-polarized charge density (SPCD), and ρ_{up} and ρ_{down} represent the up and down-spin-polarized charge densities. When the electronic states of the spin-up and spin-down-polarized charges were asymmetric, the corresponding NM-GeC system exhibited magnetism.

3. Results and Discussion

The crystal structure of the pristine two-demensional GeC is depicted in Figure 1a. GeC is an indirect semiconductor with a bandgap of 2.3 eV. The conduction band minimum (CBM) and the valence band maximum (VBM) are located at points Γ and X, respectively, as shown in Figure 1b. According to the density of state (DOS) in Figure 1c, the Ge atom is the main contributor to the CBM of GeC, and the C atom is the main contributor to the valence band maximum (VBM). Considering the symmetry of the electronic states of spin-up and spin-down, the pristine GeC is non-magnetic.

The adsorption energies of NM-GeC were compared at the four possible symmetric positions. The adsorption energies with the most stable structures are listed in Table 1, and their top and side views of the charge density difference (CDD) are depicted in Figure 2. It can be seen that all these NM-GeC systems exhibit high thermodynamic stability. The most stable adsorption positions differ with NM adatoms. The F and Cl atoms prefer to adsorb at site T_{Ge}, the H and P atoms prefer site T_{C} and the B, C, N, O and S atoms prefer site T_{H}. The adsorption heights (D) were 1.11 Å (H), 1.11 Å (B), 0.54 Å (C), 0.91 Å (N), 1.19 Å (O), 1.82 Å (F), 1.62 Å (P), 1.81 Å (S) and 2.26 Å (Cl). For the NM-GeC systems with the same adsorption position, the lower that the adsorption energy was, the shorter that the adsorption height was and the stronger that the interaction between the adatom and the substrate atoms was. In B-, C-, N-, O-, F-, S- and Cl-GeC, the planar structure of 2D GeC was deformed for these strong interactions. Especially in C-GeC, the substrate C atom was sucked out of the GeC plane. Similar adatom-induced reconstructions of the host material were found in the NM-GaN monolayer [51].

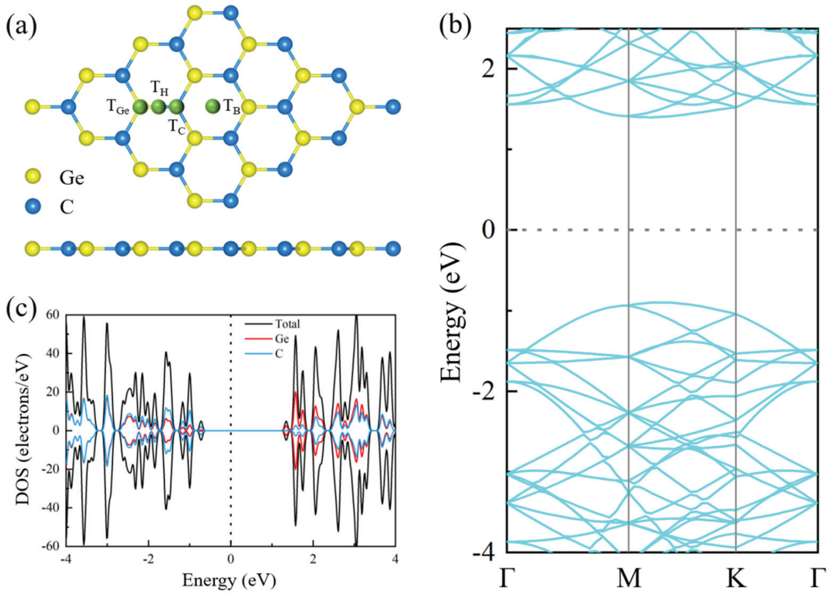

Figure 1. (**a**) The crystal structure, (**b**) the energy band structure and (**c**) the density of states (DOS) of pristine 2D GeC. T_C is above the C atom, T_{Ge} is above the Ge atom, T_H is above the Ge-C bond and T_B is above the center of the hexagonal structure. The spin-up component is above the Brillouin region, whereas the spin-down component is below the Brillouin region. The Fermi level is set to zero and is represented by a vertical black dotted line.

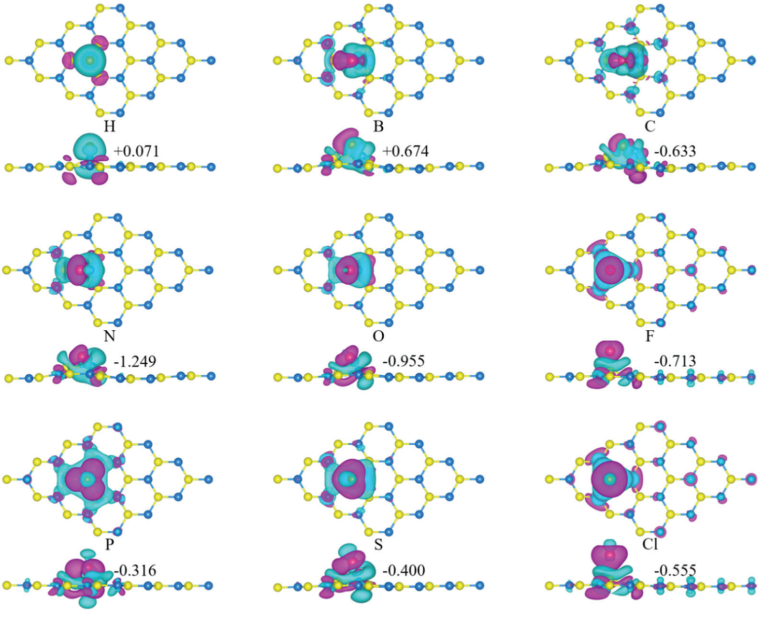

Figure 2. The charge density differences in the non-metal atoms adsorbed into GeC systems. Blue denotes the depletion of electrons, whereas purple represents the accumulation of electrons. The isovalue is set to 0.001 e/Å^3. The blue, yellow and red balls are the C, Ge and NM atoms, respectively.

Table 1. The adsorption energy (E_{ad}), charge transferred from the adatom to the GeC substrate (C), magnetic moment (M_{total}), bandgap (E_g) and the adsorption height (d) of the non-metal atoms adsorbed into GeC systems.

Adsorption Atom	Adsorption Site	E_{ad} (eV)	C (e)	M_{total} (μ_B)	E_g (eV)	d (Å)
H	T_C	−3.252	+0.071	0	0	1.11
B	T_H	−5.416	+0.674	0	0	1.11
C	T_H	−9.343	−0.633	0	0.71	0.54
N	T_H	−7.929	−1.249	1	0.28	0.91
O	T_H	−5.973	−0.955	0	1.83	1.19
F	T_{Ge}	−4.583	−0.713	0.55	0	1.82
P	T_C	−4.089	−0.316	1	0	1.62
S	T_H	−4.092	−0.400	0	1.90	1.81
Cl	T_{Ge}	−2.933	−0.555	0.55	0	2.26

Charge transfer occurs between the NM adatom and the substrate atoms. The NM-GeC systems adsorbed at the same position were similar in their distributions of CDD. The contributions of the same substrate atoms were equal or equidistant to the adsorbed atoms. The amount of charge transferred was determined by the relative electronegativity between the adatoms and the substrate atoms. The detailed amount of charge transferred from the adatom to the GeC was calculated by Bader charge [52,53], as +0.071|e| (H), +0.674|e| (B), −0.633|e| (C), −1.249|e| (N), −0.955|e| (O), −0.713|e| (F), −0.316|e| (P), −0.400|e| (S) and −0.555|e| (Cl). Positive values indicate charge transfer from the adatoms to the GeC, whereas negative values imply charge transfer from the GeC to the adatoms. In all the NM-GeC, only H and B atoms acted as charge donors, whereas other NM atoms acted as charge acceptors. The F and Cl atoms with stronger electronegativity had a greater influence on the substrate atoms, whose charge transfer occurred not only with the atoms near the adatoms, but also with the atoms farther away. For the NM atoms adsorbed at T_{Ge}, the F atoms attracted more charge than the Cl atoms due to stronger electronegativity.

The energy band structures and the DOS of the NM-GeC systems are shown in Figures 3 and 4, respectively. It can be seen that the electronic states of the spin-up and spin-down exhibit asymmetry in N-, F-, P- and Cl-GeC, suggesting that the corresponding GeC systems were magnetic. P-GeC exhibited half-metallic properties, in which the spin-down component was metallic and the spin-up component was semiconducting. F- and Cl-GeC became magnetic metals, whose spin-up and spin-down components were asymmetric and both metallic. H- and B-GeC turned into non-magnetic metals. The C-, N-, O-, and S-GeC systems were still semiconductors, with band gaps of 0.71 eV (C), 0.28 eV (N), 1.83 eV (O) and 1.90 eV (S). Only the N-GeC system showed magnetism.

The distribution of the spin-polarized charge densities (SPCDs) were further analyzed in the N-, F-, P- and Cl-GeC systems, as depicted in Figure 5. It can be seen that the distribution of the SPCD also shows similarities associated with the adsorption position. The same adatoms at equal distances made the same contributions to system magnetism, and the contributions of the substrate atoms should not be neglected. The distribution of the spin-polarized charge densities was extended into a large space, not just into the substrate atoms nearby, but also into those farther away, suggesting a long-range magnetic coupling interaction. This long-range magnetization is similar to that in the NM doped SiC [54].

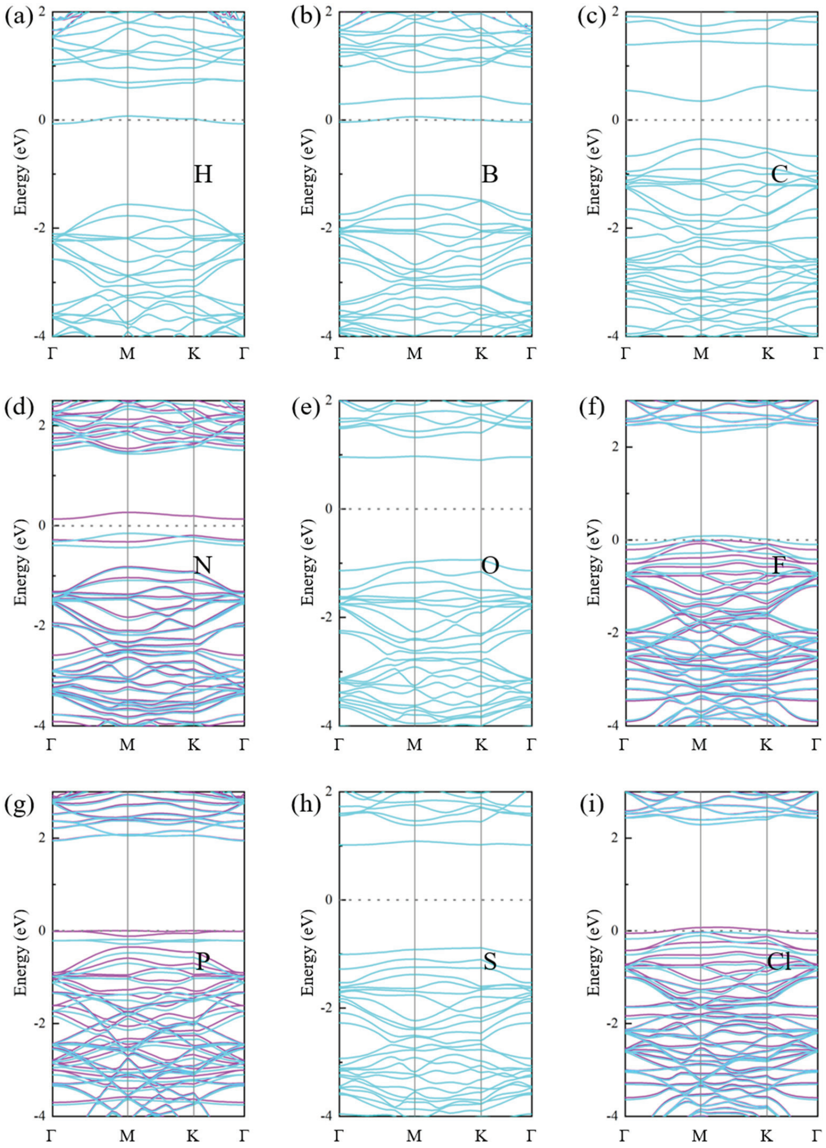

Figure 3. The band structures of the non-metal atoms adsorbed into GeC systems: (**a**) H-GeC, (**b**) B-GeC, (**c**) C-GeC, (**d**) N-GeC, (**e**) O-GeC, (**f**) F-GeC, (**g**) P-GeC, (**h**) S-GeC, (**i**) Cl-GeC. The blue and purple lines indicate the spin-up and the spin-down components of the energy levels. The Fermi level is shifted to zero.

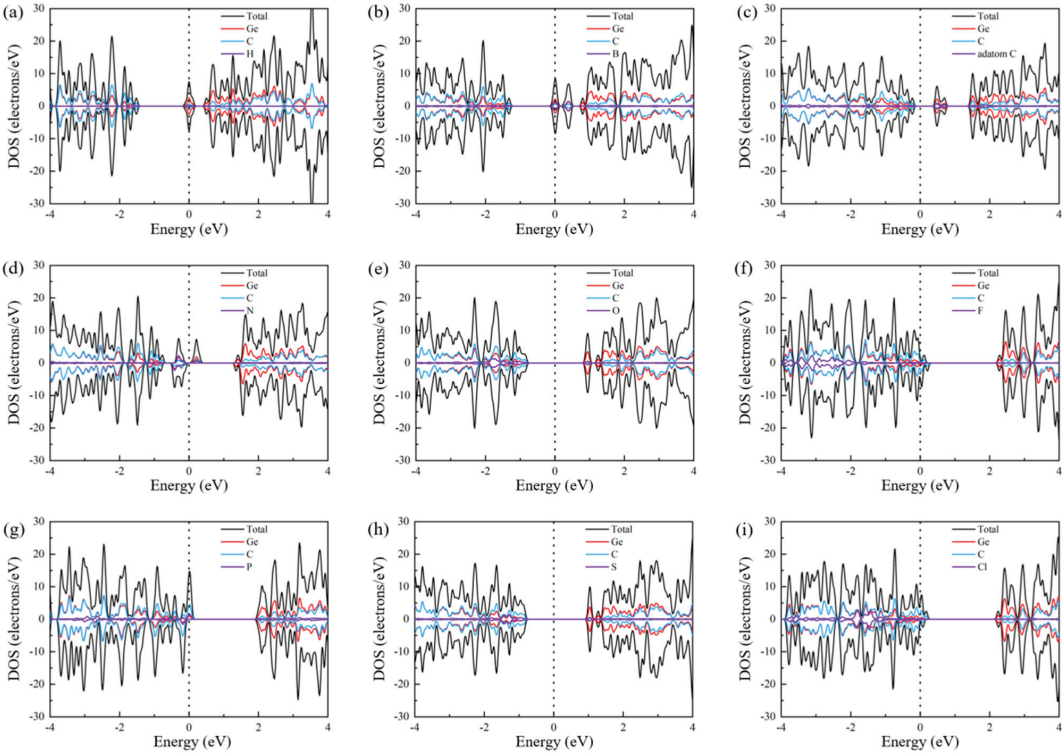

Figure 4. Density of states of (**a**) H-GeC, (**b**) B-GeC, (**c**) C-GeC, (**d**) N-GeC, (**e**) O-GeC, (**f**) F-GeC, (**g**) P-GeC, (**h**) S-GeC and (**i**) Cl-GeC. The spin-up component is above the Brillouin region, the spin-down component is below the Brillouin region and the Fermi level is set to zero and is represented by a vertical black dotted line.

The quantitative calculation of the magnetic moment was performed by the SPCD, and it is listed in Table 1. For the metallic NM-GeC, the corresponding magnetic moments were 0 μ_B (H), 0 μ_B (B), 0.55 μ_B (F) and 0.55 μ_B (Cl). For the semiconducting NM-GeC, they were 0 μ_B (C), 1 μ_B (N), 0 μ_B (O), 1 μ_B (P) and 0 μ_B (S). It can be seen that the adatoms with similar SPCD distributions responded to the same magnetic moment, such as N and P; O and S; and F and Cl.

The magnetism in the semiconducting NM-GeC can be explained by the orbital hybridization of NM atoms [39]. In the C-, N- and P-GeC systems, there occurred an sp^3 orbital hybridization in the NM atoms, forming four orbits with similar energies. The valence electrons of NM atoms occupied the four orbits with the same spinning direction according to Hund's rule and then formed four covalent bonds with the nearest IV group substrate atoms. The spinning state of the unbonded electr\ons of the NM atom determines the magnetism of NM-GeC. The remaining spinning electrons were 0 (C), 1 (N) and 1 (P), and the corresponding magnetic moments were 0 μ_B (C), 1 μ_B (N) and 1 μ_B (P). In the O-, and S-GeC systems, only two covalent bonds were constructed between the NM atoms and the nearest substrate atoms. The corresponding NM-GeC systems exhibited non-magnetic behavior. Although the number of covalent bonds was different, the formation of covalence bonds between the NM atom and the neighboring atoms was identical to construct more stable structures. Magnetism induced by NM adatoms expanded the application of 2D GeC in nano-spintronics devices.

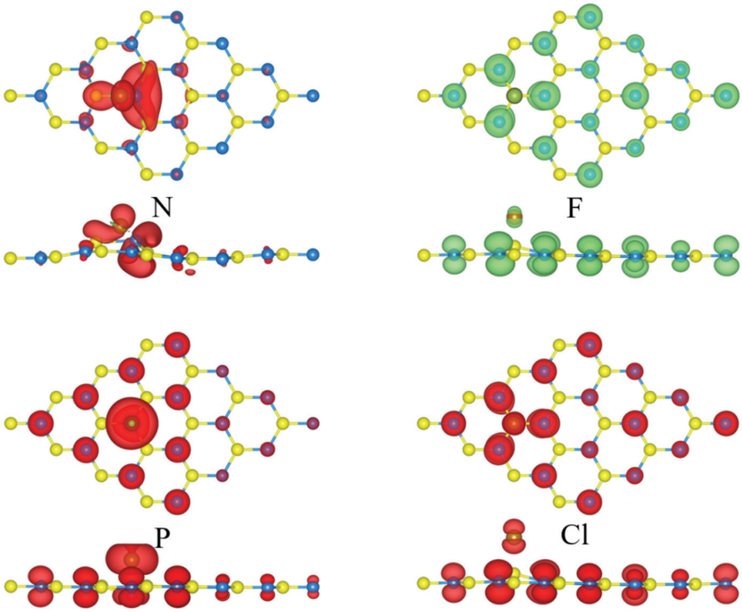

Figure 5. The spin-polarized charge densities of the non-metal atoms adsorbed into the GeC system. The green and red areas represent the contribution of the spin-up and spin-down charges, respectively. The isovalue is set to 0.001 e/ Å^3.

The work function of the pristine GeC and the NM-GeC are depicted in Figure 6. The work function of GeC is 4.26 eV, which is similar to the value of conventional 2D field electron emission devices [55–58]. With the adsorption of NM atoms, the work functions of H-, B- and N-GeC were decreased, reaching a minimum of 3.37 eV in H-GeC. This indicates that less energy was required for electrons to escape to the vacuum level in NM-GeC. The corresponding electron-emitting capacity was enhanced by the adsorption of NM atoms.

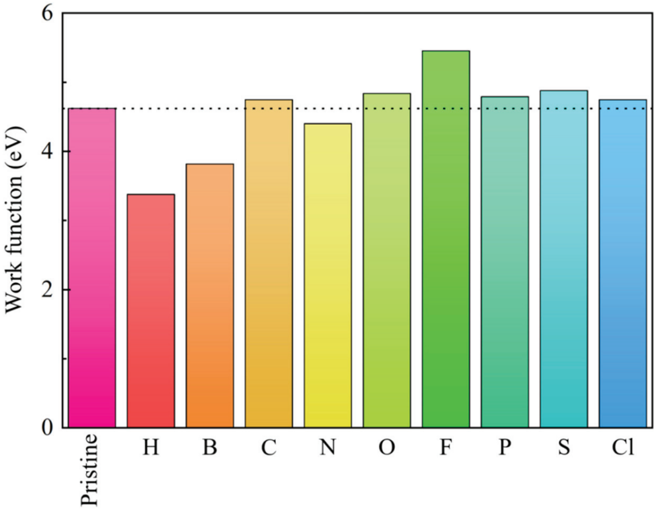

Figure 6. The work function of the intrinsic GeC and the NM-GeC systems.

The optical spectra of the pristine GeC and the NM-GeC were compared with the solar spectrum [59], as shown in Figure 7. The absorption spectrum of the pristine GeC extended from the ultraviolet to the visible light regions. The strongest absorption peak was located at a wavelength of 120 nm, with an absorption coefficient of 1.03×10^6 cm^{-1}, and strong visible light absorption occurred in the range of 400 to 600 nm. In the ultraviolet light region, the absorption coefficients of NM-GeC decreased. In the visible light region, a blueshift occurred in the absorption peaks in H-GeC, and a redshift occurred in that of C-GeC, with a strong absorption peak at 530 nm. Although applications in photocatalysts are limited by the bandgap, the 2D NM-GeC shows its fantastic advantages as a photovoltaic cell and ultraviolet photoelectric detector.

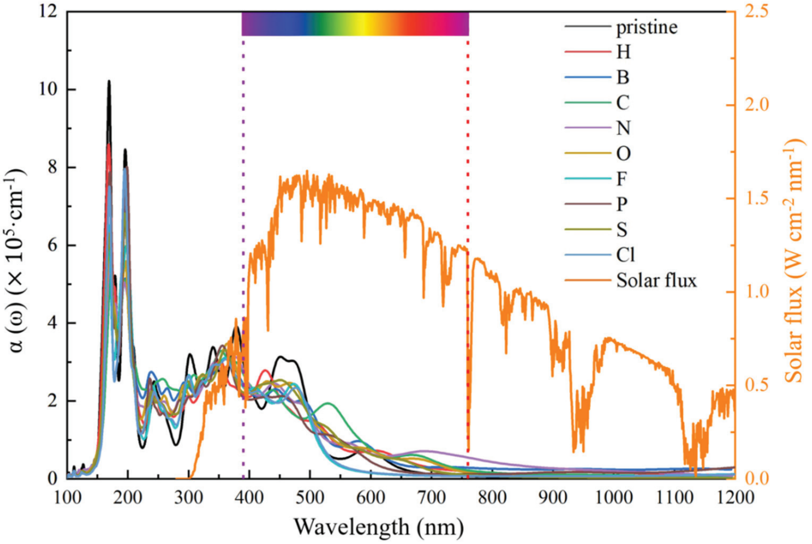

Figure 7. The absorption spectra of the pristine GeC and the NM-GeC systems.

4. Conclusions

Nine NM-atoms adsorbed into GeC systems were constructed based on the principle of favorable thermodynamics. The most stable adsorption positions were distinguished with NM atoms. F and Cl atoms were more likely to absorb at site T_{Ge}, H and P atoms preferred site T_C, and the B, C, N, O and S atoms preferred site T_H. C-GeC exhibited the strongest adsorption and the shortest adsorption height. The adsorption of NM atoms induced variations in the properties of NM-GeC. F- and Cl-GeC became magnetism metals, P-GeC turned into a half-metal and H- and B-GeC systems exhibited the properties of non-magnetic metals. C- and O-GeC were non-magnetic semiconductors, whereas N-GeC appeared as a magnetic semiconductor. The work function decreased in the H-, B- and N-SiC systems and achieved a minimum in the H-GeC system. The absorption spectrum of C-GeC redshifted in the visible light region and had a strong absorption peak at 530 nm. Magnetism in semiconducting NM-GeC is explained by the spinning states of the unbonded electrons of the NM atoms. After the covalence electrons of NM atoms formed covalent bonds with adjacent IV group atoms, the remaining spinning electrons determined the magnetism of the NM-GeC system. These electrical, magnetic and optical properties caused by the adsorption of non-metal atoms extend the application of 2D GeC, especially in field electron-emitting, spin electronics, photovoltaic cells and ultraviolet photoelectric detectors. Our discussion on the magnetism of semiconducting NM-GeC provides a reference for other NM 2D materials.

Author Contributions: Conceptualization, L.Z. and Z.C.; methodology, L.Z. and Z.C.; software, L.Z. and Z.C.; validation, L.Z. and Z.C.; formal analysis, L.Z.; investigation, L.Z.; resources, L.Z. and Z.C.; data curation, L.Z. and Z.C.; writing—original draft preparation, L.Z.; writing—review and editing, L.Z. and Z.C.; visualization, L.Z. and Z.C.; supervision, Z.C.; project administration, L.Z.; funding acquisition, L.Z. All authors have read and agreed to the published version of the manuscript.

Funding: This research was funded by [Lin Zhang] grant number [11904285], and the APC was funded by [the National Natural Science Foundation of China].

Institutional Review Board Statement: Not applicable.

Informed Consent Statement: Not applicable.

Data Availability Statement: Not applicable.

Acknowledgments: This work was supported by the National Natural Science Foundation of China (No. 11904285).

Conflicts of Interest: The authors declare no conflict of interest.

References

1. Novoselov, K.S.; Geim, A.K.; Morozov, S.V.; Jiang, D.; Katsnelson, M.I.; Grigorieva, I.V.; Dubonos, S.V.; Firsov, A.A. Two-dimensional gas of massless Dirac fermions in graphene. *Nature* **2005**, *438*, 197–200. [CrossRef] [PubMed]
2. Li, D.; Kaner, R.B. Graphene-based materials. *Science* **2008**, *320*, 1170–1171. [CrossRef] [PubMed]
3. Krishnamurthy, M.; Drucker, J.S.; Challa, A. Epitaxial growth and characterization of $Ge_{1-x}C_x$ alloys on Si (100). *J. Appl. Phys.* **1995**, *78*, 7070–7073. [CrossRef]
4. Mélinon, P.; Masenelli, B.; Tournus, F.; Perez, A. Playing with carbon and silicon at the nanoscale. *Nat. Mater.* **2007**, *6*, 479–490. [CrossRef]
5. Pino-Rios, R.; Chigo-Anota, E.; Shakerzadeh, E.; Cardenas-Jiron, G. $B_{12}N_{12}$ cluster as a collector of noble gases: A quantum chemical study. *Phys. E.* **2020**, *115*, 113697. [CrossRef]
6. Miró, P.; Audiffred, M.; Heine, T. An atlas of two-dimensional materials. *Chem. Soc. Rev.* **2014**, *43*, 6537–6554. [CrossRef]
7. Cui, Z.; Wang, M.J.; Lyu, N.; Zhang, S.; Ding, Y.C.; Bai, K.F. Electronic, magnetism and optical properties of transition metals adsorbed puckered arsenene. *Superlattices Microstruct.* **2021**, *152*, 106852. [CrossRef]
8. Sun, M.; Tang, W.; Li, S.; Chou, J.-P.; Hu, A.; Schwingenschlögl, U. Molecular doping of blue phosphorene: A first-principles investigation. *J. Phys. Condens. Matter* **2019**, *32*, 055501. [CrossRef] [PubMed]
9. Wang, Q.H.; Kalantar-Zadeh, K.; Kis, A.; Coleman, J.N.; Strano, M.S. Electronics and optoelectronics of two-dimensional transition metal dichalcogenides. *Nat. Nanotechnol.* **2012**, *7*, 699–712. [CrossRef]
10. Cui, Z.; Wang, X.; Ding, Y.C.; Li, E.L.; Bai, K.F.; Zheng, J.S.; Liu, T. Adsorption of CO, NH_3, NO, and NO_2 on pristine and defective g-GaN: Improved gas sensing and functionalization. *Appl. Surf. Sci.* **2020**, *530*, 147275. [CrossRef]
11. Sun, M.L.; Chou, J.P.; Ren, Q.; Zhao, Y.; Yu, J.; Tang, W. Tunable Schottky barrier in van der Waals heterostructures of graphene and g-GaN. *Appl. Phys. Lett.* **2017**, *110*, 173105. [CrossRef]
12. Ferdous, N.; Islam, S.; Park, J.; Hashimoto, A. Tunable electronic properties in stanene and two dimensional silicon-carbide heterobilayer: A first principles investigation. *AIP Adv.* **2019**, *9*, 025120. [CrossRef]
13. Ravindra, P.; Rerat, M.; Darrigan, C.; Causa, M. A theoretical study of stability, electronic, and optical properties of GeC and SnC. *J. Appl. Phys.* **2000**, *88*, 6462–6466.
14. Ghojavand, A.; Hashemifar, S.J.; Ahmadpour, M.T.; Shapeev, A.V.; Alhaji, A.; Hassanzada, Q. Ab initio analysis of structural and electronic properties and excitonic optical responses of eight Ge-based 2D materials. *J. Appl. Phys.* **2020**, *127*, 214301. [CrossRef]
15. Li, D.; Li, S.; Zhong, C.; He, J. Tuning magnetism at the two-dimensional limit: A theoretical perspective. *Nanoscale* **2021**, *13*, 19812–19827. [CrossRef]
16. Yuan, J.; Cai, Y.; Shen, L.; Xiao, Y.; Ren, J.-C.; Wang, A.; Feng, Y.P.; Yan, X. One-dimensional thermoelectrics induced by Rashba spin-orbit coupling in two-dimensional BiSb monolayer. *Nano Energy* **2018**, *52*, 163–170. [CrossRef]
17. Komsa, H.; Kotakoski, J.; Kurasch, S.; Lehtinen, O.; Kaise, U.; Krasheninnikov, A. Two-dimensional transition metal dichalcogenides under electron irradiation: Defect production and doping. *Phys. Rev. Lett.* **2012**, *109*, 035503. [CrossRef]
18. Sun, M.L.; Schwingenschlögl, U. Unique omnidirectional negative Poisson's ratio in δ-phase carbon monocalclgenides. *J. Phys. Chem. C* **2021**, *125*, 4133–4138. [CrossRef]
19. Bratschitsch, R. Optoelectronic devices: Monolayer diodes light up. *Nat. Nanotechnol.* **2014**, *9*, 247–248. [CrossRef]
20. Sun, M.L.; Yi, L.; Yuan, Y.; Schwingenschlögl, U. Ultrahigh carrier mobility in the two dimensional semiconductors B_8Si_4, B_8Ge_4, and B_8Sn_4. *Chem. Mater.* **2021**, *33*, 6475–6483. [CrossRef]
21. Sun, M.L.; Schwingenschlögl, U. δ-CS: A direct-band-gap semiconductor combining auxeticity, ferroelasticity, and potential for high-efficiency solar cells. *Phys. Rev. Appl.* **2020**, *14*, 044015. [CrossRef]
22. Pospischil, A.; Furchi, M.M.; Mueller, T. Solar-energy conversion and light emission in an atomic monolayer p–n diode. *Nat. Nanotechnol.* **2014**, *9*, 257–261. [CrossRef] [PubMed]

23. Sun, M.; Schwingenschlögl, U. B_2P_6: A Two-Dimensional Anisotropic Janus Material with Potential in Photocatalytic Water Splitting and Metal-Ion Batteries. *Chem. Mater.* **2020**, *32*, 4795–4800. [CrossRef]
24. Luo, Y.; Ren, C.; Xu, Y.; Yu, J.; Wang, S.; Sun, M.L. A first principles investigation on the structural, mechanical, electronic, and catalytic properties of biphenylene. *Sci. Rep.* **2021**, *11*, 19008. [CrossRef] [PubMed]
25. Wang, S.; Ren, C.D.; Tian, H.Y.; Yu, J.; Sun, M. MoS_2/ZnO van der Waals heterostructure as a high-efficiency water splitting photocatalyst: A first-principles study. *Phys. Chem. Chem. Phys.* **2018**, *20*, 13394–13399. [CrossRef]
26. Cui, Z.; Bai, K.; Ding, Y.; Wang, X.; Li, E.; Zheng, J.; Wang, S. Electronic and optical properties of janus MoSSe and ZnO vdWs heterostructures. *Superlattices Microstruct.* **2020**, *140*, 106445. [CrossRef]
27. Sun, S.Y.; Hussain, T.; Zhang, W.; Karton, A. Blue phosphorene monolayers as potential nano sensors for volatile organic compounds under point defects. *Appl. Surf. Sci.* **2019**, *486*, 52–57. [CrossRef]
28. Kooti, M.; Keshtkar, S.; Askarieh, M.; Rashidi, A. Progress toward a novel methane gas sensor based on SnO_2 nanorods-nanoporous graphene hybrid. *Sens. Actuator B Chem.* **2019**, *281*, 96–106. [CrossRef]
29. Abdullah, Q.; Yam, F.; Hassan, Z.; Bououdina, M. Hydrogen gas sensing performance of GaN nanowires-based sensor at low operating temperature. *Sens. Actuators B Chem.* **2014**, *204*, 497–506. [CrossRef]
30. Peng, Q.; Liang, C.; Ji, W.; De, S. A first-principles study of the mechanical properties of g-GeC. *Mech. Mater.* **2013**, *64*, 135–141. [CrossRef]
31. Pan, L.; Liu, H.; Wen, Y.; Tan, X.; Lv, H.; Shi, J.; Tang, X. First-principles study of monolayer and bilayer honeycomb structures of group-IV elements and their binary compounds. *Phys. Lett. A* **2010**, *375*, 614–619. [CrossRef]
32. Gao, X.; Shen, Y.; Ma, Y.; Wu, S.; Zhou, Z. A water splitting photocatalysis: Blue phosphorus/g-GeC van der Waals heterostructure. *Appl. Phys. Lett.* **2019**, *114*, 093902. [CrossRef]
33. Chen, X.; Zhang, H.; Zhang, Y. Transition metal doped graphene-like germanium carbide: Screening of high performance electrocatalysts for oxygen reduction, oxygen evolution, or hydrogen evolution. *Colloids Surf. A Physicochem. Eng. Asp.* **2021**, *630*, 127628. [CrossRef]
34. Guilhon, I.; Teles, L.K.; Marques, M.; Pela, R.; Bechstedt, F. Influence of structure and thermodynamic stability on electronic properties of two-dimensional SiC, SiGe, and GeC alloys. *Phys. Rev. B* **2015**, *92*, 075435. [CrossRef]
35. Zhao, Q.; Xiong, Z.; Qin, Z.; Chen, L.; Wu, N.; Li, X. Tuning magnetism of monolayer GaN by vacancy and nonmagnetic chemical doping. *J. Phys. Chem. Solids* **2015**, *91*, 1–6. [CrossRef]
36. Cui, Z.; Luo, Y.; Yu, J.; Xu, Y. Tuning the electronic properties of $MoSi_2N_4$ by molecular doping: A first principles investigation. *Phys. E Low-Dimens. Syst. Nanostruct.* **2021**, *134*, 114873. [CrossRef]
37. Sun, M.L.; Ren, Q.Q.; Zhao, Y.M.; Chou, J.P.; Yu, J.; Tang, W.C. Electronic and magnetic properties of 4D series transition metal substituted graphene: A first-principles study. *Carbon* **2017**, *120*, 265–273. [CrossRef]
38. Santos, E.; Ayuela, A.; Sanchez-Portal, D. First-principles study of substitutional metal impurities in graphene: Structural, electronic and magnetic properties. *New J. Phys.* **2010**, *12*, 053012. [CrossRef]
39. Sun, M.; Tang, W.; Ren, Q.; Wang, S.-K.; Yu, J.; Du, Y. A first-principles study of light non-metallic atom substituted blue phosphorene. *Appl. Surf. Sci.* **2015**, *356*, 110–114. [CrossRef]
40. Sahin, H.; Cahangirov, S.; Topsakal, M.; Bekaroglu, E.; Akturk, E.; Senger, R.T.; Ciraci, S. Honolayer honeycomb structures of group-IV elements and III–V binary compounds: First-principles calculations. *Phys. Rev. B* **2009**, *80*, 155453. [CrossRef]
41. Tuan, V.V.; Nguyen, T.T.; Duy, P.; Hoat, D.M.; Nguyen, T.T.B.; Tong, H.D.; Hoi, B.D.; Nguyen, C.V.; Phuc, H.V.; Nguyen, N.H. Surface functionalization of GeC monolayer with F and Cl: Electronic and optical properties. *Superlattices Microstruct.* **2020**, *137*, 106359.
42. Behzad, S. Direct to indirect band gap transition in two-dimensional germanium carbide through Si substitution. *Results Phys.* **2019**, *13*, 102306. [CrossRef]
43. Kresse, G.; Furthmüller, J. Efficiency of ab-initio total energy calculations for metals and semiconductors using a plane-wave basis set. *Comput. Mater. Sci.* **1996**, *6*, 15–50. [CrossRef]
44. Kresse, G.; Furthmüller, J. Efficient iterative schemes for ab initio total-energy calculations using a plane-wave basis set. *Phys. Rev. B* **1996**, *54*, 1169. [CrossRef]
45. Kresse, G.; Joubert, D. From ultrasoft pseudopotentials to the projector augmented-wave method. *Phys. Rev. B* **1999**, *59*, 1758. [CrossRef]
46. Perdew, J.P.; Burke, K.; Ernzerhof, M. Generalized gradient approximation made simple. *Phys. Rev. Lett.* **1996**, *77*, 3865. [CrossRef]
47. Grimme, S.; Antony, J.; Ehrlich, S.; Krieg, H. A consistent and accurate ab initio parametrization of density functional dispersion correction (DFT-D) for the 94 elements H-Pu. *J. Chem. Phys.* **2010**, *132*, 154104–154119. [CrossRef]
48. Hybertsen, M.S.; Louie, S.G. Electron correlation in semiconductors and insulators: Band gaps and quasiparticle energies. *Phys. Rev. B* **1986**, *34*, 5390. [CrossRef]
49. Toll, J.S. Causality and the Dispersion Relation: Logical Foundations. *Phys. Rev.* **1956**, *104*, 1760. [CrossRef]
50. Fox, A.M. *Optical Properties of Solids*; Oxford University Press: Oxford, UK, 2001; Volume 3.
51. Tang, W.; Sun, M.; Yu, J.; Chou, J.-P. Magnetism in non-metal atoms adsorbed graphene-like gallium nitride monolayers. *Appl. Surf. Sci.* **2018**, *427*, 609–612. [CrossRef]
52. Henkelman, G.; Arnaldsson, A.; Jónsson, H. A fast and robust algorithm for Bader decomposition of charge density. *Comput. Mater. Sci.* **2005**, *36*, 354–360. [CrossRef]

53. Sanville, E.; Kenny, S.D.; Smith, R.; Henkelman, G. Improved grid-based algorithm for Bader charge allocation. *J. Comput. Chem.* **2007**, *28*, 899–908. [CrossRef] [PubMed]
54. Zhang, L.; Cui, Z. Electronic, Magnetic, and Optical Performances of Non-Metals Doped Silicon Carbide. *Front. Chem.* **2022**, *10*, 898174. [CrossRef] [PubMed]
55. Cai, Y.; Zhang, G.; Zhang, Y.-W. Layer-dependent Band Alignment and Work Function of Few-Layer Phosphorene. *Sci. Rep.* **2014**, *4*, 6677. [CrossRef]
56. Yu, Y.-J.; Zhao, Y.; Ryu, S.; Brus, L.E.; Kim, K.S.; Kim, P. Tuning the Graphene Work Function by Electric Field Effect. *Nano Lett.* **2009**, *9*, 3430–3434. [CrossRef]
57. Jiao, N.; He, C.; Zhang, C.X.; Peng, X.; Zhang, K.W.; Sun, L.Z. Modulation effect of hydrogen and fluorine decoration on the surface work function of BN sheets. *AIP Adv.* **2012**, *2*, 022125. [CrossRef]
58. Soo, H.C.; Zhang, S.L.; Woo, C.Y. Layer-number-dependent work function of MoS_2 nanoflakes. *J. Korean Phys. Soc.* **2014**, *64*, 1550–1555.
59. The AM 1.5G Spectrum was Taken from the NREL Website. Available online: http://rredc.nrel.gov/solar/spectra/am1.5 (accessed on 1 January 2003).

nanomaterials

Article

A Simple Grinding Method for Preparing Ultra-Thin Boron Nanosheets

Haoran Wang [1], Zuxin Sun [1], Zuoshan Wei [2] and Yuying Wu [1,*]

[1] Key Laboratory of Liquid-Solid Structure Evolution and Processing of Materials, Ministry of Education, Shandong University, Jinan 250061, China; whr15706442929@163.com (H.W.); sunnyzx199207@gmail.com (Z.S.)
[2] Shandong Key Laboratory of Advanced Aluminum Materials and Technology, Binzhou Institute of Technology, Binzhou 256600, China; 15376251006@163.com
* Correspondence: wuyuying@sdu.edu.cn

Abstract: The preparation of boron nanosheets has very strict requirements of the preparation environment and substrate. In this work, the boron nanosheets were tried to prepare by the grinding method, using β-B alloy with stable chemical properties and large crystal plane spacing. Its morphology and chemical bonds of boron nanosheets were analyzed by scanning microscope (SEM), transmission microscope (TEM), and X-ray photoelectron spectroscopy (XPS). The results show that the two-dimensional boron nanosheets can be prepared from β-B powder by the grinding method. There are very few B-O bonds in boron particles, and the B-B bonds are principally dominant. In addition to a few B-O bonds, including some B-B bonds change to B_6O bonds which are not completely oxidized, indicating that boron has certain oxidation resistance.

Keywords: boron; nanosheet; microstructure; nanocrystalline materials

Citation: Wang, H.; Sun, Z.; Wei, Z.; Wu, Y. A Simple Grinding Method for Preparing Ultra-Thin Boron Nanosheets. *Nanomaterials* **2022**, *12*, 1784. https://doi.org/10.3390/nano12111784

Academic Editor: Jihoon Lee

Received: 15 April 2022
Accepted: 20 May 2022
Published: 24 May 2022

1. Introduction

Since boron nanosheets [1] have good chemical and physical properties, they can be used in medicine, aerospace, nuclear energy, electronic transmission, and other fields. At present, due to the easy oxidation of boron nanosheets and the high cost of the bottom-up preparation method, it needs very harsh synthesis conditions, ultra-high vacuum degrees, and sensitive temperature change. Graphene has the corresponding bulk phase layered structure in nature, and its monolayer structure can be easily analyzed. Geim [2] successfully prepared the monolayer graphene in 2004 by using a simple mechanical stripping method. However, boron has strong covalent bonds both in and out of the plane, and, thus, it is impossible to obtain monolayer structures directly through mechanical stripping.

As early as 1997, Boustani [3] calculated by the first principles that the pentagram and hexagram composed of boron atoms could be used as the basic units to form quasiplanar structures, and it was the first theoretical prediction that the monolith boron could stably exist. Subsequently, the Lau research team calculated and predicted that monolayer boron nanosheets could stably exist in the form of curly triangular lattices [4]. Yakobson [5], Zhao [6] and Gao [7] et al. calculated results showing that the monolayer boron nanosheets can be grown from MgB_2 on the Ag (111) and Au (111) substrates, providing the preparation direction and theoretical support for experimental preparation of borylene [8]. Mannix [9] prepared boron nanosheets with an atomic thickness on the Ag surface under ultra-high vacuum conditions. Xu [10] explored the porous monolith of few-layered boron nitride for effective water cleanup. Feng [11] used molecular beam epitaxy (MBE) to grow boron sheets on Ag (111) surface under ultra-high vacuum (UHV) conditions and successfully obtained 2D boron sheets.

In this study, boron nanosheets were prepared by grinding β-B alloy with stable chemical properties, large size, and large intercellular space. β-B is obtained by extraction of Cu-5B alloy.

2. Experiment and Discussion

First, the melt reaction method was used to obtain a Cu-5B alloy ingot. The ingot was cut into small pieces and put into a centrifugal tube. The Cu-5B alloy strips were obtained by using a single-roll cooling device (Melting temperature 1500 °C, rotating speed 1800 r/min). The obtained alloy strips were first corroded by nitric acid and the boron powder was obtained by vacuum drying. Then, the grinding was carried out using an agate mortar for 2 h.

Figure 1 shows the images of boron powder before and after grinding. It could be seen that boron mainly exists as some rod-shaped and massive boron particles (Figure 1a). Figure 1b,c show EDS analysis of boron particles, which shows a boron atomic ratio of 99%, so it can be considered that the boron particles before grinding are relatively pure boron. As can be seen in Figure 1d, after grinding, some boron particles in the boron powder changed from block to sheets, and the thickness of the boron nanosheets reached nanometer level. Compared with the microcrystals before grinding, the thickness of boron nanosheets is decreased significantly, indicating that this method can be used to prepare the boron nanosheets. As shown in Figure 1e XRD spectrum of boron nanosheets after grinding. The XRD pattern of the sample is shown in the figure, with black brackets marking the crystal face of β-B. The lattice constants of β -b are as follows: A = B = 10.952 Å, C = 23.824 Å (according to PDF85-0409) [12]. MALDI-TOF-MS is used to detect the stable unit of boron. The result in Figure 1f shows that the relative atomic mass of 453.36 possesses the highest relative intensity, corresponding to B42 (B: 10.81 1) [13]. As can be seen in Figure 1g, the EELS analysis of boron element in boron nanosheets, it can be seen that boron has a very high peak strength at 200 eV.

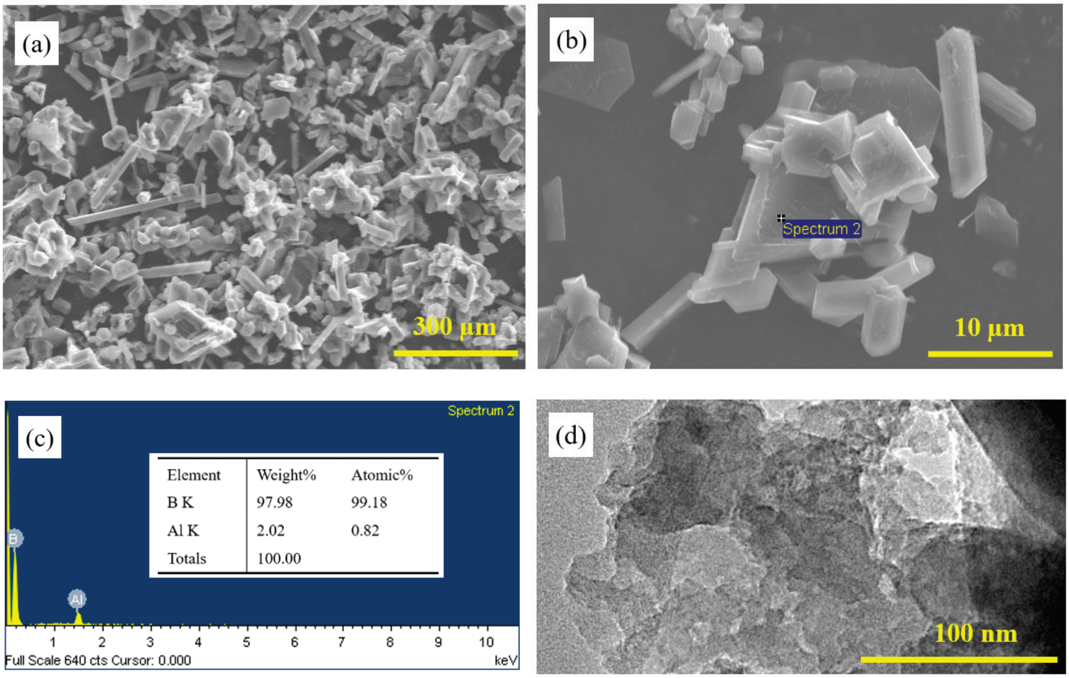

Element	Weight%	Atomic%
B K	97.98	99.18
Al K	2.02	0.82
Totals	100.00	

Figure 1. *Cont.*

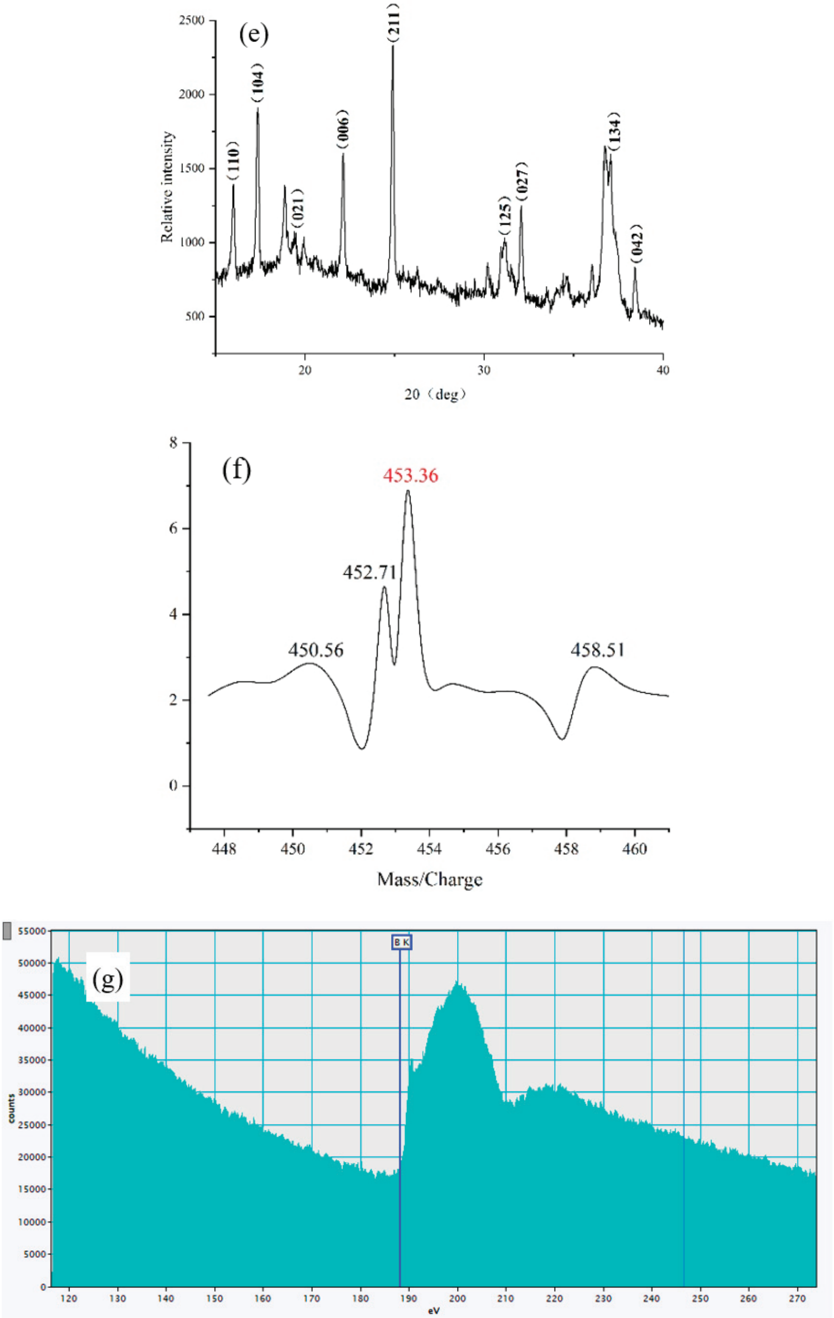

Figure 1. Images of boron particles and boron nanosheets before and after grinding (**a**) SEM image of original boron particles extracted from Cu-5B alloy, (**b**,**c**) EDS spectrum of boron particles, (**d**) TEM image of boron nanosheets after grinding, (**e**) XRD spectrum of boron nanosheets after grinding, (**f**) MALDI-TOF-MS result for the extracted boron powder, (**g**) the EELS analysis of boron element in boron nanosheets.

As can be seen in Figure 2a, some multiple boron nanosheets overlapped together and boron nanospheres with a size of about 5 nm were adsorbed at the same time. The extremely thin boron nanosheets are almost transparent under the electron beam, as shown in Figure 2b,c. The number of layers of the boron nanosheet can be seen by the crimped edges. Figure 3b shows 5layers of boron nanosheets with a size of about 40 nm. As can be observed from magnified Figure 2c,d, the process of stripping boron nanosheets from multiple layers to several layers and finally to double layers can be seen. It is indicated that the preparation of boron nanosheets by this method is through the slip between layers rather than the dissociation between layers. It is the reason why the boron nanosheet size is smaller than that of the original boron particles, the average size is about 30 nm. Figure 2e is the lattice fringe image of the boron nanosheet, with the magnified area marked by the circle. It can be measured that the exposed crystal face of the boron nanosheet is (006), and, accordingly, it can be inferred that β-B fractured along the C-axis in the grinding process. Corresponding to the crystal structure model of β-B in Figure 2f, the fracture occurred between two B12 icosahedrons (shown in green polyhedrons). β-B has a B12 icosahedron at both the vertex and the center of the edge of a single cell, and two B28 polyhedra (yellow polyhedra part in the figure) are triple fused in the middle of the cell, connected by a gap boron atom. Based on the structural model of β-B, it is believed that β-B stripping perpendicular to the C-axis may be caused by the repulsion between the B12 icosahedrons and the attraction between B12 and B28, resulting in the rupture of covalent bond between B12 units. To further characterize whether boron was contaminated by oxidation during the grinding process and the change of boron chemical environment before and after the grinding process, XPS analysis was performed.

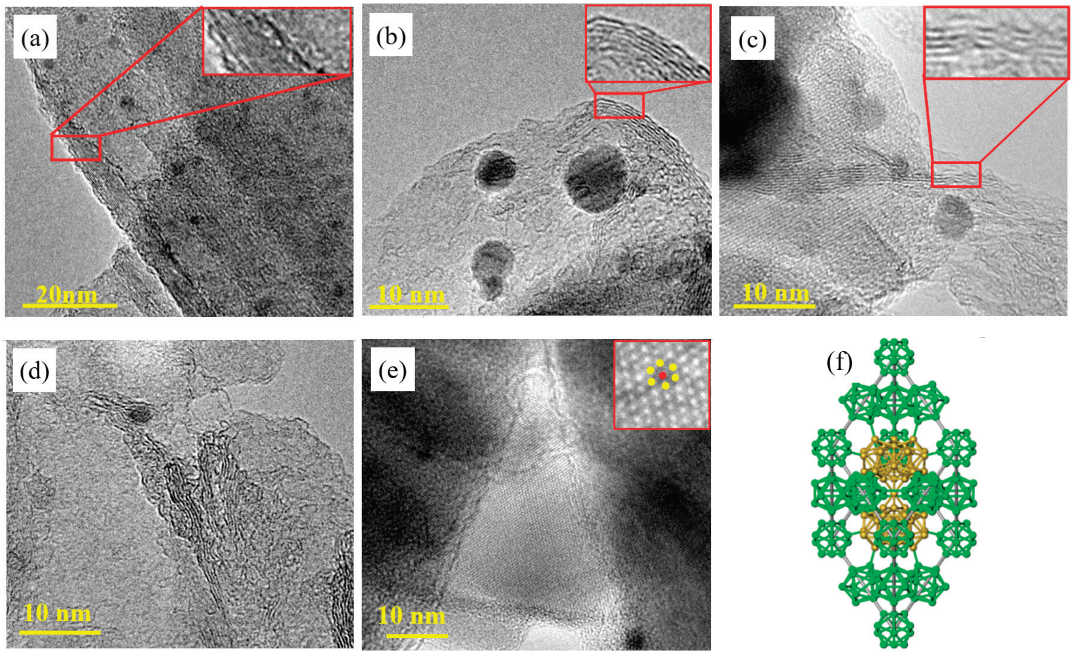

Figure 2. TEM images of boron nanosheets and their peeling processes (**a**) Overlapping boron nanosheets, (**b**) 5-layers boron nanosheets, (**c**–**e**) 2–3 layers of boron nanosheets, and their enlarged peeling processes, (**f**) Structure model of β-B.

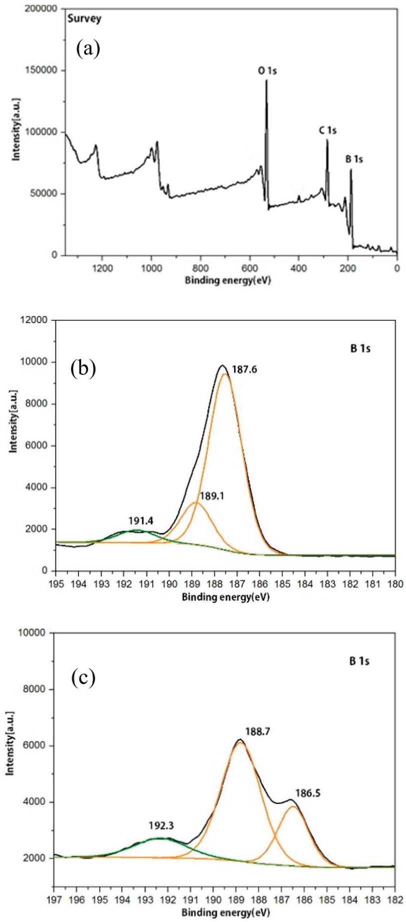

Figure 3. XPS results of boron powder before and after grinding (**a**) Full-scale survey (**b**) Before grinding, breakdown drawing of B 1s peak (**c**) After grinding, breakdown drawing of B 1s peak.

Figure 3a is the full XPS spectrum of boron powder. Strong B1s, C1s, and O1s [14] core levels are observed in the spectrum. We fix the C1s peak at 284.8 eV as the reference to decompose the B 1s band before and after grinding, as shown in Figure 3b,c. Before grinding, the B 1s band had three peaks, indicating the existence of three different chemical environments for boron. The binding energy of block B 1s is about 189–190 eV [15]. For boron powder, the binding energy value shifts to lower energy. These two low binding energy peaks (189.1 eV and 187.6 eV) are the red-shifted relative to the location of the block boron, which is most likely the existence of two different B-B bonds in the block boron. The peak observed at 191.4 eV is attributed to the complete oxidation state of boron in B_2O_3, and the binding energy value is consistent with previous reports [16]. At the same time, it is observed that the proportion of boron oxide peak is very small, and mainly B-B peak with the binding energy of 187.6 eV related to B-B bonding is the most dominant.

The decomposition of B1s peak after grinding is shown in Figure 3c [17]. There were also three peaks. It can be seen that the two low binding energy peaks shift further to lower binding energies [18]. The B-B bond at the lowest binding energy (187.6 eV) before grinding is dominant, and the lower binding energy (188.7 eV) after grinding is dominant, indicating that the grinding process changes the state of two different B-B bonds. It was reported in the literature [9] that B_6O has two different combined boron states, whose binding energies are 185.4 and 187.2 eV, respectively. It is speculated that incomplete oxidation of boron nanosheets obtained after grinding is highly likely to occur, resulting in the bonding mode of B_6O. Thus, the lowest binding energy peak corresponds to B_6O, the lower binding energy peak corresponds to the B-B bonds before grinding, and the high binding energy peak still corresponds to the fully oxidized B_2O_3. At the same time, compared with before grinding, the proportion of fully-oxidized B_2O_3 does not increase, indicating that boron has a certain antioxidation ability.

In conclusion, there are few B_2O_3 bonding and B-B bonding in two different chemical environments in boron particles before grinding. After grinding, only a few B_2O_3 bonds exist in the boron nanosheets, and the state of some B-B bonds changes, forming the incomplete-oxidized B_6O bonds, but B-B bonds still account for most of them.

3. Conclusions

Two-dimensional boron nanosheets were prepared from β-B powder by grinding. The thickness of the boron nanosheets is different, and their size is about 40 nm. Through the analysis of XPS bonding and the chemical environment of boron, there are very few B-O bonds in boron particles, and the B-B bonds are principally dominant. In addition to a few B_2O_3 bonds, some B-B bonds change to B_6O bonds, related to incomplete oxidation, indicating that boron has certain oxidation resistance.

Author Contributions: Conceptualization, H.W. and Z.S.; methodology, Z.S.; software, H.W. and Y.W.; formal analysis, Z.S.; writing—original draft preparation, H.W., Z.S., Z.W. and Y.W.; writing—review and editing, H.W. and Y.W.; visualization, H.W., Z.S. and Z.W.; supervision, Y.W.; project administration, Y.W.; funding acquisition, Y.W. All authors have read and agreed to the published version of the manuscript.

Funding: This work was supported by the National Key Research and Development Program of China (2021YFB3400800).

Data Availability Statement: Not applicable.

Conflicts of Interest: The authors declare no conflict of interest.

References

1. Zhao, S. Preparation of Boron Nanosheets and Their Strengthening Effect on Copper Matrix Composites. Ph.D. Thesis, Shandong University, Jinan, China, 2020.
2. Novoselov, K.S.; Geim, A.K.; Morozov, S.V.; Jiang, D.; Zhang, Y.; Dubonos, S.V.; Grigorieva, I.V.; Firsov, A.A. Electric field effect in atomically thin carbon films. *Science* **2004**, *306*, 666–669. [CrossRef] [PubMed]
3. Boustani, I. Systematic ab initio investigation of bare boron clusters: Determination of the geometry and electronic structures of B-n (n = 2–14). *Phys. Rev. B* **1997**, *55*, 16426–16438. [CrossRef]
4. Lua, K.C.; Pati, R.; Pandey, R.; Pineda, A.C. First-principles study of stability and electronic properties of sheets and nanotubes of elemental boron. *Chem. Phys. Lett.* **2006**, *418*, 549–554.
5. Liu, X.L.; Li, Q.C.; Ruan, Q.Y.; Rahn, M.S.; Yakobson, B.I.; Hersam, M.C. Borophene synthesis beyond the single-atomic-layer limit. *Nat. Mater.* **2022**, *21*, 35–40. [CrossRef] [PubMed]
6. Zhang, L.Z.; Yan, Q.B.; Du, S.X.; Su, G.; Gao, H.-J. Boron Sheet Adsorbed on Metal Surfaces: Structures and Electronic Properties. *J. Phys. Chem. C* **2012**, *116*, 18202–18206. [CrossRef]
7. Zhang, L.Z.; Yan, Q.B.; Du, S.X.; Yakobson, B.I. Two-Dimensional Boron Monolayers Mediated by Metal Substrates. *Angew. Chem. Int. Ed.* **2015**, *54*, 13022–13026. [CrossRef] [PubMed]
8. Fan, Q. Preparation and Properties of Two-Dimensional Boron Halide Nanosheets by Liquid Phase Stripping. Ph.D. Thesis, Beijing University of Chemical Technology, Beijing, China, 2020.
9. Mannix, A.J.; Zhou, X.F.; Kiraly, B.; Wood, J.D.; Alducin, D.; Myers, B.D.; Liu, X.L.; Oganov, A.R.; Hersam, M.C.; Guisinger, N.P. Synthesis of borophenes: Anisotropic, two-dimensional boron polymorphs. *Science* **2015**, *350*, 1513–1516. [CrossRef] [PubMed]
10. Xu, C.Y.; Zeng, J.J.; Gu, X.R.; Wang, Y.; Li, E.C.; Zhang, C.; Ge, C.; Jin, C.; Miao, M.; Jin, Z.; et al. Porous monolith of few-layered boron nitride for effective water cleanup. *J. Mater. Chem. A* **2022**, *10*, 846–854. [CrossRef]
11. Feng, B.J.; Zhang, J.; Zhong, Q.; Li, W.; Li, S.; Li, H.; Cheng, P.; Meng, S.; Chen, L.; Wu, K. Experimental realization of two-dimensional boron sheets. *Nat. Chem.* **2016**, *8*, 564–569. [CrossRef] [PubMed]
12. Zarechnaya, E.Y.; Dubrovinsky, L.; Dubrovinskaia, N.; Miyajima, N.; Filinchuk, Y.; Chernyshov, D.; Dmitriev, V. Synthesis of an orthorhombic high pressure boron phase. *Sci. Technol. Adv. Mater.* **2008**, *9*, 044209–044214. [CrossRef] [PubMed]

13. Sun, Z.; Wu, Y.; Han, X.; Zhang, G.; Liu, X. Growth mechanism of alpha-boron and beta-boron in a copper melt at ambient pressure and its stabilities. *CrystEngComm* **2017**, *19*, 3947. [CrossRef]
14. Atuchin, V.V.; Kesler, V.G.; Kokh, A.E.; Pokrovsky, L.D. X-ray photoelectron spectroscopy study of b-BaB_2O_4 optical surface. *Appl. Surf. Sci.* **2004**, *223*, 352–360. [CrossRef]
15. Ong, C.W.; Huang, H.; Zheng, B.; Kwok, R.W.M.; Hui, Y.Y.; Lau, W.M. X-ray photoemission spectroscopy of nonmetallic materials: Electronic structures of boron and B_xO_y. *J. Appl. Phys.* **2004**, *95*, 3527–3534. [CrossRef]
16. Zheng, Q.; Cao, Y.H.; Huang, N.J.; Zhang, R.Y.; Zhou, Y. Selective exposure of BiOI oxygen-rich {110} facet induced by BN nanosheets for enhanced photocatalytic oxidation performance. *Acta Phys. Chim.* **2021**, *37*, 2009063. [CrossRef]
17. Atuchin, V.V.; Kesler, V.G.; Zaitsev, A.I.; Molokeev, M.S.; Aleksandrovsky, A.S.; Kuzubov, A.A.; Ignatova, N.Y. Electronic structure of α-SrB4O7: Experiment and theory. *J. Phys. Condens. Matter.* **2013**, *25*, 085503. [CrossRef]
18. Atuchin, V.V.; Pokrovsky, L.D.; Kesler, V.G.; Isaenko, L.I.; Gubenko, L.I. Structure and chemistry of LiB_3O_5 (LBO) optical surfaces. *J. Ceram. Proc. Res.* **2003**, *4*, 84–87.

nanomaterials

Article

Tunable Switching Behavior of GO-Based Memristors Using Thermal Reduction

Muayad Abujabal [1], Heba Abunahla [2], Baker Mohammad [2] and Anas Alazzam [1,]*

[1] System on Chip Lab, Department of Mechanical Engineering, Khalifa University, Abu Dhabi P.O. Box 127788, United Arab Emirates; 100057733@ku.ac.ae
[2] System on Chip Lab, Department of Electrical Engineering and Computer Science, Khalifa University, Abu Dhabi P.O. Box 127788, United Arab Emirates; heba.abunahla@ku.ac.ae (H.A.); baker.mohammad@ku.ac.ae (B.M.)
* Correspondence: anas.alazzam@ku.ac.ae

Abstract: This work reports on the fabrication of a novel planar reduced graphene oxide (rGO) memristor (MR) device. For the first time in the literature, the MR tunable resistive switching behavior is controlled by the GO reduction time at a constant temperature. The device is fabricated using standard microfabrication techniques on a flexible cyclic olefin copolymer substrate (COC). Thermal reduction of the GO layer at low temperatures (100 °C) avoids the drawbacks of chemical reduction methods such as toxicity and electrode metal damage during fabrication, while allowing for fine-tuning of the MR's switching behavior. The device has analog switching characteristics, with a range of different resistance states. By taking advantage of the slow nature of GO thermal annealing, the switching properties of the rGO memristors can be precisely controlled by adjusting the reduction period. At short annealing times (i.e., $T < 20$ h), the devices switch from high to low resistance states, while at longer annealing times the switching behavior is reversed, with the device switching from low to high resistance states (LRS to HRS). Resistive switching occurs as a result of the diffusion and removal of the oxygen functional groups in the GO film caused by Joule heating induced by the electric current. Complete electrical characterization tests are presented along with wettability and X-ray diffraction (XRD) tests. This work opens a new vision for realizing rGO-based MR devices with tunable switching properties, broadening the application horizon of the device.

Keywords: graphene oxide; reduction; thermal; memristor; switching; analog; oxidation

Citation: Abujabal, M.; Abunahla, H.; Mohammad, B.; Alazzam, A. Tunable Switching Behavior of GO-Based Memristors Using Thermal Reduction. *Nanomaterials* **2022**, *12*, 1812. https://doi.org/10.3390/nano12111812

Academic Editors: Jihoon Lee and Ming-Yu Li

Received: 21 April 2022
Accepted: 23 May 2022
Published: 25 May 2022

1. Introduction

The memristor device (MR) is a two-terminal electrical component that was first proposed by Leon Chua in 1971 as the fourth fundamental circuit element that connects electric charge and magnetic flux [1]. MR has a closed hysteresis *I-V* characteristic that is pinched at zero and can switch between two resistance states. The low-resistance state is referred to as the "ON state" while the high-resistance state is referred to as the "OFF state". HP labs fabricated the first MR in 2008, using TiO_2 as the active switching layer [2]. After this, the interest in MR devices has dramatically increased as their unique features make them a great candidate for many emerging applications such as memory, computing, security, and sensing [3–6].

The sensing applications of MR have gained momentum due to the great ability of the device to change its fingerprint *I-V* characteristics according to the surrounding environments and the interactions taking place in the device's active area. Tzouvadaki et al. [7,8] developed a bio-functionalized silicon nanowire MR for cancer detection by attaching anti-PSA antibodies; the sensor functioned by exhibiting a voltage gap, or a non-zero current at zero volts. Additionally, the silicon nanowire was used to develop a sensor for drug monitoring in a manner similar to that used in cancer detection [9]. The silicon nanowire is analogous to enzymatic sensors in which biomolecules are attached to the device [10]. MR devices have been used as non-enzymatic sensors, and a device based on TiO_2 fabricated as a crossbar was used to detect glucose at concentrations comparable to those found in human blood samples by tracking changes in the ON/OFF ratio [11]. These applications demonstrate MR's versatility and its suitability to be deployed in biosensing applications. Device structure is a key factor for deploying MR devices in sensing applications as it should facilitate the interaction between the device's active area and the surrounding environment or the applied molecules. Thus, planar MR devices are considered a great asset for sensing applications.

In recent years, graphene and graphene-related compounds have garnered considerable attention [12]. Concurrently, graphene-based resistive switching devices have been developed [13]. In these devices, graphene and graphene oxide (GO) are used to fabricate the electrodes as well as the active resistive switching material [13–15]. For instance, GO has been used as an active layer in the development of artificial neural networks (ANNs) that mimic the behavior of neurons and the way the human brain retains information [3]. Moreover, reduced GO (rGO)-based memristors have also been used in the development of sensors [5]. GO is a two-dimensional substance formed from graphene that is decorated with oxygen functional groups [16]. The low cost and ease of manufacturing make GO especially attractive. GO-based memristor devices can be produced using a variety of standard fabrication procedures. GO can be used in its natural state [17] or it can be changed by chemical, electrochemical, thermal, or photothermal processes [18].

To the best of our knowledge, this is the first study to examine thermal reduction for the fabrication of planar rGO-based MR devices on a flexible polymer substrate. It details the development of a low-cost planar MR device that consists of Au-rGO-Au. On top of a cyclic olefin copolymer (COC) substrate, the electrodes and rGO layer are stacked in a planar metal/GO/metal configuration. The device is fabricated using standard microfabrication techniques, with the GO layer being thermally reduced at a constant temperature. Planar devices benefit from their simplicity of fabrication, which permits mass production and incorporation into low-cost disposable electronics. Due to its adaptability in applications such as flexible sensors and wearable devices, flexible electronics are gaining appeal [19]. Additionally, the planar structure has a large surface area, which provides more space for the electrochemical reactions [20]. In this work, the MR switching behavior of the device is controlled at low annealing temperatures (100 °C). This results in increased biocompatibility and safety during fabrication when compared to other reduction methods of GO. Thermal annealing at a low temperature has critical advantages over chemical reduction, which is ineffective when acid-sensitive metals are used. Furthermore, unlike previous approaches, it does not necessitate direct access to the GO film. Additionally, it requires less equipment than photothermal and chemical techniques. By carefully tweaking the reduction process, different electrical properties can be achieved for a variety of applications, ranging from computation to sensing. The obtained devices displayed unipolar analog switching characteristics with controllable switching behavior due to the degree of reduction of the GO film between the two gold electrodes. By varying the degree of reduction of the GO layer, two distinct device behaviors were achieved. Adjusting the duration of heating is sufficient for regulating the reduction process. The resulting resistive switching behavior has a great potential for a variety of applications in different fields; memristive sensors exploit the resistive switching ability to detect various quantities and substances. The thermal reduction approach of graphene oxide facilitates the construction of biocompatible sensors to detect biomolecules in enzymatic or non-enzymatic approaches. Additionally, the memristor exhibits an analog switching behavior when GO is highly reduced, and the multiple resistance states make it a prime candidate to build multi-bit memory cells for high density memory. Additionally, it can support in-memory computing and neuromorphic computing, especially for artificial neural networks (ANN).

2. Materials and Methods

2.1. Device Fabrication

As shown in Figure 1, the planar MR devices reported in this work are fabricated using standard microfabrication techniques. The lithography photomask is fabricated using a direct photolithography system (Dilase Kloe 650, Kloe-france, Saint-Mathieu-de-Tréviers, France). The electrodes are designed to be square in shape, 3 mm long, and separated by a 20 μm gap, as illustrated in Figure 1. The first stage of the device fabrication includes the deposition of a thin layer of gold using a sputter (Q300TT from Quorum, Laughton, East Sussex, United Kingdom) on a clean cyclic olefin copolymer substrate (COC) (TOPAS Advanced Polymers 5013 from microfluidic ChipShop, Jena, Germany) (Step 1). Following that, a layer of photoresist (PR1813 from micro resist technology GmbH, Berlin, Germany) is deposited using a spin coater (WS650Hzb-23NPP UD-3 from Laurell Technologies Corporation, North Wales, PA, United State) and then baked for five minutes at 70 °C. The wafer is then subjected to ultraviolet light via the photomask (step 2). The photoresist patterned layer is then developed using a suitable developer, washed in DI water, and then the gold layer is etched with gold etchant (TechniEtch ACI2 potassium iodide/iodine etchant from Microchemicals GmbH, Ulm, Germany) (steps 3 and 4). Following acetone removal of the photoresist layer, the wafer is thoroughly washed with DI water. After patterning the electrodes, the GO (Graphenea, San Sebastián, Spain) layers are deposited (Stage 2). The deposition of GO begins with a five-minute oxygen plasma treatment (PDC-002 from Harrick Plasma, Ithaca, NY, United States) of the COC substrate to improve the adherence of GO flakes and the surface's wettability [21] (step 1). Then, spin coating is used to deposit a thin layer of GO on the substrate (step 2). The wafer with GO layers is then baked for two minutes at 70 °C on a hot plate. The GO deposition (on top of the substrate) and baking steps are carried out three times (steps 3 and 4). It is important to note that the patterned electrodes are protected with scotch tape during GO deposition. In this work, the reduction of GO is achieved by heating the device at 100 °C in an air environment. As described in Section 3, the heating time is adjusted and its effect on the memristor device switching behavior is studied and analyzed.

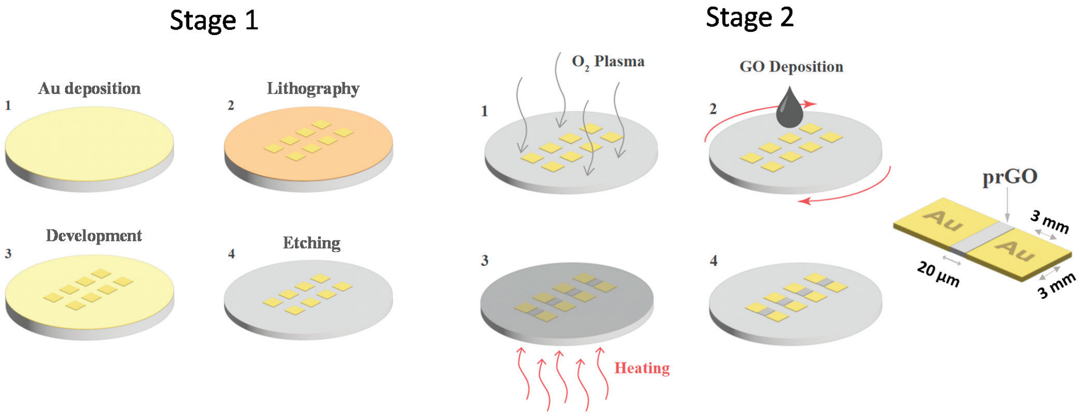

Figure 1. Memristor device fabrication steps. Stage 1 includes the patterning of the gold electrodes, while Stage 2 involves the deposition of the GO layers between the planar electrodes.

2.2. Device Characterization

Microphotographs of the fabricated memristor devices are captured using a field emission scanning electron microscope (FESEM) (JEOL, JSM-7610F, Tokyo, Japan). In addition, detailed material characterizations utilizing an X-ray diffractometer (XRD) (Bruker, D2 Phaser, Billerica, MA, USA), Raman spectroscopy and atomic force microscopy (AFM) are performed on the devices. Detailed electrical characterization is performed using Keithley

4200-SCS parameter analyzer (from Tektronix, Beaverton, OR, USA). One electrode is connected to the biasing terminal, while the second electrode is kept grounded. The voltage sweeping mode is used to measure the current-voltage (*I-V*) characteristics of the fabricated devices, with a voltage step of 0.05 V and range up to 15 V. Additionally, the pulse mode is utilized to study the effect of applying constant voltage over time on the device switching behavior.

3. Results and Discussion

3.1. Material Characterization

3.1.1. Wettability and Contact Angle

Due to the presence of oxygen functional groups that form hydrogen bonds, GO is known to have hydrophilic characteristics, resulting in low contact angles [22,23]. By reducing GO to rGO form, the hydrophobicity of the material is increased, hence increasing the contact angle between water droplets and GO surfaces [24]. By measuring the contact angle at various locations across the GO surface, this contact angle can be used to investigate the effect of baking time on the degree of reduction of the deposited GO. In this work, four fresh COC substrates are coated with GO after being treated with O_2 plasma. Following that, three substrates are baked at a temperature of 100 °C for different durations (4 h, 8 h, and 12 h). Figure 2a–d show droplets of the same volume (5 μL) above the four samples. The four droplets have distinct contact angles. The effect of baking duration on the water contact angle is shown in Figure 2e. Without reduction, GO film has a contact angle of about 43°. After 4 h of annealing, the average contact angle is increased to around 68° and then almost saturates for 8 and 12 h annealing time. This experiment proves that heating the GO on COC substrate at 100 °C for a sufficient duration (i.e., $\geq$4 h) leads to the elimination of oxygen groups, making the material less hydrophilic, and thus achieving GO reduction.

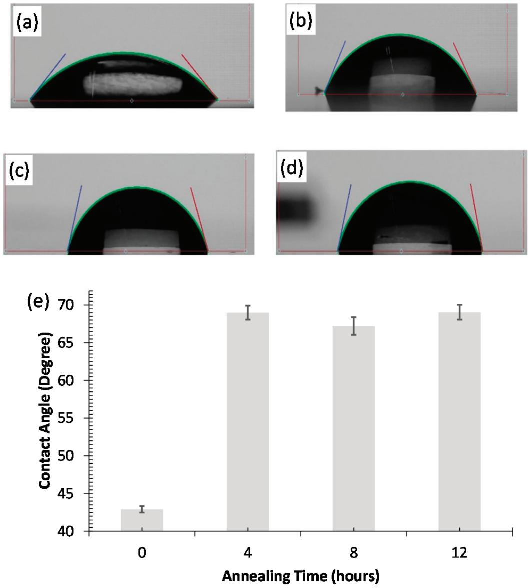

Figure 2. Images of water droplets on four COC wafers coated with GO (**a**) without baking, and (**b**–**d**) baked at a temperature of 100 °C for 4 h, 8 h, and 12 h, respectively. (**e**) The variation in the water contact angle on GO-coated COC wafers vs. the annealing time (four readings for each sample).

3.1.2. XRD and FESEM Analysis

The results achieved in the previous section can be further verified by X-ray diffraction (XRD) analysis. Figure 3a,b shows the XRD pattern for two COC wafers coated with GO; one is not reduced, the other is annealed for 12 h at 100 °C, and both are compared to bare COC. The pristine GO shows a typical GO diffraction (Figure 3a) peak at 2θ = 7 with another intense peak at 2θ = 17 that is attributed to the COC wafer interacting with the X-ray beam [25]. Subtracting the COC diffractometer from that of GO leaves the typical GO peak at 2θ = 7. After reduction, the peak at 2θ = 7 drops in intensity and shifts to a greater 2θ. Huang et al. [26] demonstrated that the intense GO peak diminishes in intensity and shifts from 2θ = 10° to 25°, which coincides with the intense COC wafer peak. The XRD pattern for the 12 h of annealed GO (Figure 3b) shows no peaks at 2θ = 7°, the expected shift for rGO peak at 2θ = 25° is overshadowed by the COC peak. When subtracting the COC pattern from the rGO pattern, the resulting diffractometer reveals a broad low intensity peak at 2θ = 10, which is typical for thermally annealed rGO.

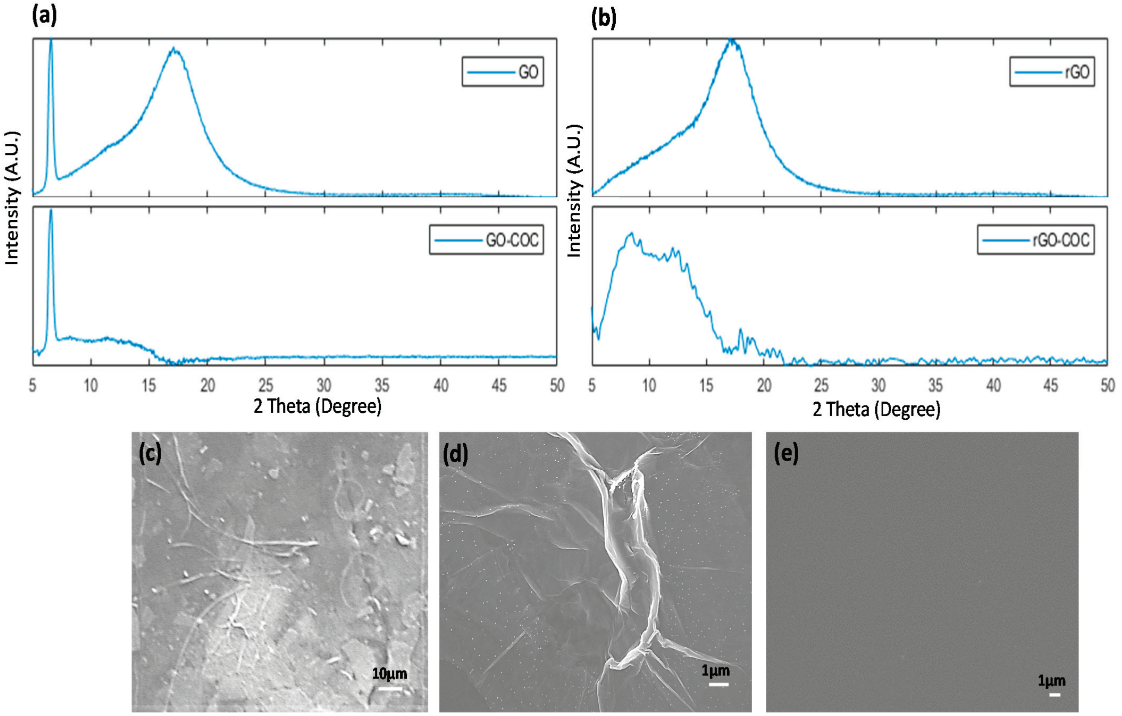

Figure 3. XRD pattern for (**a**) COC coated with pristine GO and diffractogram of the COC substrate subtracted from GO XRD, (**b**) GO reduced thermally for 12 h and diffractogram of the COC substrate subtracted from rGO XRD. (**c**–**e**) present microphotographs of the GO, rGO, and COC, respectively, captured using a field emission scanning electron microscope.

The deposited GO and rGO are further analyzed using Field Emission Scanning Electron Microscopy to determine their microstructures. Figure 3c–e show three SEM images of GO, rGO annealed for 12 h, and a bare COC substrate, respectively. The images in Figure 3c,d show a uniform distribution of the GO flakes with the presence of few wrinkles and defects and overlapping flakes. The SEM image of the bare COC substrate in Figure 3e reveals a uniform surface free of defects. The surface and microstructure features of GO and rGO are the results of the deposition process and thermal annealing.

3.1.3. Raman Spectroscopy and AFM Analysis

The Raman spectra of a GO and rGO sample are revealed in Figure 4a. Raman spectroscopy analysis is conducted to investigate the structure of GO before and after thermal annealing. Two characteristic D (1340 cm^{-1}) and G (1580 cm^{-1}) peaks for GO are visible in Figure 4a. The presence of the D peak indicates disorders and defects in the GO film [27]. The ratio of the intensities of the D to G peaks is a measure of density of the disorders and defects in the form of sp^2 to sp^3 carbon ratio [28]. Before reduction, the D to G ratio is at 0.9, and after reduction the intensity ratio increases to 1.1. The increase in the intensity can be attributed to increased defects after the reduction process.

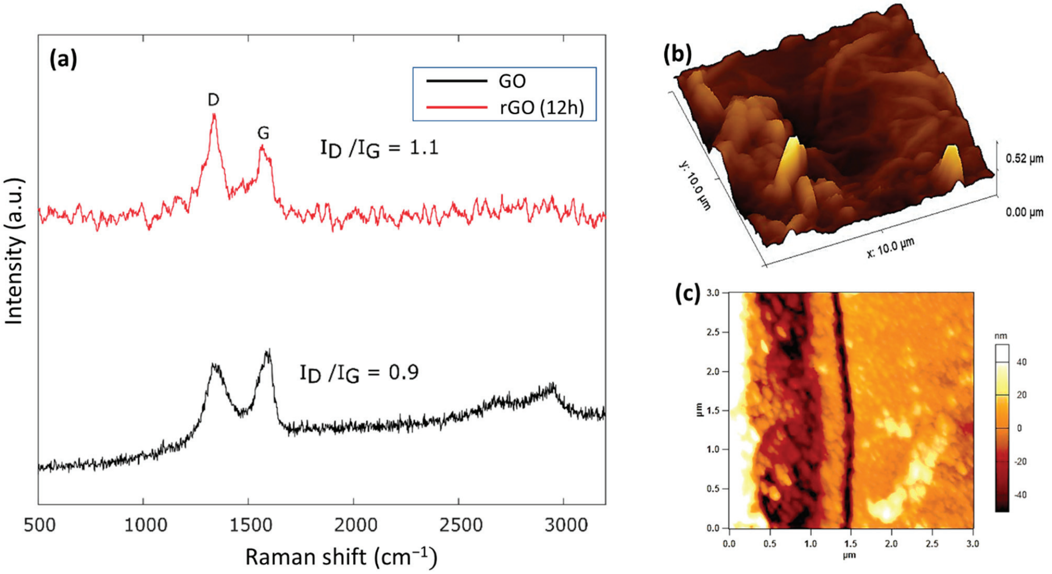

Figure 4. (**a**) Raman spectra of GO and rGO reduced for 12 h on COC substrate. (**b**) Surface morphology of GO layer as deposited on COC substrate; the root-mean-square roughness is measured at 62 nm. (**c**) AFM image of GO; the thickness of GO can be estimated as 100 nm.

The GO layer is further analyzed using Atomic-forced microscopy (AFM), as shown in Figure 4b. The GO surface has a root-mean-square roughness of 62 nm. AFM is also used to measure the thickness of the deposited GO layer. As shown in Figure 4c, the thickness of GO can be estimated as 100 nm.

3.2. Electrical Characterization

3.2.1. Switching Characteristics

The MR devices fabricated in this work are characterized using a Keithley 4200-SCS parameter analyzer in sweeping mode to measure the *I-V* curves. Figure 5a presents the *I-V* characteristics of the fresh device reduced for 4 h. The test is carried out by applying consecutive voltage sweeps; the sweeps start from 0 V to Vmax, where Vmax is the maximum voltage specified for each sweep, ranging from 3 V to 15 V. As shown, at low voltage sweeps (3 V and 5 V) (Figure 5a), the MR has very high resistance (10^8 Ohm) and shows minimal or no resistive switching behavior because of the very small current. Upon increasing Vmax to 10 V, the resistance of the device decreases with a very small OFF/ON ratio approaching 1. However, at 15 V sweep the device shows high resistance in the forward sweep and turns to the ON state with lower resistance during the reverse sweep, as in Figure 5a. Figure 5b shows the characteristics of two pristine devices reduced for 4 h, one under the application of −15 V and another under +15 V sweeps; the resulting

I-V curve is the same for both devices with similar characteristics (i.e., current, resistance ratio). This switching behavior is unipolar switching since only voltage magnitude controls the resistance state, whereas in bipolar behavior the magnitude and polarity influence the resistance switching.

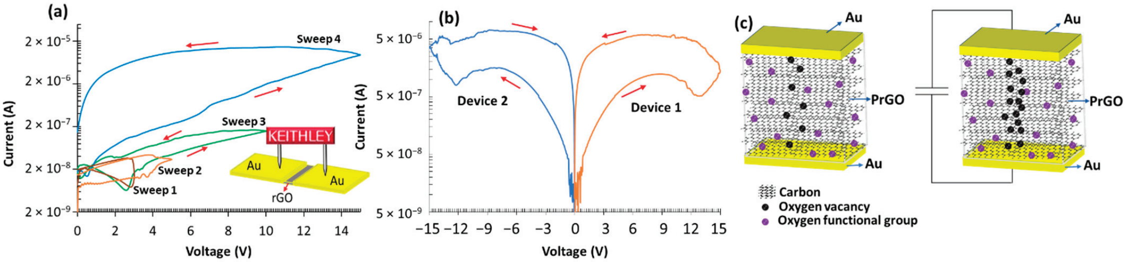

Figure 5. (**a**) *I-V* curves for 4 h rGO device generated by the parameter analyzer, multiple voltage sweeps are visible from 3 V to 15 V. (**b**) the *I-V* curve for two devices at ∓15 V sweeps, the hysteresis curve is mirrored, indicating unipolar switching. (**c**) A schematic of the switching mechanism takes place in the devices in (**a**,**b**), the GO layers are reduced by Joule heating, each subsequent sweep further reduces the GO flakes.

Understanding the resistive switching phenomena in GO-based MR devices and the mechanisms involved are essential [29]. Switching behavior describes the relation between the voltage magnitude and its polarity with resistive switching, while the switching mechanism describes the changes in the bulk GO flakes during resistive switching events. For GO-based MR devices, there are two main switching mechanisms in the literature [29]; metallic filamentary conduction is the most commonly used to explain resistive switching that takes place in GO devices [30,31]. This mechanism is dependent on the use of electrochemically active metal electrodes such as copper (Cu) in vertical and crossbar configurations [32]. When voltage is applied to the active electrode, the electrode material is dissolved, and the resulting ions migrate through the GO layer towards the passive electrode. Therefore, a conductive metallic filament is formed by the accumulating of ions, turning the MR ON. The filament is ruptured upon voltage polarity reversal returning the device to the OFF state [31,32]. MR devices that follow this mechanism typically exhibit abrupt and sudden current changes when the metallic filament is fully formed or ruptured [29]. The second mechanism is related to oxidation and reduction within the bulk GO layers. Graphene is a 2D material made of single-atom-thick flakes; graphene in this case is formed of electrically conductive sp^2 bonds. GO, on the other hand, is formed by insulating sp^3 bonds that are created by oxidizing the graphene flakes. When an electric field is applied, the oxygen functional groups in low conductivity areas are detached, converting the sp^3 bonds to sp^2 bonds, thereby locally increasing the conductivity of the GO film. This mechanism is more prevalent in planar devices and memristors using inert metal electrodes (i.e., gold and platinum) [33,34].

The device proposed in this work has a planar structure utilizing inert metal (gold) electrodes with a gap of 20 μm. Since the metallic filament conduction mechanism requires thin vertical devices (active layer thickness << 1 μm) [32,35] with electrochemically active electrodes (i.e., Al, Cu), the second mechanism–the oxidation-reduction in bulk GO–better fits the presented device, due to its relatively large electrode spacing and the use of inert gold electrodes. Moreover, as shown in Figure 5a,b, when resistance switching occurs, the current changes slowly and gradually from the high resistance state to the low resistance (OFF to ON) with no abrupt changes in current, confirming that oxidation-reduction reactions induced by the electric field [36] and Joule heating within the bulk GO film are responsible for resistive switching. Figure 5c presents a schematic that summarizes the reduction in bulk GO switching mechanism associated with the devices reported in Figure 5a,b.

3.2.2. Tuning MR Switching Via Annealing Time

In this work, tuning of the MR switching behavior is achieved by controlling the heating time of the fabricated devices, as presented in Figure 6. To elaborate, multiple fresh wafers are fabricated with different annealing times (4 h (a), 8 h (b),14 h (c), 20 h (d), 30 h (e), and 40 h (f)). All devices are tested using the same methodology by applying 15 V voltage sweeps. As shown in Figure 6, the fabricated devices have two different hysteresis curves; at a short reduction time (4 h, 8 h and 14 h), the memristor turns to a low resistance state. Around 20 h, a change in switching behavior occurs, and switching is reversed by transitioning from a low to a high resistance state for all reduction times greater than 20 h.

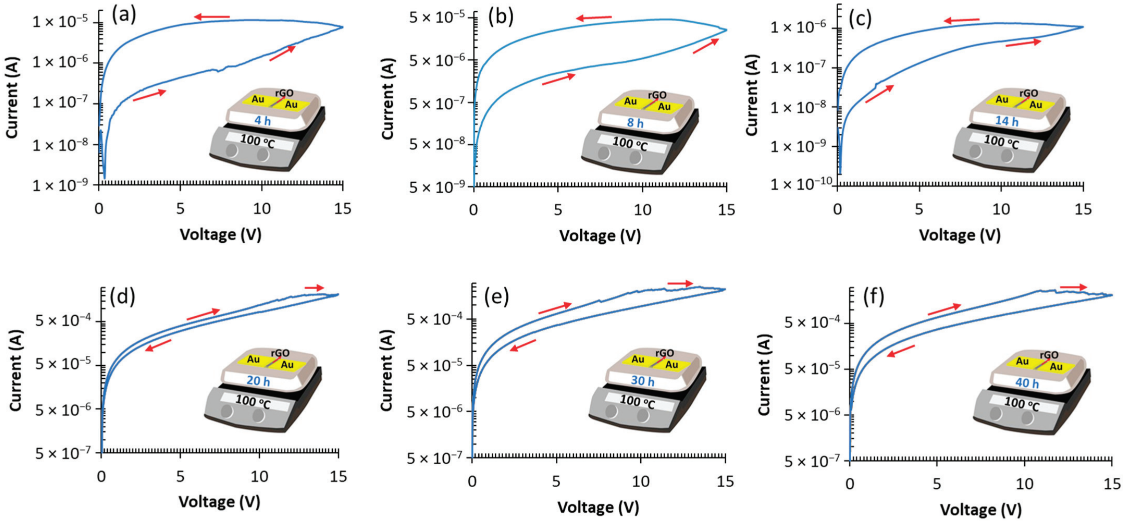

Figure 6. The switching characteristics for devices annealed over six different periods from 4 h to 40 h. (**a**–**c**) present switching from HRS to LRS, while (**d**–**f**) show switching from LRS to HRS.

Thermal annealing of GO is a transient process. Here, we give insight into the impact of annealing time on the resistive switching behavior. Prolonged annealing time increases the conductivity of GO. The measured maximum resistance ratio varies with annealing time, as shown in Figure 6a–f. The maximum resistance ratio of 17 for 4-h samples is calculated at 7.5 V. As the annealing increases, the resistance ratio drops for 8-h samples, the maximum resistance ratio is 9.3 measured at an increased voltage of 8.5 V. At 14 h of annealing, the maximum resistance ratio drops to 2.9 at 9.8 V. Devices with 20-h reduction time have a maximum ON/OFF ratio of 1.6 measured at 12 V. At 30 h of annealing, a maximum ON/OFF ratio of 2.3 is realized at 9.8 V. Devices with 40-h reduction duration have a slightly higher resistance ratio of 2.4 when compared to 30 h, measured at 11 V. The decrease in the resistance ratio as annealing time increases (up to 14 h) can be attributed to the amount of oxygen functional groups within the graphene flakes. At a short annealing time (4 h), the graphene is still highly oxidized, which results in very high initial resistance, and as increasing voltage sweeps are applied, the GO is locally reduced by Joule heating produced by the applied voltage and the current passing through the device. At 8-h reduction, more oxygen groups are removed by thermal annealing during fabrication leaving fewer oxygen groups within the GO flakes to be removed by Joule heating induced by the electrical current during the writing process. Thus, the higher initial oxygen content allows for a higher resistance ratio. The decrease in the resistance ratio for 14 h devices in Figure 6c is also linked to the amount of oxygen functional groups present within the rGO flakes. After 14 h of annealing, more oxygen groups are removed. Since the ON/OFF ratio is created by the local reduction of GO by Joule heating, the lack of oxygen groups within the GO flakes allows for limited resistive switching.

As presented in Figure 6d–f, at longer reduction periods (20 h and more) the MR resistive switching behavior is reversed, the device starts at low resistance, and when a threshold voltage is reached during a voltage sweep, the device switches to a high resistance state. The threshold voltage is tied to the degree of reduction of the GO flakes; at 20 h of annealing, resistive switching starts at 13 V, and drops to 10 V for the 30- and 40-h samples. Moreover, the devices reduced for 20 h or more show significantly higher current levels in both the forward and backward sweeps. At 14 h reduction time and less, the maximum current reached is below 1 μA, however, Figure 6f shows current levels that are about 100 times higher at a current peak of 2.7 mA for the 40 h samples. The resistance ratio is also lower; at 20 h, the maximum average resistance ratio occurs is 1.6 which occurs at 12 V. As annealing time is increased to 30 h, the threshold voltage drops to 10 V and the OFF/ON ratio increases to 2.3 at 9.8 V. At 40 h of reduction, the *I-V* curve shown is similar to that of 30 h with minuscule changes; the similarities are due to reduction process of graphene oxide. Thermal annealing of GO at low temperatures (100 °C) is a slow process, and therefore the 30 h and 40 h devices produce comparable results. Compared to the mechanism explained in Section 3.2.1 for devices reduced for ≤14 h, a different mechanism occurs for 20 h reduction or more. To elaborate, in such devices, the GO is highly reduced, but some oxygen groups still exist. By applying a high voltage sweep (i.e., 15 V), the remaining oxygen species within the bulk GO form a resistive barrier by local oxidation of GO, thus increasing the resistance. The GO is no longer being reduced by voltage as in the case of 4–14 h, but the diffusion of remaining oxygen groups is responsible for resistive switching [3].

It is worth mentioning that reduction of GO at 100 °C occurs at slow rate, which enables the tunable resistive switching by varying the reduction time, which is the main novelty of this work. Higher annealing temperatures accelerate the reduction process. Nonetheless, if the GO is reduced too rapidly at elevated temperatures, this may alter the switching behavior such that the behavior observed in this study may no longer be observed. Thus, annealing at higher temperatures reduces the ability to control the reduction process and achieve precise device resistance tuning. As evident in the work of Slobodian et al. [37], where they measured the reduction of GO versus annealing temperature in terms of weight loss percentage, the reported results show the rate of reduction changes significantly with temperature especially above 100 °C. At 100 °C, it is revealed that the rate of reduction is enough to observe the effects via fine reduction of the GO film.

3.2.3. Tuning MR Switching via DC and Sweep Voltage

To further investigate the switching characteristics of the GO-based MR devices fabricated in this work, constant DC voltage bias is applied to a fresh device, and the resistance response is logged over time. Figure 7a presents the resistance over time, under the application of 6 V DC voltages, for a pristine device annealed at 100 °C for 12 h. As shown, in 400 s, the device resistance drops from 47 MΩ to 1.3 KΩ and then reaches a saturation resistance state. The steep decline in the resistance of the active rGO layer within the memristor indicates localized reduction by the current-induced Joule heating effect. The final stagnation resistance of the device electrically reduced by joule heating in Figure 7a resembles the devices thermally reduced for 20 h and more. To elaborate, the same device is tested with linear voltage sweeps and the resultant *I-V* curves are plotted in Figure 7b. It is clear that the switching direction of the device is reversed to be from low resistance state to high resistance state in an analog manner. As depicted, under the application of a voltage sweep that is equal to or exceeds the switching threshold voltage, the resistance increases by Joule heating, inducing solid phase dissolution of oxygen functional groups [33]. By increasing the resistance, the current drops and a high voltage level is needed to recreate the Joule heating effect. By increasing the write voltage, a new high resistance state can be written. This novel tunable behavior of the MR device is considered a great asset as it broadens the application horizon of the device.

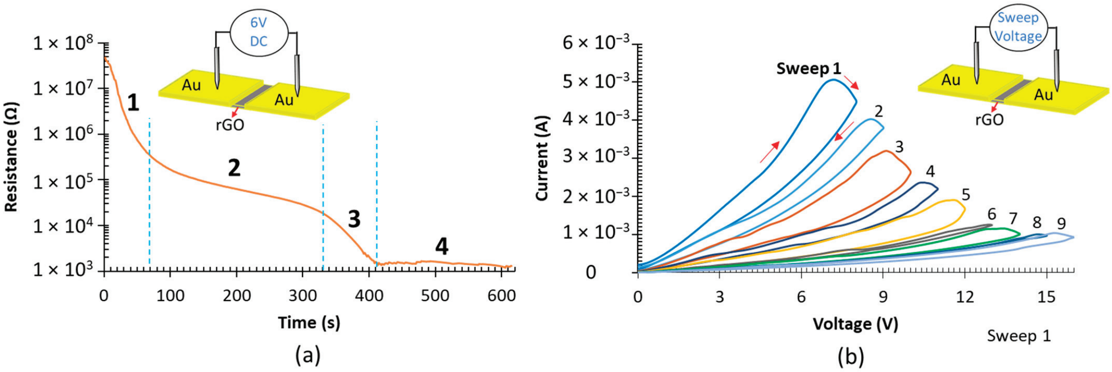

Figure 7. Tunable MR switching behavior. (**a**) Fresh device annealed for 12 h is tested under the application of 6 V DC bias. (**b**) *I-V* curves for device in (**a**) after the application of the DC voltage bias.

The electrical behavior of the memristor devices reported in this work is further investigated by applying 100 consecutive voltage sweeps at 15 V, across a 4 h reduced device. As shown in Figure 8a, during the first sweeps, the memristor exhibits resistive switching behavior, where the resistance decreases between the forward and the backward sweeps. After each sweep, the resistance decreases when compared to the previous sweep. Additionally, the ON/OFF ratio decreases until the sixth sweep, where the resistances in the forward and backward sweeps are equal (ON/OFF ratio = 1). From the 6th sweep until the 14th sweep, the resistance decreases further with the same resistance ratio (ON/OFF ratio = 1). After the 14th sweep, the device no longer behaves as a memristor, and all consequent sweeps coincide. After that, as presented in Figure 8b, a 20 V dual sweep is applied to the same device; the resistance increases at 18 V, and the device switches to a higher resistance state. Therefore, it can be concluded that after around 14 sweeps at 15 V, a 4 h device will change switching behavior and the resistance can increase with future sweeps via applying higher voltage magnitude.

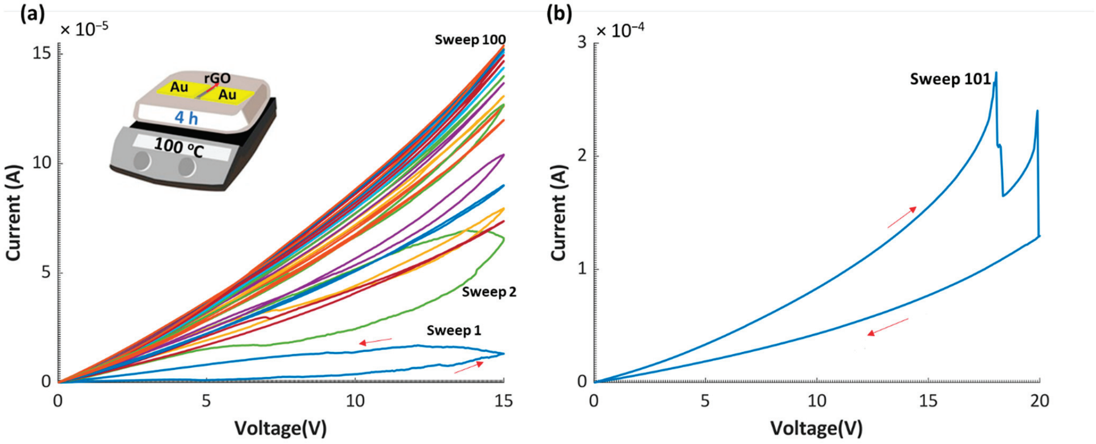

Figure 8. Tunable MR switching behavior. (**a**) A fresh device annealed for 4 h is tested for 100 cycles under the application of 15 V sweep. (**b**) *I-V* curve under the application of 20 V sweep for the same device after performing the test in (**a**).

4. Conclusions

In conclusion, this work presented a novel thermally reduced graphene oxide memristor in a planar Au/rGO/Au configuration. The presented device had a unique tunable resistive switching behavior controlled by adjusting the reduction time of the GO layer. At shorter reduction times, the device switched from OFF to ON, and increasing the reduction time reversed the switching to be from the ON to OFF state. In both stages, the devices exhibited analog switching behavior. The use of symmetric gold electrodes resulted in a unipolar switching behavior where the voltage amplitude controlled the switching and writing process irrespective of polarity. The resistive switching phenomenon was linked to the oxidation-reduction of the oxygen species within the bulk GO flakes. Moreover, a unique switching behavior was achieved by further reducing the MR devices using a suitable DC bias. This led to reversing the switching direction of the MR resistance state and achieving multi-state switching characteristics. The novel methodologies reported in this work provided new insights to develop rGO-based MR devices with highly tunable characteristics to adapt the target applications.

Author Contributions: A.A. conceived the presented idea. A.A. and B.M. supervised the findings of this work. M.A. carried out the experiments and performed the analysis with feedback from all other authors. H.A. planned and assisted the electrical characterization experiments. B.M. secured the fund. M.A. and H.A. wrote the original manuscript with input from all authors. All authors discussed the results and contributed to the final manuscript. M.A. and H.A. contributed equally to the manuscript. All authors have read and agreed to the published version of the manuscript.

Funding: This publication is based upon work supported by the Khalifa University of Science and Technology under Awards No. [RC2-2018-020].

Data Availability Statement: All data generated or analyzed during this study are included in this published article.

Conflicts of Interest: The authors declare no conflict of interest.

References

1. Marani, R.; Gelao, G.; Perri, A.G. A review on memristor applications. *arXiv* **2015**, arXiv:1506.06899.
2. Zhao, Q.; Xie, Z.; Peng, Y.-P.; Wang, K.; Wang, H.; Li, X.; Wang, H.; Chen, J.; Zhang, H.; Yan, X. Current status and prospects of memristors based on novel 2D materials. *Mater. Horizons* **2020**, *7*, 1495–1518. [CrossRef]
3. Abunahla, H.; Halawani, Y.; Alazzam, A.; Mohammad, B. NeuroMem: Analog graphene-based resistive memory for artificial neural networks. *Sci. Rep.* **2020**, *10*, 9473. [CrossRef] [PubMed]
4. Shen, Z.; Zhao, C.; Qi, Y.; Mitrovic, I.Z.; Yang, L.; Wen, J.; Huang, Y.; Li, P.; Zhao, C. Memristive non-volatile memory based on graphene materials. *Micromachines* **2020**, *11*, 341. [CrossRef] [PubMed]
5. Abunahla, H.; Mohammad, B.; Mahmoud, L.; Darweesh, M.; Alhawari, M.; Abi Jaoude, M.; Hitt, G.W. Memsens: Memristor-based radiation sensor. *IEEE Sens. J.* **2018**, *18*, 3198–3205. [CrossRef]
6. Carrara, S. The Birth of a New Field: Memristive Sensors. A Review. *IEEE Sens. J.* **2020**, *21*, 12370–12378. [CrossRef]
7. Tzouvadaki, I.; Madaboosi, N.; Soares, R.; Chu, V.; Conde, J.; De Micheli, G.; Carrara, S. Bio-functionalization study of memristive-biosensors for early detection of prostate cancer. In Proceedings of the 2015 11th Conference on Ph. D. Research in Microelectronics and Electronics (PRIME), Glasgow, UK, 29 June–2 July 2015; pp. 17–20.
8. Tzouvadaki, I.; Madaboosi, N.; Taurino, I.; Chu, V.; Conde, J.; De Micheli, G.; Carrara, S. Study on the bio-functionalization of memristive nanowires for optimum memristive biosensors. *J. Mater. Chem. B* **2016**, *4*, 2153–2162. [CrossRef] [PubMed]
9. Tzouvadaki, I.; Aliakbarinodehi, N.; De Micheli, G.; Carrara, S. The memristive effect as a novelty in drug monitoring. *Nanoscale* **2017**, *9*, 9676–9684. [CrossRef]
10. Tian, K.; Prestgard, M.; Tiwari, A. A review of recent advances in nonenzymatic glucose sensors. *Mater. Sci. Eng. C* **2014**, *41*, 100–118. [CrossRef]
11. Hadis, N.S.M.; Abd Manaf, A.; Herman, S.H.; Ngalim, S.H. High R off/R on ratio liquid based memristor sensor using sol gel spin coating technique. In Proceedings of the 2015 IEEE SENSORS, Busan, Korea, 1–4 November 2015; pp. 1–4.
12. Geim, A.K.; Novoselov, K.S. The rise of graphene. In *Nanoscience and Technology: A Collection of Reviews from Nature Journals*; World Scientific: Singapore, 2010; pp. 11–19.
13. Yao, J.; Lin, J.; Dai, Y.; Ruan, G.; Yan, Z.; Li, L.; Zhong, L.; Natelson, D.; Tour, J.M. Highly transparent nonvolatile resistive memory devices from silicon oxide and graphene. *Nat. Commun.* **2012**, *3*, 1101. [CrossRef]
14. Romero, M.F.J.; Toral, L.A.; Ohata, A.; Morales, S.D.P.; García, R.F.J.; Godoy, M.A.; Rodríguez, S.N. Laser-Fabricated Reduced Graphene Oxide Memristors. *Nanomaterials* **2019**, *9*, 897. [CrossRef] [PubMed]

15. Hong, S.K.; Kim, J.E.; Kim, S.O.; Choi, S.-Y.; Cho, B.J. Flexible resistive switching memory device based on graphene oxide. *IEEE Electron Device Lett.* **2010**, *31*, 1005–1007. [CrossRef]
16. Dreyer, D.R.; Park, S.; Bielawski, C.W.; Ruoff, R.S. The chemistry of graphene oxide. *Chem. Soc. Rev.* **2010**, *39*, 228–240. [CrossRef] [PubMed]
17. Porro, S.; Ricciardi, C. Memristive behaviour in inkjet printed graphene oxide thin layers. *RSC Adv.* **2015**, *5*, 68565–68570. [CrossRef]
18. Porro, S.; Accornero, E.; Pirri, C.F.; Ricciardi, C. Memristive devices based on graphene oxide. *Carbon* **2015**, *85*, 383–396. [CrossRef]
19. Aleksandrova, D. Five Benefits of Flexible Electronics for Displays and Sensors. FlexEnable. Available online: https://www.flexenable.com/blog/five-benefits-of-flexible-electronics-for-displays-and-sensors/ (accessed on 17 February 2020).
20. Abunahla, H.; Mohammad, B.; Alazzam, A.; Jaoude, M.A.; Al-Qutayri, M.; Abdul Hadi, S.; Al-Sarawi, S.F. MOMSense: Metal-oxide-metal elementary glucose sensor. *Sci. Rep.* **2019**, *9*, 5524. [CrossRef] [PubMed]
21. Alazzam, A. Solution-based, flexible and transparent patterned reduced graphene oxide electrodes for lab-on-chip applications. *Nanotechnology* **2019**, *31*, 075302. [CrossRef]
22. Alamoodi, N.; Alazzam, A. Droplet Coalescence by Selective Wettability Enhancement in Microfluidic Devices. *Nanomaterials* **2020**, *10*, 737. [CrossRef]
23. Alazzam, A.; Alamoodi, N. Microfluidic devices with patterned wettability using graphene oxide for continuous liquid–liquid two-phase separation. *ACS Appl. Nano Mater.* **2020**, *3*, 3471–3477. [CrossRef]
24. Dawaymeh, F.; Abbas, Y.; Khaleel, M.; Alazzam, A.; Alamoodi, N. Tuning the Surface Wettability of Cyclic Olefin Copolymer by Plasma Treatment and Graphene Oxide Deposition and Reduction. *Polymers* **2021**, *13*, 2305. [CrossRef]
25. El Fissi, L.; Vandormael, D.; Houssiau, L.; Francis, L.A. Surface functionalization of cyclic olefin copolymer (COC) with evaporated TiO_2 thin film. *Appl. Surf. Sci.* **2016**, *363*, 670–675. [CrossRef]
26. Huang, H.-H.; De Silva, K.K.H.; Kumara, G.; Yoshimura, M. Structural evolution of hydrothermally derived reduced graphene oxide. *Sci. Rep.* **2018**, *8*, 6849. [CrossRef]
27. Ferrari, A.C.; Robertson, J. Interpretation of Raman spectra of disordered and amorphous carbon. *Phys. Rev. B* **2000**, *61*, 14095. [CrossRef]
28. Panin, G.N.; Kapitanova, O.O.; Lee, S.W.; Baranov, A.N.; Kang, T.W. Resistive switching in Al/graphene oxide/Al structure. *Jpn. J. Appl. Phys.* **2011**, *50*, 70110. [CrossRef]
29. Romero, F.J.; Toral, A.; Medina-Rull, A.; Moraila-Martinez, C.L.; Morales, D.P.; Ohata, A.; Godoy, A.; Ruiz, F.G.; Rodriguez, N. Resistive switching in graphene oxide. *Front. Mater.* **2020**, *7*, 17. [CrossRef]
30. van den Hurk, J.; Menzel, S.; Waser, R.; Valov, I. Processes and Limitations during Filament Formation and Dissolution in GeS x-based ReRAM Memory Cells. *J. Phys. Chem. C* **2015**, *119*, 18678–18685. [CrossRef]
31. Mohammad, B.; Abi Jaoude, M.; Kumar, V.; Al Homouz, D.M.; Nahla, H.A.; Al-Qutayri, M.; Christoforou, N. State of the art of metal oxide memristor devices. *Nanotechnol. Rev.* **2016**, *5*, 311–329. [CrossRef]
32. Pradhan, S.K.; Xiao, B.; Mishra, S.; Killam, A.; Pradhan, A.K. Resistive switching behavior of reduced graphene oxide memory cells for low power nonvolatile device application. *Sci. Rep.* **2016**, *6*, 26763. [CrossRef]
33. Wei, H.; Zhou, P.; Sun, Q.; Wang, L.; Geng, Y.; Zhang, D.; Wang, X. The nano-scale resistive memory effect of graphene oxide. In Proceedings of the 2012 IEEE Nanotechnology Materials and Devices Conference (NMDC2012), Waikiki Beach, HI, USA, 16–19 October 2012; pp. 54–57.
34. Khurana, G.; Misra, P.; Katiyar, R.S. Forming free resistive switching in graphene oxide thin film for thermally stable nonvolatile memory applications. *J. Appl. Phys.* **2013**, *114*, 124508. [CrossRef]
35. Qi, Y.; Shen, Z.; Zhao, C.; Mitrovic, I.; Xu, W.; Lim, E.; Yang, L.; He, J.; Luo, T.; Huang, Y. Resistive switching behavior of solution-processed AlOx and GO based RRAM at low temperature. *Solid-State Electron.* **2020**, *168*, 107735. [CrossRef]
36. Ekiz, O.O.; Urel, M.; Guner, H.; Mizrak, A.K.; Dana, A. Reversible electrical reduction and oxidation of graphene oxide. *Acs Nano* **2011**, *5*, 2475–2482. [CrossRef] [PubMed]
37. Slobodian, O.M.; Lytvyn, P.M.; Nikolenko, A.S.; Naseka, V.M.; Khyzhun, O.Y.; Vasin, A.V.; Sevostianov, S.V.; Nazarov, A.N. Low-temperature reduction of graphene oxide: Electrical conductance and scanning kelvin probe force microscopy. *Nanoscale Res. Lett.* **2018**, *13*, 139. [CrossRef] [PubMed]

nanomaterials

Article

Development of Electrolyzer Using NiCo(OH)$_2$ Layered Double Hydroxide Catalyst for Efficient Water Oxidation Reaction

Rafia Nimal [1], Rashida Yahya [1], Afzal Shah [1,*], Muhammad Abdullah Khan [2], Muhammad Abid Zia [3] and Iltaf Shah [4,*]

[1] Department of Chemistry, Quaid-i-Azam University, Islamabad 45320, Pakistan; rafia.numal@gmail.com (R.N.); rashidayahya34@gmail.com (R.Y.)
[2] Renewable Energy Advancement Laboratory, Department of Environmental Sciences, Quaid-i-Azam University, Islamabad 45320, Pakistan; abdullah42pk@gmail.com
[3] Department of Chemistry, University of Education Lahore, Attock Campus, Attock 43600, Pakistan; abid@ue.edu.pk
[4] Department of Chemistry, College of Science, United Arab Emirates University, Al Ain P.O. Box 15551, United Arab Emirates
* Correspondence: afzalshah@qau.edu.pk or afzals_qau@yahoo.com (A.S.); altafshah@uaeu.ac.ae (I.S.)

Abstract: Over the past decade, layered double hydroxides (LDH) have been the subject of extensive investigations owing to their remarkable water splitting catalytic activity. Stability and porosity are several of the features of LDH which help them to serve as efficient oxygen evolution reaction (OER) catalysts. Based on these considerations, we synthesized NiCo(OH)$_2$ LDH and probed its OER electrocatalytic performance. The synthesized catalyst was subjected to X-ray diffraction, scanning electron microscopy, and X-ray photoelectron spectroscopy for structural analysis and investigation of its surface morphology, surface composition, and oxidation states. The LDH-NiCo(OH)$_2$ was anchored over the FTO surface and the fabricated electrode was found to exhibit a much lower OER onset potential of 265 mV, a much higher current density of 300 mAcm^{-2} and a smaller Tafel slope of 41 mVdec^{-1}. Moreover, the designed catalyst was found to be stable up to 2500 repeated voltametric scans. These figures of merit regarding the structure and performance of the designed LDH are expected to provide useful insights into the fundamental understanding of the OER catalysts and their mechanisms of action, thus enabling the more rational design of cost effective and highly efficient electrocatalysts for use in water splitting.

Keywords: NiCo(OH)$_2$ layered double hydroxides; electrocatalysis; oxygen evolution reaction; onset potential; current density; stability

Citation: Nimal, R.; Yahya, R.; Shah, A.; Khan, M.A.; Zia, M.A.; Shah, I. Development of Electrolyzer Using NiCo(OH)$_2$ Layered Double Hydroxide Catalyst for Efficient Water Oxidation Reaction. *Nanomaterials* **2022**, *12*, 1819. https://doi.org/10.3390/nano12111819

Academic Editors: Jihoon Lee and Ming-Yu Li

Received: 24 April 2022
Accepted: 21 May 2022
Published: 26 May 2022

1. Introduction

Energy demand has been increasing worldwide due to population growth, industrial development, and improvement in the standard of living. About 80% of this energy requirement is fulfilled by fossil fuels. However, although fossil fuels are the primary sources of energy, their reserves deplete with time. The non-sustainability of fossil fuels, and their associated environmental challenges, have prompted scientists to search out more abundant and sustainable energy sources [1–3]. Tidal, wind, and solar resources are renewable, clean, and eco-friendly, but their reliability is an issue due to daily and seasonal variations [4]. Hence, there is a need for a more sustainable energy source. In this regard, water splitting is a viable option, as it is renewable and abundantly available. Moreover, water splitting is a greener and more portable source, as its products can be put in storage or treated directly without creating any environmental risks [5,6]. In the 19th century, Paets van Troostwijk and Nicholson/Carlisle unveiled the method for the electrochemical splitting of water [7]. The concept of green energy relies on this discovery, and extensive efforts have been devoted to the advancement of water splitting [8,9]. However, so far, this abundant and environmentally friendly energy source has not yet been fully adopted worldwide. The reason for this is the high energy demanding anodic reaction of water electrolysis, i.e., the oxygen evolution reaction (OER). Thus, the affordability of water splitting is a challenge in the adoption of water as a greener energy source. A plethora of research teams are engaged in the search for cheaper catalysts that could trigger OER at the lowest possible potential.

The typical electrocatalytic splitting of water is carried out in a special electrolyzer containing a cathode for water reduction reactions and an anode for water oxidation reactions. Such electrolyzers contain suitable electrolytes for the facile transportation of ions between the two electrodes [10]. Water splitting involves two half reactions: a hydrogen evolution reaction (HER) and an oxygen evolution reaction (OER) [11]. In hypothetical terms, water splitting takes place when the applied voltage reaches 1.23 V, releasing hydrogen and oxygen gases from the electrode surfaces. However, in actual practice both HER and OER demand a substantial overpotential (η) [12,13]. The OER at the anode must cross a higher energy barrier/overpotential as it has more sluggish kinetics than the HER. Therefore, water splitting efficiencies rely mostly on OER [14]. The mechanism of OER is complex and strongly dependent on the structure and properties of the electrode surface. An effective OER electrocatalyst must contain adequate adsorption sites for efficient charge transfer between the electrode and adsorbed species. Another important factor determining the efficiency of the OER catalysts is the binding strength between the electrode surface and the reaction intermediates (e.g., HO*, O*, and HOO*). Generally, OER taking place on the active sites of the electrocatalysts involves four elementary steps: first, the formation of OH* intermediate from the adsorbed water molecules; second, the decomposition of OH* to O*; third, the subsequent reaction of O* with another adsorbed H_2O molecule to form OOH*; and finally, the formation and release of an O_2 molecule. Theoretically, the overpotential and OER activity are governed mainly by the rate-determining step. The formation of OOH* from O* is considered as the rate determining step, as it occurs at a potential higher than 1.23 V [15–20]. Researchers are trying to design electrocatalysts which could generate an OER signal closer to 1.23 V to minimize the overpotential (which is the main reason why the use of water splitting as an energy source is so expensive). Moreover, an ideal OER electrocatalyst should be efficient, stable, abundant, and cost effective. Understanding the structure–activity relationship is crucial for designing an effective water oxidation electrocatalyst [21–23].

Precious metal-based materials (usually RuO_2 and IrO_2) have been used for a long time to attain favorable OER kinetics. However, the scarcity and high cost of noble metals hinder their large-scale use for the commercial production of renewable fuel. Therefore, for achieving sustainable OER, electrocatalysts are prepared from earth-abundant metals and their activity and stability are examined. As such, researchers are preparing electrocatalysts for water electrolysis using cheaper earth-abundant elements (Ni, Co, and Fe), rather than benchmarked expensive catalysts such as Pt [24]. Ni has emerged as a promising non-noble metal electrocatalyst for water splitting owing to its abundance, lower cost, corrosion resistance, and ability to catalyze OER at a lower overpotential. Therefore, hydroxides of Ni-based electrocatalysts have excelled amongst other options in catalyzing OER. By the incorporation of other metals, the performance of individual Ni oxides can be improved. In this regard, Co is a promising candidate for OER catalysis [25,26]. Due to a number of advantages, layered double hydroxides, which belong to the two-dimensional materials family, have gained considerable interest for use in OER since 2013. Their main advantages are their larger surface area, greater surface-to-volume ratio, significantly exposed active sites, and higher efficiency than 0D and 1D materials. Their multilayer structural adjustment can be controlled by intercalation, topological transformation, or by assembling other functional materials. Their chemical composition can be tuned by changing the ratio of cations. Their ordered porosities support the transportation of water molecules and the release of gaseous products. They have configurable active site orientation, as well as increased structural stability [27]. Hence, the current work is focused on LDH and the utilization of its unique structure for water splitting catalysis.

Multiple parameters can decide the performance of a water splitting electrocatalyst, with overpotential, current density, Tafel slope, and charge transfer resistance being the most commonly evaluated parameters for the assessment of OER performance [28,29]. Based on these considerations, we synthesized $NiCo(OH)_2$ layered double hydroxide and explored its OER activity. The LDH-$NiCo(OH)_2$ fabricated FTO is the first example of a highly stable, efficient, and inexpensive OER catalyst that demonstrates the low onset potential, high current density, low charge transfer resistance, long-term cyclability, and low Tafel slope desired for an OER catalyst. Hence, the results of our investigations are expected to provide valuable insights into the electrocatalytic role of LDH and improve our fundamental understanding of the relationship of structure and OER catalytic mechanism of action.

2. Experimental Section

2.1. Chemicals and Materials

Nickel(II) nitrate hexahydrate ($Ni(NO_3)_2{\cdot}6H_2O$, purity above 97%), cobalt(II) nitrate hexahydrate ($Co(NO_3)_2{\cdot}6H_2O$, extra pure), ammonium hydroxide of 99.99% purity, anhydrous potassium chloride of ≥99% purity, 5 μL Nafion (10% Aldrich solution), benzyl alcohol (HPLC grade), and an acetone solution of ≥99.8% purity, were all purchased from Beijing Chemicals Co., Ltd., Beijing, China. Analytical-grade ethanol was used. All these chemicals and reagents were used as purchased and solutions were made in deionized water.

2.2. Physical Characterization

X-ray diffraction (XRD) analysis was performed using an XRD spectrometer (D-8 Discover, Bruker, Germany) within a 10–80 (2θ degrees) range by utilizing CuKα radiation. The surface morphology was analyzed using a field-emission scanning electron microscope (JSM-7600F, JEOL, Tokio, Japan). X-ray photoelectron spectroscopy (XPS) analysis was executed by using Kratos Nova with an Al Kα energy source at 1486.6 eV. Scans were conducted at an anode voltage of 15 kV and a 10 mA current. The pass energy was set to 160 eV for survey scans and 20 eV for high-resolution scans. The binding energy was calibrated by referencing the charge to the hydrocarbon C 1s peak at 285.0 eV.

2.3. Synthesis of LDH-$NiCo(OH)_2$

A simple co-precipitation method was used for the synthesis of layered double hydroxide. A solution was prepared by dissolving 0.64 mmol $Ni(NO_3)_2$ and 1.28 mmol $Co(NO_3)_2$ in 14 mL benzyl alcohol. The resulting solution was then stirred for 2 h at room temperature. In the next step, the solution was charged by the dropwise addition of 14 mL ammonia solution and heated to 165 °C for further two hours. The resulting precipitated solution was allowed to cool naturally and sonicated for 10 min to undo the agglomeration of particles in order to obtain a good separation. The final material was dried under nitrogen and put in a desiccator for 48 h for further drying.

2.4. Cleaning of the FTO Electrode

Conductive FTO glass (FTO, Omniscience, South Korea) (1 cm × 1 cm × 2 mm, $16\ \Omega\ cm^{-2}$) was used as a substrate for modification with the synthesized electrocatalyst. Prior to the deposition of the active material, the FTO substrate was washed properly. FTO glass was initially sonicated with acetone for 15 min and then with ethanol for another 15 min so that any organic impurity was dissolved and removed from the surface of the FTO. After thorough cleaning, the substrate was parched in a muffle furnace at a temperature of 120 °C for around 90 min for degassing. This treatment leads to a less bumpy surface and an ultimately smooth coating of active material.

2.5. Formation of Catalytic Ink and Working Electrode Fabrication

To carry out electrochemical studies, a working electrode was first fabricated with catalytic ink. An ink of the chosen catalyst was prepared by the accumulation of 5 mg of the synthesized $NiCo(OH)_2$ in 250 μL methanol/ethanol (analytical grade) and 5 μL of Nafion binder, followed by sonication for 3–4 h. After sonication, the ink of the desired material was coated over the surface of FTO via the drop casting method. The modified FTO was then dried in oven at 70 °C for 24 h. After drying, the coated FTO (with mass loading of 0.294 mg cm^{-2}) was ready for use as a working electrode.

2.6. Electrochemical Water Oxidation Studies

All electrochemical experiments were conducted on a Potentiostat/Galvanostat/ZRA 02529 (Interface 5000E) Gamry workstation (Warminster, PA, USA). The OER activity of the electrocatalyst was studied in 1 M KOH in a three-electrode system. The FTO coated with the desired catalyst was used as the working electrode, Ag/AgCl (3.0 M KCl) as the reference electrode, and platinum wire as a counter electrode. All the potentials in this work were measured with reference to Ag/AgCl. For conversion to the RHE scale, the following equation was used:

$$E_{(RHE)} = E_{(Ag/AgCl)} + 0.197 + (0.059 \times pH)$$

3. Results and Discussion

3.1. Structural and Morphological Analysis

XRD was performed for the phase categorization of the synthesized material. The XRD pattern of the electrocatalyst obtained in the 2θ range of 10–80 is displayed in Figure 1.

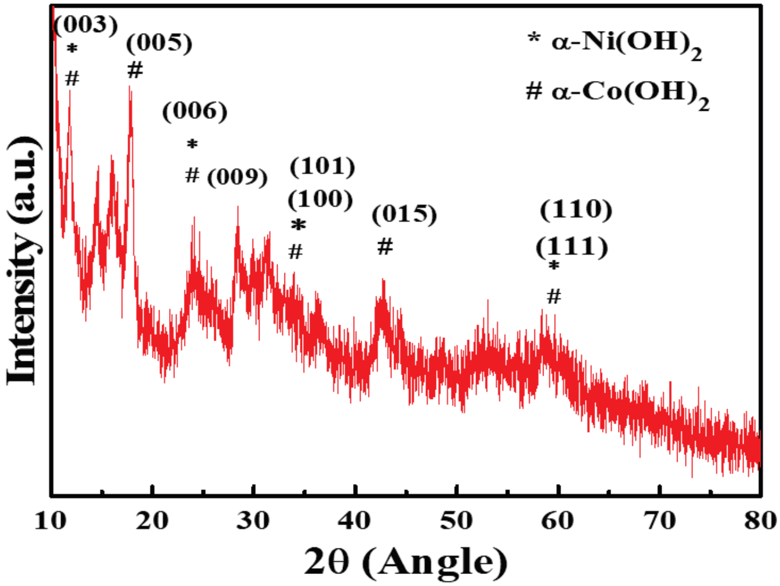

Figure 1. XRD pattern of $NiCo(OH)_2$-LDH.

The peaks for $NiCo(OH)_2$ appear at 2θ values between 11 and 60. The detectable diffraction peaks of $NiCo(OH)_2$ are in good agreement with those reported previously and can be referenced to α-$Ni(OH)_2$ and α-$Co(OH)_2$, matching JCPDS No: 38-0715 and JCPDS No: 01-087-0645 [30,31], respectively. The XRD pattern, which typically shows a steep rise in the low-angle section and noticeable asymmetry in the high-angle section, is suggestive of layer stacking, as observed in the case of the synthesized material. It also indicates that the synthesized material is loose and defective, with turbo static phases observed in the case of various α-type hydroxides [32–34]. The lesser diffraction intensity and noisy profile are indicative of poor crystallinity, as required for LDH. A loose, less crystalline structure with defective sites is generally required for good catalytic activity, as such structures provide a greater surface area and larger number of active sites for the adsorption of reactants and intermediates [35–38].

SEM provides information about surface roughness, porosity, inter-metallic distribution, material homogeneity, and particle size. SEM was performed to analyze the surface morphology and texture of the synthesized material. The surface morphology was observed at different magnifications. Figure 2 reveals that the material has a characteristic layered structure, having pores that offer a large surface area for increased OER catalytic activity. The SEM-EDS results indicate that the Ni/Co ratio is nearing 1:1.

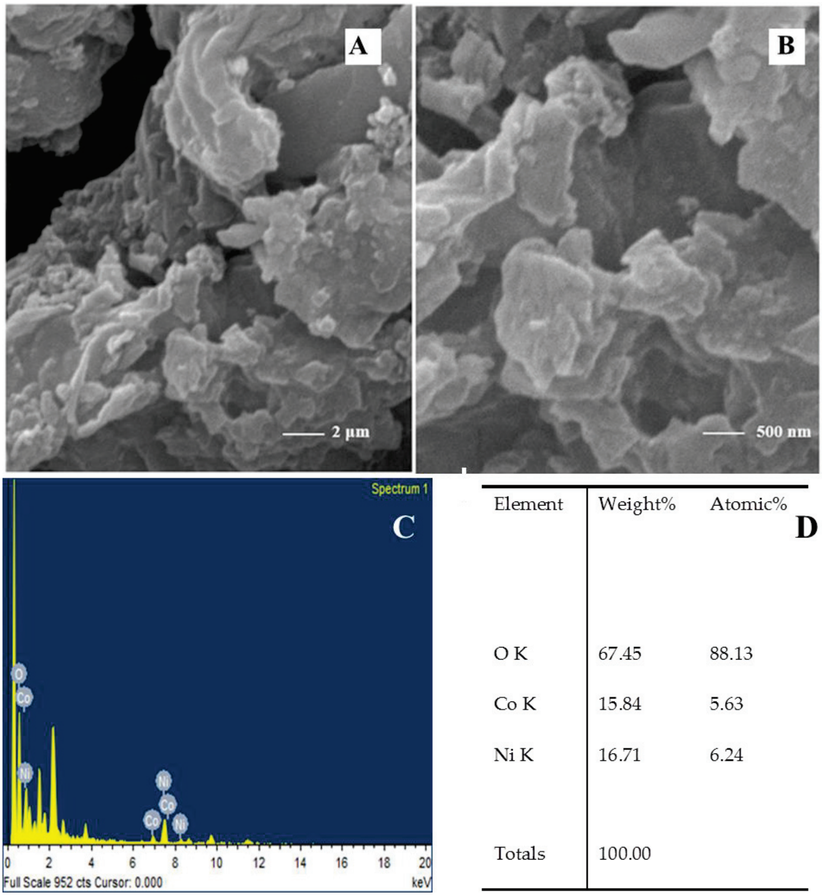

Element	Weight%	Atomic%
O K	67.45	88.13
Co K	15.84	5.63
Ni K	16.71	6.24
Totals	100.00	

Figure 2. (**A**,**B**) SEM analysis, (**C**) EDS analysis, and (**D**) percentage of elements in NiCo(OH)$_2$-LDH powdered sample.

The high-resolution Ni 2p, Co 2p, and O 1s XPS scans of the NiCo(OH)$_2$ LDH sample were further investigated to determine the surface chemical states of nickel and cobalt ions, as well as the types of oxygen-containing species present (Figure 3). The O 1s signals in Figure 3B at the binding energy value of 531.2 eV and 529.5 eV can be ascribed to the oxygen atoms on the M-O-H groups of the nickel and cobalt hydroxides and the oxygen atoms on the M-O groups of cobalt oxide, respectively. The binding energy spectrum of

Ni extends from 850 to 890 eV, with two clear shakeup satellites close to two spin-orbit doublets at 870.2 eV and 853 eV with a spin–energy separation of 17.2 eV, as shown in Figure 3D, and can be identified as Ni $2p_{1/2}$ and Ni $2p_{3/2}$ signals assigned to the Ni^{2+} state. Moreover, the O 1s, along with Ni $2p_{3/2}$ energy at 853 eV, indicates Ni-O bond formation at the surface, as reported by McIntyre and coworkers [39]. The two main peaks in Figure 3C (one at a binding energy of 781.6 eV and the other at one of 797.1 eV with two weak shake-up satellites) can be attributed to Co $2p_{3/2}$ and Co $2p_{1/2}$ orbitals. Zhang and coworkers have reported similar results for a nickel-cobalt layered double hydroxide nanoflake array, where a shoulder peak in the higher binding energy area indicates the presence of oxidized cobalt [40]. Moreover, the O 1s signal, along with Co $2p_{3/2}$ at 781.6 eV, suggests CoO bond formation at the surface, as reported by McIntyre and coworkers [39].

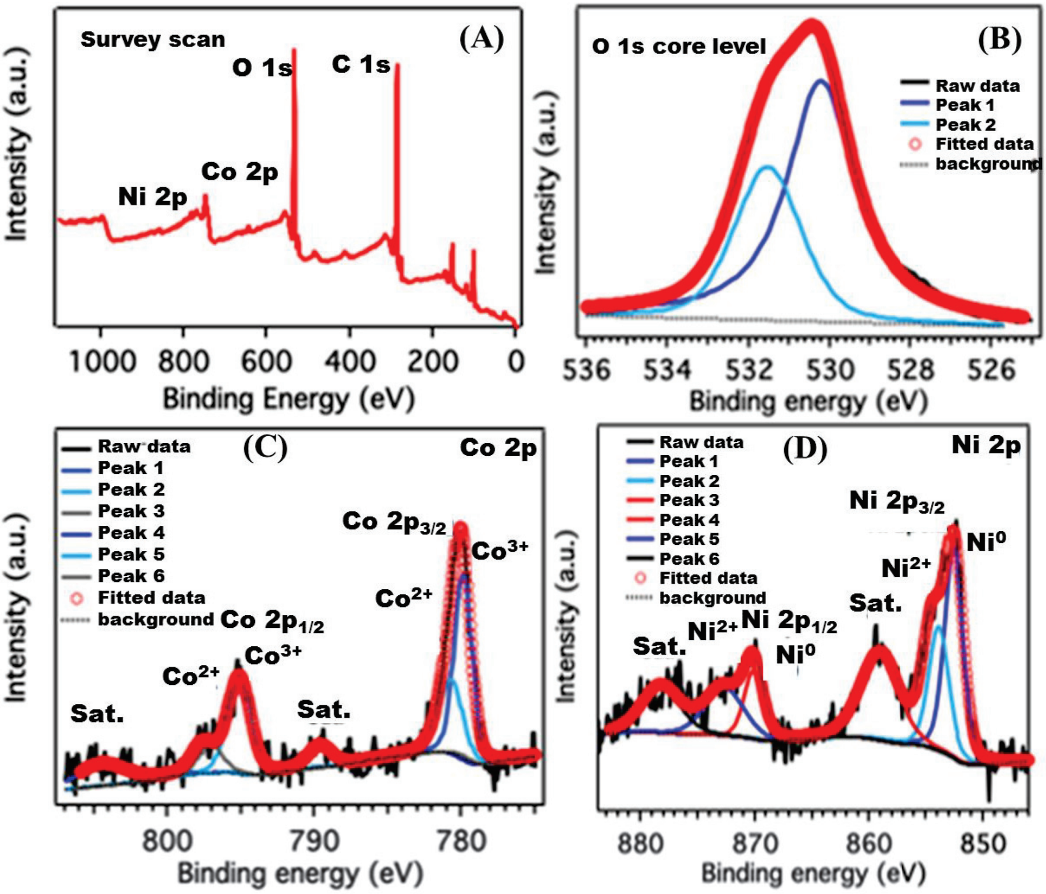

Figure 3. (**A**) Core-level XPS survey spectrum for $NiCo(OH)_2$-LDH. The fitted and de-convoluted high-resolution XPS spectra of (**B**) oxygen are referred to as O (1s), for (**C**) cobalt are referred to as Co (2p), and for (**D**) nickel are referred to as Ni(2p).

3.2. Electrochemical Water Oxidation Studies

Linear scan voltammetry (LSV) was used to examine the catalytic OER efficiency of $NiCo(OH)_2$-LDH/FTO, $NiCo_2O_4$/FTO, and NiOOH/FTO. These three electrocatalysts were synthesized using the same co-precipitation method. By recording the LSV scans shown in Figure 4A under similar experimental conditions, it can be noted that the OER signals at $NiCo(OH)_2$-LDH/FTO, $NiCo_2O_4$/FTO, and NiOOH/FTO have current density values of 300, 100 and 30 $mAcm^{-2}$, respectively. $NiCo(OH)_2$-LDH/FTO shows an onset potential of 265 mV and an over-potential of 350 mV at the current density of 10 $mAcm^{-2}$, while $NiCo_2O_4$/FTO and NiOOH/FTO show over-potentials of 480 mV and 610 mV at the current density of 10 $mAcm^{-2}$. The comparative study of these three electrocatalysts reveals that $NiCo(OH)_2$-LDH/FTO displays the attributes of a promising OER catalyst, as is obvious due to its lower overpotential and significantly higher current density. Hence, among the three synthesized catalysts, $NiCo(OH)_2$-LDH was used for further electrochemical studies. At the practical potential of 2.4 V vs. RHE, $NiCo(OH)_2$/FTO registered the maximum current density of 300 $mAcm^{-2}$. Figure 4A,B indicate that O_2 evolution starts at a 265 mV higher potential than the theoretical value of 1230 mV.

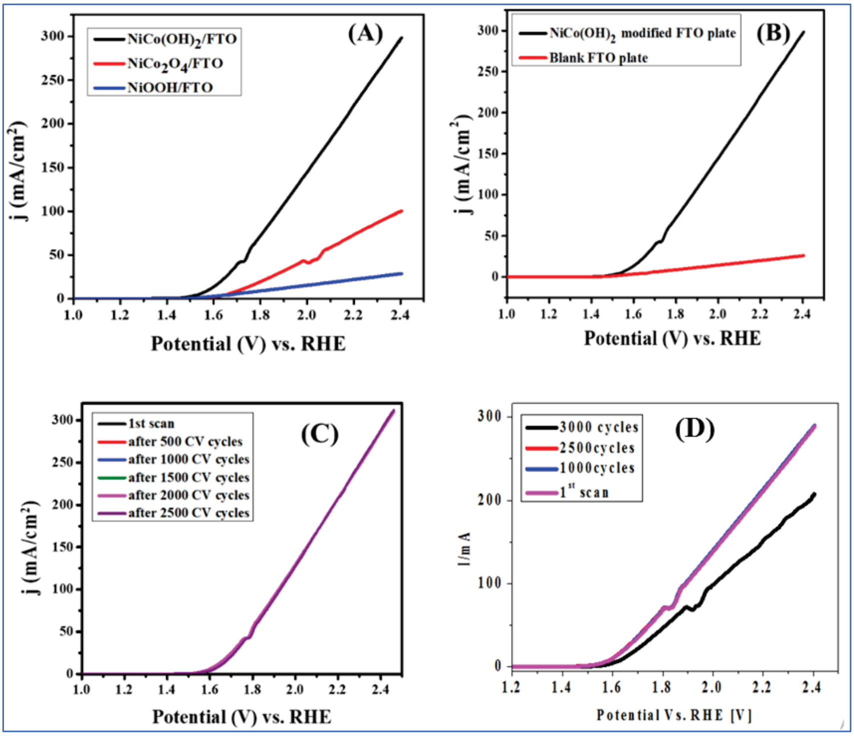

Figure 4. (**A**) LSV curves of $NiCo(OH)_2$/FTO, $NiCo_2O_4$/FTO, and NiOOH/FTO; (**B**) LSV of $NiCo(OH)_2$/FTO for OER activity in 1 M KOH solution at a scan rate of 10 mV/s; (**C**) LSVs of $NiCo(OH)_2$/FTO before and up to repeated 2500 CV cycles; (**D**) LSVs showing current loss after 2500 repeated CV cycles.

The electrocatalyst was tested for durability by recording LSVs after scanning consecutive CV cycles at a 50 mV/s scan rate. Before and after every 500 cycles of CV, an LSV scan was run. By plotting the LSV scans, it is seen that all 2500 curves overlap and show no loss in the current and shape of voltammograms, as demonstrated in Figure 4C. Hence, durability, which is a prime objective of the practical implementation of the catalyst, was achieved, as the synthesized catalyst qualified repeating cycling tests by retaining its efficiency even after the use of up to 2500 CV cycles. Figure 4D suggests the upper stability limit of the catalyst.

The electrochemically active surface area (ECSA) of $NiCo(OH)_2$ (LDH) was calculated using the scan rate dependent cyclic voltammograms presented in Figure 5A. The non-Faradaic capacitive current accompanying the double-layer charging was calculated by assuming that all measured current in this range is attributable to double-layer charging.

The non-Faradaic potential was set between 1.2 and 1.28 V vs. RHE. By plotting the current versus scan rate, linear plots were obtained for anodic and cathodic currents, as shown in Figure 5B. The value of double-layer capacitance (C_{dl}) was determined from the average slopes. By dividing the value of C_{dl} (4 mF) by the specific capacitance C_{sp} (0.040 mFcm^{-2}), the ECSA of the electrocatalyst with a value of 100 cm^2 was obtained. This large surface area of the electrocatalyst might be one of the factors responsible for the enhanced OER electrocatalytic activity of NiCo(OH)$_2$ (LDH). The catalytic roughness factor (RF), with a value of 100 cm^2, was calculated by dividing the ECSA by the geometric area of the electrode (1 cm^2). In general, a higher RF value is suggestive of greater catalytic activity.

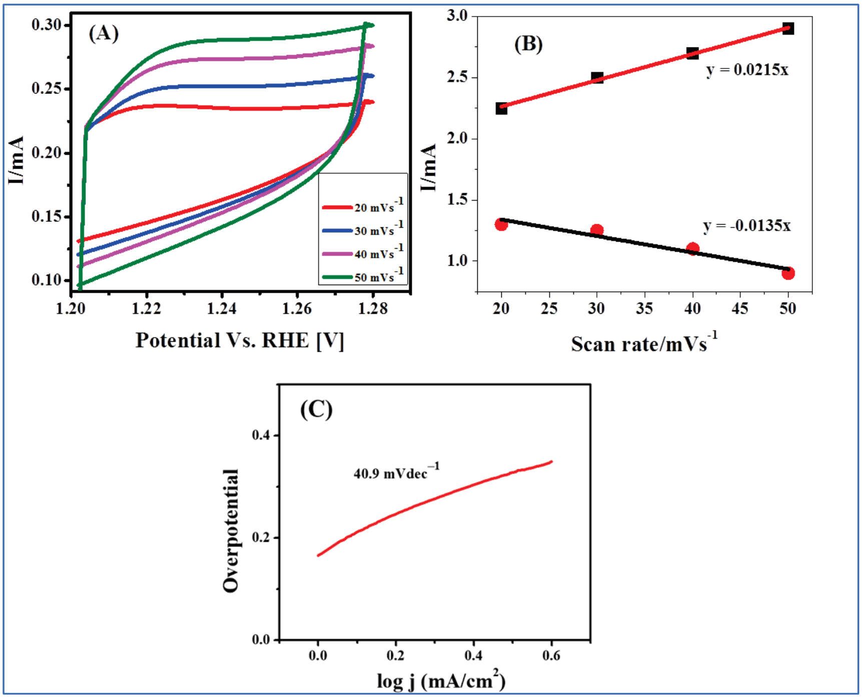

Figure 5. (**A**) CVs of NiCo(OH)$_2$-LDH/FTO electrocatalyst performed in the non-Faradaic region at various scan rates from 10 to 50 mVs^{-1}; (**B**) plot of anodic and cathodic currents against scan rate for NiCo(OH)$_2$-LDH/FTO electrocatalyst; (**C**) Tafel plot based on the data (during the OER) obtained from LSV for the NiCo(OH)$_2$/FTO electrocatalyst.

Tafel slope was calculated using the OER fitted LSV curves. For the Tafel graph, overpotential was plotted as a function of log (j), as shown in Figure 5C. Tafel slope value gives information about both the reaction kinetics and about the amount of adsorbed species generated at the surface of the catalyst. The small value (40.9 mV/dec) of the Tafel slope using data obtained at NiCo(OH)$_2$/FTO indicates that the designed electrocatalyst facilitates rapid charge transport. The lower Tafel slope value demonstrates the need for a smaller overpotential, which is the key requirement for electrocatalytic oxygen evolution. Table 1 shows a comparison of the OER performance of the Ni and Co containing electrocatalysts in terms of Tafel slope, onset potential, overpotential, and maximum current density in solutions containing 1 M KOH electrolyte.

Table 1. Comparison of the OER performance parameters of our synthesized and reported Ni- and Co-based electrocatalysts.

Catalyst	Substrate	Current Density ($mAcm^{-2}$)	Overpotential (η) at 10 $mAcm^{-2}$	Onset Potential (mV)	Tafel Slope ($mVdec^{-1}$)	Refs.
NiCo LDH@ZIF-67-V_O/NF	NF	200	290 mV	260	58	[41]
NiCoON NSAs/NF	NF	50	247 mV	247	35	[42]
NiO/$NiCo_2O_4$	GC	70	357 mV	300	130	[43]
Ni_3FeN	GC	150	421 mV	340	116	[44]
NiCo-S@CoFeA-TT	GCE	90	268 mV	250	62	[45]
$FeNi_8Co_2$ LDH	NF	40	210 mV	190	42	[46]
$NiCo_2O_4$/NiMn LDH	NF	80	310 mV	310	99	[47]
Fe–Co-2.3Ni–B	GC	50	274 mV	240	38	[48]
NCO−HNSs	FTO	90	340 mV	300	51	[49]
$NiCo(OH)_2$-LDH	FTO	300	350 mV	265	41	This work

Charge transfer is another crucial factor for the assessment of the performance catalysts. Electrochemical impedance was performed at the bare and modified FTO under OER conditions. The EIS analysis of $NiCo(OH)_2$-LDH was carried out in 1.0 M KOH solution. The respective Nyquist plot is presented in Figure 6A. The semicircular pattern reveals a property of the charge transfer mechanism. The charge transfer resistance (R_{ct}), which is the resistance present between the catalytic surface and the electrolyte interface, is equal to the semicircle diameter. R_{ct} controls the OER charge transfer kinetics. In the inset of Figure 6A simplified Randles circuit (RCR) is given in which R_s indicates the solution resistance, R_{ct} is the charge transfer resistance and CPE is the constant phase element. A simplified Randles circuit (RCR) with resistors and capacitor was fitted to the EIS data to obtain the R_{ct}, with a value of 3.7 Ω obtained for $NiCo(OH)_2$/FTO. This lower value of R_{ct} is another factor responsible for the pronounced electrocatalytic activity of the synthesized catalyst.

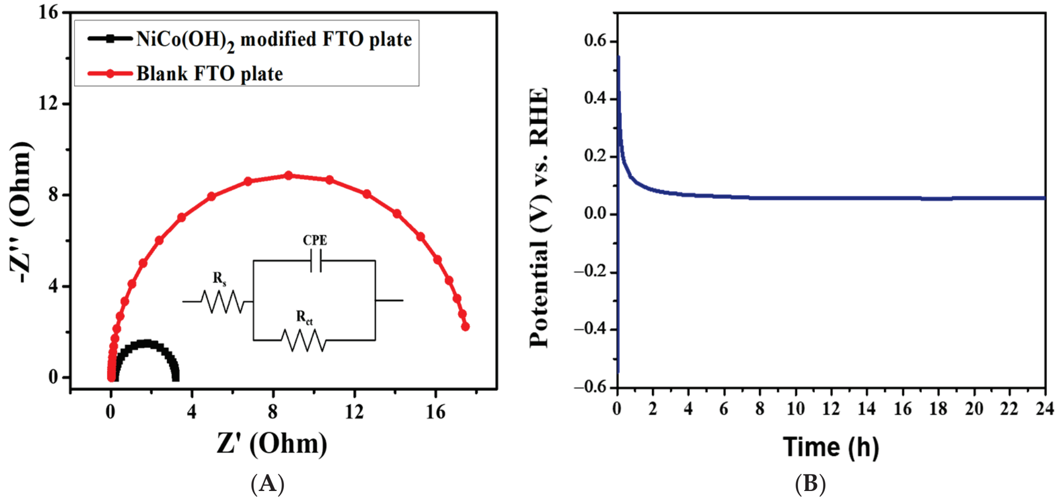

Figure 6. (**A**) Nyquist plot using EIS data obtained for $NiCo(OH)_2$/FTO in a 1 M KOH solution. (**B**) Stability of $NiCo(OH)_2$/FTO.

Chronoamperometry was performed to examine the stability and durability of the $NiCo(OH)_2/FTO$ at a constant potential of 1.6 V for 24 h in 1 M KOH solution. The chronoamperogram shown in Figure 6B displays its stability and validates the LSV results of no current loss during the OER catalytic performance for up to 2500 consecutive CV cycles. Thus, $NiCo(OH)_2$-LDH is a promising example of a highly durable and inexpensive electrocatalyst material for water oxidation.

4. Conclusions

An efficient, stable, and inexpensive water oxidation electrocatalyst, $NiCo(OH)_2$-LDH, was synthesized via a facile co-precipitation method. The synthesized electrocatalyst was characterized through XRD, SEM, and XPS. Characterization studies revealed the formation of the catalyst in the form of layered double hydroxides. SEM results pointed to the porous and layered structure of the synthesized catalyst. XPS demonstrated the oxidation states and surface configurations of Ni and Co. Electrochemical water oxidation studies were examined for $NiCo(OH)_2/FTO$ through LSV, CV, EIS, and chronoamperometry. The catalytic activity of the material deposited on the FTO was measured in 1 M KOH. LSV data showed the onset potential of 265 mV, maximum current density of up to 300 A, and overpotential of 350 V at a current density of 10 $mAcm^{-2}$ using $NiCo(OH)_2/FTO$ for electrocatalytic water oxidation. At the electrochemically active surface area of 100 cm^2, the charge transfer resistance of just 3.7 Ω and Tafel slope around 41 $mVdec^{-1}$ revealed the intrinsically favorable catalytic properties of the synthesized LDH. Chronoamperometry results and the similarity of the LSV scans of up to 2500 repeating cyclic voltammetric cycles confirmed the long-term stability of the synthesized catalyst.

Author Contributions: R.N. and R.Y., Conceptualization, Investigation, Methodology, Writing—original draft. A.S. and M.A.K., Supervision, Project administration, Writing—review and editing. M.A.Z. and I.S., Funding acquisition, Resources, Visualization, Writing—review and editing. All authors have read and agreed to the published version of the manuscript.

Funding: The Higher Education Commission of Pakistan is gratefully acknowledged for NRPU Project No. 6815.

Institutional Review Board Statement: Not applicable.

Informed Consent Statement: Not applicable.

Data Availability Statement: The data presented in this study are available on request from the corresponding author.

Acknowledgments: Iltaf Shah graciously acknowledges the generous support from UAE University (UPAR 12S091).

Conflicts of Interest: The authors declare no conflict of interest.

References

1. Shah, A.; Zahid, A.; Subhan, H.; Munir, A.; Iftikhar, F.J.; Akbar, M. Heteroatom-doped carbonaceous electrode materials for high performance energy storage devices. *Sustain. Energy Fuels* **2018**, *2*, 1398–1429. [CrossRef]
2. Akbar, M.; Shah, A.; Iftikhar, F.J.; Ali, G.; Han, H.; Rahman, G. In-situ formation of an efficient trimetallic (Cu-Zn-Ag) electrocatalyst for water oxidation. *Int. J. Energy Res.* **2021**, *45*, 2931–2944. [CrossRef]
3. Rashed, A.H.; Shah, A. The role of private sector in the implementation of sustainable development goals. *Environ. Dev. Sustain.* **2021**, *23*, 2931–2948. [CrossRef]
4. Nautiyal, A.; Ramlal, A. Clean Energy Sources for a better and sustainable environment of future generations. In *Energy: Crises, Challenges and Solutions*; Singh, P., Singh, S., Kumar, G., Baweja, P., Eds.; John Wiley & Sons: Hoboken, NJ, USA, 2021; pp. 151–168.
5. Aljar, M.A.A.; Zulqarnain, M.; Shah, A.; Akhter, M.S.; Iftikhar, F.J. A review of renewable energy generation using modified titania for photocatalytic water splitting. *AIP Adv.* **2020**, *10*, 070701. [CrossRef]
6. Aftab, S.; Shah, A.; Nisar, J.; Ashiq, M.N.; Akhter, M.S.; Shah, A.H. Marketability prospects of microbial fuel cells for sustainable energy generation. *Energy Fuels* **2020**, *34*, 9108–9136. [CrossRef]
7. Fabbri, E.; Schmidt, T.J. Oxygen evolution reaction—The enigma in water electrolysis. *ACS Publ.* **2018**, *8*, 9765–9774. [CrossRef]
8. Zulqarnain, M.; Shah, A.; Khan, M.A.; Iftikhar, F.J.; Nisar, J. $FeCoSe_2$ nanoparticles embedded in g-C_3N_4: A highly active and stable bifunctional electrocatalyst for overall water splitting. *Sci. Rep.* **2020**, *10*, 6328. [CrossRef]

9. Chen, D.; Zhu, J.; Mu, X.; Cheng, R.; Li, W.; Liu, S.; Pu, Z.; Lin, C.; Mu, S. Nitrogen-Doped carbon coupled $FeNi_3$ intermetallic compound as advanced bifunctional electrocatalyst for OER, ORR and Zn-air batteries. *Appl. Catal. B Environ.* **2020**, *268*, 118729. [CrossRef]
10. Li, P.; Zhao, R.; Chen, H.; Wang, H.; Wei, P.; Huang, H.; Liu, Q.; Li, T.; Shi, X.; Zhang, Y. Recent advances in the development of water oxidation electrocatalysts at mild pH. *Small* **2019**, *15*, 1805103. [CrossRef]
11. Ji, X.; Zhang, Y.; Ma, Z.; Qiu, Y. Oxygen Vacancy-rich Ni/NiO@ NC Nanosheets with Schottky Heterointerface for Efficient Urea Oxidation Reaction. *ChemSusChem* **2020**, *13*, 5004–5014. [CrossRef]
12. Takeguchi, T.; Yamanaka, T.; Takahashi, H.; Watanabe, H.; Kuroki, T.; Nakanishi, H.; Orikasa, Y.; Uchimoto, Y.; Takano, H.; Ohguri, N. Layered perovskite oxide: A reversible air electrode for oxygen evolution/reduction in rechargeable metal-air batteries. *J. Am. Chem. Soc.* **2013**, *135*, 11125–11130. [CrossRef]
13. Ishaque, M.; Shah, A.; Iftikhar, F.J.; Akbar, M. Development of transition metal based electrolyzer for efficient oxygen evolution reaction. *J. Renew. Sustain. Energy* **2020**, *12*, 024102. [CrossRef]
14. Tahir, M.; Pan, L.; Idrees, F.; Zhang, X.; Wang, L.; Zou, J.J.; Wang, Z.L. Electrocatalytic oxygen evolution reaction for energy conversion and storage: A comprehensive review. *Nano Energy* **2017**, *37*, 136–157. [CrossRef]
15. Anantharaj, S.; Karthick, K.; Kundu, S. Evolution of layered double hydroxides (LDH) as high performance water oxidation electrocatalysts: A review with insights on structure, activity and mechanism. *Mater. Today Energy* **2017**, *6*, 1–26. [CrossRef]
16. Fang, Y.H.; Liu, Z.P. Mechanism and tafel lines of electro-oxidation of water to oxygen on RuO_2 (110). *J. Am. Chem. Soc.* **2010**, *132*, 18214–18222. [CrossRef] [PubMed]
17. Curutchet, A.; Colinet, P.; Michel, C.; Steinmann, S.N.; Le Bahers, T. Two-sites are better than one: Revisiting the OER mechanism on CoOOH by DFT with electrode polarization. *Phys. Chem. Chem. Phys.* **2020**, *22*, 7031–7038. [CrossRef]
18. Rong, X.; Parolin, J.; Kolpak, A.M. A fundamental relationship between reaction mechanism and stability in metal oxide catalysts for oxygen evolution. *ACS Catal.* **2016**, *6*, 1153–1158. [CrossRef]
19. Moysiadou, A.; Lee, S.; Hsu, C.S.; Chen, H.M.; Hu, X. Mechanism of oxygen evolution catalyzed by cobalt oxyhydroxide: Cobalt superoxide species as a key intermediate and dioxygen release as a rate-determining step. *J. Am. Chem. Soc.* **2020**, *142*, 11901–11914. [CrossRef]
20. Dau, H.; Limberg, C.; Reier, T.; Risch, M.; Roggan, S.; Strasser, P. The mechanism of water oxidation: From electrolysis via homogeneous to biological catalysis. *ChemCatChem* **2010**, *2*, 724–761. [CrossRef]
21. Alobaid, A.; Wang, C.; Adomaitis, R.A. Mechanism and kinetics of HER and OER on NiFe LDH films in an alkaline electrolyte. *J. Electrochem. Soc.* **2018**, *165*, J3395. [CrossRef]
22. Abid, A.G.; Manzoor, S.; Usman, M.; Munawar, T.; Nisa, M.U.; Iqbal, F.; Ashiq, M.N.; Haq, M.N.; Shah, A.; Imran, M. Scalable synthesis of Sm_2O_3/Fe_2O_3 hierarchical oxygen vacancy-based gyroid-inspired morphology: With enhanced electrocatalytic activity for oxygen evolution performance. *Energy Fuels* **2022**, *35*, 17820–17832. [CrossRef]
23. Sadaqat, M.; Nisar, L.; Hussain, F.; Ashiq, M.N.; Shah, A.; Ehsan, M.F.; Joya, K.S.; Najam-Ul-Haq, M. Zinc-telluride nanospheres as an efficient water oxidation electrocatalyst displaying a low overpotential for oxygen evolution. *J. Mater. Chem. A* **2019**, *7*, 26410–26420. [CrossRef]
24. Anantharaj, S.; Noda, S. Amorphous catalysts and electrochemical water splitting: An untold story of harmony. *Small* **2020**, *16*, 1905779. [CrossRef]
25. Babar, P.; Lokhande, A.; Gang, M.; Pawar, B.; Pawar, S.; Kim, J.H. Thermally oxidized porous NiO as an efficient oxygen evolution reaction (OER) electrocatalyst for electrochemical water splitting application. *J. Ind. Eng. Chem.* **2018**, *60*, 493–497. [CrossRef]
26. Li, Y.; Bao, X.; Chen, D.; Wang, Z.; Dewangan, N.; Li, M.; Xu, Z.; Wang, J.; Kawi, S.; Zhong, Q. A Minireview on nickel based heterogeneous electrocatalysts for water splitting. *ChemCatChem* **2019**, *11*, 5913–5928. [CrossRef]
27. Cai, Z.; Bu, X.; Wang, P.; Ho, J.C.; Yang, J.; Wang, X. Recent advances in layered double hydroxide electrocatalysts for the oxygen evolution reaction. *J. Mater. Chem. A* **2019**, *7*, 5069–5089. [CrossRef]
28. Anantharaj, S.; Kundu, S. Do the evaluation parameters reflect intrinsic activity of electrocatalysts in electrochemical water splitting? *ACS Energy Lett.* **2019**, *4*, 1260–1264. [CrossRef]
29. Anantharaj, S.; Ede, S.; Karthick, K.; Sankar, S.S.; Sangeetha, K.; Karthik, P.; Kundu, S. Precision and correctness in the evaluation of electrocatalytic water splitting: Revisiting activity parameters with a critical assessment. *Energy Environ. Sci.* **2018**, *11*, 744–771. [CrossRef]
30. Aghazadeh, M.; Ghaemi, M.; Sabour, B.; Dalvand, S. Electrochemical preparation of α-$Ni(OH)_2$ ultrafine nanoparticles for high-performance supercapacitors. *J. Solid State Electrochem.* **2014**, *18*, 1569–1584. [CrossRef]
31. Youssry, S.M.; El-Hallag, I.; Kumar, R.; Kawamura, G.; Matsuda, A.; El-Nahass, M.N. Synthesis of mesoporous $Co(OH)_2$ nanostructure film via electrochemical deposition using lyotropic liquid crystal template as improved electrode materials for supercapacitors application. *J. Electroanal. Chem.* **2020**, *857*, 113728. [CrossRef]
32. Song, J.M.; Ni, J.J.; Zhang, J.; Ling, D.; Niu, H.L.; Mao, C.J.; Zhang, S.Y.; Shen, Y.H. A facile synthesis of graphene-like cobalt–nickel double hydroxide nanocomposites at room temperature and their excellent catalytic and adsorption properties. *J. Nanopart. Res.* **2014**, *16*, 1–15. [CrossRef]
33. Wang, X.; Zheng, Y.; Yuan, J.; Shen, J.; Hu, J.; Wang, A.J.; Wu, L.; Niu, L. Porous NiCo diselenide nanosheets arrayed on carbon cloth as promising advanced catalysts used in water splitting. *Electrochim. Acta* **2017**, *225*, 503–513. [CrossRef]

34. Yang, R.; Zhou, Y.; Xing, Y.; Li, D.; Jiang, D.; Chen, M.; Shi, W.; Yuan, S. Synergistic coupling of CoFe-LDH arrays with NiFe-LDH nanosheet for highly efficient overall water splitting in alkaline media. *Appl. Catal. B Environ.* **2019**, *253*, 131–139. [CrossRef]
35. Zhao, Y.; Yang, X.; Tian, J.; Wang, F.; Zhan, L. Methanol electro-oxidation on Ni@ Pd core-shell nanoparticles supported on multi-walled carbon nanotubes in alkaline media. *Int. J. Hydrog. Energy* **2010**, *35*, 3249–3257. [CrossRef]
36. Chen, L.; Zhang, Y.; Wang, H.; Wang, Y.; Li, D.; Duan, C. Cobalt layered double hydroxides derived CoP/Co_2P hybrids for electrocatalytic overall water splitting. *Nanoscale* **2018**, *10*, 21019–21024. [CrossRef] [PubMed]
37. Sun, J.; Li, S.; Zhang, Q.; Guan, J. Iron–cobalt–nickel trimetal phosphides as high-performance electrocatalysts for overall water splitting. *Sustain. Energy Fuels* **2020**, *4*, 4531–4537. [CrossRef]
38. Yan, X.; Hu, Q.T.; Wang, G.; Zhang, W.D.; Liu, J.; Li, T.; Gu, Z.G. NiCo layered double hydroxide/hydroxide nanosheet heterostructures for highly efficient electro-oxidation of urea. *Int. J. Hydrogen Energy* **2020**, *45*, 19206–19213. [CrossRef]
39. McIntyre, N.S.; Cook, M.G. X-ray photoelectron studies on some oxides and hydroxides of cobalt, nickel, and copper. *Anal. Chem.* **1975**, *47*, 2208–2213. [CrossRef]
40. Zhang, J.; Xiao, K.; Zhang, T.; Qian, G.; Wang, Y.; Feng, Y. Porous nickel-cobalt layered double hydroxide nanoflake array derived from ZIF-L-Co nanoflake array for battery-type electrodes with enhanced energy storage performance. *Electrochim. Acta* **2017**, *226*, 113–120. [CrossRef]
41. Chen, W.; Zhang, Y.; Huang, R.; Zhou, Y.; Wu, Y.; Hu, Y.; Ostrikov, K.K. Ni–Co hydroxide nanosheets on plasma-reduced Co-based metal–organic nanocages for electrocatalytic water oxidation. *J. Mater. Chem. A* **2019**, *7*, 4950–4959. [CrossRef]
42. Li, Y.; Hu, L.; Zheng, W.; Peng, X.; Liu, M.; Chu, P.K.; Lee, L.Y.S. Ni/Co-based nanosheet arrays for efficient oxygen evolution reaction. *Nano Energy* **2018**, *52*, 360–368. [CrossRef]
43. Zhang, Z.; Liang, X.; Li, J.; Qian, J.; Liu, Y.; Yang, S.; Wang, Y.; Gao, D.; Xue, D. Interfacial engineering of NiO/$NiCo_2O_4$ porous nanofibers as efficient bifunctional catalysts for rechargeable zinc–air batteries. *ACS Appl. Mater. Interfaces* **2020**, *12*, 21661–21669. [CrossRef]
44. Gu, Y.; Chen, S.; Ren, J.; Jia, Y.A.; Chen, C.; Komarneni, S.; Yang, D.; Yao, X. Electronic structure tuning in Ni_3FeN/r-GO aerogel toward bifunctional electrocatalyst for overall water splitting. *ACS Nano* **2018**, *12*, 245–253. [CrossRef]
45. Hafezi Kahnamouei, M.; Shahrokhian, S. Mesoporous nanostructured composite derived from thermal treatment CoFe Prussian blue analogue cages and electrodeposited NiCo-S as an efficient electrocatalyst for an oxygen evolution reaction. *ACS Appl. Mater. Interfaces* **2020**, *12*, 16250–16263. [CrossRef]
46. Long, X.; Xiao, S.; Wang, Z.; Zheng, X.; Yang, S. Co intake mediated formation of ultrathin nanosheets of transition metal LDH—an advanced electrocatalyst for oxygen evolution reaction. *Chem. Commun.* **2015**, *51*, 1120–1123. [CrossRef]
47. Yang, L.; Chen, L.; Yang, D.; Yu, X.; Xue, H.; Feng, L. NiMn layered double hydroxide nanosheets/$NiCo_2O_4$ nanowires with surface rich high valence state metal oxide as an efficient electrocatalyst for oxygen evolution reaction. *J. Power Sources* **2018**, *392*, 23–32. [CrossRef]
48. Nsanzimana, J.M.V.; Peng, Y.; Xu, Y.Y.; Thia, L.; Wang, C.; Xia, B.Y.; Wang, X. An efficient and earth abundant oxygen evolving electrocatalyst based on amorphous metal borides. *Adv. Energy Mater.* **2018**, *8*, 1701475. [CrossRef]
49. Wang, H.Y.; Hsu, Y.Y.; Chen, R.; Chan, T.S.; Chen, H.M.; Liu, B. Ni^{3+} induced formation of active NiOOH on the spinel Ni–Co oxide surface for efficient oxygen evolution reaction. *Adv. Energy Mater.* **2015**, *5*, 1500091. [CrossRef]

nanomaterials

MDPI

Article

Polarization Sensitive Photodetectors Based on Two-Dimensional WSe_2

Andrey Guskov [1], Sergey Lavrov [1,*] and Rinat Galiev [2]

[1] Department of Nanoelectronics, MIREA—Russian Technological University, 119454 Moscow, Russia; guskov@mirea.ru
[2] V.G. Mokerov Institute of Ultra High Frequency Semiconductor Electronics of RAS, 117105 Moscow, Russia; rgaliev@isvch.ru
* Correspondence: sdlavrov@mail.ru; Tel.: +7-499-215-65-65 (ext. 3003)

Abstract: In this work we show the possibility of imparting polarization-sensitive properties to two-dimensional films of graphene-like semiconductors, using WSe_2 as an example, by the application of ordered silver triangular nanoprisms. In addition, such nanoprisms made it possible to increase the optical sensitivity of optical detectors created on two-dimensional films by a factor of five due to surface plasmon resonance. The peculiarities of the surface plasmon resonance were shown by theoretical modeling, and the optimal conditions of its occurrence were determined. This article demonstrates an effective approach to creating spectrally selective, polarization-sensitive detectors based on two-dimensional graphene-like semiconductors.

Keywords: 2D semiconductors; transition metal dichalcogenides; photodetectors; surface plasmon resonance

1. Introduction

The main physical parameters of optical radiation are amplitude, polarization, frequency, and phase. Most optical sensors allow detection of light intensity only and are not sensitive to its polarization. The ability to analyze the optical polarization of the detected light greatly expands the capabilities of numerous applications, such as polarization-encoded quantum key distribution [1], biomedical applications [2], remote optical sensing techniques, object recognition [3], and polarization optical mapping [4].

For use in these applications, detectors must have high quantum efficiency and, at the same time, be compact enough to achieve a high level of integration and flexibility. To date, commercially available devices do not meet these requirements. To achieve polarization sensitivity, additional non-integrable polarizing filters or polarizers are installed directly in front of the optical detector, which significantly increases their size. In addition, flexible integrated devices are better integrated into optical systems, while classical photodetectors, due to their large size, are not suitable for flexible applications. The only possible approach to ensure the above requirements is the transition to new materials.

Among such new materials suitable for creating optical sensors, nanomaterials show the greatest promise. Some of them have significant optical anisotropy due to their shape, which allows selective detection of polarization. Such materials include nanowires [5] and carbon nanotubes [6], which are composed into ordered clusters and used as an active, flexible light-sensitive element. However, the creation of such structures is excessively time-consuming, because complex technological techniques are needed for their structuring and ordering.

Another approach is to use two-dimensional (2D) semiconductor films. These films, due to their unique quantum-dimensional effects, allow the creation of highly sensitive photodetectors [7] and sensors [8]. 2D semiconductors, such as transition metal dichalcogenides, were first obtained a relatively short time after the discovery of graphene in 2004. Since then, numerous attempts have been made to create optical detectors based on

Citation: Guskov, A.; Lavrov, S.; Galiev, R. Polarization Sensitive Photodetectors Based on Two-Dimensional WSe_2. *Nanomaterials* **2022**, *12*, 1854. https://doi.org/10.3390/nano12111854

Academic Editors: Jihoon Lee and Ming-Yu Li

Received: 29 April 2022
Accepted: 26 May 2022
Published: 29 May 2022

them. Some of these materials, such as $ReSe_2$, have their own optical anisotropy due to the nature of their crystallographic structure. Thus, a polarization-sensitive photodetector was designed that allowed the detection of two polarization components independently of each other [9]. The only drawback of the above device is a not very high polarization selectivity, which limits the possibility of its application.

An alternative to the use of 2D materials that do not have sufficient intrinsic optical anisotropy is to create anisotropy using plasmonic effects. For example, the possibility of using elliptical plasmonic structures to achieve polarization sensitivity through local surface plasmon resonance (LSPR) was shown [10]. In this case, the 2D material used did not possess optical anisotropy at all, but when using gold structures, it became polarization sensitive. However, in this work, gold structures were used, which reduces the efficiency of such materials. Most importantly, the possibility of only local plasmon resonance near the metal/dielectric structure was taken into account, and not the surface resonance. At the same time, surface plasmon resonance (SPR) theoretically allows the increase of optical absorption up to 100%. Until now the possibility of SPR in such structures had not been investigated.

Different theoretical modeling approaches can be used to describe such structures. For example, it is shown in [11] that upgraded local density or generalized gradient approximations to density functional theory can be successfully applied to estimate the optical parameters of nanoscale hybrid metal–silicon materials. Moreover, for example, it was successfully demonstrated in [12] that ab initio molecular dynamics simulation approaches can be used to calculate the parameters of 2D graphitic-like aluminum nitride materials. Finite element modeling is another possible option for evaluating the optical properties of such complex three-dimensional systems, which is most widely used to estimate the effects of plasmonic amplification [13].

In this work, we investigated the possibility of creating highly efficient polarization-sensitive detectors by using SPR. For this purpose, arrays of triangular nanoprisms were created on the surface of the WSe_2 monolayer film, which also made it possible to enhance the photosensitivity of the created photodetectors. To study the peculiarities of the surface plasmon resonance emergence, theoretical modeling of optical absorption for the created structures was performed, and the regularities of optical anisotropic absorption were determined.

2. Materials and Methods

There are many possible variations of the form factors of plasmonic structures designed to enhance the absorption of optical radiation in their adjacent materials by LSPR. To date, the effectiveness of spheres [14], ordered nanodiscs [15], PbS [16] and Ag [17] quantum dots, nanocubes [18], spherical dimers, nanostars, nanorods [14], grid arrays [19], and complex-shaped structures [20] has been demonstrated. However, only asymmetric nanostructures can have optical anisotropy, which significantly narrows their list of possible forms. For example, quantum dots, spheres, nanodiscs, or similar symmetric structures cannot be used for this purpose.

In such low-dimensional structures there are three main mechanisms that can be involved in increasing the absorption in the semiconductor layer, which is described in great detail in [21].

The first of them is the scattering of optical radiation on plasmonic elements. Usually, this mechanism plays a decisive role when the radiation scattered in this way further passes through the bulk layer of the semiconductor, being absorbed in it. Thus, scattering is required simply to increase the path length of the electromagnetic wave in the semiconductor. However, in this case, this effect makes almost no contribution. This is due to the fact that the plasmonic elements are located above the semiconductor, and most of the scattered radiation escapes into the air medium above. Moreover, the small thickness of the semiconductor, even if the scattered radiation reaches its surface, does not allow it to be effectively absorbed.

The second is the local surface plasmon resonance, which manifests itself in the collective oscillation of the electron density near the metal–semiconductor boundary. In the film itself there is a significant increase in the intensity of the electromagnetic wave, which in turn leads to an increase in the photocurrent. This effect is mainly dominant and allows one to obtain an increase in optical absorption using almost any form-factor of plasmonic structures on the surface of the semiconductor as shown in our work. The third mechanism is the surface plasmon resonance, which occurs mainly along long metal films, which also leads to redistribution of the electromagnetic field in the structures adjacent to it. It is worth noting that, in our case, only the latter two mechanisms yield contributions.

Therefore, the next factor in selecting the shape of the nanostructures is the effective generation of local surface plasmon resonance. For this purpose, such structures should possess sharp angles, which will enhance the electromagnetic field in their immediate vicinity. On this basis, the most effective form should have multipoint stars such as those mentioned in [14]. However, the characteristic sizes of such structures should be comparable to the length of the incident electromagnetic wave, which leads to technological difficulties in creating such defect-free structures with strictly specified geometric parameters, especially if they have a three-dimensional shape. Moreover, such multi-beam structures, for obvious reasons, begin to lose their anisotropic properties when the number of beams increases.

The next important factor is the mutual arrangement of such structures: if they are disordered, such as nanotubes lying on a substrate, then individually they will have optical anisotropy, but in the cumulative arrangement, this will be absent. For this reason, it is necessary to use asymmetric plasmonic structures, the arrangement of which relative to each other must be strictly ordered. The structures must be located as close to each other as possible. This is necessary because total amplification over the entire surface area of the functional material is more important than the amplification value of a single plasmonic structure.

The most effective material for the plasmonic element is silver, as it is extremely efficient at generating standing plasmonic waves [22]. So, for example, a comparison of metals used to create plasmonic materials is described in detail in [23]. In this work it is shown that the quality factor for localized surface plasmon resonances (at the 635 nm wavelength) in silver is two times higher than in gold. That is why in our work silver was chosen as a material for plasmonic structures. We also performed theoretical simulations for absorption in a 2D semiconductor film for different compositions of plasmonic structures (see Supplementary Materials S1). Thus, the simulation shows that the absorption in the TMD film is higher by 30% when using Ag rather than Au. It was also found that the choice of material of plasmonic elements does not affect their anisotropic absorption.

That is why the ordered plasmonic structures in the form of triangular silver nanoprisms were chosen in this work. Such nanoprisms are optimal candidates for optical amplification, as they fully satisfy all the above parameters. The prisms were arranged relative to each other in the form of a square rectangular matrix. This ordering of elements is usually the most commonly used for such problems. More so, it is optimal when creating detectors sensitive to polarization due to its symmetry. Schematic representation of a photodetector based on such a plasmonic structure is shown in Figure 1.

The distance between the elements of the matrix will hereafter be referred to as the period T of the plasmonic structures. The characteristic size of the plasmon element itself was chosen as a circle circumscribed around its triangular base. We considered it important to maintain the ratio of the open area of the TMD surface to the surface occupied by the plasmonic structures. Thus, we exclude the possibility of changing the efficiency of photodetectors only by changing the active area of the light-irradiated semiconductor. Three sets of plasmonic structures that have different periods were created: 200, 300, and 500 nm. A detailed description of the choice of the form factor of plasmonic structures is presented in Supplementary Materials S2. Thus, the optimal thickness of the plasmonic structures was estimated by simulation and the most efficient geometrical parameters were selected.

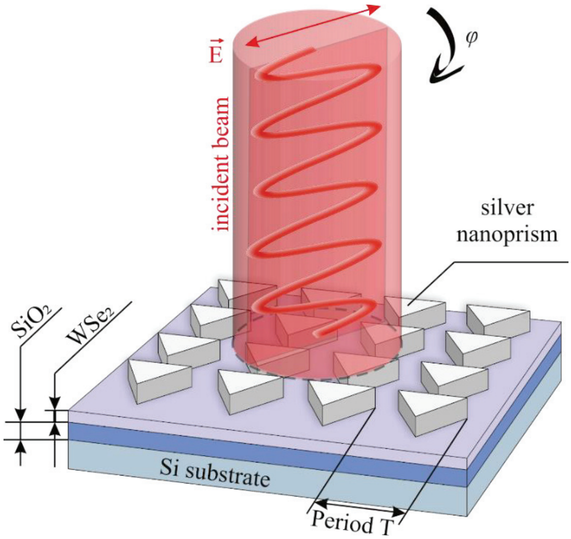

Figure 1. Schematic representation of an ordered triangular silver nanoprism on the surface of a 2D WSe_2 film.

Standard silicon wafers with an oxide layer 90 nm thick were used as substrates for photodetectors, and two-dimensional WSe_2 films were deposited on their surface by CVD method. To confirm the absence of defects in the semiconductor films and its homogeneity, standard techniques of luminescence microscopy, AFM, SEM, and nonlinear optical microscopy were employed. The standard technological route of electron-beam lithography was used to create ordered plasmonic structures with the required parameters.

The contact pads with the electrodes were created in gold with a titanium sublayer. Gold is used because it is not vulnerable to oxidation, has low contact resistance, and is more resistant to mechanical damage. The photosensitive region with plasmonic structures on the semiconductor film is located in the gaps between the electrodes, providing the application of the electric field to the film. Contact pads were provided for probe measurements. Figure 2 shows images of the created plasmonic structures.

As will be shown below, the highest optical absorption occurs only when the plasmonic structures are sufficiently close to each other, at which point the most effective plasmon resonance occurs. However, fabricating the closely spaced plasmonic structures comprises significant technological difficulties. The constraints come from the electron-beam lithography process parameters, such as resist thickness in accordance with feature height and lateral size, density of the pattern, etc. For example, for making a very small gaps (about 100 nm and less) lift-off pattern by means of convenient EBL it is necessary to have rather thin high aspect ratio resist walls (lamellas) in order to provide a reliable lift-off process. On the other hand, such thin resist lamellas are hard to stay in place—they tend to collapse or delaminate, especially when they are based on the poor adhesion sublayer like TMD monolayer, even when the test runs on the bare Si substrate have shown perfect results.

To estimate the created photodetectors' photosensitivity and to study their polarization sensitivity, the standard method of photocurrent registration was used. The laser beam was focused on the surface of the semiconductor film, to which a constant voltage was applied through tungsten probes connected to the contact pads. The photocurrent value was read using a picoammeter. Changing the polarization of laser radiation was achieved by rotating the half-wave plate. Laser radiation with a wavelength of 635 nm was focused onto a spot with a diameter of 4 μm on the surface of the sample between the electrode structures. Such a large beam diameter is necessary to provide simultaneous illumination of several periods of plasmonic structures. The power density on the sample surface was 550 W/cm^2.

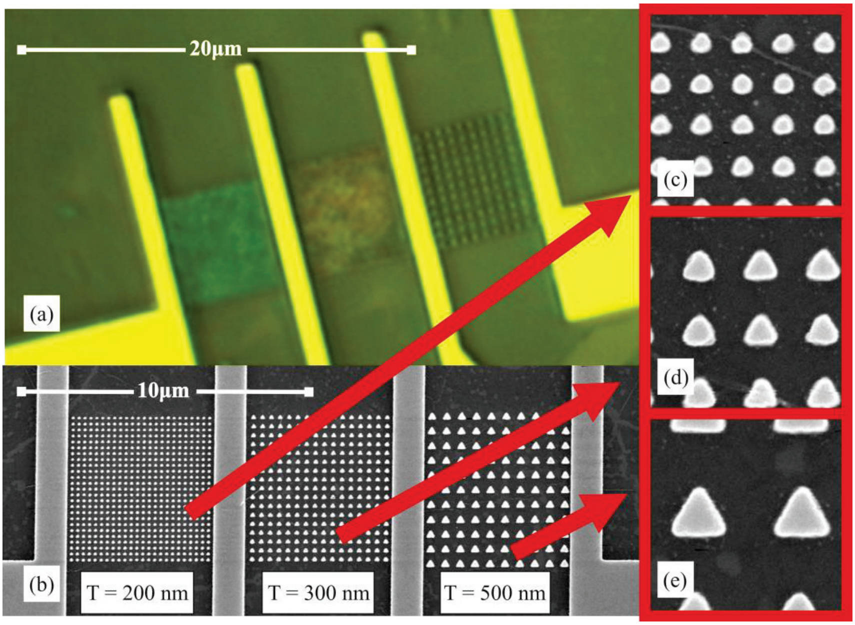

Figure 2. Image of the created photodetectors: (**a**) optical image, (**b**) SEM image of the overall structure, (**c**–**e**) SEM images of nanoprisms with periods T = 200, 300, and 500 nm, respectively.

The geometrical parameters of such low-dimensional structures significantly affect the final characteristics of the created devices [24]. At the same time, their influence can be highly nonlinear. Therefore, in order to evaluate the photodetector efficiency and determine the influence of the plasmonic structure parameters on the photodetector properties, we performed additional physical simulations of optical absorption in a two-dimensional WSe_2 film.

The simulation consisted of creating an exact copy of the device considered in this work to estimate the distribution of electromagnetic fields in its structure. The model was composed of a silicon substrate, a 90 nm thick oxide layer, a 0.86 nm thick WSe_2 monolayer film [25], and a 100 nm thick silver plasmonic structure in the form of triangular prisms placed on top of each other. Only one of the structure's elementary cells, which included one plasmonic element, was simulated. As can be seen from the images shown in Figure 2, the created structures are not geometrically ideal, which was taken into account during modeling.

Since the photocurrent of such detectors depends linearly on the optical absorption in the two-dimensional semiconductor layer, the optical absorption is a determinant of its photosensitivity. The most important results of the calculations were optical amplification (the ratio of local power density to the power density of the radiation incident on the structure), optical absorption in the semiconductor film, and polarization-dependent absorption (the ratio of absorption in the semiconductor film for two mutually perpendicular polarizations of incident light). Optical amplification makes it possible to locally visualize the patterns of LSPR occurrence, and polarization-dependent absorption makes it possible to estimate the sensitivity of the created photodetectors to optical polarization.

3. Results

Obviously, these materials possess the maximum optical absorption near their bandgap. However, this does not mean that the plasmonic structures have the greatest polarization anisotropy at the same wavelengths. Therefore, it was necessary to select the optimal wavelengths of optical radiation incident on the created structures. For this purpose, we simulated optical absorption in the created photodetectors at different wavelengths and the azimuthal angle of the incident optical radiation polarization.

The results of this simulation for the plasmonic structure with period T = 500 nm are shown in Figure 3. For greater clarity, the optical absorption was normalized separately for each value of the incident wavelength, which allows a more detailed evaluation of the anisotropy contribution for each wavelength. The non-normalized raw data are presented in Supplementary Materials S3 (they in fact exactly repeat the absorption value for the WSe_2 monolayer film).

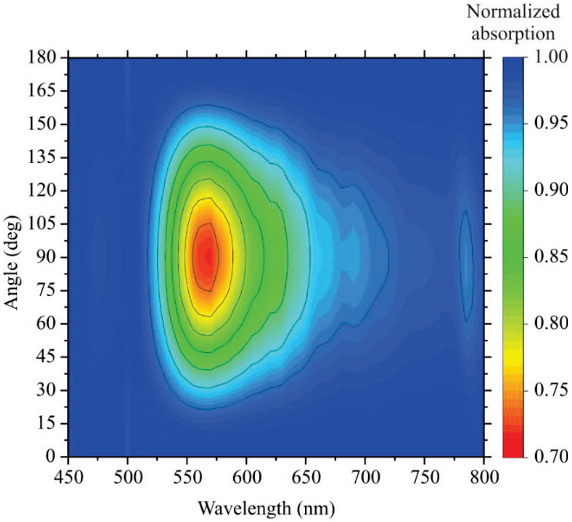

Figure 3. Calculated polarization-dependent absorption in the created photodetector (T = 500 nm) for different values of wavelength and azimuthal angle of the incident optical radiation polarization.

Thus, the results show that the polarization selectivity (for the T = 500 structure) appears only in a small wavelength range of 550–660 nm. In this case, for optical applications, it is most optimal to use pump wavelengths located as closely as possible to the value of the band gap width of the used semiconductor. Other created structures (with periods of T = 200 and 300) obtained results similar in the form of dependences, but smaller in magnitude (Supplementary Materials S3). Of the most common sources of laser radiation, the dpss lasers with a wavelength of λ = 635 nm are the most closely matched to the indicated wavelengths. Therefore, this wavelength of excitation radiation was used for the experimental analysis of the properties of the created photodetectors.

To confirm the obtained theoretical data, the photosensitivity of the created photodetectors was experimentally measured. Due to the large difference in absolute values for each of the plasmonic structures, the normalized photosensitivity is shown in Figure 4a. The actual photosensitivities range from 1.87 to 1.58 uA/W for photodetectors with period structures of 200 nm, 1.50 to 1.29 uA/W for period 300 nm, and 1.31 to 0.85 uA/W for period 500 nm. The photosensitivity of the semiconductor without plasmonic structures was 0.39 uA/W. It is worth noting that such a low photosensitivity is due to the high-power density of the incident radiation, as, with its increase, the value of the photoresponse drops exponentially [26]. Thus, plasmonic structures have allowed the photosensitivity of the created photodetectors to increase considerably. For photodetectors with the period of structures of 200 nm, photosensitivity was increased by a factor of 4.8.

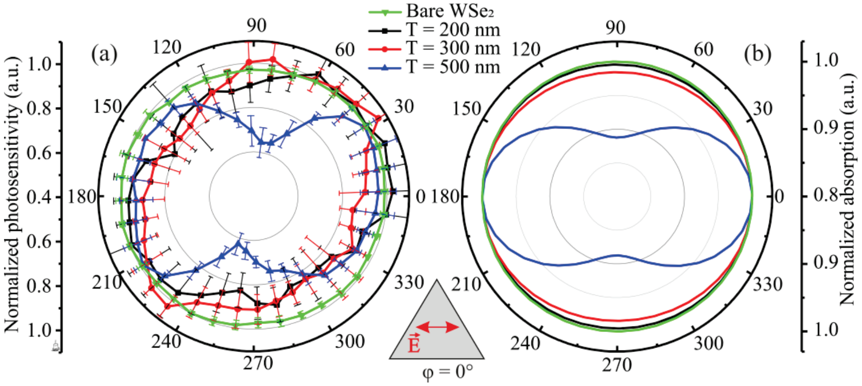

Figure 4. (**a**) Experimentally obtained values of photosensitivity at different polarization angles of incident radiation for photodetectors with plasmonic nanoprisms and (**b**) theoretically calculated absorption in WSe_2 monolayer with plasmonic structures on its surface at incident radiation with wavelength λ = 635 nm. The inset below schematically shows the polarization direction at angle φ = 0°.

Figure 4b shows the theoretically calculated normalized values of optical absorption in 2D WSe_2 film with plasmonic structures on its surface obtained at the incident wavelength of 635 nm.

From the obtained theoretical and experimental results, it clearly follows that polarization selectivity at the selected wavelength occurs only for triangular nanoprisms with the period T = 500 nm. Therefore, theoretically, the ratio of optical absorption can reach 1.13 times, while the experimental value of photosensitivity is much higher, 1.6 times. For plasmonic structures with a different period, no polarization selectivity was found.

It can be seen that the absolute values for the experimental and theoretical data are different. It should be noted that the optical coefficients used in the simulation may vary slightly from the real values, which can lead to distortions of the theoretical data. At the same time, the creation of plasmonic structures on the semiconductor film surface should not change its own optical coefficients. This conclusion can be drawn because the gentlest techniques for creating a metal layer on the TMD surface are used. Thermal vapor deposition is considerably less degrading than magnetron or laser sputtering. At the same time, silver is not a refractory material and requires a relatively low temperature for its evaporation. It should also be noted that the WSe_2 film used is quite inert and does not interact with the metal. Therefore, we can assume that the metal sputtering itself does not greatly affect the change in the optical parameters of the film. However, it is not possible to measure this directly in principle.

Moreover, the theoretical models created may differ somewhat from their real embodiments. Thus, we cannot reliably determine the homogeneity of plasmonic structures' vertical walls or accurately estimate the geometry of their faces. For example, they may have the shape of an inclined parallelepiped. We have analyzed all their geometric features, but there will still definitely remain discrepancies, which of course will lead to differences between theoretical and experimental results.

The obtained theoretical and experimental data for plasmonic structures with a period of T = 500 nm indicate a 180-degree periodicity of polarization-dependent absorption in a semiconductor film on the azimuthal angle of incidence of laser radiation polarization. In this case, the phases of the azimuthal dependences also coincide. The maximum corresponds to the case when the polarization is parallel to the base of the triangle φ = 0° (the polarization direction is indicated in the inset below in Figure 4).

In order to analyze the reason for this regularity, a simulation of the local amplification of optical radiation in the semiconductor layer was performed. The results of the simulation (the cross section is conducted in the middle of the semiconductor volume) for different incident polarizations of optical radiation in the calculated unit cell with the period of plasmonic structures T = 500 nm are shown in Figure 5a–g. It can be noted that, near the metallic plasmonic structures, there is the greatest increase in the power density of the optical radiation, the distribution of which strongly depends on the polarization parameters. When the incident polarization rotates, the greatest amplification is observed at the corners of the triangle, which are adjacent to the base parallel to the polarization of the incident light. However, such local amplification occupies a relatively small surface area, and therefore it is not its local peak value that is important, but the average value of amplification over the whole area of the semiconductor.

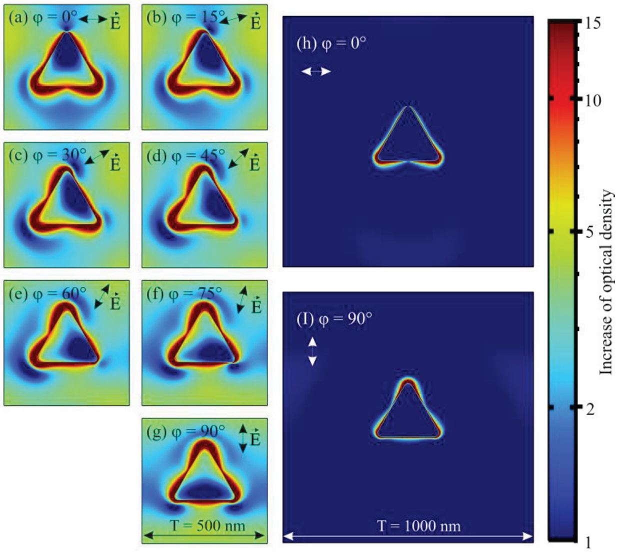

Figure 5. Calculated optical radiation amplification distribution in the layer of 2D WSe$_2$ films for plasmonic structures at the incident radiation wavelength λ = 635 nm (**a**–**g**) for the created photodetectors with period T = 500 nm, (**h**,**i**) for photodetectors with doubled spacing between them.

The results show that the amplification of optical radiation occurs on the entire surface of the semiconductor, which is located in the calculated unit cell. For example, for the polarization incidence angle φ = 0°, the amplification to the left and right of the triangular prism increases fivefold and to the top and bottom is close to unity. As the polarization rotates, such a symmetrical field distribution pattern also begins to rotate following the polarization (Figure 5a–g). Such amplification of optical radiation so far away (more than the wavelength of incident radiation) from the plasmonic structure can be explained by interaction between plasmonic structures, leading to SPR.

To verify this assertion, a simulation of optical radiation amplification was performed for a triangular nanoprism of the same size but with twice the distance between them. The results of this simulation are shown in Figure 5h,i. They show that the amplification is located only in a very small region in the immediate vicinity of the plasmonic structures and does not spread farther. This field distribution is characteristic of the LSPR. It was found that, for such modified structures, polarization anisotropy is completely absent (see Supplementary Materials S4), which fully confirms the occurrence of polarization selectivity due to the interaction between the plasmonic structures and not due to their anisotropic shape. Moreover, single triangular prisms, by virtue of their shape, should possess 60-degree symmetry of polarization dependences, which also does not correspond to the obtained results. In addition, it was found that the polarization selectivity of nanoprisms can be altered by rotating the prisms within the ordered matrix in which they are placed (see Supplementary Materials S5). The maximum value of polarization-dependent absorption is observed when one of the sides of the triangle is parallel to the axes of the square matrix in which they are ordered. It has been demonstrated that it is possible to completely get rid of polarization-dependent absorption by rotating the triangular nanoprisms by 15 degrees.

Thus, if it is known that the maximum ratio of optical selectivity in such structures is achieved at azimuthal angles of incidence of laser radiation φ = 0° and φ = 90°, then it is possible to estimate the maximum possible polarization selectivity for such structures. Thus, Figure 6a,b shows the calculated absorption in the WSe_2 monolayer based on this model as a function of wavelength and period of plasmonic nanoprisms for polarization angles φ = 0° and φ = 90°, respectively. Figure 6c shows the polarization absorption ratio for this structure, which was obtained by dividing the absorption values at polarization angles φ = 0° and φ = 90° by each other. The results show that by changing the period of the structures, the polarization selectivity can be achieved over the entire visible optical range. Moreover, as can be seen from the presented results, such a change also leads to the appearance of spectral absorption selectivity. Based on the obtained results, the maximum polarization selectivity can be obtained using triangular nanoprisms with T = 600 and an incident wavelength of 675 nm. Theoretically, the accurate selection of parameters of plasmonic structures and pump wavelengths will increase the polarization selectivity at least an additional five times for the created photodetectors.

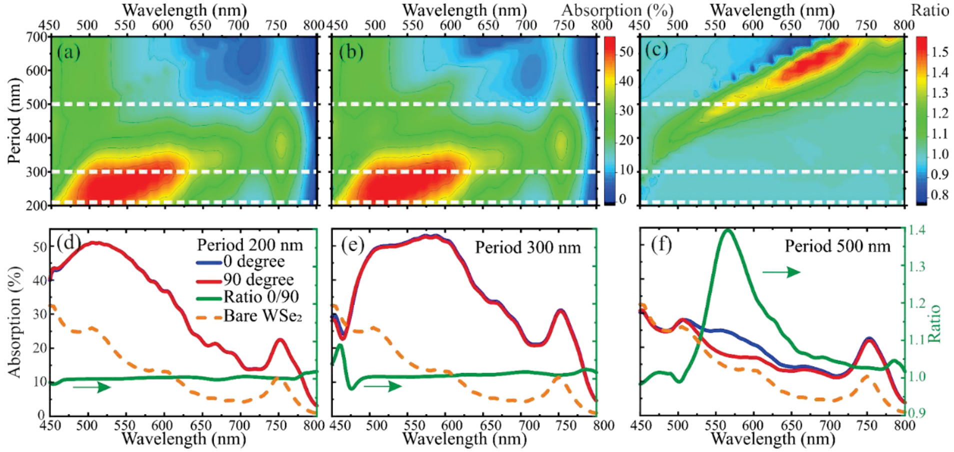

Figure 6. Simulation results of the optical absorption dependence in a two-dimensional WSe_2 film on the plasmonic structure period and the incident radiation wavelength with (**a**) φ = 0° and (**b**) φ = 90°. (**c**) The absorption ratio at φ = 0° to φ = 90°. Dependence of optical absorption for different azimuthal angles of incident polarization at (**d**) T = 200 nm, (**e**) T = 300 nm, and (**f**) T = 500 nm.

Additionally, Figure 6d–f shows absorption spectra for plasmonic structures with the same periods T = 200, 300, and 500 as for the created photodetectors. They show values of optical absorption for different values of azimuthal angles of incident polarization of laser radiation and their ratio. For comparison, all graphs additionally show the spectral absorption in the semiconductor film without a plasma structure deposited on its surface. Thus, it can be seen that the maximum value of anisotropy does not coincide with the value of the bandgap width of the semiconductor. For triangular nanoprisms with a period of T = 200 and T = 300, polarization absorption anisotropy is absent over the entire visible wavelength range. For triangular nanoprisms with period T = 500, significant anisotropy is observed at a wavelength of about 560 nm.

The ultraviolet wavelength range up to 200 nm was also investigated using theoretical simulations. The results are presented in Supplementary Materials S6. In the ultraviolet range, the absorption in the TMD film is not high. This effect is due to changes in light interference conditions in the TMD/SiO_2/Si structure. It is also determined that the absorption anisotropy in the ultraviolet region has a rather small value not exceeding 1.15 (versus 1.4 in the visible range). Moreover, the spectral width of such absorption anisotropy peaks is very narrow, which greatly complicates their possible use.

4. Conclusions

In summary, in this work, polarization-sensitive photodetectors based on two-dimensional semiconductor films that initially do not have polarization sensitivity were developed. For this, arrays of ordered asymmetric silver nanoprisms were used, due to which a surface plasmon resonance appeared in a semiconductor film. It was experimentally shown that the polarization selectivity (the maximum ratio of photosensitivities for mutually perpendicular polarizations of the incident light) of the developed detectors is 1.6 times. It was found that the use of ordered metal structures makes it possible to increase the photosensitivity of the detectors by a factor of five. Using physical modeling, we showed that the efficiency of such structures can be significantly increased over the entire visible spectral range by varying the corresponding form factors of plasmonic structures.

Supplementary Materials: The following supporting information can be downloaded at: https://www.mdpi.com/article/10.3390/nano12111854/s1, Figure S1: Simulation results of the optical absorption dependence in a two-dimensional WSe_2 film on the Ag (a–c) and Au (d–f) plasmonic structure period and the incident radiation wavelength with (a,d) $\varphi = 0^\circ$ and (b,e) $\varphi = 90^\circ$. (c,f) The absorption ratio at $\varphi = 0^\circ$ to $\varphi = 90^\circ$; Figure S2: Dependence of the optical radiation absorption in the two-dimensional WSe_2 film on the thickness of the plasmon element for two values of the polarization rotation angle φ of the incident electromagnetic wave. Form-factor of the plasmon element: triangular nanoprism with period T = 500 nm. The incident radiation wavelength is 635 nm; Figure S3: 3D distribution of the optical gain in the simulated unit cell for different thicknesses of triangular nanoprisms and angle φ: (a–c) Thicknesses of 50, 100, 200 nm for angle $\varphi = 0^\circ$. (d–f) Thicknesses of 50, 100, 200 nm for angle $\varphi = 90^\circ$. The blue isosurface shows an optical gain of 10, the red one 20; Figure S4: Dependence of optical radiation absorption in two-dimensional WSe_2 film as a function of the size of plasmonic structures D and their period T. The results were obtained for two values of the incidene light polarization angle (a) $\varphi = 0^\circ$, (b) $\varphi = 90^\circ$, and (c) absorption ratio. The incident wavelength was 635 nm; Figure S5: Calculated polarization-dependent absorption in the created photodetector for different values of wavelength and azimuthal angle of the incident optical radiation polarization. (a–c) Normalized absorption for T = 200nm, T = 300nm, T = 500nm, respectively. (d–f) Non-normalized absorption for the same periods; Figure S6: Calculated polarization-dependent absorption in WSe_2 monolayer with double period T = 1000 nm plasmonic structures (see Figure 5h–i) on its surface at incident radiation with wavelength $\lambda = 635$ nm; Figure S7: Absorption dependence in two-dimensional WSe_2 film on the rotation angle Θ of triangular nanoprisms for two values of the polarization rotation angle of the incident electromagnetic wave φ; Figure S8: (a) Absorption spectrum of the structures as a function of plasmon period T and radiation polarization, (b) absorption ratio at $\varphi = 0^\circ$ and $\varphi = 90^\circ$.

Author Contributions: Conceptualization, S.L. and A.G.; methodology, S.L. and A.G.; software, A.G.; validation, S.L.; formal analysis, S.L. and A.G.; investigation, A.G. and R.G.; resources, R.G. and S.L.; data curation, S.L.; writing—original draft preparation, A.G.; writing—review and editing, S.L.; visualization, A.G.; supervision, S.L.; project administration, S.L.; funding acquisition, S.L. All authors have read and agreed to the published version of the manuscript.

Funding: This work was supported by the Ministry of Education and Science of the Russian Federation (state task № FSFZ-0706-2020-0022).

Institutional Review Board Statement: Not applicable.

Informed Consent Statement: Not applicable.

Data Availability Statement: The data presented in this study are available on request from the corresponding author.

Acknowledgments: The research was done using the equipment of RTU MIREA shared research facilities.

Conflicts of Interest: The authors declare no conflict of interest.

References

1. Ye, T.Y.; Li, H.K.; Hu, J.L. Information Leakage Resistant Quantum Dialogue with Single Photons in Both Polarization and Spatial-Mode Degrees of Freedom. *Quantum Inf. Process.* **2021**, *20*, 209. [CrossRef]
2. Baumann, B.; Harper, D.J.; Eugui, P.; Gesperger, J.; Lichtenegger, A.; Merkle, C.W.; Augustin, M.; Woehrer, A. Improved Accuracy of Quantitative Birefringence Imaging by Polarization Sensitive OCT with Simple Noise Correction and Its Application to Neuroimaging. *J. Biophotonics* **2021**, *14*, e202000323. [CrossRef] [PubMed]
3. Li, N.; Zhao, Y.; Pan, Q.; Kong, S.G.; Chan, J.C.W. Illumination-Invariant Road Detection and Tracking Using LWIR Polarization Characteristics. *ISPRS J. Photogramm. Remote Sens.* **2021**, *180*, 357–369. [CrossRef]
4. Kim, S.; Cense, B.; Joo, C. Single-Pixel, Single-Input-State Polarization-Sensitive Wavefront Imaging. *Opt. Lett.* **2020**, *45*, 3965. [CrossRef]
5. Chi, X.; Zou, K.; Gu, C.; Zichi, J.; Cheng, Y.; Hu, N.; Lan, X.; Chen, S.; Lin, Z.; Zwiller, V.; et al. Fractal Superconducting Nanowire Single-Photon Detectors with Reduced Polarization Sensitivity. *Opt. Lett.* **2018**, *43*, 5017. [CrossRef]
6. Ren, X.; Ji, Z.; Chen, B.; Zhou, J.; Chu, Z.; Chen, X. Carbon Nanotube Far Infrared Detectors with High Responsivity and Superior Polarization Selectivity Based on Engineered Optical Antennas. *Sensors* **2021**, *21*, 5221. [CrossRef]
7. Cong, R.; Qiao, S.; Liu, J.; Mi, J.; Yu, W.; Liang, B.; Fu, G.; Pan, C.; Wang, S. Ultrahigh, Ultrafast, and Self-Powered Visible-Near-Infrared Optical Position-Sensitive Detector Based on a CVD-Prepared Vertically Standing Few-Layer MoS2/Si Heterojunction. *Adv. Sci.* **2018**, *5*, 1700502. [CrossRef] [PubMed]
8. Han, T.; Liu, H.; Wang, S.; Chen, S.; Yang, K. The Large-Scale Preparation and Optical Properties of MoS2/WS2 Vertical Hetero-Junction. *Molecules* **2020**, *25*, 1857. [CrossRef]
9. Zhang, E.; Wang, P.; Li, Z.; Wang, H.; Song, C.; Huang, C.; Chen, Z.G.; Yang, L.; Zhang, K.; Lu, S.; et al. Tunable Ambipolar Polarization-Sensitive Photodetectors Based on High-Anisotropy ReSe2 Nanosheets. *ACS Nano* **2016**, *10*, 8067–8077. [CrossRef] [PubMed]
10. Chen, S.; Cao, R.; Chen, X.; Wu, Q.; Zeng, Y.; Gao, S.; Guo, Z.; Zhao, J.; Zhang, M.; Zhang, H. Anisotropic Plasmonic Nanostructure Induced Polarization Photoresponse for MoS2-Based Photodetector. *Adv. Mater. Interfaces* **2020**, *7*, 1902179. [CrossRef]
11. Oliveira, M.I.A.; Rivelino, R.; De Brito Mota, F.; Gueorguiev, G.K. Optical Properties and Quasiparticle Band Gaps of Transition-Metal Atoms Encapsulated by Silicon Cages. *J. Phys. Chem. C* **2014**, *118*, 5501–5509. [CrossRef]
12. Kakanakova-Georgieva, A.; Gueorguiev, G.K.; Sangiovanni, D.G.; Suwannaharn, N.; Ivanov, I.G.; Cora, I.; Pécz, B.; Nicotra, G.; Giannazzo, F. Nanoscale Phenomena Ruling Deposition and Intercalation of AlN at the Graphene/SiC Interface. *Nanoscale* **2020**, *12*, 19470–19476. [CrossRef]
13. Gao, M.; Zheng, X.; Khan, I.; Cai, H.; Lan, J.; Liu, J.; Wang, J.; Wu, J.; Huang, S.; Li, S.; et al. Resonant Light Absorption and Plasmon Tunability of Lateral Triangular Au Nanoprisms Array. *Phys. Lett. A* **2019**, *383*, 125881. [CrossRef]
14. Cristiano, M.N.; Tsoulos, T.V.; Fabris, L. Quantifying and Optimizing Photocurrent via Optical Modeling of Gold Nanostar-, Nanorod-, and Dimer-Decorated MoS2 and MoTe2. *J. Chem. Phys.* **2020**, *152*, 14705. [CrossRef] [PubMed]
15. Du, W.; Zhao, J.; Zhao, W.; Zhang, S.; Xu, H.; Xiong, Q. Ultrafast Modulation of Exciton-Plasmon Coupling in a Monolayer WS2-Ag Nanodisk Hybrid System. *ACS Photonics* **2019**, *6*, 2832–2840. [CrossRef]
16. Simsek, E.; Mukherjee, B.; Guchhait, A.; Chan, Y.T. Enhanced Absorption with Quantum Dots, Metal Nanoparticles, and 2D Materials. In *Quantum Dots and Nanostructures: Growth, Characterization, and Modeling XIII*; Huffaker, D.L., Eisele, H., Dick, K.A., Eds.; SPIE: Washington, DC, USA, 2016.
17. Song, Y.; Huang, H.C.; Lu, W.; Li, N.; Su, J.; Cheng, S.B.; Lai, Y.; Chen, J.; Zhan, J. Ag@WS2 Quantum Dots for Surface Enhanced Raman Spectroscopy: Enhanced Charge Transfer Induced Highly Sensitive Detection of Thiram from Honey and Beverages. *Food Chem.* **2021**, *344*, 128570. [CrossRef] [PubMed]
18. Deng, H.; Liang, W.; Long, Y. Broadband Light Harvesting Enhancement of MoS2/Graphene Bilayer Solar Cell via Metal Nanosquare Arrays-Dielectric-Metal Structure. *Plasmonics* **2019**, *14*, 703–709. [CrossRef]
19. Wang, J.; Wang, G.; Liu, C. Plasmonic Behaviors of Two-Dimensional Ag/SiO_2 Nanocomposite Gratings: Roles of Gap Diffraction and Localized Surface Plasmon Resonance Absorption. *Plasmonics* **2019**, *14*, 921–928. [CrossRef]
20. Buryakov, A.M.; Ivanov, M.S.; Khusyainov, D.I.; Gorbatova, A.V.; Bilyk, V.R.; Klimov, E.A.; Galiev, G.B.; Vilarinho, P.M.; Mishina, E.D. Effects of Crystallographic Orientation of GaAs Substrate and the Period of Plasmon Grid on THz Antenna Performance. *Ann. Phys.* **2021**, *533*, 2100041. [CrossRef]
21. Yang, Y.; Liu, W.G.; Lin, Z.T.; Pan, R.H.; Gu, C.Z.; Li, J.J. Plasmonic Hybrids of Two-Dimensional Transition Metal Dichalcogenides and Nanoscale Metals: Architectures, Enhanced Optical Properties and Devices. *Mater. Today Phys.* **2021**, *17*, 100343. [CrossRef]
22. Rycenga, M.; Cobley, C.M.; Zeng, J.; Li, W.; Moran, C.H.; Zhang, Q.; Qin, D.; Xia, Y. Controlling the Synthesis and Assembly of Silver Nanostructures for Plasmonic Applications. *Chem. Rev.* **2011**, *111*, 3669–3712. [CrossRef] [PubMed]

23. West, P.R.; Ishii, S.; Naik, G.V.; Emani, N.K.; Shalaev, V.M.; Boltasseva, A. Searching for Better Plasmonic Materials. *Laser Photonics Rev.* **2010**, *4*, 795–808. [CrossRef]
24. Guskov, A.; Avdizhiyan, A.; Lavrov, S.; Galiev, R.; Gorbatova, A.; Buryakov, A.; Mishina, E. Sensitivity Enhancement of Two-Dimensional WSe2-Based Photodetectors by Ordered Ag Plasmonic Nanostructures. *Appl. Phys. Express* **2021**, *14*, 75005. [CrossRef]
25. He, J.; Tao, L.; Zhang, H.; Zhou, B.; Li, J. Emerging 2D Materials beyond Graphene for Ultrashort Pulse Generation in Fiber Lasers. *Nanoscale* **2019**, *11*, 2577–2593. [CrossRef] [PubMed]
26. Chen, T.; Sheng, Y.; Zhou, Y.; Chang, R.J.; Wang, X.; Huang, H.; Zhang, Q.; Hou, L.; Warner, J.H. High Photoresponsivity in Ultrathin 2D Lateral Graphene:WS 2: Graphene Photodetectors Using Direct CVD Growth. *ACS Appl. Mater. Interfaces* **2019**, *11*, 6421–6430. [CrossRef]

nanomaterials

Article

Effectiveness of Oxygen during Sintering of Silver Thin Films Derived by Nanoparticle Ink

Feng Feng [1], Haofeng Hong [1], Xing Gao [1,2,*], Tian Ren [1], Yuan Ma [3] and Pingfa Feng [1,4,*]

[1] Division of Advanced Manufacturing, Shenzhen International Graduate School, Tsinghua University, Shenzhen 518055, China; feng.feng@sz.tsinghua.edu.cn (F.F.); hhf19@mails.tsinghua.edu.cn (H.H.); rt20@mails.tsinghua.edu.cn (T.R.)
[2] Shenzhen Jinzhou Precision Technology Corp., Shenzhen 518116, China
[3] Shenzhen Tsingding Technology Co., Ltd., Shenzhen 518133, China; ma.yuan@tsingding.com
[4] Department of Mechanical Engineering, Tsinghua University, Beijing 100084, China
* Correspondence: gaoxing@jinzhou.com.cn (X.G.); fengpf@mail.tsinghua.edu.cn (P.F.)

Abstract: Silver nanoparticle (NP) inks have been widely used in the ink-jet printing field because of their excellent properties during low-temperature sintering. However, the organic dispersant used to prevent the aggregation and sedimentation of NPs can hinder the sintering process and result in the high resistivity of sintered films. In this study, silver thin films derived from silver NP ink with polyvinylpyrrolidone (PVP) dispersant were sintered in different atmospheres of pure nitrogen, air, and pure oxygen. The effect of the oxygen content in the sintering atmosphere on the thermal properties of the ink, the electrical resistivity and microstructure of the sintered films, and the amount of organic residue were studied by using differential scanning calorimetry, the four-point probe method, scanning electron microscopy, Fourier transform infrared spectroscopy, etc. The mechanism of optimizing the film resistivity by influencing the decomposition of the PVP dispersant and the microstructure evolution of the silver thin films through the sintering atmosphere was discussed. The results demonstrated that an oxygen-containing atmosphere could be effective for silver NPs in two ways. First, the oxygen content could enhance the diffusion ability of silver atoms, thus accelerating the stage transition of microstructural evolution at low temperatures. Second, the oxygen content could enable the PVP to decompose at a temperature much lower than in conditions of pure nitrogen, thus helping to finalize the densification of a silver film with a low resistivity of 2.47 μΩ·cm, which is approximately 1.5-fold that of bulk silver. Our findings could serve as a foundation for the subsequent establishment of ink-jet printing equipment and the optimization of the sintering process for printing silver patterns on flexible substrates.

Keywords: silver thin film; nanoparticle (NP) ink; sintering; oxygen; polyvinylpyrrolidone (PVP); dispersant decomposition; electrical resistivity

Citation: Feng, F.; Hong, H.; Gao, X.; Ren, T.; Ma, Y.; Feng, P. Effectiveness of Oxygen during Sintering of Silver Thin Films Derived by Nanoparticle Ink. *Nanomaterials* **2022**, *12*, 1908. https://doi.org/10.3390/nano12111908

Academic Editors: Jihoon Lee and Ming-Yu Li

Received: 11 May 2022
Accepted: 29 May 2022
Published: 2 June 2022

1. Introduction

The direct printing of conductive ink has emerged as an important alternative to traditional lithography, which is a complex multistep method for producing conductive thin films or patterns that generates a lot of waste [1]. Many examples of the use of metallic inks in printed electronics have been reported, such as printed circuit boards [2–4], light-emitting diodes (LEDs) [5,6], flexible displays [7,8], radio frequency identification (RFID) tags [9,10], solar cells [11,12], and transparent electrodes [13,14].

Regarding printing techniques, metal can be printed by using inks containing metallic nanoparticles (NPs) or low-viscosity inks with organometallic precursors; then, sintering is carried out to form the conductive thin films or patterns. NP-based inks are more commonly used because they can achieve a low electrical resistivity, i.e., a high conductivity, due to their higher solid content [15]. Such a technique is efficient in terms of material utilization, scalable and simple in the terms of processing, and adaptable to various types of substrates [16–18].

Many metals have available NP inks, such as silver [1,19], gold [20,21], and copper [22–24]. Silver-based inks are currently preferred due to their excellent electrical conductivity and stability in air, and silver is relatively inexpensive compared to gold [16,25]. Additives such as polyvinylpyrrolidone (PVP) [26–28], polyacrylic acid (PAA) [8,29,30], 2-amino-2-methyl-1-propanol (AMP) [31], and tetradecane [32] are generally added to improve the ink's uniformity during preparation, avoiding aggregation and thus improving the reliability of the printing process.

The sintering of printed metal NPs is necessary to obtain a high conductivity. The NP coalescence of a metal usually occurs at temperatures far below its bulk-form melting temperature, because there is a strong correlation between the size and the melting point of NPs, which can be derived by surface energy and thermodynamic theory [33]. During sintering, a higher conductivity can be achieved by improving the contact between NPs, which increases the removal of the organic additives [34], and so a higher sintering temperature is generally required [35]. However, for flexible substrates, the sintering temperatures cannot be too high, as this would damage the substrates, resulting in poor electrical conductivity due to the residual organic additives, particularly the dispersant with its high decomposition temperature.

Different methods have been proposed to solve the above problem, e.g., modifying the surface of silver NPs [36], using chemical reagents to remove the dispersant on the surface of silver NPs [37,38], thinning the dispersant layer on the NP surface [17], and using a dispersant with a low decomposition temperature [39,40]. These methods generally focus on the optimization of the organic dispersant, but no previous publication has reported a systematic study on the effect of an oxygen-containing atmosphere on sintered silver thin films. In this study, the effects of different sintering atmospheres on the microstructure and electrical properties of silver thin films were studied by using a silver NP ink with a PVP dispersant. It was found that the oxygen content in the sintering atmosphere could effectively promote the grain size enlargement and the decomposition of the PVP dispersant, resulting in a favorable electrical conductivity, which could provide a new basis for fabricating high-performance conductive thin films and developing practical equipment for ink-jet printing on flexible substrates.

2. Experimental Details

The ink used in this study was composed of silver NPs that were uniformly dispersed with the aid of a PVP dispersant in a solution containing isopropanol and diethylene glycol methyl ether. The viscosity of the ink measured by a viscometer (LAWSON, DHJ-5S, Ningbo, China) was 10 cp at 25 °C, and the surface tension of the ink measured by the automatic surface tension meter (Zibo Boshan Haifen Instrument Factory, HZ-800, Zibo, China) was 29 mN/m at 25 °C.

The thermodynamic properties of the ink during the thermal sintering process were characterized by using a differential scanning calorimeter (DSC, Mettler-Toledo, DSC3, Zurich, Switzerland), in which the ink was heated from room temperature to 600 °C at a ramp rate of 10 $^{\circ}\mathrm{C}\cdot\mathrm{min}^{-1}$, and the mass change of the sample, i.e., the thermogravimetric (TG) data, and the DSC data were recorded.

A flow chart of the sample preparation and sintering process is shown in Figure 1. The ink was spin-coated on a square glass sheet with a side length of 10 mm by a homogenizer (Zhangqiu Crown, 12A, Zhangqiu, China) and then dried in an oven at 75 °C for 10 min. The coated samples were heat-treated in a tube furnace (HF-Kejing, OFT-1200X, Hefei, China) under atmospheres of various oxygen contents and temperatures for 30 min. The oxygen content of the sintering atmosphere was controlled by the mass flow controller (Sevenstar, D07, Beijing, China), which uses two channels of oxygen (99.999% pure) and nitrogen (99.999% pure); the oxygen contents used in this study were 0%, 21% (denoted as air hereafter), and 100%. The heat treatment temperature ranged from 150 °C to 450 °C.

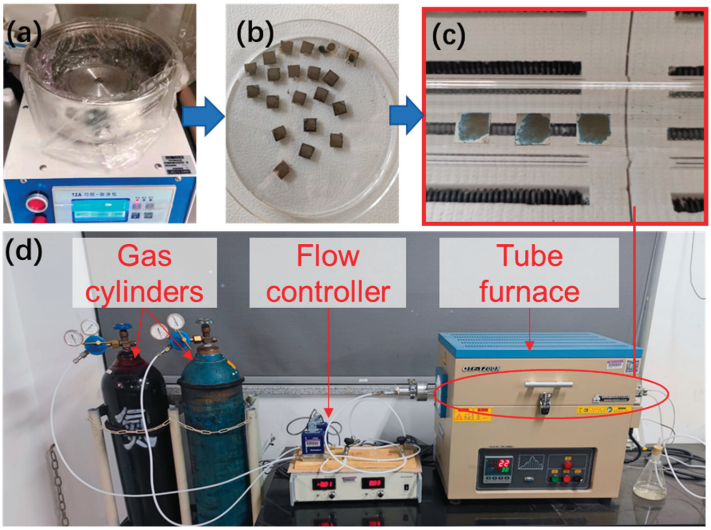

Figure 1. Flow chart of sample preparation and sintering. (**a**,**b**) Preparation of silver thin films to be sintered using a homogenizer; (**c**) thin films sintered in a tube furnace; (**d**) sintering equipments.

The electrical resistivity of the sintered samples was measured by a four-point probe meter (HELPASS, HPS2526, Changzhou, China). The microscopic morphology of the films was characterized using a scanning electron microscope (SEM, Carl Zeiss, ZEISS SUPRA 55, Oberkochen, Germany), and both the surface and cross-section of the films were observed. Fourier transform infrared (FTIR) spectroscopy (Nicolet, iS50, Waltham, MA, USA) was used to detect the residual organic matter in the samples after sintering.

3. Results

3.1. Thermal Analysis of Silver NP Ink

The thermal analysis results for the ink are illustrated in Figure 2a. It could be observed that the sample mass decreased as the temperature gradually increased from room temperature, and a mass reduction of 69.17% at 184 °C was recorded under both atmospheres of pure oxygen and pure nitrogen. The mass loss measured in the TG analysis at this stage was caused by the volatilization of the solvents isopropanol and diethylene glycol methyl ether in the ink, which corresponded to the two endothermic peaks in the DSC results located at about 70 °C and 160 °C, respectively.

The sample mass under both atmospheres changed slowly above 200 °C. The TG data indicated that the total mass of the samples in pure oxygen decreased by 0.954% from 200 °C to 600 °C, while that in pure nitrogen only decreased by 0.485%. The DSC curves under the two atmospheres were different above 200 °C. There was an obvious exothermic peak between 280 °C and 330 °C in pure oxygen, which was caused by the separation and combustion of the organic dispersant coated on the silver NPs, based on the report by Yan et al. [41]. In order to verify that the exothermic peak originated from the oxidative decomposition of PVP, a thermal analysis of PVP K30 (M_W = 40,000), which is often used as an auxiliary for reducing silver nanowire and as a stabilizer for silver NPs in inks [42], was carried out and is shown in Figure 2b. It could be seen that the PVP in oxygen experienced an exothermic phenomenon from 200 °C, with several exothermic valleys around 300–500 °C, and the mass loss at this stage was significant. The endothermic phenomenon in this temperature range is related to the breaking and decomposition of PVP [43,44]. The mass loss in nitrogen was concentrated around 450 °C, and the DSC indicated that there was an endothermic phenomenon at this temperature. Therefore, it could be inferred that PVP endothermically decomposed above 400 °C in an oxygen-deficient environment, while the presence of oxygen caused the decomposition of PVP at temperatures around 300 °C.

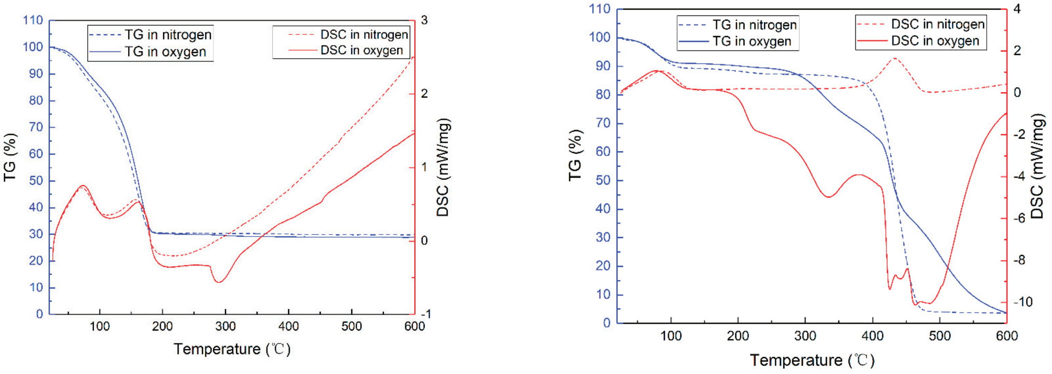

(**a**) (**b**)

Figure 2. (**a**) TG−DSC curves of silver NP ink in the atmospheres of pure oxygen and pure nitrogen; (**b**) TG−DSC curves of silver PVP K30 in the atmospheres of pure oxygen and pure nitrogen.

As shown in Figure 2a, the mass loss of the ink in the endothermic peak stage around 300 °C was 0.60%, which constituted the majority of the mass loss above 200 °C. However, the DSC curve in pure nitrogen did not show similar changes. It was found that the endothermic and exothermic conditions and mass loss of the ink and PVP were consistent, and it could be determined that the mass loss above 200 °C in the silver nanoparticle ink was mainly due to the oxidative decomposition of the organic dispersant PVP. It is worth mentioning that there is a certain difference in the endothermic peak positions between the ink and PVP, which may be due to the difference in the molecular weight of PVP and the change in properties caused by the extremely thin PVP wrapped around the NPs.

The DSC and TG data implied that the solvents in the ink could volatilize completely through sintering at 200 °C, but the removal of the dispersant PVP was much more difficult. Even in the pure oxygen atmosphere, PVP could only be removed above 330 °C.

3.2. Enhancement of Film Conductivity

The resistivity of the films sintered under different atmospheres and temperatures is plotted in Figure 3. A significant reduction in resistivity could be observed as the sintering temperature increased from 150 °C to 350 °C under all the atmospheres. The lowest resistivity was 2.47 μΩ·cm, which was approximately 1.5-fold that of bulk silver. The resistivity curves in air and pure oxygen were quite similar, and there was a slight rise in resistivity at the sintering temperature of 450 °C. Under the atmospheres of pure nitrogen, the resistance continued to decrease at the sintering temperature of 450 °C. Generally, the resistivity of the films sintered under an atmosphere containing oxygen was much lower than those without oxygen. Therefore, it can be summarized that oxygen promoted the high electrical performance of the sintered films. Moreover, the small difference between the curves of pure oxygen and air might be due to the fact that the amount of oxygen supplied in both atmospheres was much higher than the reaction demand for the decomposition of PVP.

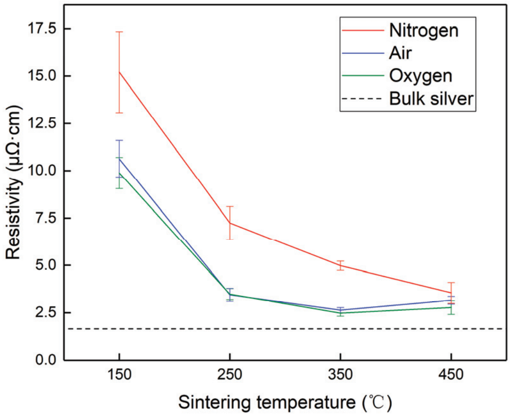

Figure 3. The resistivity curves under various sintering atmospheres and temperatures.

3.3. Microstructure of Sintered Films

The original morphology of the silver NPs can be observed in Figure 4, where the SEM image of a sample after drying at 75 °C depicts silver NPs in the ink with a particle size of approximately 30–70 nm. Figure 5 shows the surface SEM images of the films sintered in oxygen, air, and nitrogen atmospheres. Compared with the original morphology of the silver NPs in the ink, the grain size of all the annealed films increased significantly, and the originally discrete NPs aggregated into larger grains.

As can be observed in Figure 5, when the samples were sintered in pure oxygen, the morphology at 150 °C was composed of large grains above 100 nm in size inlaid with particles of the original size, as shown in Figure 5a. The morphology of the film sintered at 250 °C, shown in Figure 5d, demonstrated the coarsening of grains, whose size could reach more than 200 nm. Most of the grains were tightly connected to form an island-like microstructure, enabling the reduction in resistivity shown in Figure 3. The microstructure became denser with larger grains at 350 °C, as shown in Figure 5g, which corresponded to the lowest resistivity. When the sintering temperature rose to 450 °C, although the grain size was further enlarged, pores appeared on the surface, which might have caused the increase in resistivity. The morphological evolution of the samples sintered in air was quite similar to that in pure oxygen, and the main difference was that the grain sizes of the samples in air were smaller than those in pure oxygen, as shown in Figure 5b,e,h,k.

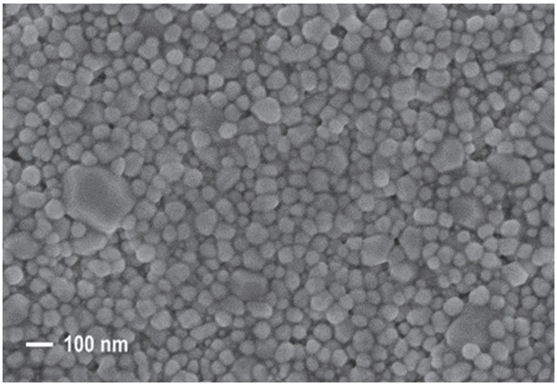

Figure 4. SEM image of silver NPs after drying at 75 °C.

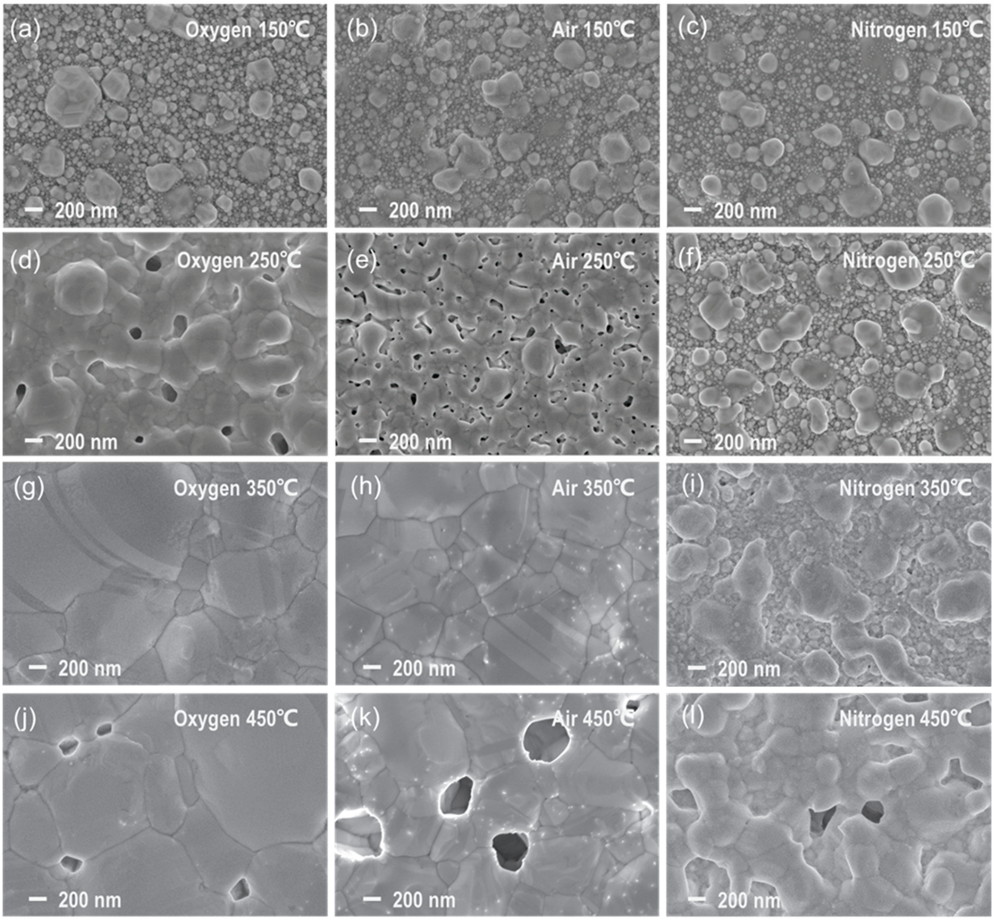

Figure 5. SEM images of the surface morphologies of silver films sintered under different atmospheres and temperatures. The columns from left to right correspond to oxygen, air, and nitrogen atmospheres, respectively. The rows from top to bottom correspond to 150, 250, 350, and 450 °C, respectively. (**a**–**c**) 150 °C; (**d**–**f**) 250 °C; (**g**–**i**) 350 °C; (**j**–**l**) 450 °C.

Comparing them with the morphologies of the samples sintered in the oxygen and air atmospheres, it could be noticed that the films sintered in nitrogen were quite different. As shown in Figure 5c,f,i,l, the grain coarsening and coalescence in nitrogen were much slower than those in the oxygen-containing atmospheres. Therefore, it could be supposed that the presence of oxygen promoted the aggregation process of NPs and thus enabled better film quality at lower temperatures.

Figure 6 presents the cross-sectional SEM images of the sintered films. In pure oxygen, a cave-like microstructure was observed inside the film sintered at 150 °C, and the fine-graininess of the silver NPs was clear. The growth of larger grains was obvious at temperatures above 250 °C, and the interconnected structures could be observed, which are beneficial for reducing the film's resistivity.

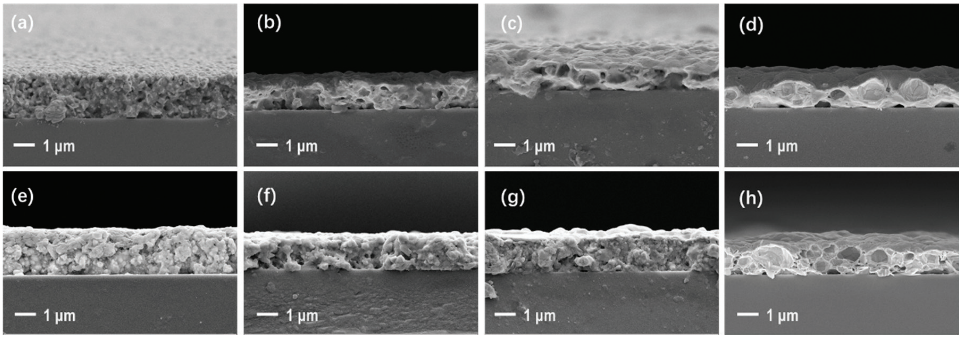

Figure 6. (**a**–**d**) SEM images of the cross-sections of silver films sintered in pure oxygen at 150, 250, 350, and 450 °C, respectively; (**e**–**h**) SEM images of the cross-sections of silver films sintered in pure nitrogen at 150, 250, 350, and 450 °C, respectively.

Compared with those sintered in oxygen, the cross-sectional microstructures of the films sintered in pure nitrogen were much poorer. Especially at high temperatures, the films sintered in oxygen showed a compact microstructure, while those sintered in nitrogen displayed poor grain growth and many internal pores, to which the high resistivity of the films sintered in nitrogen shown in Figure 3 could be attributed.

The average grain size was calculated by statistically analyzing the grain sizes in the SEM image, and it is illustrated in Figure 7a. The analysis was carried out using the SEM image analysis software Nano Measurer 1.2; the error bars represent standard deviation, and at least 100 dispersed grains were measured to ensure the accuracy. The grain size increased along with the sintering temperature for each atmosphere, consistent with the findings in Figures 5 and 6. According to the report by Volkman et al. [45], a higher temperature could promote the coalescence process among NPs, resulting in the formation of larger grains during sintering. Jang et al. [46] found that the silver NP patterns sintered in air had larger grain sizes than those in nitrogen at the same temperature, and the larger grain sizes could contribute to a lower resistivity. The other factor promoting the coalescence of silver grains was the oxygen content in the sintering atmosphere. In pure nitrogen, the average grain size sintered at 350 °C was lower than 200 nm, while those in air and pure oxygen could be above 500 nm and 700 nm, respectively.

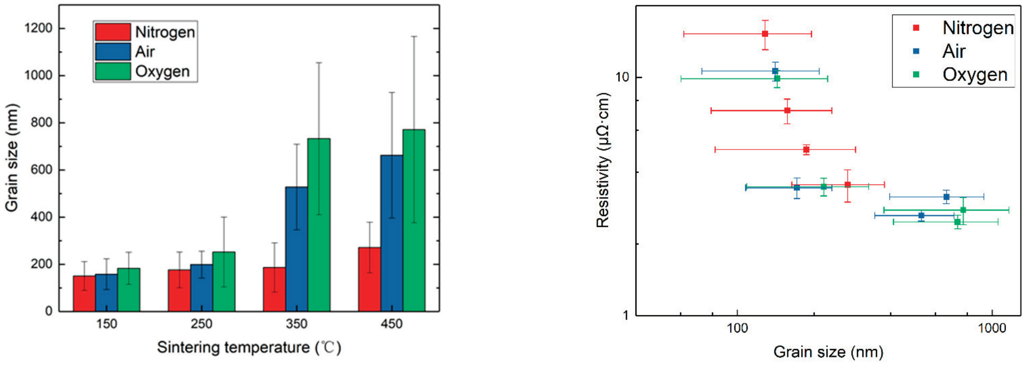

(**a**) (**b**)

Figure 7. (**a**) The average grain sizes of films sintered under different atmospheres and temperatures; (**b**) the relationship between film resistivity and grain size considering all the samples in this study.

The relationship between the mean grain size and the resistivity of the sintered films is illustrated in Figure 7b. The resistivity of the films sintered in all atmospheres gradually decreased along with the increase in grain size. When the grain size was below 200 nm, the resistivity curves basically overlapped, implying that the microstructural evolution under different atmospheres generally advanced along a similar route, although the progress in pure nitrogen required a higher temperature relative to those in oxygen and air. It could be speculated that the grain size was the dominant factor for the electrical resistivity when the organic dispersant was not decomposed.

When the grain size was further enlarged, the resistivity data under various atmospheres became scattered, indicating that the influence of factors other than grain size became significant. These factors might include the interface resistivity caused by residual organics and the newly formed pores in the film structure at high temperatures.

3.4. Organic Residue during Sintering

To reveal the changes in the organic residues in silver NP films sintered under different atmospheres and temperatures, FITR experiments were carried out. Figure 8 illustrates the FTIR spectrum of PVP and silver NP ink after sintering in air or nitrogen at a temperature of 75–350 °C. The peaks at 2953 cm^{-1} (C–H stretch) and 1638 cm^{-1} (C=O stretch) could be observed in the non-treated samples, which indicated the characteristic bands of PVP. In all the films sintered at temperatures below 250 °C, there was a peak at 1068 cm^{-1} (C–N stretch).

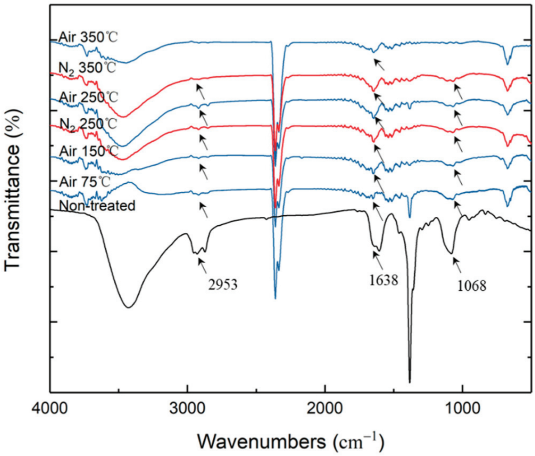

Figure 8. FTIR spectra of silver NP ink after sintering under air and pure nitrogen at various temperatures.

Significant differences according to the atmosphere occurred when the temperature was raised to 350 °C. For the film sintered in air, the peaks of both the C–N stretch and the C–H stretch almost disappeared at 350 °C, indicating that PVP was decomposed. For the film sintered in nitrogen, these peaks remained. By using the normalized calculation relative to the sample dried at 75 °C, the absorbance values at the C–H and C–N stretch of the sample after sintering at 350 °C in air were only 2% and 8%, respectively. For the samples sintered in nitrogen, these values were 82% and 60%, respectively.

4. Discussion

Combining the observations in this study and the reports in the literature [47,48], the structural evolution of the grain morphology of silver NPs during sintering can be divided into four stages: the initial stage, the Ostwald ripening stage, the particle coalescence stage, and the densification stage, as depicted in Figure 9. In the initial stage, the silver NPs have a uniform grain size of tens of nm, and the organic dispersant PVP is capsulated around the NPs. When the temperature is raised, some grains can be enlarged due to the mechanism of Ostwald ripening, while their adjacent grains become smaller because of mass transfer and dissolution [49]. The driving force of Ostwald ripening is the system's tendency to reduce its surface free energy, which is very high for a system composed of NPs [33]. The temperature is further raised to introduce the third stage of particle coalescence, which occurs when two or more silver NPs collide and merge to form a large particle [50]. The small grains can be completely absorbed into the large ones. The neighboring larger grains can form a "neck" and finally completely fuse together through the diffusion of silver atoms, resulting in a loose network structure for the entire film. Because the surface free energy of the silver grains is significantly decreased, the driving force of the Ostwald ripening is weaker, and the coalescence of the grains becomes the main mechanism of grain size enlargement at this stage. Continued heating can promote the further coarsening of the grains and the densification of the film surface, thus forming a compact network structure critical for reducing the electrical resistivity. However, it should be noted that overheating may occur if the temperature is too high, which produces pores that compromise the film's conductivity, as illustrated by Figures 3 and 5.

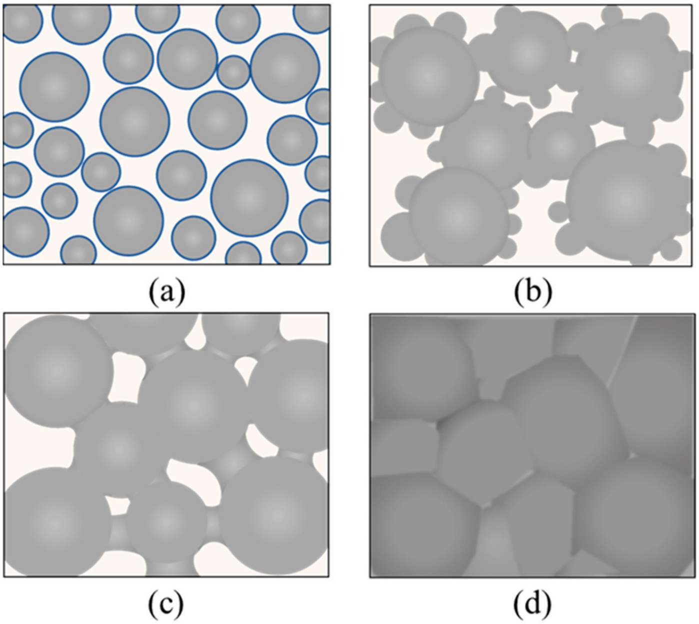

Figure 9. Schematic diagram of the sintering process of silver NPs in four stages: (**a**) initial stage; (**b**) Ostwald ripening stage; (**c**) particle coalescence stage; (**d**) densification stage.

A significant point that should be noted in this study is the differences caused by the various sintering atmospheres. As shown in Figures 5–7, the differences in grain size and the microscopic morphology of the films sintered in pure nitrogen and oxygen-containing atmospheres indicated that oxygen content was beneficial for the formation of large grains at lower temperatures. The largest contrast could be observed in Figure 10. At 150 °C, the films sintered in nitrogen and oxygen were similar, and they were both in the second stage of Ostwald ripening, with the presences of coarse grains and smaller NPs. At 250 °C, the films sintered in oxygen were obviously in the third stage of particle coalescence, with wide necks, and all the smaller particles were consumed; however, the film sintered in nitrogen was still generally in the second stage, because many smaller NPs remained, although narrow necks had begun to appear.

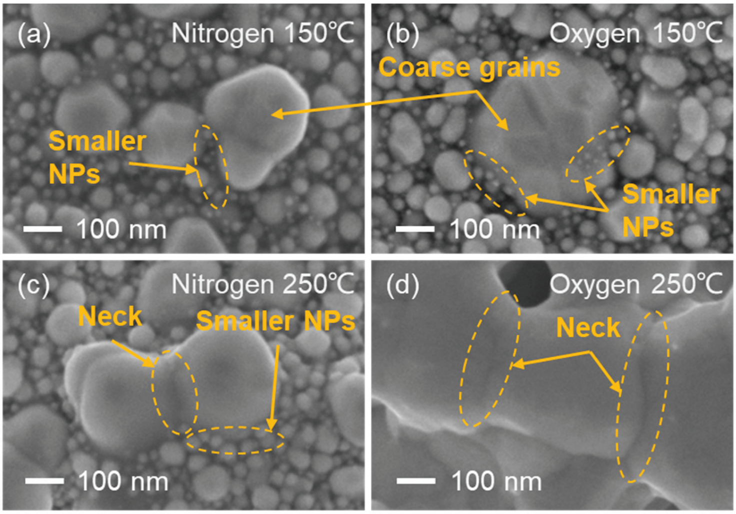

Figure 10. SEM images of microstructural difference between films sintered in different conditions. (**a**) nitrogen at 150 °C; (**b**) oxygen at 150 °C; (**c**) nitrogen at 250 °C; (**d**) oxygen at 250 °C.

Therefore, the oxygen content in the sintering atmosphere could substantially enhance the grain enlargement, enabling the transition from the Ostwald ripening stage to particle coalescence at a lower temperature. In addition, it should be noted that such a stage transition in oxygen was accomplished at a temperature below 250 °C, when the decomposition of PVP had not yet begun according to the thermal analysis results shown in Figure 2. As reported by Yan et al. [51], the organic dispersant in silver NP ink had an important influence on the sintering process, because it was found through FTIR that the carboxyl oxygen atoms of PVP interacted with silver NPs on the surface. When the temperature was low, the particles were encapsulated by PVP, and the sintering mechanism at this time depended on surface diffusion; when the temperature was raised to decompose the dispersant, the sintering process turned to volumetric diffusion. However, the fact that the stage transition in oxygen was accomplished below 250 °C when the PVP was not decomposed implies that there was a difference in the mechanism of grain size enlargement within the scope of this study. In their study of silver thin film deposition [52], Presland et al. found that oxygen could increase the surface diffusion coefficient of silver atoms by hundreds of folds. They studied the formation of hillocks in the deposition of silver thin films and found that the diffusion flux of silver atoms during film growth was affected by oxygen partial pressure [53]. Jeong et al. confirmed that the mixing of oxygen helped to reduce the free energy of silver NPs during the coalescence stage, so that the evolution mechanism of the NPs changed, and the incomplete coalescence of silver NPs occurred earlier in the experimental group with excess oxygen, which promoted the rapid development of the silver film and significantly reduced the number and size of the pores in the silver film [54]. These phenomena are consistent with the evolution of silver NPs sintered below the decomposition temperature of PVP in this study. Silver in an oxygen-containing atmosphere has a stronger surface diffusion ability, and the surface diffusion and coalescence between particles are enhanced, so the films sintered in an atmosphere with a higher oxygen content have larger particles. Therefore, the effect of the oxygen content on improving the diffusion of silver atoms during sintering was significant even with the presence of the original PVP dispersant in the film.

Moreover, the effect of the oxygen content on lowering the PVP decomposition temperature could contribute to the final sintering stage of film densification shown in Figure 10. As indicated by Figure 5, the temperature at which film densification could be finalized was approximately 350 °C for the oxygen-containing atmosphere and 450 °C for the pure nitrogen atmosphere. The temperatures of the initiation of PVP decomposition were about 280 °C in oxygen and 400 °C in nitrogen, respectively, as shown in Figure 2. As suggested in the related literature [33–55], the encapsulation of silver NPs by organic dispersants significantly affects the sintered morphology and consequently the properties of sintered silver thin films. Thus, it could be supposed that the breaching of the PVP dispersant capsulation of the silver NPs through enabling its decomposition is a prerequisite condition for the stage transition from particle coalescence to film densification, because the presence of PVP would limit the volumetric diffusion of silver NPs.

Besides the abovementioned effects of oxygen content, which could benefit our understanding of the sintering mechanisms of silver NPs, the findings in this study could also be instructive for engineering applications and equipment development for the ink-jet printing of silver thin films. First, as illustrated in Figure 3, the curves of electrical resistivity of the films sintered in air and pure oxygen were similar, and the micromorphological evolution of the films was also similar, as shown in Figure 5, indicating that the oxygen content in air was sufficient to ensure adequate grain growth from original silver NPs and PVP decomposition during sintering. The feasibility of using air as a sintering atmosphere instead of employing an oxygen-rich gas supply could help to simplify ink-jet printing equipment and lower its cost. Second, the optimal electrical conductivity could be achieved at approximately 350 °C in an oxygen-containing atmosphere, while such a temperature could damage the typical flexible substrates such as PET. Therefore, the application of heat for the practical sintering of as-printed silver circuits on a flexible substrate should be as brief as possible and concentrated on the silver NPs to avoid heat transfer from the silver film to the substrate. Based on the information discussed above, we developed an ink-jet printing system with a heating strategy that considers the absorbent properties of silver NPs and substrates and used it to fabricate high-performance samples, which will be reported in a forthcoming paper.

5. Conclusions

In this study, an investigation of the effect of the atmospheric oxygen content during the sintering of silver thin films derived from NP ink was carried out. The thermal properties of the silver NP ink and PVP dispersant were analyzed; the electrical conductivity of silver thin films sintered under different atmospheres and temperatures was compared; and the microstructure of the silver films and organic residue was analyzed. Combined with a discussion of the mechanisms of grain size and resistivity evolution, the following conclusions could be drawn:

(1) The thermal analysis of the NP ink and PVP showed that the decomposition temperature of PVP was above 400 °C in pure nitrogen, and the presence of oxygen in the sintering atmosphere lowered the onset temperature of PVP decomposition to 280 °C.

(2) The oxygen content significantly reduced the resistivity of the sintered thin films, and the optimal resistivity achieved in the film sintered at 350 °C in oxygen was 2.47 $\mu\Omega\cdot$cm, which is only 1.5-fold that of bulk silver. In addition, the resistivity–temperature curves of the films sintered in air and pure oxygen were quite similar.

(3) Compared with their counterparts in nitrogen, the silver NPs coalesced and coarsened much more rapidly when sintered in an oxygen-containing atmosphere, demonstrating that the oxygen content contributed to the enlargement of the silver grain size.

(4) The thin films sintered in an oxygen-containing atmosphere had less organic residue, which enhanced the silver diffusion to form a dense microstructure, thereby increasing the film's conductivity.

Author Contributions: Conceptualization, F.F., X.G. and Y.M.; methodology, H.H. and T.R.; data curation, H.H.; writing—original draft preparation, F.F. and H.H.; writing—review and editing, X.G., Y.M. and P.F.; project administration, P.F. All authors have read and agreed to the published version of the manuscript.

Funding: This study was supported by the National Natural Science Foundation of China under grant no. 51875311, the Guangdong Basic and Applied Basic Research Foundation under grant no. 2020A1515011199, and the Shenzhen Natural Science Foundation under grant no. WDZC20200817152115001.

Institutional Review Board Statement: Not applicable.

Data Availability Statement: The data presented in this study are available from the corresponding authors upon a reasonable request.

Acknowledgments: The authors would like to thank the Testing Technology Center of Materials and Devices, Tsinghua Shenzhen International Graduate School (https://mdtc.sz.tsinghua.edu.cn (accessed on 1 June 2022)) for the assistance with measurements and analysis.

Conflicts of Interest: The authors declare no conflict of interest.

References

1. Nayak, L.; Mohanty, S.; Nayak, S.K.; Ramadoss, A. A review on inkjet printing of nanoparticle inks for flexible electronics. *J. Mater. Chem. C* **2019**, *7*, 8771–8795. [CrossRef]
2. Shin, K.-Y.; Lee, M.; Kang, H.; Kang, K.; Hwang, J.Y.; Kim, J.-M.; Lee, S.-H. Characterization of Inkjet-Printed Silver Patterns for Application to Printed Circuit Board (PCB). *J. Electr. Eng. Technol.* **2013**, *8*, 603–609. [CrossRef]
3. Zhuo, L.; Liu, W.; Zhao, Z.; Yin, E.; Li, C.; Zhou, L.; Zhang, Q.; Feng, Y.; Lin, S. Cost-Effective silver nano-ink for inkjet printing in application of flexible electronic devices. *Chem. Phys. Lett.* **2020**, *757*, 137904. [CrossRef]
4. Kang, B.J.; Oh, J.H. Geometrical characterization of inkjet-printed conductive lines of nanosilver suspensions on a polymer substrate. *Thin Solid Films* **2010**, *518*, 2890–2896. [CrossRef]
5. Zhou, L.; Xiang, H.Y.; Shen, S.; Li, Y.Q.; Chen, J.D.; Xie, H.J.; Goldthorpe, I.A.; Chen, L.S.; Lee, S.T.; Tang, J.X. High-performance flexible organic light-emitting diodes using embedded silver network transparent electrodes. *ACS Nano* **2014**, *8*, 12796–12805. [CrossRef]
6. Kim, M.; Jee, H.; Lee, J. Photo-Sintered Silver Thin Films by a High-Power UV-LED Module for Flexible Electronic Applications. *Nanomaterials* **2021**, *11*, 2840. [CrossRef]
7. Matsuhisa, N.; Inoue, D.; Zalar, P.; Jin, H.; Matsuba, Y.; Itoh, A.; Yokota, T.; Hashizume, D.; Someya, T. Printable elastic conductors by in situ formation of silver nanoparticles from silver flakes. *Nat. Mater.* **2017**, *16*, 834–840. [CrossRef]
8. Shen, W.; Zhang, X.; Huang, Q.; Xu, Q.; Song, W. Preparation of solid silver nanoparticles for inkjet printed flexible electronics with high conductivity. *Nanoscale* **2014**, *6*, 1622–1628. [CrossRef]
9. Salmerón, J.F.; Molina-Lopez, F.; Briand, D.; Ruan, J.J.; Rivadeneyra, A.; Carvajal, M.A.; Capitán-Vallvey, L.F.; de Rooij, N.F.; Palma, A.J. Properties and Printability of Inkjet and Screen-Printed Silver Patterns for RFID Antennas. *J. Electron. Mater.* **2013**, *43*, 604–617. [CrossRef]
10. Sanchez-Romaguera, V.; Wünscher, S.; Turki, B.M.; Abbel, R.; Barbosa, S.; Tate, D.J.; Oyeka, D.; Batchelor, J.C.; Parker, E.A.; Schubert, U.S.; et al. Inkjet printed paper based frequency selective surfaces and skin mounted RFID tags: The interrelation between silver nanoparticle ink, paper substrate and low temperature sintering technique. *J. Mater. Chem. C* **2015**, *3*, 2132–2140. [CrossRef]
11. Maisch, P.; Tam, K.C.; Lucera, L.; Egelhaaf, H.-J.; Scheiber, H.; Maier, E.; Brabec, C.J. Inkjet printed silver nanowire percolation networks as electrodes for highly efficient semitransparent organic solar cells. *Org. Electron.* **2016**, *38*, 139–143. [CrossRef]
12. Karunakaran, S.K.; Arumugam, G.M.; Yang, W.; Ge, S.; Khan, S.N.; Lin, X.; Yang, G. Recent progress in inkjet-printed solar cells. *J. Mater. Chem. A* **2019**, *7*, 13873–13902. [CrossRef]
13. Kahng, Y.H.; Kim, M.-K.; Lee, J.-H.; Kim, Y.J.; Kim, N.; Park, D.-W.; Lee, K. Highly conductive flexible transparent electrodes fabricated by combining graphene films and inkjet-printed silver grids. *Sol. Energy Mater. Sol. Cells* **2014**, *124*, 86–91. [CrossRef]
14. Wu, X.; Wang, S.; Luo, Z.; Lu, J.; Lin, K.; Xie, H.; Wang, Y.; Li, J.Z. Inkjet Printing of Flexible Transparent Conductive Films with Silver Nanowires Ink. *Nanomaterials* **2021**, *11*, 1571. [CrossRef] [PubMed]
15. Tobjörk, D.; Aarnio, H.; Pulkkinen, P.; Bollström, R.; Määttänen, A.; Ihalainen, P.; Mäkelä, T.; Peltonen, J.; Toivakka, M.; Tenhu, H.; et al. IR-sintering of ink-jet printed metal-nanoparticles on paper. *Thin Solid Films* **2012**, *520*, 2949–2955. [CrossRef]
16. Kamyshny, A.; Magdassi, S. Conductive nanomaterials for printed electronics. *Small* **2014**, *10*, 3515–3535. [CrossRef]
17. Yaqoob, A.A.; Umar, K.; Ibrahim, M.N.M. Silver nanoparticles: Various methods of synthesis, size affecting factors and their potential applications—A review. *Appl. Nanosci.* **2020**, *10*, 1369–1378. [CrossRef]
18. Yong, Y.; Nguyen, M.T.; Tsukamoto, H.; Matsubara, M.; Liao, Y.C.; Yonezawa, T. Effect of decomposition and organic residues on resistivity of copper films fabricated via low-temperature sintering of complex particle mixed dispersions. *Sci. Rep.* **2017**, *7*, 45150. [CrossRef]
19. Theodorakos, I.; Zacharatos, F.; Geremia, R.; Karnakis, D.; Zergioti, I. Selective laser sintering of Ag nanoparticles ink for applications in flexible electronics. *Appl. Surf. Sci.* **2015**, *336*, 157–162. [CrossRef]
20. Reiser, B.; Gonzalez-Garcia, L.; Kanelidis, I.; Maurer, J.H.M.; Kraus, T. Gold nanorods with conjugated polymer ligands: Sintering-free conductive inks for printed electronics. *Chem. Sci.* **2016**, *7*, 4190–4196. [CrossRef]

21. Coutts, M.J.; Cortie, M.B.; Ford, M.J.; McDonagh, A.M. Rapid and Controllable Sintering of Gold Nanoparticle Inks at Room Temperature Using a Chemical Agent. *J. Phys. Chem. C* **2009**, *113*, 1325–1328. [CrossRef]
22. Lim, S.; Joyce, M.; Fleming, P.D.; Aijazi, A.T.; Atashbar, M. Inkjet Printing and Sintering of Nano-Copper Ink. *J. Imaging Sci. Technol.* **2013**, *57*, 1–7. [CrossRef]
23. Joo, S.J.; Park, S.H.; Moon, C.J.; Kim, H.S. A highly reliable copper nanowire/nanoparticle ink pattern with high conductivity on flexible substrate prepared via a flash light-sintering technique. *ACS Appl. Mater. Interfaces* **2015**, *7*, 5674–5684. [CrossRef] [PubMed]
24. Kanzaki, M.; Kawaguchi, Y.; Kawasaki, H. Fabrication of Conductive Copper Films on Flexible Polymer Substrates by Low-Temperature Sintering of Composite Cu Ink in Air. *ACS Appl. Mater. Interfaces* **2017**, *9*, 20852–20858. [CrossRef]
25. Rajan, K.; Roppolo, I.; Chiappone, A.; Bocchini, S.; Perrone, D.; Chiolerio, A. Silver nanoparticle ink technology: State of the art. *Nanotechnol. Sci. Appl.* **2016**, *9*, 1–13. [CrossRef] [PubMed]
26. Borodko, Y.; Habas, S.E.; Koebel, M.; Yang, P.; Frei, H.; Somorjai, G.A. Probing the interaction of poly (vinylpyrrolidone) with platinum nanocrystals by UV-Raman and FTIR. *J. Phys. Chem. B* **2006**, *110*, 23052–23059. [CrossRef]
27. Liu, L.; Wei, T.; Guan, X.; Zi, X.; He, H.; Dai, H. Size and Morphology Adjustment of PVP-Stabilized Silver and Gold Nanocrystals Synthesized by Hydrodynamic Assisted Self-Assembly. *J. Phys. Chem. C* **2009**, *113*, 8595–8600. [CrossRef]
28. Mirzaei, A.; Janghorban, K.; Hashemi, B.; Bonyani, M.; Leonardi, S.G.; Neri, G. Characterization and optical studies of PVP-capped silver nanoparticles. *J. Nanostruct. Chem.* **2016**, *7*, 37–46. [CrossRef]
29. Panáček, A.; Prucek, R.; Hrbáč, J.; Nevečná, T.j.; Šteffková, J.; Zbořil, R.; Kvítek, L. Polyacrylate-Assisted Size Control of Silver Nanoparticles and Their Catalytic Activity. *Chem. Mater.* **2014**, *26*, 1332–1339. [CrossRef]
30. Huang, Q.; Shen, W.; Xu, Q.; Tan, R.; Song, W. Properties of polyacrylic acid-coated silver nanoparticle ink for inkjet printing conductive tracks on paper with high conductivity. *Mater. Chem. Phys.* **2014**, *147*, 550–556. [CrossRef]
31. Chen, S.; Guan, Y.; Li, Y.; Yan, X.; Ni, H.; Li, L. A water-based silver nanowire ink for large-scale flexible transparent conductive films and touch screens. *J. Mater. Chem. C* **2017**, *5*, 2404–2414. [CrossRef]
32. Ryu, K.; Moon, Y.-J.; Park, K.; Hwang, J.-Y.; Moon, S.-J. Electrical Property and Surface Morphology of Silver Nanoparticles After Thermal Sintering. *J. Electron. Mater.* **2015**, *45*, 312–321. [CrossRef]
33. Buffat, P.; Borel, J.P. Size effect on the melting temperature of gold particles. *Phys. Rev. A* **1976**, *13*, 2287–2298. [CrossRef]
34. Anto, B.T.; Sivaramakrishnan, S.; Chua, L.-L.; Ho, P.K.H. Hydrophilic Sparse Ionic Monolayer-Protected Metal Nanoparticles: Highly Concentrated Nano-Au and Nano-Ag "Inks" that can be Sintered to Near-Bulk Conductivity at 150 °C. *Adv. Funct. Mater.* **2010**, *20*, 296–303. [CrossRef]
35. Taher, A.A.; Takhakh, A.M.; Thahab, S.M. Study and optimization of the mechanical properties of PVP/PVA polymer nanocomposite as a low temperature adhesive in nano-joining. *IOP Conf. Ser. Mater. Sci. Eng.* **2020**, *671*, 012145. [CrossRef]
36. Li, X.; Zheng, B.; Xu, L.; Wu, D.; Liu, Z.; Zhang, H. Study on Properties of Conductive Adhesive Prepared with Silver Nanoparticles Modified by Silane Coupling Agent. *Rare Metal. Mater. Eng.* **2012**, *41*, 24–27. [CrossRef]
37. Magdassi, S.; Grouchko, M.; Berezin, O.; Kamyshny, A. Triggering the sintering of silver nanoparticles at room temperature. *ACS Nano* **2010**, *4*, 1943–1948. [CrossRef]
38. Wakuda, D.; Keun-Soo, K.; Suganuma, K. Room-Temperature Sintering Process of Ag Nanoparticle Paste. *IEEE Trans. Compon. Packag. Technol.* **2009**, *32*, 627–632. [CrossRef]
39. Zhang, R.; Moon, K.-S.; Lin, W.; Wong, C.P. Preparation of highly conductive polymer nanocomposites by low temperature sintering of silver nanoparticles. *J. Mater. Chem.* **2010**, *20*, 2018–2023. [CrossRef]
40. Chou, K.-S.; Lai, Y.-S. Effect of polyvinyl pyrrolidone molecular weights on the formation of nanosized silver colloids. *Mater. Chem.* **2004**, *83*, 82–88. [CrossRef]
41. Yan, J.; Zou, G.; Hu, A.; Zhou, Y.N. Preparation of PVP coated Cu NPs and the application for low-temperature bonding. *J. Mater. Chem.* **2011**, *21*, 15981–15986. [CrossRef]
42. Gao, Y.; Song, L.; Jiang, P.; Liu, L.F.; Yan, X.Q.; Zhou, Z.P.; Liu, D.F.; Wang, J.X.; Yuan, H.J.; Zhang, Z.X.; et al. Silver nanowires with five-fold symmetric cross-section. *J. Cryst. Growth* **2005**, *276*, 606–612. [CrossRef]
43. Maensiri, S.; Nuansing, W.; Klinkaewnarong, J.; Laokul, P.; Khemprasit, J. Nanofibers of barium strontium titanate (BST) by sol-gel processing and electrospinning. *J. Colloid Interface Sci.* **2006**, *297*, 578–583. [CrossRef] [PubMed]
44. Lee, D.Y.; Lee, K.-H.; Lee, M.-H.; Cho, N.-I.; Kim, B.-Y. Synthesis of electrospun $BaSrTiO_3$/PVP nanofibers. *J. Sol.-Gel Sci. Technol.* **2009**, *53*, 43–49. [CrossRef]
45. Volkman, S.K.; Yin, S.; Bakhishev, T.; Puntambekar, K.; Subramanian, V.; Toney, M.F. Mechanistic Studies on Sintering of Silver Nanoparticles. *Chem. Mater.* **2011**, *23*, 4634–4640. [CrossRef]
46. Jang, S.; Rahman, M. Effect of sintering atmospheres on printed silver nanoparticle patterns for flexible electronics application. *Appl. Phys. A* **2021**, *127*, 1–14. [CrossRef]
47. Tang, Y.; He, W.; Wang, S.; Tao, Z.; Cheng, L. New insight into the size-controlled synthesis of silver nanoparticles and its superiority in room temperature sintering. *CrystEngComm* **2014**, *16*, 4431–4440. [CrossRef]
48. Li, M.; Xiao, Y.; Zhang, Z.; Yu, J. Bimodal sintered silver nanoparticle paste with ultrahigh thermal conductivity and shear strength for high temperature thermal interface material applications. *ACS Appl. Mater. Interfaces* **2015**, *7*, 9157–9168. [CrossRef]
49. Sun, Y.; Mayers, B.; Herricks, T.; Xia, Y. Polyol Synthesis of Uniform Silver Nanowires: A Plausible Growth Mechanism and the Supporting Evidence. *Nano Lett.* **2003**, *3*, 955–960. [CrossRef]

50. Yang, F.; Hu, B.; Peng, Y.; Hang, C.; Chen, H.; Lee, C.; Wei, J.; Li, M. Ag microflake-reinforced nano-Ag paste with high mechanical reliability for high-temperature applications. *J. Mater. Sci. Mater. Electron.* **2019**, *30*, 5526–5535. [CrossRef]
51. Yan, J. A Review of Sintering-Bonding Technology Using Ag Nanoparticles for Electronic Packaging. *Nanomaterials* **2021**, *11*, 927. [CrossRef] [PubMed]
52. Sharma, S.K.; Spitz, J. Hillock formation, hole growth and agglomeration in thin silver films. *Thin Solid Films* **1980**, *65*, 339–350. [CrossRef]
53. Presland, A.E.B.; Price, G.L.; Trimm, D.L. Hillock formation by surface diffusion on thin silver films. *Surf. Sci.* **1972**, *29*, 424–434. [CrossRef]
54. Jeong, E.; Lee, S.-G.; Bae, J.-S.; Yu, S.M.; Han, S.Z.; Lee, G.-H.; Choi, E.-A.; Yun, J. Effects of substantial atomic-oxygen migration across silver—Oxide interfaces during silver growth. *Appl. Surf. Sci.* **2021**, *568*, 150927. [CrossRef]
55. Wang, S.; Li, M.; Ji, H.; Wang, C. Rapid pressureless low-temperature sintering of Ag nanoparticles for high-power density electronic packaging. *Scr. Mater.* **2013**, *69*, 789–792. [CrossRef]

nanomaterials

Article

Nanohollow Titanium Oxide Structures on Ti/FTO Glass Formed by Step-Bias Anodic Oxidation for Photoelectrochemical Enhancement

Chi-Hsien Huang [1,†], Yu-Jen Lu [2,3,†], Yong-Chen Pan [4,†], Hui-Ling Liu [4], Jia-Yuan Chang [4], Jhao-Liang Sie [1], Dorota G. Pijanowska [5,*] and Chia-Ming Yang [1,2,4,6,7,8,*]

[1] Department of Materials Engineering, Ming Chi University of Technology, New Taipei 243, Taiwan; chhuang@mail.mcut.edu.tw (C.-H.H.); eharoger@gmail.com (J.-L.S.)
[2] Department of Neurosurgery, Chang Gung Memorial Hospital at Linkou, Taoyuan City 333, Taiwan; alexlu0416@gmail.com
[3] The College of Medicine, Chang Gung University, Taoyuan City 333, Taiwan
[4] Department of Electronic Engineering, Chang Gung University, Taoyuan City 333, Taiwan; pan890808@gmail.com (Y.-C.P.); hll20121219@gmail.com (H.-L.L.); d0827110@cgu.edu.tw (J.-Y.C.)
[5] Nalecz Institute of Biocybernetics and Biomedical Engineering, Polish Academy of Sciences, 02-109 Warsaw, Poland
[6] Institute of Electro-Optical Engineering, Chang Gung University, Taoyuan City 333, Taiwan
[7] Biosensor Group, Biomedical Engineering Research Center, Chang Gung University, Taoyuan City 333, Taiwan
[8] Artificial Intelligence Research Center, Chang Gung University, Taoyuan City 333, Taiwan
* Correspondence: dpijanowska@ibib.waw.pl (D.G.P.); cmyang@mail.cgu.edu.tw (C.-M.Y.); Tel.: +48-22-6599143 (ext. 141) (D.G.P.); +886-3-2118800 (ext. 5960) (C.-M.Y.)
† These authors contributed equally to this work.

Abstract: In this study, a new anodic oxidation with a step-bias increment is proposed to evaluate oxidized titanium (Ti) nanostructures on transparent fluorine-doped tin oxide (FTO) on glass. The optimal Ti thickness was determined to be 130 nm. Compared to the use of a conventional constant bias of 25 V, a bias ranging from 5 V to 20 V with a step size of 5 V for 3 min per period can be used to prepare a titanium oxide (TiO_x) layer with nanohollows that shows a large increase in current of 142% under UV illumination provided by a 365 nm LED at a power of 83 mW. Based on AFM and SEM, the TiO_x grains formed in the step-bias anodic oxidation were found to lead to nanohollow generation. Results obtained from EDS mapping, HR-TEM and XPS all verified the TiO_x composition and supported nanohollow formation. The nanohollows formed in a thin TiO_x layer can lead to a high surface roughness and photon absorbance for photocurrent generation. With this step-bias anodic oxidation methodology, TiO_x with nanohollows can be obtained easily without any extra cost for realizing a high current under photoelectrochemical measurements that shows potential for electrochemical-based sensing applications.

Keywords: TiO_x; anodic oxidation; photoelectrochemical; nanohollows

Citation: Huang, C.-H.; Lu, Y.-J.; Pan, Y.-C.; Liu, H.-L.; Chang, J.-Y.; Sie, J.-L.; Pijanowska, D.G.; Yang, C.-M. Nanohollow Titanium Oxide Structures on Ti/FTO Glass Formed by Step-Bias Anodic Oxidation for Photoelectrochemical Enhancement. *Nanomaterials* **2022**, *12*, 1925. https://doi.org/10.3390/nano12111925

Academic Editors: Jihoon Lee and Ming-Yu Li

Received: 29 April 2022
Accepted: 2 June 2022
Published: 4 June 2022

1. Introduction

Photosensitive metal-oxide semiconductors with different energy band gaps (Eg) have been studied for many applications, including solar cells [1,2], photodetectors [3,4], photocatalysts [5,6], water splitting [7,8] and photoelectrochemistry (PEC) [9,10]. In general, extra carriers can be generated based on the absorption of photons with an energy higher than the band gap of a semiconductor (e.g., $h\nu \geq Eg$) [11]. In electronic devices, such as solar cells and photodetectors, the photon-to-current efficiency and frequency response determined for photosensitive semiconductors can be considered the key performance parameters. In electrochemical devices, oxidation and reduction occur on the surfaces of photosensitive electrodes with the help of extra photoinduced charged carriers, which can be used to enhance chemical reactions and sensing performance. Therefore, the most common materials, including titanium oxide (TiO_2) [12,13], ferric oxide (Fe_2O_3) [14,15] and zinc oxide (ZnO) [16,17], have been investigated widely for decades due to their natural abundance, high chemical stabilities, low costs and low toxicities, especially for realizing superior performance by means of various nanostructures [18]. TiO_2 is the most promising material due to its various fabrication techniques and biocompatibility [19]. In general, self-organized nanotube arrays of these kinds of materials have the advantages of high surface areas fabricated by using the electrochemical anodization of a metal foil that can be obtained with specific bias-setting conditions and electrolytes [20–22]. For example, highly ordered TiO_2 nanotube arrays were fabricated using titanium (Ti) foils at 35 V in a solution of 0.25 wt% of NH_4F and 0.75 wt% of H_2O in ethylene glycol [23]. In this way, TiO_2 nanotubes with inner diameters and wall thicknesses of 130 and 15 nm, respectively, were created [24]. These kinds of electrodes are undesirable for applications since only a pure metal foil can be used as the substrate. However, transparent backside electrodes integrated with nanotube arrays are highly desirable in photovoltaics and photoelectrochemical-cell biorelevant applications due to short charge-transportation lengths and high light-harvesting efficiencies [25]. According to their effective and extra signals, photoelectrochemical biosensors with the advantages of high signal-to-noise ratios, good repeatabilities, low costs and simple instrumentations have attracted extensive interest in biology [26], medicine [27] and environmental monitoring [28]. In previous studies, TiO_2 nanorods were prepared on FTO glass by using a hydrothermal method in a solution containing an equal ratio of 37 wt% of HCl and deionized (DI) water [29]. Titanium iso-propoxide was injected into the prepared solution, which we stored in a Teflon-coated container fixed with an autoclave at 150 °C for 6 h. This developed electrode was proven to be applicable to a photoelectrochemical sensor for beta-amyloid peptide detection. In addition, electrochemical anodization is an easy and efficient method for growing self-organized nanotubes that has been commonly investigated for decades. With the assistance of an electrical field and F^- ions in an electrolyte, Ti-based oxidation can be obtained with the structures of nanotubes or nanopores [30]. Recently, the anodization of Ti thin films deposited on glass substrates through a sputtering modification was studied for water splitting [25,31] and electrochromic devices [32]. Compared to a Ti layer deposited by an evaporator, TiO_2 nanotubes formed on a sputtered Ti layer have five-fold higher photocurrent densities [25]. However, the nanotubes' adhesion to glass substrates and pinholes during their growth is still a concern in real applications [25]. To avoid the cracking or peeling of TiO_2 nanotubes, extra efforts for the modification process of Ti deposition [25,31] and post treatments, which limit their flexibility in real applications, have been addressed [33].

Based on previous literature [34], TiO_2 nanotubes fabricated on a Ti foil by using electrochemical anodic oxidation can be used for photoelectrochemical measurements with signal enhancements [35]. However, these fabricated TiO_2 nanotubes show no clear oxidation and reduction peaks in CV measurements due to their natural electrochemical properties [36] and potential biodamage due to front-side ultraviolet (UV) illumination during the photoelectrochemical operation [37]. For this work, a new process flow of electrode fabrication using a sputtered Ti thin film deposited on FTO glass and following different settings for anodic oxidation was designed to overcome the limitations of biosensing applications based on conventional Ti foils. The concept involved completely oxidizing the entire Ti layer into TiO_x for realizing a better photoelectrochemical response. Therefore, Ti films with different thicknesses and step biases for anodic oxidation were investigated for TiO_x formation with the creation of nanostructures, and their electrochemical and photoelectrochemical behaviors were characterized. Detailed material analyses were performed to obtain a clear understanding of the fabricated TiO_x layer with embedded nanohollows.

2. Materials and Methods

2.1. Electrode Fabrication

To fabricate a reliable electrode with TiO_x nanostructures with the possibility of back-side illumination for reducing damage to biospecies, fluorine-doped tin oxide (FTO) glass substrates (NSG TEC A7, Pilkington, Lathom, UK) with sheet resistances of 10 Ω/sq were selected and cut to dimensions of 25 mm × 10 mm × 1.1 mm for sputtered-titanium (Ti) layer depositions and subsequent electrochemical anodic oxidations. FTO glass substrates were first cleaned in solvents in the sequence of acetone, methanol and DI water for 10 min per solution with an ultrasonication process. Then, FTO glass substrates were dried with a nitrogen (N_2) stream. To obtain better adhesion between the Ti film and FTO glass substrates, the FTO glass substrates were pretreated with CF_4 plasma before titanium layer deposition. The CF_4 plasma treatment was performed using inductively coupled plasma-reactive ion etching (ICP-RIE; KD-ICP/RIE, Kao Duen, New Taipei City, Taiwan) with generation-power, bias-power, period, gas flow-rate and pressure settings of 300 W, 50 W, 3 min, 20 sccm and 100 mTorr, respectively. To reduce ion bombardment at the surface, a stainless shielding filter was placed on top of the FTO glass substrate [38]. The above cleaning and CF_4 plasma procedure not only removed surface contamination but also created a good surface quality for subsequent Ti thin film depositions. By using a radio frequency (RF) magnetron sputtering system with a titanium target with a purity of 99.99% (TIC36KRD, Summit, Taipei, Taiwan), Ti thin films with different thicknesses were deposited onto an FTO glass substrate controlled by a time mode according to a deposition rate calculated from previous test experiments and checked by using a surface profiler (Alpha Step DeltakXT, Bruker, Billerica, MA, USA). Before the deposition process, the chamber was pumped down to a base pressure of 10^{-6} mTorr using a turbo-molecular pump. The flow rate of argon (Ar), RF power and pressure for Ti deposition were 40 sccm, 70 W and 8 mTorr, respectively. The substrate temperature was increased to 300 °C to improve the quality of the Ti film deposition. After sputtering Ti films on FTO glass, the Ti thin films were densified by using rapid thermal annealing (RTA; RTA1000M-V, SJ High Tech Co., Taipei, Taiwan) under ambient N_2 at 500 °C for 1 min to improve the film quality. Figure 1 shows the step-by-step process flow for all experimental groups, including Ti thickness and anodic oxidation, for TiO_x electrode fabrication.

The 2-electrode electrochemical setup was used to anodize the Ti layer deposited onto the FTO glass, as shown in Figure 2a. All the anodization experiments were performed at room temperature in a conventional two-electrode system using a Ti/FTO glass substrate as the working electrode and ITO glass (RLO-I7, Ruilong, Miaoli, Taiwan) with dimensions of 6 cm × 2.6 cm × 0.7 mm and a resistivity of 5 Ω/sq as the counter electrode. Based on our preliminary data, the results obtained for the ITO counter electrodes are similar to those obtained for platinum (Pt) electrodes. Therefore, disposable ITO glass was used to replace the conventional Pt electrode to obtain the same fresh surface for the counter electrode in the anodic oxidation process. The Ti film was anodized in a mixed solution of 92% ethylene glycol and 270 mM ammonium fluoride (NH_4F) [39]. During the electrochemical anodizing process, a controllable DC power source was used to supply the required constant bias voltage or step-bias voltage. To study the efficiency of anodization, various Ti film thicknesses, including 50 nm, 130 nm and 200 nm, were studied first in constant-bias anodic-oxidation (CBAO) experiments with a fixed bias of 25 V for 10 min. These 3 groups were named CBAO-Ti50n, CBAO-Ti130n and CBAO-Ti200n, respectively. Then, in the second part of the anodic-oxidation bias voltage evaluation, all experimental groups with fixed Ti thicknesses of 130 nm were treated with a step-bias anodic oxidation (SBAO) method using the following voltage settings: increasing the step voltage of 5 V, 10 V, 15 V and 20 V and a period of 3 or 5 min for each step of voltage. These 2 experimental groups were named SBAO3m-Ti130n and SBAO5m-Ti130n, respectively.

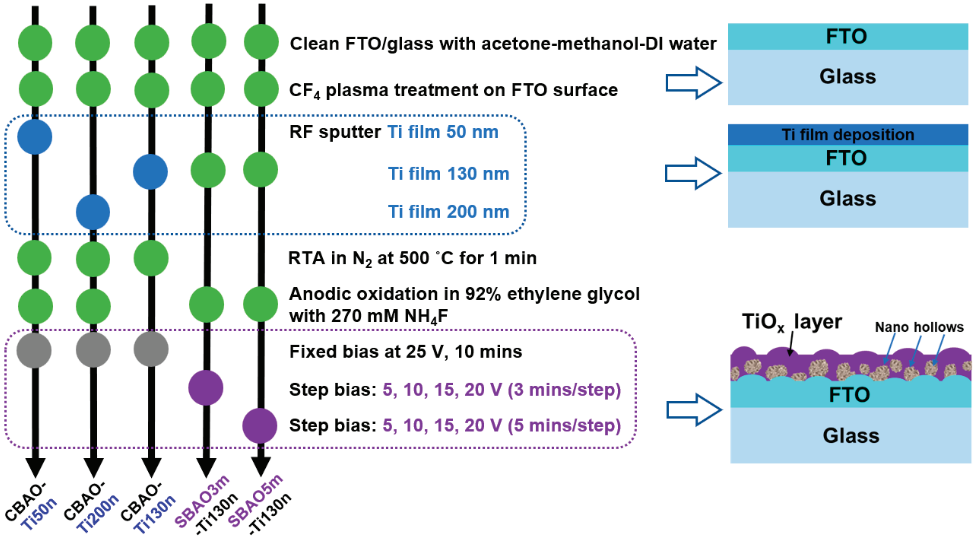

Figure 1. The detailed process flow for all experimental groups with the corresponding cross-sectional schematic plot.

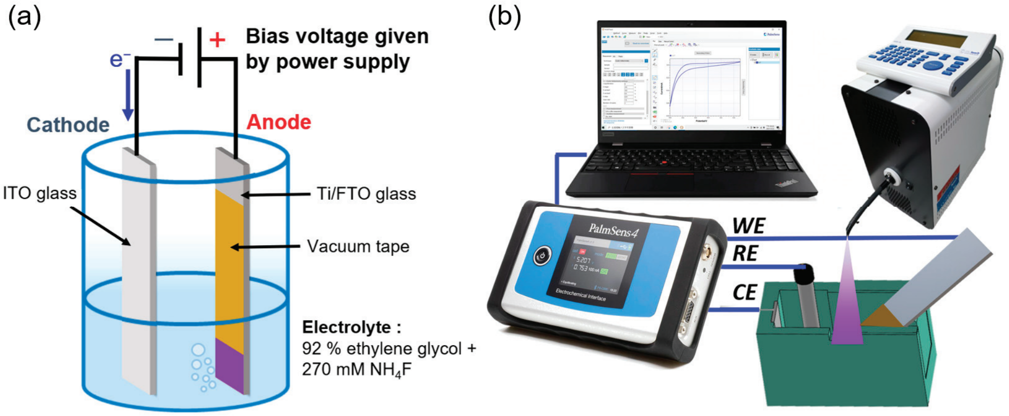

Figure 2. (**a**) The experimental setting for anodic oxidation, including electrolyte, counter and working electrodes, and (**b**) the photoelectrochemical measurement system setup.

2.2. Photoelectrochemical Response

A standard three-electrode system with a commercial potentiostat (PalmSens4, PalmSens, Houten, The Netherlands) was established for photoelectrochemical measurements, as shown in Figure 2b. The three electrodes that were used were as follows: a nanostructured TiO_x-layer grown on Ti/FTO glass encapsulated with vacuum tape for an area of 1.0 × 1.0 cm^2 as the working electrode, a commercial Ag/AgCl reference electrode (ALS, RE-1S, Tokyo, Japan) and a platinum (Pt) sheet (Pt10101, ING-JING, New Taipei City, Taiwan) with dimensions of 1.0 × 1.0 cm^2 as the counter electrode. A cyclic voltammetry (CV) measurement was performed in a 0.1X PBS background solution containing 5 mM of ferricyanide ($K_3[Fe(CN)_6]$). The scan rate and range of CV measurement were 0.1 V/s and from −0.6 V to 0.8 V, respectively. To generate an extra photocurrent for the CV measurement, ultraviolet (UV) illumination at a wavelength of 365 nm with a power of 83 mW was applied to the fabricated TiO_x nanostructured electrode using an LED (pE-4000, CoolLED, Andover, UK). The photoelectrochemical performance of the prepared electrodes was further tested by conducting linear-sweep voltammetry (LSV) measurements under chopped UV illumination with a power of 83 mW and an on/off cycle with a period of 56 s in a 0.1X PBS solution. A scan rate of 0.05 V/s, with a scan range of −0.4 V to 1.0 V, was used to compare measurements with or without continuous UV illumination.

2.3. Material Characterization

To obtain a detailed understanding of the correlation between the material properties and electrochemical behavior of this novel TiO_x nanostructure layer, various material analyses were performed for samples using the same process conditions. First, the morphologies and microstructures of the fabricated samples were characterized by using an atomic-force microscope (AFM; Nanoview 1000, Utek Material, Taipei, Taiwan). During each measurement, the distance between the tip and the sample was controlled in tapping mode to scan the surfaces for all samples. AFM images and calculated average surface-roughness (Ra) values were obtained using the data-analysis software WSxM (Version 5 develop 8.4, Nanotec Electronica, Madrid, Spain). Additionally, scanning electron microscopy (SEM) was performed to compare AFM results obtained through investigation on a top view of TiO_x/FTO glass layers. Furthermore, to investigate the cross-sectional layer distribution and nanostructure, a dual-focused ion beam (FIB; Versa 3D, FEI Company, Hillsboro, OR, USA) was used to slice the whole structure first, and then, a field-emission scanning-electron microscope (FE-SEM; SU8220, Hitachi, Tokyo, Japan) was used to obtain images of the nanostructures. The lattice structure and elemental mapping analysis were observed using high-resolution transmission electron microscopy (HR-TEM; JEM-2100, JEOL, Tokyo, Japan) operated at 200 kV with a point resolution of 0.19 nm.

X-ray diffraction analysis (XRD; PANalytical Empyrean, Malvern Panalytical, Almelo, The Netherlands) with Cu Kα radiation ($\lambda = 0.15406$ nm) was performed to observe the crystalline phase with parameters of 45 kV, 40 mA and a 2θ range of 10°–70°. The compositions and chemistries of the nanostructured TiO_x layers were investigated by using X-ray photoelectron spectroscopy (XPS; PHI 5000 VersaProbe III, ULVAC-PHI Inc., Chigasaki, Japan) performed in an ultra-high vacuum chamber with an Al Kα ($h\nu = 1486.6$ eV) monochromatic X-ray source. The binding energies were calibrated with reference to the C *1s* peak at 284.8 eV. A detailed analysis and comparison are presented in the results and discussion section.

3. Results

3.1. Material Characterization

To obtain a clear understanding of the effects of anodic oxidation on Ti/FTO glass samples, various material analyses, including AFM, SEM, TEM, EDS and XPS, were performed. After an anodic oxidation, all the samples were subjected to AFM measurements to confirm their surface morphologies and surface roughnesses. AFM images of CBAO-Ti130n, SBAO3m-Ti130n and SBAO5m-Ti130n samples are shown in Figure 3a–c, respectively. For the CBAO-Ti130n sample, some small roughnesses were observed with an average roughness (Ra) of 1.57 nm. With step-bias anodic oxidation, the surface roughnesses of the SBAO3m-Ti130n and SBAO5m-Ti130n samples increased significantly to 12.15 nm and 9.84 nm, respectively. Moreover, some nanometer-scale grains were observed in both the samples. To obtain a better understanding, top-view and cross-sectional-view SEM images were captured for all the three samples. The top-view images of CBAO-Ti130n, SBAO3m-Ti130n and SBAO5m-Ti130n are shown in Figure 4a–c, respectively. In general, the top-view SEM images well matched the AFM results obtained for the surface roughnesses and morphologies. The CBAO-Ti130n sample showed a flat surface but with some small particles. With step-bias anodic oxidation, grains with clear boundaries formed on both the SBAO3m-Ti130n and SBAO5m-Ti130n samples. The grains and their boundaries in SBAO samples result in a high surface roughness, which matched the increase in Ra measured by AFM. To confirm the potential mechanism of grain formation through anodic oxidation, cross-sectional SEM images of CBAO-Ti130n, SBAO3m-Ti130n and SBAO5m-Ti130n are shown in Figure 4d–f, respectively. For the CBAO-Ti130n sample, it can be observed that the TiO_X, the FTO and the glass layers stacked from top to bottom all met the thickness and distribution requirements of the process conditions. For the SBAO groups, an FTO layer with a thickness of approximately 310 nm and a TiO_X layer with obvious nanohollows can be observed in Figure 4e,f. The total thicknesses of the TiO_X layer for the SBAO3m-Ti130n and SBAO5m-Ti130n samples were approximately 165 nm and 173 nm, respectively. This can be used to support the small difference in the level of the anodic oxidation of the Ti layer that was 130 nm over different time periods from 3 min to 5 min. These nanohollows with dimensions of approximately 100 nm in height can lead to grain formation and an increased surface roughness. To confirm the correlation between roughness and crystallization, the XRD spectra for CBAO-Ti130n, SBAO3m-Ti130n, SBAO5m-Ti130n and FTO/glass (e.g., the control sample of substrate) are presented in Figure 5. No clear crystallization peak of titanium oxide was found for any of the three samples, but all the peaks can be referred to the FTO [40]. It can be concluded that the crystallization of TiO_X is not strong and shows a more amorphous structure [41]. It can be reasonably assumed that the high surface roughness in the SBAO5m-Ti130n group is mainly due to the nanohollow structure and is not due to the orientation of the crystallization.

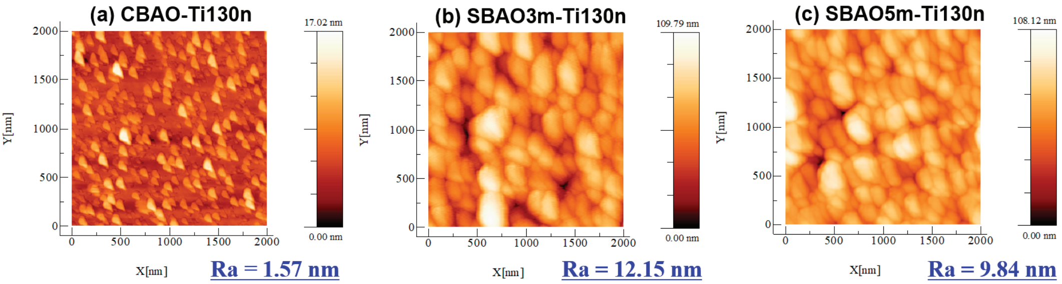

Figure 3. AFM image of the surface morphology for the sample with a 130 nm-thick Ti/FTO glass with different anodization conditions: (**a**) CBAO-Ti130n, (**b**) SBAO3m-Ti130n and (**c**) SBAO5m-Ti130n.

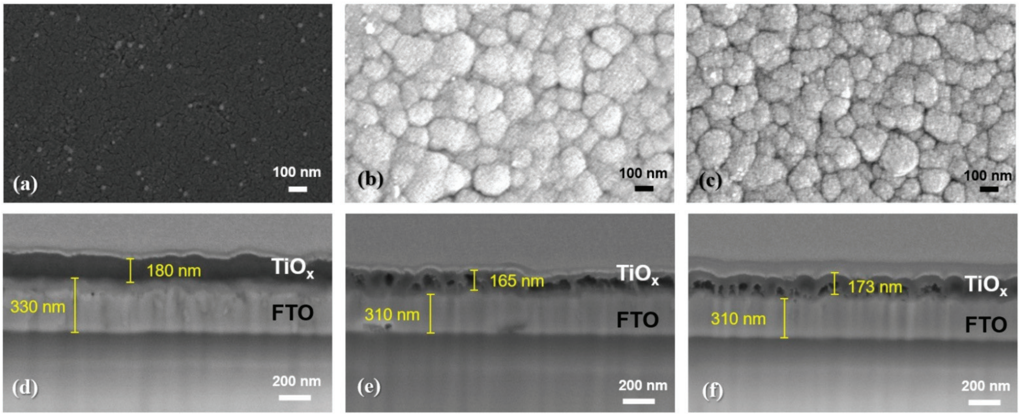

Figure 4. Top-view SEM images with the same magnitudes and scale bars of 100 nm for the surfaces of samples prepared with 130 nm-thick Ti/FTO glass with different anodization conditions: (**a**) CBAO-Ti130n, (**b**) SBAO3m-Ti130n and (**c**) SBAO5m-Ti130n. Cross-sectional SEM image with the same magnitude and scale bar of 200 nm for (**d**) CBAO-Ti130n, (**e**) SBAO3m-Ti130n and (**f**) SBAO5m-Ti130n samples.

To further confirm the composition of the layer distribution, an FIB was used to cut the SBAO3m-Ti130n sample into a thin slice for HR-TEM imaging with a corresponding EDS mapping. The title-view SEM image was captured after the FIB cutting, as shown in Figure 6a. An e-beam-deposited Pt line was used to shield the area, and then, the surrounding area was cut by using a focused ion beam. This sliced sample was used for a TEM analysis. As shown in Figure 6b, a periodic arrangement of the Ti layer with different orientations was clearly observed under a magnification of 600 K. To evaluate the composition of this sliced sample, the separated elemental mapping images recorded by using EDS for different atoms, including Si, O, Sn, Ti, Au and Pt, are shown in Figure 6c. The area of Si atoms with respect to the glass can be observed from the left side. Then, the area of Sn and Ti atoms can be seen from the FTO and TiO_x. In these three areas, O atoms can also be found. The area of each kind of atom can be clearly distinguished. On the right side, an area of thin Au and Pt layers can be observed, which originated from the post-deposited conductive metal layer and shielding layer used for FIB, respectively. Then, a stacked mapping image of all six atoms was rearranged, as shown in Figure 6d. The area of the TiO_x layer can be clearly observed and matched to the previous SEM image, as shown in Figure 4e. Some small white areas can be found in the TiO_x layer, as shown in Figure 6d, which can be attributed to the nanohollows. To further check the atom distribution, the line scanning for an elemental analysis using EDS is also presented for all six atoms, as shown in Figure 6e. The EDS scanning line is marked in the TEM image, as shown in the inset of Figure 6e. The atom distribution across the scanning line for all six atoms is shown in Figure 6f. From approximately 0 nm to 50 nm, a high intensity of Si and O atoms in the glass substrate (e.g., SiO_2) could be expected. An increase in the intensity of the Sn atoms accompanied by a decrease in the intensity of the Si atoms from 50 nm to 80 nm could be attributed to the interface between the FTO and the glass layer. The total thickness of the FTO can be estimated to be the depth with a high intensity of Sn from 50 nm to 350 nm. Then, the Ti concentration increased for the TiO_x layer from 350 nm to 500 nm. A Au layer could be found on top of the TiO_x layer. Finally, a Pt shielding layer prepared in the FIB process was observed. Based on these EDS elemental-mapping and line-scanning results, the thickness of each layer was found to be approximately consistent with the SEM images and fabrication processes. In the meantime, some peaks in the green line due to a high concentration of Ti atoms in the depth analysis and some white areas in the stacked mapping image were observed, which provided strong evidence for TiO_x formation and nanohollows, respectively. All the results obtained from the SEM, TEM and EDS mapping were fully matched to the expected results for the SBAO3m-Ti130n sample. It can be inferred with high confidence that TiO_x nanohollows were formed during the step-bias anodic oxidation of the Ti layers in the developed experiments. To confirm the composition of this fabricated nano-hollowed TiO_x layer, XPS was used to study the chemical states of the surface of this sample for all the possible atoms. As shown in Figure 7a, strong Ti and O peaks can be found from the surface XPS analysis. The Ti and O atomic ratios were 35.3% and 62.2%, respectively. To analyze the chemical binding of this TiO_x layer in detail, the XPS spectra for Ti *2p* and O *1s*, measured for the SBAO3m-Ti130n sample, were rearranged with de-convolutions, as shown in Figure 7b,c, respectively. The Ti $2p_{3/2}$ and Ti $2p_{1/2}$ binding peaks were located at 458.6 eV and 464.2 eV, respectively. This result matches published results, which demonstrates the presence of Ti^{4+} in the TiO_x lattice [42]. A Ti *2p* peak appeared at 457.3 eV, which can be attributed to the small amount of Ti^{3+} present in the TiO_x layer [42]. The O *1s* spectrum could be fitted with two peaks, as shown in Figure 7c. The peak at 530.2 eV can be attributed to Ti-O bonds in the TiO_x lattice, and the peak at 531.4 eV can be attributed to surface hydroxyl groups or adsorbed oxygen [43].

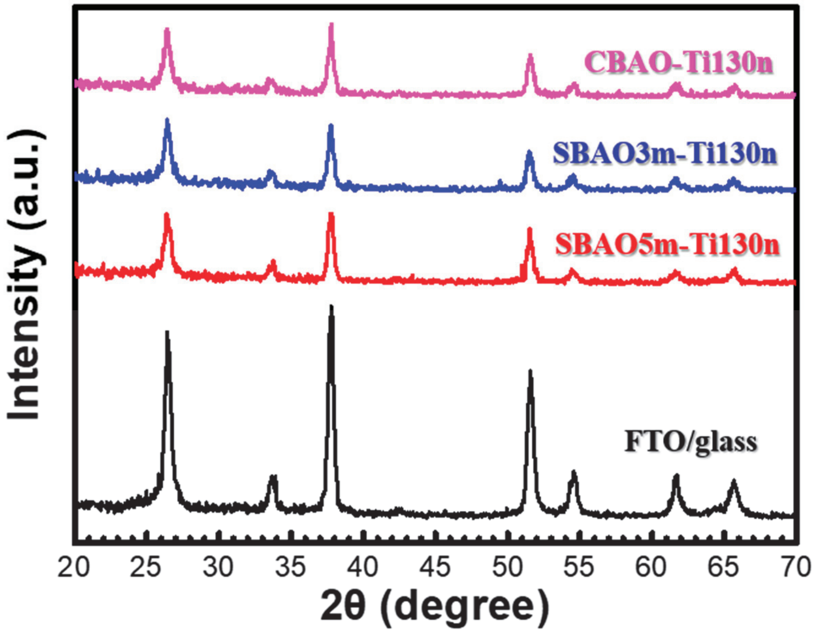

Figure 5. XRD spectra obtained for the CBAO-Ti130n, SBAO3m-Ti130n, SBAO5m-Ti130n and FTO/glass samples.

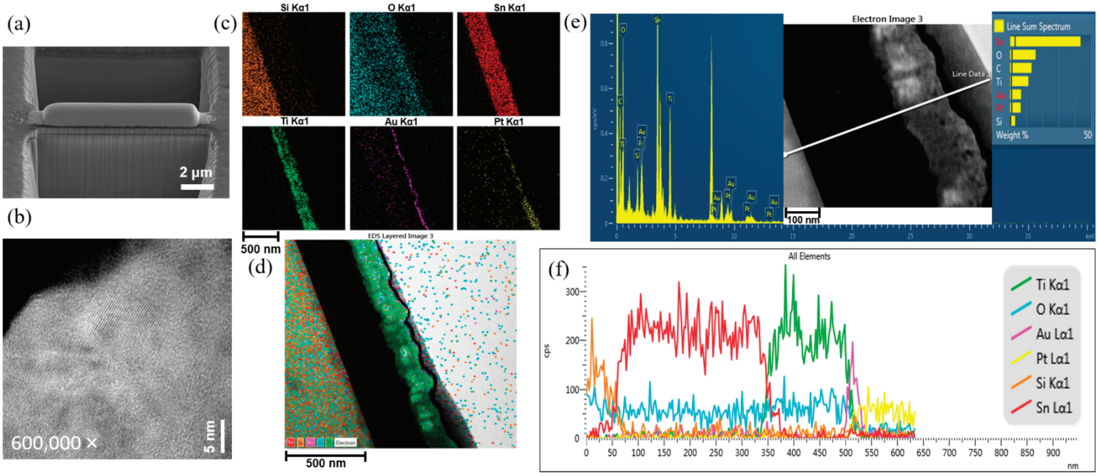

Figure 6. (**a**) SEM image recorded after FIB cutting, (**b**) HR-TEM image with a scale bar of 5 nm, (**c**) separated EDS mapping of different atoms, including Si, Sn, O, Ti, Au and Pt, with a scale bar of 500 nm, (**d**) stacked EDS mapping for all five atoms, including Sn, Si, Au, O and Ti, with a scale bar of 500 nm, (**e**) EDS spectrum obtained via line scanning, shown as a marked line in the inset and (**f**) intensity distribution of the scanning line obtained for all six atoms mentioned above for the SBAO3m-Ti130n sample with embedded nanohollows in the anodic oxidized TiO_X layer.

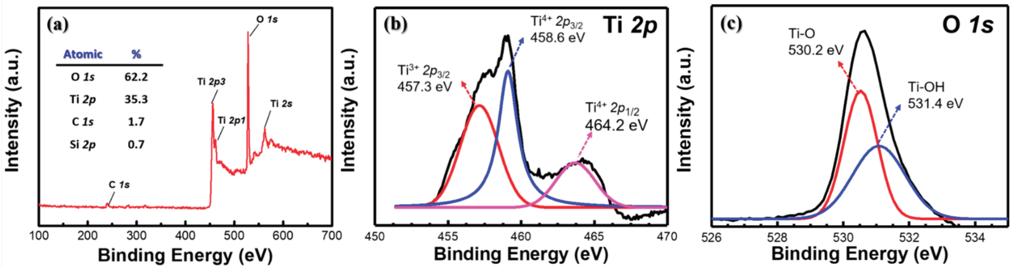

Figure 7. (**a**) Full-scale, (**b**) high-resolution Ti *2p* and (**c**) O *1s* XPS spectra obtained for the SBAO3m-Ti130n sample with embedded nanohollows in the anodic oxidized TiO_x layer.

3.2. Photoelectrochemical Measurements

3.2.1. Effect of Ti Thickness

To evaluate the electrochemical and photoelectrochemical behaviors, cyclic voltammetry (CV) curves were collected for the experimental groups with different Ti thicknesses with a constant bias anodic oxidation at 25 V for 10 min. As shown in Figure 8a,b, CV curves with and without the UV illumination of CBAO-Ti50n, CBAO-Ti130n and CBAO-Ti200n could be clearly observed. To evaluate the correlation between the electrode status and CV behavior, CV curves for FTO glass, Ti/FTO glass and TiO_2 deposited through atomic-layer deposition (ALD) on an FTO glass electrode were also presented as reference groups. First, CV curves without UV illumination presented the typical behaviors, which could be used to check the surface material and its oxidation and reduction peaks, as shown in Figure 8a. The sample with the FTO surface had a typical CV curve and clear peaks, and the samples with the Ti or ALD TiO_2 surfaces both showed no oxidation nor reduction peaks, which matched the results reported in the literature [44,45]. For the CBAO-Ti50n sample, the peak currents for oxidation and reduction both showed similar behaviors but with smaller values than those obtained for the FTO sample. In this sample, the electrochemical behavior was found to be close to that of FTO, which suggests that some parts of FTO under the Ti layer were exposed after CBAO. This also means that the Ti layer can be partly peeled off from the FTO layer during CBAO. A Ti thickness of 50 nm may not be sufficient for a CBAO treatment at 25 V for 10 min. For samples with thicker Ti layers, the current, typical oxidation and reduction peaks were all reduced with the same anodic oxidation on Ti surfaces. In the CBAO-Ti130n group, the peak currents were reduced to approximately 59% compared to those obtained for CBAO-Ti50n. For the CBAO-Ti200n group, no peak could be found, which can be attributed to the surface composed of more TiO_x that resulted in a lower conductivity for a smaller current. To confirm the photoelectrochemical behaviors of the same groups, CV measurements with UV illumination at a wavelength of 365 nm with a power of 83 mW were performed, and the results are shown in Figure 8b. Due to the energy gap and absorbance of TiO_x, UV illumination at 365 nm can be absorbed by TiO_x and then transferred to an extra photocurrent [46]. However, a photocurrent will not be induced in FTO or Ti samples under UV illumination due to a lack of absorbance and the energy band gaps of these materials [47]. No increment in current was found for the CBAO-Ti50n sample with UV illumination, which can be attributed to a very rare TiO_x layer that was formed, with the sample's response mainly dominated by FTO. This behavior was consistent with that expected from the electrochemical characterization shown in Figure 8a. As the Ti thickness increased, the current under illumination was higher than the current without illumination, which is shown for the sample with Ti thicknesses of 130 nm and 200 nm. The maximum current in the CBAO-Ti200n sample was not high enough under UV illumination. To improve the photo responses of the CV curves, a Ti thickness of 130 nm was selected as a first fix in the process condition. Then, the anodic oxidation procedure was modified as shown in the second part of the figure to reduce the possibility of Ti peeling off from the FTO surface and to ensure that more Ti remained on the FTO to be oxidized as a TiO_x layer.

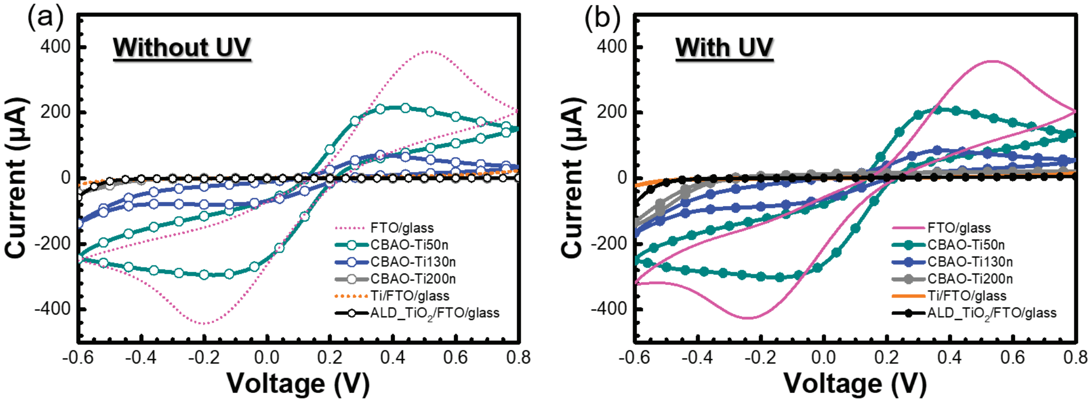

Figure 8. CV curves measured for different electrodes, including FTO glass, CBAO-Ti50n, CBAO-Ti130n, CBAO-Ti200n, Ti/FTO glass and ALD TiO_2/FTO glass in 0.1X PBS solution containing 5 mM ferricyanide $K_3[Fe(CN)_6]$ at a scan rate of 0.1 V/s (**a**) without and (**b**) with UV illumination at wavelength of 365 nm and power of 83 mW.

3.2.2. Effects of Anodic Oxidation Conditions

Due to the partial peeling off of the 50-nm-thick Ti layer under constant bias anodic oxidation and the sample with a 200-nm-thick Ti layer having a very low current, a modification in the anodic oxidation with gradual step increases of bias voltage, called step-bias anodic oxidation, was applied to samples with Ti thicknesses of 130 nm. As shown in Figure 9a–c, CV curves with and without UV illumination for CBAO-Ti130n, SBAO3m-Ti130n and SBAO5m-Ti130n, respectively, can be clearly observed. With the SBAO procedure, the current became higher than that for CBAO, both shown at 3 min and 5 min, which can be attributed to an increased oxidation of the Ti layer. It can be clearly observed that the SBAO groups both showed higher current increments with UV illumination, which can be attributed to the effects of TiO_x formation. Moreover, the oxidation and reduction peaks could not be found in SBAO groups due to the TiO_x's material behavior, which was similar to the results obtained from Section 3.2.1. The current ratios at −0.6 V for SBAO3m-Ti130n and SBAO5m-Ti130n increased by 142% and 56%, respectively. It can be concluded that the photon-to-current efficiency increased for the sample prepared by SBAO. The highest photocurrent could be found in the SBAO3m-Ti130n group. To further evaluate the photochemical behavior, linear-sweeping voltammetry (LSV) curves were obtained for these three samples to study the separation of photo-generated electron-hole pairs based on the increased photocurrent. LSV was performed at a scan rate of 0.05 V/s and then with different conditions, including chopped and with and without UV illumination at 365 nm with a power of 83 mW. As shown in Figure 10a, the current measured without the UV illumination was very low, and the current measured with the UV illumination increased with an increasing bias voltage. For chopped illumination with a period of 56 sec at a duty cycle of 50%, the on-off behavior of the photocurrent could be clearly observed between the curve with and without UV illumination. The curves obtained for the same measurement conditions for the SBAO3m-Ti130n and SBAO5m-Ti130n samples are shown in Figure 10b,c, respectively. The highest photocurrent and the fastest transient response could be observed in the SBAO5m-Ti130n sample. The response and recovery times of the photoresponse were within a few ms, which matches the published results for TiO_x [48–50]. With this great enhancement in current shown in both the CV and LSV measurements, TiO_x prepared by using SBAO can be considered a potential candidate for photocatalyst and photoelectrochemical applications. Based on all the material analyses, step-bias anodic oxidation on a Ti layer was proven to create a TiO_x layer composited with nanohollows following an increase in surface roughness and a 142% increment in the photocurrent under UV illumination at 365 nm with a power of 83 mW. This proposed process of step-bias anodic oxidation with only simple modifications to the parameter settings not only improves the stability for conventional fixed-bias anodic oxidation but also leads to a superior photoresponse, which can be suggested for applications in photocatalysis and photoelectrochemistry. In particular, photoelectrochemical sensing could be enhanced through back-side illumination through a transparent substrate composed of FTO glass to reduce photo-induced damage for biospecies detection, such as antibody and cell detection.

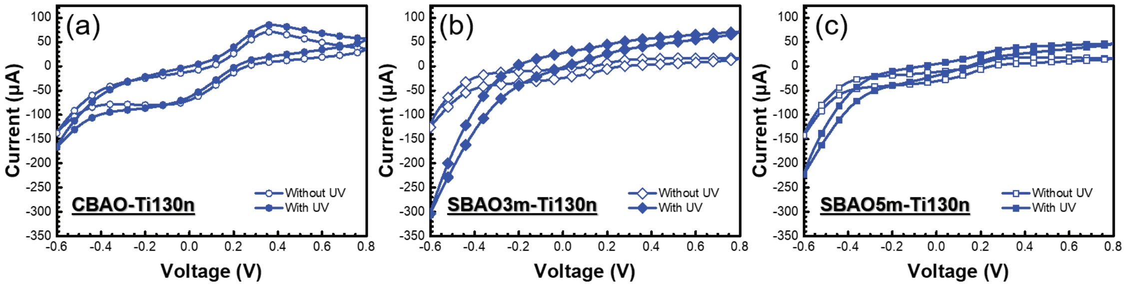

Figure 9. CV curves measured with and without UV illumination for different electrodes, including (**a**) CBAO-Ti130n, (**b**) SBAO3m-Ti130n and (**c**) SBAO5m-Ti130n electrodes, in 0.1X PBS solution containing 5 mM $K_3[Fe(CN)_6]$ at a scan rate of 0.1 V/s.

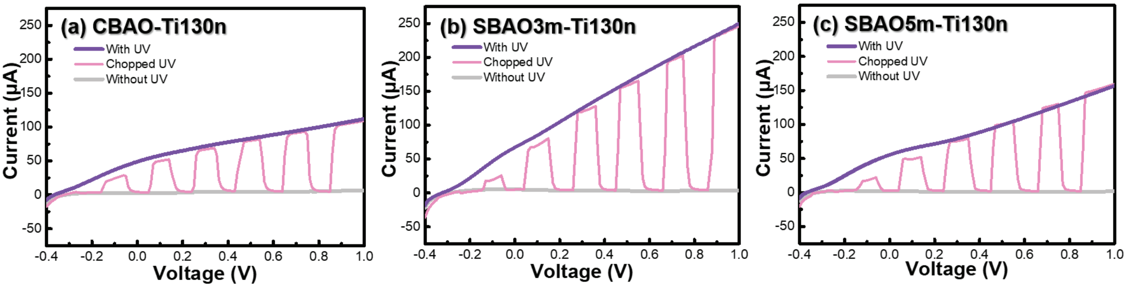

Figure 10. Different LSV curves measured with, without, and with chopped UV illumination at 365 nm with a power of 83 mW in 0.1X PBS solution at a scan rate of 0.05 V/s from −0.4 V to 1 V for (**a**) CBAO-Ti130n, (**b**) SBAO3m-Ti130n and (**c**) SBAO5m-Ti130n samples, respectively.

4. Conclusions

In summary, a TiO_x layer with nanohollow structures was successfully grown onto Ti/FTO glass by using the variable step-bias anodic oxidation of a Ti layer. To obtain a detailed insight into the physicochemical material properties and electrochemical features of the novel TiO_x nanostructure layer, various material analyses were performed for samples using the same process conditions, including AFM, SEM, XRD, HR-TEM, EDS and XPS. After an optimization of the experiments, a Ti layer thickness of 130 nm and step-bias settings of 5 V, 10 V, 15 V and 20 V for 3 min per step are suggested, which can result in a stable TiO_x layer with a thickness of approximately 160 nm. The average surface roughness of this layer is 12.15 nm. Nanohollows with diameters of approximately 100 nm were observed by using SEM. The current ratio was increased by 142% in photoelectrochemical measurements of this fabricated TiO_x layer embedded with nanohollows under UV illumination at a power of 83 mW. Further applications of this developed nanohollow-structured TiO_x electrode are suggested for photoelectrochemical biosensing and photocatalysis.

Author Contributions: Conceptualization, Y.-J.L., D.G.P. and C.-M.Y.; methodology, C.-H.H., Y.-J.L., Y.-C.P. and C.-M.Y.; formal analysis, investigation, data curation and validation, C.-H.H., Y.-C.P., H.-L.L., J.-Y.C., J.-L.S. and C.-M.Y.; visualization, Y.-J.L., D.G.P. and C.-M.Y.; writing—original draft preparation and original manuscript writing, C.-H.H., D.G.P. and C.-M.Y.; writing—review and editing, D.G.P. and C.-M.Y.; supervision, D.G.P. and C.-M.Y. All authors have read and agreed to the published version of the manuscript.

Funding: This work was funded by the Chang Gung Memorial Hospital, Taiwan, under the contract numbers CMRPD2L0171, CMRPD2I0012 and CMRPD2K0021 and by the Ministry of Science and Technology of Taiwan under the contract numbers MOST 108-2221-E-182-060-MY3, 108-2628-E-182-002-MY3, 111-2923-E-182-001-MY3 and 110-2221-E-131-011.

Institutional Review Board Statement: Not applicable.

Informed Consent Statement: Not applicable.

Data Availability Statement: The data presented in this study are available upon request from the corresponding authors.

Acknowledgments: The authors would like to express their deepest gratitude toward the Precious Instrument Utilization Center at National Central University for the FIB and TEM analyses under contract numbers MOST 107-2731-M-008-001, MOST 108-2731-M-008-001 and MOST 110-2731-M-008-001.

Conflicts of Interest: The authors declare no conflict of interest.

References

1. Orozco-Messana, J.; Daly, R.; Zanchetta-Chittka, I.F. Cu_2O–ZnO heterojunction solar cell coupled to a $Ni(OH)_2$-rGO-PPy supercapacitor within a porous stoneware tile. *Ceram. Int.* **2020**, *46*, 24831–24837. [CrossRef]
2. Cho, S.I.; Sung, H.K.; Lee, S.J.; Kim, W.H.; Kim, D.-H.; Han, Y.S. Photovoltaic Performance of Dye-Sensitized Solar Cells Containing ZnO Microrods. *Nanomaterials* **2019**, *9*, 1645. [CrossRef] [PubMed]
3. Xie, Y.; Wei, L.; Wei, G.; Li, Q.; Wang, D.; Chen, Y.; Yan, S.; Liu, G.; Mei, L.; Jiao, J. A self-powered UV photodetector based on TiO_2 nanorod arrays. *Nanoscale Res. Lett.* **2013**, *8*, 188. [CrossRef] [PubMed]
4. Chen, K.J.; Hung, F.Y.; Chang, S.J.; Young, S.J. Optoelectronic characteristics of UV photodetector based on ZnO nanowire thin films. *J. Alloy. Compd.* **2009**, *479*, 674–677. [CrossRef]
5. Tang, M.; Lu, S.; He, L.; Zhu, X.; Feng, W.; Zhang, W. Preparation, Characterization of $ZnTiO_3$/ZnO Composite Materials and Their Photocatalytic Performance. *Nanomaterials* **2022**, *12*, 1345. [CrossRef]
6. Tian, Q.; Wu, W.; Sun, L.; Yang, S.; Lei, M.; Zhou, J.; Liu, Y.; Xiao, X.; Ren, F.; Jiang, C.; et al. Tube-Like Ternary α-Fe_2O_3@SnO_2@Cu_2O Sandwich Heterostructures: Synthesis and Enhanced Photocatalytic Properties. *ACS Appl. Mater. Interfaces* **2014**, *6*, 13088–13097. [CrossRef]
7. Wang, Z.; Gu, Y.; Zheng, L.; Hou, J.; Zheng, H.; Sun, S.; Wang, L. Machine Learning Guided Dopant Selection for Metal Oxide-Based Photoelectrochemical Water Splitting: The Case Study of Fe_2O_3 and CuO. *Adv. Mater.* **2022**, *34*, 2106776. [CrossRef]
8. Kim, J.; Heo, J.N.; Do, J.Y.; Chava, R.K.; Kang, M. Electrochemical Synergies of Heterostructured Fe_2O_3-MnO Catalyst for Oxygen Evolution Reaction in Alkaline Water Splitting. *Nanomaterials* **2019**, *9*, 1486. [CrossRef]
9. Movsesyan, L.; Maijenburg, A.W.; Goethals, N.; Sigle, W.; Spende, A.; Yang, F.; Kaiser, B.; Jaegermann, W.; Park, S.-Y.; Mul, G.; et al. ZnO Nanowire Networks as Photoanode Model Systems for Photoelectrochemical Applications. *Nanomaterials* **2018**, *8*, 693. [CrossRef]
10. Ning, J.; Mu, C.; Guo, X.; Yang, R.; Jonathan, R.; Jiao, W.; Wu, X.; Jian, X. Efficient defect engineering and in-situ carbon doping in ultra-fine TiO_2 with enhanced visible-light-response photocatalytic performance. *J. Alloy. Compd.* **2022**, *901*, 163490. [CrossRef]
11. Kment, S.; Riboni, F.; Pausova, S.; Wang, L.; Wang, L.; Han, H.; Hubicka, Z.; Krysa, J.; Schmuki, P.; Zboril, R. Photoanodes based on TiO_2 and α-Fe_2O_3 for solar water-splitting—Superior role of 1D nanoarchitectures and of combined heterostructures. *Chem. Soc. Rev.* **2017**, *46*, 3716–3769. [CrossRef] [PubMed]
12. Yu, J.; Wu, Z.; Gong, C.; Xiao, W.; Sun, L.; Lin, C. Fe^{3+}-Doped TiO_2 Nanotube Arrays on Ti-Fe Alloys for Enhanced Photoelectrocatalytic Activity. *Nanomaterials* **2016**, *6*, 107. [CrossRef] [PubMed]
13. Yang, Z.; Xu, W.; Yan, B.; Wu, B.; Ma, J.; Wang, X.; Qiao, B.; Tu, J.; Pei, H.; Chen, D.; et al. Gold and Platinum Nanoparticle-Functionalized TiO_2 Nanotubes for Photoelectrochemical Glucose Sensing. *ACS Omega* **2022**, *7*, 2474–2483. [CrossRef] [PubMed]
14. Liang, R.; He, Z.; Zhou, C.; Yan, G.; Wu, L. MOF-Derived Porous Fe_2O_3 Nanoparticles Coupled with CdS Quantum Dots for Degradation of Bisphenol A under Visible Light Irradiation. *Nanomaterials* **2020**, *10*, 1701. [CrossRef] [PubMed]
15. Shi, Y.; Li, H.; Wang, L.; Shen, W.; Chen, H. Novel α-Fe_2O_3/CdS cornlike nanorods with enhanced photocatalytic performance. *ACS Appl. Mater. Interfaces* **2012**, *4*, 4800–4806. [CrossRef]
16. Gong, A.; Feng, Y.; Liu, C.; Chen, J.; Wang, Z.; Shen, T. A promising ZnO/Graphene van der Waals heterojunction as solar cell devices: A first-principles study. *Energy Rep.* **2022**, *8*, 904–910. [CrossRef]

17. Zheng, L.; Liu, M.; Zhang, H.; Zheng, Z.; Wang, Z.; Cheng, H.; Wang, P.; Liu, Y.; Huang, B. Fabrication of ZnO Ceramics with Defects by Spark Plasma Sintering Method and Investigations of Their Photoelectrochemical Properties. *Nanomaterials* **2021**, *11*, 2506. [CrossRef]
18. Chen, J.; Dai, S.; Liu, L.; Maitz, M.F.; Liao, Y.; Cui, J.; Zhao, A.; Yang, P.; Huang, N.; Wang, Y. Photo-functionalized TiO_2 nanotubes decorated with multifunctional Ag nanoparticles for enhanced vascular biocompatibility. *Bioact. Mater.* **2021**, *6*, 45–54. [CrossRef]
19. Konatu, R.T.; Domingues, D.D.; Escada, A.L.A.; Chaves, J.A.M.; Netipanyj, M.F.D.; Nakazato, R.Z.; Popat, K.C.; Grandini, C.R.; Alves Claro, A.P.R. Synthesis and characterization of self-organized TiO_2 nanotubes grown on Ti-15Zr alloy surface to enhance cell response. *Surf. Interfaces* **2021**, *26*, 101439. [CrossRef]
20. Kmentova, H.; Kment, S.; Wang, L.; Pausova, S.; Vaclavu, T.; Kuzel, R.; Han, H.; Hubicka, Z.; Zlamal, M.; Olejnicek, J.; et al. Photoelectrochemical and structural properties of TiO_2 nanotubes and nanorods grown on FTO substrate: Comparative study between electrochemical anodization and hydrothermal method used for the nanostructures fabrication. *Catal. Today* **2017**, *287*, 130–136. [CrossRef]
21. Park, J.; Cimpean, A.; Tesler, A.B.; Mazare, A. Anodic TiO_2 Nanotubes: Tailoring Osteoinduction via Drug Delivery. *Nanomaterials* **2021**, *11*, 2359. [CrossRef]
22. Rho, W.Y.; Chun, M.H.; Kim, H.S.; Kim, H.M.; Suh, J.S.; Jun, B.H. Ag Nanoparticle–Functionalized Open-Ended Freestanding TiO_2 Nanotube Arrays with a Scattering Layer for Improved Energy Conversion Efficiency in Dye-Sensitized Solar Cells. *Nanomaterials* **2016**, *6*, 117. [CrossRef] [PubMed]
23. Kuang, D.; Brillet, J.; Chen, P.; Takata, M.; Uchida, S.; Miura, H.; Sumioka, K.; Zakeeruddin, S.M.; Grätzel, M. Application of highly ordered TiO_2 nanotube arrays in flexible dye-sensitized solar cells. *ACS Nano* **2008**, *2*, 1113–1116. [CrossRef] [PubMed]
24. Du, K.; Liu, G.; Chen, X.; Wang, K. Fast charge separation and photocurrent enhancement on black TiO_2 nanotubes co-sensitized with Au nanoparticles and PbS quantum dots. *Electrochim. Acta* **2018**, *277*, 244–254. [CrossRef]
25. Krysa, J.; Lee, K.; Pausova, S.; Kment, S.; Hubicka, Z.; Ctvrtlik, R.; Schmuki, P. Self-organized transparent 1D TiO_2 nanotubular photoelectrodes grown by anodization of sputtered and evaporated ti layers: A comparative photoelectrochemical study. *Chem. Eng. J.* **2017**, *308*, 745–753. [CrossRef]
26. Yue, Z.; Lisdat, F.; Parak, W.J.; Hickey, S.G.; Tu, L.; Sabir, N.; Dorfs, D.; Bigall, N.C. Quantum-dot-based photoelectrochemical sensors for chemical and biological detection. *ACS Appl. Mater. Interfaces* **2013**, *5*, 2800–2814. [CrossRef]
27. Wang, G.L.; Xu, J.J.; Chen, H.Y.; Fu, S.Z. Label-free photoelectrochemical immunoassay for α-fetoprotein detection based on TiO_2/CdS hybrid. *Biosens. Bioelectron.* **2009**, *25*, 791–796. [CrossRef]
28. Li, H.; Li, J.; Yang, Z.; Xu, Q.; Hu, X. A novel photoelectrochemical sensor for the organophosphorus pesticide dichlofenthion based on nanometer-sized titania coupled with a screen-printed electrode. *Anal. Chem.* **2011**, *83*, 5290–5295. [CrossRef]
29. Lu, Y.J.; Purwidyantri, A.; Liu, H.L.; Wang, L.W.; Shih, C.Y.; Pijanowska, D.G.; Yang, C.M. Photoelectrochemical Detection of β-amyloid Peptides by a TiO_2 Nanobrush Biosensor. *IEEE Sens. J.* **2020**, *20*, 6248–6255. [CrossRef]
30. Prakasam, H.E.; Varghese, O.K.; Paulose, M.; Mor, G.K.; A Grimes, C. Synthesis and photoelectrochemical properties of nanoporous iron (III) oxide by potentiostatic anodization. *Nanotechnology* **2006**, *17*, 4285–4291. [CrossRef]
31. Zelny, M.; Kment, S.; Ctvrtlik, R.; Pausova, S.; Kmentova, H.; Tomastik, J.; Hubicka, Z.; Rambabu, Y.; Krysa, J.; Naldoni, A.; et al. TiO_2 Nanotubes on Transparent Substrates: Control of Film Microstructure and Photoelectrochemical Water Splitting Performance. *Catalysts* **2018**, *8*, 25. [CrossRef]
32. Berger, S.; Ghicov, A.; Nah, Y.C.; Schmuki, P. Transparent TiO_2 nanotube electrodes via thin layer anodization: Fabrication and use in electrochromic devices. *Langmuir* **2009**, *25*, 4841–4844. [CrossRef] [PubMed]
33. Krýsa, J.; Krýsová, H.; Hubička, Z.; Kment, Š.; Maixner, J.; Kavan, L. Transparent rutile TiO_2 films prepared by thermal oxidation of sputtered Ti on FTO glass. *Photochem. Photobiol. Sci.* **2019**, *18*, 891–896. [CrossRef] [PubMed]
34. Sahrin, N.T.; Nawaz, R.; Fai Kait, C.; Lee, S.L.; Wirzal, M.D.H. Visible Light Photodegradation of Formaldehyde over TiO_2 Nanotubes Synthesized via Electrochemical Anodization of Titanium Foil. *Nanomaterials* **2020**, *10*, 128. [CrossRef]
35. Valeeva, A.A.; Dorosheva, I.B.; Kozlova, E.A.; Sushnikova, A.A.; Kurenkova, A.Y.; Saraev, A.A.; Schroettner, H.; Rempel, A.A. Solar photocatalysts based on titanium dioxide nanotubes for hydrogen evolution from aqueous solutions of ethanol. *Int. J. Hydrog. Energy* **2021**, *46*, 16917–16924. [CrossRef]
36. Nguyen, T.T.; Cao, T.M.; Balayeva, N.O.; Pham, V.V. Thermal Treatment of Polyvinyl Alcohol for Coupling MoS_2 and TiO_2 Nanotube Arrays toward Enhancing Photoelectrochemical Water Splitting Performance. *Catalysts* **2021**, *11*, 857. [CrossRef]
37. Lei, B.-X.; Liao, J.-Y.; Zhang, R.; Wang, J.; Su, C.-Y.; Kuang, D.-B. Ordered crystalline TiO_2 nanotube arrays on transparent FTO glass for efficient dye-sensitized solar cells. *J. Phys. Chem. C* **2010**, *114*, 15228–15233. [CrossRef]
38. Huang, C.H.; Wang, I.S.; Ho, K.I.; Lin, Y.T.; Chou, C.; Chan, C.F.; Lai, C.S. High polarization and low-repulsion HfO_2 thin film for alkali metal ion detections by plasma system with a complementary filter. *IEEE Sens. J.* **2013**, *13*, 2459–2465. [CrossRef]
39. Khudhair, D.; Bhatti, A.; Li, Y.; Hamedani, H.A.; Garmestani, H.; Hodgson, P.; Nahavandi, S. Anodization parameters influencing the morphology and electrical properties of TiO_2 nanotubes for living cell interfacing and investigations. *Mater. Sci. Eng. C* **2016**, *59*, 1125–1142. [CrossRef]
40. Lin, T.; Liao, M.; Zhao, S.; Fan, H.; Zhu, X. Anodic TiO_2 nanotubes produced under atmospheric pressure and in vacuum conditions. *Ceram. Int.* **2018**, *44*, 1764–1770. [CrossRef]
41. Kathirvel, S.; Su, C.; Yang, C.-Y.; Shiao, Y.-J.; Chen, B.-R.; Li, W.-R. The growth of TiO_2 nanotubes from sputter-deposited Ti film on transparent conducting glass for photovoltaic applications. *Vacuum* **2015**, *118*, 17–25. [CrossRef]

42. Xie, W.; Li, R.; Xu, Q. Enhanced photocatalytic activity of Se-doped TiO_2 under visible light irradiation. *Sci. Rep.* **2018**, *8*, 8752. [CrossRef]
43. Bharti, B.; Kumar, S.; Lee, H.N.; Kumar, R. Formation of oxygen vacancies and Ti^{3+} state in TiO_2 thin film and enhanced optical properties by air plasma treatment. *Sci. Rep.* **2016**, *6*, 32355. [CrossRef] [PubMed]
44. Giurlani, W.; Sergi, L.; Crestini, E.; Calisi, N.; Poli, F.; Soavi, F.; Innocenti, M. Electrochemical stability of steel, Ti, and Cu current collectors in water-in-salt electrolyte for green batteries and supercapacitors. *J. Solid State Electrochem.* **2022**, *26*, 85–95. [CrossRef]
45. Sopha, H.; Krbal, M.; Ng, S.; Prikryl, J.; Zazpe, R.; Yam, F.K.; Macak, J.M. Highly efficient photoelectrochemical and photocatalytic anodic TiO_2 nanotube layers with additional TiO_2 coating. *Appl. Mater. Today* **2017**, *9*, 104–110. [CrossRef]
46. Han, H.; Moon, S.I.; Choi, S.; Enkhtuvshin, E.; Kim, S.J.; Jung, S.Y.; Thao, N.T.T.; Song, T. Enhanced photoelectrochemical characteristic of TiO_2 nanotubes via surface plasma treatment. *Ceram. Int.* **2021**, *47*, 30741–30746. [CrossRef]
47. In, S.I.; Almtoft, K.P.; Lee, H.S.; Andersen, I.H.; Qin, D.; Bao, N.; Grimes, C.A. Low temperature synthesis of transparent, vertically aligned anatase TiO_2 nanowire arrays: Application to dye sensitized solar cells. *Bull. Korean Chem. Soc.* **2012**, *33*, 1989–1992. [CrossRef]
48. Liu, D.; Liu, F.; Liu, J. Effect of vanadium redox species on photoelectrochemical behavior of TiO_2 and TiO_2/WO_3 photo-electrodes. *J. Power Sources* **2012**, *213*, 78–82. [CrossRef]
49. Hao, C.; Wang, W.; Zhang, R.; Zou, B.; Shi, H. Enhanced photoelectrochemical water splitting with $TiO_2@Ag_2O$ nanowire arrays via p-n heterojunction formation. *Sol. Energy Mater. Sol. Cells* **2018**, *174*, 132–139. [CrossRef]
50. Ho, H.C.; Chen, K.; Nagao, T.; Hsueh, C.H. Photocurrent Enhancements of TiO_2-Based Nanocomposites with Gold Nanostructures/Reduced Graphene Oxide on Nanobranched Substrate. *J. Phys. Chem. C* **2019**, *123*, 21103–21113. [CrossRef]

nanomaterials

Article

Role of Ambient Hydrogen in HiPIMS-ITO Film during Annealing Process in a Large Temperature Range

Ming-Jie Zhao [1,2], Jin-Fa Zhang [1], Jie Huang [1], Zuo-Zhu Chen [1], An Xie [3], Wan-Yu Wu [4], Chien-Jung Huang [5], Dong-Sing Wuu [6], Shui-Yang Lien [1,2,4,*] and Wen-Zhang Zhu [1,2]

[1] School of Opto-Electronic and Communication Engineering, Xiamen University of Technology, Xiamen 361024, China; 2015000077@xmut.edu.cn (M.-J.Z.); jfzhang2019@stu.xmut.edu.cn (J.-F.Z.); huangjie@stu.xmut.edu.cn (J.H.); 2022031141@s.xmut.edu.cn (Z.-Z.C.); wzzhu@xmut.edu.cn (W.-Z.Z.)
[2] Fujian Key Laboratory of Optoelectronic Technology and Devices, Xiamen University of Technology, Xiamen 361024, China
[3] School of Materials Science and Engineering, Xiamen University of Technology, Xiamen 361024, China; anxie@xmut.edu.cn
[4] Department of Materials Science and Engineering, Da-Yeh University, Dacun, Changhua 51591, Taiwan; wywu@mail.dyu.edu.tw
[5] Department of Applied Physics, National University of Kaohsiung, Kaohsiung University Rd., Kaohsiung 81148, Taiwan; chien@nuk.edu.tw
[6] Department of Applied Materials and Optoelectronic Engineering, National Chi Nan University, Nantou 54561, Taiwan; dsw@ncnu.edu.tw
* Correspondence: sylien@xmut.edu.cn

Abstract: Indium tin oxide (ITO) thin films were prepared by high power impulse magnetron sputtering (HiPIMS) and annealed in hydrogen-containing forming gas to reduce the film resistivity. The film resistivity reduces by nearly an order of magnitude from 5.6×10^{-3} Ω·cm for the as-deposited film to the lowest value of 6.7×10^{-4} Ω·cm after annealed at 700 °C for 40 min. The role of hydrogen (H) in changing the film properties was explored and discussed in a large temperature range (300–800 °C). When annealed at a low temperature of 300–500 °C, the incorporated H atoms occupied the oxygen sites (H_o), acting as shallow donors that contribute to the increase of carrier concentration, leading to the decrease of film resistivity. When annealed at an intermediate temperature of 500–700 °C, the H_o defects are thermally unstable and decay upon annealing, leading to the reduction of carrier concentration. However, the film resistivity keeps decreasing due to the increase in carrier mobility. Meanwhile, some locally distributed metallic clusters formed due to the reduction effect of H_2. When annealed at a high temperature of 700–800 °C, the metal oxide film is severely reduced and transforms to gaseous metal hydride, leading to the dramatic reduction of film thickness and carrier mobility at 750 °C and vanish of the film at 800 °C.

Keywords: indium tin oxide (ITO); HiPIMS; rapid thermal annealing (RTA); hydrogen-containing forming gas; hydrogen doping

Citation: Zhao, M.-J.; Zhang, J.-F.; Huang, J.; Chen, Z.-Z.; Xie, A.; Wu, W.-Y.; Huang, C.-J.; Wuu, D.-S.; Lien, S.-Y.; Zhu, W.-Z. Role of Ambient Hydrogen in HiPIMS-ITO Film during Annealing Process in a Large Temperature Range. *Nanomaterials* **2022**, *12*, 1995. https://doi.org/10.3390/nano12121995

Academic Editors: Jihoon Lee and Ming-Yu Li

Received: 1 May 2022
Accepted: 6 June 2022
Published: 10 June 2022

1. Introduction

Transparent conductors characterized by high conductivity and high transparency in the visible light spectrum have been widely used in many optoelectronic applications, such as photovoltaic cells, flat panel displays, light-emitting diodes and smart windows [1–4]. Indium tin oxide (ITO) is an excellent transparent conductor. Although it has been investigated for decades, it is still regarded as the most typical and important transparent conductor due to its high optical transmission, low electrical resistivity, high stability against harsh environments and easy processing properties. ITO film is usually prepared by DC or RF magnetron sputtering, which is capable of depositing uniform, large-area ITO film with a high deposition rate [5–7]. However, the film quality is somewhat inferior, especially when deposited at low temperatures. Persistent efforts have been devoted to improving film quality, aiming at increasing the optical and electrical properties of the film with various approaches, including doping, process parameter optimization, post-deposition thermal or chemical treatment and deposition method innovation [8–12].

Recently, high power impulse magnetron sputtering (HiPIMS) is emerging as a method for deposition of metal oxide films, including ITO films [13–17]. The high power impulses can generate high-density plasma containing highly excited/ionized sputtered species and reactive agents (oxygen radicals), favoring the synthesis of compounds. In addition, the film conformality can be enhanced thanks to the highly energetic plasma species, which is applicable for a 3D substrate such as devices with a high aspect ratio. Adding hydrogen gas to the sputter gas during film deposition or to the ambient during the annealing process and hydrogen plasma treatment has been proved to be effective approaches to reducing the film resistivity [18–21]. Moreover, hydrogen incorporation in oxide film by either annealing in an H_2 ambient at elevated temperature or hydrogen plasma treatment has been reported in the literature. However, these approaches have not been applied to ITO films prepared by the HiPIMS method. Furthermore, the role of hydrogen in influencing the properties of ITO film is still controversial so far. Some researchers stated that incorporated H exists as interstitial (H_i) or occupies the oxygen sites (H_o), both of which act as a shallow donor in metal oxide films, leading to the increase of carrier concentration and the decrease of film resistivity [22,23]. Some researchers argued that neither the interstitial hydrogen nor the substitutional hydrogen was likely the origin of incremental free carrier concentration in the film. Rather, oxygen vacancy defects created by H_2 reduction contribute to incremental free carriers [24–30]. The experimental conditions are not exactly the same as the existing reports. For instance, the investigated temperature ranges (not higher than 500 °C in most of the research in the literature), the hydrogen source (hydrogen plasma or hydrogen-containing atmosphere with various hydrogen proportions) and the introduction stage (during the film deposition process or annealing process) varied from each other. To clarify the role of hydrogen, investigations should be taken in a larger temperature range with consistent experiment setups throughout the temperature range. Nevertheless, this is still in lack so far. Furthermore, most research on the hydrogen annealing effects of ITO films focused on the analysis of the variation of oxygen sub-stoichiometry state of the film influenced by the annealing process. However, less attention has been paid to the possible material exchange between the film and the annealing ambient, such as the adsorption/desorption of hydrogen, hydroxyl groups, water, etc.

Previously, ITO films were prepared through the HiPIMS method by our group [31,32]. In this work, the films were annealed in hydrogen-containing forming gas to reduce film resistivity. The role of hydrogen in influencing the film properties is explored and discussed at a large temperature of 300–800 °C.

2. Materials and Methods

ITO thin films were deposited on a quartz glass substrate and silicon substrate by an in-line sputtering system (Ljuhv, SP-122I, Zhubei City, Taiwan) using a high-purity (99.99%) ceramic target consisting of 90 wt.% In_2O_3 and 10 wt.% SnO_2 (supplied by Heqi Target Material Technology, Zhangzhou, China). The target has a dimension of 30.7 cm (length) × 12.5 cm (width) × 0.6 cm (thickness). The sputtering system was described in detail in References [31,32]. The film deposition parameters (working pressure and sputtering power) have been optimized and reported in previously published papers. The base pressure of the process chamber was lower than 6.7×10^{-5} Pa. The high-purity (99.999%) Ar with a flow rate of 40 sccm was used as the plasma gas. The sputtering pressure was kept at 8.0 Pa during the film deposition process. The average power, duty cycle, pulse frequency and pulse length were set at 500 W, 10%, 1000 Hz and 100 us, respectively. The substrate was not heated during the film deposition process. The size of the deposited samples was 5 cm×5 cm. The inhomogeneity of film thickness was evaluated by a nine-point method. The film thicknesses (d) at nine points distributed in a substrate of 10 cm × 10 cm were measured by a step profiler. The inhomogeneity determined by

$(d_{\max} - d_{\min})/(d_{\max} + d_{\min})$ is within 2%. The deposition time was 10 min. The deposition rate was 8 nm/min. The deposition parameters for the HIPIMS process are summarized in Table 1.

Table 1. Deposition parameters for the high-power impulse magnetron sputtering (HIPIMS) process.

Parameter	Value
Base pressure ($\times 10^{-5}$ Pa)	6.7
Working pressure (Pa)	8.0
Distance of substrate-to-target (mm)	52
Average power (W)	500
Flow rate of Ar (sccm)	40
Deposition temperature (°C)	25
Frequency (Hz)	1000
Pulse length (μs)	100
Duty cycle (%)	10

The obtained ITO film was annealed in a forming gas containing 5% hydrogen (H_2) and 95% nitrogen (N_2) at 300–800 °C for 40 min using a rapid thermal annealing system (Eaststar Labs, RTP-300, Beijing, China). The forming gas with a total flow rate of 1 L/min was introduced into the furnace during the whole process. The annealing process consisted of three stages: (1) the temperature rose from room temperature to 200 °C in 20 s, then held for 20 s; (2) the temperature rose from 200 °C to the aiming temperature (300, 400, 500, 600, 700, 750 and 800 °C for each specimen, respectively), then held for 40 min; (3) The temperature fell from the aiming temperature to room temperature in about 500 s. Parameters for the annealing process of ITO film are summarized in Table 2.

Table 2. Parameters for the annealing process of ITO film.

Parameter	Value
Temperature (°C)	300–800
Duration (min)	40
Atmosphere	N_2 (95%) + H_2 (5%)
Gas flow rate (L/min)	1

The film thickness (d) was measured from the field emission scanning electron microscope (FESEM, sigma 500, Zeiss, Oberkochen, Germany) and captured images of a cross-section of the ITO/quartz specimens before and after the annealing process. The infrared (IR) absorption spectra of the films were measured with a Fourier transform infrared (FTIR, Bruker Vertex80v, Ettlingen, Germany) spectrometer. The depth distribution of elements in the film was analyzed using time-of-flight secondary ion mass spectrometry (TOF-SIMS, ION-TOF, TOF-SIMS V, Muenster, Germany). The crystal structure of the film was analyzed by grazing X-ray diffraction (GIXRD, Rigaku, TTRAXIII, Ibaraki, Japan) spectra using Cu-Kα radiation (λ = 0.154 nm) as the X-ray source. The X-ray incidents with an angle of 1°. The surface morphology of the films was observed by FESEM and atomic force microscopy (AFM, Park, XE7, Suwon, Korea). The roughness (R_q) of the film surface was obtained by statistical analysis of the AFM data. The cross-section of the film was prepared by a focused ion beam (FIB, FEI Helios, Hillsboro, OR, USA) and observed by a high-resolution transmission electron microscope (TEM, FEI Talos F200X, Hillsboro, OR, USA). The electrical properties were measured by a four-point probe station (Ossila, T2001A3, Sheffield, UK) and a Hall effect system (Hall, Ecopia, HMS5000, Anyang, Korea). The transmittance of the specimens was measured by a spectrometer (PerkinElmer Lambda 850, Waltham, MA, USA). The film transmittance (T) was obtained by deducting the transmittance of bare quartz glass substrate from that of ITO/quartz specimens. The film characterization was performed on samples on quartz glass substrate except for the analyses of SIMS and XPS, which were performed on samples on a silicon substrate.

3. Results and Discussion

Figure 1 shows the variation of film thickness with annealing temperature. The inset shows the FESEM images of a cross-section of the specimens for the measurement of film thickness. The graphs in Figure 1 present seven different specimens separated from the deposited sample. The discrepancy of the original film thickness should be within 2%. The thickness of the as-deposited film was 78.2 nm. The film thickness is almost unchanged after annealing at 300 and 400 °C. Then, it modestly decreases after annealed at 500–700 °C, possibly due to the partial reduction of the oxide film by H_2. Finally, it dramatically decreased after annealed at 750 °C and totally vanished after annealed at 800 °C due to severe reduction and vaporization of the film. The chemical reaction of the film material and the ambient gas will be discussed later.

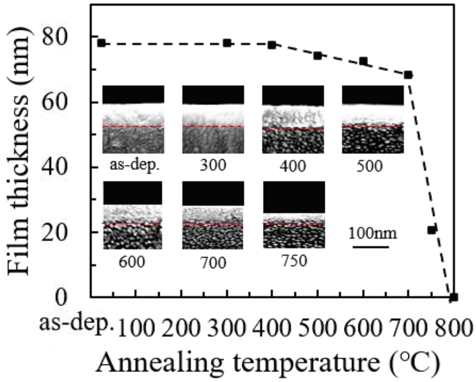

Figure 1. The variation of thickness of ITO film with annealing temperature. The inset shows the corresponding FESEM images of the specimens for the measurement of film thickness.

Generally, the Sn content and O content in the film are important factors that influence the number of donor defects such as Sn substitutions and oxygen vacancies, thus leading to the variation of carrier concentration in the film. Therefore, most research elaborated on the oxygen sub-stoichiometry states of the ITO film. In previous works, the relative Sn doping efficiency (reflected by the areal ratio of $Sn^{4+}/(Sn^{4+} + Sn^{2+})$ in the Sn 3d XPS peaks) and the relative oxygen vacancy concentration (reflected by the areal ratio of $O_V/(O_V + O_L)$ in the O 1s XPS peak) in the HiPIMS-ITO film have been investigated as functions of working pressure and average power during the film deposition process [31,32]. The same analyses have been performed on the samples in this work. The results are listed in Table 3 and compared with previous works of our group. The Sn doping efficiency first decreases with annealing temperature at 25–500 °C, then increases with annealing temperature at 500–750 °C. The variation of Sn doping efficiency is in the range of 69.8–75.0% when the annealing temperature varies from 25 to 800 °C. In contrast, in our previous works, the variations of Sn doping efficiency are in the ranges of 32.6–69.6% and 65.6–82.2%, as the average power varies in the range of 200–600 W and the working pressure varies in the range of 5.3–10.0 Pa, respectively. The oxygen vacancy concentration is shown in Table 3 first increases with annealing temperature at 25–500 °C, then decreases with annealing temperature at 500–750 °C. The variation of oxygen vacancy concentration is in the range of 42.0–47.6% when the annealing temperature varies in the range of 25–800 °C. In contrast, in our previous works, the variations of oxygen vacancy concentrations are in the ranges of 39.0–48.1% and 42.1–53.5%, as the average power varies in the range of 200–600 W and the working pressure varies in the range of 5.3–10.0 Pa, respectively. Therefore, the variations of Sn doping efficiency and oxygen vacancy concentration with annealing temperature in this work are much smaller than with average power and working pressure in our previous work. However, the annealing treatment leads to a much larger variation in the carrier concentration ($\Delta N_c = 9.3 \times 10^{20}$ cm^{-3}, see the results of Hall effect measurement) compared to the smaller $\Delta N_c = 2.2 \times 10^{20}$ cm^{-3} and $\Delta N_c = 5.6 \times 10^{20}$ cm^{-3} by varying average power and working pressure. Although the variations in Sn doping efficiency and oxygen vacancy defects would influence the carrier concentration in the film, they may not be the dominant factors. Therefore, we infer that the variation of carrier concentration with annealing temperature should be primarily attributed to the possible material exchange between the film and the annealing ambient rather than the Sn doping efficiency or the slight oxygen sub-stoichiometry state. Therefore, the analysis of the hydrogen-related defects is of main concern in this work.

Table 3. The Sn doping efficiency and oxygen vacancy concentration at different annealing temperatures.

Temperature (°C)	$Sn^{4+}/(Sn^{4+} + Sn^{2+})$ (%)	$O_V/(O_V + O_L)$ (%)
25	75.0	45.1
300	73.0	45.6
400	70.2	47.2
500	69.3	47.6
600	70.0	46.5
700	71.9	44.1
750	69.8	42.0

The hydrogen centers in ITO film were studied by FTIR absorption spectra, as shown in Figure 2. The assignment of the infrared absorption peaks in the FTIR spectra is summarized in Table 4. The peak located at 3680 cm^{-1} origins from the vibration of OH species [33]. The peak at 520 cm^{-1} is attributed to the vibration of the In-O bond [34,35]. The peak intensity slightly decreases with increasing annealing temperature at 300–700 °C, possibly due to the removal of weak In-O bonds by annealing. A broad band in the range of 1291–2260 cm^{-1} was observed for the as-deposited film, which possibly originated from the C, H and H_2O-related impurities in the film. It becomes weaker with increasing annealing temperature at 300–700 °C due to the removal of these impurities by annealing. It has been reported in the case of AZO films deposited by reactive HiPIMS stored in ambient air contain hydroxyl groups in the bulk of the film, and these groups are released after subsequent annealing in reducing atmosphere [36]. The film resistivity significantly decreases after this release. In this case, a similar phenomenon may occur in HiPIMS-ITO films. The water content in the as-deposited film is quite high and drops after annealing. The release of the adsorbed water may contribute to the decrease of film resistivity after annealing. However, the intensity of the broadband becomes stronger and with featured peaks superimposed on it after annealing at 750 °C. The featured peaks should be assigned to the stretching vibration of Si-H, C-O, H_2O and O-H bonds [37–44]. It is speculated that these featured peaks originated from the adsorbent on the film surface, which is porous and rough, as observed by FESEM.

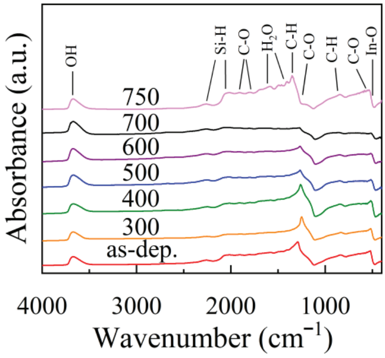

Figure 2. The FTIR spectra for ITO films deposited at different temperatures.

Table 4. Assignments of the infrared absorption peaks of ITO film.

Wavenumber (cm^{-1})	Assignments
3680	Si-OH
2260, 2020	Si-H
1904, 1802	C-O
1603, 1460	water
1350,832	C-H
1291, 531	C-O
520	In-O

Figure 3a,b shows the SIMS depth profile for the as-deposited and 500 °C-annealed ITO films, respectively. The intensity (in the unit of counts per second, CPS) in the SIMS spectra reflects the relative concentration of the certain element. The variation of the concentration of certain elements along the depth direction can be observed in the spectra. For the as-deposited ITO film, the intensity of H and C at the near-surface of the film is almost 1.5 orders higher than that in the bulk of the film, suggesting that the H and C in the as-deposited film are probably uptake from the ambient due to ambient exposure of the specimens. The Sn element seems to be unevenly distributed along the depth of the film. For the 500 °C-annealed ITO film, the distribution of C is similar to that of the as-deposited film. However, the C content in the annealed film is smaller than that in the as-deposited film both at the near film surface and in the bulk of the film. The integral SIMS intensity of C from 0 to 80 nm for both the as-deposited and annealed film was calculated. The result shows that the integral intensity of C decreases from 1.7×10^5 CPS·nm/s to 9.1×10^4 CPS·nm/s, suggesting the C related impurity was eliminated after annealing. This is in accordance with the analysis of FTIR results. However, the intensity of H in the bulk of the film increases to the level that is close to the near-surface of the film. Meanwhile, the amount of hydrogen tends to have lowered around 40 nm of etching. This result suggests that hydrogen redistribution and hydrogen adsorption from the ambient may occur during the annealing process. To verify the hydrogen adsorption, the integral SIMS intensity of H from 0–80 nm for both the as-deposited and annealed film was calculated. The integral intensity of H increases from 4.3×10^5 CPS·nm/s to 5.0×10^5 CPS·nm/s, indicating that more hydrogen atoms were incorporated into the film. In addition, the Sn element exhibits a more even distribution along the direction perpendicular to the substrate. However, the comparison between the concentrations of different elements cannot be made since the spectra do not give the absolute intensity of the corresponding elements. Therefore, the hydrogen concentrations in the SIMS spectra are not necessarily high since the relative intensity does not give the absolute concentrations.

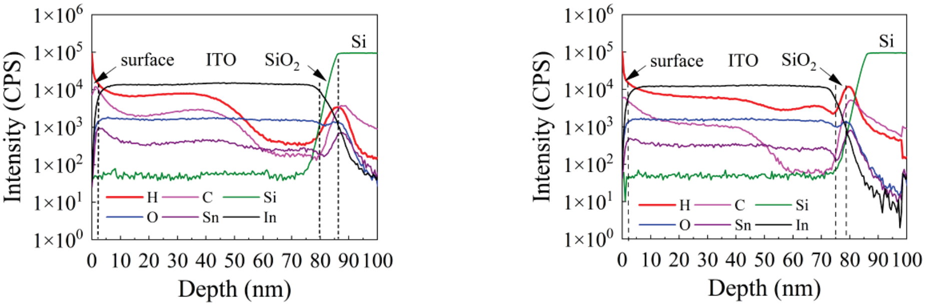

(**a**)

(**b**)

Figure 3. The SIMS depth profile for the (**a**) as-deposited ITO film and (**b**) 500 °C-annealed ITO film, respectively.

Figure 4a shows the XRD patterns of ITO films annealed at different temperatures. The diffraction peaks for the as-deposited film are all identified to be belonging to the diffraction by (2 1 1), (2 2 2), (4 0 0), (4 3 1), (4 4 0) and (6 2 2) planes of cubic bixbyite In_2O_3 lattice (JCPDS Card No. 06-0416). The multiple-peak feature of the pattern reveals the poly-crystal nature of the film with (2 2 2)-planes as the preferentially orientated planes. The cubic bixbyite crystal phase is stable after annealing at 300–500 °C. The full width at half maximum (FWHM, β) of the (2 2 2) peak decreases with increasing annealing temperature, as shown in Figure 4b, indicating that the grains grew larger after annealed. The grain size (D) was calculated according to Scherrer's formula [45]:

$$D = \frac{0.94\lambda}{\beta \cos\theta} \tag{1}$$

where λ is the wavelength of the incident X-ray (0.154 nm), and θ is the diffraction position. The grain size increases with annealing temperature, as shown in Figure 4b. Noticeably, an emerging peak located at 41.38° was observed when the annealing temperature increased to 600–750 °C, which is assigned to the diffraction by In_3Sn alloy (JCPDS Card No. 07-0345). The existence of the In_3Sn phase suggests that the oxide films are partially reduced to the alloy phase after being annealed at such a high temperature. Similarly, In/Sn clusters have been observed in ITO film after H_2 plasma treatment and annealing treatment in H_2 containing atmosphere reported by other groups [19,20].

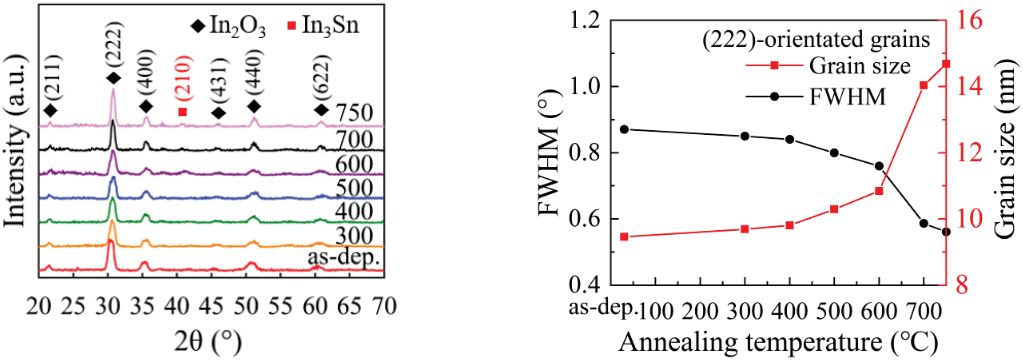

(**a**) (**b**)

Figure 4. (**a**) XRD patterns of the ITO films annealed at different temperatures. (**b**) The variation of full width at half maximum (FWHM, β) of the (2 2 2) peak and corresponding grain size with annealing temperature.

Figure 5a–g shows the SEM images for the ITO films. The corresponding AFM images were embedded at the top right corner of the SEM images. The surface roughness of the film is plotted as a function of annealing temperature in Figure 5h. The surface of the as-deposited film consists of uniform grains with clear boundaries. However, the grain boundaries become blurred after annealing at 300 °C. Then, they become clear again when the annealing temperature increases to 400 and 500 °C. The blurred grain boundaries seem to be on a transition stage of molten-to-recrystallization, which exhibits a surface morphology with seemingly amorphous characteristics. The grain size seems to slightly increase as the annealing temperature increases from room temperature to 500 °C. However, coarse grains were observed when the annealing temperature increased to higher than 600 °C. Voids started to appear at 700 °C. Suspected clusters were observed after annealing at 750 °C. The emergence of coarse grains, voids and clusters are likely to be caused by violent structural evolution such as precipitation of metal particles and escape of gaseous materials. As a result, the surface roughness generally increases with annealing temperature, as shown in Figure 5h. The porous and rough film surface after being annealed at 750 °C is more likely to accommodate adventitious contaminants, which is in accordance with the analysis of the FTIR spectra.

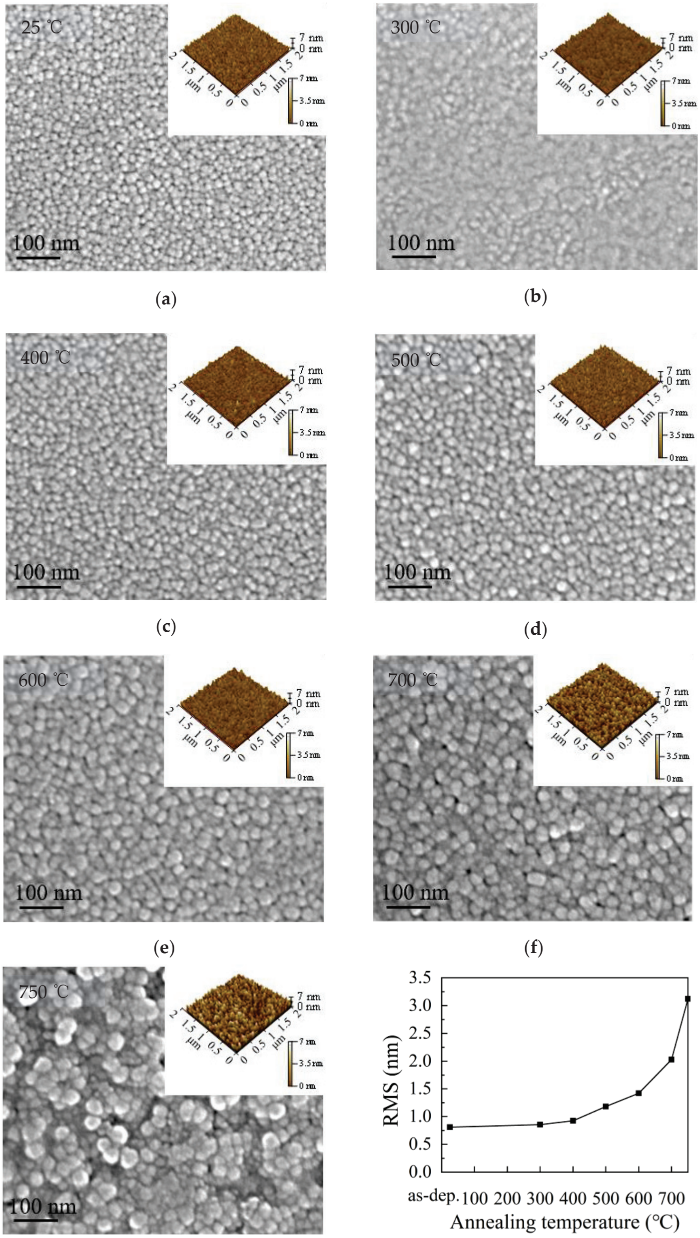

(**a**) (**b**)

(**c**) (**d**)

(**e**) (**f**)

(**g**) (**h**)

Figure 5. (**a**–**g**) The SEM images for the as-deposited and annealed ITO films (the corresponding AFM images were embedded at the top right corner of the SEM images). (**h**) The variation of film surface roughness with annealing temperature.

Figure 6a,c shows the TEM images with a magnification of 58 K of as-deposited and 500 °C-annealed ITO films, respectively. Both films exhibit columnar crystals. However, the columnar crystals grew larger after annealing. In addition, a thin amorphous layer was observed at the film/substrate interface for the as-deposited specimen, whereas it disappeared after annealed, suggesting that the crystallinity of the film increases after annealing. Some small lighter-colored regions were observed in the TEM images with a magnification of 58 K (Figure 6c). Since In_3Sn metallic phase was observed in the XRD patterns for ITO films deposited at $\geq$600 °C, the lighter-colored region is suspected to be the metallic clusters. Although the XRD peak corresponding to In_3Sn metallic phase was not observed for the film annealed at 500 °C, it is possible that the proportion of the metallic phase is too small to cause distinct diffraction that can be observed by XRD. Therefore, the observations of TEM and XRD are in accordance with each other. Figure 6b,d show the high-resolution TEM images with a magnification of 820 K, which exhibit clear grains corresponding to the (2 2 2), (4 0 0), (2 2 1) and (4 4 0) planes of the cubic bixbyite In_2O_3 lattice with an interplanar distance of 2.93 Å, 2.53 Å, 4.11 Å and 1.78 Å, respectively.

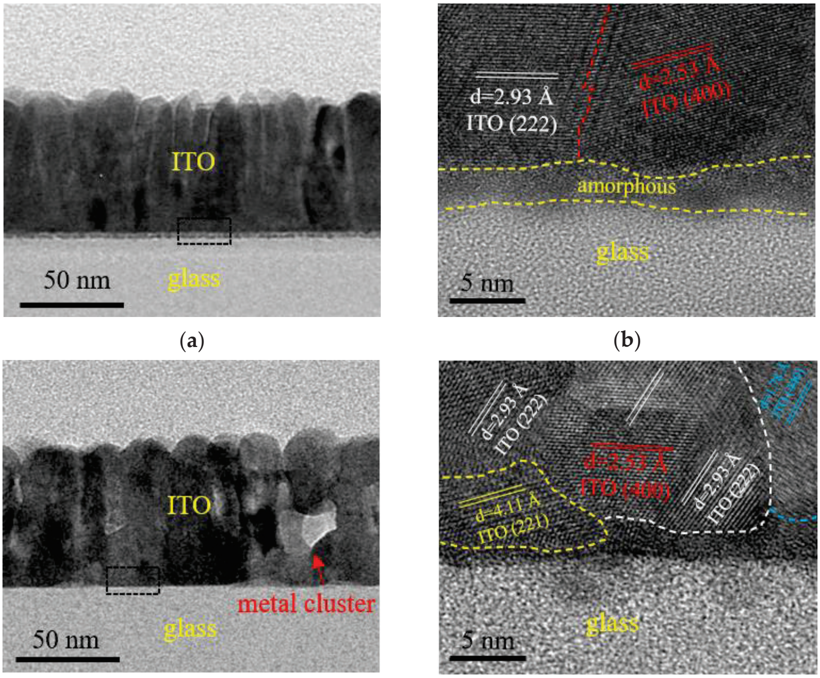

(**a**) (**b**)

(**c**) (**d**)

Figure 6. The TEM images for (**a**,**b**) as-deposited and (**c**,**d**) 500 °C-annealed ITO film. The magnification of the images in (**a**,**c**) and (**b**,**d**) is 58 K and 820 K, respectively.

Based on the analysis of our experimental data and the information obtained from the literature, different mechanisms for the effect of hydrogen on the film are proposed to dominate in three temperature zones. When annealed at a low temperature (300–500 °C), H is incorporated into the film and exists in the forms of interstitials (H_i) and substitutions (H_o) at the oxygen sites. H_i and H_o have been reported to act as shallow donors in several oxide semiconductors, including In_2O_3 and SnO_2 [22,23]. However, it has been reported that H_i in SnO_2 is thermally unstable at near room temperature and tends to decay upon annealing, while H_o in SnO_2 is more thermally stable up to ≈500 °C [46]. Therefore, it is predicted that the carrier concentration would increase due to the introduction of H_o defects by annealing in hydrogen-containing atmosphere. In this temperature range, some donor defects can also be introduced by removing oxygen atoms that could be released in the form of water molecules after combination with hydrogen. However, this seems not to be the dominant mechanism as the variation of oxygen vacancy concentration is small. In addition, the release of the adsorbed water after annealing, as indicated by the FTIR results, may also contribute to the decrease of film resistivity. The film thickness was slightly reduced due to the creation of oxygen vacancies and the release of the adsorbed water after annealing. When annealed at an intermediate temperature (500–700 °C), the H_o defects are thermally unstable and expected to decay with annealing temperature. Meanwhile, some metallic clusters are formed locally in the film (observed by XRD and TEM) due to the reduction of the oxide film by H_2 as expressed by the following reactions:

$$\mathrm{In_2O_{3-x} + H \rightarrow In + H_2O\ (g)} \tag{2}$$

$$\mathrm{SnO_{2-x} + H \rightarrow Sn + H_2O\ (g)} \tag{3}$$

where g denotes the gaseous phase. In this temperature zone, the film thickness modestly decreases due to the lattice contraction as many vacancy defects exist in the film and the partial reduction of the oxide. The decrease in oxygen vacancy concentration is possibly due to the redistribution of oxygen atoms between the metallic cluster region and the oxide lattice region. Namely, the oxygen vacancies in the oxide lattice region may be passivated by the oxygen atoms released from the metallic cluster region. However, this seems not to be the main reason for the decrease in carrier concentration as the variation of oxygen vacancy concentration is small. When annealed at a high temperature (700–800 °C), the metal oxide film was severely reduced to metallic particles and further reacted with hydrogen, releasing gaseous hydride as expressed by the following reactions [47,48]:

$$\mathrm{In + H \rightarrow InH_3\ (g)} \tag{4}$$

$$\mathrm{Sn + H \rightarrow SnH_4\ (g)} \tag{5}$$

In this temperature zone, the film thickness would be dramatically decreased until it totally vanished after being annealed at 800 °C.

Figure 7a shows the variation of carrier concentration and mobility of the film with annealing temperature. The carrier concentration increases with annealing temperature in the range of 300–500 °C before it decreases with annealing temperature in the range of 500–750 °C. Assume that the carrier concentration only depended on the oxygen vacancy concentration with a directly proportional relationship, the increments of carrier concentration would be expected to be 2.8×10^{20} cm^{-3} and 1.4×10^{20} cm^{-3} after annealed at 500 °C taking the variations of carrier concentration with working pressure ($\Delta N_c = 1.2 \times 10^{20}$ cm^{-3}) and average power ($\Delta N_c = 6.0 \times 10^{19}$ cm^{-3}) as references, respectively. Actually, a much large increment ($\Delta N_c = 8.0 \times 10^{20}$ cm^{-3}) was observed. Therefore, the variation of carrier concentration should be primarily ascribed to the creation and decay of the H_o dopant, although the evolution of carrier concentration is approximately the same as the evolution of the oxygen vacancy concentration reported in Table 3. The H_o dopant in ITO film is thermally stable and active in contributing free electrons to the conduction band at a low temperature of 300–500 °C. However, the H_o dopants are thermally unstable at higher temperatures (>500 °C) and tend to decay with increasing annealing temperature, leading to a decrease in carrier concentration. The mobility of free electrons slightly decreases after annealed at 300 °C, possibly due to the amorphous-like structure of the film surface. Further, increasing the annealing temperature to 400–700 °C leads to an increase in mobility, which should be ascribed to the increase in grain size and the reduction of grain boundary scattering. However, The electron mobility sharply decreases after annealed at 750 °C. On the one hand, the sharp decrease in mobility should be ascribed to the severe surface scattering as the film thickness is greatly reduced to 20.6 nm after annealed. On the other hand, the scattering by increased density of point defects and metallic inclusion should play a role in decreasing the electron mobility in the film. As a result, the film resistivity (ρ) shown in Figure 7b decreases with annealing temperature at 300–700 °C, then dramatically increases after being annealed at 750 °C.

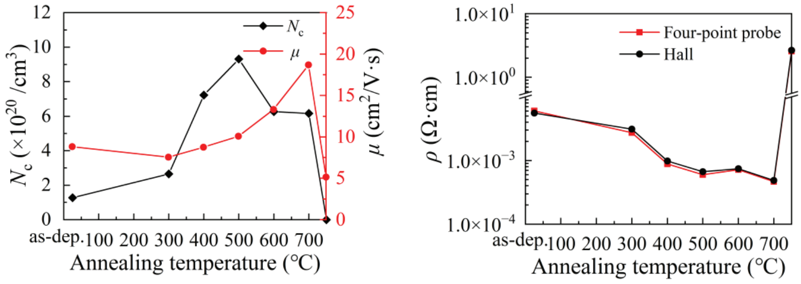

(**a**) (**b**)

Figure 7. The variation of (**a**) carrier concentration (N_c), mobility (μ) and (**b**) resistivity (ρ) of the film with annealing temperature.

Figure 8a shows the transmittance (T) spectra for the ITO films annealed at different temperatures. The films all exhibit a similar high transmittance of >80% in the visible light range (350–800 nm). The film transmittance sharply decreases at the ultraviolet light range (300–350 nm) for the as-deposited film, and the films annealed at 300–700 °C due to the band-to-band transition. The film annealed at 750 °C is highly transparent due to the very small thickness (28 nm). The absorbance (α) spectra plotted in Figure 8b were calculated using the following expression [49]:

$$\alpha = \frac{1}{d} ln\left(\frac{1}{T}\right) z \tag{6}$$

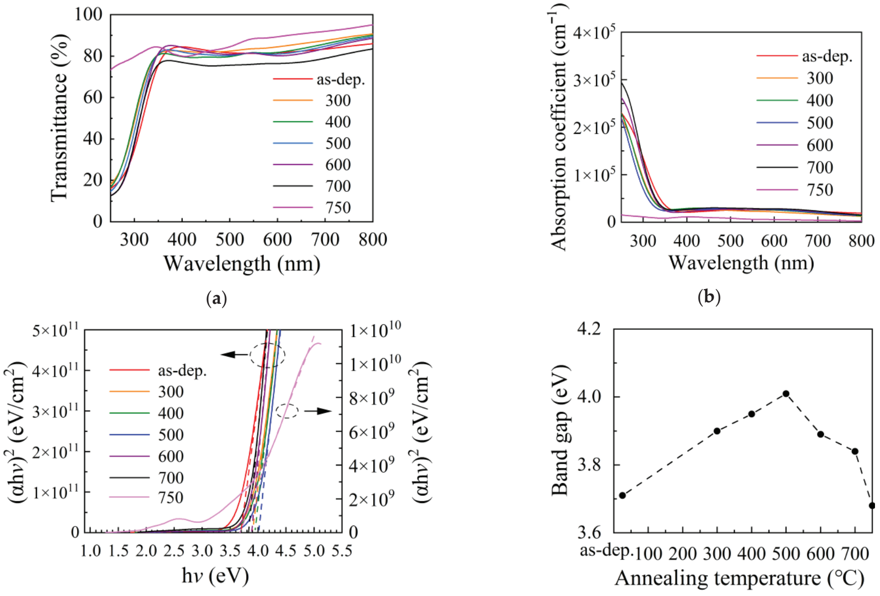

(**a**) (**b**)

(**c**) (**d**)

Figure 8. (**a**) The transmittance spectra, (**b**) light absorption coefficient (α) spectra and (**c**) Tauc's plots for the ITO films annealed at different temperatures. (**d**) The variation of optical band gap with annealing temperature.

The absorbance is very weak in the visible light range (350–800 °C) for all films and sharply increases in the shorter light range due to band-to-band transition. The extremely weak absorption of the ITO film annealed at 750 °C should be due to the small film thickness. The absorption edge in the transmittance and absorbance spectra exhibit a blue shift after annealing treatment, indicating that the optical band gap changed after annealing. The optical band gap was obtained from the Tauc plot in Figure 8c according to the following formula [50]:

$$(\alpha \mathrm{h}v)^2 = \mathrm{A}\left(\mathrm{h}v - E_\mathrm{g}\right) \tag{7}$$

where hv is the energy of incident photons, A is a constant, and E_g is the optical band gap. Figure 8d shows the variation of the optical band gap with annealing temperature. The optical band gap increases with annealing temperature at 300–500 °C. Then, it decreases with annealing temperature at 500–750 °C. This developing trend seems to be positively related to that of free carrier concentration, suggesting that the Moss–Burstein effect, which often arises in heavily doped semiconductors and manifests as widening of optical band gap by increasing carrier concentration, plays an important role in influencing the optical band gap. The existence of metallic clusters does not lead to observable deterioration of the optical properties of the film, although deterioration has been observed in ITO treated by H_2 plasma and annealed in an H_2-containing atmosphere reported by other groups [18,20].

Table 5 lists the main results in this study and previous results for HiPIMS-ITO films and ITO films prepared by other techniques. The annealing processes in the table were all carried out in hydrogen-containing ambient (with different H_2/N_2 ratios). For the as-deposited films prepared by DC magnetron sputtering (DCMS) and RF magnetron sputtering (RFMS), the resistivity is (3.4–6.2) × 10^{-4} Ω·cm and the average transmittance in the visible light range (Ave. T) is 70–90% [21,51,52]. After annealed at 500 °C, the resistivity decreases to (2.2–4.1) × 10^{-4} Ω·cm and the Ave. T is improved to 86–90%. For the ITO films prepared by sol-gel method and annealed at 600 °C, the resistivity is 4.4 × 10^{-2} Ω·cm and the Ave. T is 86% [53]. For the ITO films prepared by e-beam evaporation, the resistivity is 4.4 × 10^{-2} Ω·cm and the Ave. T is 32% [54]. These values are significantly improved to 5.8 × 10^{-4} Ω·cm and 61% after annealed at 200 °C. For the as-deposited HiPIMS-ITO films, the resistivity is (4.0–6.0) × 10^{-3} Ω·cm and the Ave. T is 78–82% [16,55,56]. The resistivity decreases to 6.7 × 10^{-4} Ω·cm and the Ave. T is almost unchanged after being annealed at 500 °C. Overall speaking, the ITO films prepared by DCMS and RFMS have the best performance in terms of the electrical and optical properties both at the as-deposited and annealed states; the ITO films prepared by HiPIMS score the secondary level at the as-deposited state but achieves similar level to the DCMS and RFMS after annealed; the ITO films prepared by e-beam evaporation have inferior performance at the as-deposited state, but the resistivity can be improved to the similar level of the DCMS and RFMS while the transmittance remains poor after annealed; the ITO films prepared by the sol-gel method have inferior performance even after annealing. The results of this work fill in the blank of the annealing data for the HiPIMS-ITO film.

Table 5. Comparison of the results of this study with previous results.

Method	H_2/N_2 Ratio (%)	Annealing Temp. (°C)	ρ (Ω·cm)		Ave. T (%)		Ref.
			As-dep.	Post-ann.	As-dep.	Post-ann.	
DCMS	50	500	3.4 × 10^{-4}	2.2 × 10^{-4}	88	90	[21]
DCMS	100	500	6.2 × 10^{-4}	2.7 × 10^{-4}	90	92	[51]
RFMS	2	500	6.0 × 10^{-4}	4.1 × 10^{-4}	70	86	[52]
Sol-gel	3.75	600	N.A.	4.4 × 10^{-2}	N.A.	86	[53]
E-beam evaporation	20	200	5.6 × 10^{-2}	5.8 × 10^{-4}	32	61	[54]
HiPIMS	N.A.	N.A.	4.0 × 10^{-3}	N.A.	N.A.	N.A.	[16]
HiPIMS	N.A.	N.A.	4.0 × 10^{-3}	N.A.	N.A.	N.A.	[55]
HiPIMS	N.A.	N.A.	6.0 × 10^{-3}	N.A.	82	N.A.	[56]
HiPIMS	5	500	5.6 × 10^{-3}	6.7 × 10^{-4}	78	78	This work

Notes: N.A. is short for not available; Ave. T is short for average transmittance in the visible light range; As-dep. is short for as-deposited; Post-ann. is short for post-annealed.

4. Conclusions

ITO films were prepared by an in-line HiPIMS system. Annealing treatment in hydrogen-containing forming gas can effectively reduce the film resistivity without observable deterioration of the optical properties. The lowest film resistivity of 6.7×10^{-4} Ω·cm was obtained after annealed at 700 °C for 40 min. The hydrogen (H_2) plays different roles in influencing the film properties at different annealing temperatures: (1) hydrogen atoms substitute the oxygen atoms (H_o), acting as shallow donors that contribute to the increase of carrier concentration at a low annealing temperature of 300–500 °C; (2) the substitutional hydrogen (H_o) is thermally unstable at an intermediate annealing temperature of 500–700 °C and decays with increasing annealing temperature, leading to the decrease of carrier concentration; In addition, metallic clusters are formed by the reduction of H_2; (3) the hydrogen gas reduces the metal oxide severely, producing volatile metal hydride, leading to a dramatic decrease of the film thickness and finally vanish of the film at a high annealing temperature of 700–800 °C. The substitutional doping of H and the modest reduction by H_2 both lead to the increase of free carrier concentration in the film and the decrease of film resistivity.

Author Contributions: Funding acquisition, S.-Y.L., M.-J.Z. and A.X.; J.-F.Z., J.H. and Z.-Z.C. performed the experiments; data analyze, J.-F.Z., M.-J.Z., S.-Y.L., W.-Y.W., C.-J.H., D.-S.W. and W.-Z.Z.; M.-J.Z. wrote the manuscript; M.-J.Z. and S.-Y.L. revised and review the manuscript; supervision, S.-Y.L. All authors took part in the investigation and discussion. All authors have read and agreed to the published version of the manuscript.

Funding: This work is partially supported by the Science and Technology Project of Xiamen (Nos. 3502ZCQ20191002, 3502Z20201003, 3502ZCQ20201001), the scientific research projects of Xiamen University of Technology (Nos. YKJ18008R, 405011904, YKJ19001R), the National Natural Science Foundation of China (No. 61704142), the Natural Science Foundation of Fujian Province (Nos. 2020H0025, 2020J02049), the National Natural Science Foundation of China Joint Fund for Cross-strait Scientific and Technological Cooperation (Grant no. U2005212).

Data Availability Statement: Not applicable.

Conflicts of Interest: The authors declare no conflict of interest.

References

1. Forouhi, A.R.; Li, G.G.; Bloomer, I. Optical characterization of ITO films used in flat panel displays. In *Metrology, Inspection, and Process Control for Microlithography X*; Jones, S.K., Ed.; International Society for Optics and Photonics: Santa Clara, CA, USA, 1996; Volume 2725, pp. 471–477.
2. Kim, K.-K.; Kim, H.; Lee, S.-N.; Cho, S. Structural, optical, and electrical properties of E-beam and sputter-deposited ITO films for LED applications. *Electron. Mater. Lett.* **2011**, *7*, 145–149. [CrossRef]
3. Saim, H.; Campbell, D. Properties of indium-tin-oxide (ITO)/silicon heterojunction solar cells by thick-film techniques. *Sol. Energy Mater.* **1987**, *15*, 249–260. [CrossRef]
4. Lee, S.J.; Lee, S.H.; Kang, H.W.; Nahm, S.; Kim, B.H.; Kim, H.; Han, S.H. Flexible electrochromic and thermochromic hybrid smart window based on a highly durable ITO/graphene transparent electrode. *Chem. Eng. J.* **2021**, *416*, 129028. [CrossRef]
5. Canhola, P.; Martins, N.; Raniero, L.; Pereira, S.; Fortunato, E.; Ferreira, I. Role of annealing environment on the performances of large area ITO films produced by rf magnetron sputtering. *Thin Solid Films* **2005**, *487*, 271–276. [CrossRef]
6. Ghorannevis, Z.; Akbarnejad, E.; Ghoranneviss, M. Structural and morphological properties of ITO thin films grown by magnetron sputtering. *J. Theor. Appl. Phys.* **2015**, *9*, 285–290. [CrossRef]
7. Demirhan, Y.; Koseoglu, H.; Turkoglu, F.; Uyanik, Z.; Ozdemir, M.; Aygun, G.; Ozyuzer, L. The controllable deposition of large area roll-to-roll sputtered ito thin films for photovoltaic applications. *Renew. Energy* **2020**, *146*, 1549–1559. [CrossRef]
8. Ritzau, K.-U.; Behrendt, T.; Palaferri, D.; Bivour, M.; Hermle, M. Hydrogen doping of Indium Tin Oxide due to thermal treatment of hetero-junction solar cells. *Thin Solid Films* **2016**, *599*, 161–165. [CrossRef]
9. Prepelita, P.; Stavarache, I.; Craciun, D.; Garoi, F.; Negrila, C.; Sbarcea, B.G.; Craciun, V. Rapid thermal annealing for high-quality ITO thin films deposited by radio-frequency magnetron sputtering. *Beilstein J. Nanotechnol.* **2019**, *10*, 1511–1522. [CrossRef]
10. Nguyen, T.; Le Rendu, P.; Dinh, N.; Fourmigué, M.; Mézière, C. Thermal and chemical treatment of ITO substrates for improvement of OLED performance. *Synth. Met.* **2003**, *138*, 229–232. [CrossRef]
11. Gupta, S.; Ada, E. Optimization of process parameters to achieve high quality as-deposited indium-tin oxide films for display applications. *J. Vac. Sci. Technol. A* **2005**, *23*, 1173–1179. [CrossRef]

12. Salami, H.; Uy, A.; Vadapalli, A.; Grob, C.; Dwivedi, V.; Adomaitis, R.A. Atomic layer deposition of ultrathin indium oxide and indium tin oxide films using a trimethylindium, tetrakis(dimethylamino)tin, and ozone precursor system. *J. Vac. Sci. Technol. A* **2019**, *37*, 010905. [CrossRef]
13. Aiempanakit, M.; Kubart, T.; Larsson, P.; Sarakinos, K.; Jensen, J.; Helmersson, U. Hysteresis and process stability in reactive high power impulse magnetron sputtering of metal oxides. *Thin Solid Films* **2011**, *519*, 7779–7784. [CrossRef]
14. Sittinger, V.; Lenck, O.; Vergöhl, M.; Szyszka, B.; Bräuer, G. Applications of HIPIMS metal oxides. *Thin Solid Films* **2013**, *548*, 18–26. [CrossRef]
15. Horwat, D.; Mickan, M.; Chamorro, W. New strategies for the synthesis of ZnO and Al-doped ZnO films by reactive magnetron sputtering at room temperature. *Phys. Status Solidi C* **2016**, *13*, 951–957. [CrossRef]
16. Carreri, F.; Sabelfeld, A.; Gerdes, H.; Bandorf, R.; Vergöhl, M.; Bräuer, G. HIPIMS ITO films from a rotating cylindrical cathode. *Surf. Coat. Technol.* **2016**, *290*, 65–72. [CrossRef]
17. Stranak, V.; Bogdanowicz, R.; Sezemský, P.; Wulff, H.; Kruth, A.; Smietana, M.; Kratochvíl, J.; Cada, M.; Hubicka, Z. Towards high quality ITO coatings: The impact of nitrogen admixture in HiPIMS discharges. *Surf. Coat. Technol.* **2018**, *335*, 126–133. [CrossRef]
18. Al-Kuhaili, M.F. Electrical conductivity enhancement of indium tin oxide (ITO) thin films reactively sputtered in a hydrogen plasma. *J. Mater. Sci. Mater. Electron.* **2020**, *31*, 2729–2740. [CrossRef]
19. Yang, S.-H.; Lee, D.-M.; Kim, J.-K.; Kang, J.-W.; Lee, J.-M. Enhanced optical and electrical properties of ITO on a PET substrate by hydrogen plasma and HCl treatment. *J. Phys. D Appl. Phys.* **2013**, *46*, 125103. [CrossRef]
20. Wang, R.X.; Beling, C.D.; Fung, S.; Djurišić, A.B.; Ling, C.C.; Kwong, C.; Li, S. Influence of annealing temperature and environment on the properties of indium tin oxide thin films. *J. Phys. D Appl. Phys.* **2005**, *38*, 2000–2005. [CrossRef]
21. Chang, S.-C. Low-pressure H2/N2 annealing on indium tin oxide film. *Microelectron. J.* **2007**, *38*, 1220–1225. [CrossRef]
22. Yin, W.; Smithe, K.; Weiser, P.; Stavola, M.; Fowler, W.B.; Boatner, L.; Pearton, S.J.; Hays, D.C.; Koch, S.G. Hydrogen centers and the conductivity of In_2O_3 single crystals. *Phys. Rev. B* **2015**, *91*, 075208. [CrossRef]
23. Bekisli, F.; Stavola, M.; Fowler, W.B.; Boatner, L.; Spahr, E.; Lüpke, G. Hydrogen impurities and shallow donors in SnO2studied by infrared spectroscopy. *Phys. Rev. B* **2011**, *84*, 035213. [CrossRef]
24. Morales-Masis, M.; Ding, L.; Dauzou, F.; Jeangros, Q.; Hessler-Wyser, A.; Nicolay, S.; Ballif, C. Hydrogen plasma treatment for improved conductivity in amorphous aluminum doped zinc tin oxide thin films. *APL Mater.* **2014**, *2*, 096113. [CrossRef]
25. Luo, S.; Kohiki, S.; Okada, K.; Shoji, F.; Shishido, T. Hydrogen Effects on Crystallinity, Photoluminescence, and Magnetization of Indium Tin Oxide Thin Films Sputter-Deposited on Glass Substrate without Heat Treatment: Hydrogen Effects on Crystallinity, PL, and Magnetization of ITO Films. *Phys. Status Solidi* **2010**, *207*, 386–390. [CrossRef]
26. Kosarian, A.; Shakiba, M.; Farshidi, E. Role of hydrogen treatment on microstructural and opto-electrical properties of amorphous ITO thin films deposited by reactive gas-timing DC magnetron sputtering. *J. Mater. Sci. Mater. Electron.* **2017**, *28*, 10525–10534. [CrossRef]
27. Álvarez-Fraga, L.; Jiménez-Villacorta, F.; Sánchez-Marcos, J.; de Andrés, A.; Prieto, C. Indium-tin oxide thin films deposited at room temperature on glass and PET substrates: Optical and electrical properties variation with the H2–Ar sputtering gas mixture. *Appl. Surf. Sci.* **2015**, *344*, 217–222. [CrossRef]
28. Luo, S.N.; Kono, A.; Nouchi, N.; Shoji, F. Effective creation of oxygen vacancies as an electron carrier source in tin-doped indium oxide films by plasma sputtering. *J. Appl. Phys.* **2006**, *100*, 113701. [CrossRef]
29. Luo, S.; Okada, K.; Kohiki, S.; Tsutsui, F.; Shimooka, H.; Shoji, F. Optical and electrical properties of indium tin oxide thin films sputter-deposited in working gas containing hydrogen without heat treatments. *Mater. Lett.* **2009**, *63*, 641–643. [CrossRef]
30. Okada, K.; Kohiki, S.; Luo, S.; Sekiba, D.; Ishii, S.; Mitome, M.; Kohno, A.; Tajiri, T.; Shoji, F. Correlation between resistivity and oxygen vacancy of hydrogen-doped indium tin oxide thin films. *Thin Solid Films* **2011**, *519*, 3557–3561. [CrossRef]
31. Zhao, M.-J.; Zhang, J.-F.; Huang, J.; Huang, Q.-H.; Wu, W.-Y.; Tseng, M.-C.; Huang, C.-J.; Kuo, H.-C.; Lien, S.-Y.; Zhu, W.-Z. Effect of power density on compositional and structural evolution of ITO thin film by HiPIMS method. *Vacuum* **2022**, *200*, 111034. [CrossRef]
32. Zhao, M.-J.; Zhang, J.-F.; Huang, Q.-H.; Wu, W.-Y.; Tseng, M.-C.; Lien, S.-Y.; Zhu, W.-Z. Effect of working pressure on Sn/In composition and optoelectronic properties of ITO films prepared by high power impulse magnetron sputtering. *Vacuum* **2021**, *196*, 110762. [CrossRef]
33. Van de Walle, C.G. Hydrogen as a Cause of Doping in Zinc Oxide. *Phys. Rev. Lett.* **2000**, *85*, 1012–1015. [CrossRef]
34. Panneerdoss, I.J.; Jeyakumar, S.J.; Ramalingam, S.; Jothibas, M. Characterization of prepared In2O3 thin films: The FT-IR, FT-Raman, UV–Visible investigation and optical analysis. *Spectrochim. Acta Part A Mol. Biomol. Spectrosc.* **2015**, *147*, 1–13. [CrossRef]
35. Jothibas, M.; Manoharan, C.; Ramalingam, S.; Dhanapandian, S.; Jeyakumar, S.J.; Bououdina, M. Preparation, characterization, spectroscopic (FT-IR, FT-Raman, UV and visible) studies, optical properties and Kubo gap analysis of In2O3 thin films. *J. Mol. Struct.* **2013**, *1049*, 239–249. [CrossRef]
36. Mickan, M.; Stoffel, M.; Rinnert, H.; Helmersson, U.; Horwat, D. Restoring the Properties of Transparent Al-Doped ZnO Thin Film Electrodes Exposed to Ambient Air. *J. Phys. Chem. C* **2017**, *121*, 14426–14433. [CrossRef]
37. Dřínek, V.; Vacek, K.; Yuzhakov, G.; Bastl, Z. Interaction between the silyl and silylen centres in the deposits prepared by pulsed laser ablation of silicon monoxide and ammonia, methylamine and dimethylamine. *Appl. Phys. A* **2005**, *81*, 1019–1023. [CrossRef]

38. Tamahkar, E.; Özkahraman, B. Potential Evaluation of PVA-Based Hydrogels for Biomedical Applications. *Hittite J. Sci. Eng.* **2015**, *2*, 165–171. [CrossRef]
39. Wu, B.; Zheng, N.; Fu, G. Small molecules control the formation of Pt nanocrystals: A key role of carbon monoxide in the synthesis of Pt nanocubes. *Chem. Commun.* **2010**, *47*, 1039–1041. [CrossRef] [PubMed]
40. Rey, J.F.Q.; Plivelic, T.S.; Rocha, R.A.; Tadokoro, S.K.; Torriani, I.; Muccillo, E.N.S. Synthesis of In2O3nanoparticles by thermal decomposition of a citrate gel precursor. *J. Nanoparticle Res.* **2005**, *7*, 203–208. [CrossRef]
41. Kulkarni, S.; Patil, D.S. Synthesis and characterization of uniform spherical shape nanoparticles of indium oxide. *J. Mater. Sci. Mater. Electron.* **2015**, *27*, 3731–3735. [CrossRef]
42. Khan, M.A.M.; Khan, W.; Ahamed, M.; Alsalhi, M.S.; Ahmed, T. Crystallite structural, electrical and luminescent characteristics of thin films of In_2O_3 nanocubes synthesized by spray pyrolysis. *Electron. Mater. Lett.* **2013**, *9*, 53–57. [CrossRef]
43. Qin, S.; Wang, J.; Zhao, C.; Zhang, S. Long-Term, Low Temperature Simulation of Early Diagenetic Alterations of Organic Matter: A FTIR Study. *Energy Explor. Exploit.* **2010**, *28*, 365–376. [CrossRef]
44. Ullah, R.; Ahmad, I.; Zheng, Y.-X. Fourier Transform Infrared Spectroscopy of "Bisphenol A". *J. Spectrosc.* **2016**, *2016*, 2073613. [CrossRef]
45. Elhalawaty, S.; Sivaramakrishnan, K.; Theodore, N.; Alford, T. The effect of sputtering pressure on electrical, optical and structure properties of indium tin oxide on glass. *Thin Solid Films* **2010**, *518*, 3326–3331. [CrossRef]
46. Oo, W.M.H.; Tabatabaei, S.; McCluskey, M.; Varley, J.B.; Janotti, A.; Van De Walle, C.G. Hydrogen donors inSnO2studied by infrared spectroscopy and first-principles calculations. *Phys. Rev. B* **2010**, *82*, 081201. [CrossRef]
47. Ugur, D.; Storm, A.; Verberk, R.; Brouwer, J.; Sloof, W. Decomposition of SnH4 molecules on metal and metal–oxide surfaces. *Appl. Surf. Sci.* **2014**, *288*, 673–676. [CrossRef]
48. Wang, X.; Andrews, L. Infrared Spectra of Indium Hydrides in Solid Hydrogen and Neon. *J. Phys. Chem. A* **2004**, *108*, 4440–4448. [CrossRef]
49. Thirumoorthi, M.; Prakash, J.T.J. Structure, optical and electrical properties of indium tin oxide ultra thin films prepared by jet nebulizer spray pyrolysis technique. *J. Asian Ceram. Soc.* **2016**, *4*, 124–132. [CrossRef]
50. Thirumoorthi, M.; Prakash, J.T.J. Structural, morphological characteristics and optical properties of Y doped ZnO thin films by sol–gel spin coating method. *Superlattices Microstruct.* **2015**, *85*, 237–247. [CrossRef]
51. Lin, T.-C.; Chang, S.-C.; Chiu, C.-F. Annealing effect of ITO and ITO/Cu transparent conductive films in low pressure hydrogen atmosphere. *Mater. Sci. Eng. B* **2006**, *129*, 39–42. [CrossRef]
52. Kim, S.J. Preparation of Indium Tin Oxide Thin Film by Rapid Thermal Annealing Treatment. *IJIRSET* **2007**, *5*, 14. [CrossRef]
53. Peng, Y.M.; Su, Y.K.; Yang, R.Y. Influence of Annealing Atmosphere on the Characteristics of Sol-Gel Derived ITO Thin Films. *Adv. Mater. Res.* **2013**, *684*, 279–284. [CrossRef]
54. Wang, R.X.; Beling, C.D.; Fung, S.; Djurisic, A.B.; Kwong, C.Y.; Li, S. The Effect of Thermal Annealing on the Properties of Indium Tin Oxide Thin Films. In Proceedings of the Conference on Optoelectronic and Microelectronic Materials and Devices, Brisbane, Australia, 8–10 December 2004; pp. 57–60. [CrossRef]
55. Sezemsky, P.; Burnat, D.; Kratochvil, J.; Wulff, H.; Kruth, A.; Lechowicz, K.; Janik, M.; Bogdanowicz, R.; Cada, M.; Hubicka, Z.; et al. Tailoring properties of indium tin oxide thin films for their work in both electrochemical and optical label-free sensing systems. *Sens. Actuators B Chem.* **2021**, *343*, 130173. [CrossRef]
56. Jun, F.; Biwen, L.; Wenbo, C.; Meiyan, C.; Fanya, J.; Min, D. Preparation of ITO Coating on PMMA by High-Power Pulse Magnetron Sputtering. *Rare Met. Mater. Eng.* **2020**, *49*, 2229–2233.

nanomaterials

Article

New Approach for Designing Zinc Oxide Nanohybrids to Be Effective Photocatalysts for Water Purification in Sunlight

Osama Saber [1,2,*], Aya Osama [1], Adil Alshoaibi [1], Nagih M. Shaalan [1,3] and Doaa Osama [1]

[1] Department of Physics, College of Science, King Faisal University, P.O. Box 400, Al-Ahsa 31982, Saudi Arabia; 217044956@student.kfu.edu.sa (A.O.); adshoaibi@kfu.edu.sa (A.A.); nmohammed@kfu.edu.sa (N.M.S.); 221445253@student.kfu.edu.sa (D.O.)
[2] Petroleum Refining Department, Egyptian Petroleum Research Institute, Nasr City, P.O. Box 11727, Cairo 11765, Egypt
[3] Physics Department, Faculty of Science, Assiut University, Assiut 71516, Egypt
[*] Correspondence: osmohamed@kfu.edu.sa; Tel.: +96-(61)-3589-9440

Abstract: Water pollution and deficient energy are the main challenges for the scientific society across the world. In this trend, new approaches include designing zinc oxide nanohybrids to be very active in sunlight. In this line, organic and magnetic species intercalate among the nanolayers of Al/Zn to build inorganic-magnetic-organic nanohybrid structures. A series of nanolayered and nanohybrid structures have been prepared through intercalating very fine particles of cobalt iron oxide nanocomposites and long chains of organic fatty acids such as n-capric acid and stearic acid inside the nanolayered structures of Al/Zn. By thermal treatment, zinc oxide nanohybrids have been prepared and used for purifying water from colored pollutants using solar energy. The optical measurements have shown that the nanohybrid structure of zinc oxide leads to a clear reduction of band gap energy from 3.30 eV to 2.60 eV to be effective in sunlight. In this line, a complete removal of the colored pollutants (naphthol green B) was achieved after ten minutes in the presence of zinc oxide nanohybrid and sunlight. Finally, this new approach for designing photoactive nanohybrids leads to positive results for facing the energy- and water-related problems through using renewable and non-polluting energy for purifying water.

Keywords: inorganic-magnetic-organic nanohybrids; zinc oxide nanohybrid; water purification; sunlight

Citation: Saber, O.; Osama, A.; Alshoaibi, A.; Shaalan, N.M.; Osama, D. New Approach for Designing Zinc Oxide Nanohybrids to Be Effective Photocatalysts for Water Purification in Sunlight. *Nanomaterials* **2022**, *12*, 2005. https://doi.org/10.3390/nano12122005

Academic Editors: Ming-Yu Li and Jihoon Lee

Received: 5 May 2022
Accepted: 7 June 2022
Published: 10 June 2022

1. Introduction

The current situation of the water and energy in the world became more critical because of deficient energy and environmental problems. Two major challenges are clear for the scientific society in the recent years: water pollution and deficient energy. These international challenges are produced through the rapidly growing population and industries which led to these energy- and environment-related problems. Many scientists have used energy to solve the problem of water pollution leading to increasing the problem of deficient energy. For saving energy, the scientists tried to discover different techniques dependent on purifying water by renewable and non-polluting energy. One of the most familiar non-polluting resources for energy is sunlight. Solar energy can produce strong oxidizing agents for converting the industrial pollutants to carbon dioxide and water through exciting active photocatalysts. Most organic dyes such as textile dyes and surfactants are not easily biodegradable. Therefore, they belong to the colored hazardous pollutants. Photocatalytic degradation seems as one of the benign solutions for purifying water from organic dyes using photocatalysts and sunlight [1–3]. For solving these environmental problems, semiconductor photocatalysts are very familiar in this trend [4–7].

Although titanium oxide was one of the most famous photocatalysts in this field, their applications were limited because it can mainly absorb UV-light which considers 4% of the solar energy [8–10]. Therefore, zinc oxide is suggested to be an alternative photocatalyst to titanium oxide because it has large excitation binding energy of 60 meV, in addition to a band gap of 3.37 eV. According to the results of Dindar and Icli [11], zinc oxide was more effective than titanium oxide in sunlight for the degradation of phenol. Many researchers confirmed this conclusion through comparing between titanium oxide and zinc oxide semiconductors through the advanced oxidation of wastewater [12,13]. However, low performance of zinc oxide was observed for photocatalytic degradation in many studies [14–16] because of the high rate of recombination reactions for the excited electrons and holes of zinc oxide which happened within nanoseconds and the low amount energy absorbed during the photocatalytic processes. These disadvantages decrease the importance of photocatalytic degradation processes in the market.

Several techniques have been used for modifying the structure of zinc oxide to solve its problems through narrowing its band gap energy to be active in sunlight. The formation of nanostructures [17], in combination with carbon nanorods and nanotubes [18], and introducing surface defects, were good solutions for improving the activity of zinc oxides. Additionally, for preventing the disadvantages of zinc oxide, doping processes with transition elements in addition to morphological changes [19] were studied to be suitable solutions for increasing the performance of zinc oxide for the photocatalytic degradation of pollutants. In this trend, the optical properties and activity of zinc oxide were developed through the morphological changes from nanoparticles [20] to nanorods [21]. In addition, the zinc oxides nanotubes [22], and nanowires [23] were suggested to be active photocatalysts [24].

Many researchers have used transition elements for doping zinc oxide to become effective photocatalysts [25–29]. Insertion of sulfur inside the structure of ZnO improved the charges separation through preventing the recombination process between electrons and holes [30]. The results of Adeel et al. showed high photocatalytic degradation of rhodamine blue and methylene blue under UV irradiation using ZnO films which were modified by the addition of Ag and Al [31]. The introduction of nitrogen using micro-emulsion method increased the optical properties and activity of ZnO nanospheres [32]. In addition, several studies concluded that the addition of aluminum and iron as dopants inside ZnO structures converted their transparent thin films to be useful for photocatalytic applications and solar cells [33–38]. This positive effect of the addition of aluminum inside zinc oxide was confirmed by our previous research [7]. Thus, the current study concentrates on improving the photocatalytic performance of ZnO structures through building nanohybrids based on organic, magnetic, and inorganic species by an unconventional technique. In the conventional methods [39], multi-steps were used for mixing one or two elements for zinc oxides. However, the main challenge is to get a homogenous structure of all elements inside the crystals of ZnO.

The nano-size spinel ferrite nanoparticles $CoFe_2O_4$ have recently attracted significant attention because of their remarkable photocatalytic properties [40–43]. Although much research has been carried out for studying the photocatalytic performance of cobalt ferrite nanoparticles, there are no articles for using $CoFe_2O_4$ as a filler for zinc oxide structures. Additionally, because of the low band gap energy of cobalt iron oxide $CoFe_2O_4$ (1.32 eV) [43], it is considered an excellent dopant and filler for reducing the band gap energy for zinc oxide.

Following this trend, the current study has used a new strategy for building zinc oxide nanohybrids with reduction in the optical band gap energy to be active in visible light for purifying water from pollutants. In this strategy, a series of zinc oxide nanohybrids based on magnetic, inorganic, and organic species were prepared through building inorganic-magnetic-organic nanohybrids according to the host–guest interaction. The inorganic-magnetic-organic nanohybrids were formed by intercalation reactions of long chains of hydrocarbons of n-capric acid and inserting magnetic nanoparticles of cobalt iron oxides nanocomposites inside the nanolayered structures of zinc and aluminum. Furthermore, longer chains of organic acid (stearic acid) were used for studying the role and the effect of organic species. Organic species are used as pillars to widen the interlayered spacing of the nanolayered structures to allow for the magnetic nanoparticles to be inserted between the nanolayers of zinc and aluminum. These nanohybrids were used for producing zinc oxide nanohybrids by thermal treatment. Zinc oxide nanohybrids were tested for purifying the water using sunlight through photocatalytic degradation of the colored pollutants. At the same time, the optical properties and activity of the nanohybrids were studied and compared with conventional photocatalysts. This strategy depends on a good distribution of magnetic nanocomposites inside the internal surfaces of the Al/Zn nanolayers in special arrangements in the nano scale producing nanohybrids based on zinc oxide doped with multi-oxides, aiming to creating new optical active centers.

2. Materials and Methods

The hetero-structured hybrids such as inorganic-magnetic-organic systems are good candidates for creating a distinguished photo-activity for ZnO which cannot be achieved through the usual methods. In order to build inorganic-magnetic-organic nanohybrids based on zinc oxide, three types of nanomaterials were prepared. The first type was very fine nanoparticles of cobalt iron oxides nanocomposite, which were used as filler for the nanohybrids. The second one was nanolayered structures based on Al/Zn LDHs. The third type depended on the long chains of hydrocarbon of organic fatty acid to expand and widen the interlayered spacing of the nanolayered structures. This widening and expansion can facilitate the insertion of magnetic nanoparticles among the nanolayers of Al/Zn LDHs. To study the important role of organic fatty acid, two different kinds of long chains of hydrocarbons were used for building the nanohybrid structures.

2.1. Preparation of Nanoparticles of Magnetic Nanocomposites

A solvent thermal technique has been used for preparing very fine nanoparticles of cobalt iron nanocomposite. Cobalt (II) acetate (0.051 mol) and Iron (II) acetate (0.026 mol) were reacted with 350 mL of methanol at room temperature for 5 h. A similar amount of ethanol was added to the mixture. To complete the reaction under super critical conditions of pressure and temperature, the mixture was placed inside an autoclave. The mixture was heated by a slow rate of 1 °C/min. to reach 260 °C under a high pressure of 75 bar. At this stage, the pressure was slowly released under a flow of nitrogen to avoid oxidation reactions. At the same time, the temperature of the autoclave decreased to the room temperature. The fine powder of the product was easily collected.

2.2. Preparation of Nanolayered Structures and Nanohybrids

Two samples of inorganic-magnetic-organic nanohybrids were prepared for designing nanolayered structure with changing the organic species. The pure nanolayered structure of Al/Zn LDH was prepared without magnetic or organic species for comparison. Al/Zn LDH was prepared through mixing aqueous solutions (0.069 M) of aluminum nitrate with zinc nitrate in presence of 0.5 M of urea. The molar ratio of aluminum to zinc was 1:3. By keeping the temperature of the mixture at 80 °C, the nanolayers of LDH were precipitated during the hydrolysis of urea because the nature of reaction medium were gradually changed from acidic to alkaline. White precipitate was obtained after 12 h of the reaction. It was filtrated and washed by distilled water. By drying at room temperature, the product was collected and coded by ZOA.

The inorganic-magnetic-organic nanohybrid was synthesized by adding 100 mL of the aqueous solution of 5% n-capric acid sodium salt during building the Al/Zn nanolayered structure. In addition, 0.5 g of the prepared nanoparticles of cobalt iron oxides nanocomposite was mixed with the aqueous solution (0.069 M) of aluminum nitrate with zinc nitrate in presence of 0.5 M of urea. By keeping the temperature of the mixture at 80 °C, the product was obtained after 12 h of the reaction. After filtration and washing, the sample was dried at 25 °C in vacuum box. The product was coded as HZ-1.

Another inorganic-magnetic-organic nanohybrid was prepared by the same procedure by changing the organic compound n-capric acid to be stearic acid, noting that the nanolayers of the Al/Zn LDH were precipitated in presence of 0.5 g of the prepared nanoparticles of cobalt iron oxides nanocomposite with the organic species. The product was collected and coded as HZ-2.

2.3. Preparation of Nanohybridsand Nanocomposite Based on Oxides

The nanolayered structure of Al/Zn LDH was thermally treated at 500 °C to produce a nanocomposite of zinc and aluminum oxides. It was represented by ZOA-500. By calcination at 500 °C, the nanohybrid HZ-1 was converted to be a stable nanohybrid composed of magnetic and non-magnetic oxides. It was represented as HZ-1-500. The inorganic-magnetic-organic nanohybrid HZ-2 was transformed to new structure of nanohybrid through the thermal treatment at 500 °C. It was represented as HZ-2-500.

2.4. Physical Characterization

Nanolayered structures and crystalline structures of the prepared samples were identified by a Bruker-AXS system with Cu-Ka radiation (Bruker Company, Karlsruhe, Germany) for X-ray diffraction analysis (XRD). An electrons probe microanalyser JED2300 (JEOLCompany, Tokyo, Japan) was used for detecting the different metals in the products through energy dispersive X-ray spectroscopy (EDX). For studying the thermal behavior of the prepared samples, a thermogravimetric analyzer TA series Q500 and TA series Q600 for differential scanning calorimetry (DSC) (T-A company, New Castle, PA, USA) were used under the flow of nitrogen. FTIR spectroscopy was performed by using a Perkin–Elmer Spectrum 400 instrument starting from 425 cm^{-1} to 4000 cm^{-1}. For determining the morphology and nanosize of the products, scanning electron microscopy (SEM) and transmission electron microscopy (TEM) JEM 2100F (JEOL Company, Tokyo, Japan) was used with different magnifications. The optical properties were measured for the prepared samples through the diffuse reflectance technique. UV/VIS/NIR Shimadzu 3600 spectrophotometer (Shimadzu, Columbia, MD, USA) was used for measuring the absorbance of liquid and solid samples.

2.5. Photocatalytic Activity

Photocatalytic degradation of aqueous solutions of industrial dyes was used for measuring the photocatalytic activity of the prepared materials for purification of water in sunlight. The photo activities of the prepared nanomaterials were studied through photocatalytic reactions of the green dyes such as naphthol green B (NGB) in the sunlight. In the current research, the low concentration of aqueous solution of NGB (4×10^{-4} M) was prepared and mixed with 0.1 g of the one of prepared nanomaterial. This sample was exposed to sunlight through an irradiation area of 10 cm^2. According to the Beer-Lambert law, the intensity of the measured spectrum of the dye can be used for expressing the low concentration of the dye. Depending on this fact, a small quantity of the green solution was extracted from the main mixture every few minutes during exposure to sunlight. Then, the UV-Vis spectrophotometer can determine the concentration through calculating the intensity of absorbance of the liquid samples at 714 nm, which is the characteristic peak of NGB. During the spring season (March) in Saudi Arabia, the photocatalysis processes were carried out in presence of sunlight starting from 10:00 a.m. to 10:20 a.m.

3. Results

3.1. Characterization of the Prepared Filler

Very fine nanoparticles of cobalt iron oxides nanocomposite were prepared and characterized to be suitable for use as a filler and inserted among the nanolayers of the nanolayered structures. In this trend, X-ray diffraction was used for confirming the structure of the prepared cobalt iron oxides nanocomposite. Figure 1a shows the X-ray diffraction pattern of the prepared cobalt iron oxides nanocomposite.

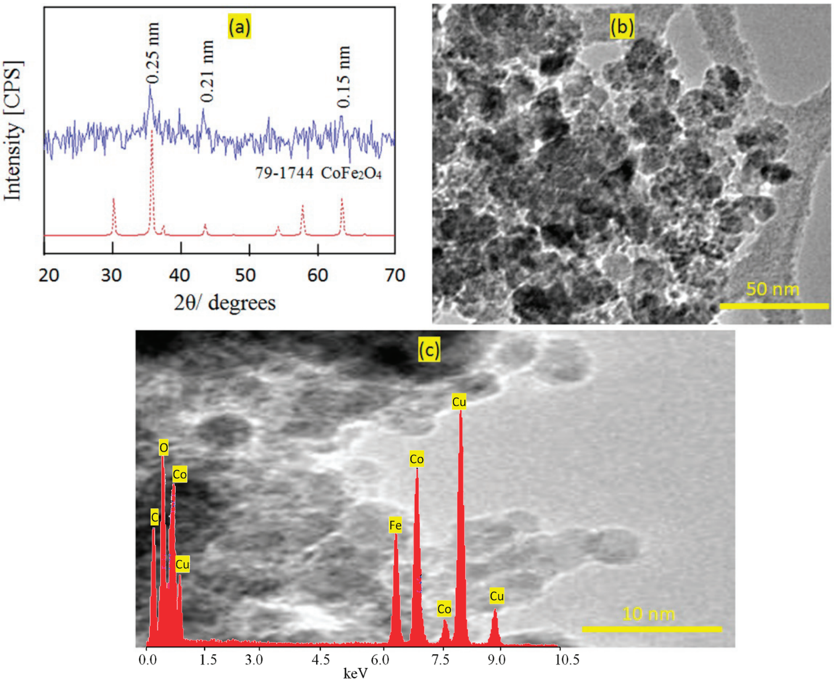

Figure 1. The prepared cobalt iron oxides nanocomposite (**a**) X-ray diffraction pattern (the red line is the standard and the blue line is the sample), (**b**) TEM image at 50 nm, and (**c**) TEM image at 10 nm (Inset: EDX spectrum).

The X-ray diffraction pattern showed weak peaks at $2\Theta = 35.56^\circ$, 41.6°, and 62.9°, agreeing with d-spacings at 0.25 nm, 0.21 nm, and 0.15 nm, respectively. According to the diffraction lines of JCPDS 79–1744, Figure 1a reveals that the prepared cobalt iron oxides have a $CoFe_2O_4$ structure. Transmission electron microscopy was used for measuring the nano size of the particles of the prepared cobalt iron oxides. Figure 1b shows strong aggregates of nanoparticles because of the magnetic behavior of the cobalt iron oxides. By magnification, very fine nanoparticles are observed in Figure 1c. Figure 1c shows that the size of the particles of the prepared cobalt iron oxides is less than 5 nm. Energy dispersive X-ray spectrometry (EDX) analysis confirmed the presence of magnetic elements through observing two sharp peaks for cobalt and iron, as shown in Figure 1c (inset).

3.2. Design of Inorganic-Magnetic-Organic Nanohybrids

Inorganic-magnetic-organic nanohybrids appear to be very creative because they can produce unlimited sets of known or unknown properties. In this way, nanohybrids were designed by a combination of zero-dimensional nanoparticles of magnetic nanocomposite and two-dimensional nanolayered structures, in addition to long chains of organic acid. This combination was achieved in an order arrangement through building Al/Zn nanolayered structures which have cationic nanolayers. In the presence of n-capric acid ($CH_3(CH_2)_8COO^-$), the long chains of the aliphatic acid were intercalated among the nanolayers for neutralizing their positive charges. At the same time, the long chains of hydrocarbons of organic compounds were working as pillars for building the nanolayered structures. In addition, these pillars expanded and widened the interlayered spacing among the nanolayers to produce enough space for existing magnetic nanoparticles of cobalt iron oxides nanocomposite. To indicate the positive role of organic species for designing this nanohybrid, a pure Al/Zn nanolayered structure was prepared for comparison. In addition, the Al/Zn nanolayered structure was modified by the nanoparticles of cobalt iron oxides nanocomposite with longer chains of hydrocarbon of stearic acid to study the effect of the organic species. The X-ray diffraction patterns of the prepared nanolayered structures and nanohybrids are displayed in Figure 2.

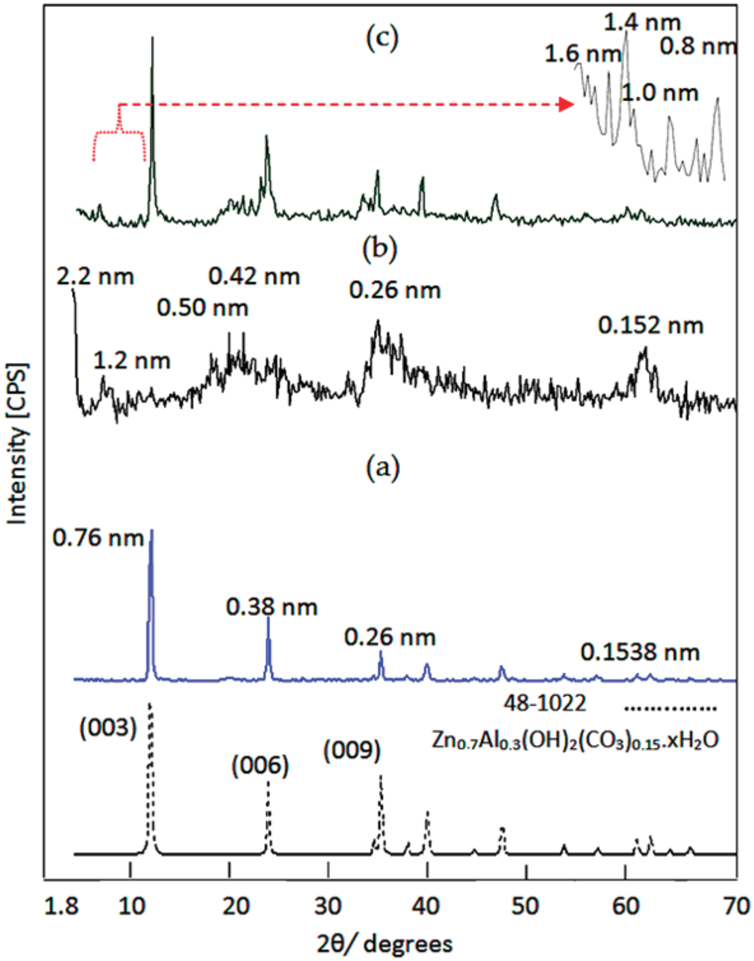

Figure 2. X-ray diffraction patterns of: (**a**) the pure Al/Zn nanolayered structure, (**b**) the nanohybrid HZ-1, and (**c**) the nanohybrid HZ-2.

Figure 2a shows the x-ray diffraction pattern of the pure Al/Zn nanolayered structure. Sharp and symmetric peaks were observed at $2\Theta = 11.62^\circ$, 23.36°, and 34.54°, aligning with the d-spacing of 0.76 nm, 0.38 nm, and 0.26 nm, respectively. These peaks are due to the reflections of the main planes (003), (006), and (009). The clear arrangement between these reflections (0.76 nm = 2 × 0.38 nm = 3 × 0.26 nm) confirmed formation of the nanolayered structures of the natural hydrotalcite (JCPDS file No. 37–629) and zinc aluminum carbonate hydroxide hydrate (JCPDS file No. 38–486). The other reflections of the planes (012), (015), (110), and (113) of the nanolayered structures of the natural hydrotalcite were observed at $2\Theta = 39.16^\circ$, 46.56°, 60.05°, and 61.44° and matched with the d-spacing of 0.23 nm, 0.19 nm, 0.17 nm, 153, and 0.150 nm, respectively. The crystal parameters (a, c) could be calculated depending on the d-spacing of the planes (003) and (110), respectively. The first parameter was $2 \times d_{(110)} = 0.306$ nm. It means that the average distance between Zn-cation and Al-cation is 0.306 nm, agreeing with the previous published data of zinc aluminum carbonate hydroxide hydrate (JCPDS file No. 38–486). The second parameter was assessed by 3 × $d_{(003)}$ = 2.28 nm. It was similar to that reported for the natural hydrotalcite.

By intercalating the long chains of hydrocarbons of n-capric acid ($CH_3(CH_2)_8COO^-$) with the Al/Zn nanolayered structures in presence of the nanoparticles of cobalt iron oxides nanocomposite, inorganic-magnetic-organic nanohybrid HZ-1 was formed through a host–guest interaction. The X-ray diffraction pattern of HZ-1, which is displayed in Figure 2b, shows new peaks at low 2Θ in addition to the disappearance of the original peaks of the nanolayered structure of LDH, noting that the peaks of the nanoparticles of magnetic nanocomposite were observed as weak peaks at $2\Theta = 35.56°$, 41.6°, and 62.9°. A sharp peak was observed at 2.2 nm indicating that the interlayered spacing of the nanolayered structure expanded and widened from 0.755 nm to 2.20 nm. This spacing could allow for the nanoparticles of cobalt iron oxides to intercalate among the nanolayers of the nanolayered structure because the peaks of cobalt iron oxides were not clear in Figure 2b. The crystal parameter (a), which depends on the reflection of the plane (110), has a little shift. At the same time, a large change was observed for the parameter (c) from 2.280 nm to 6.60 nm. It means that the nanohybrid HZ-1 consists of nanolayered structures having organic species and magnetic nanoparticles.

With intercalating longer chains of organic compounds, stearic acid ($CH_3(CH_2)_{16}COO^-$) and the nanoparticles of cobalt iron oxides nanocomposite inside the pure Al/Zn nanolayered structures, HZ-2 was formed to build another inorganic-magnetic-organic nanohybrid. Figure 2c shows the main peaks of the Al/Zn LDH in addition to appearing as new peaks after building the nanohybrid HZ-2. The new peaks of the nanohybrid HZ-2 were observed at 1.6 nm and 1.4 nm, as seen in Figure 2c (inset). It indicated that the interlayered spacing of the nanolayered structure expanded and widened from 0.755 nm to become higher. This expansion could allow for the nanoparticles of cobalt iron oxides to intercalate among the nanolayers of the nanolayered structure because the characteristic peak of cobalt iron oxides overlaps with the peak of nanolayered structure at $2\Theta = 35.56°$, as shown in Figure 3c. It means that the nanohybrid HZ-2 consists of nanolayered structures that have organic species and magnetic nanoparticles.

This finding was confirmed by transmission electron microscopy (TEM) and energy dispersive X-ray spectrometry (EDX). TEM images of the nanohybrid HZ-1 are displayed in Figure 3. Figure 3a shows that the nanohybrid HZ-2 has nanoplatelets with a size of less than 50 nm. Furthermore, very fine nanoparticles, which are marked by arrows, were observed in Figure 3c,d, representing the magnetic nanoparticles cobalt iron oxides. Through magnification, Figure 3c confirmed the presence of the magnetic nanoparticles among the nanolayers of nanohybrid. In addition, Figure 3d shows one particle started to intercalate with the nanolayered structure. By EDX analysis, the different elements were identified in the nanohybrid HZ-2, as shown in Figure 3e. Figure 3e shows sharp peaks for the non-magnetic elements zinc and aluminum. In addition, the magnetic elements cobalt and iron were observed by weak peaks.

In order to identify the function groups of the nanohybrids HZ-1 and HZ-2, the infrared spectra (FT-IR) was used and is displayed in Figure 4. For the nanohybrid HZ-1, the absorption band was observed at 3434 cm^{-1}, indicating the stretching mode of hydroxyl groups as seen in Figure 5a. The presence of long chains of hydrocarbon of n-capric acid was clear in the IR spectrum because the stretch absorption of carbon–hydrogen was observed by sharp peaks at 2924 cm^{-1} and 2953 cm^{-1}. In addition, the bending mode of the carbon–hydrogen was clear through an observing band at 1468 cm^{-1}. The symmetric stretching vibration of carboxylate, which belonged to the aliphatic acid, was observed at 1554 cm^{-1}. Furthermore, the absorption at 1411 cm^{-1} is assigned to the asymmetric stretching vibration of carboxylate. The bands observed below 1000 cm^{-1} could be ascribed to Zn-O and Al-O.

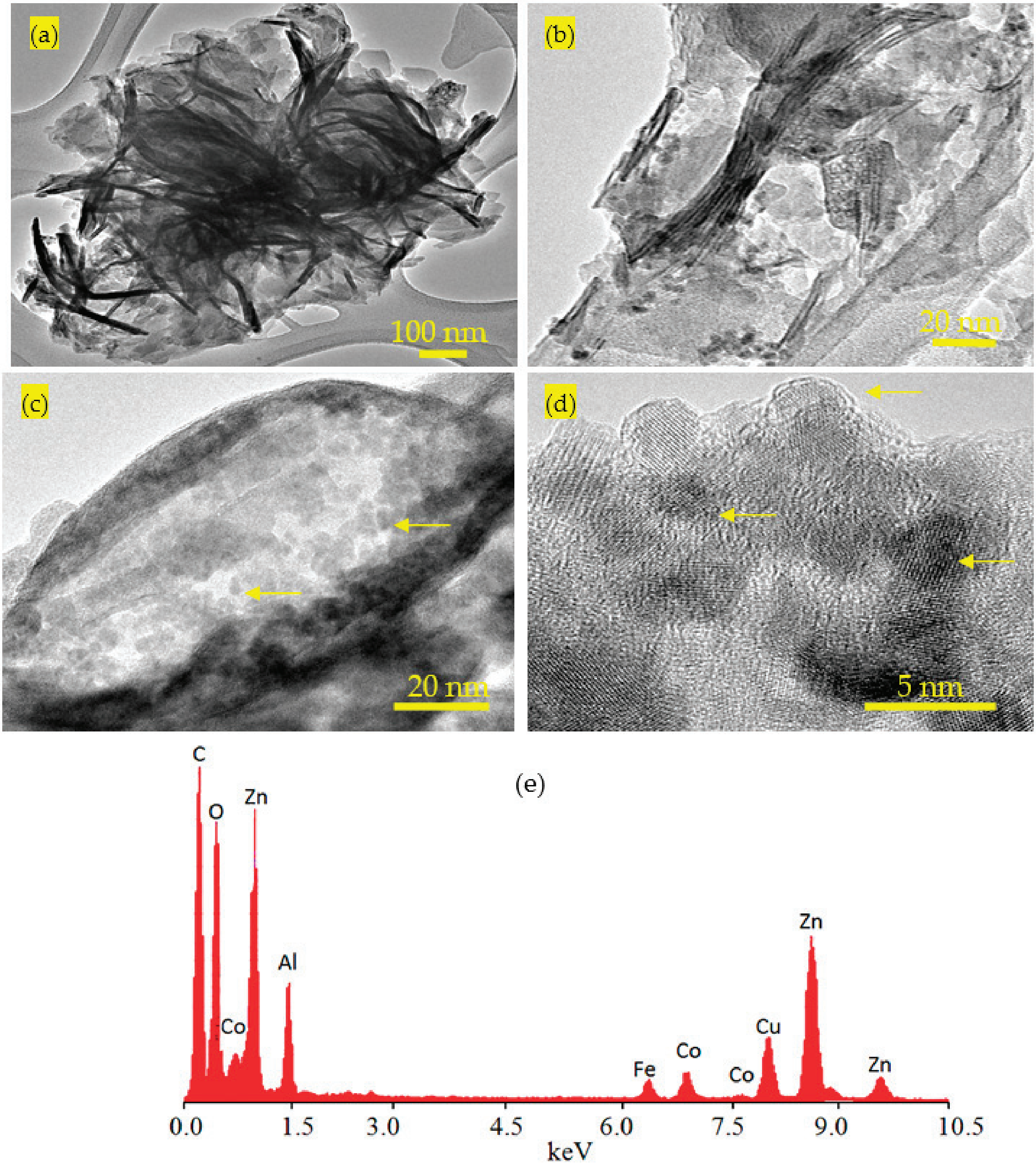

Figure 3. TEM images of the nanohybrid HZ-1: (**a**) at 100 nm, (**b**,**c**) at 20 nm, (**d**) at 5 nm (the yellow arrows are due to the intercalated nanoparticles), and (**e**) EDX spectrum.

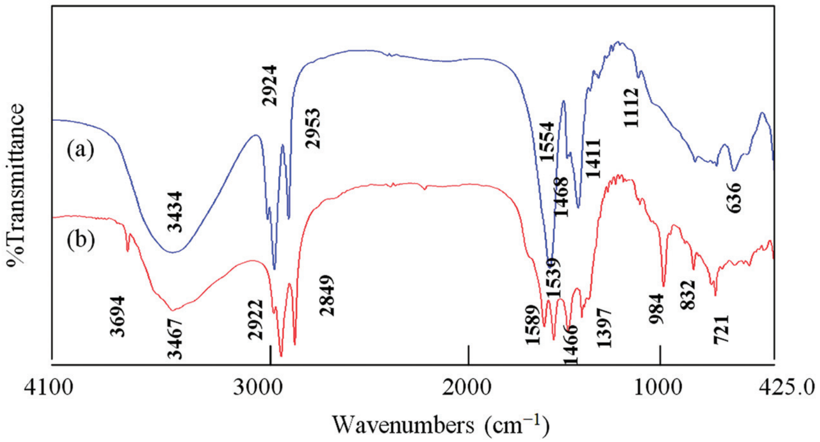

Figure 4. FT-IR spectra of: (**a**) the nanohybrid HZ-1 and (**b**) the nanohybrid HZ-2.

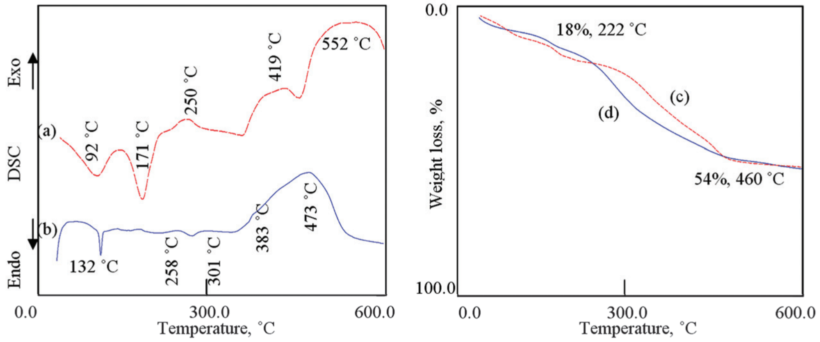

Figure 5. Thermal analyses of: (**a**) DSC curve of HZ-1, (**b**) DSC curve of HZ-2, (**c**) TG curve of HZ-1, and (**d**) TG curve of HZ-2.

For the nanohybrid HZ-2, Figure 4b confirms the formation of inorganic-magnetic-organic nanohybrid through observing the main bands of stearic acid. The presence of long chains of hydrocarbon was confirmed by observing sharp peaks at 2922 cm^{-1} and 2849 cm^{-1}, indicating the stretch absorption of carbon–hydrogen. Additionally, the bending mode of the carbon–hydrogen was clear through observing the band at 1466 cm^{-1}. The symmetric stretching vibration of carboxylate, which belonged to the aliphatic acid, was observed at 1589 cm^{-1}. Furthermore, the absorption at 1397 cm^{-1} is assigned to the asymmetric stretching vibration of carboxylate. In addition, the absorption band of the hydroxyl groups of the nanolayered structure was observed at 3467 cm^{-1}. In the same trend, the presence of different kinds of hydroxyl groups were confirmed by observing another band for hydroxyl groups at 3694 cm^{-1}. It indicated that the presence of the nanoparticles of cobalt iron oxides among the nanolayers affect the vibrational mode of hydroxyl groups. It means that the confinement of the nanoparticles of $CoFe_2O_4$ among the nanolayers affect the hydroxyl groups which are closer to these nanoparticles.

The thermal gravimetric analysis and differential scanning calorimetry (TGA-DSC curves) were used to study the thermal behavior of the prepared nanohybrids. Figure 5 indicates that the thermal decomposition of both HZ-1 and HZ-2 can give information for the nature of the interlayer species inside the nanohybrids. The DSC curve of the nanohybrid HZ-1 shows two series of peaks, as shown in Figure 5a. The first series is endothermic peaks at 92 °C and 171 °C, which are ascribed to the removal of the surface and interlayered water. The second series is exothermic peaks at 250 °C, 419 °C, and 552 °C, representing the oxidation reactions of the chains of hydrocarbon of n-capric acid. From the TG curve (Figure 5c), the weight loss of 18%, which happened up to 222 °C, represents the internal content of water inside the nanohybrid HZ-1. In the same way, the weight loss of 36%, which occurred up to 460 °C, is due to the internal content of organic species inside the nanohybrid HZ-1. The DSC curve of the nanohybrid NHA-2 is similar to that of the nanohybrid HZ-2, as seen in Figure 5b. Figure 5b shows endothermic and exothermic peaks, indicating the removal of water and oxidation reactions of the long chains of hydrocarbon of stearic acid. In the same way, similar behavior was observed for the TG curve of HZ-2, as shown in Figure 5d. The thermal analyses results confirmed formation of the nanohybrids HZ-1 and HZ-2.

3.3. Design of Nanohybrids Based on Oxides

The main reason for designing nanohybrids with organic and inorganic species is directed to produce stable and effective zinc oxides nanohybrids and nanocomposites with distinguished properties. Therefore, the prepared nanohybrids were thermally treated at 500 °C to remove unstable species and create new active sites.

X-ray diffraction has been used to identify the produced structures from the calcination of the nanohybrids. Figure 6 shows X-ray diffraction patterns of ZOA-500, HZ-1-500, and HZ-2-500. The XRD pattern of ZOA-500 exhibited new weak peaks at 2Θ = 32.01°, 34.32°, 36.49°, 47.71°, 7.05°, and 62.81°, in addition to disappearance of the original peaks of the nanolayered structures, as shown in Figure 6a. By comparing the diffraction lines of the zinc oxide crystal (JCPDS No. 36-1451) and the standard entire diffraction pattern of zincite phase (JCPDS No. 75-576), ZOA-500 has a similar structure for zinc oxide. However, the broad and diffuse peaks of ZOA-500 indicated that the structure of ZOA-500 is not pure because of the presence of the amorphous structure of aluminum oxide inside the zincite phase. In case of the nanohybrid HZ-1-500, Figure 6b shows clear and sharp peaks at 0.28 nm, 0.26 nm, and 0.24 nm, indicating a crystalline structure. Furthermore, weak peaks were observed at 0.19 nm, 0.16 nm, 0.15 nm, and 0.14 nm. These diffraction lines agree with the peaks of the zinc oxide crystal (JCPDS No. 36-1451) and the standard entire diffraction pattern of the zincite phase (JCPDS No. 75-576). In addition, a weak peak was observed at 0.30 nm and marked with (*) in Figure 6b. At the same time, Figure 6b reveals that the characteristic peak of cobalt iron oxides is observed at 0.25 nm and overlaps with the peak of zinc oxide at 0.24 nm.

For the nanohybrid HZ-2-500, Figure 6c shows that the characteristic peaks of zinc oxide were observed at 0.28 nm, 0.26 nm, and 0.24 nm, agreeing with the crystalline structure of the sample HZ-1-500. This similarity was confirmed by observing weak peaks at 0.19 nm, 0.16 nm, 0.15 nm, and 0.14 nm. These diffraction lines agree with the peaks of the zinc oxide crystal (JCPDS No. 36-1451) and the standard entire diffraction pattern of zincite phase (JCPDS No. 75-576). At the same time, Figure 6c revealed that the characteristic peak of cobalt iron oxides at 0.25 nm were not clear in the sample NH-2-500. These XRD results can conclude that both HZ-1-500 and HZ-2-500 have a zincite phase doping with aluminum and cobalt iron oxides.

To confirm the presence of magnetic elements inside the ZnO crystals, the chemical composition of HZ-1-500 was measured through scanning electron microscopy (SEM) and energy dispersive X-ray spectrometry (EDX). SEM images showed that HZ-1-500 has one phase, as shown in Figure 7a. In addition, SEM image indicated that this phase consisted of nanoparticles. The chemical composition of this phase was determined by the EDX equipment, which is attached to SEM. The EDX spectrum confirmed the presence of magnetic elements Co and Fe. Furthermore, Figure 7b shows that the atomic percentages of cobalt and iron in the nanoparticles of HZ-1-500 are 1.24% and 0.96%; respectively. In addition, the atomic percentage of aluminum was 18.64%. At the same time, Figure 7b revealed that the highest percentage is due to zinc. It means that HZ-1-500 is composed of zinc oxide doping with Al, Co, and Fe.

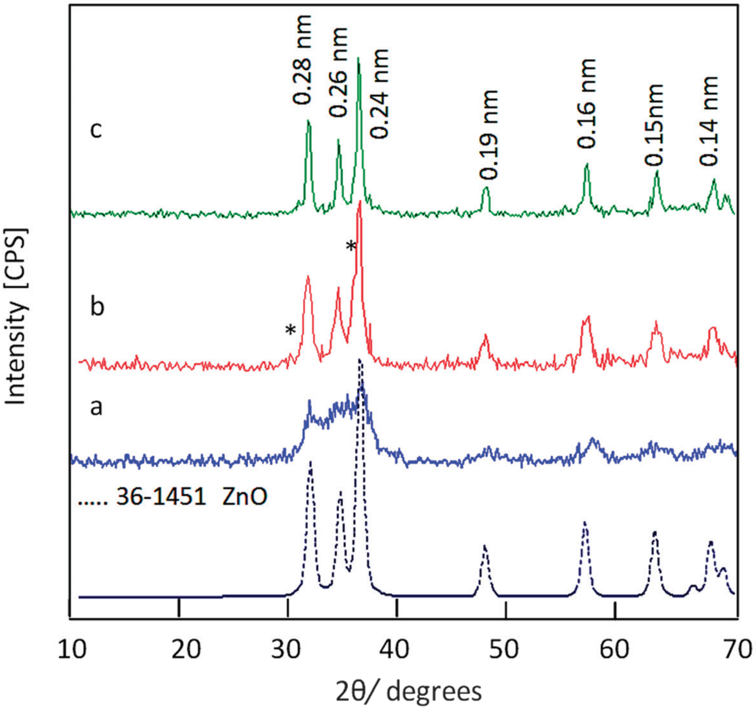

Figure 6. X-ray diffraction patterns of: (**a**) ZOA-500, (**b**) HZ-1-500 (the * is due to cobalt iron oxides), and (**c**) HZ-2-500.

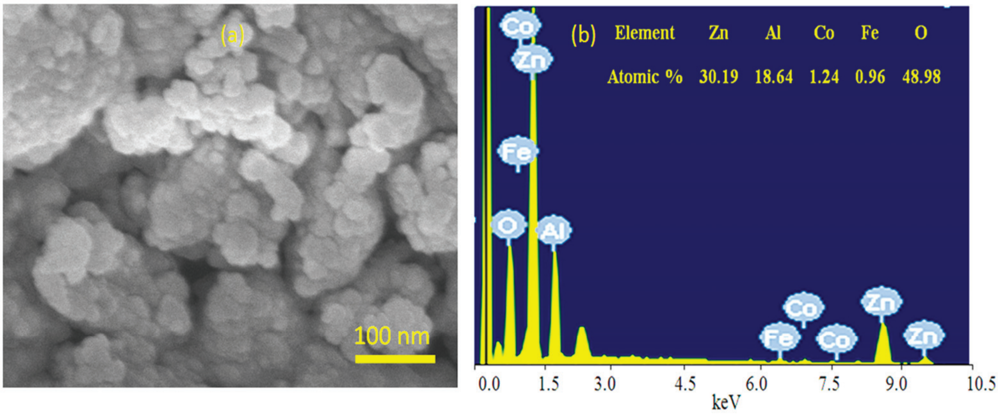

Figure 7. Images and spectrum of HZ-1-500: (**a**) SEM and (**b**) EDX with chemical composition.

TEM images of HZ-2-500 confirmed this finding, as shown in Figure 8. Clear nanoparticles were observed for HZ-1-500, as seen in Figure 8a. It indicated that the width of HZ-1-500 is 20 nm. Additionally, very fine white spots were observed and marked by the arrow on the surface of the nanoparticles. These spots represent the cobalt iron oxides nanocomposites. These white spots became clearer by magnification, as seen in Figure 8b. Figure 8b shows the combination between the zinc oxide particles with the particles of cobalt iron oxides. Energy dispersive X-ray spectrometry (EDX) analysis of HZ-1-500 confirmed the presence of magnetic elements through observing two weak peaks for cobalt and iron, as seen in Figure 8c. Furthermore, inorganic elements (zinc, aluminum and oxygen) were also observed by sharp peaks in Figure 8c.

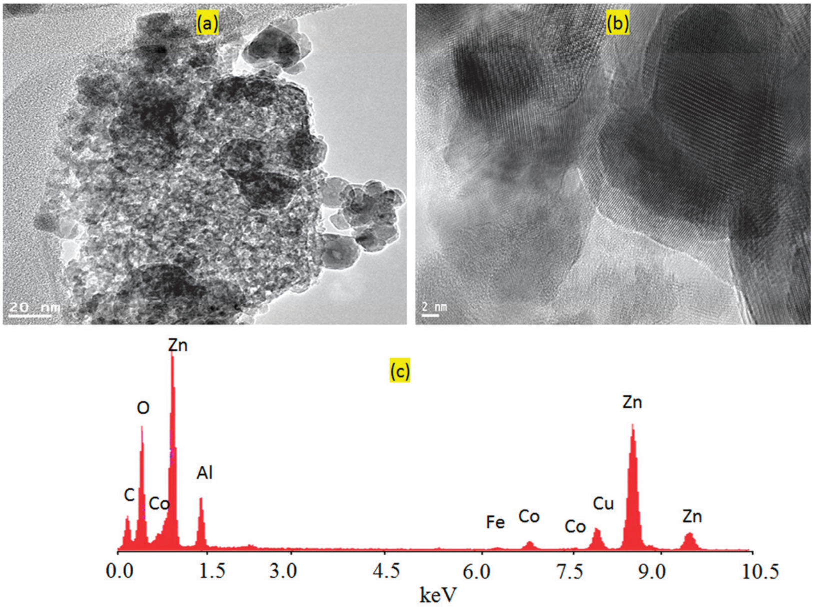

Figure 8. TEM images and EDX of HZ-1-500: (**a**) 20 nm, (**b**) 2 nm, and (**c**) EDX spectrum.

According to the results of XRD and the images of TEM in addition to SEM-EDX analysis, the zinc oxide nanohybrids were produced from the thermal decomposition of the inorganic-magnetic-organic nanohybrid, as shown in Figure 9.

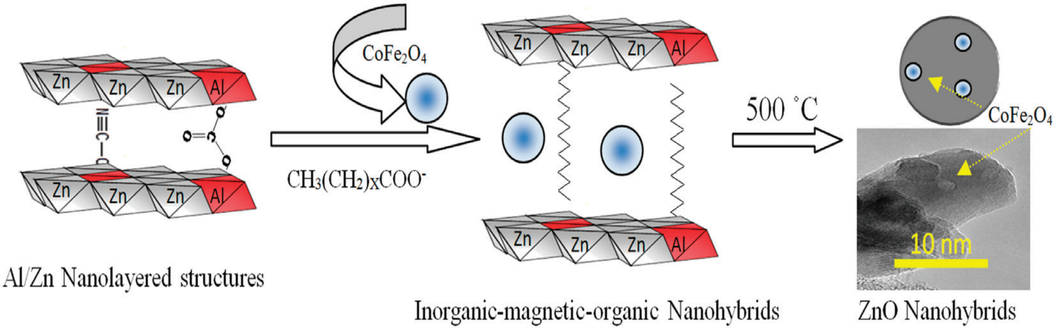

Figure 9. Schematic representation of zinc oxide nanohybrids based on inorganic-magnetic-organic nanohybrids.

Figure 9 shows a schematic representation for transforming the inorganic-magnetic-organic nanohybrid to zinc oxides nanohybrids. It indicates that the presence of the magnetic nanoparticles of cobalt iron oxides nanocomposite among the nanolayers of Al/Zn gave a good chance for incorporation of cobalt iron oxides nanocomposite with the nanoparticles of the Al-doped ZnO, which was produced during the thermal decomposition of organic species. This combination, which happened during the crystallization process of zinc oxide, created new optical active sites for HZ-1-500. According to the similarity between the results of XRD, FIIR, and thermal analyses of both nanohybrids HZ-1 and HZ-2, a similar process happened to produce HZ-2-500.

3.4. Optical Properties

Zinc oxide is familiar for the researchers in the field of optical application as one of the most famous photo-active materials. However, its optical applications are concentrated in the UV-region. Therefore, many studies were published in literature for developing the structure and the morphology of zinc oxide to advance its optical behavior through increasing the range of its absorbance and decreasing its band gap energy

In this way, the optical absorbance and the band gap energy of the prepared nanohybrids were studied and compared by using the UV-Vis absorption technique which considers one of the main means for giving significant details about their optical properties. Figure 10 shows the UV-Vis absorbance of ZOA-500, HZ-1-500, and HZ-2-500 in addition to their band gap energy. Figure 10a indicates that ZOA-500 is active in the UV region because it has absorption in the range of wavelengths of 200–350 nm. At the same time, there is no absorption in the visible region above 400 nm. By modifying the structure of ZOA-500 through building nanohybrid with magnetic nanocomposites and n-capric acid, the optical properties of HZ-1-500 improved, as shown in Figure 10b. A new absorbance band was observed in the visible region at 630 nm. At the same time, the absorbance edge shifted to higher wavelength at 700 nm. This positive effect was also observed for HZ-2-500, as shown in Figure 10c. Figure 10c shows clear absorbance for HZ-2-500, starting from 700 nm to 200 nm with two maxima at 600 nm and 350 nm. It means that the intercalation of magnetic nanoparticles inside the interlayered space of the nanohybrid led to good and ordered dispersion inside the structure of zinc oxide, in addition to creating new optical active centers for ZnO after calcination.

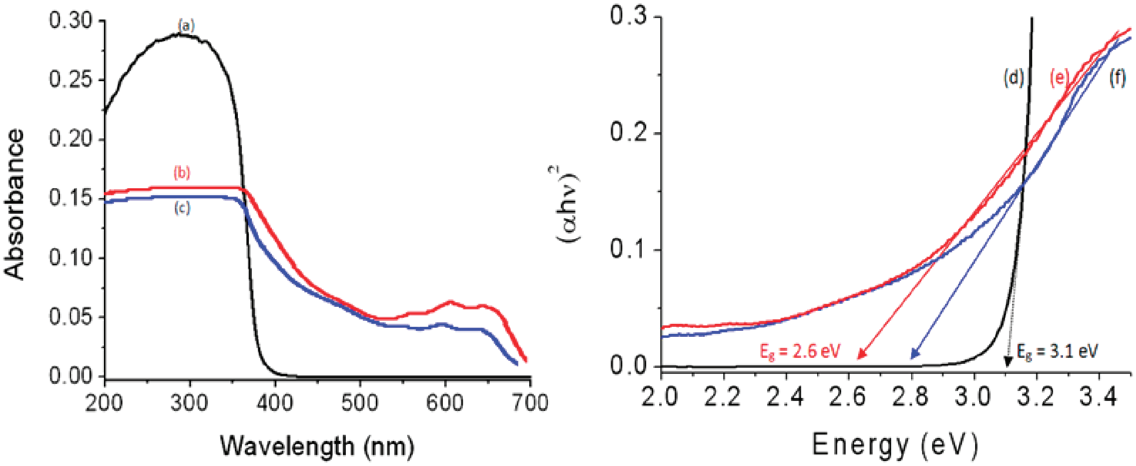

Figure 10. UV-Vis absorbance of: (**a**) ZOA-500, (**b**) HZ-1-500, (**c**) HZ-2-500, and band gap energy of (**d**) ZOA-500, (**e**) HZ-1-500, and (**f**) HZ-2-500.

These results were confirmed by calculating their optical band gap energies. The band gap energy was determined through plotting the relation $(\alpha h\nu)^2$ against energy ($h\nu$), as seen in Figure 10d–f. The band gap energy E_g of ZOA was calculated by drawing the tangent to the axis of energy to determine the optical band gap energy at $(\alpha h\nu)^2$ of 0. It showed 3.10 eV indicating a little shift from the band gap of pure ZnO because of the doping of aluminum inside the zinc oxide structure [7]. In the case of HZ-1-500, a large change was observed for the band gap energy because Figure 10e shows 2.60 eV. This strong effect of the nanohybrid structure was also observed for HZ-2-500 as shown in Figure 10f. Figure 10f revealed the narrowing of the band gap energy for HZ-2-500 to be 2.79 eV. The comparison with the pure zinc oxide showed strong narrowing for band gap energy because the reduction was from 3.30 eV to 2.60 and 2.79 eV for both the nanohybrids, indicating that the inorganic–magnetic-organic nanohybrids have a strong positive effect on the optical properties of zinc oxide.

3.5. Optical Activity

It is known that the improvement of the optical properties of the products of zinc oxides leads to positive effects for their photo activities. In order to indicate these positive effects, the prepared products have been used as photocatalysts to be appropriate means for increasing the photocatalytic activity of zinc oxide to decompose and remove pollutants by sunlight in short time. In this way, the green dye of naphthol green B was used to be specimen for industrial pollutants. The photo activities of zinc oxides (doped or undoped), and their products based on the nanohybrids structure were studied through photocatalytic degradation of naphthol green B. By measuring the absorbance of the liquid portion after exposure of the green solution of dyes to the sunlight for few minutes in the presence of the one of the prepared photocatalyst, the degradation of the main structure of the pollutant was observed through decreasing the intensity of the absorbance band at a wavelength of 714 nm, as seen in Figure 11a,b. At the same time, the reduction of the intensity of the absorption peaks at 322 nm, 280 nm, and 230 nm indicated the degradation of the naphthyl rings in the dye.

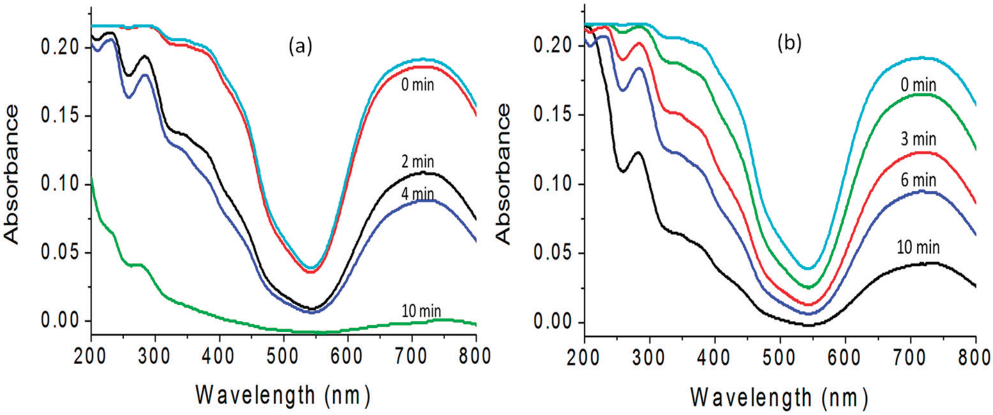

Figure 11. Photocatalytic degradation of naphthol green B in sunlight by: (**a**) HZ-1-500 and (**b**) HZ-2-500.

This blank experiment, which was performed without a photocatalyst, indicated the high stability of naphthol green B in sunlight. The photocatalytic degradation of the green dye was studied as a function of the time of sunlight exposure in the presence of the photocatalyst, as seen in Figure 11. When the aqueous solution of naphthol green B was mixed with the photocatalyst for 10 min in the dark, an appropriate change was observed, indicating that these photocatalysts have low adsorption power. For reference, it was used as 0 min irradiation.

Figure 11a showed the photo catalytic degradation of NGB under sunlight in the presence of HZ-1-500. By increasing the irradiation time, the photocatalytic degradation of naphthol green B increased. After 10 min of sunlight exposure, the green color was completely removed, indicating high activity for HZ-1-500. In the case of using HZ-2-500, the activity became lower, as shown in Figure 11b. The photocatalytic degradation of naphthol green B was arrived to 78% after 10 min of sunlight irradiation time. It means that the nanohybrid HZ-2-00 needs more than 10 min to completely remove the colored pollutant. It means that the nanohybrid HZ-1-500 is active and effective in sunlight because it completely destroyed the green dye at shorter time.

The high performance of the zinc oxide nanohybrids HZ-1-500 and HZ-2-500 was clear after comparison with the ZOA-500 and the pure zinc oxide. Where the complete removal of the green dye happened after 360 min of solar energy in presence of ZOA-500, in the case of the pure zinc oxide, the complete removal of the green dyes was achieved after 840 min of sunlight irradiation time. It means that the zinc oxide nanohybrids became very active in sunlight. In order to indicate the effect of the organic species on the optical activity, the kinetics of photocatalytic decolorization and degradation of naphthol green B were studied for both HZ-1-500 and HZ-2-500 through the next relation:

$$\ln([C_o]/[C]) = k \times t \tag{1}$$

The concentration of naphthol green B at certain times is coded as [C]. In the case of $[C_o]$, it represents the concentration of naphthol green B at t = 0. The rate reaction constant is k. To determine kinetically the type of reactions, $\ln([C_o]/[C]$ was plotted in Y-axis against the irradiation time in minutes on the X-axis.

Figure 12 shows a straight line indicating pseudo-first-order reactions for the reactions of photocatalytic degradation and decolorization of naphthol green B in the case of using both HZ-1-500 and HZ-2-500.

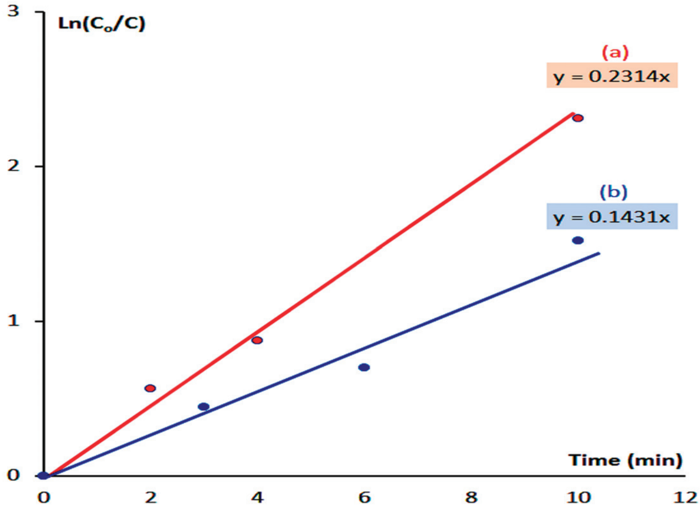

Figure 12. Kinetics study of the photocatalytic degradation of naphthol green B in sunlight by: (**a**) HZ-1-500 and (**b**) HZ-2-500.

Figure 12b shows that the photo activity of HZ-2-500 led to the rate reaction constant of the photocatalytic degradation of naphthol green B in 0.143 min^{-1}. By using HZ-1-500, Figure 12a indicates that the rate reaction constant increased to 0.294 min^{-1}. The kinetics study concluded that the rate of photocatalytic degradation of naphthol green B in the presence of HZ-1-500 increased to be higher than that of HZ-2-500. It means that the low band gap of HZ-1-500 accelerated the photocatalytic degradation of naphthol green B. In addition, the zinc oxide nanohybrid, which was based on pure nanohybrid HZ-1 is better than the zinc oxide nanohybrid, which was produced from mixed phases between nanohybrid and nanolayered LDH.

3.6. Discussion

The fast photocatalytic degradation of the green dyes in sunlight showed the excellent activity of the prepared zinc oxide nanohybrid HZ-1-500 which was produced from inorganic-magnetic-organic nanohybrids. The high performance of HZ-1-500 can be explained through the novel approach for building the nanohybrid structure of HZ-1-500. The intercalation of the fine nanoparticles of $CoFe_2O_4$ nanocomposite among the nanolayers of Al/Zn created a good chance for incorporation of this nanocomposite with zinc oxide structures during the crystallization process. Therefore, HZ-1-500 has a good crystalline structure for zinc oxide and there are no peaks for aluminum or cobalt iron oxides. This good incorporation of $CoFe_2O_4$ nanocomposite with the crystals of zinc oxide partially failed for the sample HZ-2-500 because XRD results showed two mixed phases: nanolayered structure and nanohybrid. It means that the nanoparticles of $CoFe_2O_4$ nanocomposite could intercalate among the nanolayers of Al/Zn for part of the nanohybrid and support on the external surface of the plates of the nanolayered structure of Al/Zn. The good incorporation of $CoFe_2O_4$ nanocomposite with the crystals of zinc oxide which doped with aluminum created new optical active centers inside zinc oxide nanohybrid HZ-1-500 and caused reduction for its band gap energy to be very effective in sunlight because of the low band gap energy of $CoFe_2O_4$ (1.32 eV) [43]. At the same time, some sites of Zn in zinc oxide are occupied by CoFe2O4 atoms, producing new optical active centers called shallow traps between the valance band and conduction band, leading to decreasing for the band gap energy [1,44].

This low band gap energy and the small size of the nanoparticles of the zinc oxide nanohybrid HZ-1-500 have a strong effect on the mechanism of the photocatalytic degradation process of the green dyes. The mechanism of the photocatalytic degradation process is controlled by two critical reactions.

$$\text{Photocatalyst} + h\nu \rightarrow h^{+}(\text{valance band}) + e^{-}(\text{conduction band}) \tag{2}$$

$$\text{Holes } (h^{+}) + H_2O \rightarrow H^{+} + {}^{\bullet}OH \text{ (free radicals)} \tag{3}$$

$$\text{Electrons } (e^{-}) + O_2 \rightarrow {}^{\bullet}O_2{}^{-} \tag{4}$$

The first one depends on the amount of energy which was absorbed by the photocatalyst as seen in the Reaction (2). The second reaction is the movement and separation of light-induced electrons-holes, as shown in the Reactions (3) and (4). The photo-generated holes, which produced in the conduction band, react with the water molecules to produce highly oxidizing agents free radicals of hydroxyl groups ($^{\bullet}OH$). At the same time, the photo-generated electrons attack the oxygen molecules, which are adsorbed on the surface of the photocatalyst or dissolved in water to produce strong oxidizing agents superoxide radical anion ($^{\bullet}O_2{}^{-}$).

In the presence of green dyes, the molecules of NGB adsorbed on the surface of the nanoparticles of zinc oxide nanohybrid. The HZ-1-500 accelerated the first reaction in sunlight to become excited because it has absorbance from the wavelength 700 nm to 200 nm, in addition to low band gap energy as shown in the following Reaction (5).

$$\text{HZ-NGB}^{*} \text{ (sunlight)} \rightarrow \text{HZ} + \text{NGB}^{+} \text{ intermediates} + \text{electrons } (e^{-}) \tag{5}$$

$$\text{Electrons } (e^{-}) + O_2 \rightarrow {}^{\bullet}O_2{}^{-} \tag{6}$$

$$\text{NGB+ intermediates} + {}^{\bullet}O_2{}^{-} \rightarrow \text{Degradation compounds} + CO_2 + H_2O \tag{7}$$

The band gap of HZ-1-500 is not very small to accelerate the recombination reactions in addition to the shallow traps which help for separating between electrons and holes. Therefore, the degradation reaction continues as shown in Equations (6) and (7). By this way, the colored pollutants disappeared after ten minutes of sunlight exposure. For testing the re-use of the optimum sample, the photocatalytic degradation of HZ-1-500 was repeated two times for the fresh sample of the green dye. The same results were observed after 10 min of sunlight exposure, indicating high recyclability of the photocatalyst.

4. Conclusions

In the present study, a dual-aim was achieved for designing zinc oxide nanohybrids to be useful and effective for purifying water in sunlight. This aim focused on a new approach for building inorganic-magnetic-organic nanohybrids and producing effective zinc oxide nanohybrids in sunlight. In this line, two nanohybrids were prepared through expanding the nanolayered structures of Al/Zn by intercalating long chains of hydrocarbons of fatty acids such as n-capric and stearic acid to facilitate the insertion of very fine nanoparticles of cobalt iron oxides among the nanolayers of Al/Zn. The characterization techniques showed that the prepared inorganic-magnetic-organic nanohybrids were useful for producing zinc oxide nanohybrids by thermal treatment. By measuring the optical properties, a clear reduction of band gap energy was observed for the prepared zinc oxide nanohybrids compared with the doped and undoped zinc oxide. This reduction of band gap energy from 3.20 eV to 2.60 eV led to high activity for the prepared zinc oxide nanohybrids in sunlight.

This high activity was proven by a complete removal of naphthol green B after 10 min of sunlight exposure in presence of the prepared zinc oxide nanohybrids. These results were confirmed by the comparison with the pure and doped zinc oxide which indicated that the pure and doped zinc oxide removed the green dyes after 360–840 min of sunlight exposure. Furthermore, the kinetic study showed that the zinc oxide nanohybrid, which was based on the pure nanohybrid, is better than the zinc oxide nanohybrid, which was produced from mixed phases between the nanohybrid and nanolayered LDH. Finally, it can be concluded that this new approach for designing photoactive nanohybrids led to positive tools for facing energy- and water-related problems through using renewable and non-polluting energy for purifying water.

Author Contributions: Conceptualization, O.S.; methodology, O.S. and A.O.; software, A.A. and N.M.S.; validation, O.S. and A.O.; formal analysis, O.S. and A.O.; investigation, O.S., A.A., N.M.S., and D.O.; resources, O.S.; data curation, O.S., A.O., and D.O.; writing—original draft preparation, O.S., A.O., and D.O.; writing—review and editing, O.S., A.A., and N.M.S.; visualization, A.O.; supervision, O.S. and A.A.; project administration, O.S.; funding acquisition, O.S. All authors have read and agreed to the published version of the manuscript.

Funding: This research was funded by the Deanship of Scientific Research in King Faisal University (Saudi Arabia), grant number AN000133, and the APC was funded by the same grant number AN000133.

Institutional Review Board Statement: Not applicable.

Informed Consent Statement: Not applicable.

Data Availability Statement: Data available in a publicly accessible repository.

Acknowledgments: The authors acknowledge the Deanship of Scientific Research at King Faisal University for the financial support under the Research Annual Track (Grant No. AN000133).

Conflicts of Interest: The authors declare no conflict of interest.

References

1. Saber, O.; Kotb, H.M.; Osama, M.; Khater, H.A. An Effective Photocatalytic Degradation of Industrial Pollutants through Converting Titanium Oxide to Magnetic Nanotubes and Hollow Nanorods by Kirkendall Effect. *Nanomaterials* **2022**, *12*, 440. [CrossRef] [PubMed]
2. Saber, O.; Shaalan, N.M.; Ahmed, F.; Kumar, S.; Alshoaibi, A. One-Step Multi-Doping Process for Producing Effective Zinc Oxide Nanofibers to Remove Industrial Pollutants Using Sunlight. *Crystals* **2021**, *11*, 1268. [CrossRef]
3. Alshoaibi, A.; Saber, O.; Ahmed, F. Enhancement of Optical Activity and Properties of Barium Titanium Oxides to Be Active in Sunlight through Using Hollandite Phase Instead of Perovskite Phase. *Crystals* **2021**, *11*, 550. [CrossRef]
4. Saber, O.; Alshoaibi, A.; Al-Yaari, M.; Osama, M. Conversion of Non-Optical Material to Photo-Active Nanocomposites through Non-Conventional Techniques for Water Purification by Solar Energy. *Molecules* **2020**, *25*, 4484. [CrossRef]
5. Saber, O.; Kotb, H.M. Designing Dual-Function Nanostructures for Water Purification in Sunlight. *Appl. Sci.* **2020**, *10*, 1786. [CrossRef]

6. Saber, O.; Aljaafari, A.; Osama, M.; Alabdulgader, H. Accelerating the Photocatalytic Degradation of Green Dye Pollutants by Using a New Coating Technique for Carbon Nanotubes with Nanolayered Structures and Nanocomposites. *ChemistryOpen* **2018**, *7*, 833–841. [CrossRef]
7. Saber, O.; Alomair, H.; Abu-Abdeen, M.; Aljaafari, A. Fast degradation of green pollutants through nanonets and nanofibers of the Al-doped zinc oxide. *Acta Metall. Sin. (Engl. Lett.)* **2018**, *31*, 533–546. [CrossRef]
8. Fujishima, A.; Honda, K. Electrochemical Photolysis of Water at a Semiconductor Electrode. *Nature* **1972**, *238*, 37–38. [CrossRef]
9. Gui, M.S.; Zhang, W.D. Preparation and modification of hierarchical nanostructured Bi_2WO_6 with high visible light-induced photocatalytic activity. *Nanotechnology* **2011**, *22*, 265601. [CrossRef]
10. Chen, X.B.; Liu, L.; Yu, P.Y.; Mao, S.S. Increasing solar absorption for photocatalysis with black hydrogenated titanium dioxide nanocrystals. *Science* **2011**, *331*, 746–750. [CrossRef]
11. Dindar, B.; Icli, S. Unusual photoreactivity of ZnO under concentrated sun light. *J. Photochem. Photobiol. A Chem.* **2001**, *140*, 263–268. [CrossRef]
12. Yeber, M.C.; Roderiguez, J.; Freer, J.; Baeza, J.; Duran, N.; Mansilla, H.D. Advanced oxidation of a pulp mill bleaching wastewater. *Chemosphere* **1999**, *39*, 1679–1688. [CrossRef]
13. Behnajady, M.A.; Modirshahla, N.; Hamzavi, R. Kinetic study on photocatalytic degradation of C.I. Acid Yellow 23 by ZnO photocatalyst. *J. Hazard. Mater. B* **2006**, *133*, 226–232. [CrossRef] [PubMed]
14. Sun, J.H.; Dong, S.Y.; Wang, Y.K.; Sun, S.P. Preparation and photocatalytic property of a novel dumbbell-shaped ZnO microcrystal photocatalyst. *J. Hazard. Mater.* **2009**, *172*, 1520–1526. [CrossRef]
15. Wang, Q.; Tang, C.; Jiang, C.; Du, D.; Wang, F.; Song, J. Role of Substrate Roughness in ZnO Nanowire Arrays Growth by Hydrothermal Approach. *Acta Metall. Sin. Engl. Lett.* **2016**, *29*, 237–242. [CrossRef]
16. Zhou, W.; Li, X.; Qin, L.; Kang, S. Facile Preparation of Ag_2ZnGeO_4 Flower-like Hierarchical Nanostructure and Its Photocatalytic Activity. *J. Mater. Sci. Technol.* **2017**, *33*, 47–51. [CrossRef]
17. Liu, C.; Xu, H.; Wang, L.; Qin, X. Facile One-Pot Green Synthesis and Antibacterial Activities of GO/Ag Nanocomposites. *Acta Metall. Sin. Engl. Lett.* **2017**, *30*, 36–44. [CrossRef]
18. Bai, X.; Wang, L.; Zong, R.; Lv, Y.; Sun, Y.; Zhu, Y. Performance enhancement of ZnO photocatalyst via synergic effect of surface oxygen defect and graphene hybridization. *Langmuir* **2013**, *29*, 3097–3105. [CrossRef]
19. Leung, Y.; Chen, X.; Ng, A.; Guo, M.; Liu, F.; Djurisic, A.; Chan, W.; Shi, X.; Van Hove, M. Green emission in ZnO nanostructures—Examination of the roles of oxygen and zinc vacancies. *Appl. Surf. Sci.* **2013**, *271*, 202–209. [CrossRef]
20. Wojnarowicz, J.; Chudoba, T.; Koltsov, I.; Gierlotka, S.; Dworakowska, S.; Lojkowski, W. Size control mechanism of ZnO nanoparticles obtained in microwave solvothermal synthesis. *Nanotechnology* **2019**, *29*, 06561. [CrossRef]
21. Pimentel, A.; Ferreira, S.H.; Nunes, D.; Calmeiro, T.; Martins, R.; Fortunato, E. Microwave Synthesized ZnO Nanorod Arrays for UV Sensors: A Seed Layer Annealing Temperature Study. *Materials* **2016**, *9*, 299. [CrossRef] [PubMed]
22. Samadipakchin, P.; Mortaheb, H.R.; Zolfaghari, A. ZnO nanotubes: Preparation and photocatalytic performance evaluation. *J. Photochem. Photobiol. A Chem.* **2017**, *337*, 91. [CrossRef]
23. Zhang, Y.; Ram, M.K.; Stefanakos, E.K.; Goswami, Y.D. Synthesis, Characterization, and Applications of ZnO Nanowires. *J. Nanomaterials* **2012**, *12*, 624520. [CrossRef]
24. Diguna, L.J.; Fitriani, A.D.; Liasari, B.R.; Timuda, G.E.; Widayatno, W.B.; Wismogroho, A.S.; Zeng, S.; Birowosuto, M.D.; Amal, M.I. Optical and Photodetection Properties of ZnO Nanoparticles Recovered from Zn Dross. *Crystals* **2021**, *11*, 6. [CrossRef]
25. Chen, H.; Zhao, L.; He, X.; Wang, G.; Wang, X.; Fang, W.; Du, X. In situ Formed Fan-Shaped Nanowires in Biomorphic SiO_2: A Multidimensional Composite of Hierarchical Porous Material and Organic Pollutant Adsorption Behavior. *Acta Metall. Sin. Engl. Lett.* **2017**, *30*, 104–112. [CrossRef]
26. Zhong, J.B.; Li, J.Z.; He, X.Y.; Zeng, J.; Lu, Y.; Hu, W.; Lin, K. Improved Photocatalytic Performance of Pd-Doped ZnO. *Curr. Appl. Phys.* **2012**, *12*, 998–1001. [CrossRef]
27. Sin, J.; Lam, S.; Lee, K.; Mohamed, A. Preparation and photocatalytic properties of visible light-driven samarium-doped ZnO nanorods. *Ceram. Int.* **2013**, *39*, 5833–5843. [CrossRef]
28. Ahmad, M.; Ahmed, E.; Zhang, Y.; Khalid, N.R.; Xu, J.; Ullah, M.; Hong, Z. Preparation of Highly Efficient Al-Doped ZnO Photocatalyst by Combustion Synthesis. *Curr. Appl. Phys.* **2013**, *13*, 697–704. [CrossRef]
29. Huang, L.; Ren, N.; Li, B.; Zhou, M. Effect of Annealing on the Morphology, Structure and Photoelectric Properties of AZO/Pt/FTO Trilayer Films. *Acta Metall. Sin. Engl. Lett.* **2015**, *28*, 281–288. [CrossRef]
30. Haja sheriff, M.H.; Murugan, S.; Manivasaham, A.; Ashok Kumar, R. Electro spray technique to enhance the physical property of Sulphur doped zinc oxide thin film. *Mater. Today Proc.* **2021**, *47*, 1717–1723. [CrossRef]
31. Riaz, A.; Ashraf, A.; Taimoor, H.; Javed, S.; Akram, M.A.; Islam, M.; Mujahid, M.; Ahmad, I.; Saeed, K. Photocatalytic and Photostability Behavior of Ag- and/or Al- Doped ZnO Films in Methylene Blue and Rhodamine B Under UV-C Irradiation. *Coatings* **2019**, *9*, 202. [CrossRef]
32. Lavand, A.B.; Malghe, Y.S. Synthesis, characterization and visible light photocatalytic activity of nitrogen-doped zinc oxide nanospheres. *J. Asian Ceram. Soc.* **2018**, *3*, 305–310. [CrossRef]
33. Hamrouni, S.; AlKhalifah, M.S.; El-Bana, M.S.; Zobaidi, S.K.; Belgacem, S. Deposition and characterization of spin-coated n-type ZnO thin film for potential window layer of solar cell. *Appl. Phys. A* **2018**, *124*, 555. [CrossRef]

34. Farrag, A.A.-G.; Balboul, M.R. Nano ZnO thin films synthesis by sol–gel spin coating method as a transparent layer for solar cell applications. *J. Sol-Gel Sci. Technol.* **2016**, *82*, 269–279. [CrossRef]
35. Yan, X.; Venkataraj, S.; Aberle, A.G. Wet-Chemical Surface Texturing of Sputter-Deposited ZnO: Al Films as Front Electrode for Thin-Film Silicon Solar Cells. *Int. J. Photoenergy* **2015**, *2015*, 548984. [CrossRef]
36. Islam, M.R.; Rahman, M.; Farhad, S.F.U.; Podder, J. Structural, optical and photocatalysis properties of sol–gel deposited Al-doped ZnO thin films. *Surf. Interfaces* **2019**, *16*, 120–126. [CrossRef]
37. Mahdavi, R.; Talesh, S.S.A. Sol-gel synthesis, structural and enhanced photocatalytic performance of Al doped ZnO nanoparticles. *Adv. Powder Technol.* **2017**, *28*, 1418–1425. [CrossRef]
38. Aydın, C.; AbdEl-sadek, M.S.; Zheng, K.; Yahia, I.S.; Yakuphanoglu, F. Synthesis, diffused reflectance and electrical properties of nanocrystalline Fe-doped ZnO via sol–gel calcination technique. *Opt. Laser Technol.* **2013**, *48*, 447–452. [CrossRef]
39. Ravichandran, K.; Sindhuja, E.; Uma, R.; Arun, T. Photocatalytic efficacy of ZnO films light intensity and thickness effects. *Surf. Eng.* **2017**, *33*, 512–520. [CrossRef]
40. Nassar, M.Y.; Mohamed, T.Y.; Ahmed, I.S.; Mohamed, N.M.; Khatab, M. Hydrothermally Synthesized Co_3O_4, α-Fe_2O_3, and $CoFe_2O_4$ Nanostructures: Efficient Nano-adsorbents for the Removal of Orange G Textile Dye from Aqueous Media. *J. Inorg. Organomet. Polym. Mater.* **2017**, *27*, 1526–1537. [CrossRef]
41. Thomas, B.; Alexander, L.K. Enhanced synergetic effect of Cr(VI) ion removal and anionic dye degradation with superparamagnetic cobalt ferrite meso–macroporous nanospheres. *Appl. Nanosci.* **2018**, *8*, 125–135. [CrossRef]
42. Hassani, A.; Eghbali, P.; Ekicibil, A.; Metin, Ö. Monodisperse cobalt ferrite nanoparticles assembled on mesoporous graphitic carbon nitride ($CoFe_2O_4$/mpg-C_3N_4): A magnetically recoverable nanocomposite for the photocatalytic degradation of organic dyes. *J. Magn. Magn. Mater.* **2018**, *456*, 400–412. [CrossRef]
43. Parhizkar, J.; Habibi, M. Hossein Investigation and Comparison of Cobalt ferrite composite nanoparticles with individual Iron oxide and Cobalt oxide nanoparticles in azo dyes removal. *J. Water Environ. Nanotechnol.* **2019**, *4*, 17–30.
44. Singh, A.P.; Kumari, S.; Shrivastav, R.; Dass, S.; Satsangi, V.R. Iron doped nanostructured TiO_2 for photoelectrochemical generation of hydrogen. *Int. J. Hydrogen Energy* **2008**, *33*, 5363–5368. [CrossRef]

nanomaterials

Article

Effect of Voidage on the Collapsing Bed Dynamics of Fine Particles: A Detailed Region-Wise Study

Syed Sadiq Ali [1], Agus Arsad [2], Kenneth L. Roberts [3] and Mohammad Asif [4,*]

[1] School of Chemical and Energy Engineering, Faculty of Engineering, Universiti Teknologi Malaysia, Johor Bahru 81310, Johor, Malaysia; sadiq.chem179@gmail.com
[2] UTM-MPRC Institute for Oil and Gas, School of Chemical and Energy Engineering, Faculty of Engineering, Universiti Teknologi Malaysia, Johor Bahru 81310, Johor, Malaysia; agus@utm.my
[3] Chemical Engineering Department, College of Engineering and Computing, University of South Carolina, Columbia, SC 29208, USA; ROBERTS0@mailbox.sc.edu
[4] Department of Chemical Engineering, King Saud University, P.O. Box 800, Riyadh 11421, Saudi Arabia
* Correspondence: masif@ksu.edu.sa; Tel.: +96-6114676849

Abstract: Bed collapse experiments provide vital information about fluidized bed hydrodynamics. In this study, the region-wise bed collapse dynamics of glass beads, titania (TiO_2), and hydrophilic nanosilica (SiO_2) particles with widely different voidages (ε) of 0.38, 0.80, and 0.98, respectively, were carefully investigated. These particles belonged to different Geldart groups and exhibited varied hysteresis phenomena and fluidization indices. The local collapse dynamics in the lower, lower-middle, upper-middle, and upper regions were carefully monitored in addition to the distributor pressure drop to obtain greater insight into the deaeration behavior of the bed. While the collapse dynamics of glass beads revealed high bed homogeneity, the upper middle region controlled the collapse process in the case of titania due to the size-based segregation along the bed height. The segregation behavior was very strong for nanosilica, with the slow settling fine agglomerates in the upper bed regions controlling its collapse dynamics. The collapse time of the upper region was 25 times slower than that of the lower region containing mainly large agglomerates. The spectral analysis confirmed the trend that was observed in the pressure transients. The clear presence of high frequency events at 20 and 40 Hz was observed in the nanosilica due to agglomerate movements. The residual air exiting the plenum was strongly affected by the bed voidage, being lowest for the nanosilica and highest for the glass beads.

Keywords: fluidization; collapse bed; hydrodynamics; bed voidage; purge flow; nanosilica

Citation: Ali, S.S.; Arsad, A.; Roberts, K.L.; Asif, M. Effect of Voidage on the Collapsing Bed Dynamics of Fine Particles: A Detailed Region-Wise Study. *Nanomaterials* **2022**, *12*, 2019. https://doi.org/10.3390/nano12122019

Academic Editors: Jihoon Lee and Ming-Yu Li

Received: 11 May 2022
Accepted: 9 June 2022
Published: 11 June 2022

1. Introduction

Fluidized beds are often preferred over packed beds due to their superior gas–solid contact, higher mass and heat transfer rates, and efficient gas–solid handling and mixing [1–6]. However, the fluidization of ultrafine and fine powders belonging to Geldart group C is difficult due to strong inter-particle forces (IPFs), which lead to severe bed non-homogeneities and poor interphase phase mixing [7–16]. The fluidization of ultrafine nanoparticles can either display agglomerate particulate fluidization (APF) or agglomerate bubbling fluidization (ABF) owing to the large agglomerate formation as a result of the IPFs. Whereas a high minimum fluidization velocity and a low bed expansion are observed in ABF, uniform particulate fluidization is the main characteristic of APF [2,17–23]. Moreover, the fluidization of ultrafine powders often exhibits the size segregation of agglomerates along the length of the bed. For example, in one case, the ABF behavior of nanosilica led to size-based stratification along the bed height such that agglomerates present in the lower bed region were five to ten times larger than those present in the upper layer [24]. In some cases, agglomerates as large as 2000 µm were found in the lower layer, which were almost ten times larger than those in the upper layer [3]. In view of these challenges, an efficient design and the successful large-scale operation of fluidized beds require a detailed understanding of their hydrodynamics.

An important tool for analyzing the fluidized bed hydrodynamics is the collapse bed study, which can provide meaningful insight into the bed's dynamic behavior. The fluid flow is instantly stopped in a steady fluidized bed, and the solid particles are allowed free fall under gravity, until the bed attains complete rest [22,25–30]. During the first phase of the collapse process, the residual air escapes as bubbles followed by the free fall of the particles. As the particles settle, a stationary layer develops at the bottom, and a dense phase, with moving particles, simultaneously sediments at the top of the layer. The interface of the stationary layer appears to move upwards, while the upper meniscus of the dense phase moves downwards until both coincide to a single surface, thereby marking the end of the collapse process. The pressure gradient gradually reaches zero as the bed attains complete rest [25,31]. The collapse phases are controlled by the IPFs, drag force, and gravitational force, which makes the collapse process an important tool for identifying the dominant forces in the bed.

By monitoring the local pressure drop transients, Asif and Ali [22] noted the occurrence of three prominent events characterizing three different phases of the collapse process. In the first phase, the bed fell rapidly until the pressure transient became zero. With the negative drag increasing with the downward fall of the particles, the pressure drop kept on decreasing, ultimately reaching a maximum negative value marked as the occurrence of the second event. The pressure drop then gradually increased again to a zero value, marking the third event and signaling the end of the collapse process. The bed height declined rapidly in the first phase, while slow solid particle settling occurred in the second phase. The bed height remained stationary in the third phase. The authors compared the time periods of all the phases by varying the initial fluid velocity and found that the total bed settling time did not depend upon the initial superficial velocity. A mathematical model of the bed collapse, proposed Nie and Liu [25], which successfully predicted the height of the interfaces and the pressure drop at different locations along the height of the bed, was used to predict the agglomerate diameter in a collapsing bed of nanosilica [32]. Another work used collapse bed experiments to study the effect of pre-mixing the nanosilica with inert Geldart group A particles as an aid for enhancing the fluidization quality [28].

The deaeration of the residual air during the collapse process critically governs the collapse process. The residual air moves upward during a bed collapse in a conventional fluidized bed [22,28,29,31,33]. However, other deaeration strategies have also been suggested in the literature [24,26,34,35]. Santos et al. [36] added a vent below the fluidized bed, which was active only during the collapse process, and termed this configuration as a double drainage arrangement. Both single (conventional) and double drainage configurations were used with FCC catalysts by the authors. The duration of the bed collapse was substantially lower for the double drainage configuration compared to that of the single drainage deaeration. Owing to the downward movement of the residual air, a negative pressure drop was prominently observed in the lower bed regions for the double drainage configuration. Cherntongchai, Innan [34] also used a modified air passage configuration and proposed a mathematical model for calculating the dense phase voidage and the solid velocity [35]. Lorences, Patience [26] used single drainage, double drainage, and zero drainage configurations to study the collapse dynamics of mixtures of VPO and FCC catalyst particles of different size distributions. While the deaeration durations were identical for the zero and single drainage configurations, shorter deaeration occurred when the double drainage configuration was used. The initial velocity did not affect the collapse process in the author's research. Ali et al. [24] studied the collapse of a pulsed flow fluidized bed using three different flow strategies, namely single drainage, dual drainage, and modified dual drainage. The square-wave flow pulsations were introduced using a solenoid valve. The modified dual drainage eliminated the initial flow spike at the beginning of the flow when the solenoid valve opened. This strategy reduced the size-based segregation of the nano-agglomerates and resulted in a smoother and faster bed collapse.

While the investigation of the collapse dynamics in the past mainly focused on the effect of the drainage configuration for the deaeration of the residual gas [24,26,34], the particle classification [17], and the fluidization assistance [27,29], there has not been any focused study on the effect of agglomeration induced size stratification along the bed height, which is a common occurrence in the case of the ultrafine nanoparticles. Any detailed investigation into this effect, however, requires a careful monitoring of the collapse dynamics in the different regions of the bed along its height to clearly delineate the effect of the size stratification of nano-agglomerates. For deeper insights into the collapse behavior, a comparison with other types of particles is also needed. Therefore, three different kinds of powders, viz., glass beads, titania, and ultrafine nanosilica, were selected in this study. We used hydrophilic nanosilica in this study owing to its strong agglomeration behavior that results in ABF behavior [3,24]. Apart from widely different voidages, these powders also significantly differ in their physical properties, and therefore belong to different groups of Geldart's classification [15]. Note that commercial grade nanosilica and titania find large-scale applications in several industries such as the paint, catalyst manufacturing, and pharmaceutical industries [37,38]. A set of pressure transducers located along the height monitored the local collapse dynamics during the progress of the collapse process in different bed regions of the fluidized bed. The dual drainage configuration for the residual gas deaeration was used. In addition, the distributor pressure drop was also monitored to obtain a better understanding of the gas flow through the distributor during deaeration.

2. Experimental

2.1. Experimental Set Up

The experimental set up schematic is shown in Figure 1. The test section was a transparent perplex column, 1.6 m in length and 0.07 m internal diameter. A 0.3 m long plenum, beneath the test section, eliminated inlet disturbances of the fluidizing air. A perforated plate distributor with 2 mm holes in a circular pitch and 2.5% open area was used to separate the test section from the plenum section. Such a distributor design ensured uniform distribution of the inlet gases across the cross-section of the test section and eliminated the dead zones. A 0.14 m diameter and 0.3 m long disengagement section at the top of the test section helped to suppress the elutriation of particles at high fluid velocities.

The dual drainage deaeration scheme was implemented by allowing another residual air exit from the bottom of the fluidized bed during the bed collapse. This was carried out by using a normally closed 2-way solenoid valve, SV2 (Omega SV 3310, Omega, Norwalk, CT, USA), placed immediately below the plenum chamber. With the start of the collapse process, the solenoid valve was simultaneously energized, thus providing an alternate passage to the escaping residual air from the collapsing bed. As shown in Figure 1, a flow totalizer (FMA-2605A-V2, Omega, Norwalk, CT, USA) was used to measure the flow of the escaping residual air from SV2.

Several sensitive bidirectional differential pressure transducers (Omega PX163-series, Omega, Norwalk, CT, USA) with a response time of 1-ms and appropriate ranges were used in the experiment. As shown in the figure, the local pressure drop transients in the lower (ΔP_1: 0–10 cm), lower middle (ΔP_2: 10–20 cm), upper middle (ΔP_3: 20–30 cm), and upper regions (ΔP_4: >30 cm above the distributor) were monitored. The global pressure drop (ΔP_g) across the entire bed, and the distributor pressure drop (ΔP_d) across the distributor were also recorded to gain insights into the reverse flow of the exiting residual air through SV2.

A data acquisition (DAQ) system (NI-DAQ-USB-6289) was used to acquire the analog input of the pressure transducers and flow totalizer and control the solenoid valve by using digital output signal. The data sampling rate was set to 100 Hz to capture the high frequency events taking place during the bed collapse.

The segregation tendency was very strong for the nanosilica, with the slow settling of fine agglomerates in the upper bed regions controlling its collapse dynamics, which was five to six times higher than that of glass and titania under similar conditions.

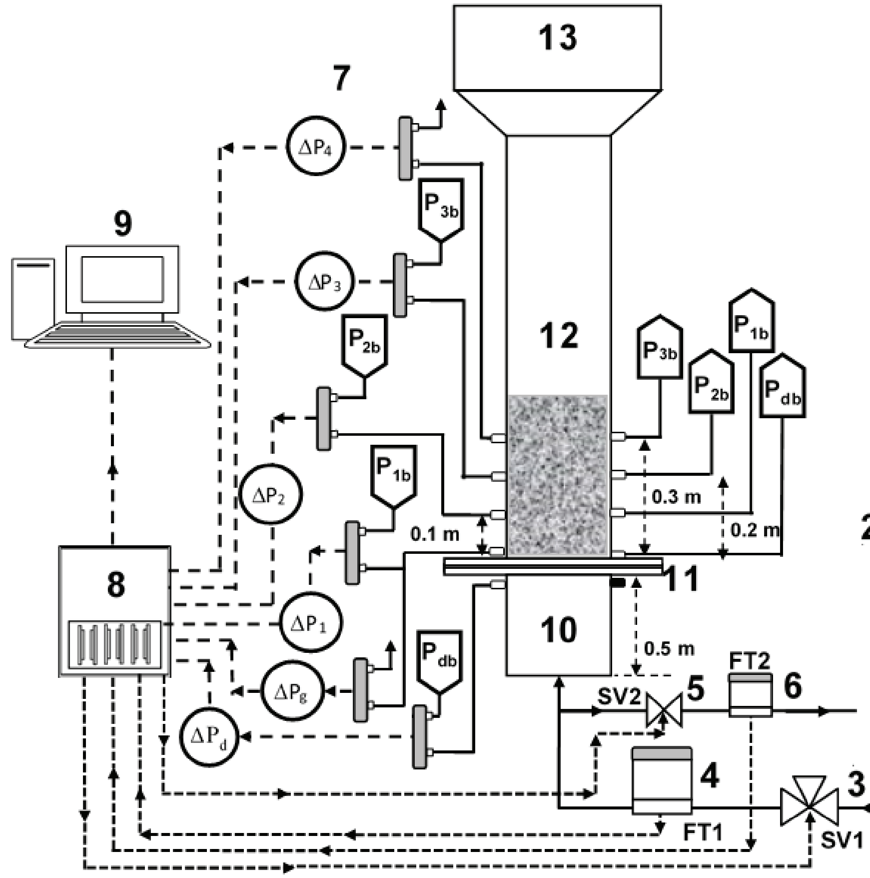

Figure 1. Experimental set-up schematic; (1) Air supply; (2) Flowmeters; (3) 3-way solenoid valve; (4) Flow totalizer; (5) 2-way solenoid valve; (6) Flow totalizer; (7) Pressure transducers; (8) Data acquisition system; (9) Computer; (10) Calming section; (11) Distributor; (12) Test section; (13) Disengagement section.

2.2. Solid Particles

Three different powders, namely glass beads, titania, and nanosilica, were used in the present work. The physical properties of the particles are listed in Table 1. We used 12 nm ultrafine hydrophilic nanosilica (Aerosil 200, Evonik GmBH, Essen, Germany) with skeletal density of 2200 kg/m^3. Its median agglomerate size was 12.5 µm (approx.), which was approximately thousand-fold larger than its primary size. The size range of titania was 0.5–90 µm. The particles' sizes were obtained using Microtrac particle size analyzer (Model S 3500, Montgomeryville, PA, USA).

Table 1. Physical properties of solid particles used in the experiments.

Powder	Particle Density (kg/m^3)	Particle Size ($\times 10^{-6}$ m)	Bulk Density (kg/m^3)	Bed Voidage(-/-)	U_{mf} ($\times 10^{-3}$ m/s)
Glass beads	2500	88–149	1547	0.38	31
TiO_2	3900	0.5–90	790	0.80	19
Nanosilica [26,39]	2200	2–100	50	0.98	30

2.3. Methodology

Two different sets of experiments were carried out. In the first set of experiments, the conventional fluidization was carried to determine the minimum fluidization velocity (U_{mf}) and fluidization quality (FI) of the different particle samples used. In the second series of experiments, the particles were fluidized at two different fluid superficial velocities (U_0) of U_{mf} and $2U_{mf}$ until the steady state fluidization was achieved, and then the airflow to the fluidization column was abruptly interrupted. The purge valve (SV2) was simultaneously opened to provide an alternate passage for residual air. Each set of experiments was performed at least twice to verify the data repeatability. To investigate the effect of height on the collapse behavior, another set of collapse experiments was carried out by adding more material in the column to raise the static bed height by 50%.

3. Results

In Section 3.1, the experimental results of the steady-state fluidization are presented for three different solid particles used in this study. The results of the bed collapse study are then considered in Section 3.2.

3.1. Conventional Fluidization

Figure 2 shows the dependence of the normalized pressure drop on the superficial velocity of the fluidization gas during the conventional fluidization experiments. The pressure drop was normalized by dividing the overall pressure drop across the entire bed $(\overline{\Delta P})$ by the effective weight of the bed

$$\overline{\Delta P} = \frac{\Delta P}{\left(\rho_b - \rho_f\right) g L} \tag{1}$$

where ρ_b, ρ_f are the bulk and fluid densities, respectively, g is the gravitational acceleration, and L is the bed length across which the pressure drop is measured. Given that the gas density is negligible, the above equation simplifies to

$$\overline{\Delta P} = \frac{\Delta P}{\left(\frac{mg}{A}\right)} \tag{2}$$

where m is the mass of the particles loaded in the bed, and A is the cross-sectional area of the bed. In the literature, the normalized pressure drop is often identified at the fluidization index since it can provide a good indication of the fluidization behavior of the powder [39]. Ideally, the fluidization index should be unity when velocity exceeds the minimum fluidization velocity, which signifies that the pressure drop across the fluidized bed should be equal to the effective bed weight.

Figure 2a shows the fluidization behavior of glass beads (size: 118 μm), which is categorized as belonging to Geldart's group A. The flow was first gradually increased up to 100 mm/s, which was more than thrice the U_{mf}. The fluidization cycle was followed by a gradual velocity decrease, thus completing the defluidization cycle. An excellent agreement between both the fluidization and defluidization cycles was clearly seen in the figure, thus indicating the absence of the hysteresis and confirming the homogeneity of the bed of glass beads.

The fluidization behavior of the titania powder is illustrated in Figure 2b. At the lowest air flow, a steep increase in the pressure drop to 0.4 was observed. However, with the further increase in the velocity, the pressure drop increase was gradual and slow before becoming almost constant at 60 mm/s. During the defluidization cycle of the experiment, a gradual velocity decrease showed smooth behavior with the pressure drop almost remaining constant as long as the velocity was greater than 40 mm/s. In this case, the hysteresis phenomenon was clearly evident as the fluidization and defluidization behaviors were significantly different. This behavior was anticipated, given that the titania powder belongs to the group C classification. Ideally, the normalized pressure drop should attain the value of unity when the bed is fully fluidized. For the fluidization of the glass beads, when $U_0 \geq 30$ mm/s, the normalized pressure drop was nearly unity ($\approx$0.92). On the contrary, the normalized pressure drop never exceeded 0.76 for the fluidization of titania. This behavior indicates the presence of non-homogeneities caused by the channeling and rat-holes through which the gas bypasses the bed solids, resulting in lower frictional losses.

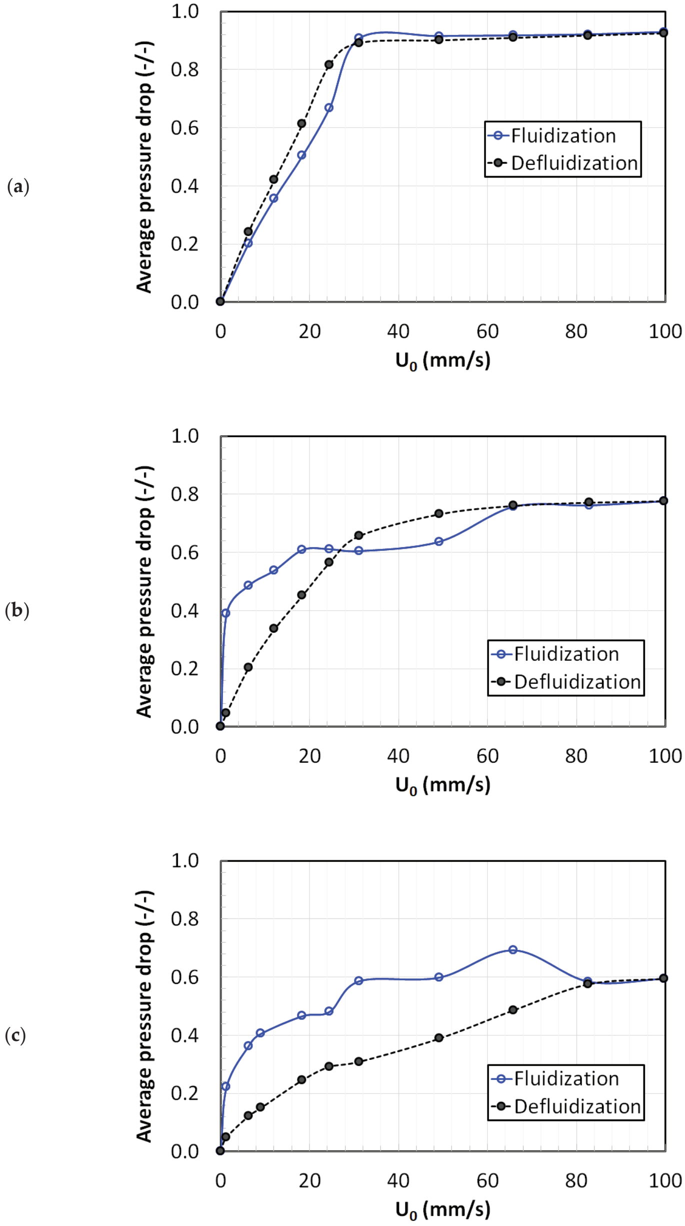

Figure 2. Hysteresis effect between fluidization and defluidization runs for conventional fluidized beds; (**a**) Glass beads; (**b**) Titania; (**c**) Nanosilica.

Figure 2c shows the fluidization behavior of the highly porous nanosilica powder ($\varepsilon = 0.98$). Silica nanoparticles form agglomerates with a wide size distribution [40]. Their fluidization shows agglomerate bubbling fluidization (ABF) [17]. The bed was composed of three main layers. The upper layer consisted of fine agglomerates while the bottom layer mainly consisted of large and rigid agglomerates. There was a transition layer of different-sized fluffy agglomerates in the middle section of the bed. The size segregation of the nanosilica bed has been reported earlier as well [24,41]. Even at $2U_{mf}$, there was hardly any motion in the lower layer, but a vigorous motion of fine agglomerates was observed in the bed's upper region. This behavior is an example of a partially fluidized bed and an indication of ABF. The fluidization and defluidization pressure drop profiles showed a substantial difference in this case. While the fluidization cycle displayed a rather unpredictable dependence of the pressure drop on the superficial velocity, a gradual decrease in velocity during the defluidization cycle showed a gradual and smooth pressure drop decrease. A pronounced hysteresis phenomenon was observed in the fluidization of nanosilica. The fluidization index was low, approximately 0.61. Such a low value of the fluidization index was a clear indication of gas channeling and bypassing. The U_{mf} values were calculated from the fluidization curves in Figure 2 and reported in Table 1.

Figure 3 shows a snapshot of the fluidization behavior of all the three powders. The glass beads displayed bubbling fluidization whereby the air moved as large bubbles through the bed. This is visible in Figure 3a encircled in red. The intensity of the bubbles increased with the increase in the fluid superficial velocity. On the other hand, the titania particles exhibited agglomerate bubbling fluidization (ABF) due to their cohesiveness, whereby the gas bubbles rapidly move upward through the bed [40]. Note that the bubbling behavior of ABF was different from that of the Group A particles, where large air bubbles dominated the fluidization behavior. The bubbles in the titania bed were smaller and irregular and erupted through channels and cavities present in the bed (marked in red in Figure 3b). The expansion was low with a substantial degree of non-homogeneities observed throughout the bed. [17]. As mentioned earlier and seen in Figure 3c, severe size-based segregation was observed during the fluidization of the nanosilica. The large and rigid agglomerates in the lower region hardly showed any movement even at high velocities whereas vigorous motion was observed in the upper layer of the fine agglomerates. The overall bed thus appeared to be only partially fluidized even at high velocities.

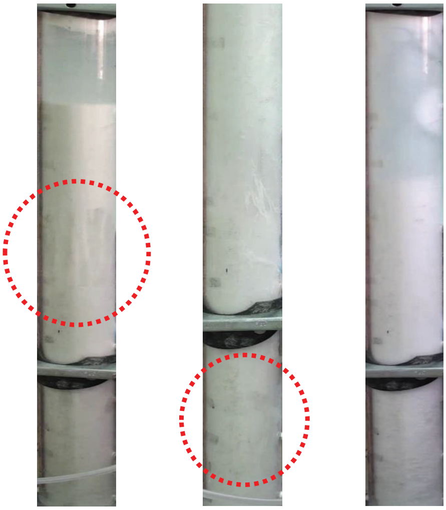
(**a**) (**b**) (**c**)

Figure 3. Digital images of solid particles fluidized bed; (**a**) Glass beads; (**b**) Titania; (**c**) Nanosilica.

3.2. Bed Collapse Dynamics

Figure 4 shows the pictorial representation of the collapse process of Geldart group A particles [24,35]. The collapse occurs in two main stages: a bubbling stage and a sedimentation stage. The bubbles escape in the first stage, while the particles settle under gravity during the second stage. A dense layer 'L_1' is created after the escape of the air bubbles, and a stationary layer of settled particles 'L_2' forms at the bottom of the bed. As more particles progressively settle in the stationary region, the interface between 'L_1' and 'L_2' rapidly moves upwards towards the upper bed interface. The upward movement of bubbles from the lower layers delays the collapse in the first stage and represents the bubbling period.

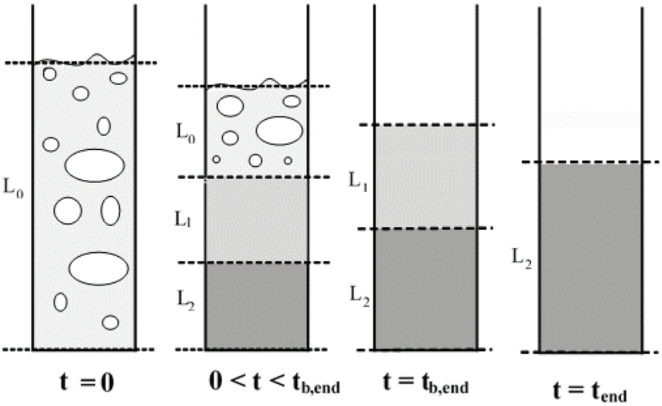

Figure 4. Schematic of the stepwise collapse process of Geldart group A particles.

Figure 5a,b show the local bed pressure drop transients for glass beads at two different air superficial velocities (U_0), i.e., $U_0 = U_{mf}$ and $U_0 = 2U_{mf}$. The dashed black vertical line indicates the commencement of the collapse process. To facilitate the comparison between different sections of the collapsing bed, the actual transient pressure drop data was normalized with respect to the steady state pressure drop before the start of the bed collapse. The upper sections of the bed displayed a delayed response to the collapse as compared to lower sections. This phenomenon was due to the movement of air bubbles during the first phase of the collapse process. The upper region transients (ΔP_4) showed the longest bubbling period, which was also the total time taken by the bubbles to escape after the start of the collapse process. Moreover, the collapse behavior of the uppermost layer was different from the other layers, as the pressure transients decreased steadily during the bubbling phase due to the downward movement of the top bed interface. The sedimentation stage of the collapse process followed an exponential decay in all bed regions before attaining a complete rest. The sedimentation stage transients were similar for all the bed regions, thus indicating the bed homogeneity and uniform size of settling particles. As the initial air superficial velocity was increased to $2U_{mf}$, the fluctuations during the first phase increased due to the higher volume of air escaping as bubbles from the top interface of the glass bed.

Figure 6a,b report the pressure transients of the collapsing bed of titania powder at $U_0 = U_{mf}$ and $U_0 = 2U_{mf}$. The bubble escape time was significantly shorter (less than half) than that of the glass beads due to the smaller bubble concentration. The bubbling stage was observed only in ΔP_3 transients with a bubbling time of approximately 0.3 s and 0.7 s for $U_0 = U_{mf}$ and $2U_{mf}$, respectively. The ΔP_3 region dominated the bed collapse process. The bubbling stage was not observed in the ΔP_2 and ΔP_4 transients, which could be attributed to the presence of cracks and channels in the upper and lower middle regions of the titania bed. Due to the poor contact between the gas and solid phases, the gas–solid drag and hence the pressure drop was low in the upper region of the bed during the collapse. As a result, the smaller agglomerates present in the upper middle layer mainly controlled the collapse process owing to size-based segregation. The size segregation of the agglomerates along the bed height also affected the sedimentation stage transients.

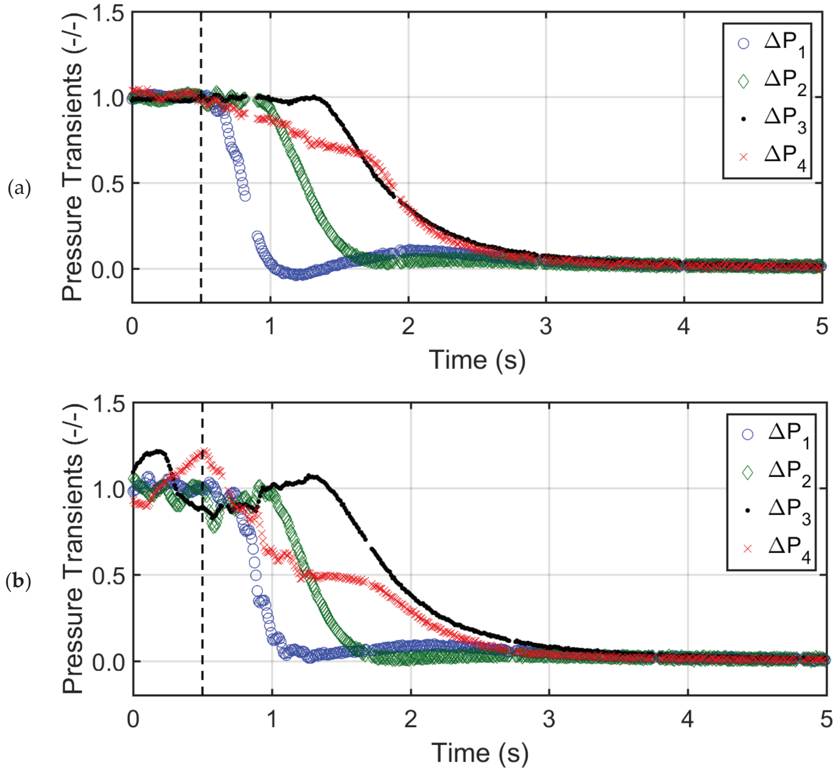

Figure 5. Pressure drop transients in different regions of the bed of glass beads for (**a**) $U_0 = U_{mf}$, (**b**) $U_0 = 2U_{mf}$.

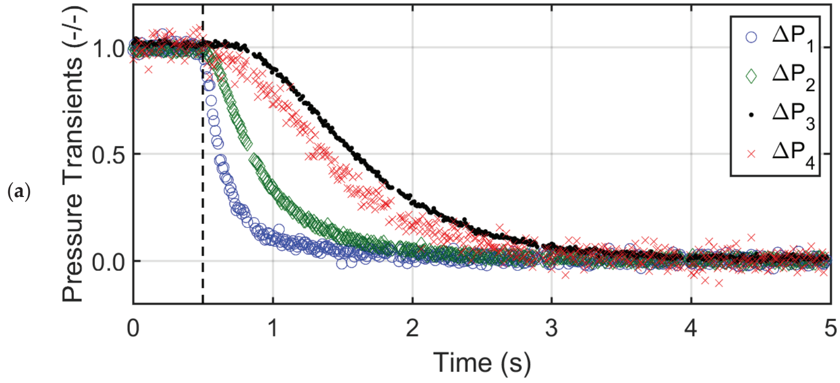

Figure 6. *Cont.*

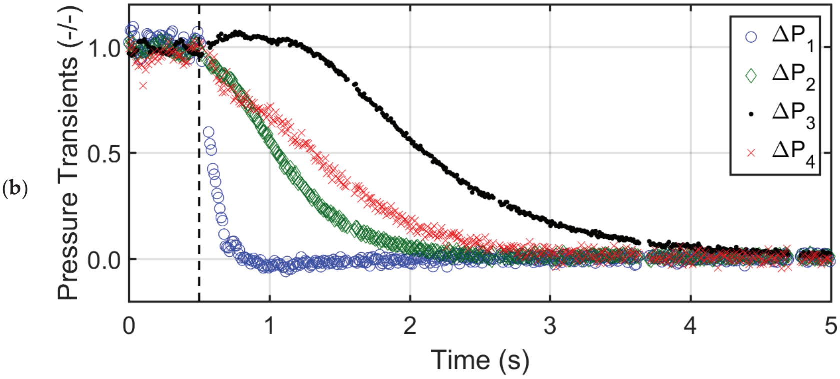

Figure 6. Pressure drop transients in different regions of the bed of titania powder for (**a**) $U_0 = U_{mf}$, (**b**) $U_0 = 2U_{mf}$.

Faster transients were observed for the lower layer that contained large agglomerates. ΔP_1 transients were followed by that of ΔP_2. Owing to the presence of fine agglomerates, the ΔP_3 transients were slowest. The collapse behavior was more pronounced for $U_0 = 2U_{mf}$ (Figure 6b). Higher velocities increased the bubble fraction, thus enhancing the bubbling time for ΔP_3 transients. The segregation behavior was also stronger at higher velocities, thereby slowing the pressure drop transients of the upper middle layer (i.e., ΔP_3). The ΔP_4 transients appeared unaffected by the velocity change as the uppermost layer apparently developed cavities or channels through which the fluidizing gas bypassed without much interaction with bed material.

Figure 7 highlights the behavior of the pressure transients in the nanosilica bed. In Figure 7a, the pressure transients, ΔP_1, ΔP_2, and ΔP_3 responded instantaneously to the collapse, whereas ΔP_4 transients decreased gradually taking approximately 25 s to settle completely. The static bed height was 0.4 m, which expanded to 0.7 m at U_{mf}, thus almost half of the bed was in the ΔP_4 region. The rapid decrease in ΔP_1, ΔP_2, and ΔP_3 transients indicated a lack of agglomerate movement in the lower regions due to the size segregation in the bed. Large rigid agglomerates constituted the lower region whereas fine agglomerates were observed in the upper region. Clearly, the size segregation in the nanosilica bed was much higher than the titania bed. The ΔP_4 transients indicated that the collapse process occurred in two stages. In the first stage, free fall of solids occurred under gravity with a rapid pressure drop decrease for approximately 1.5 s. During the second stage, the response was sluggish due to a gradual agglomerate settling and slow deaeration of the residual air through the bed and the purge.

The data analysis in the frequency domain can identify the presence of periodically recurring events in the bed, which cannot otherwise be clearly identified from the time domain data analysis [42]. Figure 8 reports the frequency spectra of the pressure drop transients recorded during the bed collapse at low frequencies using fast the Fourier transform (FFT) algorithm of MATLAB R2015a (Mathworks, Natick, MA, USA). For the case of the glass beads, the multiple low frequency peaks observed in Figure 8a indicate bubble movement. Given that the bed voidage of the glass beads at U_{mf} is approximately 0.38, its bulk density is high, leading to high pressure drop values in all the regions of the glass bed. This behavior is clearly evident from the dc component of the signal, which is <400 Pa in all the transients. The dc component refers to the amplitude of the non-fluctuating component of the signal, which is equal to the mean value of the signal.

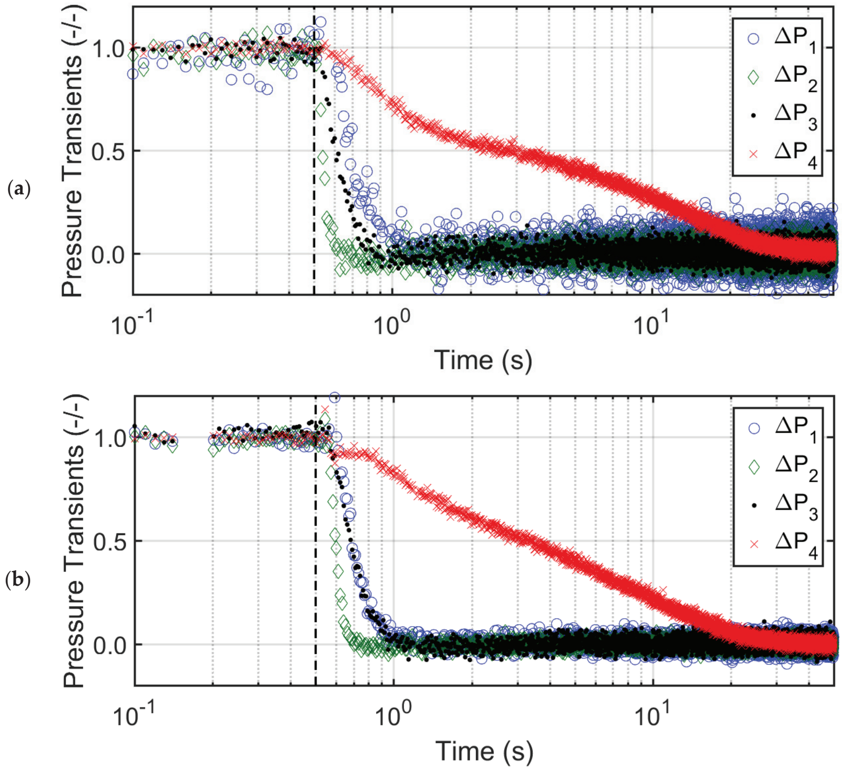

Figure 7. Pressure drop transients in different regions of the bed of nanosilica for (**a**) $U_0 = U_{mf}$, (**b**) $U_0 = 2U_{mf}$.

This situation is substantially different for the titania, with a significantly higher voidage ($\varepsilon = 0.80$) and a lower bulk density than that of glass. Therefore, pressure drop values, i.e., the dc components of the signals are substantially lower than those of glass (Figure 8b). Ideally, the dc components of ΔP_1, ΔP_2, ΔP_3 should be identical given that $\Delta L_1 = \Delta L_2 = \Delta L_3$. Therefore, the lower ΔP_1 indicates the presence of gas bypassing due to the non-homogeneities in the lower layer of the titania bed. The same phenomenon was also prominently observed in the upper layer, where ΔP_4 transients were recorded. No low frequency event was observed in this region unlike ΔP_2 and ΔP_3, where weak bubble movement with a frequency of 0.5 Hz was observed. Due to the local non-homogeneities, the bubble movement in the lower region appeared to be suppressed.

The spectral analysis corroborates the different bubbling phenomenon occurring in the glass and titania beds discussed earlier. The smaller and irregular gas bubbles were observed in the titania bed while homogeneous intense bubbling occurred throughout the bed of glass beads. In Figure 8c, no evidence of bubbling was noticed in the low frequency range for the nanosilica. However, the magnitude of the dc component, (i.e., pressure drop) was highest for ΔP_4, which kept on decreasing for ΔP_3 and ΔP_2 while being the lowest for ΔP_1. The large and rigid agglomerates in the lower regions behaved like a fixed bed, where the pressure drop varied inversely with the agglomerate size as predicted by the Ergun equation. Therefore, the gradually increasing dc component along the bed height (Figure 8c) indicated that the size of the agglomerates decreased with the distance from the distributor, thereby leading to the size-based segregation of agglomerates. The upper region of the nanosilica bed is clearly seen to contribute the most to the pressure drop.

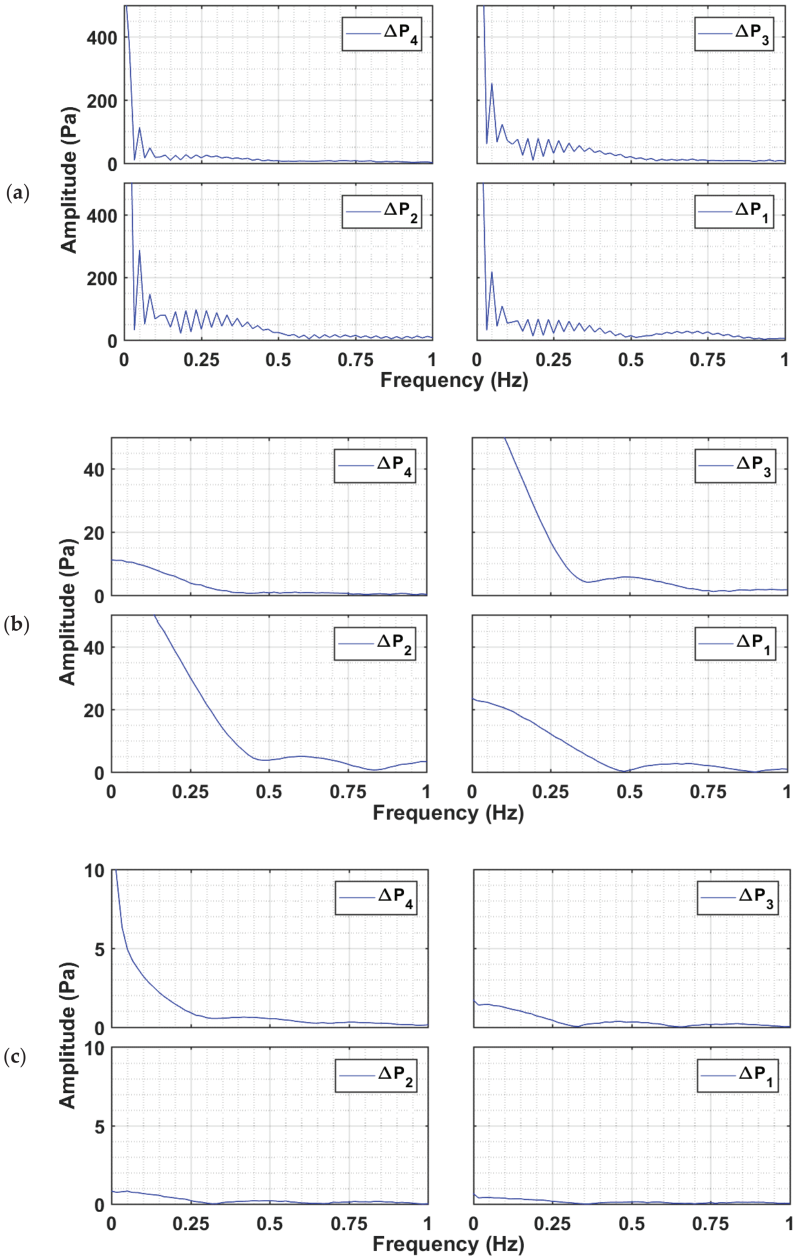

Figure 8. Power spectral analysis at low frequencies (0–1 Hz) of pressure transients in different bed regions of the collapsing bed at U_{mf} and bed height H of (**a**) glass beads, (**b**) titania, and (**c**) nanosilica.

Figure 9 reports the power spectra at higher frequencies (10–50 Hz) for all the three powders. No high frequency events were observed for the case of the glass and titania. However, the nanosilica shows two distinct peaks at 20 Hz and 40 Hz in Figure 9c, which clearly indicate the presence of high frequency events. The highest intensity fluctuation occurred in the ΔP_3 transients. The feeble peaks in the ΔP_4 region indicate lower intensity fluctuations caused by fine agglomerates present in the upper region due to segregation.

The presence of high intensity fluctuations was clearly observed in Figure 7a, which were predominantly present during the sedimentation stage for regions with large agglomerates, while the fine and smaller agglomerates in the upper region were still settling under the gravity. The interaction of the larger agglomerates with their smaller counterparts appeared to the main reason for the high frequency events observed for the nanosilica.

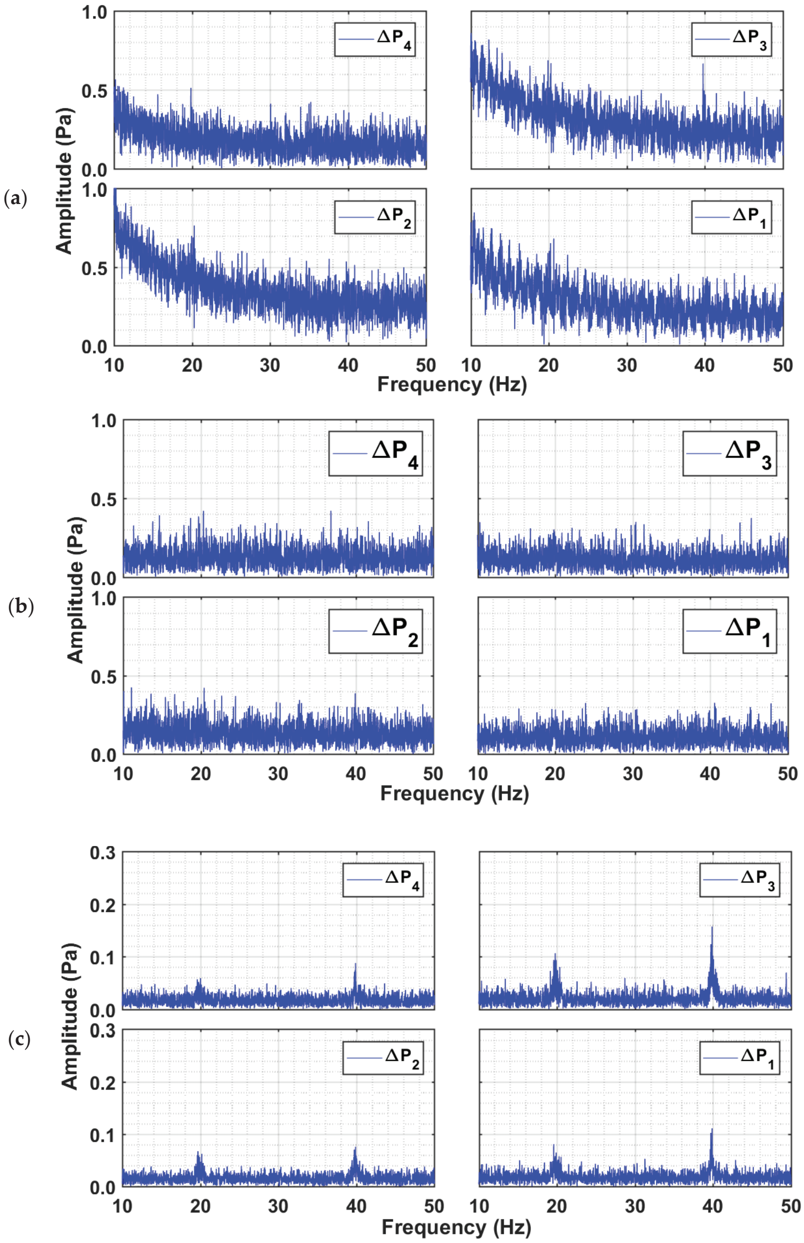

Figure 9. Power spectral analysis at low frequencies (10–50 Hz) of pressure transients in different bed regions of the collapsing bed at U_{mf} and bed height H of (**a**) glass beads, (**b**) titania, and (**c**) nanosilica.

Figure 10 shows the effect of the height and the velocity on the global bed pressure drop transients for the beds of glass beads, titania, and nanosilica. Apart from the velocity, the effect of height on the bed dynamics was also considered by increasing the bed height by 50%, represented as 1.5 H in the figure. The global pressure drop included the combined effect of all the bed regions. A smooth overall collapse was clearly seen for all the cases. A substantial change in the velocity ($U_0 = U_{mf}$ and $U_0 = 2U_{mf}$) failed to make any significant difference on the collapse time irrespective of the bed material used. Similar observations were made earlier by Lorences, Patience [26]. However, increasing the height by 50% affected the collapse time in all cases. In the case of the titania, the shorter beds were slower than the longer beds. Moreover, shorter titania beds were more sensitive to the initial superficial velocity at which the collapse was initiated. While the increase in the bed height did not significantly affect the collapse time for the glass beds, a 50% increase in the height increased the collapse time for the nanosilica by approximately 100%.

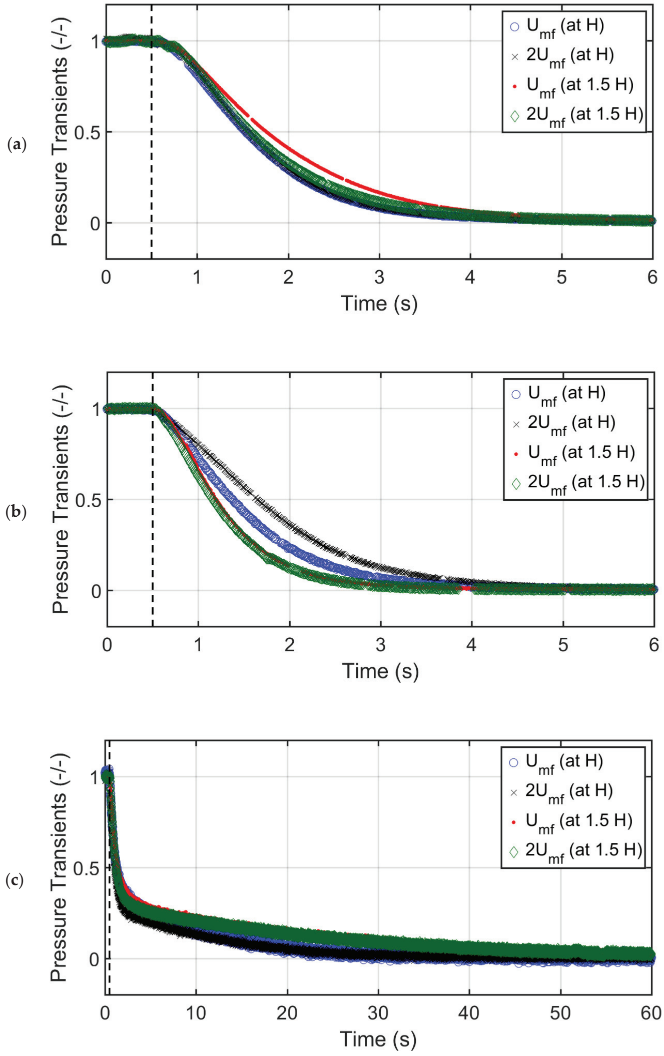

Figure 10. Global pressure drop of the collapsing particles bed at U_{mf} and $2U_{mf}$ bed heights H and 1.5 H for (**a**) glass beads, (**b**) titania, and (**c**) nanosilica.

Table 2 presents a comparison of the collapse times for all three cases. The collapse time was much higher for nanosilica as compared to those of glass beads and titania, with similar collapse times. The collapse times for glass beads, titania, and nanosilica varied from 4.7–6.6 s, 4.1–7.1 s, and 22.3–43.6 s, respectively. As mentioned earlier, unlike other cases, the bed height significantly affected the collapse time of the nanosilica. A 50% increase in the bed height led to an almost 100% increase in the collapse time for nanosilica. Adding to the bed material to increase the initial bed height led to a higher concentration of fine agglomerates in the upper region, which attained greater height in the column owing to bed expansion. These fine agglomerates took much longer to settle during collapse. Surprisingly, the trend was reversed for the titania bed. Adding to the bed material shortened the collapse time. This is a clear indication that increasing the bed material did not correspondingly increase the gas–solid contact. Instead, greater bed non-homogeneity in the bed developed, thereby reducing the gas–solid drag. As a result, the collapse time was reduced.

Table 2. Total bed collapse time (in seconds) evaluated using global pressure drop transients.

Static Bed Height	**H**		**1.5 H**	
Initial Flow Rate	U_{mf}	$2U_{mf}$	U_{mf}	$2U_{mf}$
Glass beads	5.0	4.7	6.6	5.8
Titania	5.7	7.1	4.2	4.1
Nanosilica	22.3	25.7	43.6	43.5

3.3. Distributor Pressure Drop

An important aspect of the present investigation was the monitoring of the distributor pressure drop during the bed collapse. The distributor pressure drop was mostly higher than the bed pressure drop given that only 2.7% of the distributor area was kept open to gas flow. Figure 11a reports the effect of the bed height and the velocity on the distributor pressure drop during the collapse of the glass bed. As the collapse process commenced, the distributor pressure drop decreased rapidly. A resultant net drag force was exerted downwards by the falling particles, which forced a portion of residual air present in the column to flow in the reverse direction across the distributor, which resulted in a rapid decrease of the pressure drop. The pressure drop became negative until reaching a global minimum before gradually rising back to zero pressure drop, while the collapsing bed reached a complete rest. The opening of the purge valve (SV2) during the collapse process provided an alternative path for residual air in the reverse direction in addition to the conventional pathway from the top of the bed. A higher initial collapse velocity resulted in a higher negative pressure drop because the bed contained a greater volume of air at higher velocities. Increasing the bed height by 50% increased the negative minimum by approximately 50% irrespective of the velocity, owing to bed homogeneity and uniform expansion.

Figure 11b reports the distributor pressure drop transients during the collapse of the titania bed. The effect of the bed height was not significant at a lower velocity as the gas bypassing occurred through channels and cracks. As a result, increasing bed solids did not increase the gas–solid drag that can cause a greater downward flow of residual air during the collapse. However, at a higher velocity, there was a substantial difference in the distributor pressure drop transients when the bed height was changed. Faster transients were observed for the longer beds as compared to those of the shorter beds.

For the case of the nanosilica particles shown in Figure 11c, the effect of the velocity and the bed height on the distributor pressure drop transients was negligible. Given that the voidage was 0.98, only 2% solids were present in the bed. Due to the extremely high bed voidage, any change either in the velocity or the bed material failed to make any difference on the deaeration of the residual gas from the nanosilica bed.

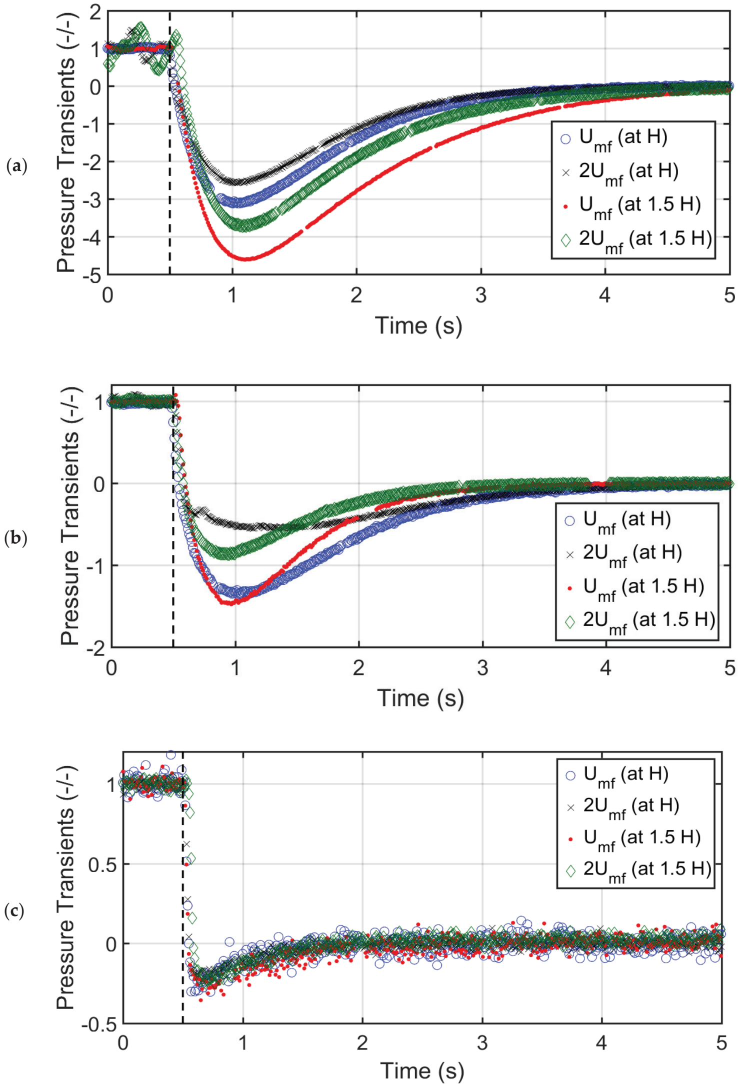

Figure 11. Distributor pressure drop of the bed at U_{mf} and $2U_{mf}$ for (**a**) glass beads, (**b**) titania, (**c**) nanosilica.

Figure 11 indicates that the bed voidage clearly affected the pressure drop minimum. The maximum negative pressure drop values attained by the glass beads, titania, and nanosilica collapse beds were approximately −4.7, −1.5 and −0.65, respectively. A low bed voidage leads to a higher specific surface area of the solid phase in the bed, resulting in greater gas–solid drag and frictional losses during the bed collapse which forces a greater amount of the residual air to pass through the distributor.

3.4. Purge Flow Transients

Figure 12 reports the airflow transients in LPM through the purge valve during the collapse process of glass beads, titania, and nanosilica particles bed. The purge flow begun with a sudden airflow spike as the collapse initiated, followed by a sluggish exponential decay. Table 3 reports the maximum airflow from the purge, recorded from Figure 12, achieved during the commencement of collapse. The lower voidage bed attained higher peak. The highest peaks attained by glass beads, titania, and nanosilica particles were 0.99, 0.54, and 0.02 LPM, respectively. The initial spike signifies the initial intensity of the bed collapse. The particles with a higher bed weight and uniform fluidization forced the downward flow of the residual air through the purge valve. Moreover, increasing the initial airflow from U_{mf} to $2U_{mf}$ did not yield any tangible effect on the purge flow. However, increasing the bed height resulted in an increase in the higher flow spike in all cases, which signifies the flow spike was dependent on the fluidized bed weight. These parameters are reported in Table 3.

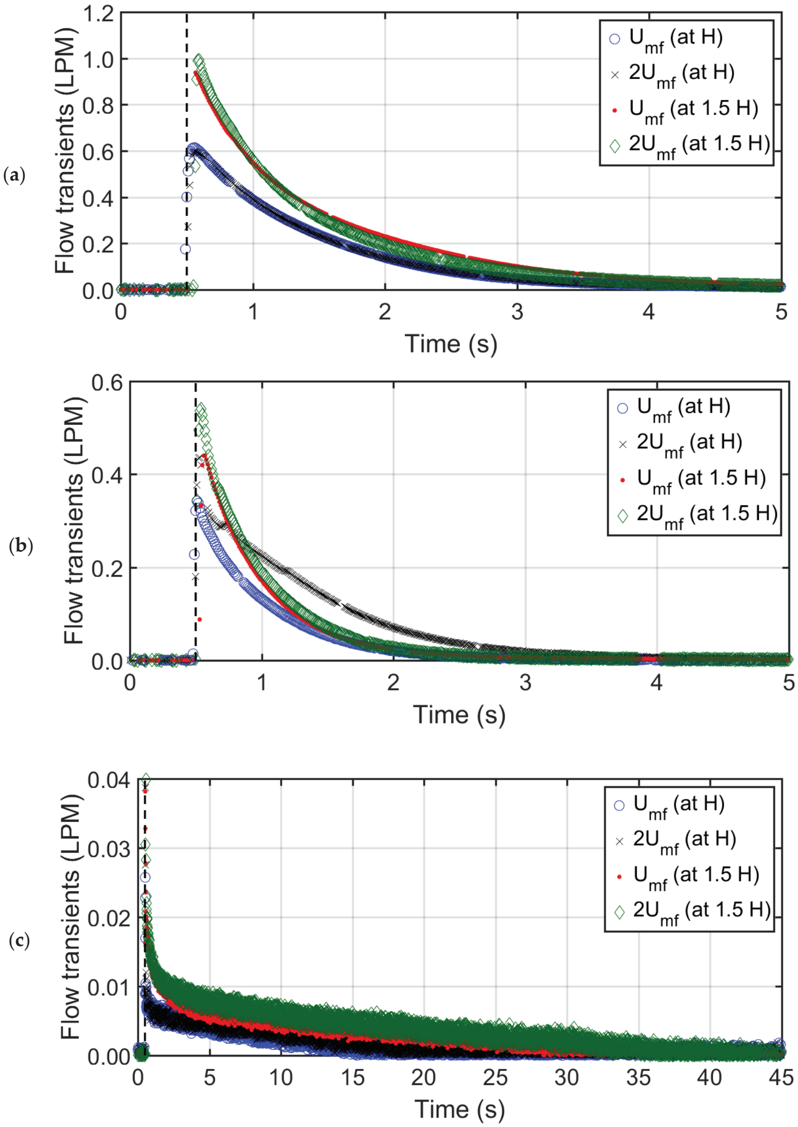

Figure 12. Purge flow transients at U_{mf} and $2U_{mf}$ for (**a**) glass beads, (**b**) titania, and (**c**) nanosilica.

Table 3. Maximum initial airflow (LPM) through purge during collapse evaluated from Figure 12.

Static Bed Height	**H**		**1.5 H**	
Initial Velocities	U_{mf}	$2U_{mf}$	U_{mf}	$2U_{mf}$
Glass beads	0.64	0.61	0.94	0.99
TiO_2	0.34	0.44	0.41	0.54
Nanosilica	0.01	0.01	0.014	0.016

The total airflow in LPM, which is the total area under the curve in Figure 12, was calculated using the trapezoid method. Thereafter, the ratio of the total airflow through purge to the volume of air that was present in the bed during the fluidization before the commencement of the collapse was calculated. The volume of air present in the bed resides in the voidage of the bed. Hence, bed voidage volume gives a good approximation of the total volume of air present under steady state. Figure 13 reports the plot of purge airflow ratio against the bed voidage. The relationship is linear with 'R^2 = 0.985' fit, which signifies that the ratio of purge airflow with bed fluid volume during fluidization decreases linearly with the bed voidage.

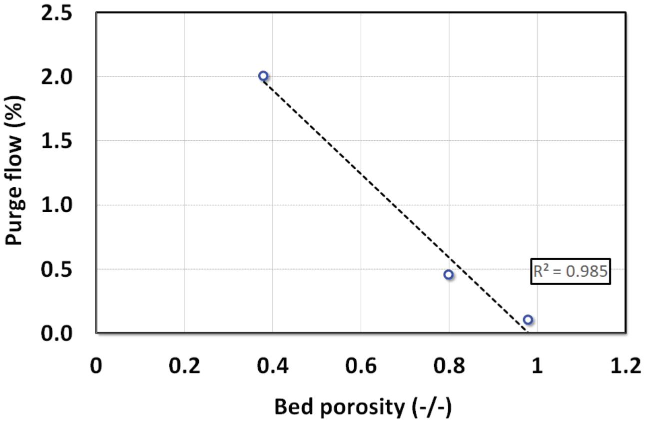

Figure 13. Effect of the bed voidage on the ratio of the purge flow to the total volume during gas deaeration.

4. Conclusions

The bed collapse behavior of three different kinds of solid particles of widely different voidages and belonging to different Geldart classifications, namely glass beads, titania, and nanosilica, was investigated in this study. First, the hysteresis behavior and fluidization index of each solid particle species was examined by analyzing the dependence of the pressure drop on the air velocity while both gradually increasing and decreasing the air flow. The glass beads (Geldart group A) showed the highest fluidization index of 0.92 with no hysteresis effects. The cohesive powder of titania (Geldart group C) showed severe gas-bypassing due to local non-homogeneities comprising cracks and channels, thereby resulting in a low fluidization index of 0.76 and a strong hysteresis effect. The fluidization index of nanosilica was even lower at 0.61 due its poor fluidization hydrodynamics with a stronger hysteresis behavior than that observed for the titania.

A dual drainage scheme was implemented by allowing the downward movement of the residual air through a purge passage located below the plenum chamber. The flowrate of the exiting air through the purge was monitored using an electronic flowmeter. Owing to the bed homogeneity, all the regions in the glass bed exhibited almost identical two-stage collapse processes, i.e., the bubbling and sedimentation stages. The bubbling time decreased with the distance from the distributor. The spectral analysis of the transients clearly indicated the bubble movement as low frequency events. The bubbling was less intense and irregular due to the gas-bypassing through the cracks and channels in the bed of the titania particles. Its transient response decreased with the distance from the distributor owing to size segregation with the upper middle layer (i.e., ΔP_3) dominating the collapse dynamics. Even stronger segregation tendencies were observed in the nanosilica bed with a significant number of fine agglomerates present in the upper region of the bed while large rigid agglomerates occupied the lower region. Therefore, the slow gravity settling of fine agglomerates in the upper region took almost 25 s whereas larger agglomerates present in the other bed regions settled in approximately 1 s only. As a result, the nanosilica bed collapse took at least five times longer than the durations of glass and titania, which showed almost identical overall collapse times. Unlike glass and titania, two distinct high frequency events at 20 Hz and 40 Hz occurred for nanosilica due to the interaction of fine agglomerates with their larger counterpart while setting down.

For glass beads, the maximum negative distributor pressure drop attained during the collapse was a function of both the velocity and bed height. The same behavior was observed with the titania bed with a change of the bed height. For the case of the nanosilica, however, the backward flow of the residual air through the distributor was rather insignificant, resulting in a low pressure drop.

Hydrophilic nanosilica with strong agglomeration behavior were used in this study. Any extension of these results to nanoparticles with APF behavior, even with similar primary dimensions and comparable bulk density, should be treated with caution.

Author Contributions: Conceptualization, S.S.A. and M.A.; Methodology, S.S.A. and M.A.; Software, S.S.A.; Validation, S.S.A.; Formal Analysis, S.S.A.; S Resources, M.A.; Data Curation, S.S.A.; Writing—Original Draft Preparation, S.S.A.; Writing—Review & Editing, A.A. and K.L.R.; Visualization, S.S.A. and M.A.; Supervision, M.A.; Funding Acquisition, M.A. All authors have read and agreed to the published version of the manuscript.

Funding: This research was funded by Researchers Supporting Project, RSP-2021/42, King Saud University, Riyadh, Saudi Arabia.

Data Availability Statement: The data that support the findings of this study are available on request from the first author, SSA.

Acknowledgments: The authors acknowledge the Researchers Supporting Project, RSP-2021/42, King Saud University, Riyadh, Saudi Arabia, for the financial support.

Conflicts of Interest: The authors declare no conflict of interest.

References

1. Lettieri, P.; Macrì, D. Effect of Process Conditions on Fluidization. *KONA Powder Part. J.* **2016**, *33*, 86–108. [CrossRef]
2. Shabanian, J.; Jafari, R.; Chaouki, J. Fluidization of Ultrafine Powders. *Int. Rev. Chem. Eng.* **2012**, *4*, 16–50.
3. Zhao, Z.; Liu, D.; Ma, J.; Chen, X. Fluidization of nanoparticle agglomerates assisted by combining vibration and stirring methods. *Chem. Eng. J.* **2020**, *388*, 124213. [CrossRef]
4. Lee, J.-R.; Lee, K.-S.; Park, Y.-O.; Lee, K.-Y. Fluidization characteristics of fine cohesive particles assisted by vertical vibration in a fluidized bed reactor. *Chem. Eng. J.* **2020**, *380*, 122454. [CrossRef]
5. Fedorov, A.V.; Yazykov, N.A.; Bulavchenko, O.A.; Saraev, A.A.; Kaichev, V.V.; Yakovlev, V.A. CuFeAl Nanocomposite Catalysts for Coal Combustion in Fluidized Bed. *Nanomaterials* **2020**, *10*, 1002. [CrossRef]
6. Ali, S.S.; Arsad, A.; Hossain, S.S.; Asif, M. A Detailed Insight into Acoustic Attenuation in a Static Bed of Hydrophilic Nanosilica. *Nanomaterials* **2022**, *12*, 1509. [CrossRef]
7. Bakhurji, A.; Bi, X.; Grace, J.R. Hydrodynamics and solids mixing in fluidized beds with inclined-hole distributors. *Particuology* **2019**, *43*, 19–28. [CrossRef]
8. Raganati, F.; Chirone, R.; Ammendola, P. Effect of Temperature on Fluidization of Geldart's Group A and C Powders: Role of Interparticle Forces. *Ind. Eng. Chem. Res.* **2017**, *56*, 12811–12821. [CrossRef]
9. Mogre, C.; Thakurdesai, A.U.; Van Ommen, J.R.; Salameh, S. Long-term fluidization of titania nanoparticle agglomerates. *Powder Technol.* **2017**, *316*, 441–445. [CrossRef]
10. Ali, S.S.; Asif, M. Effect of particle mixing on the hydrodynamics of fluidized bed of nanoparticles. *Powder Technol.* **2017**, *310*, 234–240. [CrossRef]

11. Ajbar, A.; Bakhbakhi, Y.; Ali, S.; Asif, M. Fluidization of nano-powders: Effect of sound vibration and pre-mixing with group A particles. *Powder Technol.* **2011**, *206*, 327–337. [CrossRef]
12. Lee, J.-R.; Lee, K.-S.; Hasolli, N.; Park, Y.-O.; Lee, K.-Y.; Kim, Y.-H. Fluidization and mixing behaviors of Geldart groups A, B and C particles assisted by vertical vibration in fluidized bed. *Chem. Eng. Process. Process Intensif.* **2020**, *149*, 107856. [CrossRef]
13. Al-Ghurabi, E.H.; Ali, S.S.; Alfadul, S.M.; Shahabuddin, M.; Asif, M. Experimental investigation of fluidized bed dynamics under resonant frequency of sound waves. *Adv. Powder Technol.* **2019**, *30*, 2812–2822. [CrossRef]
14. Asif, M.; Al-Ghurabi, E.H.; Ajbar, A.; Kumar, N.S. Hydrodynamics of Pulsed Fluidized Bed of Ultrafine Powder: Fully Collapsing Fluidized Bed. *Processes* **2020**, *8*, 807. [CrossRef]
15. Geldart, D. Types of Gas Fluidization. *Powder Technol.* **1973**, *7*, 285–292. [CrossRef]
16. An, K.; Andino, J.M. Enhanced fluidization of nanosized TiO_2 by a microjet and vibration assisted (MVA) method. *Powder Technol.* **2019**, *356*, 200–207. [CrossRef]
17. Raganati, F.; Chirone, R.; Ammendola, P. Gas-solid fluidization of cohesive powders. *Chem. Eng. Res. Des.* **2018**, *133*, 347–387. [CrossRef]
18. Shabanian, J.; Chaouki, J. Influence of interparticle forces on solids motion in a bubbling gas-solid fluidized bed. *Powder Technol.* **2016**, *299* (Suppl. C), 98–106. [CrossRef]
19. Van Ommen, J.R.; Valverde, J.M.; Pfeffer, R. Fluidization of nanopowders: A review. *J. Nanoparticle Res.* **2012**, *14*, 737. [CrossRef]
20. Tamadondar, M.R.; Zarghami, R.; Tahmasebpoor, M.; Mostoufi, N. Characterization of the bubbling fluidization of nanoparticles. *Particuology* **2014**, *16*, 75–83. [CrossRef]
21. Ali, S.S.; Basu, A.; Alfadul, S.M.; Asif, M. Nanopowder Fluidization Using the Combined Assisted Fluidization Techniques of Particle Mixing and Flow Pulsation. *Appl. Sci.* **2019**, *9*, 572. [CrossRef]
22. Asif, M.; Ali, S.S. Ali, Bed collapse dynamics of fluidized beds of nano-powder. *Adv. Powder Technol.* **2013**, *24*, 939–946. [CrossRef]
23. Hoorijani, H.; Zarghami, R.; Nosrati, K.; Mostoufi, N. Investigating the hydrodynamics of vibro-fluidized bed of hydrophilic titanium nanoparticles. *Chem. Eng. Res. Des.* **2021**, *174*, 486–497. [CrossRef]
24. Ali, S.S.; Arsad, A.; Asif, M. Effect of modified inlet flow strategy on the segregation phenomenon in pulsed fluidized bed of ultrafine particles: A collapse bed study. *Chem. Eng. Process. Process Intensif.* **2021**, *159*, 108243. [CrossRef]
25. Nie, Y.; Liu, D. Dynamics of collapsing fluidized beds and its application in the simulation of pulsed fluidized beds. *Powder Technol.* **1998**, *99*, 132–139. [CrossRef]
26. Lorences, M.J.; Patience, G.S.; Díez, F.V.; Coca, J. Fines effects on collapsing fluidized beds. *Powder Technol.* **2003**, *131*, 234–240. [CrossRef]
27. Ali, S.S.; Asif, M.; Ajbar, A. Bed collapse behavior of pulsed fluidized beds of nano-powder. *Adv. Powder Technol.* **2014**, *25*, 331–337. [CrossRef]
28. Ali, S.S.; Al-Ghurabi, E.H.; Ibrahim, A.A.; Asif, M. Effect of adding Geldart group A particles on the collapse of fluidized bed of hydrophilic nanoparticles. *Powder Technol.* **2018**, *330*, 50–57. [CrossRef]
29. Ali, S.S.; Hossain, S.K.S.; Asif, M. Dynamics of partially collapsing pulsed fluidized bed. *Can. J. Chem. Eng.* **2021**, *99*, 2333–2344. [CrossRef]
30. Al-Ghurabi, E.H.; Shahabuddin, M.; Kumar, N.S.; Asif, M. Deagglomeration of Ultrafine Hydrophilic Nanopowder Using Low-Frequency Pulsed Fluidization. *Nanomaterials* **2020**, *10*, 388. [CrossRef]
31. Gutfinger, C.; Goldshtein, A.; Weinstein, H. A model for the collapse of a fluidized bed. *Adv. Powder Technol.* **2005**, *16*, 49–59. [CrossRef]
32. Ali, S.S.; Al-Ghurabi, E.H.; Ajbar, A.; Mohammed, Y.A.; Boumaza, M.; Asif, M. Effect of Frequency on Pulsed Fluidized Beds of Ultrafine Powders. *J. Nanomater.* **2016**, *2016*, 12. [CrossRef]
33. Jeong, S.W.; Lee, D.H. Bed collapse and expansion characteristics of multi-walled carbon nanotubes in fluidized beds. *Adv. Powder Technol.* **2018**, *29*, 751–755. [CrossRef]
34. Cherntongchai, P.; Innan, T.; Brandani, S. Mathematical description of pressure drop profile for the 1-valve and 2-valve bed collapse experiment. *Chem. Eng. Sci.* **2011**, *66*, 973–981. [CrossRef]
35. Cherntongchai, P.; Brandani, S. A model for the interpretation of the bed collapse experiment. *Powder Technol.* **2005**, *151*, 37–43. [CrossRef]
36. Santos, E.; Hemati, M.; Andreux, R.; Ferschneider, G. Gas and solid behaviours during defluidisation of Geldart—A particles. *Powder Technol.* **2011**, *211*, 156–164. [CrossRef]
37. Mallakpour, S.; Naghdi, M. Polymer/SiO_2 nanocomposites: Production and applications. *Prog. Mater. Sci.* **2018**, *97*, 409–447. [CrossRef]
38. Xu, Z.; Ma, X.; Gao, Y.-E.; Hou, M.; Xue, P.; Li, C.M.; Kang, Y. Multifunctional silica nanoparticles as a promising theranostic platform for biomedical applications. *Materials Chemistry Frontiers* **2017**, *1*, 1257–1272. [CrossRef]
39. Al-Ghurabi, E.H.; Ajbar, A.; Asif, M. Improving fluidization hydrodynamics of group C particles by mixing with group B particles. *Appl. Sci.* **2018**, *8*, 1469. [CrossRef]
40. Zhu, C.; Yu, Q.; Dave, R.N.; Pfeffer, R. Gas fluidization characteristics of nanoparticle agglomerates. *AIChE J.* **2005**, *51*, 426–439. [CrossRef]

41. Ali, S.S.; Asif, M. Fluidization of nano-powders: Effect of flow pulsation. *Powder Technol.* **2012**, *225*, 86–92. [CrossRef]
42. Briens, L.A.; Ellis, N. Hydrodynamics of three-phase fluidized bed systems examined by statistical, fractal, chaos and wavelet analysis methods. *Chem. Eng. Sci.* **2005**, *60*, 6094–6106. [CrossRef]

nanomaterials

Article

Atomistic Insights into the Phase Transformation of Single-Crystal Silicon during Nanoindentation

Young Jin Chung, Gi Hun Lee and Hyeon Gyu Beom *

Department of Mechanical Engineering, Inha University, 100 Inha-ro, Incheon 22212, Korea;
dudwls6426@naver.com (Y.J.C.); solafide27@gmail.com (G.H.L.)
* Correspondence: hgbeom@inha.ac.kr; Tel.: +82-32-860-7310

Abstract: The influence of the indenter angle on the deformation mechanisms of single-crystal Si was analyzed via molecular dynamics simulations of the nanoindentation process. Three different types of diamond conical indenters with semi-angles of 45°, 60°, and 70° were used. The load–indentation depth curves were obtained by varying the indenter angles, and the structural phase transformations of single-crystal Si were observed from an atomistic view. In addition, the hardness and elastic modulus with varying indenter angles were evaluated based on the Oliver–Pharr method and Sneddon's solution. The simulation results showed that the indenter angle had a significant effect on the load–indentation depth curves, which resulted from the strong dependence of the elastic and plastic deformation ratios on the indenter angle during indentations.

Keywords: nanoindentation; indenter angle; phase transformation; silicon; atomistic simulation

1. Introduction

The highly localized stress near the indenter tip induces characteristic plastic responses in the material [1]. For instance, thin films consisting of single-crystal Si beneath a rigid indenter exhibit phase transformations during indentation [2,3]. When the stress in single-crystal Si with a diamond cubic structure (Si-I) increases to nearly 12 GPa, the cubic diamond phase is transformed to a β-tin structure (Si-II) [4]. For the unloading procedure, metastable phases such as body-centered cubic (Si-III) or rhombohedral distortion (Si-XII) can occur [5,6]. This phase transformation in single-crystal Si during indentation has been found to be an important factor that determines its mechanical properties. However, Jang et al. [1] investigated triangular pyramidal indenters with four different indenter angles and experimentally demonstrated that the transformation behavior of Si was strongly dependent on the shape of the indenter.

Micro-Raman analysis and transmission electron microscopy (TEM) are too restricted to provide sufficient explanations for the sequence of phase transformations [7]. An atomistic analysis via molecular dynamics (MD) simulations can effectively elucidate the essential features of phase transformations, compared to the limited observations from experiments [8–10]. Recently, several atomistic studies on the nanoindentation of thin-film Si have been conducted by Sun et al. [11], Wang et al. [12], and Jiao et al. [13]. However, these computational studies focused on the use of a spherical indenter. Different geometries of the indenter tip significantly influence the stresses and strains of the material beneath the indenter, which may induce deviations in the mechanical properties from theoretical values [14,15].

The present study investigates the effect of the indenter angle on the indentation behavior of single-crystal Si using MD simulations. Nanoindentations were performed using a perfect conical indenter, and the indenter semi-angles were chosen as 45°, 60°, and 70°. MD simulations were conducted at temperatures of 1 K and 300 K. The relationship between the indenter angle and the deformation mechanism of single-crystal Si was analyzed through load–indentation depth (P-h) curves and atomistic views. In addition, mechanical

Citation: Chung, Y.J.; Lee, G.H.; Beom, H.G. Atomistic Insights into the Phase Transformation of Single-Crystal Silicon during Nanoindentation. *Nanomaterials* **2022**, *12*, 2071. https://doi.org/10.3390/nano12122071

Academic Editor: Ana B. Pereiro

Received: 16 May 2022
Accepted: 12 June 2022
Published: 16 June 2022

properties such as hardness and elastic modulus were evaluated using the *P*-*h* curve, as suggested by Oliver and Pharr [16] and Sneddon [17].

2. MD Simulation Method

The atomistic model used in this study is shown in Figure 1. The *x*-, *y*-, and *z*-axes of the model are oriented along the [100], [010], and [001] crystallographic directions, respectively. The dimensions of the Si substrate were chosen as $L_x = 50a$, $L_y = 35a$, and $L_z = 50a$, where a is the Si lattice constant of 0.5431 nm. Periodic boundary conditions were applied in the *x*- and *z*-directions. The conical indenter was composed of a carbon diamond structure (C) with a lattice parameter of 0.3576 nm, and was located 1 nm above the Si substrate. To analyze the Si substrate's response under the conical indenter, the indenter semi-angles (α) were chosen as 45°, 60°, and 70°.

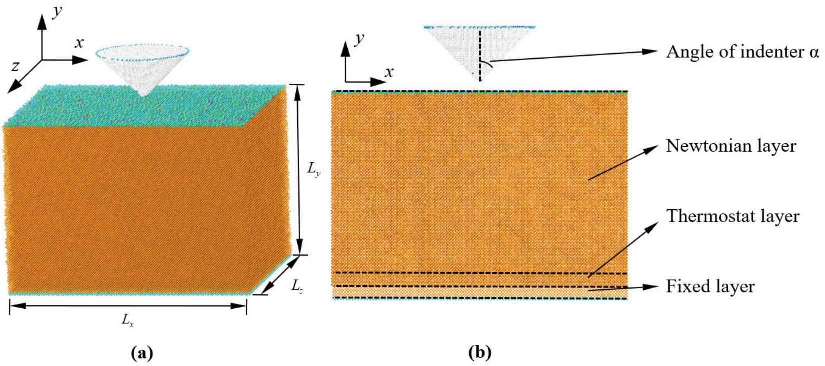

Figure 1. Computational model of a Si single-crystal substrate with a conical indenter: (**a**) three-dimensional model; (**b**) schematic diagram of the Si substrate and conical indenter.

The Si substrate consisted of fixed, thermostat, and Newtonian layers [12,18]. The fixed layer at the bottom of the substrate was treated as a rigid body for structural stability, and the thermostat layer above the fixed layer was used to ensure reasonable outward heat conduction away from the Newtonian layer through an NVT ensemble. The layer above the thermostat layer was the Newtonian layer, where the behavior of atoms was only governed by the forces between them, with no other constraints [19].

It is important to consider the interatomic potential to obtain accurate simulation results. Although many potential functions have been developed to describe the interaction between Si atoms, it has been demonstrated by many researchers that the Tersoff potential provides a reasonable deformation mechanism of Si [20]. In the present study, the Tersoff potential was used to compute the interaction between Si atoms (Si–Si) and diamond atoms (C–C) [21]. The interaction potential between the Si and C atoms was modeled using Morse potential [19].

Before the indentation procedure, the temperature of the Si substrate was equilibrated at either 1 K or 300 K. To equilibrate the temperature of the substrate, an NVE ensemble with a velocity rescaling method was used in the Newtonian layer [22,23]. Subsequently, the indentation load was applied by displacing the conical indenter into the substrate. The indentation speed was set to 50 m/s and the indentation depth was 3 nm. Retreating of the indenter was then conducted at the same speed. MD simulations were conducted using the open source MD program Large-Scale Atomic/Molecular Massively Parallel Simulator (LAMMPS) [24], and the atomistic configurations of the results were visualized using AtomViewer [25] and AtomEye [26].

3. Structural Phases of Si

Various structural phases of Si were observed during the nanoindentation simulation. The Si phases of Si-I, Si-II, BCT-5, Si-III (R8), and Si-XII (BC8) are schematically described in Figure 2 [27]. The Si-I phase is the initial diamond cubic structure with four-fold coordination, and Si-II is the tetragonal (β-tin) structure with six-fold coordination [2]. BCT-5 is the five-coordinated body-centered tetragonal structure that consists of four neighbors at a distance of 0.244 nm and one neighbor at 0.231 nm [28]. The Si-III (R8) and Si-XII (BC8) phases have four-fold coordination with similar structures [29].

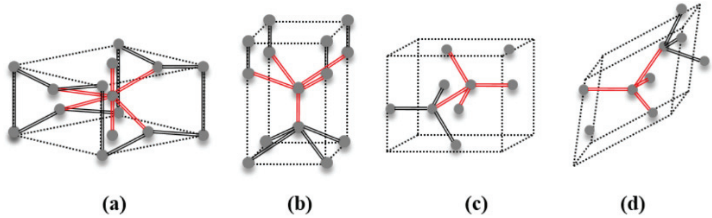

Figure 2. Crystallographic structures of the Si phases observed during nanoindentation: (**a**) Si-II, a tetragonal (β-tin) structure with six-fold coordination; (**b**) BCT-5, a body-centered tetragonal structure with five-fold coordination; (**c**) Si-III (BC8), a cubic structure with four-fold coordination; and (**d**) Si-XII (R8), a rhombohedral distortion structure with four-fold coordination.

4. Theoretical Method

4.1. Sneddon's Solution

To investigate the deformation mechanism of the Si substrate during the loading procedure in more detail, the load of the indenter was compared with Sneddon's solution [17], which is the relationship between a frictionless non-rigid cone and an elastic half plane. Sneddon's solution is given by Equation (1).

$$P = \frac{2}{\pi} E^* \tan\alpha \times h^2, \tag{1}$$

where P is the load applied to the indenter, α is the semi-angle of the conical indenter, h is the indentation depth, and E^* is the reduced modulus. The reduced modulus was defined by Oliver and Pharr [16], as given in Equation (2).

$$\frac{1}{E^*} = \frac{1-\nu_s^2}{E_s} + \frac{1-\nu_i^2}{E_i}, \tag{2}$$

where E and ν are the elastic modulus and Poisson's ratio, respectively. The subscripts s and i indicate the substrate and indenter, respectively. The elastic modulus and Poisson's ratio for the substrate and indenter are E_s = 130 GPa, E_i = 1056.48 GPa, ν_s = 0.3459, and ν_i = 0.103, respectively [30,31].

4.2. Calculation of Mechanical Properties

In nanoindentation, hardness (H) is defined as follows [16]:

$$\mathrm{H} = \frac{P_{\max}}{\mathrm{A_c}}, \tag{3}$$

where $P_{\max}$ is the maximum indentation load and $\mathrm{A_c}$ is the projected contact area. For the conical indenter, the projected contact area is expressed as follows:

$$\mathrm{A_c} = \pi(\tan\alpha \times h_c)^2, \tag{4}$$

where α is the semi-angle of the cone indenter and h_c is the contact depth. In this study, we assumed that $h_c = h$ for the actual projected contact area [32,33].

The elastic modulus values of Si were calculated from the unloading line using Sneddon's solution [17]. To measure the elastic modulus of the Si substrate, Equation (2) is modified to

$$E_s = \left(1 - \nu_s^2\right) \times \left(\frac{1}{E^*} - \frac{1 - \nu_i^2}{E_i}\right)^{-1}, \tag{5}$$

where E and ν are the elastic modulus and Poisson's ratio, respectively, and the subscripts s and i indicate the substrate and indenter, respectively. E^* is the reduced modulus. According to Sneddon, the reduced modulus of the substrate is defined as given in Equation (6).

$$E^* = \frac{1}{2h\tan\alpha}\frac{dP}{dh} = \frac{1}{2h\tan\alpha}S, \tag{6}$$

where h is the indentation depth, α is the semi-angle of the conical indenter, and the stiffness, S, is the slope of the unloading line. Typically, S is measured for the top one-third of the unloading line. In this study, S was measured in the range of 2.5 to 2.96 nm for the unloading line.

5. Results and Discussion

5.1. *P-h Curves*

To analyze the dependence of the Si substrate's deformation mechanism on the indenter angle, the load–indentation depth (*P-h*) curves for indenter angles of 45°, 60°, and 70° were obtained, as shown in Figure 3. The black solid lines were obtained from Sneddon's solution, corresponding to Equation (1). It is well known that if the indented material shows perfectly elastic deformation, then the unloading line falls on the loading line in the *P-h* curve [16]. In contrast, if plastic deformations largely occur in the indented material, the unloading line does not fall on the loading line.

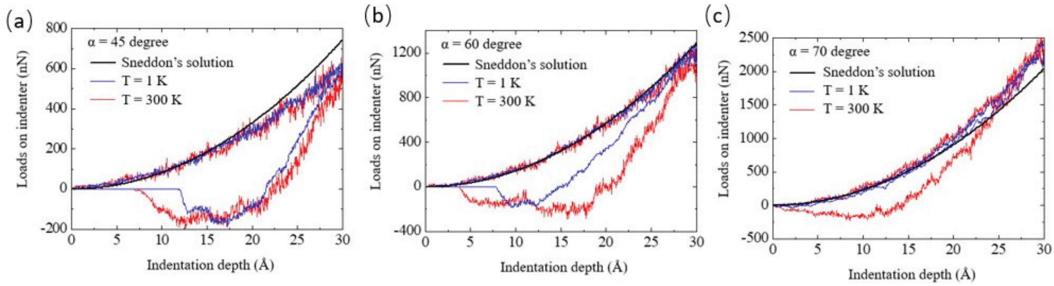

Figure 3. Load−indentation depth curves at temperatures of 1 and 300 K for indenter angles (α) of (**a**) 45°, (**b**) 60°, and (**c**) 70°.

In our simulation results, the discrepancies between the loading and unloading lines decreased with increasing indenter angles. The effect of temperature on the discrepancy could also be observed for the 60° and 70° indenter angles, whereas there was little difference between the 1 K and 300 K plots for the 45° indenter angle. In addition, the load curve for an indenter semi-angle of 45° was smaller than that obtained from Sneddon's solution. In contrast, the load curves for the 60° and 70° indenter angles were similar and larger than those derived from Sneddon's solution. It is worth noting that these discrepancies resulted from the frictionless assumption used in Sneddon's solution [17,34,35]. Hence, it can be speculated that the fraction of plastic deformation, with respect to the total deformation under loading, decreased with the increasing indenter angle.

5.2. Loading Procedure

Cross-sectional views of the transformed region at an indentation depth of 3 nm are shown in Figure 4. Figure 4a,b illustrate the cases of the 45°, 60°, and 70° indenter semi-angles at 1 K and 300 K, respectively. To identify the Si phases, the original Si phase atoms (Si-I) were not captured, while the transformed Si atoms were depicted using three colors; the blue, red, and green atoms indicate the Si-II, BCT-5, and Si-III and Si-XII phases, respectively.

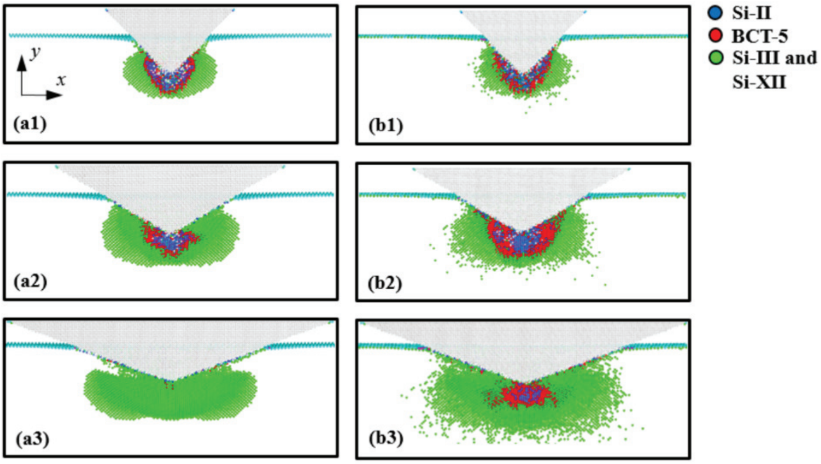

Figure 4. Cross-sectional views of the (001) plane of the transformed Si substrate at an indentation depth of $h = 3$ nm. Images (**a1**–**a3**) correspond to indenter angles of 45°, 60°, and 70° at a temperature of 1 K, and (**b1**–**b3**) correspond to indenter angles of 45°, 60°, and 70° at 300 K, respectively.

As shown in Figure 4, the distributions of the transformed Si phases were quite different depending on the indenter angle. When the Si substrate was indented by the 45° indenter, the structure of the Si atoms at the interfacial area between the indenter and the substrate was transformed from diamond to the Si-II and BCT-5 phase structures. However, the number of transformations to the Si-II and BCT-5 phases at the interfacial area decreased with increasing indenter angles. These transformed phase distributions are associated with pressure concentration [1,36,37]. To monitor the pressure distribution induced by the conical indenter, the (001) plane cross-sectional views of the Si substrate at a temperature of 1 K were captured and are presented in Figure 5. Here, the color of the atoms indicates the level of hydrostatic pressure. The pressure distributions depicted in Figure 5 matched well with the phase distributions of the Si atoms shown in Figure 4a.

To analyze the detailed behavior of the phase transformations, the ratio of the Si-II and BCT-5 atoms ($N_{\text{Si-II and BCT-5}}$) to the total transformed atoms (N_{Total}) was calculated (Table 1). It has been previously reported [13,18] that the Si-II and BCT-5 phases are related to plastic deformation, while metastable Si phases, such as Si-III and Si-XII, are associated with elastic deformation. This trend was also observed in our simulation results, as shown in Figures 3 and 4. For example, the transformed atoms in the case of the 70° indenter at 1 K were almost the same as those of the Si-III and Si-XII phases (Figure 4(a3)). However, at a temperature of 300 K (Figure 4(b3)), a large number of transformations to the Si-II and BCT-5 phases occurred at the subsurface. This trend was evident in the *P*-*h* curves shown in Figure 3c. Therefore, the ratio of the Si-II and BCT-5 atoms to the total number of transformed atoms ($N_{\text{Si-II and BCT-5}}/N_{\text{Total}}$) can be used as the ratio of plastic deformation to total deformation.

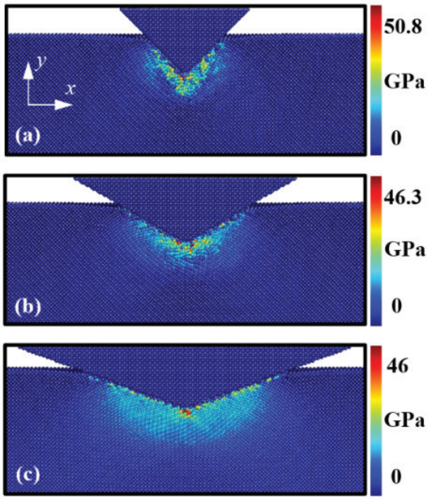

Figure 5. Cross-sectional views of the (001) plane of the hydrostatic pressure distribution in the Si substrate at an indentation depth of h = 3 nm. Images (**a**–**c**) correspond to indenter angles of 45°, 60°, and 70° at a temperature of 1 K, respectively.

Table 1. Ratio of Si-II and BCT-5 atoms ($N_{\text{Si-II and BCT-5}}$) to the total number of transformed atoms at the maximum indentation depth (N_{Total}).

Indenter Angle	$N_{\text{Si-II and BCT-5}}/N_{\text{Total}}$	
	1 K	**300 K**
45°	0.34	0.363
60°	0.162	0.362
70°	0.032	0.164

In addition, it can be seen that the ratio of Si-II and BCT-5 atoms at 300 K is larger than that at 1 K, implying that more plastic deformation occurs at 300 K than at 1 K. These results can be explained by the relationship between the temperature and pressure required for phase transformation. Khayyat et al. [38] utilized a Vickers diamond indenter (equivalent cone semi-angle of 70.3°) and experimentally showed that the pressure required to cause transformation increases with decreasing temperature. As shown in Table 1, this effect of temperature on the ratio was observed for the 60° and 70° indenters, whereas only a small discrepancy between the ratios at 1 K and 300 K was observed for the 45° indenter angle. This indicates that while the influence of temperature on plastic deformation is significant for the 60° and 70° indenters, it is not as significant for the 45° indenter angle, which is consistent with the P-h curve results.

The phase transformation in the Si substrate during indenter loading is shown in Figure 6. Figure 6a–c illustrate the 60° indenter case at the indentation depths of 1 nm, 2 nm, and 3 nm, respectively. As the hydrostatic pressure beneath the indenter tip increases with loading (Figure 5b), the area of phase transformations to Si-II, BCT-5, Si-III, and Si-XII structures increases in the substrate. Specifically, the number of Si-II and BCT-5-phase atoms (related to plastic deformation) increases beneath the indenter tip, where the location matches the large hydrostatic pressure zone. The results indicate that the phase transformation behavior of the Si structure is dependent on the hydrostatic pressure distribution.

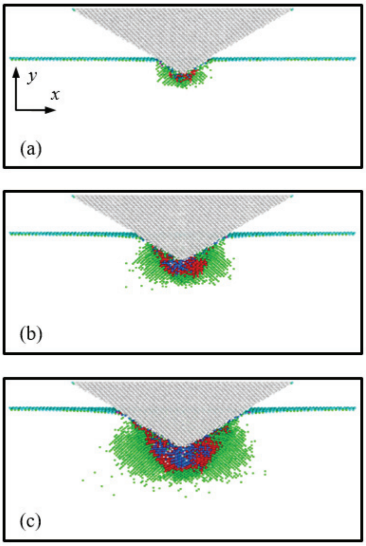

Figure 6. Cross-sectional views of the (001) plane of the transformed Si substrate during indenter loading. Images (**a**–**c**) correspond to the 60° indenter angle case at the indentation depths of 1 nm, 2 nm, and 3 nm, respectively.

5.3. Unloading Procedure

To analyze the deformation mechanism of the substrate under unloading conditions, the ratio of the final depth (h_f) to the maximum indentation depth ($h_{\max}$) was plotted as a function of the indenter angle (Figure 7) [38]. The final depth was defined as the point at which $P = 0$ in the unloading line. In the range $0 \leq h_f/h_{\max} \leq 1$, the lower bound corresponds to the case of perfect elastic recovery, while the upper bound indicates the fully plastic deformation case. As displayed in Figure 7, the ratio increased with decreasing indenter angle, and the ratio at 300 K was larger than that at 1 K. These results indicate that at a temperature of 1 K, the Si substrate indented by a blunt indenter recovers in a more elastic manner, and elastic recovery is greater. In particular, the ratio for the 70° indenter angle at 1 K was 0.143, which indicates that almost perfect elastic recovery occurs in the Si substrate.

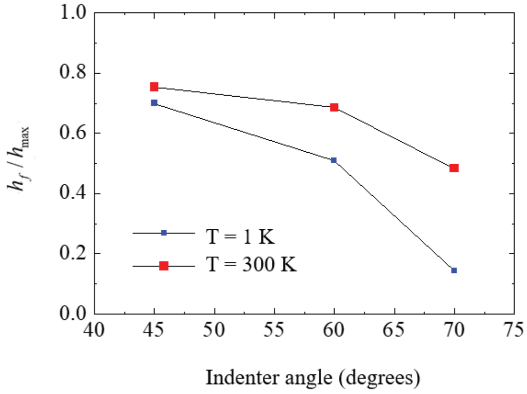

Figure 7. Ratio of the final depth, h_f, to the maximum indentation depth, $h_{\max}$, versus the indenter angle α.

The distribution of residual transformed atoms in the substrate after unloading is shown in Figure 8. Figure 8a,b illustrate the cases of indenter angles of 45°, 60°, and 70° at temperatures of 1 K and 300 K, respectively. From a comparison with Figure 4, it can be seen that most of the Si-III and Si-XII atoms disappeared, and the amorphous-phase Si comprising Si-II, BCT-5, Si-III, and Si-XII atoms was formed in the substrate. In addition, it can be observed that the shape of amorphous Si was similar to the distribution of Si-II and BCT-5 atoms at an indentation depth of 3 nm. For instance, for the 45° indenter angle, cone-shaped amorphous Si was formed in the substrate, which was similar to the distribution of the Si-II and BCT-5 atoms at an indentation depth of 3 nm, as shown in Figure 4. In contrast, for the 70° indenter angle at 1 K, most of the transformed atoms returned to the original Si structure and only a few transformed atoms remained at the surface, as shown in Figure 8(a3).

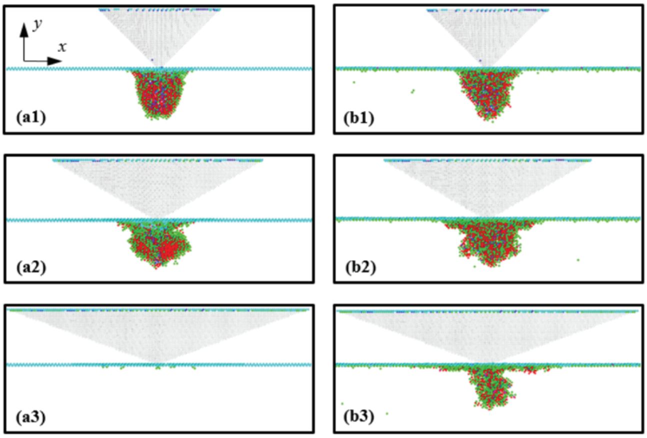

Figure 8. Views of the residual transformed atoms in the (001) plane of the Si substrate after unloading. Images (**a1**–**a3**) correspond to indenter angles of 45°, 60°, and 70° at a temperature of 1 K, and (**b1**–**b3**) correspond to indenter angles of 45°, 60°, and 70° at 300 K, respectively.

To study the ratio of elastic recovery under unloading, the ratio of atoms that returned to their original structure upon unloading to the total number of transformed atoms at an indentation depth of 3 nm, ($N_{\text{Returned atom}}/N_{\text{Total}}$), was calculated (Table 2). From the results given in Table 2, it is evident that the ratio $N_{\text{Returned atom}}/N_{\text{Total}}$ increased with increasing indenter angle and the ratio at 1 K was larger than that at 300 K, which indicates that the elastic recovery occurred more readily under blunter indenter unloading and at lower temperatures. These atomistic configuration results are consistent with the *P-h* curve trend shown in Figure 2.

Table 2. Ratio of atoms that returned to the original structure upon unloading ($N_{\text{Returned atom}}$) to the total number of transformed atoms at the maximum indentation depth (N_{Total}).

Indenter Angle	$N_{\text{Returned atom}}/N_{\text{Total}}$	
	1 K	**300 K**
45°	0.546	0.47
60°	0.783	0.736
70°	0.955	0.877

Figure 9 shows the phase transformation in the Si substrate during the unloading procedure. Figure 9a–c illustrate the 60° indenter case at the indentation depths of 2 nm, 1 nm, and 0 nm, respectively. During indenter unloading, most of the Si-III- and Si-XII-phase atoms disappear, while the Si-II- and BCT-5-phase atoms remain in the Si substrate. The phase transformation behavior under the unloading procedure describes that the Si-III and Si-XII phases are associated with the elastic deformation of Si, whereas Si-II and BCT-5 phases are related to the plastic deformation of Si [18,22].

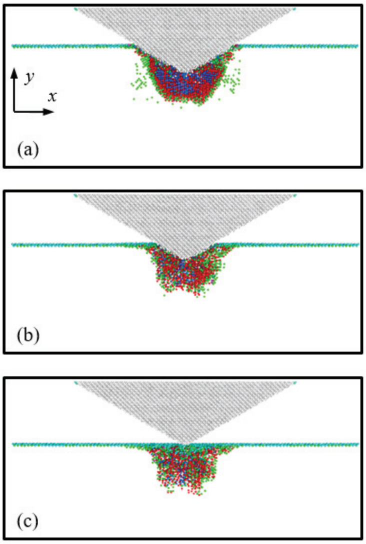

Figure 9. Cross-sectional views of the (001) plane of the transformed Si substrate during indenter unloading. Images (**a**–**c**) correspond to the 60° indenter angle case at the indentation depths of 2 nm, 1 nm, and 0 nm, respectively.

5.4. Mechanical Properties

The hardness (H) of the Si substrate was presented as a function of the indentation depth (*h*) for each indenter angle at 300 K, and the results are shown in Figure 10. The hardness was calculated from the *P*-*h* curve using Equations (3) and (4). For the 45° and 60° indenters, it was observed that the hardness decreased with increasing indentation depth, and then converged to a constant value. However, for the 70° indenter, the hardness remained almost constant during loading. This trend is also demonstrated by the indentation size effect [32,39,40], which appeared strongly in the case of the sharper indenter because of the relatively small penetration volume.

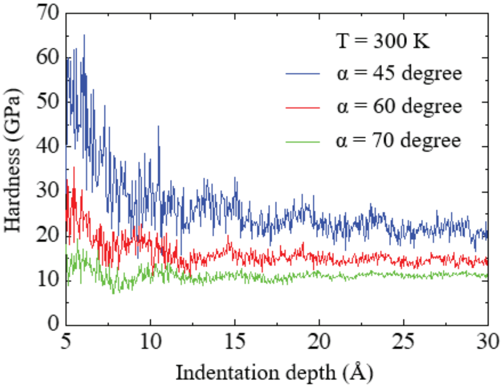

Figure 10. Hardness–indentation depth curves at a temperature of 300 K for the three indenter angles.

From Figure 10, the convergence values of hardness were obtained as 20.1, 14.21, and 11.36 GPa for the indenter semi-angles of 45°, 60°, and 70°, respectively, which are the average values at an indentation depth ranging from 2.9 to 3 nm. Experimental values of the hardness of single-crystal Si have been reported to be 12–14 GPa at 300 K [41]. Thus, the result of the 60° indenter was found to be in good agreement with experimental values. In addition, it can be seen that the obtained hardness decreases with increasing indenter angle. This angle-dependent hardness is associated with plastic flow. According to Prasad et al. [42], the hardness values decreased with an increase in the elastic deformation zone surrounding the plastic zone. As shown in Figure 4b, the size of the elastic zone surrounding the plastic zone increases with increasing indenter angle. Hence, it is reasonable to conclude that the hardness of Si depends on the indenter angle at the atomic scale.

The elastic modulus of the Si substrate was calculated for each indenter angle at 300 K using Equations (5) and (6), and the results are presented in Figure 11. The experimental value of the elastic modulus of Si in the (010) plane was reported to be 130 GPa [29,43]. As shown in Figure 9, although the obtained elastic modulus decreased with increasing indenter angle, the values were within a reasonable range when compared to experimental values. When α = 45°, the difference between the obtained result and the experimental value was 5.3%, while for α = 60° and 70°, the differences were 2.9% and 6.5%, respectively. Therefore, it can be concluded that the results obtained for the indenter with a 60° semi-angle were best fitted to the experimental values.

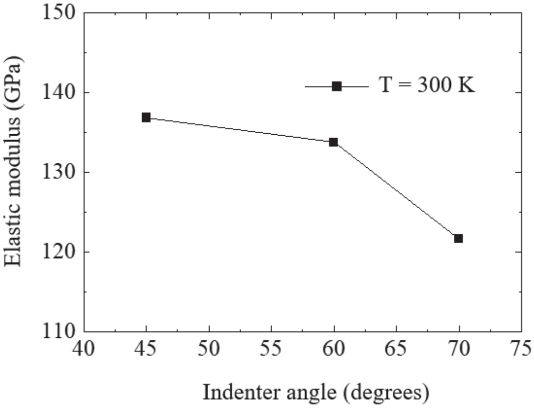

Figure 11. Computed elastic modulus values at a temperature of 300 K for the three indenter angles.

6. Conclusions

This research revealed atomistic insights into the effect of indenter shape on the phase transformation behavior of a Si substrate via MD simulations. Upon indenter loading, phase transformations to Si-II, BCT-5, Si-III, and Si-XII were observed beneath the indenter tip. For the indenter unloading procedure, the number of Si-III and Si-XII atoms significantly decreased, but the Si-II- and BCT-5-phase atoms remained in the Si substrate. The results exhibited that the Si-III and Si-XII phases describe elastic recovery, while the Si-II and BCT-5 phases describe plastic deformation. Among the three conical indenters with semi-angles of 45°, 60°, and 70°, the 70° indenter case showed greater elastic recovery, which was elucidated based on the *P-h* curve and atomistic deformation behaviors. Furthermore, the mechanical properties of hardness and elastic modulus decreased with increasing indenter angle, and the 60° indenter case showed good agreement with previous experiments. The present findings obtained from MD simulations are expected to give useful insights into the deformation mechanism of thin-film Si under nanoindentation testing.

Author Contributions: Conceptualization, Y.J.C. and H.G.B.; data curation, Y.J.C.; investigation, Y.J.C.; methodology, Y.J.C. and H.G.B.; project administration, H.G.B.; supervision, H.G.B.; validation, G.H.L. and H.G.B.; visualization, Y.J.C. and G.H.L.; writing–original draft, Y.J.C.; writing–review and editing, G.H.L. and H.G.B. All authors have read and agreed to the published version of the manuscript.

Funding: This work was supported by an Inha University research grant.

Conflicts of Interest: The authors declare no conflict of interest.

Abbreviations

Si-I	Silicon single crystal with diamond cubic structure
Si-II	Silicon with tetragonal structure
Si-III	Silicon cubic structure with four-fold coordination
Si-XII	Silicon rhombohedral distortion structure with four-fold coordination.
BCT-5	Silicon with five-coordinated body-centered tetragonal structure
TEM	Transmission electron microscopy
MD	Molecular dynamics
P-h curves	Load–indentation depth curves
LAMMPS	Large-Scale Atomic/Molecular Massively Parallel Simulator
$N_{\text{Si-II and BCT-5}}$	Number of Si-II and BCT-5 atoms
N_{Total}	Number of transformed Si atoms at the maximum indentation depth
$N_{\text{Returned atom}}$	Number of Si atoms returned to the original structure upon unloading
h_f	Final depth (the point at which $P = 0$ in the unloading line.)
h_{max}	Maximum indentation depth
H	Hardness
E	Elastic modulus

References

1. Jang, J.-I.; Lance, M.; Wen, S.; Tsui, T.Y.; Pharr, G. Indentation-induced phase transformations in silicon: Influences of load, rate and indenter angle on the transformation behavior. *Acta Mater.* **2005**, *53*, 1759–1770. [CrossRef]
2. McMahon, M.I.; Nelmes, R.J. New high-pressure phase of Si. *Phys. Rev. B* **1993**, *47*, 8337–8340. [CrossRef] [PubMed]
3. Domnich, V.; Gogotsi, Y.; Dub, S. Effect of phase transformations on the shape of the unloading curve in the nanoindentation of silicon. *Appl. Phys. Lett.* **2000**, *76*, 2214–2216. [CrossRef]
4. Jamieson, J.C. Crystal Structures at High Pressures of Metallic Modifications of Silicon and Germanium. *Science* **1963**, *139*, 762–764. [CrossRef] [PubMed]
5. Crain, J.; Ackland, G.; Maclean, J.R.; Piltz, R.O.; Hatton, P.D.; Pawley, G.S. Reversible pressure-induced structural transitions between metastable phases of silicon. *Phys. Rev. B* **1994**, *50*, 13043–13046. [CrossRef]
6. Juliano, T.; Domnich, V.; Gogotsi, Y. Examining pressure-induced phase transformations in silicon by spherical indentation and Raman spectroscopy: A statistical study. *J. Mater. Res.* **2004**, *19*, 3099–3108. [CrossRef]
7. Mann, A.B.; Heerden, D.V.; Pethica, J.B.; Bowes, P.; Weihs, T.P. Contact resistance and phase transformations during nanoindentation of silicon. *Philos. Mag. A* **2002**, *82*, 1921–1929. [CrossRef]
8. Goel, S.; Faisal, N.H.; Luo, X.; Yan, J.; Agrawal, A. Nanoindentation of polysilicon and single crystal silicon: Molecular dynamics simulation and experimental validation. *J. Phys. D Appl. Phys.* **2014**, *47*, 275304. [CrossRef]
9. Lee, G.H.; Na, S.M.; Chung, Y.J.; Beom, H.G. Atomistic aspects of the temperature effect on fracture toughness of a silicon single crystal. *Comput. Mater. Sci.* **2021**, *195*, 110489. [CrossRef]
10. Lee, G.H.; Beom, H.G. Mixed-mode fracture toughness testing of a Cu/Ag bimetallic interface via atomistic simulations. *Comput. Mater. Sci.* **2020**, *183*, 109806. [CrossRef]
11. Sun, J.; Xu, B.; Zhou, X.; Han, J.; Yang, Z.; Jiang, J.; Ma, A.; Wu, G.; Chu, P. Investigation of indenter-size-dependent nanoplasticity of silicon by molecular dynaimics simulation. *ACS Appl. Electron. Mater.* **2020**, *2*, 3039–3047. [CrossRef]
12. Wang, Y.; Minhaj, M.; Wang, X.; Shi, J. Deformation behaviors and inverse Hall-Petch effect in nanoindentation of silicon: An atomistic simulation study with experimental validation. *J. Manuf. Process.* **2021**, *74*, 319–331. [CrossRef]
13. Jiao, S.; Huang, Q.; Tu, W.; Chen, J.; Sun, Z. Investigation on the phase transformation of monocrystalline silicon during nanoindentation at cryogenic temperature by molecular dynamics simulation. *Phys. B Condens. Matter* **2018**, *555*, 139–144. [CrossRef]
14. Bouzakis, K.-D.; Michailidis, N.; Hadjiyiannis, S.; Skordaris, G.; Erkens, G. The effect of specimen roughness and indenter tip geometry on the determination accuracy of thin hard coatings stress–strain laws by nanoindentation. *Mater. Charact.* **2002**, *49*, 149–156. [CrossRef]

15. Santos, J.A.C.; Rebêlo, L.M.; Araujo, A.C.; Barros, E.B.; de Sousa, J.S. Thickness-corrected model for nanoindentation of thin films with conical indenters. *Soft Matter* **2012**, *8*, 4441–4448. [CrossRef]
16. Oliver, W.C.; Pharr, G.M. An improved technique for determining hardness and elastic modulus using load and displacement sensing indentation experiments. *J. Mater. Res.* **1992**, *7*, 1564–1583. [CrossRef]
17. Sneddon, I.N. The relation between load and penetration in the axisymmetric boussinesq problem for a punch of arbitrary profile. *Int. J. Eng. Sci.* **1965**, *3*, 47–57. [CrossRef]
18. Sun, J.; Ma, A.; Jiang, J.; Han, J.; Han, Y. Orientation-dependent mechanical behavior and phase transformation of mono-crystalline silicon. *J. Appl. Phys.* **2016**, *119*, 095904. [CrossRef]
19. Cheong, W.C.D.; Zhang, L.C. Molecular dynamics simulation of phase transformations in silicon monocrystals due to nano-indentation. *Nanotechnology* **2000**, *11*, 173–180. [CrossRef]
20. Zhang, N.; Deng, Q.; Hong, Y.; Xiong, L.; Li, S.; Strasberg, M.; Yin, W.; Zou, Y.; Taylor, C.R.; Sawyer, G.; et al. Deformation mechanisms in silicon nanoparticles. *J. Appl. Phys.* **2011**, *109*, 063534. [CrossRef]
21. Du, X.; Zhao, H.; Zhang, L.; Yang, Y.; Xu, H.; Fu, H.; Li, L. Molecular dynamics investigations of mechanical behaviours in monocrystalline silicon due to nanoindentation at cryogenic temperatures and room temperature. *Sci. Rep.* **2015**, *5*, 16275. [CrossRef]
22. Tersoff, J. Modeling solid-state chemistry: Interatomic potentials for multicomponent systems. *Phys. Rev. B* **1989**, *39*, 5566–5568. [CrossRef] [PubMed]
23. Goel, S.; Beake, B.; Chan, C.-W.; Faisal, N.; Dunne, N. Twinning anisotropy of tantalum during nanoindentation. *Mater. Sci. Eng. A* **2015**, *627*, 249–261. [CrossRef]
24. Plimpton, S. Fast Parallel Algorithms for Short-Range Molecular Dynamics. *J. Comput. Phys.* **1995**, *117*, 1–19. [CrossRef]
25. Begau, C.; Hua, J.; Hartmaier, A. A novel approach to study dislocation density tensors and lattice rotation patterns in atomistic simulations. *J. Mech. Phys. Solids* **2012**, *60*, 711–722. [CrossRef]
26. Kim, D.E.; Oh, S.I. Atomistic simulation of structural phase transformations in monocrystalline silicon induced by nanoindentation. *Nanotechnology* **2006**, *17*, 2259–2265. [CrossRef]
27. Li, J. AtomEye: An efficient atomistic configuration viewer. *Model. Simul. Mater. Sci. Eng.* **2003**, *11*, 173–177. [CrossRef]
28. Boyer, L.L.; Kaxiras, E.; Feldman, J.L.; Broughton, J.Q.; Mehl, M.J. New low-energy crystal structure for silicon. *Phys. Rev. Lett.* **1991**, *67*, 715–718. [CrossRef]
29. Hu, J.Z.; Merkle, L.D.; Menoni, C.S.; Spain, I.L. Crystal data for high-pressure phases of silicon. *Phys. Rev. B* **1986**, *34*, 4679–4684. [CrossRef] [PubMed]
30. Hopcroft, M.A.; Nix, W.D.; Kenny, T.W. What is the Young's Modulus of Silicon? *J. Microelectromech. Syst.* **2010**, *19*, 229–238. [CrossRef]
31. Al-Sayegh, R.; Makatsoris, C. Vision-Augmented Molecular Dynamics Simulation of Nanoindentation. *J. Nanomater.* **2015**, *2015*, 857574. [CrossRef]
32. Voyiadjis, G.Z.; Yaghoobi, M. Large scale atomistic simulation of size effects during nanoindentation: Dislocation length and hardness. *Mater. Sci. Eng. A* **2015**, *634*, 20–31. [CrossRef]
33. Saraev, D.; Miller, R.E. Atomistic simulation of nanoindentation into copper multilayers. *Model. Simul. Mater. Sci. Eng.* **2005**, *13*, 1089–1099. [CrossRef]
34. Lim, Y.Y.; Chaudhri, M.M. Indentation of elastic solids with a rigid Vickers pyramidal indenter. *Mech. Mater.* **2006**, *38*, 1213–1228. [CrossRef]
35. Li, L.; Song, W.; Xu, M.; Ovcharenko, A.; Zhang, G. Atomistic insights into the loading—Unloading of an adhesive contact: A rigid sphere indenting a copper substrate. *Comput. Mater. Sci.* **2015**, *98*, 105–111. [CrossRef]
36. Li, J.; Fang, Q.; Zhang, L.; Liu, Y. Subsurface damage mechanism of high speed grinding process in single crystal silicon revealed by atomistic simulations. *Appl. Surf. Sci.* **2015**, *324*, 464–474. [CrossRef]
37. Dai, H.; Chen, G.; Zhou, C.; Fang, Q.; Fei, X. A numerical study of ultraprecision machining of monocrystalline silicon with laser nano-structured diamond tools by atomistic simulation. *Appl. Surf. Sci.* **2017**, *393*, 405–416. [CrossRef]
38. Khayyat, M.M.O.; Hasko, D.G.; Chaudhri, M.M. Effect of sample temperature on the indentation-induced phase transitions in crystalline silicon. *J. Appl. Phys.* **2007**, *101*, 083515. [CrossRef]
39. Nix, W.D.; Gao, H. Indentation size effects in crystalline materials: A law for strain gradient plasticity. *J. Mech. Phys. Solids* **1998**, *46*, 411–425. [CrossRef]
40. Lucas, M.; Gall, K.; Riedo, E. Tip size effects on atomic force microscopy nanoindentation of a gold single crystal. *J. Appl. Phys.* **2008**, *104*, 113515. [CrossRef]
41. Vandeperre, L.; Giuliani, F.; Lloyd, S.; Clegg, W. The hardness of silicon and germanium. *Acta Mater.* **2007**, *55*, 6307–6315. [CrossRef]
42. Prasad, K.E.; Chollacoop, N.; Ramamurty, U. Role of indenter angle on the plastic deformation underneath a sharp indenter and on representative strains: An experimental and numerical study. *Acta Mater.* **2011**, *59*, 4343–4355. [CrossRef]
43. Hall, J.J. Electronic effects in the elastic constants of n-type silicon. *Phys. Rev.* **1967**, *161*, 756–761. [CrossRef]

nanomaterials

Article

Enhancing the Low-Temperature CO Oxidation over CuO-Based α-MnO_2 Nanowire Catalysts

Yan Cui †, Huikang Song †, Yiyu Shi †, Pengxiang Ge, Mindong Chen * and Leilei Xu *

Collaborative Innovation Center of Atmospheric Environment and Equipment Technology, Jiangsu Key Laboratory of Atmospheric Environment Monitoring and Pollution Control, School of Environmental Science and Engineering, Nanjing University of Information Science & Technology, Nanjing 210044, China; cuiyan@nuist.edu.cn (Y.C.); nuistshk@163.com (H.S.); syyee@163.com (Y.S.); gepx@nuist.edu.cn (P.G.)

* Correspondence: chenmd@nuist.edu.cn (M.C.); leileixu88@nuist.edu.cn (L.X.); Tel.: +86-25-5873-1089 (M.C.)

† These authors contributed equally to this work.

Abstract: A series of CuO-based catalysts supported on the α-MnO_2 nanowire were facilely synthesized and employed as the CO oxidation catalysts. The achieved catalysts were systematically characterized by XRD, SEM, EDS-mapping, XPS and H_2-TPR. The catalytic performances toward CO oxidation had been carefully evaluated over these CuO-based catalysts. The effects of different loading methods, calcination temperatures and CuO loading on the low temperature catalytic activity of the catalyst were investigated and compared with the traditional commercial MnO_2 catalyst with a block structure. It was found that the slenderness ratio of a CuO/α-MnO_2 nanowire catalyst decreases with the increase in CuO loading capacity. The results showed that when CuO loading was 3 wt%, calcination temperature was 200 °C and the catalyst that was supported by the deposition precipitation method had the highest catalytic activity. Besides, the α-MnO_2 nanowire-supported catalysts with excellent redox properties displayed much better catalytic performances than the commercial MnO_2-supported catalyst. In conclusion, the CuO-based catalysts that are supported by α-MnO_2 nanowires are considered as a series of promising CO oxidation catalysts.

Keywords: CuO-based catalyst; α-MnO_2 nanowire; low-temperature catalytic activity; CO oxidation

Citation: Cui, Y.; Song, H.; Shi, Y.; Ge, P.; Chen, M.; Xu, L. Enhancing the Low-Temperature CO Oxidation over CuO-Based α-MnO_2 Nanowire Catalysts. *Nanomaterials* **2022**, *12*, 2083. https://doi.org/10.3390/nano12122083

Academic Editors: Jihoon Lee and Ming-Yu Li

Received: 31 May 2022
Accepted: 14 June 2022
Published: 16 June 2022

1. Introduction

Carbon monoxide is generally considered to be a fuel, resulting from the incomplete combustion of fuel. The environmental pollution it causes has become a serious problem all over the world, which has a great impact on human health and living environment [1,2]. At present, CO degradation technologies mainly include adsorption, separation, biodegradation, combustion, plasma catalysis, photocatalysis, catalytic oxidation and so on [3]. Among them, catalytic oxidation has been widely used because of its advantages of high purification efficiency, low reaction temperature and low cost [4]. Therefore, the design and development of catalysts with advanced performance is the key to solve CO catalytic oxidation. It was found that noble metals (Au [5], Pt [6] and Rh [7]) as the active center supported on specific metal oxides (CeO_2 [8], MnO_2 [9], ZrO_2 [10] and Fe_2O_3 [11]) with excellent oxygen storage capacity usually have high activity for CO catalytic oxidation. However, due to the high price and scarce resources of precious metals, their large-scale application is greatly limited. In the past few decades, various transition metal oxides (Co_3O_4, CuO, Fe_2O_3 and MnO_2) have proved to show excellent catalytic activity in CO catalytic oxidation. Co_3O_4-based catalysts have been widely studied for their low temperature catalytic activity that is similar to that of noble metal catalysts. However, the rapid deactivation of Co_3O_4-based catalysts occurs under high humidity [12,13]. In contrast, CuO-based catalysts have poor low temperature activity but high humidity tolerance. Therefore, the preparation of CuO-based catalysts with excellent low temperature activity has always been a research focus and challenge in the field of CO catalytic oxidation [14].

In order to design and prepare highly efficient CuO-based catalysts, the effect of catalyst supports and preparation strategies have been extensively studied. Among many catalysts supports, MnO_2 has been widely studied because of its low cost, environmental friendliness and high activity [15]. It is well known that the physicochemical properties of MnO_2 with different morphologies are often different. The common one-dimensional structures of MnO_2 include block structure, nanorods, nanotube and nanowires. Among these morphologies, MnO_2 of a nanowire structure plays an important role because nanowire with a one-dimensional structure can be used as the basic assembly unit of two- or three-dimensional structural materials [16,17]. In addition, composites with novel structures and properties can be prepared easily. Compared with traditional MnO_2 with a bulk structure, nanostructured MnO_2 materials generally have better physicochemical properties, such as a higher specific surface area, lower density and adjustable chemical properties [18]. In addition, various studies have shown that MnO_2 materials with nanowire morphology usually have a high surface area and strong metal-support interactions. Compared with other morphologies of MnO_2 nanomaterials, MnO_2 nanowire usually has higher catalytic activity [19,20]. Therefore, nanowire is the main form of MnO_2 nanomaterials. MnO_2 nanowires generally have more surface oxygen adsorption, stronger reducibility, higher specific surface area and lower Mn-O bond strength than MnO_2 nanorods. Therefore, it has a better catalytic performance in the catalytic combustion of dimethyl ether and the catalytic oxidation of toluene. Saputra et al. [21] found that MnO_2 nanowire exhibited higher activity than MnO_2 nanorods and MnO_2 nanofibers in the co-degradation of phenol by reactive oxygen species and hydroxyl groups. In addition, compared with nanorod and nanotube MnO_2, MnO_2 nanowires as supports have stronger interactions with Ag and exhibit higher toluene oxidation activity. Among the MnO_2 nanomaterials (α-MnO_2, β-MnO_2), α-MnO_2 nanowire also showed the best catalytic activity for CO, even after Co_3O_4 nanoparticles were decorated. Liang et al. [22] synthesized four MnO_2 nanomaterials with different crystal types. They found that the order of activity of CO catalytic oxidation is $\alpha = \delta > \gamma > \beta$-$MnO_2$ because the [2 × 2] and [1 × 1] tunnel structures of α-MnO_2 can occupy more space to obtain more CO adsorption sites. On the other hand, the strong catalytic performance of α-MnO_2 for CO oxidation is due to the prolonged length of the Mn-O bond that is caused by twisted [MnO_6], which may be conducive to the fracture of Mn-O bond, thus promoting CO oxidation. Therefore, α-MnO_2 reacts easily with CO, which further improves its catalytic performance.

In addition, various studies have been carried out to improve the CO catalytic oxidation activity of MnO_2 nanowires. In order to achieve this goal, effective strategies, including element-doped surface engineering and combination with other active substances have been extensively developed [23]. Metal loading and doping are two commonly used modification methods for preparing catalysts. Both can significantly improve the catalytic activity of MnO_2 nanowires [24,25]. The loading method can disperse the metal or metal oxide on the surface of the catalyst carrier highly uniformly, and the catalyst with higher activity can be obtained due to the formation of a strong metal-support interaction. The doping method is to replace the metal cations in the main metal oxides with different cations, which can greatly change the chemical bonding on the surface of the main metal oxides and improve their catalytic performance [26,27]. The active sites in the catalytic system may be oxygen atoms near the dopant or the dopant itself. Therefore, the activity of MnO_2 nanowires can be further improved by dispersing more active components on their surfaces. Gao et al. [28] found that hydrothermal doping of Cu significantly improved the CO oxidation activity and water resistance of α-MnO_2 nanowires. For γ-MnO_2, Zn-doped MnO_2 achieves a 90% CO conversion at 160 °C and shows the best CO oxidation activity in other elements that are doped with γ-MnO_2. Li et al. [29] synthesized α-MnO_2 with a porous surface structure by acid treatment. It has rich adsorption sites for O_2, thus enhancing the catalytic oxidation activity of MnO_2 to CO. In addition, combining Au, Ag and CuO with MnO_2 nanomaterials can effectively improve the efficiency of CO catalytic oxidation. Xu et al. [30]

also studied the effect of a Ag-supported catalyst on CO catalytic oxidation activity on α-MnO_2 nanowires, and the $T_{90\%}$ of Ag/α-MnO_2 could reach below 100 °C.

In this study, α-MnO_2 material with a perfect nanowire structure was successfully prepared by a one-step hydrothermal method. The nanowires with excellent structural properties and thermal stability could be used as CuO-based catalyst supports. A series of CuO-based α-MnO_2 nanowire catalysts were prepared by initial impregnation and deposition precipitation methods for CO catalytic oxidation reaction at a low temperature. The catalysts were characterized by X-ray powder diffraction (XRD), scanning electron microscopy (SEM), energy-dispersed spectroscopy (EDS) mapping, X-ray photoelectron spectroscopy (XPS), etc. The effects of different loading methods, calcination temperature, CuO loading and the mesoscopic structure of MnO_2 on CO oxidation activity at low temperature were studied.

2. Materials and Methods

2.1. Synthesis of α-MnO_2 Nanowire Support

The α-MnO_2 nanowire support was synthesized by a hydrothermal method according to the scheme that was previously reported [31]. Specifically, 3 mmol of $MnSO_4 \cdot H_2O$ was first dissolved in 40 mL of deionized water and stirred for 5 min until the $MnSO_4 \cdot H_2O$ solution was clarified. Then, 2 mmol of $KMnO_4$ was also dissolved in 40 mL of deionized water and stirred for 5 min. After that, the $KMnO_4$ solution was gradually added to the $MnSO_4 \cdot H_2O$ solution to obtain the brown suspension, and the stirring was continued for 30 min. The stirred brown suspension was transferred to a Teflon reactor and hydrothermal reaction at 160 °C for 12 h. The brown-black liquid that was obtained after the hydrothermal treatment was washed six times with ethanol. The solid that was obtained by centrifugation was placed in a vacuum drying oven at 100 °C for 12 h, and then the α-MnO_2 nanowire support was obtained.

2.2. CuO-Based α-MnO_2 Nanowire Catalyst Preparation

The CuO-based supported α-MnO_2 nanowire catalysts containing x wt% CuO ($x = m_{CuO}/(m_{CuO} + m_{support}) \times 100\%$) were synthesized by a deposition precipitation method. To be specific, α-MnO_2 nanowire was dispersed in $Cu(NO_3)_2 \cdot 3H_2O$ solution, and then Na_2CO_3 (0.01 M) solution was added droplet by droplet to adjust the pH to 8~9. The mixed solution was fully stirred for 30 min and then stood for 1h. After filtration, it was washed with deionized water and dried for 12 h in an oven of 120 °C. Then, the CuO-based α-MnO_2 nanowire catalysts with different CuO loading were obtained by calcination at 200 °C for 5 h and were denoted as xCuO/α-MnO_2-200-DP (x = 1, 3, 5, 10, 20 and 30). Meanwhile, a series of catalysts defined as 3CuO/α-MnO_2-T-DP (T = 120, 200, 300 and 400) were synthesized under the same preparation process at a different calcination temperature, where "T" refers to the calcination temperature of the catalyst. In order to clarify the influence of the loading mode on the performance of the catalyst, the CuO-based α-MnO_2 nanowire catalyst by incipient impregnation method was denoted as 3CuO/α-MnO_2-200-IMP.

In addition, the CuO that was supported on a commercial MnO_2 catalyst (3CuO/C-MnO_2-200-DP) indicated that the special morphology of α-MnO_2 nanowire also promoted the catalytic activity of CO catalytic oxidation. The commercial MnO_2 that was used in this study was the most common one in the market, and it was normal to have fewer impurities in the commercial MnO_2.

2.3. Catalyst Characterizations

X-ray powder diffraction (XRD) patterns of all catalysts were performed on a Smart Lab/3 kW Intelligent multifunctional X-ray Diffractometer (Shimadzu, Kyoto, Japan) (Cu Kα radiation 40 kV/100 mA, the step of 5°/min, 2θ = 10–80°). Scanning electron microscopy (SEM) and energy-dispersed spectroscopy (EDS) mapping measurements of all catalysts were carried out on a scanning electron microscopy (FEI TECNAI G2 F20, Hillsboro, OR, USA). The sample was glued to the conductive adhesive, and gold spraying was performed for 45 s and 10 mA using Oxford Quorum SC7620 sputtering coater (Quorum, UK). The morphology of the sample was photographed with a ZEISS Gemini SEM 300 scanning electron microscope. The X-ray photoelectron spectroscopy (XPS) measurements were tested on an Escalab 250Xi (Thermo Fisher Scientific, Waltham, MA, USA) that was equipped with an Al Kα X-ray source to determine the elemental composition and chemical states of the elements. The powder of the sample was spread and coated on conductive tape on the sample holder. The binding energies were calibrated using the C 1s line at 284.5 eV as the reference.

H_2 temperature-programmed reduction (H_2-TPR) experiments were carried out in a self-made fixed-bed reactor (assemble). The consumption curve of H_2 was recorded and analyzed by an online LC-D200 mass spectrometer (TILON, Seoul, Korea). A mixture of H_2 (0.4 mL/min) and Ar (7.6 mL/min) was introduced into the reactor. After the H_2 signal baseline (m/z = 2) was stabilized, a H_2-TPR experiment was performed at a heating rate of 20 °C/min from room temperature to 800 °C.

2.4. Catalyst Evaluation

The catalytic activity of CO oxidation of the catalyst in this system had been tested in a vertical fixed-bed continuous flow reactor that was equipped with quartz tubes (I.D. = 10.00 mm). The temperature of the reaction should be the center temperature of the catalyst bed and it was detected and controlled by the thermocouple that was located in the center of the catalyst bed. The gas flows of the feed gases are controlled by the mass flow controllers (MFC, Brooks Instrument, Hatfield, UK) and used as feed 1 vol % CO, 20 vol. % O_2 and balanced N_2. The catalyst weighed 0.1 g and was injected with CO reaction gas with a total flow of 20 mL/min. The CO oxidation corresponding to the gas hourly space velocity (GHSV) was 12,000 mL/(g·h) gas, and the catalytic activity of CO oxidation over different catalysts was tested in the specified temperature range. Finally, a GC-680 gas chromatograph (Perkin Elmer, Waltham, MA, USA) with a thermal conductivity detector (TCD) was used for an on-line analysis of the outlet gas. The catalytic activity of the catalyst was reflected and expressed by CO conversion. The conversion rate of CO was calculated based on the formula below:

$$C_{CO} = \frac{F_{CO,Inlet} - F_{CO,Outlet}}{F_{CO,Intlet}} \times 100\% \tag{1}$$

$F_{CO,Inlet}$ represented the flow rate of CO species into; $F_{CO,outlet}$ represented the flow rate of CO species out of the reactor.

3. Results and Discussion

3.1. Characterizations of the Catalysts

3.1.1. XRD Analysis

In order to study the crystal phase structure of the supports and catalysts, a series of materials were analyzed by XRD. In Figure 1, the diffraction peaks of α-MnO_2 that were located at 2θ = 12.78°, 18.11°, 25.71°, 37.52°, 41.97°, 49.86°, 56.37°, 65.11° and 69.71° could be ascribed to the α-MnO_2 phase (PDF#44-0141) [30]. Specific, obvious diffraction peaks correspond to the (1 1 0), (2 0 0), (2 2 0), (2 1 1), (3 0 1), (4 1 1), (6 0 0), (5 2 1), (0 0 2) and (5 4 1) crystal planes of the MnO_2 structure, respectively. Figure 1a shows the XRD patterns of 3CuO/α-MnO_2-200-DP and 3CuO/α-MnO_2-200-IMP under different loading methods. As can be seen from the figure, the MnO_2 diffraction peak intensity of the 3CuO/α-MnO_2-200-DP catalyst that was prepared by the deposition precipitation method (DP) loaded with CuO was significantly stronger than 3CuO/α-MnO_2-200-IMP that was prepared by the initial impregnation method (IMP). The catalytic activity test showed that the CO catalytic oxidation activity of 3CuO/α-MnO_2-200-DP was significantly better than that of 3CuO/α-MnO_2-200-IMP.The test also proved that the (2 2 0) and (6 0 0) crystal planes of α-MnO_2 may play a dominant role in CO catalytic oxidation. At the same time, compared with the 3CuO/α-MnO_2-200-IMP, the characteristic peak of CuO in the 3CuO/α-MnO$_2$-200-DP catalyst was much lower. The results showed that the CuO dispersion on the surface of the 3CuO/α-MnO$_2$-200-DP catalyst was significantly higher than that of 3CuO/α-MnO$_2$-200-IMP.

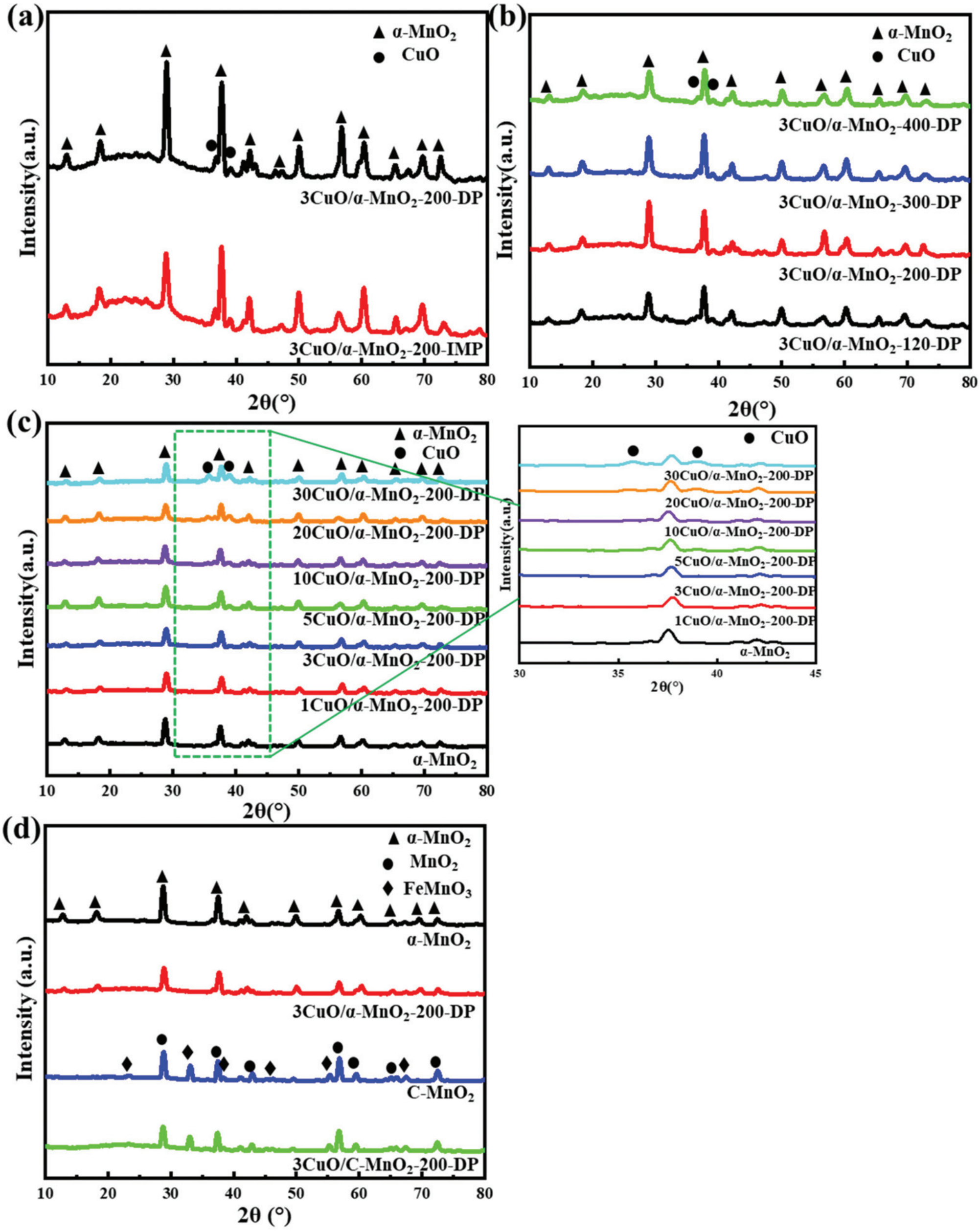

Figure 1. XRD patterns of (**a**) 3CuO/α-MnO$_2$-200-DP and 3CuO/α-MnO$_2$-200-IMP catalysts under different loading methods; (**b**) 3CuO/α-MnO$_2$-T-DP (T = 120, 200, 300, 400) catalysts with different calcination temperatures; (**c**) xCuO/α-MnO$_2$-200-DP (x = 0, 1, 3, 5, 10, 20, 30) catalysts with different CuO loading; (**d**) α-MnO$_2$ nanowire, commercial MnO$_2$ (C-MnO$_2$) and corresponding catalysts.

In general, calcination at higher temperatures was always accompanied by an increase in mean particle size and a decrease in specific surface area due to pore clogging. In addition to reducing the surface area, higher calcination temperatures reduced the active ingredients, ultimately leading to a reduction in the active interface sites. On the other hand, the CuO/α-MnO_2 catalyst generated $CuMn_2O_4$ at higher temperature and deactivates [32]. Figure 1b shows the XRD patterns of $3CuO/\alpha$-MnO_2-T-DP at different calcination temperatures. When the calcination temperature raised from 120 °C to 300 °C, the intensity of the XRD diffraction peak increased and the diffraction peak was the strongest at 300 °C. This ought to be attributed to the collapse of the nanowire framework at the calcination temperature as high as 300 °C, which made the dispersion of CuO worse. However, when the calcination temperature raised to 400 °C, the peak intensity decreased, which was caused by the formation of $CuMn_2O_4$. Moreover, due to the low content of $CuMn_2O_4$, its characteristic diffraction peak cannot be displayed in the XRD pattern.

The XRD patterns of the pure α-MnO_2 nanowire support and xCuO/α-MnO_2-200-DP catalysts with different CuO loading are shown in Figure 1c. As can be seen from the figure, almost all the xCuO/α-MnO_2-200-DP nanowire catalysts showed wide and clear XRD peaks, indicating that all the catalysts displayed good crystallinity. As the CuO loading increased, two diffraction peaks were detected at the $2\theta = 35.5°$ and $38.8°$, which were the diffraction peaks of CuO (PDF#05-0661) [33]. On the other hand, with the increase in CuO content, the intensity of the CuO diffraction peak also increased, indicating that the grain size of CuO increased. At the same time, the characteristic peak intensity of the (2 2 0) and (2 1 1) crystal planes of α-MnO_2 decreased obviously.

Figure 1d shows the XRD patterns of pure α-MnO_2 nanowire, commercial MnO_2 and corresponding catalysts. As can be seen from the figure, the diffraction peak of C-MnO_2 was the same as that of MnO_2 (PDF#72-1984). In addition, the diffraction peak of impurity $FeMnO_3$ (PDF#75-0894) was observed in the C-MnO_2 diffraction peak by comparison [34]. The characteristic peak of CuO cannot be clearly seen in the figure, due to the low loading of CuO. On the other hand, it indicated the high dispersion of CuO on the catalyst's surface.

3.1.2. SEM Observation

SEM images of the α-MnO_2 nanowire support and xCuO/α-MnO_2-200-DP catalysts were analyzed, as shown in Figure 2. The $5CuO/\alpha$-MnO_2-200-DP and $30CuO/\alpha$-MnO_2-200-DP with different CuO loadings were selected as representative catalysts. Figure 2a,b shows the morphology of pure α-MnO_2 nanowire. It was found that the nanowire had a uniform morphology, smooth surface, and large aspect ratio (length: 5–15 μm, width: 100–200 nm). Figure 2c,e, respectively, show the $5CuO/\alpha$-MnO_2-200-DP and $30CuO/\alpha$-MnO_2-200-DP nanowires' catalysts' structure. When the CuO loading increased from 0% to 5%, α-MnO_2 nanowire support retained its morphology, while the 30% CuO loading catalyst showed irregular nanowire. At the same time, the aspect ratio of α-MnO_2 nanowires decreases with the increase in CuO loading. The CuO loading was observed on the surface of the $5CuO/\alpha$-MnO_2-200-DP and $30CuO/\alpha$-MnO_2-200-DP catalysts.

The spatial dispersion of Mn and Cu elements in the nanowire structure could be characterized and analyzed by scanning transmission electron microscopy (STEM) and energy dispersive spectroscopy mapping (EDS-mapping) of the $3CuO/\alpha$-MnO_2-200-DP and $3CuO/\alpha$-MnO_2-200-IMP catalysts. It could be seen from Figure 3 that the supported metal Cu element was uniformly distributed on the surface of the catalysts. In addition, the dispersion of Cu element in the $3CuO/\alpha$-MnO_2-200-DP catalyst was significantly higher than that of the $3CuO/\alpha$-MnO_2-200-IMP catalyst, indicating that the catalyst that was prepared by the precipitation deposition method could better distribute the Cu element on the catalyst's surface.

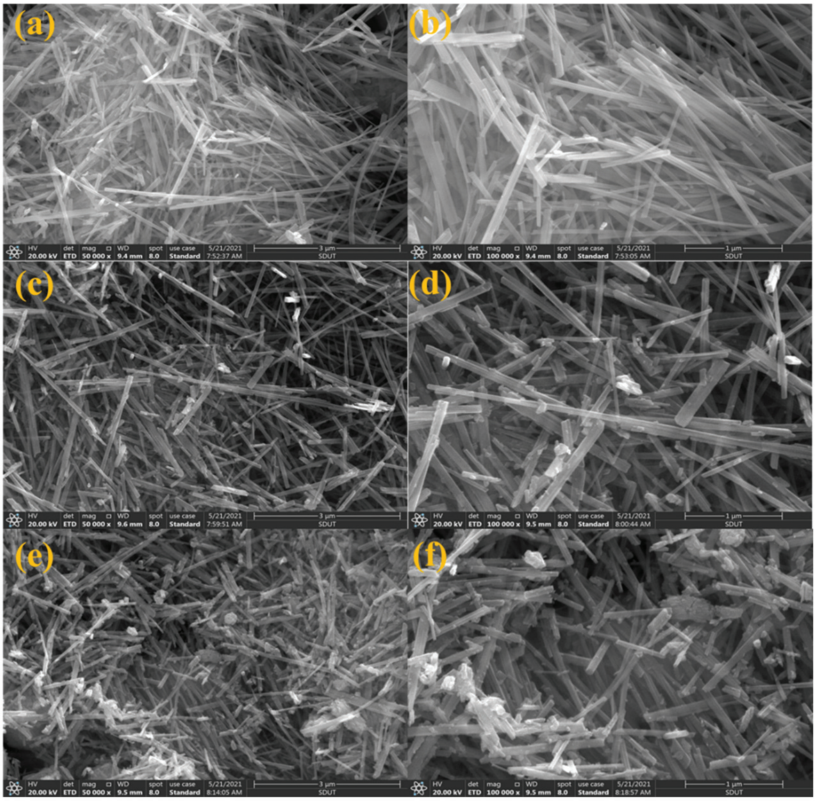

Figure 2. SEM images of α-MnO_2 nanowire support (**a**,**b**), 5CuO/α-MnO_2-200-DP (**c**,**d**) and 30CuO/α-MnO_2-200-DP (**e**,**f**) catalysts.

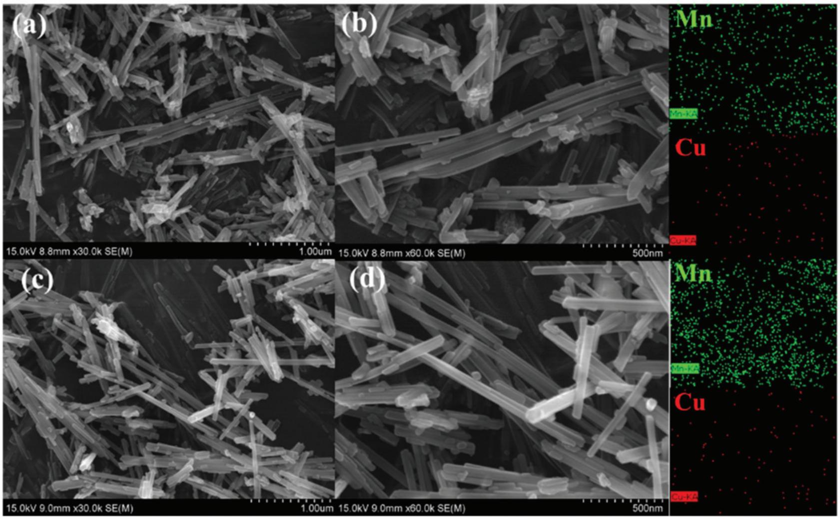

Figure 3. STEM and EDS element mapping images showing the spatial distribution of Mn and Cu elements: (**a**,**b**) 3CuO/α-MnO_2-200-DP, (**c**,**d**) 3CuO/α-MnO_2-200-IMP.

3.1.3. XPS Analysis

An XPS analysis of a series of prepared catalysts provided further evidence of surface chemical coordination, valence and composition states. Their XPS curves were shown in Figures 4–7. It can be seen from Figure 7 that the XPS spectrum of Mn 3s had a double peak structure, and the double peak spacing of all catalysts was 4.5 eV. Therefore, it could be concluded that the Mn species in all catalysts existed in the form of MnO_2. It can be seen from Figure 4a,c that the XPS distribution of Mn 2p and O 1s catalysts under different loading modes was almost the same, because the addition of a small amount of CuO did not affect the overall element concentration ratio of Mn and O. It can be observed from Figure 4b that these catalysts have two main peaks at 933.3 eV and 953.03 eV, which may be attributed to Cu $2p_{3/2}$ and Cu $2p_{1/2}$, respectively. In addition, it was noteworthy that the Cu $2p_{3/2}$ peak was almost accompanied by an oscillating satellite peak in the range of 940.38–943.28 eV. This was accompanied by three satellite peaks with Cu $2p_{3/2}$ peaks at 940.4 eV (I), 941.8 eV (II), and 943.4 eV (III). It was well known that the satellite peak was caused by the transfer of electrons from the ligand orbit to the 3d orbit of Cu, which confirmed the existence of Cu^{2+} in the divalent form of the $3d^9$ structure, rather than the species level of Cu^+ or Cu^0 with d-filled energy [35,36]. Meanwhile, the XPS spectrum of Cu 2p varies greatly under different loading modes. The peak intensity of the Cu 2p spectrum of the 3CuO/α-MnO_2-200-IMP catalyst was significantly lower than that of the 3CuO/α-MnO_2-200-DP catalyst. The peak intensity of the Cu 2p spectrum of the 3CuO/α-MnO_2-200-IMP catalyst was significantly lower than that of the 3CuO/α-MnO_2-200-DP catalyst. The main reason for this was the different CuO dispersion over these catalysts. Specifically, the CuO dispersion of the 3CuO/α-MnO_2-200-IMP catalyst was poorer than the 3CuO/α-MnO_2-200-DP catalyst. According to the XPS survey spectra results (Table 1), the surface concentration of the Cu element over the 3CuO/α-MnO_2-200-DP catalyst was 2.9%, which was similar to the content of the Cu element that was added. However, the surface concentration (1.7%) of the Cu element in the 3CuO/α-MnO_2-200-IMP catalyst was much lower than the theoretical value. These results indicated that the deposition-precipitation method could better disperse the CuO than the initial impregnation method over the α-MnO_2 nanowire support.

The XPS spectra of Mn 2p, O 1s and Cu 2p at different calcination temperatures of the 3CuO/α-MnO_2-*T*-DP catalyst are shown in Figure 5. As can be seen from Figure 5a, these catalysts had two main peaks at 654.0 eV and 642.1 eV, which belong to Mn $2p_{1/2}$ and Mn $2p_{3/2}$ spin orbits, respectively. It should be noted that these two peaks were characteristic signals of Mn (IV). All these indicated the occurrence of interfacial reactions and the formation of MnO_2. To show the redox characteristics of the prepared catalyst, the surface oxidation state of copper was also studied [37]. As can be seen from Figure 5b, the XPS peaks that are centered on 954.0 eV and 933.0 eV belong to Cu $2p_{1/2}$ and Cu $2p_{3/2}$, respectively. The binding energy of Cu 2p increased with the increase in calcination temperature. Meanwhile, with the increase in calcination temperature, the peak intensity corresponding to Cu 2p decreased, which may be caused by the decrease in Cu species' concentration on the catalyst surface, caused by the increase in calcination temperature. To further investigate the properties of various oxygen substances on the 3CuO/α-MnO_2-*T*-DP catalyst, the XPS spectrum of O 1s of 3CuO/α-MnO_2-*T*-DP are shown in Figure 5c. All the catalysts show two peaks of different oxygen species. Specifically, the peaks of 529.9 eV and 531.2 eV can be attributed to the lattice oxygen (O_{latt}) and surface-adsorbed oxygen (O_{ads}) of CuO_x and α-MnO_2, respectively. Combined with the data after peak fitting in Table 2, with the increase in calcination temperature, the acromial area ratio also decreased correspondingly. The oxygen vacancy concentration of 3CuO/α-MnO_2-200-DP was the highest. According to previous reports [38], the formation of oxygen anion radicals was due to the increased adsorption of environmental oxygen by surface oxygen vacancies, which will further improve the performance of catalysts.

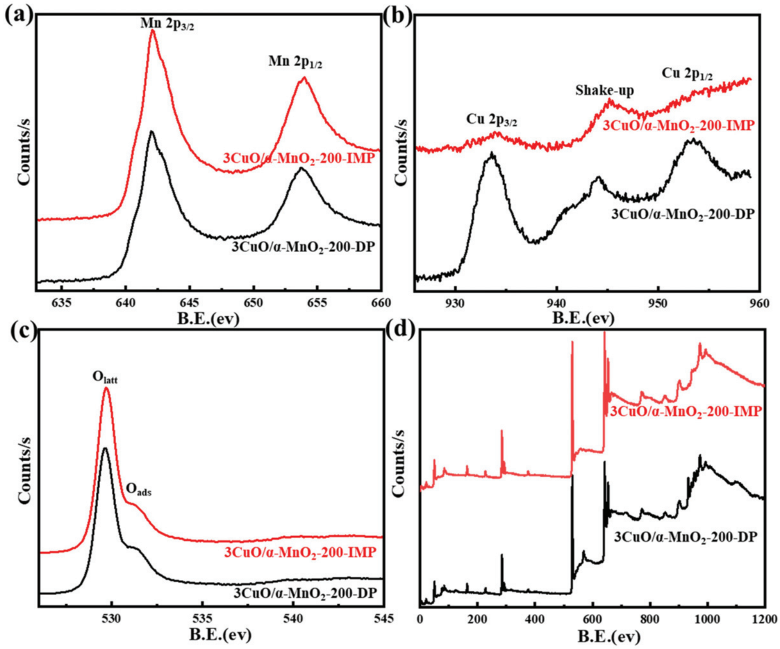

Figure 4. XPS spectra of Mn 2p (**a**), Cu 2p (**b**), O 1s (**c**) and survey spectrum (**d**) for 3CuO/α-MnO_2-200-DP and 3CuO/α-MnO_2-200-IMP catalysts under different loading methods.

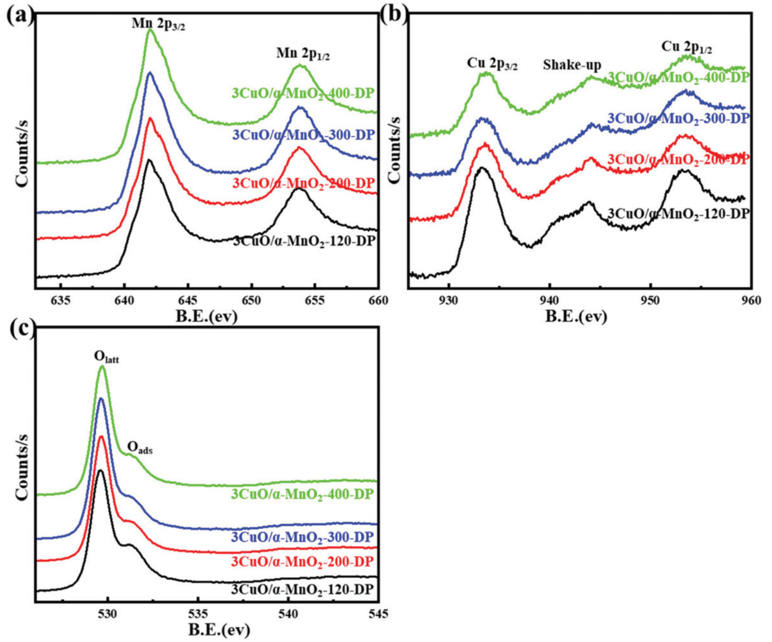

Figure 5. XPS spectra of Mn 2p (**a**), Cu 2p (**b**) and O 1s (**c**) for 3CuO/α-MnO_2-*T*-IMP catalysts with different calcination temperatures.

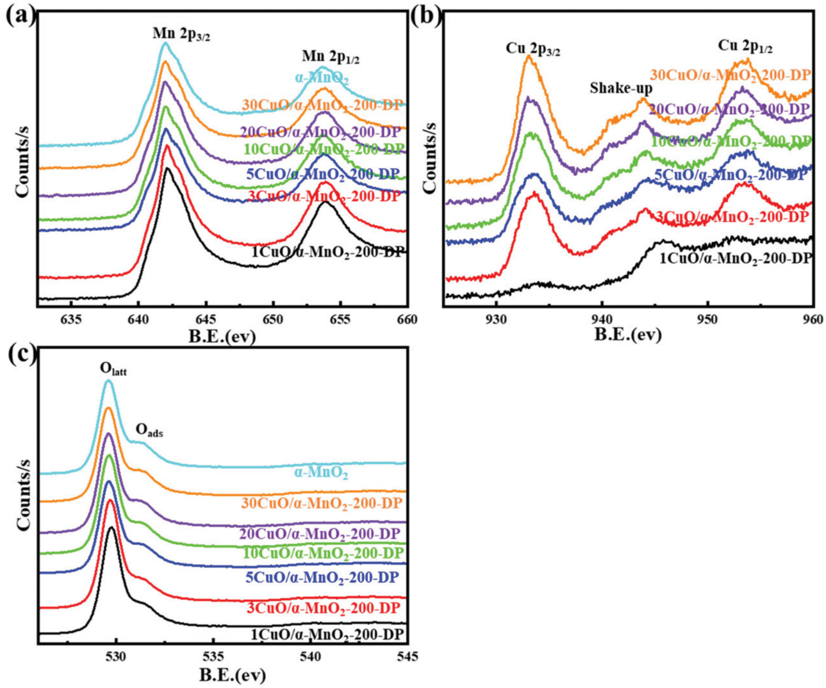

Figure 6. XPS spectra of Mn 2p (**a**), Cu 2p (**b**) and O 1s (**c**) for *x*CuO/α-MnO$_2$-200-DP catalysts with different CuO loading.

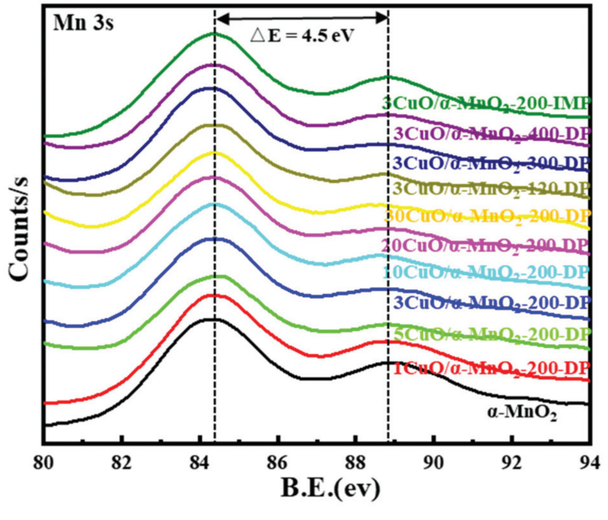

Figure 7. XPS spectra of Mn 3s for catalysts.

Table 1. The surface atomic concentration ratio of Mn, Cu, O of the catalysts based on XPS.

Samples	Mn (%)	Cu (%)	O (%)
α-MnO_2	21.1	/	46.4
1CuO/α-MnO_2-200-DP	20.8	0.9	45.8
3CuO/α-MnO_2-200-DP	18.1	2.9	51.1
5CuO/α-MnO_2-200-DP	18.0	4.0	44.6
10CuO/α-MnO_2-200-DP	17.8	5.6	43.8
20CuO/α-MnO_2-200-DP	16.5	7.0	39.4
30CuO/α-MnO_2-200-DP	10.0	16.9	40.0
3CuO/α-MnO_2-120-DP	20.4	1.2	45.5
3CuO/α-MnO_2-300-DP	17.7	2.2	44.4
3CuO/α-MnO_2-400-DP	16.9	2.0	41.5
3CuO/α-MnO_2-200-IMP	17.6	1.7	45.9

Table 2. O 1 s peak areas of the catalysts based on XPS.

Samples	O 1s Main Peak Area	O 1s Shoulder Peak Area	O 1s Shoulder Peak Area Ratio (%)
α-MnO_2	129,671.0	32,166.2	19.8
1CuO/α-MnO_2-200-DP	140,985.7	32,068.2	18.5
3CuO/α-MnO_2-200-DP	118,838.6	32,724.9	21.6
5CuO/α-MnO_2-200-DP	138,945.0	32,733.5	19.1
10CuO/α-MnO_2-200-DP	137,120.8	34,822.0	20.3
20CuO/α-MnO_2-200-DP	129,100.5	33,846.1	20.7
30CuO/α-MnO_2-200-DP	129,861.6	32,378.3	20.0
3CuO/α-MnO_2-120-DP	129,997.5	32,051.5	19.8
3CuO/α-MnO_2-300-DP	132,452.1	34,305.7	20.6
3CuO/α-MnO_2-400-DP	134,830.5	33,962.0	20.1
3CuO/α-MnO_2-200-IMP	134,777.2	32,518.3	19.4

Figure 6 shows the XPS spectra of Mn 2p, O 1s and Cu 2p in xCuO/α-MnO_2-200-DP catalysts with different CuO loadings. As can be seen from Figure 6a, these catalysts had two main peaks at 652.7 eV and 642.0 eV, which were Mn $2p_{1/2}$ and Mn $2p_{3/2}$, respectively. This indicated that Mn existed in the form of Mn^{4+} in the xCuO/α-MnO_2-200-DP catalyst. In order to show the redox characteristics of the prepared catalyst, the surface oxidation state of copper was also studied [39]. As can be seen from Figure 6b, these catalysts had two main peaks at 953.0 eV and 933.0 eV, namely Cu $2p_{1/2}$ and Cu $2p_{3/2}$. It was noteworthy that the peak intensity of the Cu 2p spectrum increased significantly with the increase in copper content, and the corresponding peak fitting results also showed that the proportion of Cu element increased. In order to clarify the properties of various oxygen-containing substances on the xCuO/α-MnO_2-200-DP catalyst, the XPS spectra of O 1s of all the xCuO/α-MnO_2-200-DP catalysts are shown in Figure 6c. According to the binding energy of surface elements, the binding energy of the xCuO/α-MnO_2-T-DP catalyst in Table 3 decreased with the increase in CuO loading. Combined with the data after peak fitting in Table 2, 3CuO/α-MnO_2-200-DP had the highest acromion area ratio of O 1s. Metal-support interactions between well-dispersed CuO and MnO_2 support produce more surface oxygen and defects. These oxygen and defects predominated when the catalysts exhibited strong CO oxidation properties, and high oxygen vacancy provided a higher catalyst performance for CO catalytic oxidation. In conclusion, different CuO loadings and calcination temperatures together affect the formation of oxygen vacancy on the surface of the catalyst, and further affect the catalytic oxidation performance of CO.

Table 3. Binding energies of surface elements in xCuO/α-MnO_2-T catalysts.

Samples	Cu $2p_{3/2}$	O 1s	Mn $2p_{3/2}$
α-MnO_2	/	529.8	642.3
1CuO/α-MnO_2-200-DP	933.2	529.7	642.2
3CuO/α-MnO_2-200-DP	933.3	529.7	642.2
5CuO/α-MnO_2-200-DP	933.2	529.6	642.1
10CuO/α-MnO_2-200-DP	933.2	529.6	642.1
20CuO/α-MnO_2-200-DP	933.1	529.6	642.1
30CuO/α-MnO_2-200-DP	933.1	529.6	642.1
3CuO/α-MnO_2-120-DP	933.2	529.6	642.1
3CuO/α-MnO_2-300-DP	933.3	529.6	642.1
3CuO/α-MnO_2-400-DP	933.4	529.7	642.2
3CuO/α-MnO_2-200-IMP	933.3	529.7	642.2

3.1.4. H_2-TPR Analysis

In order to study the interaction between catalyst support and CuO, a H_2-TPR analysis was systematically carried out on the catalysts of commercial MnO_2 and α-MnO_2 nanowire that were loaded with CuO under different CuO loadings, different calcination temperatures and different loading methods. The typical H_2-TPR curve is shown in Figure 7.

Figure 8a shows the H_2-TPR curves of α-MnO_2 nanowire catalyst under different loading modes. With the loading of CuO, the reduction peak of the catalyst moved towards a low temperature, and the reduction in catalyst by precipitation deposition was improved more obviously. This meant that the interaction between CuO and α-MnO_2 nanowire was stronger. Figure 8b shows the H_2-TPR curves of the 3CuO/α-MnO_2-T-DP nanowire catalysts that were calcined at 120 °C, 200 °C, 300 °C and 400 °C. With the increase in calcination temperature, the relative position between the two reduction peaks of the catalyst basically remained unchanged, and the H_2-TPR curve of the catalysts that were calcined at 200 °C and 300 °C moved to a higher temperature. The increase in CuO composition at this temperature required a higher temperature to completely reduce the catalyst. This indicated that the excellent reduction performance could be reduced by high loading. Figure 8c shows the H_2-TPR curve of α-MnO_2 nanowire with two main peaks, the maximum values of which were concentrated at 372 °C and 613 °C, respectively. The first peak at 372 °C was attributed to the reduction in MnO_2 to Mn_3O_4, while the second peak at 613 °C was attributed to the reduction in Mn_3O_4 to MnO [40]. However, after loading different amounts of CuO, all the xCuO/α-MnO_2-200-DP catalysts showed a two-stage reduction peak like that of pure α-MnO_2 nanowires, and there was no characteristic reduction peak of CuO species. Meanwhile, the addition of CuO to α-MnO_2 nanowire changed the reduction behavior of α-MnO_2 nanowire. With the increase in CuO loading, the continuous reduction peaks of MnO_2 to Mn_3O_4 and Mn_3O_4 to MnO also shift to lower temperatures. This finding clearly indicated that the CuO had a significant effect on the reduction performance of the xCuO/α-MnO_2-200-DP catalyst. Figure 8d shows the H_2-TPR curves of commercial MnO_2 and α-MnO_2 nanowire catalysts before and after CuO loading. Unlike α-MnO_2 nanowire, the reduction peak of the commercial MnO_2 catalyst that was loaded with CuO shifts to a high temperature. This meant that the reduction performance of commercial MnO_2 that was loaded with CuO was significantly reduced, indicating that the interaction between CuO and commercial MnO_2 was weak. The structural advantages of α-MnO_2 nanowires and their ability to interact with oxides were shown from the side view.

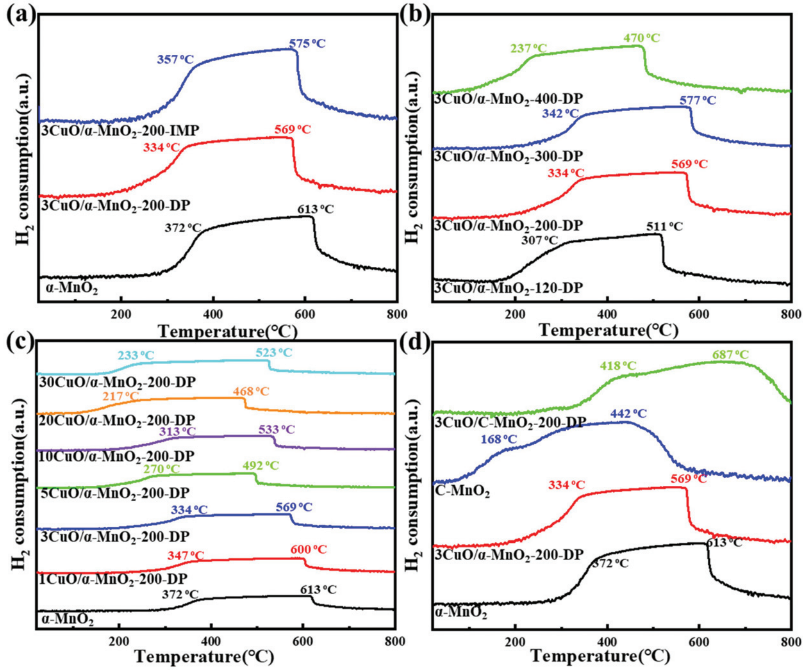

Figure 8. H_2-TPR profiles of (**a**) α-MnO_2, 3CuO/α-MnO_2-200-DP and 3CuO/α-MnO_2-200-IMP catalysts under different loading methods; (**b**) 3CuO/α-MnO_2-*T*-DP (*T* = 120, 200, 300, 400) catalysts with different calcination temperatures; (**c**) *x*CuO/α-MnO_2-200-DP (*x* = 0, 1, 3, 5, 10, 20, 30) catalysts with different CuO loading; (**d**) α-MnO_2 nanowire, commercial MnO_2 (C-MnO_2) and corresponding catalysts.

3.2. Catalytic Performance for CO Oxidation

3.2.1. Catalytic Activity

In order to study the influence of the loading mode on the catalytic activity, the catalytic oxidation reaction of 3CuO/α-MnO_2-200-DP (deposition precipitation method) and the 3CuO/α-MnO_2-200-IMP (initial impregnation method) catalyst CO was studied. The results are shown in Figure 9a. As can be seen in the figure, the 100% CO conversion temperature of the 3CuO/α-MnO_2-200-DP catalyst was 80 °C. The catalytic activity of the 3CuO/α-MnO_2-200-IMP catalyst was much lower than that of the 3CuO/α-MnO_2-200-DP catalyst, and the complete transformation of CO can be realized until 170 °C. This shows that the sedimentation method has obvious advantages over the traditional initial impregnation method.

To study the influence of calcination temperature on the catalytic activity of the 3CuO/α-MnO_2-*T*-DP catalyst, the CO catalytic oxidation reaction was studied at calcination temperatures of 200 °C, 300 °C and 400 °C, and catalyst samples dried only at 120 °C without calcination, as shown in Figure 9b. As can be seen from the figure, the catalytic activity of 3CuO/α-MnO_2-*T*-DP catalyst decreases as the calcination temperature increases from 200 °C to 400 °C. The catalytic activity of catalysts that have been calcined at 120 °C, was lower than that of the catalyst samples that have been calcined at 200 °C to 400 °C. This may be because $Cu(NO_3)_2 \cdot 3H_2O$ did not decompose completely due to the low temperature of catalyst samples that were calcined above 200 °C during the loading process. The calcination temperature of the catalysts had great influence on the dispersion, structure and metal–surface interaction strength of the catalysts. It can be seen from the XRD pattern that the CuO diffraction peak intensity of 3CuO/α-MnO_2-*T*-DP catalyst was different to some extent. The CuO diffraction peak of 3CuO/α-MnO_2-300-DP was the strongest, indicating that the CuO species were poorly dispersed. Therefore, the different catalytic activity of the 3CuO/α-MnO_2-*T*-DP catalyst at different calcination temperatures may be related to the dispersion of CuO active sites. In addition, the difference in catalytic activity of 3CuO/α-MnO_2-*T*-DP catalysts at different calcination temperatures may also be caused by the thermal shrinkage of the catalyst skeleton and the agglomeration of CuO species.

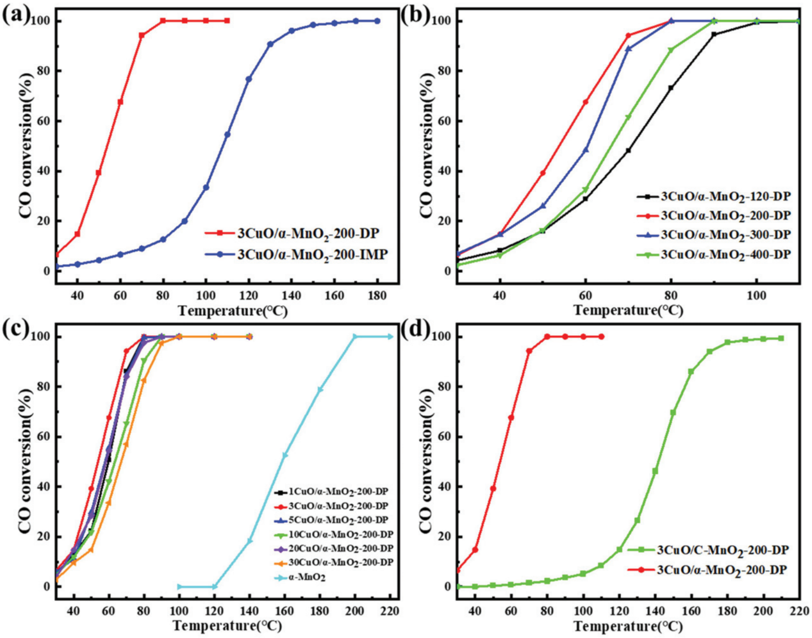

Figure 9. (**a**) 3CuO/α-MnO_2-200-DP and 3CuO/α-MnO_2-200-IMP catalysts under different loading modes; (**b**) 3CuO/α-MnO_2-*T*-DP (*T* = 120, 200, 300, 400) catalysts; (**c**) *x*CuO/α-MnO_2-200 (*x* = 0, 1, 3, 5, 10, 20, 30) catalyst; and (**d**) CO conversion of pure α-MnO_2 nanowires and commercial MnO_2 catalysts supported by CuO by precipitation deposition at different reaction temperatures.

Secondly, the catalytic activity of CO oxidation on the *x*CuO/α-MnO_2-200-DP catalyst with CuO loading was evaluated in detail, as shown in Figure 9c. As can be seen from the figure, pure α-MnO_2 nanowire catalyst started to activate at 120 °C. With the increase in reaction temperature, CO conversion gradually increased until reaching 100% at about 200 °C. Compared with pure α-MnO_2 nanowire carrier, the *x*CuO/α-MnO_2-200-DP catalyst had higher catalytic activity, especially in the 30–100 °C region. These results indicated that CuO species were the main active center of CO oxidation and the main cause of CO oxidation at a low temperature. To show the difference more clearly in the catalytic activity of the *x*CuO/α-MnO_2-200-DP catalysts with different CuO loads, the CO conversion of the *x*CuO/α-MnO_2-200-DP catalysts was analyzed at 60 °C, as shown in Figure 10. When the CuO load increased from 0 wt% to 3 wt%, the catalytic activity of the *x*CuO/α-MnO_2-200-DP catalyst was significantly enhanced at a low temperature. The 3CuO/α-MnO_2-200-DP catalyst showed the highest catalytic activity among all the catalysts, which showed a significant advantage compared with previous studies. However, a further increase in CuO from 3 wt% to 30 wt% lead to a decrease in catalytic activity. The possible reason was that the one-dimensional structure of α-MnO_2 nanowires, especially the aspect ratio of the catalyst, decreases significantly with the increase in CuO load, resulting in a poor dispersion of CuO on the surface of the supports.

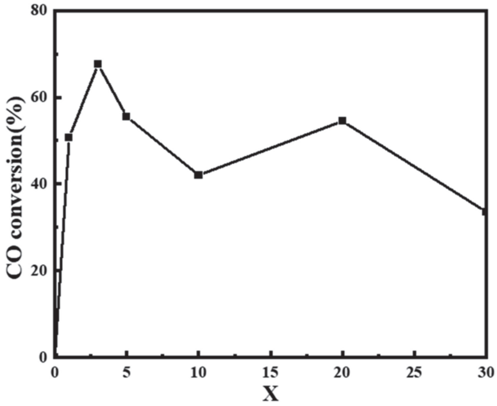

Figure 10. CO conversion and conversion of *x*CuO/α-MnO_2-200-DP (*x* = 0, 1, 3, 5, 10, 20, 30) catalysts with different CuO loading at 60 °C.

Meanwhile, in order to study the influence of the nanowire structure and redox performance of the catalyst support on the catalytic activity, commercial MnO_2 was used as the contrast carrier for the CO catalytic oxidation reaction and the same loading method was used to prepare the contrast catalyst. Figure 9d shows the catalytic activity of comparative catalysts. In the figure, the 100% CO conversion temperature of the 3CuO/α-MnO_2-200-DP catalyst was 80 °C, while the CO conversion of the 3CuO/C-MnO_2-200-DP catalyst was close to 100% only when the temperature was above 200 °C. The catalytic activity of the 3CuO/C-MnO_2-200-DP catalyst was like the α-MnO_2 nanowire support without the CuO load. The advantages of the structure and properties of α-MnO_2 nanowire support were illustrated.

3.2.2. Long-Term Stability Test

A long-term stability test was carried out to evaluate the catalytic stability of the prepared CuO-based catalyst under the specific reaction conditions ($CO/O_2/N_2$ = 1/20/79, GHSV = 12,000 mL·g^{-1}·H^{-1}, 80 °C, 1 atm). The CO oxidation stability of these catalysts was tested for 12 h, and 3CuO/α-MnO_2-200-DP was selected as the representative catalyst. As can be seen from Figure 11, the 3CuO/α-MnO_2-200-DP catalyst showed excellent stability during the entire 12 h stability test, with the activity remaining at 100% and no significant deactivation. These results indicate that the 3CuO/α-MnO_2-200-DP catalyst not only had high temperature activity, but also had good stability.

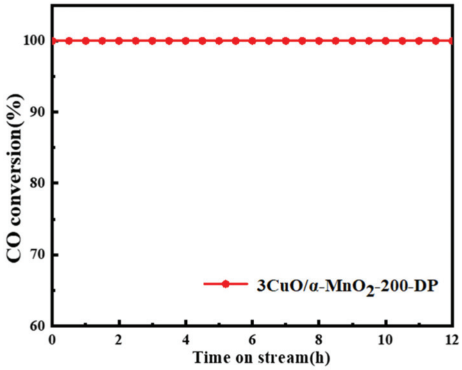

Figure 11. Stability of 3CuO/α-MnO_2-200-DP catalyst at 80 °C for 12 h.

4. Conclusions

In summary, a series of CuO/α-MnO$_2$ nanowire catalysts with different CuO loadings, different calcination temperatures and different loading modes were synthesized as the supports of a CO catalytic oxidation catalyst. The slenderness ratio of the CuO/α-MnO$_2$ nanowire catalyst decreases with the increase in loading capacity. The results showed that when CuO loading was 3 wt%, calcination temperature was 200 °C and the catalyst that was supported by the deposition precipitation method had the highest catalytic activity. Compared with the commercial MnO$_2$ catalyst, the synthetic α-MnO$_2$ nanowire catalyst has better redox performance and better low-temperature catalytic activity due to the particularity of the microstructure. Compared with commercial MnO$_2$, it was a better catalyst support for CO catalytic oxidation. The CuO particles that were calcined at 200 °C by the precipitation deposition method showed better dispersion on the surface of a α-MnO$_2$ nanowire support, which proved that the precipitation deposition method was superior to the traditional initial impregnation method. In addition, CuO as the active center of CO oxidation formed a strong intermetallic synergistic effect on the surface of the α-MnO$_2$ nanowire support, which further enhanced the CO oxidation activity of the α-MnO$_2$ nanowire support at a low temperature. Because of these advantages, α-MnO$_2$ nanowire is considered as a promising support for the CO oxidation of CuO-based catalysts, and has stronger catalytic activity, especially at low temperatures.

Author Contributions: Conceptualization, M.C. and Y.C.; formal analysis, H.S. and P.G.; investigation, H.S. and Y.C.; resources, M.C.; data curation, Y.S.; writing—original draft preparation, Y.C.; writing—review and editing, L.X.; funding acquisition, M.C. All authors have read and agreed to the published version of the manuscript.

Funding: This research was funded by the National Natural Science Foundation of China (grant number 21976094, 22176100, 21871144) and the Postgraduate Research & Practice Innovation Program of Jiangsu Province in 2022 (KYCX22_1216).

Data Availability Statement: The data supporting the findings of this study are available by reasonable request to chenmd@nuist.edu.cn.

Conflicts of Interest: The authors declare no conflict of interest.

References

1. Namasivayam, A.M.; Korakianitis, T.; Crookes, R.J.; Bob-Manuel, K.D.H.; Olsen, J. Biodiesel, Emulsified Biodiesel and Dimethyl Ether as Pilot Fuels for Natural Gas Fuelled Engines. *Appl. Energy* **2010**, *87*, 769–778. [CrossRef]
2. Neidell, M.J. Air Pollution, Health, and Socio-Economic Status: The Effect of Outdoor Air Quality on Childhood Asthma. *J. Health Econ.* **2004**, *23*, 1209–1236. [CrossRef] [PubMed]
3. Prado, O.J.; Veiga, M.C.; Kennes, C. Removal of Formaldehyde, Methanol, Dimethylether and Carbon Monoxide from Waste Gases of Synthetic Resin-Producing Industries. *Chemosphere* **2008**, *70*, 1357–1365. [CrossRef] [PubMed]
4. Lee, J.G.; An, K. Catalytic Co Oxidation on Nanocatalysts. *Top. Catal.* **2018**, *61*, 986–1001. [CrossRef]
5. Wang, L.; Wang, L.; Zhang, J.; Wang, H.; Xiao, F.-S. Enhancement of the Activity and Durability in CO Oxidation over Silica-Supported Au Nanoparticle Catalyst Via Ceox Modification. *Chin. J. Catal.* **2018**, *39*, 1608–1614. [CrossRef]
6. Zheng, B.; Wu, S.; Yang, X.; Jia, M.; Zhang, W.; Liu, G. Room Temperature Co Oxidation over Pt/MgFe$_2$O$_4$: A Stable Inverse Spinel Oxide Support for Preparing Highly Efficient Pt Catalyst. *ACS Appl. Mater. Interfaces* **2016**, *8*, 26683–26689. [CrossRef]
7. Camposeco, R.; Hinojosa-Reyes, M.; Castillo, S.; Nava, N.; Zanella, R. Synthesis and Characterization of Highly Dispersed Bimetallic Au-Rh Nanoparticles Supported on Titanate Nanotubes for CO Oxidation Reaction at Low Temperature. *Environ. Sci. Pollut. Res.* **2021**, *28*, 10734–10748. [CrossRef]
8. Zhang, X.; Li, G.; Tian, R.; Feng, W.; Wen, L. Monolithic Porous CuO/CeO$_2$ Nanorod Composites Prepared by Dealloying for CO Catalytic Oxidation. *J. Alloys Compd.* **2020**, *826*, 154149. [CrossRef]
9. Kong, F.; Zhang, H.; Chai, H.; Liu, B.; Cao, Y. Insight into the Crystal Structures and Surface Property of Manganese Oxide on Co Catalytic Oxidation Performance. *Inorg. Chem.* **2021**, *60*, 5812–5820. [CrossRef]
10. Murthy, P.R.; Munsif, S.; Zhang, J.-C.; Li, W.-Z. Influence of CeO$_2$ and ZrO$_2$ on the Thermal Stability and Catalytic Activity of Sba-15-Supported Pd Catalysts for Co Oxidation. *Ind. Eng. Chem. Res.* **2021**, *60*, 14424–14433. [CrossRef]
11. Sun, L.; Zhan, W.; Li, Y.-A.; Wang, F.; Zhang, X.; Han, X. Understanding the Facet-Dependent Catalytic Performance of Hematite Microcrystals in a Co Oxidation Reaction. *Inorg. Chem. Front.* **2018**, *5*, 2332–2339. [CrossRef]

12. Baidya, T.; Murayama, T.; Nellaiappan, S.; Katiyar, N.K.; Bera, P.; Safonova, O.; Lin, M.; Priolkar, K.R.; Kundu, S.; Rao, B.S.; et al. Ultra-Low-Temperature Co Oxidation Activity of Octahedral Site Cobalt Species in CO_3O_4 Based Catalysts: Unravelling the Origin of the Unique Catalytic Property. *J. Phys. Chem. C* **2019**, *123*, 19557–19571. [CrossRef]
13. Lou, Y.; Wang, L.; Zhao, Z.; Zhang, Y.; Zhang, Z.; Lu, G.; Guo, Y.; Guo, Y. Low-Temperature CO Oxidation over CO_3O_4-Based Catalysts: Significant Promoting Effect of Bi_2O_3 on CO_3O_4 Catalyst. *Appl. Catal. B Environ.* **2014**, *146*, 43–49. [CrossRef]
14. Cui, Y.; Xu, L.; Chen, M.; Lv, C.; Lian, X.; Wu, C.-E.; Yang, B.; Miao, Z.; Wang, F.; Hu, X. Co Oxidation over Metal Oxide (La_2O_3, Fe_2O_3, PrO_2, Sm_2O_3, and MnO_2) Doped Cuo-Based Catalysts Supported on Mesoporous $Ce_{0.8}Zr_{0.2}O_2$ with Intensified Low-Temperature Activity. *Catalysts* **2019**, *9*, 724. [CrossRef]
15. Ren, Y.; Ma, Z.; Qian, L.; Dai, S.; He, H.; Bruce, P.G. Ordered Crystalline Mesoporous Oxides as Catalysts for Co Oxidation. *Catal. Lett.* **2009**, *131*, 146–154. [CrossRef]
16. Song, H.; Xu, L.; Chen, M.; Cui, Y.; Wu, C.-E.; Qiu, J.; Xu, L.; Cheng, G.; Hu, X. Recent Progresses in the Synthesis of MnO_2 Nanowire and Its Application in Environmental Catalysis. *RSC Adv.* **2021**, *11*, 35494–35513. [CrossRef]
17. Zhao, G.-Y.; Li, H.-L. Electrochemical Oxidation of Methanol on Pt Nanoparticles Composited MnO_2 Nanowire Arrayed Electrode. *Appl. Surf. Sci.* **2008**, *254*, 3232–3235. [CrossRef]
18. Ren, Y.; Ma, Z.; Dai, S. Nanosize Control on Porous Beta-MnO_2 and Their Catalytic Activity in Co Oxidation and N_2O Decomposition. *Materials* **2014**, *7*, 3547–3556. [CrossRef]
19. Jampaiah, D.; Velisoju, V.K.; Venkataswamy, P.; Coyle, V.E.; Nafady, A.; Reddy, B.M.; Bhargava, S.K. Nanowire Morphology of Mono- and Bidoped Alpha-MnO_2 Catalysts for Remarkable Enhancement in Soot Oxidation. *ACS Appl. Mater. Interfaces* **2017**, *9*, 32652–32666. [CrossRef]
20. Du, H.; Wang, Y.; Arandiyan, H.; Younis, A.; Scott, J.; Qu, B.; Wan, T.; Lin, X.; Chen, J.; Chu, D. Design and Synthesis of CeO_2 Nanowire/MnO_2 Nanosheet Heterogeneous Structure for Enhanced Catalytic Properties. *Mater. Today Commun.* **2017**, *11*, 103–111. [CrossRef]
21. Saputra, E.; Muhammad, S.; Sun, H.; Patel, A.; Shukla, P.; Zhu, Z.H.; Wang, S. Alpha-MnO_2 Activation of Peroxymonosulfate for Catalytic Phenol Degradation in Aqueous Solutions. *Catal. Commun.* **2012**, *26*, 144–148. [CrossRef]
22. Liang, S.; Bulgan, F.T.G.; Zong, R.; Zhu, Y. Effect of Phase Structure of MnO_2 Nanorod Catalyst on the Activity for Co Oxidation. *J. Phys. Chem. C* **2008**, *112*, 5307–5315. [CrossRef]
23. Zhang, Y.; Deng, S.; Luo, M.; Pan, G.; Zeng, Y.; Lu, X.; Ai, C.; Liu, Q.; Xiong, Q.; Wang, X.; et al. Defect Promoted Capacity and Durability of N-$MnO_{2\text{-}X}$ Branch Arrays Via Low-Temperature NH_3 Treatment for Advanced Aqueous Zinc Ion Batteries. *Small* **2019**, *15*, 1905452. [CrossRef]
24. Selvakumar, K.; Duraisamy, V.; Venkateshwaran, S.; Arumugam, N.; Almansour, A.I.; Wang, Y.; Liu, T.X.; Kumar, S.M.S. Development of Alpha-MnO_2 Nanowire with Ni- and (Ni, Co)-Cation Doping as an Efficient Bifunctional Oxygen Evolution and Oxygen Reduction Reaction Catalyst. *ChemElectroChem* **2022**, *9*, e202101303. [CrossRef]
25. Wang, J.; Luo, H.; Liu, P. Highly Dispersed Gold Nanoparticles on Metal-Doped Alpha-MnO_2 Catalysts for Aerobic Selective Oxidation of Ethanol. *Catal. Commun.* **2020**, *142*, 106030. [CrossRef]
26. Li, X.; Cheng, H.; Liang, G.; He, L.; Lin, W.; Yu, Y.; Zhao, F. Effect of Phosphine Doping and the Surface Metal State of Ni on the Catalytic Performance of Ni/Al_2O_3 Catalyst. *Catalysts* **2015**, *5*, 759–773. [CrossRef]
27. Hashem, A.M.; Abuzeid, H.M.; Narayanan, N.; Ehrenberg, H.; Julien, C.M. Synthesis, Structure, Magnetic, Electrical and Electrochemical Properties of Al, Cu and Mg Doped MnO_2. *Mater. Chem. Phys.* **2011**, *130*, 33–38. [CrossRef]
28. Gao, J.; Jia, C.; Zhang, L.; Wang, H.; Yang, Y.; Hung, S.-F.; Hsu, Y.-Y.; Liu, B. Tuning Chemical Bonding of MnO_2 through Transition-Metal Doping for Enhanced CO Oxidation. *J. Catal.* **2016**, *341*, 82–90. [CrossRef]
29. Zhang, Z.; Tian, Y.; Zhao, W.; Wu, P.; Zhang, J.; Zheng, L.; Ding, T.; Li, X. Hydroxyl Promoted Preferential and Total Oxidation of Co over Epsilon-MnO_2 Catalyst. *Catal. Today* **2020**, *355*, 214–221. [CrossRef]
30. Xu, R.; Wang, X.; Wang, D.S.; Zhou, K.B.; Li, Y.D. Surface Structure Effects in Nanocrystal MnO_2 and Ag/MnO_2 Catalytic Oxidation of CO. *J. Catal.* **2006**, *237*, 426–430. [CrossRef]
31. Tuan Sang, T.; Tripathi, K.M.; Kim, B.N.; You, I.-K.; Park, B.J.; Han, Y.H.; Kim, T. Three-Dimensionally Assembled Graphene/Alpha-MnO_2 Nanowire Hybrid Hydrogels for High Performance Supercapacitors. *Mater. Res. Bull.* **2017**, *96*, 395–404.
32. Qian, K.; Qian, Z.; Hua, Q.; Jiang, Z.; Huang, W. Structure-Activity Relationship of CuO/MnO_2 Catalysts in CO Oxidation. *Appl. Surf. Sci.* **2013**, *273*, 357–363. [CrossRef]
33. Kumar, J.P.; Ramachatyulu, P.V.R.K.; Prasad, G.K.; Singh, B. Montmorillonites Supported with Metal Oxide Nanoparticles for Decontamination of Sulfur Mustard. *Appl. Clay Sci.* **2015**, *116*, 263–272. [CrossRef]
34. Papadas, I.T.; Ioakeimidis, A.; Vamvasakis, I.; Eleftheriou, P.; Armatas, G.S.; Choulis, S.A. All-Inorganic P-N Heterojunction Solar Cells by Solution Combustion Synthesis Using N-Type $FeMnO_3$ Perovskite Photoactive Layer. *Front. Chem.* **2021**, *9*, 803. [CrossRef]
35. Tafur, J.P.; Abad, J.; Roman, E.; Fernandez Romero, A.J. Charge Storage Mechanism of MnO_2 Cathodes in Zn/MnO_2 Batteries Using Ionic Liquid-Based Gel Polymer Electrolytes. *Electrochem. Commun.* **2015**, *60*, 190–194. [CrossRef]
36. Kawai, J.; Maeda, K.; Nakajima, K.; Gohshi, Y. Relation between Copper L X-ray Fluorescence and 2p X-ray Photoelectron Spectroscopies. *Phys. Rev. B* **1993**, *48*, 8560–8566. [CrossRef]
37. Du, J.; Xiao, G.; Xi, Y.; Zhu, X.; Su, F.; Kim, S.H. Periodate Activation with Manganese Oxides for Sulfanilamide Degradation. *Water Res.* **2020**, *169*, 115278. [CrossRef]

38. Mckinney P V, Reduction of palladium oxide by carbon monoxide. *J. Am. Chem. Soc.* **1932**, *54*, 4498–4504. [CrossRef]
39. Freitas, I.C.; Damyanova, S.; Oliveira, D.C.; Marques, C.M.P.; Bueno, J.M.C. Effect of Cu Content on the Surface and Catalytic Properties of Cu/ZrO_2 Catalyst for Ethanol Dehydrogenation. *J. Mol. Catal. A Chem.* **2014**, *381*, 26–37. [CrossRef]
40. Sun, M.; Lan, B.; Lin, T.; Cheng, G.; Ye, F.; Yu, L.; Cheng, X.; Zheng, X. Controlled Synthesis of Nanostructured Manganese Oxide: Crystalline Evolution and Catalytic Activities. *CrystEngComm* **2013**, *15*, 7010–7018. [CrossRef]

Article

Pulsed Fluidization of Nanosilica: Rigorous Evaluation of the Efficacy of Pulsation Frequency

Mohammad Asif [1,*], Ebrahim H. Al-Ghurabi [1] and Amanullah Fatehmulla [2]

[1] Department of Chemical Engineering, King Saud University, P.O. Box 800, Riyadh 11421, Saudi Arabia; ealghurabi@ksu.edu.sa
[2] Department of Physics and Astronomy, College of Science, King Saud University, P.O. Box 2455, Riyadh 11451, Saudi Arabia; aman@ksu.edu.sa
* Correspondence: masif@ksu.edu.sa; Tel.: +966-56-981-7045

Abstract: Assisted fluidization techniques can significantly improve the hydrodynamics of difficult-to-fluidize solids. Among these techniques, the pulsed flow strategy is highly promising owing to its cost-effectiveness and amenability to implementation for largescale processing. Using commercial-grade, highly porous nanosilica that shows strong agglomeration behavior, we implemented the pulsed flow with square-wave pulsation schemes of 0.05, 0.10, and 0.25 Hz frequencies, and compared their effectiveness in each case. Besides the conventional approach of assessing their efficacy using the pressure drop data, we have proposed a new approach in this work that consists of computing the power of the overall pressure drop transient signals. Using the theoretical value, i.e., the effective bed weight per unit area as a reference, the percentage increase in the power was 27 ± 4, 71 ± 5, and 128 ± 4, respectively, for 0.05, 0.10, and 0.25 Hz pulsation frequencies. In fact, the average pressure drop values were substantially higher when the partial bed collapse occurred between successive pulsations when compared with the case of low-frequency pulsations. The pulsation frequency also affected the evolution of local bed dynamics in various bed regions during the expansion and collapse of the bed. Moreover, the local and global pressure transients have shown interesting mutual correlations which were otherwise not evident from their individual transient profiles.

Keywords: nanosilica; fluidization; pulsed flow; pulsation frequency; assisted fluidization; efficacy; bed dynamics

Citation: Asif, M.; Al-Ghurabi, E.H.; Fatehmulla, A. Pulsed Fluidization of Nanosilica: Rigorous Evaluation of the Efficacy of Pulsation Frequency. *Nanomaterials* **2022**, *12*, 2158. https://doi.org/10.3390/nano12132158

Academic Editors: Jihoon Lee and Ming-Yu Li

Received: 14 April 2022
Accepted: 21 June 2022
Published: 23 June 2022

1. Introduction

Notwithstanding inherent advantages associated with the use of fine and ultrafine powders, their processing remains hugely challenging. This was pointed out long ago by Geldart [1], who examined the effect of the physical properties of the solid particles on their gas-phase fluidization behavior. For particles with a size smaller than 30 µm, the solids, when contacted with an upward gas flow, show cohesive and non-homogeneous fluidization behavior with poor contact and insufficient mixing between the two phases. This leads to poor transport of heat and mass that could ultimately compromise the effectiveness of the process.

A commonly used strategy to improve the fluidization hydrodynamics of difficult-to-fluidize cohesive solids has been the use of assisted fluidization techniques [2]. These techniques mostly require the input of additional extra energy to the system mainly to counteract the interparticle forces, thereby enhancing the fluidization behavior. For instance, subjecting the fluidized bed to mechanical vibration leads to a greater bed homogeneity and reduced minimum fluidization velocity (U_{mf}) in addition to uniform product quality [3–12]. Given that the transition of the fixed bed to the fluidized bed mode of gas–solid contact occurs at the U_{mf}, it is therefore considered a critical fluidization parameter. Similarly, a pulsation of the inlet flow promotes deagglomeration, reduces the U_{mf}, and suppresses the hysteresis phenomenon [13–24]. Another assisted fluidization strategy widely reported in the literature utilizes the acoustics perturbations generated from a sound source. When the acoustic frequency matches the natural frequency of the system, resonance occurs, which leads to the development of standing waves, thereby causing high-intensity disturbances in the pressure transients. This lowers the U_{mf} and improves the quality of fluidization [25–29]. Mixing with inert particles of appropriate physical properties has also been reported as a strategy to enhance the fluidization hydrodynamics of difficult-to-fluidize particles [30–33]. In some cases, a combination of two different assisted fluidization techniques has been utilized to improve the fluidization quality and suppress the size segregation of the bed material along the height [20,34–36].

For largescale gas–solid processing, the efficacy of the energy augmentation using the assisted fluidization technique is of critical importance for the economic feasibility of the process. In this context, the pulsed flow assisted fluidization technique stands out on two main counts. First, unlike mechanical vibrations and acoustic perturbations, additional energy input and its associated capital and operating costs are not required. Second, the existing process units can be easily and economically retrofitted to introduce flow pulsations.

Pulsed flow introduces intense pressure fluctuations, which cause additional dissipation of energy and can therefore help to improve fluidization hydrodynamics. Simple flow pulsation strategy, e.g., square-wave flow pulsations, can be implemented by regularly interrupting the inlet fluid flow. Once the flow is stopped, the collapse process begins. As a result of regular expansion and collapse of the bed due to pulsed flow, the solid phase mostly remains in a state of vigorous perpetual motion, thus leading to additional frictional losses, which are otherwise not possible with conventional fluidization.

Pulsation frequency can be adjusted to cause either partial or total collapse of the bed between two successive pulsation events. Further lowering the pulsations frequency beyond that required for complete collapse would provide additional time for the adjustment of solid particles before the next pulsation event [14,17,24].

The efficacy of assisted fluidization techniques has mostly been assessed in terms of the U_{mf} reduction and the fluidization index, which is a good indication of the correspondence between the overall pressure drop and the bed's effective weight. While a qualitative indication of the quality of the fluidization using this approach is possible, a precise evaluation of the power augmentation as a result of applying the assisted fluidization technique is nonetheless not feasible. In this study, we therefore set out to make a rigorous estimation of the energy dissipation per unit time from the pressure transients as a tool to discern the efficacy of the pulsed flow with different pulsation frequencies in a highly porous bed of nanosilica. The proposed approach, although presented here in the context of pulsed flow, can be extended to other assisted fluidization techniques as well. We have considered three different square-wave frequencies: 0.05, 0.10, and 0.25 Hz. While low frequency yields sufficient time between two consecutive pulsation events, higher frequencies, i.e., 0.10 Hz and 0.25 Hz, respectively, allow complete and partial collapse of the bed between successive pulsations. Following the conventional approach, we examined the effect of the pulsation frequency on the average values of the local as well as the overall pressure drop as a function of the gas flow. Next, the correlation between the local and global dynamics of different bed regions in response to the pulsations has been analyzed. Finally, the energy dissipation per unit time has been evaluated from the overall pressure signal to evaluate the effect of the pulsed flow frequency on the power input.

2. Experimental

The schematic of the experimental set used in this study is shown in Figure 1. The test section was a 1.5 m long transparent Perspex column with an internal diameter of 70 mm, which was preceded by a perforated plate distributor and a 0.5 m long plenum chamber. The fractional open area of the distributor was kept low to ensure uniform gas distribution by eliminating the dead zones [37,38].

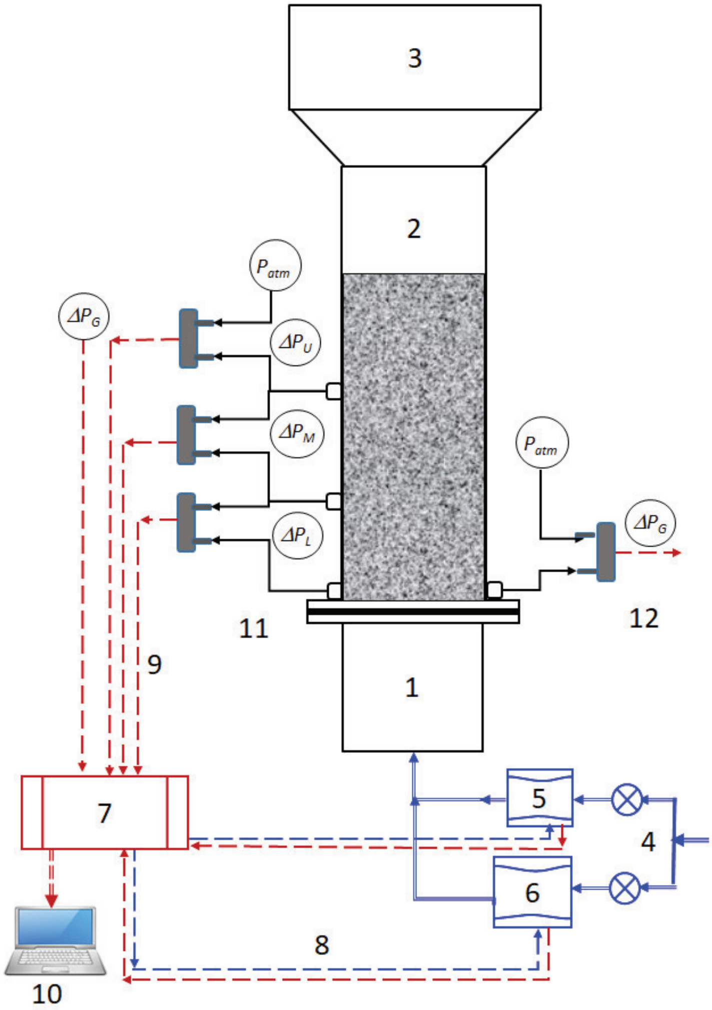

Figure 1. Experimental setup schematic. (1) Wind-box; (2) Test section; (3) Disengagement section; (4) Compressed air supply; (5) Mass flow controller (low flow); (6) Mass flow controller (high flow); (7) Data acquisition system (DAQ); (8) Analog output (AO) signals (blue broken lines) (9) Analog input (AI) signals (red broken lines); (10) Laptop with LabVIEW software; (11) Pressure taps for upper (ΔP_U), middle (ΔP_M), and lower (ΔP_L) pressure drops; (12) Pressure taps for global pressure drop (ΔP_G).

Several sensitive pressure transducers with appropriate ranges were used for monitoring the bed transients. Local bed dynamics were monitored in the lower (ΔP_L), middle (ΔP_M), and upper (ΔP_U) regions of the fluidized bed. Overall bed transients (ΔP_G) were also monitored with a pressure transducer of relatively larger range as compared to the ones used for monitoring local transients. The bottom tap of this transducer was located close to the distributor, whereas the upper tap was kept open to the atmosphere as shown in Figure 1. The transient pressure drop data were recorded at a frequency of 100 Hz with an 18-bit data acquisition system (DAQ) (Model: USB-6289, National Instruments, Austin, TX, USA) controlled using LabVIEW 2019 software obtained from National Instruments, Austin, TX, USA.

We used commercial-grade hydrophilic nanosilica (Aerosil 200, Evonik GmbH, Wolfgang, Germany), which is widely used in bulk quantities in various applications, e.g., rubber, plastics, concrete, agriculture, and cosmetics, with an estimated 3.3 million tons of global consumption in 2015 [39]. Due to multi-level agglomeration caused by interparticle forces, the particle size distribution of its sieved sample ranged from 2 to 200 µm, which was three orders of magnitude greater than the actual size of the nanoparticle [14]. The bulk density was 44 kg/m^3 with an overall bed void fraction of approximately 0.98.

Compressed air was used as the fluidizing gas. Its flow was controlled by using two different electronic mass flow controllers. Both flow controllers were connected to the DAQ to generate pulsed flow. Square-wave flow pulsation schemes were implemented for three different frequencies: 0.25, 0.10, and 0.05 Hz. For 0.25 Hz, the gas flow was maintained for two seconds followed by another two seconds of pause, thus completing one cycle. Likewise, gas flow durations were kept for five seconds and ten seconds followed by a pause of Perspex column the same duration for the 0.10 and 0.05 Hz cases, respectively. These frequencies were carefully chosen to cover the full spectrum of the bed collapse such that 0.25 Hz flow pulsation allowed only a partial collapse of the bed before the next pulsation event. However, 0.10 Hz was just sufficient to ensure the complete bed collapse in most cases before the start of the next pulsation, whereas a 0.05 Hz flow pulsation ensured a complete bed collapse and its settlement before the next flow pulse.

Our experimental strategy consisted of using 36 velocities such that 18 different flows were conducted out by gradually increasing the flow whereas the next 18 flows consisted of gradually decreasing the flow, thereby completing both the fluidization and defluidization cycles of an experimental run. At a fixed flow of the fluidizing gas, four complete pulses, each of 20 s duration, were carried out for a 0.05 Hz pulsed flow. Similarly, five complete pulses, each of 10 s duration, were considered for 0.1 Hz pulsations for each individual flow. In the case of 0.025 Hz, however, we considered eight pulses, each of 4 s duration, for a given flowrate. These aspects of our experiments are highlighted in Figure 2, which shows the power spectra of the velocity data for a complete experimental run. A prominent peak in Figure 2a at 0.048 Hz corresponds to the pulsation frequency, while another peak at 0.0124 Hz corresponds to the time duration of 80 s for which the velocity was held constant, thereby yielding four identical flow pulses with a time period of 20 s. In Figure 2b, we likewise note a prominent peak at 0.098 Hz, indicating the frequency of flow pulsation. Another peak at 0.020 Hz corresponds to the flow changes introduced after 50 s. In the case of 0.25 Hz, flow pulsation is depicted in Figure 2c with velocity step changes introduced at an interval of 32 s, where each pulse lasted only four seconds.

A 30 s snapshot of the velocity and pressure drop transients in real time is shown in Figure 3. As seen in Figure 3a, the flow lasted for 10 s and was interrupted for the next 10 s for a 0.05 Hz pulsed flow, which was reduced to five seconds for the 0.1 Hz and further reduced to 2 s for the 0.25 Hz pulsed flow. From the overall dynamics shown in Figure 3b it is obvious that the collapse process for 0.05 Hz is complete, with the bed coming to a complete rest with subsequent adjustment, if any, before the next pulse of flow is introduced. In the case of 0.1 Hz, however, the flow interruption duration was just sufficient for the total bed collapse to complete between two successive pulsation events. As the pulsation frequency was raised to 0.25 Hz, there was a notable change in the bed dynamics. The overall pressure hardly dropped to 50 Pa before the next flow pulse was introduced. This means that the 0.25 Hz flow pulsation frequency allowed only a partial bed collapse. As a result of different dynamics seen with different frequencies, a significant difference in the bed hydrodynamics is expected.

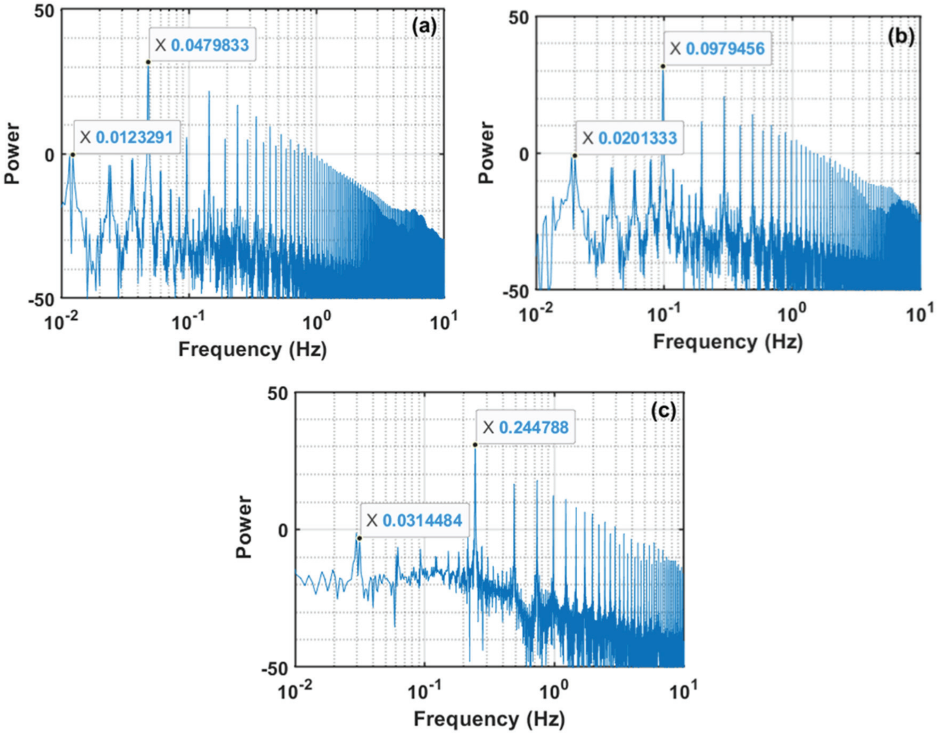

Figure 2. Power spectra (in dB) of the velocity data for (**a**) 0.05 Hz, (**b**) 0.10 Hz, (**c**) 0.25 Hz.

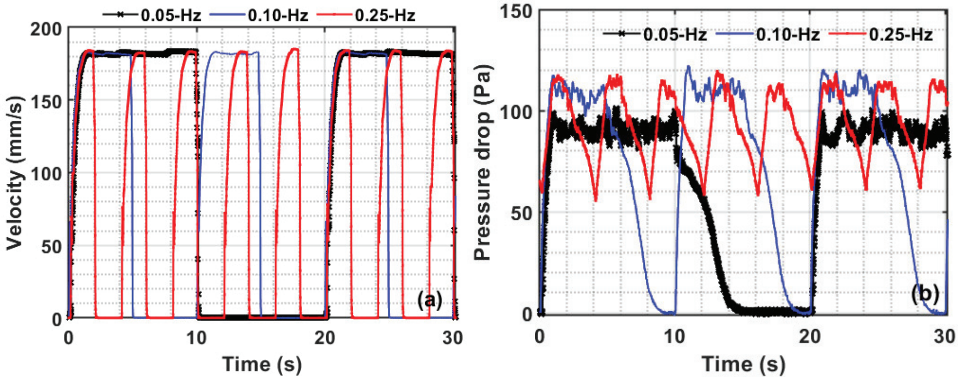

Figure 3. Pulsed flow transients for (**a**) the velocity and (**b**) the upper region pressure drop for different frequencies of the pulsed flow.

In view of the square-wave flow pulsations, the following equations were used for computing the mean values of the velocities (U_0) and the pressure drops (ΔP),

$$U_0 = \frac{1}{N}\sum_{i=1}^{N}\sum_{j=n_1}^{n_2}\frac{U_{0ij}}{(n_2 - n_1 + 1)}, \tag{1}$$

$$\Delta P = \frac{1}{N}\sum_{i=1}^{N}\sum_{j=n_1}^{n_2}\frac{\Delta p_{ij}}{(n_2 - n_1 + 1)}, \tag{2}$$

where U_{0ij} and Δp_{ij} are the j^{th} data points of the i^{th} pulse for the velocity and the pressure drop, respectively. For 0.25 Hz pulsations as an example, there were eight pulses ($N = 8$), each of four-second duration, with data acquired with a sampling frequency of 100 Hz, thereby yielding 400 data points. The part of the pulse with zero flow was not considered. For the remaining part of the pulse comprised of 200 data points, its initial rise time and the latter part of the pulse were also discarded. Therefore, we used $n_1 = 60$ and $n_2 = 160$ for the 0.25 Hz pulsed flow.

3. Results and Discussion

In the following, the effect of the gas flow on the local and overall pressure drop is first examined for various pulsation frequencies. The correlation between the dynamics of different bed regions is highlighted next. Finally, the influence of the pulsation frequency on the energy dissipation per unit time is discussed.

3.1. Dependence of the Local Pressure Drop on Gas Velocity

During the square-wave pulsed flow, the flow stoppage initiated the collapse, thereby causing a simultaneous decline in the pressure drop as well. However, for the evaluation of the average pressure drop, the pressure drop magnitudes for the fully developed were considered [24]. The variation in the local pressure drop in the upper region of the fluidized bed with the velocity is shown in Figure 4 for various pulsed flows. The case of conventional fluidization with no pulsation is also depicted in the figure for the sake of comparison. The 0.25 Hz and 0.1 Hz cases show close agreement with much greater pressure drop as compared to 0.05 Hz, which was still slightly higher than the conventional fluidized bed. This behavior is seen for both when the flow was gradually increased (Figure 4a) followed by a gradual decrease (Figure 4b). The steady increase in the pressure drop with the velocity occurs due to the bed expansion, which causes a greater input of bed solids in the upper region. A higher pressure drop indicates a greater expansion of the fluidized bed.

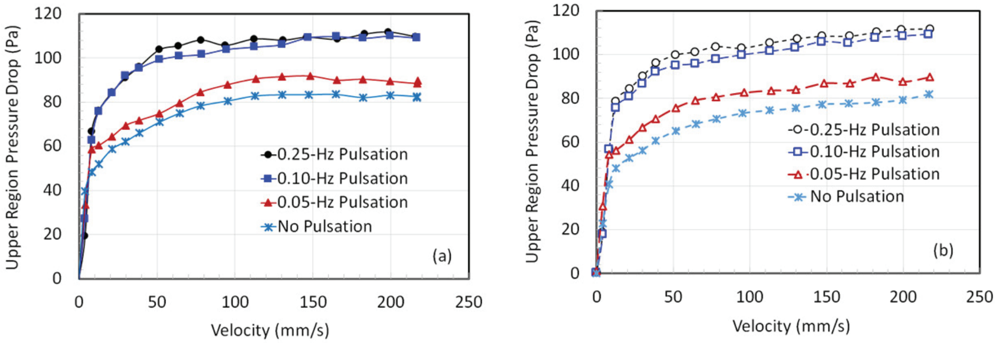

Figure 4. Local pressure drop variation with the velocity in the upper region with (**a**) increasing velocity and (**b**) decreasing velocity.

The pressure drop variation with the flow in the middle region of the fluidized bed is highlighted in Figure 5. The pressure drop at higher velocities, i.e., above 50 mm/s, is comparable for all cases during the fluidization cycle (Figure 5a). Similar behavior is also observed during the defluidization cycle in Figure 5b. At lower velocities in Figure 5a, below the U_{mf}, the pressure drop for 0.25 and 0.1 Hz is higher than that for 0.05 Hz. Assuming the applicability of the Ergun equation for flow in fixed beds, a higher pressure drop can be attributed to the smaller size of agglomerates [14].

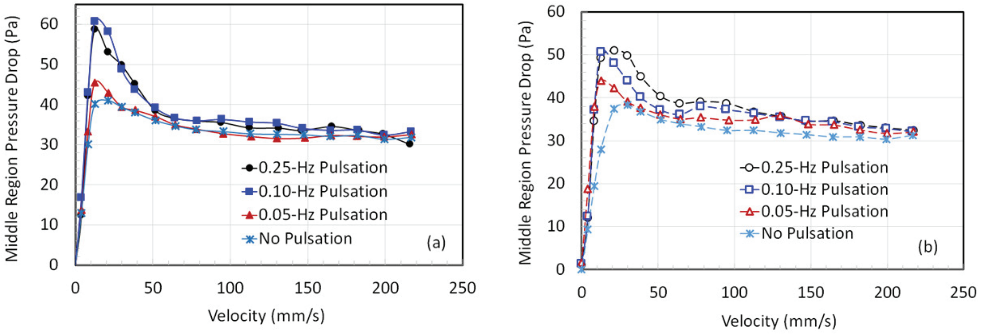

Figure 5. Local pressure drop variation with the velocity in the middle region with (**a**) increasing velocity and (**b**) decreasing velocity.

The pressure drop variation with the velocity in the lower region of the pulsed bed is shown in Figure 6 for both fluidization (Figure 6a) and defluidization (Figure 6b) cycles. The highest frequency pulsed flow in this case differs from all other cases especially during the gradual velocity decrease cycle of the experimental run (Figure 6b). This is caused by the partial collapse of the pulsed bed where the frequent collapse events cause a greater compaction, thus leading to higher frictional losses in the lower region.

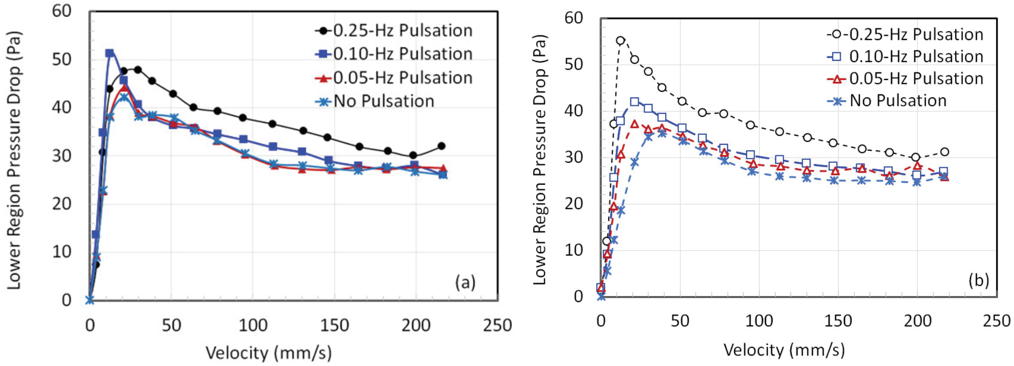

Figure 6. Local pressure drop variation with the velocity in the lower region with (**a**) increasing velocity and (**b**) decreasing velocity.

Next, in Figure 7, we consider the overall total pressure drop across the fluidized bed. The experimental data of the fluidization (Figure 7a) and defluidization (Figure 7b) cycles show the absence of hysteresis behavior. Moreover, the 0.25 and 0.10 Hz pulsed flows show good agreement with a significantly higher pressure drop than the corresponding 0.05 Hz case, which happens to be marginally higher than the one for the un-pulsed flow (conventional fluidization). A clear difference is seen in the defluidization cycle of the experiment. The 0.05 Hz flow pulsation clearly yields a slightly higher pressure drop than that for the un-pulsed flow. Likewise, 0.25 Hz pulsation causes a higher pressure drop than the one for 0.10 Hz. Note that the effective weight per unit area of the fluidized bed is approximately 149 Pa, whereas we often obtain pressure drop values as high as 185 Pa for the fully fluidized bed with the introduction of flow pulsations. This issue will be discussed in detail in Section 3.3.

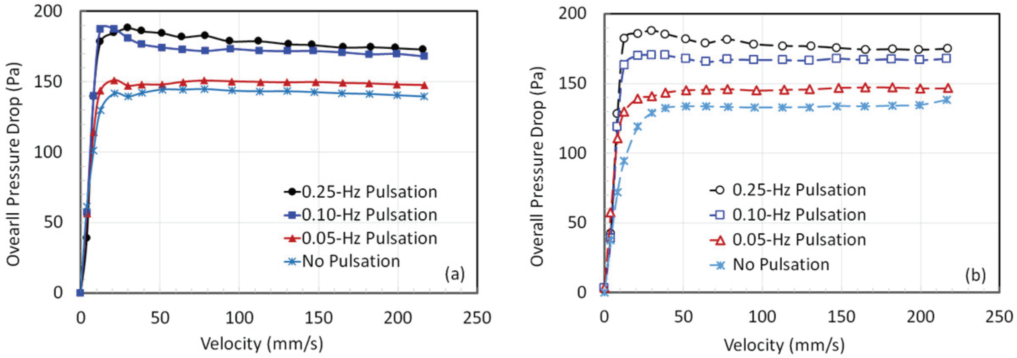

Figure 7. Variation of the total pressure drop with the velocity in pulsed beds with (**a**) increasing velocity and (**b**) decreasing velocity.

A close look at Figure 7b also reveals that pulsation helps lower the U_{mf}. However, any clear difference between the 0.1 and 0.25 Hz is hardly noticeable. In fact, earlier studies relied on the evaluation of the agglomerate diameter either from the U_{mf} or the bed collapse data to assess the effect of the flow pulsation [15,16]. Such an approach is based on the validity of a theoretical model capable of describing the experimental data. Therefore, any error in the predictive capability of the model will consequently affect the assessment of the efficacy of the assisted fluidization technique.

We have presented the normalized pressure drop behavior in Figure 8 where the actual experimental pressure drop was divided by the effective bed weight per unit area. In the literature this parameter is sometimes called the fluidization index [33,40,41]. The results shown in the figure are quite revealing, especially during the defluidization leg of the experiment when the velocity was gradually decreased. In the absence of flow pulsation, the fluidization index was almost 0.9. This means that the pressure drop was less than the effective solid weight per unit bed area. When the low frequency flow pulsations of 0.05 Hz were introduced, the fluidization quality improved. The value of the normalized pressure drop was approximately 0.99. At 0.10 Hz, we noted an increase in the normalized pressure drop to a value of approximately 1.12 for most velocities. This is a more than 20% increase in the pressure drop compared to what was obtained without pulsations. Increasing the frequency to 0.25 Hz further increased the normalized pressure drop to approximately 1.2.

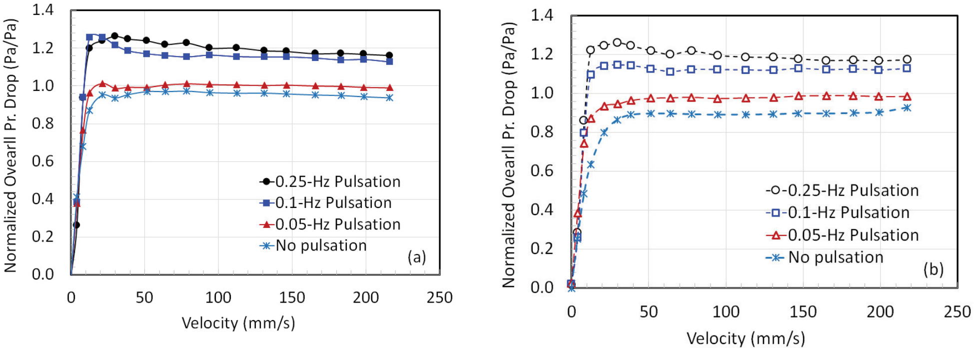

Figure 8. Variation in the normalized pressure drop with the velocity in the pulsed bed with (**a**) increasing velocity and (**b**) decreasing velocity.

The fluidized bed pressure drop is essentially caused by frictional losses, which arise from changes in the kinetic and potential energy, as well as by gas–solid interphase and solid–solid intra-phase drag. During the bed collapse, the potential energy converts into kinetic energy as the solids fall downwards. This causes an increase in the gas–solid interphase drag, leading to greater energy dissipation. In fact, this phenomenon also occurs during the expansion of the bed. Thus, the frequent collapse and expansion of the pulsed bed led to greater energy dissipation as compared to the case of conventional fluidization. As the pulsation frequency increased, greater energy dissipation took place, which was reflected in greater frictional losses. In the present case, 0.25 Hz pulsations caused a substantially greater power augmentation in the pulsed bed as compared to the one for conventional fluidization.

3.2. Bed Dynamics and Their Inter-Region Correlation

The dynamics in various bed regions were examined by utilizing the experimental data of the entire spectrum of several pulses at a fixed flow rate. First, let's consider the case of 0.05 Hz in Figure 9 with 10 s of gas flow followed by another 10 seconds of pause at a velocity of 182 mm/s. There were four complete pulses with a total duration of over 80 seconds, with approximately 8000 pressure-transient data points for each of the three regions in addition to data points for the overall pressure drop transients. The results are shown in Figure 9a. At the beginning of the flow pulse, all regions immediately responded to the change in flow. The vigorous solid motion was captured by the disturbances in the pressure transients. Once the flow was stopped, the bed collapse started. As expected, the effect of the bed fall was felt first in the lower portion, followed by the middle region, and subsequently the upper part.

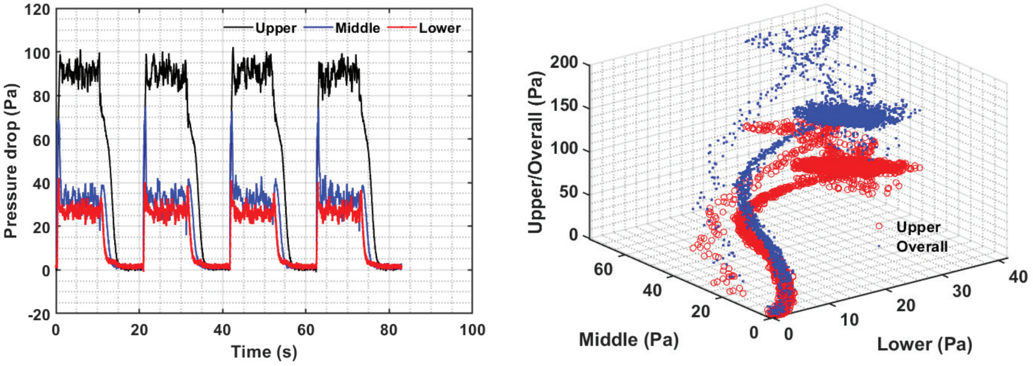

(**a**) (**b**)

Figure 9. (**a**) Bed transients in different regions of the pulsed fluidized bed and (**b**) inter-region pressure drop data correlation for 0.05 Hz at 182 mm/s.

Because the dynamics in all three bed regions occurred simultaneously, they were therefore correlated. The mutual interdependence regional dynamics are presented in Figure 9b, which also depicts the transients of the overall bed pressure drop. Note that the global dynamics data were recorded using the pressure transducer with its lower port above the distributor and the upper port open to the atmosphere. The highest data concentration is seen in the form of a circular disk. It represents the steady part of the flow pulse where the gas velocity was constant. There are two different branches, with different amounts of data points, seen in the figure; one leads toward the data disk and the other emanates from it. The branch with fewer data represents the bed expansion, while the other branch shows the bed collapse. This is a clear indication that expansion transients are faster than collapse transients.

The case of 0.10 Hz pulse with five seconds of gas flow followed immediately by another five seconds of flow interruption at 182 mm/s is considered in Figure 10. There were five complete pulses with a total duration of over 50 seconds, as seen in Figure 10a.

There is a substantial consistency in the dynamics of all the five pulses. Expectedly, pressure transients in all the regions immediately responded to the flow change, clearly evident at the start of the flow pulse. The middle region transient immediately peaks, whereas the lower region lags behind. The motion of the solid phase in the bed was once again evident from the disturbances occurring in the pressure transients. The steady part of the pulse was significantly less dense than the previous case of 0.05 Hz pulse. Once the bed collapse begins with the flow interruption, the upper region transients show significant lag compared with the transients of the other two regions, yet the complete bed occurred before the next flow pulse.

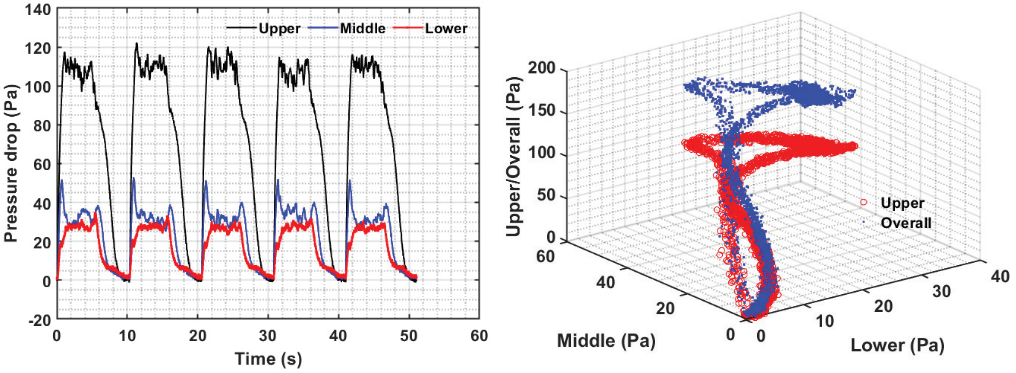

(**a**) (**b**)

Figure 10. (**a**) Bed transients in different bed regions and (**b**) inter-region pressure drop data correlation for 0.10 Hz at 182 mm/s.

The interdependence of the dynamics of all three regions is shown in Figure 10b. The data in the form of the circular disk are significantly smaller than the 0.01 Hz counterpart due to the much shorter time during which the bed is under relatively steady flow conditions. Two different branches, leading to and emanating from the circular data region, are once again clearly visible. Faster expansion transients possess fewer data as compared to the collapse dynamics. The curvature in the expansion branch arose from the faster transients displayed by the middle portion of the bed as compared to the transients of the lower portion.

The case of 0.25 Hz flow pulsations is shown in Figure 11 with two seconds of flow followed by the remaining two seconds of flow cessation. There was a total of eight pulses for a fixed velocity with a total duration of 32 seconds. Unlike the previous case of 0.05 Hz and 0.1 Hz, only a partial collapse of the bed occurred such that solids in the upper portion of the pulsed bed remained in a state of perpetual motion. The lowest pressure drop remained approximately 60 Pa, while the peaks were significantly higher than that for 0.05 Hz and slightly higher than that for 0.10 Hz pulsations. The middle region appeared relatively insensitive to pulsations as compared to the other two regions, i.e., the upper and lower regions. Another peak in the middle region pressure transients after the start of the collapse is due to the addition of the solid mass from the upper part. This significantly slows the transients of the middle region. Moreover, the central portion of the bed was never settled during the pulsed flow. Transients in the lower portion were pronounced with a prominent initial peak and a steep drop in pressure with the bed fall. This behavior significantly differed from that seen for the 0.05 and 0.10 Hz pulsed flows.

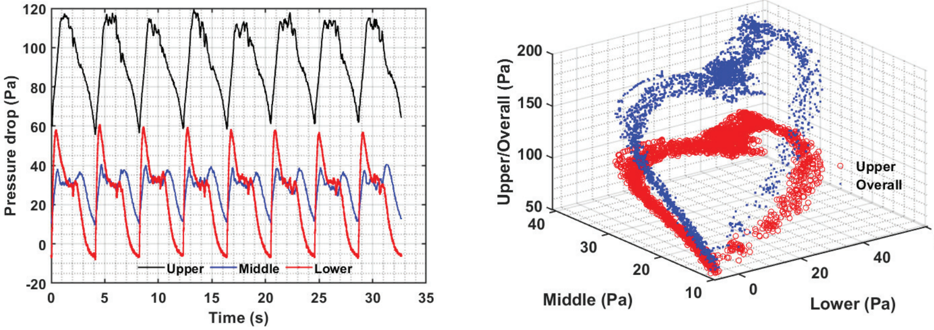

(**a**) (**b**)

Figure 11. (**a**) Bed transients in different bed regions and (**b**) inter-region pressure drop data correlation for 0.25 Hz at 182 mm/s.

The transient behavior seen in Figure 10a is also clearly reflected in Figure 11b. The faster transients in the lower bed region now shift the data branch movement counterclockwise toward the disk-shaped data region. Note that the upper region or the overall pressure drop was always above 50 Pa. Similarly, the middle region pressure drop always remained above 10 Pa, while the lower region pressure drop became negative toward the end of the collapse.

3.3. Energy Dissipation per Unit Time

To investigate the effect of the pulsation on the power augmentation, we have used the commonly suggested approach, which consists of evaluating the square of the signal over time (T) as follows:

$$Power = \lim_{T \to \infty} \frac{1}{T} \int_0^T \Delta P_G^2 dt, \tag{3}$$

where ΔP_G is the overall pressure drop signal across the pulsed bed. Four different cases are depicted in Figure 12 for the estimation of the integral in Equation (3). Only one complete pulse is shown in the figure for each of the three cases, i.e., 0.25, 0.1, and 0.05-Hz, at 182 mm/s. However, the power was computed using all four pulses for 0.05 Hz, five pulses for 0.10 Hz, and eight pulses for 0.25 Hz for a fixed velocity to ensure precise evaluation of the expression in Equation (3). In addition, the power of the theoretical case was also computed by noting that the theoretical pressure drop is equal to the effective bed weight, which is shown for the case of 0.05 Hz pulsation in Figure 12a. The shaded area shown in the figure corresponds to $\int_0^T \Delta P_G dt$ of a single pulse. Therefore, the greater the shaded area, the higher the power or the energy dissipation per unit time. As the frequency increases, the shaded area also increases, thus clearly indicating a greater dissipation of energy.

The power of the overall pressure drop (ΔP_G) signal of a fully fluidized bed is shown in Figure 13. Figure 13a shows the case when the fluidization velocity gradually increased, whereas Figure 13b considers the case of gradual decrease in velocity. The influence of the flow velocity on the magnitude of the power is insignificant. However, as the frequency increased, the energy dissipation due to the pulsation also increased. The theoretical values computed from the effective bed weight lie in the range of 9800 Pa^2, while those for the 0.05 Hz computed from the experimental data ranged from 11,750 to 12,800 Pa^2. These values increased to approximately 17,000 and 22,000 Pa^2 for 0.10 Hz and 0.25 Hz, respectively.

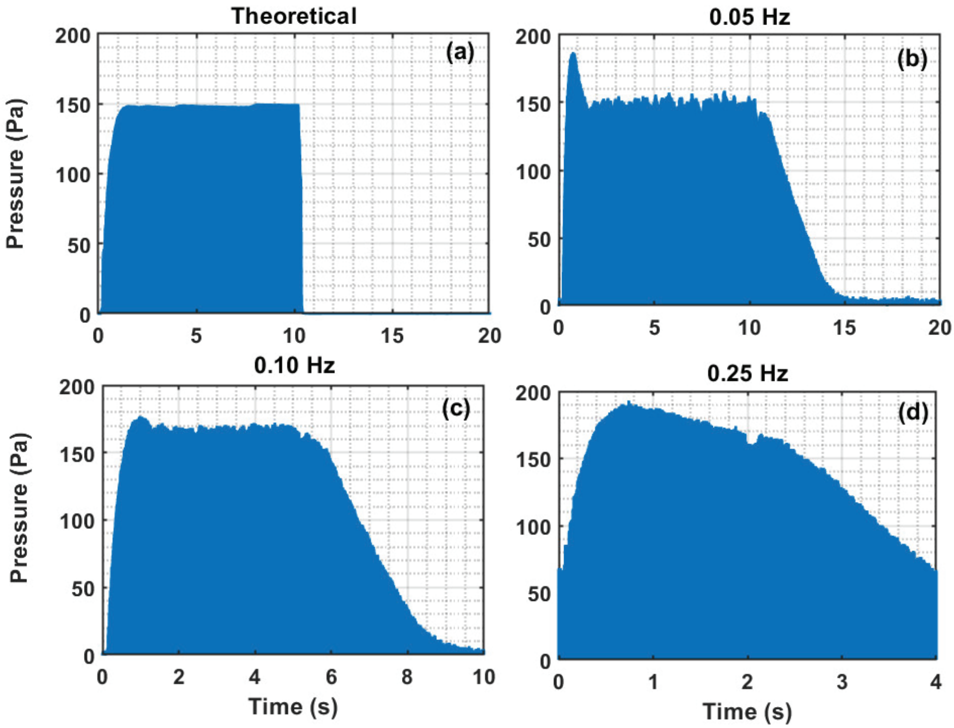

Figure 12. Shaded area used in the evaluation of the integral expression used in Equation (3); (**a**) Theoretical values (effective bed weight) based on 0.05 Hz pulsation, (**b**) 0.05-Hz pulsation, (**c**) 0.10-Hz pulsation, (**d**) 0.25-Hz pulsation.

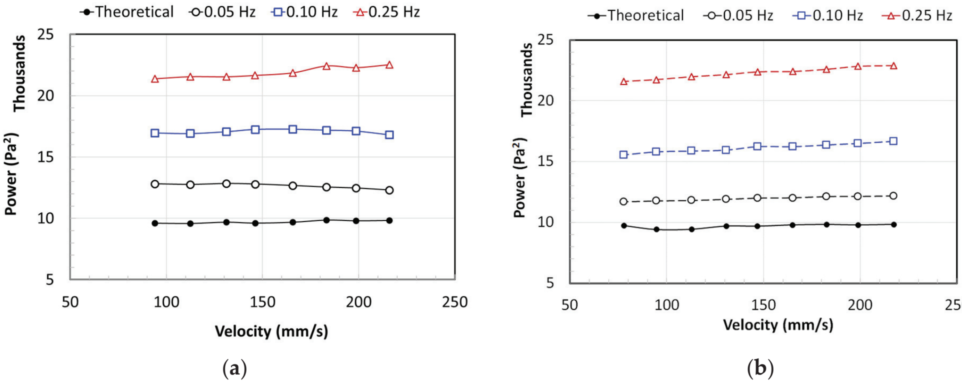

(**a**)

(**b**)

Figure 13. Power evaluated using Equation (3) while (**a**) increasing velocity and (**b**) decreasing velocity.

The data are summarized in Table 1, which presents the average values and standard deviations. Clearly, there is an almost 27 ± 4% increase in the energy dissipation when the pulsed flow of 0.05-Hz is used. This increases to 71 ± 5% with a 0.10 Hz and 128 ± 4% with a 0.25 Hz pulsed flow.

Table 1. Comparison of power input for different pulsation frequencies.

	Theoretical	**0.05-Hz**	**0.10-Hz**	**0.25-Hz**
Mean	9705	12,308	16,588	22,085
Std. Deviation	129	393	545	472

4. Conclusions

The fluidization of ultrafine and fine powders is often difficult due to the small size of the solid particles, which causes the inter-particle forces to dominate other forces acting on the particles. The fluidization of such powders would reveal poor interphase mixing with severe gas bypassing due to the heterogeneities developed in the bed. Assisted techniques are therefore often required to improve fluidization quality. The efficacy of assisted fluidization techniques has however been mostly evaluated qualitatively in the literature. This mainly consisted of examining the dependence of the pressure drop on the fluidizing gas velocity and evaluating the U_{mf}. Any decline in the U_{mf} is considered as an enhancement of the fluidization quality of the powder.

In the present study, we have extensively investigated the fluidization hydrodynamics of ultrafine nanosilica powder, which was subjected to a square-wave pulsed flow of three widely different pulsation frequencies. In addition to the overall pressure drop, the pressure drop characteristics of the lower, middle, and upper portions of the bed were carefully monitored. The dynamics of the upper portion differed from the two lower portions of the bed owing to the bed expansion, which was higher for high-frequency flow pulsations. Moreover, the progress of the collapse process was also felt differently in different portions of the bed when the frequency was changed. For example, the dynamic response of the middle bed region was slowest in comparison to the lower and upper bed regions when incomplete collapse of the bed occurred between two successive pulsation events. These characteristics of the bed dynamics were clearly highlighted by the three- dimensional plot that presented the correlation between the different parts of the pulsed bed. Finally, we have used the signal of the overall pressure drop to compute the power of the signal. A significant improvement in the power was observed when higher frequencies were used. The low-frequency pulsations (0.05 Hz), when compared with unassisted conventional technique, led to an increase of 27%, with further enhancement to 71% and 128%, for a 0.10 Hz and a 0.25 Hz pulsed fluidized bed, respectively.

Author Contributions: Conceptualization, M.A. and E.H.A.-G.; methodology, M.A. and E.H.A.-G.; software, M.A.; validation, M.A.; formal analysis, M.A.; investigation, E.H.A.-G.; resources, M.A.; data curation, M.A. and E.H.A.-G.; writing—original draft preparation, M.A. and A.F.; writing—review and editing, M.A. and A.F.; supervision, M.A.; project administration, M.A.; funding acquisition, M.A. All authors have read and agreed to the published version of the manuscript.

Funding: Researchers Supporting Project, RSP-2021/42, King Saud University, Riyadh, Saudi Arabia.

Institutional Review Board Statement: Not applicable.

Informed Consent Statement: Not applicable.

Data Availability Statement: The data is available on reasonable request from the corresponding author (M.A.).

Acknowledgments: The authors would like to thank the Researchers Supporting Project, RSP-2021/42, King Saud University, Riyadh, Saudi Arabia, for financial support.

Conflicts of Interest: The authors declare no conflict of interest. The funders had no role in the design of the study; in the collection, analyses, or interpretation of data; in the writing of the manuscript; or in the decision to publish the results.

References

1. Geldart, D. Types of Gas Fluidization. *Powder Technol.* **1973**, *7*, 285–292. [CrossRef]
2. Raganati, F.; Chirone, R.; Ammendola, P. Gas–solid fluidization of cohesive powders. *Chem. Eng. Res. Des.* **2018**, *133*, 347–387. [CrossRef]
3. Janssen, L.; Marring, E.; Hoogerbrugge, J.; Hoffmann, A. The mechanical behaviour of vibrated, aerated beds of glass and starch powder. *Chem. Eng. Sci.* **1998**, *53*, 761–772. [CrossRef]
4. Lee, J.-R.; Lee, K.-S.; Park, Y.-O.; Lee, K.-Y. Fluidization characteristics of fine cohesive particles assisted by vertical vibration in a fluidized bed reactor. *Chem. Eng. J.* **2020**, *380*, 122454. [CrossRef]
5. Lehmann, S.; Hartge, E.-U.; Jongsma, A.; Deleeuw, I.-M.; Innings, F.; Heinrich, S. Fluidization characteristics of cohesive powders in vibrated fluidized bed drying at low vibration frequencies. *Powder Technol.* **2019**, *357*, 54–63. [CrossRef]
6. Nam, C.H.; Pfeffer, R.; Dave, R.N.; Sundaresan, S. Aerated vibrofluidization of silica nanoparticles. *Aiche J.* **2004**, *50*, 1776–1785. [CrossRef]
7. Valverde, J.M.; Castellanos, A. Effect of vibration on agglomerate particulate fluidization. *Aiche J.* **2006**, *52*, 1705–1714. [CrossRef]
8. Barletta, D.; Poletto, M. Aggregation phenomena in fluidization of cohesive powders assisted by mechanical vibrations. *Powder Technol.* **2012**, *225*, 93–100. [CrossRef]
9. Barletta, D.; Russo, P.; Poletto, M. Dynamic response of a vibrated fluidized bed of fine and cohesive powders. *Powder Technol.* **2013**, *237*, 276–285. [CrossRef]
10. Cruz, M.A.A.; Passos, M.L.; Ferreira, W.R. Final Drying of Whole Milk Powder in Vibrated-Fluidized Beds. *Dry. Technol.* **2005**, *23*, 2021–2037. [CrossRef]
11. Hoorijani, H.; Zarghami, R.; Nosrati, K.; Mostoufi, N. Investigating the hydrodynamics of vibro-fluidized bed of hydrophilic titanium nanoparticles. *Chem. Eng. Res. Des.* **2021**, *174*, 486–497. [CrossRef]
12. Lee, J.-R.; Lee, K.-S.; Hasolli, N.; Ok Park, Y. Fluidization and mixing behaviors of Geldart groups A, B and C particles assisted by vertical vibration in fluidized bed. *Chem. Eng. Processing—Process Intensif.* **2020**, *149*, 107856. [CrossRef]
13. Akhavan, A.; van Ommen, J.R.; Nijenhuis, J.; Wang, X.S.; Coppens, M.-O.; Rhodes, M.J. Improved Drying in a Pulsation-Assisted Fluidized Bed. *Ind. Eng. Chem. Res.* **2009**, *48*, 302–309. [CrossRef]
14. Al-Ghurabi, E.H.; Shahabuddin, M.; Kumar, N.S.; Asif, M. Deagglomeration of Ultrafine Hydrophilic Nanopowder Using Low-Frequency Pulsed Fluidization. *Nanomaterials* **2020**, *10*, 388. [CrossRef] [PubMed]
15. Ali, S.S.; Al-Ghurabi, E.H.; Ajbar, A.; Mohammed, Y.A.; Boumaza, M.; Asif, M. Effect of Frequency on Pulsed Fluidized Beds of Ultrafine Powders. *J. Nanomater.* **2016**, *2016*, 4592501. [CrossRef]
16. Ali, S.S.; Asif, M. Fluidization of nano-powders: Effect of flow pulsation. *Powder Technol.* **2012**, *225*, 86–92. [CrossRef]
17. Asif, M.; Al-Ghurabi, E.H.; Ajbar, A.; Kumar, N.S. Hydrodynamics of Pulsed Fluidized Bed of Ultrafine Powder: Fully Collapsing Fluidized Bed. *Processes* **2020**, *8*, 807. [CrossRef]
18. Dong, L.; Zhang, Y.; Zhao, Y.; Peng, L.; Zhou, E.; Cai, L.; Zhang, B.; Duan, C. Effect of active pulsing air flow on gas-vibro fluidized bed for fine coal separation. *Adv. Powder Technol.* **2016**, *27*, 2257–2264. [CrossRef]
19. Dong, L.; Zhou, E.; Cai, L.; Duan, C.; Zhao, Y.; Luo, Z. Fluidization Characteristics of a Pulsing Dense-Phase Gas-Solid Fluidized Bed for High-Density Separation of Fine Anthracite. *Energy Fuels* **2016**, *30*, 7180–7186. [CrossRef]
20. Jia, D.; Cathary, O.; Peng, J.; Bi, X.; Lim, C.J.; Sokhansanj, S.; Liu, Y.; Wang, R.; Tsutsumi, A. Fluidization and drying of biomass particles in a vibrating fluidized bed with pulsed gas flow. *Fuel Process. Technol.* **2015**, *138*, 471–482. [CrossRef]
21. Zhou, C.; Dong, L.; Zhao, Y.; Fan, X. Studies on Bed Density in a Gas-Vibro Fluidized Bed for Coal Cleaning. *ACS Omega* **2019**, *4*, 12817–12826. [CrossRef] [PubMed]
22. Zhou, E.; Zhang, Y.; Zhao, Y.; Luo, Z.; He, J.; Duan, C. Characteristic gas velocity and fluidization quality evaluation of vibrated dense medium fluidized bed for fine coal separation. *Adv. Powder Technol.* **2018**, *29*, 985–995. [CrossRef]
23. Ireland, E.; Pitt, K.; Smith, R. A review of pulsed flow fluidisation; the effects of intermittent gas flow on fluidised gas-solid bed behaviour. *Powder Technol.* **2016**, *292*, 108–121. [CrossRef]
24. Ali, S.S.; Hossain, S.K.S.; Asif, M. Dynamics of partially collapsing pulsed fluidized bed. *Can. J. Chem. Eng.* **2021**, *99*, 2333–2344. [CrossRef]
25. Al-Ghurabi, E.H.; Ali, S.S.; Alfadul, S.M.; Shahabuddin, M.; Asif, M. Experimental investigation of fluidized bed dynamics under resonant frequency of sound waves. *Adv. Powder Technol.* **2019**, *30*, 2812–2822. [CrossRef]
26. Ammendola, P.; Chirone, R.; Raganati, F. Fluidization of binary mixtures of nanoparticles under the effect of acoustic fields. *Adv. Powder Technol.* **2011**, *22*, 174–183. [CrossRef]
27. Si, C.; Wu, J.; Wang, Y.; Zhang, Y.; Liu, G. Effect of acoustic field on minimum fluidization velocity and drying characteristics of lignite in a fluidized bed. *Fuel Process. Technol.* **2015**, *135*, 112–118. [CrossRef]
28. Viscusi, A.; Ammendola, P.; Astarita, A.; Raganati, F.; Scherillo, F.; Squillace, A.; Chirone, R.; Carrino, L. Aluminum foam made via a new method based on cold gas dynamic sprayed powders mixed through sound assisted fluidization technique. *J. Mater. Process. Technol.* **2016**, *231*, 265–276. [CrossRef]
29. Zhu, C.; Liu, G.; Yu, Q.; Pfeffer, R.; Dave, R.N.; Nam, C.H. Sound assisted fluidization of nanoparticle agglomerates. *Powder Technol.* **2004**, *141*, 119–123. [CrossRef]
30. Ali, S.S.; Al-Ghurabi, E.H.; Ibrahim, A.A.; Asif, M. Effect of adding Geldart group A particles on the collapse of fluidized bed of hydrophilic nanoparticles. *Powder Technol.* **2018**, *330*, 50–57. [CrossRef]

31. Ajbar, A.; Alhumazi, K.; Asif, M. Improvement of the fluidizability of cohesive powders through mixing with small proportions of group a particles. *Can. J. Chem. Eng.* **2005**, *83*, 930–943. [CrossRef]
32. Al-Ghurabi, E.H.; Ajbar, A.; Asif, M. Enhancement of CO_2 Removal Efficacy of Fluidized Bed Using Particle Mixing. *Appl. Sci.* **2018**, *8*, 1467. [CrossRef]
33. Al-Ghurabi, E.H.; Ajbar, A.; Asif, M. Improving Fluidization Hydrodynamics of Group C Particles by Mixing with Group B Particles. *Appl. Sci.-Basel* **2018**, *8*, 1469. [CrossRef]
34. Ali, S.S.; Basu, A.; Alfadul, S.M.; Asif, M. Nanopowder Fluidization Using the Combined Assisted Fluidization Techniques of Particle Mixing and Flow Pulsation. *Appl. Sci.* **2019**, *9*, 572. [CrossRef]
35. An, K.; Andino, J.M. Enhanced fluidization of nanosized TiO_2 by a microjet and vibration assisted (MVA) method. *Powder Technol.* **2019**, *356*, 200–207. [CrossRef]
36. Zhao, Z.; Liu, D.; Ma, J.; Chen, X. Fluidization of nanoparticle agglomerates assisted by combining vibration and stirring methods. *Chem. Eng. J.* **2020**, *388*, 124213. [CrossRef]
37. Asif, M.; Kalogerakis, N.; Behie, L.A. Hydrodynamics of liquid fluidized beds including the distributor region. *Chem. Eng. Sci.* **1992**, *47*, 4155–4166. [CrossRef]
38. Asif, M.; Kalogerakis, N.; Behie, L.A. Distributor effects in liquid fluidized beds of low-density particles. *Aiche J.* **1991**, *37*, 1825–1832. [CrossRef]
39. Market Analysis Report. NanoSilica Market Size, Share & Trends Analysis Report by Product (P Type, S Type, and Type III), by Application (Rubber, Healthcare, Food, Coatings, Plastics, Concrete, Gypsum, Battery, Electronics, Cosmetics), and Segment Forecasts, 2018–2025. 20 June 2022. Available online: https://www.grandviewresearch.com/industry-analysis/nanosilica-market (accessed on 12 April 2022).
40. Marring, E.; Hoffmann, A.C.; Janssen, L. The effect of vibration on the fluidization behaviour of some cohesive powders. *Powder Technol.* **1994**, *79*, 1–10. [CrossRef]
41. Escudero, D.; Heindel, T. Minimum fluidization velocity in a 3D fluidized bed modified with an acoustic field. *Chem. Eng. J.* **2013**, *231*, 68–75. [CrossRef]

nanomaterials

Article

Performance Enhancement of SPR Biosensor Using Graphene–MoS_2 Hybrid Structure

Haoyuan Cai [1,2,3], Mengwei Wang [1,2,3], Zhuohui Wu [1,2,3], Jing Liu [4,*] and Xiaoping Wang [1,2,3,*]

[1] Ocean College, Zhejiang University, Zhoushan 316021, China; hycai@zju.edu.cn (H.C.); wmw@zju.edu.cn (M.W.); zhuohui_wu@zju.edu.cn (Z.W.)
[2] Key Laboratory of Ocean Observation-Imaging Testbed of Zhejiang Province, Zhejiang University, Zhoushan 316021, China
[3] The Engineering Research Center of Oceanic Sensing Technology and Equipment, Ministry of Education, Zhoushan 316021, China
[4] School of Information Engineering, Jimei University, Xiamen 361021, China
* Correspondence: jingliu@jmu.edu.cn (J.L.); xpwang@zju.edu.cn (X.W.)

Abstract: We investigate a high-sensitivity surface plasmon resonance (SPR) biosensor consisting of a Au layer, four-layer MoS_2, and monolayer graphene. The numerical simulations, by the transfer matrix method (TMM), demonstrate the sensor has a maximum sensitivity of 282°/RIU, which is approximately 2 times greater than the conventional Au-based SPR sensor. The finite difference time domain (FDTD) indicates that the presence of MoS_2 film generates a strong surface electric field and enhances the sensitivity of the proposed SPR sensor. In addition, the influence of the number of MoS_2 layers on the sensitivity of the proposed sensor is investigated by simulations and experiments. In the experiment, MoS_2 and graphene films are transferred on the Au-based substrate by the PMMA-based wet transfer method, and the fabricated samples are characterized by Raman spectroscopy. Furthermore, the fabricated sensors with the Kretschmann configuration are used to detect okadaic acid (OA). The okadaic acid–bovine serum albumin bioconjugate (OA-BSA) is immobilized on the graphene layer of the sensors to develop a competitive inhibition immunoassay. The results show that the sensor has a very low limit of detection (LOD) of 1.18 ng/mL for OA, which is about 22.6 times lower than that of a conventional Au biosensor. We believe that such a high-sensitivity SPR biosensor has potential applications for clinical diagnosis and immunoassays.

Keywords: biosensor; MoS_2; graphene; SPR sensor; high sensitivity

Citation: Cai, H.; Wang, M.; Wu, Z.; Liu, J.; Wang, X. Performance Enhancement of SPR Biosensor Using Graphene–MoS_2 Hybrid Structure. *Nanomaterials* **2022**, *12*, 2219. https://doi.org/10.3390/nano12132219

Academic Editors: Jihoon Lee and Ming-Yu Li

Received: 5 June 2022
Accepted: 26 June 2022
Published: 28 June 2022

1. Introduction

Surface plasmon resonance (SPR) is one of the most powerful optical-sensing technologies due to its high sensitivity, real-time, and label-free detection [1–6]. SPR-based biosensors have many practical applications, such as medical diagnostics, food safety, virus detection, etc., as they can be coupled with various molecular recognition elements, either chemical receptors (nanomaterials, molecularly imprinted polymers (MIPs), etc.) or bioreceptors (enzymes, nucleic acids, antibodies, etc.) [7–10]. In general, Ag and Au are widely used as plasmonic materials for SPR sensors. Au film is preferred because of its excellent resistance to corrosion and oxidation in different external environments [11]. However, bioreceptors are poorly immobilized on the surface of Au film, limiting the sensitivity of the Au-based SPR biosensor.

Many chemical methods are used to enhance the immobilization of bioreceptors. Among them, the self-assembly monolayer (SAM) has been widely proven to be particularly effective because of its simplicity of fabrication, reproducibility, and good temperature stability [12–14]. Many studies have reported using SAMs to improve the sensitivity of SPR sensors. Taylor et al. [13] report a limit of detection (LOD) of 0.3 ng/mL for Tetrodotoxin

(TTX) by using a mixed SAM layer. Kawaguchi et al. [14] employ the PEG-based SAM layer for detecting TNT with a LOD of 0.008 ng/mL.

In addition to these chemical methods, many biosensors, based on metallic nanoslits [15] or nanoholes structures [16,17], are proposed to enhance the sensitivity of the SPR sensors. However, the fabrication processes of these structures often involve complicated steps or require expensive, time-consuming electron beam lithography. Moreover, large-area fabrication is challenging.

To solve this problem, a large-area thin graphene layer is used to cover the Au film surface to improve the sensitivity of the SPR sensor [18,19]. Graphene is a monoatom thin planar sheet of sp_2 carbon atoms well organized in the form of a honeycomb lattice. It provides better support for biomolecule adsorption due to its rich π conjugation structure and large surface area, making it a suitable dielectric layer for SPR sensing [20,21]. For example, Verma et al. [22] exploit graphene and silicon to improve the sensitivity of SPR biosensors. Wu et al. [23] employ 10-layer graphene to improve sensitivity, and the performance can be nearly 25% enhanced. At a certain wavelength range, more graphene layers result in higher sensor sensitivity. However, due to the large imaginary part of graphene, too many graphene layers will produce excessive an amount of damping in plasmonic waves, resulting in reduced detection accuracy.

In addition to graphene, other 2D materials, such as molybdenum disulfide (MoS_2), have gained much attention for sensing applications. Monolayer MoS_2 has many unique advantages, such as higher light absorption efficiency (5%), large direct bandgap (1.8 eV), and larger work function (5.1 eV), so it is widely used in the field of SPR sensing [24–26]. For example, Xue et al. [27] design a high-sensitivity SPR sensor by coating seven layers of MoS_2 on the surface of a sensor. They demonstrate that the highest sensitivity is about 190°/RIU and the LOD of Hg^{2+} for the sensor is 1.0 pM. In addition, the emergence of the chemical vapor deposition (CVD) technique makes the large-area growth of MoS_2 possible, which further facilitates the development of MoS_2-based SPR sensors [28].

In this work, we propose a high-sensitivity SPR biosensor based on the graphene–MoS_2 structure. MoS_2 films are used to absorb more light energy and the monolayer graphene is used as the biomolecular recognition element due to its large surface area. Theoretical optimization, based on the transfer matrix method (TMM), shows that a maximum sensitivity ~282°/RIU is achieved, when the Au-based substrate is modified with four-layer MoS_2 and monolayer graphene. The mechanism of sensitivity enhancement is discussed and explained theoretically. In the experiment, a PMMA-based wet transfer method is used to transfer MoS_2 and graphene film on the Au-based substrate and the high-refractive-index (RI) sensitivity of the fabricated sensor is verified. In addition, the proposed biosensor is used to detect okadaic acid (OA) by the indirect competitive inhibition method. The experimental results demonstrate that the graphene–MoS_2 hybrid structure can greatly reduce the LOD of the SPR biosensor.

2. Numerical Simulation

Design the Proposed SPR Biosensor

In Figure 1, the designed SPR sensor is based on a prism, Cr layer, Au layer, few-layer MoS_2, and monolayer graphene. In this structure, BK7 glass is used as a coupling prism and Au is used as a plasmonic material to excite the SPR effect. Few-layer MoS_2 films are used to absorb more light energy and the monolayer graphene is used as the biological recognition component, which further improves sensor sensitivity. In the simulation, the thickness of the Cr layer is 5 nm and the thickness of the Au layer is 50 nm. The wavelength of the incident light source is 632.8 nm. At this wavelength, the RI of BK7 glass is 1.516 [29]. The RI of Au is obtained from the Drude–Lorentz model [30]. The RI of graphene is 3 + 1.1487i [31] and its thickness can be expressed as $d_G = L*0.34$ nm, where L is the number of graphene layers. The RI of the MoS_2 layer is 5.9 + 0.8i [32] and its thickness can be denoted as $d_M = M*0.65$ nm, where M is the number of MoS_2 layers.

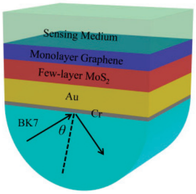

Figure 1. Schematic illustration of the designed SPR sensor.

To evaluate sensing performance, we compare the RI sensitivities of three different structures: the conventional Au-based sensor, the MoS_2-based sensor, and the graphene–MoS_2 hybrid-structure sensor. TMM is used to calculate the reflectivity curves of various structures and the calculated results are shown in Figure 2. The sensitivity calculation formula of the SPR sensor is $S = \Delta\theta/\Delta n$, where $\Delta\theta$ is the variation in resonance angle and Δn is the variation in the RI of the sensing medium. Figure 2a is the reflectivity curves of the conventional Au-based sensor, and the thickness of the Au film is 50 nm. From this figure, the resonance angle increases ~0.71° when n_s changes from 1.330 to 1.335. Thus, the sensitivity of the Au-based sensor is 142°/RIU. In Figure 2b, we use the four-layer MoS_2 to enhance the sensitivity and the sensitivity is calculated to be 256°/RIU. The high sensitivity is because the presence of the MoS_2 layer increases the efficiency of light absorption of the sensor. Most of the incident light energy is transferred to free electrons on the sensor surface, so more surface plasmons are generated, which results in the higher sensitivity [33,34]. In Figure 2c, the monolayer graphene is covered on top of the MoS_2 layer to further improve the sensitivity. The resonance angle shifts by ~1.41° and the sensitivity increases to 282°/RIU. Obviously, the monolayer graphene does not significantly enhance the RI sensitivity of the proposed sensor. This is due to the fact that the light absorption efficiency of graphene is lower than that of MoS_2. The primary function of the monolayer graphene is used as a biomolecular recognition component. In biological experiments, the graphene provides a large surface area for adsorbing biomolecules, which lowers the LOD of the sensor [35].

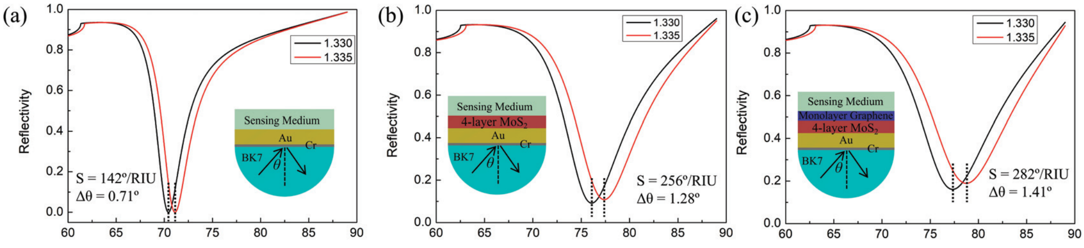

Figure 2. Reflectivity curves change with incident angles for (**a**) conventional Au-based sensor, (**b**) MoS_2-based sensor, (**c**) graphene–MoS_2 hybrid-structure sensor.

To study the influence of the number of MoS_2 layers on the sensitivity of the graphene–MoS_2 hybrid-structure sensor, we calculate the reflectivity curves in a different sensing medium, as shown in Figure 3. According to Figure 3, the SPR curves become wider and the resonance angle obviously shifts to higher angle values with the increase in the MoS_2 layers. This is due to the relatively high RI in the real parts of the MoS_2 material, which produces excessive amount of damping in the plasmonic wave [36]. Furthermore, we can see that the sensitivity first increases and then decreases with the increase in MoS_2 layers. This can be explained that as the number of MoS_2 layers continuously increases, the resonance angle will increase to 90°, but the detection angle cannot reach 90°, limiting the sensitivity of the SPR sensor [37]. When the number of MoS_2 layers is four (M = 4), the highest sensitivity of 282°/RIU is obtained, which is significantly improved as compared to the other reported works [22,23,27].

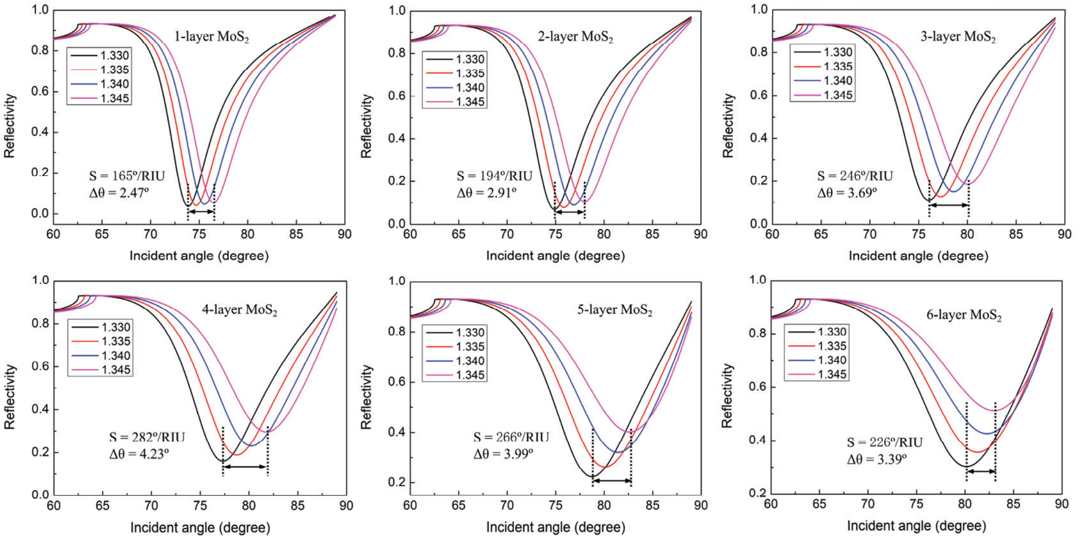

Figure 3. Reflectivity curves change with incident angles for graphene–MoS$_2$ hybrid-structure sensor in different sensing medium, where the number of MoS$_2$ layers increases from M = 1 to M = 6.

In order to clearly demonstrate the electric field enhancement of the proposed sensor, we compare the electric field distribution in two configurations of the conventional Au-based sensor and the graphene–MoS$_2$ hybrid-structure sensor with four-layer MoS$_2$ at resonance condition. The finite difference time domain (FDTD) method is used to simulate the electric field distribution and the calculated results are shown in Figure 4. Compared with the Au-based sensor, the electric field of the proposed sensor in Figure 4b can have an evident improvement by coating the MoS$_2$ and graphene film. On one hand, the graphene–MoS$_2$ hybrid structure improves the absorption of light energy. On the other hand, the absorbed light energy is transferred to the free electrons, resulting in strong coupling on the graphene surface, ultimately enhancing the surface electric field. The electric-field-enhanced region has a more sensitive response to the slight variation in RI of the sensing medium.

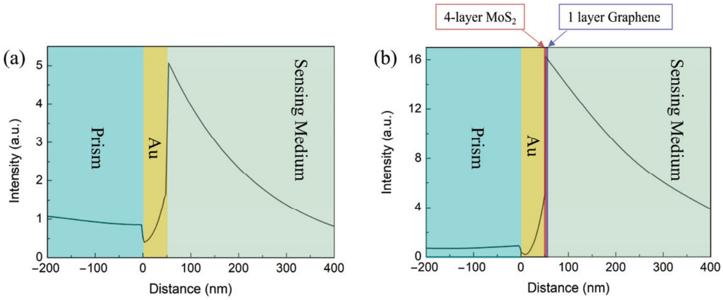

Figure 4. *Cont.*

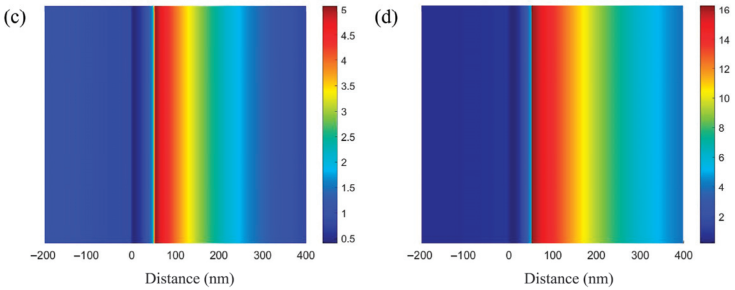

Figure 4. The electric field distributions for (**a**,**c**) conventional Au-based sensor and (**b**,**d**) graphene–MoS_2 hybrid-structure sensor.

3. Experiment

3.1. Materials and Reagents

NaCl, H_2SO_4, HCl, NaOH, H_2O_2, anisole, KOH, acetone, and poly (methyl methacrylate) (PMMA, molecular weight ≥20,000) were obtained from Sinopharm Chemical Reagent Co., Ltd. (Shanghai, China). N-hydroxysuccinimide (NHS), 1-ethyl-3-(3-dimethylaminopropyl)-carbodiimide hydrochloride (EDC), ethanolamine and phosphate-buffered saline (PBS) were purchased from Shanghai Aladdin Biochemical Technology Co., Ltd. Okadaic acid (OA) with >95% purity (HPLC-grade), the okadaic acid–bovine serum albumin bioconjugate (OA-BSA), and anti-OA monoclonal antibody (OA-mAb) were purchased from Anti Biological Technology Co., Ltd. (Shenzhen, China). A 0.2 M NaOH solution was used as the regenerant. All reagents and solvents are analytical grade and were used without further purification. Deionized water (18.2 MΩ·cm) was used throughout the work.

3.2. Sample Fabrication

3.2.1. The Fabrication of the Conventional Au-Based Sensor

The conventional Au-based sensor and graphene–MoS_2 hybrid-structure sensor with different numbers of MoS_2 layers are fabricated in this paper and the fabrication processes are shown in Figure 5. First, a 5 nm Cr layer and 50 nm-thick Au layer were sequentially deposited on the polished BK7 glass substrate by magnetron sputtering, where the Cr layer was used as an adhesion layer (See Figure 5c,d). The SEM image of Au-based sensor is shown in Figure 6. We can see that the thickness of the Au film is 49.6 nm.

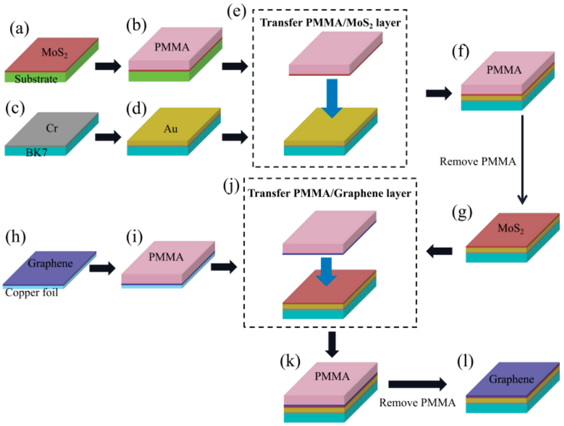

Figure 5. Schematic diagram of fabrication processes of the graphene–MoS_2 hybrid-structure sensor. (**a**) MoS_2 deposition using CVD, (**b**) PMMA spin-coating, (**c**) Cr deposition using magnetron sputtering, (**d**) Au deposition using magnetron sputtering, (**e**) separation of PMMA/MoS_2 from

SiO_2/Si substrate using KOH, (**f**) PMMA/MoS_2 transferring to Au-based substrate, (**g**) PMMA removal using acetone, (**h**) monolayer-graphene deposition using CVD, (**i**) PMMA spin-coating, (**j**) etching the Cu foil using $FeCl_3$, (**k**) PMMA/graphene transferring to MoS_2-based substrate, (**l**) PMMA removal using acetone.

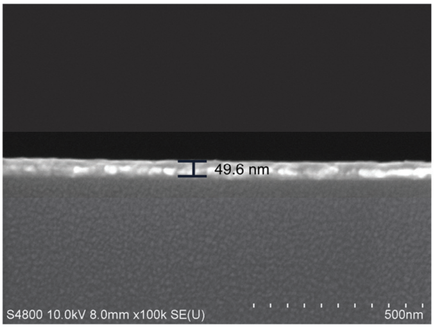

Figure 6. The SEM images of the conventional Au-based sensor.

3.2.2. The Transfer Process of MoS_2 Film

Continuous 2~6-layer MoS_2 film purchased from SixCarbon Technology was grown on SiO_2/Si substrate by CVD technique. The few-layer MoS_2 films were transferred onto the Au-based substrate by a PMMA-based wet transfer method [38]. In the MoS_2 transfer process, first, MoS_2 grown on SiO_2/Si substrate was spin-coated with PMMA (4% in anisole) at 3000 rpm for 1 min and baked at 120 C for 3 min. Then, samples with the PMMA coating were then soaked in a 2 mol/L KOH solution for 2 h, in which the PMMA/MoS_2 layer was separated from the Si substrate due to etching of SiO_2. Next, the PMMA/MoS_2 layers were washed in DI water, scooped using an Au-based substrate, dried under ambient conditions, and baked at 80 °C for 1 h. Finally, the acetone was used to dissolve the PMMA. We can complete the transfer of MoS_2 to obtain the MoS_2-based substrate (See Figure 5a–g).

3.2.3. The Transfer Process of Graphene Film

The monolayer graphene purchased from SixCarbon Technology was synthesized on Cu foil using the CVD technique. Similar to the transfer method of the MoS_2 layer, we transferred the monolayer graphene on MoS_2-based substrate to obtain the proposed biosensor. First, a thin layer of PMMA was spin-coated onto the surface of graphene/Cu foil at 500 rpm for 10 s, followed by 20 s at 2500 rpm. Then, the PMMA/graphene/Cu foil was baked at 120 °C for 3 min; then, the Cu foil was etched in a 1 mol/L $FeCl_3$ solution for 1 h. After the Cu foil was dissolved, the PMMA–graphene film was repeatedly washed with sufficient DI water. Next, the PMMA/graphene sample was carefully transferred onto the surface of MoS_2-based substrate. Then, the sample was dried at 90 °C for 60 min to enable the PMMA–graphene layer to firmly adhere to the substrate. Finally, the acetone was used to dissolve the PMMA and the fabricated samples were thoroughly washed with DI water (See Figure 5h–l). Through the above steps, we fabricated the graphene–MoS_2 hybrid-structure sensor with different numbers of MoS_2 layers.

The photograph of the fabricated graphene–MoS_2 hybrid-structure sensor with different layers of MoS_2 and monolayer graphene is shown in Figure 7. We can see the different colors correspond to the different numbers of MoS_2 layers. Raman spectra of fabricated samples are characterized by EnSpectrR532 at a laser wavelength of 532 nm and the corresponding spectra are shown in Figure 8. In the low-frequency region, two strong peaks E^1_{2g} and A_{1g}, which locate at 382.9 cm^{-1} and 406.5 cm^{-1}, respectively, are shown in Figure 8a. As the layer number increases from 2-layer to 6-layer, a slight red shift in the E^1_{2g} band and a slight blue shift in the A_{1g} band are observed. These findings suggest that MoS_2 films are successfully transferred in graphene–MoS_2 hybrid structure [39]. In the high-frequency band, the black line in Figure 8b indicates two characteristic peaks of graphene at 1581.2 cm^{-1} (G-band) and 2679.1 cm^{-1} (2D-band). According to previous reports, the number of graphene layers depends on the intensity ratios I_{2D}/I_G. When the I_{2D}/I_G of this spectrum is approximately 2, it represents a typical spectrum of monolayer graphene [40]. In addition, for the red, blue, and pink lines, both the G and 2D peaks of graphene appear in the same location. These results indicate that monolayer graphene film was successfully transferred in a graphene–MoS_2 hybrid structure.

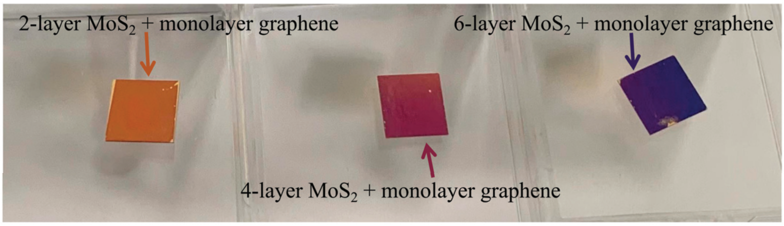

Figure 7. Photograph of the fabricated graphene–MoS_2 hybrid-structure sensor with different layers of MoS_2 and monolayer graphene.

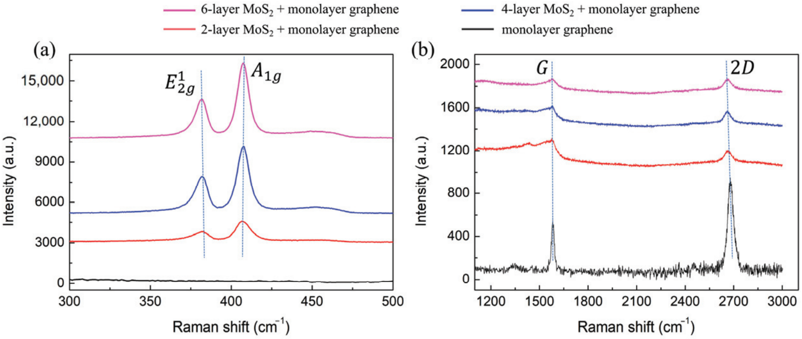

Figure 8. Raman spectra of monolayer graphene on SiO_2 substrate and the fabricated graphene–MoS_2 hybrid-structure sensor with different layers of MoS_2 for (**a**) 300~500 cm^{-1}; (**b**) 1100~3100 cm^{-1}.

3.3. RI-Sensing Experiments

In this section, we compare the RI sensitivity of the Au-based sensor and the proposed sensor with different layers of MoS_2. The Abbe refractive index meter was used to measure the RI of the NaCl solutions at room temperature (26 °C). The NaCl solution with concentration ranges of 0.1 g/L, 0.25 g/L, 0.5 g/L, 1 g/L, 2.5 g/L, 5 g/L, and 10 g/L were prepared, and their corresponding refractive indices are 1.33152, 1.33154, 1.33158, 1.33165, 1.33189, 1.33229, and 1.33308, respectively. In the experiment, deionized water was first injected into the sensor for a sufficient time to ensure the stability of the baseline. Then, the NaCl solution and deionized water were sequentially injected as a cycle, and the process was repeated to test different concentrations of NaCl solutions. Every concentration was measured three times, and the results were recorded in computer software. Figure 9 shows the response signal for the conventional Au-based biosensor in different RI solutions. From the linear fitting curve of Figure 9b, the RI sensitivity is 13,951.2 pixel/RIU with linearity of 0.98519. Similarly, NaCl solutions with different concentrations were injected into the sensing region of proposed sensor with different layers of MoS_2. The response spectra are shown in Figures 10a, 11a and 12a. In Figures 10b, 11b and 12b, linear fittings are conducted to obtain the corresponding sensitivities. The sensitivity values are 17,003.4, 25,819.9, and 21,783.3 pixel/RIU for the proposed sensors with 2, 4, and 6 layers of MoS_2, respectively, and all the correlation coefficients (R^2) are higher than 0.98. When the number of MoS_2

layers is four, the maximum sensitivity is obtained, which is 1.85 times that of conventional Au-based sensor. A good agreement is observed between the experimental results and the theoretical calculation results.

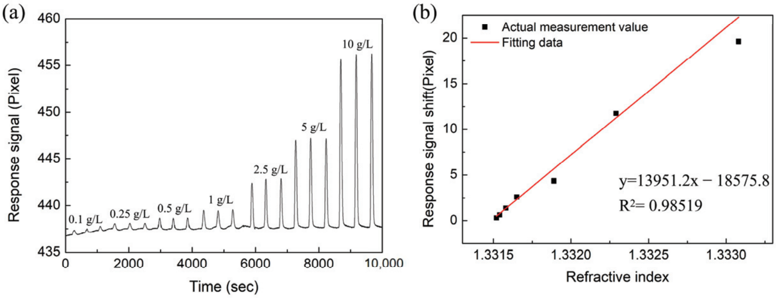

Figure 9. (**a**) The response curves of NaCl solution with different concentrations for the conventional Au-based biosensor. (**b**) The corresponding linear fitting line.

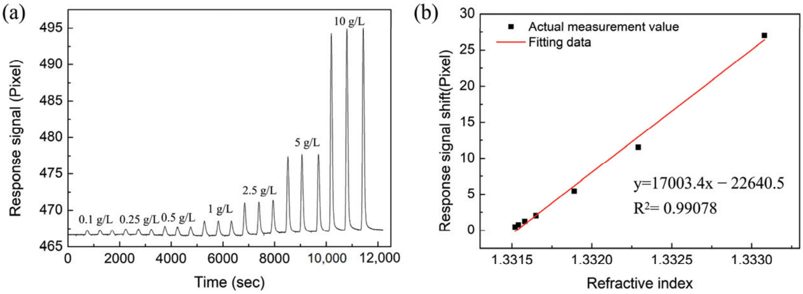

Figure 10. (**a**) The response curves of NaCl solution with different concentrations for the proposed biosensor based on two layers of MoS_2. (**b**) The corresponding linear fitting line.

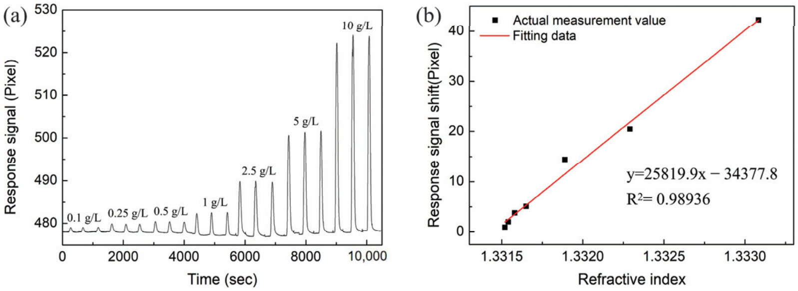

Figure 11. (**a**) The response curves of NaCl solution with different concentrations for the proposed biosensor based on four layers of MoS_2. (**b**) The corresponding linear fitting line.

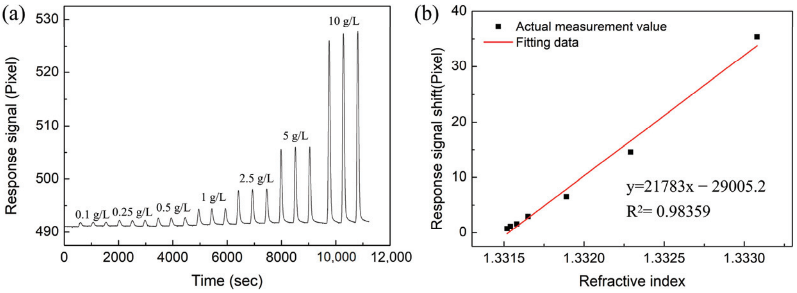

Figure 12. (**a**) The response curves of NaCl solution with different concentrations for the proposed biosensor based on six layers of MoS_2. (**b**) The corresponding linear fitting line.

3.4. Okadaic Acid Detection Experiment

3.4.1. Fabrication of SPR Immunosensor

The surface of graphene has abundant functional groups, which can be covalently bound to antigen or antibody molecules. For the pretreatment of the graphene-based SPR-sensing chip, the chip was rinsed thoroughly with plenty of water, and dried with nitrogen. Then, the carboxyl group of graphene was activated by NHS/EDC mixture solution (M:M = 4:1, v:v = 1:1) for 30 min, followed by washing in plenty of water. Afterwards, the OA-BSA conjugate (1 mg/mL) was dissolved in PBS buffer and was dropped onto the chip surface and incubated for 1 h. Finally, a 1 mol/L ethanolamine solution (pH 8.5) was used to block the nonspecific interaction on the biosensor surface.

3.4.2. Determination of OA

The low-molecular-weight analyte OA was detected by the proposed SPR sensor with four-layer MoS_2 by an indirect competition inhibition method [41,42], and the schematic diagram of the detection process for OA is shown in Figure 13. Figure 14a demonstrates the specific interaction process of OA-mAb and OA-BSA immobilized on the sensor chip surface. First, PBS buffer was injected over the sensor chip to obtain a stable baseline before the measurement. Then, the OA-mAb solution (5 µg/mL) was injected into the reactor. The free OA-mAb was captured by OA-BSA on the sensor chip surface and the response signal was increased. At the end of the detection cycle, the captured antibodies were removed by injecting NaOH (0.2 M) solution for the regeneration, and the response signal returned to the original baseline position.

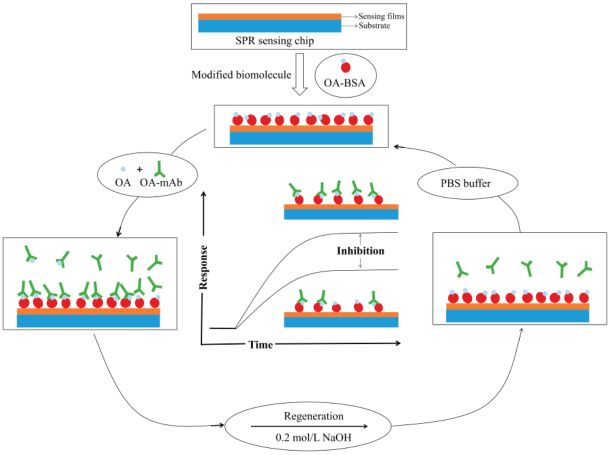

Figure 13. The schematic diagram of the detection process for OA.

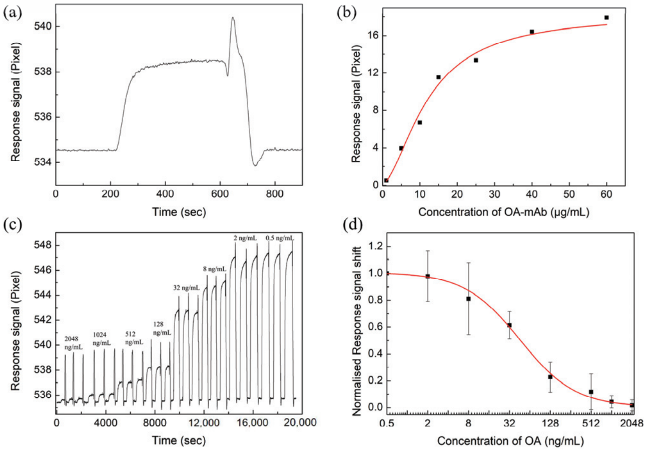

Figure 14. (**a**) The specific interaction process between OA-mAb (5 μg/mL) and the OA-BSA followed by regeneration step. (**b**) The shift in response signal with increasing concentration of OA-mAb. (**c**) The SPR response signal curves of OA solution at different concentrations for the proposed SPR biosensor. (**d**) Calibration curve for the detection of OA by indirect competitive inhibition.

For the indirect competition inhibition method, the concentration of antibody is a key parameter affecting sensitivity. To obtain the appropriate antibody concentration, a series of concentrations of OA-mAb (1~60 μg/mL) were injected into the sensor chip. Figure 14b shows the resonant pixel shifts with an increasing concentration of OA-mAb. The resonant pixel shift increases rapidly before the antibody concentration reaches 15 μg/mL, followed by a slower rate of increase. Therefore, a 15 μg/mL OA-mAb concentration was used in subsequent OA experiments.

Firstly, the OA standard solutions were incubated with the 15 μg/mL OA-mAb solution for 30 min. Subsequently, the equilibrated mixtures, containing a series of OA concentrations (0.5~2048 ng/mL) and 15 μg/mL OA-mAb, were injected into the sensor chip. The reproducibility of the immune reaction was assessed by analysis of each concentration of OA mixture solutions three times. The obtained SPR response signal curves are shown in Figure 14c. From Figure 14c, it can be seen that the shift in the resonant pixel decreases with the increase in the OA concentration in the solution. This is due to the OA in free solution inhibiting the binding interaction of OA-mAb with the OA-BSA immobilized on the sensor chip, resulting in a decrease in the response signal. The extent of reduction is directly proportional to the OA concentration. Figure 14d is the percentage of inhibition with respect to the OA concentration. It can be inferred from the sigmoidal calibration curve that the linear detection range of the proposed OA biosensor is from 4 ng/mL to 512 ng/mL. The LOD is estimated to be 1.18 ng/mL based on the LOD formula [43], which is approximately 22.6 times lower than the conventional Au-based sensor (26.7 ng/mL).

4. Conclusions

In this work, a high-sensitivity SPR biosensor composed of MoS_2 and graphene is proposed, and its performance was investigated through a simulation and experiments. MoS_2 films with a high light absorption efficiency were utilized to promote the transfer of electrons, which resulted in a significant enhancement of the electric field on the sensor's surface. Monolayer graphene was employed as the biological recognition component to further increase the sensitivity of the sensors. The numerical results show that the maximum sensitivity ~282°/RIU is achieved, when the sensor is modified with four-layer MoS_2 and monolayer graphene. In the experiment, the proposed sensor was used to measure the RI sensitivity and detect the OA concentration. The result of the RI experiments show that the RI sensitivity of the proposed sensor is approximately 1.85 times higher than the conventional Au sensor. In addition, the LOD of OA for the proposed sensor is 1.18 ng/mL, which is about 22.6 times lower than the conventional Au sensor. These results suggest that this device has the potential for clinical diagnostics and chemical detection.

Author Contributions: Original draft preparation, H.C.; methodology, M.W.; investigation, Z.W. and H.C.; writing—review and editing, H.C.; revision, J.L. and X.W. All authors have read and agreed to the published version of the manuscript.

Funding: National Natural Science Foundation of China (NSFC) (61775191); Science Fund for Distinguished Young Scholars of Fujian Province under Grant 2020J06025; Youth Talent Support Program of Jimei University under Grant ZR2019002; Innovation Fund for Young Scientists of Xiamen under Grant 3502Z20206021; Xiamen Marine and Fishery Development Special Fund under Grant 20CZB014HJ03; Fujian Provincial Natural Science Foundation under Grant 2020J01712; and Youth Talent Support Program of Fujian Province (Eyas Plan of Fujian Province 2021).

Institutional Review Board Statement: Not applicable.

Informed Consent Statement: Not applicable.

Data Availability Statement: The data presented in this study are available on request from the corresponding author upon reasonable request.

Conflicts of Interest: The authors declare no conflict of interest.

References

1. Sun, Y.; Cai, H.; Wang, X.; Zhan, S. Optimization methodology for structural multiparameter surface plasmon resonance sensors in different modulation modes based on particle swarm optimization. *Opt. Commun.* **2019**, *431*, 142–150. [CrossRef]
2. Priyabrata, P. Surface Plasmon Resonance. *Appl. Biochem. Biotechnol.* **2014**, *2*, 79–92.
3. Hoa, X.D.; Kirk, A.G.; Tabrizian, M. Towards integrated and sensitive surface plasmon resonance biosensors: A review of recent progress. *Biosens. Bioelectron.* **2007**, *23*, 151–160. [CrossRef] [PubMed]
4. Zeng, S.; Baillargeat, D.; Ho, H.P.; Yong, K.T. Nanomaterials enhanced surface plasmon resonance for biological and chemical sensing applications. *Chem. Soc. Rev.* **2014**, *43*, 3426–3452. [CrossRef]
5. Sun, Y.; Cai, H.; Wang, X.; Zhan, S. Layer analysis of axial spatial distribution of surface plasmon resonance sensing. *Anal. Chim. Acta* **2020**, *1136*, 141–150. [CrossRef]
6. Balevicius, Z.; Paulauskas, A.; Plikusiene, I.; Mikoliunaite, L.; Bechelany, M.; Popov, A.; Ramanavicius, A.; Ramanaviciene, A. Towards the application of Al_2O_3/ZnO nanolaminates in immunosensors: Total internal reflection spectroscopic ellipsometry based evaluation of BSA immobilization. *J. Mater. Chem. C Mater. Opt. Electron. Devices* **2018**, *6*, 8778–8783. [CrossRef]
7. Ozga, K.; Kawaharamura, T.; Ali, U.A.; Oyama, M.; Nouneh, K.; Slezak, A.; Fujita, S.; Piasecki, M.; Reshak, A.H.; Kityk, I.V. Second order optical effects in Au nanoparticle-deposited ZnO nanocrystallite films. *Nanotechnology* **2008**, *19*, 185709. [CrossRef]
8. Chiu, N.; Tu, Y.; Huang, T. Enhanced Sensitivity of Anti-Symmetrically Structured Surface Plasmon Resonance Sensors with Zinc Oxide Intermediate Layers. *Sensors* **2014**, *14*, 170–187. [CrossRef]
9. Balciunas, D.; Plausinaitis, D.; Ratautaite, V.; Ramanaviciene, A.; Ramanavicius, A. Towards electrochemical surface plasmon resonance sensor based on the molecularly imprinted polypyrrole for glyphosate sensing. *Talanta* **2022**, *241*, 123252. [CrossRef]
10. Bruna, M.; Borini, S. Optical constants of graphene layers in the visible range. *Appl. Phys. Lett.* **2009**, *94*, 031901. [CrossRef]
11. Homola, J.; Piliarik, M. Surface Plasmon Resonance (SPR) Sensors. *Springer Ser. Chem. Sens. Biosens.* **2006**, *4*, 45–67.
12. Ahijado-Guzmán, R.; Prasad, J.; Rosman, C.; Henkel, A.; Tome, L.; Schneider, D.; Rivas, G.; Sönnichsen, C. Plasmonic Nanosensors for Simultaneous Quantification of Multiple Protein–Protein Binding Affinities. *Nano Lett.* **2014**, *14*, 5528–5532. [CrossRef] [PubMed]
13. Taylor, A.; Ladd, J.; Etheridge, S.; Deeds, J.; Hall, S.; Jiang, S. Quantitative detection of tetrodotoxin (TTX) by a surface plasmon resonance (SPR) sensor. *Sens. Actuators B Chem.* **2008**, *130*, 120–128. [CrossRef]
14. Kawaguchi, T.; Shankaran, D.; Kim, S.; Gobi, K.; Matsumoto, K.; Toko, K.; Miura, N. Fabrication of a novel immunosensor using functionalized self-assembled monolayer for trace level detection of TNT by surface plasmon resonance. *Talanta* **2007**, *72*, 554–560. [CrossRef] [PubMed]
15. Lee, K.; Lee, C.; Wang, W.; Wei, P. Sensitive biosensor array using surface plasmon resonance on metallic nanoslits. *J. Biomed. Opt.* **2007**, *12*, 044023–044025. [CrossRef]
16. Stewart, M.E.; Anderton, C.R.; Thompson, L.B.; Maria, J.; Gray, S.K.; Rogers, J.A.; Nuzzo, R.G. Nanostructured Plasmonic Sensors. *Chem. Rev.* **2008**, *108*, 494–521. [CrossRef]
17. Sherry, L.J.; Jin, R.; Mirkin, C.A.; Schatz, G.C.; Van Duyne, R.P. Localized Surface Plasmon Resonance Spectroscopy of Single Silver Triangular Nanoprisms. *Nano Lett.* **2006**, *6*, 2060–2065. [CrossRef]
18. Choi, S.H.; Kim, Y.L.; Byun, K.M. Graphene-on-silver substrates for sensitive surface plasmon resonance imaging biosensors. *Opt. Express* **2011**, *19*, 458–466. [CrossRef]

19. Farmani, A.; Mir, A. Graphene Sensor Based on Surface Plasmon Resonance for Optical Scanning. *IEEE Photonics Technol. Lett.* **2019**, *31*, 643–646. [CrossRef]
20. Shrivastav, A.M.; Mishra, S.K.; Gupta, B.D. Localized and propagating surface plasmon resonance based fiber optic sensor for the detection of tetracycline using molecular imprinting. *Mater. Res. Express* **2015**, *2*, 35007–35011. [CrossRef]
21. Elias, D.C.; Gorbachev, R.V.; Mayorov, A.S.; Morozov, S.V.; Zhukov, A.A.; Blake, P.; Ponomarenko, L.A.; Grigorieva, I.V.; Novoselov, K.S.; Guinea, F.; et al. Dirac cones reshaped by interaction effects in suspended graphene. *Nat. Phys.* **2011**, *7*, 701–704. [CrossRef]
22. Verma, R.; Gupta, B.D.; Jha, R. Sensitivity enhancement of a surface plasmon resonance based biomolecules sensor using graphene and silicon layers. *Sens. Actuators B Chem.* **2011**, *160*, 623–631. [CrossRef]
23. Wu, L.; Chu, H.S.; Koh, W.S.; Li, E.P. Highly sensitive graphene biosensors based on surface plasmon resonance. *Opt. Express* **2010**, *18*, 14395–14400. [CrossRef] [PubMed]
24. Radisavljevic, B.; Radenovic, A.; Brivio, J.; Giacometti, V.; Kis, A. Single-layer MoS_2 transistors. *Nat. Nanotechnol.* **2011**, *3*, 147–150. [CrossRef]
25. Britnell, L.; Ribeiro, R.M.; Eckmann, A.; Jalil, R.; Belle, B.D.; Mishchenko, A.; Kim, Y.J.; Gorbachev, R.V.; Georgiou, T.; Morozov, S.V.; et al. Strong light-matter interactions in heterostructures of atomically thin films. *Science* **2013**, *340*, 1311–1314. [CrossRef]
26. Sachs, B.; Britnell, L.; Wehling, T.O.; Eckmann, A.; Jalil, R.; Belle, B.D.; Lichtenstein, A.I.; Katsnelson, M.I.; Novoselov, K.S. Doping mechanisms in graphene-MoS_2 hybrids. *Appl. Phys. Lett.* **2013**, *103*, 251607. [CrossRef]
27. Xue, T.; Qi, K.; Hu, C. Novel SPR sensing platform based on superstructure MoS_2 nanosheets for ultrasensitive detection of mercury ion. *Sens. Actuators B Chem.* **2019**, *284*, 589–594. [CrossRef]
28. Kang, Z.; Cheng, Y.; Zheng, Z.; Cheng, F.; Chen, Z.; Li, L.; Tan, X.; Xiong, L.; Zhai, T.; Gao, Y. MoS2-Based Photodetectors Powered by Asymmetric Contact Structure with Large Work Function Difference. *Nano-Micro Lett.* **2019**, *11*, 34. [CrossRef]
29. Zhao, X.; Wang, Z.; Mu, Y.; Zhang, H.; Jin, Q. Simultaneous Multiwavelength Detection Based on Surface Plasmon Resonance Technique. *Lab. Robot. Autom.* **2000**, *2*, 104–107. [CrossRef]
30. Chlebus, R.; Chylek, J.; Ciprian, D.; Hlubina, P. Surface Plasmon Resonance Based Measurement of the Dielectric Function of a Thin Metal Film. *Sensors* **2018**, *18*, 3693. [CrossRef]
31. Vahed, H.; Nadri, C. Sensitivity enhancement of SPR optical biosensor based on Graphene–MoS_2 structure with nanocomposite layer. *Opt. Mater.* **2019**, *88*, 161–166. [CrossRef]
32. Srivastava, T.; Jha, R. Black Phosphorus: A New Platform for Gaseous Sensing Based on Surface Plasmon Resonance. *IEEE Photonics Technol. Lett.* **2018**, *30*, 319–322. [CrossRef]
33. Ouyang, Q.; Zeng, S.; Jiang, L.; Hong, L.; Xu, G.; Dinh, X.; Qian, J.; He, S.; Qu, J.; Coquet, P.; et al. Sensitivity Enhancement of Transition Metal Dichalcogenides/Silicon Nanostructure-based Surface Plasmon Resonance Biosensor. *Sci. Rep.* **2016**, *6*, 28190. [CrossRef] [PubMed]
34. Cai, H.; Shan, S.; Wang, X. High Sensitivity Surface Plasmon Resonance Sensor Based on Periodic Multilayer Thin Films. *Nanomaterials* **2021**, *11*, 3399. [CrossRef] [PubMed]
35. Szunerits, S.; Maalouli, N.; Wijaya, E.; Vilcot, J.; Boukherroub, R. Recent advances in the development of graphene-based surface plasmon resonance (SPR) interfaces. *Anal. Bioanal. Chem.* **2013**, *405*, 1435–1443. [CrossRef] [PubMed]
36. Sharma, A.K.; Kaur, B. Simulation and analysis of 2D material (MoS_2/$MoSe_2$) based plasmonic sensor for measurement of organic compounds in infrared. *Optik* **2018**, *157*, 161–169. [CrossRef]
37. Su, M.; Chen, X.; Tang, L.; Yang, B.; Zou, H.; Liu, J.; Li, Y.; Chen, S.; Fan, D. Black phosphorus (BP)–graphene guided-wave surface plasmon resonance (GWSPR) biosensor. *Nanophotonics* **2020**, *9*, 4265–4272. [CrossRef]
38. Kim, N.; Choi, M.; Kim, T.W.; Choi, W.; Park, S.Y.; Byun, K.M. Sensitivity and Stability Enhancement of Surface Plasmon Resonance Biosensors based on a Large-Area Ag/MoS2 Substrate. *Sensors* **2019**, *19*, 1894. [CrossRef]
39. Yu, H.; Chong, Y.; Zhang, P.; Ma, J.; Li, D. A D-shaped fiber SPR sensor with a composite nanostructure of MoS_2-graphene for glucose detection. *Talanta* **2020**, *219*, 121324. [CrossRef]
40. Gong, W.; Jiang, S.; Li, Z.; Li, C.; Xu, J.; Pan, J.; Huo, Y.; Man, B.; Liu, A.; Zhang, C. Experimental and theoretical investigation for surface plasmon resonance biosensor based on graphene/Au film/D-POF. *Opt. Express* **2019**, *27*, 3483. [CrossRef]
41. Mitchell, J. Small Molecule Immunosensing Using Surface Plasmon Resonance. *Sensors* **2010**, *10*, 7323–7346. [CrossRef] [PubMed]
42. Kim, C.; Lee, L.; Min, J.; Lim, M.; Jeong, S. An indirect competitive assay-based aptasensor for detection of oxytetracycline in milk. *Biosens. Bioelectron.* **2014**, *51*, 426–430. [CrossRef] [PubMed]
43. Shrivastav, A.M.; Usha, S.P.; Gupta, B.D. Highly sensitive and selective erythromycin nanosensor employing fiber optic SPR/ERY imprinted nanostructure: Application in milk and honey. *Biosens. Bioelectron.* **2017**, *90*, 516–524. [CrossRef] [PubMed]

nanomaterials

Review

Single-Element 2D Materials beyond Graphene: Methods of Epitaxial Synthesis

Kirill A. Lozovoy [1,*], Ihor I. Izhnin [2], Andrey P. Kokhanenko [1], Vladimir V. Dirko [1], Vladimir P. Vinarskiy [1], Alexander V. Voitsekhovskii [1], Olena I. Fitsych [3] and Nataliya Yu. Akimenko [4]

[1] Faculty of Radiophysics, National Research Tomsk State University, Lenin Av. 36, 634050 Tomsk, Russia; kokh@mail.tsu.ru (A.P.K.); vovenmir@gmail.com (V.V.D.); vinarskiy2017@gmail.com (V.P.V.); vav43@mail.tsu.ru (A.V.V.)
[2] Scientific Research Company "Electron-Carat", Stryjska St. 202, 79031 Lviv, Ukraine; i.izhnin@carat.electron.ua
[3] P. Sagaidachny National Army Academy, Gvardijska St. 32, 79012 Lviv, Ukraine; o.fitsych@ukr.net
[4] Department of Engineering Systems and Technosphere Safety, Pacific National University, Tihookeanskaya St. 136, 680035 Khabarovsk, Russia; n_akimenko@inbox.ru
* Correspondence: lozovoymailbox@gmail.com

Abstract: Today, two-dimensional materials are one of the key research topics for scientists around the world. Interest in 2D materials is not surprising because, thanks to their remarkable mechanical, thermal, electrical, magnetic, and optical properties, they promise to revolutionize electronics. The unique properties of graphene-like 2D materials give them the potential to create completely new types of devices for functional electronics, nanophotonics, and quantum technologies. This paper considers epitaxially grown two-dimensional allotropic modifications of single elements: graphene (C) and its analogs (transgraphenes) borophene (B), aluminene (Al), gallenene (Ga), indiene (In), thallene (Tl), silicene (Si), germanene (Ge), stanene (Sn), plumbene (Pb), phosphorene (P), arsenene (As), antimonene (Sb), bismuthene (Bi), selenene (Se), and tellurene (Te). The emphasis is put on their structural parameters and technological modes in the method of molecular beam epitaxy, which ensure the production of high-quality defect-free single-element two-dimensional structures of a large area for promising device applications.

Keywords: 2D materials; two-dimensional allotropes; graphene analogs; molecular beam epitaxy; borophene; aluminene; gallenene; indiene; thallene; silicene; germanene; stanene; plumbene; phosphorene; antimonene; bismuthene; selenene; tellurene

Citation: Lozovoy, K.A.; Izhnin, I.I.; Kokhanenko, A.P.; Dirko, V.V.; Vinarskiy, V.P.; Voitsekhovskii, A.V.; Fitsych, O.I.; Akimenko, N.Y. Single-Element 2D Materials beyond Graphene: Methods of Epitaxial Synthesis. *Nanomaterials* **2022**, *12*, 2221. https://doi.org/10.3390/nano12132221

Academic Editors: Jihoon Lee and Ming-Yu Li

Received: 30 May 2022
Accepted: 24 June 2022
Published: 28 June 2022

1. Background

Today, two-dimensional materials are one of the key research topics for scientists around the world [1–5]. Since 2004, when the first representative of a new class of materials, a monolayer of carbon atoms, was experimentally obtained in the work by Geim and Novoselov [6], we have seen a real boom in publications on this topic. Over the years, there has been a quantitative and qualitative leap both in the study of graphene itself and of other two-dimensional allotropes—*transgraphenes*, or *X-enes* (Figure 1a). As a characteristic numerical indicator confirming the above, we can cite data on the growth in the number of publications that include the keyword "2D material" in the international information and analytical systems of scientific citation Scopus and Web of Science (Figure 1b). By 2022, the number of publications crossed a milestone—more than 10,000 publications on the topic of 2D materials per year (30 articles per day or 1 article every hour).

This interest in two-dimensional materials is not surprising, since, thanks to their remarkable mechanical, thermal, electrical, magnetic, and optical properties, they promise to revolutionize electronics. Among the outstanding characteristics of 2D materials, the following can be distinguished: very high mobility of charge carriers, extreme strength of graphene due to strong carbon–carbon bonds, the ability to control energy structure and bandgap by changing the material composition, and a simple defect structure due only to the presence of vacancies and impurities. In addition, under certain conditions, exotic quantum effects can manifest in these materials: they can be topological insulators and high-temperature superconductors. The unique properties of 2D materials make them promising for the creation of completely new types of devices for functional electronics, nanophotonics, and quantum technologies [7–12].

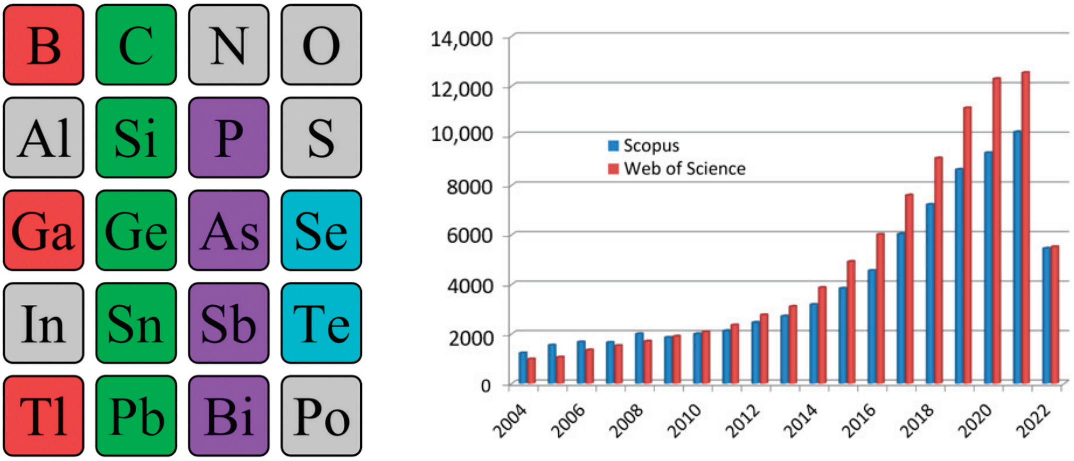

(**a**) (**b**)

Figure 1. Single-element 2D materials (**a**) and number of publications with the keyword "2D material" in scientific analytical databases Scopus and Web of Science (**b**). In the excerption from the periodic table, synthesized single-element two-dimensional materials are highlighted: group IIIA—red, group IVA—green, group VA—violet, group VIA—blue.

Nowadays, the following existing two-dimensional allotropic modifications can be distinguished: graphene (C) and its analogs (*transgraphenes* or *X-enes*) borophene (B), aluminene (Al), gallenene (Ga), indiene (In), thallene (Tl), silicene (Si), germanene (Ge), stanene (Sn), plumbene (Pb), phosphorene (P), arsenene (As), antimonene (Sb), bismuthene (Bi), selenene (Se), and tellurene (Te) (Figure 1a).

They are very closely related to graphene and transgraphene derivatives functionalized by hydrogen ions (graphane $(CH)_n$, silicane $(SiH)_n$, germanane $(GeH)_n$, and other *transgraphanes* (or *X-anes*) with the general formula $(GH)_n$, where G is one of the elements that form the initial two-dimensional material: C, Si, Sn, Pb, B, P, etc.) or other ligands (for example, metal cations, hydroxyl groups, organic radicals, with the general formula $(GR)_n$) [13].

Among the methods for creating two-dimensional materials, it is necessary to distinguish simple exfoliation techniques, chemical deposition methods, and molecular beam epitaxy. It is the latter method that makes it possible to obtain structures of the best quality: with low roughness, controlled thickness, and a high degree of uniformity over the substrate area. To achieve the desired quality, special attention must be paid to the selection of a suitable substrate and careful control of the deposition conditions, such as temperature and growth rate.

In this work, two-dimensional allotropes of various elements are considered. A review of the latest advances in growing single-element 2D materials by epitaxial methods is given. At the same time, the emphasis is put on their structural parameters and technological modes in the method of molecular beam epitaxy, which ensures the production of high-quality defect-free single-element two-dimensional structures of a large area, which are necessary for promising device applications.

2. Structural Characteristics of Single-Element 2D Materials

The concept of a two-dimensional allotropic modification of silicon was proposed in 1994 [14]. Subsequently, the new material was actively studied by theorists and was named "silicene" by analogy with graphene [15]. All graphene-like materials of elements of group IVA are characterized by mixed sp^2–sp^3 hybridization [16]. Unlike graphene (Figure 2a), the lattice of silicene, germanene, stanene, and plumbene is not absolutely flat, but curved. Their structure can be represented as two sublattices displaced relative to each other in the vertical direction (Figure 2b). Such curved honeycomb structure and ordered buckling of the surface lead to exceptional stability and increased flexibility compared with graphene. This geometry defines the wide spectrum of their potential applications in electronics [17–19]. Such a buckled hexagonal structure was also observed in all further works on the synthesis of transgraphenes of group IVA [20–58].

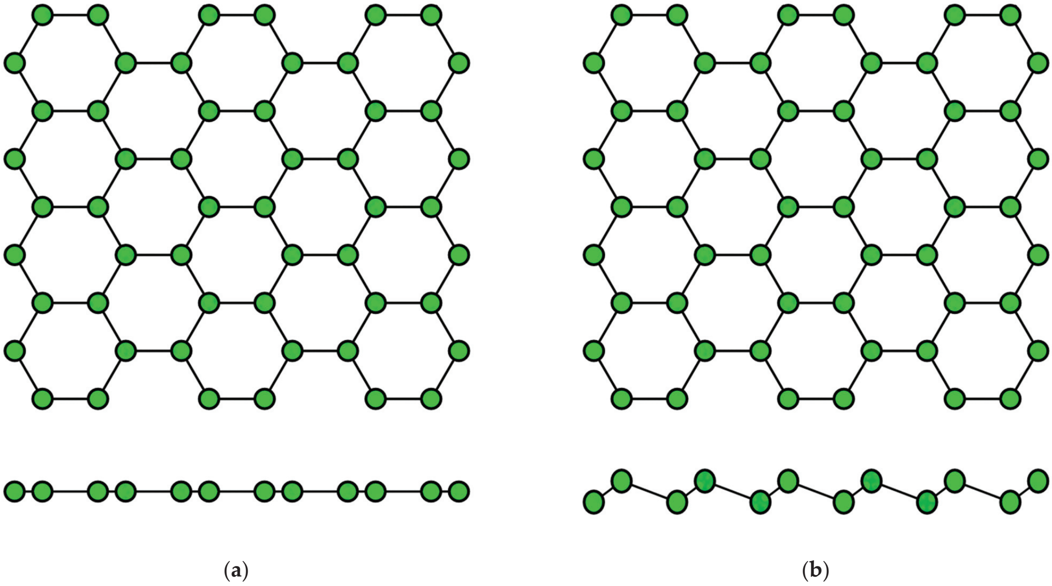

Figure 2. Honeycomb lattice of graphene (**a**) and graphene-like structure of two-dimensional materials of group IVA (**b**) (on this and following figures colored balls represent atoms and black lines represent interatomic bonds).

The data on the lattice parameters of group IVA graphene-like 2D materials (silicene, germanene, stanene, and plumbene) such as the distance l between nearest atoms in the honeycomb structure, the lattice constant a, and the displacement parameter between the upper and lower atoms δ are reviewed in Table 1.

Borophene, aluminene, gallenene, indiene, and thallene—representatives of group IIIA transgraphenes—can have various modifications of the crystal lattice [59–73].

Borophene has a flat or curved structure, consisting of many equilateral triangles, forming a two-dimensional network (Figure 3). In this case, its structure can be considered as a solid solution of the composition $B_{1-v}V_v$, where v is the concentration of vacancies V of boron atoms. When there are no vacancies of boron atoms, borophene has a curved lattice with the parameter $\delta \approx 0.08$ nm (Figure 3a), and in the presence of vacancies with the concentration $v = 1/6$, its structure becomes flat (Figure 3b). Borophene structures with a different v are also possible. The distance between boron atoms in the borophene structure is about 0.17 nm [2,59].

Table 1. Structural parameters of the buckled honeycomb lattice of graphene and group IVA transgraphenes.

Material	Distance l between Atoms	Lattice Constant a	Buckling Parameter δ	References
	nm	**nm**	**nm**	
Graphene	0.14	0.25	0	[3–5]
Silicene	0.23	0.39	0.08	[20–31]
Germanene	0.25	0.40	0.09	[32–37]
Stanene	0.28	0.47	0.10	[38–44]
Plumbene	0.30	0.49	0.10	[45–47]

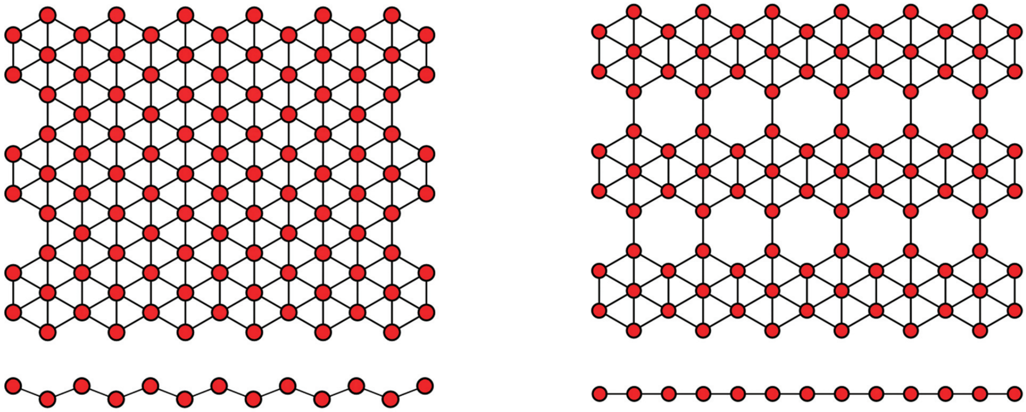

(**a**) (**b**)

Figure 3. Variants of the structure of the crystal lattice of borophene for (**a**) $v = 0$ and (**b**) $v = 1/6$.

Gallenene has a flat honeycomb structure similar to graphene (Figure 2a), or a slightly curved configuration such as group IVA transgraphenes (Figure 2b). The crystal lattice parameters of gallenene have the following values: the distance between the gallium atoms is $l = 0.25$ nm, the lattice constant a is about 0.39 nm, and the buckling parameter $\delta = 0$–0.08 nm [63,64].

Aluminene has not yet been synthesized experimentally, but theoretical calculations using the density functional theory predict the possibility of its existence with a crystal lattice such as graphene, borophene, or even phosphorene (Figure 4). Thus, aluminene can have a flat, buckled, or puckered structure [67,68]. For the graphene-like modification of the aluminene crystal lattice, the distance between aluminum atoms is predicted to be $l \approx 0.26$ nm [65].

The two-dimensional allotropic modification of indium (indiene) is also predicted only theoretically so far. Presumably, it can have three variants of the crystal structure: flat (like in graphene) (Figure 2a), buckled (like in transgraphenes of group IVA) (Figure 2b), or puckered (like in phosphorene) (Figure 4a). For all modifications of indiene, the calculated distance between indium atoms is $l \approx 0.29$ nm, and the lattice constant is $a \approx 0.5$ nm for the flat geometry and $a \approx 0.425$ nm for the buckled one at $\delta \approx 0.15$ nm [65,70–72].

The last representative of group IIIA transgraphenes, thallene, was synthesized in 2020 on the $NiSi_2/Si(111)$ surface [73] in the form of a flat honeycomb structure similar to graphene (Figure 2a), with parameter $l \approx 0.38$ nm. Density functional theory calculations predict for a free-standing thallene $l = 0.3$ nm (Table 2).

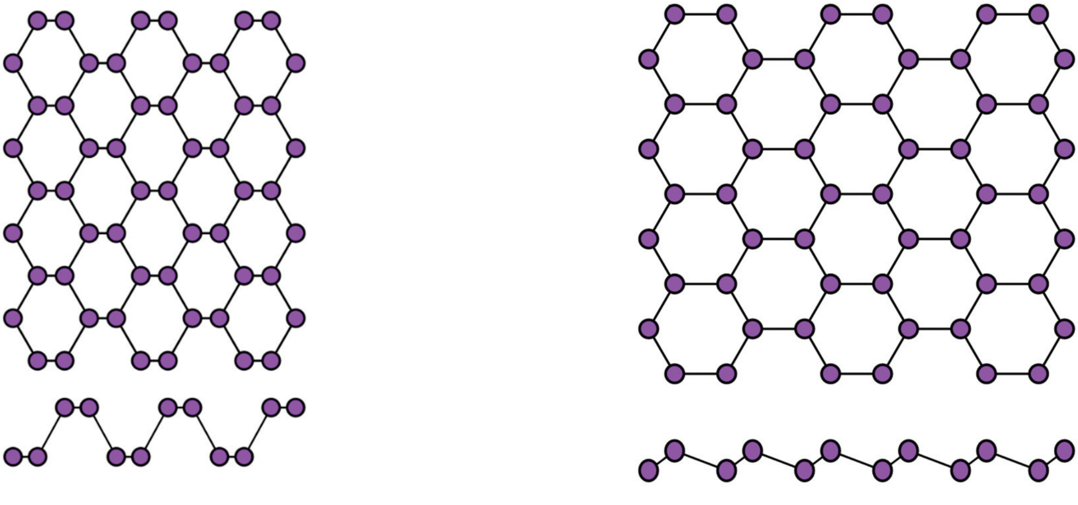
(**a**) (**b**)

Figure 4. Two variants of the crystal structure of phosphorene: (**a**) puckered (α-phase) and (**b**) buckled (β-phase).

Table 2. Parameters of the honeycomb lattice of group IIIA transgraphenes (materials predicted only theoretically and not obtained experimentally are marked with * sign).

Material	Distance *l* between Atoms	Lattice Constant *a*	Buckling Parameter δ	References
	nm	nm	nm	
Borophene	0.17	0.29	0–0.08	[2,59]
Aluminene *	0.26	0.45	-	[65]
Gallenene	0.25	0.39	0–0.08	[63,64]
Indiene *	0.29	0.43–0.50	0–0.15	[65,70–72]
Thallene	0.30–0.38	0.50–0.65	0	[73]

The first representative of transgraphenes of group VA, phosphorene can be in two modifications: puckered (or α-phase) (Figure 4a) and buckled (or β-phase) (Figure 4b). The lattice parameters of phosphorene have the following values: the distance between phosphorus atoms is l = 0.23 nm, the lattice constant a is about 0.33 nm, and the buckling parameter δ = 0.12 nm [72,74].

For the two-dimensional modification of arsenic (arsenene), theoretical calculations predict the following lattice parameters: the distance between arsenic atoms is l = 0.25 nm, the lattice constant a is about 0.36 nm, and the buckling parameter δ = 0.14 nm [75,76].

Experimental studies of the synthesis of two-dimensional antimony (antimonene) turned out to be quite successful, and today this material has already been fabricated on a large number of substrates [77–82]. The distance between antimony atoms ranges from 0.29 nm and more, depending on the substrate; the lattice constant is slightly more than 0.4 nm and $\delta \approx 0.17$ nm [75,78].

For bismuthene, a two-dimensional allotropic modification of bismuth, the lattice constant of a curved graphene-like structure was calculated to be a = 0.434 nm [72]. However, its actual value may increase depending on the substrate [83] (Table 3).

Table 3. Parameters of the honeycomb lattice of group VA transgraphenes.

Material	Distance *l* between Atoms	Lattice Constant *a*	Buckling Parameter δ	References
	nm	Nm	nm	
Phosphorene	0.23	0.33	0.12	[72,74]
Arsenene	0.25	0.36	0.14	[75,76]
Antimonene	0.29	0.40	0.17	[75,78]
Bismuthene	0.30	0.43	0.17	[72,83]

Finally, let us take a look at the structural properties of single-element 2D materials from the group VIA. The stable states of the two-dimensional modification of selenium (selenene) were first calculated within the framework of the density functional theory in 2017 [84]. Then, their electrical, thermoelectric, and thermal properties were theoretically investigated [85–88]. Two modifications of the crystal lattice are predicted for selenene and tellurene (Figure 5).

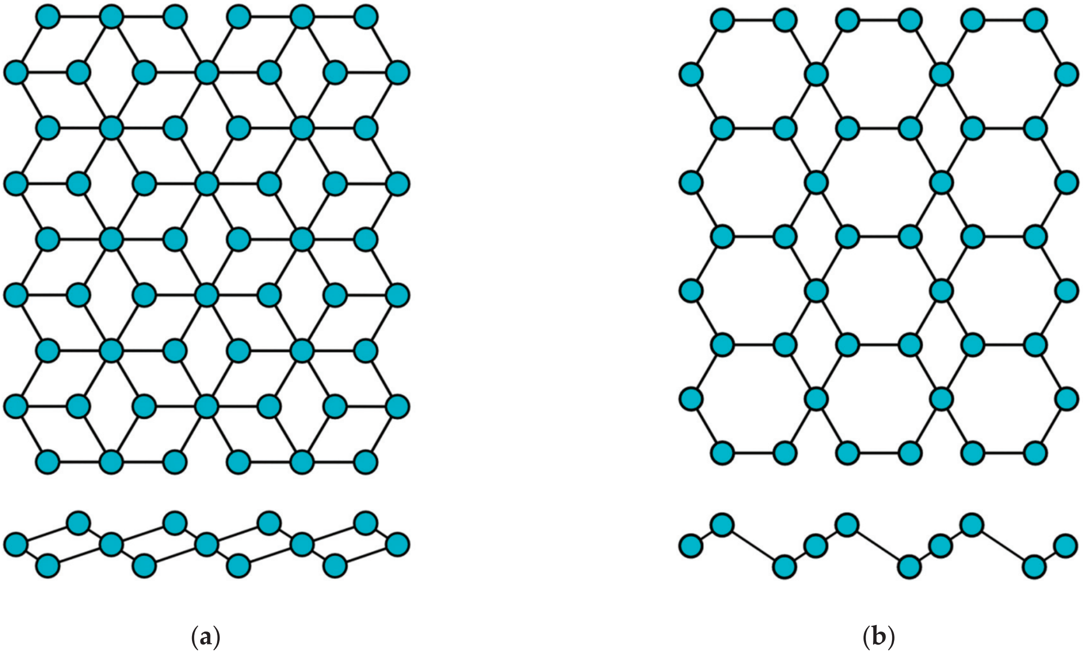

Figure 5. Two variants of the crystal structure of selenene and tellurene: (**a**) α-phase and (**b**) β-phase.

According to the theoretical calculations, the distance between atoms in selenene should be $l \approx 0.27$ nm [88]. The two-dimensional tellurium layer (tellurene) has the same crystal structure modifications as selenene (Figure 5), and its lattice parameter *l* is about 0.3 nm [88–90] (Table 4).

Table 4. Parameters of the honeycomb lattice of group VIA transgraphenes.

Material	Distance *l* between Atoms	Lattice Constant *a*	Buckling Parameter δ	References
	nm	nm	nm	
Selenene	0.27	0.37	0.18	[88]
Tellurene	0.30	0.42	0.22	[88–90]

Thus, numerous experimental studies confirmed the curved structure of transgraphenes and also showed that such a structure is more flexible than that of graphene, which makes it possible to control the energy spectra by adjusting the synthesis conditions.

3. Epitaxial Fabrication of Single-Element 2D Materials

3.1. Group IIIA Single-Element 2D Materials

We will begin our consideration of two-dimensional allotropic modifications with elements of the main subgroup of the third group of the periodic table of chemical elements. Borophene, the first representative of 2D materials of group IIIA, was first synthesized experimentally on Ag(111) substrate in 2015 [59,60]. Earlier attempts at heteroepitaxial fabrication of borophene were complicated by a low barrier of the formation of three-dimensional boron islands [91]. Therefore, it was necessary to carefully select a suitable substrate in order to overcome this unwanted 3D island formation. A low threshold for nucleation of two-dimensional clusters was found on a number of metal substrates, which facilitated the formation of extended layers of large-area single-crystal borophene. Among them are Al(111) [92], Au(111) [93], Cu(111) [94], and Ir(111) [95] (Figure 6). In this case the nearest-neighbor distance of the potential substrate for the fabrication of 2D material should match with the lattice parameter a of the honeycomb lattice. In addition to metal substrates, the possibility of obtaining layers of two-dimensional boron modification on surfaces such as transition metal diborides [96,97] with the (0001) orientation is predicted.

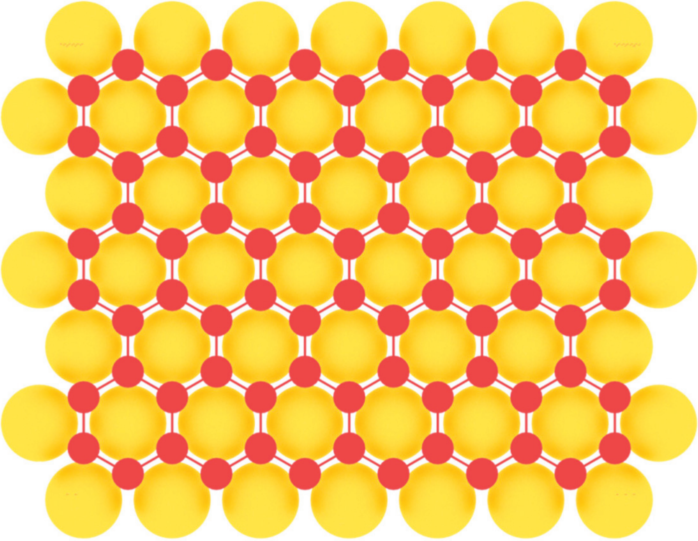

Figure 6. Model of borophene layer on a metal substrate.

After the first successful experimental works [59,60], borophene was successfully fabricated on the Al(111) surface in 2018 [92]. Aluminum belongs to the same group IIIA of the periodic table and has minimal lattice mismatch with borophene, which ensured its successful production on this substrate. Borophene was deposited on the Al(111) surface held at 230 °C. The obtained borophene had a honeycomb lattice with $a \approx 0.3$ nm. In another recent study [95], borophene was synthesized on the surface of Ir(111) upon deposition of boron at 550 °C. All experimental studies confirm the possibility of coexistence of several borophene phases depending on the growth conditions and the substrate [91,98,99].

The monatomic layer of two-dimensional gallium was first obtained in 2018 by the exfoliation method in [63]. Like borophene, gallenene was obtained by molecular beam epitaxy on surfaces such as GaN(0001) (two monolayers thick) [100] and Si(111) (one monolayer) [64]. A characteristic feature of gallenene is the covalent bond between adjacent two-dimensional layers, in contrast to other 2D materials, such as, for example, graphite or transition metal dichalcogenides, in which the layers are linked together by weak van der Waals forces. Due to this, the gallium layers demonstrate significantly higher temperature stability [101,102].

In the work [100], two monolayer gallium film with honeycomb lattice was heteroepitaxially grown on GaN(0001) layer with the thickness about 3 μm, which was deposited by metal organic chemical vapor deposition on Al_2O_3(0001) substrates using AlN buffer layer. The substrates were chemically cleaned before loading into epitaxy equipment. Several cycles of argon ion sputtering with the energy 700 eV and subsequent annealing were performed to prepare the surface. Two monolayers of gallium were then epitaxially grown at 650 °C from a high-purity gallium (99.995%) source with the deposition rate of 0.4 ML/min (monolayers per minute) at ultra-high vacuum conditions (the base pressure was lower than $2{\cdot}10^{-10}$ Torr). This led to formation of 2 ML thick gallenene layer with the lattice constant 0.32 nm [100]. The authors also suggested using silver as capping protective layer for subsequent ex situ characterization of gallenene samples.

In the work [64], base pressure maintained at $1{\cdot}10^{-10}$ Torr. Gallium atoms were thermally evaporated on clean Si(111) (7 × 7) surface from a quartz crucible. Reconstructed gallium surface was prepared by depositing 1/3 ML of gallium atoms on the silicon surface at room temperature and annealing at 550 °C for 30 min. The gallium films then were epitaxially grown on the Ga/Si(111) surface at the temperature of 50 °C with the deposition rate of 0.2 ML/min. The gallium layer grown on Si(111) (7 × 7) was used as the substrate for the growth of gallenene. Ga/Si(111) surface is better for obtaining high-ordered gallium monolayer than Si(111) (7 × 7) because gallium atoms passivate the dangling bonds on silicon surface, which is beneficial to the diffusion of the deposited atoms. Depositing Ga atoms on Ga/Si(111) surface, an ordered Ga monolayer can be obtained. At low coverage, the Ga atoms formed two-dimensional domains with random distribution. With the gallium coverage increasing, the size of domains increased. In the area where the gallium atoms were absence, the gallium superstructure was still clearly visible. When the coverage reached 1.4 ML, the Ga/Si(111) reconstructed structure was completely covered, and the growth of the gallium monolayer was completed [64].

Finally, quite recently, there was a report on the heteroepitaxial growth of the last single-element 2D-material of group IIIA, thallene [73]. As far as we know, as of early 2022, this work is the only article dedicated to thallene. The experiment was carried out under ultra-high vacuum conditions. The reconstructed Si(111) (7 × 7) surface was formed by long-term annealing of Si(111) wafers at 600 °C followed by short-term annealing at 1280 °C. One monolayer of thallium was deposited on the prepared surface at room temperature, which was then annealed at the temperature of 300 °C. For thallium evaporation a tantalum crucible was used. The next step was room temperature deposition of one monolayer of nickel, followed by annealing at 300 °C. Under these conditions, nickel atoms diffuse through the thallium layer, forming one monolayer with the composition $NiSi_2$ under the thallium layer. The last stage was the annealing of the system at the temperature of 375 °C for 5 min in order to leave 2/3 ML of thallium on the $NiSi_2$ surface. As a result, a Tl/$NiSi_2$/Si(111) sample with a thallene monolayer was obtained [73].

As far as we know, the rest of the group IIIA transgraphenes (aluminene and indiene) have not been experimentally realized yet.

3.2. Group IVA Single-Element 2D Materials

Unlike graphene, a monolayer of carbon atoms with sp^2-hybridization, which can be fabricated by simple exfoliation of single layers from graphite due to weak interlayer interaction, atom-thick layers of silicon, germanium, tin, or lead are not so readily exfoliated from the corresponding bulk materials because they have sp^3-hybridization with strong covalent bonds. Consequently, the current task is to find methods of synthesis of transgraphenes other than exfoliation technique. Moreover, one of the basic methods of fabrication of silicene, germanene, stanene, and plumbene today is the heteroepitaxy on the surfaces matched by the lattice parameter [24].

For the first time, silicene was experimentally obtained by epitaxial methods in 2012 on Ag (111) substrate [20,21]. In this work, Ag(111) plates were cleaned by Ar^+ sputtering with the energy 1.5 keV. Then, the substrates were annealed at the 500–600 °C to obtain atomically smooth silver surface. Silicon was deposited with the rate of 0.01–0.03 ML/min on the silver surface heated to 200–300 °C [20,21]. Later on, research on the growth of silicene on Ag(111) surface at various temperatures was carried out, and the important role of the substrate temperature in the formation of transgraphene structures was established [25]. It was shown that the number of defects in a honeycomb lattice increases with temperature, and silicene does not form at the temperatures of 330 °C or higher.

After that, silicene was synthesized on Ir(111) [24], Pb(111) [48], ZrB_2(0001) [26], MoS_2 [27], ZrC [28], Ru [29], and graphite [30] surfaces. For some substrates, to obtain uniform monolayer with honeycomb lattice, post-growth annealing of the synthesized structures was implemented. As in the previous case of single-element 2D materials of group IIIA, to serve a perfect surface for the group IVA buckled allotropes formation, the substrate should have lattice constant close to that of the desired 2D material, so that three of six atoms in the honeycomb mesh coincide with the nearest three atoms of the substrate (Figure 7).

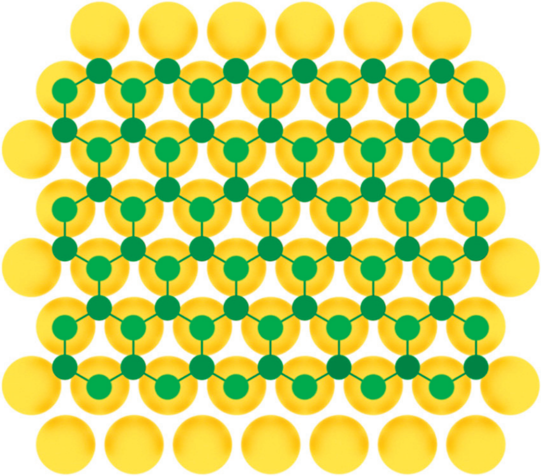

Figure 7. Model of buckled silicene layer on a metal substrate (two colors are used for silicon atoms at different height positions).

Unlike silicene, researchers failed to fabricate germanene on Ag(111) surface because germanium and silver atoms form solid solution on the surface. However, thanks to the efforts of experimenters, germanene was finally synthesized on the Au(111) substrate in 2014 [35]. The atomically clean Au(111) surface was prepared by Ar^+ ion sputtering and annealing. The honeycomb germanene structure was obtained by 1 ML germanium deposition at a temperature of 200 °C. At the same period, germanene was grown on the Pt(111) surface [36]. However, in this case, post-deposition annealing was conducted at the temperatures of 300–500 °C for half an hour.

Then, germanene was heteroepitaxially fabricated on Al(111) substrate [32]. As well as the previously used Au(111) and Pt(111), the Al(111) surface has a honeycomb structure with the lattice parameter a = 0.405 nm, which is close to germanene. The germanium deposition at very low growth rate of about 0.005 nm/min was used in this study while keeping the substrate at the temperature of 87 °C.

Later, the growth of germanene was carried out on other surfaces: Sb(111) [49], highly oriented pyrolytic graphite [50,51], MoS_2 [33], hexagonal AlN [37], Cu(111) [52], Ge_2Pt [53,54], and germanium [55].

The next representative of group IVA transgraphenes, stanene, was first synthesized on $Bi_2Te_3(111)$ surface in 2015 [41]. $Bi_2Te_3(111)$ films with thicknesses of up to 40 nm were heteroepitaxially grown on Si(111) substrate. Tin atoms were deposited from effusion cell with the rate of 0.4 ML/min at room temperature on obtained $Bi_2Te_3(111)$ surface.

After that, a whole series of works on fabrication of stanene on various surfaces appeared. For example, single-layer stanene was fabricated on Sb(111) and InSb(111) substrates cleaned by Ar^+ ion sputtering followed by annealing at the 400 °C [42,43]. Tin atoms were deposited with 0.3 ML/min growth rate at ambient or slightly elevated temperatures, forming strained layers of stanene.

Then, layers of large-area stanene with small lattice buckling parameter were obtained on Ag(111) substrate using Ag_2Sn as an intermediate layer [44]. In one of the latest works [12], high-quality multilayer stanene with a thickness of one to five monolayers was successfully fabricated on PbTe(111) surface. In addition, stanene was fabricated on Cu(111) [56], MoS_2 [57], and Au(111) [58] surfaces.

Finally, in 2019 the epitaxial fabrication of the last graphene-like material of group IVA, plumbene, was realized [45–47]. As far as we know, plumbene has been successfully synthesized on just two surfaces before 2022.

In the research by Yuhara et al. [45], large-area plumbene sheet was fabricated on Pd(111) substrate, cleaned by Ar^+ ion sputtering with the energy of 2 keV, followed by annealing at 850 °C. Lead deposition rate was maintained at 0.4 ML/min. At the first stage of growth $Pd_{1-x}Pb_x(111)$ solid solution formed, and then lead atoms segregated onto the surface, forming plumbene structure.

In the latest experimental work [47], plumbene was grown on the surface of Fe monolayer on Ir(111) substrate. To prevent intermixing of iron and lead atoms, the synthesis was performed at rather low temperature of 140 K. The distinctive feature of this method is that an almost flat plumbene monolayer with low buckling parameter forms.

3.3. Group VA Single-Element 2D Materials

Phosphorene was first produced by an exfoliation technique [103] and later fabricated in the method of molecular beam epitaxy on Au(111) substrate [104]. In work [104], clean Au(111) substrate was prepared by repeated Ar^+ bombardment with ion energy of 1.5 keV at the pressure of about $1 \cdot 10^{-5}$ Torr and subsequent annealing at 500 °C. Phosphorus was deposited by evaporation from a crucible containing bulk black phosphorus at 260 °C. During the deposition process, the substrate temperature was below 260 °C, so the initial growth stage involved the condensation of P_4 molecules from the gas phase onto Au(111) surface. Then, the system was annealed at 250 °C for 60 min until well-defined monolayer phosphorus with a hexagonal structure appeared [104]. This was achieved due to the close lattice parameters of phosphorene and the substrate (Figure 8).

Later, this result was confirmed in the work [105], along with the observation of formation of one-dimensional chain structures of phosphorus on Au(111) surface. Au(111) substrate was cleaned by Ar^+ ion sputtering with the energy of 1.0 keV, followed by annealing at a temperature of about 600 °C. Phosphorus flux was generated by thermal decomposition of InP in a Knudsen cell at 470 °C. The substrate temperature was kept at 210–230 °C. As a result, graphene-like structure of phosphorus atoms arranged in a buckled honeycomb lattice was obtained [105].

The electronic structure of this two-dimensional modification of phosphorus was revealed in the further work by Golias et al. [106]. They also prepared clean Au(111) surface by repeated cycles of Ar^+ bombardment with ion energy 1 keV followed by annealing at 620 °C for 5 min and subsequently at 420 °C for 20 min. Black phosphorus crystal heated to 300 °C was used as a source. Two variants of growth process were tested: one with the

Au(111) substrate held at 230 °C during deposition and another where phosphorus was deposited at room temperature, and then the sample was annealed at 250 °C for 15 min.

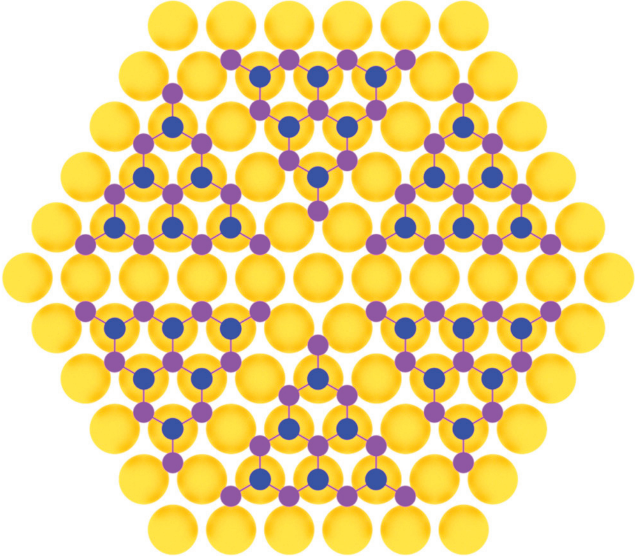

Figure 8. Model of phosphorene layer on a metal substrate (two colors are used for phosphorus atoms at different height positions).

In the later work by Zhang et al. [107] two distinct superstructures of heteroepitaxial phosphorene on Au(111) were determined with (5 × 5) periodicity (Figure 8). They also used the substrate temperature near the 250 °C, which is line with the authors of previous works. In the very recent work [108], phosphorene was also synthesized on copper oxide surface on Cu(111) substrate using on-surface reaction and segregation approaches.

The first monolayer antimonene samples were obtained by exfoliation techniques [109–112]. It was shown that free-standing antimonene demonstrates exceptional air stability, but for the creation of defect-free large-area antimonene sheets the epitaxial methods were necessary. Moreover, further experimental attempts were quite successful and now antimonene have been synthesized by the method of molecular beam epitaxy on rather large numbers of substrates, such as Ge(111) [77], $PdTe_2$ [78], Ag(111) [79], Pb(111) [80], Bi_2Te_3 [81], Cu(111) and Cu(110) [82], and Sb_2Te_3 [113]. Furthermore, van der Waals epitaxy was used to form antimonene sheets on mica substrates [114] and single-crystalline graphene [115].

In the work [77], the authors studied the growth of antimonene on Ge(111) surface. Use of Ge(111) surface is prospective for electronics. In these experiments, high-purity Sb crystals were evaporated using a Knudsen cell. The substrate temperature was varied from room temperature to 330 °C, and the deposition rate was changed between 0.2 and 70 nm/min. Ge(111) substrates were prepared firstly by chemical treatment, then by annealing at the temperature of 600–700 °C for more than 1 h. For some samples, an additional Ar^+ sputtering step with ion energy 2 keV was used before annealing. Sputtering and annealing were repeated until a sharp c(2 × 8) diffraction pattern was observed. After varying growth parameters in wide intervals, it was revealed that 2D antimony sheets were formed in narrow range of temperatures from 200 to 300 °C. For the growth rates it was established that better-quality layers are fabricated using two-step growth with the nucleation of antimony clusters at high rates (about 20 nm/min) and subsequent growth of islands at much lower rates. It was also shown that the lattice constant of antimonene depends on the thickness and changes from 0.41 nm for one layer to 0.43 nm for five layers [77].

Authors of the work [78] noted that they selected PdTe2 substrate for the synthesis of antimonene. This selection was made because PdTe2 substrate has hexagonal lattice with the constant of 0.41 nm (close to the calculated one for antimonene), along with the chemical stability of $PdTe_2$ surface and absence of formation of an alloy with antimony. High-purity antimony was evaporated from Knudsen cell and deposited onto the freshly cleaved from the single crystal $PdTe_2$ substrate. The substrate temperature was held at 130 °C during growth. This deposition resulted in formation of highly ordered buckled honeycomb antimonene structure [78].

Despite the fact that antimony tends to form alloys with metals, some groups reported the fabrication of antimonene on silver [79,116] and copper [82] substrates. In all cases, the first atoms of antimony formed an alloy with the substrate, and subsequent deposition led to the formation of buckled honeycomb antimonene structure. However, all the prospective properties of antimonene are still not realized due to insufficient quality of the fabricated antimonene, especially in the areas of edges of 2D sheets.

As far as the arsenene is concerned, there are numerous theoretical works devoted to the prediction of properties of this novel 2D material [75]. However, there is only one experimental report on the fabrication of arsenene by liquid-phase exfoliation method [76].

The same is true for bismuthene, and there are just a couple of experimental evidences of its fabrication [83,117]. In the breakthrough work [83], bismuthene was fabricated on SiC(0001) surface. Moreover, in the very latest work [117], two-dimensional hexagonal bismuth structures were obtained on the surface of 2 ML thick $HfTe_2$ surface deposited on InAs(111)/Si(111) substrate. Furthermore, the attempts to obtain bismuthene on other surfaces (such as Si(111), graphite, graphene, Au(111), and other noble metals) are constantly being made.

3.4. Group VIA Single-Element 2D Materials

To date, selenene was synthesized only by physical vapor deposition on Si(111) substrate in the work [118].

Tellurene was first obtained on flexible mica substrates by van der Waals epitaxy in 2014 in [119]. Thereafter, tellurium was successfully grown heteroepitaxially on highly oriented pyrolytic graphite [89] and graphene [120] (Figure 9).

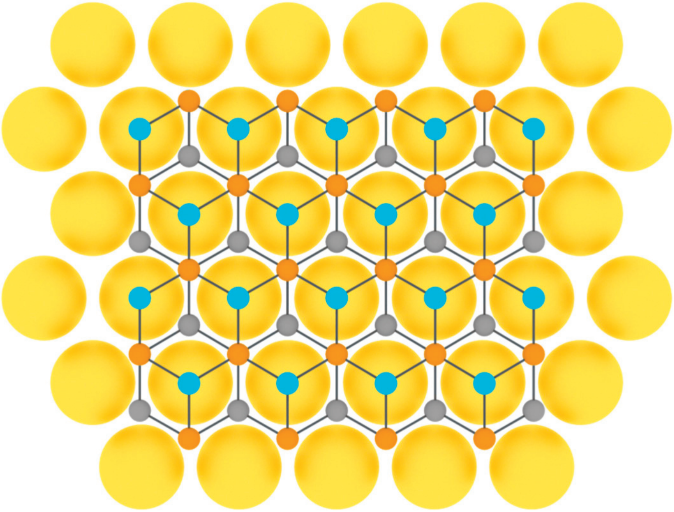

Figure 9. Model of tellurene layer on a substrate (three colors are used for tellurium atoms at different height positions).

In the work [120], different phases of two-dimensional tellurene were obtained in monolayer and few-layer films using van der Waals epitaxy of tellurium films on the surface of graphene, grown by molecular beam epitaxy on 6H-SiC(0001) substrate. High-purity tellurium (99.999%) was evaporated from a Knudsen cell at 227 °C onto the graphene/SiC substrate kept at room temperature.

In [89], tellurium atoms were deposited on a carefully annealed substrate of highly oriented pyrolytic graphite under the conditions of a molecular beam epitaxy setup at the base pressure of order of 1.5 10^{-10} Torr. The flux of tellurium was generated from a standard Knudsen cell operated at 270 °C. The substrate temperature was held constant at 130 °C during deposition. Reflection high-energy electron diffraction operated at 15 keV was employed to monitor the sample surface during the growth process, and the streaky diffraction pattern showed an atomically smooth surface of the grown tellurium film, which was confirmed by STM measurements [89].

Thus, a proper substrate and growth conditions play a key role in providing an opportunity to form large-size high-quality single-element two-dimensional materials beyond graphene.

4. Brief Outlook into the Perspectives of Single-Element 2D Materials

At present, two-dimensional materials are considered as one of the most promising materials for next-generation nanoelectronics and nanophotonics [121,122]. The family of two-dimensional crystals includes dielectrics (for example, hexagonal boron nitride and transition metal oxides), topological insulators (bismuthene telluride), semiconductors (molybdenum and tungsten disulfides), semimetals (graphene), metals (titanium disulfide), and superconductors (niobium diselenide) [3,4]. Among the single-element transgraphenes considered in this review, the type of conductivity changes from metal (for group IIIA elements), passes through semimetal (for group IVA elements), and ends with groups VA and VIA semiconductor materials (Table 5). This fact determines the enormous spectrum of possible device applications of single-element 2D materials.

For example, a high-speed field-effect transistor based on silicene operating at room temperature has already been implemented [8], as well as a field-effect transistor based on tellurene [123]. Among other things, tellurene also possesses unique thermoelectric properties [124] and anomalously low thermal conductivity [125–127]. In 2D materials such as stanene and bismuthene, due to their large atomic number, nontrivial topological properties are expected, the appearance of highly conductive channels, and the absence of certain types of carrier scattering near the boundaries. In this regard, they can be considered contenders for the creation of effective interconnections [9,128]. Aluminene and antimonene are proposed as materials for creating nanocapacitors due to their high ability to accumulate the charge [129]. In addition, superconducting states are also predicted for aluminene and gallenene [130,131]. Possible spheres of single-element 2D materials applications are summarized in Table 5.

Active research continues, aimed at finding new and investigating the discovered mechanical, electrical, magnetic, and optical properties of single-element 2D materials [132–139]. Fascinating novel physical phenomena are also theoretically predicted for materials of this family that are still waiting to be experimentally discovered and investigated. Among them are various plasmonic effects and quantum Hall effect in 2D boron [91], high-temperature quantum spin Hall effect in bismuthene [83], strain-induced magnetism in aluminene [140], massless Dirac fermions, and superconductivity in gallenene [131].

Most of the papers reviewed in this work are aimed at developing methods for the creation of high-quality layers of single-element 2D materials, which make it possible to study all of their unique physical properties and potential applications in emerging nanodevices of functional electronics. Undoubtedly, the fabrication of 2D materials of the required quality dictates a proper selection of the surface for synthesis (according to the crystal structure and lattice constant of the growing material). The next stage is rigorous preparation of the growth substrate using multiple ion sputtering and high-temperature annealing to obtain an atomically smooth layer without impurities and defects. The final step is precise control of the growth conditions, such as deposition temperature (usually less than 500 °C) and extremely low growth rates (on the order of 0.1 mL/min). The coverages of the deposited materials should be mostly chosen to equal the whole number of monolayers and no more than about 5 mL because the growth mechanism tends to transform to the island one at higher effective thicknesses.

Table 5. Physical properties and application fields of transgraphenes (materials predicted only theoretically and not obtained experimentally are marked with * sign).

Material	Band Gap, eV	Type of Conductivity	Possible Fields of Application
Borophene	0	Metal	bio-imaging tools, microelectronics devices, composites, interconnections, energy storage
Aluminene *	0	Metal	nanocapacitor, superconductor, gas sensor, energy storage
Gallenene	0	Metal	superconductor, electrical contacts, sensors, plasmonics, photonics nanostructures
Indiene * (planar) Indiene * (buckled)	0 1	Metal Semiconductor	memory device, LED, solar cell, light filter, optoelectronics applications
Thallene	0.14	Semimetal	2D topological insulator
Graphene	0	Semimetal	field-effect transistor, phototransistor, superconductor, optical modulator, plasmonics, photovoltaics applications
Silicene	0.01	Semimetal	field-effect transistor, biosensor, spintronics, plasmonics, quantum information applications
Germanene	0.02	Semimetal	field-effect transistor, nanomedicine, topological quantum field-effect transistor
Stanene	0.07	Semimetal	2D topological insulator, superconductor, field-effect transistor, interconnections
Plumbene	0.42	Semiconductor	2D topological insulator, superconductor, field-effect transistor, energy storage
Phosphorene (puckered) Phosphorene (buckled)	1.67 1.98	Semiconductor	field-effect transistor, phototransistor, biosensor, bio-imaging tools
Arsenene (puckered) Arsenene (buckled)	0.90 1.96	Semiconductor	field-effect transistor, biosensor
Antimonene (puckered) Antimonene (buckled)	0.28 0.76	Semiconductor	field-effect transistor, nanocapacitor, photodetector, sensor, bio-imaging tools
Bismuthene	0.32	Semiconductor	2D topological insulator, field-effect transistor, biosensor, bio-imaging tools, interconnections
Selenene	0.75	Semiconductor	field-effect transistor, phototransistor
Tellurene	1.13	Semiconductor	field-effect transistor, optical modulator, thermoelectric material, piezoelectric material

Extensive amount of research is underway to improve the technology for growing high quality 2D crystals [141–145]. Physical and mathematical models of growth of 2D materials by various growth mechanisms, taking into account formation of 2D and 3D islands, as well as ways to prevent possible nucleation of unwilling three-dimensional islands, are proposed [146–149]. There are also theoretical and experimental works devoted to various derivatives of transgraphenes, including chemical functionalization with various ligands [150–152].

Completely new, unexpected fields of application of transgraphenes and their derivatives are being proposed [153–158]. For instance, a material such as borophene is predicted to serve as an effective energy storage and also may form nanotubes analogous to those of graphene, which may have even higher electrical conductivity that suggests the possibility of their use as contacts and interconnections in nanodevices [91]. Multi-layer gallenene structures are expected to have significantly higher temperature stability than bulk material [102]. Strained layers of stanene have potential as possible room-temperature device applications due to a very wide bandgap induced by elastic strains [42,43]. Plumbene is calculated to have controllable sign reversal Seebeck coefficient and the large tunability of thermal conductivity [159]. An opportunity to manage band gap in wide ranges was experimentally established for antimonene [112].

In order to realize all the promising properties of single-element 2D allotropes, one needs to understand how to create defect-free large-area single-crystal structures and multilayer 2D materials. Many of the prospective properties of these materials are still not realized due to insufficient quality of the fabricated sheets. Therefore, careful preparation of the substrate and the creation of special conditions in the epitaxy chamber are required for the preferred formation of islands by the two-dimensional mechanism at the initial stages of epitaxial growth. In this regard, molecular beam epitaxy has a major advantage compared to other fabrication techniques. Epitaxial methods usually yield large-scale 2D sheets with the area limited mainly by the width of atomic terraces on the substrate. Moreover, thorough pre-epitaxial preparation of the substrate ensures uniform two-dimensional wetting of the atomically flat surface by depositing atoms with limited nucleation of unwilling volumetric clusters [128]. Nevertheless, the problem of co-existence of differently rotated 2D grains with various phases in such large-area structures is still not solved. Hence, it is necessary to comprehensively develop the technology of epitaxial synthesis of 2D materials. Thus, the successful fabrication of graphene-like materials is possible only with the correct choice of the growth surface, its careful preparation, and precise control of the growth conditions [160,161].

Besides molecular beam epitaxy, there are some other methods of producing single-element 2D materials. The basic technologies among them are exfoliation techniques (including mechanical [109], liquid-phase [162], and molten salt exfoliation [163]), chemical vapor deposition [164], and physical vapor deposition [118]. Moreover, some less-used methods can be mentioned, such as pulsed laser deposition [165] and atomic layer deposition [166]. The important challenge for the research groups among the world is to develop all these methods simultaneously in order to produce 2D nanostructures of better quality.

After the synthesis of transgraphene, researchers are faced with the huge (and mostly unsolved) problem of separation of 2D sheets or transferring of this 2D material from metallic to other device-ready substrates. Moreover, single-element two-dimensional transgraphenes are dramatically unstable when exposed to the air, resulting in their rapid oxidation. This issue demands a decision of questions connected with encapsulation of fabricated layers to prevent them from chemical destruction. Along with the task of controlled fabrication of large-scale high-quality samples, these are the three pivotal limitations that hinder further characterization and device applications of single-element transgraphenes.

Fabrication of remaining transgraphenes (aluminene, indiene, and possible two-dimensional allotropes of heavier elements) is also strongly anticipated to complete the puzzle of synthesized single-element 2D materials in the periodic table.

The star of single-element two-dimensional materials lit up very recently, and it has strong potential that could really shine in the very near future.

Author Contributions: Conceptualization, K.A.L., I.I.I., A.P.K., A.V.V. and O.I.F.; formal analysis, N.Y.A.; investigation, K.A.L., I.I.I., A.P.K., V.V.D., V.P.V. and O.I.F.; writing—original draft preparation, K.A.L. and V.P.V.; writing—review and editing, K.A.L.; visualization, V.V.D. and N.Y.A.; supervision, I.I.I. and A.P.K.; project administration, K.A.L. and A.V.V.; funding acquisition, K.A.L. All authors have read and agreed to the published version of the manuscript.

Funding: This research was funded by Russian Science Foundation grant number 21-72-10031.

Institutional Review Board Statement: Not applicable.

Informed Consent Statement: Not applicable.

Data Availability Statement: The authors declare that the data supporting the findings of this study are available within the article.

Acknowledgments: The reported study was supported by grant from the Russian Science Foundation No. 21-72-10031, https://rscf.ru/project/21-72-10031/ (accessed on 30 May 2022).

Conflicts of Interest: On behalf of all authors, the corresponding author states that there is no conflict of interest.

References

1. Khan, K.; Tareen, A.K.; Iqbal, M.; Wang, L.; Ma, C.; Shi, Z.; Ye, Z.; Ahmad, W.; Sagar, R.U.R.; Shams, S.S.; et al. Navigating recent advances in monoelemental materials (Xenes)-fundamental to biomedical applications. *Prog. Solid State Chem.* **2021**, *63*, 100326. [CrossRef]
2. Zhou, D.; Li, H.; Si, N.; Li, H.; Fuchs, H.; Niu, T. Epitaxial Growth of Main Group Monoelemental 2D Materials. *Adv. Funct. Mater.* **2020**, *31*. [CrossRef]
3. Ponomarenko, V.P.; Popov, V.S.; Popov, S.V.; Chepurnov, E.L. Photo- and Nanoelectronics Based on Two-Dimensional Materials. Part I. Two-Dimensional Materials: Properties and Synthesis. *J. Commun. Technol. Electron.* **2020**, *65*, 1062–1104. [CrossRef]
4. Li, X.; Tao, L.; Chen, Z.; Fang, H.; Li, X.; Wang, X.; Xu, J.-B.; Zhu, H. Graphene and related two-dimensional materials: Structure-property relationships for electronics and optoelectronics. *Appl. Phys. Rev.* **2017**, *4*, 021306. [CrossRef]
5. Molle, A.; Goldberger, J.; Houssa, M.; Xu, Y.; Zhang, S.-C.; Akinwande, D. Buckled two-dimensional Xene sheets. *Nat. Mater.* **2017**, *16*, 163–169. [CrossRef]
6. Novoselov, K.S.; Geim, A.K.; Morozov, S.V.; Jiang, D.; Zhang, Y.; Dubonos, S.V.; Grigorieva, I.V.; Firsov, A.A. Electric field effect in atomically thin carbon films. *Science* **2004**, *306*, 666–669. [CrossRef]
7. Acun, A.; Zhang, L.; Bampoulis, P.; Farmanbar, M.; Van Houselt, A.; Rudenko, A.N.; Lingenfelder, M.; Brocks, G.; Poelsema, B.; I Katsnelson, M.; et al. Germanene: The germanium analogue of graphene. *J. Phys. Condens. Matter* **2015**, *27*, 443002. [CrossRef]
8. Tao, L.; Cinquanta, E.; Chiappe, D.; Grazianetti, C.; Fanciulli, M.; Dubey, M.; Molle, A.; Akinwande, D. Silicene field-effect transistors operating at room temperature. *Nat. Nanotechnol.* **2015**, *10*, 227–231. [CrossRef]
9. Houssa, M.; van den Broek, B.; Iordanidou, K.; Lu, A.K.A.; Pourtois, G.; Locquet, J.P.; Afanas'ev, V.; Stesmans, A. Topological to trivial insulating phase transition in stanene. *Nano Res.* **2016**, *9*, 774–778. [CrossRef]
10. Mortazavi, B.; Dianat, A.; Cuniberti, G.; Rabczuk, T. Application of silicene, germanene and stanene for Na or Li ion storage: A theoretical investigation. *Electrochim. Acta* **2016**, *213*, 865–870. [CrossRef]
11. Garg, P.; Choudhuri, I.; Pathak, B. Stanene based gas sensors: Effect of spin–orbit coupling. *Phys. Chem. Chem. Phys.* **2017**, *19*, 31325–31334. [CrossRef] [PubMed]
12. Liao, M.; Zang, Y.; Guan, Z.; Li, H.; Gong, Y.; Zhu, K.; Hu, X.-P.; Zhang, D.; Xu, Y.; Wang, Y.-Y.; et al. Superconductivity in few-layer stanene. *Nat. Phys.* **2018**, *14*, 344–348. [CrossRef]
13. Lozovoy, K.A.; Dirko, V.V.; Vinarskiy, V.P.; Kokhanenko, A.P.; Voitsekhovskii, A.V.; Akimenko, N.Y. Two-dimensional materials of group IVA: Latest advances in epitaxial methods of growth. *Russ. Phys. J.* **2022**, *64*, 1583–1591. [CrossRef]
14. Takeda, K.; Shiraishi, K. Theoretical possibility of stage corrugation in Si and Ge analogs of graphite. *Phys. Rev. B* **1994**, *50*, 14916–14922. [CrossRef] [PubMed]
15. Guzman-Veri, G.G.; Lew Yan Voon, L.C. Electronic structure of silicon-based nanostructures. *Phys. Rev. B.* **2007**, *76*, 075131. [CrossRef]
16. Molle, A.; Grazianetti, C.; Tao, L.; Taneja, D.; Alam, H.; Akinwande, D. Silicene, silicene derivatives, and their device applications. *Chem. Soc. Rev.* **2018**, *47*, 6370–6387. [CrossRef]
17. Jose, D.; Datta, A. Structures and electronic properties of silicene clusters: A promising material for FET and hydrogen storage. *Phys. Chem. Chem. Phys.* **2011**, *13*, 7304–7311. [CrossRef]
18. Houssa, M.; Dimoulas, A.; Molle, A. Silicene: A review of recent experimental and theoretical investigations. *J. Phys. Condens. Matter* **2015**, *27*, 253002. [CrossRef]
19. Le Lay, G. Silicene transistors. *Nat. Nanotechnol.* **2015**, *10*, 202–203. [CrossRef]
20. Vogt, P.; De Padova, P.; Quaresima, C.; Avila, J.; Frantzeskakis, E.; Asensio, M.C.; Resta, A.; Ealet, B.; Le Lay, G. Silicene: Compelling Experimental Evidence for Graphenelike Two-Dimensional Silicon. *Phys. Rev. Lett.* **2012**, *108*, 155501. [CrossRef]
21. Lin, C.-L.; Arafune, R.; Kawahara, K.; Tsukahara, N.; Minamitani, E.; Kim, Y.; Takagi, N.; Kawai, M. Structure of Silicene Grown on Ag(111). *Appl. Phys. Express* **2012**, *5*, 045802. [CrossRef]
22. Ezawa, M. Monolayer Topological Insulators: Silicene, Germanene, and Stanene. *J. Phys. Soc. Jpn.* **2015**, *84*. [CrossRef]
23. Balendhran, S.; Walia, S.; Nili, H.; Sriram, S.; Bhaskaran, M. Elemental Analogues of Graphene: Silicene, Germanene, Stanene, and Phosphorene. *Small* **2015**, *11*, 640–652. [CrossRef] [PubMed]
24. Meng, L.; Wang, Y.; Zhang, L.; Du, S.; Wu, R.; Li, L.; Zhang, Y.; Li, G.; Zhou, H.; Hofer, W.A.; et al. Buckled Silicene Formation on Ir(111). *Nano Lett.* **2013**, *13*, 685–690. [CrossRef] [PubMed]

25. Jamgotchian, H.; Colignon, Y.; Hamzaoui, N.; Ealet, B.; Hoarau, J.Y.; Aufray, B.; Bibérian, J.P. Growth of silicene layers on Ag(111): Unexpected effect of the substrate temperature. *J. Phys. Condens. Matter* **2012**, *24*, 172001. [CrossRef]
26. Fleurence, A.; Friedlein, R.; Ozaki, T.; Kawai, H.; Wang, Y.; Yamada-Takamura, Y. Experimental Evidence for Epitaxial Silicene on Diboride Thin Films. *Phys. Rev. Lett.* **2012**, *108*, 245501. [CrossRef]
27. Chiappe, D.; Scalise, E.; Cinquanta, E.; Grazianetti, C.; van der Broek, B.; Fanciulli, M.; Houssa, M.; Molle, A. Two-Dimensional Si Nanosheets with Local Hexagonal Structure on a MoS_2 Surface. *Adv. Mater.* **2013**, *26*, 2096–2101. [CrossRef]
28. Aizawa, T.; Suehara, S.; Otani, S. Silicene on Zirconium Carbide (111). *J. Phys. Chem. C* **2014**, *118*, 23049–23057. [CrossRef]
29. Huang, L.; Zhang, Y.-F.; Zhang, Y.-Y.; Xu, W.; Que, Y.; Li, E.; Pan, J.-B.; Wang, Y.; Liu, Y.; Du, S.-X.; et al. Sequence of Silicon Monolayer Structures Grown on a Ru Surface: From a Herringbone Structure to Silicene. *Nano Lett.* **2017**, *17*, 1161–1166. [CrossRef]
30. De Crescenzi, M.; Berbezier, I.; Scarselli, M.; Castrucci, P.; Abbarchi, M.; Ronda, A.; Jardali, F.; Park, J.; Vach, H. Formation of Silicene Nanosheets on Graphite. *ACS Nano* **2016**, *10*, 11163–11171. [CrossRef]
31. Jahangirov, S.; Topsakal, M.; Akturk, E.; Sahin, H.; Ciraci, S. Two- and One-Dimensional Honeycomb Structures of Silicon and Germanium. *Phys. Rev. Lett.* **2009**, *102*, 236804. [CrossRef]
32. Derivaz, M.; Dentel, D.; Stephan, R.; Hanf, M.-C.; Mehdaoui, A.; Sonnet, P.; Pirri, C. Continuous Germanene Layer on Al(111). *Nano Lett.* **2015**, *15*, 2510–2516. [CrossRef]
33. Zhang, L.; Bampoulis, P.; Rudenko, A.N.; Yao, Q.; van Houselt, A.; Poelsema, B.; Katsnelson, M.I.; Zandvliet, H.J.W. Structural and electronic properties of germanene on MoS_2. *Phys. Rev. Lett.* **2016**, *116*, 256804. [CrossRef] [PubMed]
34. Dávila, M.E.; Le Lay, G. Few layer epitaxial germanene: A novel two-dimensional Dirac material. *Sci. Rep.* **2016**, *6*, 20714. [CrossRef] [PubMed]
35. Dávila, M.E.; Xian, L.; Jahangirov, S.; Rubio, A.; Le Lay, G. Germanene: A novel two-dimensional germanium allotrope akin to graphene and silicene. *New J. Phys.* **2014**, *16*. [CrossRef]
36. Li, L.; Lu, S.-Z.; Pan, J.; Qin, Z.; Wang, Y.-Q.; Wang, Y.; Cao, G.-Y.; Du, S.; Gao, H.-J. Buckled Germanene Formation on Pt(111). *Adv. Mater.* **2014**, *26*, 4820–4824. [CrossRef] [PubMed]
37. d'Acapito, F.; Torrengo, S.; Xenogiannopoulou, E.; Tsipas, P.; Marquez Velasco, J.; Tsoutsou, D.; Dimoulas, A. Evidence for germanene growth on epitaxial hexagonal (h)-AlN on Ag(111). *J. Phys. Condens. Matt.* **2016**, *28*, 045002. [CrossRef]
38. Webb, R. Future stuff: Stanene. *New Sci.* **2014**, *224*, 38–39. [CrossRef]
39. Gross, M. Stanene the next miracle material? *Chem. Ind.* **2014**, *78*, 24–27.
40. Sahoo, S.K.; Wei, K. A Perspective on Recent Advances in 2D Stanene Nanosheets. *Adv. Mater. Interfaces* **2019**, *6*, 1900752. [CrossRef]
41. Zhu, F.; Chen, W.; Xu, Y.; Gao, C.-L.; Guan, D.-D.; Liu, C.-H.; Qian, D.; Zhang, S.-C.; Jia, J.-F. Epitaxial growth of two-dimensional stanene. *Nat. Mater.* **2015**, *14*, 1020–1025. [CrossRef] [PubMed]
42. Gou, J.; Kong, L.; Li, H.; Zhong, Q.; Li, W.; Cheng, P.; Chen, L.; Wu, K. Strain-induced band engineering in monolayer stanene on Sb(111). *Phys. Rev. Mater.* **2017**, *1*, 054004. [CrossRef]
43. Xu, C.-Z.; Chan, Y.-H.; Chen, P.; Wang, X.; Flötotto, D.; Hlevyack, J.A.; Bian, G.; Mo, S.-K.; Chou, M.-Y.; Chiang, T.-C. Gapped electronic structure of epitaxial stanene on InSb(111). *Phys. Rev. B* **2018**, *97*, 035122. [CrossRef]
44. Yuhara, J.; Fujii, Y.; Nishino, K.; Isobe, N.; Nakatake, M.; Xian, L.; Rubio, A.; Le Lay, G. Large area planar stanene epitaxially grown on Ag(1 1 1). *2D Mater.* **2018**, *5*, 025002. [CrossRef]
45. Yuhara, J.; He, B.; Matsunami, N.; Nakatake, M.; Le Lay, G. Graphene's latest cousin: Plumbene epitaxial growth on a "Nano WaterCube". *Adv. Mater.* **2019**, *31*, 1901017. [CrossRef]
46. Yuhara, J.; Le Lay, G. Beyond silicene: Synthesis of germanene, stanene and plumbene. *Jpn. J. Appl. Phys.* **2020**, *59*, SN0801. [CrossRef]
47. Bihlmayer, G.; Sassmannshausen, J.; Kubetzka, A.; Blügel, S.; von Bergmann, K.; Wiesendanger, R. Plumbene on a Magnetic Substrate: A Combined Scanning Tunneling Microscopy and Density Functional Theory Study. *Phys. Rev. Lett.* **2020**, *124*, 126401. [CrossRef]
48. Stepniak-Dybala, A.; Krawiec, M. Formation of silicene on ultrathin Pb(111) films. *J. Phys. Chem. C* **2019**, *123*, 17019–17025. [CrossRef]
49. Gou, J.; Zhong, Q.; Sheng, S.; Li, W.; Cheng, P.; Li, H.; Chen, L.; Wu, K. Strained monolayer germanene with 1 × 1 lattice on Sb(111). *2D Mater.* **2016**, *3*, 045005. [CrossRef]
50. Persichetti, L.; Jardali, F.; Vach, H.; Sgarlata, A.; Berbezier, I.; De Crescenzi, M.; Balzarotti, A. van der Waals Heteroepitaxy of Germanene Islands on Graphite. *J. Phys. Chem. Lett.* **2016**, *7*, 3246–3251. [CrossRef]
51. Peng, W.B.; Xu, T.; Diener, P.; Biadala, L.; Berthe, M.; Pi, X.D.; Borensztein, Y.; Curcella, A.; Bernard, R.; Prévot, G.; et al. Resolving the Controversial Existence of Silicene and Germanene Nanosheets Grown on Graphite. *ACS Nano* **2018**, *12*, 4754–4760. [CrossRef] [PubMed]
52. Qin, Z.; Pan, J.; Lu, S.; Shao, Y.; Wang, Y.; Du, S.; Gao, H.-J.; Cao, G. Direct Evidence of Dirac Signature in Bilayer Germanene Islands on Cu(111). *Adv. Mater.* **2017**, *29*, 1606046. [CrossRef] [PubMed]
53. Yao, Q.; Zhang, L.; Kabanov, N.S.; Rudenko, A.N.; Arjmand, T.; Soleimani, H.R.; Klavsyuk, A.L.; Zandvliet, H.J.W. Bandgap opening in hydrogenated germanene. *Appl. Phys. Lett.* **2018**, *112*, 171607. [CrossRef]

54. Van Bremen, R.; Bampoulis, P.; Aprojanz, J.; Smithers, M.; Poelsema, B.; Tegenkamp, C.; Zandvliet, H.J.W. Ge2Pt hut clusters: A substrate for germanene. *J. Appl. Phys.* **2018**, *124*, 125301. [CrossRef]
55. Zhuang, J.; Liu, C.; Zhou, Z.; Casillas, G.; Feng, H.; Xu, X.; Wang, J.; Hao, W.; Wang, X.; Dou, S.X.; et al. Dirac Signature in Germanene on Semiconducting Substrate. *Adv. Sci.* **2018**, *5*, 1800207. [CrossRef]
56. Deng, J.; Xia, B.; Ma, X.; Chen, H.; Shan, H.; Zhai, X.; Li, B.; Zhao, A.; Xu, Y.; Duan, W.; et al. Epitaxial growth of ultraflat stanene with topological band inversion. *Nat. Mater.* **2018**, *17*, 1081–1086. [CrossRef]
57. Chen, K.-C.; Lee, L.-M.; Chen, H.-A.; Sun, H.; Wu, C.-L.; Chen, H.-A.; Lin, K.-B.; Tseng, Y.-C.; Kaun, C.-C.; Pao, C.-W.; et al. Multi-layer elemental 2D materials: Antimonene, germanene and stanene grown directly on molybdenum disulfides. *Semicond. Sci. Technol.* **2019**, *34*, 105020. [CrossRef]
58. Pang, W.; Nishino, K.; Ogikubo, T.; Araidai, M.; Nakatake, M.; Le Lay, G.; Yuhara, J. Epitaxial growth of honeycomb-like stanene on Au(111). *Appl. Surf. Sci.* **2020**, *517*, 146224. [CrossRef]
59. Mannix, A.J.; Zhou, X.-F.; Kiraly, B.; Wood, J.D.; Alducin, D.; Myers, B.D.; Liu, X.; Fisher, B.L.; Santiago, U.; Guest, J.R.; et al. Synthesis of borophenes: Anisotropic, two-dimensional boron polymorphs. *Science* **2015**, *350*, 1513–1516. [CrossRef]
60. Feng, B.; Zhang, J.; Zhong, Q.; Li, W.; Li, S.; Li, H.; Cheng, P.; Meng, S.; Chen, L.; Wu, K. Experimental realization of two-dimensional boron sheets. *Nat. Chem.* **2016**, *8*, 563–568. [CrossRef]
61. Penev, E.S.; Kutana, A.; Yakobson, B.I. Can Two-Dimensional Boron Superconduct? *Nano Lett.* **2016**, *16*, 2522–2526. [CrossRef] [PubMed]
62. Liu, X.; Li, Q.; Ruan, Q.; Rahn, M.S.; Yakobson, B.I.; Hersam, M.C. Borophene synthesis beyond the single-atomic-layer limit. *Nat. Mater.* **2021**, *21*, 35–40. [CrossRef] [PubMed]
63. Kochat, V.; Samanta, A.; Zhang, Y.; Bhowmick, S.; Manimunda, P.; Asif, S.A.S.; Stender, A.S.; Vajtai, R.; Singh, A.K.; Tiwary, C.S.; et al. Atomically thin gallium layers from solid-melt exfoliation. *Sci. Adv.* **2018**, *4*, e1701373. [CrossRef] [PubMed]
64. Tao, M.-L.; Tu, Y.-B.; Sun, K.; Wang, Y.-L.; Xie, Z.-B.; Liu, L.; Shi, M.-X.; Wang, J.-Z. Gallenene epitaxially grown on Si(1 1 1). *2D Mater.* **2018**, *5*, 035009. [CrossRef]
65. Khalil, B.A.; Gaston, N. Two-dimensional aluminium, gallium, and indium metallic crystals by first-principles design. *J. Phys. Condens. Matter.* **2021**, *33*, 125901.
66. Kamal, C.; Chakrabarti, A.; Ezawa, M. Aluminene as highly hole-doped graphene. *New J. Phys.* **2015**, *17*. [CrossRef]
67. Yuan, J.-H.; Yu, N.; Xue, K.-H.; Miao, X. Stability, electronic and thermodynamic properties of aluminene from first-principles calculations. *Appl. Surf. Sci.* **2017**, *409*, 85–90. [CrossRef]
68. Yeoh, K.H.; Yoon, T.L.; Rusi; Ong, D.S.; Lim, T.L. First-principles studies on the superconductivity of aluminene. *Appl. Surf. Sci.* **2018**, *445*, 161–166. [CrossRef]
69. Lukačević, I.; Pajtler, M.V.; Muževič, M.; Gupta, S.K. Prospects for experimental realization of two-dimensional aluminium allotropes. *J. Mater. Chem. C* **2019**, *7*, 2666–2675. [CrossRef]
70. Singh, D.; Gupta, S.K.; Lukačević, I.; Sonvane, Y. Indiene 2D monolayer: A new nanoelectronic material. *RSC Adv.* **2016**, *6*, 8006–8014. [CrossRef]
71. Singh, D.; Gupta, S.K.; Lukačević, I.; Muževič, M.; Sonvane, Y.; Ahuja, R. Effect of electric field on optoelectronic properties of indiene monolayer for photoelectric nanodevices. *Sci. Rep.* **2019**, *9*, 17300. [CrossRef] [PubMed]
72. Le, M.-Q.; Nguyen, H.-T.; Bui, T.-L. Fracture of 28 buckled two-dimensional hexagonal sheets. *Mech. Adv. Mater. Struct.* **2021**, 1–13. [CrossRef]
73. Gruznev, D.V.; Bondarenko, L.V.; Tupchaya, A.Y.; Mihalyuk, A.N.; Eremeev, S.V.; Zotov, A.V.; Saranin, A.A. Thallene: Graphene-like honeycomb lattice of Tl atoms frozen on single-layer $NiSi_2$. *2D Mater.* **2020**, *7*, 045026. [CrossRef]
74. Zhu, Z.; Tománek, D. Semiconducting Layered Blue Phosphorus: A Computational Study. *Phys. Rev. Lett.* **2014**, *112*, 176802. [CrossRef]
75. Xu, Y.; Peng, B.; Zhang, H.; Shao, H.; Zhang, R.; Zhu, H. First-principle calculations of optical properties of monolayer arsenene and antimonene allotropes. *Ann. Phys.* **2017**, *529*, 1600152. [CrossRef]
76. Beladi-Mousavi, S.M.; Pourrahimi, A.M.; Sofer, Z.; Pumera, M. Atomically Thin 2D-Arsenene by Liquid-Phased Exfoliation: Toward Selective Vapor Sensing. *Adv. Funct. Mater.* **2018**. [CrossRef]
77. Fortin-Deschênes, M.; Waller, O.; Menteş, T.O.; Locatelli, A.; Mukherjee, S.; Genuzio, F.; Levesque, P.; Hébert, A.; Martel, R.; Moutanabbir, O. Synthesis of Antimonene on Germanium. *Nano Lett.* **2017**, *17*, 4970–4975. [CrossRef]
78. Wu, X.; Shao, Y.; Liu, H.; Feng, Z.; Wang, Y.-L.; Sun, J.-T.; Liu, C.; Wang, J.-O.; Liu, Z.-L.; Zhu, S.-Y.; et al. Epitaxial Growth and Air-Stability of Monolayer Antimonene on $PdTe_2$. *Adv. Mater.* **2016**, *29*, 1605407. [CrossRef]
79. Shao, Y.; Liu, Z.-L.; Cheng, C.; Wu, X.; Liu, H.; Liu, C.; Wang, J.-O.; Zhu, S.-Y.; Wang, Y.-Q.; Shi, D.-X.; et al. Epitaxial Growth of Flat Antimonene Monolayer: A New Honeycomb Analogue of Graphene. *Nano Lett.* **2018**, *18*, 2133–2139. [CrossRef]
80. Jałochowski, M.; Krawiec, M. Antimonene on Pb quantum wells. *2D Mater.* **2019**, *6*, 045028. [CrossRef]
81. Lei, T.; Li, J.-M.; Li, F.-S.; Wang, J.-O.; Ibrahim, K.; Zhang, K. Anisotropic electronic structure of antimonene. *Appl. Phys. Lett.* **2019**, *115*, 221602. [CrossRef]
82. Niu, T.; Zhou, W.; Zhou, D.; Hu, X.; Zhang, S.; Zhang, K.; Zhou, M.; Fuchs, H.; Zeng, H. Modulating Epitaxial Atomic Structure of Antimonene through Interface Design. *Adv. Mater.* **2019**, *31*, e1902606. [CrossRef] [PubMed]
83. Reis, F.; Li, G.; Dudy, L.; Bauernfeind, M.; Glass, S.; Hanke, W.; Thomale, R.; Schäfer, J.; Claessen, R. Bismuthene on a SiC substrate: A candidate for a high-temperature quantum spin Hall material. *Science* **2017**, *357*, 287–290. [CrossRef] [PubMed]

84. Xian, L.; Paz, A.P.; Bianco, E.; Ajayan, P.M.; Rubio, A. Square selenene and tellurene: Novel group VI elemental 2D materials with nontrivial topological properties. *2D Mater.* **2017**, *4*, 041003. [CrossRef]
85. Wang, D.; Tang, L.-M.; Jiang, X.-X.; Tan, J.-Y.; He, M.-D.; Wang, X.-J.; Chen, K.-Q. High Bipolar Conductivity and Robust In-Plane Spontaneous Electric Polarization in Selenene. *Adv. Electron. Mater.* **2018**, *5*, 1800475. [CrossRef]
86. Lin, C.; Cheng, W.; Chai, G.; Zhang, H. Thermoelectric properties of two-dimensional selenene and tellurene from group-VI elements. *Phys. Chem. Chem. Phys.* **2018**, *20*, 24250–24256. [CrossRef]
87. Liu, G.; Gao, Z.; Li, G.-L.; Wang, H. Abnormally low thermal conductivity of 2D selenene: An ab initio study. *J. Appl. Phys.* **2020**, *127*, 065103. [CrossRef]
88. Ramírez-Montes, L.; López-Pérez, W.; Gonzalez-Hernandez, R.; Pinilla, C. Large thermoelectric figure of merit in hexagonal phase of 2D selenium and tellurium. *Int. J. Quantum Chem.* **2020**, *120*, 26267. [CrossRef]
89. Chen, J.; Dai, Y.; Ma, Y.; Dai, X.; Ho, W.; Xie, M. Ultrathin β-tellurium layers grown on highly oriented pyrolytic graphite by molecular-beam epitaxy. *Nanoscale* **2017**, *9*, 15945–15948. [CrossRef]
90. Zhu, Z.; Cai, X.; Yi, S.; Chen, J.; Dai, Y.; Niu, C.; Guo, Z.X.; Xie, M.; Liu, F.; Cho, J.-H.; et al. Multivalency-Driven Formation of Te-Based Monolayer Materials: A Combined First-Principles and Experimental study. *Phys. Rev. Lett.* **2017**, *119*, 106101. [CrossRef]
91. Zhang, Z.; Penev, E.S.; Yakobson, B.I. Two-dimensional boron: Structures, properties and applications. *Chem. Soc. Rev.* **2017**, *46*, 6746–6763. [CrossRef] [PubMed]
92. Li, W.; Kong, L.; Chen, C.; Gou, J.; Sheng, S.; Zhang, W.; Li, H.; Chen, L.; Cheng, P.; Wu, K. Experimental realization of honeycomb borophene. *Sci. Bull.* **2018**, *63*, 282–286. [CrossRef]
93. Kiraly, B.; Liu, X.; Wang, L.; Zhang, Z.; Mannix, A.J.; Fisher, B.L.; Yakobson, B.I.; Hersam, M.C.; Guisinger, N.P. Borophene Synthesis on Au(111). *ACS Nano* **2019**, *13*, 3816–3822. [CrossRef] [PubMed]
94. Wu, R.; Drozdov, I.K.; Eltinge, S.; Zahl, P.; Ismail-Beigi, S.; Božović, I.; Gozar, A. Large-area single-crystal sheets of borophene on Cu(111) surfaces. *Nat. Nanotechnol.* **2019**, *14*, 44–49. [CrossRef]
95. Vinogradov, N.A.; Lyalin, A.; Taketsugu, T.; Vinogradov, A.S.; Preobrajenski, A. Single-phase borophene on Ir(111): Formation, structure, and decoupling from the support. *ACS Nano.* **2019**, *13*, 14511–14518. [CrossRef]
96. Suehara, S.; Aizawa, T.; Sasaki, T. Graphenelike surface boron layer: Structural phases on transition-metal diborides (0001). *Phys. Rev. B* **2010**, *81*, 085423. [CrossRef]
97. Qin, N.; Liu, S.; Li, Z.; Zhao, H.; Wang, S. First-principles studies for the stability of a graphene-like boron layer on CrB2(0001) and MoB2(0001). *J. Phys. Condens. Matter* **2011**, *23*, 225501. [CrossRef]
98. Penev, E.S.; Bhowmick, S.; Sadrzadeh, A.; Yakobson, B.I. Polymorphism of Two-Dimensional Boron. *Nano Lett.* **2012**, *12*, 2441–2445. [CrossRef]
99. Wu, X.; Dai, J.; Zhao, Y.; Zhuo, Z.; Yang, J.; Zeng, X.C. Two-Dimensional Boron Monolayer Sheets. *ACS Nano* **2012**, *6*, 7443–7453. [CrossRef]
100. Zhang, H.-M.; Sun, Y.; Li, W.; Peng, J.-P.; Song, C.-L.; Xing, Y.; Zhang, Q.; Guan, J.; Li, Z.; Zhao, Y.; et al. Detection of a Superconducting Phase in a Two-Atom Layer of Hexagonal Ga Film Grown on Semiconducting GaN(0001). *Phys. Rev. Lett.* **2015**, *114*, 107003. [CrossRef]
101. Steenbergen, K.G.; Gaston, N. Thickness dependent thermal stability of 2D gallenene. *Chem. Commun.* **2019**, *55*, 8872–8875. [CrossRef] [PubMed]
102. Lambie, S.; Steenbergen, K.G.; Gaston, N. Modulating the thermal and structural stability of gallenene via variation of atomistic thickness. *Nanoscale Adv.* **2021**, *3*, 499–507. [CrossRef]
103. Castellanos-Gomez, A.; Vicarelli, L.; Prada, E.; Island, J.O.; Narasimha-Acharya, K.L.; Blanter, S.I.; Groenendijk, D.J.; Buscema, M.; Steele, G.A.; Alvarez, J.V.; et al. Isolation and characterization of few-layer black phosphorus. *2D Mater.* **2014**, *1*, 025001. [CrossRef]
104. Zhang, J.L.; Zhao, S.; Han, C.; Wang, Z.; Zhong, S.; Sun, S.; Guo, R.; Zhou, X.; Gu, C.D.; Di Yuan, K.; et al. Epitaxial Growth of Single Layer Blue Phosphorus: A New Phase of Two-Dimensional Phosphorus. *Nano Lett.* **2016**, *16*, 4903–4908. [CrossRef] [PubMed]
105. Xu, J.-P.; Zhang, J.-Q.; Tian, H.; Xu, H.; Ho, W.; Xie, M. One-dimensional phosphorus chain and two-dimensional blue phosphorene grown on Au(111) by molecular-beam epitaxy. *Phys. Rev. Mater.* **2017**, *1*, 061002. [CrossRef]
106. Golias, E.; Krivenkov, M.S.; Varykhalov, A.Y.; Sánchez-Barriga, J.; Rader, O. Band Renormalization of Blue Phosphorus on Au(111). *Nano Lett.* **2018**, *18*, 6672–6678. [CrossRef] [PubMed]
107. Zhang, W.; Enriquez, H.; Tong, Y.; Bendounan, A.; Kara, A.; Seitsonen, A.P.; Mayne, A.J.; Dujardin, G.; Oughaddou, H. Epitaxial synthesis of blue phosphorene. *Small* **2018**, *14*, 1804066. [CrossRef]
108. Zhou, D.; Meng, Q.; Si, N.; Zhou, X.; Zhai, S.; Tang, Q.; Ji, Q.; Zhou, M.; Niu, T.; Fuchs, H. Epitaxial Growth of Flat, Metallic Monolayer Phosphorene on Metal Oxide. *ACS Nano* **2020**, *14*, 2385–2394. [CrossRef]
109. Ares, P.; Aguilar-Galindo, F.; Rodríguez-San-Miguel, D.; Aldave, D.A.; Díaz-Tendero, S.; Alcami, M.; Martín, F.; Gómez-Herrero, J.; Zamora, F. Mechanical Isolation of Highly Stable Antimonene under Ambient Conditions. *Adv. Mater.* **2016**, *28*, 6332–6336. [CrossRef]
110. Gibaja, C.; Rodríguez-San-Miguel, D.; Ares, P.; Gomez-Herrero, J.; Varela, M.; Gillen, R.; Maultzsch, J.; Hauke, F.; Hirsch, A.; Abellán, G.; et al. Few-Layer Antimonene by Liquid-Phase Exfoliation. *Angew. Chem. Int. Ed.* **2016**, *55*, 14345–14349. [CrossRef]

111. Gu, J.; Du, Z.; Zhang, C.; Ma, J.; Li, B.; Yang, S. Liquid-Phase Exfoliated Metallic Antimony Nanosheets toward High Volumetric Sodium Storage. *Adv. Energy Mater.* **2017**, *7*, 1700447. [CrossRef]
112. Wang, X.; He, J.; Zhou, B.; Zhang, Y.; Wu, J.; Hu, R.; Liu, L.; Song, J.; Qu, J. Bandgap-Tunable Preparation of Smooth and Large Two-Dimensional Antimonene. *Angew. Chem. Int. Ed.* **2018**, *57*, 8668–8673. [CrossRef] [PubMed]
113. Lei, T.; Liu, C.; Zhao, J.-L.; Li, J.-M.; Li, Y.-P.; Wang, J.-Q.; Wu, R.; Qian, H.J.; Wang, H.-Q.; Ibrahim, K. Electronic structure of antimonene grown on Sb_2Te_3(111) and Bi_2Te_3 substrates. *J. Appl. Phys.* **2016**, *119*, 015302. [CrossRef]
114. Ji, J.; Song, X.; Liu, J.; Yan, Z.; Huo, C.; Zhang, S.; Su, M.; Liao, L.; Wang, W.; Ni, Z.; et al. Two-dimensional antimonene single crystals grown by van der Waals epitaxy. *Nat. Commun.* **2016**, *7*, 13352. [CrossRef] [PubMed]
115. Sun, X.; Lu, Z.; Xiang, Y.; Wang, Y.; Shi, J.; Wang, G.-C.; Washington, M.A.; Lu, T.-M. van der Waals Epitaxy of Antimony Islands, Sheets, and Thin Films on Single-Crystalline Graphene. *ACS Nano* **2018**, *12*, 6100–6108. [CrossRef]
116. Mao, Y.-H.; Zhang, L.-F.; Wang, H.-L.; Shan, H.; Zhai, X.-F.; Hu, Z.-P.; Zhao, A.-D.; Wang, B. Epitaxial growth of highly strained antimonene on Ag(111). *Front. Phys.* **2018**, *13*, 138106. [CrossRef]
117. Xenogiannopoulou, E.; Tsoutsou, D.; Tsipas, P.; Fragkos, S.; Chaitoglou, S.; Kelaidis, N.; Dimoulas, A. Ultrathin epitaxial Bi film growth on 2D HfTe2 template. *Nanotechnology* **2022**, *33*, 015701. [CrossRef]
118. Qin, J.; Qiu, G.; Jian, J.; Zhou, H.; Yang, L.; Charnas, A.; Zemlyanov, D.Y.; Xu, C.-Y.; Xu, X.; Wu, W.; et al. Controlled Growth of a Large-Size 2D Selenium Nanosheet and Its Electronic and Optoelectronic Applications. *ACS Nano* **2017**, *11*, 10222–10229. [CrossRef]
119. Wang, Q.; Safdar, M.; Xu, K.; Mirza, M.; Wang, Z.; He, J. Van der Waals Epitaxy and Photoresponse of Hexagonal Tellurium Nanoplates on Flexible Mica Sheets. *ACS Nano* **2014**, *8*, 7497–7505. [CrossRef]
120. Huang, X.; Guan, J.; Lin, Z.; Liu, B.; Xing, S.; Wang, W.; Guo, J. Epitaxial Growth and Band Structure of Te Film on Graphene. *Nano Lett.* **2017**, *17*, 4619–4623. [CrossRef]
121. Hess Bonding, structure, and mechanical stability of 2D materials: The predictive power of the periodic table. *Nanoscale Horiz.* **2021**, *6*, 856–892. [CrossRef] [PubMed]
122. McCreary, A.; Kazakova, O.; Jariwala, D.; Al Balushi, Z.Y. An outlook into the flat land of 2D materials beyond graphene: Synthesis, properties and device applications. *2D Mater.* **2021**, *8*, 013001. [CrossRef]
123. Wang, Y.; Qiu, G.; Wang, R.; Huang, S.; Wang, Q.; Liu, Y.; Du, Y.; Goddard, W.A., III; Kim, M.J.; Xu, X.; et al. Field-effect transistors made from solution-grown two-dimensional tellurene. *Nat. Electron.* **2018**, *1*, 228–236. [CrossRef]
124. Sharma, S.; Singh, N.; Schwingenschlögl, U. Two-Dimensional Tellurene as Excellent Thermoelectric Material. *ACS Appl. Energy Mater.* **2018**, *1*, 1950–1954. [CrossRef]
125. Gao, Z.; Tao, F.; Ren, J. Unusually low thermal conductivity of atomically thin 2D tellurium. *Nanoscale* **2018**, *10*, 12997–13003. [CrossRef] [PubMed]
126. Wu, W.; Qiu, G.; Wang, Y.; Wang, R.; Ye, P. Tellurene: Its physical properties, scalable nanomanufacturing, and device applications. *Chem. Soc. Rev.* **2018**, *47*, 7206–7212. [CrossRef]
127. Cai, X.; Han, X.; Zhao, C.; Niu, C.; Jia, Y. Tellurene: An elemental 2D monolayer material beyond its bulk phases without van der Waals layered structures. *J. Semicond.* **2020**, *41*, 081002. [CrossRef]
128. Grazianetti, C.; Martella, C.; Molle, A. The Xenes generations: A taxonomy of epitaxial single-element 2D materials. *Phys. Status Solidi RRL* **2020**, *14*, 1900439. [CrossRef]
129. Kansara, S.; Gupta, S.K.; Sonvane, Y.; Hussain, T.; Ahuja, R. Theoretical Investigation of Metallic Nanolayers For Charge-Storage Applications. *ACS Appl. Energy Mater.* **2018**, *1*, 3428–3433. [CrossRef]
130. Serifi, I.; Kanga, N.B.J.; Drissi, L.B.; Saidi, E.H. Electron-phonon contribution in aluminene: Superconductive and transport properties. *Superlattices Microstruct.* **2021**, *151*, 106822. [CrossRef]
131. Petrov, M.; Bekaert, J.; Milošević, M.V. Superconductivity in gallenene. *2D Mater.* **2021**, *8*, 035056. [CrossRef]
132. John, R.; Merlin, B. Optical properties of graphene, silicene, germanene, and stanene from IR to far UV A first principles study. *J. Phys. Chem. Solids* **2017**, *110*, 307–315. [CrossRef]
133. Mukhopadhyay, T.; Mahata, A.; Adhikari, S.; Asle Zaeem, M. Effective mechanical properties of multilayer nano-heterostructures. *Sci. Rep.* **2017**, *7*, 15818. [CrossRef] [PubMed]
134. Shi, Z.; Singh, C.V. The ideal strength of two-dimensional stanene may reach or exceed the Griffith strength estimate. *Nanoscale* **2017**, *9*, 7055–7062. [CrossRef] [PubMed]
135. Lew Yan Voon, L.C.; Zhu, J.; Schwingenschlögl, U. Silicene: Recent theoretical advances. *Appl. Phys. Rev.* **2018**, *3*, 040802. [CrossRef]
136. Shubham; Swarup, A. Electrochemical properties of stanene as an efficient anode material for Na-ion batteries. *Comput. Condens. Matter* **2018**, *14*, 84–88. [CrossRef]
137. Tokmachev, A.M.; Averyanov, D.V.; Parfenov, O.E.; Taldenkov, A.N.; Karateev, I.A.; Sokolov, I.S.; Kondratev, O.A.; Storchak, V.G. Emerging two-dimensional ferromagnetism in silicene materials. *Nat. Commun.* **2018**, *9*, 1672. [CrossRef]
138. Cheng, H.-P.; Liu, S.; Chen, X.; Zhang, L.; Fry, J.N. First-principles study of magnetism and electric field effects in 2D systems. *AVS Quantum Sci.* **2020**, *2*, 027101. [CrossRef]
139. Parfenov, O.E.; Averyanov, D.V.; Tokmachev, A.M.; Sokolov, I.S.; Karateev, I.A.; Taldenkov, A.N.; Storchak, V.G. High-Mobility Carriers in Germanene Derivatives. *Adv. Funct. Mater.* **2020**, *30*. [CrossRef]

140. Pandey, D.; Kamal, C.; Chakrabarti, A. Strain induced magnetism and half-metallicity in alkali metal substituted aluminene. *AIP Conf. Proc.* **2019**, *2115*, 030351. [CrossRef]
141. Kort-Kamp, W.J.M. Topological phase transitions in the photonic spin Hall effect. *Phys. Rev. Lett.* **2017**, *119*, 147401. [CrossRef] [PubMed]
142. Yu, X.-L.; Wu, J. Evolution of the topological properties of 2D group IVA materials and device design. *Phys. Chem. Chem. Phys.* **2018**, *20*, 2296–2307. [CrossRef] [PubMed]
143. Zhai, X.; Wen, R.; Zhou, X.; Chen, W.; Yan, W.; Gong, L.-Y.; Pu, Y.; Li, X. Valley-Mediated and Electrically Switched Bipolar-Unipolar Transition of the Spin-Diode Effect in Heavy Group-IV Monolayers. *Phys. Rev. Appl.* **2019**, *11*, 064047. [CrossRef]
144. Krukovskii, K.V.; Kashin, O.A.; Luchin, A.V.; Kohanenko, A.P.; Dirko, V.V.; Lozovoi, K.A.; Kashina, O.N.; Bobrov, D.I. Microstructure and properties of a silicon coating deposited on a titanium nickelide substrate using molecular-beam epitaxy equipment. *J. Phys. Conf. Ser.* **2021**, *1954*, 012024. [CrossRef]
145. Dirko, V.V.; Lozovoy, K.A.; Kokhanenko, A.P.; Voitsekhovskii, A.V. High-resolution RHEED analysis of dynamics of low-temperature superstructure transitions in Ge/Si(001) epitaxial system. *Nanotechnology* **2022**, *33*, 115603. [CrossRef]
146. Lozovoy, K.A.; Korotaev, A.G.; Kokhanenko, A.P.; Dirko, V.V.; Voitsekhovskii, A.V. Kinetics of epitaxial formation of nanostructures by Frank–van der Merwe, Volmer–Weber and Stranski–Krastanow growth modes. *Surf. Coat. Technol.* **2020**, *384*, 125289. [CrossRef]
147. Dirko, V.V.; Lozovoy, K.A.; Kokhanenko, A.P.; Voitsekhovskii, A.V. Thickness-dependent elastic strain in Stranski–Krastanow growth. *Phys. Chem. Chem. Phys.* **2020**, *22*, 19318–19325. [CrossRef]
148. Lozovoy, K.A.; Zhou, Y.; Smith, R.; Lloyd, A.; Kokhanenko, A.P.; Dirko, V.V.; Akimenko, N.Y.; Grigoryev, D.V.; Voitsekhovskii, A.V. Thickness-dependent surface energy and formation of epitaxial quantum dots. *Thin Solid Films* **2020**, *713*, 138363. [CrossRef]
149. Vinarskiy, V.P.; Kokhanenko, A.P.; Lozovoy, K.A. Modelling of epitaxial growth of two-dimensional film. *J. Phys. Conf. Ser.* **2021**, *2140*, 012001. [CrossRef]
150. Nakano, H.; Tetsuka, H.; Spencer, M.J.S.; Morishita, T. Chemical modification of group IV graphene analogs. *Sci. Technol. Adv. Mater.* **2018**, *19*, 76–100. [CrossRef]
151. Pang, Z.-X.; Wang, Y.; Ji, W.-X.; Zhang, C.-W.; Wang, P.-J.; Li, P. Two-dimensional ligand-functionalized plumbene: A promising candidate for ferroelectric and topological order with a large bulk band gap. *Phys. E Low-Dimens. Syst. Nanostruct.* **2020**, *120*, 114095. [CrossRef]
152. Kumbhakar, P.; Gowda, C.C.; Mahapatra, P.L.; Mukherjee, M.; Malviya, K.D.; Chaker, M.; Chandra, A.; Lahiri, B.; Ajayan, P.; Jariwala, D.; et al. Emerging 2D metal oxides and their applications. *Mater. Today* **2021**, *45*, 142–168. [CrossRef]
153. Shahid, M.U.; Mohamed, N.M.; Muhsan, A.S.; Khatani, M.; Bashiri, R.; Zaine, S.N.A.; Shamsudin, A.E. Dual functional passivating layer of graphene/TiO2 for improved performance of dye-synthesized solar cells. *Appl. Nanosci.* **2018**, *8*, 1001–1013. [CrossRef]
154. Nagarajan, V.; Chandiramouli, R. Investigation on adsorption properties of CO and NO gas molecules on aluminene nanosheet: A density functional application. *Mater. Sci. Eng. B* **2018**, *229*, 193–200. [CrossRef]
155. Pandey, D.; Kamal, C.; Chakrabarti, A. First-principles study of adsorption of 3d and 4d transition metal atoms on aluminene. *Comput. Condens. Matter* **2018**, *16*, e00319. [CrossRef]
156. Pandey, D.; Kamal, C.; Dutt, R.; Chakrabarti, A. Improved gas adsorption on functionalized aluminene surface: A first-principles study. *Appl. Surf. Sci.* **2020**, *531*, 147364. [CrossRef]
157. Balabai, R.; Solomenko, A. Flexible 2D layered material junctions. *Appl. Nanosci.* **2019**, *9*, 1011–1016. [CrossRef]
158. Gutiérrez, Y.; García-Fernández, P.; Junquera, J.; Brown, A.S.; Moreno, F.; Losurdo, M. Polymorphic gallium for active resonance tuning in photonic nanostructures: From bulk gallium to two-dimensional (2D) gallenene. *Nanophotonics* **2020**, *9*, 4233–4252. [CrossRef]
159. Zhang, B.; Guo, F.; Zhang, L.; Zhu, M.; Zhang, Y. Controllable sign reversal of Seeback coefficient and the large tenability of ZT value of plumbene: A first-principles study. *J. Mater. Chem. C* **2021**, *9*, 16645. [CrossRef]
160. Liu, Y.; Zhang, S.; He, J.; Wang, Z.M.; Liu, Z. Recent Progress in the Fabrication, Properties, and Devices of Heterostructures Based on 2D Materials. *Nano-Micro Lett.* **2019**, *11*, 1–24. [CrossRef]
161. Izhnin, I.I.; Kurbanov, K.R.; Lozovoy, K.A.; Kokhanenko, A.P.; Dirko, V.V.; Voitsekhovskii, A.V. Epitaxial fabrication of 2D materials of group IV elements. *Appl. Nanosci.* **2020**, *10*, 4375–4383. [CrossRef]
162. Hu, C.-X.; Shin, Y.; Read, O.; Casiraghi, C. Dispersant-assisted liquid-phase exfoliation of 2D materials beyond graphene. *Nanoscale* **2021**, *13*, 460–484. [CrossRef] [PubMed]
163. Kamali, A.R. *Green Production of Carbon Nanomaterials in Molten Salts and Applications*; Springer Nature: Singapore, 2020; 162p.
164. Choi, S.H.; Yun, S.J.; Won, Y.S.; Oh, C.S.; Kim, S.M.; Kim, K.K.; Lee, Y.H. Large-scale synthesis of graphene and other 2D materials towards industrialization. *Nat. Commun.* **2022**, *13*, 1484. [CrossRef] [PubMed]
165. Koh, A.T.T.; Foong, Y.M.; Chua, D.H.C. Cooling rate and energy dependence of pulsed laser fabricated graphene on nickel at reduced temperature. *Appl. Phys. Lett.* **2010**, *97*, 114102. [CrossRef]
166. Tan, L.K.; Liu, B.; Teng, J.H.; Guo, S.; Low, H.Y.; Loh, K. Atomic layer deposition of a MoS_2 film. *Nanoscale* **2014**, *6*, 10584–10588. [CrossRef] [PubMed]

nanomaterials

Review

Applications of Nano Hydroxyapatite as Adsorbents: A Review

Iresha Lakmali Balasooriya [1,†], Jia Chen [1,†], Sriyani Menike Korale Gedara [1], Yingchao Han [1,2,*] and Merita Nirmali Wickramaratne [3]

[1] State Key Laboratory of Advanced Technology for Materials Synthesis and Processing, Biomedical Materials and Engineering Research Center of Hubei Province, Wuhan University of Technology, Wuhan 430070, China; iresha.balasooriya@gmail.com (I.L.B.); 265998@whut.edu.cn (J.C.); sriyanimenike@gmail.com (S.M.K.G.)

[2] Foshan Xianhu Laboratory of the Advanced Energy Science and Technology Guangdong Laboratory, Xianhu Hydrogen Valley, Foshan 528200, China

[3] Faculty of Medicine, Sabaragamuwa University of Sri Lanka, Belihuloya 70140, Sri Lanka; meritanirmali@gmail.com

* Correspondence: hanyingchao@whut.edu.cn

† These authors contributed equally to this work.

Abstract: Nano hydroxyapatite ($Ca_{10}(PO_4)_6(OH)_2$, HAp) has aroused widespread attention as a green and environmentally friendly adsorbent due to its outstanding ability in removing heavy metal ions, radio nuclides, organic pollutants and fluoride ions for wastewater treatment. The hexagonal crystal structure of HAp supports the adsorption mechanisms including ionic exchange reaction, surface complexation, the co-precipitation of new partially soluble phases and physical adsorption such as electrostatic interaction and hydrogen bonding. However, nano HAp has some drawbacks such as agglomeration and a significant pressure drop during filtration when used in powder form. Therefore, instead of using nano HAp alone, researchers have worked on modificationsand composites of nano HAp to overcome these issues and enhance the adsorption capacity. The modification of cationic doping and organic molecule grafting for nano HAp can promote the immobilization of ions and then increase adsorption capacity. Developing nano HAp composite with biopolymers such as gelatin, chitosan and chitin has proven to obtain a synergetic effect for improving the adsorption capacity of composites, in which nano HAp fixed and dispersed in polymers can playmuch more of a role for adsorption. This review summarizes the adsorption properties and adsorbent applications of nano HAp as well as the methods to enhance the adsorption capacity of nano HAp.

Keywords: nanohydroxyapatite; adsorption; heavy metal; radionuclide; organic pollutants; fluoride ions

Citation: Balasooriya, I.L.; Chen, J.; Korale Gedara, S.M.; Han, Y.; Wickramaratne, M.N. Applications of Nano Hydroxyapatite as Adsorbents: A Review. *Nanomaterials* **2022**, *12*, 2324. https://doi.org/10.3390/nano12142324

Academic Editors: Jihoon Lee, Ming-Yu Li and Abdelhamid Elaissari

Received: 31 May 2022
Accepted: 4 July 2022
Published: 6 July 2022

1. Introduction

Hydroxyapatite ($Ca_{10}(PO_4)_6(OH)_2$, HAp) is a major constituent of mammalian hard tissues [1] and exists in natural phosphate mineral rocks [2]. Hydroxyapatite has attracted the scientific community due to its characteristics such as biocompatibility, hydrophilicity, surface functional groups, acidity, basicity, porosity, etc. Hydroxyapatite (HAp) synthetic particles have a wide range of applications in medical, environmental remediation and industry fields. They are used in biomedical devices [3], dental implants [4], biodegradable scaffolds [5] as coatings on bone implants [6] and other types of orthopedic implants [7] (Shokri et al., 2021). HAp is also used in the development of drug delivery systems for targeted treatment [8–10]. It also serves as a chromatographic adsorbent and a catalyst [11–15].

The HAp crystal possesses a hexagonal structure with a six fold c-axis perpendicular to three equivalent a-axes at angles of 120° to each other. In HAp, the OH^- ions are aligned in columns parallel to the c-axis, along with Ca^{2+} and ${PO_4}^{3-}$ ions [16]. All these ions/groups and their special properties such as flexible substitutability in HAp support the adsorption mechanisms in different methods. Many investigators have reported that the sorption by

HAp is taking place by ionic exchange reaction, surface complexation, the co-precipitation of new partially soluble phases and physical adsorption such as electrostatic interaction and hydrogen bonding (Figure 1).

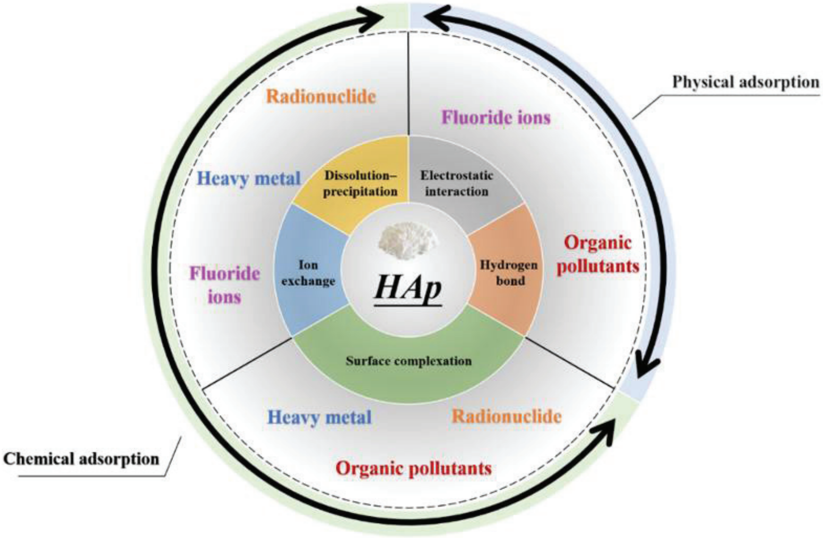

Figure 1. Adsorption mechanism of hydroxyapatite and its application.

The pathway of ionic exchange is related to the HAp properties. Ions that existed in the crystal lattice (Ca^{2+}, OH^{-}) can be replaced by foreign ions. Ca^{2+} in HAp can be substituted by divalent cations such as Pb^{2+}, Cu^{2+}, Cd^{2+} and Sr^{2+} [17]. For example, strontiapatite ($Sr_{10}(PO_4)_6(OH)_2$), formed by a substitution of calcium by strontium, is almost 107 times less soluble than hydroxyapatite [18]. Strontium substitution in natural apatites is as high as 11% [19]. The group of OH^- in HAp can take place by F^{-}, so it can also remove halogen ions. Similarly, radio nuclides intend to be absorbed by HAp via the mechanism of ions exchange. The dynamic process of HAp dissolution–precipitation can provide PO_4^{3-} ions and OH^- ions for removing foreign ions, metal ions and radionuclide and halogen ions, which is considered an important mechanism. The surface complexation mechanism, which takes an important place in the adsorption process, is dominated by the phosphate, calcium and hydroxyl groups [20]. Due to the unique surface effects of nanoparticles, there is anactive adsorption site in the HAp surface. Calcium ions exposed to the surface exhibit positively charged, easy sorption and negatively charged groups such as carboxylic acid or phosphate. The carboxyl in HAp surface possesses negative charges, forming the adsorption of cation adsorption sites. Therefore, by means of complexation the absorption of heavy metal, radial ions and organic pollutants can be achieved. In addition, substances opposite to the charge of the adsorption site can be adsorbed by HAp via electrostatic interaction belonging to physical adsorption. Hydrogen bonds play an important role in the adsorption of specific substances. The OH^- is located at the corners of the hydroxyapatite cell. When exposed to the crystal surface, it possibly forms a hydrogen bond with the ion to be adsorbed, which can be used in removing halogen ions and organic pollutants [21]. Compared with the larger scales such asmicro and centi, nano HAp exhibits excellent efficiency as an absorbent material due to its specific properties, such as a small size, a highly specific surface area and a more active site. The highly specific surface area takes a high surface energy, which means the process of ionic exchange surface and co-precipitation are promoted. Meanwhile, a more active site means atoms are exposed on the surface. It can form bonding with foreign substances when it is in contact with the external environment. The application of nano HAp as an adsorbent has been studied by many researchers recently. This paper reviews the up-to-date status of the applications of nano HAp as adsorbents for heavy metal ions, radionuclides, organic pollutants and fluoride ions in aqueous solutions.

2. Adsorption of Heavy Metals from Aqueous Solutions

With the rapid development of industries, wastewater containing heavy metals is increasingly discharged into the environment. As a consequence, heavy metal pollution has become one of the most serious environmental problems today [22]. This kind of pollution is concealed, persistent and permanent [23]. Additionally, it degrades the quality of the water and threatens the health and safety of animals and human beings by means of the food chain [23]. Therefore, it is important to improve and instigate innovative technologies for treating wastewater containing heavy metal. At present, the adsorption method is recognized as an economical and effective method for treating heavy metal wastewater. It has the following advantages: (1) The operation and design of the adsorption process are flexible, and it is suitable for efficient adsorption in most cases. (2) Adsorption materials can be reused through desorption. Many studies have recommended nano HAp as a suitable adsorbent for removing heavy metal ions such as Cd^{2+} [24–29], Co^{2+} [30,31] (Cr^{6+} [32,33], Cu^{2+} [34–37], Fe^{3+} [38]), Hg^{2+} [39], Ni^{2+} [40–42], Pb^{2+} [43–45], Zn^{2+} [46–48] (and As^{5+} [49] from aqueous solutions. The heavy metal ions adsorption by nano HAp is reported to be dependent on factors such as temperature, pH values. A comparison of the adsorption capacities of different adsorbents for the removal of heavy metal ions from aqueous solutions is presented in Table 1. NanoHAp and its composites display better adsorption capacities on Cd^{2+}, Pb^{2+} and Zn^{2+} compared with other materials.

Table 1. Comparison of the adsorption capacities of nano HAp and its composites with other absorbents on heavy metal ions.

Adsorbates	Adsorbents	Adsorption Capacity (mg/g)	Refs.
Cd(II)	Synthetic nano crystallite hydroxyapatite	142.857	[27]
	Nanohydroxyapatite/chitosan composite	243.90	[28]
	Hydroxyapatite-magnetite-bentonite composite	310.36	[29]
	Unmodified nanodiamond (ND)	40.9	[50]
	Oxidized nanodiamond (Ox-ND-1.5)	52.9	[50]
	Oxidized nanodiamond (Ox-ND-3)	67.9	[50]
Co(II)	Hydroxyapatite/chitosan composite	10.63	[31]
	Calcined *Umbonium vestiariums* nail shell (CUVS)	93.46	[51]
Cr(VI)	Nano Hydroxyapatite	2.18	[32]
	Fe_3O_4@n-HApGel composite (In-situ)	18.45	[33]
	Fe_3O_4@n-HApGel composite (Hydro)	27.06	[33]
	Unmodified nanodiamond (ND)	33.6	[50]
	Oxidized nanodiamond (Ox-ND-1.5)	44.1	[32]
	Oxidized nanodiamond (Ox-ND-3)	55.9	[50]
Cu(II)	n-HAp	4.7	[36]
	n-HAp/chitin composite	5.4	[36]
	n-HAp/chitosan composite	6.2	[36]
	Unmodified nanodiamond (ND)	25.2	[50]
	Oxidized nanodiamond (Ox-ND-1.5)	30.5	[50]
	Oxidized nanodiamond (Ox-ND-3)	44.5	[50]
	Neem bark nanoporous adsorbent (nANB)	21.23	[52]

Table 1. *Cont.*

Adsorbates	Adsorbents	Adsorption Capacity (mg/g)	Refs.
Fe(III)	n-HAp	4.238	[38]
	n-HAp/chitin composite	5.800	[38]
	n-HAp/chitosan composite	6.753	[38]
	Unmodified nanodiamond (ND)	26.8	[50]
	Oxidized nanodiamond (Ox-ND-1.5)	31.3	[50]
	Oxidized nanodiamond (Ox-ND-3)	45.7	[50]
Hg(II)	Chitosan/nanohydroxyapatite composite	111.6	[39]
	Magnetic mesoporous silica/chitosan (MMS/CS)	478.47	[53]
	Exfoliated graphene oxide–L-cystine	79.36	[54]
Ni(II)	Hydroxyapatite/chitosan composite	8.54	[31]
	Nanocrystalline calcium hydroxyapatite	46.17	[41]
	Activated carbon (AC) prepared from waste Parthenium	54.35	[55]
Pb(II)	Hydroxyapatite/chitosan composite	12.04	[31]
	Nano hydroxyapatite	357.14	[44]
	Nanohydroxyapatite–alginate composite adsorbents	270.3	[45]
	Mg_2Al-LS-LDH composite	∼123	[56]
Zn(II)	Nano hydroxyapatite	57.504	[46]
	Neem bark nanoporous adsorbent (nANB)	11.904	[52]

2.1. Adsorption Affinity of Different Heavy Metal Ions on Nano Hydroxyapatite

Nano HAp exhibits different removal efficiencies for different heavy metal ions. Gupta et al. reported the order of heavy metal removal efficiencies as (Pb > Co > Ni) [31]. Zou et al. discussed the adsorption and desorption process of divalent ions by HAp and found that the order of adsorption capacities was Hg^{2+}> Pb^{2+}> Zn^{2+}> Ni^{2+}> Cu^{2+}> Co^{2+}> Cd^{2+} ions [57]. The desorption results showed that $Hg^{2+}$was more easily desorbed than other ions; this can be attributed to the physical adsorption [57]. The studies of Chen et al. show the order of heavy metal ions removed from aqueous solutions as Pb^{2+}> Cu^{2+}> Cd^{2+} and suggest that this is inversely proportional to the hydrated ionic radii as Pb^{2+} (4.01 Å) > Cu^{2+} (4.19 Å) > Cd^{2+} (4.26 Å) [24]. Mobasherpour et al. observed a heavy metal affinity to the nano HAp in a sequence of Pb^{2+}>Cd^{2+}> Ni^{2+} and proposed that the preference of nano HAp for a metal may be clarified by the electro negativity of the metal ions and their cation/anion state [26]. The different adsorbent efficiencies of HAp for various ions can be attributed to the different ionic radii and electronegativity of each ion.

2.2. Adsorption Mechanisms of Heavy Metal Ions on Nano Hydroxyapatite

The adsorption mechanisms of heavy metal ions on HAp are identified to be through dissolution–precipitation, ionic exchange reaction and surface complexation with calcium, phosphate and hydroxyl groups (Figure 2). After the kinetic model fitting of the adsorption process of heavy metal ions (Pt^{2+}, Cu^{2+} …) by HAp, it was found that the Lagergren pseudo-second order kinetic equation better describes the process [58,59].

Dissolution–precipitation is the main adsorption mechanism that has obtained the attention of researchers recently. As nano HAp has a greater solubility than HAp, it is dissolved easily in the aqueous solution, forming $H_2PO_4^-$ groups which can react with heavy metal ions and form a precipitate [60].

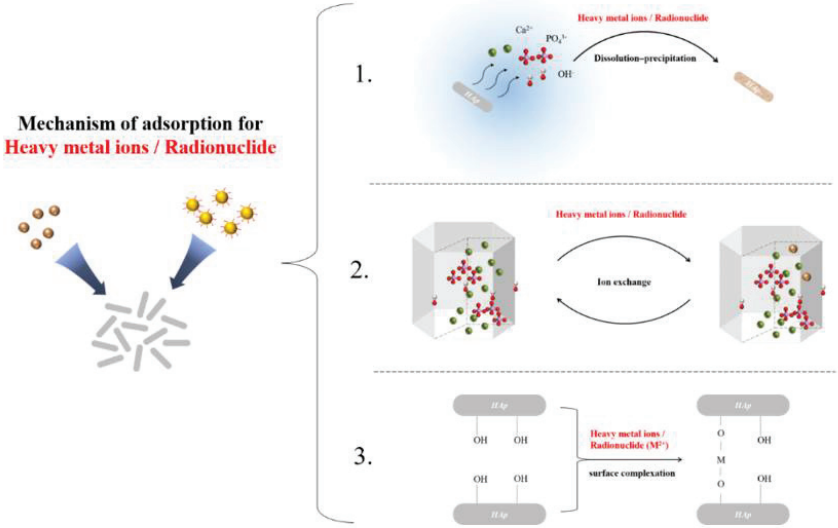

Figure 2. Adsorption mechanism of HAp for heavy metal ions or radionuclide.

The following reactions (Equations (1) and (2)) present the dissolution–precipitation mechanism (considering a divalent heavy metal ion M^{2+})

Dissolution:

$$Ca_{10}(PO_4)_6(OH)_{2\,(aq)} + 14H^+_{(aq)} \rightarrow 10Ca^{2+}_{(aq)} + 6H_2PO_4{}^-_{(aq)} + 2H_2O_{(l)} \tag{1}$$

$$10M^{2+}{}_{(aq)} + 6H_2PO_4{}^-_{(aq)} + 2H_2O_{(l)} \rightarrow 14H^+_{(aq)} + M_{10}(PO_4)_6(OH)_{2\,(S)} \tag{2}$$

Precipitation:

In the ion exchange mechanism, the heavy metal ions from the aqueous solution replace the Ca^{2+} ions of the nano HAp lattice partially, resulting in more stable heavy metal apatites [60].

The reaction below (Equation (3)) presents the ion exchange mechanism (considering a divalent heavy metal ion M^{2+})

$$Ca_{10}(PO_4)_6(OH)_2 + xM^{2+} \rightarrow xCa^{2+} + Ca_{(10\text{-}x)}M_x(PO_4)_6(OH)_2 \tag{3}$$

Other than the two main mechanisms above, metal complexation on the nano HAp surface also takes place as a secondary mechanism (Equations (4) and(5)). The phosphate and hydroxyl groups on the HAp crystal surface facilitate the complexation mechanism [60].

Meanwhile, which mechanism plays a dominant role in the adsorption process depends on the nature of the adsorbed ions. For example, the adsorption process of Cd^{2+} is divided into two stages. The first stage is the complexation of ions on the HAp surface, followed by the replacement reaction between heavy metal ions and Ca ions in the HAp crystal, achieving the purpose of removing heavy metals [61]. On the other hand, the adsorption of Pb^{2+} ions is realized through the process of dissolution and precipitation [62]. Zhu et al. used layered HAp to carry out the adsorption experiment in the system of complex heavy metal ions [63]. The results showed that, in the solution of Cd^{2+}, Pb^{2+}, Ni^{2+}, Cu^{2+} and Zn^{2+} with the same concentration, Pb is easier to be adsorbed due to it having a higher K_d value. $Pb_{10}(PO_4)_6(OH)_2$ is more easily formed by the reaction with phosphate dissolved from HAp [63].

A number of studies have found that the sorption of adsorbate on the synthesized apatites reduces the final pH to values around 6 [25,64,65]. They also found the total quantities of the displaced H^+ are comparable to the initial metal ion concentrations in the solution. This result elucidates that heavy metal sorption affects the proton discharge from the HAp surface ≡POH sites into the aqueous solution [25].

Considering a divalent heavy metal ion M^{2+},

$$\text{HAp-OH}_{(aq)} + \text{M}^{2+}{}_{(aq)} \leftrightarrow \text{HAp-O-M}^{+}{}_{(aq)} + \text{H}^{+}{}_{(aq)} \quad (4)$$

$$2\text{HAp-OH}_{(aq)} + \text{M}^{2+}{}_{(aq)} \leftrightarrow (\text{HAp-O})_2\,\text{M}_{(aq)} + 2\text{H}^{+}{}_{(aq)} \quad (5)$$

2.3. Factors Affecting the Adsorption of Heavy Metal Ions on Nano hydroxyapatite

2.3.1. Effect of pH

The pH level of the solution has a great influence on the surface charge of the adsorbent, the ion exchange processes and the solution chemistry of the metal ions. Previous studies have demonstrated that the adsorption capacity of HAp on heavy metal ions increases with an increase in pH in an acidic medium. Proton-competitive sorption reactions can explain this phenomenon. At lower pH values (2~6), H^+ ions compete with metal ions for surface binding sites of nano HAp, resulting in a lower adsorption rate than at higher pH values. At higher initial pH values (6~11), the presence of the H^+ ion in the solution is decreased, and the surface of the adsorbent is also deprotonated, increasing the metal ions adsorption [27,31,36,38,45]. However, a slight decline in sorption capacity was observed at an alkaline medium. This decline in sorption capacity in an alkaline medium was attributed to the precipitation of heavy metal hydroxides [27,31,36,38,45].

2.3.2. Effect of Adsorbent Dosage

Several studies have reported the importance of sorbent dosage because it determines the sorbent capacity for a certain initial solute concentration. Elkady et al. observed a rapid increase in Cd^{2+} removal efficiency while increasing the HAp amount from 0.1 to 0.5 g, with a slight increase above 0.5 g [25]. This could be explained by the increase in sorption sites with increasing HAp amounts. Elkady et al. also observed a decrease in the amount of cadmium removed, per gram of HAP [25]. With the increase in the HAp amount from 0.1 to 1.5 g, they further clarified it with the unreacted adsorbent sites on HAp that existed during the sorption process. In the experiment of Cu^{2+} adsorption using the composite of HAp/biochar nanocomposite, Jung et al. observed an increment in the percentage removal of Cu(II) from 26.87% to 96.02% as the adsorbent dosage increased from 0.01 to 0.04 g, then reaching a constant of 100% with further increases in the dosage [66]. This was explained by the greater availability of binding sites. However, they observed the lowest adsorption capacity of 33.33 mg/g with an adsorbent dosage of 0.06 g which may be attributed to the reduction of adsorption sites caused by material agglomeration. In addition, for the low concentration of metal ions, the adsorption sites could not reach the over-saturation point due to the excessive concentration of adsorbents, so it is critical to select the appropriate amount of adsorbent [66].

2.3.3. Effect of the Initial Heavy Metal Ion Concentration

Many researchers have examined the effect of the initial heavy metal ion concentration on the adsorption capacity. Elkady et al. observed an immediate reduction of adsorption with a fixed amount of HAp and suggested it was due to the deficiency of the available active sites of HAp required for the reaction [25]. They also observed an increase in the sorption capacities of nano HAp with an increasing cadmium concentration. This was possibly due to the increase in mass transfer driving force, which increases the rate of cadmium ions passing from the solution to the nano HAp particle surface [25]. (Elkady et al., 2011).

2.3.4. Effect of Contact Time

Evidence from the study by Elkady et al. suggests that the cadmium sorption process is rapid at the beginning (in the first 60 min) and then becomes slow [25]. This effect was explained by Elkady et al. using the larger surface area of the sorbent available for the Cd^{2+} sorption at the beginning, resulting in a rapid process [25]. Later, the process becomes slow as a result of the sudden exhaustion of the sorption sites by cadmium ions. Mortada et al. also proposed a similar conclusion: the adsorption rate of hydroxyapatite nanorods on heavy metals gradually slowed down with the extension of time and reached the platform in 30 min, indicating that this nanorod material has a good adsorption performance [67].

2.3.5. Effect of Solution Temperature

The solution temperature affects both the rate and extent of heavy metal sorption. The temperature dependency of the sorption process also offers evidence of potential sorbate–sorbent interaction. Elkady et al. examined the percentage of cadmium sorption by nano HAp with increasing temperatures [25]. Their results showed an increasing trend of sorption percentage with increasing temperatures. Elkady et al. proposed that the Cd^{2+} adsorption is stimulated by the temperature and also by the diffusion of Cd^{2+} through HAp particles [25].

2.3.6. Effect of Agitation Speed

The agitation affects the distribution of the solute in the solution as well as the formation of the external boundary film. Elkady et al. observed a relationship between the agitation speed and the percentage of cadmium removal for values between 0 and 500 rpm [25]. Their results elucidated the effect of external diffusion on the sorption kinetic mechanism. An increase in the agitation speed reduces the resistance of the boundary layer to mass transfer in the solution and increases the kinetic energy of hydrated ions. However, above 500 rpm, the cadmium removal percentage decreased, possibly as a result of an increase in the desorption tendency of adsorbate ions or the similar speed of adsorbent particles and adsorbate ions [25].

2.3.7. Effect of Foreign Ion

In practical applications, foreign ions are often involved in most conditions, and the interaction of these ions with the HAp surface affects the adsorption process of heavy metals in the solution. Jung et al. tested the adsorption capacity of HAp in the presence of Na^+, $NO_3{}^-$, $ClO_4{}^-$ and Cl^- in the solution and found that foreign ions had no obvious effect on the adsorption process at pH=5.8.When it is taken to pH=4.0, with the increase in ionic strength, the adsorption capacity of copper ions is improved, especially NaCl [66]. A possible reason for this is that the anion acts as a bridge to form HAp≡Cl-Cu, which further shows good adsorption performance at high ion concentrations [66].

2.4. Multiple Metal Solute System

The metal ion adsorption of an aqueous solution is intensely influenced by the competition between the metal ions to occupy the limited sites. Consequently, the removal efficiency of the adsorbent for the interested metals will decrease. Hence, understanding the overall heavy metal adsorption capacity of nano HAp, particularly in multiple metal solute systems, is important.

Chen et al. investigated the efficiency of nano hydroxyapatite on adsorbing aqueous Cd, Pb and Cu [24]. The results indicated a higher potential of nano HAp to adsorb aqueous Pb than other metals. Chen et al. developed a selectivity coefficient measurement and an isotherm equation, which were used to evaluate the competitive adsorption of the metals on nano HAp in multiple metal systems [24]. The results also revealed that the adsorption capability of nano HAp for individual metal ions was reduced by the competitive adsorption of multiple metals on nano HAp. Chen et al. suggested that the level of decrease was influenced by the adsorption affinity of nano HAp to the other metal ions existing in a single-metal system (i.e., $Pb^{2+} > Cu^{2+} > Cd^{2+}$) [24]. Although the adsorption of aqueous metal ions depends on many factors, this study found that the ratios of metal ions displaced by other competitive metal ions were moderately consistent over a wide concentration range in multiple metal systems.

The OH^- and PO_4^{3-} groups in HAp are hard Lewis bases, whereas Pb^{2+} is a hard Lewis acid. Cd^{2+} and Ni^{2+} are considered soft Lewis acids. The greater affinity of Pb compared to Cd and Ni towards HAp could be a result of that. As the electronegativity of Pb is greater than Cd and Ni, it results in a greater affinity in the electrostatic and inner-sphere surface complexation reactions. Compared to cations with larger ionic radii, the cations with ionic radii smaller than Ca^{2+} (0.099 nm) have a lesser opportunity to incorporate into a HAp structure [68]. Hence, the precipitation of larger cations such as Pb^{2+} (0.118 nm) and Cd^{2+} (0.097 nm) is favorable over the precipitation of smaller cations such asNi^{2+} (0.072 nm) and Ca^{2+} [26]

2.5. Enhancing the Heavy Metal Ion Adsorption Capacity of Nano Hydroxyapatite

Nanohydroxyapatite (HAp) can be used as an environmentally friendly adsorbent of heavy metal ions. However, the agglomeration and precipitation of nano HAp will result in the loss of adsorption capacity to heavy metal ions. Guo et al. suggested an alternative to inhibit the agglomeration of nano HAp and to easily separate the material from the aqueous solution after the adsorption of heavy metal ions by dispersing and fixing nano HAp in a polymer [60]. Guo et al. proposed sodium alginate as a suitable candidate polymer that can easily exchange its Na^+ ion with heavy metal ions to form gels [60]. They expected to fix HAp particles with sodium alginate and predicted the HAp-alginate composite to increase the adsorption capacity and removal efficiency with the integrated function of both components. Guo et al. suggested that nano HAp can be used as an adsorbent for heavy metal ions with alginate fixation to separate from the aqueous solution [60].

Although HAp has a good adsorption capacity, it creates a pressure drop during the field applications due to its powder form. To overcome this, Gopalakannan et al. suggested embedding HAp in a polymeric matrix, producing a hybrid composite [33]. Gopalakannan et al. investigated the Cr(VI) adsorption capacity of magnetic particles reinforced nanohydroxyapatite/gelatin composite, and they expected the HAp/ polymer hybrid composite to show excellent mechanical strength, a high sorption capacity and a higher specific surface area [33]. Their results indicated that the synthesized magnetic biocomposites exhibited a higher chromium adsorption capacity compared to nano HAp alone. As the amine group of gelatin and Lewis acid metal ions (Fe^{3+} and Ca^{2+}) of the adsorbent easily protonate, creating a positive surface, negatively charged chromate anions are attracted by electrostatic attraction with surface complexation. Gopalakannan et al. also investigated the sorption capacity of insitu and hydrothermal synthesized adsorbents and observed that the adsorbents synthesized in the hydrothermal method possess a greater adsorption capacity than those in the insitu method, as the former have a high surface area, pore width and pore volume [33].

Gandhi et al. synthesized a chitin/chitosan nano HAp composite for copper (II) removal [36]. They expected that the high metal ion adsorption potential of chitin and chitosan combined with the adsorption ability will result in a higher adsorption capacity [36]. The results indicated the sorption capacities of the adsorbents in a sequence of nano HAp < nano HAp/chitin composite < nano HAp/chitosan composite [36]. Kousalya et al. examined the adsorption capacity of nano HAp/chitin and nano HAp/chitosan composites, which could possess higher mechanical strength, biocompatibility and biodegradability than the components alone [38]. The sorption mechanism of Fe(III) by nano HAp and the two composites was dominated by adsorption and ion exchange [38]. Fe(III) sorption by chelation was also observed in nano HAp/chitin and nano HAp/chitosan composites as a result of the lone pair of electrons from nitrogen, which has also taken place as a result of amino and hydroxyl groups in the composites [38]. Therefore, Kousalya et al. observed a high increase in the sorption capacity in nano HAp/chitin and nano HAp/chitosan composites compared to nano HAp alone due to the overall effect of chitin with nano HAp and chitosan with nano HAp [38].

Gupta et al. investigated the adsorption capacity of HAp/chitosan composite on the removal of Pb^{2+}, Co^{2+} and Ni^{2+} from an aqueous solution [31]. They identified that chitosan binds HAp and forms aggregates to prevent the dispersion of HAp in an aqueous solution, which results in the convenience of recovering HAp. Similarly to pure HAp, HAp/chitosan composite also showed the order of removal efficiency as Pb > Co > Ni [31].

Salah et al. found that the sorption capacity of nano hydroxyapatite/chitosan composite (122 mg/g) to Cd^{2+} was greater than nano HAp alone(92 mg/g) [28]. They suggested the sorption capacity could be increased by increasing the initial Cd^{2+} concentration and also the nano HAp/Cd^{2+} mass ratio. Moreover, they identified that the regeneration capacity of the sorbent was satisfactory [28].

In addition to compounding HAp with other materials, the surface modification of HAp can be also an effective method to remove heavy metals. Oulguidoum et al. grafted 1, 3-benzenedisulfonate on a HAp surface and then carried out adsorption experiments on Pb^{2+}, Zn^{2+} and Cd^{2+} ions [69]. The results indicated that, compared with the blank control group, the adsorption ability of the materials on these ions had increased significantly, which was attributed to the enhancement of the metal immobilization by the grafted groups [69]. Moreover, the grafted material still showed good adsorption performance after three cycles of adsorption–desorption, indicating the reversibility of adsorption at the solid surface sites [69].

3. Adsorption of Radionuclides from Aqueous Solutions

Radioactive metals are considered hazardous contaminants in the environment due to their radioactivity, toxicity and potential to be carcinogenic to humans. Hence, it is very important to select an appropriate and effective method to remove radioactive metals from water. The present methods for radioactive metal (i.e., U, Sr, Co, etc.) removal from nuclear wastewaters include precipitation, reverse osmosis, ion exchange, adsorption and ultrafiltration [70]. Most of these methods are expensive and involve high maintenance. As the adsorption process is a simple and low-cost process, many researchers have investigated the use of adsorbents. Hydroxyapatite [71–81], aluminum oxide [82], silicon dioxide [83], hematite [84], akageneite [85,86] zeolite [87], activated carbon [88] and titanium [89] are some of the adsorbents previously studied. HAp has been widely studied for its application as an efficient radioactive ion adsorbent. It has been recommended for the adsorption of radionuclides such as UO_2^{2+} [73,74,77], Sr^{2+} [71,80] and Co^{2+} [90] by many researchers. A comparison of the adsorption capacities of several adsorbents for the removal of radionuclides from aqueous solutions is presented in Table 2. Compared with other absorbents, nano HAp has a good absorption capacity in U.

Table 2. Comparison of the adsorption capacities of nano HAp and its composites with other absorbents on Radionuclide.

Adsorbates	Adsorbents	(mg/g)	Refs.
Sr (II)	Nanocrystalline bio-hydroxyapatite	5.35	[71]
	Commercial-hydroxyapatite	0.76	[71]
	$[MeNH_3]5.5[Me_2NH_2]0.5In10S18{\cdot}7H_2O$	151.2	[91]
U (VI)	In situ-grown nanohydroxyapatite on magnetic Ca Al-layered double hydroxides	261.1	[73]
	Hydroxyapatite from bones combustion	20	[74]
	Bio-hydroxyapatite (Bio-HAP600)	384.6	[92]
	γ-Fe_2O_3	87.35	[93]

3.1. Adsorption Mechanisms of Radionuclides on Nano Hydroxyapatite

Two promising reaction mechanisms have been suggested for the reaction of HAp with uranium. They are the dissolution of HAp followed by the precipitation of chernikovite and autunite [73,94] by surface adsorption or complexation [95]. According to previous studies, the precipitation of chernikovite and autunite can scarcely occur with a low uranium concentration (4700 ppm) in the removal process. Therefore, surface complexation is recognized as the main uranium removal method in low concentrations of uranium [74] (Li et al., 2012) (Figure 2).

Handley-Sidhu et al. suggested the following equations (Equations (6)–(8)) on the mechanisms of Sr^{2+} adsorption on nano HAp [71].

Surface adsorption:

$$OH + M^{2+} \rightarrow \equiv O{-}M^{2+} + H^{+} \tag{6}$$

$$O_3P{-}OH^{+} + M^{2+} \rightarrow \equiv O_3P{-}O{-}M^{2+} + H^{+} \tag{7}$$

Ion exchange:

$$Ca^{2+} + M^{2+} \rightarrow \equiv M^{2+} + Ca^{2+} \tag{8}$$

Further, it has proven that the Lagergren pseudo-second order kinetic equation can better match the process of radionuclide adsorption on HAp [96].

3.2. Factors Affecting the Adsorption of Radionuclide Ions on Nano Hydroxyapatite

Effect of the pH Variation

Bulk precipitation is the main mechanism of Uranium(VI) removal by HAp, and the formed precipitates intensely relate to the pH of the solution. In a solution where pH is between the mildly acidic and the moderate alkaline region, uranium is precipitated as its phosphate salts, such as $(UO_2)_3(PO_4)_2$ or $Ca(UO_2)_2(PO_4)_2$. Uranium may precipitate as calcium dioxouranium(VI) carbonate ($CaUO_2(CO_3)_2$) or as calcium uranate ($CaUO_4$ and/or Ca_3UO_6) in strongly alkaline regions [73]. According to Krestou et al., in the neutral pH region, the form of uranium removed from the solution was very stable but it was unstable in the high alkaline region, in which a considerable amount of uranium (VI) was redissolved in the aqueous media [73] (Krestou et al., 2004). Therefore, many studies have suggested that HAp has a strong affinity to efficiently remove U(VI) around pH 5 to 6, but U sorption is partly reversible in the high alkaline region, facilitating the remobilization of the contaminant [73,97].

4. Adsorption of Organic Pollutants from Aqueous Solutions

Researchers have examined different adsorbent materials such as activated carbon [98], biochar [99,100], natural clay [101], carbon aerogels [102], HAp, etc. for organic pollutant removal from an aqueous solution. Hydroxyapatite is a biomaterial widely used in water pollution control as a result of its excellent adsorption affinity, inexpensive nature, accessibility and environment ally friendly nature. The use of nano-sized hydroxyapatite is advantageous over normal-sized hydroxyapatite due to the high surface area and reactivity as well as the ability to disperse throughout an aqueous solution (Table 3). A comparison of the adsorption capacities of different adsorbents for the removal of organic pollutants from aqueous solutions is presented in Table 3. For all organic pollutants, nano HAp shows an excellent adsorption capacity compared to other absorbents.

Table 3. Comparison of the adsorption capacities of nano HAp and its composites with other absorbents on organic pollutants.

Adsorbates	Adsorbents	Q (mg/g)	Conditions	Refs.
Phenol	Hydroxyapatite nanopowders	10.33	333 K, pH 6.4	[103]
	Natural clay	15	298 K, pH 5	[101]

Table 3. *Cont.*

Adsorbates	Adsorbents	Q (mg/g)	Conditions	Refs.
Nitrobenzene	Hydroxyapatite–gelatin nanocomposite	42.373		[104]
	Nanocrystalline hydroxyapatite	8.993	298 K	[105]
	Hydrophobic cotton fibers adsorbent	16.85	293 K	[106]
Reactive Blue 19 dye	Uncalcined nanohydroxyapatite	90.09	293 K, pH 3	[107]
	Calcined nanohydroxyapatite	74.97	293 K, pH 3	[107]
	Chitosan coated magnetic hydroxyapatite	26.4	pH 5	[108]
Reactive red 198 dye	HA	21.5		[109]
	Yttrium substituted HA	25.3		[109]
	Native pretreated dried *Potamogeton crispus*	14.3		[110]
	Acid pretreated dried *Potamogeton crispus*	26.8		[110]
	Alkali pretreated dried *Potamogeton crispus*	44.2		[110]
Methylene blue dye	Microwave-HAp	33.3		[111]
	MnO2-loaded biochar	248.96		[112]
Congo red dye	HAp-CS	769	pH 2–10	[113]
	Zinc peroxide (ZnO2) nanomaterial	208		[114]
Tetracycline	Zinc (II)-modified hydroxyapatites	168.5	298 K, pH 5	[102]
	Mn-N-doped carbon aerogels (MCA)	917.2	pH 4	[115]

4.1. Adsorption Mechanisms of Organic Pollutants on Nano HAp

There are threemain adsorption mechanisms of HAp that affect organic pollutants: electrostatic attraction, surface adsorption and hydroxyl bond(Figure 3). The process of adsorption conformsmore to theLagergren pseudo-second order kinetic equation.

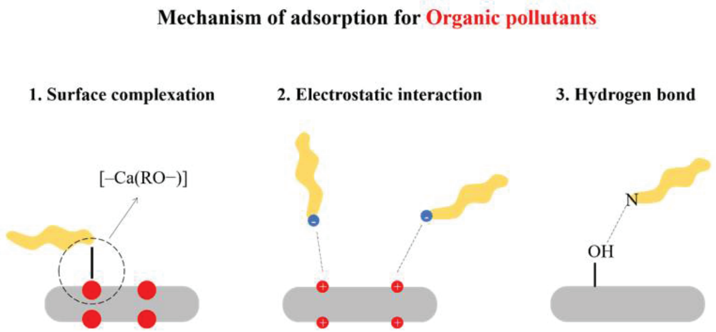

Figure 3. Adsorption mechanism of HAp for organic pollutants.

In the dissociation of phenolic compounds, their oxygen gains the greatest effective charge, acting as adsorption centers in the adsorption onto HAp. Molecules containing hydroxyl-groups contest with water molecules in the solution for the surface calcium ions of HAp. They are adsorbed onto HAp in an ionic form by forming [–Ca(RO−)] complexes [103].

The reactive blue 19 dye adsorption on HAp in acidic pH may be explained by the electrostatic attraction between the positively charged ≡CaOH$^+$ groups on the HAp surface and the negatively charged sulfonyl (–OSO$_{3-}$) and sulfonic (–SO$_{3-}$) groups of the reactive blue 19 dye [107]

The adsorption of reactive red 198 dye on HAp can be explained as follows. The dye molecules are adsorbed through the electrostatic attractions between the ionized sulphonyl groups of the dye molecule and the positively charged Ca^{2+} of the HAp surface. The dipole–dipole hydrogen bonding interaction occurs between the azoic group of the dye molecule and the hydroxyl groups of HAp, as well as the electrostatic interactions which may occur between the cationic groups of a dye such as Na^+ with anionic groups of HAp such as OH^- and $PO_4{}^{3-}$ [109].

The mechanism of the HAp adsorption of methylene blue can be explained as follows: under alkaline conditions, the negative charge on the surface of hydroxyapatite and the key group of methylene blue play a dominant role. Under acidic conditions, the electrostatic effect does not exist because the surface of hydroxyapatite is positively charged, and the adsorption is achieved by the (P-OH) group of HAp-particles and the (N) of the methylene blue molecule. Therefore, the adsorption mechanism is related to the external condition [111].

4.2. Factors Affecting the Adsorption of Organic Pollutants on Nano Hydroxyapatite

4.2.1. Effect of pH

The pH of the adsorption medium is considered the most critical parameter in the phenol adsorption process by nano HAp, because the charge of both the adsorbate and the adsorbent depends on the pH of the solution. Lin et al. studied the effect of the initial pH of the solution on the phenol adsorption onto nano HAp and found that the adsorption capacity is decreased with increasing pH up to 8.2, and then the adsorption capacity is increased by further increasing the pH to the alkaline value [103]. The maximal adsorption capacity was observed at pH 2 [103].

In the nitrobenzene adsorption process, the pH of the adsorption medium is the most vital parameter. Wei et al. found that the adsorption capacity of nanocrystalline HAp decreases sharply when the pH is higher than 6.0, and the maximum adsorption capacity of nanocrystalline HAp on nitrobenzene was at pH 2.0 [105].

Vasugi et al. studied the reactive red 198 dye adsorption capacity of nano HAp under different pH values and learned that nano HAp showed a better dye removal capacity in acidic pH and that the maximum dye removal capacity was observed at pH 6 [109].

Ciobanu et al. examined the removal rate of reactive blue 19 dye by nano HAp under different pH values [107]. Ciobanu et al. found that nano HAp exhibited a higher adsorption capacity in acidic pH and a lower adsorption capacity in basic pH, while the maximum adsorption was seen at pH 3 [107].

Allam et al. (2016) proposed that when the pH value in the solution is higher or lower than the HAp isoelectric point, the charge on the surface of the nanoparticles will change because the HAp isoelectric point is between 6 and 7.2, which will affect the mechanism of organic matter adsorption [111].

4.2.2. Effect of Contact Time

Lin et al. studied the effect of contact time on the phenol adsorption by HAp nanopowders [103]. They found that the adsorption equilibrium of phenol was achieved after 2 h and observed no remarkable changes for longer contact times [103].

Wei et al., examined the effect of contact time on the adsorption of the nitrobenzene on nanocrystalline HAp for initial nitrobenzene concentrations of 5, 10 and 50 mg/L [105]. For the three concentrations above, the adsorption equilibrium of nitrobenzene was obtained within 1 min [105]. They observed no further changes in prolonging contact times. The equilibrium time of different initial nitrobenzene concentrations exhibited that initial nitrobenzene concentrations had little effect on the adsorption equilibrium time [105].

Vasugi et al. investigated the effect of contact time on the reactive red 198 dye removal percentage by HA [109]. They observed an increase in the dye removal percentage with time and found that, above 360 min, it approaches equilibrium [109] Ciobanu et al. examined the effect of contact time on the reactive blue 19 dye removal by nano HAp at an initial pH of 3 with a nano HAp dose of 2 g/L and an initial reactive blue 19 dye concentration of 65 mg/L under 20 °C temperature [107]. They observed a rapid increase in the amounts of the dye adsorbed onto nano HAp within the first 30 min, changing slightly in the subsequent 3 h when the maximum adsorption was reached [107]. Thereafter, no further adsorption occurs with a longer contact time, indicating the reaching of equilibrium [107].

4.2.3. Effect of Adsorbent Dosage

Lin et al. investigated the effect of the nano HAp adsorbent dose on the percentage of phenol removal [103]. They identified an obvious increase in the phenol adsorption percent with increasing HAp dosages [103]. The phenol adsorption percent increased rapidly from 32.5 to 35.5% with the increase in HAp dosage from 2 to 4 g/L [103] This was attributed to the increase in the number of adsorption sites with the increase in the HAp adsorbent dosage [103]. As the HAp dosage was further increased to 12 g/L, the phenol adsorption percent increased slightly to 37.0% [103]. The results also revealed the possibility to remove phenol completely with sufficient HAp in the solution [103].

Wei et al. examined the effect of the adsorbent dose on the nitrobenzene removal by nano HAp over the 2.0–10 g/L range of the adsorbent, keeping all other parameters constant [105]. They observed an increase in the percent removal for nitrobenzene with the increasing adsorbent dosage [105]. A rapid increase in the nitrobenzene removal efficiency from 66.2 to 70.9% was observed with the increase in nano crystalline HAp dosage from 2 to 5 g/L [105]. This increase in the nitrobenzene removal efficiency was attributed to an increase in the adsorbent concentration, which increased the available surface area and adsorption sites [105] When the nanocrystalline HAp dosage was further increased to 10 g/L, the nitrobenzene removal efficiency increased slightly to 72.6% [105].

Vasugi et al. evaluated the effect of nano HAp adsorbent dosage on the percentage of reactive red 198 dye removal [109]. At a pH of 6 and under a constant adsorbate concentration of 50 mg/L, they observed an increase in the dye removal percentage with the increasing adsorbent dosage as a result of the increase in the surface area available for adsorption [109]. A maximum of 89% was attained for dye removal by nano HAp [109].

Ciobanu et al. studied the effect of nano HAp adsorbent dose on the reactive blue 19 dye removal [107]. The dye adsorption percent was studied with different adsorbent concentrations (1–20 g/L) under constant conditions, including an adsorbate concentration of 65 mg/L, an initial pH of 3, a contact time of 3 h and a temperature at 20 °C [107]. Ciobanu et al. found an obvious increase in the dye adsorption percent with the increasing adsorbent dosage. The maximum adsorption capacity was observed at a nano HAp adsorbent dose of 2 g/L [107].

4.3. Enhancing the Organic Pollutant Adsorption Capacity of Nano Hydroxyapatite

Even though the adsorption by nano HAp is recognized as a promising method for nitrobenzene removal from wastewater, there are some drawbacks of nano HAp, such as poor strength, low stability and a significant pressure drop during filtration when used in powder form [116]. To prevail over these limitations and to enhance the adsorption capacity of nano HAp, several scientists have attempted to composite nano HAp with biopolymers [104,113,117]. (Wei et al. examined the possibility of using hydroxyapatite–gelatin nanocomposite for the nitrobenzene removal from an aqueous solution [104]. The study by Wei et al. revealed that the adsorption process of the hydroxyapatite–gelatin nanocomposite was fast, and it takes only 1 min to reach a steady state [104]. Wei et al. estimated the maximum adsorption capacity to be 42.373 mg/g, which was higher than many previously reported adsorbents for nitrobenzene removal [104].

Vasugi et al. investigated the reactive red 198 dye adsorption by nano HAp and a trivalent cation (yttrium) substituted HAp (Y-HAp) [109]. The study revealed that Y-HAp showed enhanced adsorption affinity compared to the pristine HAp due to the presence of additional adsorption sites owing to the difference in the oxidation state of the substituent and its related charge balance [109].

Hou et al. prepared the composite of HAp and chitosan, which was used to adsorb Congo red dye [113]. Compared with the adsorption capacity of pure HAp (305 mg/g), the adsorption capacity of composite material increased by more than two times (769 g/mg) [113]. The characterization results show that the adsorption process not only includes electrostatic adsorption but also involves complexation, ion exchange and hydrogen bonding [113].

Guan et al. prepared polyalcohol modified HAp nanoparticles with a core-shell structure using D-Fructose-1, 6-phosphate trisodium salt octahydrate ($C_6H_{11}Na_3O_{12}P_2 \cdot 8H_2O$, DFP) as a phosphorus source [118]. The material has a large surface area of 203.18 m^2/g, so it shows good adsorption performance for organic excitements such as methyl orange and Congo red [118].

5. Adsorption of Fluoride Ions from Aqueous Solutions

The consumption of drinking water with higher levels of fluoride leads to serious health effects on human beings, including fluorosis. According to the World Health Organization, the maximum acceptable fluoride concentration in drinking water is 1.5 mg/L [119]. To remove excess fluoride from water, different defluoridation methods have been adopted. These methods include ion exchange [120], adsorption [121], precipitation [122] electrolysis [123], nanofiltration [124] and reverse osmosis [125].

Among the mentioned methods, adsorption is considered effective because it is an easy, versatile and cost-effective method. Researchers have investigated various adsorbent materials for fluoride removal from an aqueous solution. Calcite [126], limestone [127], nanohydroxyapatite [128–134], montmorillonite [135], mixed metal oxides [136], activated carbon [137], activated alumina [138], layered double hydroxides [139], clays [140] and rare earths-loaded chitosan beads [141] are some of them. Among these adsorbents, nano HAp has attracted researchers' interest due to its chemical composition, crystal structure, excellent defluoridation capacity, low cost and availability. Several attempts have been made to composite nano HAp with polymers and also to use surface modification techniques to enhance the fluoride removal capacity of nano HAp. A comparison of the defluoridation capacities of different adsorbents including HAp for the fluoride removal from aqueous solutions is presented in Table 4. Nano HAp is a promising material for removing F^- compared to other materials.

Table 4. Comparison of the adsorption capacities of nano HAp and its composites with other absorbents on fluoride ions.

Adsorbate	Adsorbents	Defluoridation Capacity(mg F^- kg^{-1})	Conditions	Refs.
	Nanohydroxyapatite	1296	T 303 K	[129]
	Nanohydroxyapatite/chitin composite	2840	T 303 K	[129]
	Nanohydroxyapatite	1845	T 303 K, pH 3	[130]
	Alginate bioencapsulated nanohydroxyapatite composite	3870	T 303 K	[131]
	Nanohydroxyapatite in gelatin polymatrix	4157	T 303 K, pH 5	[132]
	Marble apatite (synthesized using ultrasonication method)	1826	T 303 K, pH 7	[142]
	Marble apatite (synthesized using conventional method)	960	T 303 K, pH 7	[142]
	Imidazolium ionic liquid modified chitosan	8.068		[143]
	Alginate beads modified with functionalized silica particles	51.02		[144]

5.1. Adsorption Mechanisms of Fluoride Ions on Nano Hydroxyapatite

The mechanism of fluoride removal by nano HAp is controlled by both adsorption and ion exchange mechanisms [130,145]. In an aqueous fluoride solution, fluoride ions are adsorbed by nano HAp according to the reaction below. In addition to this, the OH^- ions of the n-HAp lattice are replaced by the F^- ions by ion exchange. (Figure 4) Based on the data of the experiment, the Lagergren pseudo-second order kinetic equation better fits its adsorption process for F^-.

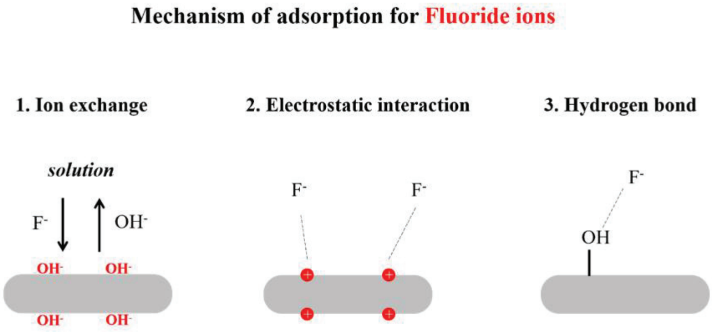

Figure 4. Adsorption mechanism of HAp for fluoride ions.

The adsorption of F^- ions on n-HAp could be expressed by the following reaction (Equation (9)):

$$Ca_{10}(PO_4)_6(OH)_2{+}nF^- \rightarrow Ca_{10}(PO_4)_6(OH)_2 — F_n^- \text{ (Hydrogen bonding)} \tag{9}$$

The fluoride removal of the n-HAp by ion exchange could be expressed by the following reactions (Equations (10)and(11)) [146]:

$$Ca_{10}(PO_4)_6(OH)_2 + F^- \rightarrow Ca_{10}(PO_4)_6FOH + OH^- \tag{10}$$

$$Ca_{10}(PO_4)_6(OH)_2 + 2F^- \rightarrow Ca_{10}(PO_4)_6F_2 + 2OH^- \tag{11}$$

In acidic media, the nano HAp surface gains a positive charge due to the higher H^+ concentration of the medium. Therefore, nano HAp attracts more fluoride ions in an acidic medium by electrostatic attractions, resulting in a higher defluoridation capacity at lower pH values. In alkaline pH, the nano HAp surface gains a negative charge and repels negatively charged fluoride ions, preventing the electrostatic attractions.

The fluoride removal of n-HAp in an acidic medium could be expressed by the following reaction (Equation (12)):

$$\begin{gathered} Ca_{10}(PO_4)_6(OH)_2{+}nF^- \rightarrow Ca_{10}(PO_4)_6(OH^+)_2 — F_n^- \text{ (Hydrogen bonding} \\ andelectrostaticattractions) \end{gathered} \tag{12}$$

5.2. Factors Affecting the Adsorption of Fluoride Ions on NanoHydroxyapatite

Several factors such as the solution pH, contact time, adsorbent dose and other anions in the medium affect the adsorption of fluoride ions on nano HAp.

5.2.1. Effect of pH

Among the factors mentioned above, the pH value plays an important role in the adsorption of fluoride ions at the water adsorbent interface. Sundaram et al. studied the fluoride adsorption on nano HAp under different pH values from 3 to 11 at room temperature with an initial fluoride concentration of 10 mg/L [130]. The removal of fluoride ions reached a maximum value of 1845 $mgF^-\ kg^{-1}$ at pH 3. At pH 11, the defluoridation was only 570 mgF$^-$ kg^{-1}. Accordingly, the defluoridation capacity increases with the decreasing pH [130]. This phenomenon is associated with the change of the adsorbent's surface charge. In an acidic medium, the surface of the adsorbent is highly protonated, and as a result, the attractive forces between the positively charged nano HAp adsorbent surface and the negatively charged fluoride surface gradually increase with decreasing pH values, resulting in an increase in the fluoride removal capacity by nano HAp. A lower defluoridation capacity by nano HAp in an alkaline medium is attributed to the nano HAp surface gaining a negative charge in the alkaline pH, resulting in repulsion between the negatively charged nano HAp surface and fluoride.

5.2.2. Effect of Contact Time

The adsorption of aqueous fluoride ions is also strongly influenced by contact time. Sundaram et al. examined the fluoride adsorption on nano HAp, varying the contact time in the range of 10–60 min with an initial fluoride concentration of 10 mg/L at room temperature [130]. (They observed that it took 30 min to reach the saturation and suggested that both ion exchange and adsorption control the fluoride sorption on nano HAp [130]. This is because, if the sorption process was only governed by the ion exchange mechanism, the saturation must have been reached very soon. As nano HAp reached saturation after 30 min, they proposed that adsorption, which is a slow process compared to ion exchange, also plays a key role in the sorption process [130].

5.2.3. Effect of Adsorbent Dose

Sundaram et al. studied the effect of nano HAp dose on percent fluoride removal by using different dosages of nano HAp ranging from 0.1 g to 1.0 g with an initial fluoride concentration of 10 mg/L [130]. They observed an increase in the percent fluoride removal with increasing adsorbent dosages. This was attributed to the added active sites resulting from the increase in the adsorbent dosage.

Jiménez-Reyes and Solache-Ríos conducted experiments using hydroxyapatite to adsorb 5 mg/L fluoride ions [147]. It has no obvious proportional relationship between the sorbent and sorbent dosage, and the following equation is used to fit the experiment data:$q_e = -3.3(\pm 0.2) \times (\ln X) - 2.2(\pm 0.2)$; $R^2 = 0.996$, where q_e is the adsorption capacity of Hap [147].

5.2.4. Effect of Other Anions in the Medium

Co-existing anions in the aqueous solution may compete with fluoride ions for adsorption sites during defluoridation and cause a negative effect on the defluoridation capacity. Sundaram et al. investigated the effect of the co-anions including Cl$^-$, $NO_3{}^-$ and $SO_4{}^{2-}$ $HCO_3{}^-$ on the defluoridation capacity of nano HAp by keeping the initial concentrations of these ions ranging from 100–500 mg/L and 10 mg/L as initial fluoride concentration at 303 K [130]. Sundaram et al, observed no significant difference in the defluoridation capacity of nano HAp in the presence of Cl$^-$, $NO_3{}^-$ and $SO_4{}^{2-}$ ions [130]. In presence of $HCO_3{}^-$ ions, the defluoridation capacity considerably decreased. Sundaram et al. concluded that the decrease in the defluoridation capacity is due to the competition of $HCO_3{}^-$ ions with the fluoride ions [130]. In another study, the interference of bicarbonate ions was explained by the increase in the solution pH due to the release of OH$^-$ ions from the $NaHCO_3$ hydrolysis and their competition with fluoride ions for active sites on nano HAp [148].

5.3. Enhancing the Fluoride Ion Adsorption Capacity of NanoHydroxyapatite

Although nanohydroxyapatite has been identified as a promising defluoridating material, its use is limited. The reasons are its brittleness and the difficulty for it to be used directly in fixed bed columns because of the significant pressure drop it causes in field applications. To overcome such technological barriers and to enhance the fluoride adsorption capacity of nanohydroxyapatite, different techniques have been used.

The collective effect of biopolymer and inorganic material has the ability to increase the mechanical properties of the composite [131]. Sundaram et al. employed nano HAp/chitin composite as adsorbents for the uptake of fluoride ions and found that it possesses a higher defluoridation capacity (DC) of 2840 mgF^- kg^{-1} than nano HAp alone, which has a DC of 1296 mgF^-kg^{-1} [129]. Sairam Sundaram et al. proposed that the enhancement in DC may be a result of adsorption by physical forces, biosorption by chitin and the fluoride ions trapped in fibrillar capillaries and voids of the polysaccharide complex of the chitin portion of the composite [129]. Sairam Sundaram et al. suggested nanoHAp/chitin composite as a promising candidate for defluoridation [129]. Pandi and Viswanathan found that the nanoHAp/Alginate composite has an enhanced DC of 3870 mg F^-/kg in comparison to nano HAp, which possessesa DC of 1296 mg F^-/kg [131]. Pandi and Viswanathan synthesized nano HAp-incorporated gelatin biocomposite (n-HAp@Gel) by the in situ coprecipitation method and investigated the removal of fluoride from an aqueous solution [132]. They observed an enhanced DC in the n-HAp@Gel biocomposite, which is 4157 mgF^-/kg compared to that of nano Hap [132]. Pandi and Viswanathan reported that in the fluoride removal mechanism, the fluoride ions are attracted by the Ca^{2+} in the gelatin polymatrix via electrostatic attraction [132]. In addition, the OH^- ions of the n-HAp lattice are replaced by F^- ions by means of ion exchange [132]. However, in the n-HAp@Gel composite, the neutralization of Ca^{2+} does not occur and, consecutively, permits the entrapping of fluoride ions from the solution as a result of the electrostatic adsorption as well as the strong Lewis acid–base interaction [132]. Pandi and Viswanathan revealed that the n-HAp@Gel composite can be successfully utilized for the adsorption of fluoride [132].

The excepted compound with organic compounds, adding inorganic substances to improve the adsorption capacity, is also a potential method. Pandi and Viswanathan prepared Fe_3O_4 /HAp /Chitosan as adsorbents to remove fluoride ions from the solution [134]. Compared with pure hydroxyapatite, the composite can reach adsorption saturation in a shorter time (20 min). Pandi and Viswanathan believed that, in addition to the ion exchange of F^- and OH^- and the electrostatic adsorption of Ca^{2+} and F^-, the adsorption mechanism also involved the complexation of Fe^{3+} and F^- [134]. Moreover, due to the magnetism of materials, it can offer the possibility of easier separation, washing and reuse [134].

Cationic doping can change the microstructure and properties of the crystal. This method is considered to improve the defluorination ability of hydroxyapatite [149,150]. Chen et al. prepared HAp doped with Al^{3+}, Mg^{2+} and La^{3+} to adsorb fluoride ions [149]. The results show that the doped ions can enhance the hydroxyl content of the crystal, thus providing more active sites for ion exchange, further improving the performance of fluoride ion adsorption [149]. Because the trivalent cations of Al^{3+} and La^{3+} are greater than the two valence cations of Mg^{2+}, the surface part has a more positive charge, which makes its adsorption ability stronger [149]. The doping ion radius does not have an effect on the adsorption performance [149]. At the same time, Chen et al. proposed that the mechanism of fluoride ion adsorption can be divided into two stages: first, fluoride ions reach the surface of the crystal through the physical adsorption; secondly, they exchange with OH^- in the hydroxyapatite crystal [149].

Surface modification technology has been verified to be efficient and effective in enhancing the adsorption capacities of adsorbents. Muthu Prabhu and Meenakshi investigated the fluoride adsorption capacity of nano HAp surface-modified by cationic surfactants, namely, cetyltrimethyl ammonium bromide (CTAB), hexadecylpyridinium chloride (HDPC) and dodecyltrimethyl ammonium bromide (DTAB) [148]. The amine salt and quaternary ammonium saltcan offer more positive sites to the adsorbents to which they are added. Even though nano HAp has a few positively charged functional groups on the surface, the cationic surfactants CTA^+, DTA^+ and HDP^+ added more positive adsorption sites to it. When a positively charged surface such as HAp is modified with a cationic surfactant, the hydrophilic groups orient away from the similarly charged substrate and towards the solution. By these means, the hydrophilic character of the adsorbent is increased, and, thus, more fluoride ions are attracted. The fluoride adsorption capacities of the three adsorbents followed the order: CTAB-HAp > DTAB-HAp > HDPC-HAp [148]. The low adsorption capacity of HDPC-HAp is a result of its pyridinium cationic head groups, which are bulkier compared to CTAB and DTAB [148] The access of fluoride to the tertiary cationic part in HDPC was blocked by the electron-rich pyridinium group, reducing the fluoride adsorption capacity compared to CTAB-HAp and DTAB-HAp [148]. Muthu Prabhu and Meenakshi, concluded that the cationic surfactant-coated HAp exhibits an excellent fluoride removal capacity over bare HAp because of the introduction of a more positive charge, especially CTAB-modified HAp compared to DTAB-HAp, HDPC-HAp powder [148]. They suggested that CTAB-HAp powder can be an auspicious defluoridating agent [148].

6. Conclusions and Future Work

The review presents the adsorption applications of nano HAp and its composites in the removal of heavy metal ions, radionuclides, organic pollutants and fluoride ions from wastewater. Nano HAp adsorbent shows a high and constant removing ability in an alkaline medium(pH 7–10)for metal ions and radionuclides. A higher alkaline region is not beneficial for the adsorbent of nano HAp; however, the acidic condition facilitates the removing of organic pollutants and fluoride ions. Usually, the sorbent capacity of nano HAp increases with a rising adsorbent dosage, but too of a high dosage cannot lead to an improvement in capacity due to the agglomeration of nano HAp. Nano HAp has the advantage of removing low concentrations, especially trace pollutants. Nano HAp shows a quick adsorption, and the adsorption rate gradually declines with the extension of contact time and reaches the platform in 30–60 min for ions; it takes more time (2–6 h) to reach the adsorption equilibrium for the majority of organic pollutants. In the future, nano HAp and its composites may be advantageous as adsorbents due to their high adsorption capacities compared to other adsorbents. Furthermore, many researchers are branching out with the modification of nano HAp, using techniques such as surface modification. However, the brittleness of HAp limits its applications. Moreover, nano HAp powder causes excessive pressure drops in field applications and therefore cannot be directly used in fixed bed columns. To overcome these technological problems, the use of composites or modification for HAp has been extensively studied. Nano-sized hydroxyapatite has its disadvantage in that the small particle size (nano-scale) makes it very difficult to separate from an aqueous solution. However magnetic adsorbents can avoid this problem, as they can be separated easily from the solution by using an external magnetic field. Hence, combining both nanotechnology and the magnetic separation technique in developing nano HAp based adsorbents would overcome the above drawback. On the other hand, the separation of nanoparticles from aqueous solutions limits the application of HAp with magnetic materials such that it only can be used in pollution removing at small volumes, such as a bottle. For its application in rivers and lakes, HAp manufactured in a layer or block is necessary. Sintering is a common forming method which can efficiently process large-scale production. However, it is difficult to preserve the excellent properties of nanoparticles. So, composites of HAp and polymers are considered as a promising method for forming. The high dispersion of nano HAp in composites should be focused on. It can be concluded that HAp is a promising material as an adsorbent for heavy metal ions, radionuclides, organic pollutants and fluoride ions in wastewater treatment. More research efforts on the practical applications development of these fascinating materials are highly recommended for the future.

Author Contributions: I.L.B.: investigation of references, writing—original draft preparation; J.C.: figure drawing, reviewing and revising; S.M.K.G.: investigation of references; Y.H.: supervision, conceptualization and methodology; M.N.W.: conceptualization and methodology. All authors have read and agreed to the published version of the manuscript.

Funding: This work was supported by the Foshan Xianhu Laboratory of the Advanced Energy Science and Technology Guangdong Laboratory (XHT2020-008) and the Science and Technology Partnership Program of the Ministry of Science and Technology of China (KY201602002).

Institutional Review Board Statement: Not applicable.

Informed Consent Statement: Not applicable.

Data Availability Statement: Data sharing is not applicable to this review.

Conflicts of Interest: The authors declare no conflict of interest.

References

1. Lowenstam, H.A.; Weiner, S. Biomineralization processes. In *On biomineralization*; Oxford University Press: Oxford, UK, 1989.
2. Chaabouni, A. Kinetic Study of the Dissolution of Tunisian Natural Phosphate or Francolite in Industrial Phosphoric Acid. *J. Adv. Chem.* **2013**, *6*, 908–916. [CrossRef]
3. Pokhrel, S. Hydroxyapatite: Preparation, Properties and Its Biomedical Applications. *Adv. Chem. Eng. Sci.* **2018**, *8*, 225–240. [CrossRef]
4. Alapati, K.; Saibaba, B.; Amarnath, M. Design and Development of Dental Implant Using Bio Ceramics. *Curr. J. Appl. Sci. Technol.* **2021**, *40*, 30–45. [CrossRef]
5. Zheng, X.; Hui, J.; Li, H.; Zhu, C.; Hua, X.; Ma, H.; Fan, D. Fabrication of novel biodegradable porous bone scaffolds based on amphiphilic hydroxyapatite nanorods. *Mater. Sci. Eng. C* **2017**, *75*, 699–705. [CrossRef]
6. Bosco, R.; Iafisco, M.; Tampieri, A.; Jansen, J.A.; Leeuwenburgh, S.C.; Beucken, J.J.V.D. Hydroxyapatite nanocrystals functionalized with alendronate as bioactive components for bone implant coatings to decrease osteoclastic activity. *Appl. Surf. Sci.* **2014**, *328*, 516–524. [CrossRef]
7. Shokri, N.; Safavi, M.S.; Etminanfar, M.; Walsh, F.C.; Khalil-Allafi, J. Enhanced corrosion protection of NiTi orthopedic implants by highly crystalline hydroxyapatite deposited by spin coating: The importance of pre-treatment. *Mater. Chem. Phys.* **2021**, *259*, 124041. [CrossRef]
8. Ginebra, M.-P.; Canal, C.; Espanol, M.; Pastorino, D.; Montufar, E.B. Calcium phosphate cements as drug delivery materials. *Adv. Drug Deliv. Rev.* **2012**, *64*, 1090–1110. [CrossRef]
9. Bose, S.; Tarafder, S.; Edgington, J.; Bandyopadhyay, A. Calcium phosphate ceramics in drug delivery. *JOM* **2011**, *63*, 93–98. [CrossRef]
10. Loca, D.; Locs, J.; Dubnika, A.; Zalite, V.; Berzina-Cimdina, L. Porous hydroxyapatite for drug delivery. In *Hydroxyapatite (Hap) for Biomedical Applications*; Elsevier: Amsterdam, The Netherlands, 2015; pp. 189–209. [CrossRef]
11. Suen, R.-B.; Lin, S.-C.; Hsu, W.-H. Hydroxyapatite-based immobilized metal affinity adsorbents for protein purification. *J. Chromatogr. A* **2004**, *1048*, 31–39. [CrossRef]
12. Cummings, L.J.; Snyder, M.A.; Brisack, K. Chapter 24 Protein Chromatography on Hydroxyapatite Columns. *Methods Enzymol.* **2009**, *463*, 387–404. [CrossRef]
13. Tsuchida, T.; Kubo, J.; Yoshioka, T.; Sakuma, S.; Takeguchi, T.; Ueda, W. Reaction of ethanol over hydroxyapatite affected by Ca/P ratio of catalyst. *J. Catal.* **2008**, *259*, 183–189. [CrossRef]
14. Dobosz, J.; Małecka, M.; Zawadzki, M. Hydrogen generation via ethanol steam reforming over Co/HAp catalysts. *J. Energy Inst.* **2018**, *91*, 411–423. [CrossRef]
15. Oh, S.C.; Xu, J.; Tran, D.T.; Liu, B.; Liu, D. Effects of Controlled Crystalline Surface of Hydroxyapatite on Methane Oxidation Reactions. *ACS Catal.* **2018**, *8*, 4493–4507. [CrossRef]
16. Orlovskii, V.P.; Komlev, V.; Barinov, S.M. Hydroxyapatite and Hydroxyapatite-Based Ceramics. *Inorg. Mater.* **2002**, *38*, 973–984. [CrossRef]
17. Nayak, A.; Bhushan, B. Hydroxyapatite as an advanced adsorbent for removal of heavy metal ions from water: Focus on its applications and limitations. *Mater. Today Proc.* **2021**, *46*, 11029–11034. [CrossRef]
18. Verbeeck, R.M.H.; Hauben, M.; Thun, H.P.; Verbeek, F. Solubility and Solution Behaviour of Strontiumhydroxyapatite. *Z. Phys. Chem.* **1977**, *108*, 203–215. [CrossRef]
19. Belousova, E.A.; Griffin, W.L.; O'Reilly, S.Y.; Fisher, N.I. Apatite as an indicator mineral for mineral exploration: Trace-element compositions and their relationship to host rock type. *J. Geochem. Explor.* **2002**, *76*, 45–69. [CrossRef]
20. Ferri, M.; Campisi, S.; Scavini, M.; Evangelisti, C.; Carniti, P.; Gervasini, A. In-depth study of the mechanism of heavy metal trapping on the surface of hydroxyapatite. *Appl. Surf. Sci.* **2019**, *475*, 397–409. [CrossRef]
21. Samant, A.; Nayak, B.; Misra, P.K. Kinetics and mechanistic interpretation of fluoride removal by nanocrystalline hydroxyapatite derived from Limacine artica shells. *J. Environ. Chem. Eng.* **2017**, *5*, 5429–5438. [CrossRef]
22. Fu, F.; Wang, Q. Removal of heavy metal ions from wastewaters: A review. *J. Environ. Manag.* **2011**, *92*, 407–418. [CrossRef]
23. Wang, Y.M. Stabilization of an elevated heavy metal contaminated site. *J. Hazard. Mater.* **2001**, *88*, 63–74. [CrossRef]
24. Chen, S.B.; Ma, Y.B.; Chen, L.; Xian, K. Adsorption of aqueous Cd^{2+}, Pb^{2+}, Cu^{2+} ions by nano-hydroxyapatite: Single- and multi-metal competitive adsorption study. *Geochem. J.* **2010**, *44*, 233–239. [CrossRef]

25. Elkady, M.; Mahmoud, M.; Abd-El-Rahman, H. Kinetic approach for cadmium sorption using microwave synthesized nano-hydroxyapatite. *J. Non-Crystall. Solids* **2011**, *357*, 1118–1129. [CrossRef]
26. Mobasherpour, I.; Salahi, E.; Pazouki, M. Comparative of the removal of Pb^{2+}, Cd^{2+} and Ni^{2+} by nano crystallite hydroxyapatite from aqueous solutions: Adsorption isotherm study. *Arab. J. Chem.* **2012**, *5*, 439–446. [CrossRef]
27. Mobasherpour, I.; Salahi, E.; Pazouki, M. Removal of divalent cadmium cations by means of synthetic nano crystallite hydroxyapatite. *Desalination* **2011**, *266*, 142–148. [CrossRef]
28. Salah, T.A.; Mohammad, A.M.; Hassan, M.A.; El-Anadouli, B.E. Development of nano-hydroxyapatite/chitosan composite for cadmium ions removal in wastewater treatment. *J. Taiwan Inst. Chem. Eng.* **2014**, *45*, 1571–1577. [CrossRef]
29. Ain, Q.U.; Zhang, H.; Yaseen, M.; Rasheed, U.; Liu, K.; Subhan, S.; Tong, Z. Facile fabrication of hydroxyapatite-magnetite-bentonite composite for efficient adsorption of Pb(II), Cd(II), and crystal violet from aqueous solution. *J. Clean. Prod.* **2019**, *247*, 119088. [CrossRef]
30. Avram, A.; Frentiu, T.; Horovitz, O.; Mocanu, A.; Goga, F.; Tomoaia-Cotişel, M. Hydroxyapatite for removal of heavy metals from wastewater. *Studia Univ. Babes-Bolyai Chem.* **2017**, *62*, 93–104. [CrossRef]
31. Gupta, N.; Kushwaha, A.K.; Chattopadhyaya, M. Adsorptive removal of Pb^{2+}, Co^{2+} and Ni^{2+} by hydroxyapatite/chitosan composite from aqueous solution. *J. Taiwan Inst. Chem. Eng.* **2012**, *43*, 125–131. [CrossRef]
32. Asgari, G.; Rahmani, A.R.; Faradmal, J.; Mohammadi, A.M.S. Kinetic and isotherm of hexavalent chromium adsorption onto nano hydroxyapatite. *J. Res. Health Sci.* **2012**, *12*, 45–53.
33. Gopalakannan, V.; Periyasamy, S.; Viswanathan, N. Fabrication of magnetic particles reinforced nano-hydroxyapatite/gelatin composite for selective Cr(vi) removal from water. *Environ. Sci. Water Res. Technol.* **2018**, *4*, 783–794. [CrossRef]
34. Bi, Y.-G.; Liu, D.; Liu, X.-M.; Zhou, S.-Q. Preparation and Characterization of Nano-Hydroxyapatite and Its Adsorption Behavior Toward Copper Ions. *Nanosci. Nanotechnol. Lett.* **2017**, *9*, 810–816. [CrossRef]
35. Brundavanam, S.; Poinern, G.E.J.; Fawcett, D. Kinetic and adsorption behaviour of aqueous Fe^{2+}, Cu^{2+} and Zn^{2+} using a 30 nm hydroxyapatite based powder synthesized via a combined ultrasound and microwave based technique. *Am. J. Mater. Sci.* **2015**, *5*, 31–40. [CrossRef]
36. Gandhi, M.R.; Kousalya, G.; Meenakshi, S. Removal of copper(II) using chitin/chitosan nano-hydroxyapatite composite. *Int. J. Biol. Macromol.* **2011**, *48*, 119–124. [CrossRef] [PubMed]
37. Song, Y.; Gao, J.; Zhang, Y.; Song, S. Preparation and characterization of nano-hydroxyapatite and its competitive adsorption kinetics of copper and lead ions in water. *Nanomater. Nanotechnol.* **2016**, *6*, 1847980416680807. [CrossRef]
38. Kousalya, G.; RajivGandhi, M.; Sundaram, C.S.; Meenakshi, S. Synthesis of nano-hydroxyapatite chitin/chitosan hybrid biocomposites for the removal of Fe(III). *Carbohydr. Polym.* **2010**, *82*, 594–599. [CrossRef]
39. Hassan, A.; Hrdina, R. Chitosan/nanohydroxyapatite composite based scallop shells as an efficient adsorbent for mercuric ions: Static and dynamic adsorption studies. *Int. J. Biol. Macromol.* **2018**, *109*, 507–516. [CrossRef]
40. El-Nagar, D.A.; Massoud, S.A.; Ismail, S.H. Removal of some heavy metals and fungicides from aqueous solutions using nano-hydroxyapatite, nano-bentonite and nanocomposite. *Arab. J. Chem.* **2020**, *13*, 7695–7706. [CrossRef]
41. Mobasherpour, I.; Salahi, E.; Pazouki, M. Removal of nickel (II) from aqueous solutions by using nano-crystalline calcium hydroxyapatite. *J. Saudi Chem. Soc.* **2011**, *15*, 105–112. [CrossRef]
42. Zamani, S.; Salahi, E.; Mobasherpour, E. Removal of Nickel from Aqueous Solution by Nano Hydroxyapatite Originated from Persian Gulf Corals. *Can. Chem. Trans.* **2013**, *1*, 173–190. [CrossRef]
43. Bi, Y.-G.; Liu, D.; Huang, M.-N. Preparation and Characterization of Nano Hydroxyapatite and Its Adsorption Behavior Toward Lead Ions. *Sci. Adv. Mater.* **2018**, *10*, 896–903. [CrossRef]
44. Googerdchian, F.; Moheb, A.; Emadi, R. Lead sorption properties of nanohydroxyapatite–alginate composite adsorbents. *Chem. Eng. J.* **2012**, *200–202*, 471–479. [CrossRef]
45. Ramesh, S.T.; Rameshbabu, N.; Gandhimathi, R.; Kumar, M.S.; Nidheesh, P.V. Adsorptive removal of Pb(II) from aqueous solution using nano-sized hydroxyapatite. *Appl. Water Sci.* **2013**, *3*, 105–113. [CrossRef]
46. Iconaru, S.L.; Motelica-Heino, M.; Guegan, R.; Predoi, M.V.; Prodan, A.M.; Predoi, D. Removal of Zinc Ions Using Hydroxyapatite and Study of Ultrasound Behavior of Aqueous Media. *Materials* **2018**, *11*, 1350. [CrossRef] [PubMed]
47. Zheng, Y.; Zhang, J. Experimental study on the adsorption of dissolved heavy metals by nano-hydroxyapatite. *Water Sci. Technol.* **2020**, *82*, 1825–1832. [CrossRef]
48. Zhou, C.; Wang, X.; Wang, Y.; Song, X.; Fang, D.; Ge, S. The sorption of single- and multi-heavy metals in aqueous solution using enhanced nano-hydroxyapatite assisted with ultrasonic. *J. Environ. Chem. Eng.* **2021**, *9*, 105240. [CrossRef]
49. Jahan, S.A.; Mollah, M.Y.A.; Ahmed, S.; Susan, M.A.B.H. Copper-doped Hydroxyapatite for Removal of Arsenic(V) from Aqueous System. *J. Sci. Res.* **2017**, *9*, 383–402. [CrossRef]
50. Ahmadijokani, F.; Molavi, H.; Peyghambari, A.; Shojaei, A.; Rezakazemi, M.; Aminabhavi, T.M.; Arjmand, M. Efficient removal of heavy metal ions from aqueous media by unmodified and modified nanodiamonds. *J. Environ. Manag.* **2022**, *316*, 115214. [CrossRef]
51. Foroutan, R.; Oujifard, A.; Papari, F.; Esmaeili, H. Calcined Umbonium vestiarium snail shell as an efficient adsorbent for treatment of wastewater containing Co (II). *3 Biotech* **2019**, *9*, 78. [CrossRef]
52. Maheshwari, U.; Mathesan, B.; Gupta, S. Efficient adsorbent for simultaneous removal of Cu(II), Zn(II) and Cr(VI): Kinetic, thermodynamics and mass transfer mechanism. *Process Saf. Environ. Prot.* **2015**, *98*, 198–210. [CrossRef]

53. He, H.; Meng, X.; Yue, Q.; Yin, W.; Gao, Y.; Fang, P.; Shen, L. Thiol-ene click chemistry synthesis of a novel magnetic mesoporous silica/chitosan composite for selective Hg(II) capture and high catalytic activity of spent Hg(II) adsorbent. *Chem. Eng. J.* **2021**, *405*, 126743. [CrossRef]
54. Kumar, A.S.K.; Jiang, S.-J. Preparation and characterization of exfoliated graphene oxide–l-cystine as an effective adsorbent of Hg(ii) adsorption. *RSC Adv.* **2015**, *5*, 6294–6304. [CrossRef]
55. Kadirvelu, K.; Senthilkumar, P.; Thamaraiselvi, K.; Subburam, V. Activated carbon prepared from biomass as adsorbent: Elimination of Ni(II) from aqueous solution. *Bioresour. Technol.* **2001**, *81*, 87–90. [CrossRef]
56. Huang, G.; Wang, D.; Ma, S.; Chen, J.; Jiang, L.; Wang, P. A new, low-cost adsorbent: Preparation, characterization, and adsorption behavior of Pb(II) and Cu(II). *J. Colloid Interface Sci.* **2015**, *445*, 294–302. [CrossRef] [PubMed]
57. Zou, X.; Zhao, Y.; Zhang, Z. Preparation of hydroxyapatite nanostructures with different morphologies and adsorption behavior on seven heavy metals ions. *J. Contam. Hydrol.* **2019**, *226*, 103538. [CrossRef]
58. Smičiklas, I.; Onjia, A.; Raičević, S.; Janaćković, Đ.; Mitrić, M. Factors influencing the removal of divalent cations by hydroxyapatite. *J. Hazard. Mater.* **2008**, *152*, 876–884. [CrossRef]
59. Yang, L.; Zhong, W.; Cui, J.; Wei, Z.; Wei, W. Enhanced removal of Cu (II) ions from aqueous solution by poorly crystalline hydroxyapatite nanoparticles. *J. Dispers. Sci. Technol.* **2016**, *37*, 956–968. [CrossRef]
60. Guo, J.; Han, Y.; Mao, Y.; Wickramaratne, M.N. Influence of alginate fixation on the adsorption capacity of hydroxyapatite nanocrystals to Cu^{2+} ions. *Colloids Surf. A Physicochem. Eng. Asp.* **2017**, *529*, 801–807. [CrossRef]
61. Corami, A.; Mignardi, S.; Ferrini, V. Cadmium removal from single- and multi-metal solutions by sorption on hydroxyapatite. *J. Colloid Interface Sci.* **2008**, *317*, 402–408. [CrossRef]
62. Crini, G. Kinetic and equilibrium studies on the removal of cationic dyes from aqueous solution by adsorption onto a cyclodextrin polymer. *Dyes Pigment.* **2008**, *77*, 415–426. [CrossRef]
63. Zhu, R.; Lai, X.; Halpert, J.E.; Yu, R.; Wang, D. ChemInform Abstract: Hierarchical Hydroxyapatite Microspheres Composed of Nanorods and Their Competitive Sorption Behavior for Heavy Metal Ions. *Eur. J. Inorg. Chem.* **2012**, *43*, 2665–2668. [CrossRef]
64. Sandrine, B.; Ange, N.; Didier, B.-A.; Eric, C.; Patrick, S. Removal of aqueous lead ions by hydroxyapatites: Equilibria and kinetic processes. *J. Hazard. Mater.* **2007**, *139*, 443–446. [CrossRef] [PubMed]
65. Xu, Y.; Schwartz, F.W.; Traina, S.J. Sorption of Zn^{2+} and Cd^{2+} on Hydroxyapatite Surfaces. *Environ. Sci. Technol.* **1994**, *28*, 1472–1480. [CrossRef] [PubMed]
66. Jung, K.-W.; Lee, S.Y.; Choi, J.-W.; Lee, Y.J. A facile one-pot hydrothermal synthesis of hydroxyapatite/biochar nanocomposites: Adsorption behavior and mechanisms for the removal of copper(II) from aqueous media. *Chem. Eng. J.* **2019**, *369*, 529–541. [CrossRef]
67. Mortada, W.I.; Kenawy, I.M.; Abdelghany, A.M.; Ismail, A.M.; Donia, A.F.; Nabieh, K.A. Determination of Cu^{2+}, Zn^{2+} and Pb^{2+} in biological and food samples by FAAS after preconcentration with hydroxyapatite nanorods originated from eggshell. *Mater. Sci. Eng. C* **2015**, *52*, 288–296. [CrossRef]
68. LeGeros, R.Z.; Legeros, J.P. *Phosphate Minerals in Human Tissues*; Springer: Berlin/Heidelberg, Germany, 1984; pp. 351–385. [CrossRef]
69. Oulguidoum, A.; Bouiahya, K.; Bouyarmane, H.; Talbaoui, A.; Nunzi, J.-M.; Laghzizil, A. Mesoporous nanocrystalline sulfonated hydroxyapatites enhance heavy metal removal and antimicrobial activity. *Sep. Purif. Technol.* **2021**, *255*, 117777. [CrossRef]
70. Cécille, L. Radioactive Waste Management and Disposal. In Proceedings of the Third European Community Conference on Radioactive Waste Management and Disposal, Luxembourg, 17–21 September 1990.
71. Handley-Sidhu, S.; Renshaw, J.C.; Yong, P.; Kerley, R.; Macaskie, L.E. Nano-crystalline hydroxyapatite bio-mineral for the treatment of strontium from aqueous solutions. *Biotechnol. Lett.* **2011**, *33*, 79–87. [CrossRef]
72. Kim, J.; Sambudi, N.S.; Cho, K. Removal of Sr^{2+} using high-surface-area hydroxyapatite synthesized by non-additive in-situ precipitation. *J. Environ. Manag.* **2019**, *231*, 788–794. [CrossRef]
73. Krestou, A.; Xenidis, A.; Panias, D. Mechanism of aqueous uranium(VI) uptake by hydroxyapatite. *Miner. Eng.* **2004**, *17*, 373–381. [CrossRef]
74. Li, S.; Bai, H.; Wang, J.; Jing, X.; Liu, Q.; Zhang, M.; Chen, R.; Liu, L.; Jiao, C. In situ grown of nano-hydroxyapatite on magnetic CaAl-layered double hydroxides and its application in uranium removal. *Chem. Eng. J.* **2012**, *193–194*, 372–380. [CrossRef]
75. Narwade, V.N.; Khairnar, R.S. Cobalt adsorption on the nano-hydroxyapatite matrix: Isotherm and kinetic studies. *Bull. Pol. Acad. Sci. Tech. Sci.* **2017**, *65*, 131–137. [CrossRef]
76. Rigali, M.J.; Brady, P.V.; Moore, R.C. Radionuclide removal by apatite. *Am. Miner.* **2016**, *101*, 2611–2619. [CrossRef]
77. Simon, F.G.; Biermann, V.; Peplinski, B. Uranium removal from groundwater using hydroxyapatite. *Appl. Geochem.* **2008**, *23*, 2137–2145. [CrossRef]
78. Su, M.; Tsang, D.C.; Ren, X.; Shi, Q.; Tang, J.; Zhang, H.; Kong, L.; Hou, L.; Song, G.; Chen, D. Removal of U(VI) from nuclear mining effluent by porous hydroxyapatite: Evaluation on characteristics, mechanisms and performance. *Environ. Pollut.* **2019**, *254*, 112891. [CrossRef]
79. Teterin, Y.A.; Kazakov, A.G.; Teterin, A.Y.; Severin, A.V.; Dvorak, S.V.; Maslakov, K.I.; Ivanov, K.E. The study of Zr adsorption on nanodispersed hydroxyapatite: X-ray photoelectron study. *J. Radioanal. Nucl. Chem. Artic.* **2019**, *321*, 341–347. [CrossRef]
80. Thomson, B.M.; Smith, C.L.; Busch, R.D.; Siegel, M.D.; Baldwin, C. Removal of Metals and Radionuclides Using Apatite and Other Natural Sorbents. *J. Environ. Eng.* **2003**, *129*, 492–499. [CrossRef]

81. Tran, T.; Kim, J.; Park, J.-S.; Chung, Y.; Han, J.; Oh, S.; Kang, S. Novel Hydroxyapatite Beads for the Adsorption of Radionuclides from Decommissioned Nuclear Power Plant Sites. *Appl. Sci.* **2021**, *11*, 1746. [CrossRef]
82. Lee, G.; Lee, W. Adsorption of uranium from groundwater using heated aluminum oxide particles. *J. Water Process Eng.* **2021**, *40*, 101790. [CrossRef]
83. Mahmoud, M.A. Adsorption of U (VI) ions from aqueous solution using silicon dioxide nanopowder. *J. Saudi Chem. Soc.* **2018**, *22*, 229–238. [CrossRef]
84. El Afifi, E.; Attallah, M.; Borai, E. Utilization of natural hematite as reactive barrier for immobilization of radionuclides from radioactive liquid waste. *J. Environ. Radioact.* **2016**, *151*, 156–165. [CrossRef]
85. Yusan, S.; Akyil, S. Sorption of uranium(VI) from aqueous solutions by akaganeite. *J. Hazard. Mater.* **2008**, *160*, 388–395. [CrossRef] [PubMed]
86. Yusan, S.; Erenturk, S.A. Adsorption equilibrium and kinetics of U(VI) on beta type of akaganeite. *Desalination* **2010**, *263*, 233–239. [CrossRef]
87. Mimura, H.; Kanno, T. Distribution and Fixation of Cesium and Strontium in Zeolite A and Chabazite. *J. Nucl. Sci. Technol.* **1985**, *22*, 284–291. [CrossRef]
88. Alahabadi, A.; Singh, P.; Raizada, P.; Anastopooulos, I.; Sivamani, S.; Dotto, G.L.; Landarani, M.; Ivanets, A.; Kyzas, G.Z.; Hosseini-Bandegharaei, A. Activated carbon from wood wastes for the removal of uranium and thorium ions through modification with mineral acid. *Colloids Surf. A Physicochem. Eng. Asp.* **2020**, *607*, 125516. [CrossRef]
89. Wang, J.; Huo, Y.; Ai, Y. Experimental and theoretical studies of chitosan modified titanium dioxide composites for uranium and europium removal. *Cellulose* **2020**, *27*, 7765–7777. [CrossRef]
90. Smičiklas, I.; Dimović, S.; Plećaš, I.; Mitrić, M. Removal of Co2+ from aqueous solutions by hydroxyapatite. *Water Res.* **2006**, *40*, 2267–2274. [CrossRef]
91. Li, W.-A.; Peng, Y.-C.; Ma, W.; Huang, X.-Y.; Feng, M.-L. Rapid and selective removal of Cs^+ and Sr^{2+} ions by two zeolite-type sulfides via ion exchange method. *Chem. Eng. J.* **2022**, *442*, 136377. [CrossRef]
92. Han, M.; Kong, L.; Hu, X.; Chen, D.; Xiong, X.; Zhang, H.; Su, M.; Diao, Z.-H.; Ruan, Y. Phase migration and transformation of uranium in mineralized immobilization by wasted bio-hydroxyapatite. *J. Clean. Prod.* **2018**, *197*, 886–894. [CrossRef]
93. Su, M.; Li, H.; Liu, Z.; Peng, H.; Huang, S.; Zhou, Y.; Liao, C.; Song, G.; Chen, D. Highly-efficient and easy separation of γ-Fe_2O_3 selectively adsorbs U(VI) in waters. *Environ. Res.* **2022**, *210*, 112917. [CrossRef]
94. Kong, L.; Ruan, Y.; Zheng, Q.; Su, M.; Diao, Z.; Chen, D.; Hou, L.; Chang, X.; Shih, K. Uranium extraction using hydroxyapatite recovered from phosphorus containing wastewater. *J. Hazard. Mater.* **2020**, *382*, 120784. [CrossRef]
95. Fuller, C.C.; Bargar, J.R.; Davis, J.A.; Piana, M.J. Mechanisms of Uranium Interactions with Hydroxyapatite: Implications for Groundwater Remediation. *Environ. Sci. Technol.* **2002**, *36*, 158–165. [CrossRef] [PubMed]
96. Yang, D.; Wang, X.; Song, G.; Zhao, G.; Chen, Z.; Yu, S.; Wang, X. One-pot synthesis of arginine modified hydroxyapatite carbon microsphere composites for efficient removal of U (VI) from aqueous solutions. *Sci. Bull.* **2017**, *62*, 1609–1618. [CrossRef]
97. Kanel, S.R.; Clement, T.P.; Barnett, M.O.; Goltz, M. Nano-Scale Hydroxyapatite: Synthesis, Two-Dimensional Transport Experiments, and Application for Uranium Remediation. *J. Nanotechnol.* **2011**, *2011*, 462382. [CrossRef]
98. Salvestrini, S.; Fenti, A.; Chianese, S.; Iovino, P.; Musmarra, D. Diclofenac sorption from synthetic water: Kinetic and thermodynamic analysis. *J. Environ. Chem. Eng.* **2020**, *8*, 104105. [CrossRef]
99. Hettithanthri, O.; Rajapaksha, A.U.; Keerthanan, S.; Ramanayaka, S.; Vithanage, M. Colloidal biochar for enhanced adsorption of antibiotic ciprofloxacin in aqueous and synthetic hydrolyzed human urine matrices. *Chemosphere* **2022**, *297*, 133984. [CrossRef]
100. Nguyen, V.-T.; Vo, T.-D.; Nguyen, T.-B.; Dat, N.D.; Huu, B.T.; Nguyen, X.-C.; Tran, T.; Le, T.-N.; Duong, T.-G.; Bui, M.-H.; et al. Adsorption of norfloxacin from aqueous solution on biochar derived from spent coffee ground: Master variables and response surface method optimized adsorption process. *Chemosphere* **2022**, *288*, 132577. [CrossRef]
101. Djebbar, M.; Djafri, F.; Bouchekara, M.; Djafri, A. Adsorption of phenol on natural clay. *Appl. Water Sci.* **2012**, *2*, 77–86. [CrossRef]
102. Chen, J.; Li, J.; Zeng, Q.; Li, H.; Chen, F.; Hou, H.; Lan, J. Efficient removal of tetracycline from aqueous solution by Mn-N-doped carbon aerogels: Performance and mechanism. *J. Mol. Liq.* **2022**, *358*, 119153. [CrossRef]
103. Lin, K.; Pan, J.; Chen, Y.; Cheng, R.; Xu, X. Study the adsorption of phenol from aqueous solution on hydroxyapatite nanopowders. *J. Hazard. Mater.* **2009**, *161*, 231–240. [CrossRef]
104. Wei, W.; Sun, R.; Jin, Z.; Cui, J.; Wei, Z. Hydroxyapatite–gelatin nanocomposite as a novel adsorbent for nitrobenzene removal from aqueous solution. *Appl. Surf. Sci.* **2014**, *292*, 1020–1029. [CrossRef]
105. Wei, W.; Sun, R.; Cui, J.; Wei, Z. Removal of nitrobenzene from aqueous solution by adsorption on nanocrystalline hydroxyapatite. *Desalinatio* **2010**, *263*, 89–96. [CrossRef]
106. Wu, Y.; Qi, H.; Li, B.; Zhanhua, H.; Li, W.; Liu, S. Novel hydrophobic cotton fibers adsorbent for the removal of nitrobenzene in aqueous solution. *Carbohydr. Polym.* **2017**, *155*, 294–302. [CrossRef] [PubMed]
107. Ciobanu, G.; Barna, S.; Harja, M. Kinetic and equilibrium studies on adsorption of Reactive Blue 19 dye from aqueous solutions by nanohydroxyapatite adsorbent. *Arch. Environ. Prot.* **2016**, *42*, 3–11. [CrossRef]
108. Nguyen, V.C.; Pho, Q.H. Preparation of Chitosan Coated Magnetic Hydroxyapatite Nanoparticles and Application for Adsorption of Reactive Blue 19 and Ni^{2+} Ions. *Sci. World J.* **2014**, *2014*, 273082. [CrossRef] [PubMed]
109. Vasugi, G.; Thamizhavel, A.; Girija, E.K. Surface modification of hydroxyapatite by yttrium ion substitution for adsorption of reactive red dye. *J. Mater. Environ. Sci.* **2017**, *8*, 714–723.

110. Gulnaz, O.; Sahmurova, A.; Kama, S. Removal of Reactive Red 198 from aqueous solution by Potamogeton crispus. *Chem. Eng. J.* **2011**, *174*, 579–585. [CrossRef]
111. Allam, K.; El Bouari, A.; Belhorma, B.; Bih, L. Removal of Methylene Blue from Water Using Hydroxyapatite Submitted to Microwave Irradiation. *J. Water Resour. Prot.* **2016**, *8*, 358–371. [CrossRef]
112. Liu, X.-J.; Li, M.-F.; Singh, S.K. Manganese-modified lignin biochar as adsorbent for removal of methylene blue. *J. Mater. Res. Technol.* **2021**, *12*, 1434–1445. [CrossRef]
113. Hou, H.; Zhou, R.; Wu, P.; Wu, L. Removal of Congo red dye from aqueous solution with hydroxyapatite/chitosan composite. *Chem. Eng. J.* **2012**, *211–212*, 336–342. [CrossRef]
114. Chawla, S.; Uppal, H.; Yadav, M.; Bahadur, N.; Singh, N. Zinc peroxide nanomaterial as an adsorbent for removal of Congo red dye from waste water. *Ecotoxicol. Environ. Saf.* **2017**, *135*, 68–74. [CrossRef]
115. Oliveira, C.; de Oliveira, A.L.M.; Chantelle, L.; Landers, R.; Medina-Carrasco, S.; Orta, M.D.M.; Filho, E.C.S.; Fonseca, M.G.F. Zinc (II) modified hydroxyapatites for tetracycline removal: Zn (II) doping or ZnO deposition and their influence in the adsorption. *Polyhedron* **2021**, *194*, 114879. [CrossRef]
116. Das, K.C.; Dhar, S.S.; Thakurata, D.G.; Das, J. Sn(II) inserted on hydroxyapatite encapsulated nickel ferrite ($NiFe_2O_4$@HAp-Sn^{2+}): A novel nanocomposite for the effective photo-degradation of rhodamine B dye. *J. Clean. Prod.* **2020**, *290*, 125172. [CrossRef]
117. Ragab, A.; Ahmed, I.; Bader, D. The Removal of Brilliant Green Dye from Aqueous Solution Using Nano Hydroxyapatite/Chitosan Composite as a Sorbent. *Molecules* **2019**, *24*, 847. [CrossRef] [PubMed]
118. Guan, Y.; Cao, W.; Guan, H.; Lei, X.; Wang, X.; Tu, Y.; Marchetti, A.; Kong, X. A novel polyalcohol-coated hydroxyapatite for the fast adsorption of organic dyes. *Colloids Surf. A Physicochem. Eng. Asp.* **2018**, *548*, 85–91. [CrossRef]
119. World Health Organization. *Guidelines for Drinking-Water Quality [Electronic Resource]: Incorporating 1st and 2nd Addenda, Vol.1, Recommendations*, 3rd ed.; World Health Organization: Geneva, Switzerland, 2008. Available online: https://apps.who.int/iris/handle/10665/204411 (accessed on 20 June 2022).
120. Meenakshi, S.; Viswanathan, N. Identification of selective ion-exchange resin for fluoride sorption. *J. Colloid Interface Sci.* **2007**, *308*, 438–450. [CrossRef]
121. Viswanathan, N.; Meenakshi, S. Selective fluoride adsorption by a hydrotalcite/chitosan composite. *Appl. Clay Sci.* **2010**, *48*, 607–611. [CrossRef]
122. Lu, N.C.; Liu, J. Removal of phosphate and fluoride from wastewater by a hybrid precipitation–microfiltration process. *Sep. Purif. Technol.* **2010**, *74*, 329–335. [CrossRef]
123. Amor, Z.; Bariou, B.; Mameri, N.; Taky, M.; Nicolas, S.; Elmidaoui, A. Fluoride removal from brackish water by electrodialysis. *Desalination* **2001**, *133*, 215–223. [CrossRef]
124. Simons, R. Trace element removal from ash dam waters by nanofiltration and diffusion dialysis. *Desalination* **1993**, *89*, 325–341. [CrossRef]
125. Bejaoui, I.; Mnif, A.; Hamrouni, B. Performance of Reverse Osmosis and Nanofiltration in the Removal of Fluoride from Model Water and Metal Packaging Industrial Effluent. *Sep. Sci. Technol.* **2014**, *49*, 1135–1145. [CrossRef]
126. Turner, B.D.; Binning, P.; Stipp, S.L.S. Fluoride Removal by Calcite: Evidence for Fluorite Precipitation and Surface Adsorption. *Environ. Sci. Technol.* **2005**, *39*, 9561–9568. [CrossRef] [PubMed]
127. Nath, S.K.; Dutta, R.K. Fluoride removal from water using crushed limestone. *Indian J. Chem. Technol.* **2010**, *17*, 120–125. Available online: http://nopr.niscair.res.in/handle/123456789/7632 (accessed on 20 June 2022).
128. Gao, S.; Cui, J.; Wei, Z. Study on the fluoride adsorption of various apatite materials in aqueous solution. *J. Fluor. Chem.* **2009**, *130*, 1035–1041. [CrossRef]
129. Sundaram, C.S.; Viswanathan, N.; Meenakshi, S. Fluoride sorption by nano-hydroxyapatite/chitin composite. *J. Hazard. Mater.* **2009**, *172*, 147–151. [CrossRef] [PubMed]
130. Sundaram, C.S.; Viswanathan, N.; Meenakshi, S. Defluoridation chemistry of synthetic hydroxyapatite at nano scale: Equilibrium and kinetic studies. *J. Hazard. Mater.* **2008**, *155*, 206–215. [CrossRef] [PubMed]
131. Pandi, K.; Viswanathan, N. Synthesis of alginate bioencapsulated nano-hydroxyapatite composite for selective fluoride sorption. *Carbohydr. Polym.* **2014**, *112*, 662–667. [CrossRef]
132. Pandi, K.; Viswanathan, N. In situ precipitation of nano-hydroxyapatite in gelatin polymatrix towards specific fluoride sorption. *Int. J. Biol. Macromol.* **2015**, *74*, 351–359. [CrossRef]
133. Pandi, K.; Viswanathan, N. Enhanced defluoridation and facile separation of magnetic nano-hydroxyapatite/alginate composite. *Int. J. Biol. Macromol.* **2015**, *80*, 341–349. [CrossRef]
134. Pandi, K.; Viswanathan, N. Synthesis and applications of eco-magnetic nano-hydroxyapatite chitosan composite for enhanced fluoride sorption. *Carbohydr. Polym.* **2015**, *134*, 732–739. [CrossRef]
135. Tor, A. Removal of fluoride from an aqueous solution by using montmorillonite. *Desalination* **2006**, *201*, 267–276. [CrossRef]
136. Prabhu, S.M.; Meenakshi, S. Enriched fluoride sorption using chitosan supported mixed metal oxides beads: Synthesis, characterization and mechanism. *J. Water Process Eng.* **2014**, *2*, 96–104. [CrossRef]
137. Karthikeyan, G.; Ilango, S.S. Fluoride sorption using Morringa Indica-based activated carbon. *J. Environ. Health Sci. Eng.* **2007**, *4*, 21–28.
138. Cheng, J.; Meng, X.; Jing, C.; Hao, J. La3+-modified activated alumina for fluoride removal from water. *J. Hazard. Mater.* **2014**, *278*, 343–349. [CrossRef] [PubMed]

139. Wei, L.; Zietzschmann, F.; Rietveld, L.C.; van Halem, D. Fluoride removal by Ca-Al-CO3 layered double hydroxides at environmentally-relevant concentrations. *Chemosphere* **2020**, *243*, 125307. [CrossRef]
140. Nabbou, N.; Belhachemi, M.; Boumelik, M.; Merzougui, T.; Lahcene, D.; Harek, Y.; Zorpas, A.A.; Jeguirim, M. Removal of fluoride from groundwater using natural clay (kaolinite): Optimization of adsorption conditions. *Comptes Rendus Chim.* **2019**, *22*, 105–112. [CrossRef]
141. Liang, P.; An, R.; Li, R.; Wang, D. Comparison of La^{3+} and mixed rare earths-loaded magnetic chitosan beads for fluoride adsorption. *Int. J. Biol. Macromol.* **2018**, *111*, 255–263. [CrossRef]
142. Mehta, D.; Mondal, P.; Saharan, V.K.; George, S. In-vitro synthesis of marble apatite as a novel adsorbent for removal of fluoride ions from ground water: An ultrasonic approach. *Ultrason. Sonochem.* **2018**, *40*, 664–674. [CrossRef]
143. Dzieniszewska, A.; Nowicki, J.; Rzepa, G.; Kyziol-Komosinska, J.; Semeniuk, I.; Kiełkiewicz, D.; Czupioł, J. Adsorptive removal of fluoride using ionic liquid-functionalized chitosan—Equilibrium and mechanism studies. *Int. J. Biol. Macromol.* **2022**, *210*, 483–493. [CrossRef]
144. Zare, K.; Banihashemi, A.; Javanbakht, V.; Mohammadifard, H. Fluoride removal from aqueous solutions using alginate beads modified with functionalized silica particles. *J. Mol. Struct.* **2022**, *1252*, 132217. [CrossRef]
145. Nayak, B.; Samant, A.; Patel, R.; Misra, P.K. Comprehensive Understanding of the Kinetics and Mechanism of Fluoride Removal over a Potent Nanocrystalline Hydroxyapatite Surface. *ACS Omega* **2017**, *2*, 8118–8128. [CrossRef]
146. Deng, L.; Wang, Y.; Zhang, X.; Zhou, J.; Huang, T. Defluoridation by fluorapatite crystallization in a fluidized bed reactor under alkaline groundwater condition. *J. Clean. Prod.* **2020**, *272*, 122805. [CrossRef]
147. Jiménez-Reyes, M.; Solache-Ríos, M. Sorption behavior of fluoride ions from aqueous solutions by hydroxyapatite. *J. Hazard. Mater.* **2010**, *180*, 297–302. [CrossRef] [PubMed]
148. Prabhu, S.M.; Meenakshi, S. Synthesis of surface coated hydroxyapatite powders for fluoride removal from aqueous solution. *Powder Technol.* **2014**, *268*, 306–315. [CrossRef]
149. Chen, Z.; Liu, Y.; Mao, L.; Gong, L.; Sun, W.; Feng, L. Effect of cation doping on the structure of hydroxyapatite and the mechanism of defluoridation. *Ceram. Int.* **2018**, *44*, 6002–6009. [CrossRef]
150. Nie, Y.; Hu, C.; Kong, C. Enhanced fluoride adsorption using Al (III) modified calcium hydroxyapatite. *J. Hazard. Mater.* **2012**, *233–234*, 194–199. [CrossRef]

nanomaterials

MDPI

Article

A Novel Electrochemical Sensor for Detection of Nicotine in Tobacco Products Based on Graphene Oxide Nanosheets Conjugated with (1,2-Naphthoquinone-4-Sulphonic Acid) Modified Glassy Carbon Electrode

M. Abd-Elsabour [1], Hesham M. Alsoghier [1], Abdulrahman G. Alhamzani [2], Mortaga M. Abou-Krisha [1,2,*], Tarek A. Yousef [2,3] and Hytham F. Assaf [1,*]

[1] Chemistry Department, Faculty of Science, South Valley University, Qena 83523, Egypt; m.sabour28@sci.svu.edu.eg (M.A.-E.); hgmohmed@gmail.com (H.M.A.)

[2] Chemistry Department, College of Science, Imam Mohammad Ibn Saud Islamic University (IMSIU), Riyadh 11623, Saudi Arabia; agalhamzani@imamu.edu.sa (A.G.A.); tayousef@imamu.edu.sa (T.A.Y.)

[3] Mansoura Laboratory, Department of Toxic and Narcotic Drug, Forensic Medicine, Medicolegal Organization, Ministry of Justice, Mansoura 35511, Egypt

* Correspondence: mmaboukrisha@imamu.edu.sa (M.M.A.-K.); elprof_3ssaf@yahoo.com (H.F.A.)

Abstract: A simple electrochemical sensor for nicotine (NIC) detection was performed. The sensor based on a glassy carbon electrode (GCE) was modified by (1,2-naphthoquinone-4-sulphonic acid)(Nq) decorated by graphene oxide (GO) nanocomposite. The synthesized (GO) nanosheets were characterized using X-ray diffraction (XRD), Raman spectroscopy, scanning electron microscope (SEM), transmission electron microscope (TEM), FT-IR, and UV-Visible Spectroscopy. The insertion of Nq with GO nanosheets on the surface of GCE displayed high electrocatalytic activity towards NIC compared to the bare GCE. NIC determination was performed under the optimum conditions using 0.10 M of Na_2SO_4 as a supporting electrolyte with pH 8.0 at a scan rate of 100 mV/s using both cyclic voltammetry (CV) and differential pulse voltammetry (DPV). This electrochemical sensor showed an excellent result for NIC detection. The oxidation peak current increased linearly with a 6.5–245 µM of NIC with $R^2 = 0.9999$. The limit of detection was 12.7 nM. The fabricated electrode provided satisfactory stability, reproducibility, and selectivity for NIC oxidation. The reliable GO/Nq/GCE sensor was successfully applied for detecting NIC in the tobacco product and a urine sample.

Keywords: adapted glassy carbon sensor; cigarette; differential pulse voltammetry; graphene oxide nanosheets synthesis; nicotine

Citation: Abd-Elsabour, M.; Alsoghier, H.M.; Alhamzani, A.G.; Abou-Krisha, M.M.; Yousef, T.A.; Assaf, H.F. A Novel Electrochemical Sensor for Detection of Nicotine in Tobacco Products Based on Graphene Oxide Nanosheets Conjugated with (1,2-Naphthoquinone-4-Sulphonic Acid) Modified Glassy Carbon Electrode. *Nanomaterials* **2022**, *12*, 2354. https://doi.org/10.3390/nano12142354

Academic Editors: Jihoon Lee, Ming-Yu Li and Dong-Joo Kim

Received: 21 April 2022
Accepted: 6 July 2022
Published: 9 July 2022

1. Introduction

Nicotine(S)3-(1-methylpyrrolidin-2-yl) pyridine (NIC) is one of the fatal toxicities of purine alkaloids which represents about 2–8% of the tobacco plants (Nicotiana genus such as N. Tabacum, N. Rustica, and N. Glauca) [1–5]. It is an oily, hygroscopic, colorless pale yellow liquid that quickly dissolves in water at room temperature [6]. Additionally, NIC is rapidly absorbed in humans and directly attacks the nervous system. The frequent intake of NIC creates many potentially harmful diseases and effects on human health, such as increased blood pressure and heartbeat, reduced healing rates, and vascular disease [7–9]. Moreover, it might lead to lung, nose, kidney, stomach, bladder, and colon cancer [10,11]. However, it can treat Alzheimer's and Parkinson's diseases [12,13].

Hence, great attention has been paid to the determination of NIC, especially in medicine, toxicology, and the tobacco industry. To date, several analytical techniques have been reported for the measurement of NIC, including high-performance liquid chromatography [14], gas chromatography [15], spectrophotometry [16], spectrofluorimetry [17], radioimmunoassay [18], amperometric assay [19], and capillary electrophoresis [4]. Unfortunately, most of these methods possess numerous disadvantages, such as being expensive and time-consuming and requiring several chemical treatment steps and many organic solvents [9,20,21]. Moreover, limited biosensors have been used to analyze NIC due to the high cost of enzymes [22,23].

On the other hand, electrochemical techniques are more convenient for detecting NIC due to their practical advantages, such as low-cost instruments, high sensitivity, good selectivity, simple operation, and rapid measurement time [8,24]. The voltammetric determination of NIC at bare electrodes is hindered by slow electrode kinetics. This is not only the electro-oxidation or reduction reaction of NIC occurring at highly positive or negative redox potentials leading to poorly reproducible results. Chemically modified electrodes are the key to enhance the electrocatalytic ability toward NIC determination due to their higher sensitivity and selectivity than typical electrodes [25].

(1,2-naphthoquinone-4-sulphonic acid) is an organic layer on the surface of the electrode in a rich active group, where there are higher chances of adsorption with the analyte. This leads to enhance the conductivity and increasing the effective surface area of the glassy carbon electrode (GCE).

Additionally, graphene oxide (GO) nanosheets have attracted much attention and are considered an excellent candidate for electrode surface modification, high specific surface area, remarkable electrical conductivity, enhanced electrocatalytic, and high mechanical properties [26–28]. The unique conjugation between a film of Nq with GO nanosheets on the surface of the GCE can improve the detecting efficiency, stability, reproducibility, and electrocatalytic properties of electrodes [29–31].

Our work aims to benefit from the conjugation between Nq layer with GO nanosheets on the surface of a glassy carbon electrode to determine the NIC for the first time. As far as we know, there are no papers of study of the electrochemical behaviors of nicotine at the GO/Nq/GCE. The mixed modification facilitates enhancing the quality of the glassy carbon electrode. This method was applied to determine Nicotine(S)3-(1-methylpyrrolidin-2-yl) pyridine, NIC. In sequence, actual samples of tobacco products were studied in an aqueous media, and satisfying results were obtained with the proposed sensor.

2. Experimental

2.1. Materials and Reagents

Graphene powder (<20 µm) and 1,2-naphthoquinone-4-sulphonic acid were purchased from Sigma Aldrich. Aldrich's stock solution of 6.2 mM NIC ($C_{10}H_{14}N_2$, 98%) was freshly prepared using deionized water and kept in the dark at 4 °C. Before use in the experiments, the stock solution was diluted using sodium sulphate (Na_2SO_4, 0.10 M) purchased from Sigma Aldrich as a supporting electrolyte. All other chemical reagents were of analytical grade and used as received without any further purification.

2.2. Apparatus

The voltammetric experimental conditions have been described in detail in previous literature [32]. Briefly, EG&G Princeton applied research potentiostat/galvanostat model 263 (USA) linked with a PC using 352 corrosion software [32,33]. A conventional three-electrode cell consisted of a GO/Nq/GCE as the working electrode, a saturated Ag/AgCl reference electrode, and an auxiliary electrode made of a bright platinum wire. A pH meter (Euteoh-India) was employed for the pH measurements. The synthesized GO was characterized by powder X-ray diffraction (XRD, X'Pert3 Powder, PA Analytical, Netherlands), Raman spectroscopy, a field-emission scanning electron microscope (SEM, QUANTA FEG250, Tokyo, Japan), transmission electron microscope (TEM, JEOL 2100 HRTEM 200V, Tokyo, Japan), FT-IR and UV-Visible spectroscopy (Perkin Elmer, Waltham, WA, USA). In this study, all measurements were carried out at room temperature.

2.3. Synthesis of GO

Synthesis of GO nanosheets were prepared according to the modified Hummers' method [34–36]. Specifically, in an ice-water bath, 1.0 g of natural graphene powder was mixed with the concentrated H_2SO_4(30 mL) and $NaNO_3$(3g). Then, 3.0 g of $KMnO_4$ was slowly added to keep the oxidation reaction temperature between 10 and 25 °C (Scheme 1). Subsequently, 100 mL of deionized water and 60 mL of 35% H_2O_2 were carefully added to reduce residual $KMnO_4$ and MnO_2. Afterward, the mixture was stirred for 30 min and then centrifuged. Finally, the product was filtered and dried in the oven at 50 °C overnight. According to the literature, GO nanosheets were synthesized from the resulting graphene oxide by magnetic stirring and heating [37,38]. Briefly, 0.50 g of dried graphene oxide nanocomposite powder was stirred with 50 mL of deionized water at 70 °C using magnetic stirring at 400 r.p.m for 12 h [38–40].

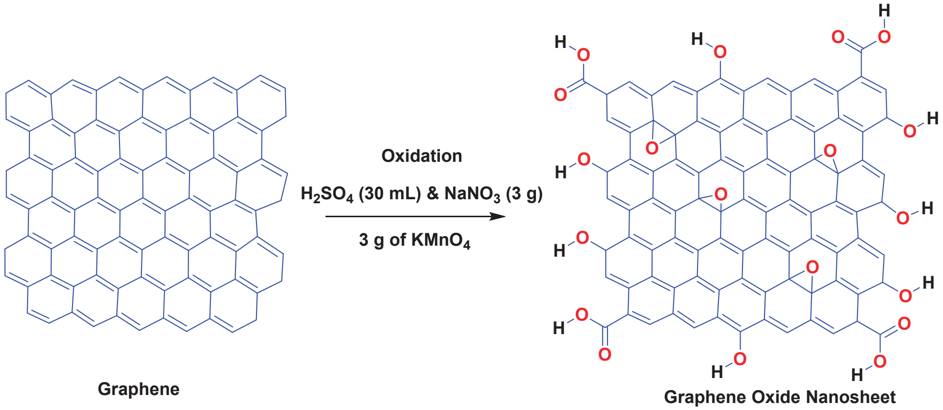

Scheme 1. Synthesis of GO using modified Hummers' method.

2.4. GO/Nq/GCE Fabrication

Before modification, a GCE (1 mm diameter) was sequentially polished with alumina powder (3 µm) to a mirror finish surface and ultrasonically cleaned with water: ethanol for 2 min and rinsed with deionized water. The modification of GCE by a layer of Nq can be obtained by electrodeposition on the cleaned surface of GCE. This was performed by dipping GCE in 0.10 M PBS containing 3.33 mM of Nq monomer and was conditioned by cyclic sweeping from −1.25 to 1.3 V vs. Ag/AgCl for 15 cycles (Section 3.2) [41]. The Nq/GCE was carefully cleaned with deionized water and dried in the air. On the other hand, the Nq/GCE was decorated by prepared GO nanosheets by dissolving the GO nanosheets in deionized water to form a suspended solution subjected to an ultrasonic device for 30 min to form a homogenous suspended solution. Then, 5.0 µL of the homogenous suspended solution (2.0 mg/mL) was cast on the surface of Nq/GCE to form GO/Nq/GCE. Finally, the GO/Nq/GCE was carefully cleaned with deionized water and dried in air. To calculate the activate surface of the different electrodes, the cyclic voltammetry of 5.0 mM of $K_3Fe(CN)_6$as the redox at the surface of bare GCE, Nq/GCE, andGO/Nq/GCE at different scan rates (from 50 to 300 mV/s) were recorded. There is a direct correlation between peak current and scan rate. By increasing the scan rate, the peak current increased for each electrode. By deriving the relationship between Ip and the square root of scan rate for different electrodes. Straight lines were obtained. Moreover, by compensation of the slope in the following Randles–Sevcik equation used [41].

$$\mathbf{Ip = 0.446\ nFAC(nFD\nu/RT)^{1/2}} \tag{1}$$

where R is the universal gas constant (J/mol.K), n is the number of electrons, C is the concentration of the electroactive species (mM), F is the Faraday constant (C/mol), ν is the scan rate (mV/s), T is the temperature in Kelvin, Ip is the peak current, D isthe diffusion coefficient (cm^2/s) and A(cm^2) is the electroactive surface area of the different types of electrodes. The accurate value of D is 5.6×10^{-6} cm^2/s [42].So the values of active surface area(A cm^2) were estimated for bare GCE, Nq/GCE, andGO/Nq/GCE as 0.0126 cm^2, 0.033 cm^2,and0.0425 cm^2, respectively. So GO/Nq/GCE provides superior conductivity to other electrodes according to the active surface area data.

2.5. Sample Preparation

For the cigarette samples analysis, leaves were boiled for 5 min in 50 mL of deionized water. The mixture was later cooled and filtered to remove suspended impurities, followed by centrifugation. Decanting the supernatant centrifuged solution resulted in a clean dark brown colored solution. A human urine sample was provided by a project team member and diluted 100 times with 0.10 M Na_2SO_4 at pH 8.0.

3. Results and Discussion

3.1. Characterization of the Synthesized GO

Figure 1A displays the XRD patterns of the GO, which demonstrates that GO was successfully synthesized. Thus, the GO exhibits a broad diffraction peak at 2θ of 11.58° due to the interlayer distance of the GO [34]. The Raman spectrum of the synthesized GO has been shown in Figure 1B to confirm the structural properties of GO. Two peaks were observed at 1345 cm^{-1} (D band) and 1581 cm^{-1} a (G band). The D (related to structural defects and amorphous carbon) to G (associated with the stretching of in-plane sp2carbons) intensity ratio (I_D/I_G) was 1.05. The Raman spectrum of the GO is consistent with previous reports [42,43].

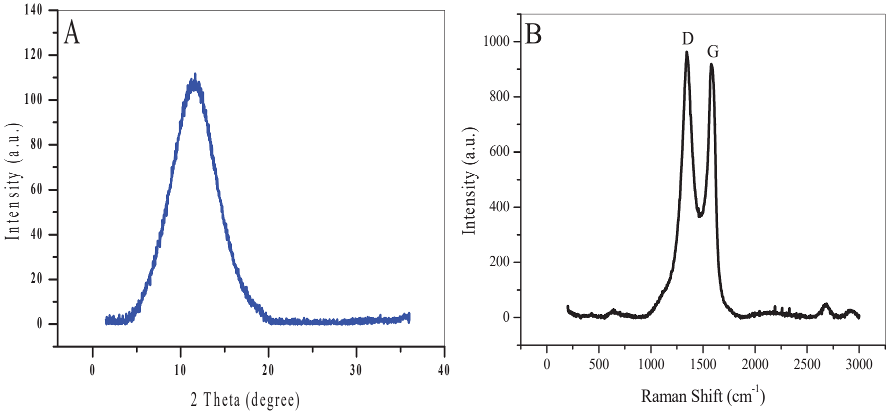

Figure 1. (**A**) XRD and (**B**) Raman spectra of the synthesized GO.

On the other hand, the SEM image of the GO is depicted in Figure 2A to examine its structural morphology. As expected, a typical wrinkled, thin sheet-like morphology is shown for the surface of GO. For further support, the features of morphology and structure of the GO can be observed by high-resolution TEM. Figure 2B clearly shows the single-layer sheets containing flake-like wrinkles and rough surfaces. This microstructure gives the stability of GO nanosheets and prevents the collapse back into graphene structure, which provides a high surface area [44].

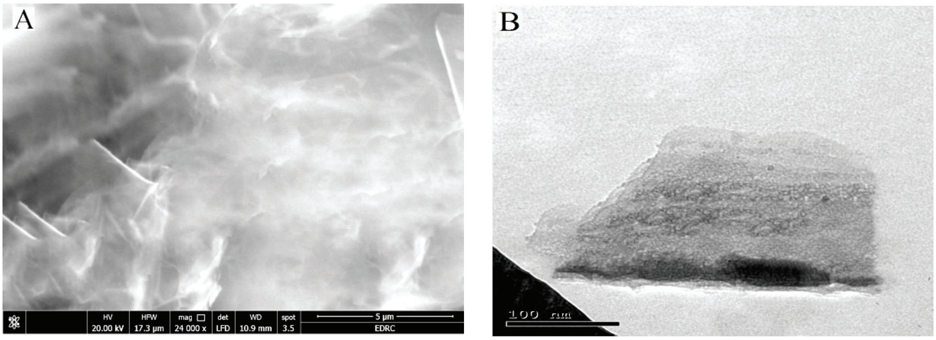

Figure 2. (**A**) SEM and (**B**) TEM images of the synthesized GO nanosheets.

Figure 3 shows the UV–Visible absorption spectrum of the aqueous solution of GO nanosheets. The observed characteristic peak (230 nm) and shoulder (301 nm) are assigned to $\pi\rightarrow\pi^*$ transition of aromatic C=C matrix of GO and $n\rightarrow\pi^*$ transition of the oxygen lone pair of electron of the carbonyl group (C=O) in GO, respectively [38,40].

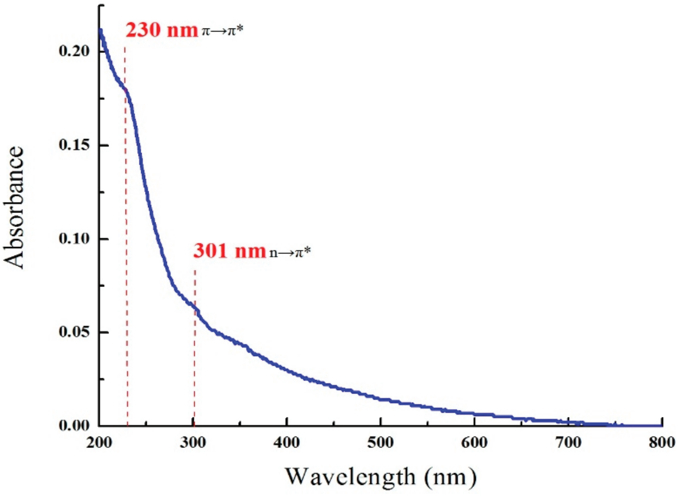

Figure 3. UV-Visible spectrum curve of the aqueous solution of GO nanosheets (0.0023g GO in 4.5 mL distilled H_2O).

FT-IR spectroscopy is vital for describing functional moieties involved on GO's surface. Figure 4 shows the site of absorption bands of functional groups in GO. The existence of broad stretching peaks at 3409 cm^{-1}, 2925 cm^{-1}, and 2857 cm^{-1} are stretching asymmetric and symmetric a hydroxyl (O–H) and C–H groups of GO matrix [38–40,45], respectively. Moreover, the C=O stretching peak of the carboxylic (COOH) group at 1724 cm^{-1}, stretching band at 1626 cm^{-1} of aromatic C=C matrix of GO, and phenolic C–O deformation, stretching, and epoxy C–O–C stretching were recognized at 1387, 1224 and 1050 cm^{-1}, respectively [38–40,46,47].

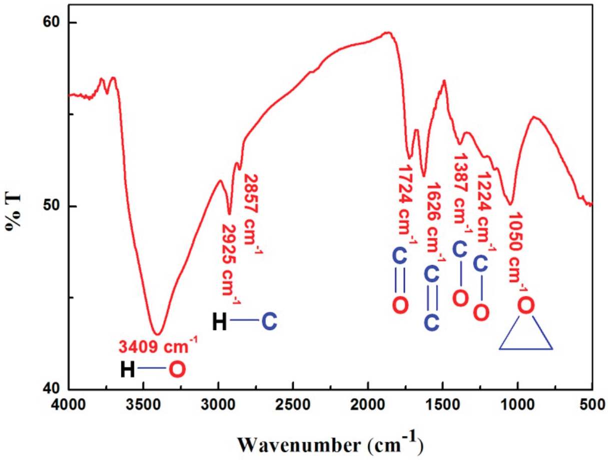

Figure 4. FT-IR spectrum curve of GO in KBr disc.

3.2. Electrochemical Behaviorof Nq

Figure 5 depicts the cyclic voltammograms (CVs) of 3.33 mM of Nq in 0.10 M PBS (pH 7.0) on the surface of GCE at a scan rate of 100 mV/s. The results illustrated the reproducible reaction with both anodic and cathodic peaks, observed at potentials 0.25 and −0.11 V. Additionally, by increasing the number of cycles, the continuous growth of Nq film was obtained. The peak separation potential $\Delta E_p = (E_{pa} - E_{pc})$ was calculated to be 0.36 V (was higher than 0.059 V) as expected for a quasi-reversible system [48]. Then, the Nq/GCE behavior in 0.10 M PBS (pH 7.0) was examined under various scan rates ranging from 25 to 500 mV/s, as displayed in Figure 6. As can be observed, both anodic and cathodic peak currents gradually increased with a raised scan rate. Furthermore, the oxidative and reductive peak potentials shifted to more positive and negative values. This behavior indicated a surface-controlled process of the electrode reactions process for the organic film of Nq formation [41,49].

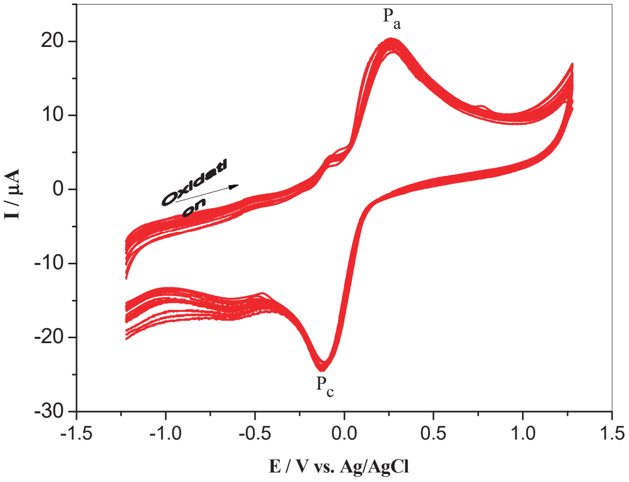

Figure 5. CVs of 3.33 mM of Nq in 0.10 M of PBS (pH 7.0) at the GCE with a scan rate of 100 mV/s.

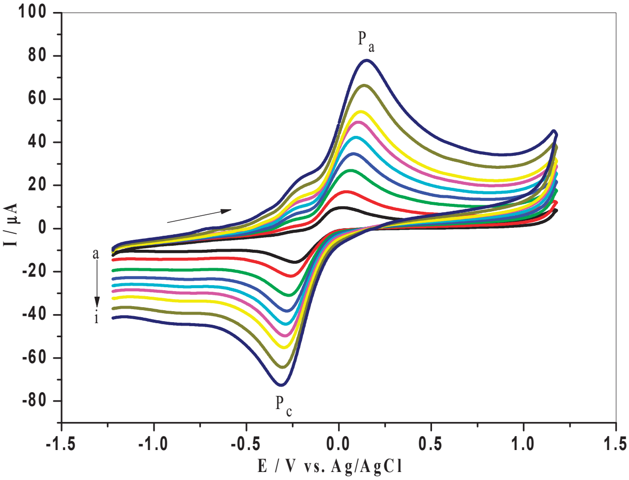

Figure 6. CVs of the Nq/GCE in 0.10 M of PBS (pH 7.0) at various scan rates (a to i: 25, 50, 100, 150, 200, 250, 300, 400, and 500 mV/s).

3.3. Voltammetric Determination of NIC

Figure 7 describes the CVs of 3.5 mM of NIC in 0.10 M Na_2SO_4 (pH 8.0) containing a bare GCE (a), the Nq/GCE (b), the GO/Nq/GCE (c), and the GO/GCE (d) at a scan rate of 100 mV/s. The results showed that the bare GCE (Figure 7, curve a) gave a poorly broad oxidation peak near 0.77 V (vs. Ag/AgCl) is ascribed to NIC oxidation. Meanwhile, in the case of Nq/GCE, GO/GCE, and GO/Nq/GCE, the peak potential of NIC oxidation appeared to be 0.85. 084 and 0.83 V, respectively, as exhibited in Figure 7 (curves b and c). The interpretation of the negative shift in the peak potential is due to the presence of both GO nanosheets and Nq films, which acted as electrocatalysts toward NIC oxidation, which accelerated the electron transfer rate. On the other hand, the usage of GO/Nq/GCE led to the enhancement and increase in the oxidation peak current of NIC by four-fold, compared to that which appeared at bar GCE. This is because the unique conjugation between the Nq film and nanosheets of GO increased the electroactive surface area that catalyzed NIC oxidation [26–28]. The absence of voltammetric response (peak) in the cathodic scan is attributed to the irreversibility of NIC oxidation as supported by the literature [24,50].

3.4. Effect of pH

The pH of the supporting electrolyte is considered an essential factor for the peak current (I_p). By examining the change of pH values from (2.0 to 9.0), it was observed that there are no current responses of NIC at a pH lower than 6.0. However, by increasing the pH value, the anodic peak of NIC increased until a maximum value was observed at pH 8.0, and then it decreased, as shown in Figure 8. This agrees with previous papers that prove that a neutral or slightly alkaline media were appropriate in the voltammetric determination of NIC [5,24]. On the other hand, the potential shifted towards less positive values by increasing the pH values, demonstrating proton participation in the oxidation process [51]. A plot of the oxidation peak potential vs. pH has three almost linear segments, and one is linear over the pH, ranging from 8.0 to 9.0 (inset Figure 8) and expressed by the following equation:

$$\mathbf{E_p(V) = 1.34 - 0.06\ Ph \quad (R^2 = 0.999)} \tag{2}$$

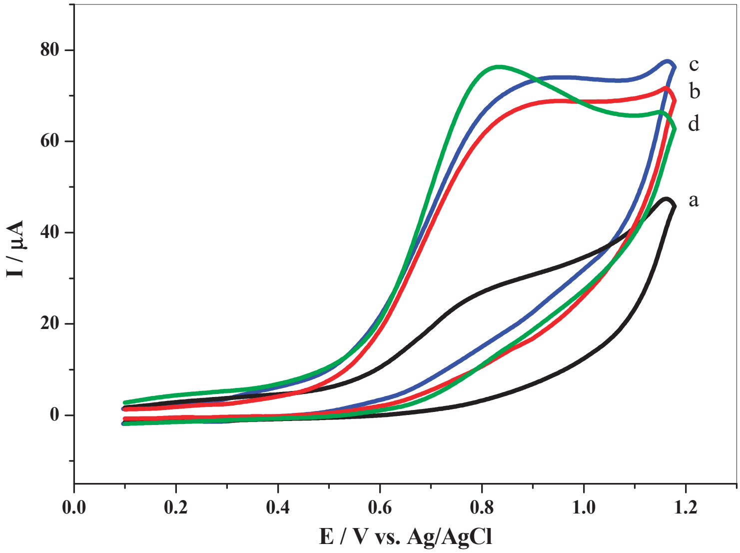

Figure 7. CVs of 3.5 mM of NIC in 0.10 M Na_2SO_4(pH 8.0) at (a) a bare GCE, (b) the Nq/GCE, and (d) the GO/GCE (c) the GO/Nq/GCE at a scan rate of 100 mV/s.

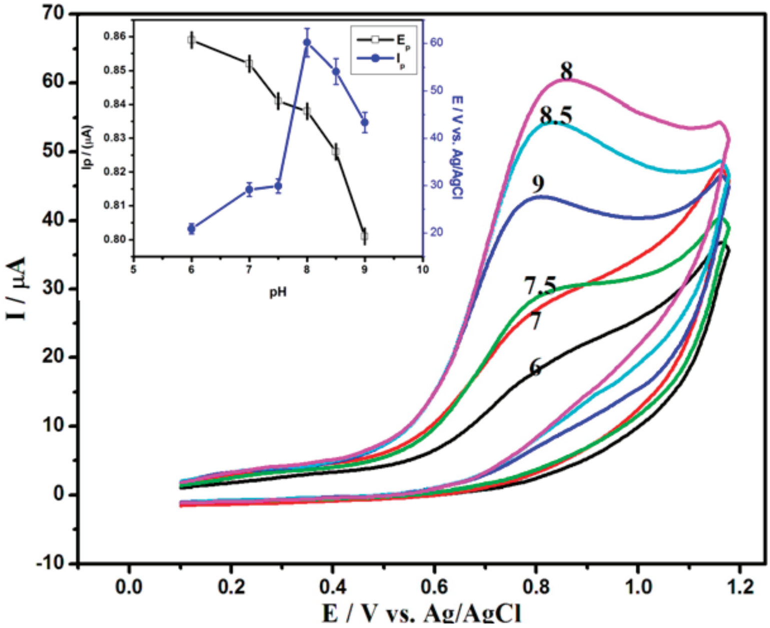

Figure 8. CVs of 3.5 mM of NIC in 0.1 M of Na_2SO_4 of various pH values: (6.0, 7.0, 7.5, 8.0, 8.5, and 9.0) at the GO/Nq/GCE with a scan rate of 100 mV/s. (inset Figure 8) A relation between pH versus both oxidation peak potential and oxidation peak current of NIC.

The calculated slope of 60 mV is very close to the theoretical value (59 mV) of the Nernst equation. Therefore, the oxidation process of NIC on the surface of GO/Nq/GCE involves the same number of protons and electrons [52–54]. This segment of the curves (∼pH 8.0–9.0) is close to the pK_{a1} due to changes in protonation of the acid–base functions in the pyrrolidine moiety. As you know, NIC has pK_{a1} = 8.02, corresponding to the protonation of pyrrolidine nitrogen, and pK_{a2} = 3.12 of pyridine nitrogen [55]. The NIC oxidation process is pH-dependent, and subsequent measurements were carried out in a buffer with pH 8.0.

3.5. Effect of Scan Rate

To achieve the optimum conditions, the influence of scan rate on the peak current of 3.5 mM of NIC in 0.10 M Na_2SO_4 (pH 8.0)on the surface of the GO/Nq/GCE was investigated. The results demonstrated a linear increase in the peak current of NIC with the increase in scan rate from 5.0 to 100 mV/s, as illustrated in Figure 9. It can be observed that the potential peak shifts toward more positive values with increasing scan rate. Of course, this behavior was characteristic of an irreversible reaction [5,24]. To assess the oxidation process of NIC at the GO/Nq/GCE, a plot of the anodic peak current of NIC vs. square root of the scan rate was recorded (inset Figure 9). A straight linear relationship was obtained, indicating the oxidation reaction of NIC under a diffusion-controlled process and can be expressed as:

$$\mathbf{I_p(\mu A) = 6.117\upsilon^{0.5} - 2.456 \quad (R^2 = 0.9984)} \tag{3}$$

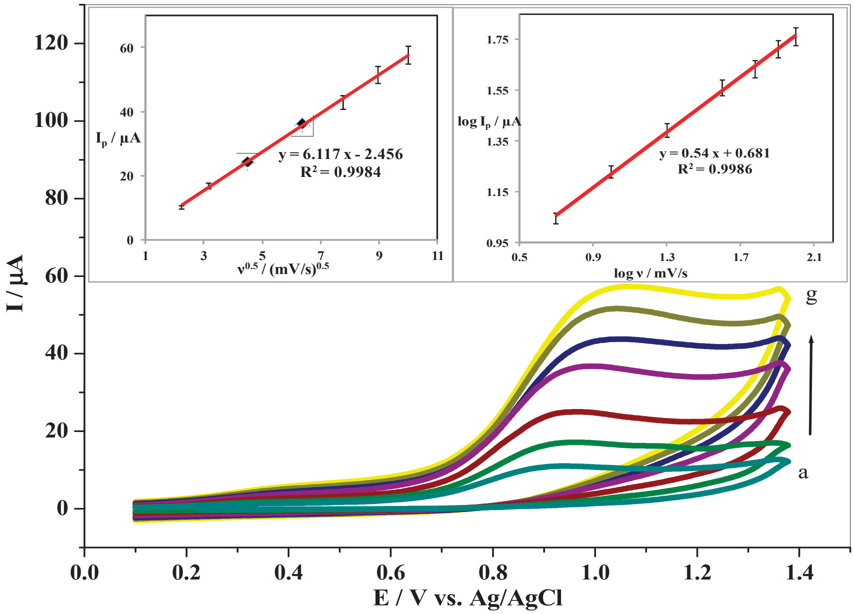

Figure 9. CVs of 3.5 mM of NIC in 0.1 M of Na_2SO_4 (pH 8.0) at the GO/Nq/GCE with various scan rates (a to g: 5, 10, 20, 40, 60, 80, and 100 mV/s).

For more support, a linear relationship with a slope of 0.54 was obtained when plotting the log peak current versus log scan rate (inset Figure 9) and can be expressed by:

$$\mathbf{\log I_p = 0.54 \log \upsilon + 0.681 \quad (R^2 = 0.996)} \tag{4}$$

The slope of the above relation (α = 0.54) is close to the theoretical value calculated, 0.5, as expected for a diffusion-controlled process [56–58].

On the other hand, the relation between Ip versus scan rate was studied, a linear relationship was found with correlation co efficient R^2 = 0.996

$$\mathbf{I_p = 2.0\ \upsilon - 23.3 \quad (R^2 = 0.996)} \tag{5}$$

Moreover, Ep and Log scan rate was determined to inform the number of electron that contributed in the oxidation process of NIC on the surface ofGO/Nq/GCE as seen in Figure 10a,b.

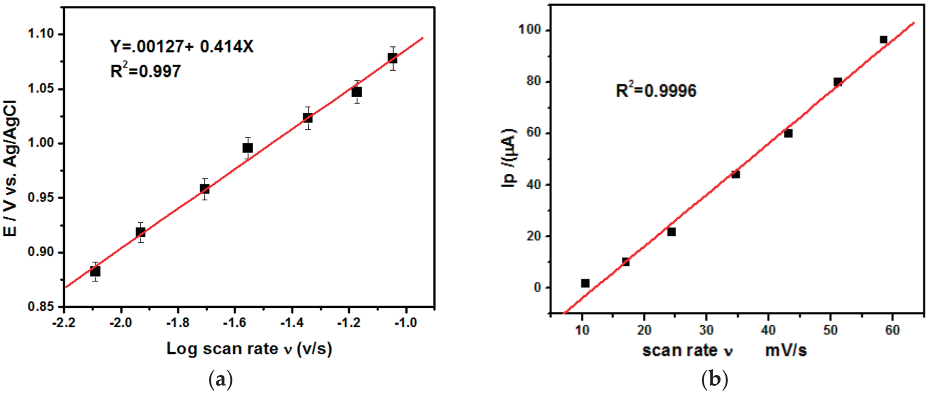

Figure 10. (**a**) The relation between oxidation peak potential of 3.5 mM of NIC in 0.1 M of Na_2SO_4 (pH 8.0) at the GO/Nq/GCE versus Log scan rate. (**b**) The relation between peak current of 3.5 mM of NIC in 0.1 M of Na_2SO_4 (pH 8.0) at the GO/Nq/GCE versus scan rate.

According to the following equation, a linear relation was obtained with correlation co-efficient R^2 = 99.6.

$$\mathbf{Ep = 0.00127 + 0.414\log \upsilon\ (R^2 = 0.997)} \quad (6)$$

The number of electrons involved was calculated from the Laviron equation:

$$\mathbf{\Delta E\ vs.\ \Delta\log(v) = 59/n\alpha} \quad (7)$$

where α is (the electron transfer coefficient) and n (refers to number of electrons). The calculated number of electrons were found to be (2.1). That is mean two electron was participated in the oxidation process of NIC. So the expected mechanism (Scheme 2) for the oxidation of NIC at the GO/Nq/GCE in alkaline media which involves substitution of CH_3 group by OH at the nitrogen of pyrrolidine ring with formation of methanol by two protons and two electrons transfer [5,59].

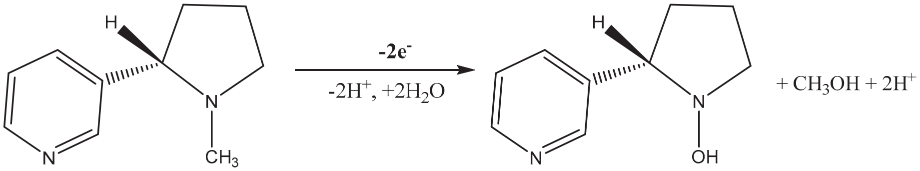

Scheme 2. Probable electrochemical oxidation mechanism of NIC.

3.6. Effect of Concentration and Calibration Curve

The DPV technique is the most appropriate technique used to examine the correlation between the peak current and the standard adding of NIC concentration, characterized by accurate electrochemical determination with a low detection limit and background current [59]. The parameters of DPV were optimized, and the influence of various NIC concentrations at the GO/Nq/GCE in 0.1 M Na_2SO_4 (pH = 8.0) was examined. Figure 11 represents the increase in the peak current of NIC by successive standard additions of NIC concentration over the wide range from 6.5 to 245 μM. An excellent linear dependence of the peak current of NIC on its concentration in the same range is shown in Figure 11. The following regression line equation can represent the obtained calibration curve:

$$\mathbf{I_p(\mu A) = 0.016\ (\mu M) + 0.573 \quad (R^2 = 0.9999)} \tag{8}$$

The limit of detection (LOD) and quantification of NIC at the GO/Nq/GCE can be determined according to LOD = 3SD/*b* and LOQ = 10SD/*b*, respectively, where *b* is the slope of the calibration curve. SD is the standard deviation of I_p of NIC, estimated from the following equation [60].

$$\mathbf{SD = 1/(n - 2)\Sigma(I_{exp} - I_{cal})^2} \tag{9}$$

where I_{exp} is the experimental value of I_p, and I_{cal} is the corresponding calculated value at the same concentration. The calculated LOD and LOQ of NIC at the proposed sensor were 12.7 and 42.4 nM, respectively.

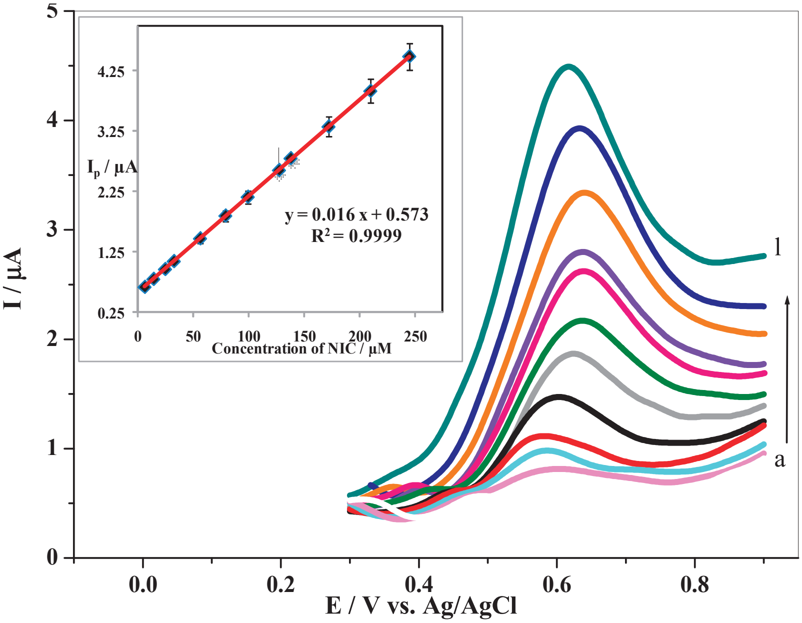

Figure 11. DPVs of 0.1 M of Na_2SO_4 (pH 8.0) containing different concentrations of NIC: (a to l: 6.5, 15, 25, 33.5, 56.5, 80, 100, 128, 138.5, 172.5, 210, and 245 µM) at the GO/Nq/GCE. Inset shows the corresponding calibration curve.

Under the optimum conditions, the sensitivity of our modified sensor was tested. The comparison of the LOD and linearity range obtained in this work with previous reports with different modified electrodes was recorded. The comparison results are epitomized in Table 1. The lower LOD and good linearity range were achieved from the presented data, reflecting the efficiency and sensitivity our modified electrode toward lower concentration of NIC.

Table 1. Comparison between our detection limit with the same techniques using different working electrodes.

Technique	Working Electrode	LOD (M)	Linear Range (μM)	Ref.
DPV	SPCE	0.6×10^{-6}	1–375	[24]
Amp	$CuWO_4$/rGO/Nf/GCE	3.5×10^{-8}	0.1–0.9	[61]
CV	MWCNTs/CuNPs	6.0×10^{-9}	1–1000	[62]
DPV	Poly(ARS)-GR/SPCE	4.6×10^{-6}	30–1000	[63]
DPV	RGO/DPA/PGE	7.60×10^{-6}	31–1900	[64]
CV	MWCNT-BPPG	1.50×10^{-6}	10–1000	[65]
SWV	p-AHNSA/GCE	0.90×10^{-6}	1–200	[66]
SWV	EA/GCE	0.70×10^{-6}	1–200	[67]
SWV	CNC/SPCE	2.00×10^{-6}	10–1000	[59]
Amp	PDA-RGO/Au/GCE	1.50×10^{-8}	0.05–500	[68]
DPV	GO/Nq/GCE	1.27×10^{-8}	6.5–245	This work

3.7. Chronoamperometric Measurements

The diffusion coefficient of NIC at the GO/Nq/GCE can be determined using the chronoamperometry method. Chronoamperograms were applied by setting the working electrode potential at 0.6 V with various concentrations of NIC (14–44 μM) in 0.10 M Na_2SO_4 (pH = 8.0) as represented in Figure 12. Plotting of I for various NIC concentrations against t^{-1} is depicted in Figure 12A. Then, the slopes of the resulting straight lines were plotted versus the different concentrations of NIC that were constructed inset Figure 12B. Using the obtained slope and applying the Cottrell equation [69],

$$\mathbf{I = nFAD^{1/2}C_b\pi^{-1/2}t^{-1/2}} \tag{10}$$

where C_b (mol cm^{-3}) is the bulk concentration, and D ($cm^2\ s^{-1}$) is the diffusion coefficient, the other symbols have their usual meaning. The D value of NIC at the GO/Nq/GCE was determined to be 4.02×10^{-7} cm^2/s is considered a satisfactory result.

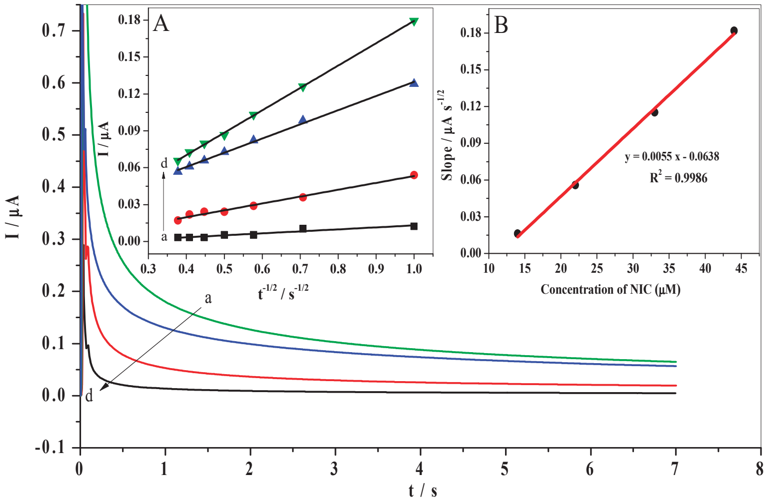

Figure 12. Chronoamperograms were obtained at the GO/Nq/GCE in 0.1 M of Na_2SO_4(pH 8.0) for different concentrations of NIC (a to d: 14, 22, 33, and 44 μM). Insets: (**A**) a plot of I vs. $t^{-1/2}$, the (**B**) plot of the slope of straight lines vs. NIC concentration.

3.8. Stability and Reproducibility

The viability of the GO/Nq/GCE could be evaluated by their stability and reproducibility towards the NIC determination. Therefore, Figure 13A shows the CVs of 3.5 mM NIC in 0.10 M Na_2SO_4 (pH 8.0) for 14 days, while the modified electrode was kept at 25 °C. The results indicate no significant change in the peak potential, and the peak current remains at 97.71% of its initial current response. Additionally, Figure 13B shows the reproducibility of the GO/Nq/GCE, taking five repetitive CVs' measurements via the same optimized protocol. It was concluded that the relative standard deviation of RSD = 0.80% in peak current. The results indicated that the fabricated electrode exhibited good stability and high reproducibility.

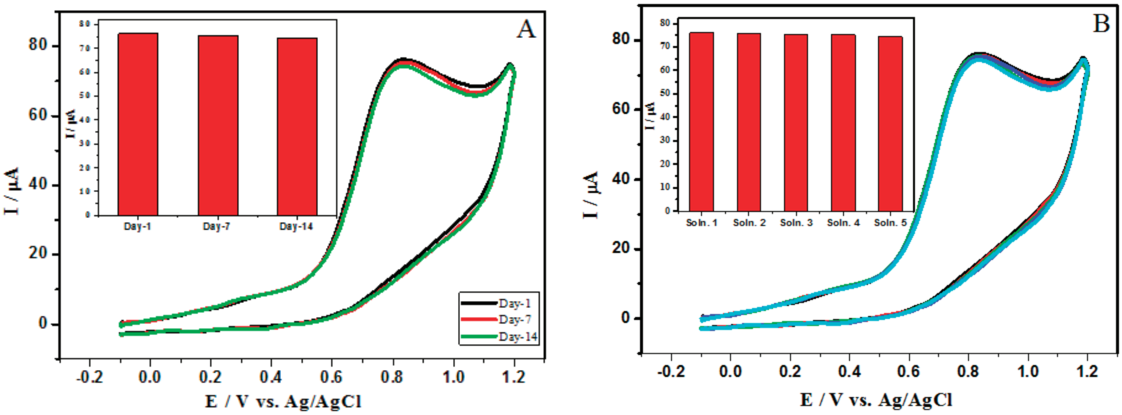

Figure 13. CVs of 3.5 mM of NIC in 0.1 M Na_2SO_4 (pH 8.0) at the GO/Nq/GCE with a scan rate of 100 mV/s for 14 days (**A**) and five repetitive CVs measurements (**B**).

3.9. Interference Study

An important parameter for a developed electrode is its selectivity towards the target analyte. The influence of some possible interferences on the determination of 3.5 mM NIC in 0.1 M Na_2SO_4 (pH 8.0) at the GO/Nq/GCE was examined. The tolerance limit was calculated as less than 5% of the relative error in this study. Figure 14 represents the results investigated from the current changes comparing the peak current of NIC only and the signal of NIC with the interfering substances. It is clear that 1000-fold concentration ratios of Na^+, K^+, Fe^{2+}, Cl^-, NO_3^-, and SO_4^{2-}, 100-fold concentration ratios of glucose and L-cysteine, and 5-fold concentration ratios of pyridine, dopamine, ascorbic acid, and uric acid did not interfere with the measurement of NIC. Additionally, there is no significant variation in the current response after adding 50-fold concentration ratios of urea, caffeine, and cotinine, a primary metabolite of NIC. These results prove the excellent selectivity of the developed sensor for the electrochemical determination of NIC in presences of other interferences.

3.10. Real Sample Analysis

Next, the content of NIC in a tobacco product and a urine sample was estimated using the GO/Nq/GCE under optimized DPV. Figure 15 depicts DPVs recorded for different concentrations of NIC standard solution, which was added to actual samples in 0.10 M Na_2SO_4. At the same time, the final NIC concentrations of 100, 110, 130, and 150 µM and the obtained results are shown in Table 2. As observed, good recoveries were obtained in the range of 99.44–100.33%. Therefore, the proposed sensor is capable of detecting NIC in actual and real samples.

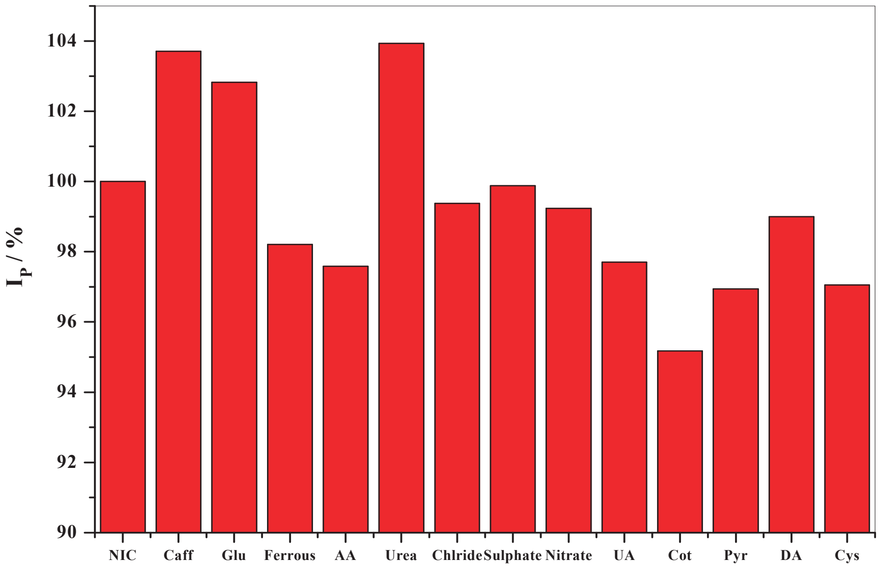

Figure 14. Measurements of 3.5 mM of NIC in 0.10 M Na_2SO_4 (pH 8.0) at the GO/Nq/GCE in the presence of the tolerance limit of foreign species.

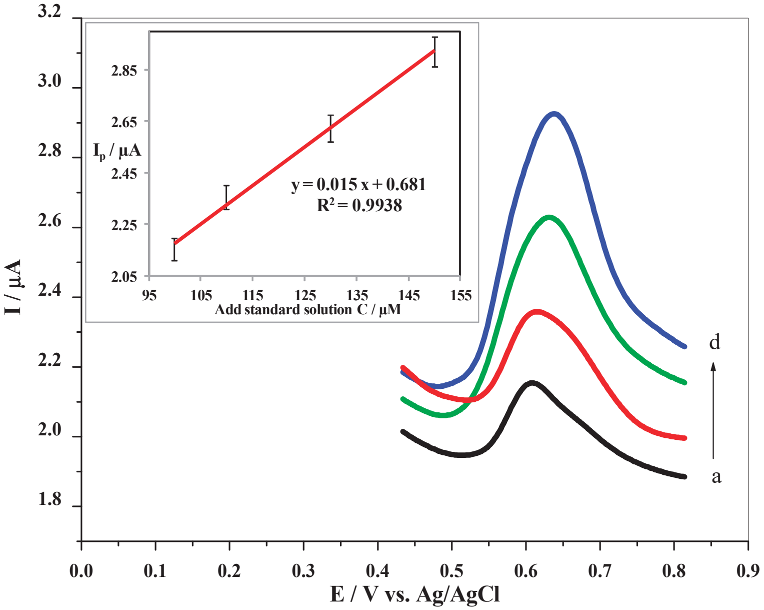

Figure 15. DPVs were recorded at the GO/Nq/GCE upon the addition of known concentrations of NIC (a to d: 100, 110, 130, and 150 µM) in 0.1 M of Na_2SO_4 (pH 8.0) with a scan rate of 100 mV/s. Inset shows the corresponding calibration curve.

Table 2. Detection of NIC in practical samples at the GO/Nq/GCE.

Sample	Added (μM)	Founded (μM)	Recovery (%)
Cigarette	0.0	21.13	–
	50	70.73	99.44
	100	121.53	100.33
Urine	50	50.07	100.14
	100	99.63	99.63
	200	199.4	99.7

4. Conclusions

In this work, we provide an electrochemical sensor used for the first time for NIC determination. The behavior of NIC was studied under optimum conditions. Using different voltammetric techniques such as Cyclic voltammetry. Differential pulse voltammetry and chronoamperometry. The sensor was built on GCE, modified by a layer film of Nq decorated by GO nanosheets. The GO nanosheets were prepared by the Hummers' method and characterized by different techniques. The fabricated electrode provided a remarkable electrochemical activity toward the oxidation of NIC compared with either bar GCE and GCE modified by Nq. The unique conjugation between Nq and nanosheets of GO has significantly increased the electroactive surface area of the electrode toward NIC.

Additionally, the GO/Nq/GCE showed high stability, reproducibility, a lower detection limit of 12.7 nM, and a linear response range from 6.5 to 450 μM with $R^2 = 0.9999$. The oxidation process of NIC is described as control diffusion. The reliable GO/Nq/GCE sensor was successfully applied for detecting NIC in the tobacco product and a urine sample.

Author Contributions: Formal analysis, H.M.A.; investigation, M.A.-E.; writing—original draft preparation, H.F.A.; H.M.A. and M.A.-E.; Funding acquisition, M.M.A.-K., A.G.A. and T.A.Y.; Investigation, H.F.A.; writing—review and editing, M.M.A.-K., A.G.A. and T.A.Y. authors designed the study, contributed to the revision of the drafts, and agreed on the final version to be submitted. All authors have read and agreed to the published version of the manuscript.

Funding: The authors extend their appreciation to the Deanship of Scientific Research at Imam Mohammad Ibn Saud Islamic University for funding this work through Research Group no. RG-21-09-72.

Institutional Review Board Statement: Not applicable.

Informed Consent Statement: Not applicable.

Data Availability Statement: Not applicable.

Conflicts of Interest: The authors declare no conflict of interest and that they have no known competing financial interests or personal relationships that could have appeared to influence the work reported in this paper.

References

1. El-Ramady, H.; Abdalla, N.; Alshaal, T.; Elhenawy, A.; Amer, M.; Shehata, A.; Paulsen, J.; Kleinwächter, M.; Selmar, D.; Taha, H. Contamination of Plant Foods with Nicotine: An Overview. DBG Reports. 2015. Available online: https://eprints.dbges.de/1088/ (accessed on 10 April 2022).
2. Rahim, S.; Rauf, A.; Rauf, S.; Shah, M.R.; Malik, M.I. Enhanced electrochemical response of a modified glassy carbon electrode by poly (2-vinlypyridine-b-methyl methacrylate) conjugated gold nanoparticles for detection of nicotine. *RSC Adv.* **2018**, *8*, 35776–35786. [CrossRef] [PubMed]
3. Scharenberg, F.; Stegemann, T.; Çiçek, S.S.; Zidorn, C. Sequestration of pyridine alkaloids anabasine and nicotine from Nicotiana (Solanaceae) by Orobanche ramosa (Orobanchaceae). *Biochem. Syst. Ecol.* **2019**, *86*, 103908. [CrossRef]
4. Marsh, A.; Clark, B.J.; Altria, K.D. Orthogonal separations of nicotine and nicotine-related alkaloids by various capillary electrophoretic modes. *Electrophoresis* **2004**, *25*, 1270–1278. [CrossRef] [PubMed]
5. Kowalcze, M.; Jakubowska, M. Voltammetric determination of nicotine in electronic cigarette liquids using a boron-doped diamond electrode (BDDE). *Diam. Relat. Mater.* **2020**, *103*, 107710. [CrossRef]

6. Hannisdal, A.; Mikkelsen, Ø.; Schrøder, K.H. Analysis of nicotine in antismoking pharmaceutical products by differential pulse polarography and voltammetry. *Collect. Czechoslov. Chem. Commun.* **2007**, *72*, 1207–1213. [CrossRef]
7. Wang, L.; Xiong, H.; Zhang, X.; Wang, S. Electrochemical behaviors of nicotine and its interaction with DNA. *Electrochem. Commun.* **2009**, *11*, 2129–2132. [CrossRef]
8. Wu, C.-T.; Chen, P.-Y.; Chen, J.-G.; Suryanarayanan, V.; Ho, K.-C. Detection of nicotine based on molecularly imprinted TiO_2-modified electrodes. *Anal. Chim. Acta* **2009**, *633*, 119–126. [CrossRef]
9. Dushna, O.; Dubenska, L.; Plotycya, S.; Rydchuk, M.; Blazheyevskiy, M. The Alternative Voltammetric Method for the Determination of Nicotine and Its Metabolite Nicotine N-Oxide. *J. Electrochem. Soc.* **2022**, *169*, 16513. [CrossRef]
10. Banerjee, J.; Al-Wadei, H.A.N.; Schuller, H.M. Chronic nicotine inhibits the therapeutic effects of gemcitabine on pancreatic cancer in vitro and in mouse xenografts. *Eur. J. Cancer* **2013**, *49*, 1152–1158. [CrossRef]
11. Yu, C.-C.; Chang, Y.-C. Enhancement of cancer stem-like and epithelial—Mesenchymal transdifferentiation property in oral epithelial cells with long-term nicotine exposure: Reversal by targeting SNAIL. *Toxicol. Appl. Pharmacol.* **2013**, *266*, 459–469. [CrossRef]
12. Suto, M.J.; Zacharias, N. Neuronal nicotinic acetylcholine receptors as drug targets. *Expert Opin. Ther. Targets* **2004**, *8*, 61–64. [CrossRef] [PubMed]
13. Newhouse, P.A.; Potter, A.; Kelton, M.; Corwin, J. Nicotinic treatment of Alzheimer's disease. *Biol. Psychiatry* **2001**, *49*, 268–278. [CrossRef]
14. Page-Sharp, M.; Hale, T.W.; Hackett, L.P.; Kristensen, J.H.; Ilett, K.F. Measurement of nicotine and cotinine in human milk by high-performance liquid chromatography with ultraviolet absorbance detection. *J. Chromatogr. B* **2003**, *796*, 173–180. [CrossRef] [PubMed]
15. Man, C.N.; Ismail, S.; Harn, G.L.; Lajis, R.; Awang, R. Determination of hair nicotine by gas chromatography–mass spectrometry. *J. Chromatogr. B* **2009**, *877*, 339–342. [CrossRef]
16. Figueiredo, E.C.; de Oliveira, D.M.; de Siqueira, M.E.P.B.; Arruda, M.A.Z. On-line molecularly imprinted solid-phase extraction for the selective spectrophotometric determination of nicotine in the urine of smokers. *Anal. Chim. Acta* **2009**, *635*, 102–107. [CrossRef]
17. Zhou, Y.; Yu, H.; Zhang, L.; Xu, H.; Wu, L.; Sun, J.; Wang, L. A new spectrofluorometric method for the determination of nicotine base on the inclusion interaction of methylene blue and cucurbit [7] uril. *Microchim. Acta* **2009**, *164*, 63–68. [CrossRef]
18. Byrd, G.D.; Davis, R.A.; Ogden, M.W. A rapid LC-MS-MS method for the determination of nicotine and cotinine in serum and saliva samples from smokers: Validation and comparison with a radioimmunoassay method. *J. Chromatogr. Sci.* **2005**, *43*, 133–140. [CrossRef]
19. Mitsubayashi, K.; Nakayama, K.; Taniguchi, M.; Saito, H.; Otsuka, K.; Kudo, H. Bioelectronic sniffer for nicotine using enzyme inhibition. *Anal. Chim. Acta* **2006**, *573*, 69–74. [CrossRef]
20. Li, Q.; Wu, J.-T.; Liu, Y.; Qi, X.-M.; Jin, H.-G.; Yang, C.; Liu, J.; Li, G.-L.; He, Q.-G. Recent advances in black phosphorus-based electrochemical sensors: A review. *Anal. Chim. Acta* **2021**, *1170*, 338480. [CrossRef]
21. Li, G.; Qi, X.; Zhang, G.; Wang, S.; Li, K.; Wu, J.; Wan, X.; Liu, Y.; Li, Q. Low-cost voltammetric sensors for robust determination of toxic Cd(II) and Pb(II) in environment and food based on shuttle-like α-Fe_2O_3 nanoparticles decorated β-Bi_2O_3 microspheres. *Microchem. J.* **2022**, *179*, 107515. [CrossRef]
22. Giuliano, C.; Parikh, V.; Ward, J.R.; Chiamulera, C.; Sarter, M. Increases in cholinergic neurotransmission measured by using choline-sensitive microelectrodes: Enhanced detection by hydrolysis of acetylcholine on recording sites? *Neurochem. Int.* **2008**, *52*, 1343–1350. [CrossRef] [PubMed]
23. Zhou, N.; Li, J.; Chen, H.; Liao, C.; Chen, L. A functional graphene oxide-ionic liquid composites–gold nanoparticle sensing platform for ultrasensitive electrochemical detection of Hg^{2+}. *Analyst* **2013**, *138*, 1091–1097. [CrossRef]
24. Mehmeti, E.; Kilic, T.; Laur, C.; Carrara, S. Electrochemical determination of nicotine in smokers' sweat. *Microchem. J.* **2020**, *158*, 105155. [CrossRef]
25. Lakshmi, D.; Whitcombe, M.J.; Davis, F.; Sharma, P.S.; Prasad, B.B. Electrochemical detection of uric acid in mixed and clinical samples: A review. *Electroanalysis* **2011**, *23*, 305–320. [CrossRef]
26. Novoselov, K.S.; Geim, A.K.; Morozov, S.V.; Jiang, D.; Zhang, Y.; Dubonos, S.V.; Grigorieva, I.V.; Firsov, A.A. Electric field effect in atomically thin carbon films. *Science* **2004**, *306*, 666–669. [CrossRef] [PubMed]
27. Fu, L.; Lai, G.; Mahon, P.J.; Wang, J.; Zhu, D.; Jia, B.; Malherbe, F.; Yu, A. Carbon nanotube and graphene oxide directed electrochemical synthesis of silver dendrites. *Rsc Adv.* **2014**, *4*, 39645–39650. [CrossRef]
28. Yang, Y.; Kang, M.; Fang, S.; Wang, M.; He, L.; Zhao, J.; Zhang, H.; Zhang, Z. Electrochemical biosensor based on three-dimensional reduced graphene oxide and polyaniline nanocomposite for selective detection of mercury ions. *Sens. Actuators B Chem.* **2015**, *214*, 63–69. [CrossRef]
29. Wang, H.-S.; Li, T.-H.; Jia, W.-L.; Xu, H.-Y. Highly selective and sensitive determination of dopamine using a Nafion/carbon nanotubes coated poly (3-methylthiophene) modified electrode. *Biosens. Bioelectron.* **2006**, *22*, 664–669. [CrossRef]
30. Sun, W.; Jiang, Q.; Yang, M.; Jiao, K. Electrochemical behaviors of hydroquinone on a carbon paste electrode with ionic liquid as binder. *Bull. Korean Chem. Soc.* **2008**, *29*, 915–920.
31. Xue, Z.; Yin, B.; Wang, H.; Li, M.; Rao, H.; Liu, X.; Zhou, X.; Lu, X. An organic indicator functionalized graphene oxide nanocomposite-based colorimetric assay for the detection of sarcosine. *Nanoscale* **2016**, *8*, 5488–5496. [CrossRef]

32. Abo-bakr, A.M.; Abd-Elsabour, M.; Abou-Krisha, M.M. An Efficient Novel Electrochemical Sensor for Simultaneous Determination of Vitamin C and Aspirin Based on a PMR/Zn-Al LDH/GCE. *Electroanalysis* **2021**, *33*, 2476–2489. [CrossRef]
33. Rageh, H.M.; Abou-Krisha, M.M.; Abo-Bakr, A.M.; Abd-Elsabour, M. Electrochemical behavior and the detection limit of ascorbic acid on a Pt modified electrode. *Int. J. Electrochem. Sci.* **2015**, *10*, 4105–4115.
34. Hummers, W.S.; Offeman, R.E. Preparation of Graphitic Oxide. *J. Am. Chem. Soc.* **1958**, *80*, 1339. [CrossRef]
35. Muzyka, R.; Kwoka, M.; Smędowski, Ł.; Díez, N.; Gryglewicz, G. Oxidation of graphene by different modified Hummers methods. *New Carbon Mater.* **2017**, *32*, 15–20. [CrossRef]
36. Dreyer, D.R.; Park, S.; Bielawski, C.W.; Ruoff, R.S. The chemistry of graphene oxide. *Chem. Soc. Rev.* **2010**, *39*, 228–240. [CrossRef]
37. Zhang, T.-Y.; Zhang, D. Aqueous colloids of graphene oxide nanosheets by exfoliation of graphene oxide without ultrasonication. *Bull. Mater. Sci.* **2011**, *34*, 25–28. [CrossRef]
38. Emiru, T.F.; Ayele, D.W. Controlled synthesis, characterization and reduction of graphene oxide: A convenient method for large scale production. *Egypt. J. Basic Appl. Sci.* **2017**, *4*, 74–79. [CrossRef]
39. Singh, R.K.; Kumar, R.; Singh, D.P. Graphene oxide: Strategies for synthesis, reduction and frontier applications. *RSC Adv.* **2016**, *6*, 64993–65011. [CrossRef]
40. Neelakandan, S.; Noel Jacob, K.; Kanagaraj, P.; Sabarathinam, R.M.; Muthumeenal, A.; Nagendran, A. Effect of sulfonated graphene oxide on the performance enhancement of acid-base composite membranes for direct methanol fuel cells. *RSC Adv.* **2016**, *6*, 51599–51608. [CrossRef]
41. Toghan, A.; Abd-Elsabour, M.; Abo-Bakr, A.M. A novel electrochemical sensor based on EDTA-NQS/GC for simultaneous determination of heavy metals. *Sensors Actuators A Phys.* **2021**, *322*, 112603. [CrossRef]
42. Chaiyakun, S.; Witit-Anun, N.; Nuntawong, N.; Chindaudom, P.; Oaew, S.; Kedkeaw, C.; Limsuwan, P. Preparation and characterization of graphene oxide nanosheets. *Procedia Eng.* **2012**, *32*, 759–764.
43. Manavalan, S.; Govindasamy, M.; Chen, S.-M.; Rajaji, U.; Chen, T.-W.; Ali, M.A.; Al-Hemaid, F.M.A.; Elshikh, M.S.; Farah, M.A. Reduced graphene oxide supported raspberry-like SrWO4 for sensitive detection of catechol in green tea and drinking water samples. *J. Taiwan Inst. Chem. Eng.* **2018**, *89*, 215–223. [CrossRef]
44. Wu, H.; Wang, J.; Kang, X.; Wang, C.; Wang, D.; Liu, J.; Aksay, I.A.; Lin, Y. Glucose biosensor based on immobilization of glucose oxidase in platinum nanoparticles/graphene/chitosan nanocomposite film. *Talanta* **2009**, *80*, 403–406. [CrossRef] [PubMed]
45. Jing, Y.; Lin, E.; Su, X.; Liu, Y.; Li, H.; Yuan, X.; Ping, L.; Fan, Y. Electrodeposition of Au nanoparticles on poly(diallyldimethylammonium chloride) functionalized reduced graphene oxide sheets for voltammetric determination of nicotine in tobacco products and anti-smoking pharmaceuticals. *RSC Adv.* **2016**, *6*, 26247–26253. [CrossRef]
46. Cheng, M.M.; Huang, L.J.; Wang, Y.X.; Tang, J.G.; Wang, Y.; Zhao, Y.C.; Liu, G.F.; Zhang, Y.; Kipper, M.J.; Wickramasinghe, S.R. Reduced graphene oxide–gold nanoparticle membrane for water purification. *Sep. Sci. Technol.* **2019**, *54*, 1079–1085. [CrossRef]
47. You, Z.; Fu, Y.; Xiao, A.; Liu, L.; Huang, S. Magnetic molecularly imprinting polymers and reduced graphene oxide modified electrochemical sensor for the selective and sensitive determination of luteolin in natural extract. *Arab. J. Chem.* **2021**, *14*, 102990. [CrossRef]
48. Mohammadi, S.Z.; Beitollahi, H.; Dehghan, Z.; Hosseinzadeh, R. Electrochemical determination of ascorbic acid, uric acid and folic acid using carbon paste electrode modified with novel synthesized ferrocene derivative and core–shell magnetic nanoparticles in aqueous media. *Appl. Organomet. Chem.* **2018**, *32*, e4551. [CrossRef]
49. Rageh, H.; Abdel-sabour, M. Pharmaceutical electrochemistry: The electrochemical behaviour of paracetamol at ZnO nanopartical/1, 2-napthaquinone-4-sulphonic acid glassy carbon modified electrode. *Anal Bioanal Electrochem.* **2017**, *9*, 351–364.
50. Suffredini, H.B.; de Santos, M.C.; De Souza, D.; Codognoto, L.; Homem-de-Mello, P.; Honório, K.M.; Da Silva, A.B.F.; Machado, S.A.S.; Avaca, L.A. Electrochemical behavior of nicotine studied by voltammetric techniques at boron-doped diamond electrodes. *Anal. Lett.* **2005**, *38*, 1587–1599. [CrossRef]
51. Levent, A.; Yardim, Y.; Senturk, Z. Voltammetric behavior of nicotine at pencil graphene electrode and its enhancement determination in the presence of anionic surfactant. *Electrochim. Acta* **2009**, *55*, 190–195. [CrossRef]
52. Khodari, M.; Rabie, E.M.; Assaf, H.F. A new electrochemical sensor based on TiO2 nanoparticles modified carbon paste electrode for voltammetric determination of phenol. *Int. J. Sci. Res.* **2015**, *5*, 1501–1505.
53. Švorc, L'.; Stanković, D.M.; Kalcher, K. Boron-doped diamond electrochemical sensor for sensitive determination of nicotine in tobacco products and anti-smoking pharmaceuticals. *Diam. Relat. Mater.* **2014**, *42*, 1–7. [CrossRef]
54. Assaf, H.F.; Salah, H.; Hashem, N.; Khodari, M.; Toghan, A. Fabrication of an electrochemical sensor based on copper waste wire recycling and its application. *Sens. Actuators A Phys.* **2021**, *331*, 112962. [CrossRef]
55. Yang, S.S.; Smetena, I. Evaluation of capillary electrophoresis for the analysis of nicotine and selected minor alkaloids from tobacco. *Chromatographia* **1995**, *40*, 375–378. [CrossRef]
56. Swain, G.M. Solid electrode materials: Pretreatment and activation. In *Handbook of Electrochemistry*; Elsevier: Amsterdam, The Netherlands, 2007; pp. 111–153.
57. Nicholson, R.S.; Shain, I. Theory of Stationary Electrode Polarography. Single Scan and Cyclic Methods Applied to Reversible, Irreversible, and Kinetic Systems. *Anal. Chem.* **1964**, *36*, 706–723. [CrossRef]
58. Rabie, E.M.; Assaf, H.F.; Shamroukh, A.A.; Khodari, M. Fabrication of a New Electrochemical Sensor Based on Carbon Paste Electrode Modified by Silica gel/MWCNTs for the Voltammetric Determination of Salicylic Acid in Tomato. *Egypt. J. Chem.* **2019**, *62*, 165–175. [CrossRef]

59. Highton, L.; Kadara, R.O.; Jenkinson, N.; Logan Riehl, B.; Banks, C.E. Metallic free carbon nanotube cluster modified screen printed electrodes for the sensing of nicotine in artificial saliva. *Electroanalysis* **2009**, *21*, 2387–2389. [CrossRef]
60. Miller, J.C.; Miller, J.N. Basic statistical methods for analytical chemistry. Part, I. Statistics of repeated measurements. A review. *Analyst* **1988**, *113*, 1351–1356. [CrossRef]
61. Karthika, A.; Karuppasamy, P.; Selvarajan, S.; Suganthi, A.; Rajarajan, M. Electrochemical sensing of nicotine using $CuWO_4$ decorated reduced graphene oxide immobilized glassy carbon electrode. *Ultrason. Sonochem.* **2019**, *55*, 196–206. [CrossRef]
62. Lo, T.W.B.; Aldous, L.; Compton, R.G. The use of nano-carbon as an alternative to multi-walled carbon nanotubes in modified electrodes for adsorptive stripping voltammetry. *Sens. Actuators B Chem.* **2012**, *162*, 361–368. [CrossRef]
63. Bai, H.; Li, C.; Wang, X.; Shi, G. A pH-sensitive graphene oxide composite hydrogel. *Chem. Commun.* **2010**, *46*, 2376–2378. [CrossRef] [PubMed]
64. Jing, Y.; Yu, B.; Li, P.; Xiong, B.; Cheng, Y.; Li, Y.; Li, C.; Xiao, X.; Chen, M.; Chen, L. Synthesis of graphene/DPA composite for determination of nicotine in tobacco products. *Sci. Rep.* **2017**, *7*, 1–9. [CrossRef] [PubMed]
65. Sims, M.J.; Rees, N.V.; Dickinson, E.J.F.; Compton, R.G. Effects of thin-layer diffusion in the electrochemical detection of nicotine on basal plane pyrolytic graphene (BPPG) electrodes modified with layers of multi-walled carbon nanotubes (MWCNT-BPPG). *Sens. Actuators B Chem.* **2010**, *144*, 153–158. [CrossRef]
66. Geto, A.; Amare, M.; Tessema, M.; Admassie, S. Voltammetric Determination of Nicotine at Poly (4-Amino-3-Hydroxynaphthalene Sulfonic Acid)-Modified Glassy Carbon Electrode. *Electroanalysis* **2012**, *24*, 659–665. [CrossRef]
67. Kassa, H.; Geto, A.; Admassie, S. Voltammetric determination of nicotine in cigarette tobacco at electrochemically activated glassy carbon electrode. *Bull. Chem. Soc. Ethiop.* **2013**, *27*, 321–328. [CrossRef]
68. Jing, Y.; Yuan, X.; Yuan, Q.; He, K.; Liu, Y.; Lu, P.; Li, H.; Li, B.; Zhan, H.; Li, G. Determination of nicotine in tobacco products based on mussel-inspired reduced graphene oxide-supported gold nanoparticles. *Sci. Rep.* **2016**, *6*, 1–8. [CrossRef]
69. Bard, A.J.; Faulkner, L.R. *Faulkner, Electrochemical Methods: Fundamentals and Applications, 2nd ed*; Wiley: New York, NY, USA, 2001. [CrossRef]

nanomaterials

Article

Ag–Se/Nylon Nanocomposites Grown by Template-Engaged Reaction: Microstructures, Composition, and Optical Properties

Valentina Krylova *, Nijolė Dukštienė and Henrieta Markevičiūtė

Department of Physical and Inorganic Chemistry, Faculty of Chemical Technology,
Kaunas University of Technology, Radvilėnų Str. 19, 50254 Kaunas, Lithuania; nijole.dukstiene@ktu.lt (N.D.); henrieta.markeviciute@ktu.edu (H.M.)
* Correspondence: valentina.krylova@ktu.lt

Abstract: Ag–Se nanostructure films were deposited on a–Se/nylon templates by a template-engaged reaction. Firstly, amorphous selenium (a–Se) was deposited on nylon by employing the chemical bath deposition method while using H_2SeO_3 and Na_2SO_3 solutions with an increasing selenium deposition time. Then, these a–Se/nylon templates were exposed into $AgNO_3$ solution at ambient temperature and pressure. The Ag–Se/nylon nanocomposites surface morphology, elemental and phase composition, and optical properties were monitored depending on the selenium deposition time on nylon. Scanning electron microscopy (SEM) analysis confirmed the development of a very complex surface composed of pyramidal-like sub-micron structures, agglomerates, and grid-like structures. Energy dispersive spectroscopy (EDS) proved the presence of carbon, oxygen, nitrogen, selenium, and silver. SEM/EDS cross-sectional analysis confirmed the multilayer character with different individual elemental composition in each film layer. X-ray diffraction analysis revealed a polycrystalline Ag_2Se phase with or without metallic Ag. The RMS value obtained from atomic force microscopy varies from 25.82 nm to 57.04 nm. From the UV-Vis spectrophotometry, the direct optical band gaps were found to be 1.68–1.86 eV. Ag–Se/nylon composites exhibit high refractive indices in the near infrared region.

Keywords: Ag_2Se; nylon 6; flexible inorganic-organic composite; ProX-SEM-EDS; optical properties

Citation: Krylova, V.; Dukštienė, N.; Markevičiūtė, H. Ag–Se/Nylon Nanocomposites Grown by Template-Engaged Reaction: Microstructures, Composition, and Optical Properties. *Nanomaterials* **2022**, *12*, 2584. https://doi.org/10.3390/nano12152584

Academic Editors: Jihoon Lee and Ming-Yu Li

Received: 22 June 2022
Accepted: 25 July 2022
Published: 27 July 2022

1. Introduction

Currently, a lot of attention is devoted to the flexible photovoltaic membranes, as they can maintain the required durability and fulfil the aesthetic, building-physics requirement(s) [1]. Therefore, the demand for a sustainable and semi-permanent energy-harvesting system, which converts solar energy to electricity, has been continuously increasing. Photovoltaic devices also need to be mechanically flexible to be employed as an energy supplier for a curved electronic device. Hybrid organic–inorganic composites are considered as very attractive and promising materials due to the diverse properties and additional functionalities as compared with those of individual components [2]. Thin films of solar light absorbers such as metal chalcogenides are of extraordinary interest for the production of solar selective coatings, large area arrays, and photovoltaic cells. The modification of flexible polymers with metal chalcogenides not only allows control an architecture of resultant solar absorbers, but also enables the creation of flexible materials with the unique microstructures and optical properties. Printing and coating methods are two main techniques to deposit thin films onto the flexible polymer surface [1]. Recently, surface modification of organic polymers with metal chalcogenides thin films via different coating techniques have been reported [3].

Owning to its high mechanical strength and high chemical and thermal stability, nylon 6 (polyamide 6) is a promising candidate for high-performance flexible energy-harvesting systems. Among a variety of metal chalcogenides, silver selenide displays many interesting properties. Ag_2Se exists in two polymorphs at atmospheric pressure: a low-temperature orthorhombic phase (α-Ag_2Se), and a high-temperature cubic phase (β-Ag_2Se) [4]. β-Ag_2Se is distinguished for its Seebeck coefficient (-150 μ VK^{-1} at 300 K [5]), large magnetoresistance [6], and excellent thermoelectric properties [7]. The Ag_2Se nanowires phase nature greatly influences electrical conductivity [8]. Authors [9] stated a super-ionic α-Ag_2Se conductor was employed in photo chargeable batteries. Environmentally friendly, an n-type nanocrystalline, Ag_2Se thin film exhibits the direct bandgap of 1.8 eV [10].

From the broad list of available literature, only a few articles have reported that a facile strategy has been developed to prepare flexible Ag_2Se films and Ag_2Se-based composite films on nylon [7,11,12]. These multiscale Ag_2Se nanoparticles with or without Ag nanoparticles on nylon exhibit a high power factor and excellent flexibility [7,12]. Through literature analysis, we did not succeed in finding any publication devoted to optical properties of Ag_2Se/nylon composites. Considering the rapid application of hybrid materials in opto-electronic modules, such study remains relevant, significant, and timely.

Template-assisted synthesis represents a straightforward, adaptable, and successful nanomaterial synthesis approach. In this approach, the templates may serve as physical scaffolds, against which other materials are assembled, or templates are engaged in synthesis as one of the reactants (template-engaged reactions). Recently, several teams have described the synthesis of Ag_2Se nanotubes [13,14], nanowires [5,15], and Se/Ag_2Se/core/shell nanocables [14] by this technique. The authors emphasised that the resulting Ag_2Se have retained the both shape and morphology of trigonal Se template with good precision.

In this study, compact Ag–Se/nylon semiconductor nanocomposites were formed via a template-engaged reaction, which could convert the amorphous selenium (a–Se) layer on nylon into an Ag–Se film. The sequential deposition method was explored. The type of the template, as well as its amount, exerts a strong influence on the structure and the properties of the resulting composites. Firstly, a–Se was deposited on nylon 6 while using the chemical bath deposition (CBD) method by mixing solutions of H_2SeO_3 and Na_2SO_3 and changing the time of selenium deposition. These a–Se/nylon templates were then exposed to the $AgNO_3$ solution. The Ag–Se/nylon nanocomposites surface morphology, elemental and phase composition, and optical properties were monitored depending on the selenium deposition time on nylon. The results were interpreted, discussed, and compared with some of the currently available state-of-the-art reports.

2. Materials and Methods

2.1. Polymer

The thermoplastic matrix which we used was semi crystalline nylon 6 *Tecamid 6*, (hereinafter referred as 'nylon') produced by Ensinger GmbH (Germany). The 500 μm-thick nylon film was opaque. The density was 1.13 g/cm^3, moisture absorption 3%, water absorption to equilibrium 9.5%. The experiments were performed on strips of $2' \, 6$ cm^2 in size. Prior to the experiments, nylon film cuts were washed with Na_2CO_3, and afterward treated in distilled water at 100 °C for 2 h. The criterion for the quality treatment of the nylon substrate surface was its uniform wetting with distilled water. After treatment, the substrates were stored in a desiccator.

2.2. Chemicals

The distilled water and as received analytical grade reagents were used to prepare freshly solutions for each experiment. Selenous acid (H_2SeO_3, 99.0%) and sodium sulphite heptahydrate ($Na_2SO_3 \cdot 7H_2O$, 99.0%) were obtained from Reachim, Russia. Sulphur acid (H_2SO_4, 96.0%), silver nitrate ($AgNO_3$, 99.0%), and sodium carbonate hydrate ($Na_2CO_3 \cdot 10H_2O$, $\geq$99.0% (calc. based on dry substance)) were purchased from Aldrich Chemical Co.

2.3. Sample Preparation and Theoretical Background

The first step involved the formation of a selenium film via the CBD method. The concentrations of H_2SeO_3 and Na_2SO_3 solutions and temperature that yielded a superior a–Se/nylon template, with respect to continuity, smoothness, and the adherence of the selenium film to the substrate, were chosen for further experiments. For Se film deposition, nylon strips were exposed in 0.1 M H_2SeO_3 and 0.15 M Na_2SO_3 solution (pH 2 adjusted with H_2SO_4) for 6, 12, 24, and 30 h at 20 ± 1 °C. The red amorphous selenium (a–Se) isolated according to the following equation [16,17]:

$$H_2SeO_{3(aq)} + 2Na_2SO_{3(aq)} \rightarrow Se_{(s)} + 2Na_2SO_{4(aq)} + H_2O. \tag{1}$$

The half reactions for the reduction and oxidation of selenous acid and the sulphite ion, respectively, are the following Equations (2) and (3):

$$H_2SeO_{3(aq)} + 4H^+{}_{(aq)} + 4e^- \rightarrow Se_{(s)} + 3H_2O, \tag{2}$$

$$SO_3{}^{2-}{}_{(aq)} + H_2O - 2e^- \rightarrow SO_4{}^{2-}{}_{(aq)} + 2H^+{}_{(aq)}. \tag{3}$$

The reduction potentials ($E^0{}_{red}$) are 0.74 V for Equation (2) and 0.17 V for Equation (3), respectively. Therefore, sodium sulphite reduces selenite readily, and the redox reaction is spontaneous [16].

For Equation (1), an acidic environment and the stoichiometry of the initial reacting materials are essential in order to prevent the formation of polythionates. Monoselenotrithionic acid forms with an excess of H_2SO_3 solution are added to the solution of H_2SeO_3 with ratio 3:1 [17]:

$$H_2SeO_{3(aq)} + 3H_2SO_{3(aq)} \rightarrow H_2SeS_2O_{6(aq)} + H_2SO_{4(aq)} + 2H_2O. \tag{4}$$

Diselenotetrathionic acid forms when H_2SO_3 solution is added to an excess of H_2SeO_3 [17]:

$$2H_2SeO_{3(aq)} + 5H_2SO_{3(aq)} \rightarrow H_2Se_2S_2O_{6(aq)} + 3H_2SO_{4(aq)} + 3H_2O. \tag{5}$$

In an acidic solution, polythionic acids decompose with the release of elemental selenium. Selenotritithionic acid $H_2SeS_2O_6$ is more stable than diselenothionic acid $H_2Se_2SO_6$, which decomposes with the release of elemental selenium at room temperature [17].

Afterward the selenium deposition, the a–Se/nylon samples were cleaned with C_2H_5OH to remove a poorly adhering film. Then a–Se/nylon samples were thoroughly washed with hot distilled water, and, between the subsequent processing steps, were stored in a desiccator. During the second stage, these a–Se/nylon templates were treated for 2 h with 0.1 M solution of $AgNO_3$ (pH 6.35) at 20 ± 1 °C temperature in a thermostatic vessel.

The solid phase formation at the template/solution interface is a dynamic non-equilibrium process requiring careful consideration of the physicochemical pathways by which they proceed. The solubility of the starting material is the determining indicator for the thermodynamic reaction feasibility in thin films deposition. The change in system Gibbs free energy is also determinant in the solid-state reaction pathway [18,19]. Additionally, the ion-exchange reactions can precede through simple mutual diffusion [20]. The highly reactive elemental Se is an excellent template for the synthesis of various metal selenides even at ambient temperature [5]. If wet films of silver and selenium are stocked together, the reaction–diffusion process starts to yield the silver selenide [21,22]. The formation of Ag_2Se phases in the Ag–Se/nylon nanocomposite could be explained through complex mechanism reactions. When refluxed in an aqueous medium containing Ag^+ cations, amorphous selenium disproportionates into Se^{2-} and $SeO_3{}^{2-}$ anions:

$$3Se_{(s)} + 3H_2O \rightarrow 2Se^{2-}{}_{(ad)} + H_2SeO_{3(ad)} + 4H^+{}_{(aq)}. \tag{6}$$

Ag^+ ions react with adsorbed chalcogenides particles (Se^{2-}, $SeO_3{}^{2-}$) to generate insoluble nanoparticles, which are in situ deposited on the a–Se/nylon template to produce

Ag–Se/nylon nanocomposites. The major reaction describing Ag_2Se formation can be written as follows [5]:

$$3Se_{(s)} + 6AgNO_{3(aq)} + 3H_2O \rightarrow 2Ag_2Se_{(s)} + Ag_2SeO_{3(s)} + 6HNO_{3(aq)}. \quad (7)$$

As the hydrophilic nylon is treated in the acidified selenium precursor solution, SO_3^{2-}, SO_4^{2-}, and SeO_3^{2-} ions can diffuse into the sub-surface space of nylon, and potentially bind to the charged sites of nylon, such as the ionised functional groups −CONH and –NH [23]. Ag^+ cations could diffuse into the a–Se/nylon template, and the formation of a sub-product within the template matrix—such as Ag_2SO_4, Ag_2SO_3, and Ag_2SeO_3—is probable.

The formed Ag–Se/nylon nanocomposites were thoroughly rinsed with hot distilled water, dried and stored in the desiccator over $CaCl_2$. Throughout the text, the obtained nanocomposites were labelled as Ag–Se-6/nylon, Ag–Se-12/nylon, Ag–Se-24/nylon and Ag–Se-30/nylon, where the added number refers to the selenium deposition time.

2.4. Testing Procedures

The solution pH was measured by using a pH-meter WTW330 (Xylem Analytics Germany Sales GmbH & Co. KG WTW, Weilheim, Germany). An optical microscope CX31 equipped with a C-5050 photo camera (Olympus Corporation, Tokyo, Japan) was used to take the images of uncoated nylon and the obtained Ag–Se/nylon composites. The X-ray diffraction (XRD) analysis was performed on a Bruker Advance D8 diffractometer with Bruker LynxEye counting detector. The operating parameters were the tube voltage of 40 kV, and the tube (emission) current of 40 mA. A Ni 0.02 mm filter selected CuKα (λ = 0.154178 nm) radiation. XRD patterns collected 2θ = 30–70° at a scanning rate of 1° min^{-1} by using the coupled two theta/theta scan type. Scanning electron microscopy coupled with energy-dispersive X-ray spectroscopy (EDS/SEM) analyses were conducted using a Phenom ProX desktop scanning electron microscope (LOT-QuantumDesign) with a high sensitivity multi-mode backscatter electron (BSE) detector. Resolution was ≤8 nm. Primary-beam energy was 0.15 kV EHT. Atomic force a NanoWizard®3 NanoScience microscope (JPK Instruments, Bruker Nano GmbH, Berlin, Germany) with pyramidal-shaped i-type silicon cantilever (0.01–0.025 ohm/cm, spring constant of 2 N/m) operated in the contact mode. The AFM images scanning area was 30 × 30 μm^2. Topographical parameters were evaluated using JPKSPM Data Processing software (Version spm-4.3.13). The diffuse reflectance spectra of the composites were recorded by using a UV-Vis spectrophotometer Lambda 35 within the range 380–1100 nm. The reflectance data were analysed applying the Kubelka Munk model [24–26].

3. Results

3.1. Optical Microscopy and ProX-SEM-EDS *Analysis*

The optical images of the uncoated nylon and corresponding Ag–Se/nylon nanocomposites are shown in Figure 1. The obtained Ag–Se/nylon nanocomposites were homogeneous, spectacularly reflecting with good adherence.

The SEM analysis (Figure 2) indicated that the progression of surface morphology changes is significantly dependent on the selenium deposition time.

As it can be seen, uncoated nylon showed fine dispersion and compact surface morphology. Different small pinholes, bumps, as well as some traces of cracking were visible on the top surface. The surface area of Ag–Se/nylon nanocomposites became larger due to the unevenness and multiple roughnesses, which can be considered as a major source of energy absorption. The surface morphology of Ag–Se-6/nylon sample contained various roads (average size 1.5–4 μm) and irregularly shaped pyramidal-like sub-micron structures (average size 0.5–1 μm). It must also be noted that these units were stacked on top of each other, indicating different stages of growth.

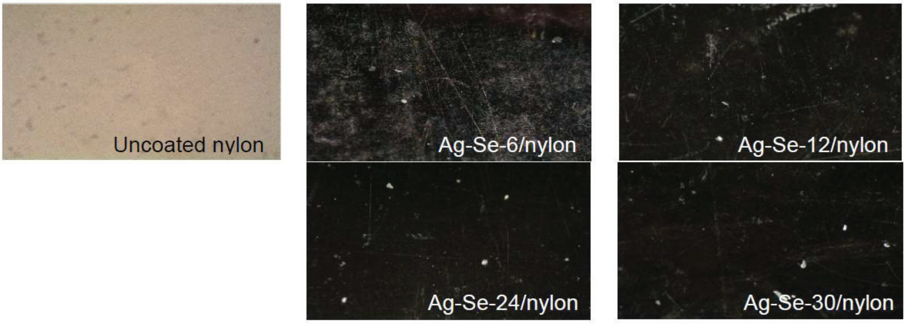

Figure 1. An image of uncoated nylon and obtained Ag–Se/nylon nanocomposites. Magnification 100×.

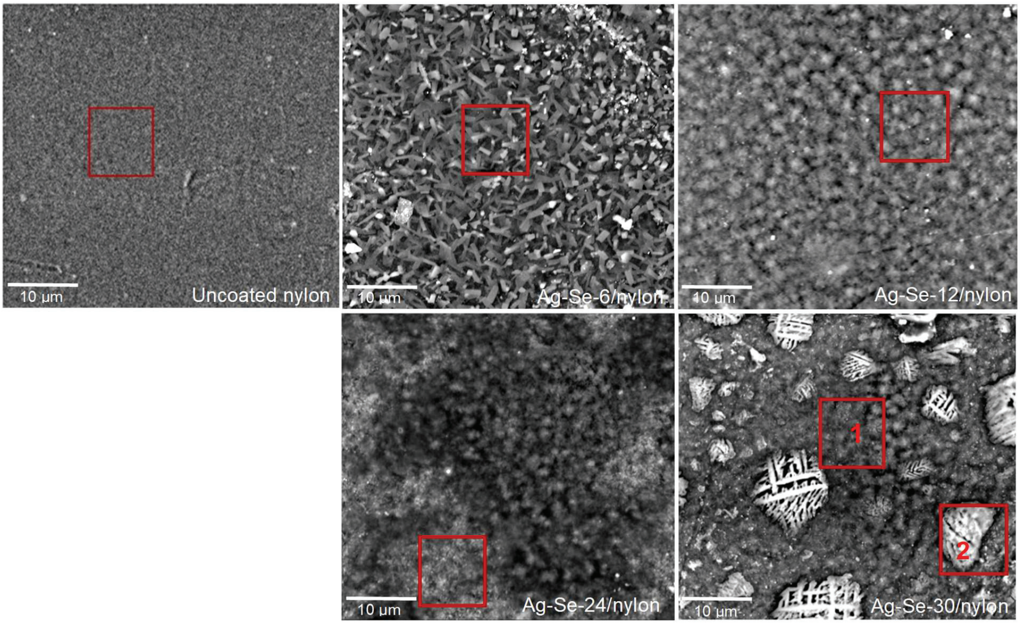

Figure 2. SEM microphotographs of uncoated nylon and Ag–Se/nylon samples with the marked area where the elemental composition was determined by Phenom ProX-SEM-EDS.

The elemental composition from SEM-EDS analysis of a large area (10 × 11.5 μm^2) of an Ag–Se-6/nylon sample confirmed the presence of carbon (C), oxygen (O), nitrogen (N), selenium (Se), sulphur (S), and silver (Ag) (Table 1). The ratio of the Ag/Se atomic concentrations *f* was 1.24, and it confirmed the overall deficiency of the silver. By increasing the selenium deposition time up to 12 h, we observed an orderly array of tightly packed spherical-like structures. The average diameter of these spherical-like structures was about 3–4 µm. Detailed analysis of the micrograph shows that these spherical-like structures in fact were clumped in various sized clusters. The dark spots are due to the pits in the surface. A similar surface morphology was also visible in the case of the Ag–Se-24/nylon sample. The different clusters of various spherical particles were formed. In addition, the more heterogeneous surface morphology is evident when compared with the Ag–Se-12/nylon sample. There were deeper (darker) areas, and, above them, there were brighter areas consisting of small >0.5 µm derivatives. As expected, Phenom ProX-SEM-EDS spectra from the Ag–Se-12/nylon and Ag–Se-24/nylon samples (Table 1) confirmed that silver, selenium, and sulphur were present in higher concentrations compared with the values of the Ag–Se-

6/nylon sample (Table 1). The ratios of f were 1.81 and 1.34 for the Ag–Se-12/nylon and Ag–Se-24/nylon samples, respectively. With a further increase in the selenium deposition time up to 30 h, significant changes in the Ag–Se-30/nylon sample surface morphology could be discerned. The varying size grains, which created different small granular islands, are visible. Various grid-like structures of irregular shapes in the size of 1–15 µm were randomly arranged on the top-surface of these granules. Granular morphology exhibited $f = 2.03$ (Table 1, Ag–Se-30/nylon sample area 1), while, for the grid-like structures, f was 2.29 (Table 1, Ag–Se-30/nylon sample area 2). The ProX-SEM-EDS spectra analysis pointed out that not only Ag_2Se nanoparticles, but also Ag was clearly concentrated on the grid-like structures. Metallic silver is the most likely impurity in the chemical deposition of Ag_2Se films [5]:

$$Se_{(s)} + 4AgNO_{3(aq)} + 3H_2O \rightarrow 4Ag_{(s)} + H_2SeO_{3(aq)} + 4HNO_{3(aq)}. \quad (8)$$

As discussed in ref. [27], excess of Ag may be incorporated in various ways: as point defects, as adsorbed metal chains, or as three-dimensional nano- or microscale inhomogeneities. The silver-rich Ag_2Se films exhibit the both negative and linear positive magnetoresistance effects [7,28], and no saturating magnetoresistance [7], which predestines them for various applications.

Table 1. Elemental composition of the Ag–Se/nylon nanocomposites obtained by EDS acquired from the surface area marked in Figure 2.

Sample	Atomic Concentrations, %						
	C	**O**	**N**	**S**	**Se**	**Ag**	**Ag/Se Concentration Ratio**
Uncoated nylon	28.68	44.96	26.36	-	-	-	-
Ag–Se-6/nylon	27.62	52.53	17.31	0.32	0.99	1.23	1.24
Ag–Se-12/nylon	25.14	52.70	17.22	0.90	1.44	2.60	1.81
Ag–Se-24/nylon	29.32	50.05	15.65	1.03	1.69	2.26	1.34
Ag–Se-30/nylon							
area 1	27.76	49.42	17.40	0.93	1.48	3.01	2.03
area 2	31.51	44.50	18.34	0.81	1.47	3.37	2.29

Extraneous elements C and N came from the nylon matrix since it is the largest part of the Ag–Se/nylon samples (Table 1). The higher content of oxygen observed in all the obtained samples as compared with that of the uncoated nylon sample distinctly supports the penetration of oxygen-containing ions, such as SeO_3^{2-}, SO_3^{2-}, or SO_4^{2-}. Although SEM/EDS is useful for the identification of the elemental distribution in micro-domains, however, it must still be appreciated that the elemental information obtained from the micron region is naturally of a heterogeneous nature when compared with bulk analyses.

As discussed above, hydrophilic nylon absorbs various ions from aqueous electrolyte solutions. To collect the relevant information, the cross-sectional analysis was performed, and the representative results are shown in Figure 3.

Three different layers with varying fractional thickness (Table 2) can be clearly identified from the cross-sectional micrographs of Ag–Se/nylon samples. The boundary between each layer is well defined: a highly dense component depicting a homogeneous diffusion layer (grey), an intermediate layer (white), which seems to be composed of coalescence particles, and, finally, the topmost (dark) layer.

The fractional thickness of the topmost layer increased with the selenium deposition time (Table 2), while the fractional thickness of the intermediate layer decreased. The fractional thickness of the diffusion layer showed a non-monotonic character. The total thickness increased with an increase of the selenium deposition time (Table 2). As an example, it was in the range of 22.83–32.33 and 27.1–39.91 µm for Ag–Se-6/nylon and Ag–Se-30/nylon, respectively. EDS analysis was performed to investigate the chemical composition from each fractional layer of the nanocomposite, and the resulting data (spot 1, spot 2 and spot 3, as marked in Figure 3) are presented in Tables 3–6, respectively.

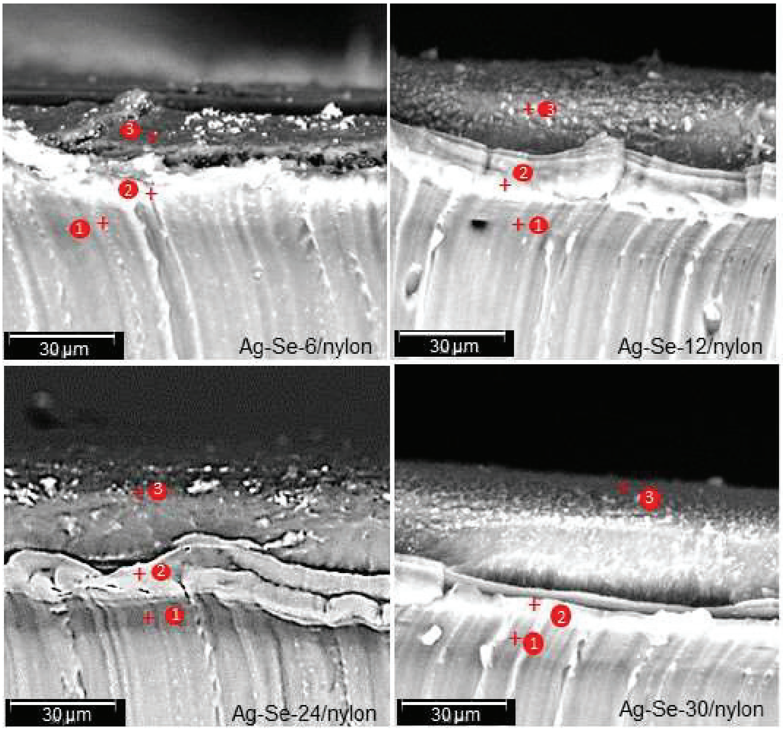

Figure 3. Cross-sectional micrographs of Ag–Se/nylon samples with marked points where the elemental composition was determined by Phenom ProX-SEM-EDS.

Table 2. Fractional thickness of Ag–Se film layers on nylon.

Layer	Fractional Thickness of the Layers, µm			
	Ag–Se-6/nylon	**Ag–Se-12/nylon**	**Ag–Se-24/nylon**	**Ag–Se-30/nylon**
Topmost (dark)	7.61–9.51	8.67–15.17	8.51–13.70	14.09–19.51
Intermediate (white)	7.61–13.31	8.67–10.14	5.15–7.87	4.34–9.76
Diffusion (grey)	7.61–9.51	8.67–13.00	8.52–11.61	8.67–10.64
Total	22.83–32.33	26.01–38.31	22.18–33.18	27.1–39.91

Table 3. Chemical composition from each fractional layer (spot 1, spot 2, and spot 3, as marked in Figure 3) of the Ag–Se-6/nylon nanocomposite obtained by EDS.

Spot	Atomic Concentrations, %						
	C	**O**	**N**	**S**	**Se**	**Ag**	**Ag/Se Concentration Ratio**
1	28.69	44.96	26.35	-	-	-	-
2	34.19	40.10	24.98	0.19	0.54	-	-
3	36.70	37.70	23.30	0.23	0.95	1.12	1.18

Table 4. Chemical composition from each fractional layer (spot 1, spot 2, and spot 3, as marked in Figure 3) of the Ag–Se-12/nylon nanocomposite obtained by EDS.

Spot	Atomic Concentrations, %						
	C	O	N	S	Se	Ag	Ag/Se Concentration Ratio
1	20.99	55.98	22.22	0.39	0.42	-	-
2	41.94	37.58	18.68	0.50	0.99	0.31	0.31
3	40.04	36.30	17.80	0.95	3.32	1.59	0.48

Table 5. Chemical composition from each fractional layer (spot 1, spot 2, and spot 3, as marked in Figure 3) of the Ag–Se-24/nylon nanocomposite obtained by EDS.

Spot	Atomic Concentrations, %						
	C	O	N	S	Se	Ag	Ag/Se Concentration Ratio
1	27.12	47.98	24.03	0.34	0.53	-	-
2	26.60	45.78	24.47	0.23	0.95	1.97	2.07
3	25.14	52.70	17.22	0.93	1.41	2.60	1.84

Table 6. Chemical composition from each fractional layer (spot 1, spot 2, and spot 3, as marked in Figure 3) of the Ag–Se-30/nylon nanocomposite obtained by EDS.

Spot	Atomic Concentrations, %						
	C	O	N	S	Se	Ag	Ag/Se Concentration Ratio
1	30.93	50.91	17.14	0.35	0.67	-	-
2	29.58	45.42	19.06	0.78	1.46	3.70	2.53
3	30.34	46.63	16.53	1.44	1.65	3.41	2.07

The results indicate that the silver, selenium, and sulphur atomic concentration of these fractional layers greatly depends on the selenium deposition time. From the depth profile EDS spectra data (Tables 3–6), it is clear that sulphur is present in all the three layers, thereby indicating that diffusion occurred during the a–Se/nylon template preparation. Likewise, in the first synthesis step, SeO_3^{2-}, SO_3^{2-}, or SO_4^{2-} ions as well as selenium nanoparticles penetrate into the polymer matrix until the concentration reaches an equilibrium value. The EDS spectra from the topmost (spot 3), intermediate (spot 2), and diffusion (spot 3) layers indicate non-homogeneous distribution of silver, selenium, and sulphur atomic concentration throughout its thickness. We note that, in all composites, silver was not detected in the diffusion layer (Tables 3–6). The calculated ratio f of the topmost layer was 1.17, 2.02, 1.84, and 2.06 for Ag–Se-6/nylon, Ag–Se-12/nylon, Ag–Se-24/nylon, and Ag–Se-30/nylon, respectively (Tables 3–6).

3.2. XRD Analysis

The crystallographic structure of the Ag–Se/nylon nanocomposites was studied by XRD analysis. Our previous XRD studies of the nylon matrix showed that the diffraction pattern features two dominant peaks at 2θ 20.1° and 23.5°, and the peak at 9.4° of lower intensity [29]. As the intensities of nylon XRD peaks sharply exceeded the XRD patterns of the obtained composites, the diffractograms are given in the 30–65° 2θ angular interval. The experimental data were interpreted by using the standard JCPDS cards and the data available in the literature [5,30]. Analysis results are presented in Figure 4.

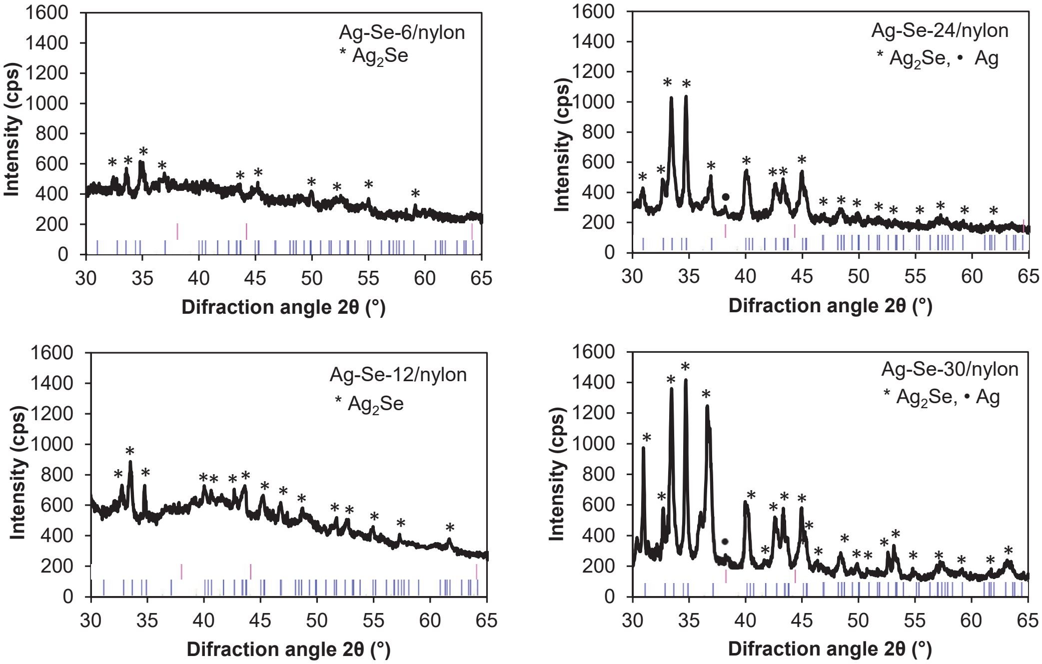

Figure 4. XRD patterns of Ag–Se films on the nylon surface. The black lines are the experimental patterns, and the pink and blue lines label the peaks from Ag (04-003-1472 (Calc., Intensity: 36.0%)) and Ag_2Se (01-071-2410 (Calc., Intensity: 91.0%)), respectively.

The Ag–Se-6/nylon nanocomposite showed diffraction peaks corresponding to the orthorhombic naumannite phase of Ag_2Se (JCPDS # 01-071-2410, λ = 0.15406 nm). As observed from the pattern, the predominant (121) peak of the orthorhombic system represents a preferred orientation along this plane. The identified peak positions coincide well with the ones reported in literature for Ag_2Se nanowires [5] and nanoparticles [30]. With a further increase in the selenium deposition time (Figure 4 Ag–Se-12/nylon sample), the intensity of the reflection (112) line increased, whereas the number of new peaks corresponding to the silver selenide phase rose. The diffractogram of the Ag–Se-24/nylon nanocomposite showed two sharp lines of nearly equal intensity along (112) and (121) planes, respectively. The orientation along (121) plane became predominant in the Ag–Se-30/nylon nanocomposite. In the Ag–Se-24/nylon and Ag–Se-30/nylon samples diffractograms, the metallic Ag phase (JCPDS # 04-003-1472, λ = 0.15406 nm) was also detected. Usually, the metallic Ag structure is depicted by a sharp XRD peak at 2θ 38.12° corresponding to a preferential (111) texture. Together with the Ag_2Se phase, a minor amount of elemental selenium may remain not reacted in the deposited film. At room temperature, deposited Se is amorphous and not detected by XRD. Since the Ag_2SeO_3, Ag_2SO_3, and Ag_2SO_4 phases were not found in Ag–Se/nylon nanocomposites, it could be assumed that the SeO_3^{2-}, SO_3^{2-}, and SO_4^{2-} ions diffused out from the a–Se/nylon template, and reacted with the silver ions to produce these compounds in solution nearby the a–Se/nylon template region. In the other case, the by-products of this reaction, due to high solubility, were removed from sample surface by rinsing with excess hot water before XRD analysis.

3.3. AFM Analysis

The 2D and 3D AFM images for scanning areas of 30 × 30 μm^2 are presented in Figure 5.

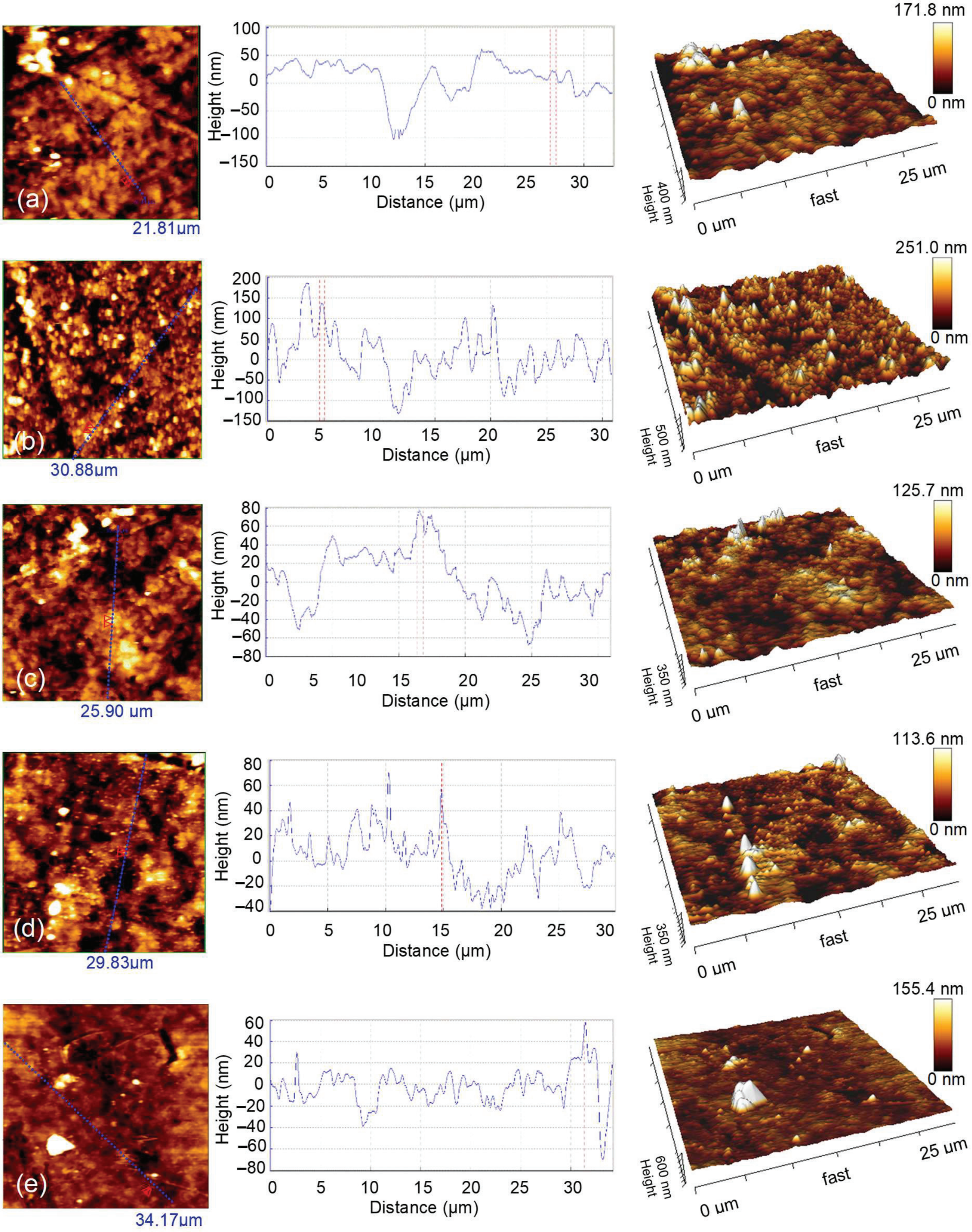

Figure 5. AFM views (left—2D views; center—profile; right—3D views) of (**a**) uncoated nylon, (**b**) Ag–Se-6/nylon, (**c**) Ag–Se-12/nylon, (**d**) Ag–Se-24/nylon, (**e**) Ag–Se-30/nylon.

The experimental results evidently indicate that the surface topography of the Ag–Se/nylon nanocomposites strongly depends on the selenium deposition time. As it can be seen, the uncoated nylon showed a morphology composed of some bulges, sags, and pores (Figure 5a). These structures of various scales also existed in the Ag–Se-6/nylon sample, and were distributed unevenly in some ranges (Figure 5b). In addition, these features possess different irregular shapes, sizes, and separations. With a further increase in the selenium deposition time (Figure 5c–e), we observed the appearance of particles agglomerates, which form separated islands. There are also various darker areas (spots and channels) filled with the several smaller grains, indicating the non-uniform growth of layers across film thickness. Alternatively, these spots and channels may represent the holes and cracks extracting down to the depth. In addition, randomly distributed pyramidal-like structures were also visible. It is difficult to notice a significant relationship between the size, shape, and the number density of morphological defects and the selenium deposition time. An examination of all AFM images indicates that the smallest number density of morphological defects is in the Ag–Se-30/nylon nanocomposite. The roughness of the composite surface strongly affects the reflectance of light and is crucial for materials application in the optoelectronic devices. The topographical parameters elucidated by using AFM analysis are gathered in Table 7.

Table 7. Surface topographical parameters average height (Z_{mean}), average roughness (R_a), root-mean-square surface roughness (R_q), and peak-to-valley roughness (R_t) obtained by AFM analysis.

Sample	Z_{mean} (nm)	R_a (nm)	R_q (nm)	R_t (nm)
Uncoated nylon	171.8	28.22	39.06	429.0
Ag–Se-6/nylon	251.0	43.19	57.04	547.0
Ag–Se-12/nylon	125.7	20.67	28.57	350.9
Ag–Se-24/nylon	113.6	18.53	25.82	369.2
Ag–Se-30/nylon	155.4	17.54	35.33	607.6

The root-mean-square surface roughness (R_q) of the obtained composites decreased with an increase of the selenium deposition time from 12 to 24 h, and, in Ag–Se-12/nylon and Ag–Se-24/nylon nanocomposites, it was lower than that of uncoated nylon, but it increased with the prolongation of the selenium deposition time up to 30 h (Table 7). The variation trend in the height and roughness values may be related to the deviation of the films composition from the stoichiometric ratio of Ag and Se (Tables 1 and 3–6) and variation in the thickness of the Ag_2Se film (Table 2). Additionally, the mobility and diffusion of the SO_3^{2-} and SeO_3^{2-} ions into the sub-surface space of nylon may enhance or inhibit the grain growth and hence affect the surface morphology (R_q) and roughness of the deposited films. The (R_q) obtained values of 25.82–57.04 nm reasonably suggest that the surface morphology is responsible for the relatively high refractive indices of the Ag–Se/nylon nanocomposites (as discussed in the section on UV-Vis analysis). The height distribution function gives the number of times that regions of a constant height occur in the morphology of the film [21]. Figure 6 shows a relatively homogeneous particle height distribution for the Ag–Se/nylon nanocomposites. Kurtosis (R_{Ku}) and skewness (R_{sk}) parameters equaled 3.1 ± 0.1 and 0.2 ± 0.05, respectively, suggesting a quasi-symmetric Gaussian distribution.

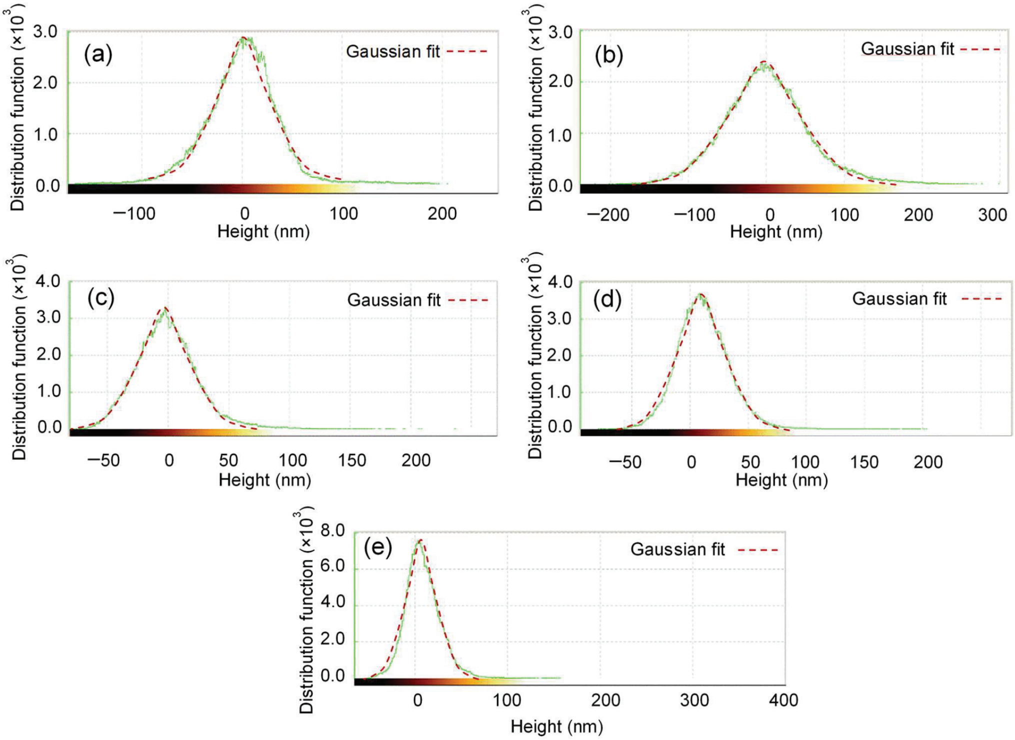

Figure 6. Histogram of the height distribution function in AFM images of (**a**) uncoated nylon, (**b**) Ag–Se-6/nylon, (**c**) Ag–Se-12/nylon, (**d**) Ag–Se-24/nylon, (**e**) Ag–Se-30/nylon samples.

3.4. UV-Vis Analysis

In the spectrum of the Ag–Se-6/nylon sample (Figure 7), the maximum absorption peak was located at 477 nm, accompanied by a shoulder peak at 584 nm.

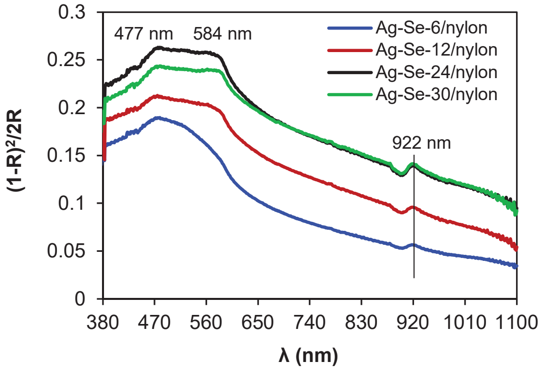

Figure 7. Optical absorption spectra of Ag–Se/nylon nanocomposites.

It is obvious that both absorption features did not shift with the selenium deposition time, but they were just subjected to an increase in their intensities. The literature reports wide absorption bands in the region between 300 and 600 nm for Ag_2Se nanoparticles [31]. In the wavelength range higher than 620 nm (near the infrared spectral range), the absorbance monotonically decreased. The peak at 922 nm possibly arises from the absorption by some large coalescing aggregates. The Kubelka–Munk method was applied to determine an optical band gap (E_{op}). The E_{op} and the reflectance are interrelated by the equations given below [25,26]: This is example 1 of an equation:

$$F\cdot(R) = \frac{(1-R)^2}{2\cdot R}\,, \tag{9}$$

$$hvF \sim \left(hv - E_{op}\right)^n, \tag{10}$$

where F—the Kubelka–Munk function, R—the reflectance, hv—the photon energy, and E_{op} is the optical band gap, n is a constant characterising the transition mode, n = 1/2 or 2 are for the allowed direct or indirect transitions, respectively.

The variation of $(hvF)^2$ versus hv for each composite is shown in Figure 8. The linear part in the higher energy region confirms the allowed direct transition mode. The intersection of a long straight-line part with the photon energy axis depicts E_{op} value. The obtained values were 1.86 eV, 1.76 eV, 1.70 eV, and 1.68 eV for Ag–Se-6/nylon, Ag–Se-12/nylon, Ag–Se-24/nylon and Ag–Se-30/nylon nanocomposites, respectively. The similar values were reported in ref. [10]. The red shift of E_{op} values with an increasing of selenium deposition time can be related to the polycrystalline structure of Ag_2Se and a relatively high surface roughness (Table 7). Additionally, the structural defects generated from the dispersed selenium nanoparticles and adsorbed SeO_3^{2-}, SO_3^{2-}, or SO_4^{2-} ions in the composites can also contribute to the band gap value [32]. The Ag_2Se had a narrow band gap (~0.15 eV) in the bulk case at room temperature [33]. The higher E_{op} values as compared with that of bulk Ag_2Se suggest that the particle sizes were within the quantum confinement regime [34].

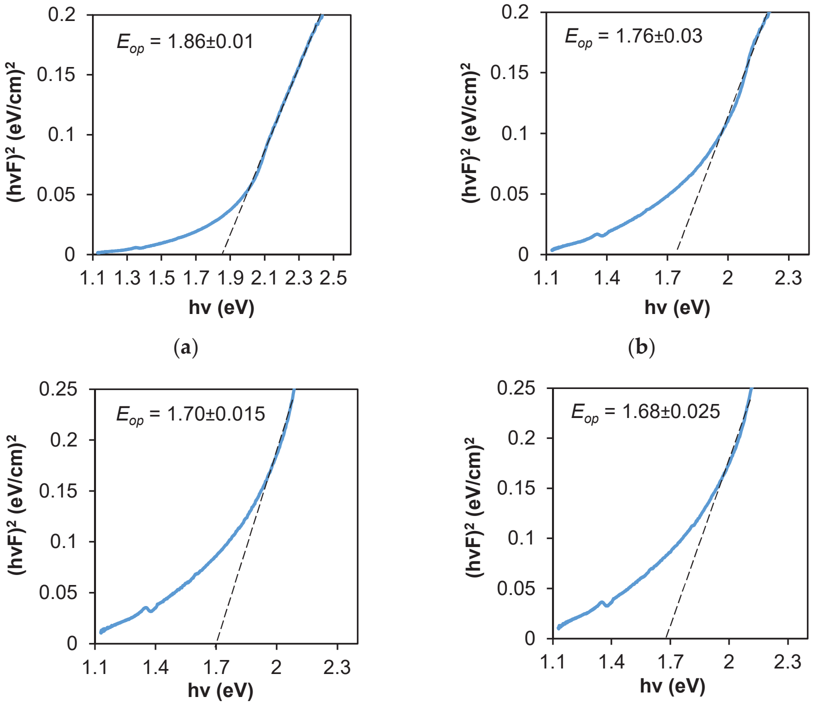

(**a**) (**b**)

(**c**) (**d**)

Figure 8. Optical band gap determination from diffuse reflectance spectra by the Kubelka–Munk method: (**a**) Ag–Se-6/nylon; (**b**) Ag–Se-12/nylon; (**c**) Ag–Se-24/nylon; (**d**) Ag–Se-30/nylon samples.

The refractive index difference of constituent materials causes a significant light scattering as well as a loss of transparency in organic-inorganic composites [35]. The following equation was applied to calculate the refractive indices (n): [36,37]:

$$n = \frac{-(R+1) \pm 2\sqrt{R}}{R-1}. \tag{11}$$

The spectral behaviour of indices (Figure 9) showed a very complex character.

In the spectral region between 380 and 477 nm, the refractive indices of all the investigated Ag–Se/nylon nanocomposites illustrated a slow decrease, which can be explained by a single oscillator model [36]. As we can observe, the refractive indices of the Ag–Se-6/nylon nanocomposite increased in the spectral interval from 477 nm to 584 nm, while, for the three other nanocomposites (Ag–Se-12/nylon, Ag–Se-24/nylon and Ag–Se-30/nylon), it remained nearly constant (the plateau region). In the region at λ > 590 nm, the refractive indices monotonically increased showing an anomalous dispersion [38]. As discussed above, various sub-micron structures, particles and agglomerates covered the nylon surface (Figure 2). These structural elements can also contribute to the anomalous dispersion [39]. At the same time, the refractive indices depend on the selenium deposition time. Specifically, Ag–Se-6/nylon nanocomposite possesses the ultra-high refractive index as compared with other samples (Figure 9). For example, the values of refractive indices for Ag–Se-6/nylon and Ag–Se-30/nylon nanocomposites at λ = 800 nm were 3.68 and 1.98, respectively and coincide well with those reported in ref. [40]. Finally, we must note that the investigated composites possessed high refractive index values. Consequently, they are promising for the development of efficient flat waveguide components and anti-reflective coatings.

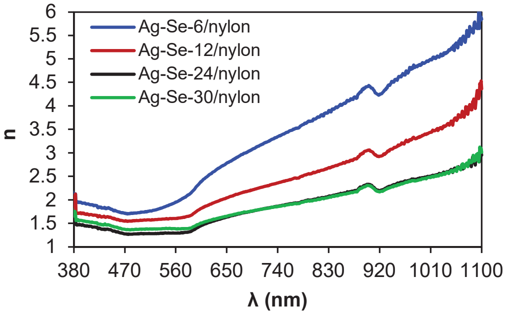

Figure 9. Variation of refractive indices of Ag–Se/nylon nanocomposites on wavelength.

4. Conclusions

Compact multilayer Ag–Se/nylon semiconductor nanocomposites were synthesised via a template-engaged reaction, which could convert the a–Se layer on nylon into an Ag–Se film. The obtained results imply that the surface morphology, and elemental and phase composition of Ag–Se/nylon nanocomposites as well as their optical properties were highly sensitive to the selenium deposition time on nylon. Scanning electron microscope (SEM) analysis confirmed the development of a very complex surface composed of pyramidal-like sub-micron structures, agglomerates, and grid-like structures. Energy dispersive spectroscopy (EDS) of large areas (10×11.5 μm^2) proved the presence of carbon, oxygen, nitrogen, sulphur, selenium, and silver. The higher content of oxygen was observed in all the obtained composites as compared with that of an uncoated nylon sample, which distinctly suggests the presence of oxygen containing ions, such as SeO_3^{2-}, SO_3^{2-}, or SO_4^{2-}. SEM/EDS cross-sectional analysis proves the multilayer character of the composite with a different individual elemental composition in each layer. X-ray diffraction analysis indicates that Ag–Se/nylon nanocomposites obtained at shorter selenium deposition times exist as polycrystalline naumannite Ag_2Se; composites obtained at longer selenium deposition times exist as a mixed-phase material composed of Ag_2Se and metallic Ag. The RMS value obtained from the atomic force microscopy varied from 25.82 nm to 57.04 nm. The direct optical band gap (E_{op}) was found to be 1.68–1.86 eV. Ag–Se/nylon nanocomposites exhibited high refractive indices in the visible and near infrared region. The presented results are promising for the optimisation of Ag_2Se/nylon nanocomposite fabrication process, which is one of the most important components in flexible electronics.

Author Contributions: Conceptualisation, V.K. and N.D.; methodology, V.K.; software, V.K.; validation, N.D., V.K. and H.M.; formal analysis, N.D.; investigation, H.M.; resources, N.D.; data curation, N.D.; writing—original draft preparation, V.K.; writing—review and editing, N.D.; visualisation, H.M.; supervision, V.K.; project administration, V.K.; funding acquisition, V.K. All authors have read and agreed to the published version of the manuscript.

Funding: This research was funded by the Doctoral Fund of Kaunas University of Technology No. A-410, approved 26 June 2019.

Institutional Review Board Statement: Not applicable.

Informed Consent Statement: Not applicable.

Data Availability Statement: Data is contained within the article.

Conflicts of Interest: The authors declare no conflict of interest.

References

1. Li, Q.; Zanelli, A. A review on fabrication and applications of textile envelope integrated flexible photovoltaic systems. *Renew. Sustain. Energy Rev.* **2021**, *139*, 110678. [CrossRef]
2. Saveleva, M.S.; Eftekhari, K.; Abalymov, A.; Douglas, T.E.L.; Volodkin, D.; Parakhonskiy, B.V.; Skirtach, A.G. Hierarchy of Hybrid Materials—The Place of Inorganics-in-Organics in it, Their Composition and Applications. *Front. Chem.* **2019**, *7*, 179. [CrossRef] [PubMed]
3. Hilal, H.S.; Zyoud, A.; Helal, M.H.S.; Bsharat, H.; Helal, H.H.; Ali, C. Effects of annealing temperature and cooling rate on photo-electrochemical performance of pristine polycrystalline metal-chalcogenide film electrodes. *Sol. Energy* **2019**, *183*, 704–715. [CrossRef]
4. Mlambo, M.; Moloto, M.J.; Moloto, N.; Mdluli, P.S. Influence of temperature and precursor concentration on the synthesis of HDA-capped Ag2Se nanoparticles. *Mater. Res. Bull.* **2013**, *48*, 2196–2200. [CrossRef]
5. Gates, B.; Mayers, B.; Wu, Y.; Sun, Y.; Cattle, B.; Yang, P.; Xia, Y. Synthesis and Characterization of Crystalline Ag $_2$ Se Nanowires Through a Template-Engaged Reaction at Room Temperature. *Adv. Funct. Mater.* **2002**, *12*, 679–686. [CrossRef]
6. Husmann, A.; Betts, J.B.; Boebinger, G.S.; Migliori, A.; Rosenbaum, T.F.; Saboungi, M.-L. Megagauss sensors. *Nature* **2002**, *417*, 421–424. [CrossRef] [PubMed]
7. Ding, Y.; Qiu, Y.; Cai, K.; Yao, Q.; Chen, S.; Chen, L.; He, J. High performance n-type Ag2Se film on nylon membrane for flexible thermoelectric power generator. *Nat. Commun.* **2019**, *10*, 841. [CrossRef]
8. Schoen, D.T.; Xie, C.; Cui, Y. Electrical Switching and Phase Transformation in Silver Selenide Nanowires. *J. Am. Chem. Soc.* **2007**, *129*, 4116–4117. [CrossRef]
9. Kobayashi, M. Review on structural and dynamical properties of silver chalcogenides. *Solid State Ionics* **1990**, *39*, 121–149. [CrossRef]
10. Pejova, B.; Najdoski, M.; Grozdanov, I.; Dey, S.K. Chemical bath deposition of nanocrystalline (111) textured Ag2Se thin films. *Mater. Lett.* **2000**, *43*, 269–273. [CrossRef]
11. Wu, M.; Cai, K.; Li, X.; Li, Y.; Liu, Y.; Lu, Y.; Wang, Z.; Zhao, W.; Wei, P. Ultraflexible and high-thermoelectric-performance sulfur-doped Ag_2Se film on nylon for power generators. *ACS Appl. Mater. Interfaces* **2022**, *14*, 4307–4315. [CrossRef]
12. Gao, Q.; Wang, W.; Lu, Y.; Cai, K.; Li, Y.; Wang, Z.; Wu, M.; Huang, C.; He, J. High power factor Ag/Ag_2Se composite films for flexible thermoelectric generators. *ACS Appl. Mater. Interfaces* **2021**, *13*, 14327–14333. [CrossRef]
13. Zhang, S.-Y.; Fang, C.-X.; Wei, W.; Jin, B.-K.; Tian, Y.-P.; Shen, Y.-H.; Yang, J.-X.; Gao, H.-W. Synthesis and Electrochemical Behavior of Crystalline Ag_2Se Nanotubes. *J. Phys. Chem. C* **2007**, *111*, 4168–4174. [CrossRef]
14. Jiang, Z.-Y.; Xie, Z.-X.; Zhang, X.-H.; Huang, R.-B.; Zheng, L.-S. Conversion of Se nanowires to Se/Ag2Se nanocables and Ag2Se nanotubes. *Chem. Phys. Lett.* **2003**, *378*, 313–316. [CrossRef]
15. Gates, B.; Wu, Y.; Yin, Y.; Yang, P.; Xia, Y. Single-Crystalline Nanowires of Ag_2Se Can Be Synthesized by Templating against Nanowires of Trigonal Se. *J. Am. Chem. Soc.* **2001**, *123*, 11500–11501. [CrossRef]
16. Greenwood, N.N.; Earnshaw, A. (Eds.). Selenium, Tellurium and Polonium. In *Chemistry of the Elements*, 2nd ed.; Elsevier Ltd., Butterworth-Heinemann: Oxford, UK, 1997; Volume 16, pp. 747–788. [CrossRef]
17. Sukyte, J.; Ivanauskas, R.; Ancutiene, I. Comparative study of selenopolythionic acids $H_2Se_nS_2O_6$ as precursors for formation of chalcogenides layers. *Chalcogenide Lett.* **2015**, *12*, 569–578.
18. Luo, Y.-R. *Comprehensive Handbook of Chemical Bond Energies*, 1st ed.; CRC Press: Boca Raton, FL, USA, 2007; p. 1688. [CrossRef]

19. Olin, Å.; Noläng, B.; Osadchii, E.G.; Öhman, L.-O.; Rosén, E. *Chemical Thermodynamics of Selenium*, 1st ed.; Elsevier Science: Amsterdam, The Netherlands, 2005; p. 894. Available online: https://www.oecd-nea.org/dbtdb/pubs/vol7-selenium.pdf (accessed on 14 April 2022).
20. Feng, S.; Xu, R. New Materials in Hydrothermal Synthesis. *Acc. Chem. Res.* **2001**, *34*, 239–247. [CrossRef]
21. Mohanty, B.C.; Murty, B.S.; Vijayan, V.; Kasiviswanathan, S. Atomic force microscopy study of thermal stability of silver selenide thin films grown on silicon. *Appl. Surf. Sci.* **2006**, *252*, 7975–7982. [CrossRef]
22. Saito, Y.; Sato, M.; Shiojiri, M. Orientation in Ag2Se polymorphic films produced by the reaction of silver films with selenium. *Thin Solid Films* **1981**, *79*, 257–266. [CrossRef]
23. Krylova, V.; Dukštienė, N. The structure of PA-Se-S-Cd composite materials probed with FTIR spectroscopy. *Appl. Surf. Sci.* **2019**, *470*, 462–471. [CrossRef]
24. Mokgalapa, N.M.; Ghosh, T.K.; Tompson, R.V.; Loyalka, S.K. Adhesion Force between a Silver Particle and Haynes 230: Role of Surface Conditions. *Nucl. Technol.* **2016**, *194*, 353–368. [CrossRef]
25. López, R.; Gómez, R. Band-gap energy estimation from diffuse reflectance measurements on sol–gel and commercial TiO2: A comparative study. *J. Sol-Gel Sci. Technol.* **2012**, *61*, 1–7. [CrossRef]
26. Nasr, M.; Viter, R.; Eid, C.; Warmont, F.; Habchi, R.; Miele, P.; Bechelany, M. Synthesis of novel $ZnO/ZnAl_2O_4$ multi co-centric nanotubes and their long-term stability in photocatalytic application. *RSC Adv.* **2016**, *6*, 103692–103699. [CrossRef]
27. Kienle, L.; Duppel, V.; Mogwitz, B.; Janek, J.; Kreutzbruck, M.V.; Leineweber, A.; Simon, A. Synthesis–Real Structure–Property: The Showcase of Silver-Rich Ag2Se. *Cryst. Growth Des.* **2011**, *11*, 2412–2421. [CrossRef]
28. Beck, G.; Janek, J. Negative and linear positive magnetoresistance effect in silver-rich silver selenide. *J. Solid State Sci.* **2008**, *10*, 776–789. [CrossRef]
29. Krylova, V.; Dukstienė, N.; Žalenkienė, S.; Baltrusaitis, J. Chemical and structural changes in polyamide based organic–inorganic hybrid materials upon incorporation of SeS2O62−precursor. *Appl. Surf. Sci.* **2017**, *392*, 634–641. [CrossRef]
30. Ayele, D.W. A facile one-pot synthesis and characterization of Ag_2Se nanoparticles at low temperature. *Egypt. J. Basic Appl. Sci.* **2016**, *3*, 149–154. [CrossRef]
31. Delgado-Beleño, Y.; Martinez-Nuñez, C.E.; Cortez-Valadez, M.; Flores-López, N.S.; Flores-Acosta, M. Optical properties of silver, silver sulfide and silver selenide nanoparticles and antibacterial applications. *Mater. Res. Bull.* **2018**, *99*, 385–392. [CrossRef]
32. Abdelrazek, E.M.; Abdelghany, A.M.; Badr, S.I.; Morsi, M.A. Structural, optical, morphological and thermal properties of PEO/PVP blend containing different concentrations of biosynthesized Au nanoparticles. *J. Mater. Res. Technol.* **2018**, *7*, 419–431. [CrossRef]
33. Zhu, C.-N.; Chen, G.; Tian, Z.-Q.; Wang, W.; Zhong, W.-Q.; Li, Z.; Zhang, Z.-L.; Pang, D.-W. Near-Infrared Fluorescent Ag_2Se-Cetuximab Nanoprobes for Targeted Imaging and Therapy of Cancer. *Small* **2017**, *13*, 1602309. [CrossRef]
34. Anthony, S.P. Synthesis of Ag2S and Ag2Se nanoparticles in self assembled block copolymer micelles and nano-arrays fabrication. *Mater. Lett.* **2009**, *63*, 773–776. [CrossRef]
35. Loste, J.; Lopez-Cuesta, J.-M.; Billon, L.; Garay, H.; Save, M. Transparent polymer nanocomposites: An overview on their synthesis and advanced properties. *Prog. Polym. Sci.* **2019**, *89*, 133–158. [CrossRef]
36. Rashad, M. Tuning optical properties of polyvinyl alcohol doped with different metal oxide nanoparticles. *Opt. Mater.* **2020**, *105*, 109857. [CrossRef]
37. Jatautė, L.; Krylova, V.; Dukštienė, N.; Lelis, M.; Tučkutė, S. Ag-In-Se films on flexible architectural textiles as efficient material for optoelectronics applications: A preliminary study. *Thin Solid Films* **2021**, *721*, 138566. [CrossRef]
38. Raj, K.R.; Murugakoothan, P. Studies on the optical and mechanical properties of non-linear optical 3-aminophenol orthophosphoric acid (3-amphph) single crystal. *Optik* **2012**, *123*, 1082–1086. [CrossRef]
39. Beaglehole, D.; Hunderi, O. Study of the Interaction of Light with Rough Metal Surfaces. I. Experiment. *Phys. Rev. B* **1970**, *2*, 309–321. [CrossRef]
40. Pandiaraman, M.; Soundararajan, N.; Vijayan, C.; Kumar, C.; Ganesan, R. Spectroscopic studies on silver selenide thin films. *J. Ovonic Res.* **2010**, *6*, 285–295.

nanomaterials

Article

Photothermal Responsivity of van der Waals Material-Based Nanomechanical Resonators

Myrron Albert Callera Aguila [1,2,3,*], Joshoua Condicion Esmenda [1,2,3], Jyh-Yang Wang [3], Yen-Chun Chen [3], Teik-Hui Lee [3], Chi-Yuan Yang [3], Kung-Hsuan Lin [3], Kuei-Shu Chang-Liao [1], Sergey Kafanov [4], Yuri A. Pashkin [4] and Chii-Dong Chen [3,*]

[1] Department of Engineering and System Science, National Tsing Hua University, Hsinchu 30013, Taiwan
[2] Nano Science and Technology Program, Taiwan International Graduate Program, Academia Sinica, Taipei 11529, Taiwan
[3] Institute of Physics, Academia Sinica, Nankang, Taipei 11529, Taiwan
[4] Department of Physics, Lancaster University, Lancaster LA1 4YB, UK
* Correspondence: maguila@gate.sinica.edu.tw (M.A.C.A); chiidong@phys.sinica.edu.tw (C.-D.C.)

Abstract: Nanomechanical resonators made from van der Waals materials (vdW NMRs) provide a new tool for sensing absorbed laser power. The photothermal response of vdW NMRs, quantified from the resonant frequency shifts induced by optical absorption, is enhanced when incorporated in a Fabry–Pérot (FP) interferometer. Along with the enhancement comes the dependence of the photothermal response on NMR displacement, which lacks investigation. Here, we address the knowledge gap by studying electromotively driven niobium diselenide drumheads fabricated on highly reflective substrates. We use a FP-mediated absorptive heating model to explain the measured variations of the photothermal response. The model predicts a higher magnitude and tuning range of photothermal responses on few-layer and monolayer $NbSe_2$ drumheads, which outperform other clamped vdW drum-type NMRs at a laser wavelength of 532 nm. Further analysis of the model shows that both the magnitude and tuning range of $NbSe_2$ drumheads scale with thickness, establishing a displacement-based framework for building bolometers using FP-mediated vdW NMRs.

Keywords: van der Waals materials; nanomechanical resonators; Fabry–Pérot interferometry; photothermal response; static displacement; absorptive heating; $NbSe_2$ drumheads

Citation: Aguila, M.A.C.; Esmenda, J.C.; Wang, J.-Y. ; Lee, T.-H.; Chen, Y.-C.; Yang, C.-Y.; Lin, K.-H.; Chang-Liao, K.-S.; Kafanov, S.; Pashkin, Y.A.; Chen, C.-D. Photothermal Responsivity of van der Waals Material-Based Nanomechanical Resonators. *Nanomaterials* **2022**, *12*, 2675. https://doi.org/10.3390/nano12152675

Academic Editors: Jihoon Lee and Ming-Yu Li

Received: 7 July 2022
Accepted: 31 July 2022
Published: 4 August 2022

1. Introduction

Nanomechanical resonators (NMRs) embedded in an optical cavity are valuable platforms for studying weak forces due to the enhanced coupling between light and motion [1]. Enhanced coupling improves the capability of nanomechanical resonators to demonstrate nonlinear dynamics [2] and sense heat transport in suspended nanostructures [3]. Resonators interacting with optical elements enjoy additional degree of spatiality [4–8], extremely large optomechanical coupling at ambient temperature [9,10], and reduced mode volume due to breakthrough technologies in focusing laser beams via free space optics [11–13], fiber optics [14–16] and near-field interactions with multiplexed on-chip optical waveguides and tapered fibre [17,18].

Heating induced by the probe laser remains a concern in the optical readout of NMRs [19,20]. Photothermal effects [3,15,21,22] emerge once the laser illuminates a region of the resonator and raises the temperature of the mechanical mode [20], while the process hinders ground-state cooling of the mechanical mode [23], it enables sensing of incident laser power with the aid of on-chip Fabry–Pérot (FP) cavities. NMRs fabricated with suspended van der Waals (vdW) materials [24–26] show promising photothermal sensitivities [27] due to reduced mass, and layer-dependent mechanical, optical, and thermal properties. Few-layer and multilayer niobium diselenide ($NbSe_2$) is a candidate vdW material for low-noise, highly responsive photodetectors at ultraviolet [28] and infrared wavelengths [29,30].

There are several approaches to quantifying the power absorbed by vdW NMRs. One can measure the mechanical mode temperature by resolving thermomechanical motion [6,31] while varying the incident laser power. Such detection requires low mass and high quality factors of NMRs, which can be difficult to ensure for vdW materials [24–26]. A less stringent yet popular method involves monitoring of the resonant frequency shift of an electromotively driven vdW NMRs [3,27], and following its dependence on the incident laser power. In both approaches, light absorption depends not only on the FP structure and wavelength, but also on the resonator displacement from the initial equilibrium position. Understanding the displacement-dependent absorptive response may provide insights into managing FP-mediated heat flow in NMRs, while experiments on NMRs fabricated from various types of vdW materials have been published, photothermal sensing with $NbSe_2$ NMRs has not yet been reported. $NbSe_2$ has low thermal conductivity [32], is flexible [33] and has large fracture strain [34]. This combination of properties enables the realization of low power, photothermal-strain-sensitive detectors.

In this paper, we explore the influence of the resonator displacement on the sensitivity of the FP-based vdW NMRs to incident light by investigating the photothermal response of electromotively driven $NbSe_2$ drumheads. We propose an FP-mediated absorptive heating model that accounts for resonator displacement to explain the observed variations in the measured photothermal response. The model consequently reveals a large tuning range of photothermal responsivity as the drumhead moves towards the bottom electrodes. We extend the model to drumheads of varying thicknesses and materials to gain insight into the geometric and material impact of FP-mediated heating on NMRs.

2. Materials and Methods

2.1. Device Design and Fabrication

Figure 1a shows the optical micrograph of devices A (circular) and B (elliptical). Bulk $NbSe_2$ flakes bought from HQ Graphene are mechanically exfoliated with PDMS stamps [8,35–37]. The flakes are then transferred on a lithographically patterned Au-Cr-SiO_2-Si substrate covered with electron-beam patterned resist CSAR-62 via dry deterministic transfer [8,36–38]. The freestanding regions of the flake above the patterned drum holes of the resist represent the drumhead resonator devices. Device A has a radius $a_A = b_A = 3.5\,\mu m$ and device B has a major radius $a_B = 4.0\,\mu m$ and a minor radius $b_B = 3.5\,\mu m$. The cross-section layout of the FP structure is shown in Figure 1b. The 40 nm-thick Au and 20 nm-thick Cr electrodes are deposited on 543 nm-thick SiO_2 to act as electrical ground and mirror. The CSAR-62 thickness s determines the designed FP cavity length.

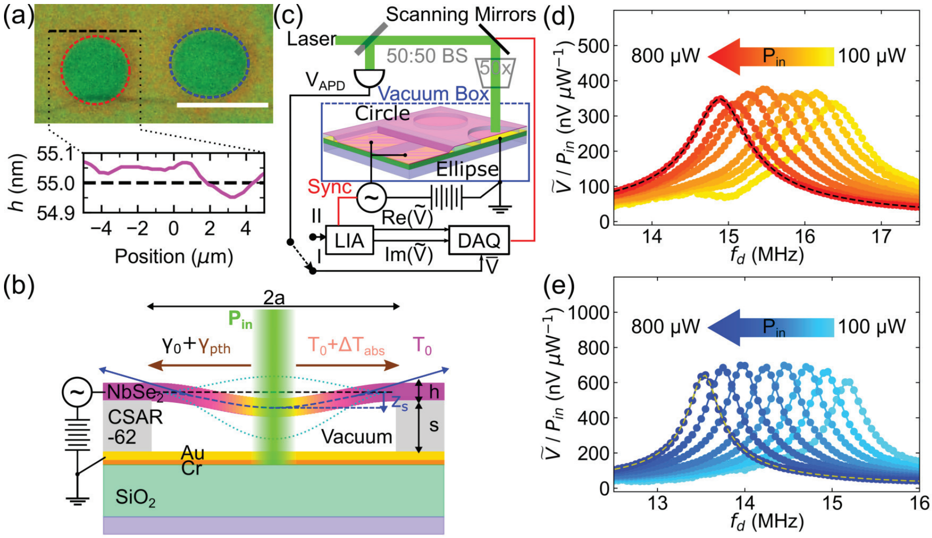

Figure 1. Measurement setup and device. (**a**) Optical micrograph of the circular (red dashed circle) and elliptical (blue dashed ellipse) drumhead resonators under study. The white scale bar corresponds to a length of 10 μm. The black dashed line on the micrograph represents the average thickness of the $NbSe_2$ flake as measured by the Multilayer Interference Approach. (**b**) Schematic diagram of laser-induced photothermal heating of an electromotively driven drumhead resonator. Cross-section showing the net tension exerted by the drumhead resonators under photothermal heating at the middle of the drumhead. (**c**) Optical interferometric setup used to track the mechanical frequency of multilayered $NbSe_2$ flake mechanical resonators. Measured driven mechanical responses of circular and elliptical drumhead resonators at increasing incident laser power are shown in (**d**,**e**), respectively. The data are represented with dot markers connected with lines. The devices are electromotively driven at $V_{DC} = 4\,\mathrm{V}$ and $V_{AC} = 0.125\,\mathrm{V}_{pk}$. The rightmost colored responses in (**d**,**e**) represent the driven responses resolved at the lowest incident powers P_{in}. The consecutive responses darken with increasing P_{in}. Dashed lines refer to the driven resonator fits.

2.2. Electromotive Actuation and Optical Detection Scheme

The mechanical drums are set into motion by an electromotive force originating from a combination of DC and oscillating voltages and as shown in Figure 1b,c. The electromotive force can be written as [2]

$$F_{em} = \frac{1}{2}\frac{dC_m}{dz}\left[V_{DC} + V_{AC}\cos(2\pi f_d t)\right]^2, \tag{1}$$

where C_m is the vacuum capacitance between the freestanding drumhead and the bottom electrode with distance defined by s, V_{DC} is the DC voltage, V_{AC} is the amplitude of the oscillating voltage at driving frequency f_d, t is time, and z is the out-of-plane (z-direction) displacement from the equilibrium position. The relation between the voltages and the time-dependent displacement for a tensioned electrostatic drum plate can be written in the form [8,39]

$$\rho h \frac{\partial^2 z(t)}{\partial t^2} + D_P \nabla^4 z(t) - \gamma \nabla^2 z(t) = \frac{F_{em}}{\pi a_{eff}^2}, \tag{2}$$

where ρ is the mass density, h is the drumhead thickness, a_{eff} is the effective radius of the drumhead, γ is the tension, and D_P is the flexural rigidity of a circular plate. Equation (2) is the general equation that determines the vibrational amplitude for electromotively-driven tensioned drum plates.

The motion is detected through the optical interferometric detection scheme at a laser wavelength $\lambda = 532\,\text{nm}$, as shown in Figure 1c. The chip containing NMR drumheads is placed in a vacuum box with optical and electrical access and a base pressure of 6×10^{-7} mBar. The laser beam, passing through a 50× objective, has a focused spot diameter of 1.9 µm and allows for spatial resolution of picometer vibrational amplitudes given the designed FP cavity length $s = 295 \pm 10$ nm as measured by a commercial stylus profilometer [8,36]. Scanning mirrors help align the spot of the probe laser beam at different positions on the drumhead. The reflected interfering light obtains redirected by the beamsplitter (50:50 BS) to the photodetector (PD). The data acquisition (DAQ) unit and the lock-in amplifier (LIA) read the PD output DC voltage $\overline{V}$ and AC voltage $\widetilde{V}(f_d)$, respectively. By using the multilayer interface approach (MIA) [36,40], the spacer height is determined from the measured $\overline{V}$ to be $s = 296\,\text{nm}$, and the drumhead thickness $h = 55\,\text{nm}$ (shown in Figure 1a), which is about 92 layers assuming a single layer thickness of 0.6 nm [35]. The LIA measures $\widetilde{V}(f_d)$ using the homodyne detection technique, with a time constant of 0.3 s and a time delay of 6 s to lock the phase at f_d and measure the steady-state response of the NMR.

2.3. Photothermal Effect

When a laser beam illuminates a region of the drumhead, the drum surface reflects a fraction of the incident laser power P_{in} for detection and absorbs some of the power accumulated in the FP cavity. The drumhead experiences radiation pressure and photothermal effects. Radiation pressure is exerted on the drumhead surface due to the momentum transfer between the drumhead and photons. This pressure is enhanced when incorporated into an FP structure due to multiple round trips of photons that are trapped between the drumhead and the bottom mirror. The tension generated from radiation pressure depends on P_{in}, λ and the reflectance of the drumhead and the reflective mirror in the FP structure [15,21]. The calculations in the Supplementary Materials show small induced tension for the highest applied P_{in}, indicating that the observed mechanical shift originates from the photothermal effect.

The photothermal effect for most van der Waals structure relies solely on laser-induced absorption [3]. The absorbed power can be described as $P_{abs} = P_{in}\chi A_{FP}$, where A_{FP} is the total absorbance of the FP cavity and χ is the power fraction absorbed by the drumhead in the FP stack. The absorbance of the FP cavity for a given drumhead thickness h depends on the difference between the spacer height s and the resonator static displacement z_s. P_{abs} heats the illuminated spot, and produces a temperature gradient due to the radial heat transfer to the drum clamps, as shown in Figure 1b. Consequently, the elevated temperature changes the mechanical tension exerted by the clamps by a photothermal tension, γ_{pth}. As illustrated in Figure 1b, γ_{pth} is added to the existing initial mechanical tension γ_0 generated by the drum displacement.

2.4. Determination of Fabry–Pérot Absorbance via Multilayer Interference Approach

The absorbances of our multilayer stack are estimated by determining the reflectance and transmittance of the substrate used for our FP devices. For simplicity, the reflectance, transmittance, and absorbance calculations assume that the laser with a wavelength $\lambda = 532\,\text{nm}$ originates from a point source in a vacuum and propagates towards the FP structure. Assuming that the thickness of the Si substrate is infinitely large, the reflection coefficient of the Au-Cr-SiO_2-Si substrate acting as a bottom mirror is $\Gamma_m = 0.665 - 0.565\text{j}$, numerically determined via MIA [36,41,42], and its corresponding reflectance is $R_m = 0.761$. For an FP cavity with a vacuum spacer, we define the reflectance of the vacuum spacer to be [36]

$$R_{FP}(h, z_s) = \left| \frac{r_h\left(1 - e^{-2j\delta_h}\right) - \left(r_h^2 - e^{-2j\delta_h}\right)\Gamma_m e^{-2j\delta_s}}{1 - r_1^2 e^{-2j\delta_h} - r_h\left(1 - e^{-2j\delta_h}\right)\Gamma_m e^{-2j\delta_s}} \right|^2, \tag{3}$$

where $r_h = (1 - \hat{n}_{res}(\lambda))/(1 + \hat{n}_{res}(\lambda))$ is the reflection coefficient of the vacuum-flake interface, $\delta_h = 2\pi\hat{n}_{res}(\lambda)h/\lambda$ is the optical phase thickness of the resonator with a complex-valued refractive index of the resonator material $\hat{n}_{res}$, and $\delta_s = 2\pi\hat{n}_{vac}(s - z_s)/\lambda$ is the optical phase thickness of the vacuum spacer, with $\hat{n}_{vac} = 1$.

Next, MIA is used to determine the substrate transmittance ($T_{sub} = 0.03$) and absorbance ($A_{sub} = 0.21$). Adding the nanomechanical resonator with a corresponding vacuum gap on the substrate leads to a vanishing transmittance of the overall FP stack $T_{FP} \approx 0$, thereby the absorbance of the FP-cavity system can be expressed as

$$A_{FP} = A_{FP}(h, z_s) \approx 1 - R_{FP}(h, z_s). \tag{4}$$

Combination of Equation (4) and Equation (3) provides the modeled absorbance A_{FP} of the drumheads as a function of h and z_s.

Apart from A_{FP}, the proportion of light absorbed by the nanomechanical resonator in the FP stack, represented by χ, is determined using the TMM package in Python [42]. Laser radiation propagates towards the surface of the FP stack, where both forward (transmitted) and backward (reflected) electric field interfere at each interface. The resonator and the substrate, especially the metal electrodes, absorb some of the energy stored in the FP cavity while the vacuum does not. The power absorbed either in the nanomechanical resonator or the substrate is quantified by obtaining the difference between the transmitted and incident intensity per material stack, and normalizing it with the incident intensity.

3. Results and Discussion

3.1. Measured Mechanical Spectra

Observation of the photothermal effect on vibrating drums requires changing P_{in} and monitoring the resonance frequency shift in the mechanical spectrum as shown in Figure 1d,e, with amplitude normalized to the incident power. Lightest colored $\widetilde{V}/P_{in}$ versus f_d responses refer to the driven responses probed with small incident powers, with the darker hue indicating higher probe powers. Figures S1 and S2 of the Supplementary Materials show the raw data of Figure 1d,e, respectively. Variations of P_{in} do not change the shape of the measured response curve, confirming that the drumhead oscillates within the linear regime even at the highest incident laser power [43]. To extract f_0, the mechanical quality factor Q_m, and their uncertainties, a linearly-driven damped oscillator model [36,44] is used to fit the measured spectra, with the amplitude $\widetilde{V}/P_{in} \propto z$. The number of reported significant figures of f_0 originates from the standard deviation of the driven damped oscillator model fit and the spacing between driving frequency values. The resulting f_0 dependences on P_{in} for devices A and B are shown in Figure 2. The Q_m of devices A and B for the range of incident powers used are 12.6 ± 0.6 and 23.4 ± 0.3, respectively. A combination of clamping losses, and imperfect, non-uniform boundaries contribute to the low quality factors observed in Figure 1d,e [36].

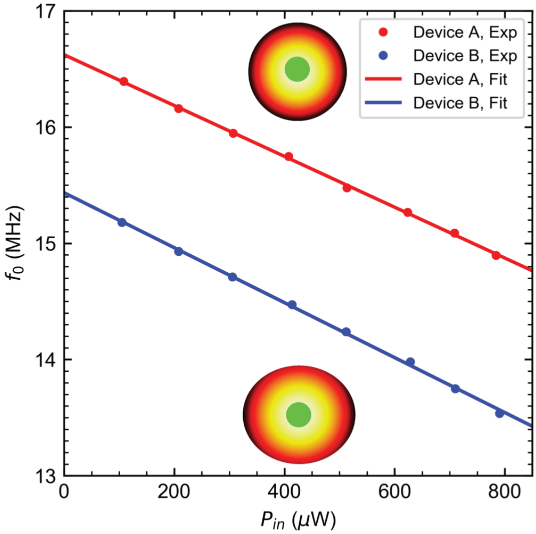

Figure 2. Dependence of the fundamental resonant frequencies of circular (device A) and elliptical (device B) resonators on the incident laser power. Insets show the position of the laser spot (green circle in the center) with a spot diameter of 1.9 µm at which the driven responses of devices A and B are measured. Data points are measured resonant frequencies from the driven responses and solid lines are linear fits. The f_0 uncertainties from the driven resonator fits are in the order of 1 kHz.

3.2. Concept and Theory

We consider the case of a tensioned circular drumhead where both D_p and γ_0 have comparable effect on the resonant frequency of the drumhead. The resonant frequency of both circular and elliptical drumheads, with an effective radius $a_{eff} = \sqrt{ab}$ and thickness h can be written as [45]

$$f_0(P_{in}) = \frac{\lambda_{01}}{2\pi}\sqrt{\frac{D_p}{\rho h a_{eff}^4}\left[\lambda_{01}^2 + \frac{(\gamma_0+\gamma_{pth})a_{eff}^2}{D_p}\right]}, \tag{5}$$

where λ_{01} is a modal parameter that is determined numerically. At $P_{in} = 0$, the drumheads oscillate at their natural resonant frequency (without heating) $f_0 = f_0(P_{in} = 0)$ corresponding to the y-intercept of both plots for circular and elliptical drumheads in Figure 2. Given f_0 values of 16.62 MHz and 15.43 MHz for device A and B, respectively, and using Equation (5), we determine the initial tension of $\gamma_{0,A} = 5.01\,\mathrm{N\,m^{-1}}$ for device A and $\gamma_{0,B} = 5.15\,\mathrm{N\,m^{-1}}$ for device B, for the given applied DC voltage. As P_{in} ramps up, the downward resonant frequency shift is observed as shown in Figure 2.

Since the frequency shift is linear for small values of P_{in}, Equation (5) can be given by its first-order Taylor polynomial

$$f_0(P_{in}) \approx f_0 + \frac{1}{2}\left[\left(\frac{\lambda_{01}}{2\pi}\right)^2 \frac{1}{\rho h a_{eff}^2}\right]\frac{\gamma_{pth}(P_{in})}{f_0}, \tag{6}$$

and the shift can be written as

$$\Delta f_0(P_{in}) = \frac{1}{2}\left(\frac{\lambda_{01}}{2\pi}\right)^2 \frac{\gamma_{pth}(P_{in})}{\rho h a_{eff}^2 f_0}. \tag{7}$$

Compressive tension is given by [27,46,47]

$$\gamma_{pth}(P_{in}) = -\frac{E_{3D}h}{1-\nu}\alpha_L \Delta T_{abs}(P_{in}), \tag{8}$$

where E_{3D} is the Young's elastic modulus, α_L is the thermal expansion coefficient of $NbSe_2$ at the bath temperature T_0, and ΔT_{abs} is the temperature difference between T_0 and the average temperature of the drumhead $T_0 + \Delta T_{abs}$. For linear changes in $T_0 + \Delta T_{abs}$, the average temperature difference is expressed as

$$\Delta T_{abs}(P_{in}) = \frac{P_{abs}(h, z_s)}{4\pi h\kappa}\eta, \tag{9}$$

where κ is the in-plane thermal conductivity of $NbSe_2$, and η is the average spot diameter factor. We estimate both χ and A_{FP} through MIA [41,42,48] whereas η is evaluated by assuming absorptive spot heating in the center of the drumheads [49].

Given these inputs, we define the photothermal responsivity Ψ as the frequency shift induced by the absorbed power. By solving Equation (7) using Equations (8) and (9), and defining Ψ as $\Psi = \Delta f_0/\Delta P_{in}$, the photothermal responsivity is expressed as

$$\Psi(z_s) = -\frac{1}{8}\left(\frac{\lambda_{01}}{2\pi}\right)^2 \frac{E_{3D}\alpha_L}{(1-\nu)mf_0}\frac{\chi A_{FP}(h, z_s)\eta}{\kappa}, \tag{10}$$

where $m = \rho\pi a_{eff}^2 h$ is the total mass of the drumhead. This quantity can be extracted experimentally from the slope of the linear fits acquired from Figure 2. In the tensioned membrane regime, $\Psi \approx \gamma_0^{-0.5}$ (see full expression in the Supplementary Materials). This dependence resembles the temperature sensitivity of string-based sensors [50], albeit the thermal tension used to gauge the temperature originated from substrate heating effects. The finding that low γ_0 is favored for temperature sensing due to high temperature sensitivity also applies to photothermal strain sensors based on drumheads. Previous works on interferometric studies of membrane NMRs demonstrate not only imperfections in the amplitude mode shape [51], but also variations of f_0 with laser beam spot position in the presence of metallic nanoparticles [52]. A localized laser heating study on membranes made from silicon nitride [53] suggests that the spot location should be accounted for when performing power-dependent bolometric tests because applying high P_{in} would induce radial dependence of the measured f_0. Figure S4 of the Supplementary Materials exhibits that devices A and B show small radial dependences of f_0 at different incident powers for a 0.2 µm misalignment away from the drum center. The misalignment range is a fraction of the spot diameter, which does not produce significant change in the radial variations of f_0 at P_{in} of Figure 2. Hence, the power dependence of the frequency shifts within the 0.2 µm radial misalignment range does not significantly deviate from that in Figure 2.

3.3. Effect of Static Displacement on the Measured Photothermal Responsivities of $NbSe_2$ Drums

Figure 3 shows the dependence of Ψ extracted from Figure 2 with the corresponding z_s and $\Psi(z_s)$ generated with Equation (10) using the resonator specifications and material properties of device A (see Table S1 of the Supplementary Materials). The wavy behavior of $\Psi(z_s)$ originates from the modulation of the FP absorbance A_{FP} of a 55 nm thick bulk $NbSe_2$ drumhead as its center moves to a distance z_s away from s. The described dependence, shown in magenta dotted lines, is simulated using Equation (4). The magnitude of Ψ comes from other material parameters in Equation (4) apart from A_{FP}.

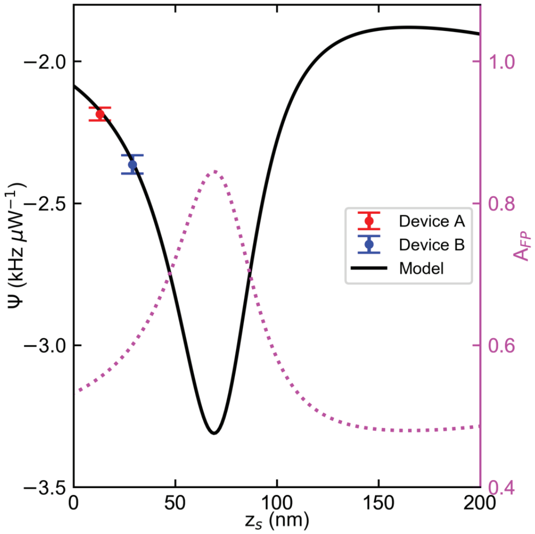

Figure 3. Photothermal responsivity and absorbance dependence of the multilayer $NbSe_2$ drumhead resonators on the static displacement. Data points are the slope extracted from the slope in Figure 2. Fitting slope uncertainties in Figure 2 for devices A and B are 35 Hz μW^{-1} and 22 Hz μW^{-1}, respectively. Solid line refers to the photothermal responsivity model. For comparison, the dependence of the simulated absorbance of the Fabry–Pérot cavity on static displacement, shown by magenta dotted line with the magnitude referenced on the right Y-axis spine, is also shown.

The negative Ψ values shown in Figure 3 imply that both devices A and B undergo heat-induced compression. Device A has $\Psi_A = -2.19$ kHz μW^{-1} for z_s = 13 nm. Device B has $\Psi_B = -2.38$ kHz μW^{-1} for $z_s = 29$ nm. The ratio of z_s between device A and device B in Figure 3 yields 2.23, which is close to the value of 2.16 obtained from the theoretically derived expression $\beta_{ellipse} a_B^4 / \beta_{circle} a_A^4$, where β is the eccentricity factor from reference [54]. The results imply that the difference in z_s of these two drums lies with geometry [8]. Physically, the compressive strain translates to an out-of-plane radial expansion of the drumhead when aided with z_s. z_s is controlled either through electromotive driving of the drumhead [3,55,56] or through slack [8,57,58]. Given the nature of the transfer process using PDMS disks [8,37], z_s likely originates from slack.

According to the model prediction in Figure 3, $\Psi = -2.10$ kHz μW^{-1} when the resonator is in its equilibrium position ($z_s = 0$). Displacing the resonator to $z_s = 69$ nm, which is a position where a dark FP fringe occurs, results in $\Psi \approx -3.33$ kHz μW^{-1}, which amounts to increases in the measured responsivities of devices A and B by 42% and 52%, respectively. Furthermore, we estimate a tuning range of 1.40 kHz μW^{-1}, which is traced from the A_{FP} difference between the dark and bright fringes.

3.4. Simulated Effect of Drumhead Thickness on the Photothermal Responsivity Profile of $NbSe_2$ Drums

To further understand the thickness dependence of the photothermal responsivity, we first visualize the effect of h on the $A_{FP}(z_s)$ profiles of bulk $NbSe_2$ films using Equation (4), as shown in Figure 4a,b. We then simulate the effect of varying h on the $\Psi(z_s)$ profiles of circular bulk $NbSe_2$ drumheads using Equation (10), as shown in Figure 5a,b. The simulated $\Psi(z_s)$ profiles are restricted to the material properties of bulk, clean devices possessing a_{eff}, f_0, FP structure and λ of device A. With these parameters, only λ_{01} is varied to decrease at an increasing thickness to maintain f_0 as shown in Figure 4d. The wavy dependencies of $\Psi(z_s)$ for multilayer bulk $NbSe_2$ originates from the $A_{FP}(z_s)$ plotted in Figure 4a,b. For $h = 6$ nm, we estimate a tuning range of roughly 12.2 kHz μW^{-1} from $\Psi(z_s = 0) = -16.30$ kHz μW^{-1}

to $\Psi(z_s = 69\,\mathrm{nm}) = -4.05\,\mathrm{kHz}\ \mu\mathrm{W}^{-1}$. For $h = 30\,\mathrm{nm}$, we obtain a tuning range of $2.78\,\mathrm{kHz}\ \mu\mathrm{W}^{-1}$ from $\Psi(z_s = 0) = -4.16\,\mathrm{kHz}\ \mu\mathrm{W}^{-1}$ to $\Psi(z_s = 86\,\mathrm{nm}) = -1.39\,\mathrm{kHz}\ \mu\mathrm{W}^{-1}$. Hence, thinner bulk $NbSe_2$ devices have larger tuning range and magnitude as compared to thicker devices. Furthermore, the simulated $\Psi(z_s)$ profile of monolayer $NbSe_2$, shown in Figure 5c as black solid lines, has larger magnitude and tuning ranges than the extrapolated bulk $NbSe_2$ $\Psi(z_s)$ curve (black dotted line).

Intuitively, the change in h modifies the properties of both the FP cavity and the nanomechanical resonators, and consequently affects $\Psi(z_s)$. In the FP domain, h modifies both A_{FP} and χ as shown in Figure 4a–c, respectively. In a non-transmissible FP cavity with known refractive indices of the resonators $\hat{n}_{res}$ [59–63], reflectance and absorbance dominate. For example, the deflection-dependent behavior of the bulk $NbSe_2$ A_{FP} transitions from an asymmetric, sinusoidal profile at thin layers to a Fano-peak profile at thicker layers, as shown in Figure 4b. Furthermore, the deflection dependence of monolayer $NbSe_2$ A_{FP} maintains an asymmetric, sinusoidal profile due to its large absorption coefficient, which is different compared to bulk $NbSe_2$ [36,59]. In device A, the values of z_s predicted to have maximum absorbance and magnitude of Ψ would have near-zero modulated reflectance, implying no detectable NMR responses by the FP cavity. Hence the estimates for the tuning range of the drumheads are upper bounds. Nevertheless, the values help confine a range of z_s that give detectable driven response and photothermal heating.

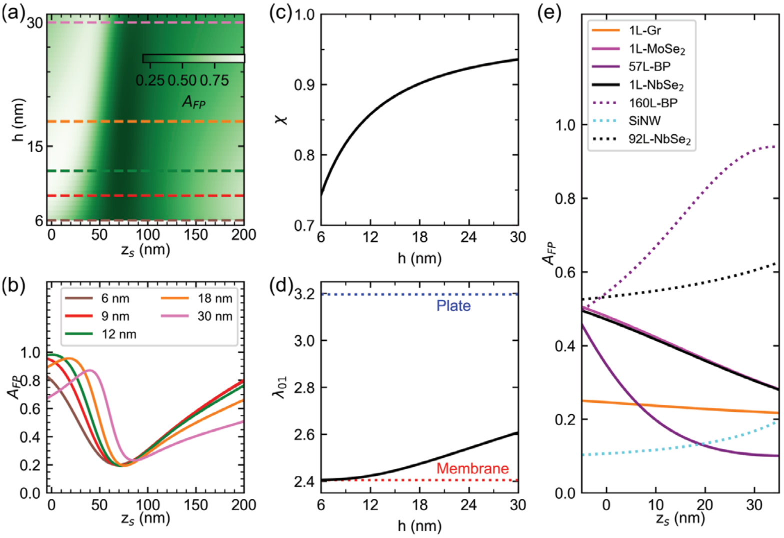

Figure 4. Dependence of the displacement-dependent Fabry–Pérot absorbance profile $A_{FP}(z_s)$ of drum NMRs on the drum thickness and displacement from equilibrium for various resonator materials. (**a**) Intensity color map of the calculated dependence of $A_{FP}(z_s)$ of bulk $NbSe_2$ on thickness and displacement from equilibrium. Colored dashed lines correspond to the $A_{FP}(z_s)$ profiles plotted in (**b**). Dependence of the absorbed power fraction χ (**c**) and fundamental mode constant λ_{01} (**d**) of bulk $NbSe_2$ resonators on thickness. (**e**) Simulated $A_{FP}(z_s)$ profile for different materials. The FP absorbances were simulated for the Fabry–Pérot structure of device A.

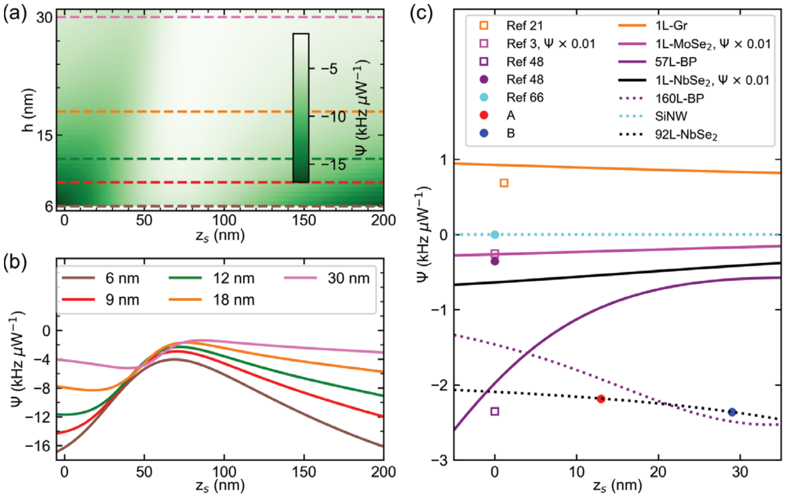

Figure 5. Dependence of the photothermal responsivity profile $\Psi(z_s)$ of drum NMRs on the thickness and displacement from equilibrium for various resonator materials. (**a**) Intensity plot of the calculated dependence of $\Psi(z_s)$ of bulk $NbSe_2$ drumheads on thickness and displacement from equilibrium. Colored dashed lines correspond to $\Psi(z_s)$ profiles displayed in (**b**). For comparison, we use the diameter, Fabry–Pérot structure, and mechanical resonant frequency of Device A in simulating the dependences. (**c**) Scatter plot of the photothermal responsivity values obtained in Figure 3, along with photothermal responsivities of other NMRs extracted from the literature. Square symbols refer to devices demonstrating highly tensioned systems such as monolayer (1L) graphene (Gr), monolayer molybdenum diselenide ($MoSe_2$), and thin black phosphorus (57L-BP) drumheads. Circular symbols refer to devices dominated by flexural rigidity such as thick black phosphorus (160L-BP) drums, silicon nanowire (SiNW) cantilever beams, and $NbSe_2$ drums (A, B). Included also are $\Psi(z_s)$ of both tension-dominated (solid lines) and flexural rigidity-dominated (dotted lines) devices having the Fabry–Pérot structure of device A.

At large displacements $z_{s,\text{large}} \geq \lambda/4$, the dependencies of A_{FP} and Ψ on $z_{s,large}$ for $NbSe_2$ drums are linear. For 55 nm thick drumheads, as shown in Figure 3, both A_{FP} and Ψ are roughly constant at $z_{s,\text{large}}$, indicating the FP cavity produces bright fringes regardless of $z_{s,\text{large}}$. For thinner drumheads described in Figures 4b and 5b, A_{FP} and consequently the magnitude of Ψ increase linearly with $z_{s,\text{large}}$ as the drumheads move to positions where the FP fringe transitions from bright to dark. Furthermore, the slope of the $A_{FP}(z_{s,\text{large}})$ profile increases at decreasing h and so does the slope of the magnitude of $\Psi(z_{s,\text{large}})$ profile. Beyond $z_{s,\text{large}} \geq 200$ nm the drumhead would collapse on the electrode when actuated by electromotive force due to pull-in instability [64].

In the nanomechanical resonator domain, the effect of the drum head thickness depends on whether the resonator operates in the low tension or high tension regime (see Supplementary Materials for the full expressions). In the regime where rigidity dominates, $\Psi \propto h^{-2}$. In the tensioned membrane regime in which the modeled multilayer and monolayer $NbSe_2$ drums in Figure 5b,c reside, $\Psi \propto h^{-0.5}$. Engineering a constant value of Ψ for any value of z_s requires thicker drum plates. For devices with larger tuning ranges of Ψ, thin $NbSe_2$ membranes are preferred, though stress-relief structures offer the possibility of thin plate structures [65].

3.5. Comparison with Reported Results of Various NMRs from Literature

We note that the $\Psi(z_s)$ curve of monolayer (1L) $NbSe_2$ in Figure 5c represents an upper bound by assuming a clean device ($\rho \approx \rho_{NbSe_2}$). These conditions result in a greater magnitude and larger tuning range of $\Psi(z_s)$ of the monolayer $NbSe_2$ than $\Psi(z_s)$ of other devices such as 165 nm thick, clamped-free silicon nanowire (SiNW) resonators [66] (cyan, solid line), graphene (1L-Gr) (orange, solid line), cryogenically-cooled monolayer diselenide (1L-MoSe$_2$) (purple, solid line) and multilayer black phosphorus (BP, magenta solid and dotted lines) drums. The shape of these $\Psi(z_s)$ is reflected in their corresponding $A_{FP}(z_s)$ dependencies as shown in Figure 4e, which uses the substrate and λ of device A. For the properties of the above-listed materials that define the magnitude of $\Psi(z_s)$, see Tables S1 and S2 of the Supplementary Materials. Note that the $\Psi(z_s)$ profiles for BP resonators assume an average, isotropic E_{3D} and κ even though these resonators have reported anisotropic properties [48]. The indicated materials have positive α_L which implies that the devices made of these materials experience compression upon the illumination by the laser beam. Only the $\Psi(z_s)$ curve of graphene experiences tension upon spot heating due to graphene's negative α_L at ambient temperature. Furthermore, the SiNW device falls under the optically-thick, bending regime, which illustrates the near-zero magnitude and tunability of Ψ with z_s.

We also see from Figure 5c that the measured Ψ of bulk NbSe$_2$ devices is comparable to that of 57L-BP device (magenta square) and significantly better than both bulk SiNW (cyan circle) and 160L-BP (magenta circle) devices. However, Ψ's of these devices are ten times smaller than the Ψ values of a 1L-MoSe$_2$ drumhead (pink square), which possesses a significantly smaller mass. We note that the values of z_s extracted from the literature are for the devices in their equilibrium position except for graphene, which has 1 nm deflection to resolve its motion [21].

The effect of the substrate and probing wavelength on the photothermal responsivity of the drumheads varies with the resonator material as its optical, thermal, and mechanical properties modify their $\Psi(z_s)$ profiles. For example, the highly-reflective substrate of device A shows improved $\Psi(z_s = 0)$ for the 160L-BP, 1L-Gr and 1L-MoSe$_2$ devices, comparable $\Psi(z_s = 0)$ to the SiNW device and decreased $\Psi(z_s = 0)$ for the 57L-BP drumhead as compared to their extracted values in the literature [3,21,48,66] (colored symbols), as shown in Figure 5c. The devices cited in the literature make use of a combination of gap heights, probe wavelength, and substrate for near-optimal FP-based detection [67] and ease in device fabrication; their photothermal responses are secondary. Nevertheless, our model demonstrates the variation of the tuning range of $\Psi(z_s)$ of thin van der Waals materials using our FP structure.

The values of $\Psi(z_s)$ reported in this work, with the exception of clean 1L-NbSe$_2$, are fractions of Ψ reported for metamaterial string [31] and graphene trampoline NMR bolometers [27] at infrared and visible wavelengths, respectively. Apart from replacing NbSe$_2$ with thermally insulating vdW materials, a strategy to improve $\Psi(z_s = 0)$ of NbSe$_2$ involves decreasing the thermal conductivity of the drumheads with high-aspect-ratio tethers that resemble a trampoline geometry. The trampoline structure is reported to increase $\Psi(z_s = 0)$ of graphene, known for its very high thermal conductivity, to 2.4×10^3 kHz μW^{-1} [27]. The structure is tricky to implement on NbSe$_2$ since the focused ion beam etching step introduces defects that alter the flake properties [68,69]. On another note, broadening the tuning range would entail engineering a partially-transparent substrate at a probe wavelength to distinguish the resonator positions of maximum absorbance and zero modulated reflectance [20]. Finally, the proposed model guides the design and fabrication of FP-based, ultrathin nanomechanical bolometers made from NbSe$_2$ and other vdW materials, whose photothermal responsivity is tunable with static displacement. Future directions include experimental demonstrations of the dependence of vdW NMR photothermal responsivity on the drumhead thickness and initial tension.

4. Conclusions

In summary, we have designed and characterized NbSe$_2$ drumheads with controllable photothermal heating using NMR static displacements in FP cavities. Our simulations show that the magnitude and tuning range of the photothermal response of drumheads increase at decreasing flake thickness. Our analysis shows that a monolayer NbSe$_2$ drumhead

NMR has promising photothermal responsivities at room temperature, while our work focuses on $NbSe_2$ devices, the design framework applies to a family of vdW materials and conventional resonator materials that absorb light.

Supplementary Materials: The following supporting information can be downloaded from: https://www.mdpi.com/article/10.3390/nano12152675/s1: Table S1: Parameters of vdW drumhead NMRs used in the calculation of the FP absorbances in Figures 3 and 4a,b,e, and photothermal responsivities in Figures 3 and 5a–c; Table S2: Parameters used in the calculation of FP absorbance and photothermal responsivities of silicon nanowire resonators in Figures 4e and 5c, respectively; Figure S1: Raw amplitude and phase response of device A; Figure S2: Raw amplitude and phase response of device B; Figure S3: Simulated temperature variation of device A; Figure S4: Dependences of the fundamental mode frequency on the laser spot position of devices A and B within twice of the misalignment range; Supplementary Material Section S1: Derivation of Photothermal Responsivities; Supplementary Material Section S2: Observed Dependencies of f_0 on the Laser Spot Position; Supplementary Material Section S3: Effect of Radiation Pressure. References [70–98] are cited in the Supplementary Materials.

Author Contributions: Conceptualization and supervision: C.-D.C.; funding acquisition: C.-D.C. and Y.A.P.; investigation: M.A.C.A., J.C.E., C.-Y.Y. and Y.-C.C.; formal analysis and methodology: M.A.C.A., J.C.E. and J.-Y.W.; software: M.A.C.A., J.C.E., T.-H.L. and K.-H.L.; resources: C.-Y.Y., K.-H.L. and C.-D.C.; writing—original draft preparation: M.A.C.A., J.C.E. and C.-D.C.; writing—review and editing: M.A.C.A., J.C.E., J.-Y.W., K.-S.C.-L., S.K., Y.A.P. and C.-D.C. All authors have read and agreed to the published version of the manuscript.

Funding: This work was funded by Academia Sinica Grand Challenge Seed Program (AS-GC-109-08), Ministry of Science and Technology (MOST) of Taiwan (107-2112-M-001-001-MY3), Cost Share Programme (107-2911-I-001-511), the Royal Society International Exchanges Scheme (grant IES\R3\170029), and iMATE (2391-107-3001).

Institutional Review Board Statement: Not applicable.

Informed Consent Statement: Not applicable.

Data Availability Statement: Data and additional details are contained within the article and in the Supplementary Materials.

Acknowledgments: We acknowledge the contribution of T.-H. Hsu and W.-H. Chang in fabricating devices and in building the experimental setup, B.-R. Guo for technical assistance, A.F. Rigosi for sharing the measured dielectric constant spectra of bulk and few-layer $NbSe_2$ and R. Frisenda for sharing the real and imaginary refractive index of single-layer $MoSe_2$. We thank the Taiwan International Graduate Program for the financial support. We extend our gratitude for the Academia Sinica Nanocore Facility.

Conflicts of Interest: The authors declare no conflict of interest.

References

1. Aspelmeyer, M.; Kippenberg, T.J.; Marquardt, F. Cavity Optomechanics. *Rev. Mod. Phys.* **2014**, *86*, 1391–1452. [CrossRef]
2. Davidovikj, D.; Alijani, F.; Cartamil-Bueno, S.J.; van der Zant, H.S.J.; Amabili, M.; Steeneken, P.G. Nonlinear Dynamic Characterization of Two-Dimensional Materials. *Nat. Commun.* **2017**, *8*, 1253. [CrossRef] [PubMed]
3. Morell, N.; Tepsic, S.; Reserbat-Plantey, A.; Cepellotti, A.; Manca, M.; Epstein, I.; Isacsson, A.; Marie, X.; Mauri, F.; Bachtold, A. Optomechanical Measurement of Thermal Transport in Two-Dimensional $MoSe_2$ Lattices. *Nano Lett.* **2019**, *19*, 3143–3150. [CrossRef]
4. Waitz, R.; Nößner, S.; Hertkorn, M.; Schecker, O.; Scheer, E. Mode Shape and Dispersion Relation of Bending Waves in Thin Silicon Membranes. *Phys. Rev. B* **2012**, *85*, 035324. [CrossRef]
5. Wang, Z.; Lee, J.; Feng, P.X. Spatial Mapping of Multimode Brownian Motions in High-Frequency Silicon Carbide Microdisk Resonators. *Nat. Commun.* **2014**, *5*, 5158. [CrossRef]
6. Davidovikj, D.; Slim, J.J.; Cartamil-Bueno, S.J.; van der Zant, H.S.; Steeneken, P.G.; Venstra, W.J. Visualizing the Motion of Graphene Nanodrums. *Nano Lett.* **2016**, *16*, 2768–2773. [CrossRef] [PubMed]
7. Kim, S.; Yu, J.; van der Zande, A.M. Nano-Electromechanical Drumhead Resonators from Two-Dimensional Material Bimorphs. *Nano Lett.* **2018**, *18*, 6686–6695. [CrossRef]
8. Esmenda, J.C.; Aguila, M.A.C.; Wang, J.; Lee, T.; Yang, C.; Lin, K.; Chang-Liao, K.; Katz, N.; Kafanov, S.; Pashkin, Y.A.; et al. Imaging Off-Resonance Nanomechanical Motion as Modal Superposition. *Adv. Sci.* **2021**, *8*, 2005041. [CrossRef]

9. Purdy, T.P.; Grutter, K.E.; Srinivasan, K.; Taylor, J.M. Quantum Correlations from a Room-Temperature Optomechanical Cavity. *Science* **2017**, *356*, 1265–1268. [CrossRef] [PubMed]
10. Delic, U.; Reseinbauer, M.; Dare, K.; Grass, D.; Vuletic, V.; Kiesel, N.; Aspelmeyer, M. Cooling of a Levitated Nanoparticle to the Motional Quantum Ground State. *Science* **2020**, *367*, 892–895. [CrossRef]
11. Bagci, T.; Simonsen, A.; Schmid, S.; Villanueva, L.G.; Zeuthen, E.; Appel, J.; Taylor, J.M.; Sørensen, A.; Usami, K.; Schliesser, A.; et al. Optical Detection of Radio Waves Through a Nanomechanical Transducer. *Nature* **2014**, *507*, 81–85. [CrossRef] [PubMed]
12. Andrews, R.W.; Peterson, R.W.; Purdy, T.P.; Cicak, K.; Simmonds, R.W.; Regal, C.A.; Lehnert, K.W. Bidirectional and Efficient Conversion between Microwave and Optical Light. *Nat. Phys.* **2014**, *10*, 321–326. [CrossRef]
13. Higginbotham, A.P.; Burns, P.S.; Urmey, M.D.; Peterson, R.W.; Kampel, N.S.; Brubaker, B.M.; Smith, G.; Lehnert, K.W.; Regal, C.A. Harnessing Electro-Optic Correlations in an Efficient Mechanical Converter. *Nat. Phys.* **2018**, *14*, 1038–1042. [CrossRef]
14. Azak, N.O.; Shagam, M.Y.; Karabacak, D.M.; Ekinci, K.L.; Kim, D.H.; Jang, D.Y. Nanomechanical Displacement Detection Using Fiber-Optic Interferometry. *Appl. Phys. Lett.* **2007**, *91*, 093112. [CrossRef]
15. Metzger, C.; Favero, I.; Ortlieb, A.; Karrai, K. Optical Self Cooling of a Deformable Fabry-Perot Cavity in the Classical Limit. *Phys. Rev. B* **2008**, *78*, 035309. [CrossRef]
16. Flowers-Jacobs, N.E.; Hoch, S.W.; Sankey, J.C.; Kashkanova, A.; Jayich, A.M.; Deutsch, C.; Reichel, J.; Harris, J.G.E. Fiber-Cavity-Based Optomechanical Device. *Appl. Phys. Lett.* **2012**, *101*, 221109. [CrossRef]
17. Basarir, O.; Bramhavar, S.; Ekinci, K.L. Motion Transduction in Nanoelectromechanical Systems (NEMS) Arrays Using Near-Field Optomechanical Coupling. *Nano Lett.* **2012**, *12*, 534–539. [CrossRef]
18. Vainsencher, A.; Satzinger, K.J.; Peairs, G.A.; Cleland, A.N. Bi-Directional Conversion Between Microwave and Optical Frequencies in a Piezoelectric Optomechanical Device. *Appl. Phys. Lett.* **2016**, *109*, 033107. [CrossRef]
19. Midolo, L.; Schliesser, A.; Fiore, A. Nano-Opto-Electro-Mechanical Systems. *Nat. Nanotechnol.* **2018**, *13*, 11–18. [CrossRef]
20. Chen, F.; Yang, C.; Mao, W.; Lu, H.; Schädler, K.G.; Reserbat-Plantey, A.; Osmond, J.; Cao, G.; Li, X.; Wang, C.; et al. Vibration Detection Schemes Based on Absorbance Tuning in Monolayer Molybdenum Disulfide Mechanical Resonators. *2D Mater.* **2018**, *6*, 011003. [CrossRef]
21. Barton, R.A.; Storch, I.R.; Adiga, V.P.; Sakakibara, R.; Cipriany, B.R.; Ilic, B.; Wang, S.P.; Ong, P.; McEuen, P.L.; Parpia, J.M.; et al. Photothermal Self-Oscillation and Laser Cooling of Graphene Optomechanical Systems. *Nano Lett.* **2012**, *12*, 4681–4686. [CrossRef] [PubMed]
22. Primo, A.G.; Kersul, C.M.; Benevides, R.; Carvalho, N.C.; Ménard, M.; Frateschi, N.C.; de Assis, P.L.; Wiederhecker, G.S.; Mayer Alegre, T.P. Accurate Modeling and Characterization of Photothermal Forces in Optomechanics. *APL Photonics* **2021**, *6*, 086101. [CrossRef]
23. Kippenberg, T.J.; Vahala, K.J. Cavity Optomechanics: Back at the Mesoscale. *Science* **2008**, *321*, 1172–1176. [CrossRef] [PubMed]
24. Barton, R.A.; Ilic, B.; van der Zande, A.M.; Whitney, W.S.; McEuen, P.L.; Parpia, J.M.; Craighead, H.G. High, Size-Dependent Quality Factor in an Array of Graphene Mechanical Resonators. *Nano Lett.* **2011**, *11*, 1232–1236. [CrossRef] [PubMed]
25. Lemme, M.C.; Wagner, S.; Lee, K.; Fan, X.; Verbiest, G.J.; Wittmann, S.; Lukas, S.; Dolleman, R.J.; Niklaus, F.; van der Zant, H.S.J.; et al. Nanoelectromechanical Sensors Based on Suspended 2D Materials. *Research* **2020**, *2020*, 8748602. [CrossRef] [PubMed]
26. Steeneken, P.G.; Dolleman, R.J.; Davidovikj, D.; Alijani, F.; van der Zant, H.S.J. Dynamics of 2D Material Membranes. *2D Mater.* **2021**, *8*, 042001. [CrossRef]
27. Blaikie, A.; Miller, D.; Aleman, B.J. A Fast and Sensitive Room-Temperature Graphene Nanomechanical Bolometer. *Nat. Commun.* **2019**, *10*, 4726. [CrossRef] [PubMed]
28. Hu, X.; Xu, E.; Xiang, S.; Chen, Z.; Zhou, X.; Wang, N.; Guo, H.; Ruan, L.; Hu, Y.; Li, C.; et al. Synthesis of $NbSe_2$ Single-Crystalline Nanosheet Arrays for UV Photodetectors. *CrystEngComm* **2020**, *22*, 5710–5715. [CrossRef]
29. Orchin, G.J.; De Fazio, D.; Di Bernardo, A.; Hamer, M.; Yoon, D.; Cadore, A.R.; Goykhman, I.; Watanabe, K.; Taniguchi, T.; Robinson, J.W.A.; et al. Niobium Diselenide Superconducting Photodetectors. *Appl. Phys. Lett.* **2019**, *114*, 251103. [CrossRef]
30. Jin, Y.; Ji, Z.; Gu, F.; Xie, B.; Zhang, R.; Wu, J.; Cai, X. Multiple Mechanisms of the Low Temperature Photoresponse in Niobium Diselenide. *Appl. Phys. Lett.* **2021**, *119*, 221104. [CrossRef]
31. Papas, D.; Ou, J.Y.; Plum, E.; Zheludev, N.I. Optomechanical Metamaterial Nanobolometer. *APL Photonics* **2021**, *6*, 126110. [CrossRef]
32. Ferreiro, J.M. Experimental and Simulation Study of Electron and Phonon Properties in Crystalline Materials. Ph.D. Thesis, University of Notre Dame, Notre Dame, IN, USA, 2019.
33. Sengupta, S.; Solanki, H.S.; Singh, V.; Dhara, S.; Deshmukh, M.M. Electromechanical Resonators as Probes of the Charge Density Wave Transition at the Nanoscale in $NbSe_2$. *Phys. Rev. B* **2010**, *82*, 155432. [CrossRef]
34. Sun, H.; Agrawal, P.; Singh, C.V. A First-Principles Study of the Relationship Between Modulus and Ideal Strength of Single-Layer, Transition Metal Dichalcogenides. *Mater. Adv.* **2021**, *2*, 6631–6640. [CrossRef]
35. Castellanos-Gomez, A.; Agraït, N.; Rubio-Bollinger, G. Optical Identification of Atomically Thin Dichalcogenide Crystals. *Appl. Phys. Lett.* **2010**, *96*, 213116. [CrossRef]
36. Aguila, M.A.C.; Esmenda, J.C.; Wang, J.Y.; Lee, T.H.; Yang, C.Y.; Lin, K.H.; Chang-Liao, K.S.; Kafanov, S.; Pashkin, Y.A.; Chen, C.D. Fabry–Perot Interferometric Calibration of Van der Waals Material-Based Nanomechanical Resonators. *Nanoscale Adv.* **2022**, *4*, 502–509. [CrossRef]

37. Pande, G.; Siao, J.Y.; Chen, W.L.; Lee, C.J.; Sankar, R.; Chang, Y.M.; Chen, C.D.; Chang, W.H.; Chou, F.C.; Lin, M.T. Ultralow Schottky Barriers in H-BN Encapsulated Monolayer WSe_2 Tunnel Field-Effect Transistors. *ACS Appl. Mater. Interfaces* **2020**, *12*, 18667–18673. [CrossRef]
38. Castellanos-Gomez, A.; Buscema, M.; Molenaar, R.; Singh, V.; Janssen, L.; van der Zant, H.S.J.; Steele, G.A. Deterministic Transfer of Two-Dimensional Materials by All-Dry Viscoelastic Stamping. *2D Mater.* **2014**, *1*, 011002. [CrossRef]
39. Suzuki, H.; Yamaguchi, N.; Izumi, H. Theoretical and Experimental Studies on the Resonance Frequencies of a Stretched Circular Plate: Application to Japanese Drum Diaphragms. *Acoust. Sci. Technol.* **2009**, *30*, 348–354. [CrossRef]
40. Pini, V.; Ramos, D.; Dominguez, C.M.; Ruz, J.J.; Malvar, O.; Kosaka, P.M.; Davis, Z.J.; Tamayo, J.; Calleja, M. Optimization of the Readout of Microdrum Optomechanical Resonators. *Microelectron. Eng.* **2017**, *183–184*, 37–41. [CrossRef]
41. Baumeister, P.W. *Optical Coating Technology*; SPIE—The International Society for Optical Engineering: Bellingham, WA USA, 2004; Volume PM137. [CrossRef]
42. Byrnes, S.J. Multilayer Optical Calculations. *arXiv* **2016**, arXiv:1603.02720v5.
43. Verbridge, S.S.; Parpia, J.M.; Reichenbach, R.B.; Bellan, L.M.; Craighead, H.G. High Quality Factor Resonance at Room Temperature with Nanostrings under High Tensile Stress. *J. Appl. Phys.* **2006**, *99*, 124304. [CrossRef]
44. Schmid, S.; Villanueva, L.G.; Roukes, M.L. *Fundamentals of Nanomechanical Resonators*; Springer Nature: Cham, Switzerland, 2016; p. 183. [CrossRef]
45. Lee, J.; Wang, Z.; He, K.; Shan, J.; Feng, P.X.L. High Frequency MoS_2 Nanomechanical Resonators. *ACS Nano* **2013**, *7*, 6086–6091. [CrossRef] [PubMed]
46. Ye, F.; Lee, J.; Feng, P.X. Electrothermally Tunable Graphene Resonators Operating at Very High Temperature up to 1200 K. *Nano Lett.* **2018**, *18*, 1678–1685. [CrossRef] [PubMed]
47. Siskins, M.; Lee, M.; Manas-Valero, S.; Coronado, E.; Blanter, Y.M.; van der Zant, H.S.J.; Steeneken, P.G. Magnetic and Electronic Phase Transitions Probed by Nanomechanical Resonators. *Nat. Commun.* **2020**, *11*, 2698. [CrossRef]
48. Islam, A.; van den Akker, A.; Feng, P.X. Anisotropic Thermal Conductivity of Suspended Black Phosphorus Probed by Opto-Thermomechanical Resonance Spectromicroscopy. *Nano Lett.* **2018**, *18*, 7683–7691. [CrossRef]
49. Kurek, M.; Carnoy, M.; Larsen, P.E.; Nielsen, L.H.; Hansen, O.; Rades, T.; Schmid, S.; Boisen, A. Nanomechanical Infrared Spectroscopy with Vibrating Filters for Pharmaceutical Analysis. *Angew. Chem. Int. Ed.* **2017**, *56*, 3901–3905. [CrossRef]
50. Larsen, T.; Schmid, S.; Grönberg, L.; Niskanen, A.O.; Hassel, J.; Dohn, S.; Boisen, A. Ultrasensitive String-Based Temperature Sensors. *Appl. Phys. Lett.* **2011**, *98*, 121901. [CrossRef]
51. De Alba, R.; Massel, F.; Storch, I.R.; Abhilash, T.; Hui, A.; McEuen, P.L.; Craighead, H.G.; Parpia, J.M. Tunable Phonon-Cavity Coupling in Graphene Membranes. *Nat. Nanotechnol.* **2016**, *11*, 741–746. [CrossRef]
52. Ramos, D.; Malvar, O.; Davis, Z.J.; Tamayo, J.; Calleja, M. Nanomechanical Plasmon Spectroscopy of Single Gold Nanoparticles. *Nano Lett.* **2018**, *18*, 7165–7170. [CrossRef]
53. Ferreiro-Vila, E.; Molina, J.; Weituschat, L.M.; Gil-Santos, E.; Postigo, P.A.; Ramos, D. Micro-Kelvin Resolution at Room Temperature Using Nanomechanical Thermometry. *ACS Omega* **2021**, *6*, 23052–23058. [CrossRef]
54. Krauthammer, T.; Ventsel, E. *Thin Plates and Shells: Theory, Analysis, and Applications*, 1st ed.; CRC Press: Boca Raton, FL, USA, 2001. [CrossRef]
55. Wong, C.L.; Annamalai, M.; Wang, Z.Q.; Palaniapan, M. Characterization of Nanomechanical Graphene Drum Structures. *J. Micromechan. Microeng.* **2010**, *20*, 115029. [CrossRef]
56. Weber, P.; Guttinger, J.; Noury, A.; Vergara-Cruz, J.; Bachtold, A. Force Sensitivity of Multilayer Graphene Optomechanical Devices. *Nat. Commun.* **2016**, *7*, 12496. [CrossRef]
57. Sazonova, V.A. A Tunable Carbon Nanotube Resonator. PhD Thesis, Cornell University, Ithaca, NY, USA, 2006.
58. Wu, C.C.; Zhong, Z. Capacitive Spring Softening in Single-Walled Carbon Nanotube Nanoelectromechanical Resonators. *Nano Lett.* **2011**, *11*, 1448–1451. [CrossRef] [PubMed]
59. Hill, H.M.; Rigosi, A.F.; Krylyuk, S.; Tian, J.; Nguyen, N.V.; Davydov, A.V.; Newell, D.B.; Walker, A.R.H. Comprehensive Optical Characterization of Atomically Thin $NbSe_2$. *Phys. Rev. B* **2018**, *98*, 165109. [CrossRef] [PubMed]
60. Weber, J.W.; Calado, V.E.; van de Sanden, M.C.M. Optical Constants of Graphene Measured by Spectroscopic Ellipsometry. *Appl. Phys. Lett.* **2010**, *97*, 091904. [CrossRef]
61. Hsu, C.; Frisenda, R.; Schmidt, R.; Arora, A.; Vasconcellos, S.M.; Bratschitsch, R.; Zant, H.S.J.; Castellanos-Gomez, A. Thickness-Dependent Refractive Index of 1L, 2L, and 3L MoS_2, $MoSe_2$, WS_2, and WSe_2. *Adv. Opt. Mater.* **2019**, *7*, 1900239. [CrossRef]
62. Wang, X.; Lan, S. Optical Properties of Black Phosphorus. *Adv. Opt. Photonics* **2016**, *8*, 618–655. [CrossRef]
63. Palik, E.D.; Prucha, E.J. *Handbook of Optical Constants of Solids*; Academic Press: Burlington, NJ, USA, 1997.
64. Zhang, W.M.; Yan, H.; Peng, Z.K.; Meng, G. Electrostatic Pull-in Instability in MEMS/NEMS: A Review. *Sens. Actuators A Phys.* **2014**, *214*, 187–218. [CrossRef]
65. Zhou, J.; Moldovan, N.; Stan, L.; Cai, H.; Czaplewski, D.A.; Lopez, D. Approaching the Strain-Free Limit in Ultrathin Nanomechanical Resonators. *Nano Lett.* **2020**, *20*, 5693–5698. [CrossRef]
66. Gil-Santos, E.; Ramos, D.; Pini, V.; Llorens, J.; Fernández-Regúlez, M.; Calleja, M.; Tamayo, J.; San Paulo, A. Optical Back-Action in Silicon Nanowire Resonators: Bolometric versus Radiation Pressure Effects. *New J. Phys.* **2013**, *15*, 035001. [CrossRef]
67. Wang, Z.; Feng, P.X. Interferometric Motion Detection in Atomic Layer 2D Nanostructures: Visualizing Signal Transduction Efficiency and Optimization Pathways. *Sci. Rep.* **2016**, *6*, 28923. [CrossRef] [PubMed]

68. Li, Z.; Chen, F. Ion Beam Modification of Two-Dimensional Materials: Characterization, Properties, and Applications. *Appl. Phys. Rev.* **2017**, *4*, 011103. [CrossRef]
69. Tomori, H.; Hoshi, N.; Inoue, D.; Kanda, A. Influence of Focused-Ion-Beam Microfabrication on Superconducting Transition in Exfoliated Thin Films of Layered Superconductor $NbSe_2$. *J. Phys. Conf. Ser.* **2019**, *1293*, 012006. [CrossRef]
70. Shaw, J.C.; Zhou, H.; Chen, Y.; Weiss, N.O.; Liu, Y.; Huang, Y.; Duan, X. Chemical Vapor Deposition Growth of Monolayer $MoSe_2$ Nanosheets. *Nano Res.* **2015**, *7*, 511–517. [CrossRef]
71. Xia, F.; Wang, H.; Jia, Y. Rediscovering Black Phosphorus as an Anisotropic Layered Material for Optoelectronics and Electronics. *Nat. Commun.* **2014**, *5*, 4458. [CrossRef] [PubMed]
72. Çakır, D.; Peeters, F.M.; Sevik, C. Mechanical and Thermal Properties of h-MX_2 (M = Cr, Mo, W; X = O, S, Se, Te) Monolayers: A Comparative Study. *Appl. Phys. Lett.* **2014**, *104*, 203110. [CrossRef]
73. Meerschaut, A.; Deudon, C. Crystal Structure Studies of the 3R-$NbSe_{1.09}S_2$ and the 2H-$NbSe_2$ Compounds: Correlation between Nonstoichiometry and Stacking Type (=Polytypism). *Mater. Res. Bull.* **2001**, *36*, 1721–1727. [CrossRef]
74. $MoSe_2$ Crystal Structure: Datasheet from "PAULING FILE Multinaries Edition—2012" in Springer Materials. Copyright 2016 Springer-Verlag Berlin Heidelberg & Material Phases Data System (MPDS), Switzerland & National Institute for Materials Science (NIMS), Japan. Available online: https://materials.springer.com/isp/crystallographic/docs/sd_0454362 (accessed on 6 July 2022).
75. Liu, H.; Du, Y.; Deng, Y.; Ye, P.D. Semiconducting Black Phosphorus: Synthesis, Transport Properties and Electronic Applications. *Chem. Soc. Rev.* **2015**, *44*, 2732–2743. [CrossRef]
76. Persson, K. Materials Data on $NbSe_2$ (SG:194) by Materials Project. 2016. Available online: https://www.osti.gov/biblio/1197331-materials-data-nbse2-materials-project (accessed on 6 July 2022).
77. Persson, K. Materials Data on $MoSe_2$ (SG:194) by Materials Project. 2014. Available online: https://www.osti.gov/dataexplorer/biblio/dataset/1191826 (accessed on 6 July 2022).
78. Wei, Q.; Peng, X. Superior Mechanical Flexibility of Phosphorene and Few-Layer Black Phosphorus. *Appl. Phys. Lett.* **2014**, *104*, 251915. [CrossRef]
79. Givens, F.L.; Fredericks, G.E. Thermal Expansion of $NbSe_2$ and TaS_2. *J. Phys. Chem. Solids* **1977**, *38*, 1363–1365. [CrossRef]
80. Bao, W.; Miao, F.; Chen, Z.; Zhang, H.; Jang, W.; Dames, C.; Lau, C.N. Controlled Ripple Texturing of Suspended Graphene and Ultrathin Graphite Membranes. *Nat. Nanotechnol.* **2009**, *4*, 562–566. [CrossRef] [PubMed]
81. Lien, H.H. Thermal Conductivity of Thin-Film Niobium Diselenide from Temperature Dependent Raman. Master's Thesis, Stevens Institute of Technology, Hoboken, NJ, USA, 2017.
82. Balandin, A.A.; Ghosh, S.; Bao, W.; Calizo, I.; Teweldebrhan, D.; Miao, F.; Lau, C.N. Superior Thermal Conductivity of Single-Layer Graphene. *Nano Lett.* **2008**, *8*, 902–907. [CrossRef] [PubMed]
83. Darvishzadeh, A.; Alharbi, N.; Mosavi, A.; Gorji, N.E. Modeling the Strain Impact on Refractive Index and Optical Transmission Rate. *Phys. B Condens. Matter* **2018**, *543*, 14–17. [CrossRef]
84. Boyd, E.J.; Uttamchandani, D. Measurement of the Anisotropy of Young's Modulus in Single-Crystal Silicon. *J. Microelectromech. Syst.* **2012**, *21*, 243–249. [CrossRef]
85. Shur, M. *Physics of Semiconductor Devices*, 1st ed.; Prentice Hall Series in Solid State Electronics; Prentice Hall: Hoboken, NJ, USA, 1990; p. 681.
86. Zheng, X.Q.; Lee, J.; Feng, P.X.L. Hexagonal Boron Nitride Nanomechanical Resonators with Spatially Visualized Motion. *Microsyst. Nanoeng.* **2017**, *3*, 17038. [CrossRef]
87. Piller, M.; Sadeghi, P.; West, R.G.; Luhmann, N.; Martini, P.; Hansen, O.; Schmid, S. Thermal Radiation Dominated Heat Transfer in Nanomechanical Silicon Nitride Drum Resonators. *Appl. Phys. Lett.* **2020**, *117*, 034101. [CrossRef]
88. Murakami, Y. *Theory of Elasticity and Stress Concentration*; Wiley: Chichester, UK, 2017. [CrossRef]
89. Ding, Z.; Jiang, J.W.; Pei, Q.X.; Zhang, Y.W. In-Plane and Cross-Plane Thermal Conductivities of Molybdenum Disulfide. *Nanotechnology* **2015**, *26*, 065703. [CrossRef] [PubMed]
90. Gu, X.; Li, B.; Yang, R. Layer Thickness-Dependent Phonon Properties and Thermal Conductivity of MoS_2. *J. Appl. Phys.* **2016**, *119*, 085106. [CrossRef]
91. Sandell, S.; Maire, J.; Chavez-Angel, E.; Torres, C.M.S.; Kristiansen, H.; Zhang, Z.; He, J. Enhancement of Thermal Boundary Conductance of Metal-Polymer System. *Nanomaterials* **2020**, *10*, 670. [CrossRef]
92. Kurek, M. Photothermal IR Spectroscopy with Perforated Membrane Micromechanical Resonators. Ph.D. Thesis, Technical University of Denmark, Lyngby, Denmark, 2017.
93. Barnes, J.; Stephenson, R.J.; Woodburn, C.N.; O'Shea, S.J.; Welland, M.E.; Rayment, T.; Gimzewski, J.K.; Gerber, C. A Femtojoule Calorimeter using Micromechanical Sensors. *Rev. Sci. Instrum.* **1994**, *65*, 3793–3798. [CrossRef]
94. Babaei Gavan, K.; van der Drift, E.W.J.M.; Venstra, W.J.; Zuiddam, M.R.; van der Zant, H.S.J. Effect of Undercut on the Resonant Behaviour of Silicon Nitride Cantilevers. *J. Micromech. Microeng.* **2009**, *19*, 035003. [CrossRef]
95. Fishlock, S.J.; O'Shea, S.J.; McBride, J.W.; Chong, H.M.H.; Pu, S.H. Fabrication and Characterisation of Nanocrystalline Graphite MEMS Resonators using a Geometric Design to Control Buckling. *J. Micromech. Microeng.* **2017**, *27*, 095015. [CrossRef]
96. Dorgan, V.E.; Behnam, A.; Conley, H.J.; Bolotin, K.I.; Pop, E. High-field Electrical and Thermal Transport in Suspended Graphene. *Nano Lett.* **2013**, *13*, 4581–4586. [CrossRef] [PubMed]

97. Hecht, E. *Optics*, 5th ed.; Pearson Education Limited: Essex, UK, 2017; p. 67.
98. Liu, K.; Wu, J. Mechanical Properties of Two-Dimensional Materials and Heterostructures. *J. Mater. Res.* **2015**, *31*, 832–844. [CrossRef]

nanomaterials

Article

The Effect of Annealing and Optical Radiation Treatment on Graphene Resonators

Yujian Liu [1,2], Cheng Li [1,2,*], Shangchun Fan [1], Xuefeng Song [3,*] and Zhen Wan [1]

[1] School of Instrumentation Science and Opto-Electronics Engineering, Beihang University, Beijing 100191, China
[2] Research Institute of Beihang University in Shenzhen, Shenzhen 518000, China
[3] Shenzhen Institute for Quantum Science and Engineering, Southern University of Science and Technology, Shenzhen 518055, China
* Correspondence: licheng@buaa.edu.cn (C.L.); songxf@sustech.edu.cn (X.S.)

Abstract: Graphene resonant sensors have shown strong competitiveness with respect to sensitivity and size. To advance the applications of graphene resonant sensors, the damage behaviors of graphene harmonic oscillators after thermal annealing and laser irradiation were investigated by morphology analysis and frequency domain vibration characteristics. The interface stress was proven to be the key factor that directly affected the yield of resonators. The resulting phenomenon could be improved by appropriately controlling the annealing temperature and size of resonators, thereby achieving membrane intactness of up to 96.4%. However, micro-cracks were found on the graphene sheets when continuous wave (CW) laser power was more than 4 mW. Moreover, the fluctuating light energy would also cause mechanical fatigue in addition to the photothermal effect, and the threshold damage power for the sinusoidally modulated laser was merely 2 mW. In this way, based on the amplitude-frequency surface morphology of the graphene resonator, the thermal time constant of the order of a few microseconds was confirmed to evaluate the damage of the graphene oscillator in situ and in real time, which could be further extended for those resonators using other 2D materials.

Keywords: graphene resonator; interface stress; film thermal damage; thermal time constant

Citation: Liu, Y.; Li, C.; Fan, S.; Song, X.; Wan, Z. The Effect of Annealing and Optical Radiation Treatment on Graphene Resonators. *Nanomaterials* **2022**, *12*, 2725. https://doi.org/10.3390/nano12152725

Academic Editor: Filippo Giubileo

Received: 21 July 2022
Accepted: 4 August 2022
Published: 8 August 2022

1. Introduction

Micro resonant sensors have been widely applied in aviation, aerospace engineering and automation due to their high sensitivity, stable performance and direct frequency signal output. The resonator is the key element of resonant sensors, which dominantly affects the performance of the whole system. To develop a high-performance resonant sensor, the material of the micro resonators should be stiff, robust and stable.

Graphene, an atom-thick two-dimensional material with a single-layer thickness of 0.335 nm, has demonstrated excellent mechanical [1], optical [2], electrical [3] and thermal properties [4]. These superior properties enable the new material with novel nanostructures to be widely applied in the field of micro-electro-mechanical systems (MEMS) or photoelectric devices [5]. To be specific, graphene exhibits a high Young's modulus of 1.0 TPa, a high tensile rate up to 20% [6] and extreme fatigue life of more than 10^9 cycles [7], which makes it an appropriate material for harmonic oscillators. Particularly, the first graphene resonator was developed by transferring graphene onto the trenches of silicon oxide [8], actuated by a modulated laser. Compared with the silicon counterpart, a graphene resonant sensor could reach 45 times higher pressure sensitivity with a 25 times smaller membrane area [9]. However, in terms of stability, the graphene resonators still cannot reach the same long-term stability as silicon resonators that can achieve a one-year frequency drift of merely 0.01% [10]. This perfect stability of silicon resonators is not only due to the craftsmanship of silicon resonators—for example, the complete sealing technology of the resonator—but also the research of the damage resource, and the compensation methods [11–13]. Thus, research about the damage mechanism of graphene resonators is of vital importance, but it has not been extensively discussed thus far. Moreover, it should be noted that, especially for a merely ~0.335 nm thick membrane, it is much easier to lose integrity.

The damage of graphene resonators can be attributed to the manufacturing process and operating conditions. For the fabrication of resonators, suspended transfer of graphene is a common step that might cause damage to the thin suspended membrane. Generally, graphene transfer in micro-mechanical systems is performed with the help of the widely used polymethyl methacrylate (PMMA) [14], Polydimethylsiloxane (PDMS) [15] or other polymers, by spin-coating on the film onto the original substrate surface [16]. Here, we focused on the commonly used transfer method with PMMA substrate. After transferring graphene to a target substrate, PMMA coating could be removed by annealing over 300 °C [17] or washed off in an acetone solution [18]. Considering the PMMA removal method, a previous study by Oshidari et al. [19] has shown that the thermal annealing procedure could be employed to improve the resonator's resonant frequency and quality factor. By using the Raman spectroscopy imaging technic, it was noticed that there is considerable strain induced in the suspended graphene flakes after annealing, including the furnace annealing [20] or laser annealing [21]. Although this extra inner stress contributes to holding the graphene sheet tightly and causes a flatter membrane surface [22], the extra strain in the annealing process would negatively induce the cracks on the graphene surface. According to Barton et al. [23], the diameter of suspended graphene would affect the performance of the fabricated device. Hence, an appropriate annealing temperature for a graphene membrane with a specific diameter should be evaluated for better performance of the graphene oscillator. Besides the transfer-induced damage in the fabrication process, the photothermal effect would also result in damage to the membrane. Generally, the laser-induced damage can be characterized by the thermal effect and the non-thermal one. For the former, graphene absorbs photons and then releases them under the irradiation of the CW laser [24]. When the applied laser power is strong enough, the energy of phonons can break chemical bonds, thereby resulting in the thermal damage to graphene. The latter could be divided into two aspects. One is due to the original defects, such as the vacancy, which would weaken the fatigue characteristics of the original material, which has been discussed in [7]. The other is due to the ultra-fast energy transfer mechanism unique to solids. When the energy transmission speed of the laser pulse was obviously faster than phonon relaxation time, electrons were excited, and thermions are created. These electrons in semiconductors could absorb energy and then cool down by giving it to other phonons on a shorter time scale than thermal diffusion [25,26]. Melting, vaporization, or sublimation might happen in this stage. Considering our experiment setup, the modulated frequency of the laser was set in the range of 10 kHz to 5 MHz. However, since the phonon relaxation time of graphene is generally in the picosecond order of magnitude [27], which is by far lower than the modulated period of (0.1 μs) the pulsed laser signal in our experiment, this effect mentioned above is not discussed in this paper.

The Raman spectroscopy technique has been used to evaluate the extent of damage by calculating the intensity of the D and G peaks [28]. However, in terms of the actual application, the Raman spectrometer lacks portability. Thus, considering that the surface morphology is suitable for early prediction regarding the resonant state before a resonant test, herein a simple method was developed based on the principle of the Fabry–Pérot (F-P) interference to evaluate the extent of damage through the resonant behaviours of a graphene oscillator. Moreover, it can be seen from the measured resonant response that the thermal time constant acted as a real-time character for monitoring the resonant state of a graphene oscillator.

2. Experiment Methods

Figure 1a shows the process of making free-standing graphene with Cu patterns, wherein a multilayer graphene was grown on the copper (Cu) foil by the chemical vapor deposition. At first, a thin film of PMMA was spin-coated onto the surface of a chemical vapor-deposited multilayer graphene (MLG). The formed MLG/PMMA film was transferred onto the surface of a copper mesh with multiple holes whose diameters were set as 20, 60 and 100 µm, respectively. Figure 1b shows the thickness of the used graphene membrane, which was measured to be 3.57 nm by AFM (FSM Precision, FM-Nanoview 6800, Suzhou, China). The sample with MLG/PMMA film was then placed in a furnace and annealed at a temperature of 300, 375 or 450 °C. Note that the annealing temperature was chosen according to the thermal decomposition characteristic of PMMA [29]. Then, an all-fibre experimental system was established to motivate and interrogate the motion of graphene sheets on the basis of Jin's work [30], as shown in Figure 1c. In view of a small divergence angle when the laser was irradiated out of the optical fibre into the F-P cavity, the air cavity distance between the fibre and the sample would cause a weak energy loss. In this case, the distance between the membrane and the fibre end-face was controlled to be less than 50 µm via a broad-band laser and an optical spectrum analyser (OSA) on basis of the F-P interference. In order to actuate the graphene membrane, the intensity of laser S was modulated with a rate of 60% and then the membrane was optically heated up and therefore shrank and expanded under the light-induced thermal stress. Then, the opto-mechanics principle in the F-P cavity was employed so as to detect this motion of the graphene, wherein the suspended graphene and the end-face of the optical fibre acted as a moving mirror and a fixed back-mirror, respectively. In this way, the deflection displacement of the suspended graphene membrane could be obtained by a photodetector (PD). For the sake of minimizing the damage caused by excessive laser power, the laser power was set to be as small as possible. To be specific, the light power for laser S and laser R was set to 0.3 mW and 2 mW, respectively. In order to batch test the resonant characteristics of the graphene membrane, the graphene sample without PMMA coating was placed on a precise translation stage with a three-dimension displacement accuracy of 1 µm (Figure 1d,e). In this way, along with the movement observation under a microscope, the light spot of the fibre laser could be adjusted properly in the centre of the membrane. Meanwhile, the photos were read out from computer in real-time, and Figure 1f showed a surface morphology comparison of graphene annealed at different temperatures. The membranes annealed at a higher temperature showed more micro-cracks.

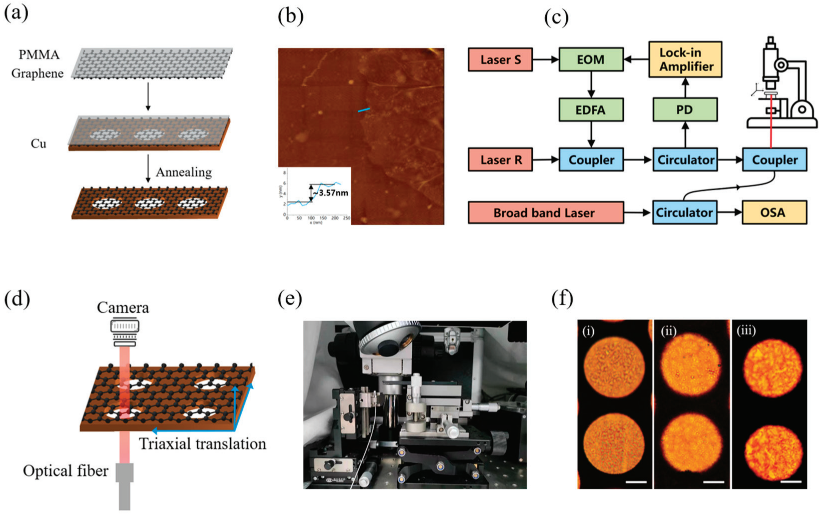

Figure 1. (**a**) The process of making free-standing graphene with Cu substrate, (**b**) the AFM topographic image of a graphene after transfer, (**c**) the experimental setup used to actuate and detect the motion of the resonators, (**d**) the schematic diagram and (**e**) experimental setup of the displacement control, (**f**) the micrographs of 60-µm graphene membranes annealed at (i) 300, (ii) 375 and (iii) 450 °C, scale bar: 20 µm.

3. Results and Discussions

3.1. Damage in the Annealing Process

In this section, the damage to the graphene harmonic oscillator after thermal annealing is presented. Graphene membranes annealed at a temperature of 300, 375 or 450 °C were first observed under an optical microscope and scanning electron microscope (SEM) (FEI, Quanta 450 FEG, Reston, VA, USA) to analyse the breakage rate of the membrane, on micro- and nano-scales, respectively. Then, the resonant characteristics, including quality factor and resonant frequency, were investigated by the aforementioned all-fibre experimental system.

After the annealing process at each temperature, the intactness of the graphene was observed by an optical microscope. It has been found that graphene with a more than 95% free-standing area has the potential to be fabricated as a well-behaved harmonic oscillator; thus, this kind of membrane was noted to be intact in this paper. To be specific, 300 graphene membranes after each annealing process were randomly selected, and the number of intact membranes was counted. The statistical results are listed in Figure 2a. Figure 2a shows that the 20 µm-diameter membranes that annealed at 300 °C exhibited the highest rate of intactness at up to 96.4%. Furthermore, graphene membranes were more easily broken with a larger diameter or annealed at a higher temperature, such as 375 °C and 450 °C. This phenomenon could be explained by the stress between PMMA and graphene. In fact, with an increase in the temperature, the decomposition of PMMA coating happened in two stages. In the first stage (at about 220 °C), the C=C bonds of PMMA were broken, while the second stage primarily involved the random scission of C-C bonds at a higher temperature (at about 300 °C) [29]. In view of the mechanical properties of PMMA, the hardness and elastic modulus of PMMA film showed an increasing tendency on account of the reduced chain length of the polymer and cross links of the polymer [31,32]. Therefore, it could be understood that, at a temperature of 300 °C, there was generally a thin film of PMMA left on the graphene surface [33], which kept the membrane rigid and protected the graphene membrane from breaking apart, which is consistent with [23]. However, when the temperature rose above 300 °C, the protection film of PMMA became thinner and left a single membrane of suspended graphene, which was much more easily damaged.

Besides the stress between the graphene and PMMA, there was also a thermal interfacial interaction between the MLG and substrate in the heating process, which would also cause damage to the graphene, especially at the edge of the entire membrane. A photo of a typical damaged graphene caused by thermal interaction between the MLG and substrate is shown in Figure 2b. To be specific, when the resonator was heated, the substrate with a positive thermal expansive efficient would impose tensile stress on the graphene with a negative thermal expansive efficient [34]. Graphene was adhered to the copper surface by the Van der Waals force. So, for some weak points where graphene and the substrate were not fitted closely, the intermolecular force was not strong enough to resist the relative slip between the membrane and the substrate. In this case, the graphene membrane tended to crimp on the metal surface. If the range of the crimp was small, little cracks were found on the graphene membrane, which is marked by point B in Figure 2b. Otherwise, if the crimping range was large, a double-layer membrane was observed, as is shown by point C in Figure 2b. In this case, the thickness of the membrane might double. The corresponding schematic diagram of graphene breakage is shown in Figure 2c.

Furthermore, in order to graphically depict the damage to the graphene membrane on a nano scale, the SEM photographs of the suspended graphene are given in Figure 3. It is worth mentioning that the small amount of PMMA on the graphene surface would lead to a poor image resolution. As a result, gold nanoparticles were sprayed on the PMMA surface to enhance its conductivity. Referring to Figure 3, the dark and bright areas of the image are representative of the broken and the suspended graphene membrane, respectively. For example, in Figure 3f, area A represents the graphene membrane and 'B' represents the broken area.

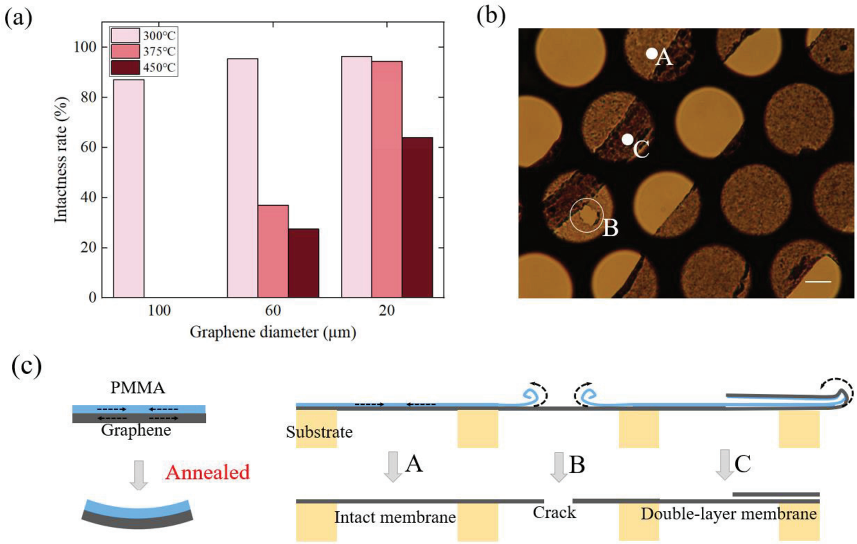

Figure 2. (**a**) The breakage rate of the annealed graphene membrane and (**b**) the microscope photograph of damaged graphene after annealing: points A, B and C represent flat graphene, graphene with a hole and double-layer graphene, respectively. Scale bar: 10 μm, (**c**) the damage mechanism of thermal interfacial interaction, where A, B and C correspond to the regionss A, B and C in Figure 2b, respectively.

In this way, these SEM images were further binarized to calculate the proportion of the damaged area. Thus, the microscopic broken rate of the membrane could be calculated as $\mathrm{num}_{\mathrm{dark}}/\mathrm{num}_{\mathrm{all},}$ wherein $\mathrm{num}_{\mathrm{dark}}$ and $\mathrm{num}_{\mathrm{all}}$ represent the number of dark pixels and all pixels, respectively. It could be concluded that a higher annealing temperature T or a larger suspended radius R would result in a larger broken area. Taking the graphene (D = 20 μm, T = 300 °C), for example, the graphene exhibited perfect intactness (100%). However, once the suspended diameter was increased to 100 μm, the breakage rate increased to 2.5%. When the annealing temperature was increased to 450 °C, the breakage rate rose rapidly to 30.9%. In the aforementioned experimental set up, the graphene breakage rate showed higher sensitivity to the annealing temperature than the suspended diameter.

Besides the breakage rate and the surface morphology of the membrane, which has been mentioned above, the resonant characteristics were also investigated, including the resonant frequency and quality factor. Among these, the resonant frequency indicates the fundamental frequency of the oscillator, and the quality factor represents the energy loss per oscillation cycle, which is calculated by $\omega_0/\Delta\omega$, where ω_0 is the natural frequency and $\Delta\omega$ is the 3 dB bandwidth of the amplitude–frequency curve. Thus, the resonant characteristics of the graphene resonators were investigated at the aforementioned three annealing temperatures, as illustrated in Figure 4.

Figure 4a shows that after annealing at 300 °C, the resonant frequency showed an inverse proportion to the diameter of the graphene membrane. For various graphene films with different diameters, the average frequencies of each 30 samples were respectively calculated as f_{20} = 1254.1 kHz (D = 20 μm), f_{60} = 338.9 kHz (D = 60 μm) and f_{100} = 153.5 kHz (D = 100 μm), and the standard deviation (STD) of frequencies were confirmed as σ_{20} = 192.7 kHz (D = 20 μm), σ_{60} = 59.0 kHz (D = 60 μm) and σ_{100} = 46.2 kHz (D = 100 μm), respectively (Figure 4a). It can be also noticed that the distribution of the resonant frequencies is more concentrated for those resonators with small radii. This is possibly because of the unpredictable breakage of the membrane, which induces more unnecessary vibration modes of the membrane. As for the Q factor, the average values were calculated to be Q_{20} = 9.8, Q_{60} = 9.5 and Q_{100} = 7.8, and the STD values were σ_{20} = 2.26 (D = 20 μm), σ_{60} = 2.50 (D = 60 μm) and σ_{100} = 3.34 (D = 100 μm), respectively (Figure 4c). The resonators with smaller diameters had higher Q factors and better consistency. Furthermore, these resonators all had a relatively low Q factor because the measurement was executed at atmospheric pressure, and the air damping caused high energy loss for the vibrating micro-membrane. In application, the quality factor could be greatly enhanced by sealing the membrane in a vacuum, which could reach an order of thousands.

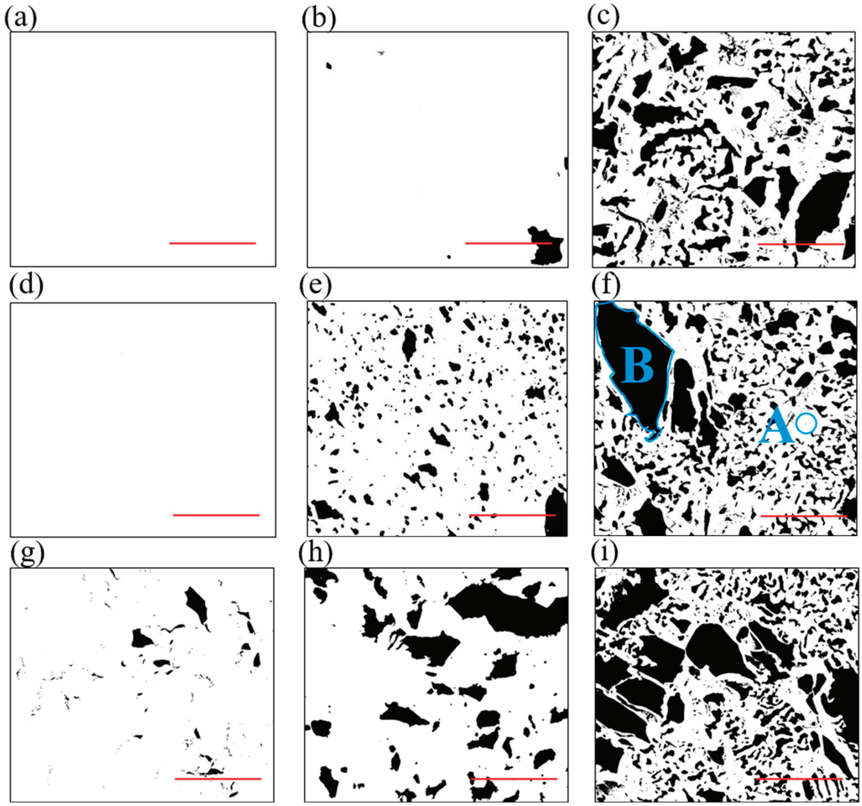

Figure 3. The binarized SEM photograph of graphene of different radius R and after annealing at different temperatures T, scale bar: 5 μm. The broken rate was noted in the brackets. (**a**) D = 20 μm, T = 300 °C (0%). (**b**) D = 20 μm, T = 375 °C (1.6%). (**c**) D = 20 μm, T = 450 °C (30.9%). (**d**) D = 60 μm, T = 300 °C (0%). (**e**) D = 60 μm, T = 375 °C (16.9%). (**f**) D = 60 μm, T = 450 °C (38.7%). (**g**) D = 100 μm, T = 300 °C (2.5%). (**h**) D = 100 μm, T = 375 °C (20.42%). (**i**) D = 100 μm, T = 450 °C (43.7%).

When the annealing temperature was set as 375 °C, 100 μm-diameter graphene was unable to support itself after annealing. Hence, the resonant data for the 100 μm diameter graphene were not included in Figure 4b. The corresponding average frequencies of the resonators were measured to be f_{20} = 3808.5 kHz (D = 20 μm) and f_{60} = 661.3 kHz (D = 60 μm), and the STD values were calculated to be 641.8 kHz and 348.4 kHz, accordingly. The Q factors were measured to be 8.93 (D = 20 μm) and 6.85 (D = 60 μm) with the corresponding STD values of 2.03 and 2.72, respectively (Figure 4d).

For a circular membrane under tension, the fundamental frequency can be expressed as [23]

$$f = \frac{2.404}{\pi D}\sqrt{\frac{E_t S}{\rho \alpha}} \tag{1}$$

where D, E_t and ρ are the diameter, the in-plain Young's modulus and the in-plain density of the graphene, respectively; S is the strain in the graphene membrane, and α is the density multiplier that describes the contaminating of the device. Moreover, the parameter $\rho\alpha$ is defined as the in-plain density of the suspended harmonic oscillator including the graphene, PMMA residues and other additional mass. For the resonators at the same annealing temperature, such as 300 °C, graphene membranes were considered to have the same in-plain mass density $\rho\alpha$. In terms of Equation (1), the ratio of the inner strain of 20 µm, 60 µm and 100 µm membranes were estimated to be S_1:S_2:S_3 = 2.69:1.78:1. This strain possibly resulted from the Van der Waals force between the graphene and the copper sidewall. At different temperatures, different mechanical energy might be introduced via distortions of the graphene lattice [21]. For the resonators with the same diameter, taking the 20 µm-diameter membrane as an example, it could be inferred that the membrane after 375 °C annealing had three times the resonant frequency compared to the counterparts annealed at 300 °C. Combining the surface appearance depicted in Figure 3, it could be inferred that the inner strain was one of the main factors that caused damage to the membrane.

Note that when the annealing temperature increased to 450 °C, the fabricated resonators of all sizes were damaged with the damaged areas as shown in Figure 2b, and no relative data were recorded in Figure 4.

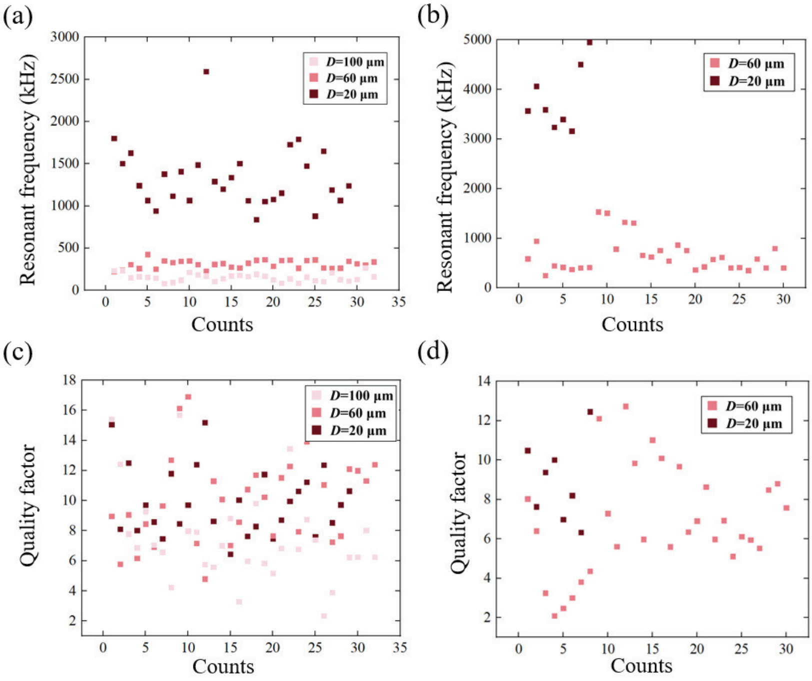

Figure 4. Statistics of resonance frequency and quality factor of graphene at different annealing temperatures and sizes: (**a**) Resonance frequency of graphene annealed at 300 °C; (**b**) the resonant frequency of graphene annealed at 375 °C; (**c**) Quality factor of graphene annealed at 300 °C; (**d**) Quality factor of graphene annealed at 375 °C.

3.2. Damage in the Laser Irradiation Process

Damage not only occurs in the fabrication process, but also in the working process of the harmonic oscillator. In the previous study on the laser-induced damage, the graphene was often tested by a Raman spectrometer [35] or microscope [36] after laser irradiation, which is ex situ. For a micro-mechanical device, it would be more helpful to perform an in situ detection of the damage situation of the graphene. At this point, the observations in this letter would provide some insight. The 300 °C -annealed 60 µm-diameter graphene membrane was placed under an optical fibre end-face and irradiated by a sinusoidal modulated laser or constant laser. Each membrane was irradiated at a certain laser power for 600 seconds, and the diameter of the damage range was then recorded. Note that the shape of the damage range was sometimes not a strict circle, but an ellipse, in which case the diameter was recorded as half of the sum of the major axis and minor axis of the ellipse. The relationship between the damaged diameter and laser power is shown in Figure 5. Under a modulated laser, cracks were found on the membrane when the power went higher than 2 mW (Figure 5a,c). For the laser with constant power, the membrane centre started to break at a laser power of about 4–5 mW (Figure 5b,d). Note that the fibre optic laser power in our experiment was first measured by a handheld optical power meter (SAMZHE, SZ-GG01, Shenzhen, China) before the sample was irradiated. This could be explained by the fact that a modulated laser would cause not only a heating effect but also alternating photothermal stress within the membrane. The photothermal stress would cause a thermal shock effect on the membrane and accelerate the damage of the membrane [37].

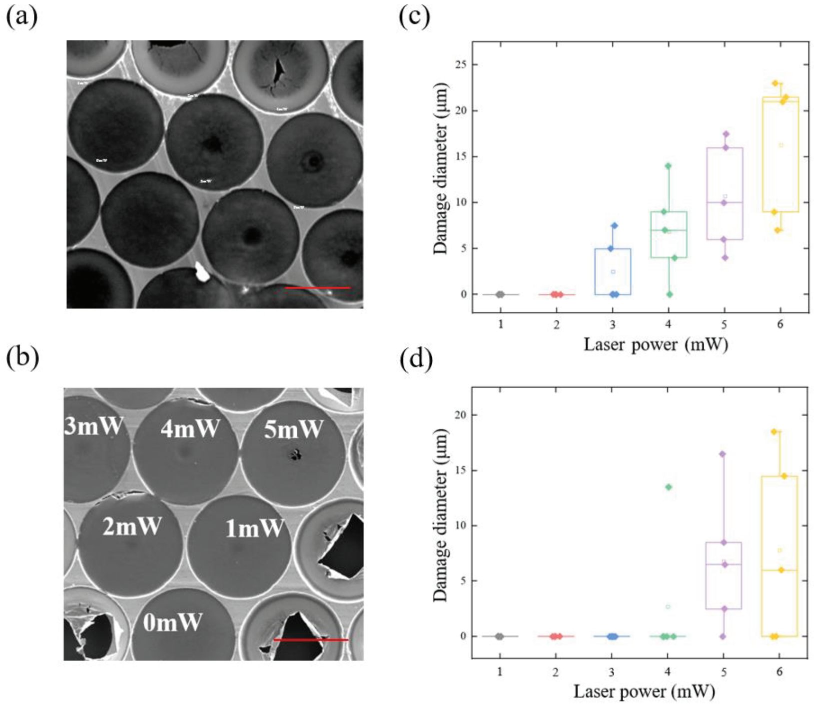

Figure 5. Surface morphology of graphene irradiated by (**a**) modulated laser, scale bar: 40 µm. and (**b**) constant laser (1–5 mW), scale bar: 40 µm. (**c**) damage radius statistics of graphene by modulated pump laser and (**d**) CW laser.

As the modulated laser was verified with a higher possibility of damaging the membrane, the effect of the modulated laser on the graphene resonant characteristics was further explored. Thus, the graphene membrane was excited with a modulated laser whose power was gradually increased from 1 mW to 5 mW. Meanwhile, the motion was recorded by a CW laser with an extremely small amount of power, so that this laser would barely damage the structure of the graphene. The experiment results were recorded in Figure 6.

From the frequency domain, Figure 6a shows that the deflection of the oscillator would first increase when the exciting laser power went up. With a further increase of the excitation optical power, the burr of the amplitude–frequency curves increased. This was because the frequency sweep needed to take about tens of seconds, during which the unstable state of the graphene exhibited a fluctuation of the reflected signal. When the laser power finally exceeded 5 mW, a hole was found in the centre of the membrane and no resonance phenomenon could be recorded anymore.

According to Metzger et al. [38], a thermomechanical response of the suspended graphene could be gained from the frequency domain feature to characterize its thermal properties. One important parameter is the thermal time constant, which describes the response time between the mechanical motion response of suspended graphene and the laser irradiation that opto-thermally actuates the membrane. According to the heat transfer theory, the process of laser irradiation onto the graphene membrane can be considered as the presence of an internal heat source. Combining the optical self-cooling of the deformable Fabry–Perot cavity, the displacement of membrane z in the frequency domain could be written as [39]:

$$z(\omega) = \alpha PR \frac{1 - i\omega\tau}{1 + \omega^2\tau^2} \tag{2}$$

where τ is the thermal time constant, R is the thermal resistance, C is the thermal capacitance ($RC = \tau$), α is an effective thermal-expansion coefficient and P is the heating power. After taking the derivative of Formula (2), the imaginary part of the response function reached the maximum amplitude when $\omega\tau = 1$. Thus, the thermal time constant τ of the graphene membrane was calculated.

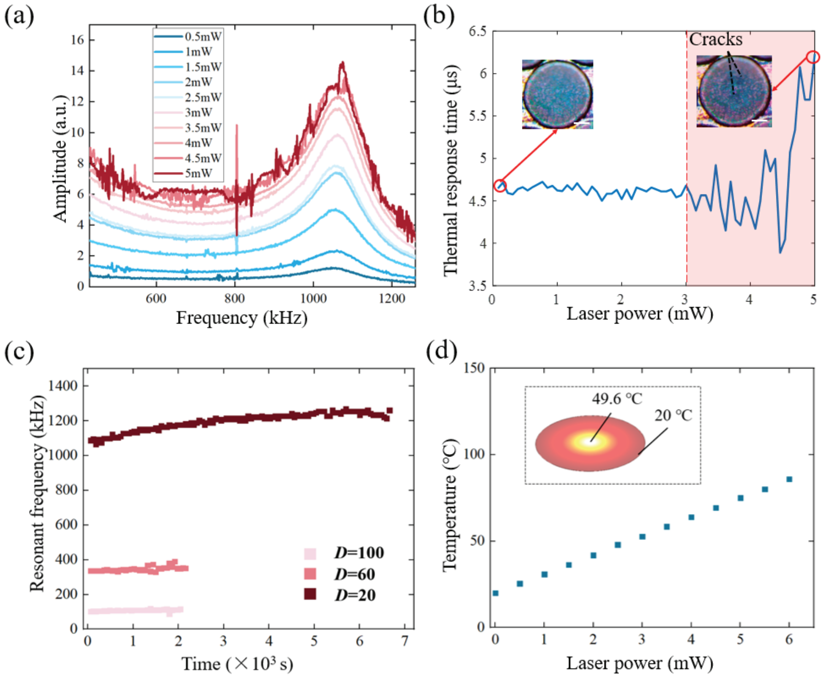

Figure 6. (**a**) The amplitude-frequency response changes when the excitation optical power increases from 0.5 mW to 5 mW. (**b**) The thermal time constant of the resonator changes when the excitation optical power increases from 1 mW to 5 mW; inset: the surface morphology of graphene. (**c**) The long-term static dwelling of graphene with different diameters. (**d**) The calculated temperature under a gaussian laser spot for graphene with three different diameters (thermal conductivity κ = 500 W/(mK)); inset: the temperature distribution of the surface.

It was found that τ started to deviate at about 3 mW (Figure 6b) and then exhibited large fluctuation. The same was the case when the real-time surface morphology started to collapse (Figure 6c), which indicated that the thermal time constant could be a parameter to evaluate the vibration state of the graphene. After that, the thermal time constant went up to about 6 μs from 4.7 μs, which meant a longer time between the actuation and the motion for a broken graphene membrane.

Then, long-term stability was considered. It was found that the graphene with a smaller diameter tended to have a longer working duration (Figure 6c, blue squares). Combining the surface appearance in Figure 6, there is a considerable possibility that the initial rate of the damage area would have a directly negative effect on the long-term static dwelling of the graphene resonators. Thus, the fabrication method of the lossless graphene membrane is a vital step for applications of graphene resonators and is worthy of further investigation. Moreover, the temperature increase of the graphene sample under a Gaussian beam was simulated with Comsol software with multi-physics fields. The simulation result showed that the thermal effect would not lead to a serious break of the C-C bonds under this laser power [40,41]. That is, it was more likely that the mechanical vibration accelerated this damage.

4. Conclusions

From the perspective of the application of graphene resonant sensors, the effect of the temperature-dependent annealing treatment on the intactness of suspended multilayer graphene was investigated through surface morphology observation to further evaluate the resonant behaviours of graphene resonators after the thermal annealing process. The experimental results showed that an annealing temperature of 300 °C leaves a certain degree of PMMA residue, which can prevent the breakage of graphene while annealing. In contrast, when the annealing temperature rose to 375 °C, more cracks, or even a total collapse, occur in the suspended membrane. In this way, although resonant frequencies that are twice as high could be achieved, the atmosphere pressure quality factor ($Q_{20} = 8.9$) of the resonator showed no synchronous improvement compared to the counterparts annealed at 300 °C ($Q_{20} = 9.8$).

Besides the annealing treatment, the effect of the laser irradiation on the intactness of the suspended multilayer graphene was also investigated. The damage was mainly caused by the modulated laser, which would induce both a thermal effect and mechanical fatigue. The damage threshold power for the modulated laser was found to be about 2–3 mW, which is about half the CW laser. Thus, the modulated laser power should be controlled carefully in application. Moreover, it was found that the fluctuation of the thermal time constant could be applied to evaluate this damage in situ and in real time.

Author Contributions: Y.L. performed the experiment and wrote the paper; C.L. conceived the idea and provided the support for the research; Z.W. and X.S. analyzed the experiment results; C.L. and S.F. proof-read the manuscript. All authors have read and agreed to the published version of the manuscript.

Funding: This work was funded by the National Natural Science Foundation of China (62173021), Beijing Natural Science Foundation (4212039), Aviation Science Foundation of China (2020Z073051002), and Science Technology and Innovation Commission of Shenzhen Municipality (JCYJ20180504165721952).

Data Availability Statement: The data presented in this study are available on request from the corresponding author.

Conflicts of Interest: The authors declare no conflict of interest.

References

1. Lee, C.; Wei, X.; Kysar, J.W.; Hone, J. Measurement of the elastic properties and intrinsic strength of monolayer graphene. *Science* **2008**, *321*, 385–388. [CrossRef]
2. Bonaccorso, F.; Sun, Z.; Hasan, T.A.; Ferrari, A.C. Graphene photonics and optoelectronics. *Nat. Photonics* **2010**, *4*, 611–622. [CrossRef]

3. Pereira, V.M.; Castro, N.A.H. Strain engineering of graphene's electronic structure. *Phys. Rev. Lett.* **2009**, *103*, 046801. [CrossRef] [PubMed]
4. Balandin, A.A.; Ghosh, S.; Bao, W. Superior thermal conductivity of single-layer graphene. *Nano Lett.* **2008**, *8*, 902–907. [CrossRef] [PubMed]
5. Xi, J.Y.; Jia, R.; Li, W.; Wang, J.; Bai, F.Q.; Eglitis, R.I.; Zhang, H.X. How does graphene enhance the photoelectric conversion efficiency of dye sensitized solar cells? An insight from a theoretical perspective. *J. Mater. Chem. A* **2019**, *7*, 2730–2740. [CrossRef]
6. Jiang, J.; Wang, J.; Li, B. Young's modulus of graphene: A molecular dynamics study. *Phys. Rev. B* **2009**, *80*, 113405. [CrossRef]
7. Cui, T.; Mukherjee, S.; Sudeep, P.M. Fatigue of graphene. *Nat. Mater.* **2020**, *19*, 405–411. [CrossRef] [PubMed]
8. Bunch, J.S.; van der Zande, A.M.; Verbridge, S.S. Electromechanical resonators from graphene sheets. *Science* **2007**, *315*, 490–493. [CrossRef]
9. Dolleman, R.J.; Vidovikj, D.D.; Cartamil-Bueno, S.J. Graphene squeeze-film pressure sensors. *Nano Lett.* **2016**, *16*, 568–571. [CrossRef]
10. Harada, K.; Ikeda, K.; Kuwayama, H. Various applications of resonant pressure sensor chip based on 3-D micromachining. *Sens. Actuator A Phys.* **1999**, *73*, 261–266. [CrossRef]
11. Greenwood, J.C. Etched silicon vibrating sensor. *J. Phys. E Sci. Instr.* **1984**, *17*, 650–652. [CrossRef]
12. Mandle, J.; Lefort, O.; Migeon, A. A new micromachined silicon high-accuracy pressure sensor. *Sens. Actuator A Phys.* **1995**, *46*, 129–132. [CrossRef]
13. Věí, J. Temperature compensation of silicon resonant pressure sensor. *Sens. Actuator A Phys.* **1996**, *57*, 179–182.
14. Kang, J.; Shin, D.; Bae, S. Graphene transfer: Key for applications. *Nanoscale* **2012**, *4*, 5527–5537. [CrossRef] [PubMed]
15. Kim, K.; Zhao, Y.; Jang, H. Large-scale pattern growth of graphene films for stretchable transparent electrodes. *Nature* **2009**, *457*, 706–710. [CrossRef]
16. Ali, U.; Karim, K.J.B.A.; Buang, N.A. A review of the properties and applications of Poly (Methyl Methacrylate) (PMMA). *Polym. Rev.* **2015**, *55*, 678–705. [CrossRef]
17. Reina, A.; Jia, X.; Ho, J. Large area, few-layer graphene films on arbitrary substrates by chemical vapor deposition. *Nano Lett.* **2009**, *9*, 30–35. [CrossRef]
18. Schmid, S.; Bagci, T.; Zeuthen, E. Single-layer graphene on silicon nitride micromembrane resonators. *J. Appl. Phys.* **2014**, *115*, 054513. [CrossRef]
19. Oshidari, Y.; Hatakeyama, T.; Kometani, R. High quality factor graphene resonator fabrication using resist shrinkage-induced strain. *Appl. Phys. Lett.* **2012**, *5*, 117201. [CrossRef]
20. Rouxinol, F.P.; Gelamo, R.V.; Amici, R.G. Low contact resistivity and strain in suspended multilayer graphene. *Appl. Phys. Lett.* **2010**, *97*, 253104. [CrossRef]
21. Robinson, J.T.; Zalalutdinov, M.K.; Cress, C.D. Graphene strained by defects. *ACS Nano* **2017**, *11*, 4745–4752. [CrossRef] [PubMed]
22. Cheng, Z.; Zhou, Q.; Wang, C. Toward intrinsic graphene surfaces: A systematic study on thermal annealing and wet-chemical treatment of SiO_2-supported graphene devices. *Nano Lett.* **2011**, *11*, 767–771. [CrossRef] [PubMed]
23. Barton, R.A.; Ilic, B.; van der Zande, A.M. High, size-dependent quality factor in an array of graphene mechanical resonators. *Nano Lett.* **2011**, *11*, 1232–1236. [CrossRef] [PubMed]
24. Currie, M.; Caldwell, J.D.; Bezares, F.J. Quantifying pulsed laser induced damage to graphene. *Appl. Phys. Lett.* **2011**, *99*, 211901. [CrossRef]
25. Yoo, J.H.; In, J.B.; Park, J.B. Graphene folds by femtosecond laser ablation. *Appl. Phys. Lett.* **2012**, *100*, 233124. [CrossRef]
26. Lenner, M.; Kaplan, A.; Palmer, R.E. Nanoscopic Coulomb explosion in ultrafast graphite ablation. *Appl. Phys. Lett.* **2007**, *90*, 153119. [CrossRef]
27. Qiu, B.; Ruan, X. Reduction of spectral phonon relaxation times from suspended to supported graphene. *Appl. Phys. Lett.* **2012**, *100*, 193101. [CrossRef]
28. Lenner, M.; Kaplan, A.; Huehon, C. Ultrafast laser ablation of graphite. *Phys. Rev. B* **2009**, *79*, 184105. [CrossRef]
29. Ferriol, M.; Gentilhomme, A.; Cochez, M. Thermal degradation of Poly (methyl methacrylate) (PMMA): Modelling of DTG and TG curves. *Polym. Degrad. Stabil.* **2003**, *79*, 271–281. [CrossRef]
30. Ma, J.; Jin, W. Fiber-optic ferrule-top nanomechanical resonator with multilayer graphene film. *Opt. Lett.* **2014**, *39*, 4769–4772. [CrossRef]
31. Süske, E.; Scharf, T.; Schaaf, P. Variation of the mechanical properties of pulsed laser deposited PMMA films during annealing. *Appl. Phys. A.* **2004**, *79*, 1295–1297. [CrossRef]
32. Nanzai, Y.; Miwa, A.; Cui, S.Z. Aging in fully annealed and subsequently strained Poly (methyl methacrylate). *Polym. J.* **2000**, *32*, 51–56. [CrossRef]
33. Xie, W.; Weng, L.; Ng, K.M. Clean graphene surface through high temperature annealing. *Carbon* **2015**, *94*, 740–748. [CrossRef]
34. Bao, W.; Miao, F.; Chen, Z. Controlled ripple texturing of suspended graphene and ultrathin graphite membranes. *Nat. Nanotechnol.* **2009**, *4*, 562–566. [CrossRef] [PubMed]
35. Roberts, A.; Cormode, D.; Reynolds, C.; Newhouse-Illige, T.; LeRoy, B.J.; Sandhu, A.S. Response of graphene to femtosecond high-intensity laser irradiation. *Appl. Phys. Lett.* **2011**, *99*, 051912. [CrossRef]
36. Beltaos, A.; Kovačević, A.; Matković, A. Damage effects on multi-layer graphene from femtosecond laser interaction. *Phys. Scr.* **2014**, *162*, 014015. [CrossRef]

37. Takeuchi, Y. *Thermal Stress*; Science Press: Beijing, China, 1977; pp. 77–79.
38. Metzger, C.; Favero, I.; Ortlieb, A. Optical self-cooling of a deformable Fabry-Perot cavity in the classical limit. *Phys. Rev. B* **2008**, *57*, 1436–1446. [CrossRef]
39. Dolleman, R.J.; Houri, S.; Davidovikj, D. Optomechanics for thermal characterization of suspended graphene. *Phys. Rev. B* **2017**, *96*, 165421. [CrossRef]
40. Renteria, J.D.; Nika, D.L.; Balandin, A.A. Graphene thermal properties: Applications in thermal management and energy storage. *Appl. Sci.* **2014**, *4*, 525–547. [CrossRef]
41. Lin, Y.; Lu, C.; Yeh, C. Graphene annealing: How clean can it be. *Nano Lett.* **2012**, *12*, 414–419. [CrossRef]

nanomaterials

MDPI

Article

Charge Transport in UV-Oxidized Graphene and Its Dependence on the Extent of Oxidation

Hwa Yong Lee [1], Mohd Musaib Haidari [1], Eun Hee Kee [1], Jin Sik Choi [1], Bae Ho Park [1], Eleanor E. B. Campbell [2] and Sung Ho Jhang [1,*]

[1] School of Physics, Konkuk University, Seoul 05029, Korea
[2] EaStCHEM, School of Chemistry, Edinburgh University, David Brewster Road, Edinburgh EH9 3FJ, UK
* Correspondence: shjhang@konkuk.ac.kr

Abstract: Graphene oxides with different degrees of oxidation are prepared by controlling UV irradiation on graphene, and the charge transport and the evolution of the transport gap are investigated according to the extent of oxidation. With increasing oxygenous defect density n_{D}, a transition from ballistic to diffusive conduction occurs at $n_{\mathrm{D}} \simeq 10^{12}\ \mathrm{cm}^{-2}$ and the transport gap grows in proportion to $\sqrt{n_{\mathrm{D}}}$. Considering the potential fluctuation related to the $e-h$ puddle, the bandgap of graphene oxide is deduced to be $E_g \simeq 30\sqrt{n_{\mathrm{D}}\ (10^{12}\ \mathrm{cm}^{-2})}$ meV. The temperature dependence of conductivity showed metal–insulator transitions at $n_{\mathrm{D}} \simeq 0.3 \times 10^{12}\ \mathrm{cm}^{-2}$, consistent with Ioffe–Regel criterion. For graphene oxides at $n_{\mathrm{D}} \geq 4.9 \times 10^{12}\ \mathrm{cm}^{-2}$, analysis indicated charge transport occurred via 2D variable range hopping conduction between localized sp^2 domain. Our work elucidates the transport mechanism at different extents of oxidation and supports the possibility of adjusting the bandgap with oxygen content.

Keywords: graphene oxide; defect density; transport gap; band gap; metal–insulator transition; 2D Mott VRH

Citation: Lee, H.Y.; Haidari, M.M.; Kee, E.H.; Choi, J.S.; Park, B.H.; Campbell, E.E.B.; Jhang, S.H. Charge Transport in UV-Oxidized Graphene and Its Dependence on the Extent of Oxidation. *Nanomaterials* **2022**, *12*, 2845. https://doi.org/10.3390/nano12162845

Academic Editor: Xuchun Gui

Received: 27 July 2022
Accepted: 15 August 2022
Published: 18 August 2022

1. Introduction

Graphene is a two-dimensional semimetal with high conductivity and mobility [1,2], and is a promising candidate for applications within electronics and optoelectronics. However, a bandgap E_g is required for certain applications and various methods have been attempted to controllably induce a bandgap in graphene. While a confinement-induced bandgap is widely investigated in graphene nanoribbons [3], a bandgap can also be induced by breaking the symmetry of the graphene lattice. As an approach to break the symmetry, functionalization of graphene with foreign atoms [4–6] such as oxygen, fluorine, and hydrogen has been tested to open a finite bandgap. For graphene oxide (GO), the bandgap is suggested to be tuned by the extent of oxidation, and $E_g \simeq 2.6$–6.5 eV is theoretically expected for fully oxidized graphene (O/C = 50%) [7–10].

The most common method to produce GO is based on wet chemistry, consisting of oxidation of graphite in strong acids, followed by a liquid exfoliation [4,11]. The degree of oxidation can be tuned by subsequent reduction via thermal or chemical treatment [12], and the transition from insulator to semimetal with increasing reduction of GO has been reported [13,14]. Despite the advantage for large-scale production of GO, this production method introduces contamination, and alternative dry oxidation methods such as plasma [4,15] and UV treatments [16,17] have been developed. Plasma oxidation produces GO by exposing graphene to an oxygen plasma, and the semimetallic graphene undergoes a transition into an insulator according to the time of exposure to the plasma [9,18]. UV/ozone treatment also controls the degree of oxidation of graphene with UV exposure time, and both methods provide convenient control over the extent of oxidation. In addition, UV oxidation causes less distortion of the graphene lattice [19,20] compared to the energetic plasma collisions that can introduce topological defects.

Transport studies of GO and observation of metal–insulator transition via oxidation or reduction reactions have been reported [9,13,14,18], but a systematic study of the transport mechanism and evolution of the transport gap for different degrees of oxidation is still required. In this paper, we produced GO samples with different extents of oxidation through UV treatment and systematically investigated the transport mechanism and the evolution of the transport gap across the metal–insulator transition.

2. Experimental

Our experiments were conducted on seven graphene field-effect-transistors (FETs) fabricated using exfoliated graphene on SiO_2 (300 nm)/Si substrates, and a device with Hall-bar geometry using graphene grown by chemical vapor deposition. For all devices, Pd (20 nm)/Au (20 nm) electrodes were deposited by e-beam lithography. Typical images of the devices are shown in Figure 1a,b. For those seven FETs prepared using exfoliated graphene, the size of the channel was unified to 2 μm × 2 μm (width × length) via oxygen plasma etching to compare later the characteristics depending on the extent of the graphene oxidation. The graphene devices were then oxidized by irradiating UV with a wavelength of 172 nm at an intensity of 20 mW/cm^2 under ambient conditions (humidity with 30 to 40%). The extent of oxidation was roughly controlled by the irradiation time. Among seven graphene FETs, groups of two devices were exposed to UV light for 15, 20, and 25 s, respectively, leaving one pristine graphene FET for reference. A laser with excitation energy of 2.33 eV was used to obtain Raman spectra of the oxidized graphene. Charge transport characteristics of the seven FETs were studied using a vacuum probe station and a Keithley 4200 semiconductor characterization system in Core Facility Center for Quantum Characterization/Analysis of Two-Dimensional Materials & Heterostructures for the temperature $77 < T < 400$ K. The graphene device with Hall-bar geometry was investigated after UV oxidation by using a quantum design PPMS for lower T down to 2 K and magnetic fields up to 7 tesla.

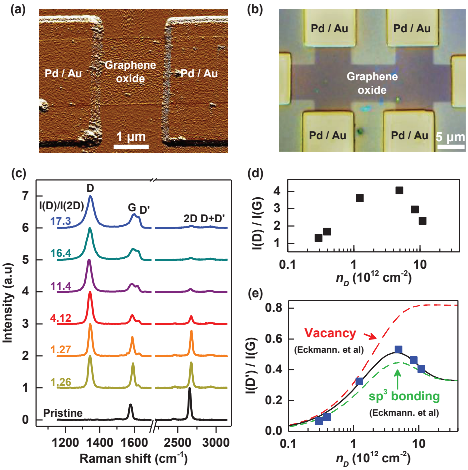

Figure 1. (**a**) Atomic force microscope image of a typical graphene FET, irradiated with UV for oxidation. (**b**) Optical image of a CVD-grown graphene device with Hall-bar geometry. (**c**) The evolution of Raman spectra of graphene devices exposed to UV light arranged according to the value of $I(D)/I(2D)$. (**d**) Values of n_D deduced from $I(D)/I(G)$ for six graphene devices irradiated with UV (**e**) $I(D')/I(G)$ as a function of n_D. The black solid line is a fit to Equation (2). Dashed lines are the evolution of $I(D')/I(G)$ either for vacancies or sp^3 sites, suggested from Ref. [21].

3. Result and Discussion

Figure 1c presents Raman spectra of pristine graphene and six graphene FETs exposed to UV light for 15, 20, or 25 s. Defect-activated D ($\sim$1345 cm^{-1}), D' ($\sim$1625 cm^{-1}), and $D + D'$ ($\sim$2930 cm^{-1}) peaks appeared for the graphene samples irradiated with UV, in addition to G ($\sim$1580 cm^{-1}) and $2D$ ($\sim$2650 cm^{-1}) peaks of pristine graphene [22]. The two graphene FETs irradiated for the same time resulted in rather different Raman spectra, possibly due to the different degrees of PMMA residues remaining on the graphene samples. Hence, in Figure 1c, Raman spectra were arranged with respect to the ratio between the D and the $2D$ peak intensities, $I(D)/I(2D)$, as the rise of D and the suppression of $2D$ peaks with increasing defect density were reported extensively as a means of quantifying defective graphene including graphene oxide [21,23–25]. Previous works on defective graphene introduced the local activation model to explain the evolution of Raman spectra, and in this model the ratio between the D and G peak intensities, $I(D)/I(G)$, allows us to estimate the defect density n_{D}, which corresponds to the degree of oxidation in our experiments [21],

$$\frac{I(D)}{I(G)} = C_{A,D} \frac{r_{A,D}^2 - r_{S,D}^2}{r_{A,D}^2 - 2r_{S,D}^2} \left[e^{-\pi^2 r_{S,D}^2 \, n_{\mathrm{D}}} - e^{-\pi^2 (r_{A,D}^2 - r_{S,D}^2) \ n_{\mathrm{D}}} \right] \tag{1}$$

Here, $C_{A,D}$ is a parameter related to the electron–phonon coupling of the D peak phonon, and $r_{S,D}$ and $r_{A,D}$ are values that indicate the size of the defect site. To deduce n_{D}, we assumed $C_{A,D} = 6$, which agrees well with the excitation laser of 532 nm and the maximum value of $I(D)/I(G) \simeq 4$ observed in our experiment [26,27] with $r_{S,D} = 1$ nm and $r_{A,D} = 3$ nm [21]. As shown in Figure 1d, values of n_{D} are deduced to be between 0.29 and 11 ($\times 10^{12}$ cm^{-2}) for the graphene samples irradiated with UV light.

To discuss the nature of the defects, we now inspect the ratio between the D' and the G peak intensities, $I(D')/I(G)$, which is sensitive to the nature of the defect. Figure 1e shows $I(D')/I(G)$ as a function of n_{D} estimated for the six irradiated graphene samples. For low defect densities, $I(D')/I(G)$ increases with n_{D}, and then starts to decrease for $n_{\mathrm{D}} \geq 4.9 \times 10^{12}$ cm^{-2} presenting a maximum value of $\simeq 0.5$. The ratio between the D' and the G peak intensities can be fitted with the following Equation (2).

$$\begin{aligned} \frac{I(D')}{I(G)} &= C_{A,D'} \frac{r_{A,D'}^2 - r_{S,D'}^2}{r_{A,D'}^2 - 2r_{S,D'}^2} \left[e^{-\pi^2 r_{S,D'}^2 \, n_{\mathrm{D}}} - e^{-\pi^2 (r_{A,D'}^2 - r_{S,D'}^2) \, n_{\mathrm{D}}} \right] \\ &+ C_S \left(1 - e^{-\pi^2 r_{S,D'}^2 \, n_{\mathrm{D}}} \right) \end{aligned} \tag{2}$$

Here, C_S is a parameter related to the defect type and $C_{A,D'}$ is a parameter related to the electron–phonon coupling of the D' peak phonon, with $r_{A,D'}$ and $r_{S,D'}$ being the length scales of the defect sites. Our data are best fitted with Equation (2) (solid line) when C_S = 0.33 and $C_{A,D'}$ = 0.63 (Figure 1e). Eckmann et al. [21] derived from their experiments C_S = 0.33 for sp^3 sites and C_S = 0.82 for vacancies. Excellent agreement with C_S = 0.33 suggests the oxidation of our graphene through UV treatment, forms sp^3 bonds. Dashed lines in Figure 1e show the evolution of $I(D')/I(G)$ for graphene with either vacancies or sp^3 sites, calculated with $C_{A,D'}$ = 0.5, $r_{S,D'} = 1.4$ nm and $r_{A,D'} = 2.6$ nm from ref. [21]. Note the slight mismatch with the curve for sp^3 sites is due to the different value of $C_{A,D'}$ determined for our samples.

Regarding n_{D} as an oxygenous defect density and a measure of the degree of oxidation of graphene, we investigate the charge transport characteristics depending on n_{D} in oxidized graphene devices. Figure 2 displays transfer characteristics of the oxidized graphene FETs at different n_{D}, measured with a fixed drain-source bias V_{DS} of 1 mV. A back-gate voltage V_{g} is applied over the 300 nm thick SiO$_2$, and the carrier density n is given by $n = \alpha(V_{\mathrm{g}} - V_{\mathrm{CNP}})$ with α = 7.2$\times$10^{10} cm^{-2} using the parallel capacitor model [28]. Here, V_{CNP} is the voltage at the charge-neutrality point. The conductivity σ monotonically decreases with increasing n_{D}. Compared to the pristine graphene, the conductivity of oxidized graphene is, for example, $\sim$1000 times smaller at $n_\mathrm{D} = 11 \times 10^{12}$ cm^{-2}. In addition, the conductivity becomes flattened near $n = 0$ with increasing n_D, discussed in terms of the so-called "transport gap" in the next paragraph. We also note for samples with $n_\mathrm{D} < 10^{12}$ cm^{-2} it follows $\sigma \propto \sqrt{n}$ (Figure 2a,b), while for $n_\mathrm{D} > 10^{12}$ cm^{-2} it shows $\sigma \propto n$ outside the flat area (Figure 2c–f). This behavior implies that charge transport transitioned from ballistic to diffusive transport at the oxidation density of $n_\mathrm{D} \simeq 10^{12}$ cm^{-2}. It is known that $\sigma \propto \sqrt{n}$ in ballistic graphene [28,29] and $\sigma \propto n$ in diffusive graphene [30,31]. The estimation of the mean free path $l = \frac{\sigma h}{2e^2} \cdot \frac{1}{\sqrt{\pi n}}$ [28,32] gives $l \simeq 4$ μm for our pristine graphene and $l \simeq 1.5$ μm for the GO FET with $n_\mathrm{D} = 0.39 \times 10^{12}$ cm^{-2}, which are twice as large and comparable to the channel length (2 μm), respectively. Additionally, $l \simeq 600, 130,$ and 5 nm, estimated for GO FETs with n_D = 1.2, 4.9, and 11 ($\times 10^{12}$ cm^{-2}), respectively, meet the condition for diffusive transport (l < channel length), consistent with our observation.

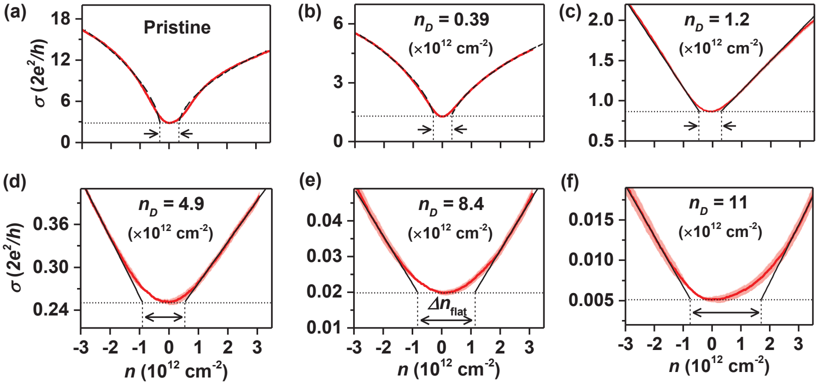

Figure 2. Transfer curves of oxidized graphene FETs with different n_D. The red shade shows the standard deviation of repeated measurements. (**a**) pristine graphene; (**b**) $n_\mathrm{D} = 0.39 \times 10^{12}$ cm^{-2}; (**c**) $n_\mathrm{D} = 1.2 \times 10^{12}$ cm^{-2}; (**d**) $n_\mathrm{D} = 4.9 \times 10^{12}$ cm^{-2}; (**e**) $n_\mathrm{D} = 8.4 \times 10^{12}$ cm^{-2}; (**f**) $n_\mathrm{D} = 11 \times 10^{12}$ cm^{-2}. Black dotted lines show the minimum conductivity σ_min. Dashed lines in (**a**,**b**) are fits to $\sigma \propto \sqrt{n}$, and solid lines in (**c**–**f**) are linear fits to the transfer curves. With increasing n_D, transfer curve becomes more flattened near $n = 0$, as indicated by the width Δn_flat.

The change in the transport mechanism observed in GO FETs happens because the scattering with oxygenous defects becomes more frequent as the extent of the oxidation increases. Figure 3a shows how the conductivity minimum σ_min and electron side mobility μ_e are reduced with increasing extent of oxidation. Field-effect mobility estimated from the electron side ($\mu_\mathrm{e} = \frac{1}{e} \cdot \frac{d\sigma}{dn}$ [24]), decreases from $\mu_\mathrm{e} \sim 2900$ (pristine) to ~ 500 ($n_\mathrm{D} = 0.29 \times 10^{12}$ cm^{-2}) and ~ 3.6 cm^2/V·s ($n_\mathrm{D} = 11 \times 10^{12}$ cm^{-2}) with increasing n_D. These results are also consistent with $\mu \simeq 30 - 2$ cm^2/V·s, reported for reduced graphene oxides at $n_\mathrm{D} \simeq 5 - 11$ $(\times 10^{12})$ cm^{-2}, synthesized by using a modified Hummer's method [26,33]. On the other hand, with the oxidation of graphene, the bandgap opens and disorder-induced localized states appear inside the bandgap, resulting in a transport gap Δ_m related to Δn_flat in Figure 2 [34,35]. To discuss the dependence of the transport gap on the oxygen content, we display in Figure 3b the flattened width Δn_flat, observed in Figure 2, as a function of n_D. Δn_flat gradually increases with n_D, while $\Delta n_\mathrm{flat} = 0.42 \times 10^{12}$ cm^{-2} for pristine graphene, associated with residual carrier densities n_0 originating from the electron(e)–hole(h) puddle [36]. The transport gap, estimated from $\Delta_\mathrm{m} = \hbar v_F \sqrt{\pi \Delta n_\mathrm{flat}}$ [37–39], overestimates the actual bandgap due to the existence of disorder potentials near the charge neutrality point ($e - h$ puddle), as illustrated in Figure 3c. Taking into account the potential fluctuation related to the $e - h$ puddle, $\delta E_{e-h} = \hbar v_F \sqrt{\pi \Delta n_0} \simeq 78$ meV from the pristine graphene device, we can infer the bandgap of UV-oxidized graphene at the different oxygenous defect densities. With $E_\mathrm{g} \simeq \Delta_\mathrm{m} - \delta E_{e-h}$, the inferred bandgap is presented as a function of

n_D in Figure 3d, together with the transport gap observed, Δ_m. E_g is seen to increase in proportion to $\sqrt{n_D}$, according to the relationship $E_g \simeq 30\sqrt{n_D}\ (10^{12}\ \mathrm{cm}^{-2})$ meV. Substitution of $n_D \simeq 1.9 \times 10^{15}$ cm^{-2} for fully oxidized graphene C_2O (epoxide) results in $E_g \simeq 1.3$ eV, comparable to $E_g \simeq 2.6$–6.5 eV calculated from theory for fully oxidized graphene [7–10]. Our results support the possibility of continuously adjusting the bandgap by tuning the oxygen content.

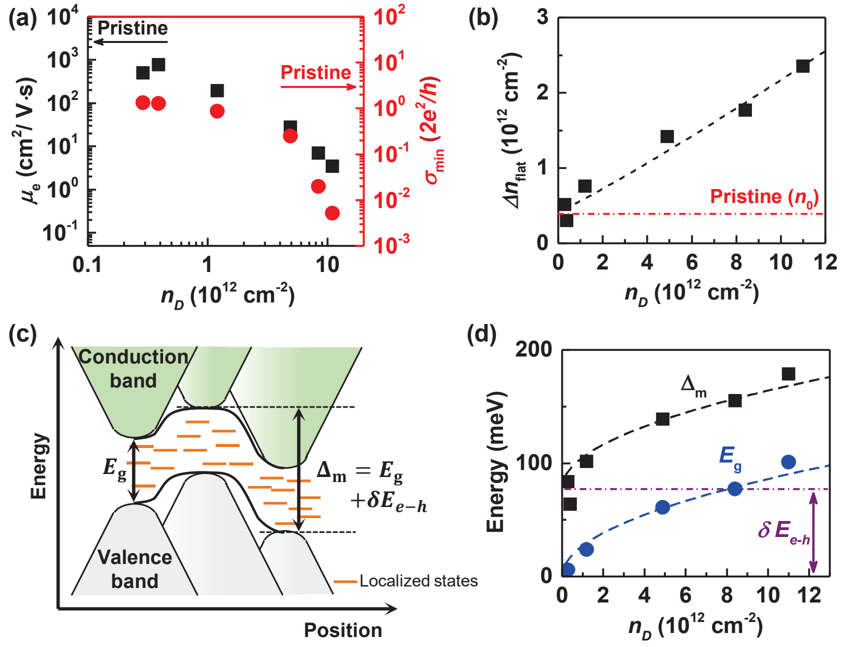

Figure 3. (**a**) Electron side mobility μ_e (black square) and conductivity minimum σ_{min} (red circle) of graphene oxide as a function of n_D. Arrows indicate the values of μ_e and σ_{min} for pristine graphene. (**b**) Δn_{flat} versus n_D. The black dashed line is a linear fit to the data. Note y-intercept n_0, associated with the electron–hole puddle in pristine graphene. (**c**) Schematic band diagram of graphene oxide and the illustration of an electron-hole puddle, affecting the transport gap observed. (**d**) Transport gap (black square) and inferred bandgap (blue circle) of graphene oxide as a function of n_D. Dashed lines are fitting curves with $\sqrt{n_D}$ and the dot-dash line indicates the size of potential fluctuation due to $e - h$ puddle.

Figure 4 shows the temperature T dependence of σ_{min} for graphene oxide with different values of n_D, studied for 77 < T < 400 K. Pristine graphene exhibits metallic behavior in which σ_{min} decreases with T. For GO samples with $n_D = 0.29$ and 0.39 ($\times 10^{12}$ cm^{-2}), conductivity minimum slightly increases with T, and the insulating behavior develops further with increasing n_D. The metal–insulator transition appears for $k_F l = 1$ and meets the Ioffe–Regel criterion, where k_F is the Fermi wavenumber and l is the mean free path with $k_F l = \sigma_{min} \frac{h}{2e^2}$ [40]. Considering $E_g \simeq 60$ meV for GO at $n_D \simeq 5 \times 10^{12}$ cm^{-2}, inferred from Figure 3d, the pronounced insulating behavior observed for $n_D \geq 4.9 \times 10^{12}$ cm^{-2} reflects that the size of opened bandgap becomes larger than the thermal energy (~26 meV at room temperature).

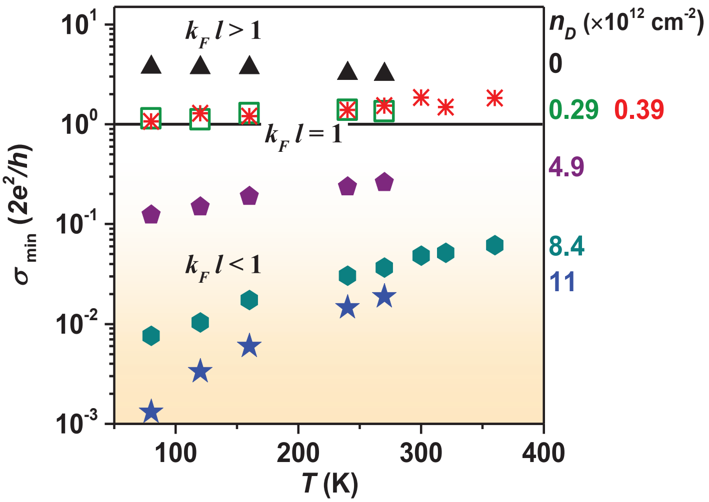

Figure 4. Temperature dependence of conductivity minimum for graphene oxides with different n_D. Solid line indicates $k_F l = 1$.

In Figure 5a, analysis shows the charge transport in GO samples for larger $n_D = 4.9,\ 8.4$, and 11×10^{12} cm^{-2} is localized and the T-dependence of σ_{min} is well explained by 2D Mott variable range hopping conduction (2D VRH) [14,41], following $\sigma = \sigma_0 \exp\left(\frac{T_0}{T}\right)^{\frac{1}{3}}$. Note that $\log \sigma_{min}$ is linear with $T^{-1/3}$ in Figure 5a. Characteristic temperature $T_0 = 900$, 17,000, and 41,000 K are obtained from the linear fits for $n_D = 4.9$, 8.4, and 11×10^{12} cm^{-2}, respectively. The localization length $\xi = \sqrt{\frac{13.8}{k_B \text{DOS(E)} T_0}}$, estimated for $0 < n < 3 \times 10^{12}$ cm^{-2}, decreases from 32–46 nm ($n_D = 4.9$) and 9–17 nm ($n_D = 8.4$) to 6–11 nm ($n_D = 11 \times 10^{12}$ cm^{-2}) with increasing n_D. Here, k_B is the Boltzmann constant, and DOS(E) is the density of states of graphene [32]. The reduction of ξ with n_D implies the size of the sp^2 domain decreases as the extent of oxidation increases [14,41]. On the other hand, charge transport in GO samples with smaller $n_D = 0.23$ and 0.39×10^{12} cm^{-2} is not explained by 2D VRH or a thermal activation model. To investigate the charge transport at metal–insulator boundaries in more detail, we prepared an additional GO FET with $n_D = 0.8 \times 10^{12}$ cm^{-2} in a Hall-bar geometry shown in Figure 1b and studied the four-probe conductivity between $2 < T < 300$ K. Figure 5b plots $\log \sigma$ of GO with $n_D = 0.8 \times 10^{12}$ cm^{-2} as a function of $T^{-1/3}$. Whereas for $15 < T < 145$ K, $\log \sigma$ is linearly proportional to $T^{-1/3}$ and agrees well with the 2D VRH model, σ is a little larger than the linear fitting curve for $145 < T < 300$ K as shown in the inset of Figure 5b. Additionally, σ becomes saturated for $2 < T < 15$ K, deviating from the linear dependence.

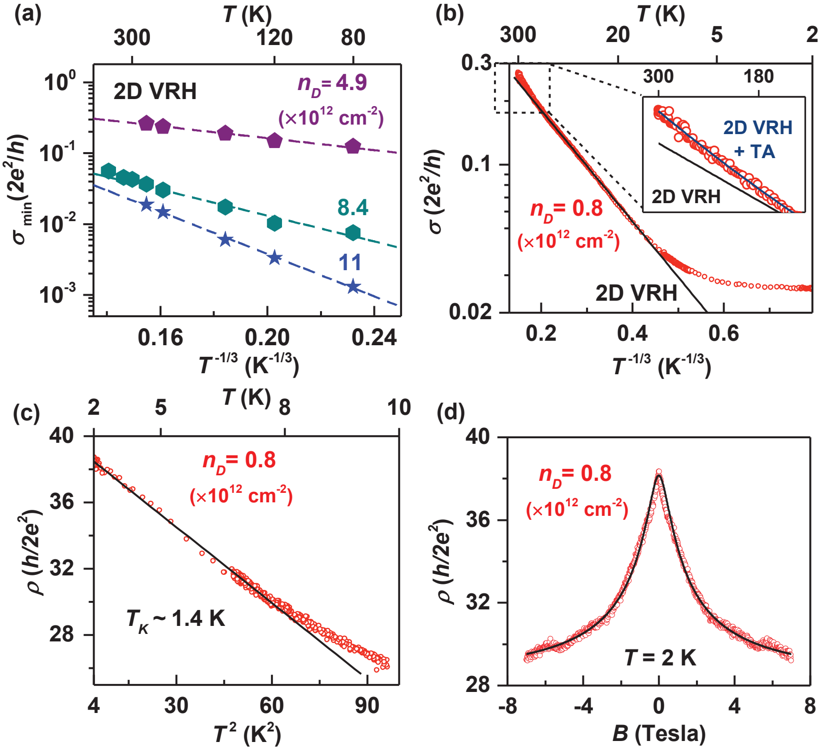

Figure 5. (**a**) $\log \sigma_{\min}$ vs. $T^{-1/3}$ for graphene oxides with n_D = 4.9, 8.4, and 11×10^{12} cm^{-2}. (**b**) $\log \sigma$ vs. $T^{-1/3}$ for graphene oxide with n_D = 0.8×10^{12} cm^{-2}, measured between $2 < T < 300$ K. For $15 < T < 145$ K, $\log \sigma$ is linearly proportional to $T^{-1/3}$ and agrees well with 2D VRH model. (Inset) $\log \sigma$ vs. $T^{-1/3}$, zoomed in for $300 < T < 140$ K. The data are best fitted considering both 2D VRH and thermal activation conduction. (**c**) ρ vs. T^2 in the low T regime for $2 < T < 10$ K for GO with $n_D = 0.8 \times 10^{12}$ cm^{-2}. (**d**) Magnetoresistance of the graphene oxide with $n_D = 0.8 \times 10^{12}$ cm^{-2}, measured at $T = 2$ K.

In the temperature range of $145 < T < 300$ K, the T-dependence of the conductivity can be explained by considering 2D VRH and thermal activation conduction (TA) together. The data are fitted well with $\sigma = \sigma_0 \exp\left(\frac{T_0}{T}\right)^{\frac{1}{3}} + \sigma_1 \exp\left(\frac{E_a}{k_B T}\right)$, as seen from the inset of Figure 5b, and an activation energy of $E_a \simeq 47$ meV is obtained. This value is larger than $E_g \simeq 27$ meV inferred from Figure 3d and can be associated with the influence of the $e - h$ puddle ($\delta E_{e-h} \simeq 78$ meV). The saturation of σ below $T < 15$ K is analyzed by considering the Kondo effect and presented in Figure 5c. The Kondo effect occurs when the charge carriers interact with the local magnetic moment of defects and the T-dependence of electrical resistivity ρ is given as follows in the low-temperature regime [42].

$$\rho = \rho_c + \rho_K \left[1 - \left(\frac{\pi}{2}\right)^4 \left(\frac{T}{T_K}\right)^2 \right] \tag{3}$$

Here, ρ_K is the Kondo resistivity at 0 K, and ρ_c is the temperature-independent resistivity parameter. T_K is the Kondo temperature, and the stronger the coupling between the magnetic moment and the charge carrier, the greater the value of T_K [42]. In Figure 5c, ρ is plotted versus T^2, and $\rho_K \simeq 20\frac{h}{e^2}$, $\rho_c \simeq 0.049\frac{h}{e^2}$ and $T_K = 1.4$ K are deduced from a linear fit. The obtained value of $T_K = 1.4$ K suggests rather weak coupling between the magnetic moment of defects and charge carriers in UV-oxidized graphene with $n_D = 0.8 \times 10^{12}$ cm^{-2}.

Figure 5d shows the magnetoresistance (MR) of the graphene oxide at $n_D = 0.8 \times 10^{12}$ cm^{-2}, measured at $T = 2$ K. A negative MR was observed in which ρ decreased as the magnetic field B increased up to 7 teslas. The negative MR is analyzed with the following equation [43] including both strong and weak localization effects.

$$\frac{\rho(B)-\rho(0)}{\rho(0)} = \frac{l_\phi}{l_c}\left[\frac{\Psi\left(\frac{2B_c+B_\phi+B_e}{B}+\frac{1}{2}\right)-\Psi\left(\frac{B_c+B_\phi}{B}+\frac{1}{2}\right)}{\ln\left(1+\frac{B_e}{B_c+B_\phi}\right)}-1\right] \tag{4}$$

Here, $\Psi(x)$ is the digamma function, and the characteristic length l_i is related to the characteristic magnetic field $\left(B_{(i=c,\phi,e)} = \frac{\hbar}{4el_i^2}\right)$. A localization length of $l_c \simeq 160$ nm, phase coherence length of $l_\phi \simeq 46$ nm, and elastic scattering length of $l_e \simeq 13$ nm are obtained from the fitting of Equation (4) to the MR data. l_ϕ is three times smaller than l_c, implying a dominant role of weak localization in the negative MR for the GO with $n_D = 0.8 \times 10^{12}$ cm^{-2}.

4. Conclusions

In summary, we have prepared graphene-oxide FETs with different degrees of oxidation by controlling the UV irradiation time on graphene, and investigated the charge transport and the evolution of the transport gap according to the extent of oxidation. With increasing oxygenous defect density n_D, the charge transport transitioned from ballistic to diffusive conduction around $n_D \simeq 10^{12}$ cm^{-2} and the transport gap grew in proportion to $\sqrt{n_D}$. Taking into account the potential fluctuation related to the $e-h$ puddle, we suggested the bandgap of GO to be $E_g \simeq 30\sqrt{n_D\ (10^{12}\ \text{cm}^{-2})}$ meV. The temperature dependence of the conductivity showed metal–insulator transitions at $n_D \simeq 0.3 \times 10^{12}$ cm^{-2} at the point where $k_F l \simeq 1$, which meets the Ioffe–Regel criterion. For GO with $n_D \geq 4.9 \times 10^{12}$ cm^{-2}, analysis indicated charge transport occurred via 2D variable range hopping conduction between localized sp^2 domains with the localization length decreasing with n_D. Finally, the Kondo effect and negative MR in the low-temperature regime were studied in GO with $n_D = 0.8 \times 10^{12}$ cm^{-2}.

Author Contributions: Conceptualization, H.Y.L. and S.H.J.; formal analysis, H.Y.L. and S.H.J.; investigation, H.Y.L.; resources, H.Y.L., M.M.H., E.H.K., J.S.C., and B.H.P.; writing—original draft preparation, H.Y.L. and S.H.J.; writing—review and editing, H.Y.L., S.H.J., and E.E.B.C.; visualization, H.Y.L. and S.H.J.; supervision, H.Y.L. and S.H.J.; project administration, H.Y.L. and S.H.J.; funding acquisition, S.H.J. All authors have read and agreed to the published version of the manuscript.

Funding: This research was supported by WTU Joint Research Grants of Konkuk University in 2017.

Institutional Review Board Statement: Not applicable.

Informed Consent Statement: Not applicable.

Data Availability Statement: Not applicable.

Conflicts of Interest: The authors declare no conflict of interest.

References

1. Novoselov, K.S.; Geim, A.K.; Morozov, S.V.; Jiang, D.E.; Zhang, Y.; Dubonos, S.V.; Grigorieva, I.V.; Firsov, A.A. Electric field effect in atomically thin carbon films. *Science* **2004**, *306*, 666–669. [CrossRef] [PubMed]
2. Morozov, S.; Novoselov, K.; Katsnelson, M.; Schedin, F.; Elias, D.C.; Jaszczak, J.A.; Geim, A. Giant intrinsic carrier mobilities in graphene and its bilayer. *Phys. Rev. Lett.* **2008**, *100*, 016602. [CrossRef] [PubMed]
3. Shen, H.; Shi, Y.; Wang, X. Synthesis, charge transport and device applications of graphene nanoribbons. *Synth. Met.* **2015**, *210*, 109–122. [CrossRef]
4. Craciun, M.; Khrapach, I.; Barnes, M.; Russo, S. Properties and applications of chemically functionalized graphene. *J. Phys. Condens. Matter* **2013**, *25*, 423201. [CrossRef]

5. Ahmad, Y.; Batisse, N.; Chen, X.; Dubois, M. Preparation and Applications of Fluorinated Graphenes. *C* **2021**, *7*, 20. [CrossRef]
6. Whitener, K.E., Jr. Hydrogenated graphene: A user's guide. *J. Vac. Sci. Technol. A Vacuum Surf. Film.* **2018**, *36*, 05G401. [CrossRef]
7. Jin, Y.; Zheng, Y.; Podkolzin, S.G.; Lee, W. Band gap of reduced graphene oxide tuned by controlling functional groups. *J. Mater. Chem. C* **2020**, *8*, 4885–4894. [CrossRef]
8. Yan, J.A.; Xian, L.; Chou, M. Structural and electronic properties of oxidized graphene. *Phys. Rev. Lett.* **2009**, *103*, 086802. [CrossRef]
9. Nourbakhsh, A.; Cantoro, M.; Vosch, T.; Pourtois, G.; Clemente, F.; van der Veen, M.H.; Hofkens, J.; Heyns, M.M.; De Gendt, S.; Sels, B.F. Bandgap opening in oxygen plasma-treated graphene. *Nanotechnology* **2010**, *21*, 435203. [CrossRef]
10. Lundie, M.; Šljivančanin, Ž.; Tomić, S. Analysis of energy gap opening in graphene oxide. *J. Phys. Conf. Ser.* **2014**, *526*, 012003.
11. Zhu, Y.; Murali, S.; Cai, W.; Li, X.; Suk, J.W.; Potts, J.R.; Ruoff, R.S. Graphene and graphene oxide: Synthesis, properties, and applications. *Adv. Mater.* **2010**, *22*, 3906–3924. [CrossRef]
12. Pei, S.; Cheng, H.M. The reduction of graphene oxide. *Carbon* **2012**, *50*, 3210–3228. [CrossRef]
13. Eda, G.; Mattevi, C.; Yamaguchi, H.; Kim, H.; Chhowalla, M. Insulator to semimetal transition in graphene oxide. *J. Phys. Chem. C* **2009**, *113*, 15768–15771. [CrossRef]
14. Negishi, R.; Akabori, M.; Ito, T.; Watanabe, Y.; Kobayashi, Y. Band-like transport in highly crystalline graphene films from defective graphene oxides. *Sci. Rep.* **2016**, *6*, 28936. [CrossRef]
15. Liu, L.; Xie, D.; Wu, M.; Yang, X.; Xu, Z.; Wang, W.; Bai, X.; Wang, E. Controlled oxidative functionalization of monolayer graphene by water-vapor plasma etching. *Carbon* **2012**, *50*, 3039–3044. [CrossRef]
16. Mulyana, Y.; Uenuma, M.; Ishikawa, Y.; Uraoka, Y. Reversible oxidation of graphene through ultraviolet/ozone treatment and its nonthermal reduction through ultraviolet irradiation. *J. Phys. Chem. C* **2014**, *118*, 27372–27381. [CrossRef]
17. Haidari, M.M.; Kim, H.; Kim, J.H.; Park, M.; Lee, H.; Choi, J.S. Doping effect in graphene-graphene oxide interlayer. *Sci. Rep.* **2020**, *10*, 8258. [CrossRef]
18. Osofsky, M.; Hernández, S.; Nath, A.; Wheeler, V.; Walton, S.; Krowne, C.; Gaskill, D. Functionalized graphene as a model system for the two-dimensional metal-insulator transition. *Sci. Rep.* **2016**, *6*, 19939. [CrossRef]
19. Ryu, G.H.; Lee, J.; Kang, D.; Jo, H.J.; Shin, H.S.; Lee, Z. Effects of dry oxidation treatments on monolayer graphene. *2D Mater.* **2017**, *4*, 024011. [CrossRef]
20. Yang, X.; Yan, M. Removing contaminants from transferred CVD graphene. *Nano Res.* **2020**, *13*, 599–610. [CrossRef]
21. Eckmann, A.; Felten, A.; Verzhbitskiy, I.; Davey, R.; Casiraghi, C. Raman study on defective graphene: Effect of the excitation energy, type, and amount of defects. *Phys. Rev. B* **2013**, *88*, 035426. [CrossRef]
22. Ferrari, A.C.; Basko, D.M. Raman spectroscopy as a versatile tool for studying the properties of graphene. *Nat. Nanotechnol.* **2013**, *8*, 235–246. [CrossRef]
23. Anno, Y.; Takeuchi, M.; Matsuoka, M.; Takei, K.; Akita, S.; Arie, T. Effect of defect-induced carrier scattering on the thermoelectric power of graphene. *Appl. Phys. Lett.* **2017**, *110*, 263501. [CrossRef]
24. Childres, I.; Jauregui, L.A.; Tian, J.; Chen, Y.P. Effect of oxygen plasma etching on graphene studied using Raman spectroscopy and electronic transport measurements. *New J. Phys.* **2011**, *13*, 025008. [CrossRef]
25. Pollard, A.J.; Brennan, B.; Stec, H.; Tyler, B.J.; Seah, M.P.; Gilmore, I.S.; Roy, D. Quantitative characterization of defect size in graphene using Raman spectroscopy. *Appl. Phys. Lett.* **2014**, *105*, 253107. [CrossRef]
26. Wang, Z.; Yao, Q.; Eigler, S. Room-temperature transport properties of graphene with defects derived from oxo-graphene. *Chem.-Eur. J.* **2020**, *26*, 6484–6489. [CrossRef] [PubMed]
27. Zhong, J.H.; Zhang, J.; Jin, X.; Liu, J.Y.; Li, Q.; Li, M.H.; Cai, W.; Wu, D.Y.; Zhan, D.; Ren, B. Quantitative correlation between defect density and heterogeneous electron transfer rate of single layer graphene. *J. Am. Chem. Soc.* **2014**, *136*, 16609–16617. [CrossRef]
28. Bolotin, K.I.; Sikes, K.J.; Hone, J.; Stormer, H.; Kim, P. Temperature-dependent transport in suspended graphene. *Phys. Rev. Lett.* **2008**, *101*, 096802. [CrossRef] [PubMed]
29. Di Bartolomeo, A. Graphene Schottky diodes: An experimental review of the rectifying graphene/semiconductor heterojunction. *Phys. Rep.* **2016**, *606*, 1–58. [CrossRef]
30. Chen, J.H.; Cullen, W.G.; Jang, C.; Fuhrer, M.; Williams, E.D. Defect scattering in graphene. *Phys. Rev. Lett.* **2009**, *102*, 236805. [CrossRef]
31. Chen, J.H.; Jang, C.; Adam, S.; Fuhrer, M.; Williams, E.D.; Ishigami, M. Charged-impurity scattering in graphene. *Nat. Phys.* **2008**, *4*, 377–381. [CrossRef]
32. Moser, J.; Tao, H.; Roche, S.; Alzina, F.; Torres, C.S.; Bachtold, A. Magnetotransport in disordered graphene exposed to ozone: From weak to strong localization. *Phys. Rev. B* **2010**, *81*, 205445. [CrossRef]
33. Eigler, S.; Enzelberger-Heim, M.; Grimm, S.; Hofmann, P.; Kroener, W.; Geworski, A.; Dotzer, C.; Röckert, M.; Xiao, J.; Papp, C.; et al. Wet chemical synthesis of graphene. *Adv. Mater.* **2013**, *25*, 3583–3587. [CrossRef]
34. Abanin, D.A.; Shytov, A.; Levitov, L. Peierls-type instability and tunable band gap in functionalized graphene. *Phys. Rev. Lett.* **2010**, *105*, 086802. [CrossRef]
35. Sehrawat, P.; Islam, S.; Mishra, P.; Ahmad, S. Reduced graphene oxide (rGO) based wideband optical sensor and the role of Temperature, Defect States and Quantum Efficiency. *Sci. Rep.* **2018**, *8*, 3537.
36. Adam, S.; Hwang, E.; Galitski, V.; Sarma, S.D. A self-consistent theory for graphene transport. *Proc. Natl. Acad. Sci. USA* **2007**, *104*, 18392–18397. [CrossRef]

37. Gallagher, P.; Todd, K.; Goldhaber-Gordon, D. Disorder-induced gap behavior in graphene nanoribbons. *Phys. Rev. B* **2010**, *81*, 115409. [CrossRef]
38. Stampfer, C.; Güttinger, J.; Hellmüller, S.; Molitor, F.; Ensslin, K.; Ihn, T. Energy gaps in etched graphene nanoribbons. *Phys. Rev. Lett.* **2009**, *102*, 056403. [CrossRef]
39. Adam, S.; Cho, S.; Fuhrer, M.; Sarma, S.D. Density inhomogeneity driven percolation metal-insulator transition and dimensional crossover in graphene nanoribbons. *Phys. Rev. Lett.* **2008**, *101*, 046404. [CrossRef]
40. Sarma, S.D.; Hwang, E. Two-dimensional metal-insulator transition as a strong localization induced crossover phenomenon. *Phys. Rev. B* **2014**, *89*, 235423. [CrossRef]
41. Vianelli, A.; Candini, A.; Treossi, E.; Palermo, V.; Affronte, M. Observation of different charge transport regimes and large magnetoresistance in graphene oxide layers. *Carbon* **2015**, *89*, 188–196. [CrossRef]
42. Chen, J.H.; Li, L.; Cullen, W.G.; Williams, E.D.; Fuhrer, M.S. Tunable Kondo effect in graphene with defects. *Nat. Phys.* **2011**, *7*, 535–538. [CrossRef]
43. Hilke, M.; Massicotte, M.; Whiteway, E.; Yu, V. Weak localization in graphene: Theory, simulations, and experiments. *Sci. World J.* **2014**, *2014*, 737296. [CrossRef] [PubMed]

nanomaterials

Article

Photocatalytic Activity of TiO_2/g-C_3N_4 Nanocomposites for Removal of Monochlorophenols from Water

Thawanrat Kobkeatthawin [1], Suwilai Chaveanghong [1], Jirawat Trakulmututa [1], Taweechai Amornsakchai [1,2], Puangrat Kajitvichyanukul [3,4,*] and Siwaporn Meejoo Smith [1,*]

[1] Center of Sustainable Energy and Green Materials and Department of Chemistry, Faculty of Science, Mahidol University, 999 Phuttamonthon Sai 4 Road, Salaya, Nakhon Pathom 73170, Thailand
[2] Center of Excellence for Innovation in Chemistry, 272 Rama VI Road, Rajthevi, Bangkok 10400, Thailand
[3] Department of Environmental Engineering, Faculty of Engineering, Chiang Mai University, 239 Huay Kaew Road, Muang District, Chiang Mai 50200, Thailand
[4] Sustainable Engineering Research Center for Pollution and Environmental Management, Faculty of Engineering, Chiang Mai University, 239 Huay Kaew Road, Muang District, Chiang Mai 50200, Thailand
[*] Correspondence: puangrat.k@cmu.ac.th (P.K.); siwaporn.smi@mahidol.edu (S.M.S.); Tel.: +66-61-6598715 (P.K.); +66-93-5939449 (S.M.S.)

Abstract: This research employed g-C_3N_4 nanosheets in the hydrothermal synthesis of TiO_2/g-C_3N_4 hybrid photocatalysts. The TiO_2/g-C_3N_4 heterojunctions, well-dispersed TiO_2 nanoparticles on the g-C_3N_4 nanosheets, are effective photocatalysts for the degradation of monochlorophenols (MCPs: 2-CP, 3-CP, and 4-CP) which are prominent water contaminants. The removal efficiency of 2-CP and 4-CP reached 87% and 64%, respectively, after treatment of 25 ppm CP solutions with the photocatalyst (40TiO_2/g-C_3N_4, 1 g/L) and irradiation with UV–Vis light. Treatment of CP solutions with g-C_3N_4 nanosheets or TiO_2 alone in conjunction with irradiation gave removal efficiencies lower than 50%, which suggests the two act synergically to enhance the photocatalytic activity of the 40TiO_2/g-C_3N_4 nanocomposite. Superoxide and hydroxyl radicals are key active species produced during CP photodegradation. In addition, the observed nitrogen and Ti^{3+} defects and oxygen vacancies in the TiO_2/g-C_3N_4 nanocomposites may improve the light-harvesting ability of the composite and assist preventing rapid electron-hole recombination on the surface, enhancing the photocatalytic performance. In addition, interfacial interactions between the MCPs (low polarity) and thermally exfoliated carbon nitride in the TiO_2/g-C_3N_4 nanocomposites may also enhance MCP degradation.

Keywords: monochlorophenol (MCPs); graphitic carbon nitride (g-C_3N_4); titanium dioxide (TiO_2); photocatalytic activity

Citation: Kobkeatthawin, T.; Chaveanghong, S.; Trakulmututa, J.; Amornsakchai, T.; Kajitvichyanukul, P.; Smith, S.M. Photocatalytic Activity of TiO_2/g-C_3N_4 Nanocomposites for Removal of Monochlorophenols from Water. *Nanomaterials* **2022**, *12*, 2852. https://doi.org/10.3390/nano12162852

Academic Editors: Jihoon Lee and Ming-Yu Li

Received: 13 July 2022
Accepted: 10 August 2022
Published: 18 August 2022

1. Introduction

In past decades, public awareness of the release of pollutants such as herbicides, pesticides, and hazardous chemicals into the environment through industrial and agricultural activities was a key driver for the implementation of new legislation and environmental standards. Monochlorophenols (MCPs), including 2-chlorophenol (2-CP), 3-chlorophenol (3-CP) and 4-chlorophenol (4-CP), are pollutants being prioritized by the United States Environmental Protection Agency [1] due to their high toxicity, carcinogenicity, environmental persistence, and low biodegradability [2,3]. MCPs have been widely used as components of pesticides, herbicides, and bactericides [4,5] used on farmlands, and are also employed in the production of dyes, pharmaceuticals, and in paper processing [6]. Since MCPs may cause DNA damage resulting in carcinogenic or mutagenic effects and histopathological changes in humans and animals [7], the effective removal of MCPs from natural waterways and soils is of vital importance. Wastewater remediation methods, including physicochemical [8,9] and biological technologies [10,11], have been applied for MCPs removal; however, these are largely ineffective for water containing high concentrations of MCPs [12,13]. On the other hand, advanced oxidation processes (AOPs) based on radical reactions, such as electrocatalysis [14], Fenton oxidation [15], and photocatalysis [16,17] showed superior performance in the removal of highly persistent MCPs. Examples include the degradation of MCPs with Co/g-C_3N_4 using peroxymonosulfate (PMS) as the oxidant [18], and the degradation of 2-CP using CNTs/AG/ITO electrodes [19]. Furthermore, photocatalytic wastewater treatments have shown great promise due to their high efficiency, the utility of cheap radiation sources for operation, the use of ambient temperatures, and that the organic pollutants can be completely mineralized, affording CO_2 and H_2O [20,21]. Regarding photoactive materials, graphitic carbon nitride (g-C_3N_4) has recently attracted attention due to its two-dimensional structure, low cost, stability, and visible-light driven bandgap [22,23]. However, fast recombination of photogenerated electron-hole pairs on pristine g-C_3N_4 and its typically low specific surface area may contribute to its low photocatalytic efficiency [24] in organic compound degradation. Notwithstanding this, g-C_3N_4 materials have recently found uses as support materials for immobilization of other semiconductors, resulting in synergic photocatalytic performance. These synergic effects arise through improved charge separation in the electron transfer processes and a further shifting of the light absorption boundary into the visible region. While several examples of composite materials exist for the photocatalytic degradation of MCPs (Table 1), the example based on bulk g-C_3N_4 and TiO_2 [25] affords only low 2-CP removal efficiency (38%) after 1 h treatment. In this study, exfoliated g-C_3N_4 nanosheets were applied to produce a series of TiO_2/g-C_3N_4 nanohybrid photocatalysts having different weight ratios of TiO_2, and their photocatalytic performance for the removal of MCPs from wastewater was investigated. The resulting nanocomposites were characterized in terms of structure, chemical composition, morphology, and optical properties. Identifications of active radical species generated in photocatalytic treated aqueous MCPs were carried out. An additional discussion on the utility of TiO_2/g-C_3N_4 based photocatalysts for remediation of pesticide contaminated water is given based on the results reported in this research and those of recent works [26–29].

Table 1. Comparison of photocatalytic activities of semiconductors based on g-C_3N_4 utilized in the degradation of aqueous MCPs.

Pollutant	Catalyst	Source	Dosage	MCP Treatment Time (h)	% Removal Efficiency	Ref
2-CP	Bulk g-C_3N_4 TiO_2 TiO_2/bulk g-C_3N_4	Xe (150 W)	4 g/L	1	9% 3% 38%	[25]
	g-C_3N_4 OH-C_3N_4	W (300 W)	0.5 g/L, 10 ppm	5	95% 85%	[29]
	10% g-C_3N_4/FST 15% g-C_3N_4/FST g-C_3N_4 5% g-C_3N_4/FST FST (FST: fibrous silica titania)	W (400 W)	0.37 g/L, 10 ppm	4	93% 70% 67% 49% 40%	[30]
3-CP	TiO_2/N-TiO_2 TiO_2	Fluorescent lamp (154 W)	0.2 g/L, 10 ppm	5	77% 36%	[31]
	TiO_2/N-TiO_2 TiO_2	Incandescent lamp (100 W)		24	30% 12%	
4-CP	g-C_3N_4/$Bi_5Nb_3O_{15}$ g-C_3N_4	-	1 g/L, 10 ppm	1	100% 72%	[32]
	g-C_3N_4 g-C_3N_4/$ZnWO_4$(1:1) g-C_3N_4/$ZnWO_4$(2:1) g-C_3N_4/$ZnWO_4$(3:1)	Xe (500 W)	0.2 g/L, 10 ppm	1.67	45% 62% 78% 88%	[33]
	C/ZnO/g-C_3N_4	Solar (300 W) UV (400 W)	0.2 g//L, 10 ppm	5	92% 72%	[34]

2. Experimental

2.1. Chemicals

All chemicals used in the experiments were of AR grade and used without further purification. Urea (CH_4N_2O), titanium (IV) oxysulfate ($TiOSO_4$), 3-chlorophenol (C_6H_5ClO), and 4-chlorophenol (C_6H_5ClO) were obtained from Kemaus, Australia. 2-Chlorophenol, ammonium oxalate ($(NH_4)_2C_2O_4$), nitric acid (HNO_3), and methanol (CH_3OH) were purchased from Merck, Germany. 5,5-Dimethyl-l-pyrroline N-oxide ($C_6H_{11}NO$) was purchased from Cayman, Japan. Benzoquinone and isopropyl alcohol were obtained from Sigma-Aldrich, St. Louis, MO, USA. Deionized water was used throughout this study.

2.2. Characterization

Powder X-ray diffraction was performed to study the crystalline structure of samples using CuK_α radiation (λ = 1.54 Å) over a 2θ range = 10–90° (Bruker AXS, D8 advance, Karlsruhe, Germany). X-ray photon spectroscopy (XPS) was employed to determine the surface electronic state of samples (XPS; AXIS Ultra DLD, Kyoto, Japan). Raman spectra were recorded using an excitation wavelength of 875 nm (Horiba, XploRA Plus, Lille, France). Sample morphologies were visualized using transmission electron microscopy (JEM-2100 Plus, JEOL, Chiyoda, Japan) and scanning electron microscopy (SEM; Hitachi: SU8010, Matsuda, Japan). Surface area measurements were carried out by N_2 sorption a 77 K, using a Micromeritics ASAP2060 instrument. The specific surface area was obtained by the Brunauer–Emmett–Teller (BET) method. Band gap energies of prepared samples were obtained by UV-Vis NIR spectrophotometer (Shimadzu, UV3600 plus, Tokyo, Japan). Electron-hole recombination in samples was investigated through photoluminescence (PL) spectra, obtained at an excitation wavelength of 320 nm (Horiba, FluoroMax, Longjumeau cedex, France). Electron paramagnetic resonance (EPR) signals of free radicals were recorded at ambient temperature (Bruker; Elexsys 500, Rheinstetten, Germany). The degradation of MCPs was monitored by measuring the absorbance with a UV-Vis spectrophotometer (Perkin Elmer, Lambda 800, Waltham, MA, USA). GC/MS was used for the separation and identification of photocatalytic degradation products (Agilent GC7890B–MSD5977B, Santa Clara, CA, USA) and utilized a HP-5MS UI column measuring 30 m × 0.25 mm × 0.25 μm. Operating conditions were as follows: sample injection volume 1 μL, initial oven temperature 60 °C for 1 min, followed by a temperature gradient of 20 °C/min to 300 °C.

2.3. Synthesis of $g\text{-}C_3N_4$

Urea powder (125 g) was added to an alumina crucible, and the powder was heated in a muffle furnace at a heating rate of 10 °C/min to 600 °C, and the sample then held at this temperature for 4 h. After cooling to room temperature, bulk g-C_3N_4 (pale yellow solid) was obtained (Bulk-CN). The bulk material was converted to g-C_3N_4 nanosheets by thermal exfoliation in the presence of nitrate. In a typical process, 2.5 g of bulk-CN was stirred in 65% HNO_3 solution (100 mL) for 12 h. After washing with deionized water, the obtained sample was annealed at 500 °C for 4 h, and then cooled to room temperature affording g-C_3N_4 nanosheets (CNNS) or the exfoliated g-C_3N_4 material.

2.4. Fabrication of TiO_2/g-C_3N_4 Nanocomposites

Composites containing different quantities of TiO_2 relative to CNNS (20–50% TiO_2 by weight) were synthesized by a hydrothermal process, with the obtained composites labelled as 20TiO_2/CNNS, 30TiO_2/CNNS, 40TiO_2/CNNS and 50TiO_2/CNNS. In this process, an appropriate quantity of $TiOSO_4$ was dispersed in deionized water (100 mL) by stirring for 15 min (magnetic stirrer), and then using an ultrasonic bath (20 min). The required quantity of g-C_3N_4 was then added, and ultrasonication continued for a further 30 min. After this, the suspension was transferred to a Teflon-lined autoclave which was closed and then heated at 180 °C for 4 h. After cooling to room temperature, the autoclave was opened and the precipitate was collected by centrifugation, then washed two times with distilled water. The obtained powder was dried at 65 °C for 24 h before analysis. As a control, TiO_2 in the absence of g-C_3N_4 was also subjected to the same process and collected as above.

2.5. Photocatalytic Activity Evaluation

The photocatalytic activity of samples was evaluated by their ability to degrade MCPs (2-CP, 3-CP and 4-CP) in aqueous solution, under UV–Visible light irradiation in a home-built metal photoreactor box (dimensions: $30 \times 80 \times 32$ cm^3) equipped with a W lamp (300 watts, Osram Ultra-Vitalux, Nové Zámky-Dolná kapsa, Slovakia). The emission spectrum obtain from the utilized light source was previously reported [35]. The light bulb was set at a distance of 25 cm from each sample solution, and the temperature of the sample was maintained at 35 °C using a water bath. The light intensity of 1.37 ± 0.05 klx was measured by a luxmeter (Extech 403125, Kaohsiung, Taiwan) at the sample solution. Following a previously reported protocol [26], 10 mg of catalyst was suspended in 10 mL of a 25 ppm aqueous MCP solution. The suspension was stirred for 1 h in the dark to achieve adsorption equilibrium, before light irradiation for certain period of time (30, 60, 90, and 120 min). The solution was then collected using a syringe equipped with a micropore filter (0.45 μm) to separate the photocatalyst. The concentration of MCP in the collected solution was obtained using UV–Vis spectrophotometry, from absorbance measurements at 274 (for 2-CP), 274 (for 3-CP) and 280 nm (for 4-CP). The MCPs removal efficiency was calculated via Equation (1) [26].

$$\% \text{ Removal efficiency} = 100 \times ((C_0 - C_t)/C_0) \quad (1)$$

where: C_0 is the initial concentration of MCPs, C_t is the concentration of MCPs after t minutes.

2.6. Identification of Active Species during Photocatalytic Degradation

Electron paramagnetic resonance (EPR) was used to detect active species such as hydroxyl (OH) and superoxide ($O_2{}^-$) radicals, with the assistance of 5,5-dimethyl-l-pyrroline N-oxide (DMPO). Hydroxyl radicals and superoxide radicals were trapped in aqueous solution and methanol, respectively. Samples for EPR measurements were prepared by adding 2 mg of photocatalyst to 2 mL of 25 ppm MCPs solution to form a suspension. This was stirred in the dark for 1 h to achieve adsorption equilibrium, and then 1 mL of DMPO (50 mM) in aqueous solution was added. Stirring was continued and the mixture irradiated with a W lamp (300 watt) for 60 min. The solution (200 μL) was then filtered through a syringe filter (0.45 μM) and EPR spectra were measured for this solution. For a comparison, EPR spectra were measured for the solution from treatment treated with photocatalyst in the dark and in the absence of irradiation (denoted as 0 min). Photolysis was also studied by irradiating the solution, in the absence of photocatalyst.

3. Result and Discussion

3.1. Structural and Chemical Properties

Powder X-ray diffraction (PXRD) patterns of the bulk-CN, CNNS, TiO_2 and $40TiO_2/CNNS$ nanocomposites are shown in Figure 1a. As all nanocomposites ($20TiO_2/CNNS$ -$50TiO_2/CNNS$) exhibit identical diffraction patterns, only that of $40TiO_2/CNNS$ is shown. Bulk-CN and CNNS display three characteristic peaks at around 13.0°, 21.6°, and 27.5°, which are assigned to the (100), (101), and (002) hexagonal crystal planes (JCPDS 87-1526), respectively [36]. The sharp peak at 27.5° is attributed to interlayer stacking of aromatic rings, with the lower intensity peak at 13.0° being due to the presence of tri-s-triazine units [37,38]. The (002) peak intensity decreases significantly on conversion of bulk-CN to CNNS, and exhibits a slight shift in 2θ, reflecting the exfoliation of bulk-CN to nanosheets with shorter stacking distances between g-C_3N_4 layers [39,40]. Titanium dioxide exhibits diffraction peaks corresponding to the (101), (112), (200), (105), (211), (204), (116), (220), and (215) planes, consistent with the material existing as tetragonal anatase (JCPDS 021-1272) [41,42]. As expected, the patterns of g-C_3N_4/TiO_2 nanocomposites exhibit peaks arising from both pure g-C_3N_4 and TiO_2, and the absence of any peak shifting in the TiO_2 peaks relative to anatase (Figure S1) indicates that coupling with g-C_3N_4 does not influence the TiO_2 lattice structure, which might be beneficial regarding the photocatalytic activity of the hybrid photocatalyst.

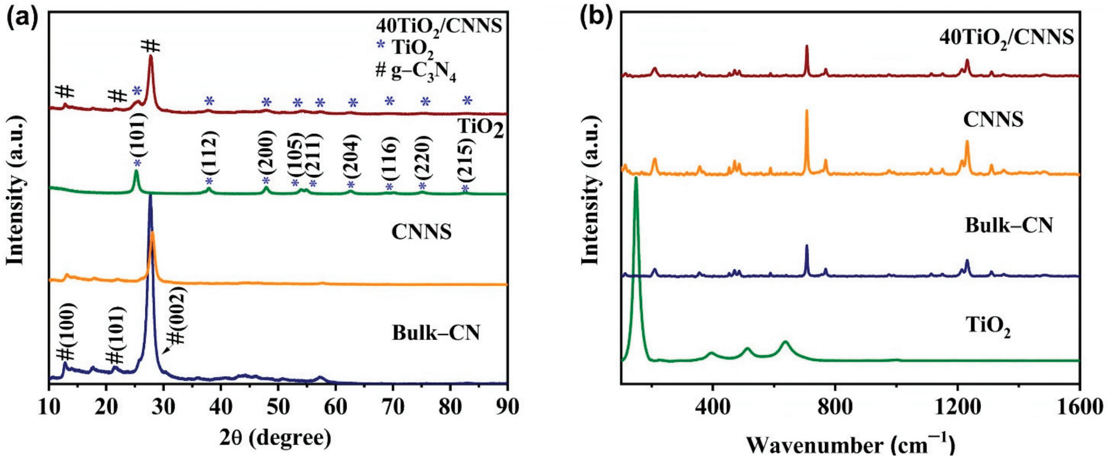

Figure 1. (**a**) PXRD patterns of bulk-CN, CNNS, TiO_2, and 40TiO_2/CNNS, (**b**) Raman spectra of bulk −CN, CNNS, TiO_2, and 40TiO_2/CNNS. An enlarged PXRD profile of 40TiO_2/CNNS is provided in Figure S1.

Raman spectra of the 40TiO_2/CNNS nanocomposite and its component materials are shown in Figure 1b. The peak at 707 cm^{-1} in CNNS and 40TiO_2/CNNS is assigned to the signature peak of g-C_3N_4, which arises due to the breathing modes of tri-s-triazine structural elements. Additionally, peaks at 1230 cm^{-1} in all CN samples are consistent with the stretching vibration modes in C-N heterocycles [43,44]. Valence state and bonding information of elements in the nanocomposites and precursor materials was obtained using X-ray photoelectron spectroscopy (XPS), with survey XPS spectra shown in Figure 2a. The nanocomposites are composed of C, N, Ti, and O, confirming the existence of TiO_2 and g-C_3N_4 in these materials. High resolution C1s spectra of g-C_3N_4, and of the nanocomposite materials, are presented in Figure 2b. All samples exhibit two C1s peaks, ascribed to the sp^2 C–C at 285.0 eV and sp^2 hybridized carbon atoms (N–C=N) in aromatic rings at 288.3 eV, respectively [45,46]. In the case of N1s spectra (Figure 2c), two different peaks located around 398.7 and 401.3 eV are visible, with the main peak at 398.7 eV arising from nitrogen atoms bonded to sp^2-hybridized carbon (C=N–C). The low intensity 401.3 eV peak is a result of N bonded to three carbon atoms N–$(C)_3$ in the aromatic moieties [47].

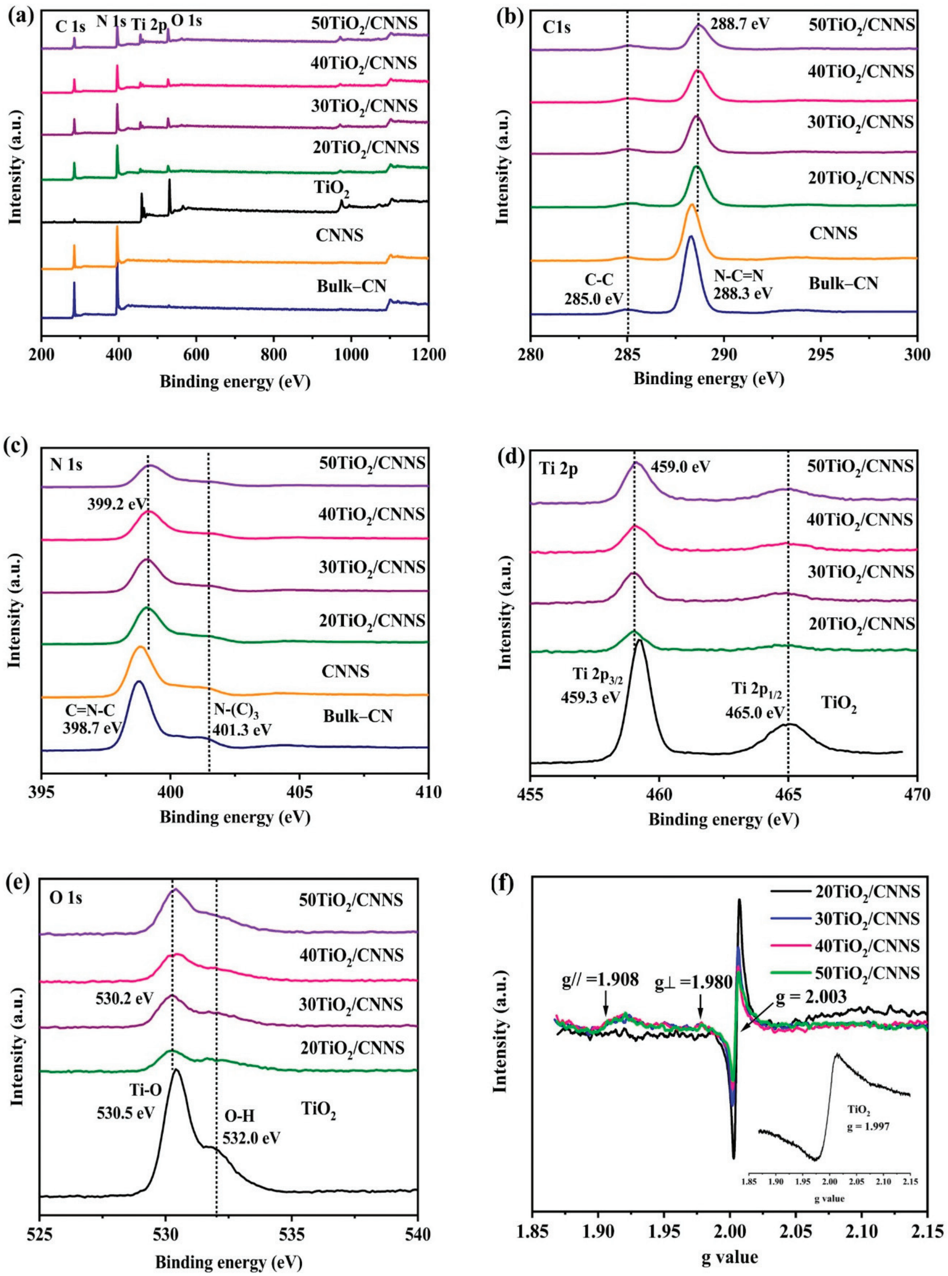

Figure 2. (**a**) Survey XPS spectra of precursor and nanocomposite samples, (**b**) C1s XPS spectra, (**c**) N1s XPS spectra, (**d**) Ti Figure 3b, f2p XPS spectra, (**e**) O1s XPS spectra, and (**f**) Solid phase EPR spectra of Ti^{3+}-TiO_2/CNNS nanocomposite and anatase TiO_2.

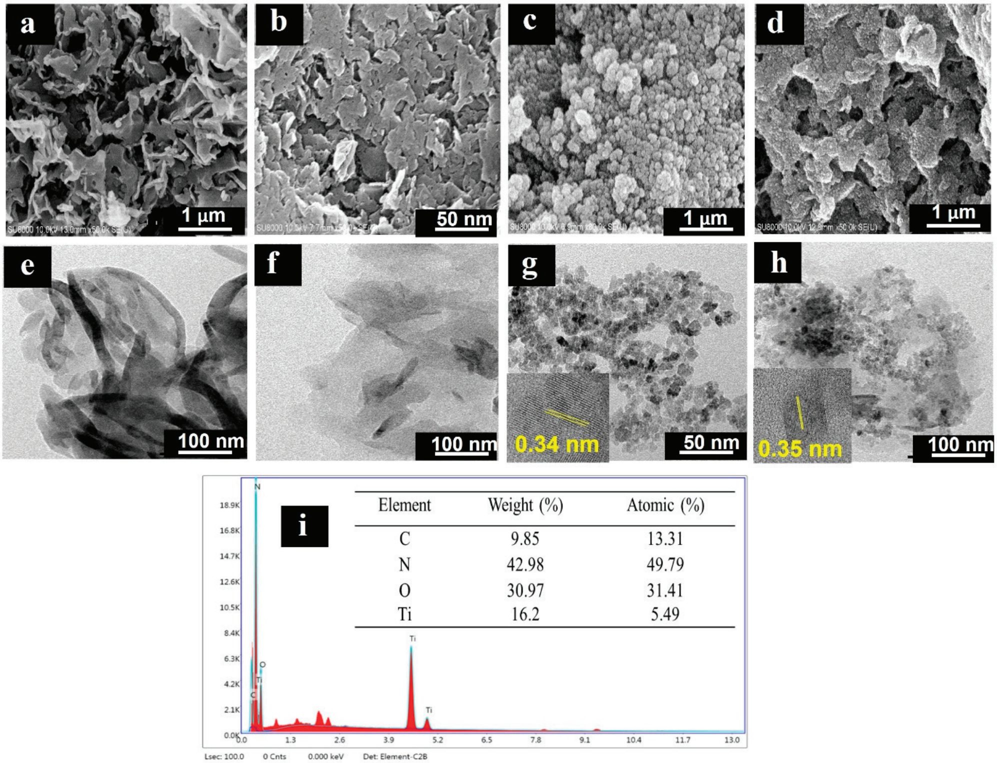

Element	Weight (%)	Atomic (%)
C	9.85	13.31
N	42.98	49.79
O	30.97	31.41
Ti	16.2	5.49

Figure 3. (**a**) SEM and TEM images of (**a**,**e**) bulk-CN, (**b**,**f**) CNNS, (**c**,**g**) TiO_2, (**d**,**h**) 40TiO_2/CNNS, and (**i**) EDX-SEM data for 40TiO_2/CNNS.

To examine the formation of defects on exfoliation EPR spectra of bulk-CN and CNNS were recorded, and these are shown in Figure S2. The EPR signal at g = 2.003 in CNNS is of significantly higher intensity than that in bulk-CN, due to the formation of N-defects on exfoliation which increases the number of unpaired electrons on C atoms [48]. In addition, the C1s and N1s peak positions in the nanocomposites are shifted relative to those of g-C_3N_4, suggestive of interactions at the interface between g-C_3N_4 and TiO_2 [49]. Peaks located at 459.2 and 464.9 eV in the high-resolution Ti 2p spectrum (Figure 2d) correspond to the Ti $2p_{3/2}$ and Ti $2p_{1/2}$ of TiO_2, respectively, confirming the presence of Ti^{4+} species in TiO_2 and its composites [50]. The O1s spectrum is given in Figure 2e, and its fitting with convolution (Figure S3) indicated three peaks with binding energies of 531.9, 530.4 and 533.23 eV which can be ascribed to oxygen bound to Ti^{4+}, oxygen vacancies (V_o) and oxygen from H_2O, respectively [51]. The formation of Ti^{3+} in nanocomposites was confirmed by solid state EPR measurements (Figure 2f). As shown in the inset, a strong EPR signal from TiO_2 was observed at g = 1.997, which is characteristic of Ti^{3+} defects ($3d^1$, S = 1/2) [51,52]. The major signal (g = 2.003) occurs from the presence of unpaired electrons on aromatic carbon centers in g-C_3N_4 [53]. The EPR signals at $g_{//}$= 1.908 and $g_{\perp}$ = 1.980 were assigned to Ti^{3+} defects in TiO_2., with the reduction in Ti^{4+} to Ti^{3+} occurring by loss of oxygen from the surface during high temperature hydrothermal treatment [54,55]. No Ti^{3+} signals were observed for the 20TiO_2/CNNS nanocomposite which reflects its low photocatalytic MCPs degradation efficiency.

The morphologies of bulk-CN, CNNS, TiO_2 and $40TiO_2/CNNS$ nanocomposites, as imaged using SEM and TEM, are shown in Figure 3. Bulk-CN (Figure 3a,e) presents a lamellar structure in line with previous reports [56]. Annealing of bulk-CN at 500 °C results in the formation of CNNS, which takes the form of nanosheets of smaller particles (Figure 3b,f). Results from N_2 adsorption–desorption isotherms indicate that the specific surface area of CNNS (91.6 $m^2\ g^{-1}$) is higher than that of Bulk-CN (68.2 $m^2\ g^{-1}$). Graphitic carbon nitride layers exfoliate during high temperature thermal oxidation as these are held together by weak intermolecular forces (Van der Waals forces and hydrogen bonding). In addition, the presence of HNO_3 assists layer separation due to the intercalation of nitrate ions, which causes interplanar swelling. Exfoliation results in reduced layer thickness and smaller particle size, which increases the specific surface area [57–59]. Pure TiO_2 consists of agglomerated spherical-like particles around 10 nm in diameter (Figure 3c,g). The interplanar distance of 0.34–0.35 nm (inset) in these particles is in agreement with the d-spacing of the (101) planes in anatase TiO_2 [60]. SEM and TEM images of $40TiO_2/CNNS$ are suggestive of TiO_2 particles being dispersed on the surface of g-C_3N_4 (Figure 3d,h) which should enhance the transfer of photogenerated electrons and result in greater photocatalytic activity. In addition, the EDX spectrum in Figure 3i highlights the elemental composition of TiO_2/g-C_3N_4 nanocomposites, which confirms the formation of heterojunctions between g-C_3N_4 and TiO_2.

3.2. Optical Properties

The UV–Vis DRS spectra of g-C_3N_4, TiO_2 and nanocomposites are shown in Figure 4a. Pristine g-C_3N_4 has a strong absorption band in the UV–Vis region with an absorption edge close to 430 nm [61]. Anatase TiO_2 exhibits similar absorption behavior, with an adsorption edge at ca. 410 nm [62]. After coupling with g-C_3N_4, the absorption edge of composites exhibits a red shift compared with that of TiO_2, as the presence of Ti^{3+} and oxygen vacancies allows for a relaxation of selection rules governing transitions in TiO_2, resulting in improved absorption profiles [63]. Band gap energies were calculated using the Tauc plot (Figure 4b) and through Equation (2).

$$Ah\nu = A(h\nu - E_g)^{1/2} \quad (2)$$

In this equation, α, h, ν, A, and E_g are the optical absorption coefficient, Planck constant, photon frequency constant, and band gap energy, respectively [64].

From Figure 4b, the band gap energy of g-C_3N_4 nanosheet is estimated to be 2.93 eV (slightly narrower than that of bulk g-C_3N_4, 2.99 eV), which is consistent with past work [65]. The band gap energy of TiO_2 obtained (3.16 eV) differs slightly from that previously reported for anatase TiO_2 materials (3.2 eV), possibly due to the presence of Ti^{3+} defects [66]. As shown in Figure 4a, $40TiO_2/CNNS$ absorbs in the visible region and exhibits the lowest bandgap energy (2.89 eV, Figure 4b), which are both advantageous features for photocatalysts. Electron-hole recombination was studied using photoluminescence analysis, with the results shown in Figure 4c. Under excitation at 320 nm, the emission peak of g-C_3N_4 occurs at 457 nm, which is consistent with UV–Vis DRS results. Bulk-CN and CNNS show high PL intensities, suggesting fast recombination of electron-hole pairs. On the other hand, TiO_2 shows a broad emission peak at 410 nm and lower intensity than that of g-C_3N_4 or CNNS. After hybridization of g-C_3N_4 and TiO_2, all composites show much weaker emission peaks, implying that recombination of charge carriers may be effectively inhibited by Ti^{3+}-V_o.

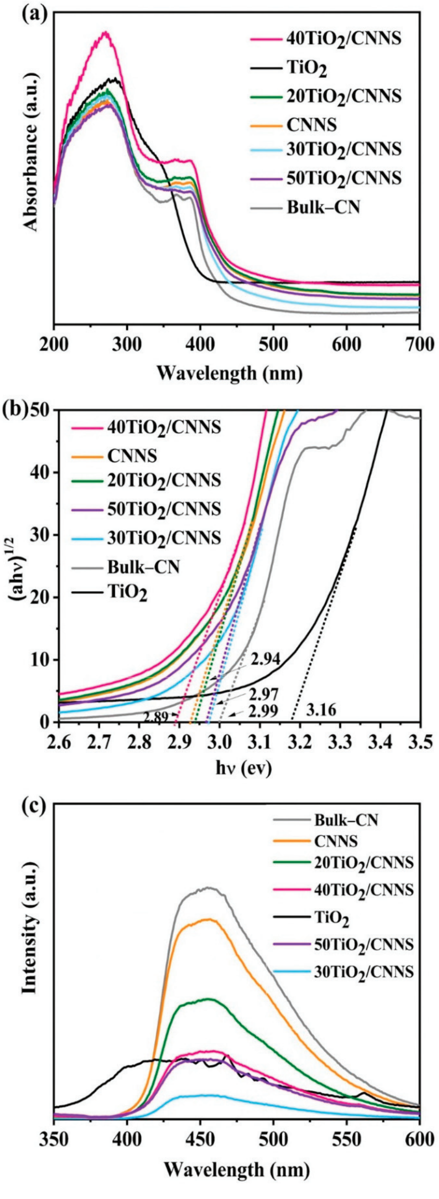

Figure 4. (**a**) Ultraviolet–visible (UV–Vis) diffuse reflectance spectra, (**b**) corresponding Tauc plot displaying band gaps of g-C_3N_4, TiO_2 and composites, and (**c**) photoluminescence spectra of bulk-CN, CNNS, and nanocomposite materials. Extrapolated dotted lines (in Figure 4b) are added to indicate energy bandgap of each sample.

3.3. Photocatalytic Degradation of MCPs

The photocatalytic performance of nanocomposites for degradation of MCPs under UV–Vis irradiation, as reported in terms of % removal efficiencies, are shown in Figure 5. Notably, as a control, photolysis was performed with 2-CP, 3-CP and 4-CP under UV–Vis irradiation without catalyst addition for 2 h (Figure S4). In these cases, absorbance values of the phototreated MCPs solutions showed no significant differences from those from untreated MCPs solutions, suggesting negligible removal of MCPs in the absence of photocatalyst. These findings agree with those from previous work [67], and reflect the structural stability of MCPs.

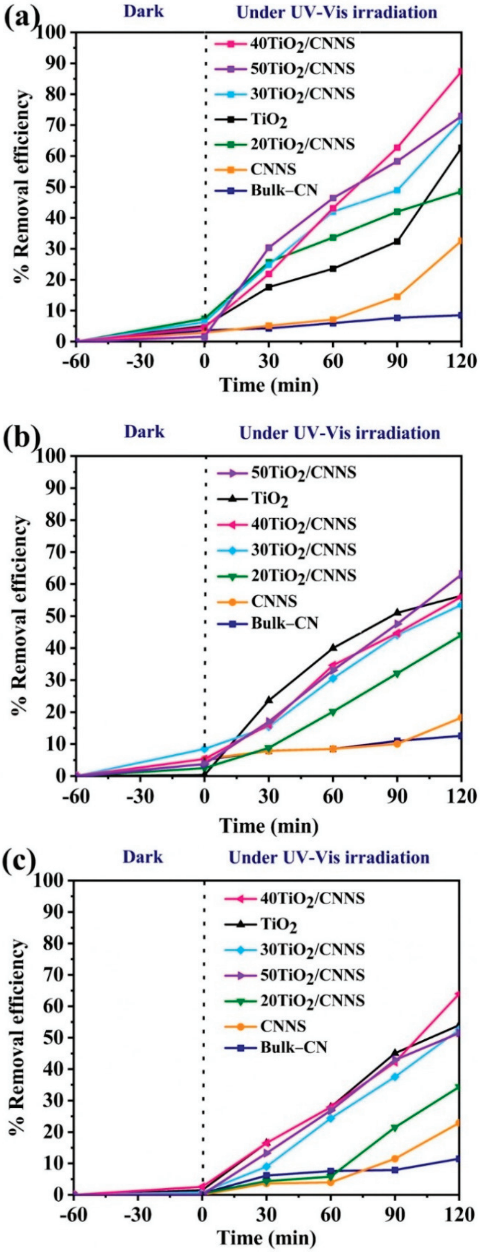

Figure 5. Photocatalytic degradation profiles for (**a**) 2-chlorophenol, (**b**) 3-chlorophenol, and (**c**) 4-chlorophenol when treated with g-C_3N_4, TiO_2, and composites under UV–Vis irradiation (25 ppm pollutant, 1 g/L catalyst loading). Plots with error bars from triplicate measurements are given in Figure S5.

Results in Figure 5 show that Bulk-CN, CNNS, and 20TiO_2/CNNS materials are only marginally effective for MCPs degradation, with removal efficiencies being less than 50% after 2 h. This is presumably due to electron-hole recombination, as implied by PL results (Figure 4b).

Notably, CNNS exhibits higher photocatalytic activity than bulk g-C_3N_4. Exfoliation results in nanosheets with a greater surface area and the addition of N-defects, both of which enhance photocatalytic activity [68,69]. Defect modification is one promising way to enhance the photocatalytic activity of g-C_3N_4, as it results in band gap narrowing and extension of the light absorption range [69]. The recombination of the photoexcited electrons and holes can also be inhibited through the midgap state generated by the introduction of the N defects, leading to enhancements in photocatalytic activity. All other composites than 20TiO_2/CNNS and TiO_2 alone show photocatalytic efficiencies greater than 50% after 2 h. The 40TiO_2/CNNS nanocomposite is the most active in degradation of 2-CP and 4-CP, giving removal efficiencies of 87% and 64% after 2 h, respectively. These results illustrate the synergistic effect of TiO_2 and g-C_3N_4, and the importance of Ti^{3+}-Vo defects, to the photocatalytic performance. As indicated earlier, 40TiO_2/CNNS has the lowest band gap energy (2.89 eV), allowing the harvesting of light in the visible region, and the introduction of Ti^{3+} provides hole traps to promote charge separation and suppress recombination. From UV–Vis DRS results (Figure 5), 30TiO_2/CNNS and 50TiO_2/CNNS show wider band gaps compared with 20Ti/CNNS and CNNS.

While the 50TiO_2/CNNS displays strong light absorption in the visible region and contain Ti^{3+} defects, no such defects were observed in 20TiO_2/CNNS which underlines the importance of both band gap and defects on photocatalytic activity. Results from UV–Vis DRS spectra indicate that 50TiO_2/CNNS exhibits a wider band gap than 40TiO_2/CNNS. Possible reasons for 40TiO_2/CNNS exhibiting the highest performance could be its low band gap energy (2.89 eV) allowing harvesting of light in the visible region, and the presence of Ti^{3+} species, providing hole traps to promote charge separation and suppress charge recombination. The nitrogen defects in CNNS and the interactions between the CNNS and TiO_2 particles (discussed herein) may account for the superior performance of these composites relative to bulk g-C_3N_4/TiO_2 in the photocatalytic degradation of 2-CP [25]. Notably, the photocatalytic activities for 2-CP degradation are higher than that obtained for 3-CP and 4-CP [70], potentially due to stronger adsorption of 2-CP over the other isomers. The photocatalytic removal efficiency of 2-, 3-, and 4-CP over the 40TiO_2/CNNS nanocomposite was ca. 87%, 64%, and 22%, respectively (Figure 5), which agrees with previous findings [70] such that the removal efficiencies of 2-CP > 3-CP > 4-CP. Additionally, the position of the Cl substituent on the aromatic ring can affect the photocatalytic degradation profile of MCPs, as ortho and para C-Cl bonds can be cleaved more easily than those of meta-Cl substituents as a result of inductive and mesomeric effects [16].

To analyze the degradation pathway of 2-chlorophenol, GC-MS was employed to visualize and identify potential breakdown products. As shown in Figure 6a, the GC trace of untreated 2-CP shows a peak corresponding to the phenol at a retention time of 4.50 min. The intensity of this peak decreases on treatment with CNNS and is completely absent after treatment with 40TiO_2/CNNS, which is in agreement with UV–Vis spectra obtained for solutions treated with this photocatalyst (Figure 6b). Intermediate products were observed at retention times of 3.68 (m/z = 63) and 3.88 (m/z = 133) min after treatment with CNNS or 40TiO_2/CNNS which, based on fragmentation data, could be acetic acid (CH_3COOH) [70,71] and C_6H_8ClOH, respectively. A possible degradation pathway for 2-CP, under optimum conditions in the presence of 40TiO_2/CNNS, is proposed in Figure 6c.

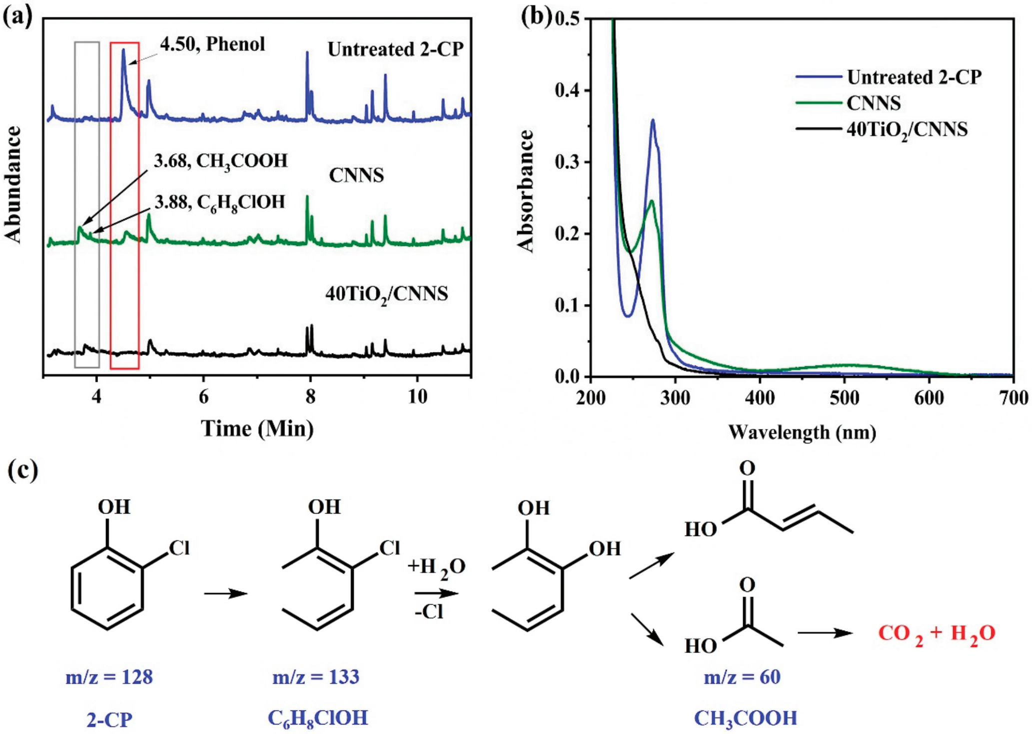

Figure 6. (**a**) GC traces of untreated 2-CP, 2-CP when treated with CNNS, and 2-CP when treated with 40TiO$_2$/CNNS. (**b**) UV–Vis spectra of 2-CP, and 2-CP treated with CNNS and 40TiO$_2$/CNNS. (**c**) A possible degradation pathway (from MS data) for 2-CP in the presence of 40TiO$_2$/CNNS.

Moreover, the generation of radical species in the CP solutions treated with photocatalyst was probed using EPR spectroscopy with DMPO as the radical spin trapping agent (Figure 7). The presence of hydroxyl radicals was tested under aqueous conditions whereas superoxide radicals were trapped in methanol solution. Under photolytic conditions, both radicals were observable (Figure 7). However, in the dark, or under photocatalytic conditions using 40TiO$_2$/CNNS, neither radical species could be detected. By contrast, signals characteristic of the formation of DMPO-OH and DMPO-O$_2^-$ adducts were observed after light irradiation for 60 min, which confirms the presence of OH and O$_2^-$ in the photocatalytic mechanism.

3.4. Photocatalytic Mechanism

To further describe the photocatalytic mechanism for the degradation of 2-CP using 40TiO$_2$/CNNS, the CB and VB edge potentials of g-C$_3$N$_4$ and TiO$_2$ were calculated, at the point of zero charge, using Equations (3) and (4) [72].

$$E_{CB} = X - E_c - 1/2E_g \quad (3)$$

$$E_{VB} = E_{CB} + E_g \quad (4)$$

In Equations (3) and (4), X is the absolute electronegativity of the atom semiconductor, being 5.8 eV for TiO$_2$ and 4.73 eV for g-C$_3$N$_4$. E$_c$ represents the energy of free electrons on the hydrogen scale (4.5 eV) [73] and E$_g$ is the band gap energy of the semiconductor. From the UV–Vis DRS spectra (Figure 4b), the E$_g$ of g-C$_3$N$_4$ is 2.94 eV and TiO$_2$ is 3.16 eV. Therefore, the reductive potentials of the conduction band (CB) are −0.28 and −1.24 V for

TiO_2 and g-C_3N_4, and the oxidation potentials of the valence band (VB) of TiO_2 and g-C_3N_4 are +2.88 and +1.70 V, respectively. Under light exposure, electrons are excited from the VB to the CB in TiO_2 ($Ti^{3+}$and V_o). Photogenerated holes thus remain in the TiO_2 valence band, while photogenerated electrons transfer from the CB of Ti^{3+} and O_v to the VB of g-C_3N_4. Electrons in the VB of g-C_3N_4 are further excited into the CB, which leads to enhanced separation between the photo-induced charge carrier and an increase in the redox ability. The electrons stored in the CB of g-C_3N_4 are then trapped on the surface and reduced to superoxide radical ions ($O_2{}^-$), while the holes in the VB of TiO_2 can oxidize OH^- or H_2O to form hydroxyl radicals (OH), which further react with chlorophenol resulting in CO_2 and H_2O products [72,73]. Therefore, the formation of Ti^{3+} and V_o is a major factor dictating the photocatalytic activity of TiO_2/CNNS nanocomposites. Classified as a type II heterojunction, the electrons on CB of g-C_3N_4 are transferred to TiO_2 which undergo a reduction reaction, whereas holes on the surface of TiO_2 are transferred to the g-C_3N_4 VB for oxidation reaction. This mechanism suggested the lowering of reduction ability of photogenerated electrons and the weakened oxidation capability of holes. The holes in the VB of g-C_3N_4 cannot adsorb water molecules near the surface of g-C_3N_4 to generate hydroxyl radicals (OH) because the reduction potential of g-C_3N_4 (+1.70 V) is less than that required to oxidize H_2O to OH (+1.99 V). However, OH species were detected by EPR from the 2-CP solution on treatment with 40TiO_2/g-C_3N_4. Therefore, the Z-scheme mechanism of 40Ti/CNNS is proposed (Figure S6), quite similar to a previous report [26].

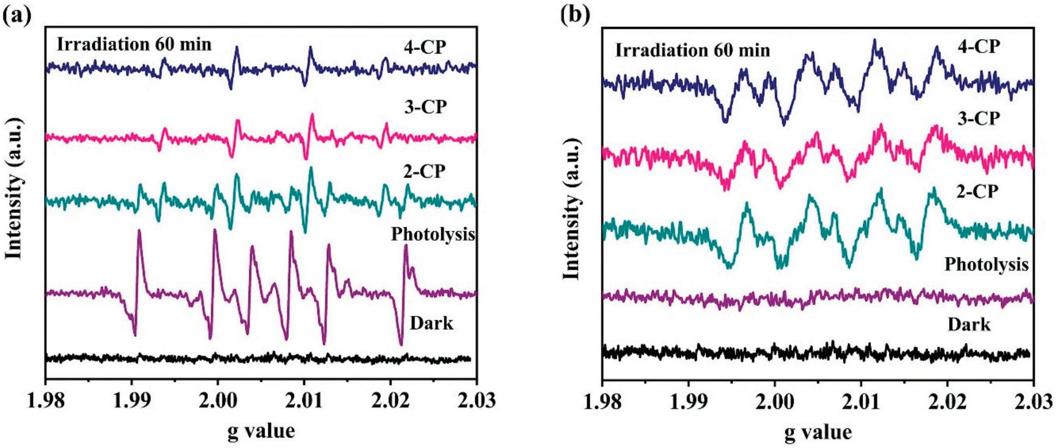

Figure 7. DMPO spin trapping EPR spectra for investigating the generation of (**a**) hydroxyl radicals in aqueous CP solutions treated with 40TiO_2/CNNS and (**b**) superoxide radicals in methanolic CP solutions treated with 40TiO_2/CNNS.

Comparatively, the content of thermally exfoliated g-C_3N_4 required in the TiO_2/CNNS nanocomposites produced in this work (weight ratio of TiO_2:CNNS = 40:60) is much higher than photocatalysts affording high removal efficiencies (>80%) of imidacloprid from aqueous solution (TiO_2:CNNS; weight ratio of TiO_2:CNNS = 96:4, [26]). Thus, the optimum CNNS content in the TiO_2/CNNS nanocomposites is varied for effective photodegradation of each pesticide. The relatively high CNNS content may enhance the number of π-π interactions at the interface between the aromatic pollutants (MCPs) and the exfoliated carbon nitride promoting surface reactions, resulting in a more facile degradation of MCPs over the TiO_2/CNNS composites described here. The polarity of MCPs ($\log K_{ow} \approx 2.5$ [74]) is quite low compared with imidachloprid ($\log K_{ow} = 0.57$ [75]), and the adsorption of MCPs is preferable on the CNNS surface (rather than TiO_2), promoting the surface photoreactions. Recent works utilizing g-C_3N_4 based photocatalysts for the removal of pesticides (endosulfan [27], and 2,4-dinitrophenylhydrazine or 2,4-DNP [28]) from water suggest that further modifications of the oxide semiconductor (e.g., adding Cu or N dopants) could also further synergically enhance the performance of the photocatalysts. The high g-C_3N_4 content (30% by weight) in the TiO_2/g-C_3N_4 based composites also correlates well with the low polarity of 2,4-DNPH [28]. Therefore, the synergetic effects obtained by incorporation of g-C_3N_4 with an oxide semiconducting material could be the results of the improved stability of photogenerated electrons and holes, as well as the increased adsorption preference sites of molecular pollutants of low polarity on the composite surface.

4. Conclusions

Exfoliated g-C_3N_4 nanosheets (CNNS) were produced via HNO_3 assisted thermal exfoliation of urea-derived bulk g-C_3N_4. The nanosheets showed larger specific surface areas than that of the bulk g-C_3N_4 and contains N vacancy defects, promoting enhanced photocatalytic activity. The addition of TiO_2 (20–50% by weight) followed by hydrothermal processing results in TiO_2/g-C_3N_4 nanocomposites, having improved photocatalytic performance over bulk g-C_3N_4, exfoliated g-C_3N_4, or TiO_2 alone for the degradation of MCPs. The highest removal efficiency of 87% was achieved from the treatment of 2-chlorophenol with 40TiO_2/CNNS, followed by UV irradiation for 2 h. Such photocatalytic performance can be attributed to the existence of nitrogen, Ti^{3+}, and V_o defects in the nanocomposites, enhancing the separation efficiency of photogenerated carriers and charge recombination suppression. It was found that OH and O_2^- radicals are active species in the photocatalytic degradation of 2-CP. These thermally exfoliated carbon nitride materials may provide preferable adsorption sites for MCPs, enhancing the photocatalytic performance of TiO_2/g-C_3N_4 nanocomposites. Further investigation of the nanocomposites obtained by greener routes or non-toxic precursors should be carried out to optimize the sustainability of photocatalytic processes.

Supplementary Materials: The following supporting information can be downloaded at: https://www.mdpi.com/article/10.3390/nano12162852/s1, Figure S1: Enlarged powder X-ray diffraction profile of the 40TiO_2/CNNS composite; Figure S2: Solid ESR spectra of bulk-CN (red) and CNNS (black); Figure S3: Convolution fitting of XPS spectrum of O1s in TiO_2; Figure S4: UV–Vis spectra of photolysis study in the absence of catalyst of (a) 2-CP, (b) 3-CP and (c) 4-CP aqueous solutions. Figure S5. Time-dependent photocatalytic degradation of a) 2-chlorophenol, b) 3-chlorophenol, and c) 4-chlorophenol when treated with g-C3N4, TiO_2 and composites under UV-Vis irradiation (25 ppm pollutant, 1g/L catalyst loading). Figure S6. Photocatalytic mechanism of utilizing 40TiO_2/CNNS for MCPs degradation

Author Contributions: Conceptualization, T.K. and S.M.S.; methodology, T.K., J.T., S.C. and S.M.S.; formal analysis, T.K.; resources, P.K. and S.M.S.; data curation, T.K.; writing-original draft preparation. T.K. and S.M.S.; writing-review and editing, T.K., J.T. and S.M.S.; visualization, T.K. and T.A.; supervision, S.M.S.; project administration, S.M.S.; funding acquisition, P.K. All authors have read and agreed to the published version of the manuscript.

Funding: This work was supported by the National Research Council of Thailand under the International Research Network-Green Technologies Network for Sustainable Environment: Food-Water-Energy Nexus (Grant no. IRN62W0005).

Institutional Review Board Statement: Not applicable for studies not involving humans or animals.

Informed Consent Statement: Not applicable.

Data Availability Statement: Data are contained within the article or supplementary material.

Acknowledgments: Authors are thankful for instrumentation support and for EPR measurements from the Center of Excellence for Innovation in Chemistry (PERCH-CIC). We thank Mahidol University-Frontier Research Facility (MU-FRF) for instrument support, and the MU-FRF scientists, Nawapol Udpuay and Suwilai Chaveanghong, for their kind assistance in Raman measurements. Authors are thankful for the support from the Sustainable Engineering Research Center for Pollution and Environmental Management, Faculty of Engineering, Chiang Mai University. Christopher Smith is highly appreciated for a proofreading task.

Conflicts of Interest: The authors declare no conflict of interest.

References

1. Jin, M.; Chen, X.; Pan, B. Simultaneous determination of 19 chlorophenols in water by liquid chromatography-mass spectrometry with solid-phase extraction. *J. Liq. Chromatogr. Relat. Technol.* **2006**, *29*, 1369–1380. [CrossRef]
2. Jiang, C.; Yu, H.; Lu, Y.; Zhu, S.; Geng, Z.; Huo, M.; Wang, X. Preparation of spike-like palladium nanoparticle electrode and its dechlorination properties. *Thin Solid Films* **2018**, *664*, 27–32. [CrossRef]
3. Lan, S.; Feng, J.; Xiong, Y.; Tian, S.; Liu, S.; Kong, L. Performance and mechanism of piezo-catalytic degradation of 4-Chlorophenol: Finding of effective piezo-dechlorination. *Environ. Sci. Technol.* **2017**, *51*, 6560–6569. [CrossRef]
4. Yang, C.-H.; Lee, C.-M. Pentachlorophenol contaminated groundwater bioremediation using immobilized *Sphingomonas* cells inoculation in the bioreactor system. *J. Hazard. Mater.* **2008**, *152*, 159–165. [CrossRef] [PubMed]
5. Onkani, S.P.; Diagboya, P.N.; Mtunzi, F.M.; Klink, M.J.; Olu-Owolabi, B.I.; Pakade, V. Comparative study of the photocatalytic degradation of 2-chlorophenol under UV irradiation using pristine and Ag-doped species of TiO_2, ZnO and ZnS photocatalysts. *J. Environ. Manag.* **2020**, *260*, 110145. [CrossRef] [PubMed]
6. Diagboya, P.N.; Olu-Owolabi, B.I.; Adebowale, K.O. Distribution and interactions of pentachlorophenol in soils: The roles of soil iron oxides and organic matter. *J. Contam. Hydrol.* **2016**, *191*, 99–106. [CrossRef]
7. Iqbinosa, E.O.; Odjadjare, E.E.; Chigor, V.N.; Igbinosa, I.H.; Emoghene, A.O.; Ekhaise, F.O.; Igiehon, N.O.; Idemudia, O.G. Toxicological Profile of Chlorophenols and Their Derivatives in the Environment: The Public Health Perspective. *Sci. World J.* **2013**, *2013*, 460215. [CrossRef]
8. Kus'mierek, K. The removal of chlorophenols from aqueous solutions using activated carbon adsorption integrated with H_2O_2 oxidation. *React. Kinet. Mech. Catal.* **2016**, *119*, 19–34. [CrossRef]
9. Soto, M.L.; Moure, A.; Domínguez, H.; Parajó, J.C. Recovery, concentration and purification of phenolic compounds by adsorption: A review. *J. Food Eng.* **2011**, *105*, 1–27. [CrossRef]
10. Lin, H.-Y. Adsorption and biodegradation of 2-chlorophenol by mixed culture using activated carbon as a supporting medium-reactor performance and model verification. *Appl. Water Sci.* **2017**, *7*, 3741–3757. [CrossRef]
11. Olaniran, A.O.; Igbinosa, E.O. Chlorophenols and other related derivatives of environmental concern: Properties, distribution and microbial degradation processes. *Chemosphere* **2011**, *83*, 1297–1306. [CrossRef] [PubMed]
12. González, L.F.; Sarria, V.; Sánchez, O.F. Degradation of chlorophenols by sequential biological-advanced oxidative process using Trametes pubescens and TiO_2/UV. *Biores. Technol.* **2010**, *101*, 3493–3499. [CrossRef] [PubMed]
13. Pedroza, A.M.; Mosqueda, R.; Alonso-Vante, N.; Rodríguez-Vázquez, R. Sequential treatment via Trametes versicolor and UV/TiO_2/RuxSey to reduce contaminants in waste water resulting from the bleaching process during paper production. *Chemosphere* **2007**, *67*, 793–801. [CrossRef]
14. Shu, X.; Yang, O.; Yao, F.; Zhong, Y.; Ren, W.; Chen, F.; Sun, J.; Ma, Y.; Fu, Z.; Wang, D.; et al. Electrocatalytic hydrodechlorination of 4-chlorophenol on Pd supported multi-walled carbon nanotubes particle electrodes. *Chem. Eng. J.* **2019**, *358*, 903–911. [CrossRef]
15. Kavitha, V.; Palanivelu, K. Degradation of 2-Chlorophenol by Fenton and Photo-Fenton Processes-A Comparative Study. *J. Environ. Sci. Health A* **2003**, *38*, 1215–1231. [CrossRef] [PubMed]
16. Aroh, A.O.; Gimba, C.E.; Omoniyi, K.I.; Abba, H.; Yilleng, M.T. Comparison of photocatalytic degradation of 4-chlorophenol and 3-chlorophenol using silver/palladium nanoparticles doped on TiO_2. *IJARBAS* **2019**, *1*, 232–254.
17. Sharma, A.; Lee, B.-K. Rapid photo-degradation of 2-chlorophenol under visible light irradiation using cobalt oxide-loaded TiO_2 /reduced graphene oxide nanocomposite from aqueous media. *J. Environ. Manag.* **2016**, *165*, 1–10. [CrossRef]
18. Xie, M.; Tang, J.; Kong, L.; Lu, W.; Natarajan, V.; Zhu, F.; Zhan, J. Cobalt doped g-C_3N_4 activation of peroxymonosulfate for monochlorophenols degradation. *Chem. Eng. J.* **2019**, *360*, 1213–1222. [CrossRef]
19. Liu, H.; Zhang, Z.; Ren, M.; Guan, J.; Lu, N.; Qu, J.; Yuan, X.; Zhang, Y.-N. Preparation of the CNTs/AG/ITO electrode with high electro-catalytic activity for 2-chlorophenol degradation and the potential risks from intermediates. *J. Hazard. Mater.* **2018**, *359*, 148–156. [CrossRef]
20. Ahmad, R.; Ahmad, Z.; Khan, A.U.; Mastoi, N.R.; Aslam, M.; Kim, J. Photocatalytic systems as an advanced environmental remediation: Recent developments, limitations and new avenues for applications. *J. Environ. Chem. Eng.* **2016**, *4*, 4143–4164. [CrossRef]
21. Kumar, A.; Pandey, G. A review on the factors affecting the photocatalytic degradation of hazardous materials. *Mater. Sci. Eng. C* **2017**, *3*, 106–114. [CrossRef]
22. Gao, M.; Feng, J.; Zhang, Z.; Gu, M.; Wang, J.; Zeng, W.; Lv, Y.; Ren, Y.; Wei, T.; Fan, Z. Wrinkled ultrathin graphitic C_3N_4 nanosheets for photocatalytic degradation of organic wastewater. *ACS Appl. Nano Mater.* **2018**, *1*, 6733–6741. [CrossRef]
23. Hong, Y.; Liu, E.; Shi, J.; Lin, X.; Sheng, L.; Zhang, M.; Wang, L.; Chen, J. A direct one-step synthesis of ultrathin g-C_3N_4 nanosheets from thiourea for boosting solar photocatalytic H_2 evolution. *Int. J. Hydrogen Energy* **2019**, *44*, 7194–7204. [CrossRef]
24. Fe, J.; Yu, J.; Jiang, C.; Cheng, B. g-C_3N_4-based heterostructured photocatalysts. *Adv. Energy Mater.* **2018**, *8*, 1701503–1701533.
25. Zada, A.; Ali, N.; Subhan, F.; Anwar, N.; Shah, M.I.A.; Ateeq, M.; Hussain, Z.; Zaman, K.; Khan, M. Suitable energy platform significantly improves charge separation of g-C_3N_4 for CO_2 reduction and pollutant oxidation under visible-light. *Prog. Nat. Sci.* **2019**, *29*, 138–144. [CrossRef]

26. Kobkeatthawin, T.; Trakulmututa, J.; Amornsakchai, T.; Kajitvichyanukul, P.; Smith, S.M. Identification of active species in photodegradation of aqueous imidacloprid over g-C_3N_4/TiO_2 Nanocomposites. *Catalysts* **2022**, *12*, 120. [CrossRef]
27. Nekooie, R.; Ghasemi, J.B.; Badiei, A.; Shamspur, T.; Mostafavi, A.; Moradian, S. Design and synthesis of g-C_3N_4/(Cu/TiO_2) nanocomposite for the visible light photocatalytic degradation of endosulfan in aqueous solutions. *J. Mol. Struct.* **2022**, *1258*, 132650. [CrossRef]
28. Dong, S.; Chen, S.; He, F.; Li, J.; Li, H.; Xu, K. Construction of a novel N-doped oxygen vacancy-rich TiO_2 N-TiO_{2-X}/g-C_3N_4 S-scheme heterostructure for visible light driven photocatalytic degradation of 2,4-dinitrophenylhydrazine. *J.Alloys Compd.* **2022**, *908*, 164586. [CrossRef]
29. Zizhen, L.; Meng, X.; Zhang, Z. Fabrication of surface hydroxyl modified g-C_3N_4 with enhanced photocatalytic oxidation activity. *Catal. Sci. Technol.* **2019**, *9*, 3979–3993.
30. Azami, M.S.; Jalil, A.A.; Hitam, C.N.C.; Hassan, N.S.; Mamat, C.R.; Adnan, R.H.; Chanlek, N. Tuning of the electronic band structure of fibrous silica titania with g-C_3N_4 for efficient Z-scheme photocatalytic activity. *Appl. Surf. Sci.* **2020**, *512*, 145744. [CrossRef]
31. Mozia, S.; Bubacz, K.; Janus, M.; Morawski, A.W. Decomposition of 3-chlorophenol on nitrogen modified TiO_2 photocatalysts. *J. Hazard. Mater.* **2012**, *128*, 128–136. [CrossRef] [PubMed]
32. Zhang, S.; Yang, Y.; Guo, Y.; Guo, W.; Wang, M.; Guo, Y.; Huo, M. Preparation and enhanced visible-light photocatalytic activity of graphitic carbon nitride/bismuth niobite heterojunctions. *J. Hazard. Mater.* **2013**, *261*, 235–245. [CrossRef] [PubMed]
33. Rathi, V.; Panneerselvam, A.; Sathiyapriya, R. Graphitic carbon nitride (g-C_3N_4) decorated $ZnWO_4$ heterojunctions architecture synthesis, characterization and photocatalytic activity evaluation. *Diam. Relat. Mater.* **2020**, *108*, 107981. [CrossRef]
34. De Sousa, J.G.M.; da Silva, T.V.C.; de Moraes, N.P.; da Silva, M.L.C.P.; da Silva Rocha, R.; Landers, R.; Rodrigues, L.A. Visible light-driven ZnO/g-C_3N_4/carbon xerogel ternary photocatalyst with enhanced activity for 4-chlorophenol degradation. *Mater. Chem. Phys.* **2020**, *256*, 123651. [CrossRef]
35. Pennetta, A.; Di Masi, S.; Piras, F.; Lü, X.; Li, J.; De Benedetto, G.E.; Mele, G. TiO_2@lipophilic porphyrin composites: New insights into tuning the photoreduction of Cr(VI) to Cr(III) in aqueous phase. *J. Compos. Sci.* **2020**, *4*, 82. [CrossRef]
36. Zou, L.-R.; Huang, G.-F.; Li, D.-F.; Liu, J.-H.; Pan, A.-L.; Huang, W.-Q. A facile and rapid route for synthesis of g-C_3N_4 nanosheets with high adsorption capacity and photocatalytic activity. *RSC Adv.* **2016**, *6*, 86688. [CrossRef]
37. Yang, Y.; Chen, J.; Mao, Z.; An, N.; Wang, D.; Fahlman, B.D. Ultrathin g-C_3N_4 nanosheets with an extended visible light-responsive range for significant enhancement of photocatalysis. *RSC Adv.* **2017**, *7*, 2333. [CrossRef]
38. Fina, F.; Callear, S.K.; Carins, G.M.; Irvine, J.T.S. Structural investigation of graphitic carbon nitride via XRD and neutron diffraction. *Chem. Mater.* **2015**, *27*, 2612–2618. [CrossRef]
39. Ma, Y.; Liu, E.; Hu, X.; Tang, C.; Wan, J.; Li, J.; Fan, J. A simple process to prepare few-layer g-C_3N_4 nanosheets with enhanced photocatalytic activities. *Appl. Surf. Sci.* **2015**, *358*, 246–251. [CrossRef]
40. Xu, J.; Zhang, L.; Shi, R.; Zhu, Y. Chemical exfoliation of graphitic carbon nitride for efficient heterogeneous photocatalysis. *J. Mater. Chem. A.* **2013**, *1*, 14766. [CrossRef]
41. Li, W.; Liang, L.; Hu, A.; Huanga, Z.; Zhou, Y.N. Generation of oxygen vacancies in visible light activated one-dimensional iodine TiO_2 photocatalysts. *RSC Adv.* **2014**, *4*, 36959. [CrossRef]
42. Majumdar, S.; Mahanta, D. Deposition of an ultra-thin polyaniline coating on a TiO_2 surface by vapor phase polymerization for electrochemical glucose sensing and photocatalytic degradation. *RSC Adv.* **2020**, *10*, 17387–17395. [CrossRef] [PubMed]
43. Wang, M.; Ma, F.; Wang, Z.; Hu, D.; Xu, X.; Hao, X. Graphitic carbon nitride, a saturable absorber material for the visible waveband. *Photonics Res.* **2018**, *6*, 307–313. [CrossRef]
44. Fan, C.; Miao, J.; Xu, G.; Liu, J.; Lv, J.; Wu, Y. Graphitic carbon nitride nanosheets obtained by liquid stripping as efficient photocatalysts under visible light. *RSC Adv.* **2017**, *7*, 37185. [CrossRef]
45. Shen, L.; Xing, Z.; Zou, J.; Li, Z.; Wu, X.; Zhang, Y.; Zhu, Q.; Yang, S.; Zhou, W. Black TiO_2 nanobelts/g-C_3N_4 nanosheets Laminated heterojunctions with efficient visible-light-driven photocatalytic performance. *Sci. Rep.* **2017**, *7*, 41978. [CrossRef]
46. Zhang, Q.; Ma, L.; Shao, M.; Huang, J.; Ding, M.; Deng, X.; Wei, X.; Xu, X. Anodic Oxidation Synthesis of One-Dimensional TiO_2 Nanostructures for Photocatalytic and Field Emission Properties. *J. Nanomater.* **2014**, *2014*, 831752. [CrossRef]
47. Ren, B.; Wang, T.; Qu, G.; Deng, F.; Liang, D.; Yang, W.; Liu, M. In situ synthesis of g-C_3N_4/TiO_2 heterojunction nanocomposites as a highly active photocatalyst for the degradation of Orange II under visible light irradiation. *Environ. Sci. Pollut. Res.* **2018**, *25*, 19122–19133. [CrossRef]
48. Wang, J.; Gao, B.; Dou, M.; Huang, X.; Ma, Z. A porous g-C_3N_4 nanosheets containing nitrogen defects for enhanced photocatalytic removal meropenem: Mechanism, degradation pathway and DFT calculation. *Environ. Res.* **2020**, *184*, 109339. [CrossRef]
49. Jiang, D.; Sun, X.; Zhang, H.; Wang, K.; Shi, L.; Du, F. Nanotube confinement-induced g-C_3N_4/TiO_2 nanorods with rich oxygen vacancies for enhanced photocatalytic water decontamination. *Appl. Phys. A* **2020**, *126*, 246. [CrossRef]
50. Du, X.; Bai, X.; Xu, L.; Yang, L.; Jin, P. Visible-light activation of persulfate by TiO_2/g-C_3N_4 photocatalyst toward efficient degradation of micropollutants. *Chem. Eng. J.* **2020**, *384*, 123245. [CrossRef]
51. Cheng, D.; Li, Y.; Yang, L.; Luo, S.; Yang, L.; Luo, X.; Luo, Y.; Li, T.; Gao, J.; Dionysiou, D.D. One step reductive synthesis of Ti^{3+} self–doped elongated anatase TiO_2 nanowires combined with reduced graphene oxide for adsorbing and degrading waste engine oil. *J. Hazard. Mater.* **2019**, *378*, 120752. [CrossRef] [PubMed]

52. Swaminathan, J.; Ravichandran, S. Insights into the defect-centered electrocatalytic behavior of reduced titania ($TiO_{1.23}$). *J. Phys. Chem. C* **2018**, *122*, 1670–1680. [CrossRef]
53. Kong, L.; Zhang, X.; Wang, C.; Xu, J.; Du, X.; Li, L. Ti^{3+} defect mediated g-C_3N_4/TiO_2 Z-scheme system for enhanced photocatalytic redox performance. *Appl. Surf. Sci.* **2018**, *448*, 288–296. [CrossRef]
54. Mohajernia, S.; Andryskova, P.; Zoppellaro, G.; Hejazi, S.; Kment, S.; Zboril, R.; Schmidt, J.; Schmuki, P. Influence of Ti^{3+} defect-type on heterogeneous photocatalytic H_2 evolution activity of TiO_2. *J. Mater. Chem. A* **2020**, *8*, 1432–1442. [CrossRef]
55. Xiong, L.-B.; Li, J.-L.; Yang, B.; Yu, Y. Ti^{3+} in the surface of Titanium Dioxide: Generation, properties and photocatalytic application. *J. Nanomater.* **2012**, *2012*, 9. [CrossRef]
56. Kathiresan, V.; Rajarathinam, T.; Lee, S.; Kim, S.; Lee, J.; Thirumalai, D.; Chang, S.-C. Cost-effective electrochemical activation of graphitic carbon nitride on the glassy carbon electrode surface for selective determination of serotonin. *Sensors* **2020**, *20*, 6083. [CrossRef]
57. Che, H.; Liu, L.; Che, G.; Dong, H.; Liu, C.; Li, C. Control of energy band, layer structure and vacancy defect of graphitic carbon nitride by intercalated hydrogen bond effect of NO_3^-toward improving photocatalytic performance. *Chem. Eng. J.* **2019**, *357*, 209–219. [CrossRef]
58. Sun, H.; Zhou, X.; Zhang, H.; Tu, W. An efficient exfoliation method to obtain graphitic carbon nitride nanosheets with superior visible-light photocatalytic activity. *Int. J. Hydrogen Energy* **2017**, *42*, 7930–7937. [CrossRef]
59. Dong, F.; Li, Y.H.; Wang, Z.Y. Enhanced visible light photocatalytic activity and oxidation ability of porous graphene-like g-C_3N_4 nanosheets via thermal exfoliation. *Appl. Surf. Sci.* **2015**, *358*, 393–403. [CrossRef]
60. Maurya, N.I.C.; Singh, S.; Gupta, A.K.; Srivastava, P.; Bahadur, L. N/Al-incorporated TiO_2 nanocomposites for improved device performance of a dye-sensitized solar cell. *Energy Environ. Sci.* **2017**, *2*, 4267–4276.
61. Yun, Y.-J.; He, J.-Y.; Zhang, D.; Wang, X.-J.; Zhao, J.; Liu, R.-H.; Li, F.-T. Simultaneous construction of dual-site phosphorus modified g-C_3N_4 and its synergistic mechanism for enhanced visible-light photocatalytic hydrogen evolution. *Appl. Surf. Sci.* **2020**, *517*, 146192.
62. Zhang, H.; Liu, F.; Wu, H.; Cao, X.; Sun, J.; Lei, W. In situ synthesis of g-C_3N_4/TiO_2 heterostructures with enhanced photocatalytic hydrogen evolution under visible light. *RSC Adv.* **2017**, *7*, 40327. [CrossRef]
63. Zhang, X.; Cai, M.; Cui, N.; Chen, G.; Zou, G.; Zhou, L. One-Step Synthesis of b-N-TiO_2/C Nanocomposites with high visible light photocatalytic activity to degrade microcystis aeruginosa. *Catalysts* **2020**, *10*, 579. [CrossRef]
64. Dong, C.; Ma, Z.; Qie, R.; Guo, X.; Li, C.; Wang, R.; Shi, Y.; Dai, B.; Jia, X. Morphology and Defects Regulation of Carbon Nitride by Hydrochloric Acid to Boost Visible Light Absorption and Photocatalytic Activity. *Appl. Catal. B* **2017**, *217*, 629–636. [CrossRef]
65. Ye, C.; Li, J.-X.; Li, Z.-J.; Li, X.-B.; Fan, X.-B.; Zhang, L.-P.; Chen, B.; Tung, C.-H.; Wu, L.-Z. Enhanced driving force and charge separation efficiency of protonated g-C_3N_4 for photocatalytic O_2 evolution. *ACS Catal.* **2015**, *5*, 6973–6979. [CrossRef]
66. Ren, R.; Wen, Z.; Cui, Z.; Hou, Y.; Guo, X.; Chen, J. Controllable synthesis and tunable photocatalytic properties of Ti^{3+}-doped TiO_2. *Sci. Rep.* **2015**, *5*, 10714. [CrossRef]
67. Zhu, M.; Lu, J.; Dong, L.; Hu, S.; Peng, S.; Zhu, C. Photochemical transformations of 2, 6-dichlorophenol and 2-chlorophenol with superoxide ions in the atmospheric aqueous phase. *J. Mol. Struct.* **2022**, *1261*, 132910. [CrossRef]
68. Liu, X.; Zhang, Q.; Cui, Z.; Ma, F.; Guo, Y.; Wang, Z.; Liu, Y.; Zheng, Z.; Cheng, H.; Dai, Y.; et al. Morphology and defects design in g-C_3N_4 for efficient and simultaneous visible-light photocatalytic hydrogen production and selective oxidation of benzyl alcohol. *Int. J. Hydrogen Energy.* **2022**, *47*, 18738–18747. [CrossRef]
69. Cai, H.; Han, D.; Wang, X.; Cheng, X.; Liu, J.; Jia, L.; Ding, Y.; Liu, S.; Fan, X. High specific surface area defective g-C_3N_4 nanosheets with enhanced photocatalytic activity prepared by using glyoxylic acid mediated melamine. *Mater. Chem. Phys.* **2020**, *256*, 123755. [CrossRef]
70. Sun, N.; Qu, Y.; Yang, C.; Yang, Z.; Yan, R.; Zhang, W.E.Z.; Li, Z.; Li, H.; Khan, I.; Sun, R.; et al. Efficiently photocatalytic degradation of monochlorophenol on in-situ fabricated $BiPO_4$/β-Bi_2O_3 heterojunction microspheres and O_2^-free hole induced selective dechloridation conversion with H_2 evolution. *Appl. Catal. B* **2020**, *263*, 118313. [CrossRef]
71. Ba-Abbad, M.M.; Takriff, M.S.; Kahum, A.A.H.; Mohamad, A.B.; Benamor, A.; Mohammad, A.W. Solar photocatalytic degradation of 2-chlorophenol with ZnO nanoparticles: Optimisation with D-optimal design and study of intermediate mechanisms. *Environ. Sci. Pollut. Res.* **2017**, *24*, 2804–2819. [CrossRef] [PubMed]
72. Bi, X.; Yu, S.; Liu, E.; Liu, L.; Zhang, K.; Zang, J.; Zhao, Y. Construction of g-C_3N_4/TiO_2 nanotube arrays Z-scheme heterojunction to improve visible light catalytic activity. *Colloids Surf. A* **2020**, *603*, 125193. [CrossRef]
73. Liao, W.; Murugananthan, M.; Zhang, Y. Synthesis of Z-scheme g-C_3N_4–Ti^{3+}/TiO_2 material: An efficient visible light photoelectrocatalyst for degradation of phenol. *Phys. Chem. Chem. Phys.* **2015**, *17*, 8877. [CrossRef] [PubMed]
74. Núñez-Gaytán, A.N.; Vera-Ávila, L.E.; Covarrubias-Herrera, M.d.R. On-line methodology for the trace level determination of the chlorinated phenol family in water samples. *J. Mex. Chem. Soc.* **2008**, *52*, 185–192.
75. Moza, P.N.; Hustert, K.; Feicht, E.; Kettrup, A. Photolysis of imidacloprid in aqueous solution. *Chemosphere* **1998**, *36*, 497–502. [CrossRef]

nanomaterials

Article

Deposition Mechanism and Characterization of Plasma-Enhanced Atomic Layer-Deposited SnO_x Films at Different Substrate Temperatures

Pao-Hsun Huang [1], Zhi-Xuan Zhang [2], Chia-Hsun Hsu [2], Wan-Yu Wu [3], Sin-Liang Ou [4], Chien-Jung Huang [5], Dong-Sing Wuu [6], Shui-Yang Lien [2,7,*] and Wen-Zhang Zhu [2]

[1] School of Ocean Information Engineering, Jimei University, Jimei District, Xiamen 361021, China
[2] School of Opto-Electronic and Communication Engineering, Xiamen University of Technology, Xiamen 361024, China
[3] Department of Materials Science and Engineering, National United University, Miaoli 36063, Taiwan
[4] Department of Biomedical Engineering, Da-Yeh University, Changhua 51591, Taiwan
[5] Department of Applied Physics, National University of Kaohsiung, Kaohsiung University Road, Kaohsiung 81148, Taiwan
[6] Department of Applied Materials and Optoelectronic Engineering, National Chi Nan University, Nantou 54561, Taiwan
[7] Department of Materials Science and Engineering, Da-Yeh University, Changhua 51591, Taiwan
* Correspondence: sylien@xmut.edu.cn or syl@mail.dyu.edu.tw

Abstract: The promising functional tin oxide (SnO_x) has attracted tremendous attention due to its transparent and conductive properties. The stoichiometric composition of SnO_x can be described as common n-type SnO_2 and p-type Sn_3O_4. In this study, the functional SnO_x films were prepared successfully by plasma-enhanced atomic layer deposition (PEALD) at different substrate temperatures from 100 to 400 °C. The experimental results involving optical, structural, chemical, and electrical properties and morphologies are discussed. The SnO_2 and oxygen-deficient Sn_3O_4 phases coexisting in PEALD SnO_x films were found. The PEALD SnO_x films are composed of intrinsic oxygen vacancies with O-Sn^{4+} bonds and then transformed into a crystalline SnO_2 phase with increased substrate temperature, revealing a direct 3.5–4.0 eV band gap and 1.9–2.1 refractive index. Lower (<150 °C) and higher (>300 °C) substrate temperatures can cause precursor condensation and desorption, respectively, resulting in reduced film qualities. The proper composition ratio of O to Sn in PEALD SnO_x films near an estimated 1.74 suggests the highest mobility of 12.89 $cm^2\ V^{-1}\ s^{-1}$ at 300 °C.

Keywords: tin oxide (SnO_x); plasma-enhanced atomic layer deposition (PEALD); substrate temperature

Citation: Huang, P.-H.; Zhang, Z.-X.; Hsu, C.-H.; Wu, W.-Y.; Ou, S.-L.; Huang, C.-J.; Wuu, D.-S.; Lien, S.-Y.; Zhu, W.-Z. Deposition Mechanism and Characterization of Plasma-Enhanced Atomic Layer-Deposited SnO_x Films at Different Substrate Temperatures. *Nanomaterials* **2022**, *12*, 2859. https://doi.org/10.3390/nano12162859

Academic Editors: Jihoon Lee and Ming-Yu Li

Received: 16 July 2022
Accepted: 15 August 2022
Published: 19 August 2022

1. Introduction

Transparent conductive oxide (TCO) materials have been widely used and intensively researched in a wide range of industries during the last half-century [1–4]. Because of its increasing use in many instruments, this large area of constantly expanding research has focused on the preparations and properties of TCO films such as tin oxide (SnO_2), indium tin oxide (ITO), zinc oxide (ZnO), aluminum-doped ZnO (AZO), and titanium oxide (TiO_2) [5–9]. Non-stoichiometric SnO_2 (SnO_x), in particular, has recently gained substantial interest as a potential functional oxide semiconductor for use in a wide range of optoelectronics due to its specific features in its stoichiometry [10]. For instance, the SnO_x films are prepared with nanocomposite porous silicon for application and used in gas microsensors [11]. Due to their superior chemical and mechanical stability over other known oxide films, SnO_x films are also employed as electron selective film candidates for solar cells and light-emitting diodes based on perovskite, quantum dots, and organic materials [12–14]. Furthermore, various experiments have been conducted to examine tin oxides with different oxygen stoichiometry, such as Sn_2O_3 [15], Sn_3O_4 [16], and Sn_5O_6 [17].

Because of its oxygen-deficient property, p-type Sn_3O_4 has gained a significant amount of interest. However, the impact of this Sn_3O_4 phase on the optical, electrical, physical, and chemical characteristics of the film, which usually coexists with the SnO_2 phase, is sometimes underestimated.

In the literature, various deposition processes such as chemical vapor deposition (CVD), low-pressure chemical vapor deposition, plasma-enhanced chemical vapor deposition (PECVD), physical vapor deposition (PVD), and so on have been employed to prepare multifunctional SnO_x films [18–21]. Currently, atomic layer deposition (ALD), as an appealing deposition process with low deposition temperature, atomic-scale thickness controllability, and remarkable conformity, permits the considerable scaling-down and 3D structuring of devices as compared to CVD and PVD [22,23]. In ALD, two self-limiting surface reactions are used, in which two reactant gases are pulsed into the chamber in two different dosages, resulting in the formation of individual mono-layers per reaction cycle. Furthermore, as a better approach, plasma-enhanced ALD (PEALD) employs plasma-generated oxidizing agents to effectively augment the reactivity between plasma species and precursors, allowing for lower deposition temperatures without affecting film quality [24–27]. Film properties are affected by different deposition modes driven by lower or higher substrate temperatures [28–30], perhaps due to precursor condensation/adsorption within an incomplete reaction or decomposition/desorption. Thus, it is important to focus on the impact of various substrate temperatures on the PEALD SnO_x films and validate which deposition mode will occur with the various substrate temperatures in order to acquire the optimal stoichiometry of oxygen and tin.

PEALD SnO_x films deposited at substrate temperatures ranging from 100 to 400 °C are investigated in this study. The metal precursor is tetrakis(dimethylamino)tin (TDMA-Sn), which reacts with oxygen and argon plasma reactants. The optical, electrical, physical, and chemical characteristics are analyzed and discussed to determine the optimal stoichiometric ratio of O to Sn.

2. Materials and Methods

2.1. Materials and PEALD Process

The SnO_x films were deposited on silicon wafers (4 inches with 450 μm and a resistivity of 50 Ω-cm) by the PEALD system (R-200, Picosun, Finland) with six source channels, where the TDMA-Sn (purity: 99.9999%, Aimou Yuan, Nanjing, China) was used as the Sn metal precursor. Each experimental variable was used for preparing five samples at different substrate temperatures, and silicon wafers were cleaned by a standard procedure, including deionized water (DI-water) for 10 s, hydrofluoric acid for 1 min, and DI water for 10 s. Before being transferred to the vacuum chamber, the silicon wafer was blow-dried with nitrogen (N_2, 99.99%). We operated the Ar and O_2 (both of them with an ultra-high purity of 99.999%) plasma in a quartz cavity by the inductive coupling of RF power. The SnO_x deposition was performed with a total of 300 ALD cycles. Table 1 shows the preparation parameters of the PEALD SnO_x films, and the substrate temperature was varied from 100 to 400 °C.

Table 1. Preparation parameters of PEALD SnO_2 films.

Parameter	Value
Bubbler temperature (°C)	50
Substrate temperature (°C)	100–400
TDMA-Sn pulse time (s)	1.6
TDMA-Sn purge time (s)	6
O_2 pulse time (s)	11
O_2 purge time (s)	5
Ar flow rate (sccm)	80
O_2 flow rate (sccm)	150
O_2 plasma power (W)	2000
TDMA-Sn carry gas flow rate (sccm)	120
TDMA-Sn dilute gas flow rate (sccm)	400

2.2. Characteristic Measurements

The ellipsometer (M-2000, J. A. Woollan Co., Lincoln, NE, USA) was used to determine the thickness, refractive index (n), and deposition rate (nm/cycle). The estimated thickness value had an error of less than ±2% to show satisfying reproducibility. The model of "air, air/SnO_x, SnO_x, SnO_x/silicon" was used to complete the fitting ellipsometric data for the PEALD SnO_x films by the Drude-Lorentz model. For the optical properties of films, all samples were measured by ultraviolet-visible spectroscopy (MFS-630, Hong-Ming Technology, New Taipei City, Taiwan) in the wavelength range from 350 to 850 nm. For the structural properties of films, the grazing incidence X-ray diffraction (XRD, Rigaku TTRAXIII, Ibaraki, Japan) with a selected 0.5° incident angle and a wavelength of 0.15418 nm was used at 50 kV and 300 mA to obtain the orientation in diffraction patterns within a 2θ range of 20° to 70°. Field emission scanning electron microscopy (FESEM, JSM-7800F, JEOL, Tokyo, Japan) at 9.6×10^{-5} Pa and atomic force microscopy (AFM, XE7, Park, Korea) at ambient conditions were used to obtain the top-view surface morphologies. Further microstructure characteristics were shown in the cross-sectional transmission electron microscopy (TEM) images. For the chemical properties of the films, the X-ray photoelectron spectroscopy (XPS, ESCALAB, 250Xi, Thermo Fisher, Waltham, MA, USA) spectra were performed and calibrated by C 1s (284.5 eV). Before XPS measurement, the surface contamination was removed by sputtering. For the electrical properties of films, the resistivity, carrier concentration, and mobility were conducted by Hall-effect measurements (HMS-5000, Side Semiconductor Technology, Ecopia, Anyang, Korea) at room temperature. Both XRD and XPS results were further analyzed by peak-differentiated and imitating methods to demonstrate the phase and bonding characteristics of the films, respectively.

3. Results and Discussion

3.1. Deposition Mechanism

The schematic deposition mechanism of the PEALD SnO_x films is shown in Figure 1. Three growth modes concerning the first (steps 1 and 3) and second self-limiting surface reactions (steps 2 and 4) are described as (a) precursor condensation (<150 °C), (b) saturation reaction (250–300 °C), and (c) thermal desorption (350–400 °C), where the reaction can be represented via the following equations [28,29]:

$$S^{\wedge}\text{–}(OH)_3 + 2\,Sn(N(CH_3)_2)_4 \rightarrow S^{\wedge}\text{–}OH\text{–}Sn(N(CH_3)_2)_4 + S^{\wedge}\text{–}O_2Sn(N(CH_3)_2)_2 + 2\,NC_2H_7\uparrow \tag{1a}$$

$$S^{\wedge}\text{–}(OH)_2 + Sn(N(CH_3)_2)_4 \rightarrow S^{\wedge}\text{–}O_2Sn(N(CH_3)_2)_2 + 2\,NC_2H_7\uparrow \tag{1b}$$

$$S^{\wedge}\text{–}(OH)_2 + Sn(N(CH_3)_2)_4 \rightarrow S^{\wedge}\text{–}O_2Sn(N(CH_3)_2)_2 + NC_2H_7\uparrow + Sn(NC_2H_7)_2\uparrow \tag{1c}$$

$$S^{\wedge}\text{–}O_2Sn(N(CH_3)_2)_2 + \textit{Plasma}\ (O^*/Ar^*/e^-) \rightarrow S^{\wedge}\text{–}SnO_2\text{–}H + (CO_X + NO_X + H_2O)\uparrow \tag{2}$$

$$S^{\wedge}\text{–}SnO_2\text{–}2H + Sn(N(CH_3)_2)_4 \rightarrow S^{\wedge}\text{–}SnO_2\text{–}Sn(N(CH_3)_2)_2 + NC_2H_7\uparrow \tag{3}$$

$$S^{\wedge}\text{–}SnO_2\text{–}Sn(N(CH_3)_2)_2 + \textit{Plasma}\ (O^*/Ar^*/e^-) \rightarrow S^{\wedge}\text{–}SnO_2\text{–}SnO_2\text{–}2H + (CO_X + NO_X + H_2O)\uparrow \tag{4}$$

where the $S^{\wedge}$ and ↑ symbols represent the substrate surface and by-product with volatile gaseous phase, respectively. In Equation (1), the TDMA-Sn molecules will react with the hydroxyl (OH) groups on the substrate surface. Equation (1a) reveals that the low substrate temperature (<150 °C) causes the condensation of the TDMA-Sn precursor mainly due to the physisorption, where it is quite mobile and oscillating on the surface. This result is similar to some other studies [28]. With the increasing substrate temperatures (200–400 °C), the physisorption becomes a minor factor and the film growth gradually turns into chemisorption as a significant factor. As shown in Equations (1b) and (1c), the thermal activation induces the irreversible break of chemical bonding and the electron transfer between the deposited surface and adsorbed molecules [31,32]. Notably, when the substrate temperature is in the range of 250–300 °C, a self-limiting PEALD process emerges as Equation (1b) due to enough heat energy, leading to the saturation reaction of precursors and oxygen radicals. However, these adsorbed precursor molecules will further desorb, as in Equation (1c), when the surface possesses excess heat energy at higher substrate temperatures of 350–400 °C. In the second self-limiting surface reaction, the plasma reaction is shown as the following formula to generate oxygen (O_2) radicals: $Ar + O_2 + e^- \rightarrow 2O^* + Ar^* + e^-$, where the asterisk mark describes the excited state. The Sn-O bonds and initial hydroxyl ligands are formed, and then the released by-products (CO_X, NO_X, and H_2O gas), as described in Equation (2), are purged. So far, one PEALD cycle has finished, and we continuously used more than one cycle to complete the film growth by repeating Equations (3) and (4).

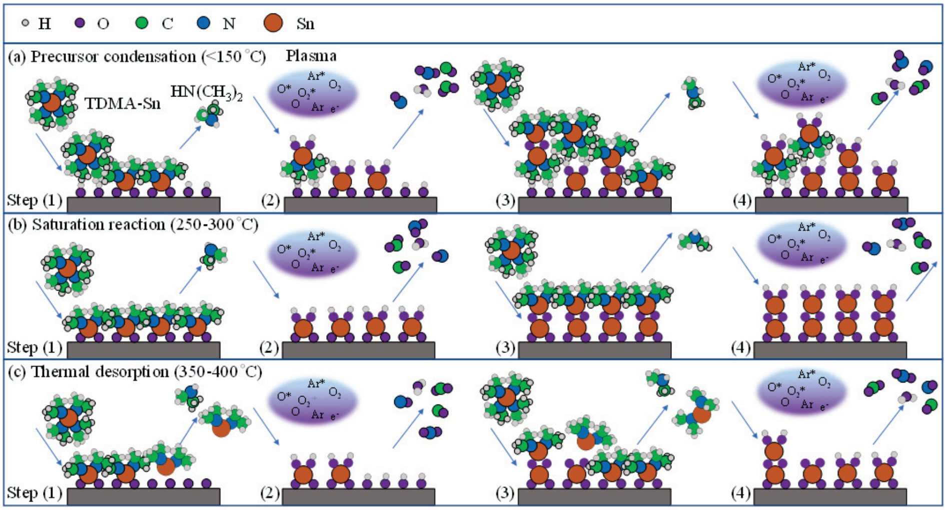

Figure 1. Deposition mechanism of PEALD SnO_x films at different substrate temperatures dividing into three growth modes: (**a**) precursor condensation (<150 °C), (**b**) saturation reaction (250–300 °C), and (**c**) thermal desorption (350–400 °C).

Figure 2a shows the substrate temperature-dependent growth per cycle (GPC) of PEALD SnO_x films on the Si wafer from 100 to 400 °C. The trend line of corresponding thickness at each GPC is plotted in Figure 2b. We calculate the GPC value by dividing the film thickness by the number of cycles. Three reaction regions are obviously demonstrated with respect to the substrate temperature. The GPC of 0.117 nm/cycle at 100 °C is mainly induced by the precursor physisorption and condensation [28,33]; however, at 150–200 °C, the GPC decreases to 0.117–0.087 nm/cycle, inferring that the surface reaction changes from physisorption to chemisorption-dominated. These low GPC values are likely due to the low chemical reaction rates at low temperatures [34,35]. The high GPC values of 0.138 nm/cycle at 250 °C and 0.131 nm/cycle at 300 °C are ascribed to the saturation of chemical-adsorbed precursors. However, the GPC rapidly drops to 0.094 nm/cycle at 350 °C and 0.082 nm/cycle at 400 °C due to the severe thermal desorption between the precursors and surface [34]. In other words, the self-limiting process as a unique feature of PEALD is verified by observing the saturation reaction of the GPC value as a function of the substrate temperature. Compared to some studies contrary to our results [28], these observations indicate that the higher substrate temperature causes the low GPC owing to the precursor's desorption [34]. In the ALD process, the saturation reaction should lead to a relatively high GPC value and simultaneously a small change in GPC, which were observed in the range of 250 to 300 °C in this study. This temperature range is reasonable as compared to the literature [36].

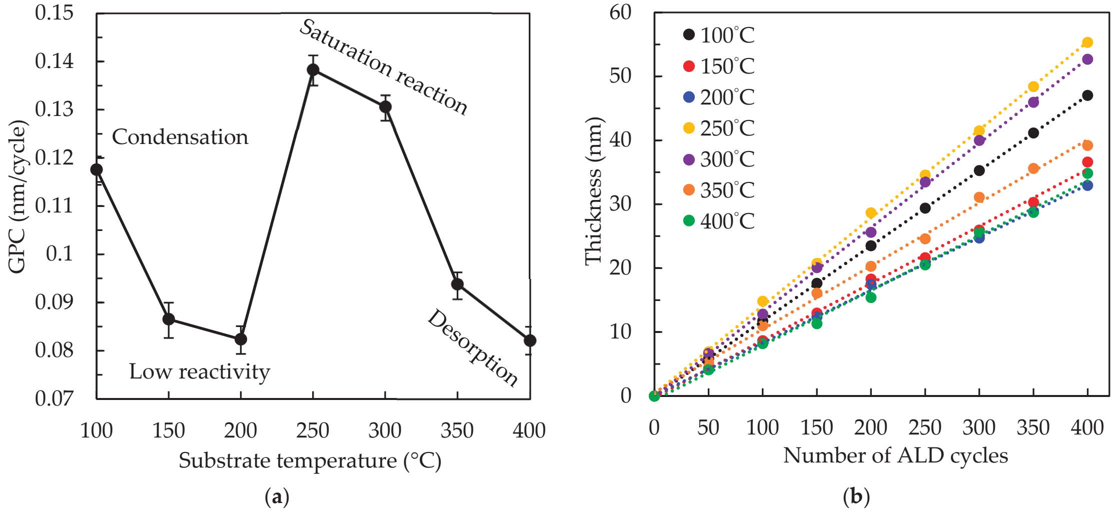

Figure 2. (**a**) The substrate temperature-dependent growth per cycle (GPC) of PEALD SnO_x films and (**b**) its trend line of corresponding thickness at each GPC.

3.2. Chemical and Electronic State of the Sn and O

Figure 3a shows the XPS full-side spectra for the films deposited at different temperatures. All the peaks are labeled and hydrogen is not detectable in XPS, while nitrogen and carbon may be contained in the films, but only in low amounts. The nitrogen content of around 2.5 at.% at 100 and 150 °C results from the unreacted ligands of TDMA-Sn, possibly due to the low reactivity at low substrate temperatures. At higher substrate temperatures (>200 °C), the nitrogen content is as low as around 0.5 at.%. In particular, Sn $3d_{3/2}$ and $3d_{5/2}$ peak at ~495.6 and~487.0 eV [37], respectively, and the O 1s peak at ~530.7 eV is commonly used for further analysis. In Figure 3b, showing the high-resolution Sn 3d peaks, the peak position is slightly different among the samples with different substrate temperatures. This is related to the Sn^{4+} and Sn^{2+} components, e.g., at respectively 487.5 eV and at 486.4 eV for the Sn5/2 peaks [38]. The Sn^{4+} and Sn^{2+} components indicate the coexistence of the SnO_2 and the metastable Sn oxide (such as Sn_3O_4). This is also supported by the O 1s spectra illustrated in Figure 3c. The spectra are deconvoluted into three peaks at 530.0 eV, associated with the lattice oxygen bonded to Sn^{2+} (O_L–Sn^{2+}); 531 ± 0.1 eV, to the lattice oxygen bonded to Sn^{4+} (O_L–Sn^{4+}); and 532 ± 0.1 eV to oxygen-deficient regions in oxides [24,39,40]. The ratio of each oxygen component to the total is calculated and shown in Figure 3d. At low temperatures (100–200 °C) the O_L–Sn^{2+} area ratio decreases from 20.07% to the lowest of 15.23%, and the oxygen vacancy (O_V) defects proportion increases from 10.25% to the highest of 12.62%, primarily due to the precursor chemisorption dominating at 200 °C.

The maximum 22.57% O_L–Sn^{2+} area ratio and the minimum 3.15% O_V proportion at 300 °C are observed. This suppression of O_V defects is mainly due to the best decomposition of the precursor at 300°C. Besides, the O_V defects proportion increases to 7.61% at 400 °C due to the out-diffusion of the oxygen atoms from SnO_2 films. It is deduced that at higher substrate temperatures, the SnO_2 decomposes thermally and oxygen breaks bonds between itself and metal and diffuses towards the film surface. The oxygen then leaves the film as O_2, and it is possible that a small amount of oxygen leaves the film as CO_2. The atomic ratios of elemental compositions, including O, Sn, and nitrogen (N), as a function of substrate temperature, are shown in Figure 3e. Notably, the high N ratio of ~2.5% at 100 °C and 150 °C dramatically decreases to ~0.5% in the range of 200–400 °C, demonstrating that the precursors are decomposed above 200°C. To analyze the stoichiometric SnO_x films, the O to Sn ratio values ($R_{O/Sn}$) are further calculated at different substrate temperatures. The $R_{O/Sn}$

of 1.517 at 100 °C increases to 1.559 and 1.645 at 150 °C and 200 °C, respectively. Then, the improved $R_{O/Sn}$ is obtained as 1.709 at 250 °C and 1.736 at 300 °C. The excessively high temperatures (350 °C and 400 °C) show a slightly decreased $R_{O/Sn}$ of 1.725 and 1.723, respectively. These results are similar to a few studies [37].

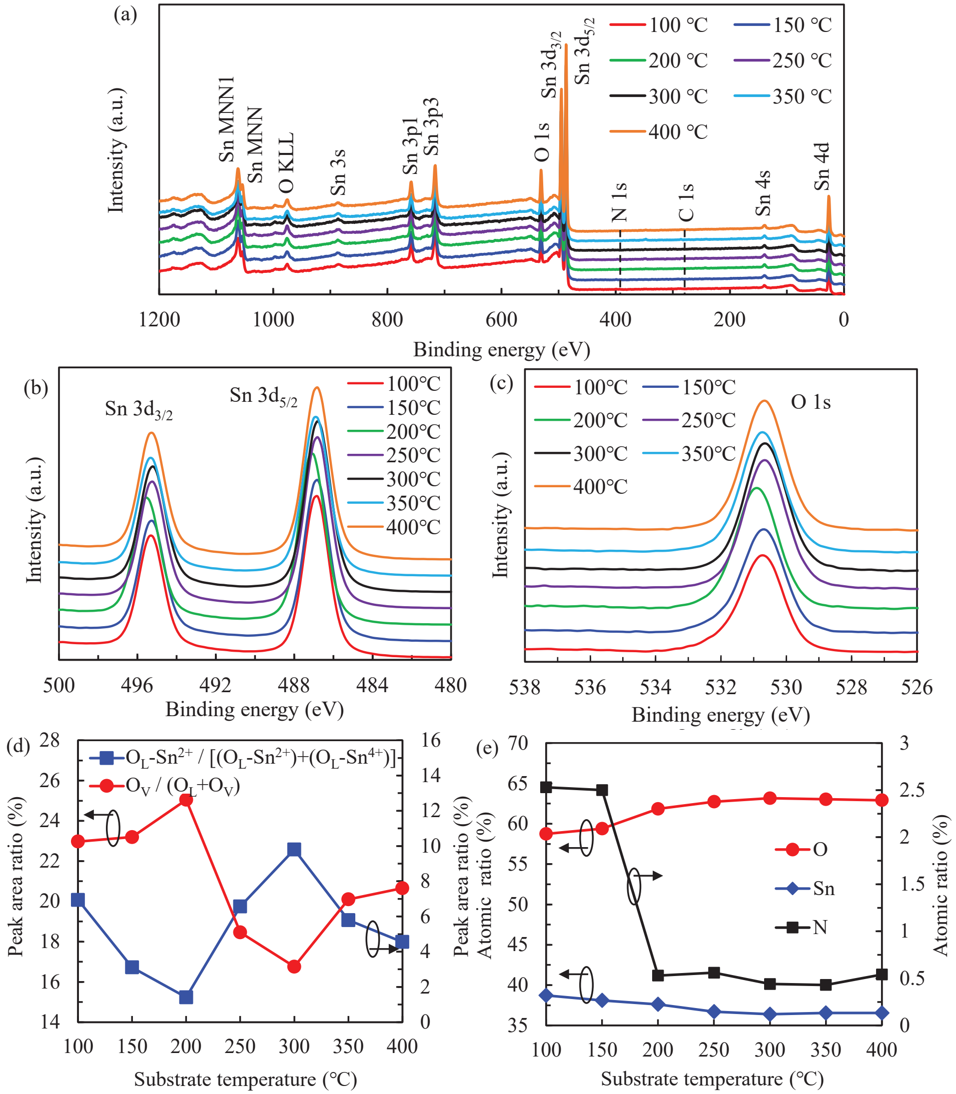

Figure 3. (**a**) XPS spectrums for the PEALD SnO_x films deposited at substrate temperatures from 100 and 400 °C. The spectra of (**b**) Sn 3d and (**c**) O 1s core level with (**d**) the peak area ratio of O_L–Sn^{2+}/[(O_L–Sn^{2+}) + (O_L–Sn^{4+})] and O_V/(O_L + O_V), and (**e**) the atomic ratio of O, Sn, and N elements.

3.3. Structural Properties of the SnO_x film

Figure 4a illustrates the XRD patterns of PEALD SnO_x films deposited at different substrate temperatures. Based on the JCPDS card (no. 41-1445), the strong peaks at 26.7°, 38.4°, and 52.1° are ascribed to (110), (200), and (211) orientations of the SnO_2 tetragonal rutile structure, respectively [24,25,41]. The weak peaks at 34.2°, 53.1°, and 62.4° correspond to (101), (220), and (310) orientations, respectively [27]. The amorphous structure of films deposited at below 200 °C is clearly observed. The reason is the low reactivity of precursor and precursor condensation induced by the low substrate temperature. With the increasing substrate temperatures, a polycrystalline SnO_2 is observed. A (110) preferred orientation is detected with the highest intensity variability when the substrate temperature is in the range of 250–400 °C. The intensity of (110) orientation increases at medium temperature (250–300 °C) due to the self-limiting growth and then decreases at higher substrate temperature (350–400 °C), owing to the decomposition and desorption of the precursor. The intensity variation of diffraction peaks indicates the consistent variation of full width at half maximum (FWHM). Figure 4b shows the FWHM variation of the preferential (110) orientation and the average crystallite size (D) of films estimated by the Scherrer function as Equation (5) [42]:

$$D = \kappa\lambda/(\beta\cos\theta), \tag{5}$$

where the $\kappa = 0.9$ is the Scherrer constant, λ is the wavelength of the X-ray sources, β is the FWHM value, and θ as Bragg angle is the peak position of the (110) orientation. The lowest FWHM value of 0.87° at 300 °C corresponds to the largest average crystallite size. Then, the FWHM value increases with increasing substrate temperature from 300 °C to 350 °C, indicating the decreased average crystallite size from 13.42 to 9.06 nm. The reason is attributed to the fact that excessively high substrate temperature above 300 °C causes the non-ideal deposition induced by severe precursor desorption and decomposition. It is observed that the diffraction peaks slightly shift with the increasing substrate temperature, suggesting a lattice expansion or contraction. For example, the peak position shifts from 26.56° at 250 °C to 26.74° at 300 °C. Similarly, the peak position then shifts toward a lower angle to 26.42° at 400 °C. The interplanar distance ($d-$spacing) is calculated as shown in Figure 4c by the Bragg formula [43]:

$$2d\sin\theta = n_d\lambda, \tag{6}$$

where n_d is the order of diffraction, and d is the dspacing. With increasing substrate temperatures from 250 °C to 400 °C, the dspacings of SnO_x films are around 3.356, 3.334, 3.349, and 3.373 Å, respectively. The standard dspacing value of pure SnO_2 is 3.347 Å. The decreased dspacing when increasing the substrate temperature from 250 to 300 °C is attributed to the decrease in oxygen vacancy defects as observed from the XPS results, causing the lattice contraction of SnO_x films [44]. In the study reported by Santara et al. [45], the oxygen interstitials (${O_i}^{2+}$) and metal interstitials may attract each other and cause lattice contraction. Thus, another possible reason for the lattice contraction observed in this study can be due to the electrostatic attraction between ${O_i}^{2+}$ and tin interstitials (${Sn_i}^{4+}$). In contrast, the increased d−spacings at 350–400 °C are due to the generated oxygen vacancy defects. The O−Sn bonds in the vicinity of oxygen-deficient regions are relaxed, leading to the lattice expansion of SnO_x films. Besides, the nearest-neighbor Sn atoms move outward from the vacancy to strengthen their neighboring bonds of the remaining oxygen lattice. Although the nearest-neighbor oxygen atoms may move inward to fill the site of oxygen vacancy defects, the net outward movement of Sn atoms is higher than the net inward movement of oxygen atoms, resulting in the lattice expansion. Other microstructural parameters, such as micro-strain (ε) and dislocation density (δ), are estimated as:

$$\boldsymbol{\varepsilon} = \beta/4\tan\theta, \tag{7}$$

$$\delta = 1/D^2, \tag{8}$$

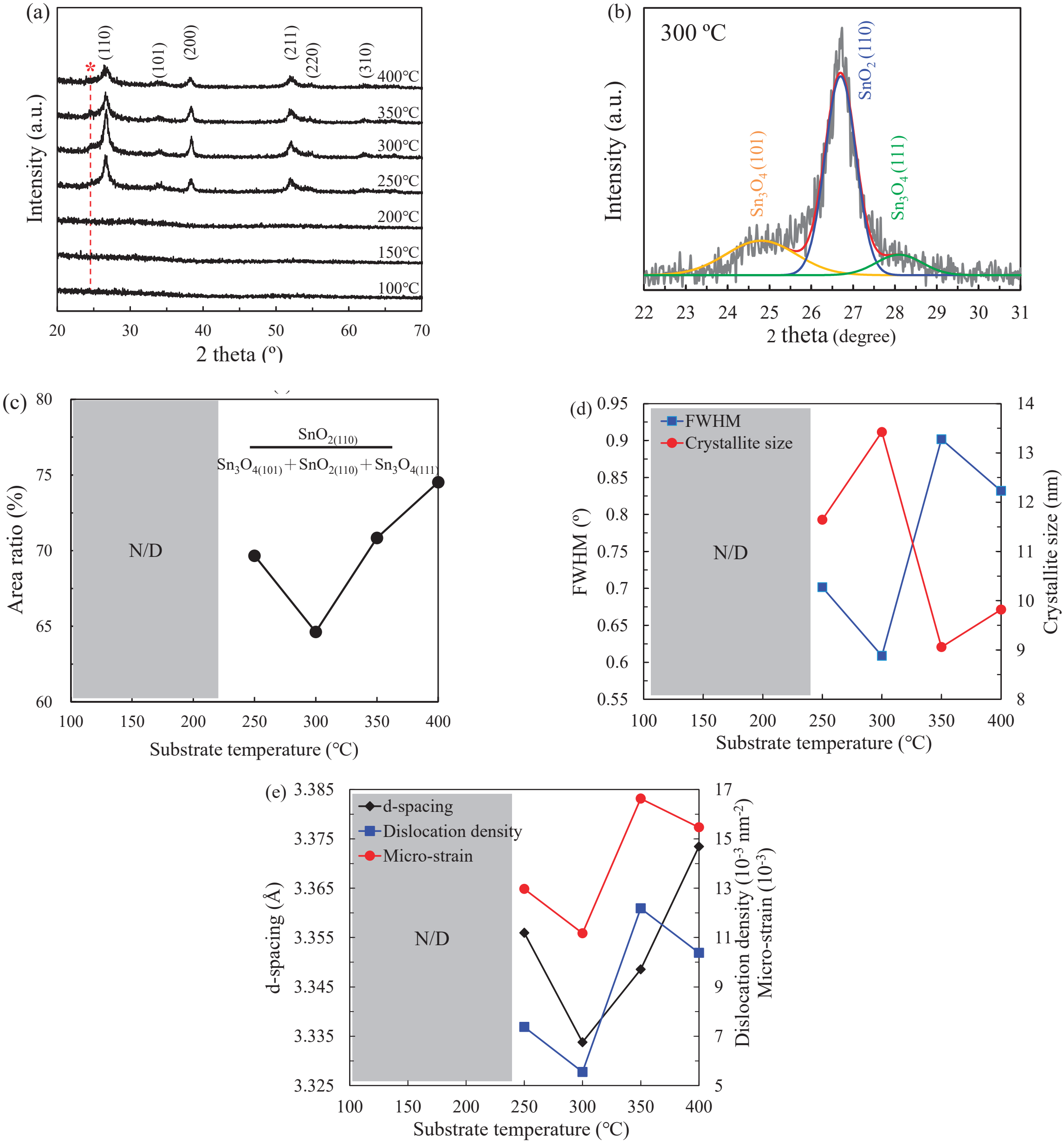

Figure 4. (**a**) XRD patterns of PEALD SnO$_x$ films deposited at substrate temperatures where the red star mark with red dash line presents another (101) orientation of Sn$_3$O$_4$. (**b**) The variation for the FWHM of the preferential (110) orientation and the average crystallite size, showing (**c**) the dependence of the average dspacing of (110) planes, the dislocation density, and the micro-strain value. (**d**) The deconvolution results of the (110) orientation deposited at 300 °C in the 2 theta of 22–31°. (**e**) The variation of the area ration of $(110)_{SnO2}$ to $[(110)_{SnO2} + (101)_{Sn3O4} + (111)_{Sn3O4}]$.

Accordingly, the film at the 300 °C substrate temperature obtains the lowest value of δ and ε. The small δ obtained at 300 °C is the number of defects measured in the crystals [43] and the released ε at 250–300 °C is mainly due to the lattice contraction. The enhanced ε at 300–350 °C can be described by the increased vacancy formation energy from external strain [46].

However, beyond the substrate temperature of 300 °C, we observe that the (110) SnO_2 peaks are not symmetrical, possibly implying the existence of other phases. For example, a diffraction peak near 25° is observed as a star, marked in Figure 4a, resulting from the oxygen-deficient SnO_x [27]. To identify whether there are other hidden peaks, the (110) peaks are deconvoluted in Figure 4d, where two shoulder peaks at 24.8° and 28.1° as (101) and (111) triclinic Sn_3O_4 phases are identified (JCPDS#16-0737) [47,48]. This means that the SnO_x films have SnO_2 as the major phase and Sn_3O_4 as the minor phase. Moreover, the triclinic Sn_3O_4 as an intermediate oxide during the phase transformation of SnO_2 is known as the oxygen-deficient SnO_x phase [49]. The $(110)_{SnO2}/[(110)_{SnO2} + (101)_{Sn3O4} + (111)_{Sn3O4}]$ peak area ratio for the different substrate temperatures is further shown in Figure 4e. The proportion of (110) orientation firstly decreases to the lowest value of 64.62% at 300 °C and then increases again at increasing substrate temperatures. This result also supports that the 300 °C substrate temperature is a critical temperature where the deposition mode changes from saturation growth to precursor decomposition or desorption.

AFM with a scanning area of 5×5 μm^2 is used to analyze the topographic and stereoscopic surface morphologies of PEALD SnO_x, films as shown in Figure 5. The films grown at 100–200 °C show a smooth microstructure with a root-mean-square (Rq) of 0.16–0.23 nm, consistent with the amorphous SnO_x films at this temperature range. The film deposited at 250 °C obtains the highest Rq value of 1.65 nm. The Rq reduces to 0.34 nm when the substrate temperature increases to 400 °C. Compared to the Rq value of SnO_x films deposited by spray pyrolysis (11.6 nm) [50] and sputtering (17.72 nm) [51], the PEALD SnO_x films provide a smoother surface that is beneficial for many applications.

The top-view FESEM images of the films are observed on the right-hand side of Figure 5. Flat and featureless morphologies of SnO_x films are observed without noticeable grain boundaries at the substrate temperature of 100–200 °C. This agrees with the amorphous structure of the films. At 250 °C, distinct clusters can be observed due to the large SnO_x grains, and a clear grain structure is visible at 300 °C; however, these obvious grain boundaries gradually disappear at the higher substrate temperatures of 350 °C and 400 °C, attributed to the decreased grain size.

Figure 6 shows the cross-sectional TEM images of SnO_x films. It is unexpected that crystallization is observed at 100 °C, shown in Figure 6a, as this is inconsistent with the XRD result. One reasonable explanation is that the amorphous structure recrystallizes by the ion beam of the TEM measurement.

In Figure 6b, the 41.49 nm-thick SnO_x film deposited at 250 °C reveals well-defined lattice fringes with a dspacing of 3.35 Å corresponding to the (110) SnO_2 tetragonal rutile structure. The film deposited at 400 °C shown in Figure 6c shows lattice fringes of 2.3 and 3.35 Å dspacings corresponding to SnO_2 (200) and (110) planes. At the Si/SnO_x interface, the silicon oxide layer is presented, and its thickness decreases from 3.9 (100 °C) to 1.5 nm (400 °C). The presence of the interfacial layer is similar to our previous research of ALD HfO_2 or Al_2O_3 [52,53], and thus the reason is believed to be attributed to the reaction between oxygen plasma radicals and the Si wafer in the first few cycles.

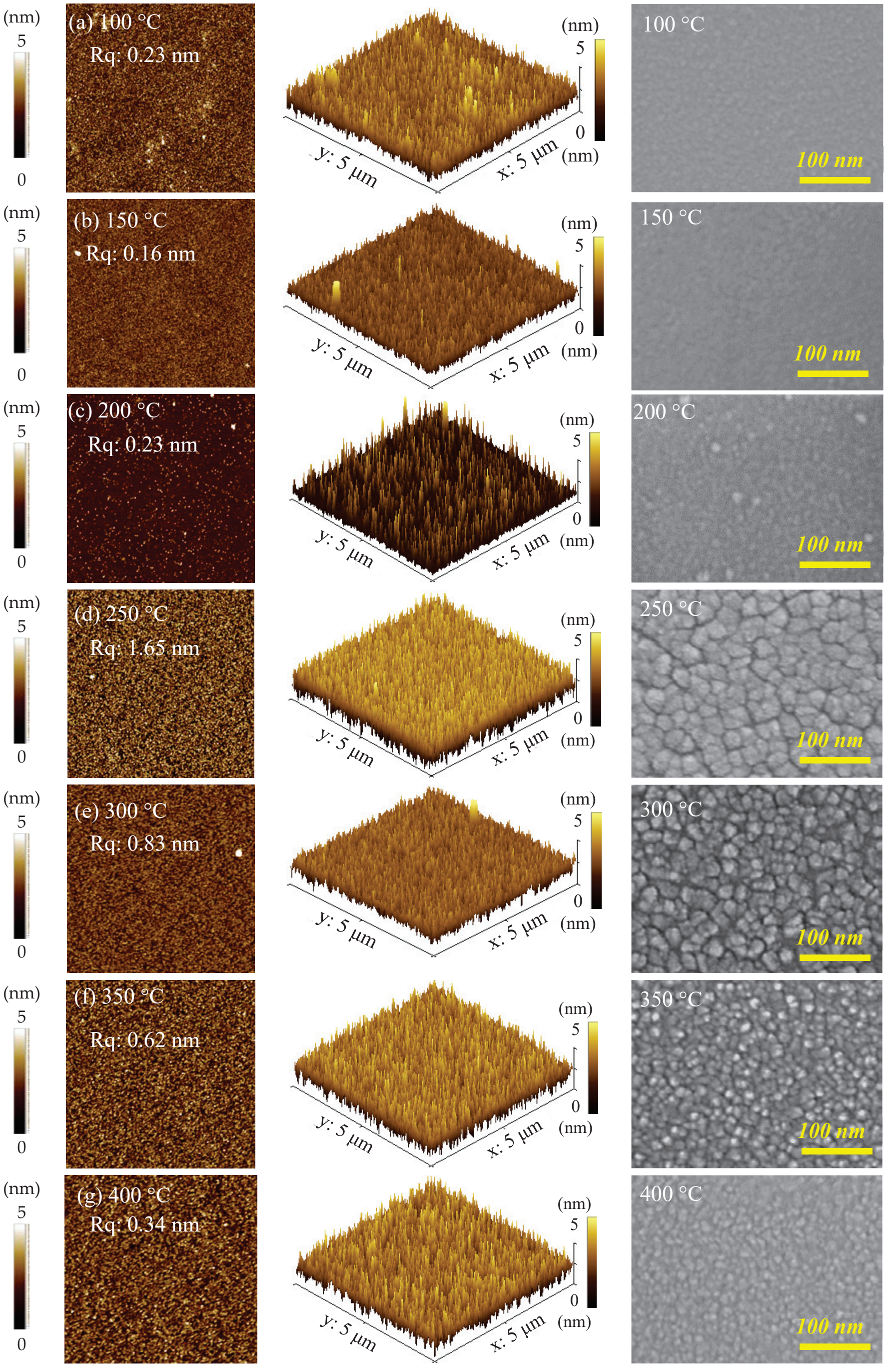

Figure 5. Topographic and stereoscopic surface morphologies of AFM with a scanning area of 5 × 5 μm^2 and top-view images of FESEM for PEALD SnO_x films deposited at various substrate temperatures from (**a**–**g**) 100 °C to 400 °C on a Si wafer.

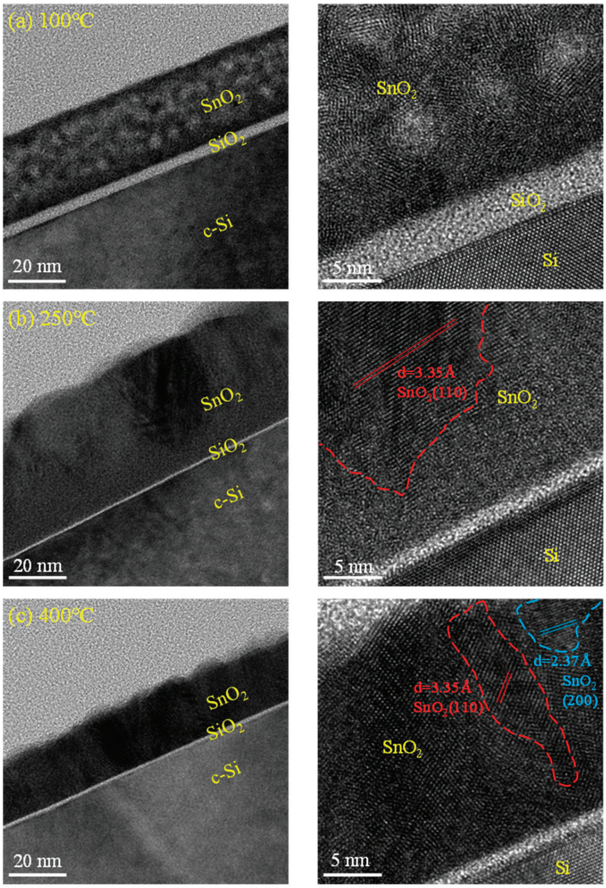

Figure 6. The TEM results of SnO_x films deposited at different substrate temperatures of (**a**) 100 °C, (**b**) 250 °C, and (**c**) 400 °C, including cross-sectional and high-resolution images.

3.4. Photoelectric Properties of the SnO_x film

Figure 7a shows the optical spectra of PEALD SnO_x films deposited at different substrate temperatures. The variation of the transmittance spectrum is inverse to that of reflectance. All samples have a transmittance of approximately 80% to 90% and a reflectance of approximately 10% to 15% in the wavelength range of 400–900 nm. The decrease in transmittance at the short wavelength of around 400 nm for the films is attributed to the absorption caused by the band-to-band transition. In addition, the absorption coefficient (α) is determined by the Beer–Lambert law equation [31,33]:

$$\alpha = 4\pi k/\lambda, \tag{9}$$

where λ is the wavelength and k is the extinction coefficient determined from ellipsometer measurements. The absorption coefficients are further used for the optical band gap determination using Tauc's plot method [54]:

$$(\alpha h\nu)^2 = A\cdot(h\nu - Eg), \tag{10}$$

where $h\nu$ is the photon energy and A is the proportionality constant [55]. As shown in Figure 7c, Eg with the V-shaped trend on the substrate temperature is observed. With the increasing substrate temperatures, the SnO_x film obtains the narrowest Eg of 3.52 eV at 200 °C, possibly due to the introduction of a shallow donor energy level of oxygen vacancies (O_V) under the conduction band [56,57]. Another reason is the smaller excited energy induced by the short-range ordered crystallite in the amorphous SnO_x crystal, leading to the increase in the carrier concentration [58,59]. Furthermore, the enhancement of Eg to 3.78 eV is obtained at 250°C, mainly owing to the presence of polycrystalline, as evidenced in XRD results. The Eg increases slightly from 3.78 to 3.85 eV at 250–300 °C and then maintains 3.83 eV at 350 °C and 400 °C.

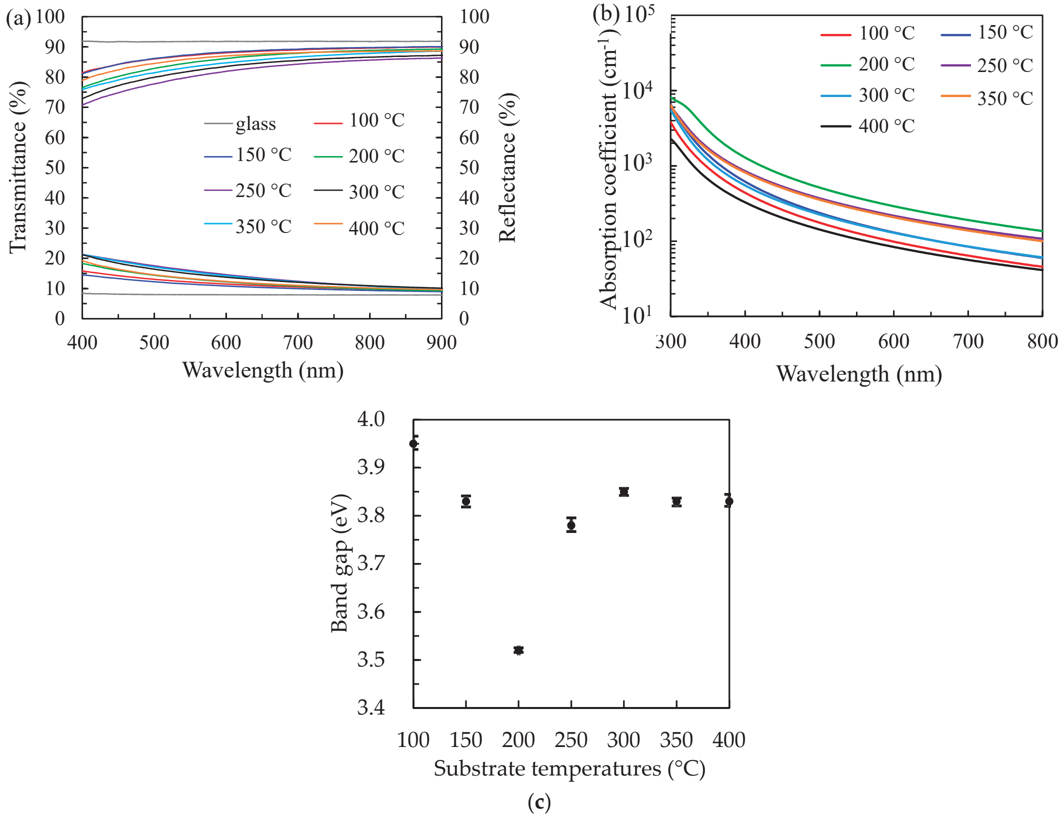

Figure 7. (**a**) The optical transmittance with reflectance and (**b**) absorption coefficient spectrums to extract (**c**) the band gap values for the PEALD SnO_x films with increasing substrate temperatures from 100 to 400 °C.

Figure 8 demonstrates the wavelength-dependent refractive index of the PEALD SnO_x films with different substrate temperatures. The refractive index is low for the samples at 100–200 °C, then varies closely at 250–350 °C, and reaches the highest value at 400 °C. This variation of the refractive index can be a reflection of the change in the film density, since they are closely related [25]. Increasing the substrate temperature from 100 to 200 °C causes the increase in packing density in the amorphous structure and the change in the chemical composition of the films (especially nitrogen proportion), hence affecting the refractive index. Meanwhile, the variation of refractive index at high substrate temperatures (250–400 °C) also corresponds to the crystallinity variation in the polycrystalline structure.

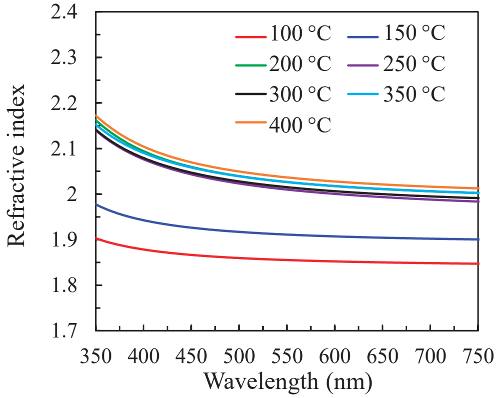

Figure 8. The wavelength-dependent refractive index of PEALD SnO_x films with increasing substrate temperatures from 100 to 400 °C.

As a transparent conductive material, the electrical properties are an important indicator for PEALD SnO_x films. As a result, the carrier concentration (*Ne*), mobility (μ), and resistivity (ρ) of PEALD SnO_x films were determined by Hall-effect measurements. In Figure 9a, the films deposited at 100°C obtained the lowest *Ne* of 1.17×10^{20} cm^{-3} and μ of 2.44 cm^2/Vs. With the increasing substrate temperatures, the *Ne* slightly increases to 1.91×10^{20} cm^{-3} at 150 °C and sharply sweeps upward to the highest 8.22×10^{20} cm^{-3} at 200 °C. After that, we observed that the *Ne* descends to 2.84×10^{20} cm^{-3} at 250 °C and even 2.18×10^{20} cm^{-3} at 300 °C. The possible reason for this trend is attributed to the variation of crystallization and the proportion of oxygen vacancies, where the change presents similar consistency to Figure 3d. Upon increasing the substrate temperature to 350 °C, the increased proportion of oxygen vacancies becomes the main reason for the suddenly increased *Ne* to 4.27×10^{20} cm^{-3}. However, we have noticed that, primarily, the μ gradually ascends with the increasing substrate temperature from 100 °C to 300 °C, maybe owing to an enhancement of the crystallinity of the films and thus electrical continuity in the lateral direction [28]. Higher substrate temperatures cause the decreased μ at 350 °C and 400 °C due to the variation of crystallinity and crystallite size in SEM results, resulting from the phase transition during the deposition. Figure 9b shows the high ρ values of SnO_x films below 150°C determined by the *Ne* and the low μ. Low ρ values at 200–400 °C are shown in the range of 1.5 to 2.6×10^{-3} Ω·cm.

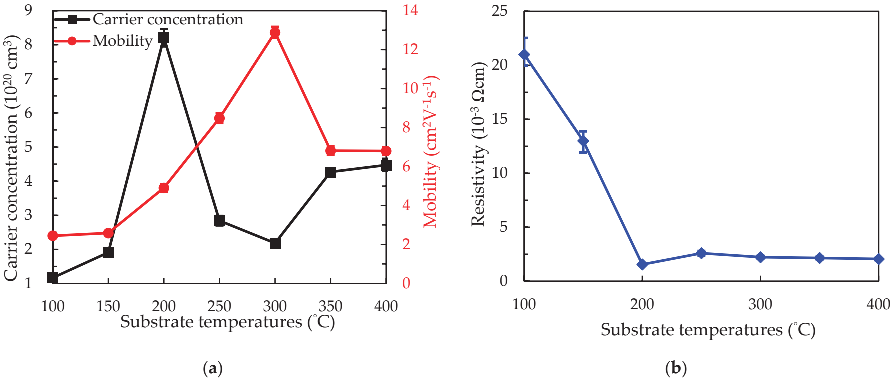

(**a**) (**b**)

Figure 9. Hall-effect measurement for the (**a**) carrier concentration (*Ne*) accompanied by the mobility (μ) and (**b**) resistivity (ρ) of SnO_x films deposited at various substrate temperatures at 100–400 °C. Five samples were measured in each series, and standard deviations are included.

4. Conclusions

In this work, PEALD SnO_x films were prepared at various substrate temperatures, and their optical, physical, and chemical properties were further studied. The deposition mechanisms associated with three temperature ranges are clearly demonstrated. The precursor condensation is observed at low substrate temperatures (100–200 °C), forming the amorphous structure with the highest carrier concentration of 8.22×10^{20} cm^{-3}. The surface reaction at 200 °C changes from physisorption to chemisorption-dominated. Meanwhile, the precursors are largely decomposed to participate in the reaction due to the dramatic decrease in the N ratio. With the increasing substrate temperatures, the PEALD SnO_x films prepared at 250–400 °C show the coexistence of SnO_2 and Sn_3O_4 phases. The lowest (110) SnO_2 ratio is obtained at 300 °C. However, the film prepared at the substrate temperature of 300 °C has the highest $O_L{-}Sn^{2+}$ and the lowest O_V ratios. The excessive 350 °C and 400 °C initiated severe precursor desorption, leading to a decrease in the GPC and mobility. The ratio of O to Sn at 300 °C is further estimated to be ~1.74 as a preferred parameter for depositing high-quality PEALD SnO_x films.

Author Contributions: Conceptualization, P.-H.H. and S.-Y.L.; formal analysis, P.-H.H., Z.-X.Z., C.-H.H., W.-Y.W., S.-L.O., C.-J.H., D.-S.W., S.-Y.L. and W.-Z.Z.; funding acquisition, P.-H.H., C.-H.H. and S.-Y.L.; investigation, P.-H.H., Z.-X.Z. and S.-Y.L.; methodology, Z.-X.Z.; writing—original draft, P.-H.H. and Z.-X.Z.; writing—review and editing, P.-H.H. and S.-Y.L. All authors have read and agreed to the published version of the manuscript.

Funding: This research was funded by the Scientific and Technological Project in Xiamen, grant number 3502ZCQ20191002; the Scientific Research Projects of Xiamen University of Technology, grant numbers 405011904, 40199029, YKJ19001R, HK-HX210106, HK-HX201243, and XPDKQ19006; the Natural Science Foundation of Fujian Province, grant numbers 2020H0025 and 2020J05151; the Education Department of Fujian Province grant number JAT190300; and the Scientific Research Projects of Jimei University, grant number ZQ2019032.

Institutional Review Board Statement: Not applicable.

Informed Consent Statement: Not applicable.

Data Availability Statement: Not applicable.

Conflicts of Interest: The authors declare no conflict of interest.

References

1. Ellmer, K. Past Achievements and Future Challenges in the Development of Optically Transparent Electrodes. *Nat. Photon.* **2012**, *6*, 809–817. [CrossRef]
2. Battaglia, C.; Cuevas, A.; De Wolf, S. High-Efficiency Crystalline Silicon Solar Cells: Status and Perspectives. *Energy Environ. Sci.* **2016**, *9*, 1552–1576. [CrossRef]
3. So, F.; Kido, J.; Burrows, P. Organic Light-Emitting Devices for Solid-State Lighting. *MRS Bull.* **2008**, *33*, 7. [CrossRef]
4. Klein, A. Transparent Conducting Oxides: Electronic Structure-Property Relationship from Photoelectron Spectroscopy with in Situ Sample Preparation. *J. Am. Ceram. Soc.* **2013**, *96*, 331–345. [CrossRef]
5. Granqvist, C.G.; Hultåker, A. Transparent and Conducting ITO Films: New Developments and Applications. *Thin Solid Films* **2002**, *411*, 1–5. [CrossRef]
6. Gorley, P.M.; Khomyak, V.V.; Bilichuk, S.V.; Orletsky, I.G.; Horley, P.P.; Grechko, V.O. SnO_2 Films: Formation, Electrical and Optical Properties. *Mater. Sci. Eng. B* **2005**, *118*, 160–163. [CrossRef]
7. Zhang, Y.; Du, G.; Liu, D.; Wang, X.; Ma, Y.; Wang, J.; Yin, J.; Yang, X.; Hou, X.; Yang, S. Crystal Growth of Undoped ZnO Films on Si Substrates under Different Sputtering Conditions. *J. Cryst. Growth* **2002**, *243*, 439–443. [CrossRef]
8. Lee, K.E.; Wang, M.; Kim, E.J.; Hahn, S.H. Structural, Electrical and Optical Properties of Sol–Gel AZO Thin Films. *Curre. Appl. Phys.* **2009**, *9*, 683–687. [CrossRef]
9. Brezesinski, T.; Wang, J.; Polleux, J.; Dunn, B.; Tolbert, S.H. Templated Nanocrystal-Based Porous TiO_2 Films for Next-Generation Electrochemical Capacitors. *J. Am. Chem. Soc.* **2009**, *131*, 1802–1809. [CrossRef]
10. Park, B.-E.; Park, J.; Lee, S.; Lee, S.; Kim, W.-H.; Kim, H. Phase-Controlled Synthesis of SnO_x Thin Films by Atomic Layer Deposition and Post-Treatment. *Appl. Surf. Sci.* **2019**, *480*, 472–477. [CrossRef]
11. Bolotov, V.V.; Korusenko, P.M.; Nesov, S.N.; Povoroznyuk, S.N.; Roslikov, V.E.; Kurdyukova, E.A.; Sten'kin, Y.A.; Shelyagin, R.V.; Knyazev, E.V.; Kan, V.E.; et al. Nanocomposite Por-Si/SnO_x Layers Formation for Gas Microsensors. *Mater. Sci. Eng. B* **2012**, *177*, 1–7. [CrossRef]

12. Song, J.; Zheng, E.; Bian, J.; Wang, X.-F.; Tian, W.; Sanehira, Y.; Miyasaka, T. Low-Temperature SnO_2-Based Electron Selective Contact for Efficient and Stable Perovskite Solar Cells. *J. Mater. Chem. A* **2015**, *3*, 10837–10844. [CrossRef]
13. Tao, H.; Wang, H.; Bai, Y.; Long, H.; Zhao, H.; Fu, Q.; Ma, Z. Effects of Sputtering Power of SnO_2 Electron Selective Layer on Perovskite Solar Cells. *J. Mater. Sci. Mater. Electron.* **2019**, *30*, 12036–12043. [CrossRef]
14. Park, M.; Song, J.; An, M.; Lim, J.; Lee, C.; Roh, J.; Lee, D. Colloidal Quantum Dot Light-Emitting Diodes Employing Solution-Processable Tin Dioxide Nanoparticles in an Electron Transport Layer. *RSC Adv.* **2020**, *10*, 8261–8265. [CrossRef]
15. Alfonso, C.; Charaï, A.; Armigliato, A.; Narducci, D. Transmission Electron Microscopy Investigation of Tin Sub-oxide Nucleation upon SnO_2 Deposition on Silicon. *Appl. Phys. Lett.* **1996**, *68*, 1207–1208. [CrossRef]
16. Zeng, W.; Liu, Y.; Mei, J.; Tang, C.; Luo, K.; Li, S.; Zhan, H.; He, Z. Hierarchical SnO_2–Sn_3O_4 Heterostructural Gas Sensor with High Sensitivity and Selectivity to NO_2. *Sens. Actuators B Chem.* **2019**, *301*, 127010. [CrossRef]
17. Hassan, M.A.M.; Salem, E.T.; Mohammed, N.J.; Agool, I.R. Tin Dioxide Nanostructure Using Rapid Thermal Oxidation Method and Hydrothermal Synthesis of CuO-SnO_2-ZnO Nano Composite Oxides. *Int. J. Nanosci. Nanoeng.* **2014**, *1*, 22.
18. Maleki, M.; Rozati, S.M. An Economic CVD Technique for Pure SnO_2 Thin Films Deposition: Temperature Effects. *Bull. Mater. Sci.* **2013**, *36*, 217–221. [CrossRef]
19. Kwoka, M.; Ottaviano, L.; Passacantando, M.; Santucci, S.; Czempik, G.; Szuber, J. XPS Study of the Surface Chemistry of L-CVD SnO_2 Thin Films after Oxidation. *Thin Solid Films* **2005**, *490*, 36–42. [CrossRef]
20. Huang, H.; Tan, O.K.; Lee, Y.C.; Tse, M.S. Preparation and Characterization of Nanocrystalline SnO_2 Thin Films by PECVD. *J. Cryst. Growth* **2006**, *288*, 70–74. [CrossRef]
21. Sberveglieri, G.; Faglia, G.; Groppelli, S.; Nelli, P.; Taroni, A. A Novel PVD Technique for the Preparation of SnO_2 Thin Films as C_2H_5OH Sensors. *Sens. Actuators B Chem.* **1992**, *7*, 721–726. [CrossRef]
22. Leskelä, M.; Ritala, M. Atomic Layer Deposition (ALD): From Precursors to Thin Film Structures. *Thin Solid Films* **2002**, *409*, 138–146. [CrossRef]
23. Parsons, G.N.; George, S.M.; Knez, M. Progress and Future Directions for Atomic Layer Deposition and ALD-Based Chemistry. *MRS Bull.* **2011**, *36*, 865–871. [CrossRef]
24. Lee, B.K.; Jung, E.; Kim, S.H.; Moon, D.C.; Lee, S.S.; Park, B.K.; Hwang, J.H.; Chung, T.-M.; Kim, C.G.; An, K.-S. Physical/Chemical Properties of Tin Oxide Thin Film Transistors Prepared Using Plasma-Enhanced Atomic Layer Deposition. *Mater. Res. Bull.* **2012**, *47*, 3052–3055. [CrossRef]
25. Kuang, Y.; Zardetto, V.; van Gils, R.; Karwal, S.; Koushik, D.; Verheijen, M.A.; Black, L.E.; Weijtens, C.; Veenstra, S.; Andriessen, R.; et al. Low-Temperature Plasma-Assisted Atomic-Layer-Deposited SnO_2 as an Electron Transport Layer in Planar Perovskite Solar Cells. *ACS Appl. Mater. Interfaces* **2018**, *10*, 30367–30378. [CrossRef]
26. Chistiakova, G.; Mews, M.; Wilks, R.G.; Bär, M.; Korte, L. In-System Photoelectron Spectroscopy Study of Tin Oxide Layers Produced from Tetrakis(Dimethylamino)Tin by Plasma Enhanced Atomic Layer Deposition. *J. Vac. Sci. Technol. A Vac. Surf. Films* **2018**, *36*, 02D401. [CrossRef]
27. Kim, H.Y.; Nam, J.H.; George, S.M.; Park, J.-S.; Park, B.K.; Kim, G.H.; Jeon, D.J.; Chung, T.-M.; Han, J.H. Phase-Controlled SnO_2 and SnO Growth by Atomic Layer Deposition Using Bis(N-Ethoxy-2,2-Dimethyl Propanamido)Tin Precursor. *Ceram. Int.* **2019**, *45*, 5124–5132. [CrossRef]
28. Choi, D.; Maeng, W.J.; Park, J.-S. The Conducting Tin Oxide Thin Films Deposited via Atomic Layer Deposition Using Tetrakis-Dimethylamino Tin and Peroxide for Transparent Flexible Electronics. *Appl. Surf. Sci.* **2014**, *313*, 585–590. [CrossRef]
29. Elam, J.W.; Baker, D.A.; Hryn, A.J.; Martinson, A.B.F.; Pellin, M.J.; Hupp, J.T. Atomic Layer Deposition of Tin Oxide Films Using Tetrakis(Dimethylamino) Tin. *J. Vac. Sci. Technol. A Vac. Surf. Films* **2008**, *26*, 244–252. [CrossRef]
30. Lee, D.-K.; Wan, Z.; Bae, J.-S.; Lee, H.-B.-R.; Ahn, J.-H.; Kim, S.-D.; Kim, J.; Kwon, S.-H. Plasma-Enhanced Atomic Layer Deposition of SnO_2 Thin Films Using $SnCl_4$ and O_2 Plasma. *Mater. Lett.* **2016**, *166*, 163–166. [CrossRef]
31. Mullings, M.N.; Hägglund, C.; Bent, S.F. Tin Oxide Atomic Layer Deposition from Tetrakis(Dimethylamino)Tin and Water. *J. Vac. Sci. Technol. A Vac. Surf. Films* **2013**, *31*, 061503. [CrossRef]
32. Tanskanen, J.T.; Bent, S.F. Insights into the Surface Chemistry of Tin Oxide Atomic Layer Deposition from Quantum Chemical Calculations. *J. Phys. Chem. C* **2013**, *117*, 19056–19062. [CrossRef]
33. Hoffmann, L.; Theirich, D.; Schlamm, D.; Hasselmann, T.; Pack, S.; Brinkmann, K.O.; Rogalla, D.; Peters, S.; Räupke, A.; Gargouri, H.; et al. Atmospheric Pressure Plasma Enhanced Spatial Atomic Layer Deposition of SnO_x as Conductive Gas Diffusion Barrier. *J. Vac. Sci. Technol. A Vac. Surf. Films* **2018**, *36*, 01A112. [CrossRef]
34. George, S.M. Atomic Layer Deposition: An Overview. *Chem. Rev.* **2010**, *110*, 111–131. [CrossRef] [PubMed]
35. Choi, D.; Park, J.-S. Highly Conductive SnO_2 Thin Films Deposited by Atomic Layer Deposition Using Tetrakis-Dimethyl-Amine-Tin Precursor and Ozone Reactant. *Surf. Coat. Technol.* **2014**, *259*, 238–243. [CrossRef]
36. Xu, L.; Zhang, Z.; Yang, L.; Yang, J.; Wang, P.; Gao, G.; Sun, C.; Ralchenko, V.; Zhu, J. Comparison of Thermal, Plasma-Enhanced and Layer by Layer Ar Plasma Treatment Atomic Layer Deposition of Tin Oxide Thin Films. *J. Cryst. Growth* **2021**, *572*, 126264. [CrossRef]
37. Hsu, C.-H.; Zhang, Z.-X.; Huang, P.-H.; Wu, W.-Y.; Ou, S.-L.; Lien, S.-Y.; Huang, C.-J.; Lee, M.-K.; Zhu, W.-Z. Effect of Plasma Power on the Structural Properties of Tin Oxide Prepared by Plasma-Enhanced Atomic Layer Deposition. *Ceram. Int.* **2021**, *47*, 8634–8641. [CrossRef]

38. Huang, P.-H.; Zhang, Z.-X.; Hsu, C.-H.; Wu, W.-Y.; Huang, C.-J.; Lien, S.-Y. Chemical Reaction and Ion Bombardment Effects of Plasma Radicals on Optoelectrical Properties of SnO_2 Thin Films via Atomic Layer Deposition. *Materials* **2021**, *14*, 690. [CrossRef]
39. Yang, Y.; Wang, Y.; Yin, S. Oxygen Vacancies Confined in SnO_2 Nanoparticles for Desirable Electronic Structure and Enhanced Visible Light Photocatalytic Activity. *Appl. Surf. Sci.* **2017**, *420*, 399–406. [CrossRef]
40. Ma, D.; Li, Y.; Zhang, P.; Lin, Z. Oxygen Vacancy Engineering in Tin(IV) Oxide Based Anode Materials toward Advanced Sodium-Ion Batteries. *ChemSusChem* **2018**, *11*, 3693–3703. [CrossRef]
41. Kumar, V.; Swart, H.C.; Gohain, M.; Bezuidenhoudt, B.C.B.; van Vuuren, A.J.; Lee, M.; Ntwaeaborwa, O.M. The Role of Neutral and Ionized Oxygen Defects in the Emission of Tin Oxide Nanocrystals for near White Light Application. *Nanotechnology* **2015**, *26*, 295703. [CrossRef] [PubMed]
42. Sapuan, S.M.; Ismail, H.; Zainudin, E.S. *Natural Fibre Reinforced Vinyl Ester and Vinyl Polymer Composites: Characterization, Properties and Applications*; Woodhead Publishing: Sawston, UK, 2018; ISBN 978-0-08-102161-3.
43. Kamble, D.L.; Harale, N.S.; Patil, V.L.; Patil, P.S.; Kadam, L.D. Characterization and NO_2 Gas Sensing Properties of Spray Pyrolyzed SnO_2 Thin Films. *J. Anal. Appl. Pyrolysis* **2017**, *127*, 38–46. [CrossRef]
44. Manh Hung, N.; Nguyen, C.V.; Arepalli, V.K.; Kim, J.; Duc Chinh, N.; Nguyen, T.D.; Seo, D.-B.; Kim, E.-T.; Kim, C.; Kim, D. Defect-Induced Gas-Sensing Properties of a Flexible SnS Sensor under UV Illumination at Room Temperature. *Sensors* **2020**, *20*, 5701. [CrossRef]
45. Santara, B.; Giri, P.K.; Imakita, K.; Fujii, M. Microscopic Origin of Lattice Contraction and Expansion in Undoped Rutile TiO_2 Nanostructures. *J. Phys. D Appl. Phys.* **2014**, *47*, 215302. [CrossRef]
46. Li, T.-H.; Li, H.-T.; Pan, J.-H. Interplay between External Strain and Oxygen Vacancies on Raman Spectra of SnO $_2$. *Chinese Phys. Lett.* **2014**, *31*, 076201. [CrossRef]
47. White, T.A.; Moreno, M.S.; Midgley, P.A. Structure Determination of the Intermediate Tin Oxide Sn_3O_4 by Precession Electron Diffraction. *Z. Krist.* **2010**, *225*, 56–66. [CrossRef]
48. Wu, J.; Xie, Y.; Du, S.; Ren, Z.; Yu, P.; Wang, X.; Wang, G.; Fu, H. Heterophase Engineering of SnO_2/Sn_3O_4 Drives Enhanced Carbon Dioxide Electrocatalytic Reduction to Formic Acid. *Sci. China Mater.* **2020**, *63*, 2314–2324. [CrossRef]
49. Zhang, F.; Lian, Y.; Gu, M.; Yu, J.; Tang, T.B. Static and Dynamic Disorder in Metastable Phases of Tin Oxide. *J. Phys. Chem. C* **2017**, *121*, 16006–16011. [CrossRef]
50. Murakami, K.; Nakajima, K.; Kaneko, S. Initial Growth of SnO_2 Thin Film on the Glass Substrate Deposited by the Spray Pyrolysis Technique. *Thin Solid Films* **2007**, *515*, 8632–8636. [CrossRef]
51. Khan, A.F.; Mehmood, M.; Rana, A.M.; Bhatti, M.T. Effect of Annealing on Electrical Resistivity of Rf-Magnetron Sputtered Nanostructured SnO_2 Thin Films. *Appl. Surface Sci.* **2009**, *255*, 8562–8565. [CrossRef]
52. Zhang, X.-Y.; Hsu, C.-H.; Lien, S.-Y.; Wu, W.-Y.; Ou, S.-L.; Chen, S.-Y.; Huang, W.; Zhu, W.-Z.; Xiong, F.-B.; Zhang, S. Temperature-Dependent HfO_2/Si Interface Structural Evolution and Its Mechanism. *Nanoscale Res. Lett.* **2019**, *14*, 83. [CrossRef] [PubMed]
53. Hsu, C.-H.; Cho, Y.-S.; Wu, W.-Y.; Lien, S.-Y.; Zhang, X.-Y.; Zhu, W.-Z.; Zhang, S.; Chen, S.-Y. Enhanced Si Passivation and PERC Solar Cell Efficiency by Atomic Layer Deposited Aluminum Oxide with Two-Step Post Annealing. *Nanoscale Res. Lett.* **2019**, *14*, 139. [CrossRef] [PubMed]
54. Sivaranjani, S.; Malathy, V.; Prince, J.J.; Subramanian, B.; Balasubramanian, T.; Sanjeeviraja, C.; Jayachandran, M.; Swaminathan, V. Thickness Dependence of Structural, Electrical and Optical Properties of Sputter Deposited Indium Tin Oxide Films. *Adv. Sci. Lett.* **2010**, *3*, 434–441. [CrossRef]
55. Karthik, K.; Revathi, V.; Tatarchuk, T. Microwave-Assisted Green Synthesis of SnO_2 Nanoparticles and Their Optical and Photocatalytic Properties. *Mol. Cryst. Liquid Cryst.* **2018**, *671*, 17–23. [CrossRef]
56. Ágoston, P.; Albe, K.; Nieminen, R.M.; Puska, M.J. Intrinsic n-Type Behavior in Transparent Conducting Oxides: A Comparative Hybrid-Functional Study of In_2O_3, SnO_2, and ZnO. *Phys. Rev. Lett.* **2009**, *103*, 245501. [CrossRef] [PubMed]
57. Buckeridge, J.; Catlow, C.R.A.; Farrow, M.R.; Logsdail, A.J.; Scanlon, D.O.; Keal, T.W.; Sherwood, P.; Woodley, S.M.; Sokol, A.A.; Walsh, A. Deep vs Shallow Nature of Oxygen Vacancies and Consequent n-Type Carrier Concentrations in Transparent Conducting Oxides. *Phys. Rev. Mater.* **2018**, *2*, 054604. [CrossRef]
58. Sharma, M.; Aljawfi, R.N.; Kumari, K.; Chae, K.H.; Gautam, S.; Dalela, S.; Alvi, P.A.; Kumar, S. Investigation of Local Atomic Structure of Ni Doped SnO_2 Thin Films via X-Ray Absorption Spectroscopy and Their Magnetic Properties. *J. Mater. Sci. Mater. Electron.* **2019**, *30*, 760–770. [CrossRef]
59. Ribic, V.; Recnik, A.; Drazic, G.; Podlogar, M.; Brankovic, Z.; Brankovic, G. TEM and DFT Study of Basal-Plane Inversion Boundaries in SnO_2-Doped ZnO. *Sci. Sinter.* **2021**, *53*, 237–252. [CrossRef]

nanomaterials

Article

Simulation of Figures of Merit for Barristor Based on Graphene/Insulator Junction

Jun-Ho Lee †, Inchul Choi †, Nae Bong Jeong, Minjeong Kim, Jaeho Yu , Sung Ho Jhang and Hyun-Jong Chung *

Department of Physics, Konkuk University, Seoul 05029, Korea
* Correspondence: hjchung@konkuk.ac.kr
† These authors contributed equally to this work.

Abstract: We investigated the tunneling of graphene/insulator/metal heterojunctions by revising the Tsu–Esaki model of Fowler–Nordheim tunneling and direct tunneling current. Notably, the revised equations for both tunneling currents are proportional to V^3, which originates from the linear dispersion of graphene. We developed a simulation tool by adopting revised tunneling equations using MATLAB. Thereafter, we optimized the device performance of the field-emission barristor by engineering the barrier height and thickness to improve the delay time, cut-off frequency, and power-delay product.

Keywords: graphene; barristor; Fowler–Nordheim tunneling; cut-off frequency; delay time; power-delay product

Citation: Lee, J.-H.; Choi, I.; Jeong, N.B.; Kim, M.; Yu, J.; Jhang, S.H.; Chung, H.-J. Simulation of Figures of Merit for Barristor Based on Graphene/Insulator Junction. *Nanomaterials* **2022**, *12*, 3029. https://doi.org/10.3390/nano12173029

Academic Editor: Jipeng Cheng

Received: 13 July 2022
Accepted: 30 August 2022
Published: 31 August 2022

1. Introduction

Graphene barristor [GB] has been introduced to break the limitation of the low $I_{\mathrm{ON}}/I_{\mathrm{OFF}}$ of the graphene field-effect transistor (GFET) [1]. Since the introduction of the barristor, not only Si, but either organic [2–5] or inorganic [6–12] materials, have been exploited to make the graphene-semiconductor junction and applied on photosensors, gas sensors, etc., with its superior $I_{\mathrm{ON}}/I_{\mathrm{OFF}}$.

Extreme temperature changes or degradation due to the environment may affect the performance of GFET or GB [13]. However, graphene-insulator-junction barristors exhibit a more stable performance compared to semiconductor-based ones [14].

In this study, we revised the models for Fowler–Nordheim tunneling (FNT) and direct tunneling (DT) in graphene/insulator/metal (GIM) junctions using the Tsu–Esaki tunneling model to reflect the graphene's linear band structure [15]. Compared to the traditional FNT equation—proportional to V^2—the revised FNT equation—proportional to V^3—fits better with the experimental data. Then, we simulated how delay time (τ), power-delay product (PDP), and cut-off frequency (f_{T}) of the field-emission barristor (FEB) could be improved by varying the tunneling-barrier height ($\varnothing_B$), and the thickness of the hexagonal boron nitride (hBN) (t_{Tunnel}) with the revised tunneling models. We also considered thermionic emission for the low barrier height and DT for the thin insulator channel. The figures of merit of the FEB were extracted from the experimentally measured *I*–*V* characteristics in [14]. Notably, we could improve the device performance by decreasing t_{Tunnel}. This is because $\varnothing_B$, followed by the channel current (I_{D}), decreased with t_{Tunnel}. However, the improvement in the device performance by increasing t_{Tunnel} has a limitation because the increase in t_{Tunnel} deteriorates the PDP. Therefore, to not only improve τ and f_{T} but also PDP, both the tunneling barrier height and t_{Tunnel} should be decreased.

2. Materials and Methods

We used the polydimethylsiloxane (PDMS) stamping method to create the bottom structure (gate electrode/hBN). Few-layer hBN was prepared on PDMS (PF Film-X4-6.5

mil bought in Gel-Film®) by mechanical exfoliation, and it was attached to the slide glass upside down. The hBN was subsequently aligned on top of the target substrate using a 3-axes manipulator. The PDMS was heated to 60 °C while it was transferred onto the target. Finally, PDMS was mechanically peeled off after the temperature was decreased to 25 °C. The top structure (hBN/graphene) was then transferred to the metal/hBN structure using the PMMA transfer method. The drain and source electrodes were deposited using an e-beam evaporator. The processes were conducted at the Core Facility Center for Quantum Characterization/Analysis of Two-Dimensional Materials and Heterostructures.

The simulation data were calculated using MATLAB R2021b. The source code implements the equations derived in the manuscript. We utilized MATLAB to calculate the current by varying the barrier height and the electric field. Using the double for loops, we obtained the current ranging from the height up to 3.0 eV and the field up to 0.4 V/nm with the discrete tunneling thickness. The source code is provided in the Supplementary Materials.

3. Results

3.1. Tunneling Current Model in GIM Junction

We derived a revised model for tunneling in graphene/insulator/metal (GIM) junctions. We started with the Tsu–Esaki model and applied the band structure of graphene. The current density tunneling from graphene to the metal can be calculated as follows [16]:

$$dJ_{g\to m} = qv_x T'(k_x) D_g(k_g) f_g(E)(1 - f_m(E)) dk_x dk_g, \tag{1}$$

where q is the elementary charge; v_x is the velocity in the x-direction, which is perpendicular to the graphene plane (to the insulator); $T'(k_x)$ is the transmission coefficient; k_g and k_x are the wave vectors of the carrier parallel and perpendicular to the graphene plane (y-z plane), respectively; and $D_g(k_g)$ is the density of states of the graphene with momentum k_g. In addition, $f_g(E)$ and $1 - f_m(E)$ indicate the Fermi–Dirac distribution of the filled states in the graphene and empty states in the metal, respectively. The density of states $D_g(k_g)$ can be obtained as $D_g(k_g)dk_g = D_g^*(k_y, k_z)dk_y dk_z\Big|_{k=k_g}$, where $k = \sqrt{{k_x}^2 + {k_y}^2}$ and $D_g^*(k_y, k_z)$ is the number of states per unit cell in the 2D momentum space. The areas of the primitive cell (S_1) in real space and reciprocal lattice space (S_2) of graphene are $S_1 = \frac{\sqrt{3}}{2}a^2$ and $S_2 = \frac{8\pi^2}{\sqrt{3}a^2}$, respectively (Figure S1a) $D_g^*(k_y, k_z) = 2 * 2 * \frac{1}{S_1} * \frac{1}{S_2} = \frac{1}{\pi^2}$, considering the spin and valley degeneracy [17,18]. Thus, $D_g(k_g)dk_g = \frac{1}{\pi^2}2\pi k_g dk_g = \frac{2}{\pi}k_g dk_g$, as shown in Figure S2b. Since graphene has a linear dispersion relation around the K-point, so that $E_g = \hbar v_F k_g$ or $v_F dk_g = \frac{1}{\hbar}dE_g$ (inset of Figure S2b), and the density of states in energy space $D_g(E_g)dE_g = \frac{2}{\pi}\frac{E_g dE_g}{(\hbar v_F)^2}$, where v_F is the Fermi velocity and $\hbar$ is the reduced Plank's constant.

Using the parabolic dispersion relation so that $E_x = \frac{\hbar^2 {k_x}^2}{2m}$, $\frac{1}{\hbar}dE_x = v_x dk_x$, Equation (1) can be re-expressed with k_x changed to E_x as follows:

$$dJ_{g\to m} = qT'(E_x) f_g(E)(1 - f_m(E)) \frac{2}{\pi\hbar^3 {v_F}^2} E_g dE_g dE_x \tag{2a}$$

As the total energy $E = E_x + E_g$, Equation (2a) can be re-expressed as:

$$dJ_{g\to m} = qT'(E_x) f_g(E)(1 - f_m(E)) \frac{2}{\pi\hbar^3 {v_F}^2} (E - E_x) dE dE_x \tag{2b}$$

Therefore, considering that $E_g > 0$,

$$J_{g\to m} = \frac{2q}{\pi\hbar^3 {v_F}^2} \int_0^\infty dE_x T'(E_x) \int_{E_x}^\infty dE f_g(E)(1 - f_m(E))(E - E_x) \tag{3}$$

Notably, $(E - E_x)$ of the integrand originates from the linear dispersion relation of graphene, which does not exist in the original transport equation.

Equation (3) is a model of the tunneling current density in a graphene/insulator/metal junction. It comprises two integral parts: the first integral indicates the tunneling probability between graphene and the metal. Because it includes the tunneling coefficient T, which is related to the barrier height and width, it has different forms depending on the tunneling mechanisms such as FNT and DT [19–22]. The difference will be described in the next subsection. The second integral is related to the carriers supplied at the interface by an applied voltage. Thus, it has an identical form for both the FNT and DT. At the temperature $T = 0$, the integrand is finite only in the interval of $\left[E_x, E_{F,g}\right]$ because the carrier tunnels only from the filled state of graphene and the empty state of the metal, as shown in Figure 1b,c. Thus, the second integral can be simplified to $\int_{E_x}^{E_{F,g}} (E - E_x)dE = \frac{1}{2}\left(E_{F,g} - E_x\right)^2$, where $E_{F,m}$ is the Fermi level of the metal. Therefore, $J_{g\to m}$ can be written as $T = 0$, as follows:

$$J_{g\to m} = \frac{q}{\pi\hbar^3 v_F^2}\int_{E_{F,m}}^{E_{F,g}} T'(E_x)\left(E_{F,g} - E_x\right)^2 dE_x, \tag{4}$$

where is the interval limit between the filled state of graphene and empty state of the metal, and $E_{F,g}$ is the Fermi level of graphene.

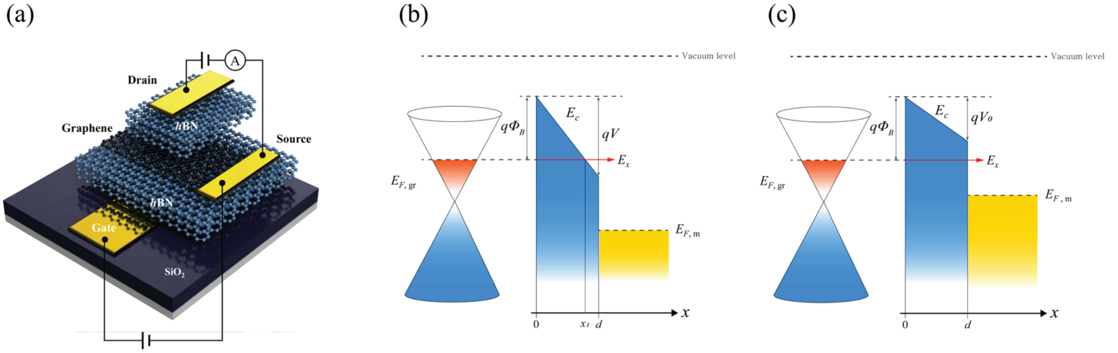

Figure 1. (**a**) A schematic of the field-emission barristor and schematic illustration of the graphene/insulator/metal (GIM) junction in Fowler–Nordheim tunneling; (**b**) an illustration of the FN tunneling. Electron tunnels through the insulator with the tunneling thickness of x_1; (**c**) an illustration of DT; electrons tunnel through the insulator with a width of d.

While the total current density is the difference between the current tunneling from graphene to metal ($J_{g\to m}$) and that from metal to graphene ($J_{m\to g}$), the total current density J of the GIM junction becomes $J_{g\to m}$ because $J_{m\to g}$ does not contribute to J. This is because $\int_{E_x}^{E_{F,g}} f_m(E)\left(1 - f_g(E)\right)dE$ becomes zero because $f_m(E) = 0$ under $E_{F,m} \leq E$.

3.2. Fowler–Nordheim Tunneling Model in GIM Junction

In Equation (4), the transmission coefficient $T(E_x)$ for FNT in the Wentzel–Kramers–Brillouin approximation can be expressed as $T(E_x) = \exp\left(-\frac{4\pi}{h}\int_0^{x_1}\sqrt{2m^*(E_c - E_x)}dx\right)$ [16,19], where $m*$ is the electron effective mass, the conduction band minimum (CBM) $E_C(x) = E_{F,g} + q\varnothing_B - q\frac{V}{d}x$, and $x_1 = \frac{\left(E_{F,g} + q\varnothing_B - E_x\right)d}{qV}$, as shown in Figure 1b. Assuming that the work function of graphene and metal are the same, $V = \left(E_{F,g} - E_{F,m}\right)/q$, where V is the potential bias between the graphene and metal. Then, the transmission coefficient can be rewritten as follows:

$$\begin{aligned} T(E_x) &= \exp\left(-\frac{4\pi\sqrt{2m^*}}{h}\int_0^{x_1} dx\sqrt{E_{F,g} + q\varnothing_B - q\frac{V}{d}x - E_x}\right) \\ &= \exp\left[\frac{8\pi\sqrt{2m^*}d}{3hqV}\left\{\left(E_{F,g} + q\varnothing_B - q\frac{V}{d}x_1 - E_x\right)^{3/2} - \left(E_{F,g} + q\varnothing_B - E_x\right)^{3/2}\right\}\right]. \end{aligned} \tag{5}$$

Since the first term in the curly bracket disappears because of the value of x_1, the tunneling coefficient can be described as follows:

$$T(E_x) = \exp\left(-\frac{8\pi\sqrt{2m^*}d}{3hqV}\left(q\varnothing_B - \left(E_x - E_{F,g}\right)\right)^{3/2}\right) \tag{6}$$

Then, Equation (4) can be rewritten for the FNT current when E_x is between $E_{F,m}$, and $E_{F,g}$ as follows:

$$J = \frac{q}{\pi\hbar^3 v_F^2}\int_{E_{F,m}}^{E_{F,g}} \exp\left(-\frac{8\pi\sqrt{2m^*}d}{3hqV}\left(q\varnothing_B - \left(E_x - E_{F,g}\right)\right)^{3/2}\right)\left(E_{F,g} - E_x\right)^2 dE_x \tag{7}$$

The exponential term in Equation (7) can be rewritten by using the following Taylor series as $\left(q\varnothing_B - \left(E_x - E_{F,g}\right)\right)^{3/2} \cong \left(q\varnothing_B\right)^{3/2} - \frac{3}{2}\left(E_x - E_{F,g}\right)\left(q\varnothing_B\right)^{1/2}$.

Then, by substituting $E_x - E_{F,g}$ with E, the FNT current J is given by the following equation:

$$J = \frac{q}{\pi\hbar^3 v_F^2}\exp\left(-\frac{8\pi\sqrt{2m^*}d}{3hqV}\left(q\varnothing_B\right)^{3/2}\right)\int_{E_{F,m}-E_{F,g}}^{0} \exp\left(E\frac{4\pi\sqrt{2m^*}d}{hqV}\left(q\varnothing_B\right)^{1/2}\right)E^2\, dE \tag{8a}$$

The integral part can be simplified as

$$\int_k^0 \exp(AE)E^2 dE = \frac{1}{A^3}\left[2 - \exp(Ak)\left(A^2k^2\right) - 2Ak + 2\right)\right] \tag{8b}$$

where $A = \frac{4\pi\sqrt{2m^*}d}{hqV}\left(q\varnothing_B\right)^{1/2}$ and $k = E_{F,m} - E_{F,g}$.

Assuming that $E_{F,g} \gg E_{F,m}$, the k is very small, as is Ak. Therefore, only the constant in Equation (8b) survives. Equation (8a) can then be rewritten as follows:

$$J = \frac{q^4V^3}{4\pi v_F^2\left(2m^*\right)^{3/2}\left(q\varnothing_B\right)^{3/2}d^3}\exp\left(-\frac{8\pi\sqrt{2m^*}d}{3hqV}\left(q\varnothing_B\right)^{3/2}\right). \tag{9}$$

Equation (9) represents a new model for the FNT current in a graphene/insulator/metal junction [15]. Notably, in the revised model, the FNT is proportional to V^3, whereas the FNT in the Tsu–Esaki model is proportional to V^2.

3.3. Direct Tunneling Model in GIM Junction

$T(E_x)$ for DT can be expressed from Equation (4) as follows [23]:

$$\begin{aligned} T(E_x) &= \exp\left(-\tfrac{4\pi\sqrt{2m^*}}{h}\int_0^d dx\sqrt{E_{F,g} + q\varnothing_B - q\tfrac{V}{d}x - E_x}\right) \\ &= \exp\left[\tfrac{8\pi\sqrt{2m^*}d}{3hqV}\left\{\left(E_{F,g} + q\varnothing_B - qV - E_x\right)^{3/2} - \left(E_{F,g} + q\varnothing_B - E_x\right)^{3/2}\right\}\right] \end{aligned} \tag{10}$$

Note that the integration interval for DT is [0, d], as shown in Figure 1c. After integrating and taking the terms up to the order of $\left(q\varnothing_B\right)^{\frac{3}{2}}$ of the Taylor series, the current density for DT can be rewritten as follows:

$$J = \frac{q}{\pi\hbar^3 v_F^2}\int_{E_{F,m}-E_{F,g}}^{0} \exp\left(\frac{4\pi\sqrt{2m^*}d}{hqV}E\left\{\left(q\varnothing_B\right)^{1/2} - \left(q\varnothing_B - qV\right)^{1/2}\right\}\right)E^2\, dE, \tag{11}$$

where E_x is located between $E_{F,m}$ and $E_{F,g}$, $qV \ll q\varnothing_B$, and $E_x - E_{F,g}$ is replaced by E. Therefore, the DT current can be rewritten as follows:

$$J = \frac{q^4 V^3}{4\pi v_F^2 (2m^*)^{3/2} d^3 \left\{ (q\varnothing_B)^{1/2} - (q\varnothing_B - qV)^{1/2} \right\}^3} \exp\left[-\frac{8\pi\sqrt{2m^*}d}{3hqV} \left\{ (q\varnothing_B)^{3/2} - (q\varnothing_B - qV)^{3/2} \right\} \right] \tag{12}$$

Equation (12) is a revised DT model for a graphene/insulator/metal junction. Compared to the DT equation based on the Tsu–Esaki model in the metal/insulator/metal junctions [15], the tunneling current in the Tsu–Esaki model is proportional to V^2, whereas the current in the revised model is proportional to V^3.

3.4. FNT Barrier Height

To calculate the barrier height using the FNT equation for the graphene/insulator junction, the FNT equation can be rewritten as follows:

$$ln\left(\frac{I_D}{V_D^3}\right) = \gamma + \beta\frac{1}{V_D} \tag{13}$$

where I_D is the drain current; V_D is the drain voltage, $\gamma = ln\frac{A_{eff}q^4}{4\pi v_F^2 (2m^*)^{3/2} (q\varnothing_B)^{3/2} d^3}$ and $\beta = -\frac{8\pi\sqrt{2m^*}d}{3hqV}\ (q\varnothing_B)^{3/2}$. In the new equation, γ is replaced with $\alpha = ln\frac{A_{eff}q^3 m}{8\pi h\varnothing_B d^2 m^*}$ from the original FNT equation because they are extracted from different second integrations in Equation (3), which are related to the density of states in the metal and graphene, respectively. However, β does not change because it is extracted from the tunneling coefficient, which is the first integration in Equation (3). Consequently, the results of the barrier height calculation using the original and revised FNT equations were not significantly different.

Figure 2a shows the replotted I_D–V_D curve of the FEB using the revised FNT equation. The graph fits well to the straight line, and its slope was estimated to be −683 V. Figure 2b shows a replotted I_D–V_D curve obtained using the traditional FNT equation. The slope of the straight line was estimated to be −689 V. The tunneling barrier heights extracted from the slopes were 2.10 eV (by the revised FNT equation) and 2.11 eV (by the traditional FNT equation), respectively. Therefore, the results of the barrier height calculation using the original and revised FNT equation were similar because they used an identical β [19–24].

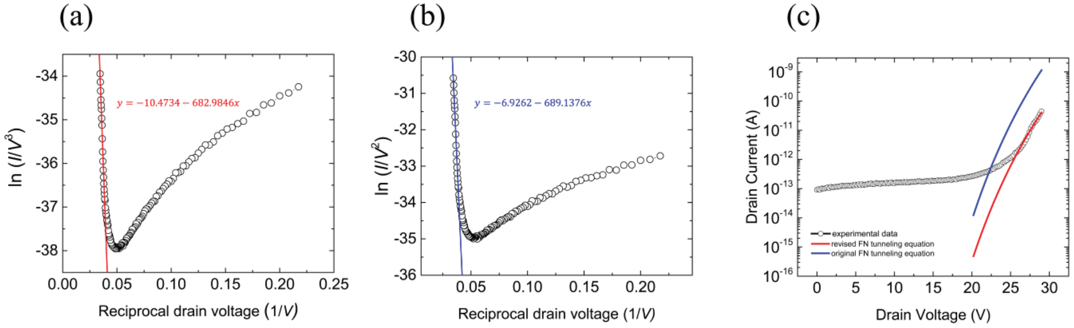

Figure 2. Fitting of FNT to calculate the tunneling barrier height with the revised and traditional equations. (**a**) Straight line (red) fitted to FNT current by the revised FNT equation. Its slope is estimated to be −683 V. A barrier height of 2.10 eV was extracted from the slope. (**b**) Straight line (blue) fitted to the FNT current by the traditional FNT equation. Its slope was estimated to be −689 V. A barrier height of 2.11 eV was extracted from the slope. (**c**) The experimental I_D–V_D curve (black) of FEB consisting of graphene and hBN, the simulated I–V curve by the revised FNT equation (red), and simulated I_D–V_D curve by the original FNT equation (blue). Further information of fitting method is explained in detail on Appendix A.

However, the discrepancy between the two models became apparent when we estimated the FNT current in the graphene/insulator junctions. In contrast to the barrier calculation, α and γ affected the tunneling current estimated using each FNT equation. Figure 2c shows the experimental data and simulated I_{D}–V_{D} curves obtained using the original (blue) and revised (red) FNT equations. The black curve indicates the measured I_{D}–V_{D}. The red line was estimated using the revised FNT equation: $I_{D,\mathrm{revised}} = {V_D}^3 \exp\left[\gamma - \frac{8\pi\sqrt{2m^* d}}{3hqV_D}(q\varnothing_B)^{3/2}\right]$. The blue line was obtained by the original FNT equation: $I_{D,original} = {V_D}^2 \exp\left[\alpha - \frac{8\pi\sqrt{2m^* d}}{3hqV_D}(q\varnothing_B)^{3/2}\right]$ [25]. The barrier heights of 2.10 eV and 2.11 eV were applied to the revised and traditional FNT equations, respectively. Although the barrier heights were similar, the simulated currents were significantly different because of the α and γ. As shown in Figure 2c, the red curve simulated by the revised FNT equation was better fitted to the experimental data. Therefore, we used the revised FNT equation to simulate the figures of merit for the FEB.

3.5. Simulation for Barrier Height Engineering to Improve Delay Time and Cut-Off Frequency

To evaluate the performance of the FEB, we extracted τ and f_{T} from the experimental *I*–*V* curve, where τ is a time delay required to charge the gate electrode with I_{ON}, and f_{T} is a maximum frequency up to which the current of the transistor could be amplified [14]. We obtained a delay time of 154 ns and a cut-off frequency of 13.8 MHz for the FEB. Compared to the performance of the graphene/Si barristor, which was simulated using NanoTCAD ViDES (Device simulator) [26], the FEB's delay time was 140 times slower than that of the graphene/Si barristor (1.1 ns), and the cut-off frequency was 92 times lower than that of the graphene/Si barristor (1.3 GHz). The low performance of the FEB originated from the low ON current (I_{ON}) because the delay time and cut-off frequency depend on I_{ON}. In the FEB, the tunneling barrier height should be decreased to improve I_{ON}. Therefore, to obtain the minimum barrier height in our device, we estimated the drain current by varying the barrier height and electric field strength between the source and drain electrodes (E_{Field}) using the revised FNT equation.

Figure 3a shows the FNT current simulated by varying $\varnothing_B$ and E_{Field}. To increase the J_{ON}, a higher E_{Field} and a lower $\varnothing_B$ are required. However, Figure 3b describes that $\Delta J_D/\Delta\varnothing_B$ ratios (slope of lines) decreased with E_{Field}. This indicates that the device requires more charge on graphene to modulate its work function. Increasing E_{Field} to improve J_{ON} requires more switching energy for the device. Therefore, the maximum E_{Field} should be determined by considering both the on-state current and the energy consumption for switching. Likewise, decreasing the tunneling barrier height is limited by thermionic emission. The thermionic emission current was estimated using the following equation:

$$J_{Thermionic} = \frac{qk_B^3}{\pi\hbar^3 v_F^2} T^3 \exp\left(-\frac{\mathrm{q}\varnothing_B}{k_B T}\right) \tag{14}$$

where k_{B} is the Boltzmann constant and T is the temperature [27].

Because the thermionic emission current exponentially depends on $\varnothing_B$ and the temperature, the total channel current under E_{Field} lower than 0.1 V/nm is affected by the thermionic emission current, as shown in Figure 3b. Therefore, an E_{Field} above 0.1 V/nm should be applied to avoid temperature dependence of the I_{D}–V_{D} characteristics. As shown in Figure 3b, these conditions for improving the delay time and cut-off frequency were satisfied when the E_{Field} was 0.2 V/nm, J_{ON} was 10^{-4} A/μm^2 with $\varnothing_B$ 0.5 eV, and J_{Off} was 10^{-10} A/μm^2 with $\varnothing_B$ 1.055 eV. The required charge (Q) to decrease $\varnothing_B$ from 1.055 eV to 0.505 eV was calculated by using the equation: $\Delta w_G = \frac{h}{2\pi} v_F \sqrt{\pi Q}$, where Δw_G is the work function shift of graphene [28]. The delay time and cut-off frequency were calculated using the following equations [29]:

$$
\begin{aligned}
\tau &= \frac{Q_{\text{on}} - Q_{\text{off}}}{J_{\text{on}}} = \frac{Q}{J_{\text{on}}} \\
f_T &= \frac{1}{2\pi}\frac{\text{d}J_{\text{D}}/\text{d}V_{\text{G}}}{\text{d}Q/\text{d}V_{\text{G}}} = \frac{1}{2\pi}\frac{\text{d}J_{\text{D}}}{\text{d}Q}
\end{aligned}
\qquad (15)
$$

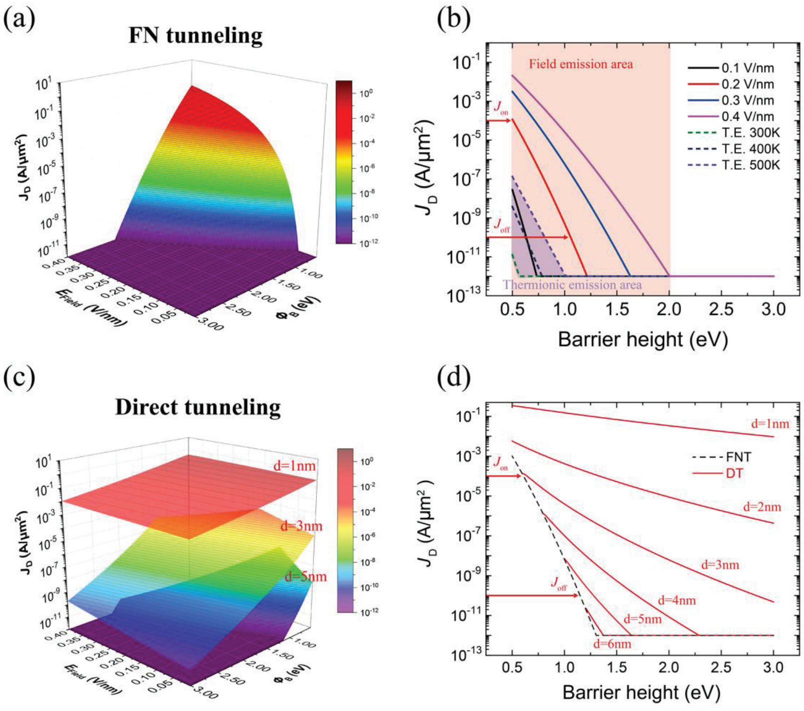

Figure 3. The simulated FNT current as a function of the tunneling barrier height and drain electric field. (**a**) A 3D plot of the FNT equation. (**b**) The channel current under a low drain electric field (0.1 V/nm) can be affected by the thermionic emission current. The $\Delta J_{\text{D}}/\Delta\varnothing_B$ ratios decreased with increasing drain electric field. The on-state current J_{on} was 10^{-4} A/μm^2 when $\varnothing_B$ was 0.5 eV, and the off-state current J_{off} was 10^{-10} A/μm^2 when $\varnothing_B$ was 1.055 eV. (**c**) A 3D plot of the DT equation for different thicknesses of the insulator. The DT current exponentially increased with a decrease in the thickness. (**d**) The simulated FNT current and DT as a function of the tunneling barrier height for different thicknesses of the insulator. The tunneling current under E_{Field} = 0.2 V/nm was simulated by using the revised FNT and revised DT equations. The DT current increased with the decreasing thickness of the insulator. J_{on} and J_{off} indicate the on-state current and off-state current, respectively.

We obtained a delay time τ of 0.18 ns and cut-off frequency f_{T} of 3.98 GHz that were better than 1.1 ns and 1.3 GHz in the graphene/Si barristor. Therefore, when the applied E_{Field} was 0.2 V/nm and $\varnothing_B$ was changed from 0.5 eV to 1.055 eV or vice versa, FEB could achieve the optimized delay time and cut-off frequency.

3.6. Simulation for Insulator Thickness Engineering to Improve Power-Delay Product

The power delay product (PDP) refers to the energy consumed during device switching. We estimated the PDP of the FEB to be 355 fJ/μm^2 from the I_{D}–V_{G} graph, which was 47 times greater than that of the graphene/Si barristor (7.5 fJ/μm^2). This high energy consumption for device switching is because the semiconductor-less device requires a high

V_D to control the FNT current. Therefore, to reduce the PDP, t_{Tunnel}, where the FNT takes place, should be reduced.

Figure 3d exhibits the DT current by varying t_{Tunnel}. When t_{Tunnel} was thinner than 2 nm, the FNT could not control the channel current because the DT current dominated the FNT current. In contrast, DT was suppressed below the off-state current in the FNT regime when t_{Tunnel} was 6 nm. Therefore, when t_{Tunnel} was 6 nm, and E_{Field} was 0.2 V/nm, we obtained a PDP of 21 fJ/μm^2 from the following equation:

$$PDP = V_D\,(Q_{\mathrm{on}} - Q_{\mathrm{off}}). \tag{16}$$

Although still greater than that of the graphene/Si barristor (7.4 fJ/μm^2), the PDP decreased to 6% of the measurement by engineering t_{Tunnel}.

4. Conclusions

In conclusion, we introduce a new model for the FNT and DT currents of graphene/insulator/metal (GIM) heterojunctions. We obtained new models by revising the supply function of the Tsu–Esaki model. Notably, the tunneling current in the revised FNT equation was proportional to V^3. We then extracted the tunneling barrier height in the graphene/insulator junction from the slope of the line in the I_D–V_D curve replotted with the axes of $ln(I/V^3)$ and $1/V$. The barrier height obtained using the revised model was not significantly different from that of the original model. However, the I_D–V_D curve estimated by the revised FNT fit better with the experimental data than the I_D–V_D curve simulated by the original FNT. Then, we simulated the τ, f_T, and PDP of the FEB by varying $\varnothing_B$ and t_{Tunnel} by using the revised FNT equation. These significantly improved by decreasing $\varnothing_B$ and increasing E_{Field}. By considering the thermionic emission at low barrier height and energy consumption at the high electric field, we obtained a τ of 0.18 ns and f_T of 3.98 GHz when E_{Field} was 0.2 V/nm, and $\varnothing_B$ was changed from 0.5 to 1.055 eV or vice versa. We improved the PDP by decreasing the t_{Tunnel}. As DT exponentially increased as the thickness decreased, we obtained a lower boundary t_{Tunnel} of 6 nm, and then the PDP decreased to 17 times lower than the experimental data.

Supplementary Materials: The following supporting information can be downloaded at: https://www.mdpi.com/article/10.3390/nano12173029/s1, Figure S1: An illustration of the reciprocal lattice space of graphene; Figure S2: The optical microscope image of the device; Supplementary Software Files: "S1 MATLAB code.zip" simulation MATLAB Code.

Author Contributions: Conceptualization, J.-H.L.; Software: J.-H.L.; Investigation, J.-H.L.; Writing—original draft preparation, J.-H.L. and I.C.; Writing—review and editing, I.C., N.B.J., M.K., J.Y., S.H.J., and H.-J.C.; Supervision, H.-J.C.; Project administration, H.-J.C.; Funding acquisition, H.-J.C. All authors have read and agreed to the published version of the manuscript.

Funding: This research was supported by a National Research Foundation of Korea (NRF) grant funded by the Korean government (MIST) (2020R1A2C1003398) and by Korea Basic Science Institute(National research Facilities and Equipment Center) grant funded by the Ministry of Education (2022R1A6C101A754).

Data Availability Statement: Data can be available upon request from the authors.

Conflicts of Interest: The authors declare no conflict of interest.

Appendix A

The fitting lines projected in Figure 2a,b were obtained by linear fitting of each plotted data. The interval of the x-axis for the linear regression ranged from 0.034 V^{-1} to 0.039 V^{-1}, corresponding to the V_D of 25.6 V and 29.0 V, respectively. This limited interval was to distinguish the FNT current from that of the DT. Then, the currents in Figure 2c were extrapolated by using each current equation (revised or traditional) with the key parameters obtained by the linear regression. Figure 2c projects the data ranges from 20 to 30 V.

References

1. Yang, H.; Heo, J.; Park, S.; Song, H.J.; Seo, D.H.; Byun, K.; Kim, P.; Yoo, I.; Chung, H.; Kim, K. Graphene Barristor, a Triode. *Science* **2012**, *336*, 1140–1143. [CrossRef] [PubMed]
2. Ojeda-Aristizabal, C.; Bao, W.; Fuhrer, M.S. Thin-Film Barristor: A Gate-Tunable Vertical Graphene-Pentacene Device. *Phys. Rev. B* **2013**, *88*, 035435. [CrossRef]
3. Parui, S.; Pietrobon, L.; Ciudad, D.; Vélez, S.; Sun, X.; Casanova, F.; Stoliar, P.; Hueso, L.E. Gate-Controlled Energy Barrier at a Graphene/Molecular Semiconductor Junction. *Adv. Funct. Mater.* **2015**, *25*, 2972–2979. [CrossRef]
4. Oh, G.; Kim, J.-S.; Jeon, J.H.; Won, E.; Son, J.W.; Lee, D.H.; Kim, C.K.; Jang, J.; Lee, T.; Park, B.H. Graphene/Pentacene Barristor with Ion-Gel Gate Dielectric: Flexible Ambipolar Transistor with High Mobility and on/off Ratio. *ACS Nano* **2015**, *9*, 7515–7522. [CrossRef] [PubMed]
5. Moon, J.S.; Seo, H.-C.; Stratan, F.; Antcliffe, M.; Schmitz, A.; Ross, R.S.; Kiselev, A.A.; Wheeler, V.D.; Nyakiti, L.O.; Gaskill, D.K.; et al. Lateral Graphene Heterostructure Field-Effect Transistor. *IEEE Electron. Device Lett.* **2013**, *34*, 1190–1192. [CrossRef]
6. Georgiou, T.; Jalil, R.; Belle, B.D.; Britnell, L.; Gorbachev, R.V.; Morozov, S.V.; Kim, Y.-J.; Gholinia, A.; Haigh, S.J.; Makarovsky, O.; et al. Vertical Field-Effect Transistor Based on Graphene—WS 2 Heterostructures for Flexible and Transparent Electronics. *Nat. Nanotechnol.* **2013**, *8*, 100–103. [CrossRef]
7. Parui, S.; Ruiter, R.; Zomer, P.J.; Wojtaszek, M.; Van Wees, B.J.; Banerjee, T. Temperature Dependent Transport Characteristics of Graphene/n-Si Diodes. *J. Appl. Phys.* **2014**, *116*, 244505. [CrossRef]
8. Tian, H.; Tan, Z.; Wu, C.; Wang, X.; Mohammad, M.A.; Xie, D.; Yang, Y.; Wang, J.; Li, L.-J.; Xu, J.; et al. Novel Field-Effect Schottky Barrier Transistors Based on Graphene-MoS 2 Heterojunctions. *Sci. Rep.* **2014**, *4*, 5951. [CrossRef]
9. Jeong, S.-J.; Gu, Y.; Heo, J.; Yang, J.; Lee, C.-S.; Lee, M.-H.; Lee, Y.; Kim, H.; Park, S.; Hwang, S. Thickness Scaling of Atomic-Layer-Deposited HfO2 Films and Their Application to Wafer-Scale Graphene Tunnelling Transistors. *Sci. Rep.* **2016**, *6*, 20907. [CrossRef]
10. Huh, W.; Jang, S.; Lee, J.Y.; Lee, D.; Lee, D.; Lee, J.M.; Park, H.G.; Kim, J.C.; Jeong, H.Y.; Wang, G.; et al. Synaptic Barristor Based on Phase-Engineered 2D Heterostructures. *Adv. Mater.* **2018**, *30*, e1801447. [CrossRef]
11. Hwang, H.J.; Heo, S.; Yoo, W.B.; Lee, B.H. Graphene—ZnO:N Barristor on a Polyethylene Naphthalate Substrate. *AIP Adv.* **2018**, *8*, 15022. [CrossRef]
12. Kim, S.Y.; Hwang, J.; Kim, Y.J.; Hwang, H.J.; Son, M.; Revannath, N.; Ham, M.H.; Cho, K.; Lee, B.H. Threshold Voltage Modulation of a Graphene–ZnO Barristor Using a Polymer Doping Process. *Adv. Electron. Mater.* **2019**, *5*, 1800805. [CrossRef]
13. Shim, J.; Kim, H.S.; Shim, Y.S.; Kang, D.-H.; Park, H.-Y.; Lee, J.; Jeon, J.; Jung, S.J.; Song, Y.J.; Jung, W.S.; et al. Extremely Large Gate Modulation in Vertical Graphene/WSe2Heterojunction Barristor Based on a Novel Transport Mechanism. *Adv. Mater.* **2016**, *28*, 5293–5299. [CrossRef] [PubMed]
14. Lee, J.-H.; Shin, D.H.; Yang, H.; Jeong, N.B.; Park, D.-H.; Watanabe, K.; Taniguchi, T.; Kim, E.; Lee, S.W.; Jhang, S.H.; et al. Semiconductor-Less Vertical Transistor with I ON/I OFF of 106. *Nat. Commun.* **2021**, *12*, 1000. [CrossRef]
15. Tsu, R.; Esaki, L. Tunneling in a Finite Superlattice. *Appl. Phys. Lett.* **1973**, *22*, 562–564. [CrossRef]
16. Gehring, A.; Selberherr, S. Modeling of Tunneling Current and Gate Dielectric Reliability for Nonvolatile Memory Devices. *IEEE Trans. Device Mater. Reliab.* **2004**, *4*, 306–319. [CrossRef]
17. Novoselov, K.S.; Geim, A.K.; Morozov, S.V.; Jiang, D.; Katsnelson, M.I.; Grigorieva, I.V.; Dubonos, S.V.; Firsov, A.A. Two-Dimensional Gas of Massless Dirac Fermions in Graphene. *Nature* **2005**, *438*, 197–200. [CrossRef]
18. Ishigami, M.; Chen, J.H.; Cullen, W.G.; Fuhrer, M.S.; Williams, E.D. Atomic Structure of Graphene on SiO 2. *Nano Lett.* **2007**, *7*, 1643–1648. [CrossRef]
19. Fowler, R.H.; Nordheim, L. Electron Emission in Intense Electric Fields. *Proc. R. Soc. Lond. Ser. A Contain. Pap. Math. Phys. Character* **1928**, *119*, 173–181. [CrossRef]
20. Simmons, J.G. Electric Tunnel Effect between Dissimilar Electrodes Separated by a Thin Insulating Film. *J. Appl. Phys.* **1963**, *34*, 2581–2590. [CrossRef]
21. Britnell, L.; Gorbachev, R.V.; Jalil, R.; Belle, B.D.; Schedin, F.; Mishchenko, A.; Georgiou, T.; Katsnelson, M.I.; Eaves, L.; Morozov, S.V.; et al. Field-Effect Tunneling Transistor Based on Vertical Graphene Heterostructures. *Science* **2012**, *335*, 947–950. [CrossRef] [PubMed]
22. Britnell, L.; Gorbachev, R.V.; Jalil, R.; Belle, B.D.; Schedin, F.; Katsnelson, M.I.; Eaves, L.; Morozov, S.V.; Mayorov, A.S.; Peres, N.M.R.; et al. Electron Tunneling through Ultrathin Boron Nitride Crystalline Barriers. *Nano Lett.* **2012**, *12*, 1707–1710. [CrossRef] [PubMed]
23. Lee, G.-H.; Yu, Y.-J.; Lee, C.; Dean, C.; Shepard, K.L.; Kim, P.; Hone, J. Electron Tunneling through Atomically Flat and Ultrathin Hexagonal Boron Nitride. *Appl. Phys. Lett.* **2011**, *99*, 243114. [CrossRef]
24. Persaud, A. Analysis of Slope-Intercept Plots for Arrays of Electron Field Emitters. *J. Appl. Phys.* **2013**, *114*, 154301. [CrossRef]
25. Gotoh, Y.; Tsuji, H.; Ishikawa, J. Relationships among the Physical Parameters Required to Give a Linear Relation between Slope and Intercept of Fowler-Nordheim Plots. *Ultramicroscopy* **2001**, *89*, 63–67. [CrossRef]
26. Logoteta, D.; Fiori, G.; Iannaccone, G. Graphene-Based Lateral Heterostructure Transistors Exhibit Better Intrinsic Performance than Graphene-Based Vertical Transistors as Post-CMOS Devices. *Sci. Rep.* **2014**, *4*, 6607. [CrossRef]

27. Liang, S.J.; Hu, W.; Di Bartolomeo, A.; Adam, S.; Ang, L.K. A Modified Schottky Model for Graphene-Semiconductor (3D/2D) Contact: A Combined Theoretical and Experimental Study. In Proceedings of the 2016 IEEE International Electron Devices Meeting (IEDM), San Francisco, CA, USA, 3–7 December 2016; pp. 14.4.1–14.4.4. [CrossRef]
28. Yu, Y.-J.; Zhao, Y.; Ryu, S.; Brus, L.E.; Kim, K.S.; Kim, P. Tuning the Graphene Work Function by Electric Field Effect. *Nano Lett.* **2009**, *9*, 3430–3434. [CrossRef]
29. Schwierz, F. Graphene Transistors. *Nat. Nanotechnol.* **2010**, *5*, 487–496. [CrossRef]

nanomaterials

Article

Independent Dual-Channel Approach to Mesoscopic Graphene Transistors

Fernando Sánchez [1], Vicenta Sánchez [2] and Chumin Wang [1,*]

[1] Instituto de Investigaciones en Materiales, Universidad Nacional Autónoma de México, Mexico City 04510, Mexico
[2] Departamento de Física, Facultad de Ciencias, Universidad Nacional Autónoma de México, Mexico City 04510, Mexico
* Correspondence: chumin@unam.mx

Abstract: Graphene field-effect transistors (GFETs) exhibit unique switch and sensing features. In this article, GFETs are investigated within the tight-binding formalism, including quantum capacitance correction, where the graphene ribbons with reconstructed armchair edges are mapped into a set of independent dual channels through a unitary transformation. A new transfer matrix method is further developed to analyze the electron transport in each dual channel under a back gate voltage, while the electronic density of states of graphene ribbons with transversal dislocations are calculated using the retarded Green's function and a novel real-space renormalization method. The Landauer electrical conductance obtained from these transfer matrices was confirmed by the Kubo–Greenwood formula, and the numerical results for the limiting cases were verified on the basis of analytical results. Finally, the size- and gate-voltage-dependent source-drain currents in GFETs are calculated, whose results are compared with the experimental data.

Keywords: independent dual-channel method; graphene field-effect transistor; edge reconstruction defects; linear dislocations; quantum capacitance

Citation: Sánchez, F.; Sánchez, V.; Wang, C. Independent Dual-Channel Approach to Mesoscopic Graphene Transistors. *Nanomaterials* **2022**, *12*, 3223. https://doi.org/10.3390/nano12183223

Academic Editors: Ana M. Benito, Hai Li and Iván Mora-Seró

Received: 22 August 2022
Accepted: 13 September 2022
Published: 16 September 2022

1. Introduction

Graphene is a one-atom-thick planar sheet of carbon atoms in a honeycomb structure, whose free-standing monolayer was isolated and characterized for the first time in 2004 by Andre Geim and Konstantin Novoselov [1]. This material possesses outstanding properties such as high specific surface area [2], very high carrier mobility with null effective mass [3], huge thermal conductivity, and giant Young's modulus [4], making it an ideal candidate for a wide range of applications [5].

When the semiconductor layer of a traditional metal–oxide–semiconductor field-effect transistor (MOSFET) is replaced by a graphene sheet, it is called as graphene field-effect transistor (GFET), whose source-drain current is extremely sensitive to the adsorbed molecules, and it is employable for use in gas and bio sensing [6–8]. Moreover, GFET constitutes a central component of far-infrared radiation and terahertz devices [9] since graphene exhibits a quick optical response based on high carrier mobility [10]. In addition, the graphene nanoribbon field-effect transistor (GNRFET) presents an elevated I_{on}/I_{off} ratio around the threshold voltage compared to the conventional Si-based CMOS [11]. Among possible disadvantages of GFETs, there are difficulties in fabricating wafer-sized high-quality graphene, as well as the apparent degradation of carrier mobility when it is placed over an oxide [12].

Additionally, GFET has a singular capacitor behavior, since the graphene ribbon, being one of the parallel plates, possesses a very low charge density around the Dirac point, which may induce large variations in its chemical potential when a small amount of electric charge is introduced into the capacitor. This fact could significantly increase the potential difference between the back gate and the graphene, because it is equal to the difference between the chemical potentials at each plate. Such small quantities of charge generating a large potential difference lead to a lower capacitance compared to geometric or classic ones (C_C) obtained using ideal metal plates. Hence, the capacitance of GFET (C_{tot}) can be calculated by including a so-called quantum capacitance (C_Q) through $C_{tot}^{-1} = C_C^{-1} + C_Q^{-1}$ [13].

On the theoretical side, GFETs can be modeled at the atomic scale by means of first-principle or semiempirical methods. For example, N/B/P co-doped seven-atom-wide armchair GNRFET was analyzed by using the density functional theory (DFT) [14], while ten-atom-width GNRFET has been studied by self-consistently solving Schrödinger–Poison equations within the tight-binding formalism [15]. Recently, mesoscopic GFETs have been extensively investigated for the detection of micron-scale biomolecules [16] and their graphene ribbons contain several billions of atoms, which impede atomic-scale first-principle modeling. In addition, such graphene ribbons usually possess numerous structural defects, which requires an innovative real-space approach [17].

In this article, the source-drain current (I_{sd}) in mesoscopic GFETs is studied by means of an independent dual-channel method that transforms the graphene ribbon with edge reconstruction defects and transversal dislocations into a set of double chains with first and second neighbor interactions within the tight-binding formalism. The electrical conductance and electronic density of states in these double chains or dual channels connected to two semi-infinite periodic leads at their ends are further addressed by means of a new transfer matrix method within the Landauer formalism and a novel real-space renormalization procedure based on the retarded Green's function, respectively. The theoretical I_{sd}, as a function of the gate voltage, is compared with experimental data obtained from GFETs of different lengths.

2. The Model

In GFETs, an extra carrier density (n_{2D}) can be induced in graphene ribbon by the application of a gate voltage (V_G), which is related to the chemical potentials of graphene (μ) and of back gate metal (μ_M) through $eV_G = \mu - \mu_M$. Figure 1 shows a schematic representation of (Figure 1a) top and (Figure 1b,c) side views of a backgated GFET with energy band diagrams for (b) $V_G = 0$ and (c) $V_G > 0$, where the diminution of μ_M due to V_G is denoted as eV_C. Hence, we have:

$$eV_G = \mu - \mu_M = \mu + eV_C, \tag{1}$$

which is equivalent to $C_{tot}^{-1} = C_C^{-1} + C_Q^{-1}$, since $C_{tot} = e\,\partial n/\partial V_G$, $C_C = e\,\partial n/\partial V_C$, $C_Q = e\,\partial n/\partial V_Q$ and $e\,V_Q = \mu - \mu_0$ with $\mu_0 = 0$ or at the Dirac point in our case [18].

In general, the capacitance per unit of area (C) of an ideal parallel-plate capacitor with a dielectric material of thickness d and a relative permittivity ε_r is $C = \varepsilon_r\varepsilon_0/d = Q/V_C$ in units of MKS [19], where ε_0 is the vacuum permittivity, $Q = en_{2D}$ is the electric charge per unit of area in the capacitor and V_C is the potential difference between the parallel plates. Hence:

$$eV_C = \frac{e^2 n_{2D} d}{\varepsilon_r \varepsilon_0}, \tag{2}$$

where e is the magnitude of the electron charge.

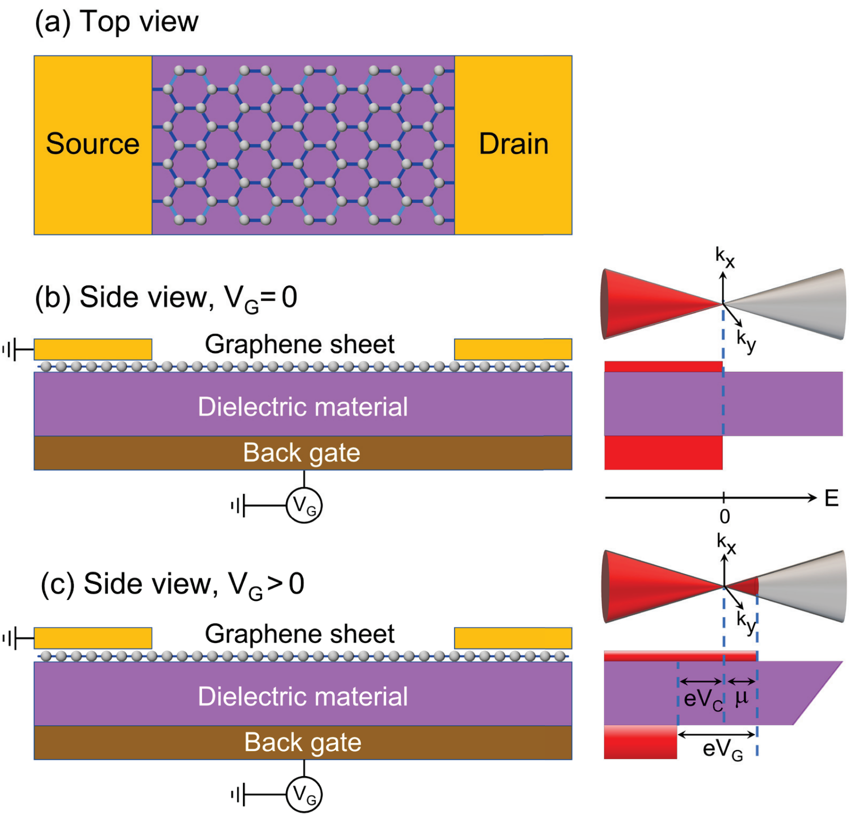

Figure 1. Schematic representations of (**a**) top and (**b**,**c**) side views of a backgated GFET with Dirac cones and energy band diagrams for (**b**) $V_G = 0$ and (**c**) $V_G > 0$, where $eV_G = eV_C + \mu$ being μ the chemical potential of graphene ribbon with respect to the Dirac point.

Let us consider an armchair-edged graphene ribbon with an even number of atoms ($2W$) in each transversal zig-zag line, as illustrated in Figure 2a. This ribbon of width $\mathcal{W} = \sqrt{3}a_S + \sqrt{3}(2W-3)\,a_0/2$ and length $\mathcal{L} = (3/2)La_0 - a_0$ is found in a backgated GFET, where W and L are integer numbers, $a_0 = 1.41$ Å and $a_S = 1.36$ Å are bond lengths between interior atoms and between the edge and next-edge atoms, respectively denoted by blue and thick blue lines in Figure 2a. This variation in interatomic distance is originated from the edge reconstruction of graphene ribbons [20]. The single-electron tight-binding Hamiltonian (H) of this graphene ribbon with null on-site energies can be written as

$$\begin{aligned} H &= \sum_{l=1}^{L}\left(t_s|l,1\rangle\langle l,2| + t\sum_{j=2}^{2W-2}|l,j\rangle\langle l,j+1| + t_s|l,2W-1\rangle\langle l,2W|\right) \\ &\quad + \sum_{l=1}^{(L-1)/2}\sum_{j=1}^{W}\left(t_{2l-1}|2l-1,2j\rangle\langle 2l,2j| + t_{2l}|2l,2j-1\rangle\langle 2l+1,2j-1|\right), \end{aligned} \tag{3}$$

where $|l,j\rangle$ is the Wannier function at site (l,j), t is the hopping integral of pristine graphene sheet and $t_s = 1.2\,t$ is that between the edge and next-edge atoms in a graphene ribbon with edge reconstructions [20] and t_l with $l = 1, 2, \cdots, L-1$ is the hopping integral between transversal zig-zag lines l and $l+1$, representing possible transversal dislocations when $t_l \neq t$.

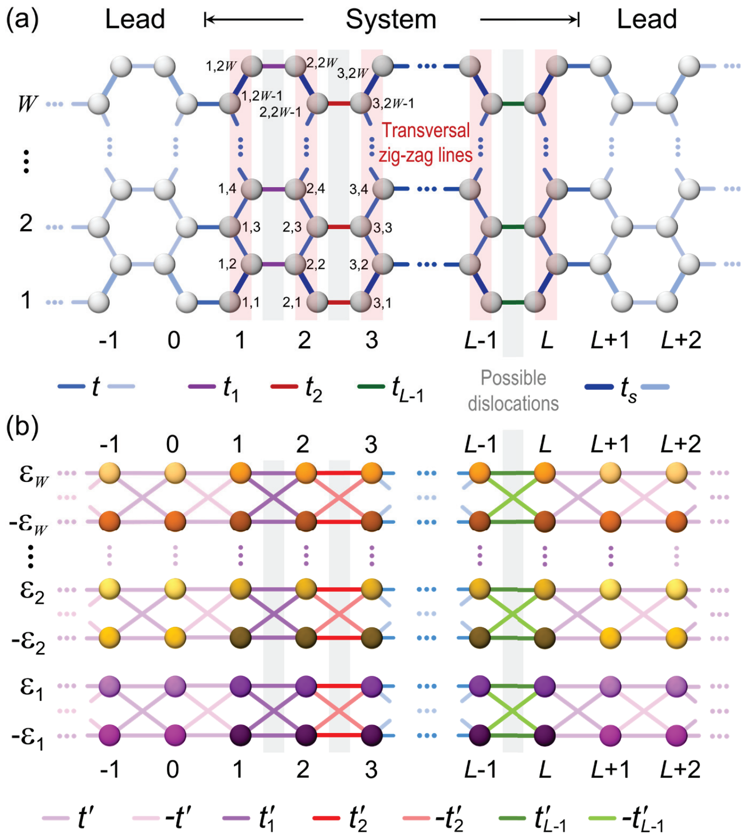

Figure 2. Sketch of (**a**) a graphene ribbon of width W and length L with hopping integrals t, t_s and t_l, being $l = 1,\ 2,\ \cdots,\ L-1$, connected to two semi-infinite periodic leads (light grey spheres) and (**b**) double chains obtained from the independent dual-channel method (Appendix A) with hopping integrals $\pm\, t'$, $\pm\, t'_l$ and on-site energies $\pm\, \varepsilon_j$ being $j = 1,\ 2, \cdots,\ W$. Red highlight and gray zones respectively indicate zig-zag lines and possible transversal dislocations.

There is a unitary transformation discussed in Appendix A that converts the Hamiltonian (3), including the edge reconstruction defects, into a set of W independent dual channels, whose Hamiltonian contains hopping integrals $t' = t/2$, $t'_l = t_l/2$ with $l = 1,\ 2,\ \cdots,\ L-1$ and on-site energies $\pm\, \varepsilon_j$ with $j = 1,\ 2, \cdots,\ W$, which are eigenvalues obtained from the Hamiltonian of an arbitrary transversal zig-zag line in Figure 2.

The extra carrier density (n_{2D}) induced by V_G in the graphene ribbon can be calculated by [21]

$$n_{2D} = \int_0^{\mu} DOS(E)\, dE = \int_0^{eV_G -\ eV_C} DOS(E)\, dE, \tag{4}$$

where

$$DOS(E) = -\frac{1}{\pi}\mathrm{Im}\{Tr\ [G^{+}(E)]\}, \tag{5}$$

is the density of states with $G^{+}(E) = \lim_{\eta \to 0^{+}} (E + i\eta - H)^{-1}$ the retarded Green's function and η the imaginary part of energy [22]. Combining Equations (2) and (4), V_C can be determined as the solution of following self-consistent equation,

$$eV_C = \frac{e^2 d}{\varepsilon_r \varepsilon_0} \int_0^{eV_G - eV_C} DOS(E)\, dE. \tag{6}$$

On the other hand, the source-drain current (I_{sd}) of GFETs at temperature T is given by [23]

$$I_{sd}(T) = V_{sd}\mathrm{g}(\mu, T), \tag{7}$$

where V_{sd} is the source-drain voltage and

$$\mathrm{g}(\mu, T) = \int_{-\infty}^{+\infty} dE \left(-\frac{\partial f_{FD}(E)}{\partial E} \right) \mathrm{g}(E, 0) = \mathrm{g}_0 \int_{-\infty}^{+\infty} dE \left(-\frac{\partial f_{FD}(E)}{\partial E} \right) \mathrm{T}(E) \tag{8}$$

is the electrical conductance of graphene ribbon at chemical potential μ within the Landauer formalism. In Equation (8), $f_{FD} = \{\exp[(E - \mu)/k_B T] + 1\}^{-1}$ is the Fermi–Dirac distribution, $\mathrm{g}_0 = 2e^2/h$ is the conductance quantum, $\mathrm{T}(E)$ is the carrier transmittance of graphene ribbon, and at zero temperature we have [24]

$$\mathrm{g}(\mu, 0) = \mathrm{g}_0 \mathrm{T}(\mu). \tag{9}$$

By means of the independent dual-channel method presented in Appendix A, an armchair-edged graphene ribbon can be transformed into a set of double chains or dual channels (see Figure 2) and then

$$\mathrm{T}(E) = \sum_{j=1}^{W} \mathrm{T}_j(E), \tag{10}$$

where $\mathrm{T}_j(E)$ is the carrier transmittance along the j-th dual channel. We further developed a new transfer matrix method to calculate $\mathrm{T}_j(E)$, which is thoroughly presented in Appendix B, and the result can be written as

$$\mathrm{T}_j(E) = \left| \frac{u_0(j)\, d_0^*(j) - d_0(j)\, u_0^*(j)}{m_{11}(j,E)\, d_0(j)\, u_0^*(j) + m_{12}(j,E)|d_0(j)\,|^2 - m_{21}(j,E)\,|u_0(j)\,|^2 - m_{22}(j,E)\, u_0(j)\, d_0^*(j)} \right|^2, \tag{11}$$

where $m_{\mu\nu}(j, E)$ are elements of the total transfer matrix, $u_0(j)$ and $d_0(j)$ are respectively initial wavefunction amplitudes at the up and down channels, both from the j-th dual channel (see Appendix B).

One of structural defects commonly observed in graphene ribbons is linear dislocation [25,26], because its presence slightly alters the free energy but may significantly modify the carrier transport. In this article, we consider a distribution of transversal dislocations following the Rudin–Shapiro (RS) sequence, which constitutes one of the closest aperiodic arrays to the random distribution [27]. A Rudin–Shapiro lattice with bond disorder can be built by using four kinds of dislocation hopping integrals $t_l = t_A,\ t_B,\ t_C$ or t_D, respectively denoted by letters A, B, C or D, whose positions along the ribbon are ordered by the substitution rules [28]

$$A \to A \oplus B = AB,\ B \to A \oplus C = AC,\ C \to D \oplus B = DB,\ D \to D \oplus C = DC \tag{12}$$

or by the addition rules expressed as

$$\begin{aligned} &S_A(k+1) = S_A(k) \oplus S_B(k),\ S_B(k+1) = S_A(k) \oplus S_C(k), \\ &S_C(k+1) = S_D(k) \oplus S_B(k), S_D(k+1) = S_D(k) \oplus S_C(k), \end{aligned} \tag{13}$$

where the symbol $\oplus$ represents the concatenation operation and $S_\alpha(k)$ is the α-type RS sequence of generation k with $\alpha = A, B, C$ or D. As a consequence, a graphene ribbon based on $S_\alpha(k)$ has $2^k + 1$ transversal zig-zag lines. To have a limited number of dislocations, let us introduce dilute RS lattices, which are built by using periodic segments to construct the RS lattice until generation $m-1$ and a single transversal dislocation is placed at the initial of next generation m. For example, when $k = m = 3$, $S_A(3) = APPP$, $S_B(3) = BPPP$, $S_C(3) = CPPP$ and $S_D(3) = DPPP$, where P denotes a periodic RS sequence with hopping integral t connecting all transversal zig-zag lines. A detailed discussion of this dilute RS lattice and the real-space renormalization method can be found in Appendix C.

Another quantity that should be considered for determining the electrical conductance is the contact resistance between the graphene ribbon and periodic leads. In the diffusive regime, the total resistance (R_{total}) can be written as [29,30]

$$R_{total} = R + 2R_c/\mathcal{W}, \tag{14}$$

where $R = R_{sheet}\mathcal{L}/\mathcal{W}$ is the electrical resistance of a graphene ribbon with length $\mathcal{L}$ and width $\mathcal{W}$, being R_{sheet} that of a square graphene sheet, and R_c is the specific contact resistance in units of $\Omega \cdot \mu\text{m}$, which can be experimentally determined by the transfer length method [31]. Hence, the total conductance defined as $G_{total} = R_{total}^{-1}$ can be calculated from Equation (14) through

$$G_{total} = \frac{G}{2(R_c/\mathcal{W})\, G + 1}, \tag{15}$$

where $G = R^{-1}$ is the conductance of graphene ribbon. For a uniform sample, the electrical resistance of a p-micron segment, $R(\mathcal{L} = p\ \mu\text{m})$, should be p/q times of $R(\mathcal{L} = q\ \mu\text{m})$ obtained from a q micrometer portion. Therefore, Equation (15) can be rewritten as

$$G_{total}(p\ \mu\text{m}) = \frac{G(p\ \mu\text{m})}{2(R_c/\mathcal{W})\, G(p\ \mu\text{m}) + 1} = \frac{G(q\ \mu\text{m})}{2(R_c/\mathcal{W})\, G(q\ \mu\text{m}) + p/q}, \tag{16}$$

where $G(p\ \mu\text{m}) = qG(q\ \mu\text{m})/p$. This equation will be used in the length variation analysis.

3. Results

The electronic density of states, $DOS^\alpha(k, E)$, of a graphene ribbon built by W dual channels based on an α-type dilute RS sequence of generation k can be written as [22]

$$DOS^\alpha(k,E) = \sum_{j=1}^{W} DOS_j^\alpha(k,E) = \sum_{j=1}^{W} \left\{ -\frac{1}{\pi} \lim_{\eta \to 0^+} \sum_{l=1}^{L(k)} \text{Im}\, [G_{l,l}^{\alpha,j}(k,z)] \right\}, \tag{17}$$

where $L(k) = 2\,(2^k + 1)$ is the number of sites in each dual channel and $G_{l,l}^{\alpha,j}(k,z)$ is the l-th diagonal element of the retarded Green's function evaluated at $z = E + i\eta$. The $DOS_j^\alpha(k,E)$ of the j-th dual channel can be rewritten as

$$\begin{aligned} DOS_j^\alpha(k,E) \quad &= -\tfrac{1}{\pi} \lim_{\eta \to 0^+} \text{Im} \Big[M^\alpha(k)\, G_{L,L}^{\alpha,j}(k,z) + P^\alpha(k)\, G_{\underline{L},\underline{L}}^{\alpha,j}(k,z) + Q^\alpha(k)\, G_{R,R}^{\alpha,j}(k,z) \\ &+ R^\alpha(k)\, G_{\underline{R},\underline{R}}^{\alpha,j}(k,z) + S^\alpha(k)\, G_{L,\underline{L}}^{\alpha,j}(k,z) + U^\alpha(k)\, G_{L,R}^{\alpha,j}(k,z) + V^\alpha(k)\, G_{L,\underline{R}}^{\alpha,j}(k,z) \\ &+ W^\alpha(k)\, G_{\underline{L},R}^{\alpha,j}(k,z) + X^\alpha(k)\, G_{\underline{L},\underline{R}}^{\alpha,j}(k,z) + Y^\alpha(k)\, G_{R,\underline{R}}^{\alpha,j}(k,z) + Z^\alpha(k) \Big], \end{aligned} \tag{18}$$

where $M^\alpha(k)\ , \cdots , Z^\alpha(k)$ are the renormalization coefficients and $G_{\mu,\nu}^{\alpha,j}(k,z)$ with $\mu, \nu = L,\ \underline{L},\ R$ or $\underline{R}$ are matrix elements of the Green's function corresponding to the left up (L), left down ($\underline{L}$), right up (R) and right down ($\underline{R}$) sites of the renormalized four-site j-th dual channel, which constitutes the basic element of the real-space renormalization method presented in Appendix C.

Figure 3 shows the electronic density of states (DOS) and the electrical conductance (g) at zero temperature in units of the conductance quantum $g_0 = 2e^2/h$ obtained from

Equation (9) as functions of the chemical potential (μ) for free-standing graphene ribbons without dislocations, whose widths are $\mathcal{W} = 0.122$ μm (red lines), 0.073 μm (dark yellow lines) and 0.037 μm (blue lines) as well as an arbitrary length of L transversal zig-zag lines. All the ribbons studied in this article are connected to two semi-infinite periodic leads at their ends, as illustrated in Figure 2a, while a surface hopping integral $t_s = 1.2\,t$ due to the edge reconstruction and an imaginary part of energy $\eta = 10^{-3}|\,t\,|$ are also included.

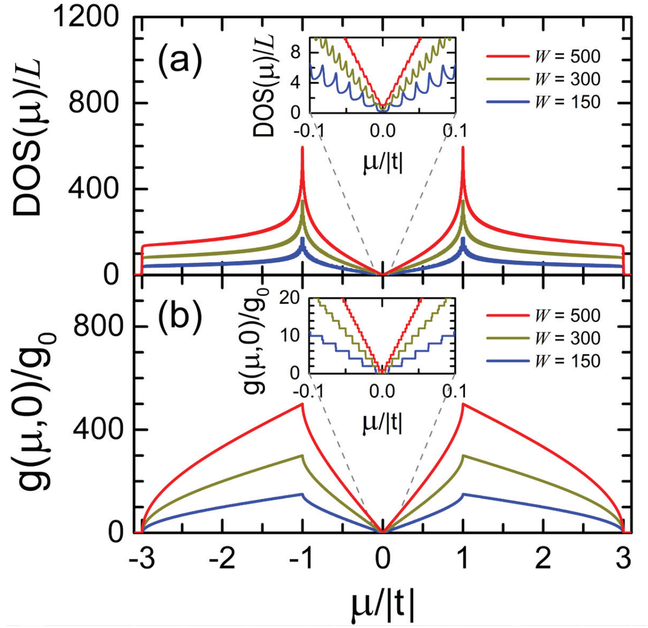

Figure 3. (**a**) Electronic density of states (DOS) and (**b**) electrical conductance (g) at $T = 0$ in units of g_0 versus the chemical potential (μ) for graphene ribbons of $\mathcal{W} = 0.122$ μm (red lines), 0.073 μm (dark yellow lines), and 0.037 μm (blue lines) with an arbitrary length of L transversal zig-zag lines and hopping integrals of t and $t_s = 1.2\,t$.

Observe the Van Hove singularities in the inset of Figure 3a, which are located at the band limits of each dual channel. The DOS spectra of Figure 3a can be analytically verified through [32]

$$DOS(E) = \frac{dS/dk}{|dE/dk\,|} = \sum_{j=1}^{W} \frac{2|E|}{\pi\sqrt{4t^2\varepsilon_j^2 - \left(E^2 - 4t^2 - \varepsilon_j^2\right)^2}}, \tag{19}$$

where $dS/dk = La/(2\pi)$ and dE/dk can be obtained from Equation (A9) in Appendix B. Note also the quantized conductance spectra in the inset of Figure 3b and the maximum values of $g(E, 0)$ around $E = \pm\, t$ in Figure 3b is equal to the number of dual channels (W).

To analyze the electrical conductance (g) of GFETs, we first self-consistently calculate V_C from Equation (6) for a given V_G and then, the chemical potential μ and g can be respectively determined using Equations (1) and (8). Figure 4 shows the electrical conductance (g) at $T = 0$ (blue lines) and at $k_BT = 0.02|\,t\,|$ (red lines) versus the gate voltage (V_G) for GFETs of $\mathcal{W} = 0.122$ μm, i.e., $W = 500$ dual channels, and $L = 4097$ zig-zag lines without dislocations, whose capacitances per unit area are (a) $C = 10$ nF/cm^2 and (b) $C = 50$ nF/cm^2. Note the quantized conductance spectra for $T = 0$, in contrast to the smoothed ones when T increases, as well as the growth of conductance with the capacitance.

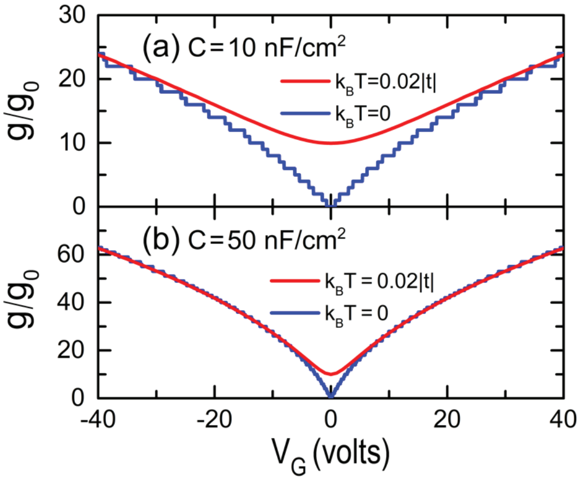

Figure 4. Normalized electrical conductance (g) by the conductance quantum g_0 at $T = 0$ and at $k_BT = 0.02|\ t\ |$ as a function of the gate voltage (V_G) for GFETs with (**a**) $C = 10\ \text{nF/cm}^2$ and (**b**) $C = 50\ \text{nF/cm}^2$, whose dimensions are $\mathcal{W} = 0.122\ \mu\text{m}$ and $L = 4097$ zig-zag lines without dislocations.

In Figure 5, the electrical conductance (g) at $k_BT = 0.026|\ t\ |$ is plotted as a function of both the back gate voltage (V_G) and the dislocation hopping integral t_A for the same graphene ribbon of Figure 4 except by the value of t_A maintaining $t_B = t_C = t_D = t$. This ribbon contains 72 *A*-type transversal dislocation lines obtained from a *A*-type dilute RS lattice with $k = 12$ and dislocations introduced from generation $m = 5$, and it is placed on a GFET with a capacitance per unit area $C = 10\ \text{nF/cm}^2$. Observe the V-shaped dependence between g and V_G, even for $t_A = 0.9\ t$, and this dependence can be noted from Figure 3b, since V_G modifies the value of chemical potential μ, as shown in Figure 1c.

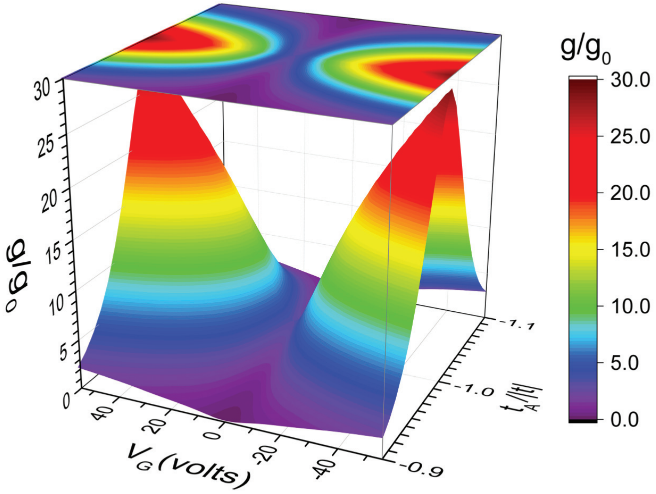

Figure 5. Electrical conductance (g) at $k_BT = 0.026|\ t\ |$ as a function of gate voltage (V_G) and dislocation hopping integral t_A for the same GFET of Figure 4a except by 72 *A*-type transversal dislocations lines placed following the dilute RS sequence with $m = 5$ and $t_B = t_C = t_D = t$.

Figure 6 shows the electrical conductance (g) at (Figure 6a) $k_BT = 0.01|t|$ and (Figure 6b) $k_BT = 0.02|t|$ with $t = -2.70$ eV [20] as functions of the gate voltage (V_G) for GFETs of

$\mathcal{W} = 0.122$ μm (i.e., $W = 500$ dual channels) and $\mathcal{L} = 0.217$ μm (red lines), 0.433 μm (green lines), and 0.866 μm (blue lines), respectively corresponding to generations $k = 10$, 11 and 12 of A-type dilute RS sequences with dislocations introduced from generation $m = 3$, hopping integrals $t_A = -2.389$ eV, $t_B = t_C = -2.74$ eV and $t_D = -2.63$ eV, where the capacitance per unit area of GFET is $C = 10$ nF/cm^2.

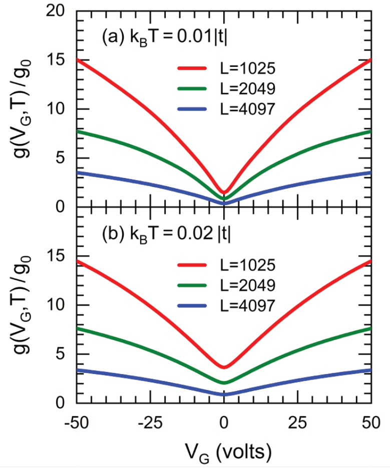

Figure 6. Conductance (g) at (**a**) $k_BT = 0.01|\ t\ |$ and (**b**) $k_BT = 0.02|\ t\ |$ as functions of the gate voltage (V_G) for GFETs with dislocations and a capacitance $C = 10$ nF/cm^2, $\mathcal{W} = 0.122$ μm (i.e., $W = 500$ dual channels) and $\mathcal{L} = 0.217$ μm (red lines), 0.433 μm (green lines), and 0.866 μm (blue lines), whose hopping integrals are $t_A = -2.389$ eV, $t_B = t_C = -2.74$ eV and $t_D = -2.63$ eV.

The results reveal a more emphasized V-shaped conductance behavior at lower temperatures, while the electrical conductance diminishes with increasing RS generation, being almost inversely proportional to the GFET length, in accordance with the Ohm's law as well as the length variation measurements carried out in GFET [33].

Finally, let us consider a specific GFET [29] built by an armchair-edged graphene ribbon placed on a substrate of silicon dioxide (SiO$_2$) of thickness $d = 285$ nm, i.e., a geometric capacitance per unit area of $C = \varepsilon_0\varepsilon_r/d \approx 12.11$ nF/cm^2. We first calculated the electrical conductance g of a graphene ribbon having a width of $W = 9009$ dual channels ($\mathcal{W} = 2.2$ μm) and a length of $L = 4097$ zig-zag lines ($\mathcal{L} = 0.866$ μm corresponding to generation 12 of the RS sequence), which contains 1024 transversal dislocation lines from a A-type dilute RS lattice with $m = 3$ and hopping integrals $t = -2.7$ eV, $t_s = 1.2\ t$, $t_A = -2.389$ eV, $t_B = t_C = -2.74$ eV and $t_D = -2.63$ eV as in Figure 6, while the analysis of system length ($\mathcal{L}$) effects on the conductance was carried out by means of Equation (16). Additionally, the contact resistance described in ref. [29] is included in the total conductance (G_{total}) using Equation (15). In Figure 7, we present the source-drain current (I_{sd}) at $T = 300$ K as a function of the gate voltage (V_G) and graphene ribbon length ($\mathcal{L}$) for the considered GFET with a source-drain voltage of $V_{sd} = 0.05$ volts, where $I_{sd}(T)$ (red spheres) was obtained from $I_{sd} = V_{sd}G_{total}$ and Equation (16) with $q = 0.866$ μm and $p = \mathcal{L}$.

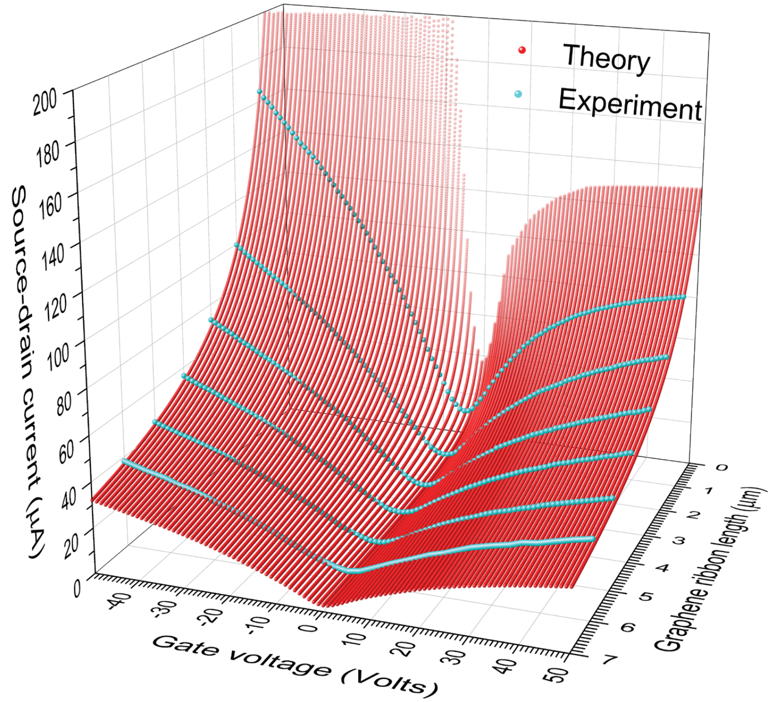

Figure 7. Theoretical source-drain current (red spheres) versus gate voltage (V_G) and graphene ribbon length ($\mathcal{L}$) for a GFET of a width $\mathcal{W} = 2.2$ μm and a capacitance per unit area $C = 12.11$ nF/cm^2, in comparison with experimental data (cyan spheres) reported from Ref. [28] for $\mathcal{L} = 1, 2, \cdots, 6$ μm.

The accordance between the theoretical (I_{sd}^T) and experimental (I_{sd}^E) source-drain currents can be quantified by means of the standard deviation (σ), given by

$$\sigma = \sqrt{\frac{1}{N}\sum_{j=1}^{N}\left\{I_{sd}^T[V_G(j)] - I_{sd}^E[V_G(j)]\right\}^2}, \tag{20}$$

where $V_G(j) = j - 51$ volts is the j-th analyzed gate voltage and $I_{sd}^E[V_G(j)]$ are digitalized experimental data (cyan spheres in Figure 7) from reference [29] with $N = 101$. The resulting σ for graphene ribbons of $\mathcal{L} = 1, 2, 3, 4, 5$ and 6 μm are respectively 3.4423, 3.0119, 2.5801, 2.7210, 1.9327 and 1.4795 μA.

Note in Figure 7 the asymmetry of I_{sd} values with respect to $V_G = 0$, whose magnitude diminishes as the ribbon length increases. This asymmetry is derived from that of the contact-resistance (R_c) spectrum in ref. [29], which is probably related to the slight doping of the used graphene ribbon [30]. In fact, the contribution of R_c to I_{sd} diminishes as the resistance of graphene ribbon (R) grows [see Equation (15)], while R in turn increases with the ribbon length. Therefore, the asymmetry of I_{sd} respect to $V_G = 0$ should decrease as the ribbon length grows.

4. Conclusions

The correlation between source-drain current and gate voltage in graphene field-effect transistors (GFETs) is investigated by means of an atomic-scale tight-binding model, where mesoscopic graphene ribbons with edge reconstruction defects and transversal dislocations are addressed by an independent dual-channel transformation, which converts armchair-edged graphene ribbons into a set of independent dual channels.

The electronic transport was studied within the Landauer formalism, and a new transfer matrix method has been further developed for each dual channel with nearest- and next-nearest-neighbor interactions, including aperiodically placed dislocations following a dilute Rudin–Shapiro (RS) sequence, which is one of the closest aperiodic arrangements to the random distribution. The Landauer conductance was confirmed by that obtained from the Kubo–Greenwood formula (see Appendix B), while the density of states from the Green's function has been verified by analytical solutions of Equation (19) for the case without dislocations.

Quantized electrical conductance spectra are observed even in presence of edge reconstruction defects along mesoscopic graphene ribbons without dislocations, whose maximum value corresponds to the number of dual channels, while the multi-step behavior is softened at finite temperatures. In addition, the back gate voltage (V_G) creates a shift of the chemical potential in graphene ribbons, which produces a V-shape correlation between the source-drain current (I_{sd}) and V_G originated from the V-shape DOS spectrum of graphene around the Dirac point. Finally, the realistic calculation of I_{sd} reveals an excellent agreement between the theoretical prediction from a single set of parameters and multiple experimental data obtained from GFETs of six different lengths [29].

The approach of independent dual-channel plus renormalization method presented in this article can be used to study biosensor devices based on GFETs by considering adsorbed molecules as Fano impurities [34]. This study is currently in process.

Author Contributions: Conceptualization, F.S., V.S. and C.W.; methodology, F.S., V.S. and C.W; software, F.S., V.S. and C.W; validation, F.S., V.S. and C.W.; formal analysis, F.S., V.S. and C.W; investigation, F.S., V.S. and C.W; resources, F.S., V.S. and C.W; data curation, F.S., V.S. and C.W; writing—original draft preparation, F.S., V.S. and C.W; writing—review and editing, F.S., V.S. and C.W; visualization, F.S., V.S. and C.W; supervision, F.S., V.S. and C.W; project administration, F.S., V.S. and C.W; funding acquisition, V.S. and C.W All authors have read and agreed to the published version of the manuscript.

Funding: This work has been partially supported by the Consejo Nacional de Ciencia y Tecnología of Mexico (CONACyT) through grant 252943 and by the National Autonomous University of Mexico through projects PAPIIT-IN110020 and PAPIIT-IN112522. The computations were performed at Miztli of DGTIC-UNAM.

Institutional Review Board Statement: Not applicable.

Informed Consent Statement: Not applicable.

Data Availability Statement: Data sharing not applicable.

Acknowledgments: The technical assistance of Alberto López (R.I.P.), Alejandro Pompa, Cain González, Silvia E. Frausto, and Yolanda Flores are fully appreciated. F.S. acknowledges the postdoctoral fellowship from CONACyT.

Conflicts of Interest: The authors declare no conflict of interest.

Appendix A. Independent Dual-Channel Method

Let us consider an armchair-edged graphene ribbon with a width of four atoms and an arbitrary length of L transversal zig-zag lines described by Hamiltonian (3), which in the matrix form following the atom numbering of Figure A1a can be written as

$$\mathbf{H}=\begin{pmatrix} \ddots & \ddots & \ddots & \vdots & \iddots & \ddots & \ddots \\ \ddots & \mathbf{h} & \mathbf{t}_1 & 0 & \cdots & \ddots & \ddots \\ \ddots & \mathbf{t}_1 & \mathbf{h} & \mathbf{t}_2 & \ddots & \vdots & \iddots \\ \cdots & 0 & \mathbf{t}_2 & \mathbf{h} & \ddots & 0 & \cdots \\ \iddots & \vdots & \ddots & \ddots & \ddots & \mathbf{t}_{L-1} & \ddots \\ \ddots & \ddots & \cdots & 0 & \mathbf{t}_{L-1} & \mathbf{h} & \ddots \\ \ddots & \ddots & \iddots & \vdots & \ddots & \ddots & \ddots \end{pmatrix}, \tag{A1}$$

where

$$\mathbf{h}=\begin{pmatrix} 0 & t_s & 0 & 0 \\ t_s & 0 & t & 0 \\ 0 & t & 0 & t_s \\ 0 & 0 & t_s & 0 \end{pmatrix},\ \mathbf{t}_1=\begin{pmatrix} 0 & 0 & 0 & 0 \\ 0 & t_1 & 0 & 0 \\ 0 & 0 & 0 & 0 \\ 0 & 0 & 0 & t_1 \end{pmatrix},\ \mathbf{t}_2=\begin{pmatrix} t_2 & 0 & 0 & 0 \\ 0 & 0 & 0 & 0 \\ 0 & 0 & t_2 & 0 \\ 0 & 0 & 0 & 0 \end{pmatrix},\ \text{and } \mathbf{t}_{L-1}=\begin{pmatrix} t_{L-1} & 0 & 0 & 0 \\ 0 & 0 & 0 & 0 \\ 0 & 0 & t_{L-1} & 0 \\ 0 & 0 & 0 & 0 \end{pmatrix} \tag{A2}$$

being t and t_s the interior- and surface-hopping integrals, whose difference is originated from the edge reconstruction of graphene ribbons [20]. In Equation (A2), t_l with $l = 1,\ 2,\ \cdots,\ L-1$ are hopping integrals that connect zig-zag lines and through them transverse dislocations can be introduced. The eigenvalues of matrix $\mathbf{h}$ are $\pm\,\varepsilon_1 = \pm\frac{1}{2}\left(t-\sqrt{t^2+4t_s^2}\right)$ and $\pm\,\varepsilon_2 = \mp\frac{1}{2}\left(t+\sqrt{t^2+4t_s^2}\right)$.

Let us further introduce a unitary transformation given by

$$\mathbf{U}=\begin{pmatrix} \ddots & \ddots & \ddots & \vdots & \iddots \\ \ddots & \mathbf{u} & 0 & 0 & \cdots \\ \ddots & 0 & \mathbf{u} & 0 & \ddots \\ \cdots & 0 & 0 & \mathbf{u} & \ddots \\ \iddots & \vdots & \ddots & \ddots & \ddots \end{pmatrix} \text{ with } \mathbf{u}=\frac{1}{\sqrt{2}}\begin{pmatrix} v_1 & -\,v_2 & v_2 & -\,v_1 \\ \varepsilon_1 v_1/t_s & -\varepsilon_2 v_2/t_s & -\varepsilon_2 v_2/t_s & \varepsilon_1 v_1/t_s \\ \varepsilon_1 v_1/t_s & \varepsilon_2 v_2/t_s & -\varepsilon_2 v_2/t_s & -\varepsilon_1 v_1/t_s \\ v_1 & v_2 & v_2 & v_1 \end{pmatrix}, \tag{A3}$$

where $v_j = \left[(\varepsilon_j/t_s)^2+1\right]^{-1/2}$ being $j = 1$ or 2.

Applying this transformation ($\mathbf{U}$) to $\mathbf{H}$ we obtain

$$\tilde{\mathbf{H}}=\mathbf{U}^{\mathrm{T}}\mathbf{H}\,\mathbf{U}=\begin{pmatrix} \ddots & \ddots & \ddots & \vdots & \iddots & \ddots & \ddots \\ \ddots & \boldsymbol{\alpha} & \boldsymbol{\beta}_1 & 0 & \cdots & \ddots & \ddots \\ \ddots & \boldsymbol{\beta}_1 & \boldsymbol{\alpha} & \boldsymbol{\beta}_2 & \ddots & \vdots & \iddots \\ \cdots & 0 & \boldsymbol{\beta}_2 & \boldsymbol{\alpha} & \ddots & 0 & \cdots \\ \iddots & \vdots & \ddots & \ddots & \ddots & \boldsymbol{\beta}_{L-1} & \ddots \\ \ddots & \ddots & \cdots & 0 & \boldsymbol{\beta}_{L-1} & \boldsymbol{\alpha} & \ddots \\ \ddots & \ddots & \iddots & \vdots & \ddots & \ddots & \ddots \end{pmatrix}, \tag{A4}$$

where

$$\boldsymbol{\alpha} = \begin{pmatrix} \varepsilon_1 & 0 & 0 & 0 \\ 0 & \varepsilon_2 & 0 & 0 \\ 0 & 0 & -\varepsilon_2 & 0 \\ 0 & 0 & 0 & -\varepsilon_1 \end{pmatrix},\ \boldsymbol{\beta}_1 = \begin{pmatrix} t'_1 & 0 & 0 & t'_1 \\ 0 & t'_1 & t'_1 & 0 \\ 0 & t'_1 & t'_1 & 0 \\ t'_1 & 0 & 0 & t'_1 \end{pmatrix},\ \boldsymbol{\beta}_2 = \begin{pmatrix} t'_2 & 0 & 0 & -t'_2 \\ 0 & t'_2 & -t'_2 & 0 \\ 0 & -t'_2 & t'_2 & 0 \\ -t'_2 & 0 & 0 & t'_2 \end{pmatrix}$$

$$\text{and } \boldsymbol{\beta}_{L-1} = \begin{pmatrix} t'_{L-1} & 0 & 0 & -t'_{L-1} \\ 0 & t'_{L-1} & -t'_{L-1} & 0 \\ 0 & -t'_{L-1} & t'_{L-1} & 0 \\ -t'_{L-1} & 0 & 0 & t'_{L-1} \end{pmatrix} \tag{A5}$$

being $t'_l = t_l/2$ with $l = 1,\ 2,\ \cdots,\ L-1$.

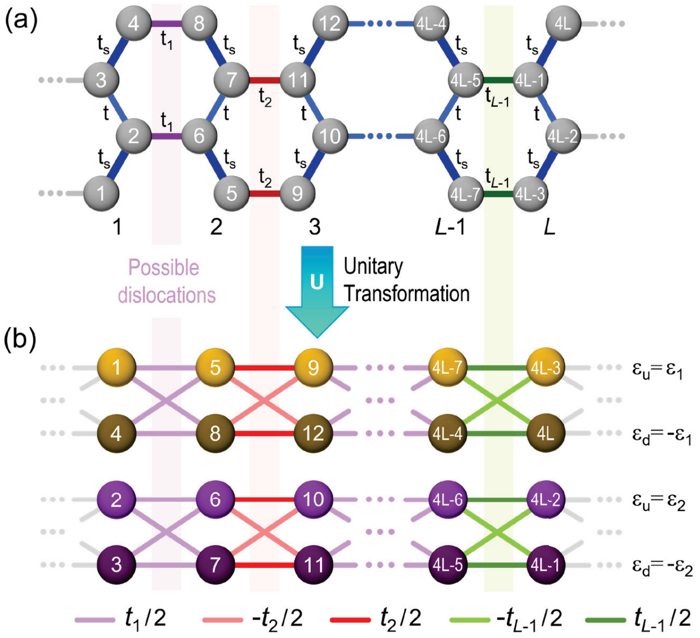

Figure A1. (**a**) Sketch of an armchair-edged graphene nanoribbon with a width of 4 atoms, arbitrary length L, null on-site energies, hopping integrals t (light blue lines), t_1 (violet lines), t_2 (red lines), t_{L-1} (green lines) and $t_s = 1.2\,t$ (thick blue lines); (**b**) by applying a unitary transformation **U**, the nanoribbon (**a**) becomes into two independent dual-channels with on-site energies ($\pm\varepsilon_1$ and $\pm\varepsilon_2$) and hopping integrals $t_1/2$ (light violet lines), $\pm t_2/2$ (light red lines) and $\pm t_{L-1}/2$ (light green lines). Numbers inside spheres denote the positions in Hamiltonian matrices (A1) and (A4) respectively before and after the application of **U**.

Hence, for a graphene ribbon with a width of four atoms and arbitrary length L, Hamiltonian **H** can be visualized as two independent dual channels, as illustrated in Figure A1b with on-site energies $\pm\varepsilon_j$ and hopping integrals $t_1/2$, $\pm\, t_2/2$ and $\pm t_{L-1}/2$. It is worth mentioning that the independent dual-channel method presented in this appendix includes the ribbon edge reconstruction, and a particular case of this method can be found in reference [35] for $t_s = t$.

Appendix B. Transfer Matrix Method for Dual Channels

Let us consider a dual channel or double chain obtained from the unitary transformation of Appendix A, as illustrated in Figure A2, whose Hamiltonian can be written as

$$\begin{aligned} H \; = & \; \varepsilon \sum_{l} (|u,l\rangle\langle u,l| - |d,l\rangle\langle d,l|) + \sum_{l} t'_l (|d,l\rangle\langle d,l+1| + |u,l\rangle\langle u,l+1| + c.c.) \\ & + \sum_{l} t'_l (|d,2l-1\rangle\langle u,2l| + |u,2l-1\rangle\langle d,2l| - |d,2l\rangle\langle u,2l+1| - |u,2l\rangle\langle d,2l+1| + c.c.), \end{aligned} \tag{A6}$$

where $t'_l = t_l/2$ is the hopping integral between transversal lines l and $l+1$, $|u\,,\,l\rangle$ and $|d,l\rangle$ are respectively the Wannier functions at the up and down sites of transversal line l. In contrast, there is no variation in hopping integrals $t'_l = t' = t/2$ in periodic leads. Moreover, the system possesses an odd number L of transversal lines, since a Rudin–Shapiro (RS) distribution of bonds is considered.

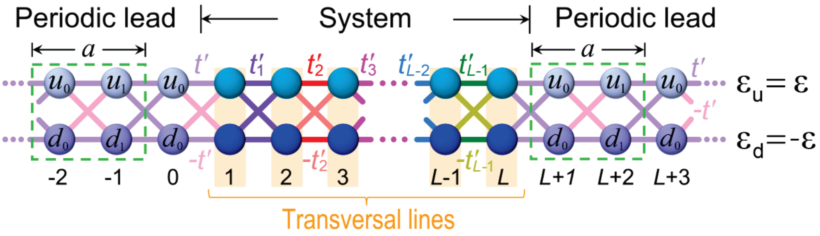

Figure A2. Dual-channel system of $2L$ sites with hopping integrals $\pm\, t'_l$ connected to two semi-infinite periodic leads with $\pm\, t'$, where the on-site energies are $\varepsilon_{\mathrm{u}} = \varepsilon$ and $\varepsilon_{\mathrm{d}} = -\varepsilon$. Green dashed lines indicate unit cells whose wavefunction amplitudes without phases are denoted on the spheres.

In these periodic dual-channel leads, the unit cell of length a is constituted by four sites and the electronic wavefunction with wavenumber k can be written as

$$|\Psi(k)\rangle = \sum_{m} \Big[u_0(k)\;|u,0\rangle + u_1(k)\; e^{ika/2}|u,1\rangle + d_0(k)\;|d,0\rangle + d_1(k)\; e^{ika/2}|d,1\rangle \Big]\; e^{ikma}, \tag{A7}$$

where m is the index of unit cells. The stationary Schrödinger equation $H|\Psi(k)\rangle = E(k)|\Psi(k)\rangle$ leads to

$$\begin{pmatrix} \varepsilon & 0 & 2\,t'\cos\,(ka/2) & -2\,i\,t'\sin\,(ka/2) \\ 0 & -\varepsilon & -2\,i\,t'\sin\,(ka/2) & 2\,t'\cos\,(ka/2) \\ 2\,t'\cos\,(ka/2) & 2\,i\,t'\sin\,(ka/2) & \varepsilon & 0 \\ 2\,i\,t'\sin\,(ka/2) & 2\,t'\cos\,(ka/2) & 0 & -\varepsilon \end{pmatrix} \begin{pmatrix} u_0(k) \\ d_0(k) \\ u_1(k) \\ d_1(k) \end{pmatrix} = E(k) \begin{pmatrix} u_0(k) \\ d_0(k) \\ u_1(k) \\ d_1(k) \end{pmatrix}, \tag{A8}$$

whose eigenvalues or dispersion relations are

$$E(k) = \begin{cases} E_{+}^{-}(k) = +\sqrt{\varepsilon^2 + 4(t')^2 - 4\,t\varepsilon\;\cos\,(ka/2)}, \text{ if } \sqrt{\varepsilon^2 + 4\,(t')^2} \le E \le\; |\varepsilon - 2\,t'| \\ E_{+}^{+}(k) = +\sqrt{\varepsilon^2 + 4(t')^2 + 4\,t\varepsilon\;\cos\,(ka/2)}, \text{ if } |\varepsilon + 2\,t'|\; \le E \le \sqrt{\varepsilon^2 + 4\,(t')^2} \\ E_{-}^{+}(k) = -\sqrt{\varepsilon^2 + 4(t')^2 + 4\,t\varepsilon\;\cos\,(ka/2)}, \text{ if } -\sqrt{\varepsilon^2 + 4\,(t')^2} \le E \le -|\varepsilon + 2\,t'| \\ E_{-}^{-}(k) = -\sqrt{\varepsilon^2 + 4(t')^2 - 4\,t\varepsilon\;\cos\,(ka/2)}, \text{ if } -\;|\varepsilon - 2\,t'|\; \le E \le -\sqrt{\varepsilon^2 + 4\,(t')^2} \end{cases} \tag{A9}$$

where a is the lattice constant indicated in Figure A2. These four dispersion relations of (A9) are plotted in Figure A3 for $t' = -\,0.5|\,t\,|$, $t_s = -\,1.2|\,t\,|$ and $\varepsilon_u = -\varepsilon_d = \frac{1}{2}\Big(|\,t\,| + \sqrt{t^2 + 4t_s^2}\Big) = 1.8\,|\,t\,|$ in the first dual channel analyzed in Appendix A.

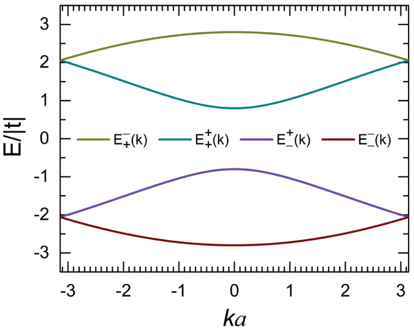

Figure A3. Dispersion relations $E_\pm^+(k)$ and $E_\pm^-(k)$ versus ka for periodic dual-channel leads with $\varepsilon_u = -\varepsilon_d = 1.8|t|$ and $t' = -0.5|t|$.

Wavefunction amplitudes $u_l(k)$ and $d_l(k)$ for $l = 0$ and 1 obtained from Equation (A8) are summarized in Table A1 for each energy band, shown for example in Figure A3.

Table A1. Amplitudes u_l and d_l in periodic dual-channel leads with $\varepsilon_u = -\varepsilon_d = \varepsilon > 0$ and $t' < 0$.

Energy Band	$u_0\ (k)$	$d_0\ (k)$	$u_1\ (k)$	$d_1\ (k)$
$\lvert\varepsilon + 2t'\rvert \le E \le \sqrt{\varepsilon^2 + 4(t')^2}$	$-i\,[C + \varepsilon + E_+^+]/S$	-1	$-i\,[C + \varepsilon + E_+^+]/S$	1
$-\sqrt{\varepsilon^2 + 4(t')^2} \le E \le -\lvert\varepsilon + 2t'\rvert$	$-i\,[C + \varepsilon + E_-^+]/S$	-1	$-i\,[C + \varepsilon + E_-^+]/S$	1
$\sqrt{\varepsilon^2 + 4(t')^2} \le E \le \lvert 2t' - \varepsilon\rvert$	$i\,[C - \varepsilon - E_+^-]/S$	1	$-i\,[C - \varepsilon - E_+^-]/S$	1
$-\lvert 2t' - \varepsilon\rvert \le E \le -\sqrt{\varepsilon^2 + 4(t')^2}$	$i\,[C - \varepsilon - E_-^-]/S$	1	$-i\,[C - \varepsilon - E_-^-]/S$	1

where $C = 2t'\cos(ka/2)$ and $S = 2t'\sin(ka/2)$.

On the other hand, for a dual-channel system of L transversal lines connected to two periodic leads represented by lines zero and $L + 1$, the wavefunction of both system and leads can be written as

$$|\Psi\rangle = \sum_{l=0}^{L+1} (A_l|u,l\rangle + B_l|d,l\rangle) \tag{A10}$$

and then, the stationary Schrödinger equation from Hamiltonian (A6) is given by

$$\begin{cases} [\varepsilon_u - E]\ A_1 + t'_0 A_0 + t'_1 A_2 - t'_0 B_0 + t'_1 B_2 = 0 \\ [\varepsilon_d - E]\ B_1 + t'_0 B_0 + t'_1 B_2 - t'_0 A_0 + t'_1 A_2 = 0 \\ [\varepsilon_u - E]\ A_2 + t'_1 A_1 + t'_2 A_3 + t'_1 B_1 - t'_2 B_3 = 0 \\ [\varepsilon_d - E]\ B_2 + t'_1 B_1 + t'_2 B_3 + t'_1 A_1 - t'_2 A_3 = 0 \\ \qquad\qquad\qquad \vdots \\ [\varepsilon_u - E]\ A_{L-1} + t'_{L-2} A_{L-2} + t'_{L-1} A_L + t'_{L-2} B_{L-2} - t'_{L-1} B_L = 0 \\ [\varepsilon_d - E]\ B_{L-1} + t'_{L-2} B_{L-2} + t'_{L-1} B_L + t'_{L-2} A_{L-2} - t'_{L-1} A_L = 0 \\ [\varepsilon_u - E]\ A_L + t'_{L-1} A_{L-1} + t'_L A_{L+1} - t'_{L-1} B_{L-1} + t'_L B_{L+1} = 0 \\ [\varepsilon_d - E]\ B_L + t'_{L-1} B_{L-1} + t'_L B_{L+1} - t'_{L-1} A_{L-1} + t'_L A_{L+1} = 0 \end{cases}, \tag{A11}$$

where $\varepsilon_u = \varepsilon$, $\varepsilon_d = -\varepsilon$ and $t'_0 = t'_L = t'$. Equations (A11) can be rewritten in matrix form as

$$\begin{pmatrix} A_{L+1} \\ B_{L+1} \end{pmatrix} = \mathbf{M}_L(E) \cdots \mathbf{M}_{2j}(E)\mathbf{M}_{2j-1}(E) \cdots \mathbf{M}_0(E) \begin{pmatrix} A_0 \\ B_0 \end{pmatrix} = \mathbf{M}_\mathrm{T}(E) \begin{pmatrix} A_0 \\ B_0 \end{pmatrix} = \begin{pmatrix} m_{11}(E) & m_{12}(E) \\ m_{21}(E) & m_{22}(E) \end{pmatrix} \begin{pmatrix} A_0 \\ B_0 \end{pmatrix}, \tag{A12}$$

where $j = 1,\ 2,\ \cdots,\ (L-1)/2$, A_0 (B_0) and A_{L+1} (B_{L+1}) are respectively wavefunction coefficients at the up (down) site of transversal lines zero and $L+1$,

$$\mathbf{M}_{2l}(E) = \frac{1}{4\,\varepsilon\,t_{2l}}\begin{pmatrix} E^2-\varepsilon^2-4\,t_{2l}^2 & -(E+\varepsilon)^2+4\,t_{2l}^2 \\ (E-\varepsilon)^2-4\,t_{2l}^2 & -E^2+\varepsilon^2+4\,t_{2l}^2 \end{pmatrix} \text{ for } l = 0,\ 1,\ \cdots,\ \frac{L-1}{2} \tag{A13}$$

$$\mathbf{M}_{2s-1}(E) = \frac{1}{4\,\varepsilon\,t_{2s-1}}\begin{pmatrix} E^2-\varepsilon^2-4\,t_{2s-1}^2 & -(E-\varepsilon)^2+4\,t_{2s-1}^2 \\ -(E-\varepsilon)^2+4\,t_{2s-1}^2 & E^2-\varepsilon^2-4\,t_{2s-1}^2 \end{pmatrix} \text{ for } s = 1,\ 2,\ \cdots,\ \frac{L+1}{2} \tag{A14}$$

and the total transfer matrix $\mathbf{M}_{\mathrm{T}}$ including connections to periodic leads $\mathbf{M}_L$ and $\mathbf{M}_0$.

For the case of an electronic plane wave incident from the left lead of Figure A1, the scattered ones by the system are a reflected wave moving to the left and another transmitted one going to the right. Hence, the wavefunction coefficients at transversal line zero and line $L+1$ can be respectively written as

$$\begin{pmatrix} A_0 \\ B_0 \end{pmatrix} = \begin{pmatrix} u_0 + r\,u_0^* \\ d_0 + r\,d_0^* \end{pmatrix} \text{ and } \begin{pmatrix} A_{L+1} \\ B_{L+1} \end{pmatrix} = \begin{pmatrix} \tau\,u_0 e^{ik(L+1)a} \\ \tau\,d_0 e^{ik(L+1)a} \end{pmatrix}, \tag{A15}$$

where r and τ are respectively the reflection and transmission coefficients satisfying $|\,r\,|^2 + |\,\tau\,|^2 = 1$. From Equations (A12) and (A15), we have

$$\begin{pmatrix} u_0 \tau e^{ik(L+1)a} \\ d_0 \tau e^{ik(L+1)a} \end{pmatrix} = \mathbf{M}_{\mathrm{T}}(E)\begin{pmatrix} u_0 + u_0^* r \\ d_0 + d_0^* r \end{pmatrix}, \tag{A16}$$

which can be rewritten as

$$\begin{pmatrix} \tau e^{ik\,La} \\ 0 \end{pmatrix} = \begin{pmatrix} u_0 e^{ika} & 0 \\ d_0 e^{ika} & 1 \end{pmatrix}^{-1} \begin{pmatrix} m_{11}(E) & m_{12}(E) \\ m_{21}(E) & m_{22}(E) \end{pmatrix}\begin{pmatrix} u_0 + r\,u_0^* \\ d_0 + r\,d_0^* \end{pmatrix}. \tag{A17}$$

Therefore, the transmittance (T) of electronic waves in a dual channel is given by

$$\mathrm{T}(E) = |\tau|^2 = \left| \frac{u_0\,d_0^* - d_0\,u_0^*}{m_{11}(E)\,d_0 u_0^* + m_{12}(E)\,|d_0\,|^2 - \ m_{21}(E)\,|u_0\,|^2 - \ m_{22}(E)\,u_0\,d_0^*} \right|^2 \tag{A18}$$

where u_0 and d_0 are given in Table A1.

The electrical conductance (g) at 0 K obtained from Equations (9) and (A18) as a function of the chemical potential (μ) is shown in Figure A4 for the graphene ribbon of Figure A1 containing $L = 9$ transversal lines (see Table A3 for generation $k = 3$) (a) without and (b) with a single transversal dislocation $t_A = 1.1\,t$, while $t_B = \ t$. These Landauer conductance spectra are further compared with those obtained from the Kubo formalism within the linear response theory. In general, the electric conductivity (σ) can be calculated by means of the Kubo–Greenwood formula [22],

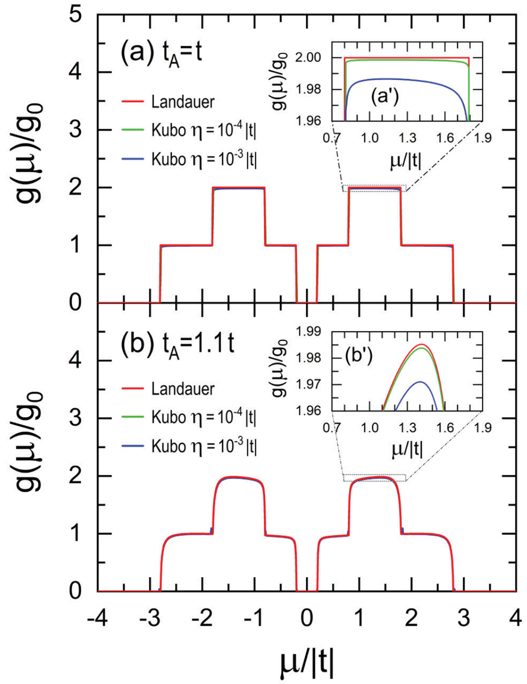

Figure A4. Electrical conductance (g) at 0 K in units of $g_0 = 2e^2/h$ obtained from the Landauer (red lines) and Kubo–Greenwood formulas using $\eta = 10^{-3}|\,t\,|$ (blue lines) and $\eta = 10^{-4}|\,t\,|$ (green lines) as functions of the chemical potential (μ) for graphene ribbons with $W = 4$, $L = 9$, $t_s = 1.2\,t$, $t_B = t$, (**a**,**a′**) $t_A = t$ and (**b**,**b′**) $t_A = 1.1\,t$, whose magnifications are shown in (**a′**) and (**b′**).

$$\sigma(\mu,\omega,T) = \frac{2\,e^2\hbar}{\pi\,m^2\Omega}\int_{-\infty}^{\infty} dE\frac{f_{FD}(E) - f_{FD}(E+\hbar\omega)}{\hbar\omega}Tr\left[\hat{p}_x \mathrm{Im}G^+(z+\hbar\omega)\hat{p}_x \mathrm{Im}G^+(z)\right], \tag{A19}$$

where e and m are respectively the electrical charge and the mass of electron, Ω is the area of graphene ribbon, and $f_{FD}(E) = \{\,1+\exp[(E-\mu)/k_BT]\,\}^{-1}$ is the Fermi–Dirac distribution with the chemical potential μ, the Boltzmann constant k_B and temperature T. $\hat{p}_x = im\,[\hat{H},x]/\hbar$ is the projection of the momentum operator along the oscillating electrical field with frequency ω, and $G^+(z)$ with $z = E + i\eta$ is the retarded one-particle Green's function. For the case of $\omega = T = 0$, Equation (A19) can be rewritten as [36].

$$g(\mu,0,0) = \sigma(\mu,0,0)\frac{\mathcal{W}}{\mathcal{L}} = \frac{2\,e^2\hbar}{\pi\,m^2\mathcal{L}^2}Tr\left[\hat{p}_x \mathrm{Im}G^+(\mu)\hat{p}_x \mathrm{Im}G^+(\mu)\right]. \tag{A20}$$

In Figure A4 the Kubo conductance spectra are obtained from Equation (A20) for two imaginary parts of energy $\eta = 10^{-3}|\,t\,|$ (blue lines) and $\eta = 10^{-4}|\,t\,|$ (green lines), where the retarded Green's function was calculated through $G(z) = (z-H)^{-1}$ from the Dyson equation for a Hamiltonian of 36 atoms since $W = 4$ and $L = 9$ for a dilute A-type RS lattice with $k = 4$ and $m = 3$ containing only dislocation hopping integrals t_A and t_B, whose boundary conditions were obtained from periodic leads of 200,000 transversal lines. Observe in Figure A4a′,b′ the coincidence between electrical conductance spectra from Landauer and Kubo formalisms when $\eta \to 0$ in the latter one.

Appendix C. Real-Space Renormalization Method for Dilute Rudin–Shapiro Dual Channels

The Rudin–Shapiro (RS) sequence of generation k, $S(k)$, can be built using the substitution rules (12) or addition rules (13). The latter can be summarized into a single equation given by

$$S_\alpha(k) = S_\beta(k-1) \oplus S_\gamma(k-1), \tag{A21}$$

whose subindices α, β and γ denote A, B, C or D-type RS sequence according to Table A2.

Table A2. Addition rules for all type Rudin–Shapiro sequences.

α-Type	β-Type	γ-Type
A	A	B
B	A	C
C	D	B
D	D	C

Let us consider an RS dual channel with bond disorder formed by alternating hopping integrals t'_A, t'_B, t'_C and t'_D, instead of letters A, B, C and D in the RS sequences, being $t'_\alpha = t_\alpha/2$ with $\alpha = A,\ B,\ C$ or D. Moreover, a dilute RS dual channel can be built using periodic RS segments of generation $m-1$ formed by hopping integrals $t' = t/2$ and placing a single hopping integral defect t'_α at the beginning of $S_\alpha(m)$, while subsequent generations of dilute RS dual channels are constructed following the standard addition rule (A21) and Table A2. For example, dilute RS dual channels with $m = 2$ are presented in Table A3.

Table A3. Dilute Rudin–Shapiro dual channels with m = 2.

Generation	*A*-Type	*B*-Type	*C*-Type	*D*-Type
1	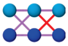	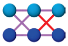	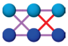	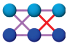
2	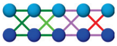	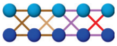	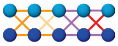	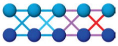
3	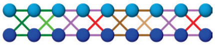	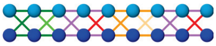	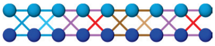	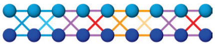

Note: Symbol meaning ● ε ● -ε — t' — $-t'$ — t'_A — $-t'_A$ — t'_B — $-t'_B$ — t'_C — $-t'_C$ — t'_D — $-t'_D$.

In this appendix, a new real-space renormalization method is developed for dilute RS dual channels, as an extension of that for single channels developed in reference [37], where the freedom degrees of interior sites are removed but their exact participation is maintained in the results. As an example, we present in Figure A5 this renormalization procedure for A-type RS dual channels by starting from generation one, which consists of six sites (blue spheres) with on-site energies $\varepsilon_u = \varepsilon$ and $\varepsilon_d = -\varepsilon$, respectively, for up and down sites, as well as hopping integrals $t' = t/2$ (violet lines) and $-t'$ (red lines). The central sites located at the second transversal line can be renormalized by reducing the six-site dual channel into a four-site one with effective on-site energies $\varepsilon^A_L(1)$, $\varepsilon^A_{\underline{L}}(1)$, $\varepsilon^A_R(1)$ and $\varepsilon^A_{\underline{R}}(1)$, respectively, for left-up, left-down, right-up and right-down sites, as well as effective hopping integrals $t'_h(1)$, $t'_{\underline{h}}(1)$, $t'_v(1)$, $t'_{\underline{v}}(1)$, $t'_d(1)$ and $t'_{\underline{d}}(1)$, correspondingly denoting up horizontal, down horizontal, left vertical, right vertical, decreasing diagonal and increasing diagonal bonds. Using the addition rule for A-type RS dual channels given by Equation (A21) and Table A2, this four sites dual channel is concatenated to another four-site renormalized B-type RS dual channel to build a six-site dual channel of generation 2, where the on-site energies of central sites are $\varepsilon^A_C(2) = \varepsilon^A_R(1) + \varepsilon^B_L(1) - \varepsilon$ and

$\varepsilon_{\underline{C}}^A(2) = \varepsilon_{\underline{R}}^A(1) + \varepsilon_{\underline{L}}^B(1) + \varepsilon$ respectively for up and down ones connected by the hopping integral $t_C^A(2) = t_{\underline{v}}^A(1) + t_v^B(1)$, represented by a double line.

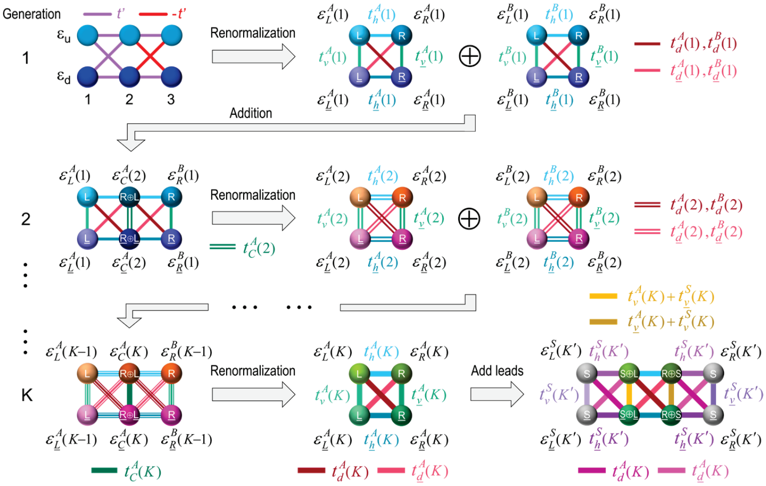

Figure A5. Schematic representation of the renormalization procedure to build an A-type RS dual channel of generation K connected to two periodic leads of generation K' (gray spheres), where the effective on-site energies $\varepsilon_l^\alpha(k,z)$ and hopping integrals $t_j^\alpha(k,z)$ are respectively denoted as $\varepsilon_l^\alpha(k)$ and $t_j^\alpha(k)$ for $\alpha = A$ or B, $l = L,\ \underline{L},\ C,\ \underline{C},\ R$ or $\underline{R}$ and $j = h,\ \underline{h},\ v,\ \underline{v},\ d,\ \underline{d},\ C$ or $\underline{C}$.

In general, for an α-type RS dual channel of generation k, similar addition and renormalization procedures were carried out. The effective on-site energies $\varepsilon_l^\alpha(k,E)$ with $l = L,\ \underline{L},\ R$ or $\underline{R}$ and hopping integrals $t_j^\alpha(k,E)$, being $l = h,\ \underline{h},\ v,\ \underline{v},\ d$ or $\underline{d}$, of four-site dual channel can be obtained from the stationary Schrödinger equation:

$$(\mathbf{H} - E\mathbf{I})|\Psi\rangle = 0 \tag{A22}$$

where $\mathbf{I}$ is the identity matrix, $\mathbf{H}$ is the Hamiltonian of a concatenated six-site dual channel built from two dual channels of generations $k-1$ and $|\Psi\rangle = \sum_j b_j|j\rangle$ is the electronic wavefunction with $j = L,\ \underline{L},\ C,\ \underline{C},\ R,$ or $\underline{R}$. Equation (A22) can be rewritten as

$$\begin{pmatrix} \varepsilon_L^\beta(k-1,E)-E & t_v^\beta(k-1,E) & t_h^\beta(k-1,E) & t_d^\beta(k-1,E) & 0 & 0 \\ t_v^\beta(k-1,E) & \varepsilon_{\underline{L}}^\beta(k-1,E)-E & t_{\underline{d}}^\beta(k-1,E) & t_{\underline{h}}^\beta(k-1,E) & 0 & 0 \\ t_h^\beta(k-1,E) & t_{\underline{d}}^\beta(k-1,E) & \varepsilon_C^\alpha(k,E)-E & t_c^\alpha(k,E) & t_h^\gamma(k-1,E) & t_d^\gamma(k-1,E) \\ t_d^\beta(k-1,E) & t_{\underline{h}}^\beta(k-1,E) & t_c^\alpha(k,E) & \varepsilon_{\underline{C}}^\alpha(k,E)-E & t_{\underline{d}}^\gamma(k-1,E) & t_{\underline{h}}^\gamma(k-1,E) \\ 0 & 0 & t_h^\gamma(k-1,E) & t_{\underline{d}}^\gamma(k-1,E) & \varepsilon_R^\gamma(k-1,E)-E & t_{\underline{v}}^\gamma(k-1,E) \\ 0 & 0 & t_d^\gamma(k-1,E) & t_{\underline{h}}^\gamma(k-1,E) & t_{\underline{v}}^\gamma(k-1,E) & \varepsilon_{\underline{R}}^\gamma(k-1,E)-E \end{pmatrix} \begin{pmatrix} b_L^\beta \\ b_{\underline{L}}^\beta \\ b_C^\alpha \\ b_{\underline{C}}^\alpha \\ b_R^\gamma \\ b_{\underline{R}}^\gamma \end{pmatrix} = \begin{pmatrix} 0 \\ 0 \\ 0 \\ 0 \\ 0 \\ 0 \end{pmatrix}, \tag{A23}$$

whose two central equations can be considered as a set of equations for b_C^α and $b_{\underline{C}}^\alpha$, with solutions given by

$$\begin{cases} b_C^\alpha = \Gamma_1^\alpha(k,E)\, b_L^\beta + \Gamma_2^\alpha(k,E)\, b_{\underline{L}}^\beta + \Gamma_3^\alpha(k,E)\, b_R^\gamma + \Gamma_4^\alpha(k,E)\, b_{\underline{R}}^\gamma \\ b_{\underline{C}}^\alpha = \Theta_1^\alpha(k,E)\, b_L^\beta + \Theta_2^\alpha(k,E)\, b_{\underline{L}}^\beta + \Theta_3^\alpha(k,E)\, b_R^\gamma + \Theta_4^\alpha(k,E)\, b_{\underline{R}}^\gamma \end{cases}, \tag{A24}$$

where

$$\begin{cases} \Gamma_1^{\alpha}(k,E) = \theta_1^{\alpha}(k,E)\,[t_h^{\beta}(k-\,1,E)\;+\;\phi_2^{\alpha}(k,E)\,t_d^{\beta}(k-\,1,E)] \\ \Gamma_2^{\alpha}(k,E) = \theta_1^{\alpha}(k,E)\,[t_{\underline{d}}^{\beta}(k-\,1,E)\;+\;\phi_2^{\alpha}(k,E)\,t_{\underline{h}}^{\beta}(k-\,1,E)] \\ \Gamma_3^{\alpha}(k,E) = \theta_1^{\alpha}(k,E)\,[t_h^{\gamma}(k-1,E)+\phi_2^{\alpha}(k,E)\,t_{\underline{d}}^{\gamma}(k-1,E)] \\ \Gamma_4^{\alpha}(k,E) = \theta_1^{\alpha}(k,E)\,[t_d^{\gamma}(k-1,E)+\phi_2^{\alpha}(k,E)\,t_{\underline{h}}^{\gamma}(k-1,E)] \end{cases} \tag{A25}$$

and

$$\begin{cases} \Theta_1^{\alpha}(k,E) = \theta_2^{\alpha}(k,E)\,[t_d^{\beta}(k-1,E)+\phi_1^{\alpha}(k,E)\,t_h^{\beta}(k-1,E)] \\ \Theta_2^{\alpha}(k,E) = \theta_2^{\alpha}(k,E)\,[t_{\underline{h}}^{\beta}(k-1,E)+\phi_1^{\alpha}(k,E)\,t_{\underline{d}}^{\beta}(k-1,E)] \\ \Theta_3^{\alpha}(k,E) = \theta_2^{\alpha}(k,E)\,[t_{\underline{d}}^{\gamma}(k-1,E)+\phi_1^{\alpha}(k,E)\,t_h^{\gamma}(k-1,E)] \\ \Theta_4^{\alpha}(k,E) = \theta_2^{\alpha}(k,E)\,[t_{\underline{h}}^{\gamma}(k-1,E)+\phi_1^{\alpha}(k,E)\,t_d^{\gamma}(k-1,E)] \end{cases}, \tag{A26}$$

where

$$\begin{cases} \theta_1^{\alpha}(k,E) = \left\{E-\varepsilon_c^{\alpha}(k,E)-\frac{[t_c^{\alpha}(k,E)]^2}{E-\varepsilon_{\underline{c}}^{\alpha}(k,E)}\right\}^{-1} \\ \theta_2^{\alpha}(k,E) = \left\{E-\varepsilon_{\underline{c}}^{\alpha}(k,E)-\frac{[t_c^{\alpha}(k,E)]^2}{E-\varepsilon_c^{\alpha}(k,E)}\right\}^{-1} \end{cases} \text{and} \begin{cases} \phi_1^{\alpha}(k,E) = \frac{t_c^{\alpha}(k,E)}{E-\varepsilon_c^{\alpha}(k,E)} \\ \phi_2^{\alpha}(k,E) = \frac{t_c^{\alpha}(k,E)}{E-\varepsilon_{\underline{c}}^{\alpha}(k,E)} \end{cases} \tag{A27}$$

with

$$\begin{cases} \varepsilon_c^{\alpha}(k,E) = \varepsilon_R^{\beta}(k-1,E)+\varepsilon_L^{\gamma}(k-1,E)-\varepsilon \\ \varepsilon_{\underline{c}}^{\alpha}(k,E) = \varepsilon_{\underline{R}}^{\beta}(k-1,E)+\varepsilon_{\underline{L}}^{\gamma}(k-1,E)+\varepsilon \\ t_c^{\alpha}(k,E) = t_{\underline{v}}^{\beta}(k-1,E)+t_v^{\gamma}(k-1,E) \end{cases}. \tag{A28}$$

Substituting Equation (A24) into (A23), we obtain the stationary Schrödinger equation of a four-site dual channel given by

$$\begin{pmatrix} \varepsilon_L^{\alpha}(k,E)-E & t_v^{\alpha}(k,E) & t_h^{\alpha}(k,E) & t_d^{\alpha}(k,E) \\ t_v^{\alpha}(k,E) & \varepsilon_{\underline{L}}^{\alpha}(k,E)-E & t_{\underline{d}}^{\alpha}(k,E) & t_{\underline{h}}^{\alpha}(k,E) \\ t_h^{\alpha}(k,E) & t_{\underline{d}}^{\alpha}(k,E) & \varepsilon_R^{\alpha}(k,E)-E & t_{\underline{v}}^{\alpha}(k,E) \\ t_d^{\alpha}(k,E) & t_{\underline{h}}^{\alpha}(k,E) & t_{\underline{v}}^{\alpha}(k,E) & \varepsilon_{\underline{R}}^{\alpha}(k,E)-E \end{pmatrix} \begin{pmatrix} b_L^{\alpha} \\ b_{\underline{L}}^{\alpha} \\ b_R^{\alpha} \\ b_{\underline{R}}^{\alpha} \end{pmatrix} = \begin{pmatrix} 0 \\ 0 \\ 0 \\ 0 \end{pmatrix}, \tag{A29}$$

where

$$\begin{cases} \varepsilon_L^{\alpha}(k,E) = \varepsilon_L^{\beta}(k-\,1,E)+\Gamma_1^{\alpha}(k,E)\,t_h^{\beta}(k-\,1,E)+\Theta_1^{\alpha}(k,E)\,t_d^{\beta}(k-1,E) \\ \varepsilon_{\underline{L}}^{\alpha}(k,E) = \varepsilon_{\underline{L}}^{\beta}(k-\,1,E)+\Theta_2^{\alpha}(k,E)\,t_{\underline{h}}^{\beta}(k-\,1,E)+\Gamma_2^{\alpha}(k,E)\,t_{\underline{d}}^{\beta}(k-1,E) \\ \varepsilon_R^{\alpha}(k,E) = \varepsilon_R^{\gamma}(k-\,1,E)+\Gamma_3^{\alpha}(k,E)\,t_h^{\gamma}(k-\,1,E)+\Theta_3^{\alpha}(k,E)\,t_{\underline{d}}^{\gamma}(k-1,E) \\ \varepsilon_{\underline{R}}^{\alpha}(k,E) = \varepsilon_{\underline{R}}^{\gamma}(k-\,1,E)+\Theta_4^{\alpha}(k,E)\,t_{\underline{h}}^{\gamma}(k-\,1,E)+\Gamma_4^{\alpha}(k,E)\,t_d^{\gamma}(k-1,E) \end{cases} \tag{A30}$$

and

$$\begin{cases} t_h^\alpha(k,E) = \Gamma_3^\alpha(k,E)\, t_h^\beta(k-1,E) + \Theta_3^\alpha(k,E)\, t_d^\beta(k-1,E) \\ t_{\underline{h}}^\alpha(k,E) = \Gamma_4^\alpha(k,E)\, t_{\underline{d}}^\beta(k-1,E) + \Theta_4^\alpha(k,E)\, t_{\underline{h}}^\beta(k-1,E) \\ t_d^\alpha(k,E) = \Gamma_4^\alpha(k,E)\, t_h^\beta(k-1,E) + \Theta_4^\alpha(k,E)\, t_d^\beta(k-1,E) \\ t_{\underline{d}}^\alpha(k,E) = \Gamma_3^\alpha(k,E)\, t_{\underline{d}}^\beta(k-1,E) + \Theta_3^\alpha(k,E)\, t_{\underline{h}}^\beta(k-1,E) \\ t_v^\alpha(k,E) = t_v^\beta(k-1,E) + \Gamma_2^\alpha(k,E)\, t_h^\beta(k-1,E) + \Theta_2^\alpha(k,E)\, t_d^\beta(k-1,E) \\ t_{\underline{v}}^\alpha(k,E) = t_{\underline{v}}^\gamma(k-1,E) + \Gamma_4^\alpha(k,E)\, t_h^\gamma(k-1,E) + \Theta_4^\alpha(k,E)\, t_{\underline{d}}^\gamma(k-1,E). \end{cases} \tag{A31}$$

These effective on-site energies and hopping integrals are those indicated in Figure A5.

On the other hand, the electronic density of states (*DOS*) for an α-type RS dual channel of generation k evaluated at energy E can be written as [22]

$$DOS^\alpha(k,E) = -\frac{1}{\pi} \lim_{\eta \to 0^+} \sum_{j=1}^{L(k)} \mathrm{Im}\,[G_{j,j}^\alpha(z)], \tag{A32}$$

where $L(k) = 2\,(1+2^k)$ is the number of sites in the dual channel and $G_{j,j}^\alpha(z)$ is the j-th diagonal element of retarded Green's function evaluated at $z = E + i\eta$. Extending the real-space renormalization method developed for Fibonacci chains [37,38], the $DOS^\alpha(k,E)$ of (A32) can be rewritten as

$$\begin{aligned} DOS^\alpha(k,E) = -\tfrac{1}{\pi} \lim_{\eta \to 0^+} \mathrm{Im}\,[&M^\alpha(k,z)\, G_{L,L}^\alpha(k,z) + P^\alpha(k,z)\, G_{\underline{L},\underline{L}}^\alpha(k,z) + Q^\alpha(k,z)\, G_{R,R}^a(k,z) \\ &+R^\alpha(k,z)\, G_{\underline{R},\underline{R}}^\alpha(k,z) + S^\alpha(k,z)\, G_{L,\underline{L}}^\alpha(k,z) + U^\alpha(k,z)\, G_{L,R}^\alpha(k,z) + V^\alpha(k,z)\, G_{L,\underline{R}}^\alpha(k,z) \\ &+W^\alpha(k,z)\, G_{\underline{L},R}^\alpha(k,z) + X^\alpha(k,z)\, G_{\underline{L},\underline{R}}^\alpha(k,z) + Y^\alpha(k,z)\, G_{R,\underline{R}}^\alpha(k,z) + Z^\alpha(k,z)], \end{aligned} \tag{A33}$$

where $M^\alpha(k,z), \;\cdots,\; Z^\alpha(k,z)$ are the renormalization coefficients and $G_{l,j}^\alpha(k,z)$ with $l,j = L,\ \underline{L},\ R$ or $\underline{R}$ are elements of the Green's function matrix, with $L(\underline{L})$ and $R(\underline{R})$ respectively being the up (down) left and right sites of the renormalized four-site dual channel, as illustrated in Figure A5. From Equation (A32) and the addition rule (A21), we have

$$DOS^\alpha(k,E) = DOS^\beta(k-1,E) + DOS^\gamma(k-1,E) - G_{C,C}^\alpha(k,z) - G_{\underline{C},\underline{C}}^\alpha(k,z), \tag{A34}$$

where subindex C denotes the central sites at the union of two renormalized dual channels. Equation (A34) can be rewritten using Equation (A33) as

$$\begin{aligned} DOS^\alpha(k,E) = -\tfrac{1}{\pi} \lim_{\eta \to 0^+} \mathrm{Im}\,[&M^\beta(k-1,z) G_{L,L}^\beta(k,z) + P^\beta(k-1,z) G_{\underline{L},\underline{L}}^\beta(k,z) + Q^\beta(k-1,z) G_{C,C}^\beta(k,z) \\ &+R^\beta(k-1,z) G_{\underline{C},\underline{C}}^\beta(k,z) + S^\beta(k-1,z) G_{L,\underline{L}}^\beta(k,z) + U^\beta(k-1,z) G_{L,C}^\beta(k,z) + V^\beta(k-1,z) G_{L,\underline{C}}^\beta(k,z) \\ &+W^\beta(k-1,z) G_{\underline{L},C}^\beta(k,z) + X^\beta(k-1,z) G_{\underline{L},\underline{C}}^\beta(k,z) + Y^\beta(k-1,z) G_{C,\underline{C}}^\beta(k,z) + Z^\beta(k-1,z) \\ &+M^\gamma(k-1,z) G_{C,C}^\gamma(k,z) + P^\gamma(k-1,z) G_{\underline{C},\underline{C}}^\gamma(k,z) + Q^\gamma(k-1,z) G_{R,R}^\gamma(k,z) + R^\gamma(k-1,z) G_{\underline{R},\underline{R}}^\gamma(k,z) \\ &+S^\gamma(k-1,z) G_{C,\underline{C}}^\gamma(k,z) + U^\gamma(k-1,z) G_{C,R}^\gamma(k,z) + V^\gamma(k-1,z) G_{C,\underline{R}}^\gamma(k,z) + W^\gamma(k-1,z) G_{\underline{C},R}^\gamma(k,z) \\ &+X^\gamma(k-1,z) G_{\underline{C},\underline{R}}^\gamma(k,z) + Y^\gamma(k-1,z) G_{R,\underline{R}}^\gamma(k,z) + Z^\gamma(k-1,z) - G_{C,C}^\gamma(k,z) - G_{\underline{C},\underline{C}}^\gamma(k,z)]. \end{aligned} \tag{A35}$$

The Dyson equation of a six-site α-type RS dual channel (see Figure A5 for $\alpha = \mathrm{A}$) given by $(z\mathbf{I} - \mathbf{H})\mathbf{G} = \mathbf{I}$ can be rewritten as

$$\begin{cases} [z-\varepsilon_{L}^{\beta}(k-1)]G_{L,j}^{\beta}(k-1,z)=\delta_{L,j}+t_{v}^{\beta}(k-1)G_{\underline{L},j}^{\beta}(k-1,z)+t_{h}^{\beta}(k-1)G_{C,j}^{\alpha}(k,z)+t_{d}^{\beta}(k-1)G_{\underline{C},j}^{\alpha}(k,z) \\ [z-\varepsilon_{\underline{L}}^{\beta}(k-1)]G_{\underline{L},j}^{\beta}(k-1,z)=\delta_{\underline{L},j}+t_{v}^{\beta}(k-1)G_{L,j}^{\beta}(k-1,z)+t_{\underline{d}}^{\beta}(k-1)G_{C,j}^{\alpha}(k,z)+t_{\underline{h}}^{\beta}(k-1)G_{\underline{C},j}^{\alpha}(k,z) \\ [z-\varepsilon_{C}^{\alpha}(k)]G_{C,j}^{\alpha}(k,z)=\delta_{C,j}+t_{h}^{\beta}(k-1)G_{L,j}^{\beta}(k-1,z)+t_{\underline{d}}^{\beta}(k-1)G_{\underline{L},j}^{\beta}(k-1,z)+t_{\underline{h}}^{\gamma}(k-1)G_{R,j}^{\gamma}(k-1,z) \\ \qquad +t_{d}^{\gamma}(k-1)G_{\underline{R},j}^{\gamma}(k-1,z)+t_{c}^{\alpha}(k)G_{\underline{C},j}^{\alpha}(k,z) \\ [z-\varepsilon_{\underline{C}}^{\alpha}(k)]G_{\underline{C},j}^{\alpha}(k,z)=\delta_{\underline{C},j}+t_{d}^{\beta}(k-1)G_{L,j}^{\beta}(k-1,z)+t_{\underline{h}}^{\beta}(k-1)G_{\underline{L},j}^{\beta}(k-1,z)+t_{\underline{d}}^{\gamma}(k-1)G_{R,j}^{\gamma}(k-1,z) \\ \qquad +t_{\underline{h}}^{\gamma}(k-1)G_{\underline{R},j}^{\gamma}(k-1,z)+t_{c}^{\alpha}(k)G_{C,j}^{\alpha}(k,z) \\ [z-\varepsilon_{R}^{\gamma}(k-1)]G_{R,j}^{\beta}(k-1,z)=\delta_{R,j}+t_{\underline{v}}^{\gamma}(k-1)G_{\underline{R},j}^{\beta}(k-1,z)+t_{h}^{\gamma}(k-1)G_{C,j}^{\alpha}(k,z)+t_{\underline{d}}^{\gamma}(k-1)G_{\underline{C},j}^{\alpha}(k,z) \\ [z-\varepsilon_{\underline{R}}^{\gamma}(k-1)]G_{\underline{R},j}^{\beta}(k-1,z)=\delta_{\underline{R},j}+t_{\underline{v}}^{\gamma}(k-1)G_{R,j}^{\beta}(k-1,z)+t_{d}^{\gamma}(k-1)G_{C,j}^{\alpha}(k,z)+t_{\underline{h}}^{\gamma}(k-1)G_{\underline{C},j}^{\alpha}(k,z) \end{cases} \tag{A36}$$

where $j = L,\ \underline{L},\ C,\ \underline{C},\ R,$ or $\underline{R}$, and then Equation (A36) represents the 36 equations of six effective sites. The two central equations of (A36) can be visualized as a system of equations for $G_{C,j}^{\alpha}(k,z)$ and $G_{\underline{C},j}^{\alpha}(k,z)$, whose solutions are

$$\begin{cases} G_{C,j}^{\alpha}(k,z) & =\Gamma_1^{\alpha}(k,z)\ G_{L,j}^{\beta}(k-1,z)+\Gamma_2^{\alpha}(k,z)\ G_{\underline{L},j}^{\beta}(k-1,z)+\Gamma_3^{\alpha}(k,z)\ G_{R,j}^{\gamma}(k-1,z) \\ & +\Gamma_4^{\alpha}(k,z)\ G_{\underline{R},j}^{\gamma}(k-1,z)+\delta_{C,j}+\theta_1^{\alpha}(k,z)\delta_{\underline{C},j} \\ G_{\underline{C},j}^{\alpha}(k,z) & =\Theta_1^{\alpha}(k,z)\ G_{L,j}^{\beta}(k-1,z)+\Theta_2^{\alpha}(k,z)\ G_{\underline{L},j}^{\beta}(k-1,z)+\Theta_3^{\alpha}(k,z)\ G_{R,j}^{\gamma}(k-1,z) \\ & +\Theta_4^{\alpha}(k,z)\ G_{\underline{R},j}^{\gamma}(k-1,z)+\delta_{\underline{C},j}+\theta_2^{\alpha}(k,z)\delta_{C,j} \end{cases}. \tag{A37}$$

Substituting Equation (A37) into (A35) and comparing it to Equation (A33), we obtain the following iteration relations for renormalization coefficients given by

$$M^{\alpha}(k,z)\ = M^{\beta}(k-1,z)+\Gamma_1^{\alpha}(k,z)\ [\Xi_1^{\alpha}(k,z)+U^{\beta}(k-1,z)]+\Theta_1^{\alpha}(k,z)\ [V^{\beta}(k-1,z)+\Omega_1^{\alpha}(k,z)] \tag{A38}$$

$$P^{\alpha}(k,z)\ =\ P^{\beta}(k-1,z)+\Gamma_2^{\alpha}(k,z)\ [\Xi_2^{\alpha}(k,z)+W^{\beta}(k-1,z)]+\Theta_2^{\alpha}(k,z)\ [X^{\beta}(k-1,z)+\Omega_2^{\alpha}(k,z)], \tag{A39}$$

$$Q^{\alpha}(k,z)\ = Q^{\gamma}(k-1,z)+\Gamma_3^{\alpha}(k,z)\ [\Xi_3^{\alpha}(k,z)+U^{\gamma}(k-1,z)]+\Theta_3^{\alpha}(k,z)\ [W^{\gamma}(k-1,z)+\Omega_3^{\alpha}(k,z)], \tag{A40}$$

$$R^{\alpha}(k,z)=\ R^{\gamma}(k-1,z)+\Gamma_4^{\alpha}(k,z)\ [\Xi_4^{\alpha}(k,z)+V^{\gamma}(k-1,z)]+\Theta_4^{\alpha}(k,z)\ [X^{\gamma}(k-1,z)+\Omega_4^{\alpha}(k,z)], \tag{A41}$$

$$\begin{aligned} S^{\alpha}(k,z)=S^{\beta}(k-1,z)&+\Gamma_2^{\alpha}(k,z)\ [\Xi_1^{\alpha}(k,z)+U^{\beta}(k-1,z)]+\Gamma_1^{\alpha}(k,z)\ [\Xi_2^{\alpha}(k,z)+W^{\beta}(k-1,z)] \\ &+\Theta_2^{\alpha}(k,z)\ [V^{\beta}(k-1,z)+\Omega_1^{\alpha}(k,z)]+\Theta_1^{\alpha}(k,z)\ [X^{\beta}(k-1,z)+\Omega_2^{\alpha}(k,z)], \end{aligned} \tag{A42}$$

$$\begin{aligned} U^{\alpha}(k,z)=\Gamma_3^{\alpha}(k,z)\ [\Xi_1^{\alpha}(k,z)+U^{\beta}(k-1,z)]&+\Gamma_1^{\alpha}(k,z)\ [\Xi_3^{\alpha}(k,z)+U^{\gamma}(k-1,z)] \\ +\Theta_3^{\alpha}(k,z)\ [V^{\beta}(k-1,z)+\Omega_1^{\alpha}(k,z)]&+\Theta_1^{\alpha}(k,z)\ [W^{\gamma}(k-1,z)+\Omega_3^{\alpha}(k,z)], \end{aligned} \tag{A43}$$

$$\begin{aligned} V^{\alpha}(k,z)=\Gamma_4^{\alpha}(k,z)\ [\Xi_1^{\alpha}(k,z)+U^{\beta}(k-1,z)]&+\Gamma_1^{\alpha}(k,z)\ [\Xi_4^{\alpha}(k,z)+V^{\gamma}(k-1,z)] \\ +\Theta_4^{\alpha}(k,z)\ [V^{\beta}(k-1,z)+\Omega_1^{\alpha}(k,z)]&+\Theta_1^{\alpha}(k,z)\ [X^{\gamma}(k-1,z)+\Omega_4^{\alpha}(k,z)], \end{aligned} \tag{A44}$$

$$\begin{aligned} W^{\alpha}(k,z)=\Gamma_3^{\alpha}(k,z)\ [\Xi_2^{\alpha}(k,z)+W^{\beta}(k-1,z)]&+\Gamma_2^{\alpha}(k,z)\ [\Xi_3^{\alpha}(k,z)+U^{\gamma}(k-1,z)] \\ +\Theta_3^{\alpha}(k,z)\ [X^{\beta}(k-1,z)+\Omega_2^{\alpha}(k,z)]&+\Theta_2^{\alpha}(k,z)\ [W^{\gamma}(k-1,z)+\Omega_3^{\alpha}(k,z)], \end{aligned} \tag{A45}$$

$$\begin{aligned} X^{\alpha}(k,z)=\Gamma_4^{\alpha}(k,z)\ [\Xi_2^{\alpha}(k,z)+W^{\beta}(k-1,z)]&+\Gamma_2^{\alpha}(k,z)\ [\Xi_4^{\alpha}(k,z)+V^{\gamma}(k-1,z)] \\ +\Theta_4^{\alpha}(k,z)\ [X^{\beta}(k-1,z)+\Omega_2^{\alpha}(k,z)]&+\Theta_2^{\alpha}(k,z)\ [X^{\gamma}(k-1,z)+\Omega_4^{\alpha}(k,z)], \end{aligned} \tag{A46}$$

$$\begin{aligned} Y^{\alpha}(k,z)\ \ =\ Y^{\gamma}(k-1,z)&+\Gamma_4^{\alpha}(k,z)\ [\Xi_3^{\alpha}(k,z)+U^{\gamma}(k-1,z)]+\Gamma_3^{\alpha}(k,z)\ [\Xi_4^{\alpha}(k,z)+V^{\gamma}(k-1,z)] \\ &+\Theta_4^{\alpha}(k,z)\ [W^{\gamma}(k-1,z)+\Omega_3^{\alpha}(k,z)]+\Theta_3^{\alpha}(k,z)\ [X^{\gamma}(k-1,z)+\Omega_4^{\alpha}(k,z)], \end{aligned} \tag{A47}$$

$$\begin{aligned} Z^{\alpha}(k,z) = {} & Z^{\beta}(k-1,z) + Z^{\gamma}(k-1,z) + \theta_1^{\alpha}(k,z)\,[Q^{\beta}(k-1,z) + M^{\gamma}(k-1,z) - 1] \\ & + \theta_2^{\alpha}(k,z)\,[R^{\beta}(k-1,z) + P^{\gamma}(k-1,z) - 1] + \phi_2^{\alpha}(k,z)\,[Y^{\beta}(k-1,z) + S^{\gamma}(k-1,z)], \end{aligned} \tag{A48}$$

with

$$\Xi_{\rho}^{\alpha}(k,z) = \Gamma_{\rho}^{\alpha}(k,z)\,[Q^{\beta}(k-1,z) + M^{\gamma}(k-1,z) - 1] + \Theta_{\rho}^{\alpha}(k,z)\,[Y^{\beta}(k-1,z) + S^{\gamma}(k-1,z)] \tag{A49}$$

and

$$\Omega_{\rho}^{\alpha}(k,z) \;=\; \Theta_{\rho}^{\alpha}(k,z)\,[R^{\beta}(k-1,z) + P^{\gamma}(k-1,z) - 1], \tag{A50}$$

where $\rho = 1,\ 2,\ 3$ or 4. The initial conditions for this renormalization method are

$$\begin{cases} M^{\alpha}(1,z) = P^{\alpha}(1,z) = Q^{\alpha}(1,z) = R^{\alpha}(1,z) \;= 1 + (\xi_-^2 + \xi_+^2)\,t_{\alpha}^2 \\ U^{\alpha}(1,z) \;= -V^{\alpha}(1,z) = W^{\alpha}(1,z) = -X^{\alpha}(1,z) = 2(\xi_-^2 - \xi_+^2)\,t_{\alpha}^2 \\ S^{\alpha}(1,z) \;= -Y^{\alpha}(1,z) = 2(\xi_-^2 + \xi_+^2)\,t_{\alpha}^2 \\ Z^{\alpha}(1,z) = (\xi_- + \xi_+) \end{cases} \tag{A51}$$

and

$$\begin{cases} t_h^{\alpha}(1,z) = -t_{\underline{h}}^{\alpha}(1,z) = -t_d^{\alpha}(1,z) = t_{\underline{d}}^{\alpha}(1,z) = (\xi_- - \xi_+)\,t_{\alpha}^2 \\ t_v^{\alpha}(1,z) = -t_{\underline{v}}^{\alpha}(1,z) = (\xi_- + \xi_+)\,t_{\alpha}^2 \\ \varepsilon_L^{\alpha}(1,z) = \varepsilon_R^{\alpha}(1,z) = (\xi_- + \xi_+)\,t_{\alpha}^2 - \varepsilon \\ \varepsilon_{\underline{L}}^{\alpha}(1,z) = \varepsilon_{\underline{R}}^{\alpha}(1,z) = (\xi_- + \xi_+)\,t_{\alpha}^2 + \varepsilon \end{cases}, \tag{A52}$$

where $\xi_{\pm} \; = (z \pm \varepsilon)^{-1}$. The elements of Green's function in Equation (A33) are numerically calculated from the Dyson equation, written as an 8×8 matrix for the dual channel of the *K*-th generation connected to two periodic leads at its ends, as illustrated at the end of Figure A5.

References

1. Novoselov, K.S.; Geim, A.K.; Morozov, S.V.; Jiang, D.; Zhang, Y.; Dubonos, S.V.; Grigorieva, I.V.; Firsov, A.A. Electric field effect in atomically thin carbon films. *Science* **2004**, *306*, 666–669. [CrossRef]
2. Bolotin, K.I.; Sikes, K.J.; Jiang, Z.; Klima, M.; Fudenberg, G.; Hone, J.; Kim, P.; Stormer, H.L. Ultrahigh electron mobility in suspended graphene. *Solid State Commun.* **2008**, *146*, 351–355. [CrossRef]
3. Balandin, A.A.; Ghosh, S.; Bao, W.; Calizo, I.; Teweldebrhan, D.; Miao, F.; Lau, C.N. Superior thermal conductivity of single-layer graphene. *Nano Lett.* **2008**, *8*, 902–907. [CrossRef]
4. Lee, C.; Wei, X.; Kysar, J.W.; Hone, J. Measurement of the elastic properties and intrinsic strength of monolayer graphene. *Science* **2008**, *321*, 385–388. [CrossRef]
5. Dhinakaran, V.; Lavanya, M.; Vigneswari, K.; Ravichandran, M.; Vijayakumar, M.D. Review on exploration of graphene in diverse applications and its future horizon. *Mater. Today Proc.* **2020**, *27*, 824–828. [CrossRef]
6. Schedin, F.; Geim, A.K.; Morozov, S.V.; Hill, E.W.; Blake, P.; Katsnelson, M.I.; Novoselov, K.S. Detection of individual gas molecules adsorbed on graphene. *Nat. Mater.* **2007**, *6*, 652–655. [CrossRef] [PubMed]
7. Béraud, A.; Sauvage, M.; Bazán, C.M.; Tie, M.; Bencherifa, A.; Bouilly, D. Graphene field-effect transistors as bioanalytical sensors: Design, operation and performance. *Analyst* **2021**, *146*, 403–428. [CrossRef] [PubMed]
8. Wang, S.; Qi, X.; Hao, D.; Moro, R.; Ma, Y.; Ma, L. Recent advances in graphene-based field-effect-transistor biosensors: A review on biosensor designing strategy. *J. Electrochem. Soc.* **2022**, *169*, 027509. [CrossRef]
9. Wang, M.; Yang, E.-H. THz applications of 2D materials: Graphene and beyond. *Nano-Struct. Nano-Objects* **2018**, *15*, 107–113. [CrossRef]
10. Liu, J.; Li, X.; Jiang, R.; Yang, K.; Zhao, J.; Khan, S.A.; He, J.; Liu, P.; Zhu, J.; Zeng, B. Recent progress in the development of graphene detector for terahertz detection. *Sensors* **2021**, *21*, 4987. [CrossRef]
11. Lone, S.; Bhardwaj, A.; Pandit, A.K.; Gupta, S.; Mahajan, S. A review of graphene nanoribbon field-effect transistor structures. *J. Electron. Mater.* **2021**, *50*, 3169–3186. [CrossRef]
12. Freitag, M.; Steiner, M.; Martin, Y.; Perebeinos, V.; Chen, Z.; Tsang, J.C.; Avouris, P. Energy dissipation in graphene field-effect transistors. *Nano Lett.* **2009**, *9*, 1883–1888. [CrossRef]
13. Yu, G.L.; Jalil, R.; Belle, B.; Mayorov, A.S.; Blake, P.; Schedin, F.; Morozov, S.V.; Ponomarenko, L.A.; Chiappini, F.; Wiedmann, S.; et al. Interaction phenomena in graphene seen through quantum capacitance. *Proc. Natl. Acad. Sci. USA* **2013**, *110*, 3282–3286. [CrossRef] [PubMed]
14. Wen, R.; Jiang, Z.; Miao, R.; Wang, L.; Liang, Y.; Deng, J.; Shao, Q.; Zhang, J. Electronic transport properties of B/N/P co-doped armchair graphene nanoribbon field effect transistor. *Diam. Relat. Mater.* **2022**, *124*, 108893. [CrossRef]

15. Radsar, T.; Khalesi, H.; Ghods, V.; Izadbakhsh, A. Effects of channel dimension and doping concentration of source and drain contacts on GNRFET performance. *Silicon* **2021**, *13*, 3337–3350. [CrossRef]
16. Saltzgaber, G.; Wojcik, P.; Sharf, T.; Leyden, M.R.; Wardini, J.L.; Heist, C.A.; Adenuga, A.A.; Remcho, V.T.; Minot, E.D. Scalable graphene field-effect sensors for specific protein detection. *Nanotechnology* **2013**, *24*, 355502. [CrossRef]
17. Sánchez, V.; Wang, C. Real space theory for electron and phonon transport in aperiodic lattices via renormalization. *Symmetry* **2020**, *12*, 430. [CrossRef]
18. Shylau, A.A.; Kłos, J.W.; Zozoulenko, I.V. Capacitance of graphene nanoribbons. *Phys. Rev. B* **2009**, *80*, 205402. [CrossRef]
19. Griffiths, D.J. *Introduction to Electrodynamics*, 4th ed.; Cambridge University Press: Cambridge, UK, 2017; pp. 106–190.
20. Son, Y.-W.; Cohen, M.L.; Louie, S.G. Energy gaps in graphene nanoribbons. *Phys. Rev. Lett.* **2006**, *97*, 216803. [CrossRef]
21. Fernández-Rossier, J.; Palacios, J.J.; Brey, L. Electronic structure of gated graphene and graphene ribbons. *Phys. Rev. B* **2007**, *75*, 205441. [CrossRef]
22. Economou, E.N. *Green's Functions in Quantum Physics*, 3rd ed.; Springer: Berlin/Heidelberg, Germany, 2006; pp. 14–16, 184.
23. Datta, S. *Lessons from Nanoelectronics. A New Perspective on Transport—Part A: Basic Concepts*, 2nd ed.; World Scientific: Singapore, 2017; pp. 32, 123.
24. Landauer, R. Electrical resistance of disordered one-dimensional lattices. *Philos. Mag.* **1970**, *21*, 863–867. [CrossRef]
25. Cao, Q.; Geng, X.; Wang, H.; Wang, P.; Liu, A.; Lan, Y.; Peng, Q. A review of current development of graphene mechanics. *Crystals* **2018**, *8*, 357. [CrossRef]
26. Yang, G.; Li, L.; Lee, W.B.; Ng, M.C. Structure of graphene and its disorders: A review. *Sci. Technol. Adv. Mater.* **2018**, *19*, 613–648. [CrossRef] [PubMed]
27. Pires, M.A.; Duarte-Queirós, S.M. Quantum walks with sequential aperiodic jumps. *Phys. Rev. E* **2020**, *102*, 012104. [CrossRef]
28. Maciá, E. *Aperiodic Structures in Condensed Matter: Fundamentals and Applications*; CRC Press: Boca Raton, FL, USA, 2009; p. 130.
29. Zhong, H.; Zhang, Z.; Xu, H.; Qiu, C.; Peng, L.-M. Comparison of mobility extraction methods based on field-effect measurements for graphene. *AIP Adv.* **2015**, *5*, 057136. [CrossRef]
30. Xia, F.; Perebeinos, V.; Lin, Y.; Wu, Y.; Avouris, P. The origins and limits of metal-graphene junction resistance. *Nat. Nanotechnol.* **2011**, *6*, 179–184, see also supplementary information. [CrossRef]
31. Schroder, D.K. *Semiconductor and Material and Device Characterization*, 3rd ed.; John Wiley & Sons: Hoboken, NJ, USA, 2005; p. 146.
32. Sutton, A.P. *Electronic Structure of Materials*; Clarendon Press: Oxford, UK, 1993; p. 58.
33. Abhilash, T.S.; De Alba, R.; Zhelev, N.; Craighead, H.G.; Parpia, J.M. Transfer printing of CVD graphene FETs on patterned substrates. *Nanoscale* **2015**, *7*, 14109–14113. [CrossRef]
34. Sánchez, V.; Sánchez, F.; Wang, C. Independent channel method for nanoribbons with dislocation and Fano defects. *Phys. Status Solidi B* **2021**, *258*, 2100095. [CrossRef]
35. Nadri, F.; Mardaani, M.; Rabani, H. Semi-analytic study on the conductance of a lengthy armchair honeycomb nanoribbon including vacancies, defects, or impurities. *Chin. Phys. B* **2019**, *28*, 017202. [CrossRef]
36. Sánchez, V.; Wang, C. Kubo conductivity in two-dimensional Fibonacci lattices. *J. Non-Cryst. Solids* **2003**, *329*, 151–154. [CrossRef]
37. Sánchez, V.; Wang, C. Application of renormalization and convolution methods to the Kubo-Greenwood formula in multidimensional Fibonacci systems. *Phys. Rev. B* **2004**, *70*, 144207. [CrossRef]
38. Sánchez, F.; Sánchez, V.; Wang, C. Renormalization approach to the electronic localization and transport in macroscopic generalized Fibonacci lattices. *J. Non-Cryst. Solids* **2016**, *450*, 194–208. [CrossRef]

nanomaterials

Article

Vanadium-Doped FeBP Microsphere Croissant for Significantly Enhanced Bi-Functional HER and OER Electrocatalyst

Shalmali Burse, Rakesh Kulkarni, Rutuja Mandavkar, Md Ahasan Habib, Shusen Lin, Young-Uk Chung, Jae-Hun Jeong * and Jihoon Lee *

Department of Electronic Engineering, College of Electronics and Information, Kwangwoon University, Nowon-gu, Seoul 01897, Korea
* Correspondence: myloveofjh@gmail.com (J.-H.J.); jihoonlee@kw.ac.kr (J.L.)

Abstract: Ultra-fine hydrogen produced by electrochemical water splitting without carbon emission is a high-density energy carrier, which could gradually substitute the usage of traditional fossil fuels. The development of high-performance electrocatalysts at affordable costs is one of the major research priorities in order to achieve the large-scale implementation of a green hydrogen supply chain. In this work, the development of a vanadium-doped FeBP (V-FeBP) microsphere croissant (MSC) electrocatalyst is demonstrated to exhibit efficient bi-functional water splitting for the first time. The FeBP MSC electrode is synthesized by a hydrothermal approach along with the systematic control of growth parameters such as precursor concentration, reaction duration, reaction temperature and post-annealing, etc. Then, the heteroatom doping of vanadium is performed on the best FeBP MSC by a simple soaking approach. The best optimized V-FeBP MSC demonstrates the low HER and OER overpotentials of 52 and 180 mV at 50 mA/cm^2 in 1 M KOH in a three-electrode system. In addition, the two-electrode system, i.e., V-FeBP || V-FeBP, demonstrates a comparable water-splitting performance to the benchmark electrodes of Pt/C || RuO_2 in 1 M KOH. Similarly, exceptional performance is also observed in natural sea water. The 3D MSC flower-like structure provides a very high surface area that favors rapid mass/electron-transport pathways, which improves the electrocatalytic activity. Further, the V-FeBP electrode is examined in different pH solutions and in terms of its stability under industrial operational conditions at 60 °C in 6 M KOH, and it shows excellent stability.

Keywords: water splitting; V-FeBP; heteroatom doping; hydrothermal approach; soaking approach

Citation: Burse, S.; Kulkarni, R.; Mandavkar, R.; Habib, M.A.; Lin, S.; Chung, Y.-U.; Jeong, J.-H.; Lee, J. Vanadium-Doped FeBP Microsphere Croissant for Significantly Enhanced Bi-Functional HER and OER Electrocatalyst. *Nanomaterials* **2022**, *12*, 3283. https://doi.org/10.3390/nano12193283

Academic Editors: Yuichi Negishi and Diego Cazorla-Amorós

Received: 9 August 2022
Accepted: 14 September 2022
Published: 21 September 2022

1. Introduction

Hydrogen is an efficient green-energy resource with its high gravimetric energy density and carbon-free nature. Hydrogen has emerged as a promising substitution for fossil fuels, which can then gradually decrease climate change and global warming [1–5]. Hydrogen also offers excellent transportability and is convenient to store in a compressed gas and liquid form, much like natural gas and oil. Currently, noble-metal-based electrocatalysts such as Pt/Pd and RuO_2/IrO_2 are the benchmark electrodes for water splitting. However, the practical production of ultra-fine hydrogen by water electrolysis is hindered due to the limited availability of these elements and high costs [6–8]. The development of highly active electrocatalysts at an affordable cost remains to be one of the major research priorities for the green hydrogen supply chain.

Over the last decade, transition metals (TMs) such as Co, Ni, Cu, Fe, W, Mo, Mn, V, etc., combined with several non-metallic elements including phosphorus, selenium, carbon, sulfur, nitrogen, etc., have been widely researched as efficient water-splitting catalysts [9–15]. The TMs possess fewer filled d-orbitals and their combination with non-metallic elements can offer superior intrinsic water-splitting capabilities and significantly enhance HER and OER kinetics [16,17]. Among them, iron (Fe) is one of the most earth-abundant elements and can offer good stability; thus, the iron-based electrodes can be a cost-effective alternative for the practical industrialization of water splitting. Fe-based compounds and structures demonstrated effective adsorption/desorption of reaction intermediates in the overall water-splitting process [9]. For example, the ultra-thin FeP nanosheets exhibited an excellent electrocatalytic oxygen-evolution performance with the Fe defects on the FeP nanosheets, which facilitated the adsorption of oxygenated intermediates and a low overpotential [18]. The Fe_2O_3/FeP heterostructure demonstrated excellent OER with the reduced reaction barrier due to the large surface area and lower charge-transfer resistance [5].

Meanwhile, phosphorus (P) is one of the most widely studied non-metallic elements that has been frequently compounded with TMs in various combinations, and remarkable advances have been made up to now [19–22]. More recently, boron (B) has emerged as another potential non-metallic element that can be combined with TMs due to its multi-centered bonding characteristics and significant charge-transfer nature [16,19,23–25].The metallic sites can be electronegative and thus can offer improved intrinsic electrocatalytic kinetics [26]. In addition, the insertion of B into the TM matrix can stabilize the atomic configurations and thus can offer enhanced stability [27]. However, the combination of B and P together with the TM has been very rarely studied up to now. As an example, the Co-B-P catalyst demonstrated significantly improved adsorption and desorption capabilities due to the faster charge-transfer kinetics [19], and the good balance between B and P in the TM matrix can induce interesting synergetic effects such as lowering the reaction-energy barrier and increasing the rate of the catalytic process.

At the same time, heteroatom doping is another technique that can be utilized for improved water-splitting performance by increasing the number of active catalytic sites and modifying the electronic states [28,29]. The heteroatom doping of metallic elements such as W, Ru, Mo, Cr and V into the existing material matrix has demonstrated improved water-splitting performances [30–33]. Among these, V doping is a promising candidate due to its multiple valence states ranging from $^{+}2$ to $^{+}5$ that can induce strong electronic interactions with other metal cations. Thus, the incorporation of V can facilitate improved intrinsic catalytic activity by increasing the number of active sites and the structural flexibility, resulting in improved overall water-splitting performances [34]. In addition, V-doping has been barely studied. To this end, the fabrication of well-balanced B and P with Fe and the incorporation of V into the FeBP matrix can be an interesting attempt at improving HER and OER kinetics. With the V-doped FeBP, enhanced electrode stability can be obtained by protecting the metallic cores due to the difference in the electronegativity [35,36]. The V-doped FeBP electrocatalysts can be a cost-effective water-splitting electrocatalyst.

In this study, the FeBP electrocatalyst was fabricated by the systematic parameter control of the hydrothermal approach, and then the heteroatom doping of vanadium was demonstrated by the soaking approach as seen in Figure S1 for efficient overall water splitting for the first time. The V-FeBP MSC demonstrates a bi-functional capability for the HER and OER operations. The two-electrode configuration of V-FeBP || V-FeBP shows a comparable performance as compared to the benchmark electrodes of Pt/C and RuO_2 in 1 M KOH. The V-FeBP MSC demonstrates the low 2-E overpotential of 1.48 V as compared to the 1.46 V of Pt/C and RuO_2. In addition, the 2-E system demonstrates nearly the same performance in real sea water as compared with the benchmarks.

2. Experimental Section

2.1. V-FeBP Electrode Fabrication

For the fabrication of the V-FeBP electrode, nickel foam (NF) was used as a substrate after the ultrasonication in 6 M HCl for 20 min. Figures S2 and S3 show the morphological and elemental analyses of the bare NF. The $Fe(NO_3)_3 \cdot 9H_2O$, H_3BO_3 and $NaH_2PO_2 \cdot H_2O$ were utilized as precursors for the Fe, B and P. The chemicals utilized for the fabrication of the V-FeBP electrode were analytical grades of high purity (Sigma-Aldrich, St. Louis, MO, USA). The FeBP electrode was firstly optimized by the hydrothermal approach in terms of the molarity of precursors, concentration ratio, reaction time, and temperature. The

CH_4N_2O (urea) was utilized as a surface-active agent to induce the 3D microstructure formation. The precursor solution was placed into a Teflon-lined autoclave with the NF, which was followed by baking at different temperatures and durations. After the FeBP electrode optimization, the vanadium (V) was doped by a soaking approach. The V concentration, soaking duration and temperature were considered for the V-doping optimization.

2.2. Morphological, Elemental, and Optical Characterizations

A scanning electronic microscope (SEM, COXEM, Daejeon, Korea) was utilized for the morphology analyses of the various FeBP and V-FeBP electrodes. Energy-dispersive X-ray spectroscopy (EDS, Thermo Fisher, Waltham, MA, USA) was adapted to characterize the elemental phases of the electrodes. The Raman measurement was performed in a NOST system (Nostoptiks, Gyeonggi-do, Korea), equipped with a 532 nm laser, spectrograph (ANDOR, SR-500, Belfast, UK), and charge-coupled device (CCD). The X-ray diffraction (XRD, D8 Advance, Bruker, Billerica, MA, USA) patterns were collected under the illumination of Cu Kα (λ = 1.5406 Å) at a scan rate of 2 °/min.

2.3. Electrochemical Characterization

The 3-electrode (3-E) electrochemical characterizations of the FeBP and V-FeBP electrodes were performed with the target electrode as a working electrode, Pt plate as a counter electrode and Ag/AgCl as a reference in an electrochemical workstation (Wizmac, Daejeon, Korea). The reversible hydrogen electrode (RHE) potential (E) was based on the following relation for the HER and OER: E [V vs. RHE] = E + 0.059 × pH + 0.197 (Ag/AgCl). The polarization curves were obtained using linear-sweep voltammetry (LSV) at a scan rate of 5 mV/s between 0.2 and −0.6 V for the HER and 1.2 and 2.2 V for the OER in 1 M KOH. No iR compensation was adapted in any of the electrochemical characterizations and the data were plotted as received. The electrochemical impedance spectroscopy (EIS) was measured in the range of 100 kHz to 0.1 Hz at the voltage corresponding to 10 mA/cm^2 vs. RHE for the HER and OER catalytic turnover region with an amplitude of 5 mV as shown in Figure S4. Cyclic voltammetry (CV) was performed at different scan rates ranging from 40 to 180 mV/s in a non-faradic region between 0.1 and 0.3 V for the HER and 1.04 and 1.14 V for the OER. From the CV plots, the anodic and cathodic currents were obtained at specific potentials for HER and OER. The electrochemical double-layer capacitance (C_{dl}) plots were obtained based on $\Delta J = (J_a - J_c)/2$ as shown in Figures S5 and S6. The slope of the C_{dl} plot was used to estimate the electrochemical surface-active area (ECSA) in Figure S7. The different C_{dl} values for the HER and OER reactions suggest different reaction processes. In addition, the 3-E and 2-E water-splitting performances were measured in different pH waters using 1 M KOH (alkaline), 0.5 M H_2SO_4 (acidic), and 1 M PBS (neutral). The natural sea water was collected from the Yellow Sea (Incheon, Korea) and river water was obtained from the Han River (Seoul, Korea).

3. Results and Discussion

In this work, the FeBP electrodes were firstly optimized, and the vanadium (V) doping was optimized on the best FeBP. Firstly, the Fe concentration ($FeN_3O_9 \cdot 9H_2O$) variation was performed between 0.1 and 3 mM for the FeBP electrode optimization as shown in Figure 1. Generally, the microspherical structures were fabricated as seen in Figure 1a–d and larger-scale images can be found in Figure S8. The microspheres were constructed with highly dense layers of croissant-like structures as seen in Figure 1(a-1–d-1). Thus, it was named 'microsphere croissant (MSC)' for the various layers of croissant bread. Along with the increased $FeN_3O_9 \cdot 9H_2O$ concentration, the density of MSCs was gradually increased as seen Figures 1a–d and S8. The size of the MSC was up to 20~30 µm. The MSC morphology with the layer-like structures can be largely advantageous for catalytic reactions due to the significantly increased surface area, allowing effective ion access and reactions [37]. The formation of the highly layered 3D structure of Fe-B-P electrocatalyst can be described as below in Equations (1)–(3).

$$Fe(NO_3)_3{\cdot}9H_2O + H_3BO_3 + NaH_2PO_2{\cdot}H_2O + CH_4N_2O + NH_4F + n{\cdot}H_2O \text{ (Precursor solution)} \tag{1}$$

$$Fe(NO_3)_3{\cdot}9H_2O + H_2O \rightarrow Fe^{3+} + 3NO_3^{\,-} + 10H^+ + 10OH^- \tag{2}$$

$$2H_3BO_3 + 2H_2O \rightarrow 2[B(OH)_4]^- + 2H^+ \tag{3}$$

$$NaH_2PO_2{\cdot}H_2O \rightarrow NaH_2PO_2 + H_2O \rightarrow Na^+ + H_2PO_2^{\,-} + H^+ + OH^- \tag{4}$$

$$NH_4F + H_2O \rightarrow NH_4^{\,+} + F^- + H^+ + OH^- \tag{5}$$

$$CH_4N_2O + H_2O \rightarrow 2NH_3 + CO_2\uparrow \rightarrow 2NH_3 + 2H_2O \rightarrow 2NH_4^{\,+} + 2OH^- \tag{6}$$

The overall deposition process is:

$$Fe^{3+} + 2[B(OH)_4]^- + H_2PO_2^{\,-} + 3NO_3^{\,-} + Na^+ + 14H^+ + 14OH^- + 3NH_4^{\,+} + F^- \rightarrow$$

$$Fe\text{-}B\text{-}P + 3NO_3^{\,-} + Na^+ + 14H^+ + 22OH^- + 3NH_4^{\,+} + HF + 2H_2O \tag{7}$$

For the fabrication of the FeBP electrode, all the precursors were taken as shown in Equation (1). The Fe, B and P were formed by the corresponding precursors as seen in Equations (2)–(4). The $Fe(NO_3)_3{\cdot}H_2O$ (iron (III) nitrate nonahydrate) generates the Fe^{3+} in Equation (2) and the H_3BO_3 (boric acid) produces the $B[(OH)_4]^-$ as the reaction intermediates in Equation (3). The NaH_2PO_2 yields the $H_2PO_2^{\,-}$ complex compound in Equation (4). Then, NH_4F breaks down into NH4$^+$ and F^- in Equation (5). The generated $NH_4^{\,+}$ ions can help to stabilize the pH in the solution and the highly electronegative F^- ions help to form H bonds, which can increase the solution conductivity and increase the reaction speed in the ionic solution. Further, $CO(NH_2)_2$ (urea) splits into $2NH_3$ and CO_2 ↑ in Equation (6). In this process, the generated $2NH_3$ reacts with the water molecules to produce two ammonium ($NH_4^{\,+}$) and two hydroxyl (OH^-) ions in Equation (6). As discussed, the ammonium and hydroxyl ions can also boost the solution conductivity and reaction speed. Finally, the possible fabrication reaction can be described as shown in Equation (7), where the main precursors take part in the formation of FeBP. The boric acid and the formation of HF during the reaction can react with water ($HF + H_2O \rightarrow H_3O + F^-$) and helps to form more hydronium ions. During the reaction, the formation of hydronium ions induces the formation of bubbles. The bubble formation helps in layered crystal growth that offers a highly electrochemically active surface area.

Figure 1e presents the At.% plots of Fe, B and P in the Fe concentration variation set. The At.% showed a gradually increased incorporation of Fe atoms with the increased Fe molarity. B was also more incorporated. However, P showed a gradually decreased incorporation, perhaps due to the high affinity of Fe and B. Additional full-range EDS spectra are provided in Figure S9. Figure 1f shows the Raman spectra of FeBP MSCs with the characteristic peaks at 172, 242, 269, 549, and 936 cm^{-1}. The Raman contour plots are shown in Figure 1(f-1–f-3). The highest Raman peaks demonstrated by the 1 mM Fe indicates the highest local crystallinity of FeBP MSC structures. Raman intensity was decreased for the other Fe concentrations. The highly local-crystalline FeBP MSC with microsheets can provide faster electron transfer and increased intrinsic electrocatalytic activity by lowering charge-transfer resistance [13]. In terms of electrochemical performance, the HER and OER LSV curves of the FeBP MSC electrodes are provided in Figure 1g,i with the corresponding overpotential values in Figure 1(g-1,i-1). The HER reaction in an alkaline medium can be described by the Volmer, Heyrovsky and Tafel steps, where the metal active sites can react with the H_2O and generate a metal–hydride bond to produce H_2 [35,38]. Volmer step: $H_2O + M + e^- \rightarrow M\text{-}H^* + OH^-$, Heyrovsky step: $M\text{-}H^* + H_2O + e^- \rightarrow M + OH^- + H_2$, Tafel step: $2M\text{-}H^* \rightarrow 2M + H_2$. The Volmer reaction is the production of M-H*, followed by the Heyrovsky step. The Tafel steps explain the whole process of producing H_2. In the water electrolysis process, the HER is a crucial half-reaction to produce hydrogen at the cathode through a two-electron transfer process with the generation of hydroxyl (OH^-) ions. In contrast, the OER entails four-proton–electron transfer reactions at the anodic metallic atomic sites [39]. $OH^- + * \rightarrow HO^* + e^-$, $HO^* + OH^- \rightarrow O^* + H_2O + e^-$, $O^* + OH^- \rightarrow HOO^* + e^-$, $HOO^* + OH^- \rightarrow * + O_2(g) + H_2O + e^-$. Starting from the hydroxyl (OH^-) generated from the HER, O_2 is evolved through the protonation of HOO* coupled with the regeneration of $2H_2O$ at the active sites. In general, the electrical current splits the water molecules into hydrogen and oxygen in alkaline water electrolysis in the presence of metal (M) sites [39]. In the HER and OER reactions, the strong M-H* and M-OH bindings are the key components of the catalytic surface and thus, the strong binding nature of H atoms and hydroxyl ions with a large surface area is important in water electrolysis. The FeBP MSC with the 1 mM Fe demonstrated the best HER and OER performances with the lowest overpotential of 105 and 220 mV at 50 mA/cm^2, as summarized in Figure 1(g-1,i-1). The 1 mM Fe demonstrated the highest double-layer capacitance (C_{dl}) values of 1.8 and 2.1 mF/cm^2 for the HER and OER, as seen in Figure 1h,j, which suggests the largest electrochemical surface area (ECSA) of the 1 mM Fe. The improved performance of the FeBP MSC can be attributed to the improved local-crystalline quality and the balance between the ternary Fe, B and P elements with the MSC morphology, which can boost the catalytic activity in an alkaline environment [40]. The MSC structure formed with the appropriate number of Fe, B and P atoms can offer rich active sites for the H and OH^- groups, and such a hierarchical structure can benefit the high reaction rate due to the large electrochemical surface area and the acceleration of charge transfer [16]. In addition, the P and B groups can act as electron donors to the d-orbitals of transition metals in the FeBP system, resulting in a high electron concentration of the Fe atoms, which can lower the reaction barriers for the H_2O and OH^- [33].

In addition to the Fe concentration variation (related data Figures S5–S10), the 100 °C reaction temperature (related data Figures S11–S14), 20 mM urea (related data Figures S15 and S16), 30% B and 70% P ($FeB_{30}P_{70}$) (related data Figures S17–S21), and 100 °C post-annealing treatment (related data Figures S22–S26) were found to offer the best optimized performance. Figure S19 shows the XRD patterns of FeBP, FeB and, FeP. The two common peaks at 44.4 and 51.8° correspond to the (111) and (200) planes of the nickel substrate in the XRD patterns [41]. Generally, the FeBP showed broader peaks with a lower intensity as compared with the FeP and FeB in Figure S19, which could be due to the increase in the short-range polycrystalline phases of FeBP. Generally, the polycrystalline phase can indicate a low electron transfer and high resistance. Thus, a lower electrochemical performance can be expected. However, a recent study showed that the short-range polycrystalline or amorphous phases can be beneficial to the improved electrochemical performance in water electrolysis [42,43]. The polycrystalline phase can offer abundant active sites and higher intrinsic electrochemical activity due to the structural flexibility and stability of the electrocatalysts.

Figure 2 shows the vanadium (V)-doped FeBP MSC electrodes after the 2nd-stage post-annealing temperature optimization. The best FeBP electrode was taken for the vanadium (V) doping by controlling the doping temperature between 25 and 80 °C in Figures S27–S29, the vanadium concentration between 0.05 and 0.4 mM in Figures S30–S32, and the soaking duration between 15~120 min in Figures S33–S35. The 0.2 mM V in the 15 min soaking reaction at 25 °C demonstrated the best HER and OER performances in Figure S35 without any change in the morphology. An adequate amount of V incorporation can induce the water-dissociation capacity and can decrease the energy barrier and reduce the impedance of charge transfer. In addition, post-annealing at an appropriate temperature can improve the crystallinity of electrodes by the reduction in point and line defects with the thermal diffusion of atoms [44,45]. In terms of the 2nd post-annealing duration optimization, the 15 min duration showed the best result in Figures S36–S38. Along with post-annealing at various temperatures for 15 min, the 50~100 °C samples showed similar morphologies before and after the annealing in Figure 2(a–b-2). However, the high-temperature-annealed samples showed a slight deformation of croissant layers at 150 °C and more deformation at 200 °C in Figure 2(c-2–d-2). The temperature of 200 °C also had a much lower density of the microsphere croissant (MSC) in Figure 2d. Excess diffusion energy at a high temperature can damage crystallinity due to defect formation and can separate the MSC from the NF during the annealing process. Further, the Raman analyses demonstrated the best intensity with the 50 °C sample, as clearly seen in Figure 2(e–e-3). It clearly demonstrates that the 50 °C sample had better crystallinity, which helps to obtain stable electrochemical activity. In addition, the 50 °C sample demonstrated uniform distributions of Fe L, B K, P K, and V L peaks, indicating the even diffusion of vanadium into the FeBP matrix, as shown by the EDS maps and line profiles in Figure 2(f–f-4,g).

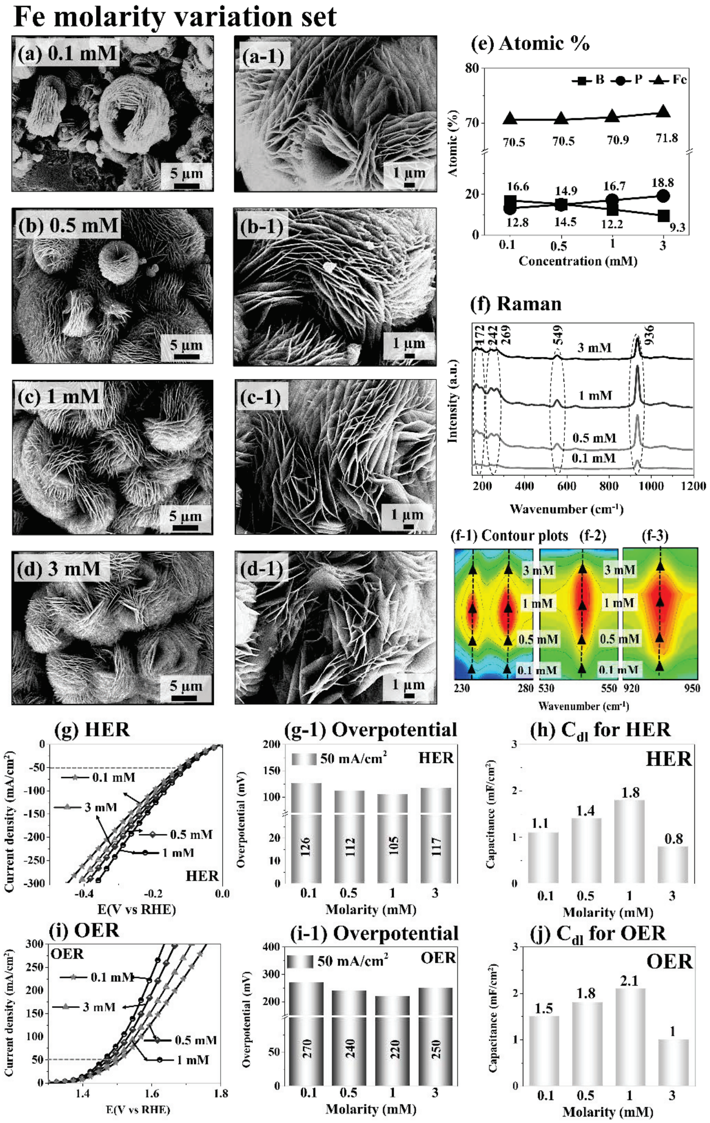

Figure 1. Fe concentration variation between 0.1~3 millimolar (mM) for the fabrication of FeBP MSC electrocatalysts at 100 °C for 12 h. A total of 20 mmol of CH_4N_2O, 6 mM $NaH_2PO_2.H_2O$ and 6 mM H_3BO_3 were used. (**a**–**d**) SEM images of FeBP electrodes. (**a-1**–**d-1**) Magnified SEM micrographs. (**e**) Atomic% graph. (**f**) Raman spectra of FeBP. (**f-1**–**f-3**) Contour plots of Raman peaks. (**g**,**i**) LSV measurements in 1 M KOH. (**g-1**,**i-1**) Overpotential bar chart at 50 mA/cm^2. (**h**) and (**j**) C_{dl} values for HER and OER.

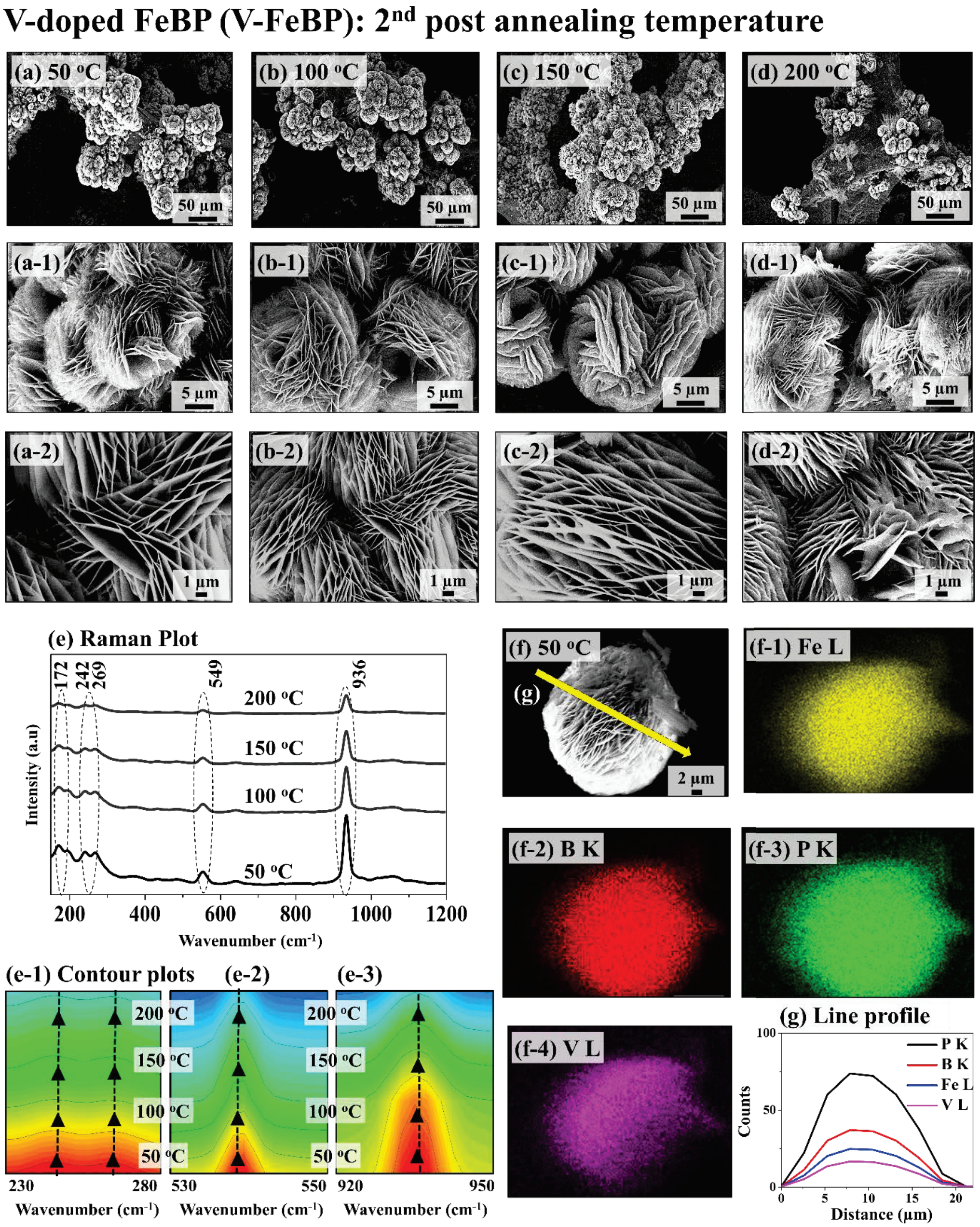

Figure 2. Post-annealing temperature variation (2nd annealing) of vanadium (V)-doped FeBP MSC electrodes between 50~200 °C for 15 min. The best FeBP was fabricated at 100 °C for 12 h with the 1 mM Fe, 3.6 mM H_3BO_3, 8.4 mM NaH_2PO_2 and 20 mM CH_4N_2O. The best FeBP was post-annealed (1st) and doped with V by a soaking approach in 0.2 mM V solution for 15 min at room temperature. (**a**–**d**) SEM micrographs. (**a-1**–**d-1**,**a-2**–**d-2**) Magnified SEM images. (**e**) Raman plot. (**e-1**–**e-3**) Contour plots of Raman peaks. (**f**–**f-4**) EDS maps of Fe L, B K, P K and V L. (**g**) Corresponding EDS line profiles.

Figure 3 shows the electrochemical characterizations of the V-FeBP MSC electrodes at the post-annealing optimization in terms of LSV, Tafel, EIS and C_{dl}. As shown in Figure 3a,e, the V-FeBP electrode annealed at 50 °C demonstrated the best HER and OER performances, and the performance gradually became worse with the increased temperature. The 50 °C sample demonstrated the lowest overpotentials of 52 mV and 210 mV at 50 mA/cm^2 for the HER and OER, as summarized in Figure 3(a-1,e-1). The bar plots in Figure 3(a-1,e-1) clearly show the overpotential values, which followed the sequence of 50 < 100 < 150 < 200 °C. The improved HER and OER performances could be due to the reduced lattice defects and better electrocatalytic activity following the appropriate heat treatment for an appropriate duration [37]. After the V doping and post-annealing optimization, the surface structure of the electrode can reorganize, and thus can introduce more active sites on the catalytic surface [46]. Additional active sites can speed up the electrochemical HER and OER reaction processes by increasing the conductivity to obtain better HER and OER performances. The V doping of the FeBP can largely improve the conductivity and electron density to enhance the electrocatalytic reaction. The addition of V can tune the electronic structure and activate more active sites. The partial electron transfer is possible from the V^{2+} to Fe^{2+} ions, which might help to improve the adsorption capacity of hydrogen protons and hydroxyl groups and improve the HER and OER processes [47]. The HER and OER Tafel analyses are shown in Figure 3b,f. The Tafel slopes can be acquired from the linear range of the HER and OER curves as shown in Figure 3b,f. The Tafel slope values in Figure 3(b-1,f-1) indicate the degree of the reaction and charge-transfer rates. The lower slope values indicate a higher electron transfer and thus a greater reaction rate. The 50 °C sample demonstrated the lowest HER and OER Tafel slope values of 98 and 72 mV/dec, as summarized in Figure 3(b-1,f-1). The HER and OER EIS measurements were performed to understand the transport characteristics of the V-FeBP electrodes. The HER and OER EIS were measured at different overpotential voltages based on the fixed current of 20 mA/cm^2 for the consistency between samples. The EIS measurements showed different R_{ct} values at different voltages around the turnover region, as seen in Figure S4 [1]. The higher voltage application showed smaller R_{ct} values and vice versa. In both the HER and OER EIS plots, the charge-transfer resistance (R_{ct}) was gradually decreased with the lower annealing temperatures, and the V-FeBP electrode annealed at 50 °C demonstrated the lowest (R_{ct}) of 25.3 and 26.4 Ω for the HER and OER EIS, which indicates that the 50 °C sample demonstrated the lower conductivity and outstanding charge-transport characteristics [1]. Further, the double-layer capacitance (C_{dl}) measurements based on the CV plots indicated the highest electrochemical active surface area of the 50 °C sample with 1.84 and 1.95 mF/cm^2 in Figure 3d,h. After doping, the electrochemical surface area of the V-FeBP MSC was significantly increased, indicating a higher electrochemical activity of electrode. The CV curves and anodic and cathodic current densities are provided in Figures S40 and S41.

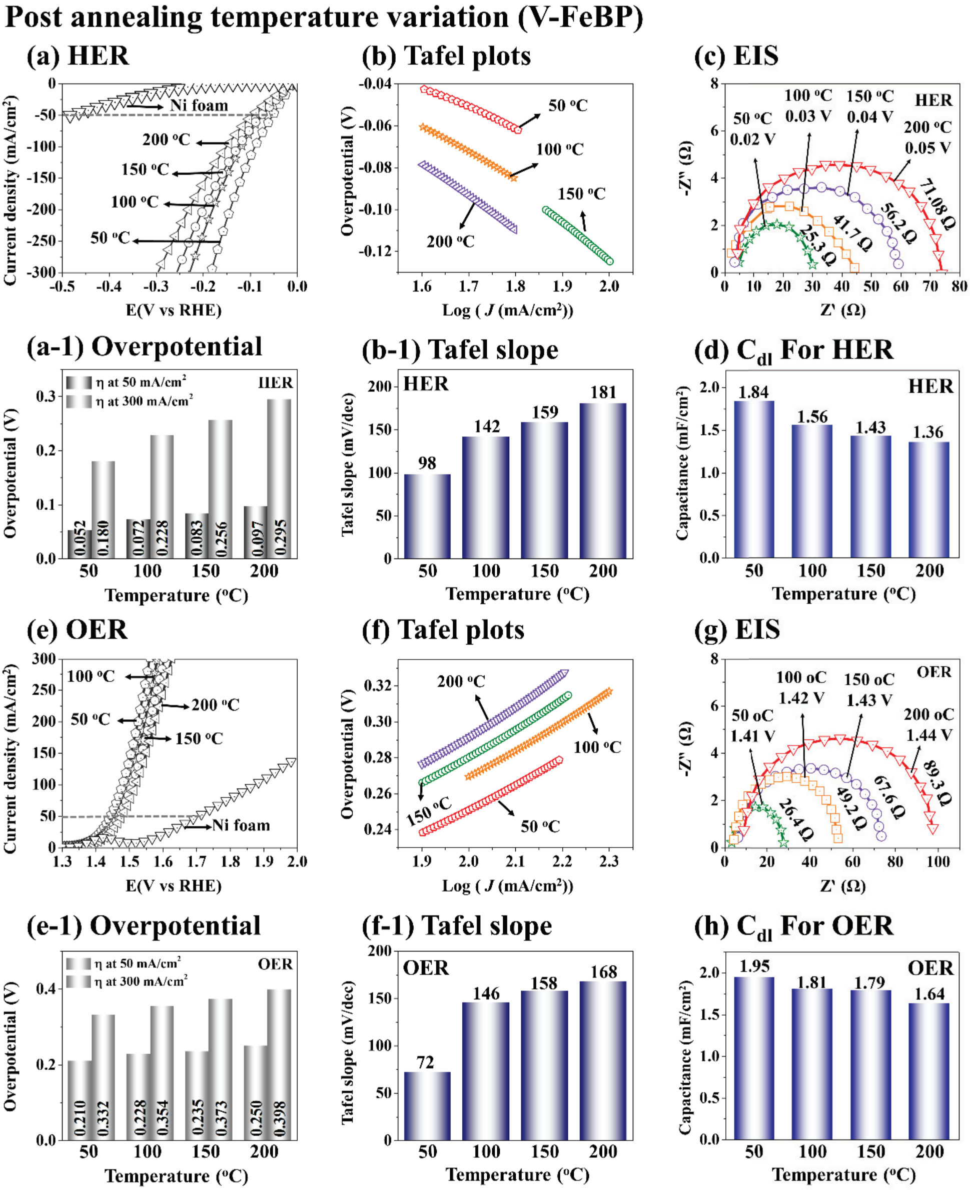

Figure 3. 3-electrode (3-E) electrochemical performance of the post-annealing temperature variation set (V-FeBP MSC electrodes). (**a**,**e**) HER and OER polarization curves of V-FeBP electrodes in 1 M KOH. (**a-1**,**e-1**) Overpotentials at 50 and 300 mA/cm^2. (**b**,**f**) Tafel slopes derived from the polarization curves. (**b-1**,**f-1**) Tafel slope values. (**c**,**g**) HER and OER Nyquist plots obtained at the fixed current of 20 mA/cm^2. (**d**,**h**) HER and OER C_{dl} values. All the electrochemical measurements were plotted as received without iR drop compensation.

Figure 4 shows the 3-E electrochemical performance comparison of V-FeBP and benchmark electrodes of Pt/C and RuO_2 in alkaline, acidic, and neutral waters. Different pH waters were prepared by 1 M KOH (pH 14), 0.5 M H_2SO_4 (pH 0) and 1 M PBS (pH 7.4). The morphological and elemental analyses of the benchmark electrodes of Pt/C and RuO_2 are provided in Figures S42 and S43. Overall, the V-FeBP and benchmark electrodes demonstrated quite stable operations in alkaline, acidic, and neutral waters in Figure 4a–f. At the same time, the benchmark electrodes demonstrated better HER and OER performances in all three solutions, as clearly seen in Figure 4(a-1–f-1). Both V-FeBP and the benchmark electrodes demonstrated similar trends in terms of performance with the overpotentials in alkaline < acidic < neutral waters, indicating that both electrode configurations demonstrated the best performances in 1 M KOH water. The higher performance in KOH can be attributed to the high electrochemical conductivity due to the ionization of OH^- [48]. KOH can offer high current density and electrode stability. In the electrochemical reaction process, the cation K^+ plays a crucial role in lowering the activation barrier for the dissociation of H_2O into $OH^- + H^+ + e^-$. KOH dissociates into K^+ and OH^- in water and H_2O can be dissociated more easily into OH^- and H^+ [49]. The lower HER and OER performances in the acidic solution could be due to the slow reaction rate with the electrode degradation in the low-pH water [50]. Similarly, the lowest performances in the neutral media could be due to the low ion migration in PBS solution, which could have resulted in the lowest kinetics during the HER and OER operations [3]. The lack of hydrogen protons or hydroxyl ions can obstruct the mass transport and cause extra energy consumption to dissociate water molecules under neutral conditions [51]. In short, the V-FeBP demonstrated good electrochemical performances with all the optimizations in terms of the LSV, Tafel, EIS, C_{dl}, TOF and stability. This could be due to the good balance between the V, Fe, B and P components and the good crystalline quality, along with the unique microsphere croissant (MSC) morphology as discussed. Additionally, the HER and OER steady-state current observations were performed by the comparison of the LSV and CA currents in a 3-E system in Figures S44 and S45. This was to show the stability of the electrodes at different current densities [52]. The V-FeBP annealed at 50 °C demonstrated stable operations at various voltages as summarized in Figures S44 and S45, indicating a good stability of the V-FeBP electrode. One thing to notice here is that the V-FeBP achieved a comparable OER result in 1 M KOH in Figure 5d, indicating that the 2-E operation of V-FeBP electrodes can largely benefit from the good OER performance.

Figure 5 shows the 2-E electrochemical performance of V-FeBP and benchmark electrodes in alkaline, acidic, and neutral media and the stability test. In the 2-E configuration, the Pt/C ‖ RuO_2 were used as the cathode and anode, and two V-FeBP electrodes were adapted as bi-functional electrodes, i.e., V-FeBP ‖ V-FeBP. Generally, the 2-E water-splitting performance trend was similar to the 3-E, i.e., alkaline < acidic < neutral waters, in Figure 5a–c. The specific overpotentials at 50 and 1500 mA/cm^2 are summarized in Figure 5(a-1–c-1). The overpotentials were 1.46 and 1.48 V at 50 mA/cm^2 and then reached 2.34 and 2.49 V at 1500 mA/cm^2 in 1 M KOH for the Pt/C ‖ RuO_2 and V-FeBP ‖ V-FeBP in Figure 5(a-1). The overpotentials were 1.49 and 1.51 V at 50 mA/cm^2 and 2.53 and 2.86 V at 1500 mA/cm^2 in 0.5 M H_2SO_4 in Figure 5(b-1). Similarly, the overpotentials were 1.51 and 1.56 V at 50 mA/cm^2 and 2.76 and 3.68 V at 1500 mA/cm^2 in 1 M PBS in Figure 5(c-1). The benchmark configuration demonstrated better water-splitting performances over the V-FeBP ‖ V-FeBP configuration due to the superior intrinsic electrochemical properties of Pt/C and RuO_2 for the HER and OER operations. Notably, the bi-functional configuration of V-FeBP demonstrated 2.18 V as compared with 2.06 V of the Pt/C ‖ RuO_2 at 1000 mA/cm^2 as identified in Figure 5a, which is a quite comparable performance to the benchmarks. This indicates that V-FeBP ‖ V-FeBP can demonstrate a compatible water-splitting performance as compared with the Pt/C ‖ RuO_2 in 1 M KOH water, with the costs of the electrode materials being several orders less.

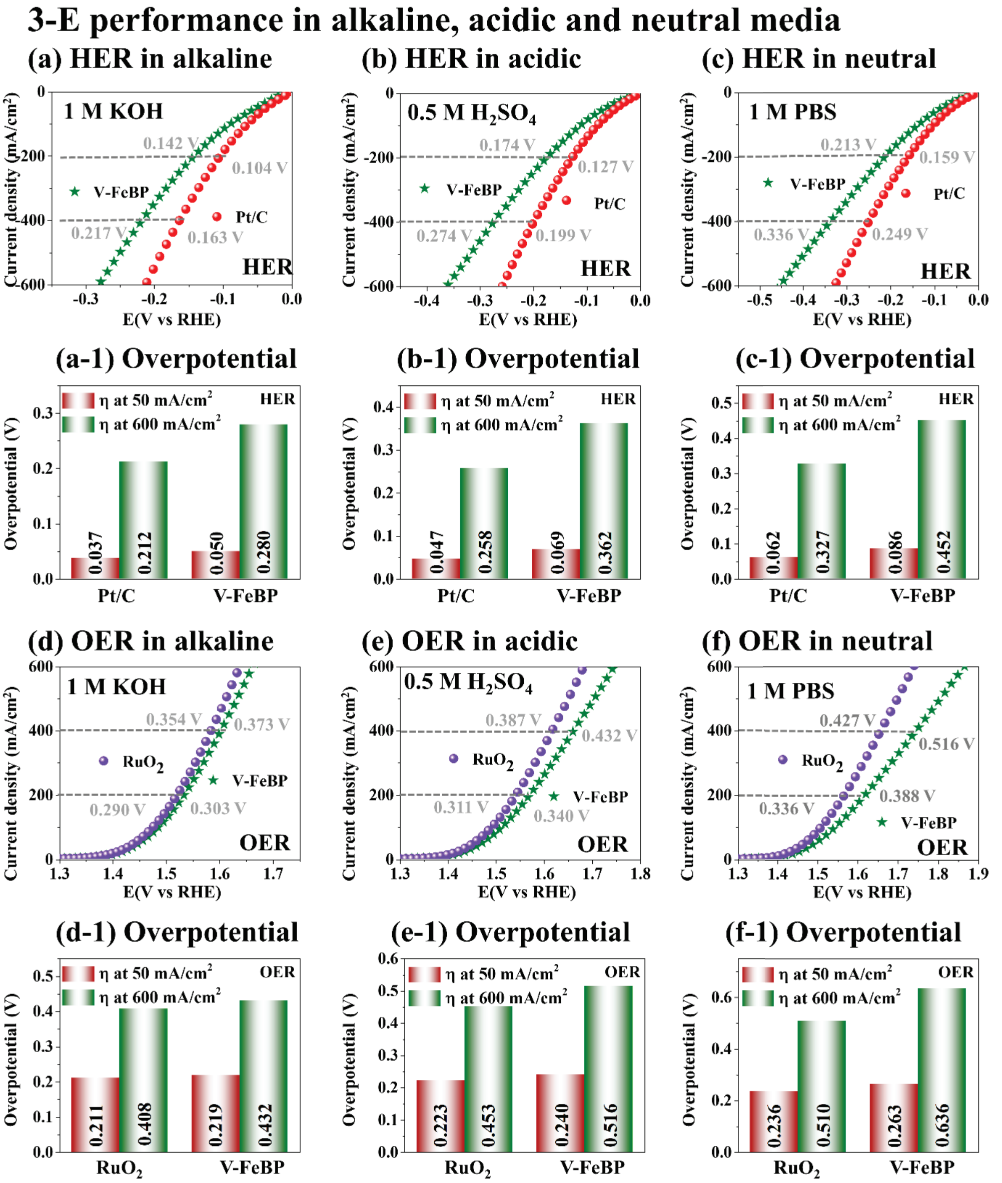

Figure 4. 3-E electrochemical performance comparison of V-FeBP and benchmark electrodes (Pt/C and RuO_2) in alkaline, acidic, and neutral waters. (**a**–**c**) HER curves in 1.0 M KOH, 0.5 M H_2SO_4, 1 M PBS. (**a-1**–**c-1**) Corresponding overpotential bar plots at 50 and 600 mA/cm^2. (**d**–**f**) HER curves. (**d-1**–**f-1**) Corresponding overpotential bar plots.

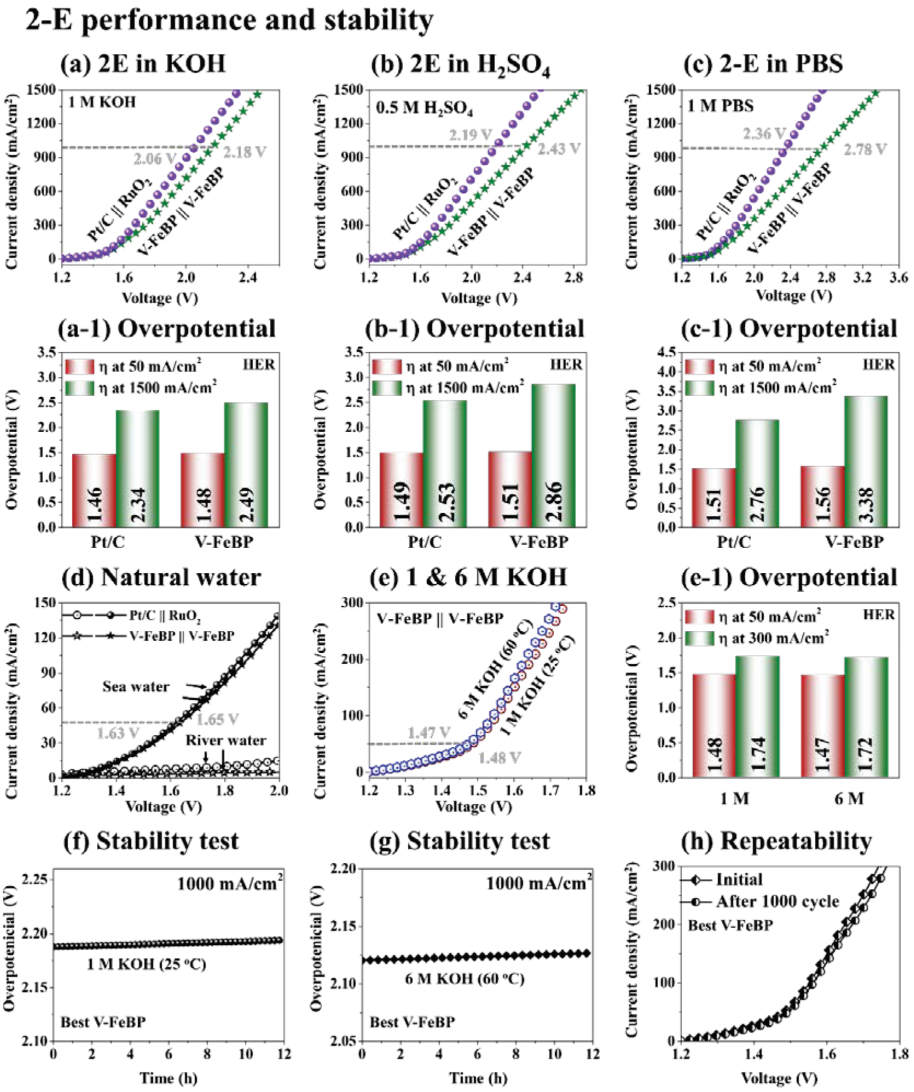

Figure 5. 2-E electrochemical performance in alkaline, acidic and neutral media and stability test. (**a**–**c**) 2-E LSV curves in 1 M KOH, 0.5 M H_2SO_4 and 1 M PBS. (**a-1**–**c-1**) Overpotentials at 50 and 1500 mA/cm^2. (**d**) 2-E LSV plots in natural sea and river waters. (**e**) 2-E LSV in 1 and 6 M KOH. (**e-1**) Overpotentials at 50 and 300 mA/cm^2. (**f**,**g**) Stability test of V-FeBP for 12 h in 1 M (25 °C) and 6 M KOH (60 °C) at 1000 mA/cm^2. (**h**) 2-electrode repeatability test of V-FeBP before and after 1000 cycles in 1 M KOH.

The 2-E performance of V-FeBP || V-FeBP and Pt/C || RuO_2 in natural sea and river waters are shown in Figure 5d. The V-FeBP || V-FeBP demonstrated a comparable overpotential of 1.63 V at 50 mA/cm^2 as compared to the 1.65 V of Pt/C || RuO_2 in sea water. The river water showed a very low current for both electrode configurations. The sea water generally demonstrated a better performance due to the presence of numerous Na^+ and Cl^- ions, which can increase the conductivity in the water, and thus the water-splitting performance can be improved. Meanwhile, the river water also includes various kinds of ion species such as Ca^+, Mg^+, Br^-, $HCO_3{}^-$, SiO_2, $SO_4{}^-$, Cl^-, F^-, etc. [53]. These anions and cations in the river water can slow down the reaction process and lower the overall current density. While the elemental compositions in both sea and river waters are similar, the majority of the ionic species in sea water ions are Na^+ and Cl^- (over 90%) and $HCO_3{}^-$, Ca^+, SiO_2, $SO_4{}^-$ constitute over 90% of the ionic species in river waters. In addition, the V-FeBP ‖ V-FeBP demonstrated a slightly improved water-splitting performance in 6 M KOH at 60 °C as compared to the 1 M KOH at 25 °C as seen in Figure 5e. The overpotential values are shown in Figure 5(e-1). The V-FeBP ‖ V-FeBP demonstrated quite a stable current in 1 M KOH at 25 °C and in 6 M KOH at 60 °C at 1000 mA/cm^2 in Figure 5f,g, which indicates a good stability of V-FeBP in industrial water-splitting conditions. The stability test at the high current of 1000 mA/cm^2 for 12 h did not show any significant difference, but there was a slightly increasing trend, likely due to the oxidation of metallic atoms and surface modifications, as shown in Figure 5f. Similarly, the chronoamperometry test did not show any degradation in the harsh industrial condition of 6 M KOH, indicating the excellent stability of V-FeBP, as shown in Figure 5g. The V-FeBP ‖ V-FeBP also demonstrated excellent repeatability after 1000 cycles in 1 M KOH, as shown in Figure 5h. The two-electrode activity after 1000 cycles showed a very negligible difference in performance, which clearly shows that the V-FeBP has good repeatability after a long operation. In addition, the HER and OER turnover frequency (TOF) of the post-annealing temperature variation set of the V-FeBP electrocatalysts was evaluated for the vanadium and iron active sites at 150 mV/cm^2, as shown in Figure S46. The TOF indicates the number of H_2 and O_2 molecules generated per atomic site per unit of time at the turnover. The TOF can be used to indicate the intrinsic water-splitting activity of each catalytic atomic active site under a specified reaction condition [38,54]. As summarized in Figure S46, the V-FeBP annealed at 50 °C demonstrated the highest HER and OER TOF values of 3.32 and 2.10 site^{-1} s^{-1}. In addition, the 2-E LSV and CA comparison of V-FeBP ‖ V-FeBP is shown in Figure S47, and the steady-state LSV and CA currents showed minor differences, as summarized in Figure S47c,d, indicating a good stability and stable operations at various voltages. The comparison of the two-electrode performance with the state-of-the-art Fe-based electrodes and transition-metal-based electrodes at 50 mA/cm^2 in 1 M KOH are shown in Figures S48 and S49 and Table 1 and Table S1. The V-FeBP was 2nd in the overpotential comparisons. Further, the three-electrode comparison with the state-of-the-art transition-metal-based electrodes at 10 mA/cm^2 in 1 M KOH is summarized in Figure S50 and Table S2. Again, the V-FeBP was one of the best.

Table 1. Comparison of 2-electrode performance with the state-of-art Fe-based electrodes at density of 50 mA/cm^2 in 1 M KOH.

Electrocatalysts	Electrolyte Solution	Overpotential [V] at 50 mA/cm^2	Year	Reference
FeNiSe	1 M KOH	1.36	2022	[55]
V/FeBP	1 M KOH	1.48	-	(This work)
Ni-Fe-MoN NTs	1 M KOH	1.62	2018	[56]
NiFe LDH@DG10	1 M KOH	1.65	2017	[57]
Fe-Ni_5P_4/NiFeOH-350	1 M KOH	1.66	2021	[9]
$Fe_{7\cdot4\%}$-NiSe	1 M KOH	1.68	2019	[58]
NFC@CNSs-700	1 M KOH	1.70	2021	[59]
R-Fe-Ni_2P	1 M KOH	1.75	2020	[60]
$(FeO)_2.(MoO_2)_3/MoO_2$	1 M KOH	1.76	2020	[61]
Ni-Fe-P/NF_0	1 M KOH	1.77	2019	[62]
Fe-Cu@CN3	1 M KOH	1.83	2021	[63]
Fe-Ni_3 S_2/NF	1 M KOH	1.84	2020	[64]
CoFeO NFs/NPCNT	1 M KOH	1.86	2019	[65]

4. Conclusions

A unique microsphere croissant (MSC) configuration of a V-FeBP electrode was demonstrated on a form of bare nickel substrate. The FeBP MSC was first optimized in terms of various synthesis parameters, and then the vanadium doping was further optimized.

Generally, the well-balanced F-B-P elements showed better electrochemical performances over the FeB and FeP. The post-annealing played an important role in improving the crystallinity of FeBP MSCs. Overall, the V-FeBP electrode demonstrated quite a comparable performance as compared with the benchmark electrodes with the low overpotential of 52 and 210 mV at 50 mA/cm^2 for the HER and OER in a three-electrode configuration in 1 M KOH. The V-FeBP || V-FeBP also demonstrated a comparable overpotential of 1.48 V at mA/cm^2 as compared with the PtC || RuO_2. This clearly indicates that V-FeBP can offer a compatible water-splitting performance in 1 M KOH water. In addition, the V-FeBP MSC demonstrated excellent stability and repeatability under industrial water-splitting conditions. This study presents an efficient approach based on the combination of the transition metal Fe combined with the non-metallic elements B and P, and the heteroatom doping of V, which can offer an alternative option for large-scale water electrolysis.

Supplementary Materials: The following are available online at https://www.mdpi.com/article/10.3390/nano12193283/s1, Figure S1: (a) Schematic representation of V-doped FeBP microsphere croissant (MSC) structure fabrication, namely V-FeBP MSC electrocatalyst. The V-FeBP MSC were fabricated by the combination of hydrothermal method and soaking approach. (a-1) V-doped FeBP MSC by the soaking approach., Figure S2. (a)–(c) SEM images of bare Ni foam (NF), Figure S3. (a)–(a-2) EDS maps of Ni and O. (b)–(b-1) Elemental line-profiles from the arrow location in (a). (c) EDS spectrum and atomic percentage of NF, Figure S4. Electrochemical impedance spectroscopy (EIS) measured at different voltages for the best V-FeBP. (a) EIS for HER. (b) EIS for OER. The EIS measurements showed different R_{ct} values at different voltages around the turnover region. The higher voltage application showed the smaller R_{ct} values and vice versa. Thus, the EIS was measured at a fixed current of 20 mA/cm^2 for the consistency between samples. The EIS was measured between 100 kHz to 0.1 Hz with an amplitude of 5 mV, Figure S5. (a)–(d) HER CV curves of various FeBP electrocatalyst with Fe concentration variation set. The CV curves were measured in the non-faradic region where there is no charge transfer reaction occur in between 0.2 and 0.3 E below 1.023 V based on the $E_{RHE} = E + 0.059 \times pH + 0.197$ (Ag/AgCl). The actual reverse sweeping voltage (E) lies between −0.723 and −0.823 V. The scan rate was varied from 40 to 180 mV/s at the interval of 20 mV/s, Figure S6. (a)–(d) OER CV curves of various V-FeBP catalyst with Fe concentration variation set. The CV scan rate is varied from 40 to 180 mV/s. The CV measurements were taken in a non-faradic region from 1.04 to 1.14 E below 1.23 V based on $E_{RHE} = E + 0.059 \times pH + 0.197$ (Ag/AgCl). The actual forward sweeping voltage (E) was between 0.017 and 0.117 V, Figure S7. (a) and (d) HER and OER anodic and cathodic current density vs scan rate plots. (b) and (e) HER and OER double layer capacitance (C_{dl}) plots. The C_{dl} plots were obtained from the anodic and cathodic current density graphs: $\Delta jH_{0.25} = (Ja - Jc)/2$ and $\Delta jO_{1.09} = (Ja - Jc)/2$, where Ja and Jc is the anodic and cathodic current. (c) and (f) Bar plots of C_{dl} values. The HER and OER C_{dl} are obtained from the extracting slope of C_{dl} plots in (b) and (e). The HER and OER C_{dl} values represent the HER and OER electrochemical surface-active area (ECSA), Figure S8. (a)–(d) SEM images of FeBP electrode fabricated with Fe concentration variation, Figure S9. (a)–(d) EDS spectra of Fe concentration variation set with corresponding atomic percentage in the given table, Figure S10. Reaction temperature variation for the FeBP electrocatalyst fabrication. The reaction temperature is varied between 80 and 140 °C. (a)–(d) SEM images. (a-1)–(d-1) Enlarged SEM images for the corresponding samples. (e) EDS spectra of 100 °C electrode. (f)–(f-3) SEM and corresponding EDS phase maps of Fe, B and P. (g) Raman spectra for FeBP. (h) and (i) Hydrogen evolution reaction (HER) and oxygen evolution reaction (OER) performance in 1 M KOH. (h-1) and (i-1) HER and OER overpotential values at 50 mA/cm^2, Figure S11. (a)–(c) EDS spectra of reaction temperature variation set. Tables show the atomic and weight percentage of Fe, B and P. (d) Atomic % of Fe, B and P, Figure S12. (a)–(d) HER CV curves of various V-FeBP electrocatalyst with reaction temperature variation set measured in the non-faradic region between 0.2 and 0.3 E. The scan rate was varied from 40 to 180 mV/s at the interval of 20 mV/s, Figure S13. (a)–(d) OER CV curves of various V-FeBP catalyst with the reaction temperature variation. The CV scan rate is varied from 40 to 180 mV/s, Figure S14. (a) and (c) HER and OER anodic and cathodic current density vs scan rate plots. (b) and (d) HER and OER double layer capacitance (C_{dl}) plots. (c) and (f) Bar plots showing C_{dl} values, Figure S15. (a) and (b) Polarization curves of HER and OER for the FeBP electrodes with the urea concentration variation, Figure S16. (a)–(c) SEM images of FeBP electrode fabricated with B and P concentration variation. (a-1)–(c-1) Enlarged SEM images for the corresponding electrodes. Other images are in the main figures, Figure S17. B and P concentration variation at 100 °C for 12 h. The total molarity of B and P was fixed at 20 mM and the ratio was varied accordingly: i.e., the $B_{30}P_{70}$ indicates 3.6 mM B and 8.4 mM of P. The Fe concentration was fixed at 1 mM. (a)–(d) SEM images for FeBP MSC electrocatalysts. (a-1)–(d-1) Enlarged SEM images. (e) Atomic % plot. (f) Raman spectra. (f-1)–(f-3) Contour plots of Raman peaks. (g) and (i) HER and OER LSV curves. (g-1) and (i-1) Overpotential values at 50 mA/Cm2 for HER and OER. (h) and (j) HER and OER C_{dl} values, Figure S18. (a)–(g) EDS spectra of B and P concentration variation set as labeled and corresponding tables of the atomic and weight percentage of Fe, B and P, Figure S19. X-ray diffraction (XRD) analysis of FeB, FeP and FeBP. Generally, the FeP and FeB demonstrated sharper peaks and the FeBP demonstrated broad peaks. This could be due to the short-range polycrystalline phase of FeBP, Figure S20. (a)–(g) HER CV curves of B and P concentration variation set as labeled. (h) Linear plots for the anodic and cathodic current density versus scan rates of the CV. (i) HER double layer capacitance (C_{dl}) plots, Figure S21. (a)–(g) OER CV curves of B and P concentration variation set as labeled. (h) Linear plots of anodic and cathodic current density versus scan rates of the CV plot. (i) OER double layer capacitance (C_{dl}) plots, Figure S22. Post annealing temperature variation between 100 and 500 °C. The best sample (1 mM Fe, 20 mM CH_4N_2O, 3.6 mM H_3BO_3 and 8.4 mM NaH_2PO_2. H_2O) fabricated at 100 °C for 12 hrs was adapted for annealing. (a)–(d) SEM images. (a-1)–(d-1) and (a-2)–(d-2) Enlarged SEM images. (e)–(e-3) SEM images and its corresponding EDS maps of Fe K, B K and P K. (f) EDS line profile plot corresponds to yellow line. (g) Atomic percentage plot. (h)–(h-3) Raman spectra and contour plots, Figure S23. (a)–(d) EDS spectra of the post-annealing temperature variation set. Inset tables show the atomic and weighting percentages of Fe, B, and P, Figure S24. Electrochemical performance of post annealing temperature variation set. (a) and (e) HER and OER polarization curves of FeBP electrodes in 1 M KOH. (a-1) and (e-1) HER and OER overpotential bar graphs at 50 and 300 mA/cm^2. (b) and (f) Tafel slopes derived from polarization curves. (b-1) and (f-1) Tafel slope values. (c) and (g) HER and OER Nyquist plots. (d) and (h) HER and OER C_{dl} values, Figure S25. (a)–(d) HER CV curves of post annealing temperature variation as labeled. (e) Linear plots for the anodic and cathodic current density versus scan rates of the CV. (f) HER double layer capacitance (C_{dl}) plots, Figure S26. (a)–(d) OER CV curves of post annealing temperature variation as labeled. (e) Linear plots for the anodic and cathodic current density versus scan rates of the CV. (f) OER C_{dl} plots, Figure S27. (a)–(d) SEM images of V-FeBP electrodes, V-doped with soaking approach at different temperature as labelled. (a-1)–(d-1) Enlarged SEM images of the corresponding electrodes, Figure S28. (a)–(d) EDS spectra and corresponding atomic percentage tables of the V-FeBP electrodes by the soaking temperature variation, Figure S29. (a) and (b) HER and OER polarization curves of the V-FeBP electrodes by the soaking temperature variation. The room temperature (RT) sample demonstrated the best HER and OER performances, Figure S30. (a)–(d) SEM images of V-FeBP electrode fabricated with the V concentration variation. (a-1)–(d-1) Enlarged SEM images for the corresponding electrodes, Figure S31. (a)–(d) EDS spectra and corresponding atomic percentage tables of the V concertation variation set, Figure S32. (a) and (b) HER and OER LSV curves of the V-FeBP electrodes with the V concentration variation. The 0.2 mM sample demonstrated the best HER and OER performances, Figure S33. (a)–(d) SEM images of V-FeBP electrodes fabricated with the soaking duration variation. (a-1)–(d-1) Enlarged SEM images for the corresponding electrodes, Figure S34. (a)–(d) EDS spectra and corresponding atomic percentage tables of the soaking time variation set, Figure S35. (a) and (b) HER and OER polarization curves of the V-FeBP electrodes with the soaking time variation. The 25-min sample demonstrated the best HER and OER performances, Figure S36. (a)–(d) SEM images of V-FeBP electrode fabricated with post annealing duration variation at 100 °C annealing temperature. (a-1)–(d-1) Enlarged SEM images for the corresponding electrodes, Figure S37. (a)–(d) EDS spectra and corresponding atomic percentage tables of the post annealing duration variation set, Figure S38. (a) and (b) Polarization curves of HER and OER for the V-FeBP electrodes of the post annealing duration variations set. The 15-mim sample demonstrated the best HER and OER performances, Figure S39. (a)–(d) EDS spectra and corresponding atomic percentage tables of the post annealing temperature variation set followed by vanadium (V) doping (V-FeBP), Figure S40. (a)–(d) HER CV plots of post annealing temperature variation set (V-FeBP). (e) Linear plot for the anodic and cathodic current density Vs scan rate. (f) HER double layer capacitance (C_{dl}) plots, Figure S41. (a)–(d) OER CV plots of post annealing temperature vernation set (V-FeBP). (e) Linear plot for the anodic and cathodic current density Vs scan rate. (f) OER C_{dl} plots, Figure S42. (a)–(a-1) SEM images of Pt/C electrode. (b) EDS spectra with the atomic and weight percentage. For the Pt/C electrode fabrication, 20 mg of Pt/C and 60 µL of 5%

Nafion (117 solutions, Sigma-Aldrich, St. Louis, MO, USA) were dispersed into an ethanol and DI water mixture solution (2 mL, 50:50 solution). The mixture solution was then ultrasonicated for 30 min for uniform dispersion. The bare Ni foam was then immersed in the solution for 30 min. The Pt/C electrode was dried at ambient, Figure S43. (a)–(a-1) Morphological analysis of RuO_2 electrode. (b) EDS spectra and atomic and weight percentage. To fabricate the RuO_2 electrode for the OER reference, 40 mg of RuO_2 and 60 µL of 5% Nafion (117 solutions, Sigma-Aldrich, St. Louis, MO, USA) were dispersed into the 2 mL mixture of ethanol and DI water at the volume ratio 50:50. The mixture was ultrasonically mixed for 30 min. The Ni foam was then dipped in the dispersion solution for 30 min followed by being dried in the air, Figure S44. HER LSV and CA current comparison of the best electrode V-FeBP (50 °C) in 1 M KOH. (a) HER polarization curves. (b) CA response at -0.034, -0.059, -0.082 and -0.101 V. (c) Bar plot comparison of current density for LSV and CA. (d) Percentage difference, Figure S45. OER LSV and CA current comparison of the best electrode V-FeBP (50 °C) in 1 M KOH. (b) CA response at 1.42, 1.45, 1.47 and 1.49 V. (c) Bar plot comparison of current density for LSV and CA. (d) Percentage difference, Figure S46. HER and OER turnover frequency (TOF) of post annealing temperature variation set (V-FeBP). (a)–(b) Vanadium active sites at 150 mV/cm^2. (c)–(d) Fe active sites at 150 mV/cm^2, Figure S47. 2-E LSV and CA comparison of the V-FeBP ‖ V-FeBP in 1 M KOH. (a) HER polarization curves. (b)–(c-1) CA responses at 1.55, 1.65, 1.81, 1.93, 2.05, 2.18, 2.30, and 2.42 V. (c)–(c-1) Bar plots comparison of current density for the LSV and CA. (d) Percentage difference, Figure S48. Comparison of 2-electrode performance with the state-of-art Fe-based electrodes at the current density of 50 mA/cm^2 in 1 M KOH. Related to Table 1 in the main text, Figure S49. Comparison of 2-electrode performance with the all state-of-art electrodes at the current density of 50 mA/cm^2 in 1 M KOH. Related to Table S1, Figure S50. Comparison of 3-electrode performance with the all state-of-art electrodes at the current density of 10 mA/cm^2 in 1 M KOH. (a) HER. (b) OER Related to Table S2, Table S1. Comparison of 2-electrode performance with the state-of-art transition metal-based electrodes at density of 50 mA/cm^2 in 1 M KOH, Table S2. Comparison of 3-electrode performance with the state-of-art transition metal-based electrodes at density of 10 mA/cm^2 in 1 M KOH. The references [66–92] are cited in Supplementary Materials.

Author Contributions: S.B., R.K., R.M., M.A.H. and S.L. participated in the experiment design and carried out the experiments. S.B., R.K., R.M., M.A.H. and S.L. participated in the characterizations and analysis of data. J.-H.J., Y.-U.C. and J.L. designed the experiments and testing methods. S.B., R.K. and J.L. carried out the writing. All authors have read and agreed to the published version of the manuscript.

Funding: Financial support from National Research Foundation of Korea (NRF) grant funded by the Korea government (MSIT) (no. NRF-2022R1H1A2091290, NRF-2020R1I1A1A01060937 and NRF-2018R1A6A1A03025242) and in part by the research grant of Kwangwoon University in 2022 is gratefully acknowledged.

Data Availability Statement: The data presented in this study are available on request from the corresponding author.

Conflicts of Interest: The authors declare no conflict of interest. The funders had no role in the design of the study; in the collection, analyses, or interpretation of data; in the writing of the manuscript, or in the decision to publish the results.

References

1. Yao, M.; Hu, H.; Sun, B.; Wang, N.; Hu, W.; Komarneni, S. Self-Supportive Mesoporous Ni/Co/Fe Phosphosulfide Nanorods Derived from Novel Hydrothermal Electrodeposition as a Highly Efficient Electrocatalyst for Overall Water Splitting. *Small* **2019**, *15*, 1905201. [CrossRef]
2. Cheng, Y.; Geng, H.; Huang, X. Advanced Water Splitting Electrocatalysts: Via the Design of Multicomponent Heterostructures. *Dalt. Trans.* **2020**, *49*, 2761–2765. [CrossRef]
3. Zhang, P.; Wang, M.; Yang, Y.; Yao, T.; Han, H.; Sun, L. Electroless Plated Ni-Bx Films as Highly Active Electrocatalysts for Hydrogen Production from Water over a Wide PH Range. *Nano Energy* **2016**, *19*, 98–107. [CrossRef]
4. Cai, L.; Lin, Z.; Wang, M.; Pan, F.; Chen, J.; Wang, Y.; Shen, X.; Chai, Y. Improved Interfacial H_2O Supply by Surface Hydroxyl Groups for Enhanced Alkaline Hydrogen Evolution. *J. Mater. Chem. A* **2017**, *5*, 24091–24097. [CrossRef]
5. Li, H.; Wen, P.; Li, Q.; Dun, C.; Xing, J.; Lu, C.; Adhikari, S.; Jiang, L.; Carroll, D.L.; Geyer, S.M. Earth-Abundant Iron Diboride (FeB_2) Nanoparticles as Highly Active Bifunctional Electrocatalysts for Overall Water Splitting. *Adv. Energy Mater.* **2017**, *7*, 1700513. [CrossRef]

6. Ahn, H.J.; Yoon, K.Y.; Kwak, M.J.; Park, J.; Jang, J.H. Boron Doping of Metal-Doped Hematite for Reduced Surface Recombination in Water Splitting. *ACS Catal.* **2018**, *8*, 11932–11939. [CrossRef]
7. Qu, S.; Huang, J.; Yu, J.; Chen, G.; Hu, W.; Yin, M.; Zhang, R.; Chu, S.; Li, C. Ni_3S_2 Nanosheet Flowers Decorated with CdS Quantum Dots as a Highly Active Electrocatalysis Electrode for Synergistic Water Splitting. *ACS Appl. Mater. Interfaces* **2017**, *9*, 29660–29668. [CrossRef]
8. Zhang, B.; Shan, J.; Wang, W.; Tsiakaras, P.; Li, Y. Oxygen Vacancy and Core–Shell Heterojunction Engineering of Anemone-Like CoP@CoOOH Bifunctional Electrocatalyst for Efficient Overall Water Splitting. *Small* **2022**, *18*, 2106012. [CrossRef]
9. Li, C.F.; Zhao, J.W.; Xie, L.J.; Wu, J.Q.; Li, G.R. Fe Doping and Oxygen Vacancy Modulated Fe-Ni_5P_4/NiFeOH Nanosheets as Bifunctional Electrocatalysts for Efficient Overall Water Splitting. *Appl. Catal. B Environ.* **2021**, *291*, 119987. [CrossRef]
10. Liu, Y.; Yu, Y.; Mu, Z.; Wang, Y.; Ali, U.; Jing, S.; Xing, S. Urea-Assisted Enhanced Electrocatalytic Activity of MoS_2-Ni_3S_2 for Overall Water Splitting. *Inorg. Chem. Front.* **2020**, *7*, 3588–3597. [CrossRef]
11. Yuan, S.; Pu, Z.; Zhou, H.; Yu, J.; Amiinu, I.S.; Zhu, J.; Liang, Q.; Yang, J.; He, D.; Hu, Z.; et al. A Universal Synthesis Strategy for Single Atom Dispersed Cobalt/Metal Clusters Heterostructure Boosting Hydrogen Evolution Catalysis at All PH Values. *Nano Energy* **2019**, *59*, 472–480. [CrossRef]
12. Jeong, J.H.; Kunwar, S.; Pandit, S.; Lee, J. CoP_2 Nanoparticles Deposited on Nanometer-Thick Pt-Coated Fluorine-Doped Tin Oxide Substrates as Electrocatalysts for Simultaneous Hydrogen Evolution and Oxygen Evolution. *ACS Appl. Nano Mater.* **2020**, *3*, 6507–6515. [CrossRef]
13. Wu, Z.; Nie, D.; Song, M.; Jiao, T.; Fu, G.; Liu, X. Facile Synthesis of Co-Fe-B-P Nanochains as an Efficient Bifunctional Electrocatalyst for Overall Water-Splitting. *Nanoscale* **2019**, *11*, 7506–7512. [CrossRef]
14. Kunwar, S.; Pandit, S.; Jeong, J.H.; Lee, J. Hybrid CoP_2–Pt–FTO Nanoarchitecture for Bifunctional Electrocatalysts in H_2 Generation by Water Splitting. *Mater. Today Sustain.* **2020**, *9*, 100045. [CrossRef]
15. Xu, K.; Guo, W.; Zhang, H.; Zhou, H.; Zhu, Z.; Zhou, Y. An efficient Vanadium/Cobalt Metaphosphate Electrocatalyst for Hydrogen and Oxygen Evolution in Alkaline Water Splitting. *Inorg. Chem. Front.* **2022**, *9*, 4808–4816. [CrossRef]
16. Xu, N.; Cao, G.; Chen, Z.; Kang, Q.; Dai, H.; Wang, P. Cobalt Nickel Boride as an Active Electrocatalyst for Water Splitting. *J. Mater. Chem. A* **2017**, *5*, 12379–12384. [CrossRef]
17. Spanos, I.; Tesch, M.F.; Yu, M.; Tüysüz, H.; Zhang, J.; Feng, X.; Müllen, K.; Schlögl, R.; Mechler, A.K. Facile Protocol for Alkaline Electrolyte Purification and Its Influence on a Ni-Co Oxide Catalyst for the Oxygen Evolution Reaction. *ACS Catal.* **2019**, *9*, 8165–8170. [CrossRef]
18. Hao, W.; Yao, D.; Xu, Q.; Wang, R.; Zhang, C.; Guo, Y.; Sun, R.; Huang, M.; Chen, Z. Highly Efficient Overall-Water Splitting Enabled via Grafting Boron-Inserted Fe-Ni Solid Solution Nanosheets onto Unconventional Skeleton. *Appl. Catal. B Environ.* **2021**, *292*, 120188. [CrossRef]
19. Chunduri, A.; Gupta, S.; Bapat, O.; Bhide, A.; Fernandes, R.; Patel, M.K.; Bambole, V.; Miotello, A.; Patel, N. A Unique Amorphous Cobalt-Phosphide-Boride Bifunctional Electrocatalyst for Enhanced Alkaline Water-Splitting. *Appl. Catal. B Environ.* **2019**, *259*, 118051. [CrossRef]
20. Liu, X.; Wu, J.; Guo, X. Ternary Boron-, Phosphorus- and Oxygen-Doped Amorphous Nickel Nanoalloys for Enhanced Activity towards the Oxygen Evolution Reaction. *Electrochem. Commun.* **2020**, *111*, 106649. [CrossRef]
21. Guo, Z.; Liu, L.; Wang, J.; Cao, Y.; Tu, J.; Zhang, X.; Ding, L. Recent Progress in CoP-Based Materials for Electrochemical Water Splitting. *Int. J. Hydrog. Energy* **2021**, *46*, 34194–34215. [CrossRef]
22. Deng, X.; Zhang, R.; Li, Q.; Gu, W.; Hao, L. Bimetallic Boron Phosphide Ni-2Fe-BP as an Active Water-Splitting Catalyst. *ChemistrySelect* **2022**, *7*, e202200091. [CrossRef]
23. Habib, M.A.; Mandavkar, R.; Burse, S.; Lin, S.; Kulkarni, R.; Patil, C.S.; Jeong, J.-H.; Lee, J. Design of Boron-Based Ternary W_3CoB_3 Electrocatalyst for the Improved HER and OER Performances. *Mater. Today Energy* **2022**, *26*, 101021. [CrossRef]
24. Popczun, E.J.; McKone, J.R.; Read, C.G.; Biacchi, A.J.; Wiltrout, A.M.; Lewis, N.S.; Schaak, R.E. Nanostructured Nickel Phosphide as an Electrocatalyst for the Hydrogen Evolution Reaction. *J. Am. Chem. Soc.* **2013**, *135*, 9267–9270. [CrossRef] [PubMed]
25. Mandavkar, R.; Habib, A.; Lin, S.; Kulkarni, R.; Burse, S.; Jeong, J.; Lee, J. Electron Enriched Ternary NiMoB Electrocatalyst for Improved Overall Water Splitting: Better Performance as Compared to the Pt/C || RuO_2 at High Current Density. *Appl. Mater. Today* **2022**, *29*, 101579. [CrossRef]
26. Saad, A.; Gao, Y.; Owusu, K.A.; Liu, W.; Wu, Y.; Ramiere, A.; Guo, H.; Tsiakaras, P.; Cai, X. Ternary Mo_2NiB_2 as a Superior Bifunctional Electrocatalyst for Overall Water Splitting. *Small* **2022**, *18*, 2104303. [CrossRef]
27. Lin, S.; Habib, A.; Mandavkar, R.; Kulkarni, R.; Burse, S.; Chung, Y.; Liu, C.; Wang, Z.; Lin, S.; Jeong, J.; et al. Higher Water-Splitting Performance of Boron-Based Porous CoMnB Electrocatalyst over the Benchmarks at High Current in 1 m KOH and Real Sea Water. *Adv. Sustain. Syst.* **2022**, *6*, 2270022. [CrossRef]
28. Zhang, H.; Maijenburg, A.W.; Li, X.; Schweizer, S.L.; Wehrspohn, R.B. Bifunctional Heterostructured Transition Metal Phosphides for Efficient Electrochemical Water Splitting. *Adv. Funct. Mater.* **2020**, *30*, 2003261. [CrossRef]
29. Zhu, Z.; Xu, K.; Guo, W.; Zhang, H.; Xiao, X.; He, M.; Yu, T.; Zhao, H.; Zhang, D.; Yang, T. Vanadium-Phosphorus Incorporation Induced Interfacial Modification on Cobalt Catalyst and Its Super Electrocatalysis for Water Splitting in Alkaline Media. *Appl. Catal. B Environ.* **2022**, *304*, 120985. [CrossRef]

30. Cheng, C.; Zheng, F.; Zhang, C.; Du, C.; Fang, Z.; Zhang, Z.; Chen, W. High-Efficiency Bifunctional Electrocatalyst Based on 3D Freestanding Cu Foam in Situ Armored CoNi Alloy Nanosheet Arrays for Overall Water Splitting. *J. Power Sources* **2019**, *427*, 184–193. [CrossRef]
31. Feng, Y.; Li, Z.; Li, S.; Yang, M.; Ma, R.; Wang, J. One Stone Two Birds: Vanadium Doping as Dual Roles in Self-Reduced Pt Clusters and Accelerated Water Splitting. *J. Energy Chem.* **2022**, *66*, 493–501. [CrossRef]
32. Wang, Q.; Zhao, H.; Li, F.; She, W.; Wang, X.; Xu, L.; Jiao, H. Mo-Doped Ni_2P Hollow Nanostructures: Highly Efficient and Durable Bifunctional Electrocatalysts for Alkaline Water Splitting. *J. Mater. Chem. A* **2019**, *7*, 7636–7643. [CrossRef]
33. Du, X.; Su, H.; Zhang, X. Cr Doped-Co9S8 Nanoarrays as High-Efficiency Electrocatalysts for Water Splitting. *J. Alloy. Compd.* **2020**, *824*, 153965. [CrossRef]
34. Khatun, S.; Roy, P. Cobalt Chromium Vanadium Layered Triple Hydroxides as an Efficient Oxygen Electrocatalyst for Alkaline Seawater Splitting. *Chem. Commun.* **2022**, *58*, 1104–1107. [CrossRef]
35. Jo, S.; Kwon, J.H.; Cho, K.Y.; Kim, D.H.; Eom, K.S. Enhanced Activity and Stability of Co-Ni-P-B Catalyst for the Hydrogen Evolution Reaction via Predeposition of Co-Ni on a Cu Substrate. *Catal. Today* **2021**, *359*, 35–42. [CrossRef]
36. Niu, Z.; Qiu, C.; Jiang, J.; Ai, L. Hierarchical CoP-FeP Branched Heterostructures for Highly Efficient Electrocatalytic Water Splitting. *ACS Sustain. Chem. Eng.* **2019**, *7*, 2335–2342. [CrossRef]
37. Farai Kuchena, S.; Wang, Y. A Full Flexible NH_4^+ Ion Battery Based on the Concentrated Hydrogel Electrolyte for Enhanced Performance. *Chem. A Eur. J.* **2021**, *27*, 15450–15459. [CrossRef]
38. Ülker, E. Hydrothermally Synthesized Cobalt Borophosphate as an Electrocatalyst for Water Oxidation in the PH Range from 7 to 14. *ChemElectroChem* **2019**, *6*, 3132–3138. [CrossRef]
39. Li, W.; Zhao, Y.; Liu, Y.; Sun, M.; Waterhouse, G.I.N.; Huang, B.; Zhang, K.; Zhang, T.; Lu, S. Exploiting Ru-Induced Lattice Strain in CoRu Nanoalloys for Robust Bifunctional Hydrogen Production. *Angew. Chem. Int. Ed.* **2021**, *60*, 3290–3298. [CrossRef]
40. Wang, F.; Zhu, J.; Liu, H. Urea Controlled Hydrothermal Synthesis of Ammonium Aluminum Carbonate Hydroxide Rods. *AIP Adv.* **2018**, *8*, 5–12. [CrossRef]
41. Xuan, C.; Wang, J.; Xia, W.; Peng, Z.; Wu, Z.; Lei, W.; Xia, K.; Xin, H.L.; Wang, D. Porous Structured Ni-Fe-P Nanocubes Derived from a Prussian Blue Analogue as an Electrocatalyst for Efficient Overall Water Splitting. *ACS Appl. Mater. Interfaces* **2017**, *9*, 26134–26142. [CrossRef] [PubMed]
42. Liu, H.; Li, X.; Ge, L.; Peng, C.; Zhu, L.; Zou, W.; Chen, J.; Wu, Q.; Zhang, Y.; Huang, H.; et al. Accelerating Hydrogen Evolution in Ru-Doped FeCoP Nanoarrays with Lattice Distortion toward Highly Efficient Overall Water Splitting. *Catal. Sci. Technol.* **2020**, *10*, 8314–8324. [CrossRef]
43. Li, S.; Zhang, G.; Tu, X.; Li, J. Polycrystalline CoP/CoP2 Structures for Efficient Full Water Splitting. *ChemElectroChem* **2018**, *5*, 701–707. [CrossRef]
44. Kyesmen, P.I.; Nombona, N.; Diale, M. Heterojunction of Nanostructured α-Fe_2O_3/CuO for Enhancement of Photoelectrochemical Water Splitting. *J. Alloys Compd.* **2021**, *863*, 158724. [CrossRef]
45. Maiti, A.; Srivastava, S.K. Ru-Doped CuO/MoS_2 Nanostructures as Bifunctional Water-Splitting Electrocatalysts in Alkaline Media. *ACS Appl. Nano Mater.* **2021**, *4*, 7675–7685. [CrossRef]
46. Han, L.; Xu, J.; Huang, Y.; Dong, W.; Jia, X. High-Performance Electrocatalyst of Vanadium-Iron Bimetal Organic Framework Arrays on Nickel Foam for Overall Water Splitting. *Chin. Chem. Lett.* **2021**, *32*, 2263–2268. [CrossRef]
47. Jeung, Y.; Jung, H.; Kim, D.; Roh, H.; Lim, C.; Han, J.W.; Yong, K. 2D-Structured V-Doped Ni(Co,Fe) Phosphides with Enhanced Charge Transfer and Reactive Sites for Highly Efficient Overall Water Splitting Electrocatalysts. *J. Mater. Chem. A* **2021**, *9*, 12203–12213. [CrossRef]
48. Yu, J.; Li, Q.; Li, Y.; Xu, C.Y.; Zhen, L.; Dravid, V.P.; Wu, J. Ternary Metal Phosphide with Triple-Layered Structure as a Low-Cost and Efficient Electrocatalyst for Bifunctional Water Splitting. *Adv. Funct. Mater.* **2016**, *26*, 7644–7651. [CrossRef]
49. Sivula, K.; Zboril, R.; Le Formal, F.; Robert, R.; Weidenkaff, A.; Tucek, J.; Frydrych, J.; Grätzel, M. Photoelectrochemical Water Splitting with Mesoporous Hematite Prepared by a Solution-Based Colloidal Approach. *J. Am. Chem. Soc.* **2010**, *132*, 7436–7444. [CrossRef]
50. Yao, Q.; Huang, B.; Zhang, N.; Sun, M.; Shao, Q.; Huang, X. Channel-Rich RuCu Nanosheets for PH-Universal Overall Water Splitting Electrocatalysis. *Angew. Chem.* **2019**, *131*, 14121–14126. [CrossRef]
51. Kyesmen, P.I.; Nombona, N.; Diale, M. Modified Annealing Approach for Preparing Multi-Layered Hematite Thin Films for Photoelectrochemical Water Splitting. *Mater. Res. Bull.* **2020**, *131*, 110964. [CrossRef]
52. Anantharaj, S.; Kundu, S.; Noda, S. Worrisome Exaggeration of Activity of Electrocatalysts Destined for Steady-State Water Electrolysis by Polarization Curves from Transient Techniques. *J. Electrochem. Soc.* **2022**, *169*, 014508. [CrossRef]
53. Zhang, Z.; Li, C.; Huang, H.; Li, J.; Zhang, X.; Li, Z.; Wei, H.; Chu, H. High-Density Nickel Phosphide Nanoparticles Loaded Reduced Graphene Oxide on Nickel Foam for Enhanced Alkaline and Neutral Water Splitting. *Electrochim. Acta* **2020**, *362*, 137172. [CrossRef]
54. Sultan, S.; Ha, M.; Kim, D.Y.; Tiwari, J.N.; Myung, C.W.; Meena, A.; Shin, T.J.; Chae, K.H.; Kim, K.S. Superb Water Splitting Activity of the Electrocatalyst $Fe_3Co(PO_4)_4$ Designed with Computation Aid. *Nat. Commun.* **2019**, *10*, 5195. [CrossRef]
55. Liu, Y.; Cao, J.; Chen, Y.; Wei, M.; Liu, X.; Li, X.; Wu, Q.; Feng, B.; Zhang, Y.; Yang, L. Regulation of the Morphology and Electrochemical Properties of Ni 0.85 Se via Fe Doping for Overall Water Splitting and Supercapacitors. *CrystEngComm* **2022**, *24*, 1704–1718. [CrossRef]

56. Zhu, C.; Yin, Z.; Lai, W.; Sun, Y.; Liu, L.; Zhang, X.; Chen, Y.; Chou, S.L. Fe-Ni-Mo Nitride Porous Nanotubes for Full Water Splitting and Zn-Air Batteries. *Adv. Energy Mater.* **2018**, *8*, 1802327. [CrossRef]
57. Jia, Y.; Zhang, L.; Gao, G.; Chen, H.; Wang, B.; Zhou, J.; Soo, M.T.; Hong, M.; Yan, X.; Qian, G.; et al. A Heterostructure Coupling of Exfoliated Ni–Fe Hydroxide Nanosheet and Defective Graphene as a Bifunctional Electrocatalyst for Overall Water Splitting. *Adv. Mater.* **2017**, *29*, 1700017. [CrossRef]
58. Zou, Z.; Wang, X.; Huang, J.; Wu, Z.; Gao, F. An Fe-Doped Nickel Selenide Nanorod/Nanosheet Hierarchical Array for Efficient Overall Water Splitting. *J. Mater. Chem. A* **2019**, *7*, 2233–2241. [CrossRef]
59. Yaseen, W.; Ullah, N.; Xie, M.; Yusuf, B.A.; Xu, Y.; Tong, C.; Xie, J. Ni-Fe-Co Based Mixed Metal/Metal-Oxides Nanoparticles Encapsulated in Ultrathin Carbon Nanosheets: A Bifunctional Electrocatalyst for Overall Water Splitting. *Surf. Interfaces* **2021**, *26*, 101361. [CrossRef]
60. Li, M.; Wang, J.; Guo, X.; Li, J.; Huang, Y.; Geng, S.; Yu, Y.; Liu, Y.; Yang, W. Structural Engineering of Fe-Doped Ni_2P Nanosheets Arrays for Enhancing Bifunctional Electrocatalysis towards Overall Water Splitting. *Appl. Surf. Sci.* **2021**, *536*, 147909. [CrossRef]
61. Chen, W.; Qian, G.; Xu, Q.; Yu, C.; Yu, M.; Xia, Y.; Yin, S. Efficient Bifunctional Catalysts for Overall Water Splitting: Porous Fe-Mo Oxide Hybrid Nanorods. *Nanoscale* **2020**, *12*, 7116–7123. [CrossRef]
62. Wang, K.; Sun, K.; Yu, T.; Liu, X.; Wang, G.X.; Jiang, L.; Xie, G. Facile Synthesis of Nanoporous Ni-Fe-P Bifunctional Catalysts with High Performance for Overall Water Splitting. *J. Mater. Chem. A* **2019**, *7*, 2518–2523. [CrossRef]
63. He, Q.; Liu, H.; Tan, P.; Xie, J.; Si, S.; Pan, J. N-Fe-Cu Co-Doped Carbon Materials for Efficient Electrocatalytic Water Splitting. *J. Solid State Chem.* **2021**, *299*, 122179. [CrossRef]
64. Lim, D.; Oh, E.; Lim, C.; Shim, S.E.; Baeck, S.H. Fe-Doped Ni3S2 Nanoneedles Directly Grown on Ni Foam as Highly Efficient Bifunctional Electrocatalysts for Alkaline Overall Water Splitting. *Electrochim. Acta* **2020**, *361*, 137080. [CrossRef]
65. Li, W.; Chen, Y.; Yu, B.; Hu, Y.; Wang, X.; Yang, D. 3D Hollow Co-Fe-P Nanoframes Immobilized on N,P-Doped CNT as an Efficient Electrocatalyst for Overall Water Splitting. *Nanoscale* **2019**, *11*, 17031–17040. [CrossRef]
66. Anantharaj, S.; Noda, S. Appropriate Use of Electrochemical Impedance Spectroscopy in Water Splitting Electrocatalysis. *ChemElectroChem* **2020**, *7*, 2297–2308. [CrossRef]
67. Yu, F.; Zhou, H.; Huang, Y.; Sun, J.; Qin, F.; Bao, J.; Goddard, W.A.; Chen, S.; Ren, Z. High-Performance Bifunctional Porous Non-Noble Metal Phosphide Catalyst for Overall Water Splitting. *Nat. Commun.* **2018**, *9*, 1–9. [CrossRef]
68. Chen, C.; Tuo, Y.; Lu, Q.; Lu, H.; Zhang, S.; Zhou, Y.; Zhang, J.; Liu, Z.; Kang, Z.; Feng, X.; et al. Hierarchical Trimetallic Co-Ni-Fe Oxides Derived from Core-Shell Structured Metal-Organic Frameworks for Highly Efficient Oxygen Evolution Reaction. *Appl. Catal. B Environ.* **2021**, *287*, 119953. [CrossRef]
69. Yu, L.; Zhou, H.; Sun, J.; Qin, F.; Yu, F.; Bao, J.; Yu, Y.; Chen, S.; Ren, Z. Cu Nanowires Shelled with NiFe Layered Double Hydroxide Nanosheets as Bifunctional Electrocatalysts for Overall Water Splitting. *Energy Environ. Sci.* **2017**, *10*, 1820–1827. [CrossRef]
70. Jiang, Y.; Lu, Y. Designing Transition-Metal-Boride-Based Electrocatalysts for Applications in Electrochemical Water Splitting. *Nanoscale* **2020**, *12*, 9327–9351. [CrossRef]
71. Palma, V.; Vaiano, V.; Matarangolo, M.; Anello, G. Comparison of Pt/C Electrocatalyst Deposition Methods for PEM Fuel Cells. *Chem. Eng. Trans.* **2018**, *70*, 1525–1530. [CrossRef]
72. Yu, H.; Quan, T.; Mei, S.; Kochovski, Z.; Huang, W.; Meng, H.; Lu, Y. Prompt Electrodeposition of Ni Nanodots on Ni Foam to Construct a High-Performance Water-Splitting Electrode: Efficient, Scalable, and Recyclable. *Nano-Micro Lett.* **2019**, *11*, 1–13. [CrossRef]
73. Anantharaj, S.; Karthik, P.E.; Noda, S. The Significance of Properly Reporting Turnover Frequency in Electrocatalysis Research. *Angew. Chemie - Int. Ed.* **2021**, *60*, 23051–23067. [CrossRef] [PubMed]
74. Han, N.; Yang, K.R.; Lu, Z.; Li, Y.; Xu, W.; Gao, T.; Cai, Z.; Zhang, Y.; Batista, V.S.; Liu, W.; et al. Nitrogen-Doped Tungsten Carbide Nanoarray as an Efficient Bifunctional Electrocatalyst for Water Splitting in Acid. *Nat. Commun.* **2018**, *9*, 1–10. [CrossRef] [PubMed]
75. Gong, M.; Zhou, W.; Kenney, M.J.; Kapusta, R.; Cowley, S.; Wu, Y.; Lu, B.; Lin, M.C.; Wang, D.Y.; Yang, J.; et al. Blending Cr2O3 into a NiO-Ni Electrocatalyst for Sustained Water Splitting. *Angew. Chemie Int. Ed.* **2015**, *54*, 11989–11993. [CrossRef]
76. Wang, J.; Zhang, M.; Yang, G.; Song, W.; Zhong, W.; Wang, X.; Wang, M.; Sun, T.; Tang, Y. Heterogeneous Bimetallic Mo-NiPx/NiSy as a Highly Efficient Electrocatalyst for Robust Overall Water Splitting. *Adv. Funct. Mater.* **2021**, *31*, 2101532. [CrossRef]
77. Ma, H.; Chen, Z.; Wang, Z.; Singh, C.V.; Jiang, Q. Interface Engineering of Co/CoMoN/NF Heterostructures for High-Performance Electrochemical Overall Water Splitting. *Adv. Sci.* **2022**, *2105313*, 2105313. [CrossRef]
78. Wang, D.; Li, Q.; Han, C.; Lu, Q.; Xing, Z.; Yang, X. Atomic and Electronic Modulation of Self-Supported Nickel-Vanadium Layered Double Hydroxide to Accelerate Water Splitting Kinetics. *Nat. Commun.* **2019**, *10*, 3899. [CrossRef]
79. Wang, P.; Qi, J.; Chen, X.; Li, C.; Li, W.; Wang, T.; Liang, C. Three-Dimensional Heterostructured NiCoP@NiMn-Layered Double Hydroxide Arrays Supported on Ni Foam as a Bifunctional Electrocatalyst for Overall Water Splitting. *ACS Appl. Mater. Interfaces* **2020**, *12*, 4385–4395. [CrossRef]
80. Bai, X.; Ren, Z.; Du, S.; Meng, H.; Wu, J.; Xue, Y.; Zhao, X.; Fu, H. In-Situ Structure Reconstitution of NiCo2Px for Enhanced Electrochemical Water Oxidation. *Sci. Bull.* **2017**, *62*, 1510–1518. [CrossRef]

81. Xu, H.; Fei, B.; Cai, G.; Ha, Y.; Liu, J.; Jia, H.; Zhang, J.; Liu, M.; Wu, R. Boronization-Induced Ultrathin 2D Nanosheets with Abundant Crystalline–Amorphous Phase Boundary Supported on Nickel Foam toward Efficient Water Splitting. *Adv. Energy Mater.* **2020**, *10*, 1902714. [CrossRef]
82. Menezes, P.W.; Indra, A.; Das, C.; Walter, C.; Göbel, C.; Gutkin, V.; Schmeißer, D.; Driess, M. Uncovering the Nature of Active Species of Nickel Phosphide Catalysts in High-Performance Electrochemical Overall Water Splitting. *ACS Catal.* **2017**, *7*, 103–109. [CrossRef]
83. Niu, J.; Yue, Y.; Yang, C.; Wang, Y.; Qin, J.; Zhang, X.; Wu, Z.S. Ultrarapid Synthesis Ni-Cu Bifunctional Electrocatalyst by Self-Etching Electrodeposition for High-Performance Water Splitting Reaction. *Appl. Surf. Sci.* **2021**, *561*, 150030. [CrossRef]
84. Tang, C.; Cheng, N.; Pu, Z.; Xing, W.; Sun, X. NiSe Nanowire Film Supported on Nickel Foam: An Efficient and Stable 3D Bifunctional Electrode for Full Water Splitting. *Angew. Chem. Int. Ed.* **2015**, *54*, 9351–9355. [CrossRef]
85. De Silva, U.; Masud, J.; Zhang, N.; Hong, Y.; Liyanage, W.P.R.; Asle Zaeem, M.; Nath, M. Nickel Telluride as a Bifunctional Electrocatalyst for Efficient Water Splitting in Alkaline Medium. *J. Mater. Chem. A* **2018**, *6*, 7608–7622. [CrossRef]
86. Zhang, R.; Tang, C.; Kong, R.; Du, G.; Asiri, A.M.; Chen, L.; Sun, X. Al-Doped CoP Nanoarray: A Durable Water-Splitting Electrocatalyst with Superhigh Activity. *Nanoscale* **2017**, *9*, 4793–4800. [CrossRef]
87. Kim, D.; Qin, X.; Yan, B.; Piao, Y. Sprout-Shaped Mo-Doped CoP with Maximized Hydrophilicity and Gas Bubble Release for High-Performance Water Splitting Catalyst. *Chem. Eng. J.* **2021**, *408*, 127331. [CrossRef]
88. Hu, E.; Feng, Y.; Nai, J.; Zhao, D.; Hu, Y.; Lou, X.W. Construction of Hierarchical Ni-Co-P Hollow Nanobricks with Oriented Nanosheets for Efficient Overall Water Splitting. *Energy Environ. Sci.* **2018**, *11*, 872–880. [CrossRef]
89. Ji, L.; Wang, J.; Teng, X.; Meyer, T.J.; Chen, Z. CoP Nanoframes as Bifunctional Electrocatalysts for Efficient Overall Water Splitting. *ACS Catal.* **2020**, *10*, 412–419. [CrossRef]
90. Jiao, L.; Zhou, Y.X.; Jiang, H.L. Metal-Organic Framework-Based CoP/Reduced Graphene Oxide: High-Performance Bifunctional Electrocatalyst for Overall Water Splitting. *Chem. Sci.* **2016**, *7*, 1690–1695. [CrossRef]
91. Sun, K.; Wang, K.; Yu, T.; Liu, X.; Wang, G.; Jiang, L.; Bu, Y.; Xie, G. High-Performance Fe–Co–P Alloy Catalysts by Electroless Deposition for Overall Water Splitting. *Int. J. Hydrogen Energy* **2019**, *44*, 1328–1335. [CrossRef]
92. Ayom, G.E.; Khan, M.D.; Choi, J.; Gupta, R.K.; van Zyl, W.E.; Revaprasadu, N. Synergistically Enhanced Performance of Transition-Metal Doped Ni2P for Supercapacitance and Overall Water Splitting. *Dalt. Trans.* **2021**, *50*, 11821–11833. [CrossRef] [PubMed]

nanomaterials

Article

Indirect Band Gap in Scrolled MoS_2 Monolayers

Jeonghyeon Na [1,†], Changyeon Park [1,†], Chang Hoi Lee [1], Won Ryeol Choi [1], Sooho Choi [2], Jae-Ung Lee [3], Woochul Yang [4], Hyeonsik Cheong [5], Eleanor E. B. Campbell [6,7] and Sung Ho Jhang [1,*]

[1] School of Physics, Konkuk University, Seoul 05029, Korea
[2] Center for Integrated Nanostructure Physics, Institute for Basic Science, Suwon 16419, Korea
[3] Department of Physics, Ajou University, Suwon 16499, Korea
[4] Department of Physics, Dongguk University, Seoul 04620, Korea
[5] Department of Physics, Sogang University, Seoul 04107, Korea
[6] EaStCHEM, School of Chemistry, Edinburgh University, David Brewster Road, Edinburgh EH9 3FJ, UK
[7] Department of Physics, Ehwa Womans University, Seoul 03760, Korea
* Correspondence: shjhang@konkuk.ac.kr
† These authors contributed equally to this work.

Abstract: MoS_2 nanoscrolls that have inner core radii of ∼250 nm are generated from MoS_2 monolayers, and the optical and transport band gaps of the nanoscrolls are investigated. Photoluminescence spectroscopy reveals that a MoS_2 monolayer, originally a direct gap semiconductor (∼1.85 eV (optical)), changes into an indirect gap semiconductor (∼1.6 eV) upon scrolling. The size of the indirect gap for the MoS_2 nanoscroll is larger than that of a MoS_2 bilayer (∼1.54 eV), implying a weaker interlayer interaction between concentric layers of the MoS_2 nanoscroll compared to Bernal-stacked MoS_2 few-layers. Transport measurements on MoS_2 nanoscrolls incorporated into ambipolar ionic-liquid-gated transistors yielded a band gap of ∼1.9 eV. The difference between the transport and optical gaps indicates an exciton binding energy of 0.3 eV for the MoS_2 nanoscrolls. The rolling up of 2D atomic layers into nanoscrolls introduces a new type of quasi-1D nanostructure and provides another way to modify the band gap of 2D materials.

Keywords: rolled structure; 1D structure; MoS_2; scrolled MoS_2; band gap; ionic liquid gating

Citation: Na, J.; Park, C.; Lee, C.H.; Choi, W.R.; Choi, S.; Lee, J.-U.; Yang, W.; Cheong, H.; Campbell, E.E.B.; Jhang, S.H. Indirect Band Gap in Scrolled MoS_2 Monolayers. *Nanomaterials* **2022**, *12*, 3353. https://doi.org/10.3390/nano12193353

Academic Editors: Filippo Giannazzo and Elias Stathatos

Received: 30 August 2022
Accepted: 22 September 2022
Published: 26 September 2022

1. Introduction

Two-dimensional (2D) atomic layers of graphene and transition metal dichalcogenides (TMDs) have been widely investigated for future applications [1]. Among TMDs, materials having semiconductor properties, such as MoS_2 and WS_2, have received a great amount of attention as materials that complement gapless graphene. The structural modifications of 2D materials, such as ripples, and folded and rolled structures, were also studied [2–4]. Since a rolled structure has a large surface area in a small volume and can transport materials through the hollow core, the nanoscrolls of 2D materials have potential for energy storage, sensors, microrockets, and photodetectors [5]. The rolling up of graphene [4,6–8], h-BN [9], and TMDs into nanoscrolls [10–21] was achieved, and the properties of nanoscrolls are of interest from theoretical and experimental viewpoints. In particular, nanoscrolls spirally wrapped from 2D sheets provide another possibility to tune the band gap of 2D materials. Theory predicts band structure changes in graphene nanoscrolls [22] and black phosphorus [23]. Chirality and radius are the most relevant factors to determine the electronic structure of nanoscrolls. One can also infer from previous studies on MoS_2 nanotubes [24] where the band gap decreased with decreasing diameter that a change in the band gap of MoS_2 can be expected upon scrolling. However, experimental studies of the band gap of MoS_2 nanoscrolls often reported contradictory results. Metallic transport with a zero band gap was claimed for a scrolled MoS_2 [13], and a small red shift of 30–60 meV in the A peak (direct band gap) compared to a MoS_2 monolayer was reported from the photoluminescence (PL) spectroscopy of MoS_2 nanoscrolls [10,16].

In this paper, we produced MoS_2 nanoscrolls that had inner core radii of ∼250 nm by rolling up MoS_2 monolayers, and investigate their optical and transport band gaps using PL and ambipolar transport in ionic-liquid-gated transistors. Combined with atomic force microscopy (AFM) to determine the structures of the nanoscrolls complemented with Raman spectroscopy, we provide a comprehensive characterization of the properties of MoS_2 nanoscrolls and verify the possibility to tune the band gap compared to the MoS_2 monolayer.

2. Materials and Methods

Experiments were performed on MoS_2 monolayers prepared with either chemical vapor deposition (CVD) or mechanical exfoliation. CVD was carried out in a two-zone quartz tube furnace with sulfur powder (∼1 g) loaded into a low-temperature T zone heated to 400 °C and MoO_3 film (∼50 nm) into a high-T zone heated to 800 °C. The CVD growth produced triangular crystals (ca. 25 μm edges) of MoS_2 on SiO_2 substrates. Exfoliated MoS_2, on the other hand, was obtained with a gold-assisted exfoliation technique [25] that yields monolayers with much larger lateral dimensions than ∼10 μm.

The method used to produce scrolls from monolayers follows the one originally introduced by Xie et al. [4]. A droplet of isopropyl alcohol (IPA) solution (IPA:deionized water volume ratio of 1:3) was placed on top of MoS_2 on the substrate. For exfoliated MoS_2, a 1 mM KOH in IPA solution was used to facilitate rolling up the monolayer.

Raman and PL measurements were conducted using a home-built confocal microscope system. A 532 nm (2.33 eV) beam of a diode-pumped solid-state (DPSS) laser was used as an excitation source. The scattered or emitted light was dispersed with a Jobin-Yvon Horiba iHR550 spectrometer (2400 grooves/mm for Raman and 300 grooves/mm for PL) and detected with a liquid-nitrogen-cooled back-illuminated charge-coupled-device (CCD) detector. In order to access the low-frequency range down to 5 cm^{-1}, volume holographic filters (OptiGrate Corp, Oviedo, FL, USA) were used to reject the Rayleigh-scattered light. Laser power was kept below 100 μW (focal spot ∼1 μm^2) to avoid damaging the samples. The PL spectrum of the scrolled MoS_2 was fitted using the multipeak Lorentzian fitting analysis of OriginPro 2016 software (Northampton, MA, USA) by setting the initial positions of A series (A_{xx}, A^-, A) and B exciton peaks to the known positions for a monolayer MoS_2 [26].

Transistors incorporating rolled-MoS_2 were fabricated on SiO_2 (300 nm)/Si substrates. The source and drain electrodes were patterned with conventional electron-beam lithography. Ti (20 nm)/Au (100 nm) electrodes were then deposited for transistors with back-gating, and Cr (30 nm)/Au (120 nm) for transistors with ionic liquid-gating to avoid the strong electrochemical reaction of Ti. Diethylmethyl(2-methoxyethyl)ammonium bis(trifluoromethylsulfonyl)imide (DEME-TFSI) was used as the ionic liquid. Ionic liquids have hygroscopicity, and moisture penetrates easily. Moisture penetration lowers the charge density of the ionic liquid and provides a channel for leakage current. To minimize this effect, the device was heated in a low vacuum for 12 hours at 370 K and then cooled for 2 hours at 200 K. Transistor characteristics with ionic liquid gating were then studied at 250 K using a vacuum probe station and a Keithley 4200 semiconductor characterization system in the core facility center for quantum characterization/analysis of two-dimensional materials and heterostructures. Backgated transistors were investigated using a Quantum Design PPMS that could reach temperatures down to 2 K.

3. Results and Discussion

3.1. Structure of Scrolled MoS_2

In total, 15 MoS_2 scrolls were produced with droplets of IPA solution, 2 of which were from CVD-grown MoS_2 and 13 from exfoliated monolayers. Figure 1a,b present optical images of typical scrolls produced from CVD-grown MoS_2 and exfoliated monolayer, respectively. Figure 1a shows MoS_2 scrolls from the center towards the edge of a triangular MoS_2 crystal. This suggests that the orientation of the nanoscroll was parallel to the edge and to the armchair direction, consistent with a previous report [13]. The formation energy for rolled-up MoS_2 scrolling in armchair orientation is lower than that for the zigzag and other chiralities [13]. MoS_2 nanoscrolls were studied on samples prepared from CVD-grown MoS_2 [10,13–16]; here, we also conducted research with scrolls prepared from exfoliated MoS_2. CVD-grown MoS_2 on a SiO_2 substrate often possesses strain as it is synthesized at high temperature and its thermal expansion coefficient is ~1000 times larger than that of the SiO_2 substrate [11]. Due to the built-in strain, CVD-grown MoS_2 is easily separated from the substrate and scrolled using the IPA solution. For exfoliated MoS_2, however, a small amount of KOH must be added to the IPA solution to help in the separation of 2D sheet from the substrate by etching SiO_2. Figure 1b shows an optical image of an exfoliated MoS_2 before scrolling (top), and an optical image of a MoS_2 nanoscroll after rolling up with a droplet of IPA + KOH solution (bottom). The nanoscroll was rolled about 10 µm from the upper edge of the 2D sheet along the direction of the red arrow shown in Figure 1b.

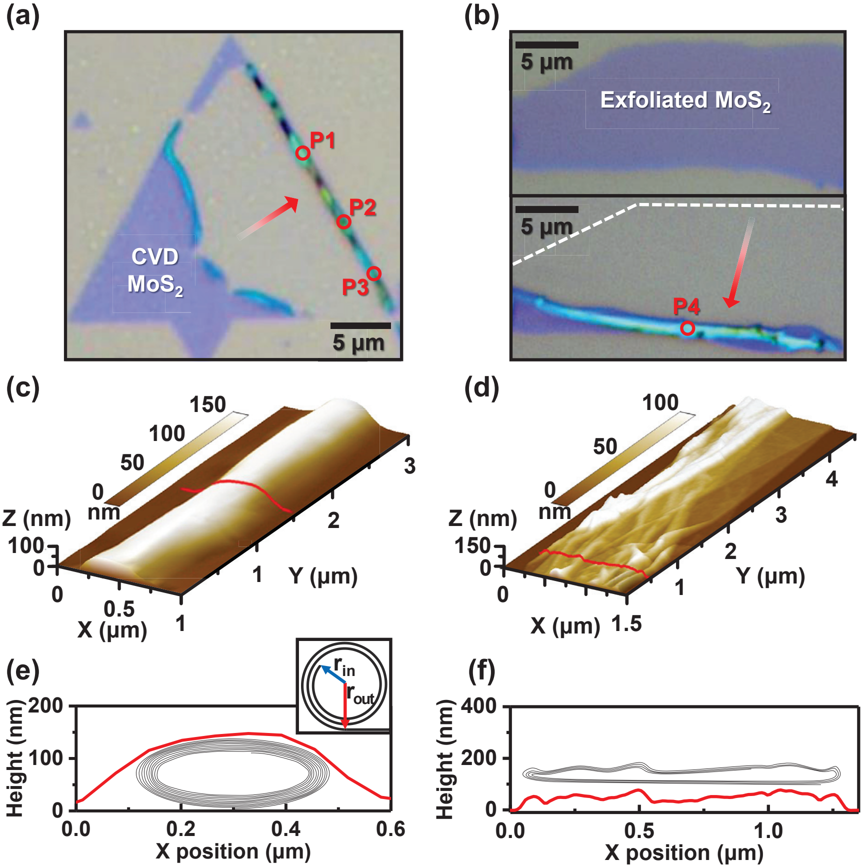

Figure 1. (**a**) Optical image of a nanoscroll produced from CVD-grown MoS_2. (**b**) Optical image of an exfoliated MoS_2 before (top) and after scrolling (bottom). (**c**,**d**) AFM 3D images of each nanoscroll in (**a**,**b**). (**e**,**f**) Schematic diagrams of internal structures and cross-sectional profiles of each following the red line shown in the AFM 3D images. (**e**) Inset shows an ideal circular scroll with an Archimedean spiral structure.

The structure of the MoS_2 nanoscrolls was studied with atomic force microscopy (AFM) for all 15 nanoscrolls. Three-dimensional AFM images are displayed in Figure 1c,d for the nanoscrolls shown in Figure 1a,b with the cross-sectional profiles of each in Figure 1e,f.

As reported for rolled-up graphene [6], the scrolls are distorted from the ideal circular–cylindrical form (inset of Figure 1e). The MoS_2 nanoscroll shown in Figure 1c had an elliptical–cylindrical structure in the cross-section due to the interaction with the underlying substrate (Figure 1e), with a height (∼150 nm) to width (∼400 nm) ratio of ∼0.4. On the other hand, the MoS_2 nanoscroll displayed in Figure 1d shows a collapsed ribbonlike structure. The height along this nanoscroll was nonuniform, with an average height (∼60 nm) to width (∼1300 nm) ratio of ∼0.05. Among the 15 investigated nanoscrolls, 3 showed an elliptical structure with a height/width ratio larger than 0.1, 7 had a collapsed ribbonlike structure, and the others showed different shapes (such as a partially collapsed structure) that did not fall exactly into these two categories (elliptical or collapsed).

The number of stacking layers in nanoscrolls can be estimated by considering both the dimension of the MoS_2 prior to scrolling and the cross-sectional profile of the nanoscroll after scrolling [6]. Using the interlayer spacing of MoS_2 nanoscrolls $t \simeq 0.65$ nm [10], the MoS_2 nanoscroll in Figure 1a,c was estimated to consist of MoS_2 that was rolled for ∼10 turns. By comparing the height of 10 stacked MoS_2 rolls (2×0.65 nm $\times 10$ layers = 13 nm) to the height of the elliptical MoS_2 nanoscroll (∼150 nm), it is reasonable to assume that a large hollow core was present in the nanoscroll. For the collapsed MoS_2 nanoscroll shown in Figure 1b,d, the height of the estimated number of stacking layers (4 layers giving 5.2 nm) was much smaller than the height of the collapsed scroll (∼60 nm), implying the presence of a hollow core within the collapsed scroll. Schematic illustrations of the internal structures of the MoS_2 nanoscrolls are given in Figure 1e,f.

To compare hollow core sizes for different shapes of scrolls, we considered the scrolls to have the form of an Archimedean spiral in the inset of Figure 1e, and regarded the innermost radius r_{in} as the hollow core radius. Following the approach in [6], we obtained $r_{\text{in}} \simeq 140$ and 410 nm for the MoS_2 nanoscrolls in Figure 1c,d, respectively. The average r_{in} of all 15 MoS_2 nanoscrolls was $\simeq$260 nm. Estimated hollow core radii of collapsed ribbonlike structures tend to be larger than those of elliptical structures, with a critical radius for collapse at around $r_{\text{in}} \simeq 250$ nm. Carbon nanoscrolls [6] and carbon nanotubes [27] also collapse as the radius of the hollow core increases.

Nanoscrolls theoretically have a radius that minimizes the sum of elastic and surface energies of the system. The following relation shows how the surface energy per unit area γ, bending stiffness D, and the length of 2D sheet B influence the r_{in} of the nanoscroll [28]

$$\frac{2\gamma t}{D} = \frac{1}{r_{\text{in}}} - \frac{1}{\sqrt{(Bt/\pi) + r_{\text{in}}^2}} \tag{1}$$

With $\gamma \simeq 400$ mJ/m^2, $D \simeq 1.6 \times 10^{-18}$ J for MoS_2 [29], and $B \simeq 5$ μm, the calculation leads to $r_{\text{in}} \simeq 3$ nm. This value is much smaller than the average $r_{\text{in}} \simeq 260$ nm from our experiments or $r_{\text{in}} \simeq 80$–350 nm reported so far from MoS_2 nanoscrolls prepared with organic solvents [13–16]. However, recent studies determined the effective bending stiffness of 2D monolayers in aqueous solution to be approximately three orders of magnitude higher than the value in vacuum [30,31] due to thermal fluctuations and static ripples. Assuming an effective bending stiffness of $\simeq 10^{-15}$ J in water/IPA, i.e., 1000 times larger than $D \simeq 10^{-18}$ J for MoS_2 in vacuum, Equation (1) results in $r_{\text{in}} \geq 100$ nm, which is consistent with our observation.

3.2. Band Gap of Scrolled MoS_2

The optical and transport band gaps of scrolled MoS_2 were determined from the PL spectroscopy and ionic-liquid gating of a FET device, respectively. Figure 2a presents the PL spectrum of the MoS_2 nanoscroll shown in Figure 1a measured at Spot P2 with the PL spectra of mono-, bi-, and trilayer MoS_2 sheets for comparison. The multipeak Lorentzian fitting of the PL spectrum of monolayer MoS_2 exhibited A_{xx} (biexciton, 1.83 eV), A^- (trion, 1.86 eV), A (1.89 eV), and B (2.01 eV) exciton peaks. A and B excitons are related to the direct gap transitions between the conduction and the spin-split valence band [26]. For the

MoS_2 nanoscroll, in addition to the A_{xx}, A^-, A and B exciton peaks, a peak also appeared at ∼1.60 eV that could be associated with the I peak from an exciton in the indirect gap. The direct band gap of monolayer MoS_2 changes into an indirect band gap in few-layer MoS_2, and as the number of layers increases, the indirect gap decreases due to the quantum confinement effect that is common in nanosystems [32]. In Figure 2a, the I peak is shown at 1.54 and 1.40 eV for bi- and trilayer MoS_2, respectively. The I peak was influenced by the interlayer coupling strength, and blue-shifted when the interaction was weak, as reported for folded and twisted MoS_2 [3,33]. Therefore, an I peak at ∼1.60 eV, observed for MoS_2 nanoscrolls, implies a weaker interlayer interaction in rolled MoS_2 compared to that in Bernal-stacked bilayer MoS_2. For scrolled MoS_2, S atoms of the top layer may sit randomly relative to the S atoms of the bottom layer, resulting in a stronger repulsion between S atoms and a larger interlayer distance, i.e., a weaker interlayer interaction. PL spectra were measured at eight spots on two different MoS_2 nanoscrolls, and the indirect band gap was in the range of 1.60 ± 0.05 eV. In addition, one can notice a relatively weaker A^- peak for the MoS_2 scroll compared to the monolayer MoS_2 sheet. The A^- (trion) peak, related to the binding of a free electron to the A exciton, is strong when excess charge is present due to doping. Impurities or defects in SiO_2 substrate result in a strong A^- peak for monolayer MoS_2 [34]. For the MoS_2 nanoscroll, the A^- peak was weaker as a significant portion of the scroll is separated from the substrate.

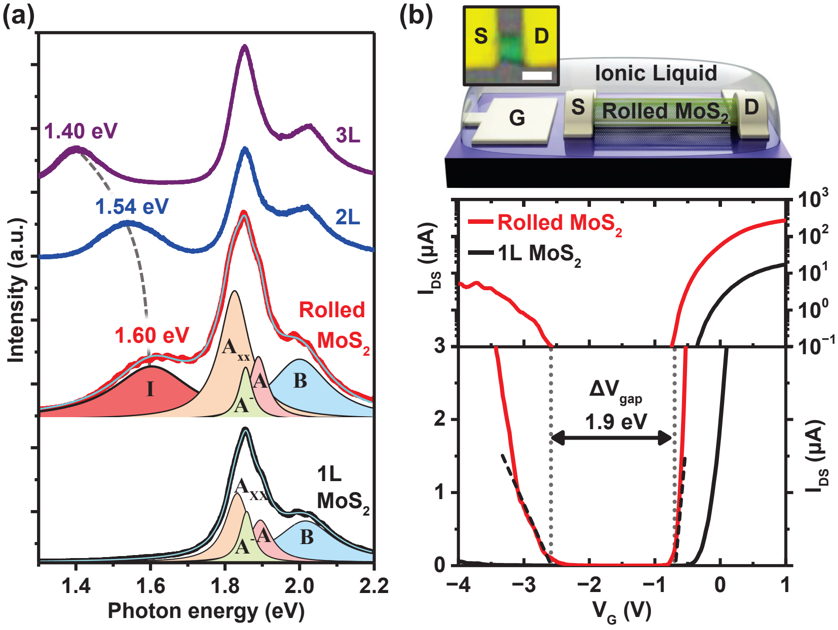

Figure 2. (**a**) PL spectrum of MoS_2 nanoscroll (red) presented along with PL spectra of mono- (black), bi- (blue) and trilayer (purple) MoS_2. Multipeak Lorentzian fittings are produced for the PL spectra of the scrolled MoS_2 and MoS_2 monolayer, and cyan solid lines represent fitted curves. (**b**) Schematic diagram of the ionic-liquid-gated transistor and an optical image of scrolled MoS_2 transistor. White scale bar indicates 1 μm (top). Transfer characteristics of MoS_2 nanoscroll and MoS_2 monolayer transistors presented in semilogarithmic (middle) and in linear scales (bottom).

To further investigate the band gap of scrolled MoS_2, ionic-liquid-gated transistors were fabricated on MoS_2 nanoscrolls and on a MoS_2 monolayer for reference. Figure 2b displays the transfer curves for an MoS_2 nanoscroll ($r_{in} \simeq 300$ nm, ∼3 stacked rolls) and MoS_2 monolayer transistors, presented with semilogarithmic (middle) and linear scales (bottom). A schematic diagram and microscopic image of the ionic-liquid-gated transistor are given at the top of Figure 2b, where the channel length was 800 nm. Ionic liquid DEME-TFSI was used as the gate dielectric. Because of the extremely large capacitance ($\simeq$8 μF/cm^2 [35]) of the electric double layer that had accumulated on the MoS_2 surface, the transport gap could be directly extracted from the transfer characteristics [36]. For a MoS_2 nanoscroll transistor, the dependence of source-drain current I_{DS} (measured at a source-drain voltage $V_{DS} = 1$ V) on the gate voltage V_G shows ambipolar behavior, and the transistor is in the off state when the Fermi level is located in the band gap of the nanoscroll. We found the threshold voltages for electron and hole conduction at $V_{th}^e \simeq -0.7$ V and $V_{th}^h \simeq -2.6$ V, respectively, which yielded a transport gap $\Delta V_{\text{gap}} = e(V_{th}^e - V_{th}^h) = 1.9$ eV for the scrolled MoS_2. The transport gap (1.9 eV) of the MoS_2 nanoscroll was larger than the optical gap (1.6 eV) by 0.3 eV, reflecting the exciton binding energy. Owing to increased dielectric screening in the MoS_2 nanoscroll, the exciton binding energy can be smaller than the value (0.45 eV) reported for a MoS_2 monolayer on a SiO_2 substrate [37].

In comparison, the transfer characteristics of the MoS_2 monolayer did not show ambipolar behavior, which is consistent with previous studies [38–40]. Sulfur vacancies induce hole-trap states inside the band gap of the MoS_2 monolayer, 300–400 meV above the top of the valence band, and prevent hole conduction in exfoliated MoS_2 monolayers. For few-layer MoS_2, the defect states are located deep in the valence band, and it is possible to observe ambipolar transport [38,40]. The transport gap ($\sim$1.9 eV) of the MoS_2 nanoscroll, determined from Figure 2b, was larger than the transport gap ($\sim$1.6 eV [38]) of the MoS_2 bilayers, and smaller than the band gap (2.36–2.71 eV [41,42]) of the MoS_2 monolayers. The ambipolar transport observed for the MoS_2 nanoscroll implies that defect states due to sulfur vacancies are located inside the valence band.

3.3. Back-Gated Field Effect Transistor Based on Scrolled MoS_2

We also studied MoS_2 nanoscrolls in a typical back-gated FET device fabricated on SiO_2/Si substrate with source and drain electrodes (Ti/Au) patterned on top of scrolls. The inset of Figure 3a presents an optical image of a MoS_2 nanoscroll FET, where electrodes were deposited on the rolled MoS_2 shown in Figure 1a. Figure 3a shows the transfer curves of the device measured at different temperatures between 2 and 300 K. When the backgate voltage varied in the range of $-80 \leq V_G \leq 70$ V, only n-type transport was observed for the nanoscroll FET, reflecting a much smaller back-gate capacitance ($\sim$10 nF/cm^2) compared with the ionic liquid gating. The source-drain current increased with increasing temperature, indicating the semiconducting nature of scrolled MoS_2.

In Figure 3b, the field effect mobility, estimated for electron transport according to the 1D mobility equation $\mu_{1D} = (\Delta G/\Delta V_G) \cdot (L^2/C_{1\text{D}})$, is displayed as a function of temperature. Here, G is the conductance, and the channel length is $L \simeq 3$ μm. The capacitance is given by $C_{1\text{D}} = \frac{2\pi\epsilon\epsilon_0 L}{\cosh^{-1}[(r_{\text{out}}+t_{\text{ox}})/r_{\text{out}}]}$, where ϵ (3.9) is the dielectric constant of SiO_2 and ϵ_0 is the permittivity of vacuum, with t_{ox} (300 nm) being the thickness of SiO_2. For the MoS_2 nanoscroll with $r_{\text{out}} \simeq 145$ nm, we have $C_{1\text{D}} \simeq 3.7 \times 10^{-16}$ F. The mobility at 300 K was estimated to be $\sim$8.8 cm^2/Vs, an order of magnitude greater than the typical value of $\sim$1 cm^2/Vs for our CVD-grown MoS_2 monolayers. The enhancement of mobility of the MoS_2 nanoscroll was first attributed to most of scroll's surface being away from the substrate. Layers lifted from the substrate could avoid charge traps and be free from the influence of the substrate roughness and surface polar phonon scattering. In addition, since the outer layer was directly connected to the inner layer, all layers within the scroll could be available as current channels, unlike in multilayered 2D materials with high interlayer resistance. On the other hand, $\mu_{1\text{D}}$, estimated from the highest transconductance in the transfer curve, increased with T, as shown in Figure 3b, while the mobility of the MoS_2 monolayer in a metallic conduction regime decreases with T, as mobility is limited by phonons at high temperatures [43]. However, the mobility of the MoS_2 monolayer, when extracted in an insulating regime at lower gate voltages that locate the Fermi energy inside the band gap, showed a much lower value and increased with temperature [43]. Therefore, the transfer curves in Figure 3a are in the insulating regime with the Fermi energy inside the band gap for the range of V_G applied, and the mobility was underestimated, particularly for lower temperatures. Scrolled MoS_2 can be less doped, as most of the scroll's surface is away from the substrate and affected less by charged impurities on the substrate.

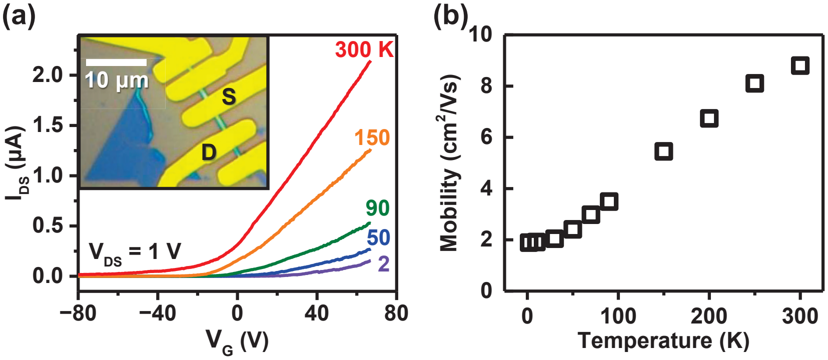

Figure 3. (**a**) Transfer characteristics of a MoS_2 nanoscroll FET, measured at different temperatures between 2 and 300 K. Inset presents an optical image of the transistor. (**b**) Estimated field-effect electron mobility of the MoS_2 nanoscroll as a function of temperature.

3.4. Raman Spectra of Scrolled MoS_2

Figure 4a displays Raman spectra of the MoS_2 nanoscroll shown in Figure 1a measured at Spots P1, P2, and P3, together with the Raman spectrum of a MoS_2 monolayer as a reference. Raman-active E^1_{2g} and A_{1g} modes are observed in both monolayer and rolled MoS_2. Compared to the E^1_{2g} (∼405 cm^{-1}) and A_{1g} (∼385 cm^{-1}) peaks of the MoS_2 monolayer, E^1_{2g} was red-shifted, and A_{1g} is blue-shifted for the MoS_2 nanoscroll, leading to a larger frequency difference between the two modes. This behavior is consistent with previous Raman studies on MoS_2 nanoscrolls [10,13,14,16]. Raman spectroscopy performed on 56 different spots from 15 different MoS_2 nanoscrolls resulted in average central positions of E^1_{2g} and A_{1g} modes at 383.6 ± 0.4 and 404.4 ± 0.6 cm^{-1}, respectively, rendering the average frequency difference between the two modes to be 20.8 ± 0.7 cm^{-1}. The frequency distance between these modes is widely used to identify the number of layers in thin MoS_2, as the distance increases with the number of layers from ∼18.8 (mono), 22.4 (bi) to 24.8 cm^{-1} (bulk) [44].

The value (∼20.8 cm^{-1}) observed for MoS_2 nanoscrolls was between those of the MoS_2 monolayer and bilayer. Considering that the average number of concentric layers in our nanoscrolls was ∼4, the observed distance between the two modes indicates a weaker interlayer interaction for the MoS_2 nanoscroll compared to the few Bernal-stacked MoS_2 layers, which is consistent with our PL results in Figure 2a. In folded or twisted MoS_2, a narrower distance between the two modes than that for the same layer number of Bernal-stacked MoS_2 was reported and attributed to the weaker interlayer interactions [3,45].

The frequency difference between the E^1_{2g} and A_{1g} modes for all 56 measurements is plotted in Figure 4b as a function of r_{out}. No clear dependence was observed for the height/width ratio or the number of stacking layers in the nanoscroll; the distance between the two peaks tended to increase with increasing r_{out}. The increase in r_{out} led to a decrease in strain due to the reduced curvature that, however, would be expected to show the opposite dependence. Suspended MoS_2 monolayers under strain show a decrease in peak separation as the strain is reduced [46]. Instead, a larger r_{out} may facilitate some parts of the layers to be Bernal-stacked, giving rise to a stronger interlayer interaction and wider distance between the two Raman peaks.

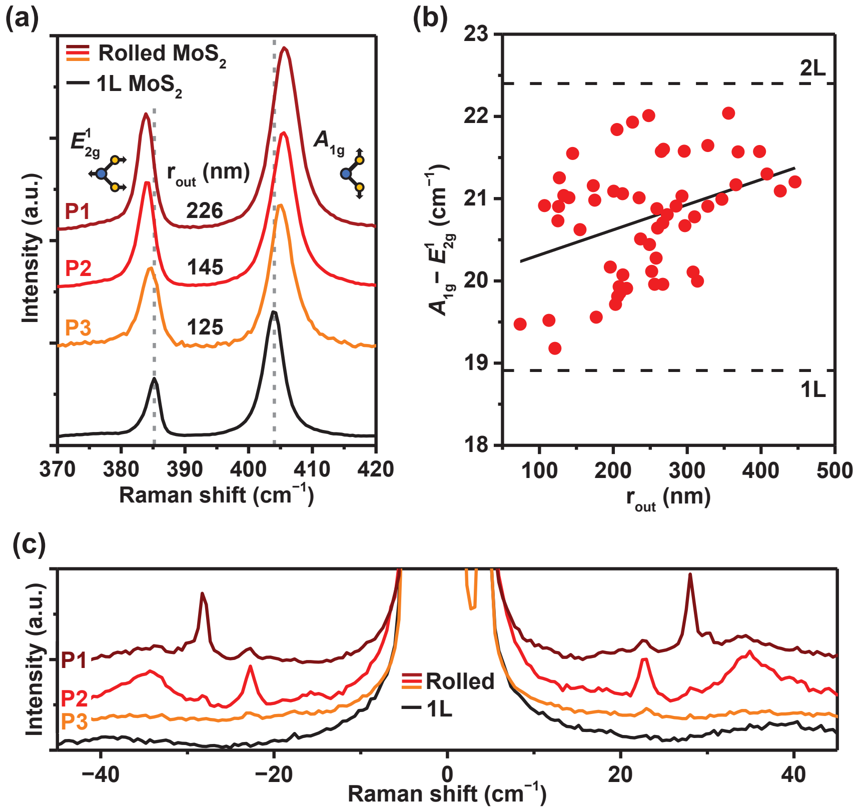

Figure 4. (**a**) Raman spectra of the MoS_2 nanoscroll measured at Spots P1, P2, and P3 indicated in Figure 1a. r_{out} estimated for each spot is indicated. The Raman spectrum of MoS_2 monolayer is also shown for reference. (**b**) Frequency difference between E_{2g}^1 and A_{1g} modes as a function of r_{out} estimated for 56 different spots on 15 different MoS_2 nanoscrolls. The solid line is the fitted slope. (**c**) Low-frequency ($\leq$45 cm^{-1}) Raman spectra of MoS_2 monolayer and the MoS_2 nanoscroll, measured at Spots P1, P2 and P3.

Figure 4c shows the ultralow-frequency ($\leq$45 cm^{-1}) Raman spectra of the MoS_2 monolayer and the MoS_2 nanoscroll measured at Spots P1, P2 and P3. For the MoS_2 monolayer, there was no peak in the frequency range. On the other hand, for the MoS_2 nanoscroll (P1 spot), a sharp peak was observed at ~28 cm^{-1} with the full width at half maximum (FWHM) of ~1 cm^{-1}, and small peaks were located at 22.5, 34.5 cm^{-1}. For Spot P2, there was a sharp peak at ~22.5 and a broad peak at 34.5 cm^{-1} with FWHM of ~1 and 10 cm^{-1}, respectively; for Spot P3, only a weak peak was seen at ~22.5 cm^{-1}. For multilayer MoS_2, shear (C mode) and layer breathing modes (LB mode) were observed in this low frequency range [47]. For MoS_2 nanoscrolls, LB modes at 21, 26, 38 cm^{-1} were reported [16]. Our results indicate that there can be LB or C mode coupling between the concentric layers of MoS_2 nanoscrolls. These modes are sensitive to the number of layers and stacking configurations [45]; therefore, the peaks appear at different frequencies for different spots depending on the detailed configuration and topology of the nanoscroll.

4. Conclusions

In summary, we formed MoS_2 nanoscrolls from both CVD-grown and exfoliated MoS_2 monolayers that had inner core radii of ~250 nm, and investigated their optical and transport band gaps. PL spectroscopy reveals that the MoS_2 monolayer, originally a direct band-gap semiconductor (∼1.85 eV (optical)), changed into an indirect band-gap semiconductor (∼1.6 eV) upon scrolling. The size of the indirect gap for MoS_2 nanoscrolls was larger than that of the MoS_2 bilayer (∼1.54 eV), implying a weaker interlayer interaction between the concentric layers in the nanoscroll compared to that in few Bernal-stacked MoS_2 layers. We also determined the transport band gap (∼1.9 eV) of MoS_2 nanoscrolls by fabricating and characterizing ambipolar ionic-liquid-gated transistors. The difference between the transport and optical gaps suggests an exciton binding energy of 0.3 eV for MoS_2 nanoscrolls. Rolling up 2D atomic layers into nanoscrolls introduces a new type of quasi-1D nanostructure and provides another way to tune the band gap of 2D materials.

Author Contributions: Conceptualization, J.N. and S.H.J.; methodology, J.N., C.P., C.H.L. and S.H.J.; formal analysis, J.N., C.P., C.H.L. and S.H.J.; investigation, J.N., C.P., C.H.L. and S.H.J.; resources, S.C., J.-U.L., W.Y., H.C.; data curation, J.N., C.P., C.H.L., W.R.C. and S.H.J.; writing—original draft preparation, C.P., C.H.L. and S.H.J.; writing—review and editing, C.P., C.H.L., E.E.B.C. and S.H.J.; visualization, C.P., C.H.L. and S.H.J.; supervision, S.H.J.; project administration, J.N., C.P., C.H.L. and S.H.J.; funding acquisition, S.H.J. All authors have read and agreed to the published version of the manuscript.

Funding: This research was supported by WTU Joint Research Grants of Konkuk University in 2017.

Data Availability Statement: Not applicable.

Conflicts of Interest: The authors declare no conflict of interest.

References

1. Manzeli, S.; Ovchinnikov, D.; Pasquier, D.; Yazyev, O.V.; Kis, A. 2D transition metal dichalcogenides. *Nat. Rev. Mater.* **2017**, *2*, 17033 . [CrossRef]
2. Deng, S.; Gao, E.; Xu, Z.; Berry, V. Adhesion energy of MoS_2 thin films on silicon-based substrates determined via the attributes of a single MoS_2 wrinkle. *ACS Appl. Mater. Interfaces* **2017**, *9*, 7812–7818. [CrossRef] [PubMed]
3. Castellanos-Gomez, A.; van der Zant, H.S.; Steele, G.A. Folded MoS_2 layers with reduced interlayer coupling. *Nano Res.* **2014**, *7*, 572–578. [CrossRef]
4. Xie, X.; Ju, L.; Feng, X.; Sun, Y.; Zhou, R.; Liu, K.; Fan, S.; Li, Q.; Jiang, K. Controlled fabrication of high-quality carbon nanoscrolls from monolayer graphene. *Nano Lett.* **2009**, *9*, 2565–2570. [CrossRef]
5. Xu, B.; Lin, X.; Mei, Y. Versatile rolling origami to fabricate functional and smart materials. *Cell Rep. Phys. Sci.* **2020**, *1*, 100244. [CrossRef]
6. Uhm, T.; Na, J.; Lee, J.U.; Cheong, H.; Lee, S.W.; Campbell, E.E.; Jhang, S.H. Structural configurations and Raman spectra of carbon nanoscrolls. *Nanotechnology* **2020**, *31*, 315707. [CrossRef]
7. Baptista-Pires, L.; Orozco, J.; Guardia, P.; Merkoçi, A. Architecting graphene oxide rolled-up micromotors: A simple paper-based manufacturing technology. *Small* **2018**, *14*, 1702746. [CrossRef]
8. Liu, Y.; Wang, L.; Zhang, H.; Ran, F.; Yang, P.; Li, H. Graphene oxide scroll meshes encapsulated Ag nanoparticles for humidity sensing. *RSC Adv.* **2017**, *7*, 40119–40123. [CrossRef]
9. Suh, D.H.; Hwang, D.Y. Formation of hexagonal boron nitride nanoscrolls induced by inclusion and exclusion of self-assembling molecules in solution process. *Nanoscale* **2014**, *6*, 5686–5690.
10. Cui, X.; Kong, Z.; Gao, E.; Huang, D.; Hao, Y.; Shen, H.; Di, C.a.; Xu, Z.; Zheng, J.; Zhu, D. Rolling up transition metal dichalcogenide nanoscrolls via one drop of ethanol. *Nat. Commun.* **2018**, *9*, 1301. [CrossRef]
11. Hao, S.; Yang, B.; Gao, Y. Fracture-induced nanoscrolls from CVD-grown monolayer molybdenum disulfide. *Phys. Status Solidi (RRL) Rapid Res. Lett.* **2016**, *10*, 549–553. [CrossRef]
12. Meng, J.; Wang, G.; Li, X.; Lu, X.; Zhang, J.; Yu, H.; Chen, W.; Du, L.; Liao, M.; Zhao, J.; et al. Rolling up a monolayer MoS_2 sheet. *Small* **2016**, *12*, 3770–3774. [CrossRef] [PubMed]
13. Wang, Z.; Wu, H.H.; Li, Q.; Besenbacher, F.; Zeng, X.C.; Dong, M. Self-scrolling MoS_2 metallic wires. *Nanoscale* **2018**, *10*, 18178–18185. [CrossRef]
14. Deng, W.; Chen, X.; Li, Y.; You, C.; Chu, F.; Li, S.; An, B.; Ma, Y.; Liao, L.; Zhang, Y. Strain Effect Enhanced Ultrasensitive MoS_2 Nanoscroll Avalanche Photodetector. *J. Phys. Chem. Lett.* **2020**, *11*, 4490–4497. [CrossRef] [PubMed]
15. Qian, Q.; Zu, R.; Ji, Q.; Jung, G.S.; Zhang, K.; Zhang, Y.; Buehler, M.J.; Kong, J.; Gopalan, V.; Huang, S. Chirality-Dependent Second Harmonic Generation of MoS_2 Nanoscroll with Enhanced Efficiency. *ACS Nano* **2020**, *14*, 13333–13342. [CrossRef] [PubMed]
16. Fang, X.; Wei, P.; Wang, L.; Wang, X.; Chen, B.; He, Q.; Yue, Q.; Zhang, J.; Zhao, W.; Wang, J.; et al. Transforming monolayer transition-metal dichalcogenide nanosheets into one-dimensional nanoscrolls with high photosensitivity. *ACS Appl. Mater. Interfaces* **2018**, *10*, 13011–13018. [CrossRef] [PubMed]
17. Zhao, B.; Wan, Z.; Liu, Y.; Xu, J.; Yang, X.; Shen, D.; Zhang, Z.; Guo, C.; Qian, Q.; Li, J.; et al. High-order superlattices by rolling up van der Waals heterostructures. *Nature* **2021**, *591*, 385–390. [CrossRef] [PubMed]

18. Zhang, S.; Gao, F.; Feng, W.; Yang, H.; Hu, Y.; Zhang, J.; Xiao, H.; Li, Z.; Hu, P. High-responsivity photodetector based on scrolling monolayer MoS_2 hybridized with carbon quantum dots. *Nanotechnology* **2021**, *33*, 105301. [CrossRef]
19. Yue, Q.; Wang, L.; Fan, H.; Zhao, Y.; Wei, C.; Pei, C.; Song, Q.; Huang, X.; Li, H. Wrapping plasmonic silver nanoparticles inside one-dimensional nanoscrolls of transition-metal dichalcogenides for enhanced photoresponse. *Inorg. Chem.* **2020**, *60*, 4226–4235. [CrossRef]
20. Wang, L.; Yue, Q.; Pei, C.; Fan, H.; Dai, J.; Huang, X.; Li, H.; Huang, W. Scrolling bilayer WS_2/MoS_2 heterostructures for high-performance photo-detection. *Nano Res.* **2020**, *13*, 959–966. [CrossRef]
21. Jiang, Z.; Zhou, W.; Hong, A.; Guo, M.; Luo, X.; Yuan, C. MoS_2 Moiré superlattice for hydrogen evolution reaction. *ACS Energy Lett.* **2019**, *4*, 2830–2835. [CrossRef]
22. Khaledian, M.; Ismail, R.; Akbari, E. Band structures of graphene nanoscrolls and their dispersion relation near the Fermi point. *RSC Adv.* **2016**, *6*, 38753–38760. [CrossRef]
23. Wang, Y.; Jiang, C.; Chen, Q.; Zhou, Q.; Wang, H.; Wan, J.; Ma, L.; Wang, J. Highly promoted carrier mobility and intrinsic stability by rolling up monolayer black phosphorus into nanoscrolls. *J. Phys. Chem. Lett.* **2018**, *9*, 6847–6852. [CrossRef]
24. Xiao, J.; Long, M.; Li, X.; Xu, H.; Huang, H.; Gao, Y. Theoretical prediction of electronic structure and carrier mobility in single-walled MoS_2 nanotubes. *Sci. Rep.* **2014**, *4*, 4327. [CrossRef]
25. Desai, S.B.; Madhvapathy, S.R.; Amani, M.; Kiriya, D.; Hettick, M.; Tosun, M.; Zhou, Y.; Dubey, M.; Ager III, J.W.; Chrzan, D.; et al. Gold-mediated exfoliation of ultralarge optoelectronically-perfect monolayers. *Adv. Mater.* **2016**, *28*, 4053–4058. [CrossRef] [PubMed]
26. Pandey, J.; Soni, A. Unraveling biexciton and excitonic excited states from defect bound states in monolayer MoS_2. *Appl. Surf. Sci.* **2019**, *463*, 52–57. [CrossRef]
27. Pugno, N.M. The design of self-collapsed super-strong nanotube bundles. *J. Mech. Phys. Solids* **2010**, *58*, 1397–1410. [CrossRef]
28. Shi, X.; Pugno, N.M.; Gao, H. Tunable core size of carbon nanoscrolls. *J. Comput. Theor. Nanosci.* **2010**, *7*, 517–521. [CrossRef]
29. Liu, Z.; Gao, J.; Zhang, G.; Cheng, Y.; Zhang, Y.W. From two-dimensional nano-sheets to roll-up structures: Expanding the family of nanoscroll. *Nanotechnology* **2017**, *28*, 385704. [CrossRef]
30. Blees, M.K.; Barnard, A.W.; Rose, P.A.; Roberts, S.P.; McGill, K.L.; Huang, P.Y.; Ruyack, A.R.; Kevek, J.W.; Kobrin, B.; Muller, D.A.; et al. Graphene kirigami. *Nature* **2015**, *524*, 204–207. [CrossRef]
31. Reynolds, M.F.; McGill, K.L.; Wang, M.A.; Gao, H.; Mujid, F.; Kang, K.; Park, J.; Miskin, M.Z.; Cohen, I.; McEuen, P.L. Capillary origami with atomically thin membranes. *Nano Lett.* **2019**, *19*, 6221–6226. [CrossRef] [PubMed]
32. Splendiani, A.; Sun, L.; Zhang, Y.; Li, T.; Kim, J.; Chim, C.Y.; Galli, G.; Wang, F. Emerging photoluminescence in monolayer MoS_2. *Nano Lett.* **2010**, *10*, 1271–1275. [CrossRef] [PubMed]
33. Liu, K.; Zhang, L.; Cao, T.; Jin, C.; Qiu, D.; Zhou, Q.; Zettl, A.; Yang, P.; Louie, S.G.; Wang, F. Evolution of interlayer coupling in twisted molybdenum disulfide bilayers. *Nat. Commun.* **2014**, *5*, 4966. [CrossRef] [PubMed]
34. Li, Y.; Qi, Z.; Liu, M.; Wang, Y.; Cheng, X.; Zhang, G.; Sheng, L. Photoluminescence of monolayer MoS_2 on $LaAlO_3$ and $SrTiO_3$ substrates. *Nanoscale* **2014**, *6*, 15248–15254. [CrossRef]
35. Shi, W.; Ye, J.; Zhang, Y.; Suzuki, R.; Yoshida, M.; Miyazaki, J.; Inoue, N.; Saito, Y.; Iwasa, Y. Superconductivity series in transition metal dichalcogenides by ionic gating. *Sci. Rep.* **2015**, *5*, 12534. [CrossRef] [PubMed]
36. Braga, D.; Gutieérrez Lezama, I.; Berger, H.; Morpurgo, A.F. Quantitative determination of the band gap of WS_2 with ambipolar ionic liquid-gated transistors. *Nano Lett.* **2012**, *12*, 5218–5223. [CrossRef] [PubMed]
37. Berghäuser, G.; Malic, E. Analytical approach to excitonic properties of MoS_2. *Phys. Rev. B* **2014**, *89*, 125309. [CrossRef]
38. Ponomarev, E.; Pásztor, Á.; Waelchli, A.; Scarfato, A.; Ubrig, N.; Renner, C.; Morpurgo, A.F. Hole transport in exfoliated monolayer MoS_2. *ACS Nano* **2018**, *12*, 2669–2676. [CrossRef]
39. Ponomarev, E.; Gutiérrez-Lezama, I.; Ubrig, N.; Morpurgo, A.F. Ambipolar light-emitting transistors on chemical vapor deposited monolayer MoS_2. *Nano Lett.* **2015**, *15*, 8289–8294. [CrossRef]
40. Chu, L.; Schmidt, H.; Pu, J.; Wang, S.; Özyilmaz, B.; Takenobu, T.; Eda, G. Charge transport in ion-gated mono-, bi-and trilayer MoS_2 field effect transistors. *Sci. Rep.* **2014**, *4*, 7293. [CrossRef]
41. Zhang, C.; Gong, C.; Nie, Y.; Min, K.A.; Liang, C.; Oh, Y.J.; Zhang, H.; Wang, W.; Hong, S.; Colombo, L.; et al. Systematic study of electronic structure and band alignment of monolayer transition metal dichalcogenides in Van der Waals heterostructures. *2D Mater.* **2016**, *4*, 015026. [CrossRef]
42. Huang, Y.L.; Chen, Y.; Zhang, W.; Quek, S.Y.; Chen, C.H.; Li, L.J.; Hsu, W.T.; Chang, W.H.; Zheng, Y.J.; Chen, W.; et al. Bandgap tunability at single-layer molybdenum disulphide grain boundaries. *Nat. Commun.* **2015**, *6*, 6298. [CrossRef] [PubMed]
43. Schmidt, H.; Wang, S.; Chu, L.; Toh, M.; Kumar, R.; Zhao, W.; Castro Neto, A.; Martin, J.; Adam, S.; Özyilmaz, B.; et al. Transport properties of monolayer MoS_2 grown by chemical vapor deposition. *Nano Lett.* **2014**, *14*, 1909–1913. [CrossRef]
44. Li, H.; Zhang, Q.; Yap, C.C.R.; Tay, B.K.; Edwin, T.H.T.; Olivier, A.; Baillargeat, D. From bulk to monolayer MoS_2: Evolution of Raman scattering. *Adv. Funct. Mater.* **2012**, *22*, 1385–1390. [CrossRef]
45. Huang, S.; Liang, L.; Ling, X.; Puretzky, A.A.; Geohegan, D.B.; Sumpter, B.G.; Kong, J.; Meunier, V.; Dresselhaus, M.S. Low-frequency interlayer Raman modes to probe interface of twisted bilayer MoS_2. *Nano Lett.* **2016**, *16*, 1435–1444. [CrossRef] [PubMed]
46. Lloyd, D.; Liu, X.; Christopher, J.W.; Cantley, L.; Wadehra, A.; Kim, B.L.; Goldberg, B.B.; Swan, A.K.; Bunch, J.S. Band gap engineering with ultralarge biaxial strains in suspended monolayer MoS_2. *Nano Lett.* **2016**, *16*, 5836–5841. [CrossRef]
47. Zhang, X.; Han, W.; Wu, J.; Milana, S.; Lu, Y.; Li, Q.; Ferrari, A.; Tan, P. Raman spectroscopy of shear and layer breathing modes in multilayer MoS_2. *Phys. Rev. B* **2013**, *87*, 115413. [CrossRef]

nanomaterials

Article

Low-Power Complementary Inverter Based on Graphene/Carbon-Nanotube and Graphene/MoS_2 Barristors

Dong-Ho Shin [1], Young Gyu You [1], Sung Il Jo [2], Goo-Hwan Jeong [2], Eleanor E. B. Campbell [3,4], Hyun-Jong Chung [1] and Sung Ho Jhang [1,*]

[1] School of Physics, Konkuk University, Seoul 05029, Korea
[2] Department of Advanced Materials Science and Engineering, Kangwon National University, Chuncheon 24341, Korea
[3] EaStCHEM, School of Chemistry, Edinburgh University, David Brewster Road, Edinburgh EH9 3FJ, UK
[4] Department of Physics, Ewha Womans University, Seoul 03760, Korea
* Correspondence: shjhang@konkuk.ac.kr

Abstract: The recent report of a p-type graphene(Gr)/carbon-nanotube(CNT) barristor facilitates the application of graphene barristors in the fabrication of complementary logic devices. Here, a complementary inverter is presented that combines a p-type Gr/CNT barristor with a n-type Gr/MoS_2 barristor, and its characteristics are reported. A sub-nW (∼0.2 nW) low-power inverter is demonstrated with a moderate gain of 2.5 at an equivalent oxide thickness (EOT) of ∼15 nm. Compared to inverters based on field-effect transistors, the sub-nW power consumption was achieved at a much larger EOT, which was attributed to the excellent switching characteristics of Gr barristors.

Keywords: complementary inverter; low power; graphene/carbon-nanotube junction; barristor

Citation: Shin, D.-H.; You, Y.G.; Jo, S.I.; Jeong, G.-H.; Campbell, E.E.B.; Chung, H.-J.; Jhang, S.H. Low-Power Complementary Inverter Based on Graphene/Carbon-Nanotube and Graphene/MoS_2 Barristors. *Nanomaterials* **2022**, *12*, 3820. https://doi.org/10.3390/nano12213820

Academic Editor: Ming-Yu Li

Received: 28 September 2022
Accepted: 25 October 2022
Published: 28 October 2022

1. Introduction

Complementary metal oxide semiconductor (CMOS) devices have led to the development of science and technology using silicon. The density of integrated circuits (IC) gradually increased and the size of devices decreased, leading to Moore's Law which showed that the integration of ICs doubled every two years. However, as silicon faced physical limitations for device scaling, new alternatives were needed [1]. Low-dimensional materials, such as nanotubes and layered materials are capable of channel dimension scaling and have excellent physical properties, presenting potential as new semiconductor materials [2–4]. In particular, graphene (Gr), which opened the research field of two-dimensional (2D) layered materials, has excellent electrical properties and its mobility can be up to ∼100,000 cm^2/Vs [5,6]. However, the absence of a band gap in graphene has limited its application in logic devices [7,8]. Transition metal dichalcogenides (TMDCs), such as MoS_2 and WS_2, have a band gap of about 1–2 eV. They have an indirect band gap in the bulk form and a direct band gap in the monolayer [9,10]. They have, therefore, been popular objects for study of their transport properties and incorporation into field-effect transistor (FET) structures [11–14]. However, the field-effect mobility was insufficient to be commercialized, and digital inverters based on TMDCs operated at high supply voltages causing high power consumption [15–17]. In addition, the majority of TMDCs were n-type, induced by structural defects and interfacial charge impurities. The lack of p-type 2D semiconductors also restricted the realization of CMOS logic function in 2D electronics [18].

In order to use graphene as the channel of a switching device, the graphene barristor, making use of the Schottky barrier at the junction between graphene and a semiconductor material, was invented [19]. The Schottky barrier formed in the junction between graphene and semiconductor, such as Si, TMDC, or organic semiconductor, etc., was modulated by changing the Fermi energy E_F of graphene by applying a voltage to a gate electrode. Since the reverse current increased exponentially as the Schottky barrier height decreased, the graphene barristors exhibited excellent switching characteristics with a low subthreshold swing (SS) [19,20]. However, most Gr/TMDC barristors were also n-type because of the n-type nature of TMDCs, hindering the development of CMOS systems using Gr/TMDC barristors. Recently, by combining graphene with a semiconducting single-walled carbon nanotube (CNT), a p-type Gr/CNT barristor was demonstrated with an on–off current ratio of 10^6 and a high mobility of $\mu \sim 5350\ \mathrm{cm^2/Vs}$ [21]. A low subthreshold swing of 70 mV/dec with an equivalent oxide thickness (EOT) of 15 nm was reported. In addition, high conductance of the CNT allowed Gr/CNT barristors to function at much lower supply voltages of 10–100 mV, making them promising candidates for low-power CMOS devices [21].

In this paper, a complementary inverter was fabricated using a p-type Gr/CNT barristor, combined with a n-type Gr/MoS_2 barristor. The potential of the device as a low power complementary inverter was investigated and compared with previously reported low-power inverters based on low-dimensional materials.

2. Materials and Experimental

Complementary inverters were fabricated based on Gr/CNT and Gr/MoS_2 barristors. Single-walled carbon nanotubes (SWCNTs), straight and longer than 10 μm, were grown sparsely by chemical vapor deposition (CVD) on a quartz substrate employing ferritin as a catalyst [22,23]. Graphene, MoS_2, and hexagonal boron nitride (h-BN) were prepared by mechanical exfoliation. Figure 1 illustrates the fabrication process of the complementary inverter using p-type Gr/CNT and n-type Gr/MoS_2 Schottky junctions. The fabrication involved several transfer processes via the polymethylmethacrylate (PMMA) transfer method [24]. Firstly, SWCNTs were transferred from the quartz substrate to a SiO_2(300 nm)/Si substrate and a CNT, isolated from other nanotubes, was identified using atomic force microscopy (AFM) and Raman spectroscopy (Figure 1a). The diameter d_t of the SWCNTs was about 1.3 nm, determined from the Raman response of the radial breathing mode (RBM) by using $d_t = 224(\mathrm{cm^{-1}})/\omega_{\mathrm{RBM}}(\mathrm{cm^{-1}})$ [25]. Graphene was then transferred onto the CNT to form a Gr/CNT junction (Figure 1b). On the other hand, a Gr/MoS_2 junction was generated on a different SiO_2/Si substrate in a similar fashion, and transferred adjacent to the Gr/CNT junction (Figure 1c). Conventional e-beam lithography was then used to create Cr(20 nm)/Au(20 nm) electrodes, as indicated in Figure 1d. Finally, a large 15 nm-thick h-BN flake was transferred covering both the Gr/CNT and the Gr/MoS_2 junctions and used as gate dielectric, followed by the deposition of top-gate electrodes (Figure 1e). An AFM cleaning technique [26] was implemented to remove residual impurities on the material's surface before each transfer process as the property of a barristor is very sensitive to the property of the junction.

For the operation of the complementary inverter, an input voltage V_{in} was applied through top-gates connected to each other. A positive V_{DD} was applied to the graphene constituting the Gr/CNT junction, and the other graphene comprising the Gr/MoS_2 junction was grounded. This circuit connection allowed both barristors to be reverse-biased. An output voltage V_{out} was then measured at the electrodes connected to the CNT and MoS_2, as shown in Figure 1e. Inverter characteristics were studied using a vacuum probe station and a Keithley 4200 semiconductor characterization system in Core Facility Center for Quantum Characterization/Analysis of Two-Dimensional Materials and Heterostructures.

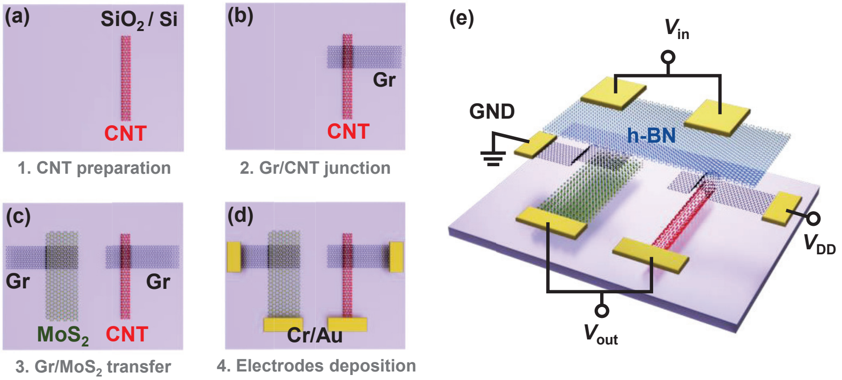

Figure 1. Fabrication processes of a complementary inverter based on Gr/CNT and Gr/MoS_2 barristors. (**a**) A semiconducting CNT is transferred from a quartz to a SiO_2(300 nm)/Si substrate. (**b**) A Gr/CNT junction is formed by the transfer of graphene onto the CNT. (**c**) A Gr/MoS_2 junction, prepared on a different substrate, is moved next to the Gr/CNT junction. (**d**) Metal (Cr/Au) electrodes are patterned and deposited. (**e**) A large h-BN flake is transferred onto the junctions to be used as a top-gate insulator and top-gate electrodes are deposited.

3. Results

Figure 2a shows a scanning electron microscope image of the Gr/MoS_2 and Gr/CNT junctions used in a complementary inverter, where the thickness of the MoS_2 was $\sim$7 nm and the diameter of the semiconducting CNT was $\sim$1.3 nm. A series connection of n-type Gr/MoS_2 and p-type Gr/CNT barristors inverted the input signal V_{in} to its inverse V_{out}. Figure 2b presents the voltage transfer characteristics (VTC) of the complementary inverter, obtained by varying V_{DD} from 1 V to 0.1 V at intervals of –0.1 V. A clear inversion of the input voltage was observed for the range of V_{DD} applied. When the input voltage was lower than –3.9 V, $V_{out} \simeq V_{DD}$, while, for $V_{in} \geq -2.4$ V, the output voltage was inverted to $V_{out} \simeq 0$. The device operated under a negative input voltage as the threshold voltages of both p-and n-barristors had negative values, as shall be seen later. The inset of Figure 2b replots the VTC at $V_{DD} = 0.4$ V in a semilogarithmic scale. The ratio between the maximum and the minimum of V_{out} was $\sim 10^3$, and increased to $\sim 10^4$ at $V_{DD} = 1.0$ V, 100 times larger than that reported earlier for a complementary inverter based on Gr/Si barristors [19]. This implies high on/off current ratios of Gr/MoS_2 and Gr/CNT barristors, and ensures a lower static power consumption at off-state. The threshold voltage of the inverter (V_M), where $V_{out} = V_{DD}/2$, was shifted to the left from –2.7 V to –3.6 V as V_{DD} decreased from 1 V to 0.1 V. The shift can be accounted for by the reverse bias-induced barrier lowering [27]. Figure 2c displays the voltage gain, defined as $\left|\frac{V_{out}}{V_{in}}\right|$, as a function of V_{in}, shown for several V_{DD} between 0.4 and 1.0 V. The gain increased from 1.4 to 5 with the increase of V_{DD} from 0.4 V to 1.0 V. The gain further increased to $\sim$ 12 at $V_{DD} = 1.6$ V (data not shown). A larger V_{DD} resulted in a larger gain due to the suppression of the contact barriers between semiconductors and metal electrodes at larger V_{DD}. However, as the power consumed by the inverter increases with V_{DD}, V_{DD} should be minimized and efforts have been made to lower the V_{DD} in logic devices [28]. The abruptness of the gain is indicated by the full width at half maximum (FWHM) being in the range of 120 and 230 mV. Figure 2d presents the power consumption of the inverter as a function of V_{in}, extracted by the expression, $P = V_{DD} \times I_{DD}$. Here, I_{DD} is the current through the inverter. The power consumption was the largest between –3.9 V < V_{in} < –2.4 V, where a transition occurred in the magnitude of resistance between the p-type Gr/CNT and n-type Gr/MoS_2 barristors, i.e., an indeterminate state. Consumed power is related to V_{DD}, and the power consumption diminished with decreasing V_{DD}. Although the static power consumption was negligible at $\sim$0.1 nW, the peak power consumption was about 30 nW at $V_{DD} = 1$ V, and reduced down to ~1 nW at $V_{DD} = 0.4$ V. Optimization, such as the adjustment of the threshold voltages for each barristor and the reduction of EOT, can still improve the characteristics of the inverter, but the observed switching power of 1 nW at $V_{DD} = 0.4$ V is lower than, or comparable to previously reported low-power complementary inverters [29–33]. The low power operation is a consequence of the barristor characteristics. The barristor controls the current exponentially via modulation of the Schottky barrier height by changing the Fermi level of graphene. Thus, fast switching is possible even at a low voltage bias. The results before optimization already show that the complementary inverter based on p-type Gr/CNT and n-type Gr/MoS_2 barristors possesses the potential as a low power inverter with a moderate gain, operating at a low V_{DD}.

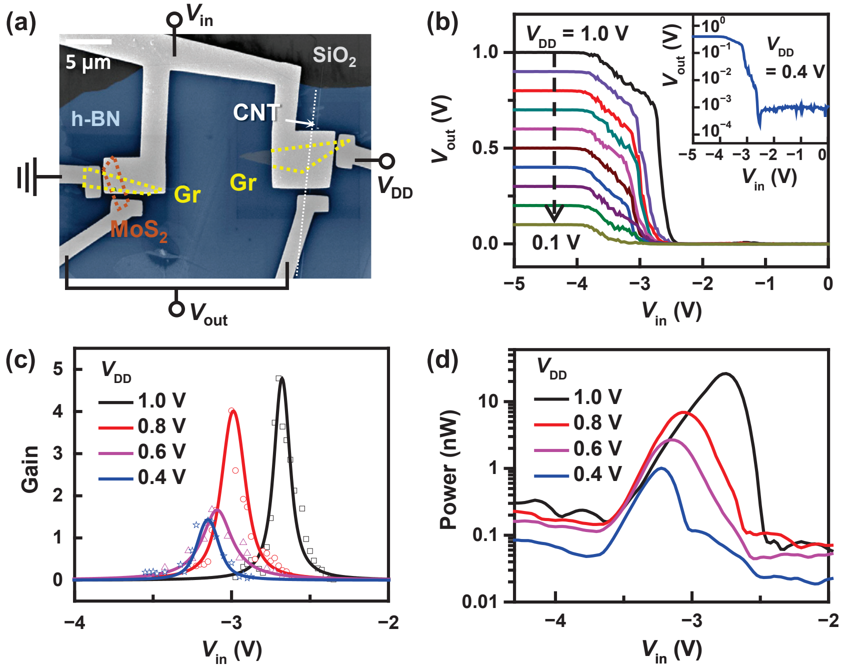

Figure 2. Inverter characteristics. (**a**) Scanning electron microscope image of Gr/MoS_2 (left) and Gr/CNT (right) junctions used in a complementary inverter. Dotted lines indicate the location of 2D layers and CNT. Both junctions are covered by a 15 nm-thick h-BN flake. (**b**) Voltage transfer characteristics of the complementary inverter at different V_{DD}. The inset shows the voltage transfer curve at $V_{DD} = 0.4$ V in a semilogarithmic scale. (**c**) Voltage gain as a function of the input voltage V_{in}. (**d**) Power consumption of the complementary inverter versus V_{in} in a semilogarithmic scale.

By applying a back-gate voltage, V_{BG}, through a SiO_2(300 nm)/Si substrate, the performance of the inverter can be improved. Although the top-gate V_{in} tunes the work function of graphene, the back-gate voltage can modulate the work function of the semiconductors (CNT and MoS_2) constituting the bottom of each junction on the substrate. Figure 3a exhibits VTC curves for $V_{DD} = 0.5$ V, measured at different V_{BG}. As V_{BG} was decreased from 5 V to –30 V, i.e., in the direction of hole-doping to the CNT and MoS_2, V_M moved to the right from –3.7 V to –2.3 V, reflecting the shifts of threshold voltage for each barristor. Figure 3b shows how the voltage gain versus V_{in} changes with V_{BG}. The voltage gain increased with decreasing V_{BG}, providing a gain of 2.7 and 2.5 at $V_{BG} = –15$ V, –30 V, respectively. The FWHM of the gain was around 160 meV. Interestingly, as shown in Figure 3c, the power consumption of the complementary inverter was reduced by 100 times as V_{BG} was decreased from 5 V to –30 V. At $V_{BG} =$ –30 V, the peak power consumed in the inverter was ∼0.2 nW. Thus, a low-power (0.2 nW) complementary inverter with gain of 2.5, operating at a low $V_{DD} = 0.5$ V, was demonstrated with an EOT of ∼15 nm, combining a p-type Gr/CNT barristor with a n-type Gr/MoS_2 barristor.

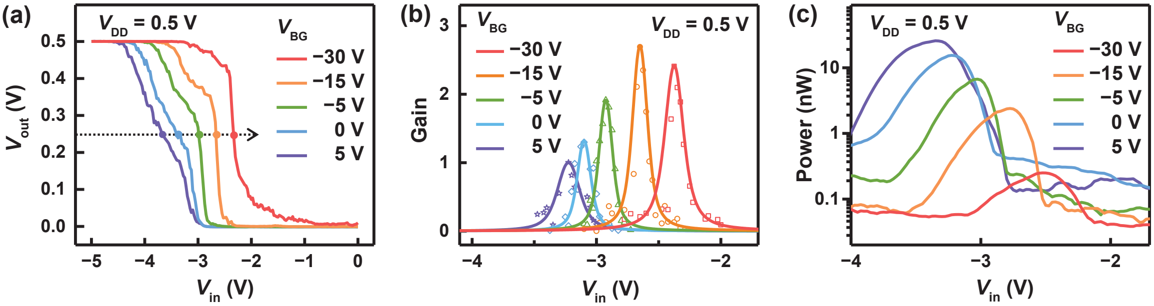

Figure 3. Inverter characteristics modulated with back-gate voltage V_{BG}. (**a**) Voltage transfer characteristics of the complementary inverter at $V_{DD} = 0.5$ V, obtained by varying V_{BG}. (**b**) Voltage gain as a function of the input voltage V_{in}, measured at different V_{BG}. (**c**) Power consumption of the inverter versus V_{in}. Peak power is reduced down to 0.2 nW at $V_{BG} = -30$ V.

The characteristics of the complementary inverter and the dependence on V_{BG} can be understood from the characteristics of individual barristors comprising the inverter. Figure 4a,b shows transfer characteristics of the p-type Gr/CNT and the n-type Gr/MoS_2 barristors, obtained by varying V_{BG}, respectively. The application of V_{BG} changed the Schottky barrier height between the graphene and the semiconductor (CNT or MoS_2) by adjusting the Fermi energy of the semiconductor, and shifted the threshold voltages in the transfer curves for each barristor. At the same time, the application of V_{BG} changed the resistance of the semiconductor itself by electrostatic doping. The total resistance of the barristor is the sum of the resistance of Gr, Gr/semiconductor junction, and the semiconductor, $R_{total} = R_{Gr} + R_{junction} + R_{semi}$, where R_{Gr} is negligible due to the semimetallic nature of the graphene. Therefore, a negative V_{BG}, which decreased the resistance of CNT by hole doping, resulted in a higher on-current, on/off ratio, effective mobility and reduced SS [21]. Note for the Gr/MoS_2 barristor, a negative V_{BG} worked in the opposite way in Figure 4b, increasing the resistance of MoS_2. Figure 4c displays the subthreshold swing of each barristor, SS = $d(V_{TG})/d(\log I_{DS})$, as a function of V_{BG}. SS increased with increasing V_{BG} for the p-type Gr/CNT barristor, and decreased for the n-type Gr/MoS_2 barristor, reflecting the change of R_{semi}. SS of each barristor crossed each other at $V_{BG} \simeq -20$ V with the value of SS $\simeq$ 160 mV/dec. The larger gain of the complementary inverter observed between $-30\text{ V} \leq V_{BG} \leq -15$ V (Figure 3b) can be attributed to the fact that both p-and n-type barristors have as small SS as possible in the range of V_{BG}. On the other hand, the dependence of the power consumption on V_{BG} can be associated with the threshold voltage of each barristor. The power consumption of a complementary inverter is expected to be lower if each component is located more in the deep subthreshold region at V_M. Therefore, adjustment of the threshold voltages, V_{Tp} and V_{Tn}, for p-and n-components, respectively, is preferred for the optimization of the inverter. The application of V_{BG} does not allow individual control over V_{Tp} and V_{Tn} and shifts both in the same direction. However, the degrees of change in E_F with respect to V_{BG} are different for the CNT and the MoS_2, and the application of V_{BG} can alter the relative distance between threshold voltages, $V_{Tn} - V_{Tp}$. Denoted in the upper axis of Figure 4c, $V_{Tn} - V_{Tp}$ is reduced from 2.6 V to 1.5 V upon the decrease of V_{BG} from 0 to -30 V. The adjustment of $V_{Tn} - V_{Tp}$ enabled the transition of the inverter to occur at lower current for V_{BG} =-30 V, reducing the power consumption of the complementary inverter down to ∼0.2 nW. In Figure 4d, the transfer curves of the Gr/CNT and the Gr/MoS_2 barristors are displayed together for selected V_{BG}. Notice that the intersection of the transfer curves occurred at a lower current regime for V_{BG} =–30 V. Figure 4e presents effective field-effect mobility of each barristor, extracted from the transfer curves shown in Figure 4a,b, and their dependence on V_{BG}. The mobility of the Gr/CNT barristor was calculated according to the 1D mobility equation, $\mu_{1D} = \frac{L}{c_g\ V_{DS}} \frac{dI_{DS}}{dV_{TG}}$, with L being the length of the junction and c_g being the capacitance per unit length. The mobility of Gr/MoS$_2$ was estimated from the 2D mobility equation, $\mu_{2D} = \frac{L}{W\ c_g\ V_{DS}} \frac{dI_{DS}}{dV_{TG}}$, with W being the width of the junction and c_g being the capacitance per unit area. When varying V_{BG} from -30 V to +10 V, the effective mobility of the Gr/CNT barristor decreased from $\sim$1300 to $\sim$400 cm^2/Vs, while μ for the Gr/MoS$_2$ barristor increased from $\sim$0.4 to $\sim$4.7 cm^2/Vs. This behavior in the effective mobility is explained by the increase in the resistance of CNT (MoS$_2$) at a positive (negative) V_{BG}, making the switching of R_{junction} less significant. Here, we find the mobility of Gr/MoS$_2$ is much lower than Gr/CNT barristor, but the mobility of Gr/MoS$_2$ can be improved up to $\sim$100 cm^2/Vs by reducing charged impurities [34,35]. Knowing the mobility and the threshold voltage of each barristor component, one can deduce the threshold of the complementary inverter with the following equation [36],

$$V_M = \frac{V_{Tn} + \sqrt{\frac{k_p}{k_n}}(V_{DD} + V_{Tp})}{1 + \sqrt{\frac{k_p}{k_n}}}, \tag{1}$$

$$k_{n,p} = (\frac{W}{L})_{n,p}\ \mu_{n,p}\ C_{ox}.$$

Here, $\mu_{n,p}$ is the mobility of either n-or p-barristor, and C_{ox} is the capacitance of the top-gate insulator per unit area. Using this equation, V_M is estimated to be -2.1 V, -2.3 V, -2.6 V, and -3.3 V when V_{BG} is -30 V, -15 V, -5 V, and 0 V, respectively. These values are in good agreement with the threshold voltage, V_M, observed in Figure 3a.

Table 1 summarizes previous reports on low-power complementary inverters based on low-dimensional materials. We find several sub-nW low-power complementary inverters realized with CNT- [32] or TMDCs-FETs [30,33]. Inverters using the TMDCs-FETs operated at relatively higher V_{DD} due to their higher contact resistance than CNT, and the inverter based on CNT-FETs exhibited a lower power consumption of $\sim$0.1 nW. The value is smaller than $\sim$0.2 nW, observed in our inverter made of Gr/CNT and Gr/MoS$_2$ barristors. However, the low-power complementary inverters employing FETs required much lower EOT compared to our device, for example at EOT $\sim$0.7 nm for the inverter realized with CNT-FETs. EOT indicates the thickness of silicon oxide that provides the same electrical performance as that of the dielectric material being used. In principle, thinner gate oxide leads to a smaller SS, reducing the power consumption of the device. Therefore, the low power consumption ($\sim$0.2 nW) achieved with a larger EOT of 15 nm for our device represents the excellent switching characteristics of Gr barristors, and further improvement can be expected by lowering the EOT. A theoretical analysis showed that SS of $\sim$50 mV/dec can be achieved in a graphene barristor with EOT $\leq$ 1 nm, overcoming the limitation of 60 mV/dec in conventional FETs [34]. Apart from our work, there have been several demonstrations of inverters based on graphene barristors incorporating Si [19], organic semiconductors [31], or cobaltite [37] as p-type semiconductors. However, these p-type Gr barristors showed relatively poor subthreshold swing (SS $\geq$ 500 mV/dec) compared to that (SS $\simeq$ 150 mV/dec) of the p-type Gr/CNT barristor, and limited the performance of the complementary inverter. On the other hand, in order to make a low-power inverter with a high gain, not only SS values of p-and n-components should be low, but transfer curves of p-and n-components should also intersect in the deep subthreshold region [38]. In this research, we relied on V_{BG} to partly adjust the threshold voltages of each component. A chemical doping of graphene [39], or separate electrostatic doping to each component can allow more precise control over the threshold voltages. In addition, such control over the threshold voltage can make the device to operate at the same input and output voltage ranges, essential for the circuit integration.

Table 1. Comparison between low-power complementary inverters.

p-Type	n-Type	V_{DD} [V]	EOT [nm]	Gain	Power [nW]	Ref
Si	MoS_2	1	18	2	2	[29]
$MoTe_2$	MoS_2	1	7	2	0.4	[30]
CNT	CNT	0.2	0.7	9	0.1	[32]
CNT	MoS_2	5	100	1.3	–	[40]
WSe_2	WS_2	1.5	2.5	40	1	[33]
Gr/Si	Gr/Si	2	–	1.2	–	[19]
Gr/DNTT	Gr/ZnO:N	2	6.5	8	> 10	[31]
Gr/BSCO	Gr/MoS_2	2	10	1.6	–	[37]
Gr/CNT	Gr/MoS_2	0.5	15	2.5	0.2	This work

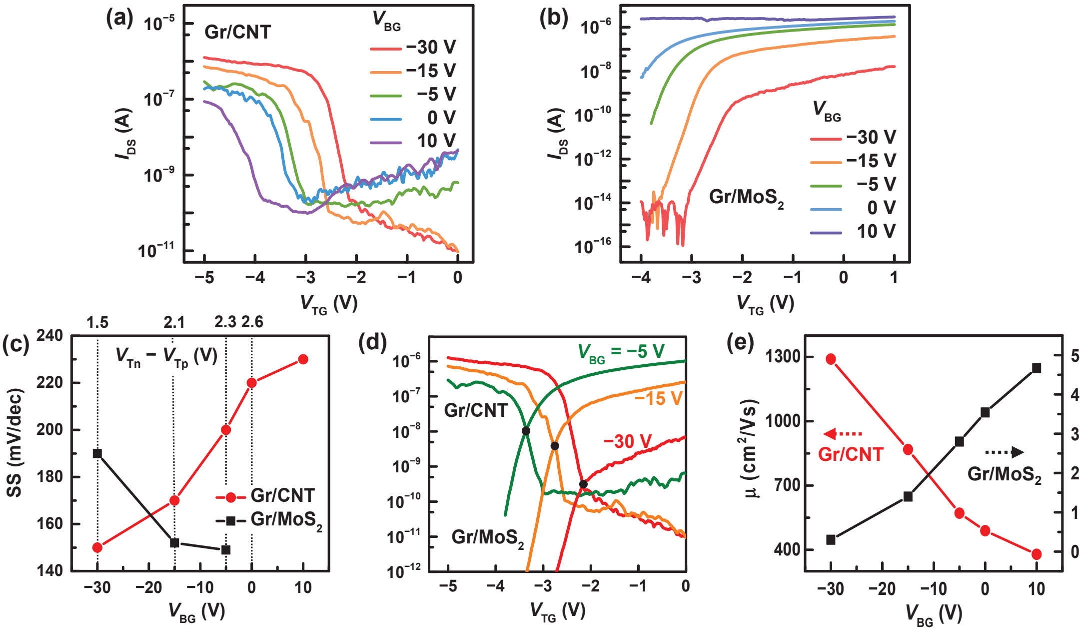

Figure 4. (**a**) Drain-source current, I_{DS}, versus V_{TG} of the Gr/CNT barristor, obtained from various V_{BG}. A reverse drain-source bias, V_{DS}, of –0.5 V is applied to the CNT so that holes cross the Schottky barrier from graphene to CNT. (**b**) Transfer curves of the Gr/MoS_2 barristor, measured at different V_{BG}. $V_{DS} = 0.5$ V is applied to the MoS_2, allowing electrons to cross the Schottky barrier from graphene to MoS_2. (**c**) Subthreshold swing of the Gr/CNT and Gr/MoS_2 barristors, deduced from transfer curves for different V_{BG}. (**d**) Transfer curves of the Gr/CNT and the Gr/MoS_2 barristors displayed together for selected V_{BG}. The intersection of the transfer curves occurred at a lower current regime with decreasing V_{BG}. (**e**) Estimated field-effect mobility as a function of V_{BG}. See the left axis for the Gr/CNT barristor and the right axis for the Gr/MoS_2 barristor.

Finally, we compare our device with a low-power inverter recently demonstrated using negative capacitance based FETs (NCFETs) by integrating a ferroelectric layer within the gate stack [41]. The complementary inverter with MoS_2 and WSe_2 NCFETs reported the lowest power consumption of 0.07 nW for the forward sweep and 0.17 nW for the reverse sweep [41]. However, the hysteresis of the inverter, theoretically existing as a result of polarization switching, is a serious obstacle to their practical use. Inverters based on graphene barristors are free from such problem of the ferroelectric negative capacitance and there is much room for the improvement with the reduction of EOT.

4. Conclusions

In conclusion, combining a p-type Gr/CNT barristor with a n-type Gr/MoS_2 barristor, a complementary inverter was fabricated and its characteristics were investigated. The complementary inverter exhibited a low switching power consumption of ∼0.2 nW and a moderate gain of ∼2.5 at $V_{DD} = 0.5$ V and at EOT of ∼15 nm. This sub-nW complementary inverter was achieved at much larger EOT compared to the inverters based on FETs, which was attributed to the excellent switching characteristics of Gr barristors. The p-type Gr/CNT barristor used in this experiment displayed an on–off current ratio of 10^5 and a high mobility of ∼1300 cm^2/Vs with a subthreshold swing of 150 mV/dec with an EOT of 15 nm. The emergence of a p-type Gr/CNT barristor with an excellent switching property, not available for Gr/TMDCs barristors, opens the possibility of logic devices based on graphene barristors.

Author Contributions: Conceptualization, Y.G.Y., H.-J.C., and S.H.J.; formal analysis, D.-H.S. and S.H.J.; investigation, D.-H.S.; resources, D.-H.S., S.I.J., G.-H.J., H.-J.C., and S.H.J.; writing—original draft preparation, D.-H.S. and S.H.J.; writing—review and editing, D.-H.S., S.H.J., and E.E.B.C.; visualization, D.-H.S. and S.H.J.; supervision, H.-J.C. and S.H.J.; project administration, D.-H.S. and S.H.J.; funding acquisition, S.H.J. All authors have read and agreed to the published version of the manuscript.

Funding: This work was supported by Konkuk University in 2017.

Institutional Review Board Statement: Not applicable.

Informed Consent Statement: Not applicable.

Data Availability Statement: The data is included in the main text.

Conflicts of Interest: The authors declare no conflicts of interest.

References

1. Solomon, P. Device innovation and material challenges at the limits of CMOS technology. *Annu. Rev. Mater. Sci.* **2000**, *30*, 681–697. [CrossRef]
2. Che, Y.; Chen, H.; Gui, H.; Liu, J.; Liu, B.; Zhou, C. Review of carbon nanotube nanoelectronics and macroelectronics. *Semicond. Sci. Technol.* **2014**, *29*, 073001. [CrossRef]
3. Novoselov, K.S.; Colombo, L.; Gellert, P.; Schwab, M.; Kim, K. A roadmap for graphene. *Nature* **2012**, *490*, 192–200. [CrossRef] [PubMed]
4. Manzeli, S.; Ovchinnikov, D.; Pasquier, D.; Yazyev, O.V.; Kis, A. 2D transition metal dichalcogenides. *Nat. Rev. Mater.* **2017**, *2*, 17033. [CrossRef]
5. Zhan, B.; Li, C.; Yang, J.; Jenkins, G.; Huang, W.; Dong, X. Graphene field-effect transistor and its application for electronic sensing. *Small* **2014**, *10*, 4042–4065. [CrossRef]
6. Banszerus, L.; Schmitz, M.; Engels, S.; Dauber, J.; Oellers, M.; Haupt, F.; Watanabe, K.; Taniguchi, T.; Beschoten, B.; Stampfer, C. Ultrahigh-mobility graphene devices from chemical vapor deposition on reusable copper. *Sci. Adv.* **2015**, *1*, e1500222. [CrossRef]
7. Kim, B.J.; Jang, H.; Lee, S.K.; Hong, B.H.; Ahn, J.H.; Cho, J.H. High-performance flexible graphene field effect transistors with ion gel gate dielectrics. *Nano Lett.* **2010**, *10*, 3464–3466. [CrossRef]
8. Yun, J.M.; Park, S.; Hwang, Y.H.; Lee, E.S.; Maiti, U.; Moon, H.; Kim, B.H.; Bae, B.S.; Kim, Y.H.; Kim, S.O. Complementary p-and n-type polymer doping for ambient stable graphene inverter. *ACS Nano* **2014**, *8*, 650–656. [CrossRef]
9. Yang, X.; Li, B. Monolayer MoS_2 for nanoscale photonics. *Nanophotonics* **2020**, *9*, 1557–1577. [CrossRef]
10. Ben Amara, I.; Ben Salem, E.; Jaziri, S. Optoelectronic response and excitonic properties of monolayer MoS_2. *J. Appl. Phys.* **2016**, *120*, 051707. [CrossRef]
11. Wang, H.; Yu, L.; Lee, Y.H.; Shi, Y.; Hsu, A.; Chin, M.L.; Li, L.J.; Dubey, M.; Kong, J.; Palacios, T. Integrated circuits based on bilayer MoS_2 transistors. *Nano Lett.* **2012**, *12*, 4674–4680. [CrossRef] [PubMed]
12. Chee, S.S.; Seo, D.; Kim, H.; Jang, H.; Lee, S.; Moon, S.P.; Lee, K.H.; Kim, S.W.; Choi, H.; Ham, M.H. Lowering the Schottky barrier height by graphene/Ag electrodes for high-mobility MoS_2 field-effect transistors. *Adv. Mater.* **2019**, *31*, 1804422. [CrossRef] [PubMed]
13. Iqbal, M.W.; Iqbal, M.Z.; Khan, M.F.; Shehzad, M.A.; Seo, Y.; Park, J.H.; Hwang, C.; Eom, J. High-mobility and air-stable single-layer WS_2 field-effect transistors sandwiched between chemical vapor deposition-grown hexagonal BN films. *Sci. Rep.* **2015**, *5*, 10699. [CrossRef]
14. Fathipour, S.; Ma, N.; Hwang, W.; Protasenko, V.; Vishwanath, S.; Xing, H.; Xu, H.; Jena, D.; Appenzeller, J.; Seabaugh, A. Exfoliated multilayer $MoTe_2$ field-effect transistors. *Appl. Phys. Lett.* **2014**, *105*, 192101. [CrossRef]

15. Yoo, H.; Hong, S.; On, S.; Ahn, H.; Lee, H.K.; Hong, Y.K.; Kim, S.; Kim, J.J. Chemical doping effects in multilayer MoS_2 and its application in complementary inverter. *ACS Appl. Mater. Interfaces* **2018**, *10*, 23270–23276. [CrossRef]
16. Tosun, M.; Chuang, S.; Fang, H.; Sachid, A.B.; Hettick, M.; Lin, Y.; Zeng, Y.; Javey, A. High-gain inverters based on WSe_2 complementary field-effect transistors. *ACS Nano* **2014**, *8*, 4948–4953. [CrossRef] [PubMed]
17. Luo, W.; Zhu, M.; Peng, G.; Zheng, X.; Miao, F.; Bai, S.; Zhang, X.A.; Qin, S. Carrier modulation of ambipolar few-layer $MoTe_2$ transistors by MgO surface charge transfer doping. *Adv. Funct. Mater.* **2018**, *28*, 1704539. [CrossRef]
18. He, Q.; Liu, Y.; Tan, C.; Zhai, W.; Nam, G.h.; Zhang, H. Quest for p-type two-dimensional semiconductors. *ACS Nano* **2019**, *13*, 12294–12300. [CrossRef]
19. Yang, H.; Heo, J.; Park, S.; Song, H.J.; Seo, D.H.; Byun, K.E.; Kim, P.; Yoo, I.; Chung, H.J.; Kim, K. Graphene barristor, a triode device with a gate-controlled Schottky barrier. *Science* **2012**, *336*, 1140–1143. [CrossRef]
20. Jahangir, I.; Uddin, M.A.; Singh, A.K.; Koley, G.; Chandrashekhar, M. Richardson constant and electrostatics in transfer-free CVD grown few-layer MoS_2/graphene barristor with Schottky barrier modulation >0.6eV. *Appl. Phys. Lett.* **2017**, *111*, 142101. [CrossRef]
21. You, Y.G.; Park, D.H.; Lee, J.H.; Choi, I.; Shin, D.H.; Jo, S.I.; Jeong, G.H.; Campbell, E.E.; Hodge, S.A.; Ferrari, A.C.; et al. *p-Type Schottky Junction Devices Based on Graphene and a Semiconducting Carbon Nanotube*; Konkuk University: Seoul, Korea, 2022. (Submitted)
22. Durrer, L.; Helbling, T.; Zenger, C.; Jungen, A.; Stampfer, C.; Hierold, C. SWNT growth by CVD on Ferritin-based iron catalyst nanoparticles towards CNT sensors. *Sens. Actuators B Chem.* **2008**, *132*, 485–490. [CrossRef]
23. Durrer, L.; Greenwald, J.; Helbling, T.; Muoth, M.; Riek, R.; Hierold, C. Narrowing SWNT diameter distribution using size-separated ferritin-based Fe catalysts. *Nanotechnology* **2009**, *20*, 355601. [CrossRef] [PubMed]
24. Jiao, L.; Fan, B.; Xian, X.; Wu, Z.; Zhang, J.; Liu, Z. Creation of nanostructures with poly (methyl methacrylate)-mediated nanotransfer printing. *J. Am. Chem. Soc.* **2008**, *130*, 12612–12613. [CrossRef] [PubMed]
25. Bandow, S.; Asaka, S.; Saito, Y.; Rao, A.M.; Grigorian, L.; Richter, E.; Eklund, P.C. Effect of the growth temperature on the diameter distribution and chirality of single-wall carbon nanotubes. *Phys. Rev. Lett.* **1998**, *80*, 3779–3782. [CrossRef]
26. Park, D.H.; Cho, Y.J.; Lee, J.H.; Choi, I.; Jhang, S.H.; Chung, H.J. The evolution of surface cleanness and electronic properties of graphene field-effect transistors during mechanical cleaning with atomic force microscopy. *Nanotechnology* **2019**, *30*, 394003. [CrossRef]
27. Sinha, D.; Lee, J.U. Ideal graphene/silicon Schottky junction diodes. *Nano Lett.* **2014**, *14*, 4660–4664. [CrossRef]
28. Riel, H.; Wernersson, L.E.; Hong, M.; Del Alamo, J.A. III–V compound semiconductor transistors—From planar to nanowire structures. *Mrs Bull.* **2014**, *39*, 668–677. [CrossRef]
29. Das, T.; Chen, X.; Jang, H.; Oh, I.K.; Kim, H.; Ahn, J.H. Highly flexible hybrid CMOS inverter based on Si nanomembrane and molybdenum disulfide. *Small* **2016**, *12*, 5720–5727. [CrossRef]
30. Du, W.; Jia, X.; Cheng, Z.; Xu, W.; Li, Y.; Dai, L. Low-power-consumption CMOS inverter array based on CVD-grown p-$MoTe_2$ and n-MoS_2. *Iscience* **2021**, *24*, 103491. [CrossRef]
31. Heo, S.; Lee, H.I.; Lee, H.; Kim, S.M.; Kim, K.; Kim, Y.J.; Kim, S.Y.; Kim, J.H.; Yoon, M.H.; Lee, B.H. Very-low-temperature integrated complementary graphene-barristor-based inverter for thin-film transistor applications. *Ann. Der Phys.* **2018**, *530*, 1800224. [CrossRef]
32. Liang, S.; Zhang, Z.; Si, J.; Zhong, D.; Peng, L.M. High-performance carbon-nanotube-based complementary field-effect-transistors and integrated circuits with yttrium oxide. *Appl. Phys. Lett.* **2014**, *105*, 063101. [CrossRef]
33. Yeh, C.H.; Liang, Z.Y.; Lin, Y.C.; Chen, H.C.; Fan, T.; Ma, C.H.; Chu, Y.H.; Suenaga, K.; Chiu, P.W. Graphene–transition metal dichalcogenide heterojunctions for scalable and low-power complementary integrated circuits. *ACS Nano* **2020**, *14*, 985–992. [CrossRef] [PubMed]
34. Tian, H.; Tan, Z.; Wu, C.; Wang, X.; Mohammad, M.A.; Xie, D.; Yang, Y.; Wang, J.; Li, L.J.; Xu, J.; et al. Novel field-effect Schottky barrier transistors based on graphene-MoS_2 heterojunctions. *Sci. Rep.* **2014**, *4*, 5951. [CrossRef] [PubMed]
35. Shim, J.; Park, J.H. Optimization of graphene-MoS_2 barristor by 3-aminopropyltriethoxysilane (APTES). *Org. Electron.* **2016**, *33*, 172–177. [CrossRef]
36. Cho, A.J.; Park, K.C.; Kwon, J.Y. A high-performance complementary inverter based on transition metal dichalcogenide field-effect transistors. *Nanoscale Res. Lett.* **2015**, *10*, 1–6. [CrossRef]
37. Yu, W.J.; Li, Z.; Zhou, H.; Chen, Y.; Wang, Y.; Huang, Y.; Duan, X. Vertically stacked multi-heterostructures of layered materials for logic transistors and complementary inverters. *Nat. Mater.* **2013**, *12*, 246–252. [CrossRef]
38. Das, S.; Dubey, M.; Roelofs, A. High gain, low noise, fully complementary logic inverter based on bi-layer WSe_2 field effect transistors. *Appl. Phys. Lett.* **2014**, *105*, 083511. [CrossRef]
39. Kim, S.Y.; Hwang, J.; Kim, Y.J.; Hwang, H.J.; Son, M.; Revannath, N.; Ham, M.H.; Cho, K.; Lee, B.H. Threshold voltage modulation of a graphene–ZnO barristor using a polymer doping process. *Adv. Electron. Mater.* **2019**, *5*, 1800805. [CrossRef]
40. Huang, J.; Somu, S.; Busnaina, A. A molybdenum disulfide/carbon nanotube heterogeneous complementary inverter. *Nanotechnology* **2012**, *23*, 335203. [CrossRef]
41. Wang, J.; Guo, X.; Yu, Z.; Ma, Z.; Liu, Y.; Lin, Z.; Chan, M.; Zhu, Y.; Wang, X.; Chai, Y. Low-power complementary inverter with negative capacitance 2D semiconductor transistors. *Adv. Funct. Mater.* **2020**, *30*, 2003859. [CrossRef]

nanomaterials

Article

High Performance 0D ZnO Quantum Dot/2D $(PEA)_2PbI_4$ Nanosheet Hybrid Photodetectors Fabricated via a Facile Antisolvent Method

Shijie Liu [1], Hao Li [1], Haifei Lu [1], Yanran Wang [1], Xiaoyan Wen [1], Shuo Deng [1], Ming-Yu Li [1,*], Sisi Liu [1,*], Cong Wang [2,*] and Xiao Li [3]

[1] School of Science, Wuhan University of Technology, Wuhan 430070, China
[2] School of Electronics and Information Engineering, Harbin Institute of Technology, Harbin 150001, China
[3] Hisense Visual Technology Co., Ltd., Qingdao 266555, China
* Correspondence: mingyuli.oliver@gmail.com (M.-Y.L.); liusisi0109@hotmail.com (S.L.); kevinwang@hit.edu.cn (C.W.)

Abstract: Two-dimensional (2D) organic−inorganic perovskites have great potential for the fabrication of next-generation photodetectors owing to their outstanding optoelectronic features, but their utilization has encountered a bottleneck in anisotropic carrier transportation induced by the unfavorable continuity of the thin films. We propose a facile approach for the fabrication of 0D ZnO quantum dot (QD)/2D $(PEA)_2PbI_4$ nanosheet hybrid photodetectors under the atmospheric conditions associated with the ZnO QD chloroform antisolvent. Profiting from the antisolvent, the uniform morphology of the perovskite thin films is obtained owing to the significantly accelerated nucleation site formation and grain growth rates, and ZnO QDs homogeneously decorate the surface of $(PEA)_2PbI_4$ nanosheets, which spontaneously passivate the defects on perovskites and enhance the carrier separation by the well-matched band structure. By varying the ZnO QD concentration, the Ion/Ioff ratio of the photodetectors radically elevates from 78.3 to 1040, and a 12-fold increase in the normalized detectivity is simultaneously observed. In addition, the agglomeration of perovskite grains is governed by the annealing temperature, and the photodetector fabricated at a relatively low temperature of 120 °C exhibits excellent stability after a 50-cycle test in the air condition without any encapsulation.

Keywords: 2D perovskite; ZnO quantum dot; antisolvent method; photodetector; outstanding stability

Citation: Liu, S.; Li, H.; Lu, H.; Wang, Y.; Wen, X.; Deng, S.; Li, M.-Y.; Liu, S.; Wang, C.; Li, X. High Performance 0D ZnO Quantum Dot/2D $(PEA)_2PbI_4$ Nanosheet Hybrid Photodetectors Fabricated via a Facile Antisolvent Method. *Nanomaterials* **2022**, *12*, 4217. https://doi.org/10.3390/nano12234217

Academic Editor: Iván Mora-Seró

Received: 7 November 2022
Accepted: 24 November 2022
Published: 27 November 2022

1. Introduction

Photodetection provides a feasible approach for interpreting the unreadable optical information by converting it into electrical signals, which has been sparking burgeoning interests for widespread applications, such as optical telecommunication, environmental monitoring, biomedical imaging, distributing sensor networks, and the internet of things [1–4]. The rapid expansion of information technology has been fueling the demand for high-performance photodetectors with a high signal-to-noise ratio, sensitivity, response speed, spectrum selectivity, and stability, which were proposed as “5S” figure-of-merits for the evaluation of photodetection capability [5]. Perovskites have emerged as promising photoactive materials with a combination of advantages over conventional semiconductors, including easy solution processability, a large absorption coefficient, a long carrier diffusion length, and high carrier mobility [6,7]. Inheriting from the excellent photoelectric capacities of their three-dimensional (3D) counterparts, 2D perovskites have been recently developed with a considerably improved atmospheric stability owing to the protection of hydrophobic organic chain spacers enclosed in $[MX_6]^{4-}$ metal halide octahedra [8], which is believed to be a savior for long-term stable perovskite-based photodetection [9]. As of now, research on the 2D perovskite-based photodetectors is still in the early embryonic stage, and their application suffers from a huge hindrance in the fabrication of continuous thin films from isolated nanosheets [10]. Recently, the one-step antisolvent method has been reported as a successful attempt for manufacturing high quality $(PEA)_2PbI_4$ thin films at relatively low temperatures owing to the accelerated nucleation and grain growth governed by polarity and saturated vapor pressure [11]. As a typical Ruddlesden—Popper (RP) phase perovskite, the Van der Waals interactions between layers within $(PEA)_2PbI_4$ nanosheets can restrict the charge-carrier transportation along out-of-plane direction [12], which remains a critical challenge of the undesirable performance in comparison to that of 3D perovskite photodetectors.

Perovskite photoactive thin films have been successfully fabricated via various approaches, i.e., chemical vapor deposition [13], mechanical exfoliation [14], electrochemical deposition [15–17], and spinning coating [18]. Alternative fabrication techniques allow the construction of heterostructures by introducing foreign low-dimensional materials, offering an efficient route for improving the optoelectronic response of the resulting perovskite thin films. For instance, the $Cs_2AgBiBr_6/WS_2$/graphene vertical heterostructure photodetectors demonstrated orientationally intensified charge transfer [19]. In addition, direct incorporation of low-dimensional materials with a high conductivity (i.e., graphene QDs [20] and MXene nanosheets [21]) can well balance the simplicity of fabrication and efficient charge transfer, which is commonly accompanied with inevitably knotty issues of the extra noise in dark and lattice miss-match in the hybrid photoactive layers. Meanwhile, ZnO QDs possess various advantages, including large resistance in the dark, high electron mobility, and a wurtzite structure [22], and the improved crystallization of $CsPbBr_3$ thin films was observed by blending with ZnO QDs [23], providing an adequate filler for the fabrication of high-performance photodetectors. In this work, we demonstrate novel 0D ZnO QD/2D $(PEA)_2PbI_4$ nanosheet hybrid photodetectors fabricated via a facile antisolvent method under atmospheric conditions. The homogeneous decoration of ZnO DQs on a 2D $(PEA)_2PbI_4$ nanosheet surface instantaneously realizes the defect passivation and construction of carrier transfer paths within the photoactive layers. With a well-balanced ZnO concentration, the normalized detectivity (D^*) of the 0D/2D hybrid perovskite photodetector radically increases to 15.40×10^9 Jones with an excellent I_{on}/I_{off} ratio of 1040. Temperature effect on the performance of photodetectors is attributed to the morphological evolution of the hybrid perovskite thin films, and superior stability of the device is observed within 50 test cycles, offering an auspicious way to overcome the breakthrough of 2D perovskite photodetectors for the "5S" requirements.

2. Materials and Methods

Chemicals and Reagents: Zinc acetate dihydrate ($C_4H_6O_4Zn{\cdot}2H_2O$, 99.0%; Sinopharm Group Chemical Reagent Co., Ltd. A. R, Shanghai, China), potassium hydroxide (KOH, 85%; Aladdin, Shanghai, China), methanol (CH_3OH, 99.5%; Sinopharm Group Chemical Reagent Co., Ltd. A. R, Shanghai, China), chloroform (CH_3Cl, 99.0%; Sinopharm Group Chemical Reagent Co., Ltd. A. R, Shanghai, China), phenethylammonium iodide (PEAI, 99.5%; Xi'an Polymer Light Co., Xi'an, China), lead iodide (PbI_2, 99.0%; Sinopharm Group Chemical Reagent Co., Ltd. A. R, Shanghai, China), and N, N-Dimethylformamide (DMF, 99.0%; Sinopharm Group Chemical Reagent Co., Ltd. A. R, Shanghai, China). All chemical reagents mentioned above were used directly, without any further purification.

Material Synthesis: The ZnO quantum dots (QDs) were prepared through an optimized solvothermal method as reported in our previous work [24]. Specifically, 1.9582 g of zinc acetate dihydrate was dissolved in 46 mL of methanol and heated up to 60 °C. Meanwhile, 0.8528 g of KOH was dissolved in 46 mL of methanol and dropped into the zinc acetate dihydrate methanol solution for 8–12 min. The mixed solution kept stirring for 2.15 h under 60 °C, and was washed twice by the precipitation method. After synthesis, the resulting ZnO QDs were dispersed in 6 mL of chloroform. The $(PEA)_2PbI_4$ precursors were prepared in the atmosphere at room temperature. Specifically, the mixture of 199.2 mg

PEAI and 184.0 mg PbI_2 was dissolved in 1 mL of DMF, and the solution was treated with ultrasonication for 20 minutes at room temperature.

Device Fabrication: Prior to spin-coating, each glass substrate with a size of 2.5×2.5 cm^2 was ultrasonicated in anhydrous ethanol (99.0%) and acetone (99%) for 20 minutes, respectively. Subsequently, 100 μL of $(PEA)_2PbI_4$ precursor solution was initially dropped on the glass substrate, and 100 μL of chloroform antisolvents with various contents of ZnO QDs: 0 mg/mL (PD1), 0.032 mg/mL (PD2), 0.048 mg/mL (PD3), 0.097 mg/mL (PD4), 0.194 mg/mL (PD5), 0.388 mg/mL (PD6), and 0.776 mg/mL (PD7). After incubation for 1 min, the photoactive thin films were spin-coated layer-by-layer at 800 rpm for 20 s and 2000 rpm for 30 s, respectively. After coating 3 layers, the samples were annealed at 120 °C for 1 min between spin-coating for each layer and were finally treated with a 10 min annealing at an identical temperature to improve crystallization. To investigate the annealing temperature effect, the samples fabricated with a 0.097 mg/mL of chloroform antisolvent were annealed on a hot plate in the atmosphere at room temperature (PD8), 80 °C (PD9), 100 °C (PD10), and 140 °C (PD11). Finally, a pair of 80 nm-thick Au electrodes with a spacing distance of 200 μM was deposited via thermal evaporation.

Device Characterization: The morphologies of ZnO QD-decorated $(PEA)_2PbI_4$ nanosheets were characterized by a transmission electron microscope (TEM, JEM-1400 Plus, JEOL, Tokyo, Japan), and scanning electron microscope (SEM) images of each sample were obtained by a Regulus8100 system (Hitachi, Tokyo, Japan). The elemental analysis of the samples was carried out by an energy dispersive X-ray spectroscopy system (EDS, Regulus8100, Hitachi, Tokyo, Japan), and the surface morphological characterization was realized with atomic force microscopy (AFM, Dimension Icon, Bruker, Karlsruhe, Germany). The crystallinity of the samples was analyzed by X-ray diffractometer (XRD, D8 Advance, Bruker, Karlsruhe, Germany; D/MAX-RB, Rigaku, Tokyo, Japan). The absorption spectra were recorded on a UV/vis spectrophotometer (UV-2600, Shimadzu, Kyoto, Japan), and the steady-state photoluminescence (PL) spectra were required by a spectrofluorophotometer (RF-6000, Shimadzu, Kyoto, Japan) with an excitation light of 350 nm. The time-resolved PL (TRPL) spectra of $(PEA)_2PbI_4$ thin films were recorded with a spectrofluorometer (Fluo Time 300, PicoQuant, Berlin, Germany) with a pumping laser of 375 nm and a probing laser of 526 nm. The photoelectric performances of all devices were measured with a semiconductor characterization system (4200, Keithley, Cleveland, OH, USA), and a monochrome adjustable light source (CME-OPS1000, Microenerg, Beijing, China) was engaged as an illumination source.

3. Results and Discussion

Figure 1 shows the effect of ZnO QD concentrations on the morphological evolution of the zero-dimensional (0D) ZnO QD and 2D $(PEA)_2PbI_4$ nanosheet hybrid thin films. The fabrication process of ZnO QD/$(PEA)_2PbI_4$ nanosheet photodetectors is depicted in Figure 1a. Briefly, the ZnO QD/$(PEA)_2PbI_4$ thin films were fabricated by blending ZnO QD chloroform solution with various concentrations after dropping 100 μL PEAI and PbI_2 mixture on glass substrate. According to previous works, highly crystallized 2D perovskite nanosheet thin films with a continuous morphology could be hardly achieved [25], and an effective approach for improving crystallinity was reported by adding antisolvents during thin film growth due to the accelerated nucleation site formation and grain growth rates [26]. Providing the distinctive polarity (μ_C = 1.06 D) of chloroform over that of DMF (μ_D = 3.82 D) [11], the nucleation site formation and grain growth rates were significantly boosted, and thus, the packed morphology of the pristine $(PEA)_2PbI_4$ nanosheet thin films was obtained, as shown in Figure 1b. As shown in Figure S1a, the ZnO QDs are well-decorated on the surface of the $(PEA)_2PbI_4$ nanosheet with an average diameter of ~6.22 nm after blending into the $(PEA)_2PbI_4$ nanosheet precursor solution. In addition, $(PEA)_2PbI_4$ nanosheets generally crystallized in the monoclinic space group C2/m with lattice parameters a = 3.25 nm, b = 0.61 nm, and c = 0.62 nm [27], and wurtzite ZnO with relatively smaller lattice parameters a = b = 0.32 nm and c = 0.52 nm [28], allowing preferential adsorption of ZnO QDs on $(PEA)_2PbI_4$ nanosheets. As a result, ZnO QDs were evenly decorated on the $(PEA)_2PbI_4$ nanosheets, as clearly witnessed in Figure S1b, and bright diffraction spots of (200) and (020) planes [29] in the selected area electron diffraction (SAED) pattern evidenced the existence of $(PEA)_2PbI_4$ in the mixed solution, as shown in Figure S1c. As shown in Figures 1 and S1d, the packed and continuous surface morphology was comparably observed for each ZnO QD/$(PEA)_2PbI_4$ nanosheet sample, with a variation of ZnO QD concentrations between 0 and 0.776 mg/mL. Meanwhile, the neglectable effect of ZnO QDs on the surface morphology can also be witnessed with a similar root-mean-squared roughness (RRMS) for the devices blending with various concentrations of 0 mg/mL (14.4 nm) and 0.097 mg/mL (17.1 nm), as shown in Figure S1e–f.

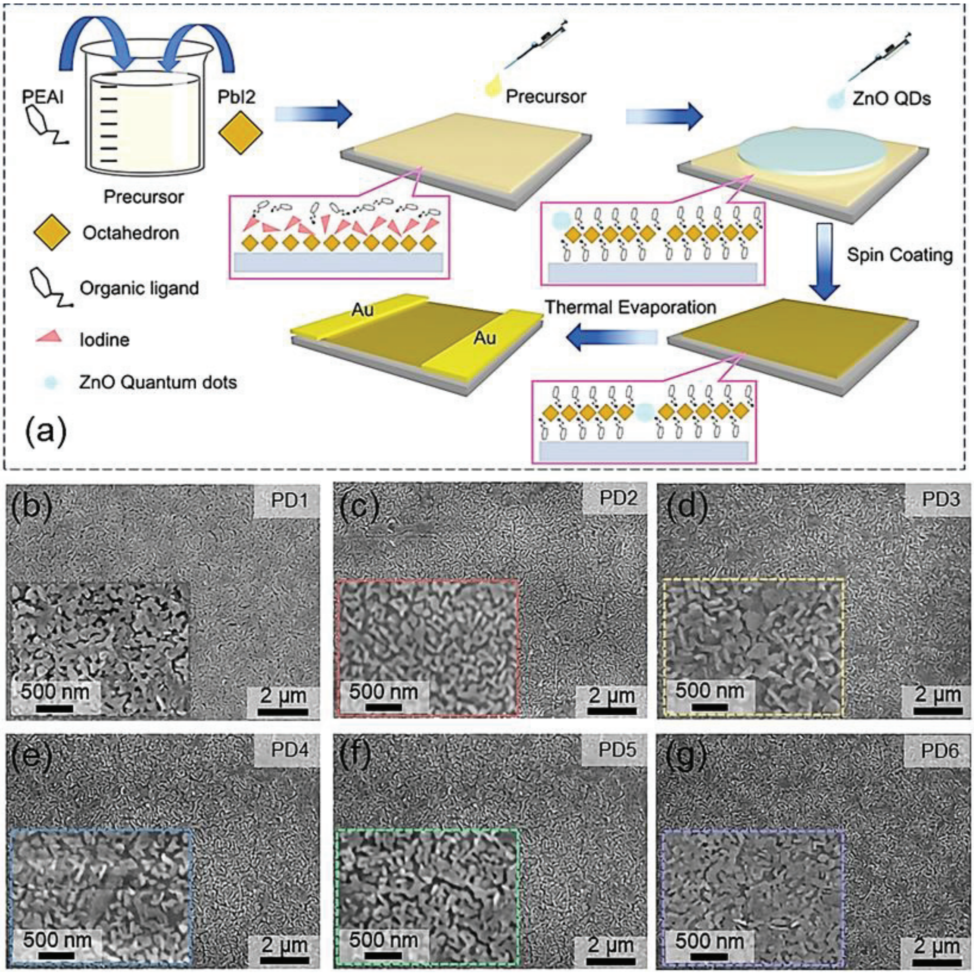

Figure 1. (**a**) Schematic diagram of the fabrication process of ZnO QD decorated $(PEA)_2PBI_4$ nanosheet photodetectors via antisolvent method. (**b**–**g**) Scanning electron microscope (SEM) images of the ZnO QD/$(PEA)_2PBI_4$ nanosheet samples with various proportions of ZnO QD: PD1 (0 mg/mL), PD2 (0.032 mg/mL), PD3 (0.048 mg/mL), PD4 (0.097 mg/mL), PD5 (0.194 mg/mL), and PD6 (0.388 mg/mL).

To further investigate the effect of ZnO QD, the developments of optical properties and crystal structures were systematically investigated with diverse concentrations between 0 and 0.776 mg/mL, as shown in Figure 2. As shown in Figure 2a, the elements N, I, Pb, O, and Zn were evenly observed throughout the whole surface of the PD4 device fabricated with 0.097 mg/mL ZnO QD antisolvent solution, indicating a uniform distribution of ZnO QD in the hybrid thin films. In terms of the elementary composition of the samples, the existence of $(PEA)_2PbI_4$ was verified with the occurrence of the $K\alpha_1$ peak at 0.392 keV of N, $M\alpha_1$ peak at 2.346 keV of Pb, and $L\alpha_1$ peak at 3.94 keV of I regardless of the ZnO QD concentration [30], and the $L\beta_1$ peak at 1.035 keV of Zn [31] can only be witnessed with the hybrid thin films blending with 0.097 mg/mL ZnO QDs, as shown in Figure 2b,c. For each sample, the characteristic peaks at 5.5°, 10.9°, 16.4°, 21.9°, 27.4°, 33.0°, and 38.7° can be assigned to the periodical diffraction peaks of (001) series of reflections ((00x), x = 2, 4, 6), (010), (012), and (014) peaks [32], as shown in Figure 2d. Practically, (002) peaks strikingly appeared in comparison with other peaks, manifesting a preferential crystallization of the thin films [33]. As revealed in Figure 2e, the noticeable exciton absorption peak of $(PEA)_2PbI_4$ [34] was constantly observed at 517 nm in the absorbance spectrum for each sample, suggesting an identical bandgap of ~2.364 eV the hybrid thin films irrespective of the ZnO QD concentration as conformed with the Tauc plots shown in Figure S2. Correspondingly, the near band emission for each sample was similarly witnessed at 526 nm without any shifting as exhibited with room temperature photoluminescence (PL) spectra in Figure 2f, and the peak intensity gradually elevated along with the increased ZnO QD concentration as observed in Figure 2f, which can be possibly induced by intensified irradiative combination with the reduced defect state density due to the surface passivation with ZnO QDs [35]. To verify the hypothesis, time-resolved photoluminescence (TRPL) spectra of the photodetectors fabricated without (PD1) and with ZnO QD (PD4) were characterized, as shown in Figure 2g. The TRPL curves were well fitted by a multiexponential function with three decay components τ_1 (the excitation relaxation), τ_2 (the interaction between excitons and phonons), and τ_3 (the recombination of excitons with defects) [36]:

$$\mathrm{I(t)} = A_1 exp(-\mathrm{t}/\tau_1) + A_2 exp(-\mathrm{t}/\tau_2) + A_3 exp(-\mathrm{t}/\tau_3) \tag{1}$$

where A_1, A_2, and A_3 denote the proportionality factor for each decay period. The average decay lifetime (τ_{avg}) of the device can be given with [37]:

$$\tau_{Avg} = A_1 \times \tau_1 + A_2 \times \tau_2 + A_3 \times \tau_3 \tag{2}$$

As summarized in Table 1, the τ_1 and τ_2 were comparable for the devices, and the significant decrease in τ_{avg} from 5.16 ns (PD1) to 0.94 ns (PD4) was primarily ascribed to the restricted recombination of excitons with defects [38], which can be beneficial for the carrier transportation within the photodetectors. As shown in the inset in Figure 2g, the continuous morphology of the thin films was observed with the PD4 device, and strong green irradiation under UV light illumination verified the high quality of the spin-coated thin films.

Table 1. Summary of TRPL decay fitting characteristics for the photodetectors PD1 and PD4 based on the decay functions.

	PD1	**PD4**
τ_1 (ns)	0.69	0.53
τ2 (ns)	3.10	3.27
τ3 (ns)	45.67	-
B_1 (%)	53.52	84.82
B_2 (%)	38.62	15.18
B_3 (%)	7.87	-
τ_{avg} (ns)	5.16	0.94

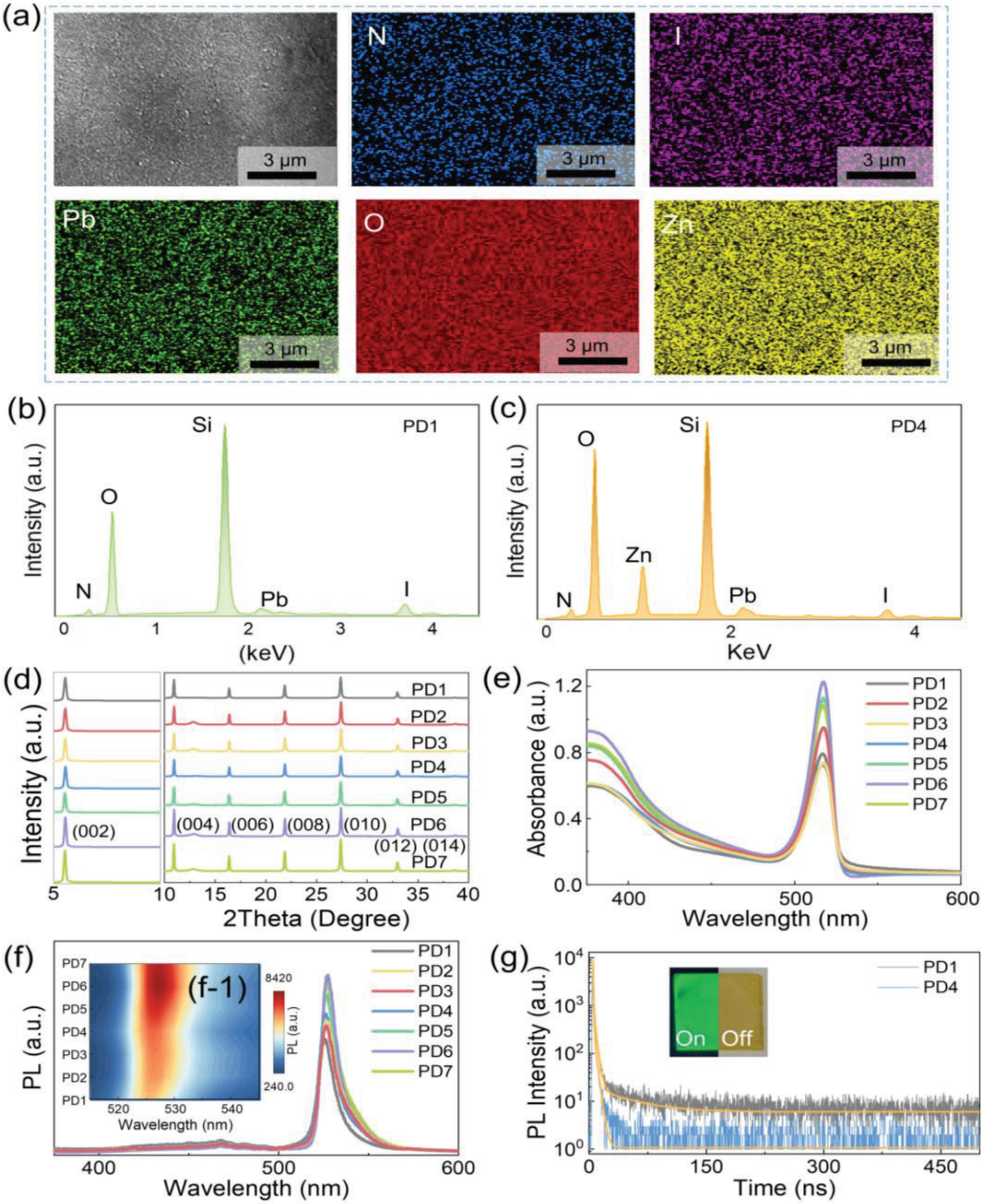

Figure 2. (**a**) Energy dispersive X-ray spectroscopy (EDS) element maps of the photodetector PD4. Energy dispersive X-ray spectroscopy (EDS) spectra of the photodetectors (**b**) PD1 and (**c**) PD4. (**d**) Corresponding X-ray diffraction (XRD) spectra. (**e**) Absorbance and (**f**) room-temperature PL spectra of the devices. (**f–1**) The contour maps of wavelength dependent PL for the devices. (**g**) Time-resolved photoluminescence (TRPL) spectra of the photodetectors PD1 and PD4. (Inset) The optical images of the sample under UV illumination (left) and white light (right).

Figure 3 shows the evolution of photoelectric performance of the hybrid ZnO QD/$(PEA)_2PbI_4$ nanosheet photodetectors as a function of ZnO QD concentrations, and the configuration of the device is depicted in Figure 3a. In order to deeply study the role of ZnO QD, the energy band diagram of the device is shown in Figure 3b. The conduction band minimum (E_C) and valence band maximum (E_V) of ZnO are 4.35 and 7.72 eV [39], and $(PEA)_2PbI_4$ possesses relatively higher E_C (3.48 eV) and E_V (5.71 eV) [40]. Thus, enhanced carrier separation can be correspondingly expected from $(PEA)_2PbI_4$ nanosheets to ZnO QDs under light illumination, overcoming the hindrance of charge transfer between isolated nanosheets within the thin films. As revealed in Figure 3c, the current in dark (I_{off}) of devices linearly elevated depending on the bias voltage without any barrier formation, and I_{off} was comparable among photodetectors, suggesting that incorporation of ZnO QD would not introduce extra noise. As shown in Figure 3d, the elevated photocurrent (I_{on}) was observed at each voltage with the increased ZnO QD concentrations from 0 to 0.097 mg/mL, resulting in a noticeable increase in I_{on} from 0.46 to 4.55 nA at 10 V under 500 nm illumination owing to improved carrier transportation induced by the efficient defect passivation and photoexcited electron separation. With the further increased concentration, the I_{on} gradually deteriorated to 0.76 nA when the concentration reached 0.776 mg/mL, as shown in Figure 3e, which can because the formation of undesirable ion scattering sites as a result of the aggregation of exceeded ZnO QDs at grain boundaries of $(PEA)_2PbI_4$ severely hindered the carrier transportation [41]. Correspondingly, the I_{on}/I_{off} ratio, an important metric to evaluate the antinoise capacity of photodetectors, radically increased by 13-folds from 78.3 to 1040 in comparison with the pristine device, as shown in Table 2. The responsivity (R_s) can be expressed as [42]:

$$R_S = \frac{I_{on} - I_{off}}{P \times S} \tag{3}$$

where P represents the light intensity (1.97 mW cm^{-2}), and S is the active area between the two electrodes (0.016 cm^{-2}). As shown in Figure 3f, the R_s is developed as a function of the ZnO QD concentrations, leading to the optimized R_s of 143.94 μA W^{-1} for the PD4 device. Given that the shot noise generally determines the total noise in photodetectors, the normalized detectivity (D^*) becomes a crucial metric for the evaluation of the devices, which can be given with [43]:

$$D^* = \frac{I_{on} - I_{off}}{P} \times \sqrt{\frac{1}{2 \times e \times S \times I_{off}}} \tag{4}$$

where e denotes the elementary charge (1.6×10^{-19} C). In contrast to the pristine device (PD1), the D^* of the PD4 device obviously elevated from 1.31×10^9 to 1.54×10^{10} Jones, as shown in Figure 3f, and the D^* gradually decreased along with the further increased ZnO QD concentration due to the strictly deteriorated I_{on}. The conversion efficiency of incident photons into electrons for photodetectors can be determined by the external quantum efficiency (EQE) [44]:

$$EQE = \frac{hc}{e\lambda} \times R_s \times 100\% \tag{5}$$

where h, c, and λ represent the Planck's constant, the velocity of light in a vacuum, and the wavelength of irradiated light, respectively. Similar to R_s, the EQE markedly boosted from 0.0035% to 0.0357% when the ZnO QD concentration increased from 0 to 0.097 mg/mL, and the deterioration in EQE was observed with further increased concentration as evidenced with Figure S3a.

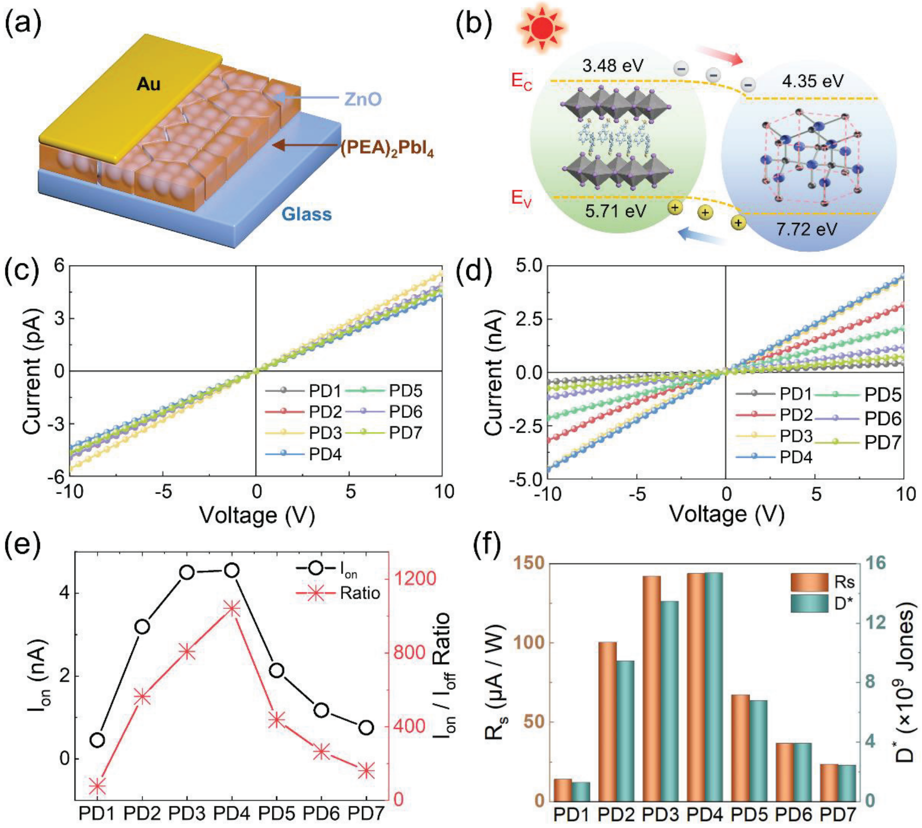

Figure 3. The photoelectric performance of the devices. (**a**) Scheme of the configuration and (**b**) the energy-band diagram of the ZnO QD/$(PEA)_2PBI_4$ nanosheet photodetector. I-V characteristics of the devices (**c**) in the dark (I_{off}) and (**d**) under illumination (I_{on}) of 500 nm UV light (1.97 mW cm^{-2}). (**e**) The I_{on} and I_{on}/I_{off} ratio of each device. (**f**) Responsivity (R_s) and normalized detectivity (D *) of each device with different contents of ZnO QDs.

Table 2. Summary of the Rs, D^*, I_{on}/I_{off} ratio, τ_{rise}, and τ_{fall} of each photodetector at 10 V bias voltage and under 500 nm light illumination.

Photodetectors	R_s (μA/W)	D^* ($\times 10^9$ Jones)	I_{on}/I_{off} Ratio	τ_{rise} (ms)	τ_{fall} (ms)
PD1	14.21	1.32	78.3	95.8	106.8
PD2	100.73	9.48	564	69.1	46.7
PD3	142.40	13.50	809	126.7	53.0
PD4	143.94	15.40	1040	53.3	87.0
PD5	67.45	6.82	437	69.0	87.7
PD6	36.99	3.93	265	42.9	89.0
PD7	23.77	2.46	173	69.1	88.2
PD8	39.81	1.73	48.6	53.3	86.6
PD9	88.31	3.96	113	37.3	72.8
PD10	130.88	9.87	473	53.4	82.1
PD11	131.11	8.88	381	53.2	92.3

The development of photoelectric performance for the photodetectors depending on the ZnO QD concentrations was further investigated at various spectrum wavelengths from

300 to 600 nm and testing periods, as shown in Figure 4. As observed in Figure 4a, the effect of ZnO QD concentrations on the R_s was consistently witnessed throughout the whole response spectra between 300 and 550 nm, and the R_s of the device PD4 was consequently superior to the photodetectors at each wavelength. Particularly, the optimized R_s was obtained at 500 nm for most devices, and the R_s of the devices PD4 (374.57 μA W^{-1}) at 300 nm was evidently higher than that at 500 nm (143.94 μA W^{-1}), which can be ascribed to the additional photogenerated carriers from ZnO QDs under UV illumination. As a result, the similar behaviors of D^* and EQE were observed depending on the variation of spectrum wavelengths, as shown in Figure S3b,c, indicating that blending with ZnO QDs can be an advantageous strategy for the improved performance for the 2D perovskite photodetectors over a broad wavelength range. As shown in Figure S3d, the I_{on}/I_{off} ratio of the device PD4 was always higher than that of the device PD1, and the decreased ratios below 375 nm were derived from the unfavorable excitation at much lower light intensities. The photodetector PD4 remained at excellent stability with a negligible deterioration after a continuous test of 50 cycles in the air, as evidenced in Figure 4b. The τ_{rise} (the period for the current elevated from 10% to 90% of the I_{on}) and τ_{fall} (the period for the current declined from 90% to 10% of the I_{on}) of each photodetector was within 150 ms, as shown in Figure 4c–i. Compared with the pristine device, the photodetectors fabricated with ZnO QDs exhibited faster τ_{rise} and τ_{fall}, suggesting accelerated carrier mobility within the hybrid thin films.

The evolution of the morphological and optical characteristics of ZnO QD/$(PEA)_2PbI_4$ nanosheet hybrid thin films fabricated with an identical ZnO QD concentration of 0.097 mg/mL was investigated with a variation of annealing temperatures from room temperature to 140 °C, as shown in Figure 5. As shown in Figure 5a–c, the uniform and dense morphology was evenly observed at each temperature, and agglomeration gradually occurred along with the increased temperature, which can be beneficial for the crystallization of the hybrid perovskite thin films [45–47]. Above 120 °C, the severe truncation was observed between grains, as shown in Figure 5d, which can be induced by the partially melt crystallization of $(PEA)_2PbI_4$ [48]. As shown in Figure 5e, there was a slight red shift of the exciton absorption peak as a function of annealing temperature, and thus, the bandgap gradually decreased from 2.368 eV to 2.362 eV due to the expansion of grain size [49], as shown in Figure 5f. As observed in Figure 5g, the PL peak initially descended depending on the annealing temperature induced by the intensified surface scattering along with morphological development, and peak intensity slightly ascended above 120 °C as a result of decreased roughness along with the melt crystallization [50]. In addition, the characteristic peaks were similarly observed without any shift depending on annealing temperatures, and the (002) peak increased after annealing in comparison with the thin films fabricated at room temperature, suggesting a preferential crystallization along [002], as evidenced in Figure 5h.

The temperature effect on the photoelectric performance of the ZnO QD/$(PEA)_2PbI_4$ nanosheet hybrid photoreactors is shown in Figure 6. As shown in Figure 6a, the I_{off} was slightly higher at relatively lower temperatures within the whole bias range due to the denser morphology, and superior I_{on} was constantly obtained with the PD4 device at each bias as observed in Figure 6b, manifesting a sufficient temperature for the high crystallinity (PEA)2PbI4 thin films at 120 °C. Therefore, the Ion at 10 V was elevated by 3.6-folds from room temperature to 120 °C, and the Ion/Ioff ratio correspondingly increased by 21.4-folds as shown in Figure 6c. Depending on the annealing temperature, a comparable trend was witnessed with the Rs, D^*, and EQE, as shown in Figure 6d–e. The increase was likewise observed for each metric as a function of temperature, and slight decreases occurred above 120 °C. As evidenced in Figures 6f and S4, the response time was similar for the devices fabricated at various temperatures, suggesting that the ZnO concentration played a more critical role in the response speed than the annealing temperature. As shown in Figure 7, the photodetector fabricated at 120 °C exhibited an optimized performance and a slowly declining response for each device depending on the wavelength derived from the effect of ZnO QDs. Correspondingly, the R_s, D *, and EQE of the PD4 device were 374 μA W^{-1}, 4.01×10^{10} Jones, and 0.1548% at 300 nm, respectively. As summarized in Table 3, the ZnO QD/$(PEA)_2PbI_4$ nanosheet hybrid photodetector PD4 possessed an outstanding performance among perovskite photodetectors [51–59], offering an approach for the fabrication of high-performance perovskite photodetectors with excellent stability.

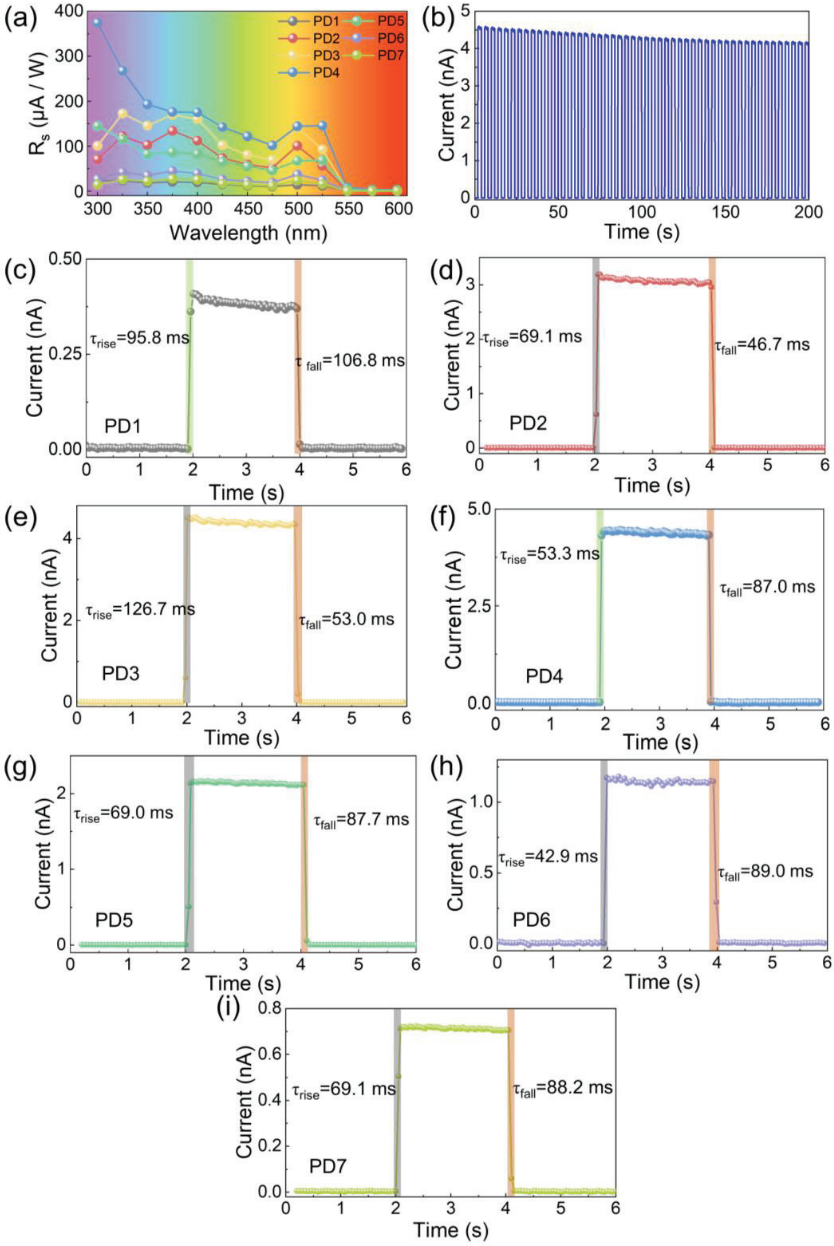

Figure 4. (**a**) The responsivity (R_s) of the photodetectors within a broadband spectrum wavelength. (**b**) Transient response of the device PD4 within multiple test cycles. Single-period response of the photodetectors (**c**) PD1, (**d**) PD2, (**e**) PD3, (**f**) PD4, (**g**) PD5, (**h**) PD6, and (**i**) PD7 under 500 nm light irradiation at 10 V bias voltage.

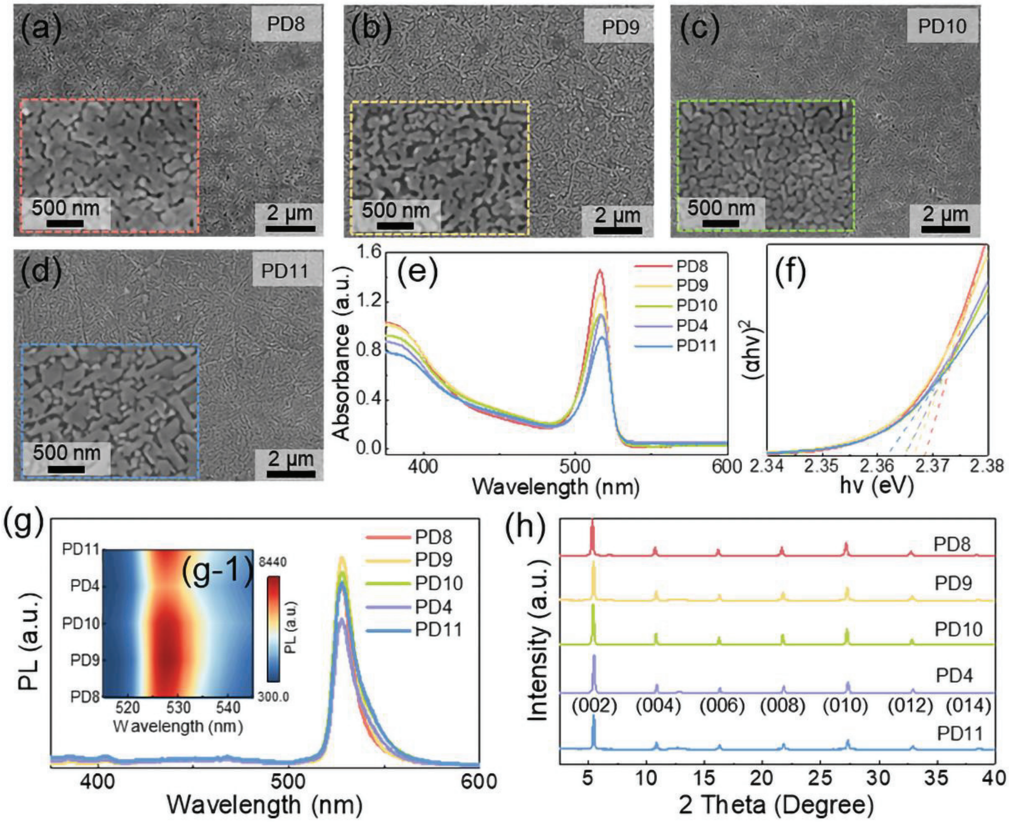

Figure 5. SEM images of the ZnO QD/(PEA)$_2$PBI$_4$ nanosheet devices fabricated with a 0.097 mg/mL ZnO QD chloroform antisolvent at different annealing temperatures: (**a**) room temperature (PD8), (**b**) 80 °C (PD9), (**c**) 100 °C (PD10), and (**d**) 140 °C (PD11). (**e**) Absorbance spectra and (**f**) Tauc plots of the samples. (**g**) The PL spectra and (**g-1**) the contour maps of wavelength-dependent PL for the devices. (**h**) XRD spectra of each sample.

Table 3. Comparison of the photodetector performance created from different perovskite materials.

Materials	I_{off} (nA)	Bias (V)	I_{on}/I_{off} Ratio	D^* ($\times 10^9$ Jones)	Ref.
$CH_3NH_3PbI_3$	1	1	3.05	900	[51]
CsPbBr3	0.488	2	1.7×10^6	0.456	[52]
$(PA)_2(MA)Pb_2I_7$	~0.1	10	$>10^3$	29.2	[53]
$MAPbI_3$	$>10^2$	15	1100	12	[54]
$(PEA)_2PbI_4$, MoS_2	$\sim 10^3$	3	500	8.09	[55]
BDAPbI4	$>10^{-2}$	10	/	~1	[56]
$MAPbI_{3\text{-}x}Br_x$	4	4	<10	20	[57]
$EA_4Pb_3Cl_{10}$	/	5	$\sim 10^4$	3.06	[58]
$(PEA)_2PbI_4$	$\sim 10^{-3}$	5	10.8	1070	[59]
$(PEA)_2PbI_4$, ZnO	4.37×10^{-3}	10	1040	15.40	This Work

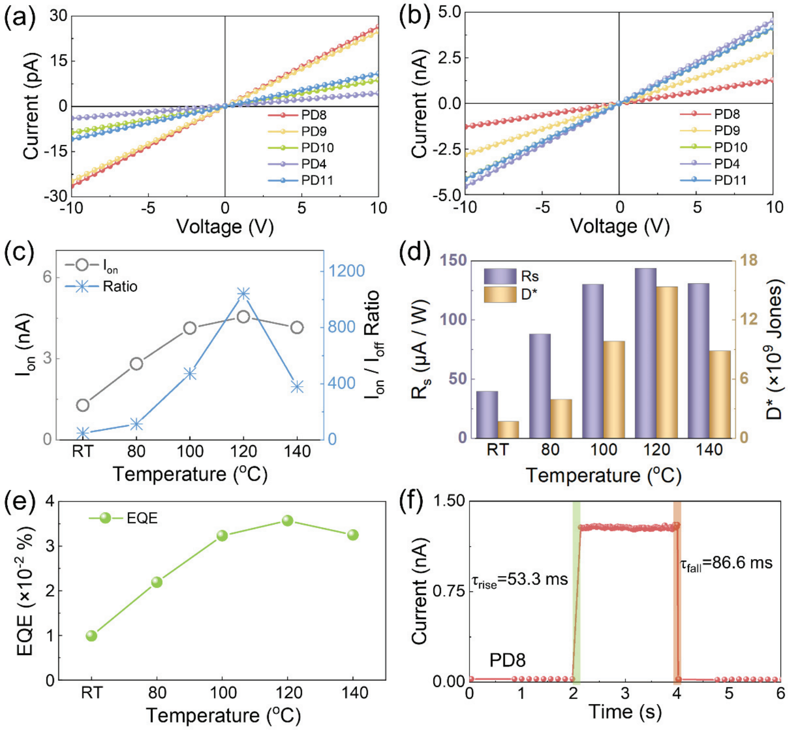

Figure 6. The photoelectric performance of the photodetectors fabricated at various annealing temperatures. I-V characteristics of the devices (**a**) in the dark and (**b**) irradiated under 500 nm UV light (1.97 mW cm^{-2}). (**c**) The plots of I_{on} and I_{on}/I_{off} ratio for each device. (**d**) R_s, D*, and (**e**) external quantum efficiency (EQE) of each device fabricated at distinct temperatures. (**f**) The transient response within a single period for the photodetector PD.

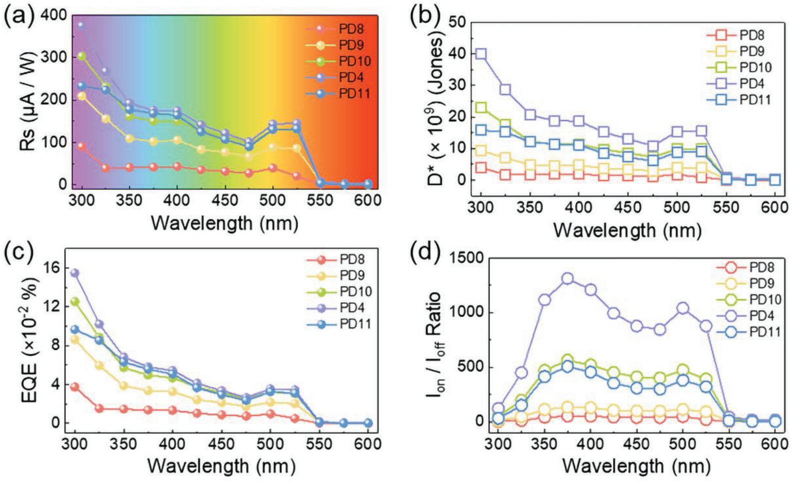

Figure 7. The spectrum dependent (**a**) responsivity (R_s), (**b**) normalized detectivity (D*), (**c**) external quantum efficiency (EQE), (**d**) I_{on}/I_{off} ratio plots with different annealing temperature.

4. Conclusions

In summary, the 0D ZnO quantum dot (QD)/2D $(PEA)_2PbI_4$ nanosheet hybrid photodetectors were fabricated via a facile ZnO QD chloroform antisolvent method under atmospheric conditions. Benefiting from the distinctive difference in polarity between the antisolvent and precursor solutions, the crystallization of the $(PEA)_2PbI_4$ thin films was effectively improved as a result of the accelerated nucleation site formation and grain growth rates. The uniform ornamentation of ZnO QDs on $(PEA)_2PbI_4$ nanosheets provided an in situ surface passivation for the surface defects as evidenced by the TRPL decay fitting, and the carrier transportation within the perovskite thin films was concurrently enhanced with the intensified charge separation induced by the well-balanced energy band levels. As a consequence, the photoelectric performance of ZnO QD/$(PEA)_2PbI_4$ nanosheet hybrid photodetectors sensitively developed with a variation of ZnO QD concentrations, resulting in excellent D * of 1.54×10^{10} Jones and I_{on}/I_{off} ratio of 1040 for the device fabricated with the 0.097 mg/mL ZnO QD antisolvent.

The annealing temperature-dependent behavior of photoconductive devices originated from the surface morphological evolution of the perovskite thin films, and the photodetector fabricated at 120 °C maintained a fast response speed within 100 ms and outstanding atmospheric stability after a 50-cycle test, offering a facile yet effective strategy for the ever-increasing demand for highly sensitive and long-term stable photodetection based on low-dimensional perovskites.

Supplementary Materials: The following supporting information can be downloaded at: https://www.mdpi.com/article/10.3390/nano12234217/s1, Figure S1: (a,b) Transmission electron microscope (TEM) images with different magnifications of ZnO QD decorated $(PEA)_2PBI_4$ nanosheets. (c) The selected area electron diffraction (SAED) pattern of the nanosheets. (d) Scanning electron microscope (SEM) images of the ZnO QD/$(PEA)_2PBI_4$ nanosheet sample blended with a proportion of 0.776 mg/mL ZnO QDs. Atomic force microscopy (AFM) images of the samples with different ZnO QD concentrations: (e) PD1 (0 mg/mL) and (f) PD4 (0.097 mg/mL); Figure S2: Tauc plot of the device blended with different proportions of ZnO QDs. Figure S3: (a) The plots of external quantum efficiency (EQE) for each device with different contents of ZnO QDs acquired at 500 nm. (b) The spectrum-dependent normalized detectivity (D *), (c) external quantum efficiency (EQE), and (d) I_{on}/I_{off} ratio plots with different contents of ZnO QDs. Figure S4: The single-period responses of the devices fabricated at (a) 80 °C (PD9), (b) 100 °C (PD10), and (c) 140 °C (PD11), respectively.

Author Contributions: M.-Y.L., S.L. (Sisi Liu) and C.W. participated in the experiment design; M.-Y.L., S.L. (Shijie Liu), H.L. (Hao Li) and Y.W. performed the experiment; H.L. (Haifei Lu) and S.D. participated in data processing and analysis; S.L. (Shijie Liu), X.W. and X.L. participated in characterization; S.L. (Shijie Liu) and M.-Y.L. wrote the manuscript. All authors have read and agreed to the published version of the manuscript.

Funding: This research was supported by the National Key Research and Development Program of China (2019YFE0121800 and 2021YFF0603500), the National Natural Science Foundation of China (grant No. 61705070, 11974266, 62075174, and 11704293), and the Fundamental Research Funds for the Central Universities (WUT:2021VA056).

Data Availability Statement: The data is available upon reasonable request from the corresponding author.

Conflicts of Interest: The authors declare no conflict of interest.

References

1. Ghosh, S.; Kumar, H.; Mukhopadhyay, B.; Chang, G.-E. Design and Modeling of High-Performance DBR-Based Resonant-Cavity-Enhanced GeSn Photodetector for Fiber-Optic Telecommunication Networks. *IEEE Sens. J.* **2021**, *21*, 9900–9908. [CrossRef]
2. Dong, T.; Simões, J.; Yang, Z. Flexible Photodetector Based on 2D Materials: Processing, Architectures, and Applications. *Adv. Mater. Interfaces* **2020**, *7*, 1901657. [CrossRef]
3. Bartolo-Perez, C.; Chandiparsi, S.; Mayet, A.S.; Cansizoglu, H.; Gao, Y.; Qarony, W.; AhAmed, A.; Wang, S.-Y.; Cherry, S.R.; Saif Islam, M.; et al. Avalanche Photodetectors with Photon Trapping Structures for Biomedical Imaging Applications. *Opt. Express* **2021**, *29*, 19024. [CrossRef]

4. Zhang, Y.; Hu, M.; Wang, Z. Enhanced Performances of P-Si/N-ZnO Self-Powered Photodetector by Interface State Modification and Pyro-Phototronic Effect. *Nano Energy* **2020**, *71*, 104630. [CrossRef]
5. Chen, J.; Ouyang, W.; Yang, W.; He, J.; Fang, X. Recent Progress of Heterojunction Ultraviolet Photodetectors: Materials, Integrations, and Applications. *Adv. Funct. Mater.* **2020**, *30*, 1909909. [CrossRef]
6. Li, J.; Zhang, G.; Zhang, Z.; Li, J.; Uddin, Z.; Zheng, Y.; Shao, Y.; Yuan, Y.; Yang, B. Defect Passivation via Additive Engineering to Improve Photodetection Performance in $CsPbI_2Br$ Perovskite Photodetectors. *ACS Appl. Mater. Interfaces* **2021**, *13*, 56358–56365. [CrossRef] [PubMed]
7. Yu, J.; Liu, G.; Chen, C.; Li, Y.; Xu, M.; Wang, T.; Zhao, G.; Zhang, L. Perovskite CsPbBr3 Crystals: Growth and Applications. *J. Mater. Chem. C* **2020**, *8*, 6326–6341. [CrossRef]
8. Loi, H.; Cao, J.; Guo, X.; Liu, C.; Wang, N.; Song, J.; Tang, G.; Zhu, Y.; Yan, F. Gradient 2D/3D Perovskite Films Prepared by Hot-Casting for Sensitive Photodetectors. *Adv. Sci.* **2020**, *7*, 2000776. [CrossRef]
9. Zhang, Y.; Li, S.; Li, Z.; Liu, H.; Liu, X.; Chen, J.; Fang, X. High-Performance Two-Dimensional Perovskite $ca_2Nb_3O_{10}$ UV Photodetectors. *Nano Lett.* **2020**, *21*, 382–388. [CrossRef] [PubMed]
10. Wang, Y.; Ma, Z.-Z.; Li, Y.; Zhang, F.; Chen, X.; Shi, Z.-F. Low-Dimensional Phases Engineering for Improving the Emission Efficiency and Stability of Quasi-2D Perovskite Films*. *Chin. Phys. B* **2021**, *30*, 067802. [CrossRef]
11. Yue, Y.; Li, M.; Li, H.; Chai, N.; Dong, Y.; Li, Z.; Chen, X.; Wang, X. One-Step Anti-Solvent Associated Method for High Performance Two-Dimensional Perovskite Photodetectors Fabrication at Low Temperature. *Chem. Eng. J.* **2022**, *441*, 135997. [CrossRef]
12. Cheng, B.; Li, T.-Y.; Wei, P.-C.; Yin, J.; Ho, K.-T.; Retamal, J.R.D.; Mohammed, O.F.; He, J.-H. Layer-Edge Device of Two-Dimensional Hybrid Perovskites. *Nat. Commun.* **2018**, *9*, 5196. [CrossRef] [PubMed]
13. Malekshahi Byranvand, M.; Behboodi-Sadabad, F.; Alrhman Eliwi, A.; Trouillet, V.; Welle, A.; Ternes, S.; Hossain, I.M.; Khan, M.R.; Schwenzer, J.A.; Farooq, A.; et al. Chemical Vapor Deposited Polymer Layer for Efficient Passivation of Planar Perovskite Solar Cells. *J. Mater. Chem. A* **2020**, *8*, 20122–20132. [CrossRef]
14. Liang, Y.; Shang, Q.; Wei, Q.; Zhao, L.; Liu, Z.; Shi, J.; Zhong, Y.; Chen, J.; Gao, Y.; Li, M.; et al. Lasing from Mechanically Exfoliated 2D Homologous Ruddlesden–Popper Perovskite Engineered by Inorganic Layer Thickness. *Adv. Mater.* **2019**, *31*, 1903030. [CrossRef] [PubMed]
15. Zanca, C.; Piazza, V.; Agnello, S.; Patella, B.; Ganci, F.; Aiello, G.; Piazza, S.; Sunseri, C.; Inguanta, R. Controlled Solution-Based Fabrication of Perovskite Thin Films Directly on Conductive Substrate. *Thin Solid Film.* **2021**, *733*, 138806. [CrossRef]
16. Jha, S.; Hasan, M.; Khakurel, N.; Ryan, C.A.; McMullen, R.; Mishra, A.; Malko, A.V.; Zakhidov, A.A.; Slinker, J.D. Electrochemical Characterization of Halide Perovskites: Stability & Doping. *Mater. Today Adv.* **2022**, *13*, 100213. [CrossRef]
17. Di Girolamo, D.; Dini, D. Electrodeposition as a Versatile Preparative Tool for Perovskite Photovoltaics: Aspects of Metallization and Selective Contacts/Active Layer Formation. *Sol. RRL* **2022**, *6*, 2100993. [CrossRef]
18. Swartwout, R.; Hoerantner, M.T.; Bulović, V. Scalable Deposition Methods for Large-Area Production of Perovskite Thin Films. *Energy Environ. Mater.* **2019**, *2*, 119–145. [CrossRef]
19. Fang, F.; Wan, Y.; Li, H.; Fang, S.; Huang, F.; Zhou, B.; Jiang, K.; Tung, V.; Li, L.-J.; Shi, Y. Two-Dimensional $Cs_2AgBiBr_6/WS_2$ Heterostructure-Based Photodetector with Boosted Detectivity via Interfacial Engineering. *ACS Nano* **2022**, *16*, 3985–3993. [CrossRef] [PubMed]
20. Subramanian, A.; Akram, J.; Hussain, S.; Chen, J.; Qasim, K.; Zhang, W.; Lei, W. High-Performance Photodetector Based on a Graphene Quantum Dot/$CH_3NH_3PbI_3$ Perovskite Hybrid. *ACS Appl. Electron. Mater.* **2019**, *2*, 230–237. [CrossRef]
21. Li, H.; Li, Z.; Liu, S.; Li, M.; Wen, X.; Lee, J.; Lin, S.; Li, M.-Y.; Lu, H. High Performance Hybrid MXene Nanosheet/CsPbBr3 Quantum Dot Photodetectors with an Excellent Stability. *J. Alloys Compd.* **2022**, *895*, 162570. [CrossRef]
22. Wu, D.; Wang, Y.; Ma, N.; Cao, K.; Zhang, W.; Chen, J.; Wang, D.; Gao, Z.; Xu, F.; Jiang, K. Single-Crystal-like ZnO Mesoporous Spheres Derived from Metal Organic Framework Delivering High Electron Mobility for Enhanced Energy Conversion and Storage Performances. *Electrochim. Acta* **2019**, *305*, 474–483. [CrossRef]
23. Shen, K.; Li, X.; Xu, H.; Wang, M.; Dai, X.; Guo, J.; Zhang, T.; Li, S.; Zou, G.; Choy, K.-L.; et al. Enhanced Performance of ZnO Nanoparticle Decorated All-Inorganic $CsPbBr_3$ Quantum Dot Photodetectors. *J. Mater. Chem. A* **2019**, *7*, 6134–6142. [CrossRef]
24. Li, Z.; Yu, X.; Zhu, Y.; Liu, S.; Wen, X.; Lu, H.; Wang, C.; Li, X.; Li, M.-Y.; Yang, Y. High Performance ZnO Quantum Dot (QD)/ Magnetron Sputtered ZnO Homojunction Ultraviolet Photodetectors. *Appl. Surf. Sci.* **2022**, *582*, 152352. [CrossRef]
25. Li, L.; Liu, J.; Zeng, M.; Fu, L. Space-Confined Growth of Metal Halide Perovskite Crystal Films. *Nano Res.* **2020**, *14*, 1609–1624. [CrossRef]
26. Huang, F.; Siffalovic, P.; Li, B.; Yang, S.; Zhang, L.; Nadazdy, P.; Cao, G.; Tian, J. Controlled Crystallinity and Morphologies of 2D Ruddlesden-Popper Perovskite Films Grown without Anti-Solvent for Solar Cells. *Chem. Eng. J.* **2020**, *394*, 124959. [CrossRef]
27. Jung, M.H. Exploration of Two-Dimensional Perovskites Incorporating Methylammonium for High Performance Solar Cells. *CrystEngComm* **2021**, *23*, 1181–1200. [CrossRef]
28. Singh, A.K.; Pal, P.; Gupta, V.; Yadav, T.P.; Gupta, V.; Singh, S.P. Green Synthesis, Characterization and Antimicrobial Activity of Zinc Oxide Quantum Dots Using Eclipta Alba. *Mater. Chem. Phys.* **2018**, *203*, 40–48. [CrossRef]
29. Yang, S.; Niu, W.; Wang, A.-L.; Fan, Z.; Chen, B.; Tan, C.; Lu, Q.; Zhang, H. Ultrathin Two-Dimensional Organic-Inorganic Hybrid Perovskite Nanosheets with Bright, Tunable Photoluminescence and High Stability. *Angew. Chem. Int. Ed.* **2017**, *56*, 4252–4255. [CrossRef]

30. Lan, J.; Lv, J.; Feng, J. Identification of Chrome Pigments in Paints with Fourier Transform Infrared Spectroscopy (FTIR), Confocal Raman Microscopy, and Scanning Electron Microscope-Energy Dispersive Spectrometer. *Environ. Forensics* **2013**, *14*, 81–86. [CrossRef]
31. Sánchez, J.D.G.; Messina, S.; Álvarez, J.C.; Nair, P.K. Optical Absorption and Light-Generated Current Density in Chemically Deposited Antimony Sulfide Selenide Thin Films Used for Solar Cell Development. *J. Mater. Sci. Mater. Electron.* **2022**, *33*, 12026–12038. [CrossRef]
32. Hu, R.; Zhang, Y.; Paek, S.; Gao, X.-X.; Li, X.; Nazeeruddin, M.K. Enhanced Stability of α-Phase $FAPbI_3$ Perovskite Solar Cells by Insertion of 2D $(PEA)_2PbI_4$ Nanosheets. *J. Mater. Chem. A* **2020**, *8*, 8058–8064. [CrossRef]
33. Adhikari, N.; Dubey, A.; Gaml, E.A.; Vaagensmith, B.; Reza, K.M.; Mabrouk, S.A.A.; Gu, S.; Zai, J.; Qian, X.; Qiao, Q. Crystallization of a Perovskite Film for Higher Performance Solar Cells by Controlling Water Concentration in Methyl Ammonium Iodide Precursor Solution. *Nanoscale* **2016**, *8*, 2693–2703. [CrossRef]
34. Tu, Y.; Xu, Y.; Li, J.; Hao, Q.; Liu, X.; Qi, D.; Bao, C.; He, T.; Gao, F.; Zhang, W. Ultrathin Single-Crystalline 2D Perovskite Photoconductor for High-Performance Narrowband and Wide Linear Dynamic Range Photodetection. *Small* **2020**, *16*, 2005626. [CrossRef]
35. Song, J.; Fang, T.; Li, J.; Xu, L.; Zhang, F.; Han, B.; Shan, Q.; Zeng, H. Organic–Inorganic Hybrid Passivation Enables Perovskite QLEDs with an EQE of 16.48%. *Adv. Mater.* **2018**, *30*, 1805409. [CrossRef]
36. Chen, H.; Guo, A.; Zhu, J.; Cheng, L.; Wang, Q. Tunable Photoluminescence of $CsPbBr_3$ Perovskite Quantum Dots for Their Physical Research. *Appl. Surf. Sci.* **2019**, *465*, 656–664. [CrossRef]
37. Zhou, L.; Yu, K.; Yang, F.; Cong, H.; Wang, N.; Zheng, J.; Zuo, Y.; Li, C.; Cheng, B.; Wang, Q. Insight into the Effect of Ligand-Exchange on Colloidal $CsPbBr_3$ Perovskite Quantum Dot/Mesoporous-TiO_2 Composite-Based Photodetectors: Much Faster Electron Injection. *J. Mater. Chem. C* **2017**, *5*, 6224–6233. [CrossRef]
38. Liu, H.; Wang, C.; Liu, D.; Luo, J. Neutral and Defect-Induced Exciton Annihilation in Defective Monolayer WS_2. *Nanoscale* **2019**, *11*, 7913–7920. [CrossRef] [PubMed]
39. Yang, L.; Wang, Y.; Xu, H.; Liu, W.; Zhang, C.; Wang, C.; Wang, Z.; Ma, J.; Liu, Y. Color-Tunable ZnO/GaN Heterojunction LEDs Achieved by Coupling with Ag Nanowire Surface Plasmons. *ACS Appl. Mater. Interfaces* **2018**, *10*, 15812–15819. [CrossRef]
40. Zhu, L.; Lu, Q.; Li, C.; Wang, Y.; Deng, Z. Graded Interface Engineering of 3D/2D Halide Perovskite Solar Cells through Ultrathin (PEA)2PbI4 Nanosheets. *Chin. Chem. Lett.* **2021**, *32*, 2259–2262. [CrossRef]
41. Lee, S.-W.; Cha, S.-H.; Choi, K.-J.; Kang, B.-H.; Lee, J.-S.; Kim, S.-W.; Kim, J.-S.; Jeong, H.-M.; Gopalan, S.-A.; Kwon, D.-H.; et al. Low Dark-Current, High Current-Gain of PVK/ZnO Nanoparticles Composite-Based UV Photodetector by PN-Heterojunction Control. *Sensors* **2016**, *16*, 74. [CrossRef]
42. Yang, Q.; Guo, X.; Wang, W.; Zhang, Y.; Xu, S.; Lien, D.H.; Wang, Z.L. Enhancing Sensitivity of a Single ZnO Micro-/Nanowire Photodetector by Piezo-Phototronic Effect. *ACS Nano* **2010**, *4*, 6285–6291. [CrossRef] [PubMed]
43. Gong, X.; Tong, M.; Xia, Y.; Cai, W.; Moon, J.S.; Cao, Y.; Yu, G.; Shieh, C.-L.; Nilsson, B.; Heeger, A.J. High-Detectivity Polymer Photodetectors with Spectral Response from 300 nm to 1450 nm. *Science* **2009**, *325*, 1665–1667. [CrossRef]
44. Xiao, H.; Liang, T.; Xu, M. Growth of Ultraflat PbI_2 Nanoflakes by Solvent Evaporation Suppression for High-Performance UV Photodetectors. *Small* **2019**, *15*, 1901767. [CrossRef] [PubMed]
45. Bi, C.; Shao, Y.; Yuan, Y.; Xiao, Z.; Wang, C.; Gao, Y.; Huang, J. Understanding the Formation and Evolution of Interdiffusion Grown Organolead Halide Perovskite Thin Films by Thermal Annealing. *J. Mater. Chem. A* **2014**, *2*, 18508–18514. [CrossRef]
46. Ma, W.; Yang, C.; Gong, X.; Lee, K.; Heeger, A.J. Thermally Stable, Efficient Polymer Solar Cells with Nanoscale Control of the Interpenetrating Network Morphology. *Adv. Funct. Mater.* **2005**, *15*, 1617–1622. [CrossRef]
47. Hsu, C.-J.; Duan, H.-S.; Yang, W.; Zhou, H.; Yang, Y. Benign Solutions and Innovative Sequential Annealing Processes for High Performance Cu2ZnSn(Se,S)4Photovoltaics. *Adv. Energy Mater.* **2013**, *4*, 1301287. [CrossRef]
48. Yu, J.C.; Kim, D.W.; Kim, D.B.; Jung, E.D.; Park, J.H.; Lee, A.-Y.; Lee, B.R.; Di Nuzzo, D.; Friend, R.H.; Song, M.H. Improving the Stability and Performance of Perovskite Light-Emitting Diodes by Thermal Annealing Treatment. *Adv. Mater.* **2016**, *28*, 6906–6913. [CrossRef] [PubMed]
49. Venkataprasad Bhat, S.; Vivekchand, S.R.C.; Govindaraj, A.; Rao, C.N.R. Photoluminescence and Photoconducting Properties of ZnO Nanoparticles. *Solid State Commun.* **2009**, *149*, 510–514. [CrossRef]
50. Yang, L.; Zhang, Y.; Ruan, W.; Zhao, B.; Xu, W.; Lombardi, J.R. Improved Surface-Enhanced Raman Scattering Properties of TiO_2Nanoparticles by Zn Dopant. *J. Raman Spectrosc.* **2009**, *41*, 721–726. [CrossRef]
51. Cao, F.; Tian, W.; Gu, B.; Ma, Y.; Lu, H.; Li, L. High-Performance UV–Vis Photodetectors Based on Electrospun ZnO Nanofiber-Solution Processed Perovskite Hybrid Structures. *Nano Res.* **2017**, *10*, 2244–2256. [CrossRef]
52. Dong, Y.; Gu, Y.; Zou, Y.; Song, J.; Xu, L.; Li, J.; Xue, J.; Li, X.; Zeng, H. Improving All-Inorganic Perovskite Photodetectors by Preferred Orientation and Plasmonic Effect. *Small* **2016**, *12*, 5622–5632. [CrossRef]
53. Han, S.; Wang, P.; Zhang, J.; Liu, X.; Sun, Z.; Huang, X.; Li, L.; Ji, C.; Zhang, W.; Teng, B.; et al. Exploring a Polar Two-Dimensional Multi-Layered Hybrid Perovskite of $(C_5H_{11}NH_3)_2(CH_3NH_3)Pb_2I_7$ for Ultrafast-Responding Photodetection. *Laser Photonics Rev.* **2018**, *12*, 1800060. [CrossRef]
54. Maculan, G.; Sheikh, A.D.; Abdelhady, A.L.; Saidaminov, M.I.; Haque, M.A.; Murali, B.; Alarousu, E.; Mohammed, O.F.; Wu, T.; Bakr, O.M. $CH_3NH_3PbCl_3$ Single Crystals: Inverse Temperature Crystallization and Visible-Blind UV-Photodetector. *J. Phys. Chem. Lett.* **2015**, *6*, 3781–3786. [CrossRef]

55. Fang, C.; Wang, H.; Shen, Z.; Shen, H.; Wang, S.; Ma, J.; Wang, J.; Luo, H.; Li, D. High-Performance Photodetectors Based on Lead-Free 2D Ruddlesden–Popper Perovskite/MoS_2 Heterostructures. *ACS Appl. Mater. Interfaces* **2019**, *11*, 8419–8427. [CrossRef] [PubMed]
56. Zhang, Y.; Liu, Y.; Xu, Z.; Yang, Z.; Liu, S. (Frank) 2D Perovskite Single Crystals with Suppressed Ion Migration for High-Performance Planar-Type Photodetectors. *Small* **2020**, *16*, 2003145. [CrossRef]
57. Fang, Y.; Dong, Q.; Shao, Y.; Yuan, Y.; Huang, J. Highly Narrowband Perovskite Single-Crystal Photodetectors Enabled by Surface-Charge Recombination. *Nat. Photonics* **2015**, *9*, 679–686. [CrossRef]
58. Wang, S.; Li, L.; Weng, W.; Ji, C.; Liu, X.; Sun, Z.; Lin, W.; Hong, M.; Luo, J. Trilayered Lead Chloride Perovskite Ferroelectric Affording Self-Powered Visible-Blind Ultraviolet Photodetection with Large Zero-Bias Photocurrent. *J. Am. Chem. Soc.* **2019**, *142*, 55–59. [CrossRef] [PubMed]
59. Lin, C.-H.; Cheng, B.; Li, T.-Y.; Retamal, J.R.D.; Wei, T.-C.; Fu, H.-C.; Fang, X.; He, J.-H. Orthogonal Lithography for Halide Perovskite Optoelectronic Nanodevices. *ACS Nano* **2018**, *13*, 1168–1176. [CrossRef] [PubMed]

nanomaterials

MDPI

Article

A Study on the Dynamic Tunning Range of CVD Graphene at Microwave Frequency: Determination, Prediction and Application

Hao Chen [1,2], Zhen-Guo Liu [1,2,3], Ming-Yang Geng [1,2], Xiang-Yu Meng [3,4], Wan-Lin Fu [4], Lu Ju [1,2,3], Bu-Yun Yu [1,2,3], Wu Yang [1,2,3], Yun-Qian Dai [3,4,*] and Wei-Bing Lu [1,2,3,*]

[1] State Key Laboratory of Millimeter Waves, School of Information Science and Engineering, Southeast University, Nanjing 210096, China
[2] Center for Flexible RF Technology, Frontiers Science Center for Mobile Information Communication and Security, Southeast University, Nanjing 210096, China
[3] Purple Mountain Laboratories, Nanjing 211111, China
[4] School of Chemistry and Chemical Engineering, Southeast University, Nanjing 210096, China
* Correspondence: daiy@seu.edu.cn (Y.-Q.D.); wblu@seu.edu.cn (W.-B.L.)

Abstract: In recent years, graphene has shown great application prospects in tunable microwave devices due to its tunable conductivity. However, the electromagnetic (EM) properties of graphene, especially the dynamic tunning characteristics, are largely dependent on experimental results, and thus are unable to be effectively predicted according to growth parameters, which causes great difficulties in the design of graphene-based tunable microwave devices. In this work, we systematically explored the impact of chemical vapor deposition (CVD) parameters on the dynamic tunning range of graphene. Firstly, through improving the existing waveguide method, the dynamic tunning range of graphene can be measured more accurately. Secondly, a direct mathematical model between growth parameters and the tunning range of graphene is established. Through this, one can easily obtain needed growth parameters for the desired tunning range of graphene. As a verification, a frequency tunable absorber prototype is designed and tested. The good agreement between simulation and experimental results shows the reliability of our mathematic model in the rapid design of graphene-based tunable microwave devices.

Keywords: graphene; CVD; tunning range; mathematic model; waveguide method

Citation: Chen, H.; Liu, Z.-G.; Geng, M.-Y.; Meng, X.-Y.; Fu, W.-L.; Ju, L.; Yu, B.-Y.; Yang, W.; Dai, Y.-Q.; Lu, W.-B. A Study on the Dynamic Tunning Range of CVD Graphene at Microwave Frequency: Determination, Prediction and Application. *Nanomaterials* **2022**, *12*, 4424. https://doi.org/10.3390/nano12244424

Academic Editor: Antonio Di Bartolomeo

Received: 10 November 2022
Accepted: 9 December 2022
Published: 11 December 2022

1. Introduction

Carbon-based materials are an important member of the material family, and their inherent excellent physical or chemical properties have attracted extensive attention in various disciplines and fields. Graphene, a planar monolayer of carbon atoms arranged in honeycomb structures, has recently sparked intense and multidisciplinary research since the advent of free-standing graphene in 2004 [1]. In terms of electromagnetic (EM) field, graphene provides a new perspective to realize active surfaces because the charge density on graphene can be electrically controlled by applying a DC voltage, which makes it outstanding in research on dynamic tunable devices, such as switches [2], regulators [3–5], plasma [6,7], stealth [8,9], beam steering [10–15], and absorbers [16–19]. Therefore, graphene has rapidly become a hot spot in the fields of materials, energy, and information technology.

The early research on graphene was mostly theoretical simulation, and its EM modeling was based on Kubo's formula [20]. During the design process, the researchers more or less ignored the feasibility of the experimental realization. Owing to the progress in manufacturing high-quality and large-scale graphene, microwave active devices based on graphene have been studied widely and constantly with experimental breakthroughs.

In 2010, roll-to-roll production of 30-inch graphene films using the chemical vapor deposition (CVD) approach was reported [21]. In 2015, the work from Bilkent University successfully modulated the conductivity of graphene at the decimeter scale using graphene sandwich structure (GSS) [22]. The emergence of these key technologies further prompted researchers to gradually shift the focus of graphene research from pure theoretical design to the combination of theory and experiment. In particular, microwave and millimeter-wave devices based on graphene have made certain progress in the world due to practical application requirements [14–19,23,24].

In the microwave range, graphene can be considered a frequency-independent resistive film [15], and its tunable sheet resistance can be controlled by applying bias voltage through GSS. This characteristic has been widely applied to the modeling and design of graphene-based microwave tunable devices, such as wavefront controllers [15], absorbers, [18,19], attenuators [25], etc. The tunning range of graphene not only provides the basis for the simulation and design of these works but also serves as an important basis for experimental feasibility, but the tunning range of graphene in these works shows apparent differences, which causes doubts in researchers' minds and is not conducive to the further application of graphene in microwave devices. In our previous work [26], the relationship between growth parameters and static sheet resistance of graphene was simply introduced. Many researchers are also committed to the study of the synthesis and also the physicochemical properties of graphene [27,28]. Raman, SEM and statistical techniques are applied to characterize the properties of graphene, such as the number of layers, growth uniformity, and so on. The microwave tunning property of graphene is largely dependent on its synthesis conditions, namely, the growth parameters for CVD process. However, the relationship between the dynamic tunning range of graphene and the growth parameters, which is of great importance to improve the design efficiency of graphene-related tunable devices, has never been studied in previously reported works. The main difficulty faced by the study of the relationship between the graphene tunning range and the growth parameters is twofold. Firstly, unlike the static sheet resistance of graphene, which can easily be obtained by the four-probe method, the dynamic sheet resistance of graphene cannot be accurately measured by existing methods because of the essential sandwich structure. Secondly, the CVD method is a sophisticated and time-consuming process, which brings trouble to either data collection or data processing.

To address these problems, in this work, firstly, with the help of transmission line theory, the measuring method of GSS is improved to help us obtain more precise tunning ranges of graphene. Secondly, the influence of growth parameters on the dynamic tunning property of graphene is investigated both qualitatively and quantitatively. To better reflect the numerical relation between the tunning and growth parameters, several statistical methods, including orthogonal experiment design [29,30] and multivariate nonlinear fitting [31,32], are adopted, based on which quantitative relations are given to easily obtain the desired tunable characteristic of graphene. At the end of this work, a tunable microwave absorber prototype is designed and used to verify the accuracy and availability of our model. The method adopted in this work is good guidance for following graphene-related works and has positive significance for promoting the combination of basic research and application research of two-dimensional (2D) materials.

2. Materials and Methods

Copper (25 μm) and CVD furnace (OTF 1200-X) were purchased from Hefei Kejing Material Technology Co. Ltd., Hefei, China, Hydrochloric acid (HCl, 36%) and nitric acid (HNO3, 70%) were purchased from Nanjing Wanqing Co. Ltd., Nanjing, China, Hydrogen (H2, 99.999%) and Methane (CH4, 99.999%) were purchased from Nanjing Shangyuan Co. Ltd., Nanjing, China, Polyvinyl chloride (PVC, 70 μm) was purchased from Shanghai Lingmin Trading Co. Ltd., Shanghai, China, Diaphragm paper (NKKTF4030) was purchased from Guangdong Canrd New Energy Technology Co. Ltd., Guangzhou, China.

Ionic liquid (methoxyethyldiethylmethylammomium bis((trifluoromethyl)sulfonyl)-imide, $C_{10}H_{20}F_6N_2O_5S_2$, CAS: 464927-84-2) was purchased from Lanzhou Institute of chemical physics. Wire mesh (125 µm, 0.5 Ω/sq) and Polydimethylsiloxane (PDMS, 1 mm) are purchased from CS New Materials Co., Ltd., Jining, China.

Large-area graphene is synthesized by CVD on copper foil. Copper foil is placed on a quartz holder in a CVD furnace. The mechanism of CVD on copper foil and the growth curve are shown in Figure 1a,b. After terminating the growth by stopping the flow of methane, the samples were cooled down to room temperature. Then we laminated 70-µm-thick PVC sheets on graphene-coated copper foils. Following the lamination, the copper foils were etched in diluted nitric acid solution and dried overnight to reduce the chemical doping of nitric acid on graphene. In order to meet the needs of subsequent measurements, the schematic diagram of the copper foil used to synthesize graphene is shown in Figure 1c. The size of each copper foil is 50 × 150 mm^2, which can be cut into two pieces, subsequently, the two pieces can be combined into a GSS, typical photographs of synthesized graphene are shown in Figure 1d.

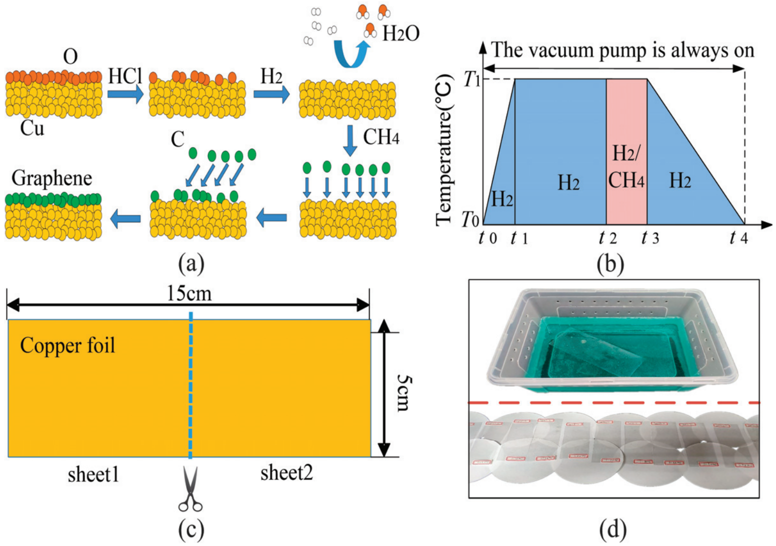

Figure 1. (**a**) Schematic diagram of CVD on copper foil. (**b**) Growth curve of graphene. (**c**) Schematic diagram of copper foil used to grow graphene. (**d**) Typical photographs during the synthesis of graphene. Upper: etching the copper foil in acid. Lower: obtained graphene samples on PVC substrate.

As shown in Figure 2a,b, the GSS structure made of PVC, graphene, and ionic liquid is used to realize dynamic control of graphene sheet resistance [15,18,19,22]. PVC acts as the transfer carrier of graphene. The diaphragm paper is used as the carrier of ionic liquid, then the positive and negative electrodes are applied to upper graphene and lower graphene respectively. The ions of the electrolyte (ionic liquid) have very low mobility; therefore, they cannot respond to the electric field of microwaves. When the electrostatic field bias is applied, the electrolyte layer polarizes and ionic double layers form on the graphene–electrolyte interface with opposite polarizations, then the sheet resistance of GSS can be tuned due to the electrostatic doping on graphene electrodes [22].

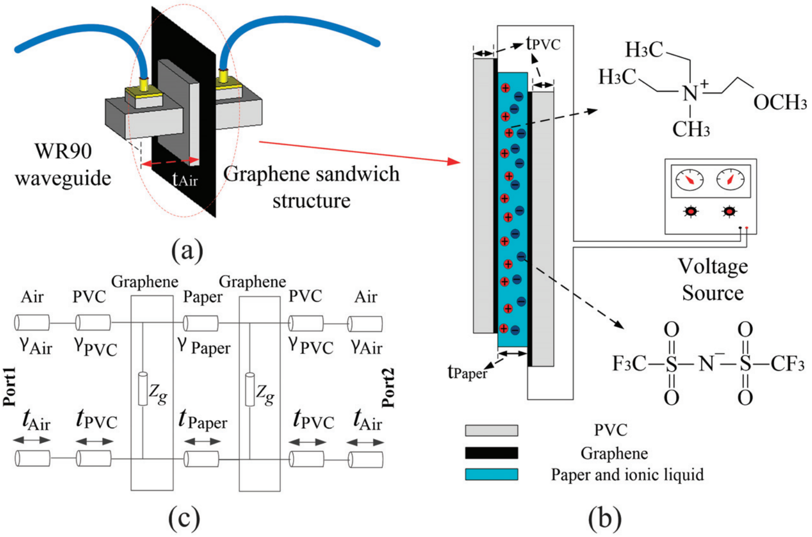

Figure 2. (**a**) Schematic diagram of the waveguide method. (**b**) Schematic diagram of GSS used to regulate graphene square resistance. (**c**) The equivalent circuit of the waveguide method.

During the measurement, each GSS is measured four times for reducing test error by changing the relative position between GSS and waveguide.

The absorption rate of the graphene-based absorber was tested by the waveguide method, and the waveguide used is WR62 (11.9–18 GHz). The absorption rate A is calculated through

$$A = 1 - R - T = 1 - |S_{11}|_2 - |S_{21}|_2, \tag{1}$$

where S_{11} and S_{21} are reflection and transmission coefficients. Due to the metallic ground structure of designed absorber, the transmission is blocked. As such, S_{21} equals zero, so A is calculated through only S_{11} parameters.

3. Results

3.1. Improvement of Waveguide Method

The dynamic tunning range of graphene is measured through the waveguide method, as shown in Figure 2a, which is a kind of noncontact measurement method. It should be noted that the dynamic tunning range is unable to be measured by the commonly used four-probe method [17,26] because the conductive part (graphene) is wrapped by its transfer substrate. The waveguide used for measuring the dynamic sheet resistance of graphene is WR90 (8.2–12.4 GHz) and the vector network analyzer used is purchased from Agilent Co. Ltd., Santa Clara, CA, USA, (ZNB-40, 10–40 GHz).

To accurately obtain the sheet resistance of graphene, we improved the calculation process of the previously reported waveguide method [33,34] with the help of transmission line theory. The equivalent circuit of the waveguide method is shown in Figure 2c. Under the main mode (TE10) of the waveguide in our study (WR90), the complex propagation constant γ and characteristic impedance Z of the medium (air, PVC, paper) in the cross-section of the waveguide can be expressed by the following Formulas (2)–(4):

$$\gamma(\omega) = j\beta(\omega), \tag{2}$$

$$\beta(\omega) = \sqrt{\left(\frac{\omega}{c}\right)^2 \varepsilon_r - \left(\frac{\pi}{a}\right)^2}, \tag{3}$$

$$Z(\omega) = \frac{\omega\mu_0}{\beta(\omega)}. \tag{4}$$

in which c is the speed of light, ε_r is the relative permittivity of the waveguide-filled medium, μ_0 is the free space permeability, $\beta(\omega)$ is the phase constant, and t is the thickness of various mediums along the waveguide direction. The thickness of air part (35 mm) can be found in the datasheet of WR90 waveguide. The thicknesses of PVC and paper are 70 μm and 50 μm, respectively, and the relative permittivity of air, PVC, and paper are 1, 3, and 2.5, respectively.

The different transfer matrices are connected in cascade to obtain the response of the entire waveguide section as shown in Formulas (5)–(7):

$$T_{\text{Total}} = T_{A\text{ir}} T_{\text{PVC}} T_{\text{Graphene}} T_{P\text{aper}} T_{\text{Graphene}} T_{\text{PVC}} T_{A\text{ir}}. \tag{5}$$

where

$$T_{\text{Air,PVC,}P\text{aper}} = \begin{pmatrix} \cos\text{h}(\gamma t) & Z\sin\text{h}(\gamma t) \\ \sin\text{h}(\gamma t)/Z & \cos\text{h}(\gamma t) \end{pmatrix} \tag{6}$$

The total transmission matrix $T_{T\text{otal}}$ can be obtained from the measured scattering parameters [35]:

$$T_{total} = \begin{pmatrix} ((1+\mathrm{S}_{11})(1-\mathrm{S}_{22})+\mathrm{S}_{12}\mathrm{S}_{21})/(2\mathrm{S}_{21}) & \mathrm{Z}_{\mathrm{Air}}((1+\mathrm{S}_{11})(1+\mathrm{S}_{22})-\mathrm{S}_{12}\mathrm{S}_{21})/(2\mathrm{S}_{21}) \\ ((1-\mathrm{S}_{11})(1-\mathrm{S}_{22})-\mathrm{S}_{12}\mathrm{S}_{21})/(2\mathrm{S}_{21}\mathrm{Z}_{\mathrm{Air}}) & ((1-\mathrm{S}_{11})(1+\mathrm{S}_{22})+\mathrm{S}_{12}\mathrm{S}_{21})/(2\mathrm{S}_{21}) \end{pmatrix}. \tag{7}$$

After obtaining T_{total}, we can derive the following relationship:

$$T_{G\text{raphene}} T_{P\text{aper}} T_{G\text{raphene}} = T_{\text{PVC}}^{-1} T_{A\text{ir}}^{-1} T_{T\text{otal}} T_{A\text{ir}}^{-1} T_{\text{PVC}}^{-1}. \tag{8}$$

Traditionally, the influence of diaphragm paper and PVC is neglected [33,36]. Under such conditions, (8) can be simplified as

$$T_{G\text{raphene}} T_{G\text{raphene}} = T_{A\text{ir}}^{-1} T_{T\text{otal}} T_{A\text{ir}}^{-1}. \tag{9}$$

The sheet resistance of graphene can be easily calculated; however, it also brings certain errors, which is not conducive to future calculations using other types of graphene transfer carriers and ionic liquid carriers.

Here, we do not ignore the influence of PVC and paper and use the definition of matrix calculation to solve the formula. Assuming that

$$T_{G\text{raphene}} = \begin{pmatrix} T_1 & T_2 \\ T_3 & \mathrm{T}_4 \end{pmatrix}, T_{P\text{aper}} = \begin{pmatrix} T_{01} & T_{02} \\ T_{03} & \mathrm{T}_{04} \end{pmatrix}, T_{\text{PVC}}^{-1} T_{A\text{ir}}^{-1} T_{T\text{otal}} T_{A\text{ir}}^{-1} T_{\text{PVC}}^{-1} = \begin{pmatrix} T_{05} & T_{06} \\ T_{07} & \mathrm{T}_{08} \end{pmatrix}, \tag{10}$$

From the previous description, it can be seen that T_{01}–T_{08} are all known values, while T_1–T_4 are the unknowns to be solved. According to (8), we can obtain the values of T_1–T_4 by listing and solving the following Equation (11):

$$\begin{cases} T_1(T_1T_{01} + T_2T_{03}) + T_3(T_1T_{02} + T_2T_{04}) = T_{05} \\ T_2(T_1T_{01} + T_2T_{03}) + T_4(T_1T_{02} + T_2T_{04}) = T_{06} \\ T_1(T_3T_{01} + T_4T_{03}) + T_3(T_3T_{02} + T_4T_{04}) = T_{07} \\ T_2(T_3T_{01} + T_4T_{03}) + T_4(T_3T_{02} + T_4T_{04}) = T_{08} \end{cases} \tag{11}$$

It should be noted that there are four groups of roots of the equation, which need to be decided by judgment. Theoretically, according to the form of the transmission matrix of graphene, (T_1, T_2; T_3, T_4) should satisfy the form of (1, 0; $1/R_{\text{S}}$, 1). Thereout, we can select the solution with practical physical significance, so that the sheet resistance of graphene can be obtained by $R_{\text{S}} = 1/T_3$.

As a verification of the improved method, we simulated the S parameters corresponding to $R\text{s}$ = 300, 500, and 800 Ω/sq and substitute them into (7), then the retrieved sheet resistance can be obtained through (9) or (11). In Figure 3a, the sheet resistance can be correctly calculated by our improved method, in contrast, appear deviations could be observed while using the traditional method, especially with the increase in frequency. For completeness, the retrieved result corresponding to R_S = 500 Ω/sq without judgment procedure is plotted in Figure 3b, the sharp jumps of the result are caused by the multi-foot of the Equation (11), which implies the necessity of the judgment procedure.

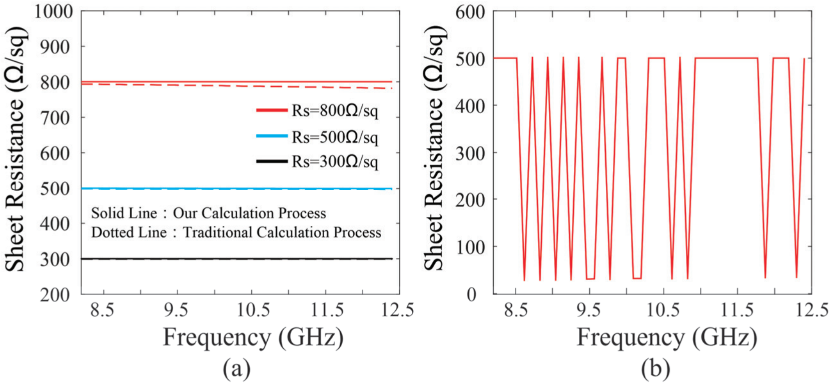

Figure 3. (**a**) Derived sheet resistance corresponding to R_S = 300, 500, and 800 Ω/sq using the traditional method and our improved method. (**b**) Derived sheet resistance corresponding to R_S = 500 Ω/sq without judgment procedure.

The improved method is important for the measurement and characterization of the sandwich structure, mathematically, the reason lies in that the matrix equation of $\mathbf{A} \times \mathbf{B} \times \mathbf{A} = \mathbf{C}$ cannot be solved directly through matrix transformation, in which, **A**, **B**, and **C** are 2 × 2 matrices. This improved method is used for the measurement of dynamic tunning range of GSS in this work, it also can be applied to other materials, such as planner or powder materials.

3.2. Impact of Growth Parameters

The mechanism of CVD on the copper foil can be understood with the help of a schematic diagram and growth curve shown in Figure 1a,b. As shown in Figure 1a, for metals such as copper having a low carbon dissolution rate, the graphene is formed with the carbon atoms depositing to the copper foil through a surface growth mechanism. Both the aim of foil pretreatment by hydrochloric acid and annealing step by hydrogen are to remove the surface oxides and other impurities of copper foil. The annealing step also increases the flatness of copper foil. Methane is used as the carbon source, which cracks at high temperature, the obtained carbon atoms will be adsorbed on the surface of copper, then the atoms nucleate and grow into graphene islands. With the constant expanding of these islands, they connect each other, thus obtaining graphene pieces.

From above, the quality of graphene the factors affecting the quality of graphene mainly include surface cleanliness, surface flatness of copper, and the amount of carbon atoms originating from methane. Combined with the growth curve shown Figure 1b, four parameters are selected for study: T_1, Δt_1, Δt_2, and *Ratio*. In which, T_1 is annealing temperature, $\Delta t_1 = t_2 - t_1$ is the annealing duration, $\Delta t_2 = t_3 - t_2$ is growth duration, *Ratio* is the flow ratio of hydrogen to methane during the growth stage.

To investigate the influence of each parameter, the specific parameter should fluctuate around an initial value while keeping the other three parameters unchanged (single variable principle). The first problem to be solved is the initial values of T_1, Δt_1, Δt_2, *Ratio*. Physically, the graphene synthesized under this group of values has the largest dynamic range, and an orthogonal experiment [29,30] is used to reduce the time consumption while ensuring the accuracy of experimental results as much as possible. The orthogonal table generated by SPSS software (v17.0) is shown in Table 1. Where the variation ranges of T_1, Δt_1, Δt_2, *Ratio* are [1000, 1050] (°C), [60, 180] (mins), [10, 30] (mins), [70:30, 50:50] (sccms), respectively. The measured results of the orthogonal experiment is shown in Figure 4, the tunning range of GSS composed of graphene sheets measured by waveguide method in group_4 is the largest, which varies from 430−1840 Ω/sq. Combining our previous work [26], it can be seen that the demands for growth parameters are consistent when pursuing the lowest static sheet resistance and the biggest tunning range of graphene. This can be understood by the best flatness and integrity of graphene sample grown under the parameter of group_4 as shown in Figure 5a. Based on which, (T_1, Δt_1, Δt_2, $Ratio$) = (1025, 180, 20, 70:30) is used as the initial value of the parameter comparison experiment.

Table 1. Variation of parameters and results in the orthogonal experiment.

Sequence	T_1 (°C)	Δt_1 (min)	Δt_2 (min)	*Ratio* (sccm)	Tunning Range (kΩ/sq)
1	1050	120	30	70:30	[0.43, 1.43]
2	1050	180	10	60:40	[0.54, 1.76]
3	1025	60	30	60:40	[0.77, 1.43]
4	1025	180	20	70:30	[0.43, 1.84]
5	1025	120	10	50:50	[0.62, 1.14]
6	1025	180	30	50:50	[0.60, 1.38]
7	1000	60	10	70:30	[0.67, 1.51]
8	1050	60	20	50:50	[0.44, 1.08]
9	1000	120	20	60:40	[0.49, 1.08]

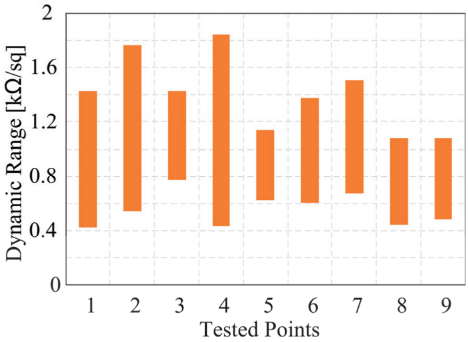

Figure 4. Calculated dynamic range of graphene samples in orthogonal experiment.

After obtaining the initial values of T_1, Δt_1, Δt_2, $Ratio$, the second set of experiments, namely, parameter comparison, is carried out to explore the influence of a single parameter on the tunning range of graphene, as shown in Table 2. The results of parameter comparison experiments are shown in Figure 6. The relations between tunning range with annealing temperature T_1, annealing duration Δt_1, growth duration Δt_2, and gas ratio are plotted in Figure 6a−d, respectively. From Figure 6a, although the lower annealing temperature T_1 will lead to relatively low growth uniformity, it also ensures the upper limit of the dynamic tunning range of graphene. For example, when the annealing temperature is 975 °C, the upper and lower limits of the dynamic range of graphene are slightly higher than those of other groups. Graphene with lower static sheet resistance can be obtained by changing annealing duration Δt_1 or gas ratio, but as shown in Figure 6b,d, the upper limit of dynamic sheet resistance is also suppressed. For these three parameters, they influence on the annealing process of the CVD procedure, either the annealing temperature or annealing duration of copper have a significant effect on the recrystallization effect of copper foil, causing the typical problems of multilayer (Figure 5b), defects (Figure 5c) and out of flatness (Figure 5d) to the final graphene samples. While the ratio of hydrogen to methane especially the amount of hydrogen largely influences the reduction degree of oxides on the copper foil. From these, we can notice that the change of the variation range in Figure 6a,b,d is relatively severe because they are directly related to copper foil. These trends can be also understood from optical microscopy (OM) of copper foil [37]. From Figure 6c, we can see that not only the uniformity but also a wide range of dynamic range of graphene can be guaranteed by changing the growth duration Δt_2, the variation trend is relatively smooth. Together with the SEM pictures in Figure 5, it can be concluded that the flatness of graphene has the greatest influence on its tunning ability (Figure 5d,f), when obvious rolling marks are observed, the corresponding tunning ranges of graphene are suppressed, this may be caused by the uneven doping effect on graphene sheets. In contrast, a few defects originating from too high T_1 or too long Δt_1 (Figure 5c,e) will increase the overall tunning range of graphene. This can be understood in that when patterns are made on graphene sheets, the effective conducting area decreases [38], leading to higher sheet resistance.

Table 2. Variation of parameters and results in the contrast experiment.

Sequence	T_1 (°C)	Δt_1 (min)	Δt_2 (min)	*Ratio* (sccm)	Tunning Range (kΩ/sq)
1	975	180	20	70:30	[0.78, 1.84]
2	1000	180	20	70:30	[1.16,1.65]
3	1025	180	20	70:30	[0.43, 1.84]
4	1050	180	20	70:30	[0.30, 1.74]
5	1075	180	20	70:30	[0.90, 2.20]
6	1025	120	20	70:30	[0.43, 1.28]
7	1025	150	20	70:30	[0.35, 1.04]
8	1025	180	20	70:30	[0.43, 1.84]
9	1025	210	20	70:30	[0.42, 1.08]
10	1025	240	20	70:30	[0.67, 2.20]
11	1025	180	10	70:30	[0.48, 1.90]
12	1025	180	15	70:30	[0.30, 1.50]
13	1025	180	20	70:30	[0.43, 1.84]
14	1025	180	25	70:30	[0.50, 1.58]
15	1025	180	30	70:30	[0.30, 1.74]
16	1025	180	20	90:10	[0.42, 0.93]
17	1025	180	20	80:20	[0.61, 1.37]
18	1025	180	20	70:30	[0.43, 1.84]
19	1025	180	20	60:40	[0.25, 1.16]
20	1025	180	20	50:50	[0.40, 1.77]

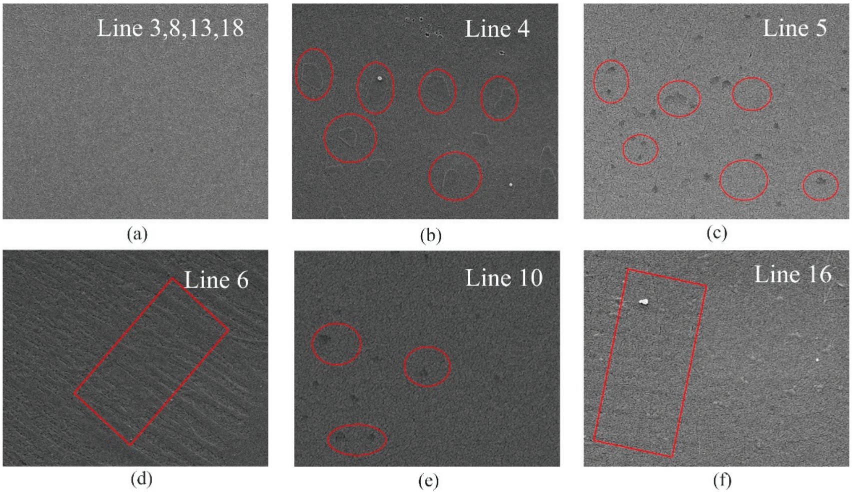

Figure 5. Typical SEM images of samples corresponding to line (**a**) 3, 8, 13, 18, (**b**) 4, (**c**) 5, (**d**) 6, (**e**) 10, and (**f**) 16 in Table 2. The scale of the pictures was 3 μm.

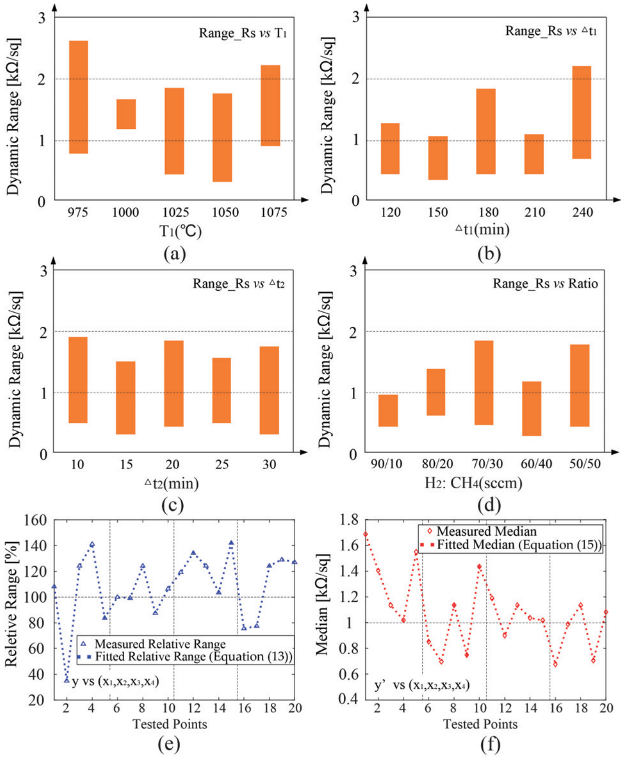

Figure 6. Calculated (**a**–**d**) dynamic range of graphene samples shown in Table 2. (**e**) Fitting results between the relative dynamic range of graphene and all four factors. (**f**) Fitting results between the median of dynamic range and all four factors.

Here, we do not define what is "good" or "bad" about graphene. Readers can change the growth parameters of graphene according to the needs of practical applications to get the desired properties. The above qualitative analysis is useful for improving the quality of graphene. However, from the aspect of the application, especially in the field of electromagnetism, either single layer, multilayer, or graphene with some defects is modeled as a surface impedance boundary with its surface resistance. In the following, we quantitatively analyze the results of this section and give readers a more practical method to select growth parameters.

3.3. Mathematic Model

To effectively process the previous data and provide guidance for the subsequent work, we fitted the data and formed the mathematic model of the relationship between the dynamic tunning range and growth parameters of graphene. Different from the static sheet resistance, the dynamic range of graphene is not a single value, but an interval. To establish a quantitative model of the interval, one can choose to fit the relation among the upper, the lower bounds of the interval, and growth parameters. However, to better reflect the nature of the interval, we refer to the concept of relative bandwidth from the index of the absorber and define the concept of relative dynamic range:

$$Reletive\_range = \frac{R_{s2} - R_{s1}}{(R_{s1} + R_{s2})/2} = f(T_1, \Delta t_1, \Delta t_2, Ratio) \tag{12}$$

in which R_{S1} and R_{S2} are the upper and lower bounds of the dynamic range. The statistical model is widely used in many fields, including the materials domain [39,40]. The specific tool is not unique, aiming at different kinds of problems. Here, in order to solve this kind of multivariable nonlinear fitting problem [31,32], the nlinfit tool in MATLAB is used [41,42], and the form of the model is as follows:

$$y = \sum_{\mathrm{i}=1}^{4} \sum_{\mathrm{j}=1}^{4} \mathrm{q}_{\mathrm{i,j}} x_{\mathrm{i}}{}^{5-\mathrm{j}} + \mathrm{q}_0. \tag{13}$$

where y represents the relative dynamic tunning range of graphene and x_1–x_4 the variation vector of annealing temperature, annealing duration, growth duration, and gas ratio, respectively. Polynomial fitting with fitting order equaling 4 is selected after comparing with other fitting functions. The values of $\mathrm{q}_{\mathrm{i,j}}$ after optimization are shown in Table 3, and the value of q_0 is 2.8767×107, the optimization process can be found in [26]. The physical significance of the model can be understood from the following aspects. Firstly, when the other three variables are fixed, and the three variables have been preliminarily optimized through orthogonal experiments, the effect of a single parameter (the fourth parameter) on the properties of GSS should be gradual rather than jump, thus smooth curve fitting (polynomial fitting is selected here) is used to preliminarily determine the variation trend of relative dynamic tunning range with the change of this parameter. Secondly, compared with individually fitting the variation trend of relative dynamic tunning range with the four parameters to form four equations:

$$\begin{cases} y_1 = f_1(x_1) \\ y_2 = f_2(x_2) \\ y_3 = f_3(x_3) \\ y_4 = f_4(x_4) \end{cases} \tag{14}$$

where y_1–y_4 denotes the change in graphene dynamic range with x_1–x_4. Equation (13) can be seen as a modified model, which not only can reflect the changing trend of graphene tunning range with a single variable but also includes the effect or other three parameters, thus increasing the reliability. As shown in Figure 6e, all measured results in the parameter comparison experiment can be correctly located on the fitted line. In addition, the model between the median of the tunning range and growth parameters of graphene is also determined using the same method:

$$y' = \frac{R_{s2} + R_{s1}}{2} = \sum_{i=1}^{4}\sum_{j=1}^{4} q'_{i,j} x_i^{5-j} + q'_0 \quad (15)$$

Table 3. Value of qi,j after optimization. (i = 1–4, j = 1–4).

i j	1	2	3	4
1	2.4885×10^{-5}	-0.1033	1.6068×10^{2}	-1.1102×10^{5}
2	1.0493×10^{-5}	-0.0075	1.9464	-2.2040×10^{2}
3	0.0037	-0.2364	5.1130	-42.2300
4	4.9760×10^{-4}	-0.1350	13.4652	-5.8628×10^{2}

Among them, y' represents the median of the tunning range of GSS. The values of $q_{i,j}$ after optimization are shown in Table 4, and the value of q'_0 is 3.7768×10^4, and the corresponding fitting result is shown in Figure 6f.

Table 4. Value of $q'_{i,j}$ after optimization. (i = 1–4, j = 1–4).

i j	1	2	3	4
1	2.4885×10^{-5}	-0.1033	1.6068×10^{2}	-1.1102×10^{5}
2	1.0493×10^{-5}	-0.0075	1.9464	-2.2040×10^{2}
3	0.0037	-0.2364	5.1130	-42.2300
4	4.9760×10^{-4}	-0.1350	13.4652	-5.8628×10^{2}

After obtaining the mathematic models, one can not only directly predict the tunning range of graphene through the growth parameters but also obtain needed growth parameters for desired tunning range. Here, we make a simple demonstration of the second function of the model, namely to deduce the required growth parameters under the circumstance of the known desired tunning range of GSS.

When considering the desired range of tunable characteristics, both (13) and (15) are needed. For instance, the desired tunning range of graphene is 400 to 1400 Ω/sq, and we predetermine that x_1 = 1025, x_3 = 20, x_4 = 70. The median of the range is 0.9 kΩ/sq, substituting it to (15), x_2 = 119.2, 159.3, 201.1, and 231.8 can be obtained. Except for the out-of-range value 119.2, we calculate the corresponding relative dynamic range of graphene under the other three values of annealing duration through (13). The relative ranges are 112.34%, 101.86% and 81.27%, respectively, thus the tunable range of graphene in a GSS can be obtained as [394.5, 1405.5] Ω/sq, [441.6, 1358.4] Ω/sq, [534.2, 1265.5] Ω/sq. We can see that the desired range is involved in the interval of [394.5, 1405.5] Ω/sq, namely, the tunning range of around 400 to 1400 Ω/sq can be obtained using the parameter x_1 = 1025, x_2 =159.3, x_3 = 20, x_4 = 70, which will be verified by a frequency tunable absorber shown in Section 4.

It should be noted that when using the model to predict the dynamic tunning range of GSS or deduce the needed parameters based on desired tunning range, one should still obey the rule of single-parameter principle, namely, the other three parameters should equal the optimized value obtained by the orthogonal experiment. The reason lies in that the data used to calculate to coefficients of the model, i.e., the data of the parameter comparison experiment is originated from the initial value of (T_1, Δt_1, Δt_2, *Ratio*) = (1025, 180, 20, 70:30), as stated in Section 3.

3.4. Application of the Model

In this section, a frequency tunable absorber is designed and fabricated to verify the effect of the mathematic model on the actual device. The overall structure of the absorber is shown in Figure 7a, which consists of a patterned GSS layer, metal ribbon layer, substrate layer, and bottom metal layer. The schematic diagram and corresponding size of the unit cell are shown in Figure 7b. The period of the unit is p = 2.7 mm, the width of the graphene ribbon is w_g = 2.2 mm, the side length of the metal ribbon is w_m = 1.6 mm. The substrate adopted here is PDMS, with relative permittivity of 2.8 and the thickness of t_{sub} = 1 mm. The thickness of the metal ribbon and bottom metal layer is t_m = 125 µm, and the sheet resistance is 0.5Ω/sq. Commercial software CST 2019 was used to simulate the model, in which unit-cell boundary condition is set up. The incident wave is vertical to the sample with the electric field perpendicular to the graphene strip. In the simulation, the sheet resistances of graphene ribbons are 400, 600, 800, 1000, and 1400 Ω/sq, respectively. As can be seen from Figure 7c, when the sheet resistance changes from 400 to 1400 Ω/sq, the central frequency of the absorption peak shifts from 14.9 to 17.0 GHz, while the absorption rate remains above 0.9, showing obvious frequency tunable absorption phenomenon.

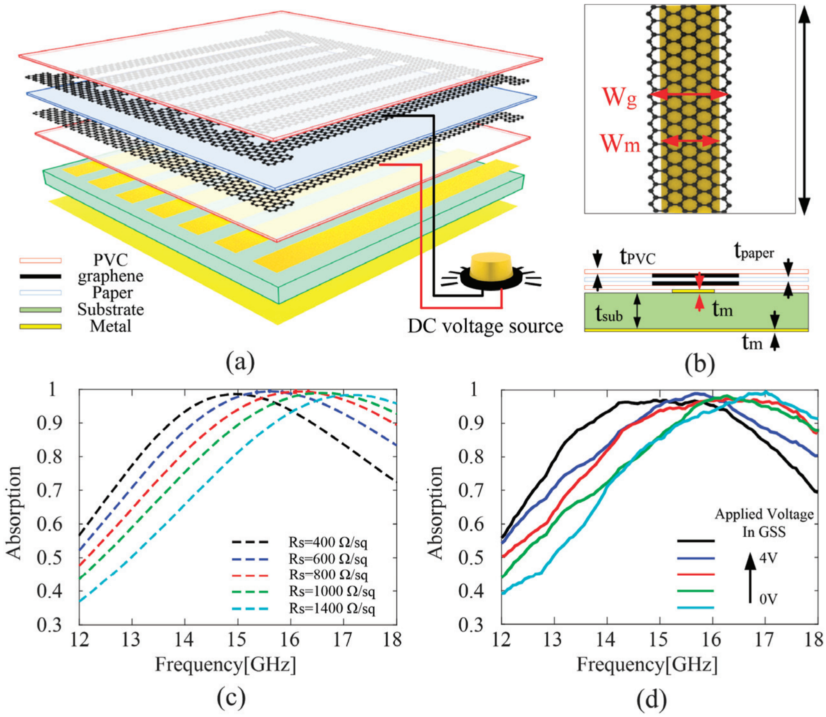

Figure 7. (**a**) Schematic of the absorber array. (**b**) Transverse view and longitudinal view of the unit cell. (**c**) Simulated and (**d**) measured results of the absorber.

To verify the simulated results and also the correctness of the mathematical model, as calculated in the last section, the parameters x_1 = 1025, x_2 =159.3, x_3 = 20, x_4 = 70 are used to synthesize the graphene with a desired tunning range of 400 to 1400 Ω/sq. The graphene ribbon and metal ribbon are realized through a laser engraving machine, the material of the metal ribbon layer and the metal ground layer is transparent metallic wire mesh. The photograph of the metal ribbon on PDMS substrate and the patterned graphene is shown Figure 8a,b while the measurement environment is shown in Figure 8c. The test results are shown in Figure 7d, several results are recorded with the increase in applied voltage, it can be seen that the absorption peak shift from around 16.9 GHz to 14.9 GHz when the applied voltage increases from 0 to 4 V, which is basically consistent with the simulated results. The slight difference may be caused by the deviation in the tunning of graphene between simulation and measurement. In addition, the imperfect adhesion between the patterned GSS layer and the metal ribbon layer will also lead to certain deviations. In general, there is good agreement between the simulation and the actual measurement, which indicates the accuracy and useability of the fitting formula in this paper.

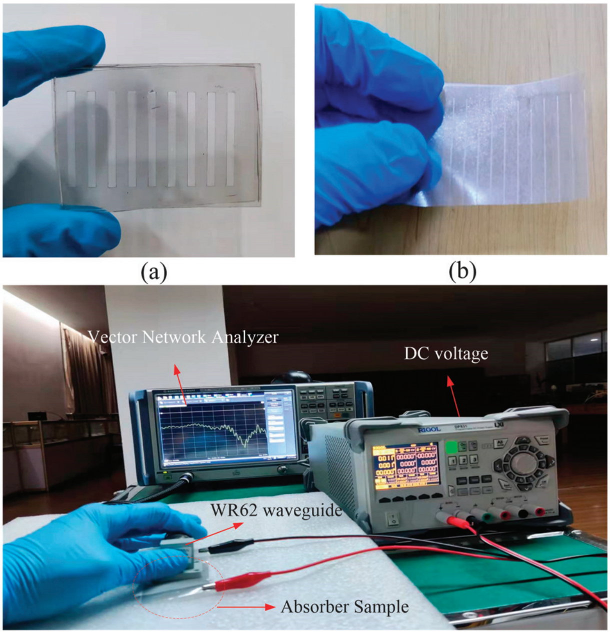

(a) (b)

(c)

Figure 8. (**a**) Fabricated metal ribbon on PDMS substrate. (**b**) Fabricated patterned graphene. (**c**) Measurement environment of the absorber.

4. Conclusions

In summary, the influences of CVD parameters on the dynamic tunning range of graphene were systematically investigated. The measurement method of GSS is improved to obtain more accurate tunning ranges of graphene. Direct mathematical models between growth parameters and the tunability of graphene are given. As a result, one can quickly and precisely predict the tunning range of graphene through the growth parameters or obtain needed growth parameters for the desired tunning range, which largely improves the design efficiency of graphene-based microwave devices. At the end of the work, the usability and accuracy of the proposed mathematic relation are verified by a frequency tunable absorber. The results of this work have positive significance for promoting the research and application of novel materials.

Author Contributions: Conceptualization, H.C. and W.-B.L.; methodology, H.C., Y.-Q.D. and W.-B.L.; software, H.C., M.-Y.G. and W.Y.; validation, H.C., M.-Y.G., X.-Y.M., W.-L.F. and L.J.; formal analysis, H.C., X.-Y.M. and Y.-Q.D.; investigation, H.C. and B.-Y.Y.; resources, Y.-Q.D. and W.-B.L.; data curation, Z.-G.L. and W.-B.L.; writing—original draft preparation, H.C.; writing—review and editing, H.C., Y.-Q.D. and W.-B.L.; visualization, H.C.; supervision, Z.-G.L.; project administration, W.-B.L.; funding acquisition, H.C. and W.-B.L. All authors have read and agreed to the published version of the manuscript.

Funding: This work was supported by the National Science Funds for Distinguished Young Scientists (61925103), National Natural Science Foundation of China (NSFC, 62101115), Project for Jiangsu Specially Appointed Professor, Fundamental Research Funds for the Central Universities (SEU: 2242022k30008, 2242022R20018; WUT: 2021IVA064, 2021III006JC), and China Postdoctoral Science Foundation (2022M710670).

Data Availability Statement: Not applicable.

Conflicts of Interest: The authors declare no conflict of interest.

References

1. Novoselov, K.S.; Geim, A.K.; Morozov, S.V.; Jiang, D.; Zhang, Y.; Dubonos, S.V.; Grigorieva, I.V.; Firsov, A.A. Electric field effect in atomically thin carbon films. *Science* **2004**, *306*, 666–669. [CrossRef] [PubMed]
2. Lee, S.H.; Choi, M.; Kim, T.-T.; Lee, S.; Liu, M.; Yin, X.; Choi, H.; Choi, C.-G.; Choi, S.-Y.; Zhang, X.; et al. Switching terahertz waves with gate-controlled active graphene metamaterials. *Nat. Mater.* **2012**, *11*, 936–941. [CrossRef] [PubMed]
3. Zhang, J.; Wei, X.; Rukhlenko, I.D.; Chen, H.-T.; Zhu, W. Electrically Tunable Metasurface with Independent Frequency and Amplitude Modulations. *ACS Photon.* **2019**, *7*, 265–271. [CrossRef]
4. Tamagnone, M.; Fallahi, A.; Mosig, J.R.; Perruisseau-Carrier, J. Fundamental limits and near-optimal design of graphene modulators and non-reciprocal devices. *Nat. Photon.* **2014**, *8*, 556–563. [CrossRef]
5. Sensale-Rodriguez, B.; Yan, R.; Kelly, M.M.; Fang, T.; Tahy, K.; Hwang, W.S.; Jena, D.; Liu, L.; Xing, H.G. Broadband graphene terahertz modulators enabled by intraband transitions. *Nat. Commun.* **2012**, *3*, 780. [CrossRef] [PubMed]
6. Long, J.; Baisong, G.; Jason, H.; Caglar, G. Graphene plasmonics for tunable terahertz metamaterials. *Nat. Nanotechnol.* **2011**, *6*, 630–634. [CrossRef]
7. Gomez-Diaz, J.; Moldovan, C.; Capdevila, S.; Romeu, J.; Bernard, L.; Magrez, A.; Ionescu, A.; Perruisseau-Carrier, J. Self-biased reconfigurable graphene stacks for terahertz plasmonics. *Nat. Commun.* **2015**, *6*, 6334. [CrossRef]
8. Chen, P.-Y.; Soric, J.; Padooru, Y.R.; Bernety, H.M.; Yakovlev, A.B.; Alù, A. Nanostructured graphene metasurface for tunable terahertz cloaking. *New J. Phys.* **2013**, *15*, 123029. [CrossRef]
9. Chen, P.-Y.; Alù, A. Atomically Thin Surface Cloak Using Graphene Monolayers. *ACS Nano* **2011**, *5*, 5855–5863. [CrossRef]
10. Lu, F.; Liu, B.; Shen, S. Infrared Wavefront Control Based on Graphene Metasurfaces. *Adv. Opt. Mater.* **2014**, *2*, 794–799. [CrossRef]
11. Yatooshi, T.; Ishikawa, A.; Tsuruta, K. Terahertz wavefront control by tunable metasurface made of graphene ribbons. *Appl. Phys. Lett.* **2015**, *107*, 053105. [CrossRef]
12. Wang, J.; Lu, W.B.; Li, X.B.; Liu, J.L. Terahertz Wavefront Control Based on Graphene Manipulated Fabry-Pérot Cavities. *IEEE Photon. Technol. Lett.* **2016**, *28*, 971–997. [CrossRef]
13. Zhang, Z.; Yan, X.; Liang, L.; Wei, D.; Wang, M.; Wang, Y.; Yao, J. The novel hybrid metal-graphene metasurfaces for broadband focusing and beam-steering in farfield at the terahertz frequencies. *Carbon* **2018**, *132*, 529–538. [CrossRef]
14. Chen, H.; Liu, Z.-G.; Lu, W.-B.; Zhang, A.-Q.; Li, X.-B.; Zhang, J. Microwave Beam Reconfiguration Based on Graphene Ribbon. *IEEE Trans. Antennas Propag.* **2018**, *66*, 6049–6056. [CrossRef]
15. Chen, H.; Lu, W.-B.; Liu, Z.-G.; Geng, M.-Y. Microwave Programmable Graphene Metasurface. *ACS Photon.* **2020**, *7*, 1425–1435. [CrossRef]
16. Yi, D.; Wei, X.C.; Xu, Y.L. A transparent microwave absorber based on patterned graphene: Design measurement and enhancement. *IEEE Trans. Nanotechnol.* **2017**, *16*, 484–490. [CrossRef]
17. Chen, H.; Lu, W.-B.; Liu, Z.-G.; Zhang, J.; Zhang, A.-Q.; Wu, B. Experimental Demonstration of Microwave Absorber Using Large-Area Multilayer Graphene-Based Frequency Selective Surface. *IEEE Trans. Microw. Theory Tech.* **2018**, *66*, 3807–3816. [CrossRef]
18. Chen, H.; Lu, W.-B.; Liu, Z.-G.; Jiang, Z.H. Flexible Rasorber Based on Graphene With Energy Manipulation Function. *IEEE Trans. Antennas Propag.* **2019**, *68*, 351–359. [CrossRef]
19. Zhang, J.; Li, Z.; Shao, L.; Zhu, W. Dynamical absorption manipulation in a graphene-based optically transparent and flexible metasurface. *Carbon* **2021**, *176*, 374–382. [CrossRef]
20. Hanson, G.W. Dyadic Green's functions and guided surface waves for a surface conductivity model of graphene. *J. Appl. Phys.* **2008**, *103*, 064302. [CrossRef]
21. Bae, S.; Kim, H.; Lee, Y.; Xu, X.; Park, J.-S.; Zheng, Y.; Balakrishnan, J.; Lei, T.; Kim, H.R.; Song, Y.I.; et al. Roll-to-roll production of 30-inch graphene films for transparent electrodes. *Nat. Nanotechnol.* **2010**, *5*, 574–578. [CrossRef] [PubMed]
22. Balci, O.; Polat, E.O.; Kakenov, N.; Kocabas, C. Graphene-enabled electrically switchable radar-absorbing surfaces. *Nat. Commun.* **2015**, *6*, 6628. [CrossRef] [PubMed]
23. Zhang, C.; Zhao, J.; Zhang, B.H.; Song, R.G.; Wang, Y.C.; He, D.P.; Cheng, Q. Multilayered Graphene-Assisted Broadband Scattering Suppression through an Ultrathin and Ultralight Metasurface. *ACS Appl. Mater. Interfaces* **2021**, *13*, 7698–7704. [CrossRef] [PubMed]
24. Zhang, C.; Long, C.; Yin, S.; Song, R.G.; Zhang, B.H.; Zhang, J.W.; He, D.P.; Cheng, Q. Graphene-based anisotropic polarization meta-filter. *Mater. Des.* **2021**, *206*, 109768. [CrossRef]

25. Zhang, A.-Q.; Liu, Z.-G.; Wei-Bing, L.; Chen, H. Graphene-Based Dynamically Tunable Attenuator on a Coplanar Waveguide or a Slotline. *IEEE Trans. Microw. Theory Tech.* **2018**, *67*, 70–77. [CrossRef]
26. Chen, H.; Geng, M.Y.; Liu, Z.G.; Lu, W.B. A quantitative study of CVD graphene on synthesis parameters and sheet resistance. In Proceedings of the 2021 IEEE 4th International Conference on Electronic Information and Communication Technology (ICEICT), Xi'an, China, 18–20 August 2021; pp. 836–839.
27. Pekdemir, S.; Onses, M.S.; Hancer, M. Low temperature growth of graphene using inductively-coupled plasma chemical vapor deposition. *Surf. Coatings Technol.* **2017**, *309*, 814–819. [CrossRef]
28. Terasawa, T.-O.; Saiki, K. Effect of vapor-phase oxygen on chemical vapor deposition growth of graphene. *Appl. Phys. Express* **2015**, *8*, 35101. [CrossRef]
29. Pallavi; Joshi, S.; Singh, D.; Kaur, M.; Lee, H.-N. Comprehensive Review of Orthogonal Regression and its Applications in Different Domains. *Arch. Comput. Methods Eng.* **2022**, *1209*, 1–21. [CrossRef]
30. Li, X.; Hao, J. Orthogonal test design for optimization of synthesis of super early strength anchoring material. *Constr. Build. Mater.* **2018**, *181*, 42–48. [CrossRef]
31. Wang, P.; Tian, C.; Liu, R.; Wang, J. Mathematical model for multivariate nonlinear prediction of SMD of X-type swirl pressure nozzles. *Process Saf. Environ. Prot.* **2019**, *125*, 228–237. [CrossRef]
32. Konishi, S. *Introduction to Multivariate Analysis: Linear and Nonlinear Modeling*; CRC Press: Boca Raton, FL, USA, 2014.
33. Zhang, J.; Liu, Z.; Lu, W.; Chen, H.; Wu, B.; Liu, Q. A low profile tunable microwave absorber based on graphene sandwich structure and high impedance surface. *Int. J. RF Microw. Comput. Eng.* **2019**, *30*, e22022. [CrossRef]
34. Xing, B.B.; Liu, Z.G.; Lu, W.B.; Chen, H. Wideband microwave absorber with dynamically tunable absorption based on gra-phene and random metasurface. *IEEE Antennas Wirel. Propag. Lett.* **2019**, *18*, 2602–2606. [CrossRef]
35. Pozar, D. *Microwave Engineering*, 3rd ed.; Wiley: Hoboken, NJ, USA, 2005.
36. Gómez-Díaz, J.S.; Perruisseau-Carrier, J.; Sharma, P.; Ionescu, A. Non-contact characterization of graphene surface impedance at micro and millimeter waves. *J. Appl. Phys.* **2012**, *111*, 114908. [CrossRef]
37. Sun, F.T.; Feng, A.H.; Chen, B.B. Effect of Copper Pretreatment on Growth of Graphene Films by Chemical Vapor Deposition. *J. Inorg. Mater.* **2020**, *35*, 1177–1182. [CrossRef]
38. Costa, F.; Monorchio, A.; Manara, G. Analysis and design of ultrathin electromagnetic absorbers comprising resistively loaded high impedance surfaces. *IEEE Trans. Antennas Propag.* **2010**, *58*, 1551–1555. [CrossRef]
39. Lookman, T.; Balachandran, P.V.; Xue, D.; Yuan, R. Active learning in materials science with emphasis on adaptive sampling using uncertainties for targeted design. *NPJ Comput. Mater.* **2019**, *5*, 1–17. [CrossRef]
40. Montgomery, D.C. *Design and Analysis of Experiments*; John Wiley & Sons: Hoboken, NJ, USA, 2017.
41. Fan, X.; Forsberg, F.; Smith, A.D.; Schröder, S.; Wagner, S.; Rödjegård, H.; Fischer, A.C.; Östling, M.; Lemme, M.C.; Niklaus, F. Graphene ribbons with suspended masses as transducers in ultra-small nanoelectro-mechanical accelerometers. *Nat. Electron.* **2019**, *2*, 394–404. [CrossRef]
42. Aamir, M.A.; Moore, J.N.; Lu, X.; Seifert, P.; Englund, D.; Fong, K.C.; Efetov, D.K. Ultra-fast calorimetric measurements of the electronic heat capacity of graphene. *arXiv* **2020**, arXiv:2020.14280. [CrossRef]

MDPI
St. Alban-Anlage 66
4052 Basel
Switzerland
www.mdpi.com

Nanomaterials Editorial Office
E-mail: nanomaterials@mdpi.com
www.mdpi.com/journal/nanomaterials

Academic Open
Access Publishing

mdpi.com

ISBN 978-3-7258-0882-3